

Artificial Intelligence Applications in Mobile Virtual Reality Technology

Lead Guest Editor: Balakrishnan Nagaraj

Guest Editors: Fadi Al-Turjman, Raffaele Mascella, and Yong Deng





Artificial Intelligence Applications in Mobile Virtual Reality Technology

Wireless Communications and Mobile Computing

Artificial Intelligence Applications in Mobile Virtual Reality Technology

Lead Guest Editor: Balakrishnan Nagaraj


Guest Editors: Fadi Al-Turjman, Raffaele Mascella,
and Yong Deng






Copyright © 2023 Hindawi Limited. All rights reserved.

This is a special issue published in “Wireless Communications and Mobile Computing.” All articles are open access articles distributed under the Creative Commons Attribution License, which permits unrestricted use, distribution, and reproduction in any medium, provided the original work is properly cited.

Chief Editor

Zhipeng Cai , USA

Associate Editors

Ke Guan , China
Jaime Lloret , Spain
Maode Ma , Singapore

Academic Editors

Muhammad Inam Abbasi, Malaysia
Ghufran Ahmed , Pakistan
Hamza Mohammed Ridha Al-Khafaji ,
Iraq
Abdullah Alamoodi , Malaysia
Marica Amadeo, Italy
Sandhya Aneja, USA
Mohd Dilshad Ansari, India
Eva Antonino-Daviu , Spain
Mehmet Emin Aydin, United Kingdom
Parameshchhari B. D. , India
Kalapraveen Bagadi , India
Ashish Bagwari , India
Dr. Abdul Basit , Pakistan
Alessandro Bazzi , Italy
Zdenek Becvar , Czech Republic
Nabil Benamar , Morocco
Olivier Berder, France
Petros S. Bithas, Greece
Dario Bruneo , Italy
Jun Cai, Canada
Xuesong Cai, Denmark
Gerardo Canfora , Italy
Rolando Carrasco, United Kingdom
Vicente Casares-Giner , Spain
Brijesh Chaurasia, India
Lin Chen , France
Xianfu Chen , Finland
Hui Cheng , United Kingdom
Hsin-Hung Cho, Taiwan
Ernestina Cianca , Italy
Marta Cimitile , Italy
Riccardo Colella , Italy
Mario Collotta , Italy
Massimo Condoluci , Sweden
Antonino Crivello , Italy
Antonio De Domenico , France
Floriano De Rango , Italy

Antonio De la Oliva , Spain
Margot Deruyck, Belgium
Liang Dong , USA
Praveen Kumar Donta, Austria
Zhuojun Duan, USA
Mohammed El-Hajjar , United Kingdom
Oscar Esparza , Spain
Maria Fazio , Italy
Mauro Femminella , Italy
Manuel Fernandez-Veiga , Spain
Gianluigi Ferrari , Italy
Luca Foschini , Italy
Alexandros G. Fragkiadakis , Greece
Ivan Ganchev , Bulgaria
Óscar García, Spain
Manuel García Sánchez , Spain
L. J. García Villalba , Spain
Miguel Garcia-Pineda , Spain
Piedad Garrido , Spain
Michele Girolami, Italy
Mariusz Glabowski , Poland
Carles Gomez , Spain
Antonio Guerrieri , Italy
Barbara Guidi , Italy
Rami Hamdi, Qatar
Tao Han, USA
Sherief Hashima , Egypt
Mahmoud Hassaballah , Egypt
Yejun He , China
Yixin He, China
Andrej Hrovat , Slovenia
Chunqiang Hu , China
Xuexian Hu , China
Zhenghua Huang , China
Xiaohong Jiang , Japan
Vicente Julian , Spain
Rajesh Kaluri , India
Dimitrios Katsaros, Greece
Muhammad Asghar Khan, Pakistan
Rahim Khan , Pakistan
Ahmed Khattab, Egypt
Hasan Ali Khattak, Pakistan
Mario Kolberg , United Kingdom
Meet Kumari, India
Wen-Cheng Lai , Taiwan

Jose M. Lanza-Gutierrez, Spain
Pavlos I. Lazaridis , United Kingdom
Kim-Hung Le , Vietnam
Tuan Anh Le , United Kingdom
Xianfu Lei, China
Jianfeng Li , China
Xiangxue Li , China
Yaguang Lin , China
Zhi Lin , China
Liu Liu , China
Mingqian Liu , China
Zhi Liu, Japan
Miguel López-Benítez , United Kingdom
Chuanwen Luo , China
Lu Lv, China
Basem M. ElHalawany , Egypt
Imadeldin Mahgoub , USA
Rajesh Manoharan , India
Davide Mattera , Italy
Michael McGuire , Canada
Weizhi Meng , Denmark
Klaus Moessner , United Kingdom
Simone Morosi , Italy
Amrit Mukherjee, Czech Republic
Shahid Mumtaz , Portugal
Giovanni Nardini , Italy
Tuan M. Nguyen , Vietnam
Petros Nicolitidis , Greece
Rajendran Parthiban , Malaysia
Giovanni Pau , Italy
Matteo Petracca , Italy
Marco Picone , Italy
Daniele Pinchera , Italy
Giuseppe Piro , Italy
Javier Prieto , Spain
Umair Rafique, Finland
Maheswar Rajagopal , India
Sujan Rajbhandari , United Kingdom
Rajib Rana, Australia
Luca Reggiani , Italy
Daniel G. Reina , Spain
Bo Rong , Canada
Mangal Sain , Republic of Korea
Praneet Saurabh , India

Hans Schotten, Germany
Patrick Seeling , USA
Muhammad Shafiq , China
Zaffar Ahmed Shaikh , Pakistan
Vishal Sharma , United Kingdom
Kaize Shi , Australia
Chakchai So-In, Thailand
Enrique Stevens-Navarro , Mexico
Sangeetha Subbaraj , India
Tien-Wen Sung, Taiwan
Suhua Tang , Japan
Pan Tang , China
Pierre-Martin Tardif , Canada
Sreenath Reddy Thummaluru, India
Tran Trung Duy , Vietnam
Fan-Hsun Tseng, Taiwan
S Velliangiri , India
Quoc-Tuan Vien , United Kingdom
Enrico M. Vitucci , Italy
Shaohua Wan , China
Dawei Wang, China
Huaqun Wang , China
Pengfei Wang , China
Dapeng Wu , China
Huaming Wu , China
Ding Xu , China
YAN YAO , China
Jie Yang, USA
Long Yang , China
Qiang Ye , Canada
Changyan Yi , China
Ya-Ju Yu , Taiwan
Marat V. Yuldashev , Finland
Sherali Zeadally, USA
Hong-Hai Zhang, USA
Jiliang Zhang, China
Lei Zhang, Spain
Wence Zhang , China
Yushu Zhang, China
Kechen Zheng, China
Fuhui Zhou , USA
Meiling Zhu, United Kingdom
Zhengyu Zhu , China

Contents

Retracted: Research on the Detection and Tracking Algorithm of Moving Object in Image Based on Computer Vision Technology

Wireless Communications and Mobile Computing
Retraction (1 page), Article ID 9897473, Volume 2023 (2023)

Retracted: Research of Schema Evolution and Implementation Scheme Optimization in AI-Enabled Embedded Systems

Wireless Communications and Mobile Computing
Retraction (1 page), Article ID 9894875, Volume 2023 (2023)

Retracted: Urban Fruit Quality Traceability Model Based on Smart Contract for Internet of Things

Wireless Communications and Mobile Computing
Retraction (1 page), Article ID 9892125, Volume 2023 (2023)

Retracted: Construction of Live Broadcast Training Platform Based on “Cloud Computing” and “Big Data” and “Wireless Communication Technology”

Wireless Communications and Mobile Computing
Retraction (1 page), Article ID 9878547, Volume 2023 (2023)

Retracted: Innovation and Development of University Education Management Informationization in the Environment of Wireless Communication and Big Data

Wireless Communications and Mobile Computing
Retraction (1 page), Article ID 9878431, Volume 2023 (2023)

Retracted: Biobjective UAV/UGV Collaborative Rendezvous Planning in Persistent Intelligent Task-Based Wireless Communication

Wireless Communications and Mobile Computing
Retraction (1 page), Article ID 9871912, Volume 2023 (2023)

Retracted: Research on Wireless Sensor Network Positioning Based on Genetic Algorithm

Wireless Communications and Mobile Computing
Retraction (1 page), Article ID 9870257, Volume 2023 (2023)

Retracted: The Construction of Immersive Learning System Based on Virtual Testing Technology of Virtual Reality

Wireless Communications and Mobile Computing
Retraction (1 page), Article ID 9867459, Volume 2023 (2023)

Retracted: Finder-MCTS: A Cognitive Spectrum Allocation Based on Traveling State Priority and Scenario Simulation in IoV

Wireless Communications and Mobile Computing
Retraction (1 page), Article ID 9860968, Volume 2023 (2023)

Retracted: Design and Analysis of Bridge Inspection System Based on Wireless Communication and Internet of Things Technology

Wireless Communications and Mobile Computing
Retraction (1 page), Article ID 9854124, Volume 2023 (2023)

Retracted: Analysis of the Needs of English-Chinese Translation Courses and Research on Teaching Strategies under the Background of Wireless Communication and Big Data

Wireless Communications and Mobile Computing
Retraction (1 page), Article ID 9852981, Volume 2023 (2023)

Retracted: Research on Tourism Route Planning Based on Artificial Intelligence Technology

Wireless Communications and Mobile Computing
Retraction (1 page), Article ID 9851837, Volume 2023 (2023)

Retracted: Application of Wireless Communication in Experimental Research of the Interface Bonding Condition between Asphalt Layers by Tensile Testing

Wireless Communications and Mobile Computing
Retraction (1 page), Article ID 9851435, Volume 2023 (2023)

Retracted: Microcomputer Control System of Bridge Dehumidification Based on Energy Consumption Optimization and Wireless Communication

Wireless Communications and Mobile Computing
Retraction (1 page), Article ID 9850742, Volume 2023 (2023)

Retracted: The Development of Data Acquisition System of Formula SAE Race Car Based on CAN Bus Communication Interface and Closed-Loop Design of Racing Car

Wireless Communications and Mobile Computing
Retraction (1 page), Article ID 9848505, Volume 2023 (2023)

Retracted: SLAM of Mobile Robot for Wireless Communication Based on Improved Particle Filter

Wireless Communications and Mobile Computing
Retraction (1 page), Article ID 9848426, Volume 2023 (2023)

Retracted: FastQR: Fast Pose Estimation of Objects Based on Multiple QR Codes and Monocular Vision in Mobile Embedded Devices

Wireless Communications and Mobile Computing
Retraction (1 page), Article ID 9841018, Volume 2023 (2023)

Retracted: A Novel Model-Based Reinforcement Learning Attitude Control Method for Virtual Reality Satellite

Wireless Communications and Mobile Computing
Retraction (1 page), Article ID 9838549, Volume 2023 (2023)

Retracted: Research on the Integration and Development of Culture and Tourism Based on Wireless Communication and Virtual Reality Technology

Wireless Communications and Mobile Computing
Retraction (1 page), Article ID 9832468, Volume 2023 (2023)

Contents

Retracted: Computer Mathematical Modeling Based on the Improved Genetic Algorithm and Mobile Computing

Wireless Communications and Mobile Computing
Retraction (1 page), Article ID 9831903, Volume 2023 (2023)

Retracted: Research on Efficient Deep Learning Algorithm Based on ShuffleGhost in the Field of Virtual Reality

Wireless Communications and Mobile Computing
Retraction (1 page), Article ID 9829420, Volume 2023 (2023)

Retracted: Geological Mineral Energy and Classification Based on Machine Learning

Wireless Communications and Mobile Computing
Retraction (1 page), Article ID 9821654, Volume 2023 (2023)

Retracted: MEC-Driven Fast Deformation Monitoring Based on GNSS Signal

Wireless Communications and Mobile Computing
Retraction (1 page), Article ID 9815756, Volume 2023 (2023)

Retracted: Analyzing the Effect of Masking Length Distribution of MLM: An Evaluation Framework and Case Study on Chinese MRC Datasets

Wireless Communications and Mobile Computing
Retraction (1 page), Article ID 9814905, Volume 2023 (2023)

Retracted: Research on Book Recommendation Algorithm Based on Collaborative Filtering and Interest Degree

Wireless Communications and Mobile Computing
Retraction (1 page), Article ID 9813784, Volume 2023 (2023)

Retracted: Mobile Communication Procurement Platform Optimization Decision Based on Overseas Retailer Investment under Supply and Demand Disruption Risk

Wireless Communications and Mobile Computing
Retraction (1 page), Article ID 9810720, Volume 2023 (2023)

Retracted: A Formal Verification Method of Compilation Based on C Safety Subset

Wireless Communications and Mobile Computing
Retraction (1 page), Article ID 9809531, Volume 2023 (2023)

Retracted: Research on Cultural Communication in College English Teaching Based on Wireless Communication and Multimedia Network Technology

Wireless Communications and Mobile Computing
Retraction (1 page), Article ID 9807351, Volume 2023 (2023)

Retracted: Network Traffic Prediction via Deep Graph-Sequence Spatiotemporal Modeling Based on Mobile Virtual Reality Technology

Wireless Communications and Mobile Computing
Retraction (1 page), Article ID 9806091, Volume 2023 (2023)

Retracted: Application of Wireless Communication Technology in Construction Project Information Management

Wireless Communications and Mobile Computing
Retraction (1 page), Article ID 9803653, Volume 2023 (2023)

Retracted: Applications of Wireless Communication in a New Dual Branch CTS Charge Pump Based on Employing Clock Matched Technology

Wireless Communications and Mobile Computing
Retraction (1 page), Article ID 9802959, Volume 2023 (2023)

Retracted: Study of Node Distribution and Density Optimization in Mobile Sensor Network 3D Space

Wireless Communications and Mobile Computing
Retraction (1 page), Article ID 9801925, Volume 2023 (2023)

Retracted: A Method of Offline Reinforcement Learning Virtual Reality Satellite Attitude Control Based on Generative Adversarial Network

Wireless Communications and Mobile Computing
Retraction (1 page), Article ID 9795831, Volume 2023 (2023)

Retracted: Information Security Situation Awareness Based on Big Data and Artificial Intelligence Technology

Wireless Communications and Mobile Computing
Retraction (1 page), Article ID 9794572, Volume 2023 (2023)

Retracted: Multimodal Emotion Recognition Model Based on a Deep Neural Network with Multiobjective Optimization

Wireless Communications and Mobile Computing
Retraction (1 page), Article ID 9792689, Volume 2023 (2023)

Retracted: Malicious Intrusion Data Mining Algorithm of Wireless Personal Communication Network Supported by Legal Big Data

Wireless Communications and Mobile Computing
Retraction (1 page), Article ID 9786042, Volume 2023 (2023)

Retracted: High-Precision 3D Reconstruction of Cooperative Markers under Motion Blur

Wireless Communications and Mobile Computing
Retraction (1 page), Article ID 9782864, Volume 2023 (2023)

Retracted: Mobile Communication Network Optimization System Based on Artificial Intelligence

Wireless Communications and Mobile Computing
Retraction (1 page), Article ID 9780784, Volume 2023 (2023)

Retracted: Research on Webcast Supervision Based on Convolutional Neural Network and Wireless Communication

Wireless Communications and Mobile Computing
Retraction (1 page), Article ID 9769208, Volume 2023 (2023)

Contents

Retracted: An Intelligent Code Search Approach Using Hybrid Encoders

Wireless Communications and Mobile Computing

Retraction (1 page), Article ID 9760642, Volume 2023 (2023)

Retracted: Facial Expression Recognition Based on Convolutional Neural Network Fusion SIFT Features of Mobile Virtual Reality

Wireless Communications and Mobile Computing

Retraction (1 page), Article ID 9760391, Volume 2023 (2023)

Retracted: Wireless Network Sensing of Urban Surface Water Environment Based on Clustering Algorithm

Wireless Communications and Mobile Computing

Retraction (1 page), Article ID 9758314, Volume 2023 (2023)

Retracted: Reform and Challenges of Ideological and Political Education for College Students Based on Wireless Communication and Virtual Reality Technology

Wireless Communications and Mobile Computing

Retraction (1 page), Article ID 9797068, Volume 2023 (2023)

Retracted: Research on the Development Path of a Cross-European e-Commerce Logistics Mode under the Background of “Internet Plus”

Wireless Communications and Mobile Computing

Retraction (1 page), Article ID 9895631, Volume 2023 (2023)

Retracted: Research and Application of Multifeature Gesture Recognition in Human-Computer Interaction Based on Virtual Reality Technology

Wireless Communications and Mobile Computing




Retraction (1 page), Article ID 9842785, Volume 2023 (2023)

Retracted: Conceptual Implementation of Artificial Intelligent based E-Mobility Controller in smart city Environment

Wireless Communications and Mobile Computing

Retraction (1 page), Article ID 9829418, Volume 2023 (2023)

Application of Virtual Reality Technology Based on Artificial Intelligence in Sports Skill Training

Jiyong Lv , Xiangzhi Jiang , and Ang Jiang 


Review Article (7 pages), Article ID 4613178, Volume 2022 (2022)

[Retracted] Computer Mathematical Modeling Based on the Improved Genetic Algorithm and Mobile Computing

Huixian Wei  and Jia Liu 

Research Article (7 pages), Article ID 1584435, Volume 2021 (2021)

[Retracted] Research on Tourism Route Planning Based on Artificial Intelligence Technology


Maobin Ding 

Research Article (7 pages), Article ID 2227798, Volume 2021 (2021)



[Retracted] Wireless Network Sensing of Urban Surface Water Environment Based on Clustering Algorithm

Qichao Zhao , Xiufeng Yang , Xuxin Dong , and Huairui Li 
Research Article (6 pages), Article ID 2829195, Volume 2021 (2021)



Corrigendum to “MEC-Driven Fast Deformation Monitoring Based on GNSS Signal”

Bo Li, Shangwei Chen, Yi Liu, Kan Xie, and Shengli Xie 
Corrigendum (1 page), Article ID 9798317, Volume 2021 (2021)




[Retracted] Geological Mineral Energy and Classification Based on Machine Learning

Yan Lv  and Lajun Lu 
Research Article (7 pages), Article ID 2788161, Volume 2021 (2021)

[Retracted] Analyzing the Effect of Masking Length Distribution of MLM: An Evaluation Framework and Case Study on Chinese MRC Datasets

Changchang Zeng  and Shaobo Li 
Research Article (17 pages), Article ID 5375334, Volume 2021 (2021)

[Retracted] Research on Wireless Sensor Network Positioning Based on Genetic Algorithm

Jing Zhang , Yajing Hu , and Hongliang Li 
Research Article (7 pages), Article ID 3996401, Volume 2021 (2021)

Development Strategy of Internet Interactive Video under the Background of 5G Converged Media and Wireless Communication

Ruomu Miao , Juan Li , and Jiayin Gao 
Research Article (5 pages), Article ID 9502279, Volume 2021 (2021)


[Retracted] Finder-MCTS: A Cognitive Spectrum Allocation Based on Traveling State Priority and Scenario Simulation in IoV

Zhong Li and Hao Shao 
Research Article (18 pages), Article ID 2270505, Volume 2021 (2021)

[Retracted] Information Security Situation Awareness Based on Big Data and Artificial Intelligence Technology

Fuguang Yao 
Research Article (6 pages), Article ID 2989118, Volume 2021 (2021)

Embedded Design of 3D Image Intelligent Display System Based on Virtual Reality Technology


Liang Li 
Research Article (9 pages), Article ID 2469603, Volume 2021 (2021)

[Retracted] Facial Expression Recognition Based on Convolutional Neural Network Fusion SIFT Features of Mobile Virtual Reality

Fuguang Yao  and Liudong Qiu
Research Article (7 pages), Article ID 5763626, Volume 2021 (2021)


Contents

[Retracted] Design and Analysis of Bridge Inspection System Based on Wireless Communication and Internet of Things Technology

Haidong Sun, Zhengtao Zhang , and Peng Li



Research Article (5 pages), Article ID 3410844, Volume 2021 (2021)

[Retracted] Innovation and Development of University Education Management Informationization in the Environment of Wireless Communication and Big Data

Weizhe Li 


Research Article (6 pages), Article ID 8493464, Volume 2021 (2021)

[Retracted] Conceptual Implementation of Artificial Intelligent based E-Mobility Controller in smart city Environment

Jayaraj Jayakumar , Balakrishnan Nagaraj , Shanty Chacko, and P. Ajay


Research Article (8 pages), Article ID 5325116, Volume 2021 (2021)

[Retracted] FastQR: Fast Pose Estimation of Objects Based on Multiple QR Codes and Monocular Vision in Mobile Embedded Devices

Yuheng Yan, Yiqiu Liang, Zihan Zhou, Bin Jiang, and Jian Xiao 

Research Article (9 pages), Article ID 9481190, Volume 2021 (2021)

Design of Management Platform Architecture and Key Algorithm for Massive Monitoring Big Data

Wen Liu , Shanshan Li, Jiangru Pan, Lijun Xu, Zheng Gu, and Ling Hai

Research Article (8 pages), Article ID 3111844, Volume 2021 (2021)

[Retracted] Malicious Intrusion Data Mining Algorithm of Wireless Personal Communication Network Supported by Legal Big Data

Kai Ji 

Research Article (7 pages), Article ID 8321636, Volume 2021 (2021)

[Retracted] Research on the Development Path of a Cross-European e-Commerce Logistics Mode under the Background of “Internet Plus”

Wangli Zhu  and Meixia Shi 


Research Article (7 pages), Article ID 6964302, Volume 2021 (2021)

[Retracted] Mobile Communication Network Optimization System Based on Artificial Intelligence

Chao Duan  and Jun Luo


Research Article (5 pages), Article ID 9999873, Volume 2021 (2021)

[Retracted] Analysis of the Needs of English-Chinese Translation Courses and Research on Teaching Strategies under the Background of Wireless Communication and Big Data

Bei Gao 

Research Article (5 pages), Article ID 3424658, Volume 2021 (2021)

[Retracted] Research on Cultural Communication in College English Teaching Based on Wireless Communication and Multimedia Network Technology

Yun Li 

Research Article (5 pages), Article ID 5123421, Volume 2021 (2021)

[Retracted] Research on Webcast Supervision Based on Convolutional Neural Network and Wireless Communication

Zhidong Sun , Jie Sun , and Xueqing Li 

Research Article (7 pages), Article ID 1191641, Volume 2021 (2021)

Visual Fatigue Alleviating in Stereo Imaging of Anaglyphs by Reducing Retinal Rivalry and Color Distortion Based on Mobile Virtual Reality Technology

Min Qi , Shanshan Cui , Qianmin Du , Yuele Xu , and David F. McAllister 




Research Article (10 pages), Article ID 1285712, Volume 2021 (2021)

[Retracted] Construction of Live Broadcast Training Platform Based on “Cloud Computing” and “Big Data” and “Wireless Communication Technology”

Zhidong Sun  and Xueqing Li 


Research Article (9 pages), Article ID 8971195, Volume 2021 (2021)

[Retracted] Research on the Integration and Development of Culture and Tourism Based on Wireless Communication and Virtual Reality Technology

HeChi Gan , YaoGuang Li , and YaNan Song 


Research Article (6 pages), Article ID 8322092, Volume 2021 (2021)

[Retracted] Application of Wireless Communication in Experimental Research of the Interface Bonding Condition between Asphalt Layers by Tensile Testing

Hua Yin , Daming Wang, Jianwei Zou, and Yaoting Zhu


Research Article (5 pages), Article ID 2488947, Volume 2021 (2021)

[Retracted] Research on the Detection and Tracking Algorithm of Moving Object in Image Based on Computer Vision Technology

Chunsheng Chen  and Din Li

Research Article (7 pages), Article ID 1127017, Volume 2021 (2021)

[Retracted] High-Precision 3D Reconstruction of Cooperative Markers under Motion Blur

Yun Shi, Cong Tao, Xiaoping Wang, and Liyan Zhang 

Research Article (9 pages), Article ID 6467337, Volume 2021 (2021)

[Retracted] MEC-Driven Fast Deformation Monitoring Based on GNSS Signal

Bo Li, Shangwei Chen, Yi Liu , Kan Xie , and Shengli Xie 

Research Article (9 pages), Article ID 9517133, Volume 2021 (2021)



Contents

[Retracted] SLAM of Mobile Robot for Wireless Communication Based on Improved Particle Filter

Daixian Zhu , Mingbo Wang, Mengyao Su, Shulin Liu, and Ping Guo



Research Article (14 pages), Article ID 9263277, Volume 2021 (2021)

[Retracted] Application of Wireless Communication Technology in Construction Project Information Management

Jie Zhang , Xin Guo , and Ying Xu 


Research Article (7 pages), Article ID 8174600, Volume 2021 (2021)

[Retracted] The Development of Data Acquisition System of Formula SAE Race Car Based on CAN Bus Communication Interface and Closed-Loop Design of Racing Car

Zhonghao Li , Da Wang , and Qiao Kang


Research Article (18 pages), Article ID 4211010, Volume 2021 (2021)

[Retracted] Multimodal Emotion Recognition Model Based on a Deep Neural Network with Multiobjective Optimization

Mingyong Li , Xue Qiu , Shuang Peng, Lirong Tang, Qiqi Li, Wenhui Yang, and Yan Ma 






Research Article (10 pages), Article ID 6971100, Volume 2021 (2021)

[Retracted] Research and Application of Multifeature Gesture Recognition in Human-Computer Interaction Based on Virtual Reality Technology

Zhao Feng, Jinlong Wu, and Taile Ni 

Research Article (5 pages), Article ID 3603693, Volume 2021 (2021)

[Retracted] Study of Node Distribution and Density Optimization in Mobile Sensor Network 3D Space

Musong Gu , Chaobang Gao , Jingjing Lyu , Wenjie Fan , and Lei You 



Research Article (7 pages), Article ID 6978812, Volume 2021 (2021)

[Retracted] Microcomputer Control System of Bridge Dehumidification Based on Energy Consumption Optimization and Wireless Communication

Xudong Zhou , Feng Xiong , Peng Li , and Qi Yu 


Research Article (5 pages), Article ID 2689878, Volume 2021 (2021)

[Retracted] Mobile Communication Procurement Platform Optimization Decision Based on Overseas Retailer Investment under Supply and Demand Disruption Risk

Deli Wang  and Wuwei Li 

Research Article (12 pages), Article ID 2630814, Volume 2021 (2021)

[Retracted] The Construction of Immersive Learning System Based on Virtual Testing Technology of Virtual Reality

Sansan Li and Dongxian Zhou 


Research Article (6 pages), Article ID 9656578, Volume 2021 (2021)

[Retracted] Research of Schema Evolution and Implementation Scheme Optimization in AI-Enabled Embedded Systems

Xiaojuan Zhang , Yongheng Zhang , Feng Zhang , and Xiuyun Yang 


Research Article (10 pages), Article ID 3591427, Volume 2021 (2021)

[Retracted] Applications of Wireless Communication in a New Dual Branch CTS Charge Pump Based on Employing Clock Matched Technology

Jiayang Li 


Research Article (9 pages), Article ID 4014795, Volume 2021 (2021)

Research on the Reform and Innovation of Preschool Education Informatization under the Background of Wireless Communication and Virtual Reality

Juan Li 






Research Article (6 pages), Article ID 3176309, Volume 2021 (2021)

[Retracted] Reform and Challenges of Ideological and Political Education for College Students Based on Wireless Communication and Virtual Reality Technology

Xing Hang 

Research Article (7 pages), Article ID 6151249, Volume 2021 (2021)

[Retracted] Biobjective UAV/UGV Collaborative Rendezvous Planning in Persistent Intelligent Task-Based Wireless Communication

Qin Wang , Hua Chen , Junwei Tian , Jia Wang , and Yu Su 



Research Article (12 pages), Article ID 9578783, Volume 2021 (2021)

[Retracted] Research on Efficient Deep Learning Algorithm Based on ShuffleGhost in the Field of Virtual Reality

Bangtong Huang, Hongquan Zhang , Zihong Chen, Lingling Li, and Lihua Shi


Research Article (11 pages), Article ID 1382781, Volume 2021 (2021)

[Retracted] Urban Fruit Quality Traceability Model Based on Smart Contract for Internet of Things

Cheng Xu , Kai Chen, Min Zuo, Hongzhe Liu , and Yanan Wu

Research Article (10 pages), Article ID 9369074, Volume 2021 (2021)

[Retracted] Network Traffic Prediction via Deep Graph-Sequence Spatiotemporal Modeling Based on Mobile Virtual Reality Technology

Kai Zhang, Xiaohu Zhao , Xiao Li, XingYi You, and Yonghong Zhu

Research Article (12 pages), Article ID 2353875, Volume 2021 (2021)



[Retracted] A Formal Verification Method of Compilation Based on C Safety Subset

Yu Tan, Dianfu Ma, and Lei Qiao 

Research Article (10 pages), Article ID 8352267, Volume 2021 (2021)


Contents

[Retracted] A Method of Offline Reinforcement Learning Virtual Reality Satellite Attitude Control Based on Generative Adversarial Network

Jian Zhang  and Fengge Wu 

Research Article (9 pages), Article ID 4238125, Volume 2021 (2021)

A Wireless Network Communication Capacity Control Technology Based on Fuzzy Wavelet Neural Network

Bing Zheng and Dawei Yun 



Research Article (10 pages), Article ID 9994200, Volume 2021 (2021)

[Retracted] Research on Book Recommendation Algorithm Based on Collaborative Filtering and Interest Degree

Zhi Hui Wang  and De Zhi Hou 

Research Article (7 pages), Article ID 7036357, Volume 2021 (2021)

[Retracted] A Novel Model-Based Reinforcement Learning Attitude Control Method for Virtual Reality Satellite

Jian Zhang  and Fengge Wu 


Research Article (11 pages), Article ID 7331894, Volume 2021 (2021)

[Retracted] An Intelligent Code Search Approach Using Hybrid Encoders

Yao Meng 

Research Article (16 pages), Article ID 9990988, Volume 2021 (2021)

Application of Virtual Display Technology of LCD Backlight Spectrum Optimization Algorithm Based on Linear Programming

Yuan Cui , Zhuyang Chen, Cheng Huang, and Qian Gao

Research Article (12 pages), Article ID 9947288, Volume 2021 (2021)

Retraction

Retracted: Research on the Detection and Tracking Algorithm of Moving Object in Image Based on Computer Vision Technology

Wireless Communications and Mobile Computing

Received 28 November 2023; Accepted 28 November 2023; Published 29 November 2023

Copyright © 2023 Wireless Communications and Mobile Computing. This is an open access article distributed under the Creative Commons Attribution License, which permits unrestricted use, distribution, and reproduction in any medium, provided the original work is properly cited.

This article has been retracted by Hindawi, as publisher, following an investigation undertaken by the publisher [1]. This investigation has uncovered evidence of systematic manipulation of the publication and peer-review process. We cannot, therefore, vouch for the reliability or integrity of this article.

Please note that this notice is intended solely to alert readers that the peer-review process of this article has been compromised.

Wiley and Hindawi regret that the usual quality checks did not identify these issues before publication and have since put additional measures in place to safeguard research integrity.

We wish to credit our Research Integrity and Research Publishing teams and anonymous and named external researchers and research integrity experts for contributing to this investigation.

The corresponding author, as the representative of all authors, has been given the opportunity to register their agreement or disagreement to this retraction. We have kept a record of any response received.

References

- [1] C. Chen and D. Li, "Research on the Detection and Tracking Algorithm of Moving Object in Image Based on Computer Vision Technology," *Wireless Communications and Mobile Computing*, vol. 2021, Article ID 1127017, 7 pages, 2021.

Retraction

Retracted: Research of Schema Evolution and Implementation Scheme Optimization in AI-Enabled Embedded Systems

Wireless Communications and Mobile Computing

Received 28 November 2023; Accepted 28 November 2023; Published 29 November 2023

Copyright © 2023 Wireless Communications and Mobile Computing. This is an open access article distributed under the Creative Commons Attribution License, which permits unrestricted use, distribution, and reproduction in any medium, provided the original work is properly cited.

This article has been retracted by Hindawi, as publisher, following an investigation undertaken by the publisher [1]. This investigation has uncovered evidence of systematic manipulation of the publication and peer-review process. We cannot, therefore, vouch for the reliability or integrity of this article.

Please note that this notice is intended solely to alert readers that the peer-review process of this article has been compromised.

Wiley and Hindawi regret that the usual quality checks did not identify these issues before publication and have since put additional measures in place to safeguard research integrity.

We wish to credit our Research Integrity and Research Publishing teams and anonymous and named external researchers and research integrity experts for contributing to this investigation.

The corresponding author, as the representative of all authors, has been given the opportunity to register their agreement or disagreement to this retraction. We have kept a record of any response received.

References

- [1] X. Zhang, Y. Zhang, F. Zhang, and X. Yang, "Research of Schema Evolution and Implementation Scheme Optimization in AI-Enabled Embedded Systems," *Wireless Communications and Mobile Computing*, vol. 2021, Article ID 3591427, 10 pages, 2021.

Retraction

Retracted: Urban Fruit Quality Traceability Model Based on Smart Contract for Internet of Things

Wireless Communications and Mobile Computing

Received 28 November 2023; Accepted 28 November 2023; Published 29 November 2023

Copyright © 2023 Wireless Communications and Mobile Computing. This is an open access article distributed under the Creative Commons Attribution License, which permits unrestricted use, distribution, and reproduction in any medium, provided the original work is properly cited.

This article has been retracted by Hindawi, as publisher, following an investigation undertaken by the publisher [1]. This investigation has uncovered evidence of systematic manipulation of the publication and peer-review process. We cannot, therefore, vouch for the reliability or integrity of this article.

Please note that this notice is intended solely to alert readers that the peer-review process of this article has been compromised.

Wiley and Hindawi regret that the usual quality checks did not identify these issues before publication and have since put additional measures in place to safeguard research integrity.

We wish to credit our Research Integrity and Research Publishing teams and anonymous and named external researchers and research integrity experts for contributing to this investigation.

The corresponding author, as the representative of all authors, has been given the opportunity to register their agreement or disagreement to this retraction. We have kept a record of any response received.

References

- [1] C. Xu, K. Chen, M. Zuo, H. Liu, and Y. Wu, "Urban Fruit Quality Traceability Model Based on Smart Contract for Internet of Things," *Wireless Communications and Mobile Computing*, vol. 2021, Article ID 9369074, 10 pages, 2021.

Retraction

Retracted: Construction of Live Broadcast Training Platform Based on “Cloud Computing” and “Big Data” and “Wireless Communication Technology”

Wireless Communications and Mobile Computing

Received 28 November 2023; Accepted 28 November 2023; Published 29 November 2023

Copyright © 2023 Wireless Communications and Mobile Computing. This is an open access article distributed under the Creative Commons Attribution License, which permits unrestricted use, distribution, and reproduction in any medium, provided the original work is properly cited.

This article has been retracted by Hindawi, as publisher, following an investigation undertaken by the publisher [1]. This investigation has uncovered evidence of systematic manipulation of the publication and peer-review process. We cannot, therefore, vouch for the reliability or integrity of this article.

Please note that this notice is intended solely to alert readers that the peer-review process of this article has been compromised.

Wiley and Hindawi regret that the usual quality checks did not identify these issues before publication and have since put additional measures in place to safeguard research integrity.

We wish to credit our Research Integrity and Research Publishing teams and anonymous and named external researchers and research integrity experts for contributing to this investigation.

The corresponding author, as the representative of all authors, has been given the opportunity to register their agreement or disagreement to this retraction. We have kept a record of any response received.

References

- [1] Z. Sun and X. Li, “Construction of Live Broadcast Training Platform Based on “Cloud Computing” and “Big Data” and “Wireless Communication Technology,” *Wireless Communications and Mobile Computing*, vol. 2021, Article ID 8971195, 9 pages, 2021.

Retraction

Retracted: Innovation and Development of University Education Management Informationization in the Environment of Wireless Communication and Big Data

Wireless Communications and Mobile Computing

Received 28 November 2023; Accepted 28 November 2023; Published 29 November 2023

Copyright © 2023 Wireless Communications and Mobile Computing. This is an open access article distributed under the Creative Commons Attribution License, which permits unrestricted use, distribution, and reproduction in any medium, provided the original work is properly cited.

This article has been retracted by Hindawi, as publisher, following an investigation undertaken by the publisher [1]. This investigation has uncovered evidence of systematic manipulation of the publication and peer-review process. We cannot, therefore, vouch for the reliability or integrity of this article.

Please note that this notice is intended solely to alert readers that the peer-review process of this article has been compromised.

Wiley and Hindawi regret that the usual quality checks did not identify these issues before publication and have since put additional measures in place to safeguard research integrity.

We wish to credit our Research Integrity and Research Publishing teams and anonymous and named external researchers and research integrity experts for contributing to this investigation.

The corresponding author, as the representative of all authors, has been given the opportunity to register their agreement or disagreement to this retraction. We have kept a record of any response received.

References

- [1] W. Li, "Innovation and Development of University Education Management Informationization in the Environment of Wireless Communication and Big Data," *Wireless Communications and Mobile Computing*, vol. 2021, Article ID 8493464, 6 pages, 2021.

Retraction

Retracted: Biobjective UAV/UGV Collaborative Rendezvous Planning in Persistent Intelligent Task-Based Wireless Communication

Wireless Communications and Mobile Computing

Received 28 November 2023; Accepted 28 November 2023; Published 29 November 2023

Copyright © 2023 Wireless Communications and Mobile Computing. This is an open access article distributed under the Creative Commons Attribution License, which permits unrestricted use, distribution, and reproduction in any medium, provided the original work is properly cited.

This article has been retracted by Hindawi, as publisher, following an investigation undertaken by the publisher [1]. This investigation has uncovered evidence of systematic manipulation of the publication and peer-review process. We cannot, therefore, vouch for the reliability or integrity of this article.

Please note that this notice is intended solely to alert readers that the peer-review process of this article has been compromised.

Wiley and Hindawi regret that the usual quality checks did not identify these issues before publication and have since put additional measures in place to safeguard research integrity.

We wish to credit our Research Integrity and Research Publishing teams and anonymous and named external researchers and research integrity experts for contributing to this investigation.

The corresponding author, as the representative of all authors, has been given the opportunity to register their agreement or disagreement to this retraction. We have kept a record of any response received.

References

- [1] Q. Wang, H. Chen, J. Tian, J. Wang, and Y. Su, "Biobjective UAV/UGV Collaborative Rendezvous Planning in Persistent Intelligent Task-Based Wireless Communication," *Wireless Communications and Mobile Computing*, vol. 2021, Article ID 9578783, 12 pages, 2021.

Retraction

Retracted: Research on Wireless Sensor Network Positioning Based on Genetic Algorithm

Wireless Communications and Mobile Computing

Received 28 November 2023; Accepted 28 November 2023; Published 29 November 2023

Copyright © 2023 Wireless Communications and Mobile Computing. This is an open access article distributed under the Creative Commons Attribution License, which permits unrestricted use, distribution, and reproduction in any medium, provided the original work is properly cited.

This article has been retracted by Hindawi, as publisher, following an investigation undertaken by the publisher [1]. This investigation has uncovered evidence of systematic manipulation of the publication and peer-review process. We cannot, therefore, vouch for the reliability or integrity of this article.

Please note that this notice is intended solely to alert readers that the peer-review process of this article has been compromised.

Wiley and Hindawi regret that the usual quality checks did not identify these issues before publication and have since put additional measures in place to safeguard research integrity.

We wish to credit our Research Integrity and Research Publishing teams and anonymous and named external researchers and research integrity experts for contributing to this investigation.

The corresponding author, as the representative of all authors, has been given the opportunity to register their agreement or disagreement to this retraction. We have kept a record of any response received.

References

- [1] J. Zhang, Y. Hu, and H. Li, "Research on Wireless Sensor Network Positioning Based on Genetic Algorithm," *Wireless Communications and Mobile Computing*, vol. 2021, Article ID 3996401, 7 pages, 2021.

Retraction

Retracted: The Construction of Immersive Learning System Based on Virtual Testing Technology of Virtual Reality

Wireless Communications and Mobile Computing

Received 28 November 2023; Accepted 28 November 2023; Published 29 November 2023

Copyright © 2023 Wireless Communications and Mobile Computing. This is an open access article distributed under the Creative Commons Attribution License, which permits unrestricted use, distribution, and reproduction in any medium, provided the original work is properly cited.

This article has been retracted by Hindawi, as publisher, following an investigation undertaken by the publisher [1]. This investigation has uncovered evidence of systematic manipulation of the publication and peer-review process. We cannot, therefore, vouch for the reliability or integrity of this article.

Please note that this notice is intended solely to alert readers that the peer-review process of this article has been compromised.

Wiley and Hindawi regret that the usual quality checks did not identify these issues before publication and have since put additional measures in place to safeguard research integrity.

We wish to credit our Research Integrity and Research Publishing teams and anonymous and named external researchers and research integrity experts for contributing to this investigation.

The corresponding author, as the representative of all authors, has been given the opportunity to register their agreement or disagreement to this retraction. We have kept a record of any response received.

References

- [1] S. Li and D. Zhou, "The Construction of Immersive Learning System Based on Virtual Testing Technology of Virtual Reality," *Wireless Communications and Mobile Computing*, vol. 2021, Article ID 9656578, 6 pages, 2021.

Retraction

Retracted: Finder-MCTS: A Cognitive Spectrum Allocation Based on Traveling State Priority and Scenario Simulation in IoV

Wireless Communications and Mobile Computing

Received 28 November 2023; Accepted 28 November 2023; Published 29 November 2023

Copyright © 2023 Wireless Communications and Mobile Computing. This is an open access article distributed under the Creative Commons Attribution License, which permits unrestricted use, distribution, and reproduction in any medium, provided the original work is properly cited.

This article has been retracted by Hindawi, as publisher, following an investigation undertaken by the publisher [1]. This investigation has uncovered evidence of systematic manipulation of the publication and peer-review process. We cannot, therefore, vouch for the reliability or integrity of this article.

Please note that this notice is intended solely to alert readers that the peer-review process of this article has been compromised.

Wiley and Hindawi regret that the usual quality checks did not identify these issues before publication and have since put additional measures in place to safeguard research integrity.

We wish to credit our Research Integrity and Research Publishing teams and anonymous and named external researchers and research integrity experts for contributing to this investigation.

The corresponding author, as the representative of all authors, has been given the opportunity to register their agreement or disagreement to this retraction. We have kept a record of any response received.

References

- [1] Z. Li and H. Shao, "Finder-MCTS: A Cognitive Spectrum Allocation Based on Traveling State Priority and Scenario Simulation in IoV," *Wireless Communications and Mobile Computing*, vol. 2021, Article ID 2270505, 18 pages, 2021.

Retraction

Retracted: Design and Analysis of Bridge Inspection System Based on Wireless Communication and Internet of Things Technology

Wireless Communications and Mobile Computing

Received 28 November 2023; Accepted 28 November 2023; Published 29 November 2023

Copyright © 2023 Wireless Communications and Mobile Computing. This is an open access article distributed under the Creative Commons Attribution License, which permits unrestricted use, distribution, and reproduction in any medium, provided the original work is properly cited.

This article has been retracted by Hindawi, as publisher, following an investigation undertaken by the publisher [1]. This investigation has uncovered evidence of systematic manipulation of the publication and peer-review process. We cannot, therefore, vouch for the reliability or integrity of this article.

Please note that this notice is intended solely to alert readers that the peer-review process of this article has been compromised.

Wiley and Hindawi regret that the usual quality checks did not identify these issues before publication and have since put additional measures in place to safeguard research integrity.

We wish to credit our Research Integrity and Research Publishing teams and anonymous and named external researchers and research integrity experts for contributing to this investigation.

The corresponding author, as the representative of all authors, has been given the opportunity to register their agreement or disagreement to this retraction. We have kept a record of any response received.

References

- [1] H. Sun, Z. Zhang, and P. Li, "Design and Analysis of Bridge Inspection System Based on Wireless Communication and Internet of Things Technology," *Wireless Communications and Mobile Computing*, vol. 2021, Article ID 3410844, 5 pages, 2021.

Retraction

Retracted: Analysis of the Needs of English-Chinese Translation Courses and Research on Teaching Strategies under the Background of Wireless Communication and Big Data

Wireless Communications and Mobile Computing

Received 28 November 2023; Accepted 28 November 2023; Published 29 November 2023

Copyright © 2023 Wireless Communications and Mobile Computing. This is an open access article distributed under the Creative Commons Attribution License, which permits unrestricted use, distribution, and reproduction in any medium, provided the original work is properly cited.

This article has been retracted by Hindawi, as publisher, following an investigation undertaken by the publisher [1]. This investigation has uncovered evidence of systematic manipulation of the publication and peer-review process. We cannot, therefore, vouch for the reliability or integrity of this article.

Please note that this notice is intended solely to alert readers that the peer-review process of this article has been compromised.

Wiley and Hindawi regret that the usual quality checks did not identify these issues before publication and have since put additional measures in place to safeguard research integrity.

We wish to credit our Research Integrity and Research Publishing teams and anonymous and named external researchers and research integrity experts for contributing to this investigation.

The corresponding author, as the representative of all authors, has been given the opportunity to register their agreement or disagreement to this retraction. We have kept a record of any response received.

References

- [1] B. Gao, "Analysis of the Needs of English-Chinese Translation Courses and Research on Teaching Strategies under the Background of Wireless Communication and Big Data," *Wireless Communications and Mobile Computing*, vol. 2021, Article ID 3424658, 5 pages, 2021.

Retraction

Retracted: Research on Tourism Route Planning Based on Artificial Intelligence Technology

Wireless Communications and Mobile Computing

Received 28 November 2023; Accepted 28 November 2023; Published 29 November 2023

Copyright © 2023 Wireless Communications and Mobile Computing. This is an open access article distributed under the Creative Commons Attribution License, which permits unrestricted use, distribution, and reproduction in any medium, provided the original work is properly cited.

This article has been retracted by Hindawi, as publisher, following an investigation undertaken by the publisher [1]. This investigation has uncovered evidence of systematic manipulation of the publication and peer-review process. We cannot, therefore, vouch for the reliability or integrity of this article.

Please note that this notice is intended solely to alert readers that the peer-review process of this article has been compromised.

Wiley and Hindawi regret that the usual quality checks did not identify these issues before publication and have since put additional measures in place to safeguard research integrity.

We wish to credit our Research Integrity and Research Publishing teams and anonymous and named external researchers and research integrity experts for contributing to this investigation.

The corresponding author, as the representative of all authors, has been given the opportunity to register their agreement or disagreement to this retraction. We have kept a record of any response received.

References

- [1] M. Ding, "Research on Tourism Route Planning Based on Artificial Intelligence Technology," *Wireless Communications and Mobile Computing*, vol. 2021, Article ID 2227798, 7 pages, 2021.

Retraction

Retracted: Application of Wireless Communication in Experimental Research of the Interface Bonding Condition between Asphalt Layers by Tensile Testing

Wireless Communications and Mobile Computing

Received 28 November 2023; Accepted 28 November 2023; Published 29 November 2023

Copyright © 2023 Wireless Communications and Mobile Computing. This is an open access article distributed under the Creative Commons Attribution License, which permits unrestricted use, distribution, and reproduction in any medium, provided the original work is properly cited.

This article has been retracted by Hindawi, as publisher, following an investigation undertaken by the publisher [1]. This investigation has uncovered evidence of systematic manipulation of the publication and peer-review process. We cannot, therefore, vouch for the reliability or integrity of this article.

Please note that this notice is intended solely to alert readers that the peer-review process of this article has been compromised.

Wiley and Hindawi regret that the usual quality checks did not identify these issues before publication and have since put additional measures in place to safeguard research integrity.

We wish to credit our Research Integrity and Research Publishing teams and anonymous and named external researchers and research integrity experts for contributing to this investigation.

The corresponding author, as the representative of all authors, has been given the opportunity to register their agreement or disagreement to this retraction. We have kept a record of any response received.

References

- [1] H. Yin, D. Wang, J. Zou, and Y. Zhu, "Application of Wireless Communication in Experimental Research of the Interface Bonding Condition between Asphalt Layers by Tensile Testing," *Wireless Communications and Mobile Computing*, vol. 2021, Article ID 2488947, 5 pages, 2021.

Retraction

Retracted: Microcomputer Control System of Bridge Dehumidification Based on Energy Consumption Optimization and Wireless Communication

Wireless Communications and Mobile Computing

Received 28 November 2023; Accepted 28 November 2023; Published 29 November 2023

Copyright © 2023 Wireless Communications and Mobile Computing. This is an open access article distributed under the Creative Commons Attribution License, which permits unrestricted use, distribution, and reproduction in any medium, provided the original work is properly cited.

This article has been retracted by Hindawi, as publisher, following an investigation undertaken by the publisher [1]. This investigation has uncovered evidence of systematic manipulation of the publication and peer-review process. We cannot, therefore, vouch for the reliability or integrity of this article.

Please note that this notice is intended solely to alert readers that the peer-review process of this article has been compromised.

Wiley and Hindawi regret that the usual quality checks did not identify these issues before publication and have since put additional measures in place to safeguard research integrity.

We wish to credit our Research Integrity and Research Publishing teams and anonymous and named external researchers and research integrity experts for contributing to this investigation.

The corresponding author, as the representative of all authors, has been given the opportunity to register their agreement or disagreement to this retraction. We have kept a record of any response received.

References

- [1] X. Zhou, F. Xiong, P. Li, and Q. Yu, "Microcomputer Control System of Bridge Dehumidification Based on Energy Consumption Optimization and Wireless Communication," *Wireless Communications and Mobile Computing*, vol. 2021, Article ID 2689878, 5 pages, 2021.

Retraction

Retracted: The Development of Data Acquisition System of Formula SAE Race Car Based on CAN Bus Communication Interface and Closed-Loop Design of Racing Car

Wireless Communications and Mobile Computing

Received 28 November 2023; Accepted 28 November 2023; Published 29 November 2023

Copyright © 2023 Wireless Communications and Mobile Computing. This is an open access article distributed under the Creative Commons Attribution License, which permits unrestricted use, distribution, and reproduction in any medium, provided the original work is properly cited.

This article has been retracted by Hindawi, as publisher, following an investigation undertaken by the publisher [1]. This investigation has uncovered evidence of systematic manipulation of the publication and peer-review process. We cannot, therefore, vouch for the reliability or integrity of this article.

Please note that this notice is intended solely to alert readers that the peer-review process of this article has been compromised.

Wiley and Hindawi regret that the usual quality checks did not identify these issues before publication and have since put additional measures in place to safeguard research integrity.

We wish to credit our Research Integrity and Research Publishing teams and anonymous and named external researchers and research integrity experts for contributing to this investigation.

The corresponding author, as the representative of all authors, has been given the opportunity to register their agreement or disagreement to this retraction. We have kept a record of any response received.

References

- [1] Z. Li, D. Wang, and Q. Kang, "The Development of Data Acquisition System of Formula SAE Race Car Based on CAN Bus Communication Interface and Closed-Loop Design of Racing Car," *Wireless Communications and Mobile Computing*, vol. 2021, Article ID 4211010, 18 pages, 2021.

Retraction

Retracted: SLAM of Mobile Robot for Wireless Communication Based on Improved Particle Filter

Wireless Communications and Mobile Computing

Received 28 November 2023; Accepted 28 November 2023; Published 29 November 2023

Copyright © 2023 Wireless Communications and Mobile Computing. This is an open access article distributed under the Creative Commons Attribution License, which permits unrestricted use, distribution, and reproduction in any medium, provided the original work is properly cited.

This article has been retracted by Hindawi, as publisher, following an investigation undertaken by the publisher [1]. This investigation has uncovered evidence of systematic manipulation of the publication and peer-review process. We cannot, therefore, vouch for the reliability or integrity of this article.

Please note that this notice is intended solely to alert readers that the peer-review process of this article has been compromised.

Wiley and Hindawi regret that the usual quality checks did not identify these issues before publication and have since put additional measures in place to safeguard research integrity.

We wish to credit our Research Integrity and Research Publishing teams and anonymous and named external researchers and research integrity experts for contributing to this investigation.

The corresponding author, as the representative of all authors, has been given the opportunity to register their agreement or disagreement to this retraction. We have kept a record of any response received.

References

- [1] D. Zhu, M. Wang, M. Su, S. Liu, and P. Guo, "SLAM of Mobile Robot for Wireless Communication Based on Improved Particle Filter," *Wireless Communications and Mobile Computing*, vol. 2021, Article ID 9263277, 14 pages, 2021.

Retraction

Retracted: FastQR: Fast Pose Estimation of Objects Based on Multiple QR Codes and Monocular Vision in Mobile Embedded Devices

Wireless Communications and Mobile Computing

Received 28 November 2023; Accepted 28 November 2023; Published 29 November 2023

Copyright © 2023 Wireless Communications and Mobile Computing. This is an open access article distributed under the Creative Commons Attribution License, which permits unrestricted use, distribution, and reproduction in any medium, provided the original work is properly cited.

This article has been retracted by Hindawi, as publisher, following an investigation undertaken by the publisher [1]. This investigation has uncovered evidence of systematic manipulation of the publication and peer-review process. We cannot, therefore, vouch for the reliability or integrity of this article.

Please note that this notice is intended solely to alert readers that the peer-review process of this article has been compromised.

Wiley and Hindawi regret that the usual quality checks did not identify these issues before publication and have since put additional measures in place to safeguard research integrity.

We wish to credit our Research Integrity and Research Publishing teams and anonymous and named external researchers and research integrity experts for contributing to this investigation.

The corresponding author, as the representative of all authors, has been given the opportunity to register their agreement or disagreement to this retraction. We have kept a record of any response received.

References

- [1] Y. Yan, Y. Liang, Z. Zhou, B. Jiang, and J. Xiao, "FastQR: Fast Pose Estimation of Objects Based on Multiple QR Codes and Monocular Vision in Mobile Embedded Devices," *Wireless Communications and Mobile Computing*, vol. 2021, Article ID 9481190, 9 pages, 2021.

Retraction

Retracted: A Novel Model-Based Reinforcement Learning Attitude Control Method for Virtual Reality Satellite

Wireless Communications and Mobile Computing

Received 28 November 2023; Accepted 28 November 2023; Published 29 November 2023

Copyright © 2023 Wireless Communications and Mobile Computing. This is an open access article distributed under the Creative Commons Attribution License, which permits unrestricted use, distribution, and reproduction in any medium, provided the original work is properly cited.

This article has been retracted by Hindawi, as publisher, following an investigation undertaken by the publisher [1]. This investigation has uncovered evidence of systematic manipulation of the publication and peer-review process. We cannot, therefore, vouch for the reliability or integrity of this article.

Please note that this notice is intended solely to alert readers that the peer-review process of this article has been compromised.

Wiley and Hindawi regret that the usual quality checks did not identify these issues before publication and have since put additional measures in place to safeguard research integrity.

We wish to credit our Research Integrity and Research Publishing teams and anonymous and named external researchers and research integrity experts for contributing to this investigation.

The corresponding author, as the representative of all authors, has been given the opportunity to register their agreement or disagreement to this retraction. We have kept a record of any response received.

References

- [1] J. Zhang and F. Wu, "A Novel Model-Based Reinforcement Learning Attitude Control Method for Virtual Reality Satellite," *Wireless Communications and Mobile Computing*, vol. 2021, Article ID 7331894, 11 pages, 2021.

Retraction

Retracted: Research on the Integration and Development of Culture and Tourism Based on Wireless Communication and Virtual Reality Technology

Wireless Communications and Mobile Computing

Received 28 November 2023; Accepted 28 November 2023; Published 29 November 2023

Copyright © 2023 Wireless Communications and Mobile Computing. This is an open access article distributed under the Creative Commons Attribution License, which permits unrestricted use, distribution, and reproduction in any medium, provided the original work is properly cited.

This article has been retracted by Hindawi, as publisher, following an investigation undertaken by the publisher [1]. This investigation has uncovered evidence of systematic manipulation of the publication and peer-review process. We cannot, therefore, vouch for the reliability or integrity of this article.

Please note that this notice is intended solely to alert readers that the peer-review process of this article has been compromised.

Wiley and Hindawi regret that the usual quality checks did not identify these issues before publication and have since put additional measures in place to safeguard research integrity.

We wish to credit our Research Integrity and Research Publishing teams and anonymous and named external researchers and research integrity experts for contributing to this investigation.

The corresponding author, as the representative of all authors, has been given the opportunity to register their agreement or disagreement to this retraction. We have kept a record of any response received.

References

- [1] H. Gan, Y. Li, and Y. Song, "Research on the Integration and Development of Culture and Tourism Based on Wireless Communication and Virtual Reality Technology," *Wireless Communications and Mobile Computing*, vol. 2021, Article ID 8322092, 6 pages, 2021.

Retraction

Retracted: Computer Mathematical Modeling Based on the Improved Genetic Algorithm and Mobile Computing

Wireless Communications and Mobile Computing

Received 28 November 2023; Accepted 28 November 2023; Published 29 November 2023

Copyright © 2023 Wireless Communications and Mobile Computing. This is an open access article distributed under the Creative Commons Attribution License, which permits unrestricted use, distribution, and reproduction in any medium, provided the original work is properly cited.

This article has been retracted by Hindawi, as publisher, following an investigation undertaken by the publisher [1]. This investigation has uncovered evidence of systematic manipulation of the publication and peer-review process. We cannot, therefore, vouch for the reliability or integrity of this article.

Please note that this notice is intended solely to alert readers that the peer-review process of this article has been compromised.

Wiley and Hindawi regret that the usual quality checks did not identify these issues before publication and have since put additional measures in place to safeguard research integrity.

We wish to credit our Research Integrity and Research Publishing teams and anonymous and named external researchers and research integrity experts for contributing to this investigation.

The corresponding author, as the representative of all authors, has been given the opportunity to register their agreement or disagreement to this retraction. We have kept a record of any response received.

References

- [1] H. Wei and J. Liu, "Computer Mathematical Modeling Based on the Improved Genetic Algorithm and Mobile Computing," *Wireless Communications and Mobile Computing*, vol. 2021, Article ID 1584435, 7 pages, 2021.

Retraction

Retracted: Research on Efficient Deep Learning Algorithm Based on ShuffleGhost in the Field of Virtual Reality

Wireless Communications and Mobile Computing

Received 28 November 2023; Accepted 28 November 2023; Published 29 November 2023

Copyright © 2023 Wireless Communications and Mobile Computing. This is an open access article distributed under the Creative Commons Attribution License, which permits unrestricted use, distribution, and reproduction in any medium, provided the original work is properly cited.

This article has been retracted by Hindawi, as publisher, following an investigation undertaken by the publisher [1]. This investigation has uncovered evidence of systematic manipulation of the publication and peer-review process. We cannot, therefore, vouch for the reliability or integrity of this article.

Please note that this notice is intended solely to alert readers that the peer-review process of this article has been compromised.

Wiley and Hindawi regret that the usual quality checks did not identify these issues before publication and have since put additional measures in place to safeguard research integrity.

We wish to credit our Research Integrity and Research Publishing teams and anonymous and named external researchers and research integrity experts for contributing to this investigation.

The corresponding author, as the representative of all authors, has been given the opportunity to register their agreement or disagreement to this retraction. We have kept a record of any response received.

References

- [1] B. Huang, H. Zhang, Z. Chen, L. Li, and L. Shi, "Research on Efficient Deep Learning Algorithm Based on ShuffleGhost in the Field of Virtual Reality," *Wireless Communications and Mobile Computing*, vol. 2021, Article ID 1382781, 11 pages, 2021.

Retraction

Retracted: Geological Mineral Energy and Classification Based on Machine Learning

Wireless Communications and Mobile Computing

Received 28 November 2023; Accepted 28 November 2023; Published 29 November 2023

Copyright © 2023 Wireless Communications and Mobile Computing. This is an open access article distributed under the Creative Commons Attribution License, which permits unrestricted use, distribution, and reproduction in any medium, provided the original work is properly cited.

This article has been retracted by Hindawi, as publisher, following an investigation undertaken by the publisher [1]. This investigation has uncovered evidence of systematic manipulation of the publication and peer-review process. We cannot, therefore, vouch for the reliability or integrity of this article.

Please note that this notice is intended solely to alert readers that the peer-review process of this article has been compromised.

Wiley and Hindawi regret that the usual quality checks did not identify these issues before publication and have since put additional measures in place to safeguard research integrity.

We wish to credit our Research Integrity and Research Publishing teams and anonymous and named external researchers and research integrity experts for contributing to this investigation.

The corresponding author, as the representative of all authors, has been given the opportunity to register their agreement or disagreement to this retraction. We have kept a record of any response received.

References

- [1] Y. Lv and L. Lu, "Geological Mineral Energy and Classification Based on Machine Learning," *Wireless Communications and Mobile Computing*, vol. 2021, Article ID 2788161, 7 pages, 2021.

Retraction

Retracted: MEC-Driven Fast Deformation Monitoring Based on GNSS Signal

Wireless Communications and Mobile Computing

Received 28 November 2023; Accepted 28 November 2023; Published 29 November 2023

Copyright © 2023 Wireless Communications and Mobile Computing. This is an open access article distributed under the Creative Commons Attribution License, which permits unrestricted use, distribution, and reproduction in any medium, provided the original work is properly cited.

This article has been retracted by Hindawi, as publisher, following an investigation undertaken by the publisher [1]. This investigation has uncovered evidence of systematic manipulation of the publication and peer-review process. We cannot, therefore, vouch for the reliability or integrity of this article.

Please note that this notice is intended solely to alert readers that the peer-review process of this article has been compromised.

Wiley and Hindawi regret that the usual quality checks did not identify these issues before publication and have since put additional measures in place to safeguard research integrity.

We wish to credit our Research Integrity and Research Publishing teams and anonymous and named external researchers and research integrity experts for contributing to this investigation.

The corresponding author, as the representative of all authors, has been given the opportunity to register their agreement or disagreement to this retraction. We have kept a record of any response received.

References

- [1] B. Li, S. Chen, Y. Liu, K. Xie, and S. Xie, "MEC-Driven Fast Deformation Monitoring Based on GNSS Signal," *Wireless Communications and Mobile Computing*, vol. 2021, Article ID 9517133, 9 pages, 2021.

Retraction

Retracted: Analyzing the Effect of Masking Length Distribution of MLM: An Evaluation Framework and Case Study on Chinese MRC Datasets

Wireless Communications and Mobile Computing

Received 28 November 2023; Accepted 28 November 2023; Published 29 November 2023

Copyright © 2023 Wireless Communications and Mobile Computing. This is an open access article distributed under the Creative Commons Attribution License, which permits unrestricted use, distribution, and reproduction in any medium, provided the original work is properly cited.

This article has been retracted by Hindawi, as publisher, following an investigation undertaken by the publisher [1]. This investigation has uncovered evidence of systematic manipulation of the publication and peer-review process. We cannot, therefore, vouch for the reliability or integrity of this article.

Please note that this notice is intended solely to alert readers that the peer-review process of this article has been compromised.

Wiley and Hindawi regret that the usual quality checks did not identify these issues before publication and have since put additional measures in place to safeguard research integrity.

We wish to credit our Research Integrity and Research Publishing teams and anonymous and named external researchers and research integrity experts for contributing to this investigation.

The corresponding author, as the representative of all authors, has been given the opportunity to register their agreement or disagreement to this retraction. We have kept a record of any response received.

References

- [1] C. Zeng and S. Li, "Analyzing the Effect of Masking Length Distribution of MLM: An Evaluation Framework and Case Study on Chinese MRC Datasets," *Wireless Communications and Mobile Computing*, vol. 2021, Article ID 5375334, 17 pages, 2021.

Retraction

Retracted: Research on Book Recommendation Algorithm Based on Collaborative Filtering and Interest Degree

Wireless Communications and Mobile Computing

Received 28 November 2023; Accepted 28 November 2023; Published 29 November 2023

Copyright © 2023 Wireless Communications and Mobile Computing. This is an open access article distributed under the Creative Commons Attribution License, which permits unrestricted use, distribution, and reproduction in any medium, provided the original work is properly cited.

This article has been retracted by Hindawi, as publisher, following an investigation undertaken by the publisher [1]. This investigation has uncovered evidence of systematic manipulation of the publication and peer-review process. We cannot, therefore, vouch for the reliability or integrity of this article.

Please note that this notice is intended solely to alert readers that the peer-review process of this article has been compromised.

Wiley and Hindawi regret that the usual quality checks did not identify these issues before publication and have since put additional measures in place to safeguard research integrity.

We wish to credit our Research Integrity and Research Publishing teams and anonymous and named external researchers and research integrity experts for contributing to this investigation.

The corresponding author, as the representative of all authors, has been given the opportunity to register their agreement or disagreement to this retraction. We have kept a record of any response received.

References

- [1] Z. H. Wang and D. Z. Hou, "Research on Book Recommendation Algorithm Based on Collaborative Filtering and Interest Degree," *Wireless Communications and Mobile Computing*, vol. 2021, Article ID 7036357, 7 pages, 2021.

Retraction

Retracted: Mobile Communication Procurement Platform Optimization Decision Based on Overseas Retailer Investment under Supply and Demand Disruption Risk

Wireless Communications and Mobile Computing

Received 28 November 2023; Accepted 28 November 2023; Published 29 November 2023

Copyright © 2023 Wireless Communications and Mobile Computing. This is an open access article distributed under the Creative Commons Attribution License, which permits unrestricted use, distribution, and reproduction in any medium, provided the original work is properly cited.

This article has been retracted by Hindawi, as publisher, following an investigation undertaken by the publisher [1]. This investigation has uncovered evidence of systematic manipulation of the publication and peer-review process. We cannot, therefore, vouch for the reliability or integrity of this article.

Please note that this notice is intended solely to alert readers that the peer-review process of this article has been compromised.

Wiley and Hindawi regret that the usual quality checks did not identify these issues before publication and have since put additional measures in place to safeguard research integrity.

We wish to credit our Research Integrity and Research Publishing teams and anonymous and named external researchers and research integrity experts for contributing to this investigation.

The corresponding author, as the representative of all authors, has been given the opportunity to register their agreement or disagreement to this retraction. We have kept a record of any response received.

References

- [1] D. Wang and W. Li, "Mobile Communication Procurement Platform Optimization Decision Based on Overseas Retailer Investment under Supply and Demand Disruption Risk," *Wireless Communications and Mobile Computing*, vol. 2021, Article ID 2630814, 12 pages, 2021.

Retraction

Retracted: A Formal Verification Method of Compilation Based on C Safety Subset

Wireless Communications and Mobile Computing

Received 28 November 2023; Accepted 28 November 2023; Published 29 November 2023

Copyright © 2023 Wireless Communications and Mobile Computing. This is an open access article distributed under the Creative Commons Attribution License, which permits unrestricted use, distribution, and reproduction in any medium, provided the original work is properly cited.

This article has been retracted by Hindawi, as publisher, following an investigation undertaken by the publisher [1]. This investigation has uncovered evidence of systematic manipulation of the publication and peer-review process. We cannot, therefore, vouch for the reliability or integrity of this article.

Please note that this notice is intended solely to alert readers that the peer-review process of this article has been compromised.

Wiley and Hindawi regret that the usual quality checks did not identify these issues before publication and have since put additional measures in place to safeguard research integrity.

We wish to credit our Research Integrity and Research Publishing teams and anonymous and named external researchers and research integrity experts for contributing to this investigation.

The corresponding author, as the representative of all authors, has been given the opportunity to register their agreement or disagreement to this retraction. We have kept a record of any response received.

References

- [1] Y. Tan, D. Ma, and L. Qiao, "A Formal Verification Method of Compilation Based on C Safety Subset," *Wireless Communications and Mobile Computing*, vol. 2021, Article ID 8352267, 10 pages, 2021.

Retraction

Retracted: Research on Cultural Communication in College English Teaching Based on Wireless Communication and Multimedia Network Technology

Wireless Communications and Mobile Computing

Received 28 November 2023; Accepted 28 November 2023; Published 29 November 2023

Copyright © 2023 Wireless Communications and Mobile Computing. This is an open access article distributed under the Creative Commons Attribution License, which permits unrestricted use, distribution, and reproduction in any medium, provided the original work is properly cited.

This article has been retracted by Hindawi, as publisher, following an investigation undertaken by the publisher [1]. This investigation has uncovered evidence of systematic manipulation of the publication and peer-review process. We cannot, therefore, vouch for the reliability or integrity of this article.

Please note that this notice is intended solely to alert readers that the peer-review process of this article has been compromised.

Wiley and Hindawi regret that the usual quality checks did not identify these issues before publication and have since put additional measures in place to safeguard research integrity.

We wish to credit our Research Integrity and Research Publishing teams and anonymous and named external researchers and research integrity experts for contributing to this investigation.

The corresponding author, as the representative of all authors, has been given the opportunity to register their agreement or disagreement to this retraction. We have kept a record of any response received.

References

- [1] Y. Li, "Research on Cultural Communication in College English Teaching Based on Wireless Communication and Multimedia Network Technology," *Wireless Communications and Mobile Computing*, vol. 2021, Article ID 5123421, 5 pages, 2021.

Retraction

Retracted: Network Traffic Prediction via Deep Graph-Sequence Spatiotemporal Modeling Based on Mobile Virtual Reality Technology

Wireless Communications and Mobile Computing

Received 28 November 2023; Accepted 28 November 2023; Published 29 November 2023

Copyright © 2023 Wireless Communications and Mobile Computing. This is an open access article distributed under the Creative Commons Attribution License, which permits unrestricted use, distribution, and reproduction in any medium, provided the original work is properly cited.

This article has been retracted by Hindawi, as publisher, following an investigation undertaken by the publisher [1]. This investigation has uncovered evidence of systematic manipulation of the publication and peer-review process. We cannot, therefore, vouch for the reliability or integrity of this article.

Please note that this notice is intended solely to alert readers that the peer-review process of this article has been compromised.

Wiley and Hindawi regret that the usual quality checks did not identify these issues before publication and have since put additional measures in place to safeguard research integrity.

We wish to credit our Research Integrity and Research Publishing teams and anonymous and named external researchers and research integrity experts for contributing to this investigation.

The corresponding author, as the representative of all authors, has been given the opportunity to register their agreement or disagreement to this retraction. We have kept a record of any response received.

References

- [1] K. Zhang, X. Zhao, X. Li, X. You, and Y. Zhu, "Network Traffic Prediction via Deep Graph-Sequence Spatiotemporal Modeling Based on Mobile Virtual Reality Technology," *Wireless Communications and Mobile Computing*, vol. 2021, Article ID 2353875, 12 pages, 2021.

Retraction

Retracted: Application of Wireless Communication Technology in Construction Project Information Management

Wireless Communications and Mobile Computing

Received 28 November 2023; Accepted 28 November 2023; Published 29 November 2023

Copyright © 2023 Wireless Communications and Mobile Computing. This is an open access article distributed under the Creative Commons Attribution License, which permits unrestricted use, distribution, and reproduction in any medium, provided the original work is properly cited.

This article has been retracted by Hindawi, as publisher, following an investigation undertaken by the publisher [1]. This investigation has uncovered evidence of systematic manipulation of the publication and peer-review process. We cannot, therefore, vouch for the reliability or integrity of this article.

Please note that this notice is intended solely to alert readers that the peer-review process of this article has been compromised.

Wiley and Hindawi regret that the usual quality checks did not identify these issues before publication and have since put additional measures in place to safeguard research integrity.

We wish to credit our Research Integrity and Research Publishing teams and anonymous and named external researchers and research integrity experts for contributing to this investigation.

The corresponding author, as the representative of all authors, has been given the opportunity to register their agreement or disagreement to this retraction. We have kept a record of any response received.

References

- [1] J. Zhang, X. Guo, and Y. Xu, "Application of Wireless Communication Technology in Construction Project Information Management," *Wireless Communications and Mobile Computing*, vol. 2021, Article ID 8174600, 7 pages, 2021.

Retraction

Retracted: Applications of Wireless Communication in a New Dual Branch CTS Charge Pump Based on Employing Clock Matched Technology

Wireless Communications and Mobile Computing

Received 28 November 2023; Accepted 28 November 2023; Published 29 November 2023

Copyright © 2023 Wireless Communications and Mobile Computing. This is an open access article distributed under the Creative Commons Attribution License, which permits unrestricted use, distribution, and reproduction in any medium, provided the original work is properly cited.

This article has been retracted by Hindawi, as publisher, following an investigation undertaken by the publisher [1]. This investigation has uncovered evidence of systematic manipulation of the publication and peer-review process. We cannot, therefore, vouch for the reliability or integrity of this article.

Please note that this notice is intended solely to alert readers that the peer-review process of this article has been compromised.

Wiley and Hindawi regret that the usual quality checks did not identify these issues before publication and have since put additional measures in place to safeguard research integrity.

We wish to credit our Research Integrity and Research Publishing teams and anonymous and named external researchers and research integrity experts for contributing to this investigation.

The corresponding author, as the representative of all authors, has been given the opportunity to register their agreement or disagreement to this retraction. We have kept a record of any response received.

References

- [1] J. Li, "Applications of Wireless Communication in a New Dual Branch CTS Charge Pump Based on Employing Clock Matched Technology," *Wireless Communications and Mobile Computing*, vol. 2021, Article ID 4014795, 9 pages, 2021.

Retraction

Retracted: Study of Node Distribution and Density Optimization in Mobile Sensor Network 3D Space

Wireless Communications and Mobile Computing

Received 28 November 2023; Accepted 28 November 2023; Published 29 November 2023

Copyright © 2023 Wireless Communications and Mobile Computing. This is an open access article distributed under the Creative Commons Attribution License, which permits unrestricted use, distribution, and reproduction in any medium, provided the original work is properly cited.

This article has been retracted by Hindawi, as publisher, following an investigation undertaken by the publisher [1]. This investigation has uncovered evidence of systematic manipulation of the publication and peer-review process. We cannot, therefore, vouch for the reliability or integrity of this article.

Please note that this notice is intended solely to alert readers that the peer-review process of this article has been compromised.

Wiley and Hindawi regret that the usual quality checks did not identify these issues before publication and have since put additional measures in place to safeguard research integrity.

We wish to credit our Research Integrity and Research Publishing teams and anonymous and named external researchers and research integrity experts for contributing to this investigation.

The corresponding author, as the representative of all authors, has been given the opportunity to register their agreement or disagreement to this retraction. We have kept a record of any response received.

References

- [1] M. Gu, C. Gao, J. Lyu, W. Fan, and L. You, "Study of Node Distribution and Density Optimization in Mobile Sensor Network 3D Space," *Wireless Communications and Mobile Computing*, vol. 2021, Article ID 6978812, 7 pages, 2021.

Retraction

Retracted: A Method of Offline Reinforcement Learning Virtual Reality Satellite Attitude Control Based on Generative Adversarial Network

Wireless Communications and Mobile Computing

Received 28 November 2023; Accepted 28 November 2023; Published 29 November 2023

Copyright © 2023 Wireless Communications and Mobile Computing. This is an open access article distributed under the Creative Commons Attribution License, which permits unrestricted use, distribution, and reproduction in any medium, provided the original work is properly cited.

This article has been retracted by Hindawi, as publisher, following an investigation undertaken by the publisher [1]. This investigation has uncovered evidence of systematic manipulation of the publication and peer-review process. We cannot, therefore, vouch for the reliability or integrity of this article.

Please note that this notice is intended solely to alert readers that the peer-review process of this article has been compromised.

Wiley and Hindawi regret that the usual quality checks did not identify these issues before publication and have since put additional measures in place to safeguard research integrity.

We wish to credit our Research Integrity and Research Publishing teams and anonymous and named external researchers and research integrity experts for contributing to this investigation.

The corresponding author, as the representative of all authors, has been given the opportunity to register their agreement or disagreement to this retraction. We have kept a record of any response received.

References

- [1] J. Zhang and F. Wu, "A Method of Offline Reinforcement Learning Virtual Reality Satellite Attitude Control Based on Generative Adversarial Network," *Wireless Communications and Mobile Computing*, vol. 2021, Article ID 4238125, 9 pages, 2021.

Retraction

Retracted: Information Security Situation Awareness Based on Big Data and Artificial Intelligence Technology

Wireless Communications and Mobile Computing

Received 28 November 2023; Accepted 28 November 2023; Published 29 November 2023

Copyright © 2023 Wireless Communications and Mobile Computing. This is an open access article distributed under the Creative Commons Attribution License, which permits unrestricted use, distribution, and reproduction in any medium, provided the original work is properly cited.

This article has been retracted by Hindawi, as publisher, following an investigation undertaken by the publisher [1]. This investigation has uncovered evidence of systematic manipulation of the publication and peer-review process. We cannot, therefore, vouch for the reliability or integrity of this article.

Please note that this notice is intended solely to alert readers that the peer-review process of this article has been compromised.

Wiley and Hindawi regret that the usual quality checks did not identify these issues before publication and have since put additional measures in place to safeguard research integrity.

We wish to credit our Research Integrity and Research Publishing teams and anonymous and named external researchers and research integrity experts for contributing to this investigation.

The corresponding author, as the representative of all authors, has been given the opportunity to register their agreement or disagreement to this retraction. We have kept a record of any response received.

References

- [1] F. Yao, "Information Security Situation Awareness Based on Big Data and Artificial Intelligence Technology," *Wireless Communications and Mobile Computing*, vol. 2021, Article ID 2989118, 6 pages, 2021.

Retraction

Retracted: Multimodal Emotion Recognition Model Based on a Deep Neural Network with Multiobjective Optimization

Wireless Communications and Mobile Computing

Received 28 November 2023; Accepted 28 November 2023; Published 29 November 2023

Copyright © 2023 Wireless Communications and Mobile Computing. This is an open access article distributed under the Creative Commons Attribution License, which permits unrestricted use, distribution, and reproduction in any medium, provided the original work is properly cited.

This article has been retracted by Hindawi, as publisher, following an investigation undertaken by the publisher [1]. This investigation has uncovered evidence of systematic manipulation of the publication and peer-review process. We cannot, therefore, vouch for the reliability or integrity of this article.

Please note that this notice is intended solely to alert readers that the peer-review process of this article has been compromised.

Wiley and Hindawi regret that the usual quality checks did not identify these issues before publication and have since put additional measures in place to safeguard research integrity.

We wish to credit our Research Integrity and Research Publishing teams and anonymous and named external researchers and research integrity experts for contributing to this investigation.

The corresponding author, as the representative of all authors, has been given the opportunity to register their agreement or disagreement to this retraction. We have kept a record of any response received.

References

- [1] M. Li, X. Qiu, S. Peng et al., "Multimodal Emotion Recognition Model Based on a Deep Neural Network with Multiobjective Optimization," *Wireless Communications and Mobile Computing*, vol. 2021, Article ID 6971100, 10 pages, 2021.

Retraction

Retracted: Malicious Intrusion Data Mining Algorithm of Wireless Personal Communication Network Supported by Legal Big Data

Wireless Communications and Mobile Computing

Received 28 November 2023; Accepted 28 November 2023; Published 29 November 2023

Copyright © 2023 Wireless Communications and Mobile Computing. This is an open access article distributed under the Creative Commons Attribution License, which permits unrestricted use, distribution, and reproduction in any medium, provided the original work is properly cited.

This article has been retracted by Hindawi, as publisher, following an investigation undertaken by the publisher [1]. This investigation has uncovered evidence of systematic manipulation of the publication and peer-review process. We cannot, therefore, vouch for the reliability or integrity of this article.

Please note that this notice is intended solely to alert readers that the peer-review process of this article has been compromised.

Wiley and Hindawi regret that the usual quality checks did not identify these issues before publication and have since put additional measures in place to safeguard research integrity.

We wish to credit our Research Integrity and Research Publishing teams and anonymous and named external researchers and research integrity experts for contributing to this investigation.

The corresponding author, as the representative of all authors, has been given the opportunity to register their agreement or disagreement to this retraction. We have kept a record of any response received.

References

- [1] K. Ji, "Malicious Intrusion Data Mining Algorithm of Wireless Personal Communication Network Supported by Legal Big Data," *Wireless Communications and Mobile Computing*, vol. 2021, Article ID 8321636, 7 pages, 2021.

Retraction

Retracted: High-Precision 3D Reconstruction of Cooperative Markers under Motion Blur

Wireless Communications and Mobile Computing

Received 28 November 2023; Accepted 28 November 2023; Published 29 November 2023

Copyright © 2023 Wireless Communications and Mobile Computing. This is an open access article distributed under the Creative Commons Attribution License, which permits unrestricted use, distribution, and reproduction in any medium, provided the original work is properly cited.

This article has been retracted by Hindawi, as publisher, following an investigation undertaken by the publisher [1]. This investigation has uncovered evidence of systematic manipulation of the publication and peer-review process. We cannot, therefore, vouch for the reliability or integrity of this article.

Please note that this notice is intended solely to alert readers that the peer-review process of this article has been compromised.

Wiley and Hindawi regret that the usual quality checks did not identify these issues before publication and have since put additional measures in place to safeguard research integrity.

We wish to credit our Research Integrity and Research Publishing teams and anonymous and named external researchers and research integrity experts for contributing to this investigation.

The corresponding author, as the representative of all authors, has been given the opportunity to register their agreement or disagreement to this retraction. We have kept a record of any response received.

References

- [1] Y. Shi, C. Tao, X. Wang, and L. Zhang, "High-Precision 3D Reconstruction of Cooperative Markers under Motion Blur," *Wireless Communications and Mobile Computing*, vol. 2021, Article ID 6467337, 9 pages, 2021.

Retraction

Retracted: Mobile Communication Network Optimization System Based on Artificial Intelligence

Wireless Communications and Mobile Computing

Received 28 November 2023; Accepted 28 November 2023; Published 29 November 2023

Copyright © 2023 Wireless Communications and Mobile Computing. This is an open access article distributed under the Creative Commons Attribution License, which permits unrestricted use, distribution, and reproduction in any medium, provided the original work is properly cited.

This article has been retracted by Hindawi, as publisher, following an investigation undertaken by the publisher [1]. This investigation has uncovered evidence of systematic manipulation of the publication and peer-review process. We cannot, therefore, vouch for the reliability or integrity of this article.

Please note that this notice is intended solely to alert readers that the peer-review process of this article has been compromised.

Wiley and Hindawi regret that the usual quality checks did not identify these issues before publication and have since put additional measures in place to safeguard research integrity.

We wish to credit our Research Integrity and Research Publishing teams and anonymous and named external researchers and research integrity experts for contributing to this investigation.

The corresponding author, as the representative of all authors, has been given the opportunity to register their agreement or disagreement to this retraction. We have kept a record of any response received.

References

- [1] C. Duan and J. Luo, "Mobile Communication Network Optimization System Based on Artificial Intelligence," *Wireless Communications and Mobile Computing*, vol. 2021, Article ID 9999873, 5 pages, 2021.

Retraction

Retracted: Research on Webcast Supervision Based on Convolutional Neural Network and Wireless Communication

Wireless Communications and Mobile Computing

Received 28 November 2023; Accepted 28 November 2023; Published 29 November 2023

Copyright © 2023 Wireless Communications and Mobile Computing. This is an open access article distributed under the Creative Commons Attribution License, which permits unrestricted use, distribution, and reproduction in any medium, provided the original work is properly cited.

This article has been retracted by Hindawi, as publisher, following an investigation undertaken by the publisher [1]. This investigation has uncovered evidence of systematic manipulation of the publication and peer-review process. We cannot, therefore, vouch for the reliability or integrity of this article.

Please note that this notice is intended solely to alert readers that the peer-review process of this article has been compromised.

Wiley and Hindawi regret that the usual quality checks did not identify these issues before publication and have since put additional measures in place to safeguard research integrity.

We wish to credit our Research Integrity and Research Publishing teams and anonymous and named external researchers and research integrity experts for contributing to this investigation.

The corresponding author, as the representative of all authors, has been given the opportunity to register their agreement or disagreement to this retraction. We have kept a record of any response received.

References

- [1] Z. Sun, J. Sun, and X. Li, "Research on Webcast Supervision Based on Convolutional Neural Network and Wireless Communication," *Wireless Communications and Mobile Computing*, vol. 2021, Article ID 1191641, 7 pages, 2021.

Retraction

Retracted: An Intelligent Code Search Approach Using Hybrid Encoders

Wireless Communications and Mobile Computing

Received 28 November 2023; Accepted 28 November 2023; Published 29 November 2023

Copyright © 2023 Wireless Communications and Mobile Computing. This is an open access article distributed under the Creative Commons Attribution License, which permits unrestricted use, distribution, and reproduction in any medium, provided the original work is properly cited.

This article has been retracted by Hindawi, as publisher, following an investigation undertaken by the publisher [1]. This investigation has uncovered evidence of systematic manipulation of the publication and peer-review process. We cannot, therefore, vouch for the reliability or integrity of this article.

Please note that this notice is intended solely to alert readers that the peer-review process of this article has been compromised.

Wiley and Hindawi regret that the usual quality checks did not identify these issues before publication and have since put additional measures in place to safeguard research integrity.

We wish to credit our Research Integrity and Research Publishing teams and anonymous and named external researchers and research integrity experts for contributing to this investigation.

The corresponding author, as the representative of all authors, has been given the opportunity to register their agreement or disagreement to this retraction. We have kept a record of any response received.

References

- [1] Y. Meng, “An Intelligent Code Search Approach Using Hybrid Encoders,” *Wireless Communications and Mobile Computing*, vol. 2021, Article ID 9990988, 16 pages, 2021.

Retraction

Retracted: Facial Expression Recognition Based on Convolutional Neural Network Fusion SIFT Features of Mobile Virtual Reality

Wireless Communications and Mobile Computing

Received 28 November 2023; Accepted 28 November 2023; Published 29 November 2023

Copyright © 2023 Wireless Communications and Mobile Computing. This is an open access article distributed under the Creative Commons Attribution License, which permits unrestricted use, distribution, and reproduction in any medium, provided the original work is properly cited.

This article has been retracted by Hindawi, as publisher, following an investigation undertaken by the publisher [1]. This investigation has uncovered evidence of systematic manipulation of the publication and peer-review process. We cannot, therefore, vouch for the reliability or integrity of this article.

Please note that this notice is intended solely to alert readers that the peer-review process of this article has been compromised.

Wiley and Hindawi regret that the usual quality checks did not identify these issues before publication and have since put additional measures in place to safeguard research integrity.

We wish to credit our Research Integrity and Research Publishing teams and anonymous and named external researchers and research integrity experts for contributing to this investigation.

The corresponding author, as the representative of all authors, has been given the opportunity to register their agreement or disagreement to this retraction. We have kept a record of any response received.

References

- [1] F. Yao and L. Qiu, "Facial Expression Recognition Based on Convolutional Neural Network Fusion SIFT Features of Mobile Virtual Reality," *Wireless Communications and Mobile Computing*, vol. 2021, Article ID 5763626, 7 pages, 2021.

Retraction

Retracted: Wireless Network Sensing of Urban Surface Water Environment Based on Clustering Algorithm

Wireless Communications and Mobile Computing

Received 28 November 2023; Accepted 28 November 2023; Published 29 November 2023

Copyright © 2023 Wireless Communications and Mobile Computing. This is an open access article distributed under the Creative Commons Attribution License, which permits unrestricted use, distribution, and reproduction in any medium, provided the original work is properly cited.

This article has been retracted by Hindawi, as publisher, following an investigation undertaken by the publisher [1]. This investigation has uncovered evidence of systematic manipulation of the publication and peer-review process. We cannot, therefore, vouch for the reliability or integrity of this article.

Please note that this notice is intended solely to alert readers that the peer-review process of this article has been compromised.

Wiley and Hindawi regret that the usual quality checks did not identify these issues before publication and have since put additional measures in place to safeguard research integrity.

We wish to credit our Research Integrity and Research Publishing teams and anonymous and named external researchers and research integrity experts for contributing to this investigation.

The corresponding author, as the representative of all authors, has been given the opportunity to register their agreement or disagreement to this retraction. We have kept a record of any response received.

References

- [1] Q. Zhao, X. Yang, X. Dong, and H. Li, "Wireless Network Sensing of Urban Surface Water Environment Based on Clustering Algorithm," *Wireless Communications and Mobile Computing*, vol. 2021, Article ID 2829195, 6 pages, 2021.

Retraction

Retracted: Reform and Challenges of Ideological and Political Education for College Students Based on Wireless Communication and Virtual Reality Technology

Wireless Communications and Mobile Computing

Received 26 September 2023; Accepted 26 September 2023; Published 27 September 2023

Copyright © 2023 Wireless Communications and Mobile Computing. This is an open access article distributed under the Creative Commons Attribution License, which permits unrestricted use, distribution, and reproduction in any medium, provided the original work is properly cited.

This article has been retracted by Hindawi following an investigation undertaken by the publisher [1]. This investigation has uncovered evidence of one or more of the following indicators of systematic manipulation of the publication process:

- (1) Discrepancies in scope
- (2) Discrepancies in the description of the research reported
- (3) Discrepancies between the availability of data and the research described
- (4) Inappropriate citations
- (5) Incoherent, meaningless and/or irrelevant content included in the article
- (6) Peer-review manipulation

The presence of these indicators undermines our confidence in the integrity of the article's content and we cannot, therefore, vouch for its reliability. Please note that this notice is intended solely to alert readers that the content of this article is unreliable. We have not investigated whether authors were aware of or involved in the systematic manipulation of the publication process.

Wiley and Hindawi regrets that the usual quality checks did not identify these issues before publication and have since put additional measures in place to safeguard research integrity.

We wish to credit our own Research Integrity and Research Publishing teams and anonymous and named external researchers and research integrity experts for contributing to this investigation.

The corresponding author, as the representative of all authors, has been given the opportunity to register their agreement or disagreement to this retraction. We have kept a record of any response received.

References

- [1] X. Hang, "Reform and Challenges of Ideological and Political Education for College Students Based on Wireless Communication and Virtual Reality Technology," *Wireless Communications and Mobile Computing*, vol. 2021, Article ID 6151249, 7 pages, 2021.

Retraction

Retracted: Research on the Development Path of a Cross-European e-Commerce Logistics Mode under the Background of “Internet Plus”

Wireless Communications and Mobile Computing

Received 1 August 2023; Accepted 1 August 2023; Published 2 August 2023

Copyright © 2023 Wireless Communications and Mobile Computing. This is an open access article distributed under the Creative Commons Attribution License, which permits unrestricted use, distribution, and reproduction in any medium, provided the original work is properly cited.

This article has been retracted by Hindawi following an investigation undertaken by the publisher [1]. This investigation has uncovered evidence of one or more of the following indicators of systematic manipulation of the publication process:

- (1) Discrepancies in scope
- (2) Discrepancies in the description of the research reported
- (3) Discrepancies between the availability of data and the research described
- (4) Inappropriate citations
- (5) Incoherent, meaningless and/or irrelevant content included in the article
- (6) Peer-review manipulation

The presence of these indicators undermines our confidence in the integrity of the article’s content and we cannot, therefore, vouch for its reliability. Please note that this notice is intended solely to alert readers that the content of this article is unreliable. We have not investigated whether authors were aware of or involved in the systematic manipulation of the publication process.

Wiley and Hindawi regrets that the usual quality checks did not identify these issues before publication and have since put additional measures in place to safeguard research integrity.

We wish to credit our own Research Integrity and Research Publishing teams and anonymous and named external researchers and research integrity experts for contributing to this investigation.

The corresponding author, as the representative of all authors, has been given the opportunity to register their

agreement or disagreement to this retraction. We have kept a record of any response received.

References

- [1] W. Zhu and M. Shi, “Research on the Development Path of a Cross-European e-Commerce Logistics Mode under the Background of “Internet Plus”,” *Wireless Communications and Mobile Computing*, vol. 2021, Article ID 6964302, 7 pages, 2021.

Retraction

Retracted: Research and Application of Multifeature Gesture Recognition in Human-Computer Interaction Based on Virtual Reality Technology

Wireless Communications and Mobile Computing

Received 1 August 2023; Accepted 1 August 2023; Published 2 August 2023

Copyright © 2023 Wireless Communications and Mobile Computing. This is an open access article distributed under the Creative Commons Attribution License, which permits unrestricted use, distribution, and reproduction in any medium, provided the original work is properly cited.

This article has been retracted by Hindawi following an investigation undertaken by the publisher [1]. This investigation has uncovered evidence of one or more of the following indicators of systematic manipulation of the publication process:

- (1) Discrepancies in scope
- (2) Discrepancies in the description of the research reported
- (3) Discrepancies between the availability of data and the research described
- (4) Inappropriate citations
- (5) Incoherent, meaningless and/or irrelevant content included in the article
- (6) Peer-review manipulation

The presence of these indicators undermines our confidence in the integrity of the article's content and we cannot, therefore, vouch for its reliability. Please note that this notice is intended solely to alert readers that the content of this article is unreliable. We have not investigated whether authors were aware of or involved in the systematic manipulation of the publication process.

Wiley and Hindawi regrets that the usual quality checks did not identify these issues before publication and have since put additional measures in place to safeguard research integrity.

We wish to credit our own Research Integrity and Research Publishing teams and anonymous and named external researchers and research integrity experts for contributing to this investigation.

The corresponding author, as the representative of all authors, has been given the opportunity to register their

agreement or disagreement to this retraction. We have kept a record of any response received.

References

- [1] Z. Feng, J. Wu, and T. Ni, "Research and Application of Multifeature Gesture Recognition in Human-Computer Interaction Based on Virtual Reality Technology," *Wireless Communications and Mobile Computing*, vol. 2021, Article ID 3603693, 5 pages, 2021.

Retraction

Retracted: Conceptual Implementation of Artificial Intelligent based E-Mobility Controller in smart city Environment

Wireless Communications and Mobile Computing

Received 1 August 2023; Accepted 1 August 2023; Published 2 August 2023

Copyright © 2023 Wireless Communications and Mobile Computing. This is an open access article distributed under the Creative Commons Attribution License, which permits unrestricted use, distribution, and reproduction in any medium, provided the original work is properly cited.

This article has been retracted by Hindawi following an investigation undertaken by the publisher [1]. This investigation has uncovered evidence of one or more of the following indicators of systematic manipulation of the publication process:

- (1) Discrepancies in scope
- (2) Discrepancies in the description of the research reported
- (3) Discrepancies between the availability of data and the research described
- (4) Inappropriate citations
- (5) Incoherent, meaningless and/or irrelevant content included in the article
- (6) Peer-review manipulation

The presence of these indicators undermines our confidence in the integrity of the article's content and we cannot, therefore, vouch for its reliability. Please note that this notice is intended solely to alert readers that the content of this article is unreliable. We have not investigated whether authors were aware of or involved in the systematic manipulation of the publication process.

Wiley and Hindawi regrets that the usual quality checks did not identify these issues before publication and have since put additional measures in place to safeguard research integrity.

We wish to credit our own Research Integrity and Research Publishing teams and anonymous and named external researchers and research integrity experts for contributing to this investigation.

The corresponding author, as the representative of all authors, has been given the opportunity to register their agreement or disagreement to this retraction. We have kept a record of any response received.

References

- [1] J. Jayakumar, B. Nagaraj, S. Chacko, and P. Ajay, "Conceptual Implementation of Artificial Intelligent based E-Mobility Controller in smart city Environment," *Wireless Communications and Mobile Computing*, vol. 2021, Article ID 5325116, 8 pages, 2021.

Review Article

Application of Virtual Reality Technology Based on Artificial Intelligence in Sports Skill Training

Jiyong Lv ¹, Xiangzhi Jiang ², and Ang Jiang ²

¹National Traditional Sports Institute, Harbin Sport University, Harbin, 150008 Heilongjiang, China

²Physical Education and Training Institute, Harbin Sport University, Harbin, 150008 Heilongjiang, China

Correspondence should be addressed to Xiangzhi Jiang; jxzeagle2008@163.com

Received 20 July 2021; Revised 16 September 2021; Accepted 18 July 2022; Published 29 July 2022

Academic Editor: Daniel G. Reina

Copyright © 2022 Jiyong Lv et al. This is an open access article distributed under the Creative Commons Attribution License, which permits unrestricted use, distribution, and reproduction in any medium, provided the original work is properly cited.

With the rapid development of science and technology and economy, it has a great impact on people's lifestyle and habits. Fewer and fewer people will actually carry out offline sports activities, and some will choose gyms and other places for offline exercise, but the high cost of gyms limits most people's desire to exercise. Our country has been actively introducing policies or measures to advocate physical exercise, but people's enthusiasm is not high or improper training leads to frequent physical injury. In view of the current situation and pain points of sports skill training, this paper first discusses the possibility of the overall application of virtual reality technology based on artificial intelligence in sports skill training. Secondly, it explores the application of virtual reality technology based on artificial intelligence in tennis, which is a highly skilled sports training. Finally, combined with the practical application of virtual reality technology based on artificial intelligence in sports skills training, it proves the advantages and influence of applying virtual reality technology based on artificial intelligence in sports skills training in the future.

1. Introduction

At present, the society is full of various Internet activities, such as video games, short videos, and online social networking, which constantly squeeze people's less affluent leisure time. People generally hope to release the pressure in video games, experience all kinds of new things in short videos, and use online social instead of offline meeting [1]. The current situation of almost not taking part in any physical exercise, coupled with unreasonable diet structure, hypertension, hyperlipidemia, obesity, low vision, low cardiopulmonary function, and other diseases, gradually appears to have younger status in some overnourished people [2]. China's relevant departments attach great importance to people's health. The CPC Central Committee and the State Council have successively issued and implemented "healthy China 2030" program outline, national fitness implementation plan, and other program outlines [3]. At the 19th National Congress of the Communist Party of China and the 13th National Games, General Secretary Xi also constantly emphasized the important role and significance of developing mass sports

[4]. In this context, our citizens have a new understanding of the importance of physical exercise to health. More and more people begin to plan for sports training in their spare time but encounter the problems of time, venue, and training skills [5]. First of all, in the fast-paced life, people's leisure time is "fragmented," few people can spend a large period of time for sports training. At the same time, the improper understanding of training skills does not play the role of physical training but causes irreversible damage to the body [6]. Based on the above problems, it has greatly hit the enthusiasm of the people for sports training. With the continuous development of science and technology, virtual reality technology based on artificial intelligence can well avoid these problems in sports skills training. This paper introduces and demonstrates this.

This paper first introduces the application of artificial intelligence virtual reality in physical education and then, combined with the case of the role of artificial intelligence virtual reality technology in tennis training skills, specifically discusses the promotion and grasp of artificial intelligence virtual reality technology in sports training skills. Finally,

according to the above analysis and discussion, we come to the conclusion that the use of artificial intelligence virtual reality technology can play a positive role in sports skills training, and through the specific cases of artificial intelligence virtual reality technology in table tennis and other sports skills training, it shows the current application of artificial intelligence virtual reality technology in sports training skills. This paper hopes that through the introduction and discussion of virtual reality technology under artificial intelligence in sports skill training, we can promote the application of virtual reality technology in sports teaching and have certain guiding significance for sports skill training.

2. Related Work

2.1. The Research Status of Artificial Intelligence Virtual Reality Technology in China. The application of artificial intelligence virtual reality technology in physical education has only been applied in recent years. Almashat and others believe that artificial intelligence virtual reality technology with its virtuality can effectively prevent the inevitable collision and other injuries in physical education. At the same time, the required teaching conditions can be presented and realized visually through the writing of computer code, which can make up for the lack of teaching conditions. A computer and a pair of glasses can be used to start sports training, which completely breaks the time and space restrictions on sports training. Using the 3D effect of artificial intelligence virtual reality technology, we can watch sports actions and skills in multiple directions without dead angle, which is conducive to tap the potential of physical education teaching [7]. Sadeghi et al. think that artificial intelligence virtual reality technology in physical education teaching can effectively avoid irreversible sports injury caused by improper operation of difficult movements by making viewers fully understand and put themselves in the training. At the same time, the real field can be set in a relatively safe field, so as to avoid accidents in sports training [8]. Pushparajah et al. also pointed out that the application of artificial intelligence virtual reality technology can effectively avoid sports accidents, reduce physical injury caused by improper sports movements, and save and make up for the cost and shortage of sports facilities [9].

Based on the research results of the above scholars, we find that the academic circles generally believe that the role of artificial intelligence virtual reality technology in sports training has the following points, to avoid irreversible body injury caused by improper or not in place actions in the training process [10], break the limitation of time and space in physical training [11], and Fully tap the teaching potential in the process of training [12]. But at the same time, most of the domestic research on virtual reality technology in sports training mostly stays at the theoretical level and lacks the analysis combined with specific cases [11]; At the same time, for the application of artificial intelligence virtual reality technology in sports training, it only expounds the advantages and application role of relevant research [13]; rarely analyzes the problems encountered in the practical application process, such as the computer hardware settings, the

uneven products of artificial intelligence virtual technology, and the public consumption concept, and puts forward the countermeasures [14].

2.2. International Research Status of Artificial Intelligence Technology. The United States first began to study artificial intelligence virtual reality technology. As early as the 1940s, the U.S. military began to simulate the training of astronauts and pilots through artificial intelligence virtual reality technology. Later, it gradually extended to civilian, such as user interface, perception, hardware, and background software. So far, the United States has established artificial intelligence virtual reality training system and virtual reality education system for space station, aviation, and satellite maintenance. In the field of simulation, George Mason University developed a simulation system in dynamic virtual environment. In terms of game software and office, Boeing and Xerox of the United States and NEC of Japan have designed a knowledge base system based on artificial intelligence virtual reality technology on the existing basis, which can effectively improve the user's sense of body and improve the application efficiency. In Europe, the United Kingdom, Germany, Sweden, and other more developed countries also actively participate in the research and application of artificial intelligence virtual reality technology, but mainly in the field of hardware and software.

To sum up, artificial intelligence virtual technology has been widely studied by researchers all over the world. The research and application of virtual reality technology focus on different countries, mostly in industry, military, medicine, entertainment, education, and so on. Among them, there is less research on sports training, but it has a good prospect.

3. Method

The basic operation scene of artificial intelligence virtual reality technology (VRT) is to bring the subjects an electronic helmet with an eye screen. The electronic helmet is equipped with an impression. The eye screen is made of liquid crystal with two micro screens. The subjects can see the virtual image on each eye screen. At the same time, the hand is equipped with a data glove, which can be used to control or issue commands to users or display graphics. According to the positioning sensor which detects the position of human body on the user's clothing, the real-time position of the subject or the position in the virtual space can be transmitted in two directions. At the same time, the user's trajectory can be recorded, and the position in the model can be modified according to the user's motion trajectory. In addition, if necessary, the subjects also need to wear foot transmission equipment. Through the above equipment, the subjects saw a computer-generated three-dimensional space, with a full-color stereo image and stereo sound, and felt the feedback force of the virtual environment, so they had a real experience in the virtual environment. The artificial intelligence virtual reality technology working scene is shown in Figure 1.



FIGURE 1: Artificial intelligence virtual reality technology working scene demonstration.

3.1. Sports Training of Virtual Reality Technology Based on Artificial Intelligence. Sports skills require athletes to be proficient and standard when doing specific actions. Therefore, in order to achieve proficiency and standard, on the one hand, athletes must continue to train; on the other hand, instructors' demonstration and training methods should be perfectly absorbed, so as to finally achieve the improvement of training level. But taking the result level of professional sports economic training as an example, most coaches mainly rely on the naked eye and experience to judge the athletes' movements in the training process, which is more dependent on the subjective consciousness of coaches, affected by the angle, distance, and lighting. Therefore, athletes need to go through repeated actions and correction or in actual operation to realize the ignored problems in training, which leads to the poor quality of economic sports training in China. The national team with the best training resources is still like this, not to mention for the public, there is no coach guidance, no professional action correction demonstration, and no sufficient and appropriate training time and training ground for athletes. We can imagine the process and result of physical training.

We can combine the actual human movement with sports biomechanics into the virtual coordinate system of digital three position human movement, so as to record the movement track in the space of combination of virtual and reality, correct the movement track to achieve the purpose of sports training, and avoid the injury caused by improper operation in the whole process. The whole process is divided into two parts. One part configures the motion capture action database and stores the data records of action modification and design. The other part generates the corresponding parameters through the trajectory of the mover and combines the two parts of data to test the action. In this part, we define the trajectory of the mover and the corresponding action by establishing a coordinate system and Euler angles in the X and Y directions. And according to the data in the database to correct and arrange the action, the final output of correct data to the specific action of the line of movement and the corresponding parameters are stored in the three-dimensional standard simulation action library for the next preparation.

Through the above system, first of all, the sports training of the volleyball team in a certain area is simulated, and the application performance of the Chinese system is tested through the training effect. Firstly, we input the data of athletes' standard service action effect through three-dimensional modeling and set them as standard parameters. Then, the space coordinate system is established for the actual movements of the athletes, and the Euler angles in the x -axis and y -axis directions are used as the reference to detect the trajectory differences between the athletes and the standard movements and record them (see Figure 2). Finally, through the system calculation results, the standard action track and the correction action track are sent back to the perspective of the athletes, and the specific correction of the athletes' movement is carried out through the control equipment such as data glove and pedal. In order to achieve the practical application of artificial intelligence virtual display technology in volleyball skill training. According to this scheme, we conducted artificial intelligence virtual reality simulation training for 10 athletes and compared the results before and after training. The results are shown in Figure 3.

It can be seen from Figure 2 that the Euler angle of the corrected trajectory is basically below 1 compared with the standard trajectory, which indicates that the simulation effect of the technology is better, and the simulation effect can be used in actual training. It can be seen from Figure 3 that the average time used to reach the same training level for 1-5 months after training is often lower than that before using the simulation training technology system. For 6~8 levels, no one can reach the level before training, but after training with the simulation system, the athletes can reach 6~8 levels, and the time is less than the time to reach 1~5 levels before training.

In the same way, the above scheme is different. For the randomly selected 10 divers, the standard action parameters are still collected first. Combined with the real diving trajectory of the athletes, the difference between the two Euler angles is calculated, and finally, the correction parameters are generated to correct the movements of the athletes. Specific data are shown in Figures 4 and 5.

As can be seen from Figure 4, after using artificial intelligence virtual technology to simulate training, the difference between the actual action parameters and the standard action parameters is about 2. Considering the complexity of diving action, combined with the actual situation, we still think that the simulation effect of artificial intelligence virtual simulation system is better, and the simulation effect can be used in practical application. It can be seen from Figure 5 that all the time, when the system reaches the same level after 1-4 is less than that before the system simulation, and for 5-7 levels, the system can reach the same level after the system simulation, and the average time is 1-4 before the system simulation, and no one has reached the level before the system simulation.

To sum up, it can be concluded that after using the artificial intelligence virtual reality technology simulation system, the effect of athletes in sports training is better; the action standard is longer; the mastery degree is better; the

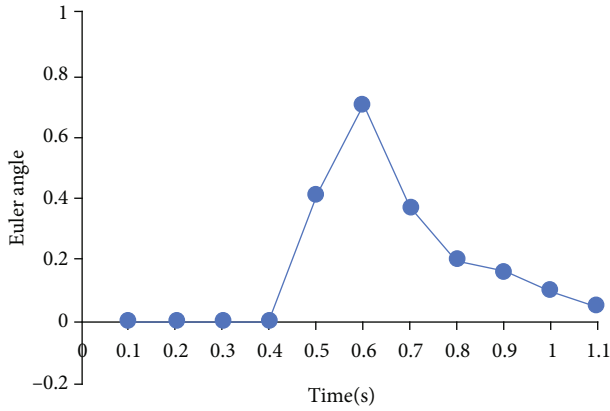


FIGURE 2: The Euler angle is indicated in volleyball.

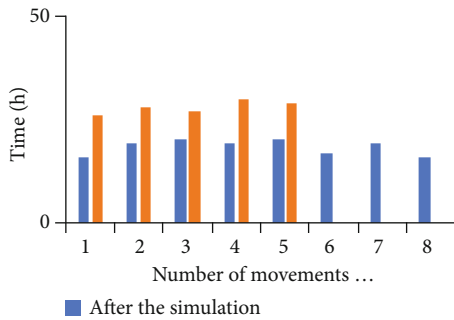


FIGURE 3: Volleyball action training effect.

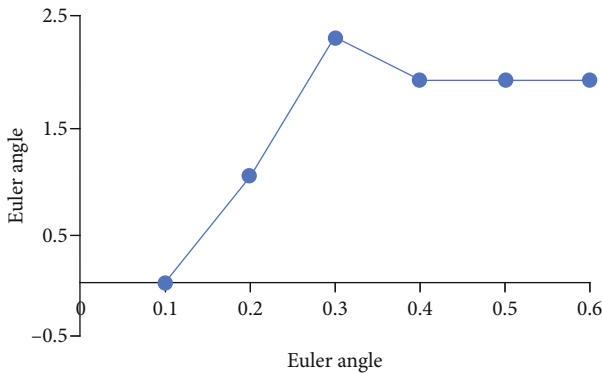


FIGURE 4: The Euler angle is indicated in diving.

time to reach the same level is shorter, that is, the action efficiency is higher; and the application of the system can effectively improve the level of athletes' sports training skills.

3.2. Virtual Reality Technology Based on Artificial Intelligence in Tennis Skills Training. With the emergence of Li Na, Deng Jie, and other world-class players of Chinese women's tennis team in the past two years, tennis is gradually known and sought after by the public. However, due to the complexity and confrontational limitations of the venue and teaching content, it is easy for the athletes to have negative emotions and suppress their learning enthusiasm

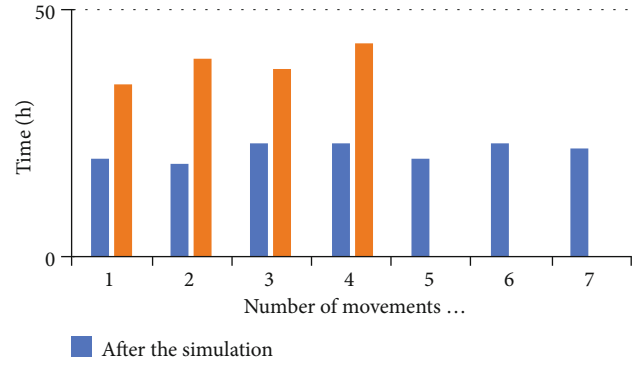


FIGURE 5: Diving action training effect.

and initiative. This situation is typical of the current situation of people's exercise, so through the application of artificial intelligence virtual reality technology in tennis, we hope to discuss the application of virtual reality technology in sports skills training.

In order to avoid the influence of the existing Tennis Foundation on the training effect, we randomly selected 40 subjects without tennis learning foundation as the research object and divided them into the control group and the experimental group, with the male to female ratio of 1:1 in each group. The control group was trained by traditional training methods, and the experimental group was trained by artificial intelligence virtual reality technology. Finally, through the comparison of the results, we hope to see the difference of the effect of virtual reality technology of artificial intelligence on tennis in interest training, sports skills training, and psychological motivation, so as to demonstrate the application of virtual reality technology of artificial intelligence in sports skills training and the application in the current situation of sports skills training in China.

After controlling the relevant irrelevant variables such as the physical fitness of the subjects, the randomness of the training and testing teachers, the teaching content, the testing content, the progress time, and the homogeneity of the place, we started the experiment according to the process. The main process is as follows: firstly, the two groups of subjects were tested in terms of body shape and physical fitness to ensure that the subjects can carry out the experiment and avoid accidents in the process of the experiment. Secondly, the tennis learning interest test is carried out as a comparison with the tennis learning interest test after training. Finally, we test the initial technique of tennis. On the one hand, we can prevent the difference of initial level between subjects from affecting the effect of different training methods. On the other hand, we can make a comparison between the initial reference data and the training effect after the completion of subsequent training. After the above tests, we officially entered the experiment. After the test, the above experimental process was measured and the data were recorded in order.

It can be seen from Figure 6 that everyone likes tennis very much. Except for a few who like or dislike tennis very much, most of them prefer tennis. We first record the distribution of likes before the experiment and then compare the

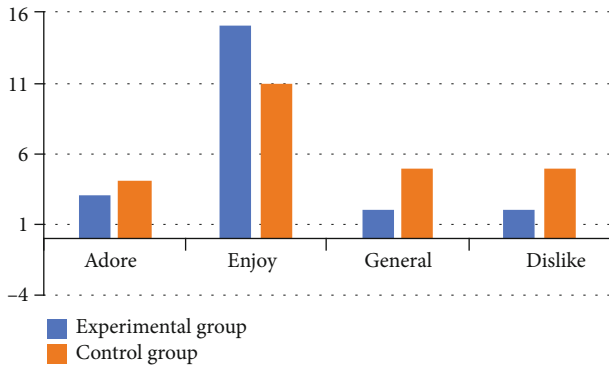


FIGURE 6: Contrast of interest in tennis before experiment.

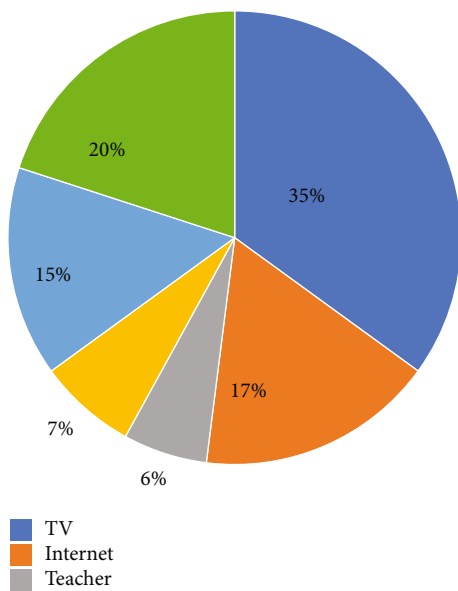


FIGURE 7: Approaches for participants to acquire tennis knowledge.

results after the follow-up and training. It can be seen from Figure 7 that the main channel for people to understand tennis is through television, followed by the Internet, which benefits from the good results of China’s National Women’s tennis team in the world in recent two years.

Finally, we will position the training score below 60 as failing, 60 to 69 as passing, 70 to 79 as average, 80 to 89 as good, and 90 to 100 as excellent. Through the statistics of the results, we found that 35% of the experimental group trained by artificial intelligence virtual reality technology got excellent, while only 10% of the control group got the evaluation. There was no significant difference between the control group and the experimental group in the general and good range, but 35% of the experimental group in the excellent group got the evaluation, while only 10% of the control group got the evaluation. For this result, we think that the average score is also normal distribution. Affected by the sample size, it is normal that there is no difference between the two groups. But the difference between the experimental group and the control group shows that the virtual reality technology based on artificial intelligence has



FIGURE 8: Virtual reality table tennis human-computer interaction scene.

higher efficiency and results in teaching and improving tennis technology. In order to further verify this result, we will further split the process and data of training skills. Due to the influence of space, I will not repeat it here.

To sum up, under the two different training methods, it is found that the effect of virtual reality technology based on artificial intelligence is far more than that of traditional training in the aspects of interest cultivation, enthusiasm promotion, and sports skills training, and the difference is significant. Therefore, in real sports training, we can try to promote the use of artificial intelligence virtual reality technology.

3.3. Application of Table Tennis Training Skills Based on Artificial Intelligence and Virtual Reality Technology. Table tennis, as one of the sports with the highest audience and popularity in China, will also have new effects after the application of virtual reality technology, such as allowing the trainer to enter the role quickly, effectively improving the boring learning process and frustration after failure. Therefore, it is more persuasive to explore the practical application of virtual reality technology based on artificial intelligence in table tennis training.

Table tennis is one of the most advantageous sports in China. A large number of excellent talents are added every year. With the deepening of education reform, a lot of experience and methods that can be copied and popularized have been created. But there are some problems in this system, such as single teaching means and training methods always copy the previous methods, regardless of the actual situation and innovation of training. As a result, the trainers’ theoretical knowledge is weak, their interest in learning gradually declines with the training process, and their enthusiasm is hit. After the introduction of artificial intelligence virtual reality technology, it can effectively stimulate the interest and enthusiasm of the trainers, as well as the theoretical basis and practical practice of training. On the successful case of the practical application of artificial intelligence virtual technology in table tennis training, this paper introduces and analyzes its reasons and characteristics, hoping to use this as a template to promote the virtual reality technology of artificial intelligence to other sports skills training.

In table tennis training, the trainers are mainly equipped with data gloves with sensors, which can accurately locate

TABLE 1: Analysis of application effect of the simulation system.

Action name	Correlation data	After applying the simulation system	Before applying the simulation system
The diving movement	Master the number of movements	7	4
The diving movement	The average time to master the movements	21.7	38.4
Delivery of service	Master the number of movements	8	5
Delivery of service	The average time to master the movements	18.2	27.8

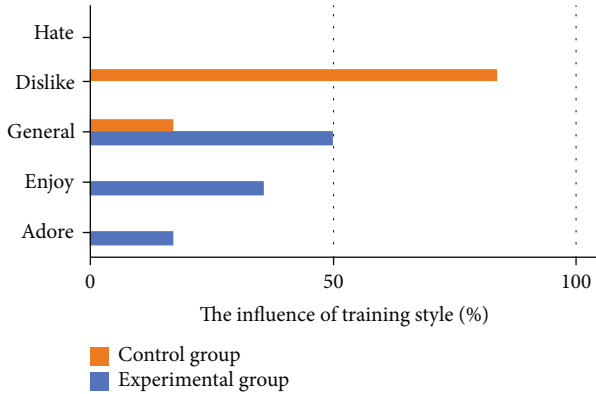


FIGURE 9: The influence of training style.

the position and movement track of the trainer's hand and send it back to the computer host, so as to obtain the interactive scene and track between the ball and the trainer in the simulation space. At the same time, the trainer's head is equipped with an electronic eye screen, which can visualize the computer simulation scene, so that the trainer can carry out table tennis training personally (schematic diagram), as shown in Figure 8.

4. Result Analysis and Discussion

To sum up, we explore the application of artificial intelligence virtual reality technology in the process of sports skills training. We found that after the application of artificial intelligence virtual reality technology, the diving movement of athletes changed from 4 before training to 7, and the average time changed from 38.4 to 21.7, nearly 70% higher. The service action technology has changed from 5 to 8, and the average time used has changed from 27.8 to 18.2, which is nearly 80% higher than 40% and 50% before using the system, indicating that the artificial intelligence virtual reality technology has very high use value and obvious use effect (see Table 1).

Similarly, in the application of artificial intelligence virtual reality technology in tennis, through the comparison and analysis of the experimental results, we found that after learning artificial intelligence virtual reality technology and traditional training technology for a period of time, it has a great impact on the interest of the subjects. The control group is from the original most like to general and not interested from 0% to 84%, while the experimental group data is from interested to very interested; at the same time, the

number of interested is also on the rise. This shows that artificial intelligence virtual reality technology plays a great role in fully mobilizing the enthusiasm of trainers and maintaining their nature (as shown in Figure 9).

In addition to the problems discussed above, artificial intelligence virtual technology in sports skills has a role that has not been widely discussed, that is, to reduce injury. In the traditional offline training, there are many reasons, such as insufficient warm-up activities, lack of standardization of technical actions, and lack of reserve of safety knowledge, which often lead to accidental injury, even irreversible injury to the body. This is also one of the current situations of sports skill training, but through the artificial virtual reality technology, we can import the standard action in advance, and then through the positioning sensor, we can locate and analyze the shortcomings of the trainer and refer to the standard action to correct the trainer. At the same time, artificial intelligence virtual reality technology is more used for operation and training in virtual three-dimensional space, which effectively avoids the injury caused by the site. There are few people to explore this aspect. I hope that this paper can attract attention after introducing and raising questions and pay attention to this issue while promoting artificial intelligence virtual reality technology.

5. Conclusion

Through the above discussion, we find that artificial intelligence virtual reality technology has gradually been promoted in the field of education and teaching, because of its immersion, interaction, and conception. Facing the current situation and problems of the training of the social mass sports skills, this paper first expounds the role of artificial intelligence virtual technology in the field of education and teaching through the general application and principle of artificial intelligence in the training of sports skills. Secondly, through the application of artificial intelligence virtual technology in tennis, it fully proves that the use of artificial intelligence virtual reality technology to solve the problems of students, athletes, people, and other different groups in sports skills sports is facing the shortcomings of the decline of enthusiasm, accidental injury, irregular movement skills, and low efficiency. Finally, the successful case of artificial intelligence virtual technology in table tennis training is given. The function and advantages of artificial intelligence virtual technology in sports skill training are illustrated by practical application. It is hoped that the application of artificial intelligence virtual

reality technology in sports training can be accelerated and played a guiding and reference role in it.

Data Availability

The data used to support the findings of this study are included within the article.

Conflicts of Interest

The authors declare that they have no conflicts of interest.

Acknowledgments

This work was supported by the grant from University Teaching Innovation Program of Heilongjiang Province of China (No. SJGZ20180030).

References

- [1] T. Richesin, R. Baldwin, and L. A. M. Wicks, "Art making and virtual reality: a comparison study of physiological and psychological outcomes," *The Arts in Psychotherapy*, vol. 75, p. 101823, 2021.
- [2] S. Skard, E. Knudsen, H. Sjøstad, and H. Thorbjørnsen, "How virtual reality influences travel intentions: the role of mental imagery and happiness forecasting," *Tourism Management*, vol. 87, p. 104360, 2021.
- [3] S. M. C. Loureiro, J. Guerreiro, and A. Japutra, "How escapism leads to behavioral intention in a virtual reality store with background music," *Journal of Business Research*, vol. 134, pp. 288–300, 2021.
- [4] N. A. Baker, J. Baird, and M. Driscoll, "Integrating virtual reality into a comprehensive chronic pain program," *Pain Medicine*, vol. 2, pp. 77–79, 2021.
- [5] P. Yeh, C. Liu, M. H. Sun, S. C. Chi, and Y. S. Hwang, "To measure the amount of ocular deviation in strabismus patients with an eye-tracking virtual reality headset," *BMC Ophthalmology*, vol. 21, no. 1, pp. 1–5, 2021.
- [6] J. Pang, X. Li, and X. Zhang, "Retracted article:Coastline land use planning and big data health sports management based on virtual reality technology," *Arabian Journal of Geosciences*, vol. 14, no. 12, pp. 73–75, 2021.
- [7] R. Almashat, R. Baakdah, T. Justinia et al., "Pediatric dentists' perception on the effect of virtual reality on patients," *Computer Methods and Programs in Biomedicine*, vol. 205, p. 105988, 2021.
- [8] H. Sadeghi, A. Maat, Y. Taverne et al., "Virtual reality and artificial intelligence for 3-dimensional planning of lung segmentectomies," *JTCVS Techniques*, vol. 7, pp. 309–321, 2021.
- [9] K. Pushparajah, K. Chu, S. Deng et al., "Virtual reality three-dimensional echocardiographic imaging for planning surgical atrioventricular valve repair," *JTCVS Techniques*, vol. 7, pp. 269–277, 2021.
- [10] M. Parger, C. Tang, Y. Xu et al., "UNOC: understanding occlusion for embodied presence in virtual reality," *IEEE Transactions on Visualization and Computer Graphics*, vol. 43, pp. 1–237, 2021.
- [11] D. Baur, C. Pfeifle, and C. E. Heyde, "Cervical spine injury after virtual reality gaming: a case report," *Journal of Medical Case Reports*, vol. 15, no. 1, pp. 11–12, 2021.
- [12] M. Takac, J. Collett, R. Conduit, and A. De Foe, "A cognitive model for emotional regulation in virtual reality exposure," *Virtual Reality*, vol. 12, pp. 22–26, 2021.
- [13] D. Colombo, A. Díaz-García, J. Fernandez-Álvarez, and C. Botella, "Virtual reality for the enhancement of emotion regulation," *Clinical Psychology & Psychotherapy*, vol. 34, pp. 65–68, 2021.
- [14] K. Meyerbröker, "Virtual reality in clinical practice," *Clinical Psychology & Psychotherapy*, vol. 29, pp. 82–85, 2021.

Retraction

Retracted: Computer Mathematical Modeling Based on the Improved Genetic Algorithm and Mobile Computing

Wireless Communications and Mobile Computing

Received 28 November 2023; Accepted 28 November 2023; Published 29 November 2023

Copyright © 2023 Wireless Communications and Mobile Computing. This is an open access article distributed under the Creative Commons Attribution License, which permits unrestricted use, distribution, and reproduction in any medium, provided the original work is properly cited.

This article has been retracted by Hindawi, as publisher, following an investigation undertaken by the publisher [1]. This investigation has uncovered evidence of systematic manipulation of the publication and peer-review process. We cannot, therefore, vouch for the reliability or integrity of this article.

Please note that this notice is intended solely to alert readers that the peer-review process of this article has been compromised.

Wiley and Hindawi regret that the usual quality checks did not identify these issues before publication and have since put additional measures in place to safeguard research integrity.

We wish to credit our Research Integrity and Research Publishing teams and anonymous and named external researchers and research integrity experts for contributing to this investigation.

The corresponding author, as the representative of all authors, has been given the opportunity to register their agreement or disagreement to this retraction. We have kept a record of any response received.

References

- [1] H. Wei and J. Liu, "Computer Mathematical Modeling Based on the Improved Genetic Algorithm and Mobile Computing," *Wireless Communications and Mobile Computing*, vol. 2021, Article ID 1584435, 7 pages, 2021.

Research Article

Computer Mathematical Modeling Based on the Improved Genetic Algorithm and Mobile Computing

Huixian Wei  and Jia Liu 

Basic Department of Information Engineering, Shijiazhuang Institute of Railway Technology, Shijiazhuang Hebei 050041, China

Correspondence should be addressed to Jia Liu; 201410734038@stu.shmtu.edu.cn

Received 8 October 2021; Revised 25 October 2021; Accepted 1 November 2021; Published 26 December 2021

Academic Editor: Balakrishnan Nagaraj

Copyright © 2021 Huixian Wei and Jia Liu. This is an open access article distributed under the Creative Commons Attribution License, which permits unrestricted use, distribution, and reproduction in any medium, provided the original work is properly cited.

In order to change the problem of data redundancy in a genetic algorithm, this paper proposes a computer mathematical model based on the combination of an improved genetic algorithm and mobile computing. Combined with the least square method, MATLAB software is used to solve the equations, determine the range of parameters, and solve the estimation parameter range and identification problems. The improved genetic algorithm combined with mobile computing and least square method to establish a mathematical model greatly increased the individual search space and increased the operation rate of 90% compared to the basic genetic algorithm or mobile computing. The results show that the improved genetic algorithm and mobile computing have a certain ability to identify the optimal solution and greatly improve the work efficiency.

1. Introduction

For big data, an efficient optimization calculation process is very important. With the rapid update of computer science, various mathematical methods have been widely used in natural science and play a key role in social science. And mathematics technology has also realized the transformation from basic mathematics to an important component of high technology. In mass mathematical analysis methods, mathematical modeling can usually be closely combined with practical problems [1]. Generally speaking, mathematical modeling is not a direct reproduction of practical problems but requires an in-depth study, detailed observation and analysis, and rational use of various mathematical theories and knowledge. In this process, a system model framework should be established first. In most cases, experiments are started through known models [2]. In fact, model solving is to build functional relations based on the known system model framework through mathematical theory and skills and estimate model parameters with system input and output data. The estimation of model parameters is closely related to data, curve fitting, and experimental error analysis, and the key lies in the application of the least square method [3]. In data fitting, the least square method is the most com-

monly used method, which is the main method of observation data research. It can observe two variables repeatedly and ensure the accuracy of data. A genetic algorithm does not limit the scope of the problem, has strong robustness, and has a variety of compatible general modes. It has been widely used in many fields, such as function optimization, automatic control, production scheduling, and image processing, and the effect is remarkable. Therefore, this paper studies the construction of a computer mathematical model based on the improved genetic algorithm and least square method [4].

2. Literature Review

A genetic algorithm (GA), based on genetic theory, simulates a survival mechanism of the fittest and exchanges information randomly, which is more suitable for optimization of complex systems. It originated in the 1960s and is a very practical optimization technology, which can be applied to multidisciplinary research [5]. The genetic algorithm will not limit the field of the problem and has strong robustness. There are many compatible and universal modes. The genetic algorithm has an obvious application effect in the fields of function optimization, combination optimization, automatic control,

production scheduling, image processing, artificial life, structure optimization, and so on. In data fitting, the least square method is often used as an important method to study observation data [6]. The least square method can observe two variables for many times, so as to obtain more accurate data. The genetic algorithm simulates the reproduction and evolution of natural biological groups from generation to generation and generates a new generation of better individuals as the solution to the problem through iteration, just as biological groups multiply and evolve from generation to generation and finally converge to a generation of biological individuals most suitable for the living environment [7]. That is the optimal solution of the problem. The genetic algorithm is widely used in engineering optimization and industrial control. Wu et al. used the genetic algorithm to optimize the cantilever structure of a certain machine, which has fast convergence speed and high calculation accuracy, and established a single-objective nonlinear optimization design mathematical model. It provides a powerful method and tool for multiobjective nonlinear structural optimization design. Gong et al. introduced an immune algorithm to improve the genetic algorithm [8]. In solving the complex problem of too many iterations of a population in TSP application, the probability of algorithm degradation was reduced by a vaccine test and annealing selection, and the phenomenon of population degradation was avoided. The sowing quality, sowing efficiency, and energy consumption of the seeder cannot be brought into full play due to the influence of sowing terrain and region [9]. Hua and others put forward a multiobjective speed control genetic algorithm optimization model based on BTO mode, determined the initial parameters of the performance optimization of the seeder under BTO mode, and obviously improved the sowing quality, sowing efficiency, and sowing energy consumption of the seeder [10]. And the operation performance of the seeder is improved. In view of the shortcomings of the basic genetic algorithm, such as slow convergence speed and premature convergence, Lei proposed an improved adaptive genetic algorithm, which automatically adjusted the crossover probability and mutation probability according to the size of the fitness value in the evolution process, so that the algorithm could jump out of the local optimal solution [11]. The simulation experiment of mobile robot path planning shows that. The improved genetic algorithm is effective and feasible and obviously improves the quality of robot path planning. The genetic algorithm is also used to solve the optimization problem of mathematical modeling in the annual college students' mathematical modeling competition [12]. Liu and others used the genetic algorithm to establish a VRP model for efficient dispatching of public bicycles in large- and medium-sized cities and tested the algorithm with standard examples [13]. The results show that the genetic algorithm can effectively solve the bicycle scheduling model. According to the principle of "seeing the sun immediately" and making a shadow sunshine map, Fu and Li put forward a method of sun shadow location [14]. They first combine the solar altitude angle and the solar declination angle. A multiobjective optimization model for sun shadow location is established with the maximum correlation coefficient between theoretical shadow length and actual shadow length and the minimum sum of

error squares as objective functions. The genetic algorithm is used to solve the problem, and the result is superior to the traditional enumeration algorithm in both accuracy and convergence speed [15]. In the annual teaching and guidance of mathematical modeling for college students, how to make college students' master genetic algorithm quickly in a short period of time is a thorny problem. The genetic algorithm has its own advantages in solving problems. It has been widely used in various researches by many scholars. Through continuous improvement, more advantages of the genetic algorithm have been gradually excavated, and some new theories and research methods about the genetic algorithm have been developed rapidly in constant practice [16]. And some new application fields have emerged, such as the application in machine learning. It has found a solution to the thorny problems left by scholars in artificial intelligence for many years. The crosscombination with some intelligent algorithms such as neural network points out the direction for solving the difficulties in computational intelligence conveniently and quickly. The characteristics of parallel processing carried by the genetic algorithm itself have greatly promoted the research of computer parallel architecture. However, the traditional standard genetic algorithm adopts fixed control parameters, which leads to poor global searching ability and immature convergence [17]. The research results of many researchers show that the traditional standard genetic algorithm cannot guarantee convergence to the global optimal solution. In recent years, the research on the improvement of the genetic algorithm has not stopped, and the optimization ability of the genetic algorithm has been greatly improved both in the direction of improvement and in the content of improvement.

The genetic algorithm used in this paper is an advanced modern optimization algorithm, which has strong parallelism and global search ability. Its coding technology and genetic operation are relatively simple, and it has low requirements on the restrictive conditions of optimization problems. At present, various genetic algorithms have been well applied in the fields of machine learning, image processing, pattern recognition, optimization control, combination optimization, management decision-making, etc. The research and popularization of genetic algorithms are of great significance to economic and social development.

3. Research Methods

3.1. Improved Genetic Algorithm

3.1.1. Operating Principle of the Basic Genetic Algorithm. The genetic algorithm, as a new computing method, is based on the basic principles of genetics, imitates the mutation and crossover mechanism of biological genetic evolution, and makes a global search for specific problems to obtain a basic genetic algorithm (SGA), which is the basis of improving the genetic algorithm.

Coding operation is adopted to express the solution space as structural data in genetic information, thus completing genetic operation. According to the precision requirement, the binary symbol is used as the fixed coding string to represent the gene model between individuals. According to the

structure of space, its value range is defined, and after coding, it is necessary to generate a number of individuals as the initial population [18]. By calculating the individual fitness evaluation function value, the individual's pros and cons are calculated. The selection operator needs to judge the fitness of the individual according to the fitness function of the individual, so as to complete the whole operation process. Matching each other according to a certain rule and generating new data individuals, the genetic algorithm is the most important method for crossover. For each random mutation point, the gene value is inversely calculated, thus forming a new individual.

3.1.2. Mobile Computing Model. A mobile computing model is the basic framework and principle that the computer system must follow to complete calculation. The mobile computing model is significantly different from the distributed computing model due to special requirements such as device disconnection, communication and computing imbalance, and energy saving caused by mobility. Therefore, support for mobility and weak connectivity should be added. The core problem of the mobile computing model is to determine how the functions of the mobile terminal and server are allocated and how to adjust dynamically according to the needs.

The concepts of location and movement determine that the architecture of the mobile computing system is loosely coupled and strongly autonomous. Loose coupling means that a group (application or device) continues to work when it is disconnected or weakly connected to the server. And as long as the connection is available, make the connection. Strong autonomy in mobile computing is determined by the characteristics of mobile computing environment. That is, it must have very little self-tolerance and very strong initiative. Due to loose coupling, strong autonomy and mobility of computing components, mobile computing systems need dynamic configuration. Component movement and management regionalization require mobile computing to fully consider resource access control policies and mechanisms.

π -calculus is a method of describing and analyzing concurrent systems and is an extension of CCS. The base entity is the channel name and the process made up of the name. The syntactic definition of the monospore π -calculus process is as follows:

$$P ::= \sum_{i \in I} \alpha_i P_i \mid P_1 \mid P_2 \mid P_1 + P_2 \mid \nu_x P \mid P, \quad \alpha ::= x(y) \mid xy, \quad (1)$$

where x, y stands for name and has two forms: the input prefix $x(y)$ means that the name y is received on channel x and the output prefix xy means that the name y is sent on channel x .

3.1.3. Convergence Verification. Function optimization is a very important part of the genetic algorithm. Given an objective function, it is necessary to find the best quality in the solution space without any constraints. With the Rastrin-

gin function as the test function, the convergence effects of crossover probability and mutation probability are analyzed.

3.1.4. Analysis of the Improvement Scheme. In the process of running the algorithm, crossover and mutation will increase the search range. At the end of the running of the algorithm, it is necessary to control the search within a certain range for the protection of individual position. If the algorithm can find a group point with high average fitness in the initial running stage, the optimal solution can be obtained. In order to keep the best individuals better, it is necessary to accelerate the convergence speed in the iterative process and ensures that the optimal value which is found before the maximum value of average fitness is obtained.

3.2. Least Square Method. The least square method has a good effect on the study of observation data. For known variables, it is necessary to satisfy a specific linear relationship and observe the variables for many times, so as to obtain observation data. The basic idea of the least square method is to find the straight line with the shortest distance between multiple groups of observations. If an n contains m unknowns, it is necessary to find the optimal value according to the linear equations. In regression analysis and variance analysis, the least square method is the best theoretical basis, and many mathematical statistics theories are developed on the basis of the least square method. In the least square method, it is known that the observed data $(x_1, y_1), (x_2, y_2) \dots (x_n, y_n)$ need to satisfy the condition $y = g(x) + \varepsilon(x)$, where $y = g(x)$ is a function and $\varepsilon(x) = y - g(x)$ is an error function. $\varepsilon_i(x) = y_i - g(x_i)$ is an observation function. This method is called the least square method. The fitting function can be expressed as

$$y = a_1\varphi_1(x) + a_2\varphi_2(x) + \dots + a_s\varphi_s(x), \quad (2)$$

where $\varphi_1(x), \varphi_2(x) \dots \varphi_s(x)$ is the basis function and the undetermined function $a_i (i = 1, 2, \dots, s)$. In order to determine $a_i (i = 1, 2, \dots, s)$, it is necessary to minimize the sum of squares of observed data distances between Y and N , so that the formula can get the minimum value.

3.3. Construction of the Computer Mathematical Model

3.3.1. Ask Questions

(1) *Question 1.* There is a straight bar with a length of 3.5 m in the square. Based on the square position, the longitude and latitude (θ) can be roughly determined to obtain the sun altitude angle and azimuth angle. The shadow length of the straight rod can be obtained according to the change of parameters, and the correlation between the coordinates of the shadow endpoint and the height of the straight rod is not high. The curve fitting analysis can be carried out by the least square method to solve the corresponding irradiation time of the shadow minimum point and then calculate the longitude. At the same time, solving latitude is constructed based on a nonlinear equation. The longitude and latitude are not unique, which directly increases the

difficulty of solving, which can be solved by the improved genetic algorithm to determine the measuring points.

(2) *Question 2.* Based on the improved genetic algorithm, the optimal solution is found, and the relevant parameters are obtained through its discrimination ability. Distinguish the model specifically:

$$y(t) = -f_1y(t-1) - \dots - f_my(t-1) + g_1k(t-1) + \dots + g_nk(t-1) + \gamma(t). \quad (3)$$

The least square method is regarded as one of the most commonly used methods to solve and distinguish the parameters.

3.3.2. Building a Model

(1) *Question 1.* Set the height of the straight rod as u , projecting on the end point of the ground based on the highest point of the straight rod, and the shadow length as OH , and set the included angle between the sun ray and the ground as β ; then,

$$\frac{P}{U} = \cot\beta. \quad (4)$$

Then, $\Delta k_{\text{latitude}} = 12 \times (f - 120)/180$. The specific relationship between the flat sun and the true sun is as follows:

$$\begin{aligned} k_{\text{真}} &= k_{\text{平}} + 9.6n \sin 2P - 7.8n \sin(P + 78) \\ k_{\text{真}} &= k_{\text{平}} + 9.6n \sin 2P - 7.8n \sin(P + 78^\circ) \end{aligned} \quad (5)$$

$$P = 280^\circ + 0.986^\circ m,$$

where m represents the date and n represents the minute. Then,

$$k_{\text{平}} = k_{\text{北}} + 4 \times (F - 120^\circ) \quad (6)$$

$$\omega = 23.5 \sin \frac{2\pi(287 + m)}{365}, \quad (7)$$

$$\sinh = \sin \alpha \sin \omega \cos \alpha \cos \omega \cos \theta.$$

Get azimuth, i.e.,

$$\begin{cases} P = OH = \sqrt{(x_0 - 0)^2 + (y_0 - 0)^2}, \\ \frac{P}{S} = \cot \beta, \\ S \cdot \cot \beta = \sqrt{x_0^2 + y_0^2}. \end{cases} \quad (8)$$

Fitting analysis is for the least square method, in which the quadratic curve expression is

$$y = fx^2 + gx + l. \quad (9)$$

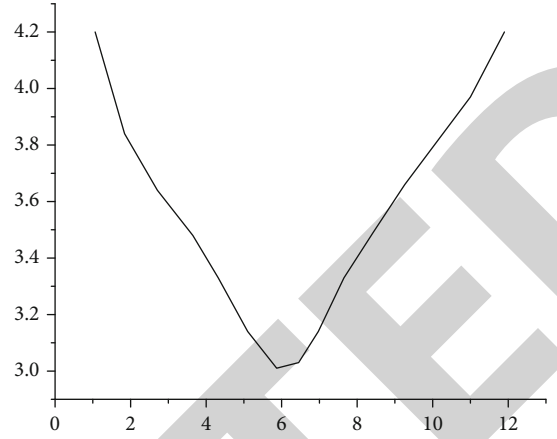


FIGURE 1: Curve of shadow length of pole changing with time.

Set the parameter as f ; when f is the minimum state, take it as the basis of optimization evaluation, and define ω based on the model to obtain the relationship between dimension and height angle. Through the least square fitting analysis, the least square model is constructed at the same time. When f is the smallest, the obtained quadratic fitting function is as follows:

$$\min F(f, g, l) = \sum_{w=1}^m (x_w - x'_w)^2 + (y_w - y'_w)^2. \quad (10)$$

Based on this research, the nonlinear equation can be obtained, namely,

$$\sin A = \frac{\cos \omega \sin \theta}{\cos (\arcsin (\sin \alpha \sin \omega \cos \alpha \cos \omega \cos \theta))}. \quad (11)$$

The equation is solved by MATLAB software to obtain the date serial number, i.e., 108, and ω is 10.6. Based on this value, the measuring place can be determined.

(2) *Question 2.* Firstly, the rows and columns of matrix strings are defined, and the number of parameters is defined. Once the parameters exceed six, the matrix distribution mode needs to be defined, and the corresponding parameters should be defined through multiple elements. Secondly, determine the specific search range, define the search range based on the improved genetic algorithm, and determine the use range for practical problems. According to the specific situation, the estimation parameter range and discrimination of measurement data are defined. Evaluate the individual's fitness again. Based on the least square method, we know that

$$L = \sum [y(t) - \lambda^K(t)\beta]^2, \quad (12)$$

where L represents the difference between the experimental estimated value and the measured value, and the smallest group is selected as the high-quality data to be output. The

TABLE 1: Experimental results of three algorithms on F1.

	Average error	Number of successes	Average convergence iteration	Optimal function value
Algorithm 1	$5.9 * 10^{-4}$	47	285	38.8
Algorithm 2	$2.9 * 10^{-4}$	84	147	38.8
Algorithm 3	$1.9 * 10^{-4}$	95	121	38.8

TABLE 2: Experimental results of three algorithms on F2.

	Average error	Number of successes	Average convergence iteration	Optimal function value
Algorithm 1	$6.5 * 10^{-4}$	34	387	-186.8
Algorithm 2	$2.5 * 10^{-4}$	78	246	-186.7
Algorithm 3	$1.2 * 10^{-4}$	90	189	-186.7

improved genetic algorithm combined with the least square method can effectively solve the key problems. Based on the genetic algorithm, the difference between the parameter value and the measured value is searched, and the fitness function of the genetic algorithm is obtained.

$$u(x) = \frac{1}{L} = \frac{1}{\sum [y(t) - \lambda^K(t)\beta]^2}. \quad (13)$$

Finally, to avoid the damage during mutation, in order to avoid parent string mutation, it is necessary to find the optimal solution without crossover and mutation and directly input the offspring. In order to facilitate the improved genetic algorithm to quickly and accurately obtain the global optimal solution, it is also necessary to construct crossover function and mutation probability to obtain

$$\begin{aligned} H < \frac{Q}{2}, P_\alpha(h) &= P_{\alpha \max} - \frac{2(P_{\alpha \max} - P_{\alpha \min})}{Q} \cdot H, \\ \frac{Q}{2} \leq H \leq Q, P_\alpha(h) &= P_{\alpha \min}, \\ H \leq \frac{Q}{2}, P_n(h) &= P_{n \max} - \frac{2(P_{n \max} - P_{n \min})}{Q} \cdot H, \\ \frac{Q}{2} \leq H \leq Q, P_n(h) &= P_{n \min}. \end{aligned} \quad (14)$$

$P_\alpha(h)$ and $P_n(h)$ represent crossover probability and mutation probability, respectively. Q stands for algebra. $P_{\alpha \max}$ and P_α and P_n represent the upper limit and the lower limit. During the simulation test, the range of P_α and P_n can be set according to the actual needs. There are too many parameters, so there will be long codes when identifying problems, and single-point crossover will be adopted, but it will hinder the expansion of the search space, which can be calculated and analyzed through two-point crossover or multipoint crossover. The whole process needs to be obtained based on the genetic algorithm. After cross-

over and mutation, the individual search space generated is relatively large, which can maximize the optimization.

4. Research Results

For question 1, use MATLAB software to make the curve of shadow length change with time as shown in Figure 1.

A total of 50 sampling parameters are counted by the input and input data of the third-order linear discrete system, and the parameters are estimated according to the combination of the improved genetic algorithm and the least square method. The initial conditions are given when calculating, and the N -link deviation before the experiment and the calculation is as follows:

$$\begin{aligned} \gamma'(0) &= \varphi, \\ \gamma_e'(0) &= 0, \\ e_n(t) &= [y'(t) - y(t)]^2, \\ L(t) &= \sum_w^n e^2(t). \end{aligned} \quad (15)$$

Therefore, $y(t)$ represents the measured value, and $y'(t)$ represents the optimal value sought by the improved genetic algorithm, i.e., [1.76, 0.95, 0.16, 1.00, 0.53, 0.07]. However, before decoding, it is necessary to clarify the parameter variation range and distinguish the results as [1.70, 0.94, 0.15].

In the comparative test, algorithm 1 adopts binary coding, single-point crossing, and roulette; algorithm 2 adopts real coding, and a selection operator adopts an adaptive proportional selection operator. Algorithm 3 is an improved algorithm in this paper. The initial population size is set at 100, and the maximum evolutionary algebra is 500. Run each algorithm for 100 times, and when the optimal solution function is searched, it indicates that the algorithm is successful in optimization and then stops operation, and record the average error between the optimal solution function

TABLE 3: Experimental results of three algorithms on F3.

	Average error	Number of successes	Average convergence iteration	Optimal function value
Algorithm 1	$5.9 * 10^{-4}$	25	366	0.5
Algorithm 2	$3.7 * 10^{-4}$	67	184	0.5
Algorithm 3	$2.6 * 10^{-4}$	80	130	0.5

value and ideal extremum when the algorithm is stopped, the average convergence algebra of successful optimization, the number of successful optimization times, and the optimal function value obtained by 100 searches. If the algorithm does not converge when it exceeds the maximum evolutionary algebra $T = 500$, it is considered that this experiment does not converge, as shown in Tables 1–3.

It can be seen from the above table that algorithm 1 is inferior to other algorithms in all results, which shows that the traditional genetic algorithm is difficult to adapt to this computer mathematical model. Algorithms 2 and 3 have more successful optimization times, avoiding premature convergence, which proves the superiority of the improved algorithm.

5. Conclusion

Mathematical modeling is to build a mathematical model according to specific problems, solve the model by mathematical methods and computer tools, and solve practical problems according to the results. In this paper, the computer mathematical model is constructed based on the improved genetic algorithm and the least square method. Through theoretical analysis, the two algorithms are verified by specific problem analysis experiments. The results show that, as a modern advanced algorithm, the improved genetic algorithm has outstanding global search ability, concise coding technology, and genetic operation method and less limitation in the optimization problem. The improved genetic algorithm has strong discrimination ability, can find the optimal solution, and greatly improves the operation efficiency and quality. The equations are solved by MATLAB software. Clear the specific use area of parameters to solve the related problems such as estimating parameter range and distinguishing. The simulation results show that the computer mathematical model based on the improved genetic algorithm and least square method can significantly expand the search space, and the operation efficiency is relatively high. The continuous improvement and perfection of the genetic algorithm are helpful to promote social progress. It is of great practical significance to the development of society.

Data Availability

The data used to support the findings of this study are available from the corresponding author upon request.

Conflicts of Interest

The authors declare no conflicts of interest.

Acknowledgments

This study was funded by the Three Three Three Talent Project of Hebei Province under Grant Project No. A202101033.

References

- [1] C. Ding, L. Chen, and B. Zhong, "Exploration of intelligent computing based on improved hybrid genetic algorithm," *Cluster Computing*, vol. 22, Supplement 4, pp. 9037–9045, 2019.
- [2] P. Dolgoplov, D. Konstantinov, L. Rybalchenko, and R. Muhitovs, "Optimization of train routes based on neuro-fuzzy modeling and genetic algorithms," *Procedia Computer Science*, vol. 149, pp. 11–18, 2019.
- [3] L. U. Zhiqiang and T. Shi, "Modeling and optimization of resource investment problem with activity splitting," *Jisuanji Jicheng Zhizao Xitong/Computer Integrated Manufacturing Systems, CIMS*, vol. 24, no. 3, pp. 602–611, 2018.
- [4] J. L. Gao, "Research on boiler water supply control system based on at89c55 and fractional order PID algorithm," *Procedia Computer Science*, vol. 154, pp. 173–180, 2019.
- [5] J. Jiang, J. Zhang, L. Zhang, X. Ran, and Y. Tang, "Passive location resource scheduling based on an improved genetic algorithm," *Sensors*, vol. 18, no. 7, p. 2093, 2018.
- [6] T. Rouabah, A. Tounsi, and N. E. Belaloui, "A mathematical epidemic model using genetic fitting algorithm with cross-validation and application to early dynamics of COVID-19 in Algeria," *Journal of Fundamental and Applied Sciences*, vol. 12, no. 3, pp. 1253–1276, 2020.
- [7] S. Dian, H. Fang, T. Zhao, Q. Wu, and S. Li, "Modeling and trajectory tracking control for magnetic wheeled mobile robots based on improved dual-heuristic dynamic programming," *IEEE Transactions on Industrial Informatics*, vol. 17, no. 2, pp. 1470–1482, 2020.
- [8] X. Gong, X. Zheng, J. Fang, and G. Liu, "Optimized layout methods based on optimization algorithms for DPOS," *Aerospace Science and Technology*, vol. 84, no. JAN., pp. 484–496, 2019.
- [9] G. M. W. Ullah and M. Nehring, "A multi-objective mathematical model of a water management problem with environmental impacts: an application in an irrigation project," *PLoS One*, vol. 16, no. 8, p. e0255441, 2021.
- [10] Y. Acuna and Y. Sun, "An efficiency-improved genetic algorithm and its application on multimodal functions and a 2D common reflection surface stacking problem," *Geophysical Prospecting*, vol. 68, no. 4, pp. 1189–1210, 2020.
- [11] M. A. Baset, I. Selim, Y. Zhou, and I. Hezam, "Stellar population analysis of galaxies based on improved flower pollination algorithm," *International Journal of Mathematical Modelling and Numerical Optimisation*, vol. 8, no. 3, pp. 183–196, 2018.

Retraction

Retracted: Research on Tourism Route Planning Based on Artificial Intelligence Technology

Wireless Communications and Mobile Computing

Received 28 November 2023; Accepted 28 November 2023; Published 29 November 2023

Copyright © 2023 Wireless Communications and Mobile Computing. This is an open access article distributed under the Creative Commons Attribution License, which permits unrestricted use, distribution, and reproduction in any medium, provided the original work is properly cited.

This article has been retracted by Hindawi, as publisher, following an investigation undertaken by the publisher [1]. This investigation has uncovered evidence of systematic manipulation of the publication and peer-review process. We cannot, therefore, vouch for the reliability or integrity of this article.

Please note that this notice is intended solely to alert readers that the peer-review process of this article has been compromised.

Wiley and Hindawi regret that the usual quality checks did not identify these issues before publication and have since put additional measures in place to safeguard research integrity.

We wish to credit our Research Integrity and Research Publishing teams and anonymous and named external researchers and research integrity experts for contributing to this investigation.

The corresponding author, as the representative of all authors, has been given the opportunity to register their agreement or disagreement to this retraction. We have kept a record of any response received.

References

- [1] M. Ding, "Research on Tourism Route Planning Based on Artificial Intelligence Technology," *Wireless Communications and Mobile Computing*, vol. 2021, Article ID 2227798, 7 pages, 2021.

Research Article

Research on Tourism Route Planning Based on Artificial Intelligence Technology

Maobin Ding 

Graduate School Hotel Tourism Department, Tongmyong University, Busan 48520, Republic of Korea

Correspondence should be addressed to Maobin Ding; 150511139@stu.sxit.edu.cn

Received 6 October 2021; Revised 30 October 2021; Accepted 6 November 2021; Published 23 December 2021

Academic Editor: Balakrishnan Nagaraj

Copyright © 2021 Maobin Ding. This is an open access article distributed under the Creative Commons Attribution License, which permits unrestricted use, distribution, and reproduction in any medium, provided the original work is properly cited.

Study on designing reasonable travel routes with the least time cost and the highest experience index was conducted. An artificial intelligence-based wireless sensor travel route planning study is proposed. First, the improved TSP route planning model is built at the least time consumption and combines the normal distributed random number (ND) with the genetic algorithm (GA) and proposes the ND-GA algorithm, analyzes the overall structure, node structure, communication mode, and network coverage of the wireless sensor network, and gives a mathematical model of wireless transmission energy consumption. Using the proposed algorithm to solve the travel route and detailed itinerary, with time, the 10-year travel route design model based on multitarget dynamic optimization finally detailed analysis of the model results and sensitivity analysis results showing that the application of AI wireless sensor technology can also make the scenic work more efficient; for example, a face recognition system can improve the speed of ticket checking. Although the application of AI technology is widely used in tourism activities, there are some problems, which require the continuous optimization and innovation of AI wireless sensor technology by relevant practitioners, so that it can better serve tourists.

1. Introduction

With the rapid development of social economy, people's living standard tourism has developed from a few luxury to popular consumption becoming an important content of people's daily life with the deepening of the reform, and opening up tourism has become one of the important industries in China; in the future, tourism will become an important driving force to promote GDP growth, so scientifically planning an optimal tourism route makes tourist cost and tourism experience be of very important significance [1]. Sensing network, Internet, and other technologies can not only provide tourists with accurate scenic spot information and tourist routes but also enrich tourists' travel experience, improve tourists' satisfaction, and improve the service quality and efficiency of tourism management, so as to improve tourists' sense of tourism experience. At the same time, tourism enterprises can also analyze, calculate, and summarize according to big data, constantly tap the market demand of the tourism industry, and improve the satisfaction of tourists. According to the analysis and positioning, so as to find

the law of the tourism market, such as different groups of preferences for different tourism cities, tourism activities, and preference for tourism transportation, these are problems to be considered and solved in the development of the tourism industry [2]. In tourism activities, the calculation and summary of big data can accurately grasp the preferences of tourists, so as to meet the various needs of tourists, enhance the experience and satisfaction of tourists, and thus promote the development of the tourism industry [3].

A sensor network represents a new computer network and integrates wireless communication technology, network technology, sensor technology, computer technology, and embedded system and can organically integrate logical information world and objective physical world, inject new data into the logical world, solve data source problem, and also realize human-computer interaction and the "ubiquitous, ubiquitous" computing concept. In a sense, the sensor network organizes the information world, the physical world, and the human society into a large three-dimensional system. Artificial intelligence (AI) is an emerging scientific

technology to study and develop theories, methods, techniques, and application systems to simulate and extend human intelligence. Since the birth of the artificial intelligence concept, it has experienced several generations of changes, and its own connotation is constantly rich. Nowadays, artificial intelligence has been integrated with the Internet of things, big data, mobile terminals, Internet+, and other concepts and constantly combined with the development of the times and national policies, so that it has entered a new stage of development and development field. At present, the concept of "AI+" is gradually being accepted by the public, and intelligent life has also ushered in a new era of development with the help of artificial intelligence. With the help of artificial intelligence, all fields of society have shown a broad development space, which not only changes the development mode of various fields but also changes the overall framework, development concept, and operation mode of various fields. Among them, artificial intelligence is widely used in the field of education, which has also attracted the attention of universities and many researchers [4].

This paper mainly considers the following three problems. First, considering the condition constraints of tourism enthusiasts and other practical factors for the different requirements of minimum time consumption, for 2015A scenic spots and several 4A scenic spots, an improved TSP model based on the ND-GA algorithm is established for the cost of aircraft, high-speed rail, and self-driving and the overall structure of the wireless sensor network at the least travel cost and gives a mathematical model of wireless transmission energy consumption. At the same time, based on the different stages of travel experience index influence factors classification and constitute tourism experience index, using particle group algorithm based projection tracing method to index allocation weight, establishing the highest tourism experience index optimization model, based on the above two optimization model introduced tourist attitude parameter to establish 10 years travel route plan multi-target planning model, and by solving the model to get 10 years detailed travel plan. Finally, considering the accommodation fee and catering fee in the next 10 years, a combined prediction model is constructed to forecast the above cost and improve the multitarget planning model built above, finally obtaining a ten-year travel route design model based on multitarget dynamic optimization and a detailed travel plan by solving the model [5, 6].

2. Research Technique

2.1. Application of AI Wireless Sensors in Tourism Activities

(1) Grasp the tourism needs of tourists

The sensor network represents a new computer network and integrates wireless communication technology, network technology, sensor technology, computer technology, and embedded system and can organically integrate logical information world and objective physical world, inject new data into the logical world, solve data source problem, and also

realize human-computer interaction and the "ubiquitous, ubiquitous" computing concept. In a sense, the sensor network organizes the information world, the physical world, and the human society into a large three-dimensional system. By taking big data as an example, a variety of data in tourism, including tourists' personal preferences and consumption habits, not only do these data have distinct personal characteristics but also it has the characteristics of a dynamic distribution [7]. As an activity that people participate in at their leisure time, tourism does not belong to people's daily activities, because there is a personalized need for tourism; the time, place, way, and purpose where they travel are different; and the data they form in tourism activities are also diverse. Big data of tourism is often not restricted by culture, region, country, language, and number of people, which can bring economic benefits to the society. Many businesses and individuals in the tourism industry want to create benefits by tapping into tourists' demand for tourism, but the data that needs to be collected is very numerous and complex, so it is more difficult to find a certain rule in it. And the application of big data solves this problem very well; businesses and individuals can tap on big data, analysis, and positioning according to previous tourism data. So as to find the law of the tourism market, such as the preferences of different groups for different tourism cities, tourism activities, and preference for tourism transportation, these are all the problems to be considered and solved in the development process of the tourism industry [8, 9]. In tourism activities, big data calculation and summary can accurately grasp the preferences of tourists, to then meet the various needs of tourists and enhance the experience and satisfaction of tourists, thus promoting the development of the tourism industry.

(2) Reduce operating costs and improve the tourist experience

Today, more and more people choose to travel on their breaks; thus, there is a growing demand for tourism information, and the requirements for the service quality of tourist attractions are also getting higher and higher. As the number of visitors increases, the workload of the scenic area staff is also getting bigger and bigger. In order to provide tourists with a better experience environment and services, the scene has to increase the scenic area staff. In the long run, it will greatly increase the cost of operations, leading to the increased difficulty of management. Thus, many scenic spots use artificial intelligence tools to replace artificial labor; not only will this reduce the cost of operations but also it can reduce the work pressure of the staff. For example, a face recognition system is set up at the entrance of the scenic area, visitors can buy tickets online, and ticket inspection is automated, so as to avoid the tedious manual ticket checking and the waste of human resources [10–12].

(3) Self-service is available for visitors

Artificial intelligence technologies such as face recognition, voice recognition, language translation, image consolidation, and tourist information sorting and transmission have

been very widely used in the tourism industry, and the audience is growing wider and wider. Previously, it has mainly provided services to companies or individuals engaged in the tourism industry, and now, a lot of AI technologies can also provide self-service to tourists, such as electronic tour guides. Visitors can open the e-tour guide function free of charge or paid through WeChat scanning code; no matter which scenic spot the tourist goes, e-guides can all locate visitors through satellite positioning, and according to the characteristics of the scenic spots, historical stories are accurately introduced. Artificial intelligence not only provides many convenience to tourists. It can also greatly reduce the possible risks in the travel process and can operate efficiently and continuously [13, 14]. Another example is that if tourists accidentally get lost after entering the scenic spot, they can find the correct tour route through the navigation system, so as to avoid some risks to a certain extent and ensure the safety of tourists in the travel process.

2.2. The Application of AI Wireless Sensors in Tourism Activities

- (1) The demand for personnel in some positions is reduced

Although the application of AI in tourism activities brings many benefits, there are also various problems in its practical application. Tourism is a pillar industry for some countries; not only can it bring great economic benefits to these countries but also it offers a lot of jobs. According to statistics, the number in direct and indirect employment in the tourism industry reached more than 76 million. Once artificial intelligence is heavily applied in tourism activities, some basic jobs, such as ticket sales, ticket checking, and other positions, will gradually reduce the demand for personnel [15, 16].

- (2) Destruction of the environment

The application of artificial intelligence technology in tourism activities will also have a greater demand for natural resources, because artificial intelligence technology is mainly on the basis of information technology and the development of information technology; then, artificial intelligence technology is widely used in tourism activities; more natural resources need to be invested to guarantee the hardware facilities in AI. It will cause some degree of damage to the environment.

- (3) There are safety risks

It is well known that AI applications require computer systems, and too reliance on computer systems can cause problems such as information security. If artificial intelligence is hacked, it could paralyze the system, causing the loss of tourist information and data or malicious use. At the same time, some criminals will also use AI technology to steal tourists' personal information and property; this brings spiritual and material losses to the tourists [17, 18].

2.3. Overall Design of the Wireless Sensor Networks

- (1) Fault tolerance: the impact of the failure of partial sensor nodes in the region is on the overall performance of the network. The fault tolerance emphasizes that the network has the ability to keep the network overall communication after some sensor nodes. If used $R_k(t)$ represents a single node K 's fault tolerance or reliability, the mathematical model of the indicator meets the Poisson distribution, and the fault tolerance (1) of a single node K within the time period $(0, t)$ is represented:

$$R_k(t) = e^{-\lambda_k} \frac{\lambda_k^k}{k!}, \quad (1)$$

where λ_k shows the failure rate of the node K in the time period T .

- (2) Scale-type (scalability) index: the number of nodes in the sensor network varies depending on the actual application requirements. If the number of nodes reaches the maximum region tolerance, this not only affects the normal communication between the nodes in the region but also increases the operating cost of the network. This indicator mainly calculates the number of sensor nodes per unit area. The area density knife is shown in

$$\mu(R) = \frac{(N \cdot \pi R^2)}{A}, \quad (2)$$

where N represents the number of nodes scattered within the region A and R is the effective communication radius of a single sensor node.

2.4. Study on the Optimal Tourist Route. The TSP question is descriptive to finding a distance between all cities given a few cities. In addition, the path that each city is only visited once and the shortest total path distance is guaranteed to first assume 2015A scenic spots as one trip, and then the optimization of the objective function is solved through the corresponding constraints to obtain the optimal multiple travel scheme [19].

2.4.1. Establishment of Excellent Tourist Route Model Constraints

- (1) Driving time

as one trip, and then the optimization of the objective function is solved through

For driving time, according to the question, it can be divided into three situations: (a) an 8-hour tour all day with no more than 3 hours of driving; (b) half-day (4 hours) tour driving time of no more than 5 hours; and (c) no tour on the day, no more than 8 hours. The TSP model is now improved

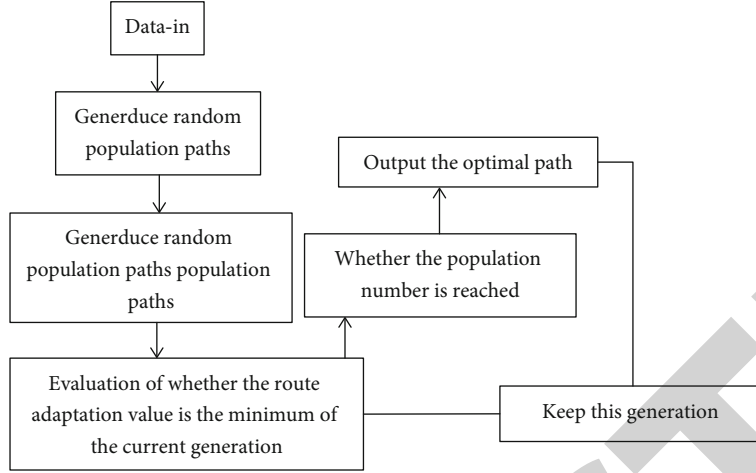


FIGURE 1: The flow chart of the ND-GA algorithm.

according to the driving time; that is, the enhanced constraints are discussed in four situations:

Situation 1: the minimum tour time of the scenic spot skj is half a day (4 hours)

Situation 2: the minimum tour time of scenic skj is one day (8 hours)

Situation 3: the minimum tour time of scenic spot skj is a day and half (12 hours)

Situation 4: the minimum tour time for the scenic spot skj is two days (16 hours)

(2) Location relationship of scenic spots and one city

The maximum distance between cities is the distance between Kuggar Old Town scenic spot in Kashgar and Kashgar. It is 1,080 km, and the driving time is about 14 hours.

$$t_1(A_{kj1}, S_{kj}) = t_1(S_{kj}, A_{kj2}) \leq 14. \quad (3)$$

(3) City-city location relationship

By calculation, according to the driving time of the two furthest transit cities which is 78 hours, there are

$$t_1(A_{ki}, A_{kj1}) = t_1(A_{kf1}, A_{ki}) \leq 78. \quad (4)$$

(4) Visit time

For a specific scenic spot, the longest minimum stay time is two days in half a day (in 4 hours).

$$t_2(S_{kj}) = 4n_{\text{standard}}n \leq 4. \quad (5)$$

3. Interpretation of Result

3.1. ND-GA Algorithm. To solve the mathematical model of energy consumption for wireless transmission, we introduce a normal distribution random number, improve the traditional genetic algorithm, obtain the ND-GA algorithm, and finally give the algorithm process; as shown in Figure 1, the model is solved.

The improved TSP model was computed based on the ND-GA algorithm to obtain 24 travel routes. Its satisfaction time is the most, and you can visit all 2015A scenic spots. Results are shown. It will take at least 12 years to visit all 5A attractions. We give a detailed analysis on one of these trips, as shown in Table 1.

3.2. The Travel Experience Is the Highest

3.2.1. Determination of the Evaluation Indicators and Their Weights. Assessing the travel experience index is both a difficult and complex inter topic. Thus, in this paper, we follow the feasibility principles and the family chooses scientific and reasonable indicators on the basis of learning and abandonment principle. At the same time, we determine the weights of each metric using the projection tracing method of the particle group algorithm, as shown in Table 2.

3.2.2. The Combination of WPGA Operators Predicts Chess Patterns to Study Changes in Future Travel Costs. Forecast the future transportation expenses, accommodation expenses, tourism and catering expenses, and tourism shopping expenses; first, we utilize three commonly used single items: prediction method gray prediction model, BP neural network prediction model, and support vector machine regression prediction mode. It is then proposed based on the combinatorial predictive model of the weighted geometric power average (WPGA) operator.

TABLE 1: Details of a single tour.

Feature spot	Circuit	Driving time between scenic spots	Visit time
Ordos Igin Holo Banner Genghis Khan Mausoleum tourist area	Xi'an-Ordos	10.07	One day
Ordos Dalat Banner Xiangshui Shawan scenic spot	Dosdarat banner	9.77	A long time
Shizuishan Pingluo County sand lake tourism scenic spot	Maoshan City-Pingluo Cou	1.20	A long time
Yinchuan town fort west film studios	Town North Fort-Lingwu City	0.93	A long time
Zhongwei Shapotou tourist scenic spot	Lingwu City-Zhongwei City, Shapotou District	1.17	A long time
Tower temple scenic spot in Huangzhong County, Xining City	Xining City-Huangzhong County	2.68	One day
Qinghai Lake scenic area	Huangzhong County-Haibei Tibetan Autonomous Prefecture	4.10	A long time
Jiayuguan cultural relics scenic spot	Gangcha County-Jiayuguan City	5.80	One day
Jiuquan City Dunhuang sand crescent spring scenic area	Jiayuguan City-Dunhuang City	3.42	A long time
Xi'an	Dunhuang City-Xi'an	1.07	

TABLE 2: Quality evaluation of tourism experience and weight allocation of index Hugh factors.

To evaluate the total target layer	Evaluation of the project layer	Weight	Evaluation factor layer	Weight	Total ranking
Tourism experience quality evaluation	Total ranking	0.23	Convenient degree (C11)	0.44	0.0217
			Punctuality (C12)	0.36	0.0644
			Punctuality (C12)	0.2	0.1399
	Travel and catering (B2)	0.15	Feature (C21)	0.38	0.1210
			Tariff (C22)	0.30	0.146
			Handy (C23)	0.32	0.1002
			Tariff (C31)	0.27	0.0055
			Handy (C32)	0.32	0.1297
	Travel accommodation (B3)	0.14	Comfort (C33)	0.45	0.1427
			Image of the scenic spot (C41)	0.32	0.1037
			Management and service (C42)	0.38	0.1158
	Tourist attraction (B4)	0.30	Local specialty characteristics (C51)	0.43	0.0599
			Tariff (C52)	0.35	0.1001
	Travel shopping (B5)	0.18	Handy (C53)	0.22	0.026

Definition 1. If the WPGA is available, $R^n \rightarrow n$. For the n element function, satisfy the following form:

$$\text{WPGA}(a_1, a_2, \dots, a_n) = \prod_{i=1}^n \frac{w_i(1 + T(a_i))}{a_i w_i(1 + T(a_i))}. \quad (6)$$

Among them, $w = (w_1, w_2, \dots, w_n)T$ is the weighted vector related to the WPGA satisfied:

$$w_i = 1, i = 1, 2, \dots, n, T(a_i) = \sum_{j=1}^n w_j \sup(a_i, a_j). \quad (7)$$

Then, the function WPGA dimension weighted power geometric average operator, simply the WPGA operator.

The combined forecast model allows the transportation fee, accommodation fee, travel catering fee, and the weight forecast prediction results of the three square monomial prediction methods [20]. The combination trend of

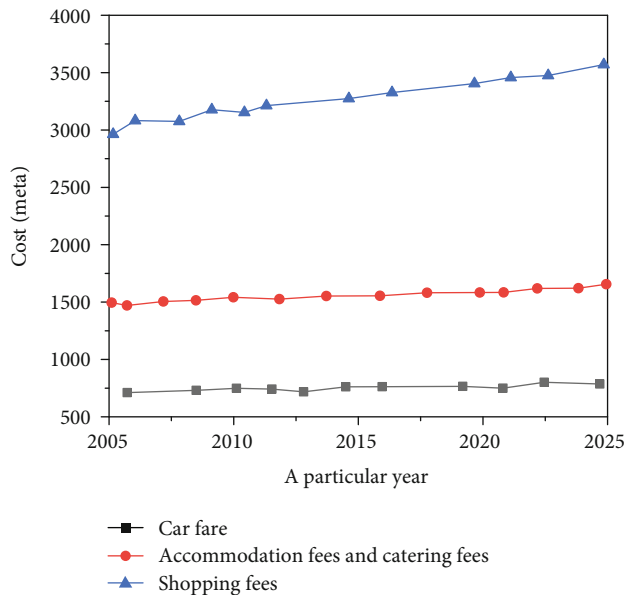


FIGURE 2: Change trends of transportation expenses, accommodation expenses, tourism catering expenses, and tourism shopping expenses.

transportation, accommodation, tourism catering, and travel shopping fees is shown in Figure 2.

4. Conclusions

With the rapid development of the tourism industry, more and more tourists have higher requirements for the quality and service of tourism activities, so the application of artificial intelligence technology provides a new development opportunity for the tourism industry. The application of AI wireless sensor technology can not only improve the work efficiency of employees but also bring convenience to tourists and enhance the experience and satisfaction of tourists. For example, according to the tourists' search records, the relevant information can be pushed to the tourists to help the tourists make better decisions. At the same time, the application of AI wireless sensor technology can also make the work of scenic spots more efficient; for example, a face recognition system can improve the speed of ticket checking. Although AI wireless sensor technology is widely used in tourism activities, there are some problems, which require the continuous optimization and innovation of AI wireless sensor technology by relevant practitioners to better serve tourists.

Data Availability

The data used to support the findings of this study are available from the corresponding author upon request.

Conflicts of Interest

The authors declare that they have no conflicts of interest.

References

- [1] W. C. Hu, H. T. Wu, H. H. Cho, and F. H. Tseng, "Optimal route planning system for logistics vehicles based on artificial intelligence," *Journal of Internet Technology*, vol. 21, no. 3, pp. 757–764, 2020.
- [2] L. Jia and L. Li, "Research on core strength training of aerobics based on artificial intelligence and sensor network," *EURASIP Journal on Wireless Communications and Networking*, vol. 2020, no. 1, Article ID 164, 16 pages, 2020.
- [3] Y. Wang and E. Liu, "Virtual reality technology of multi UAVearthquake disaster path optimization," *Mathematical Problems in Engineering*, vol. 2021, no. 8, Article ID 5525560, 9 pages, 2021.
- [4] Y. C. Fan, F. Liu, X. Ning et al., "Improved-learning method for multirobot formation and path planning with concave obstacles," *Journal of Sensors*, vol. 2021, Article ID 4294841, 14 pages, 2021.
- [5] Y. Zhao, Y. Li, X. Zhang, G. Geng, W. Zhang, and Y. Sun, "A survey of networking applications applying the software defined networking concept based on machine learning," *IEEE Access*, vol. 7, no. 99, pp. 95397–95417, 2019.
- [6] A. Machmudah and S. Parman, "Bezier curve collision-free route planning using meta-heuristic optimization," *International Journal of Artificial Intelligence & Robotics (IJAIR)*, vol. 3, no. 1, pp. 1–14, 2021.
- [7] I. Ahmad, R. Md Noor, R. Alroobaea et al., "Aiding traffic prediction servers through self-localization to increase stability in complex vehicular clustering," *Complexity*, vol. 2021, no. 3&4, Article ID 6627539, 11 pages, 2021.
- [8] Z. Chen, Y. Lian, and Z. Lin, "Research on business English autonomous learning based on artificial intelligence and improved BP network model," *Journal of Intelligent and Fuzzy Systems*, vol. 3, pp. 1–12, 2020.
- [9] Z. Zhang and L. I. Fang, "Research on the water pollution monitoring and rapid decision-making system based on artificial intelligence agent," *Journal of Environmental Protection and Ecology*, vol. 20, no. 3, pp. 1565–1573, 2019.
- [10] Q. Liu and Z. Huang, "Research on intelligent prevention and control of covid-19 in China's urban rail transit based on artificial intelligence and big data," *Journal of Intelligent and Fuzzy Systems*, vol. 39, no. 6, pp. 9085–9090, 2020.
- [11] M. Huang, S. Liu, Y. Zhang, K. Cui, and Y. Wen, "Research on the university intelligent learning analysis system based on AI," *Journal of Intelligent and Fuzzy Systems*, vol. 31, pp. 1–10, 2021.
- [12] V. L. Mango, M. Sun, R. T. Wynn, and R. Ha, "Should we ignore, follow, or biopsy? Impact of artificial intelligence decision support on breast ultrasound lesion assessment," *American Journal of Roentgenology*, vol. 214, no. 6, pp. 1445–1452, 2020.
- [13] K. C. Leonard, F. Hasan, H. F. Sneddon, and F. You, "Can artificial intelligence and machine learning be used to accelerate sustainable chemistry and engineering?," *ACS Sustainable Chemistry & Engineering*, vol. 9, no. 18, pp. 6126–6129, 2021.
- [14] J. Licato and Z. Zhang, "Correction to: evaluating representational systems in artificial intelligence," *Artificial Intelligence Review*, vol. 52, no. 4, pp. 2743–2751, 2019.
- [15] A. Y. Nesterov, A. V. Nikonorov, and A. V. Kupriyanov, "On the work of the Samara branch of the RAS scientific council on the methodology of artificial intelligence and cognitive

Retraction

Retracted: Wireless Network Sensing of Urban Surface Water Environment Based on Clustering Algorithm

Wireless Communications and Mobile Computing

Received 28 November 2023; Accepted 28 November 2023; Published 29 November 2023

Copyright © 2023 Wireless Communications and Mobile Computing. This is an open access article distributed under the Creative Commons Attribution License, which permits unrestricted use, distribution, and reproduction in any medium, provided the original work is properly cited.

This article has been retracted by Hindawi, as publisher, following an investigation undertaken by the publisher [1]. This investigation has uncovered evidence of systematic manipulation of the publication and peer-review process. We cannot, therefore, vouch for the reliability or integrity of this article.

Please note that this notice is intended solely to alert readers that the peer-review process of this article has been compromised.

Wiley and Hindawi regret that the usual quality checks did not identify these issues before publication and have since put additional measures in place to safeguard research integrity.

We wish to credit our Research Integrity and Research Publishing teams and anonymous and named external researchers and research integrity experts for contributing to this investigation.





The corresponding author, as the representative of all authors, has been given the opportunity to register their agreement or disagreement to this retraction. We have kept a record of any response received.

References

- [1] Q. Zhao, X. Yang, X. Dong, and H. Li, "Wireless Network Sensing of Urban Surface Water Environment Based on Clustering Algorithm," *Wireless Communications and Mobile Computing*, vol. 2021, Article ID 2829195, 6 pages, 2021.

Research Article

Wireless Network Sensing of Urban Surface Water Environment Based on Clustering Algorithm

Qichao Zhao ^{1,2}, Xiufeng Yang ^{1,2}, Xuxin Dong ^{2,3} and Huairui Li ⁴

¹School of Remote Sensing and Information Engineering, North China Institute of Aerospace Engineering, Langfang Hebei 065000, China

²Hebei Remote Sensing Information Processing and Application of Collaborative Innovation Center, Langfang Hebei 065000, China

³School of Electronic and Information Engineering, Hebei University of Technology, Tianjin 300131, China

⁴Beijing Insights Value Technology CO., LTD., Beijing 100071, China

Correspondence should be addressed to Qichao Zhao; 20150401161@m.scnu.edu.cn

Received 8 October 2021; Revised 26 October 2021; Accepted 15 November 2021; Published 6 December 2021

Academic Editor: Balakrishnan Nagaraj

Copyright © 2021 Qichao Zhao et al. This is an open access article distributed under the Creative Commons Attribution License, which permits unrestricted use, distribution, and reproduction in any medium, provided the original work is properly cited.

To improve the wireless sensing image extraction technology of urban surface water environment, a regional FCM clustering method combined with water index was proposed in this paper. The normalized water index (NDWI) was obtained by calculating the fusion multispectral wireless sensing image. Through the combination with normalized water index, fuzzy clustering results were obtained by RFCM algorithm proposed in this paper. The optimal threshold was selected to defuzzify the fuzzy clustering results, and finally, the extraction results of urban surface water were obtained. The accuracy of the proposed algorithm was compared with that of the traditional surface water extraction algorithm. The experimental results showed that the size of different neighborhood regions affected the water extraction accuracy. In W city, the kappa coefficient of MFCM16 was 0.41% higher than that of MFCM8, and the overall classification accuracy of MFCM16 was 1.33% higher than that of MFCM. In G city area, the kappa coefficient of MFCM16 was 1.81% higher than that of MFCM8, and the overall classification accuracy of MFCM16 was 1.7% higher than that of MFCM. Comparing the RFCM algorithm with other algorithms, the RFCM algorithm obtained the best experimental results, to reduce the “salt-and-pepper phenomenon” effect.

1. Introduction

With the development of wireless sensing technology, especially the improvement of wireless sensing image processing level, wireless sensing is increasingly widely used in various social fields. In terms of urban planning, wireless sensing can realize dynamic monitoring of land use, supervision and control of air quality, urban ecological environment planning and construction, etc. [1]. Urban surface is a subsystem of urban ecosystem. As an important part of urban ecosystem, it plays an important role in improving urban ecological environment quality and improving residents' living standards [2]. In recent years, many cities at home and abroad have applied wireless sensing technology to surface information extraction to dynamically master the coverage area, optimize the spatial structure of green space, improve the potential of sustainable development of the city, and realize the overall planning [3].

Compared with the traditional way, the extraction of green space information by aerial wireless sensing image has the advantages of wide field of view, strong macroscopic view, clear and realistic image, large amount of information, short repetition cycle, and convenient data collection. It is very economical in terms of manpower, material resources, and financial resources and has a short time and high efficiency. Wireless sensing is a comprehensive earth detection technology developed in the century [4]. That is, collect information about an object without directly touching it. It usually refers to the acquisition of various ground object information from the air or space by some kind of sensor and the extraction and analysis of this information, so as to measure and judge the nature or characteristics of the ground object. With the development of space technology, optical technology, sensor technology, computer technology, and modern communication technology, wireless sensing technology has made great

progress [5]. Since the rise of the century, the development of wireless sensing technology is increasingly rapid, on the basis of aerial photogrammetry, with the rapid development of modern science and technology such as space technology and electronic computer, as well as the needs of the development of geoscience, biology, and other disciplines; as an emerging technical discipline gradually developed, it has formed a relatively complete basic theoretical system and a series of technical support [6]. As a means of information acquisition, wireless sensing technology has penetrated into various fields of the national economy, such as agriculture, forestry, geology, meteorology, oceanography, environment, urban planning and land management, and other professional fields and departments [7]. Zhao et al. proposed the main methods of urban wireless sensing summarized as postclassification comparison method, multitemporal complex method, image difference ratio method, vegetation index method, principal component analysis, and transformation vector analysis [8]. Song et al. proposed a new urban land use classification method, which determines urban building density based on image texture to determine land use type. They used panchromatic spectral images to conduct experiments in Athens, Greece, which is higher than the traditional maximum likelihood method. This method can be used for urban wireless sensing monitoring such as urban land use change, urban expansion, and illegal building monitoring [9]. Awad et al. adopted the difference method, used spatial texture information and set certain constraints to eliminate the change information of agricultural land, and accurately extracted the annual urban expansion area [10]. Based on the current research, MFCM algorithm only considers the fixed neighborhood of each pixel to improve the robustness of the algorithm [11]. Most of the mature monitoring system instruments are imported. The imported instruments have high precision and many measuring indexes, but they are expensive and cumbersome to operate. The wireless frequency domain used in China needs to be specially applied to the radio department. There are also some independent research and development monitoring systems, but compared with foreign countries, there are still some problems, such as the number of monitoring stations and limited scope. In particular, in the wireless sensor network, the application of wireless sensor network technology is less. Real-world objects, however, are irregular neighborhood areas. On the basis of the current research, this paper proposes a regional FCM clustering method combined with water index, which calculates the normalized water index (NDWI) through the fusion of multispectral wireless sensing images. Combined with normalized water index, fuzzy clustering results were obtained by RFCM algorithm proposed in this paper. The optimal threshold was selected to defuzzify the fuzzy clustering results, and finally, the extraction results of urban surface water were obtained. The accuracy of the proposed algorithm was compared with that of the traditional surface water extraction algorithm. The experimental results showed that the size of different neighborhood regions affected the water extraction accuracy. In W city, the kappa coefficient of MFCM16 was 0.41% higher than that of MFCM8, and the overall classification accuracy of MFCM16 was 1.33% higher than that of MFCM. In G city area, the

kappa coefficient of MFCM16 was 1.81% higher than that of MFCM8, and the overall classification accuracy of MFCM16 was 1.7% higher than that of MFCM. Comparing the RFCM algorithm with other algorithms, the RFCM algorithm obtained the best experimental results, to reduce the “salt-and-pepper phenomenon” effect [12]. The innovation of sensor technology and communication technology makes wireless sensor network technology more perfect, which is often used in environmental monitoring. Using wireless sensor network to monitor water quality and obtain water quality data for storage and remote transmission can well solve the shortcomings of traditional monitoring methods and achieve real-time, low-cost, and long-term measurement of the environment.

2. Methods

2.1. Wireless Sensing Data Preprocessing. Two-scene gF-2 domestic high-resolution wireless sensing images (Guangzhou and Wuhan) were used to extract urban surface water. (1) Firstly, radiometric calibration and atmospheric correction are performed on the multispectral data and panchromatic data, and then, a 1 m resolution multispectral wireless sensing image is obtained by using NND (Nearest Neighbor Diffusion) image fusion algorithm. (2) Use morphological shadow index to remove building shadow. (3) Normalized water index (NDWI) was obtained by using fusion multispectral wireless sensing images. (4) Combined with normalized water index, fuzzy clustering results were obtained by using the RFCM algorithm proposed in this paper. (5) Select the optimal threshold to defuzzify the fuzzy clustering results, and finally, obtain the extraction results of urban surface water. (6) Artificial vectorized real surface water data is used to verify the effectiveness of the algorithm, and the accuracy of the algorithm is compared with that of the traditional surface water extraction algorithm [13].

2.2. Water Index. Water index method is a combination of single-band threshold method and multiband spectral logic operation, so as to improve the difference between water body and other ground objects and effectively suppress the influence of background noise (shadow, black impervious surface, ice and snow, etc.). Water index method is to use the water body in visible light reflectance which is generally low, less than 10%, generally 4%-5%, and gradually decreases with the increase of wavelength, but in the near-infrared band, water body almost shows full absorption. In order to enhance the difference between water body and other ground objects, the ratio calculation of visible band and near-infrared band is carried out or different weights are given to the band based on the above principle. At present, the mainstream water index includes normalized water index (NDWI), improved normalized water index (MNDWI), enhanced water index (EWI), and automated water extraction index (AWEI). However, gF-2 domestic high-resolution wireless sensing image has only one panchromatic band, which consists of four multispectral bands, namely, red, green, blue, and near middle red, without middle infrared band and thermal infrared band. Therefore,

normalized water index (NDWI) is adopted in this paper. The specific calculation is shown in Formula (1). This water index has a good suppression effect on background noise [14].

$$\text{NDWI} = \frac{\rho_{\text{Green}} - \rho_{\text{NIR}}}{\rho_{\text{Green}} + \rho_{\text{NIR}}}, \quad (1)$$

where ρ_{Green} is the surface reflectance of green band and ρ_{NIR} is the surface reflectance of near-infrared band.

2.3. Regional FCM Clustering Algorithm

2.3.1. Principle of Regional FCM Clustering Algorithm. RFCM (regional fuzzy C-means) clustering algorithm is derived from traditional FCM algorithm and improved FCM algorithm. The traditional FCM algorithm only considers the information of the pixel itself, not the spatial information of the pixel neighborhood. The improved FCM algorithm MFCM (modified FCM) considers the spatial information of the pixel neighborhood, but it only considers the spatial information of the fixed window in the pixel regular neighborhood. Real objects are irregular neighborhood areas (image objects). The regional FCM clustering algorithm will determine the size of the neighborhood region according to the spatial heterogeneity of the pixel and the neighborhood pixel. The principle of the RFCM algorithm only adds spatial information of pixel neighborhood region on the basis of the FCM algorithm and considers the membership degree constraint of pixel neighborhood region. Finally, the membership degree was obtained by iterative optimization of RFCM objective function considering neighborhood region constraints, and the category of pixels was determined according to the optimal threshold of membership degree. The objective function J_{RFCM} of region FCM is shown in

$$J_{\text{RFCM}} = \sum_{i=1}^C \sum_{j=1}^N \mu_{ij}^m \|x_j - v_i\|^2 + a \sum_{i=1}^C \sum_{j=1}^N \|\bar{x}_j - \text{region} - v_i\|^2, \quad (2)$$

where u_{ij} represents the membership degree that pixel J belongs to category I ; $m \in [0, 1]$ represents a weighting coefficient; $\|x_j - v_i\|^2$ represents the feature space distance between pixel J and cluster center v_i . A is the constraint parameter of neighborhood area; $\|\bar{x}_j - \text{region} - v_i\|^2$ represents the feature space distance between the mean value of the feature space of the pixel in the neighborhood of pixel J and v_i of the cluster center. By introducing Lagrange theory to optimize the objective function of regional FCM, a constraint function O_{RFCM} is constructed, as shown in

$$O_{\text{RFCM}} = \sum_{i=1}^C \sum_{j=1}^N \left(\mu_{ij}^m \|x_j - v_i\|^2 + a \sum_{i=1}^C \sum_{j=1}^N \|\bar{x}_j - \text{region} - v_i\|^2 \right) + \gamma \left(1 + \sum_{i=1}^C \mu_{ij} \right), \quad (3)$$

where λ stands for Lagrange multiplier; $\sum_{i=1}^C \mu_{ij}$ represents the sum of the membership degree of each category for the J TH pixel, where $\sum_{i=1}^C \mu_{ij} = 1$.

2.3.2. Calculation of Neighborhood Area. The key of RFCM algorithm is the calculation of neighborhood area. The size of neighborhood area is determined by the spectral difference between center pixel and neighborhood pixel. PSI index method is adopted in this paper to determine neighborhood area, which is more reasonable than fixed window neighborhood area [15]. The basic theory of the algorithm is a series of direction lines diverging from the center of the pixel in different directions as shown in Figure 1. The spectral heterogeneity of the pixel on each direction line and the central pixel is calculated. If the spectral heterogeneity is less than the threshold value and the length of the direction line is less than the threshold value, the pixel is determined as the neighborhood area of the central pixel. The calculation of spectral heterogeneity measure is shown in

$$P_d(i, k) = \sum_{s=1}^n |p_s(i) - p_s(k)|, \quad (4)$$

where $p_d(i, k)$ represents the heterogeneity measure value of the current pixel I and the neighborhood pixel K on the direction line D , $p_s(i)$ and $p_s(k)$ represent the spectral value of the center pixel and the current neighborhood pixel on band S , respectively, and N represents the number of bands. Under the condition of two thresholds, each direction line expands simultaneously from the center pixel. One threshold condition is that when the current pixel heterogeneity value is greater than the spectral constraint threshold $T1$, diffusion stops on this direction line. Another threshold condition is that the length of the direction line between the current pixel and the center pixel is less than the threshold $T2$, so the search in this direction is stopped to prevent the neighborhood on the direction line from being too large. Finally, the neighborhood region pixels that meet the conditions in each direction of the central pixel are counted, and the pixel set obtained is the neighborhood region of the pixel.

2.3.3. The Specific Process of RFCM Algorithm. Set the number of clustering $2 \leq C \leq C_{\text{num-max}} - 1$ and parameter $M > 1$, and terminate the algorithm ϵ , the maximum number of iterations n_{max} , spectral difference measure threshold, and direction line length threshold. According to the neighborhood region calculation method, the neighborhood region of each pixel of the image is determined, and $\bar{x}_j - \text{region}$ of each pixel is calculated. Initialize $v_i^{(0)}$ of each cluster center. The membership function $v_i^{(0)}$ was calculated by using the current clustering center μ_{ij}^{OP} , and then, μ_{ij}^{OP} of various clustering centers was calculated according to the membership function ϵ . According to the threshold v_i^{OP} and the maximum number of iterations n_{max} , if $\|v^{n+1} - v^n\| < \epsilon$ or the number of iterations $n \geq n_{\text{max}}$, the iteration is terminated. When the algorithm converges, the membership degree of

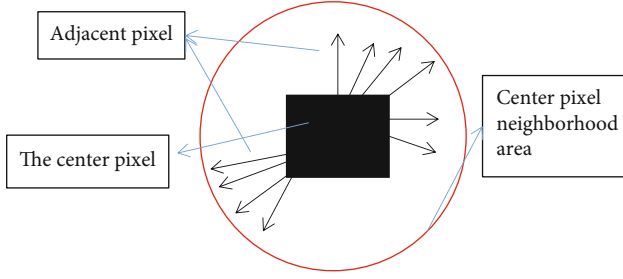


FIGURE 1: Schematic diagram of neighborhood area calculation.

each cluster center and each pixel to each cluster center is obtained, and the fuzzy clustering result is completed. Finally, the fuzzy clustering results are defuzzified according to the optimal threshold value, and the fuzzy clustering results are transformed into deterministic classification to realize the final clustering of wireless sensing images.

Compared with the spectral features of wireless sensing image, the water index improves the separability of water body and other ground objects and has a good suppression effect on background noise. Therefore, the normalized water index and shadow index are stacked with spectral features as the input features of RFCM clustering algorithm in the experiment. At the same time, in RFCM clustering algorithm, the spatial information of homogeneous neighborhood region of pixels is considered. Based on the advantages of the above two aspects, an urban surface water extraction algorithm integrating water index and RFCM was designed and applied to surface water extraction from domestic gF-2 wireless sensing images in complex urban environment.

2.4. Design Objectives of Water Environment Monitoring System Based on Wireless Sensor Network

- (1) The construction of intelligent system and the application of wireless sensing technology to achieve the measurement and monitoring of water quality
- (2) To achieve reliable, high-speed, and low-power wireless transmission of water monitoring data
- (3) Collect data and monitor data: the host computer and the web page display the location of specific water areas and sensor nodes in water and display the latest time recorded data of various water quality parameters measured by sensor nodes
- (4) Under low power consumption, it can work normally for a long time

3. Results and Analysis

The RFCM algorithm proposed in this paper is compared and analyzed with the improved MFCM algorithm (8×8 and 16×16 were considered as MFCM8 and MFCM16 in the experiment), K -means clustering algorithm, NDWI threshold algorithm (TH), and object-oriented method (OBIA). In the experiment, OA and kappa coefficients of

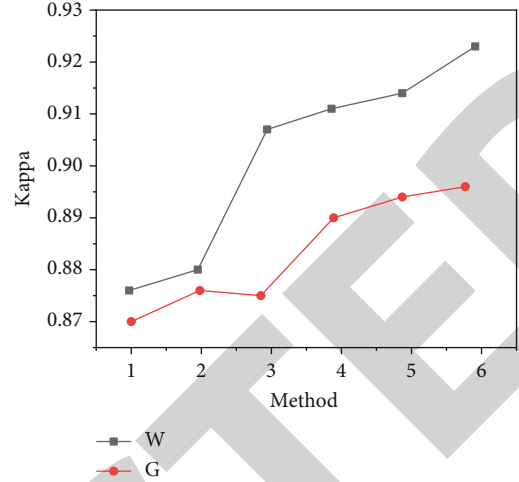


FIGURE 2: Experimental results of kappa coefficient.

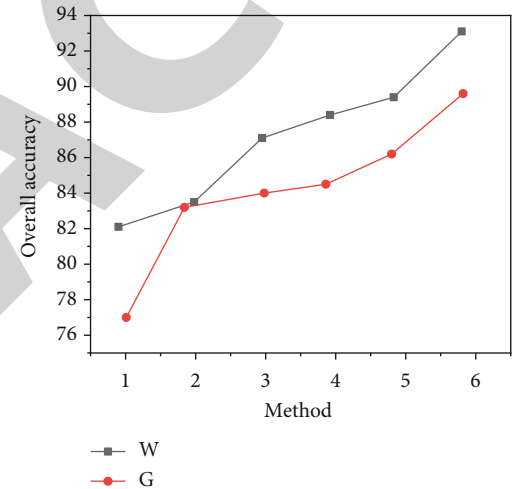


FIGURE 3: The overall accuracy of the experimental results.

overall classification accuracy were used for statistical and quantitative evaluation of accuracy, and visual discrimination was used for qualitative evaluation [16].

The classified kappa coefficients and overall accuracy of the two research areas in G city and W city are shown in Figures 2 and 3.

The kappa coefficient in G city is 89.88%, the kappa coefficient in W city is 92.49%, and the overall classification accuracy in G city is 89.14%. The overall classification accuracy of W city is 92.58%, and the classification accuracy of the method considering regional spatial information (MFCM and RFCM) and the object-oriented method (OBIA) is higher than that of the pixel-based method (K -means) and the water index threshold method (TH) and has a lower misclassification error rate and missed classification error rate [17]. Among them, in W city, the kappa coefficient of RFCM was 1%, 1.5%, and 1.3% higher than that of OBIA, MFCM8, and MFCM16, respectively. The OA of RFCM was 3.86%, 5.82%, and 4.48% higher than that of OBIA, MFCM8, and MFCM16, respectively. In city G, the

TABLE 1: Statistical table of “noise” of surface water extraction results.

Laboratory area	TH	K-means	MFCM8	MFCM16	OBIA	RFCM
W	5048	1466	1269	1140	750	469
G	8277	655	250	225	85	64

kappa coefficient of RFCM was 0.2%, 2.3%, and 0.7% higher than that of OBIA, MFCM8, and MFCM16, respectively, and the overall classification accuracy (OA) of RFCM was 3.2%, 5.83%, and 4.12% higher than that of OBIA, MFCM8, and MFCM16, respectively [18]. The OBIA method maintains the integrity of ground object better than *K*-means and TH method. RFCM and MFCM algorithms not only maintain the integrity of ground object but also better retain local details of ground object. Compared with other OBIA, *K*-means, TH, MFCM8, and MFCM16 algorithms, the RFCM algorithm can not only maintain the integrity of ground object but also better retain local details of ground object. The fine surface water bodies are effectively identified, the boundary information of surface water bodies is maintained well, and the influence of shadow of urban buildings is eliminated at the same time [19]. The improved FCM algorithm also considered the neighborhood regions with different window sizes of rules. Experimental results showed that the size of different neighborhood regions affected the water extraction accuracy. In W city, the kappa coefficient of MFCM16 was 0.41% higher than that of MFCM8, and the overall classification accuracy of MFCM16 was 1.33% higher than that of MFCM. In G city area, the kappa coefficient of MFCM16 was 1.81% higher than that of MFCM8, and the overall classification accuracy of MFCM16 was 1.7% higher than that of MFCM.

The “salt-and-pepper” phenomenon of the experimental results was quantitatively counted, and the speckle noise was defined as the water area less than the water area. Table 1 shows that compared with other algorithms, the RFCM algorithm can obviously eliminate the “salt-and-pepper phenomenon” of surface water extraction. In the comparison experiment of the six algorithms, TH has the worst effect and has a large number of noise spots. Due to the phenomenon of “same object, different spectrum, foreign object in the same spectrum” of high-resolution data, a large number of isolated noise points are caused. *K*-means algorithm is better than TH algorithm and MFCM8 and MFCM16 algorithms. Thirdly, MFCM algorithm significantly reduces the “noise” spots of surface water, which proves that the spatial information of pixel neighborhood has a certain inhibitory effect on the “noise” spots of water. The OBIA algorithm is better than MFCM8 and MFCM16. The RFCM algorithm achieves the best experimental results and has a significant effect on reducing “salt-and-pepper phenomenon” [20].

4. Conclusions

In this paper, a regional FCM clustering method combined with water index is proposed, which calculates the normalized water index (NDWI) from the fusion of multispectral wireless sensing images. Through the design of wireless

sensor network water environment monitoring system, combined with normalized water index, fuzzy clustering results were obtained by the RFCM algorithm proposed in this paper. The optimal threshold was selected to defuzzify the fuzzy clustering results, and finally, the extraction results of urban surface water were obtained. The accuracy of the proposed algorithm was compared with that of the traditional surface water extraction algorithm. Comparing the RFCM algorithm with other algorithms, the RFCM algorithm obtained the best experimental results, to reduce the “salt-and-pepper phenomenon” effect. The algorithm in some details of surface water extraction was not taken into account and will continue to be studied in the future.

Data Availability

The data used to support the findings of this study are available from the corresponding author upon request.

Conflicts of Interest

The authors declare no conflicts of interest.

Acknowledgments


The study was supported by the (1) Natural Science Foundation of Hebei Province, spectral characteristics and remote sensing identification method of black and odorous water bodies in urban and rural areas at county scale, Project No. D2020409005; (2) Scientific Research Foundation of Higher Education Institutions of Hebei Province, remote sensing recognition model of black and odorous water in Beijing-Tianjin-Hebei region based on high-resolution image, Project No. ZD2019138; and (3) National Defense Basic Scientific Research Program of China, Project No. JCKY2019407D004.

References

- [1] C. Yu, L. Wang, J. Zhao, L. Hao, and Y. Shen, “Remote sensing image classification based on rbf neural network based on fuzzy *c*-means clustering algorithm,” *Journal of Intelligent and Fuzzy Systems*, vol. 38, no. 4, pp. 3567–3574, 2020.
- [2] L. Zhang and A. Li, “Region-of-interest extraction based on saliency analysis of co-occurrence histogram in high spatial resolution remote sensing images,” *IEEE Journal of Selected Topics in Applied Earth Observations and Remote Sensing*, vol. 8, no. 5, pp. 2111–2124, 2015.
- [3] Y. Cao, Y. Xun, Y. Han et al. et al., “Feature extraction of wireless sensing images based on bat algorithm and normalized chromatic aberration,” *IFAC-PapersOnLine*, vol. 52, no. 24, pp. 318–323, 2019.

Corrigendum

Corrigendum to “MEC-Driven Fast Deformation Monitoring Based on GNSS Signal”

Bo Li,¹ Shangwei Chen,^{1,2} Yi Liu,^{1,3} Kan Xie,^{1,4} and Shengli Xie^{1,5} 

¹*School of Automation, Guangdong University of Technology, Guangzhou, China*

²*Guangdong Key Laboratory of IoT Information Technology (GDUT), Guangzhou, China*

³*Key Laboratory of Intelligent Detection and the Internet of Things in Manufacturing, Ministry of Education (GDUT), Guangzhou, China*

⁴*Guangdong-HongKong-Macao Joint Laboratory for Smart Discrete Manufacturing (GDUT), Guangzhou, China*

⁵*111 Center for Intelligent Batch Manufacturing Based on IoT Technology (GDUT), Guangzhou, China*

Correspondence should be addressed to Kan Xie; kxie@gdut.edu.cn

Received 23 September 2021; Accepted 23 September 2021; Published 30 November 2021

Copyright © 2021 Bo Li et al. This is an open access article distributed under the Creative Commons Attribution License, which permits unrestricted use, distribution, and reproduction in any medium, provided the original work is properly cited.

In the article titled “MEC-Driven Fast Deformation Monitoring Based on GNSS Signal” [1], the funding statement was omitted in error and is as follows: “This work is partially supported by the Key Research and Development Program of Guangdong Province (2019B010141001).”

References

- [1] B. Li, S. Chen, Y. Liu, K. Xie, and S. Xie, “MEC-driven fast deformation monitoring based on GNSS signal,” *Wireless Communications and Mobile Computing*, vol. 2021, Article ID 9517133, 9 pages, 2021.

Retraction

Retracted: Geological Mineral Energy and Classification Based on Machine Learning

Wireless Communications and Mobile Computing

Received 28 November 2023; Accepted 28 November 2023; Published 29 November 2023

Copyright © 2023 Wireless Communications and Mobile Computing. This is an open access article distributed under the Creative Commons Attribution License, which permits unrestricted use, distribution, and reproduction in any medium, provided the original work is properly cited.

This article has been retracted by Hindawi, as publisher, following an investigation undertaken by the publisher [1]. This investigation has uncovered evidence of systematic manipulation of the publication and peer-review process. We cannot, therefore, vouch for the reliability or integrity of this article.

Please note that this notice is intended solely to alert readers that the peer-review process of this article has been compromised.

Wiley and Hindawi regret that the usual quality checks did not identify these issues before publication and have since put additional measures in place to safeguard research integrity.

We wish to credit our Research Integrity and Research Publishing teams and anonymous and named external researchers and research integrity experts for contributing to this investigation.

The corresponding author, as the representative of all authors, has been given the opportunity to register their agreement or disagreement to this retraction. We have kept a record of any response received.

References

- [1] Y. Lv and L. Lu, "Geological Mineral Energy and Classification Based on Machine Learning," *Wireless Communications and Mobile Computing*, vol. 2021, Article ID 2788161, 7 pages, 2021.

Research Article

Geological Mineral Energy and Classification Based on Machine Learning

Yan Lv  and Laijun Lu 

College of Earth Sciences, Jilin University, Changchun Jinlin, 130061, China

Correspondence should be addressed to Yan Lv; 1530509005@stu.suda.edu.cn

Received 7 October 2021; Revised 25 October 2021; Accepted 1 November 2021; Published 26 November 2021

Academic Editor: Balakrishnan Nagaraj

Copyright © 2021 Yan Lv and Laijun Lu. This is an open access article distributed under the Creative Commons Attribution License, which permits unrestricted use, distribution, and reproduction in any medium, provided the original work is properly cited.

In order to mine geological mineral energy and study on geological mineral energy classification, a method based on a wireless sensor was proposed. Of logistic regression, artificial neural networks, random forests, and main wireless sensor algorithms of support vector machine (SVM) with the model in the application of the energy mineral resource prediction practice effects are reviewed and discuss the practical application in the process of sample selection, the wrong points existing in the cost, the uncertainty evaluation, and performance evaluation of the model using wireless sensor algorithm, random forest of the probability distribution of mineralization in the study area is calculated, and five prospecting potential areas are delineated. The results show that the ratio of ore-bearing unit and non-ore-bearing unit is 1 : 1, and the best random forest training model is obtained. 70% of the training sample set was randomly selected as the training set, and the remaining 30% was used as the test set to construct the random forest model. The training accuracy of the model is 96.7%, and the testing accuracy is 96.5%. Both model training accuracy and model testing accuracy are very high, which proves the accuracy of RF model construction and achieves satisfactory results. In this study, a wireless sensor is successfully applied to 3D mineral energy prediction, which makes a positive exploration for mineral resource prediction and evaluation in the future. Finally, the prediction of mineral resource energy based on a wireless sensor is an important trend of future development.

1. Introduction

The reserves of mineral resources are a symbol of economic development. With the increasing social demand for mineral resources and the increasing difficulty of prospecting for mineral resources, the research on new theories and methods of prediction and evaluation of mineral resource energy has been promoted. Mineral resource energy evaluation has gone through three stages: the stage of mineral deposit statistical prediction, marked by the application of probability statistics and multivariate statistics [1]. The stage of resource and energy prediction and evaluation based on the theory of seeking difference is mainly marked by the theory and method of “geological anomaly mineralization and metallogenic prediction” initiated in 1990 and “comprehensive information metallogenic prediction” [2]. In the stage of “digital ore prospecting” and resource and energy prediction and evaluation, the application of data science in mineral

exploration is emphasized, and the practical problems in mineral exploration are solved by data analysis theory and method, with “triple” metallogenic prediction and resource evaluation theory and method as the main symbol [3]. The introduction of nonlinear and complexity theory and model into mineral resource evaluation is a rising research field in the world, and the representative one is the prediction theory and model of multiple formation proposed by Cheng Qiuming. In recent years, with the advent of the age of geological information, all kinds of geological data show an explosive growth trend, which brings challenges and opportunities to the development and innovation of mineral resource prediction and evaluation theories and methods. In order to solve the high dimension, high computational complexity, and uncertainty and realize multisource heterogeneous prospecting space data intelligent mining and integration, wireless sensor methods to dig deeper into the geological data, information fusion, and prediction

evaluation provide a useful tool and have become the focus in the current energy mineral resource prediction and frontier [4].

The core of mineral prediction is feature extraction and integration of geospatial data. The current research focus and frontier focus on feature extraction and integration of deep-level mineralized information. Deep mineralization information refers to the mineralization information that is difficult to be identified by traditional methods and technologies, including hidden mineralization information, deep mineralization information, and specific information extracted under complex geological background [5]. Mining and integration of deep mineralization information are the keys to successfully discover concealed ore and deep ore. In the era of big data, how to carry out deep-level mineralization information mining and integration based on a wireless sensor is the frontier field of mineral prediction [6]. Nurmaini et al. found in the study that when large sample MNIST data set was used, SVM accuracy was 0.88 and CNN accuracy was 0.98. When the small sample COREL1000 data set was used, the accuracy of SVM was 0.86 and CNN was 0.83 [7]. Aravinda and Lin proposed the 3D prediction process of deep mineral resources, namely, “geological information integration - quantitative extraction of metallogenic information - three-dimensional quantitative prediction,” and studied the 3D quantitative analysis of geological body shape, quantitative extraction of ore-controlling geological factors, and three-dimensional quantitative prediction of ore bodies [8]. Siomos et al., with the application of three-dimensional comprehensive information metallogenic prediction method, carried out a case study on large-scale three-dimensional metallogenic prediction [9].

Based on this, this paper proposes a method based on a wireless sensor. Random forest has higher prediction accuracy and stability and can make energy evaluation on the importance of ore control elements. This study has successfully applied a wireless sensor to 3D mineral energy prediction, which makes a positive exploration for mineral resource prediction and evaluation in the future.

2. Mineral Resource Prediction by a Wireless Sensor

2.1. Random Forest Algorithm. Random forest is an important ensemble algorithm in the wireless sensor model. It is a combinatorial classifier composed of a decision tree classifier set proposed by Breiman in 2001 on the basis of decision tree and bagging method. The basic idea of random forest is to merge multiple unrelated decision trees together, and each tree has the same distribution [10, 11]. The classification error of the model depends on the classification ability of the decision tree and the correlation between the trees. For the classification algorithm, the new input samples are classified and predicted according to the decision tree in the forest.

2.1.1. Decision Tree. Decision tree is also a prediction model in a wireless sensor, which represents the mapping between

object attributes and object values. It uses the structure of tree to divide data records into three types of nodes: root node, middle node, and leaf node. A leaf node of tree represents the record set corresponding to the leaf node of decision tree under certain conditions. The decision tree is generated by repeatedly establishing lower-level nodes in branch subsets [12]. CART is a typical binary decision tree, which can do both classification and regression. The CART algorithm uses the Gini coefficient as impurity to measure the impurity of a set sample. For a classification problem with characteristic variable M , there are n samples in the training sample set T ; then, the Gini coefficient of the training sample set is

$$G(T) = 1 - \sum_{i=1}^n P_i^2. \quad (1)$$

In the formula, P_i represents the conditional probability of the occurrence of the i th category in the classification results. According to a certain classification standard S (such as j attribute values of attribute A), the sample is divided into K subsets, which are, respectively, T_1, T_2, \dots, T_k ; then, the Gini coefficient of this classification is

$$G(T, S) = \sum_{i=1}^k \frac{n_i}{n} * G(T_i). \quad (2)$$

The smaller the Gini coefficient is, the higher the purity of the subsample after dichotomy is, and the branching of the decision tree generated by this splitting method can represent the direct difference between different categories, because the division standard S with the minimum Gini coefficient is selected as the optimal splitting attribute and the optimal splitting node [13].

2.1.2. Bagging Method. The bagging method, also known as the self-help method, adopts equiprobabilistic random repeated sampling technique with put back to select training data to construct classifier and finally combine. In other words, every time a fixed number of samples are randomly collected from the original training set, the samples are put back and the next round of random sampling is conducted again. Since the data outside the bag does not participate in the model fitting, it can be used to estimate the classification accuracy without bias. The realization process is as follows: (1) T training samples are extracted from the original sample set D with the method of random sampling with replacement in each round, and n independent training sets are obtained through n rounds of extraction. (2) The NTH weak learner is obtained by using a training set D_n each time. (3) For the classification problem, the final strong learner can be obtained by adopting the majority voting method for the N weak learners obtained in the previous step; (4) for regression problems, the arithmetic mean of regression results is used as the final strong learner. Random forest is applied to mineral prediction, and its characteristic variables are the ore-controlling elements in the energy

prediction model, and its classification ability is used to judge the characteristics of ore-bearing attributes [14–16].

2.2. Support Vector Machine Regression Model

2.2.1. Model Principle. Support vector machine (SVM) is based on the statistical learning theory developed wireless sensor method, it can be through the kernel function can be used to convert the actual problem to high-dimensional feature space and through the structure in the high-dimensional space linear discriminant function to realize nonlinear discriminant in the original space, usually can get global optimal solution of support vector machine (SVM). Moreover, it has good generalization ability for large volume and high-dimensional data sets. In this chapter, the principle of the SVM model is firstly described based on the classification model, and then, it is extended to regression problems. The basic principles of the SVM model are as follows:

Let me define my matrix $m \times n$, X , and my column vector W , Y , where X is the input variable; x_i is the column vector: $[x_1, x_2, x_3, \dots, x_n]^T$; m is the sample number; n is the number of attribute features; W is the corresponding weight; and Y is the output variable.

$$\begin{aligned} X &= [x_1, x_2, x_3, \dots, x_m], \\ Y &= [y_1, y_2, y_3, \dots, y_m], \\ W &= [w_1, w_2, w_3, \dots, w_n]. \end{aligned} \quad (3)$$

The partition hyperplane in the sample space is defined by a linear equation:

$$W^T X + b = 0. \quad (4)$$

In the formula, normal vector W determines the direction of the hyperplane. The displacement term b determines the distance between the hyperplane and the origin. In this definition, the distance between any point x in the sample space and the hyperplane is

$$r = \frac{|W^T X + b|}{\|W\|}. \quad (5)$$

Considering the dichotomous problem, in order to obtain a good classification effect, if all samples are correctly classified, the sample points should meet the following constraints:

$$y_i = \begin{cases} +1, & W^T x_i + b \geq +1, \\ -1, & W^T x_i + b \leq -1. \end{cases} \quad (6)$$

The training sample point closest to the hyperplane and satisfying formula (5) is defined as the support vector; then, the sum of the distance between the two dissimilar support

vectors and the hyperplane is defined as

$$\gamma = \frac{2}{\|W\|}. \quad (7)$$

In the formula, γ is called interval, and the support vector machine algorithm is to find the hyperplane with the maximum interval γ , that is, to find the model parameter W, b that satisfies the constraint of formula (5) and maximizes γ :

$$\max_{W,b} \frac{2}{\|W\|} \text{ s.t. } y_i (w^T x_i + b) \geq 1, \quad i = 1, 2, \dots, m. \quad (8)$$

Obviously, in order to maximize the interval, only maximizing $\|W\|^{-1}$ is equivalent to minimizing $\|W\|^2$, and the relaxation factor ξ and regularization parameter C are added on this basis:

$$\min_{w,b} \frac{1}{2} \|W\|^2 + C \sum_{i=1}^m \xi_i \text{ s.t. } y_i (w^T x_i + b) \geq 1 - \xi_i, \quad i = 1, 2, \dots, m. \quad (9)$$

The duality problem can be obtained through the Lagrange bearing method used for (9):

$$L(w, b, \xi, a, \mu) = \frac{1}{2} \|w\|^2 + C \sum \xi - \sum a \{y(w^T X + b) - 1 + \xi\} - \sum \mu \xi. \quad (10)$$

The support vector machine model with maximum soft interval can be obtained by solving the equation above, where the relaxation factor ξ is the classification error term. The degree of punishment for misclassification samples is controlled by regularization parameter C .

The SVM classification model is extended to the regression problem, and the error function with regularization term in the linear regression model is considered:

$$\frac{1}{2} \sum_{n=1}^N \{h(x_n, w) - y_n\}^2 + \frac{\lambda}{2} \|w\|^2. \quad (11)$$

To ensure the sparsity of the model, the quadratic error term is replaced, where $h(x_n, w) = W^T X + b$ can obtain a new error function:

$$\frac{1}{2} \|w\|^2 + C \sum E(h(x_n, w) - y_n). \quad (12)$$

Same as the classification model, relaxation factor ξ is introduced, where

$$\begin{aligned} y_n &\leq h(x_n, w) + \varepsilon + \xi, \\ y_n &\geq h(x_n, w) - \varepsilon - \xi. \end{aligned} \quad (13)$$

After sorting out, the final error function of the SVM

TABLE 1: Data basis of 3D geological modeling.

Profile name	Scale	The number of	Detection depth (m)
Topographic geological map	1:5000	1	The earth's surface
Geological map of bedrock	1:5000	1	The earth's surface
Pillar contrast map of ore bed	1:5000	2	1000
Borehole bar diagram	1:200	147	70~1030
Geological prospecting section	1:2000	21	1000~1200
CSAMT comprehensive interpretation profile	1:10000	12	2000
Middle section of CSAMT comprehensive interpretation	1:10000	3	500, 1000, 1500

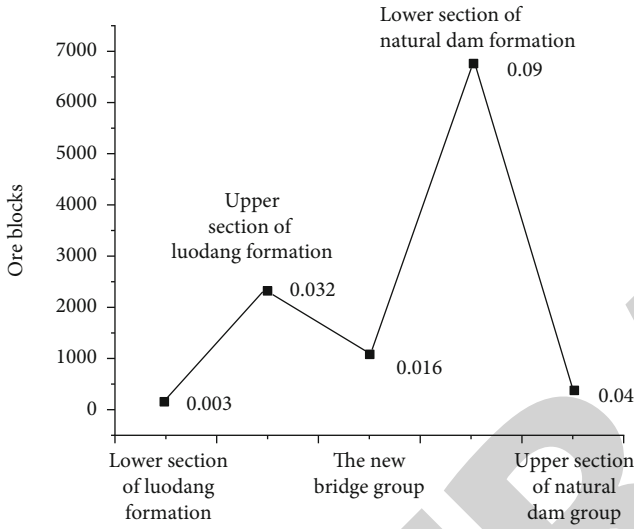


FIGURE 1: Ore-bearing statistics of strata.

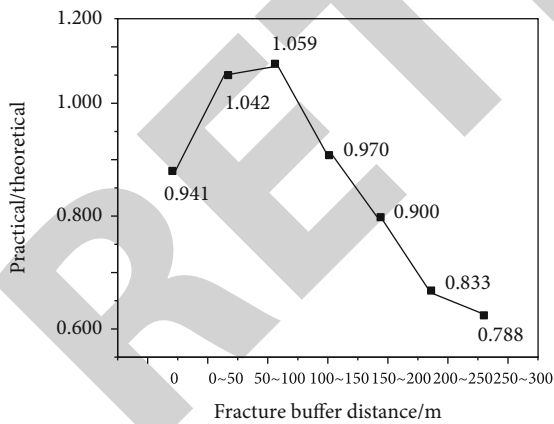


FIGURE 2: Statistics of ore-bearing rate in fracture buffer.

regression model is

$$\frac{1}{2} \|W\|^2 + C \sum (\hat{\xi} + \xi). \quad (14)$$

The specific solving process of this model is the same as that of the SVM classification model.

3. Three-Dimensional Geological Modeling

3D geological modeling is an important basis for 3D geological mapping, deep geological survey, and large-scale 3D metallogenic prediction of key metallogenic zones and also an important way to solve some deep geological problems and study geological laws. Surpac6.3, the 3D modeling software of GEMCOM International Mining Software Co., LTD., was adopted for this 3D geological modeling based on plane geological map, borehole data, exploration line profile, and geophysical comprehensive interpretation map. The modeling data are shown in Table 1. Section modeling method was adopted to construct three-dimensional solid models of stratum, rock mass, fault, low resistivity anomaly, and ore body in the study area “vertical cube” [17]. The coordinate range of modeling in this study is 2899615~2903025 m from north to south, 792980~796250 m from east to west, and 1000~2050 m above sea level. Considering the spacing of boreholes, the spacing of geological section exploration lines, the amount of data after subdividing 3D geological solid model blocks, and the computer computing capacity, the running speed of the computer can be improved as much as possible on the premise that the size of block units can meet the calculation accuracy of 3D metallogenic prediction. Therefore, the whole solid model area was divided into blocks according to the block unit size of 25 m × 25 m × 25 m, and the total number of block units divided in the whole research area was 3,099,906. There are a large number of vein ore bodies in the study area. When dividing the whole study area with the above-mentioned unit block size, as long as ore bodies are included, they are assigned as vertical blocks of ore bodies, and there are a total of 14064 known ore bodies. It should be pointed out that it is extremely inaccurate to divide ore bodies at this scale for reserve estimation, but the block model constructed is intended to serve as positive sample markers in a wireless sensor [18, 19].

4. Three-Dimensional Energy Prediction

4.1. Extraction of Favorable Metallogenic Information. In the process of energy prediction, it is the prediction model that finally decides which GIS layer participates in the model operation. The prediction model is based on the prospecting model, through the cube (or grid unit) to establish the characteristic variables of different parts, and combined with the

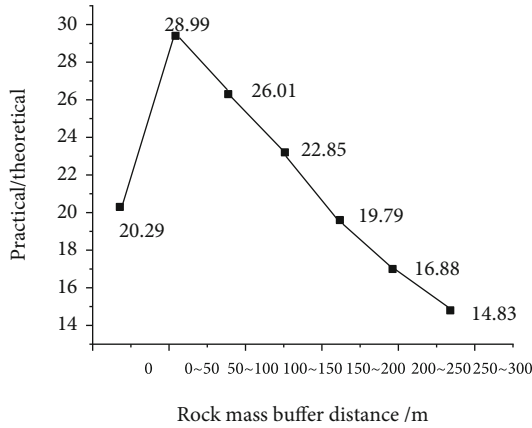


FIGURE 3: Statistics of ore-bearing rate of rock mass buffer.

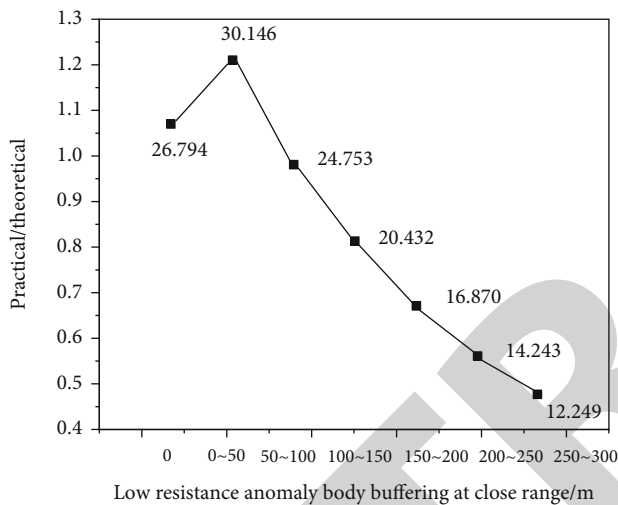


FIGURE 4: CSAMT low resistance anomaly buffer ore-bearing rate statistics.

known ore body (or ore point) to analyze and extract the favorable conditions for mineralization, and finally, the ore-controlling elements and their favorable metallogenic range are combined to form the prediction model. In this study, favorable information of mineralization was extracted from stratigraphy, structure, rock mass, and geophysics.

4.2. Formation Favorable Information. Five stratigraphic units are mainly modeled in this study. The number of ore bodies contained in different stratigraphic blocks is shown in Figures 1–4. If we consider the difference of distribution range of different strata, we can use the concept of ore-bearing ratio for comparative analysis. The ore-bearing rate can be obtained by the number of ore bearing in different strata/the number of formation blocks (Figure 1). The ore-bearing rate is the highest in the lower Tiantianba Formation, followed by the upper, Xinqiao, upper and lower Tiantianba Formation of Luodang Formation. Through the statistical analysis of the above two aspects, it can be found that the main ore-bearing strata in the Hongnipo mining area are the lower member of Tiantianba Formation and the upper member of Luodang Formation.

4.3. Construct Favorable Information. The formation of Hongnipo copper deposit is closely related to regional basement faults. From the perspective of extraction of favorable metallogenic information energy, the number of fault blocks in the study area is 41462, and the number of superposition with ore bodies is 110, so the ore-bearing rate of the fault is 0.0025, reaching a certain level of ore-bearing rate. Therefore, the fault is the ore controlling factor for energy prediction. In addition, ore-forming migration channels are often characterized by fault buffer zones. In this paper, the “expansion buffer method” is used to quickly build the fault buffer of different distances and then determine the best fault buffer distance through the analysis of ore bearing. The expansion buffering method adopts the expansion algorithm in morphological analysis and applies it to the 3D block model. The size of the cube model in this study is 25 m, and one square is buffered each time, 25 m distance. The buffer of $0 \sim N * 25$ m can be obtained by N times of buffering, and the model obtained by $n - 1$ times of buffering can be removed to achieve different grades of fracture buffer block model. Statistical results of fracture buffer in this study are shown in Figure 2. When the fracture buffer is 100 m, it is the optimal fracture buffer distance. In addition to the direct analysis of faults and their buffer zones, favorable metallogenic information can often be mined by energy analysis of the characteristic parts of faults in energy prediction.

4.4. Favorable Information of Rock Mass. In this three-dimensional geological modeling of rock mass, only gabbro and gabbro intercalated breccia are constructed, which are collectively referred to as “rock mass” in energy prediction. In the block model, the total number of rock mass is 35812, among which the number of ore-bearing blocks is 584, and the ore-bearing rate is 0.016, reaching a certain level of ore-bearing rate. Therefore, rock mass is the ore-controlling factor for energy prediction. Similarly, through statistical analysis of “expansion buffer method” in this study, when the rock mass buffer range is 50 m, the ratio of actual and theoretical ore concentration in the buffer reaches 28.993, so the rock mass buffer distance is determined to be 50 M (Figure 3).

4.5. Geophysical Favorable Information. The CSAMT method adopted in this study plays an important role in stratigraphic division, fault location, and rock mass inference. In addition, through the superposition analysis of apparent resistivity profile and known ore body, combined with the ore-controlling environment of the study area and the interpretation and inference results of each survey line, 12 middle-low resistivity abnormal areas are delineated on 12 comprehensive interpretation profiles, and then, three-dimensional reconstruction is carried out to form mineralized abnormal bodies. The total number of vertical blocks of abnormal mineralized bodies is 32033, including 1407 ore blocks, and the ore-bearing rate is 0.044. Since the apparent resistivity is continuous and the medium and low resistivity are defined as relative regions, information leakage can be reduced as much as possible by making buffers. The

TABLE 2: Quantitative prediction model of copper mine.

Types of ore deposits	Ore-controlling factors	Element type	Characteristics of the variable	The eigenvalue	
Volcanic sedimentary metamorphism Type E copper (iron) ore	Formation	Ore formation	A natural dam group	A natural dam group	
			The new bridge group	The new bridge group	
			Fall dang group	Fall dang group	
	Structure	Ore-controlling fracture	Fracture zone	Basement faults	The fracture
				Rupture zone	The 100 MB buffer
		Tectonic site		Azimuth anomaly	(0, 0.1)
				Structural isodensity	(1.045, 1.492)
	Rock mass	Favorable ore-forming rock	Rock contact zone	Degree of central symmetry	(0.001, 0.210)
				Structural frequency	(0, 1.375)
				Gabbro	Gabbro
	Geophysical	Abnormal apparent resistivity	Favorable rock characteristics	Rock buffer zone	Buffer 50 m
				Rock mass differentiation	(0.07, 3.04)
				CSAMT abnormal	Low resistivity abnormal body
				CSAMT exception buffer	Buffer 50 m

“expansion buffer method” was adopted to analyze the ore-bearing rate under different buffer zones, and the optimal buffer distance was determined to be 50 m (Figure 4). Based on the above extraction of metallogenic information and combined with the regional mineral characteristics of the study area, the three-dimensional energy prediction model of copper mine is formed (Table 2), as shown in Table 2.

4.6. *Classification of Ore-Forming Energy.* The ore-forming energy anomalies delineated in the study area are classified according to the following principles:

- (1) There should be 3 or more geochemical sampling points within the anomaly
- (2) For small anomalies with sampling points less than 3, if they belong to the same third-order catchment basin, several small anomaly groups with the same anomaly source can be divided into one anomaly according to the drainage distribution and the relationship between sampling points
- (3) The anomaly numbers are individually numbered according to the four geochemical subzones, in the form of “E3-2,” where *E* represents the comprehensive anomaly of metallogenic energy, 3 represents geochemical partition, and 2 is the sequence number of the anomaly

5. Conclusions

In this study, a machine learn-based study on geological and mineral energy and mineral energy classification was proposed, and a three-dimensional geological entity model was constructed. After the cube of the entity model, the

three-dimensional quantitative prediction model of the study was determined through the extraction of metallogenic information. Under the guidance of the quantitative prediction model, the wireless sensor algorithm was used to carry out the 3D quantitative prediction based on the wireless sensor algorithm. The training accuracy of the model and the test accuracy of the model were over 96%, which proved the accuracy of the RF model construction and achieved satisfactory results. In this study, a wireless sensor is successfully applied to 3D mineral energy prediction, which makes a positive exploration for mineral resource prediction and evaluation in the future. Finally, the prediction of mineral resource energy based on a wireless sensor is an important trend of future development.

Data Availability

The data used to support the findings of this study are available from the corresponding author upon request.

Conflicts of Interest

The authors declare no conflicts of interest.

References

- [1] X. Huang, J. Sun, S. M. Srinivasan, and R. S. Sangwan, “Comparative study of disease classification using multiple machine learning models based on landmark and non-landmark gene expression data,” *Procedia Computer Science*, vol. 185, no. 1, pp. 264–273, 2021.
- [2] Y. Chen, J. Tao, J. Wang et al., “The novel sensor network structure for classification processing based on the wireless sensor method of the acgan,” *Sensors*, vol. 19, no. 14, p. 3145, 2019.

Retraction

Retracted: Analyzing the Effect of Masking Length Distribution of MLM: An Evaluation Framework and Case Study on Chinese MRC Datasets

Wireless Communications and Mobile Computing

Received 28 November 2023; Accepted 28 November 2023; Published 29 November 2023

Copyright © 2023 Wireless Communications and Mobile Computing. This is an open access article distributed under the Creative Commons Attribution License, which permits unrestricted use, distribution, and reproduction in any medium, provided the original work is properly cited.

This article has been retracted by Hindawi, as publisher, following an investigation undertaken by the publisher [1]. This investigation has uncovered evidence of systematic manipulation of the publication and peer-review process. We cannot, therefore, vouch for the reliability or integrity of this article.

Please note that this notice is intended solely to alert readers that the peer-review process of this article has been compromised.

Wiley and Hindawi regret that the usual quality checks did not identify these issues before publication and have since put additional measures in place to safeguard research integrity.

We wish to credit our Research Integrity and Research Publishing teams and anonymous and named external researchers and research integrity experts for contributing to this investigation.

The corresponding author, as the representative of all authors, has been given the opportunity to register their agreement or disagreement to this retraction. We have kept a record of any response received.

References

- [1] C. Zeng and S. Li, "Analyzing the Effect of Masking Length Distribution of MLM: An Evaluation Framework and Case Study on Chinese MRC Datasets," *Wireless Communications and Mobile Computing*, vol. 2021, Article ID 5375334, 17 pages, 2021.

Research Article

Analyzing the Effect of Masking Length Distribution of MLM: An Evaluation Framework and Case Study on Chinese MRC Datasets

Changchang Zeng^{1,2} and Shaobo Li^{1,2,3}

¹Chengdu Institute of Computer Application, Chinese Academy of Sciences, Chengdu 610041, China

²University of Chinese Academy of Sciences, Beijing 100049, China

³State Key Laboratory of Public Big Data, Guizhou University, Guiyang 550025, China

Correspondence should be addressed to Changchang Zeng; zengchangchang16@mailsucas.ac.cn

Received 1 October 2021; Revised 22 October 2021; Accepted 1 November 2021; Published 23 November 2021

Academic Editor: Balakrishnan Nagaraj

Copyright © 2021 Changchang Zeng and Shaobo Li. This is an open access article distributed under the Creative Commons Attribution License, which permits unrestricted use, distribution, and reproduction in any medium, provided the original work is properly cited.

Machine reading comprehension (MRC) is a challenging natural language processing (NLP) task. It has a wide application potential in the fields of question answering robots, human-computer interactions in mobile virtual reality systems, etc. Recently, the emergence of pretrained models (PTMs) has brought this research field into a new era, in which the training objective plays a key role. The masked language model (MLM) is a self-supervised training objective widely used in various PTMs. With the development of training objectives, many variants of MLM have been proposed, such as whole word masking, entity masking, phrase masking, and span masking. In different MLMs, the length of the masked tokens is different. Similarly, in different machine reading comprehension tasks, the length of the answer is also different, and the answer is often a word, phrase, or sentence. Thus, in MRC tasks with different answer lengths, whether the length of MLM is related to performance is a question worth studying. If this hypothesis is true, it can guide us on how to pretrain the MLM with a relatively suitable mask length distribution for MRC tasks. In this paper, we try to uncover how much of MLM's success in the machine reading comprehension tasks comes from the correlation between masking length distribution and answer length in the MRC dataset. In order to address this issue, herein, (1) we propose four MRC tasks with different answer length distributions, namely, the short span extraction task, long span extraction task, short multiple-choice cloze task, and long multiple-choice cloze task; (2) four Chinese MRC datasets are created for these tasks; (3) we also have pretrained four masked language models according to the answer length distributions of these datasets; and (4) ablation experiments are conducted on the datasets to verify our hypothesis. The experimental results demonstrate that our hypothesis is true. On four different machine reading comprehension datasets, the performance of the model with correlation length distribution surpasses the model without correlation.

1. Introduction

In the field of natural language processing (NLP), machine reading comprehension (MRC) is a challenging task and has received extensive attention. According to the definition of Burges, machine reading comprehension refers to the following: "A machine comprehends a passage of text if, for any question regarding that text that can be answered correctly by a majority of native speakers, that machine can provide

a string which those speakers would agree both answers that question, and does not contain information irrelevant to that question [1]."

Generally, MRC tasks can be roughly divided into four categories based on the answer form: cloze test, multiple choice, span extraction, and free answering [2, 3]. Most of the early reading comprehension systems were based on retrieval technology; that is, we search in the article according to the questions and find the relevant sentences as the

answers. However, information retrieval mainly depends on keyword matching, and in many cases, the answers found by relying solely on text matching are not related to the questions.

With the development of machine learning (especially deep learning) and the release of large-scale datasets, the efficiency and quality of the MRC model have been greatly improved. In some benchmark datasets, the accuracy of the MRC model has exceeded the human performance [4]. In recent years, pretrained language models (PTMs) have brought revolutionary changes to the field of MRC. Among them, the most representative pretrained model is the BERT proposed by Google in 2018 [5]. BERT uses unsupervised learning to pretrain on a large-scale corpus and creatively uses MLM and NSP subtasks to enhance the language ability of the model [5]. After the author released the code and pretrained models, BERT was immediately used by researchers in various NLP tasks, and the previous SOTA results were refreshed frequently and significantly.

Recently, many efforts have been devoted to improve pretrained models, and various pretrained models have been proposed, such as BERT-wwm [6], ERNIE 1.0 [7], ERNIE 2.0 [8], SpanBERT [9], and MacBERT [10]. We can see that all of them have improved the masked language model (MLM) of the BERT model in different ways. However, the BERT model itself (the paradigm of the pretraining process, transformer-based model, and fine-tuning process) has not been significantly modified. This shows the importance of MLM. MLM is a self-supervised training objective of predicting missing tokens in a sequence from placeholders, which is widely used in various PTMs [11]. With the development of training objectives, many variants of MLM have been proposed, such as whole word masking [6], entity masking [7, 8], phrase masking [7, 8], and span masking [9].

In different MRC tasks, the length of the answer text is often different, and the answer is either a word, a phrase, or a sentence. Similarly, in different variants of MLM, the text length of the mask is also different. For example, the whole word masking improves the MLM objective of BERT by using the whole word instead of the word piece [6]; the span masking performs the replacement at the span level and not for each token individually [9]; the entity masking masks entities that are usually composed of multiple words, while the phrase masking masks an entire phrase composed of multiple words as a conceptual unit [7, 8].

How to choose a masking scheme for MRC tasks with different answer lengths has become a question worth studying. At the same time, it also makes us wonder whether the length of MLM is related to their performance in MRC tasks with different answer lengths. If this hypothesis is true, maybe it can guide us on how to pretrain an MLM with a relatively suitable mask length distribution for various MRC tasks.

However, for different variants of MLM, there are many inconsistencies in their corpora, training methods, evaluation tasks, and benchmark datasets. Therefore, it is difficult to perform ablation experiments on the existing MRC datasets and these publicly released pretrained models to quantitatively measure the performance improvements brought about by different masking schemes.

To address the above issues, we design a set of controlled experiments to verify our hypothesis. In summary, our main contributions are as follows:

- (1) Four MRC tasks with different answer length distributions are proposed, including the short span extraction task, long span extraction task, short cloze task, and long cloze task
- (2) We create MRC datasets for these four tasks and statistically analyze the answer word length distribution on these four datasets
- (3) Using uniform hyperparameters, we trained MLMs with different masking length distributions
- (4) We conducted ablation experiments on the above dataset to verify our hypothesis. The experiment result shows that the consistency of the masking length distribution and the answer length distribution does affect the performance of the model. On four different machine reading comprehension datasets, the performance of the model with correlation length distribution surpasses the model without correlation

2. Related Works

2.1. Existing Masked Language Models (MLMs). Recently, many efforts have been devoted to improve masked language models (MLMs). In this section, we briefly introduce several existing MLMs, including word piece masking, whole word masking, entity masking, phrase masking, span masking, and N -gram masking.

2.1.1. Word Piece Masking. Word piece masking is the MLM used in the original version of BERT [5], where the “Word-Piece tokenizer” is used in the data preprocessing to split the input sequence into subwords, which is very effective in dealing with out-of-vocabulary (OOV) words. In Chinese text tokenization, when a sentence is tokenized with a “WordPiece tokenizer,” it will be split into Chinese characters. Then, tokens are selected randomly for masking, and 15% of the tokens will be randomly selected. Among the selected tokens, for each word, it has an 80% probability of being replaced with [MASK], 10% will be replaced with a random token, and 10% will remain unchanged. It should be noted that each token is masked independently according to the above probability, rather than all selected tokens being masked at the same time.

2.1.2. Whole Word Masking. Whole word masking (WWM) is an upgraded version of BERT [5] released by Google, which mitigates the drawbacks of masking partial Word-Piece tokens in the original BERT [6]. In the whole word masking, if a subword of a complete word is masked, the other parts of the same word will also be masked; that is, the whole word will be masked at the same time. In the Chinese version of BERT released by Google, Chinese is segmented at the granularity of characters, and the Chinese word segmentation (CWS) [12] is not considered. Therefore,

Cui et al. applied the whole word masking to Chinese [6] and masked the whole word instead of masking Chinese characters.

2.1.3. *N-Gram Masking.* *N*-gram In reference [10], Cui et al. believed that the idea of *N*-gram masking was first proposed by Devlin et al. [5]. Devlin et al.'s paper [5] did not include the phrase “*N*-gram masking,” but according to their model name on the SQuAD leaderboard, the academic community usually admits that they were the first to propose this concept [10]. In *N*-gram masking, a sequence of *N* words is treated as a whole unity. During pretraining of MLM, all words in the same unit are masked, instead of masking only one word or character. *N*-gram masking is used in many advanced pretraining models. For example, MacBERT [10] uses an *N*-gram masking scheme for selecting candidate tokens for masking, with a percentage of 40%, 30%, 20%, and 10% for the word-level unigram to 4-gram. To a certain extent, the span masking, entity-level masking, and phrase-level masking can be regarded as special cases of the *N*-gram masking scheme [5, 9].

2.1.4. *Explicitly N-Gram Masking.* Explicitly *N*-gram masking is an explicit *N*-gram masking scheme, in which the *N*-gram is replaced by a single [MASK] symbol [13]. When predicting masked tokens, explicit *N*-gram identities are directly used instead of token sequences. In addition, explicitly *N*-gram masking uses a generator model to sample reasonable *N*-gram identities as an optional *N*-gram mask and predicts it in both a coarse-grained manner and a fine-grained manner to achieve comprehensive relation modeling. Explicitly *N*-gram masking is proposed by the Baidu team in 2021 [13].

2.1.5. *Entity-Level Masking.* Entities usually contain important information in the sentences, such as a person, location, organization, and product. Unlike selecting random tokens for masking, entity-level masking masks the whole named entities, which are usually composed of multiple words [7, 8]. Before masking, the text needs to be segmented using named entity recognition tools. In entity-level masking, the MLM implicitly learned the information about longer semantic dependency, such as the relationship between entities.

2.1.6. *Phrase-Level Masking.* A phrase is a small group of words or characters as a conceptual unit. Phrase-level masking masks the whole phrase which is composed of several words [7, 8], and it is similar to the *N*-gram masking scheme [5, 9, 10]. For English, vocabulary analysis and chunking tools are used to get the boundaries of phrases in sentences, and we use some language-related segmentation tools to get word/phrase information in other languages (such as Chinese) [7, 8]. In this way, the prior knowledge of phrases is considered to be learned implicitly during the training procedure, such as syntactic and semantic information.

2.1.7. *Span Masking.* Span masking was proposed in the SpanBERT [9], in which contiguous random spans are masked, rather than individual tokens. The process of span

masking is, first, iteratively selecting contiguous random spans until the 15% masking budget is spent. In each iteration, the length of the span is selected according to the geometric distribution. Then, randomly select the starting point of the span. Third, replace all the tokens in the same selected span with [MASK], random or original tags according to the 80%-10%-10% rule in BERT [5], where the span constitutes the unit. Therefore, it forces the model to use only the context in which the span occurs to predict the entire span.

2.1.8. *Multilevel Masking.* Multilevel masking uses multiple schemes at the same time. For example, the knowledge masking proposed in the ERNIE 1.0 [7] masking can be regarded as a kind of multilevel masking scheme, which uses both phrase-level masking and entity-level masking. The knowledge masking treats a phrase or entity as a unit, which is usually composed of several words. All words in the same unit are masked, instead of masking only one word or character. The knowledge masking does not directly add knowledge embedding but is considered to be learning information about knowledge, such as entity attributes and event types, to guide word embedding learning [7].

2.1.9. *Dynamic Masking.* Static masking is used in the MLM of the original BERT, and the masking is performed only once during the data preprocessing before MLM training, which means that the same words are masked in the input sequence provided to the model on each epoch. In order to avoid masking the same words multiple times and make full use of the input sequence, dynamic masking is proposed. In the dynamic masking process, the “dupe_factor” is defined, and the input sequence will be the duplicated “dupe_factor”; then, the same sequence will have different masks [14]. Before providing the input sequence to the model each time, the masking operation will be performed repeatedly. Therefore, the model will see different masking versions of the same sequence. Dynamic masking is adopted by many pre-trained models, such as RoBERTa [14].

2.2. *Interpretability of Masked Language Models.* With various advanced MLMs, many pretrained language models have achieved state-of-the-art performance when adapted to MRC tasks. The black box nature of MLM and related pretrained models has inspired many works trying to understand them.

Many efforts have been devoted to uncover whether the MLM calculates various types of structured information by probing analysis or evaluating the performance of simple classifiers on representations [15–20]. Popular methods also include analyzing self-attention weights and evaluating the performance of classifiers with different representations as inputs [19]. A possible explanation for the success of masked language model (MLM) training is that these models have learned to represent semantic information or syntactic information [21].

2.2.1. *Semantic Information.* With the MLM probing study, Ettinger applied a set of diagnostic methods derived from human language experiments to the BERT model and found that BERT has a certain understanding of semantic roles [19, 22].

Tenney et al. used a set of detection tasks derived from traditional NLP pipelines to quantify the encoding position of specific types of semantic information, and the experimental results show that BERT encodes information about entity types, relationships, semantic roles, and prototype roles [18, 19].

2.2.2. Syntactic Information. Through the probes of MLM, Goldberg assessed the extent to which the BERT model captures English syntactic phenomena and found that the BERT models perform remarkably well on the syntactic test cases. The experimental results show that BERT considers subject-predicate agreement when completing the cloze task, even for meaningless sentences and sentences with participle clauses between the subject and the verb [19, 23].

Wu et al. proposed a perturbation masking technique to evaluate the impact of one word on the prediction of another word in MLM. They concluded that BERT “naturally” learns some syntactic information, although it is not very similar to linguistically annotated resources [19, 24].

2.2.3. Distributional Information. Most recently, Sinha et al. [21] surprisingly found that most of MLM’s high performance can in fact be explained by the “distributional prior” rather than its ability to replicate “the types of syntactic and semantic abstractions traditionally believed necessary for language processing [18].” In other words, they found that the success of MLM in downstream tasks is almost entirely because they can model high-order word co-occurrence statistics. To prove this, they pretrained MLMs on sentences with a randomly shuffled word order and showed that after fine-tuning many downstream tasks, these models can still achieve high accuracy, including tasks designed specifically to be challenging for models that ignore the word order. According to some parametric syntactic probes, these models perform surprisingly well, which indicates possible deficiencies when testing the representation for syntactic information [21].

3. Motivation and Approach

Firstly, as described in Section 2.1, most of the existing MLMs adopt different mask rules to improve their performance. Some take a word as a mask unit; some take phrases, entities, or spans as mask units; and others adopt multilevel masking schemes. As we can see, the length of the masked text is one of the basic variables in the above masking schemes. However, at present, there is a lack of quantitative research and analysis on the performance of MLM with different masking lengths. The whole word masking [6] only masks words, and entity and phrase masking schemes [7, 8] mask only entities or phrases. Span masking [9] simply uses geometric distribution in the process of selecting spans. N -gram masking in MacBERT [10] also just masks different N -grams in a fixed probability. However, for MRC tasks with different answer lengths, if different masking lengths of MLM are used, will the performance achieved be different? There is no relevant research yet. In addition, some MLMs use a multilevel masking scheme, such as the knowl-

edge masking in ERNIE [7, 8]. However, what is the optimal proportion of masking schemes of different levels? It is also a question worth studying. If there is a correlation between performances of MLM and masking lengths in MRC tasks with different answer lengths, then we can choose an appropriate length for an MLM according to the length distribution in the MRC dataset.

Secondly, from the interpretability of MLM described in Section 2.2, we can see that the theoretical analysis of the MLM is very challenging. There are many empirical studies trying to understand why MLMs are so effective, and one possible explanation for the impressive performance of MLMs is that these models have learned semantic information and syntactic information. A lot of work has been devoted to revealing whether MLM calculates various types of structured information [15–20, 22–24].

However, the most recent studies have pointed out that the success of MLM may actually come from the word distribution information it learns to a large extent, and they found that the success of MLM in downstream tasks is almost entirely because they can model high-order word co-occurrence statistics [21].

Inspired by this research, we wonder whether the distribution of masking length will also affect the performance of MLM in MRC tasks with different answer lengths. In this work, we try to uncover how much of MLM’s success comes from the correlation between masking length distribution and answer length in the MRC dataset. We treat the distribution of answer lengths in the MRC dataset and the masking length of MLMs as latent variables and treat the performance of different MLMs on downstream MRC tasks with different answer distributions as functions of latent variables. Assuming that the distribution of the answer length in the MRC dataset is correlated with the masking length of the MLM, then pretraining on a large corpus allows MLM to learn the hidden information of different lengths. Therefore, in the downstream MRC task, the MLM whose masking length is closest to the answer length distribution in the MRC dataset should achieve better performance.

The key starting point of our research work is to propose an evaluation framework to quantitatively verify whether masking schemes of different lengths will affect the results of the MLM in MRC tasks with different answer lengths. However, using the existing pretrained models and MRC dataset to create a verification framework is challenging because there are too many different factors affecting performance. Since there are many inconsistencies in the pretraining corpus, pretraining methods, downstream tasks, and evaluation datasets used by different pretrained models, therefore, it is difficult to conduct ablation experiments on different masking schemes.

To address the above issues, we first design four MRC tasks and construct the related datasets with different answer lengths. Next, using unified hyperparameters, we retrain several MLMs with different masking lengths according to the answer lengths of the above MRC datasets. Then, ablation experiments are carried out, and we evaluate the performance of different MLMs on the above MRC dataset. The key points of our experiment are as follows.

3.1. New MRC Tasks and Datasets. When designing the MRC tasks and datasets, we integrate the mainstream MRC tasks, namely, the cloze test, multiple choice, span extraction, and free answering [2, 3], and we adopt two kinds of MRC tasks, including the span extraction tasks and two multiple-choice cloze tasks. The answer length of these two tasks can also be divided into two categories: long answer and short answer. Finally, we construct four MRC datasets, namely, the short span dataset, long span dataset, short cloze dataset, and long cloze dataset. In addition, because the Chinese corpus is composed of Chinese characters, there is no well-marked word boundary, which is conducive to eliminate the influence of word boundary information in the pretrained model. Therefore, we chose to create Chinese MRC datasets.

3.2. Training MLM from Scratch. Existing MLMs usually integrate a variety of improvements, such as MLM in the SpanBERT [9] which uses both span masking and SBO pre-training tasks [9] at the same time. In order to eliminate the influence of the prior knowledge embedded in the pretrained model, in this experiment, we do not directly use the existing MLMs, but we conducted MLM training from scratch by ourselves, thereby eliminating the interference variables.

3.3. Unified Pretraining Corpora. When training MLMs with different masking lengths, we use the same pretraining corpora to eliminate the impact of word distribution in different corpora.

3.4. Answer Length Distribution of Datasets. In this article, in order to quantitatively verify whether masking schemes of different lengths will affect the performance of the MLM, we have counted the length distributions of different datasets.

3.5. Masking Length Distribution of MLMs. In the process of training different MLMs, we use the weighted average answer length distribution in the dataset as the MLM mask length to quantitatively verify whether masking schemes of different lengths will affect the results of the MLM.

3.6. Unified Masking Ratios. During the experiment, we fixed the masking ratio to be the same as the original version of BERT. That is, select 15% of the text in the paragraph, and 80% of the selected text are replaced by [MASK], 10% are replaced by random tokens, 10% are replaced by original tokens, and 10% remain unchanged. We perform this replacement at the sequence level; that is, each time, all tokens in a sequence are replaced with “mask” or random tokens or remain unchanged.

3.7. Unified Pretraining Hyperparameters. In order to eliminate the influencing factors, we use the same model hyperparameters in the pretraining of different MLMs.

4. Proposed MRC Tasks

According to the style of the answers and questions, MRC tasks can be roughly divided into four categories: cloze test, multiple choice, span extraction, and free answering [2, 3].

When designing MRC tasks and datasets required for ablation experiments, we integrate the main characteristics of these MRC tasks, and we adopt two kinds of MRC tasks, including the span extraction tasks and two multiple-choice cloze tasks. The answer length of these two tasks can also be divided into two categories: long answer and short answer. Finally, the four MRC tasks are as follows:

- (1) Span extraction tasks with short answers
- (2) Span extraction tasks with long answers
- (3) Multiple-choice cloze tasks with short answers
- (4) Multiple-choice cloze tasks with long answers

We believe these tasks are representative of most of the current MRC tasks. Among them, the number of tokens in the short answer of span extraction tasks is set to be greater than 3 and less than 7, and the size of the long answer is greater than 6 and less than 10; the number of tokens in the short answer of multiple-choice cloze tasks is greater than 6 and less than 15, and the size of the long answer is greater than 16 and less than 30.

In the following subsections, we briefly introduce the definitions of typical MRC tasks and the two types of MRC tasks we used in the experiment.

4.1. Typical MRC Tasks. Generally, the definition of a typical MRC task is given below.

Definition 1. A typical machine reading comprehension task could be formulated as a supervised learning problem. Given the training examples $\{p, q, a\}$, where p is a passage and q is a question, the goal of a typical machine reading comprehension task is to learn a predictor f which takes the passage p and a corresponding question q as inputs and gives the answer a as output, which could be formulated as the following formula [2–4]:

$$a = f(p, q), \quad (1)$$

and it is necessary that a majority of native speakers would agree what the question q does regarding that text p , and the answer a is a correct one which does not contain information irrelevant to that question.

4.2. Span Extraction Tasks with Different Answer Lengths. In order to quantitatively verify whether masking schemes with different lengths will affect the performance of MLM, we propose two span extraction tasks with different answer lengths for Chinese machine reading comprehension. Table 1 shows an example of the proposed span extraction task.

The definition of the span extraction task is as follows.

Definition 2. Given a serial of training samples, each sample contains a passage about a public service event, a corresponding question, and the answer to this question. The answer should be a span which is directly extracted from the passage. The goal of the span extraction machine reading comprehension task is to train the machine so that it can

TABLE 1: An example of the proposed span extraction task.

<p>Context: 传染病的医学治疗属于传染病医学领域，在某些情况下传播学的研究属于流行病学领域。一般来说，感染最初由初级保健医生或内科专家诊断。例如，“简单”肺炎通常由内科医师或肺科医师(肺科医师)治疗。因此，传染病专家的工作需要与病人和全科医生以及实验室科学家、免疫学家、细菌学家和其他专家合作。</p> <p>Question: 病传播可以归入哪些研究领域的范畴?</p> <p>Answer: 行病学</p>	<p>Context: The medical treatment of infectious diseases belongs to the field of infectious disease medicine. In some cases, the research of communication belongs to the field of epidemiology. In general, infection is initially diagnosed by a primary care physician or medical expert. For example, “simple” pneumonia is usually treated by a physician or pulmonary physician (pulmonary physician). Therefore, the work of infectious disease experts requires cooperation with patients and general practitioners, as well as laboratory scientists, immunologists, bacteriologists, and other experts.</p> <p>Question: What research areas can disease transmission fall into?</p> <p>Answer: The field of epidemiology</p>
--	--

TABLE 2: An example of the proposed multiple-choice cloze task.

<p>Passage: 2001年初苹果开始销售带有CD-RW驱动器的电脑。强调Mac电脑的DVD播放能力。DVD-ROM和DVD-RAM驱动器作为标准配置。[BLANK1]苹果在可写CD技术方面“迟到了”。他认为Mac电脑可以成为一个“数字中心”并促成一种“新兴的数字生活方式”。苹果随后将对其iTunes音乐播放器软件进行更新。时推出一项颇具争议的“翻录、混合、刻录”广告活动。[BLANK2]。[BLANK3]iPod是苹果第一款成功的手持设备。[BLANK4]如失败的Power MacG4cube、面向教育的EMAC和面向专业人士的钛(后来的铝)PowerBook G4笔记本电脑。直到1989年苹果公司发布了他们的第一台便携式电脑。[BLANK5]。[BLANK6]很快在1991年被第一条PowerBook线取代。</p> <p>Options: A: “一些人认为这鼓励了媒体盗版” B: “伴随着iPod的发布” C: “一种小型便携式设备” D: “史蒂夫·乔布斯承认” E: “Macintosh便携式电脑” F: “苹果继续推出产品”</p> <p>Answer: D, F, E, C, A, B</p>	<p>Passage: In early 2001, Apple began selling computers with CD-RW drives, emphasized the DVD playback capability of MAC computers, and took DVD-ROM and DVD-RAM drives as standard configurations. [BLANK1] Apple was “late” in the technology of writable CD, but he believed that the MAC could become a “Digital Center” to connect and promote an “emerging digital lifestyle.” Apple will then update its iTunes music player software, and launch a controversial “rip, mix, and burn” advertising campaign. [BLANK2], [BLANK3], iPod is Apple’s first successful handheld device [BLANK4], such as the failed Power MacG4cube, the EMAC for education, and the titanium (later aluminum) PowerBook G4 laptop for professionals. Until 1989, Apple released their first portable computer, [BLANK5]. [BLANK6], which was soon replaced by the first PowerBook line in 1991.</p> <p>Options: A: “some people think this encourages media piracy” B: “with the release of iPod” C: “a small portable device” D: “Steve Jobs admitted that” E: “Macintosh laptop” F: “Apple continues to launch products”</p> <p>Answer: D, F, E, C, A, B</p>
--	---

find the correct answers in the given passage. The task can be simplified by predicting the start and end pointers of the right answer in the given passage.

4.3. *Multiple-Choice Cloze Tasks with Different Answer Lengths.* We also proposed two multiple-choice cloze tasks with different answer lengths for Chinese machine reading comprehension. The form of our multiple-choice cloze tasks is similar to the CMRC2019 task [25], but redundant fake answers are removed. Table 2 shows an example of the proposed multiple-choice cloze task.

The definition of the multiple-choice cloze task is as follows.

Definition 3. Generally, the reading comprehension task can be described as a triple $\langle P, Q, A \rangle$, where P represents Passage, Q represents Question, and A represents Answer. Specifically, for the multiple-choice cloze-style reading comprehension task, we select several sentences in the passages and replace them with special marks (for example, [BLANK]), forming an incomplete passage. The selected sentences form a candidate list, and the machine should fill in the blanks with these candidate sentences to form a complete passage [2–4, 25].

5. Evaluation Metrics

In this paper, we use F1 and EM to measure the performance of the pretrained model in the span extraction tasks.

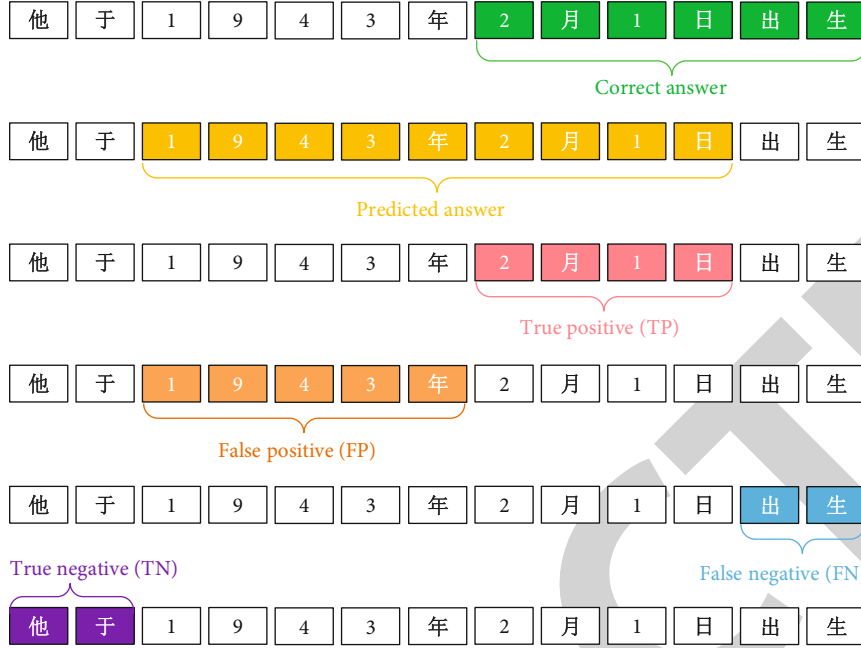


FIGURE 1: The true positive (TP), false positive (FP), true negative (TN), and false negative (FN).

5.1. *F1 Score.* F1 is a commonly used MRC task evaluation metric. The equation of F1 for a single question is as follows:

$$F1 = \frac{2 \times \text{Precision} \times \text{Recall}}{\text{Precision} + \text{Recall}}, \quad (2)$$

where P denotes the token-level Precision for a single question and R denotes the Recall for a single question [2–4].

5.2. *Precision.* Precision represents the percentage of the maximum span overlap between the tokens in the correct answer and the tokens in the predicted answer. In order to calculate Precision, we first need to obtain the true positive (TP), false positive (FP), true negative (TN), and false negative (FN), as shown in Figure 1.

As shown in Figure 1, for a single question in the proposed dataset, the true positive (TP) is equal to the maximum common span (MCS) between the predicted answer and the correct answer. The false positive (FP) indicates the span not in the correct answer but in the predicted answer, while the false negative (FN) indicates the span not in the predicted answer but in the correct answer [2–4]. The Precision of a single question is calculated as follows:

$$\text{Precision} = \frac{\text{TP}}{\text{TP} + \text{FP}}. \quad (3)$$

5.3. *Recall.* Recall represents the percentage of correct answers that have been correctly predicted in the question [2–4]. According to the above definitions of the true positive (TP), false positive (FP), and false negative (FN), the Recall

of a single answer is calculated as follows:

$$\text{Recall} = \frac{\text{TP}}{\text{TP} + \text{FN}}, \quad (4)$$

where Recall represents the recall rate of a single problem, NumTP represents the number of true positive (TP) tokens, and NumFN represents the number of false negative (FN) tokens.

5.4. *Exact Match.* Exact Match represents the percentage of questions where the answer generated by the system exactly matches the correct answer, which means that every word is the same. Exact Match is usually abbreviated as EM. In the span extraction MRC task, the answer to the question is a sentence, and some words in the predicted answer may be included in the correct answer, while other words are not included in the correct answer [2–4]. For example, if the MRC task contains N questions, each question corresponds to a correct answer. The answer can be a word, a phrase, or a sentence, and the number of predicted answers exactly the same as the correct answer is M . Exact Match can be calculated as follows:

$$\text{Exact Match} = \frac{M}{N}. \quad (5)$$

5.5. *Accuracy.* In this paper, we use Accuracy to measure the performance of the pretrained model in the multiple-choice cloze tasks. Accuracy is defined as the ratio of the number of correctly predicted samples to the total number of samples for a given test dataset.

For example, suppose that an MRC task contains N questions; each question corresponds to one correct answer;

the answers can be a word, a phrase, or a sentence; and the number of questions that the system answers correctly is M . The equation for the Accuracy is as follows:

$$\text{Accuracy} = \frac{M}{N}. \quad (6)$$

In addition, in order to make the assessment more reliable, following the evaluation method of CMRC2019 [25], we adopt two metrics to evaluate the systems on our datasets, which are Question-level Accuracy (QAC) and Passage-level Accuracy (PAC).

The Question-level Accuracy (QAC) is the ratio between the correct prediction and the total blanks, which can be calculated by the following formula [25]:

$$\text{QAC} = \frac{\#\text{Correctly Answered Questions}}{\#\text{Total Questions}}. \quad (7)$$

Similar to the QAC, Passage-level Accuracy (PAC) measures how many passages have been correctly answered. We only count the passages where all blanks have been correctly predicted [25].

Passage-level Accuracy (PAC) is used to measure how many passages are answered exactly correctly. Similar to the Exact Match, only paragraphs where all blanks are correctly predicted are considered to be exactly correctly predicted samples. Passage-level Accuracy (PAC) can be calculated by the following formula [25]:

$$\text{PAC} = \frac{\#\text{Exactly Correct Paragraphs}}{\#\text{Total Paragraphs}}. \quad (8)$$

6. Dataset Construction

As mentioned above, in order to eliminate the influence of interference factors on the experiment as much as possible, we designed four MRC tasks: short span extraction task, long span extraction task, short multiple-choice cloze task, and long multiple-choice cloze task. In this section, we further construct four Chinese MRC datasets for these MRC tasks. Unlike the English text, a feature of the Chinese text is that there are no obvious spaces to mark word boundaries, so the influence of word boundary information on the results can be further eliminated. So in this article, we use Chinese as the language of the dataset. Below, we will briefly introduce the construction methods of these MRC datasets.

6.1. Span Extraction Dataset with Different Answer Lengths. The corpus of our span extraction datasets comes from the paragraphs in the Chinese SQuAD dataset [26]. The Stanford Question Answering Dataset (SQuAD) [27] is one of the most popular machine reading comprehension datasets, containing more than 100,000 questions generated by humans, and the answer to each question is a span of text in a related context [20]. Since its release in 2016, SQuAD1.1 has quickly become the most widely used MRC dataset. Now, it has been updated to SQuAD2.0 [4, 28].

The Chinese SQuAD dataset [26] is translated from the original SQuAD through machine translation and manual correction, including SQuAD1.1 [27] and SQuAD2.0 [28]. Because some translations cannot find the answers in the original text (the answer translation and document translation are different), the amount of data is reduced compared to the original English version of SQuAD. After data cleaning, the Chinese SQuAD dataset contains 125,892 questions and 36,100 paragraphs, and the number of unanswerable questions is 49,443 [26]. Among them, each paragraph includes a number of different contexts, and each context includes multiple question-and-answer pairs. Then, we divided the paragraphs in the Chinese SQuAD dataset according to the length of the answer and obtained the long span extraction dataset and the short span extraction dataset, where the number of tokens in the short answer of span extraction tasks is set to be greater than 3 and less than 7, and the size of the long answer is greater than 6 and less than 10. The statistics of our span extraction datasets is shown in the sections below.

6.2. Multiple-Choice Cloze Dataset with Different Answer Lengths. The corpus source of our multiple-choice cloze dataset is the NLPCC 2017 corpus [29]. The cleaned NLPCC 2017 corpus contains 50,000 news articles with summaries, and the average number of tokens in an article is 1036 [29].

We first divide the above corpus into several paragraphs and then divide each paragraph into sentences using commas, periods, semicolons, exclamation marks, and question marks as the dividing point. Then, when constructing the multiple-choice cloze dataset with short answers, for each paragraph, we randomly select 9 sentences as candidate long answers, and the number of tokens in these sentences is greater than 6 and less than 15. When constructing the multiple-choice cloze dataset with long answers, for each paragraph, we also randomly select 9 sentences as candidate long answers, and the number of tokens in these sentences is greater than 16 and less than 30. After selecting the candidate answers, we randomly shuffle the order of the answers to obtain candidate options in the form of multiple choices. The statistics of our multiple-choice cloze datasets is shown in sections below.

6.3. Dataset Analysis. In this subsection, we analyze the paragraphs, questions, and answers in the proposed datasets. Specifically, we explore (1) the statistics of the data size and (2) the length distribution of the answer lengths in the train set, development set, and test set of the proposed datasets. As we can see, the statistics of the proposed span extraction datasets are given in Table 3, and Table 4 shows the statistics of the proposed multiple-choice cloze datasets.

6.4. Distribution of Answer Lengths. We have separately counted the distribution of answer lengths in these four datasets. Tables 5 and 6 show the answer length distributions of the train set, development set, and test set. For example, in the short span extraction dataset, there are 16,171 answers that have 4 tokens in the training set, and 3344 answers that have 4 tokens in the development set, while 4147 in the test set.

TABLE 3: Statistics of the proposed span extraction datasets.

	Short span extraction			Long span extraction		
	Train set	Dev set	Test set	Train set	Dev set	Test set
Paragraph #	600	150	200	600	150	200
Passage #	15,265	2770	2484	7756	1163	1565
Question #	31,390	6774	8309	12,053	2376	5812
Max tokens in a context #	512	512	512	512	512	512
Max answer tokens #	6	6	6	9	9	9
Min answer tokens #	4	4	4	7	7	7

TABLE 4: Statistics of the proposed multiple-choice cloze datasets.

	Short multiple-choice cloze			Long multiple-choice cloze		
	Train set	Dev set	Test set	Train set	Dev set	Test set
Passages #	4500	1000	1000	4500	1000	1000
Blanks #	40,500	9000	9000	40,500	9000	9000
Max tokens in a passage #	1000	1000	1000	1000	1000	1000
Max answer tokens #	14	14	14	29	29	29
Min answer tokens #	7	7	7	17	17	17
Options #	9	9	9	9	9	9

TABLE 5: The answer length distributions of the proposed span extraction datasets.

(a)

Short span dataset						
Tokens #	Train #	PP (%)	Dev #	PP (%)	Test #	PP (%)
4	16,171	51.52%	3344	49.37%	4147	49.91%
5	8566	27.29%	1828	26.99%	2230	26.84%
6	6653	21.19%	1602	23.65%	1932	23.25%
Total	31,390	100.00%	6774	100.00%	8309	100.00%

(b)

Long span dataset						
Tokens #	Train #	PP (%)	Dev #	PP (%)	Test #	PP (%)
7	5040	41.82%	819	34.47%	2071	35.63%
8	4192	34.78%	980	41.25%	2390	41.12%
9	2821	23.40%	577	24.28%	1351	23.25%
Total	12,053	100.00%	2376	100.00%	5812	100.00%

Based on the data in the above table, we have also given the illustration of answer length distribution ratios in different MRC datasets. For example, it can be seen from Figure 2(a). The blue squares represent the proportion of answers with length 4, the red squares represent the proportion of answers with length 5, and the green squares represent the proportion of answers with length 5.

6.5. Dataset Comparison. The statistics of the proposed dataset have been given in the previous section. In this section, we compare the proposed dataset with the other MRC datasets. The comparison of the number of questions is shown in

Table 7. In contrast to prior MRC datasets, the question size of the proposed dataset is at a medium level.

Next, the statistics of the context size are given in Table 8. As we can see, in contrast to prior MRC datasets, the context size of the proposed dataset is also at a medium level.

We also compared the question style, answer style, source of corpora, and generation method of each dataset, as shown in Table 9.

7. MLMs with Different Masking Lengths

In order to quantitatively verify whether masking schemes of different lengths will affect the performance of the MLM, in the previous section, we have proposed MRC tasks and constructed MRC datasets with different answer lengths. In this section, as shown in Figure 3, we use the above datasets and tasks to propose an evaluation framework for masked language models (MLMs) with different masking lengths. However, existing MLMs usually integrate various improvements. To eliminate the influence of the prior knowledge embedded in the existing MLMs, in this experiment, we do not directly use the existing MLMs but conduct MLM training from scratch by ourselves. We trained four different MLMs, namely, short span MLM, long span MLM, short cloze MLM, and long cloze MLM. When training our MLMs, we used different masking lengths according to the average distribution of answer lengths in the proposed four MRC datasets.

7.1. Masking Schemes. The key point of our mask scheme used in our experiment is that the probability distribution of different masking lengths is equal to the proportional distribution of different answer lengths in the corresponding dataset. For example, as shown in Figure 3, in the short multiple-choice cloze dataset, the answer length distribution

TABLE 6: The answer length distributions of the proposed multiple-choice cloze datasets.

(a)						
Short cloze dataset						
Tokens #	Train #	PP (%)	Dev #	PP (%)	Test #	PP (%)
7	4428	10.93%	974	10.82%	1016	11.29%
8	4630	11.43%	1022	11.36%	1037	11.52%
9	5020	12.40%	1166	12.96%	1077	11.97%
10	5260	12.99%	1212	13.47%	1154	12.82%
11	5389	13.31%	1149	12.77%	1253	13.92%
12	5427	13.40%	1205	13.39%	1200	13.33%
13	5308	13.11%	1171	13.01%	1136	12.62%
14	5038	12.44%	1101	12.23%	1127	12.52%
Total	40,500	100.00%	9000	100.00%	9000	100.00%

(b)						
Long cloze dataset						
Tokens #	Train #	PP (%)	Dev #	PP (%)	Test #	PP (%)
17	5209	12.86%	1132	12.58%	1174	13.04%
18	4919	12.15%	1114	12.38%	1072	11.91%
19	4367	10.78%	999	11.10%	982	10.91%
20	3983	9.83%	891	9.90%	875	9.72%
21	3637	8.98%	762	8.47%	770	8.56%
22	3187	7.87%	714	7.93%	715	7.94%
23	2980	7.36%	655	7.28%	602	6.69%
24	2627	6.49%	576	6.40%	590	6.56%
25	2275	5.62%	546	6.07%	570	6.33%
26	2162	5.34%	467	5.19%	504	5.60%
27	1885	4.65%	408	4.53%	427	4.74%
28	1776	4.39%	385	4.28%	396	4.40%
29	1493	3.69%	351	3.90%	323	3.59%
Total	40,500	100.00%	9000	100.00%	9000	100.00%

is shown in Figure 3(e). Suppose that the total number of answers with length l in the dataset is X_l , and the length of l ranges from min to max. Then, we can calculate the actual distribution ratio of the length of each answer as shown in the following formula:

$$D_l = \frac{X_l}{\sum_{l=\min}^{\max} X_l}. \quad (9)$$

Among them, D_l is the distribution ratio of the number of answers with length l to the total number of answers.

Then, we treat the distribution ratios as the probabilities and use them as the probabilities of different lengths being selected in the MLM. The pie chart of this probability distribution is shown in Figure 3(a).

When training the MLM for the dataset, we take D_l as the selected probability of different masking lengths; that is, in the MLM, if the number of samples with masking

length of l is M_l and the value range of l is also set to min to max, then the masked probability of each masking length is P_l , which we set as follows:

$$P_l = M_l. \quad (10)$$

Then, we use P_l as the probability to randomly select masked sequences with the length of l from the training corpus as training samples and set the total number of selected training samples to T . Then, the final number of masked samples with length l is N_l :

$$N_l = P_l T. \quad (11)$$

Next, we get the probability distributions of the mask lengths for four different datasets:

$$\begin{aligned} P_l^{ss} &= \frac{X_l^{ss}}{\sum_{l=\min}^{\max} X_l^{ss}}, \\ P_l^{sc} &= \frac{X_l^{sc}}{\sum_{l=\min}^{\max} X_l^{sc}}, \\ P_l^{ls} &= \frac{X_l^{ls}}{\sum_{l=\min}^{\max} X_l^{ls}}, \\ P_l^{lc} &= \frac{X_l^{lc}}{\sum_{l=\min}^{\max} X_l^{lc}}, \end{aligned} \quad (12)$$

where the P_l^{ss} is the selected probability of the masked sequences with the length of l in the short span dataset, and the P_l^{sc} , P_l^{ls} , and P_l^{lc} are the probabilities of the masked sequences with the length of l in the short cloze dataset, long span dataset, and long cloze dataset, respectively.

In the MLM training process, first, we duplicate the input sequence 10 times and then choose different ways to mask it. We use iterative sampling to mask the sequence. In each iteration, we will randomly select the current mask length according to the above probability distribution, such as l . Then, we randomly select a sequence with l consecutive tokens from the paragraphs. This process will be cycled until the masking budget has been spent. Following BERT, the masking budget is set to 15%, which means that 15% of the text in the paragraph will be selected.

Then, for each selected sequence, we also replace it with a proportion of 80%-10%-10%. As shown in Figure 3, in the following span masking scheme in SpanBERT [9], we perform this replacement at the sequence level, rather than separately for each token; i.e., each selected sequence has an 80% probability of being replaced with "mask" and 10% probability of being replaced with random tokens, and 10% remains the same.

Finally, the actual number of masked samples of the masked sequence of length l is as follows:

$$\text{Real_}N_l = 80\% \times N_l. \quad (13)$$

The number of masked samples which are randomly

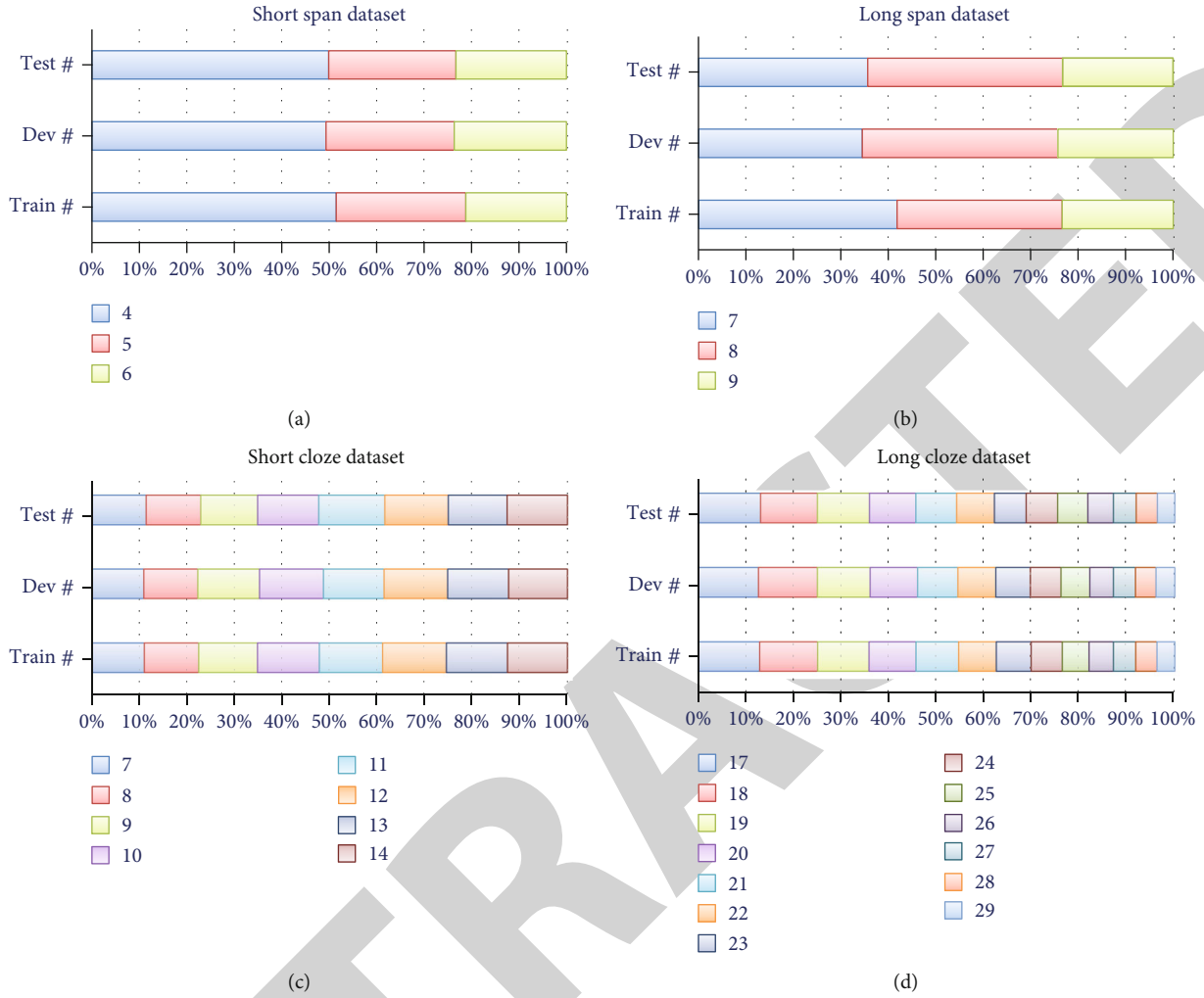


FIGURE 2: The illustration of answer length distribution ratios in different MRC datasets. (a) The short span dataset. (b) The long span dataset. (c) The short cloze dataset. (d) The long cloze dataset.

TABLE 7: The number of questions of each MRC dataset.

Dataset	Question #	Train question #	Dev question #	Test question #	Percentage of the train set
SQuAD2.0	151,054	130,319	11,873	8862	86.27%
SQuAD1.1	107,702	87,599	10,570	9533	81.33%
TQA	26,260	15,154	5309	5797	57.71%
MovieQA	21,406	14,166	2844	4396	66.18%
MCScript	13,939	9731	1411	2797	69.81%
DREAM	10,197	6116	2040	2041	59.98%
ARC-E	5197	2251	570	2376	43.31%
WikiQA	3047	2118	296	633	69.51%
ARC-C	2590	1119	299	1172	43.20%
ProPara	488	391	54	43	80.12%
Short span	46,473	31,390	6774	8309	67.54%
Long span	20,241	12,053	2376	5812	59.55%
Short cloze	58,500	40,500	9000	9000	69.23%
Long cloze	58,500	40,500	9000	9000	69.23%

TABLE 8: The number of contexts of each MRC dataset.

Dataset	Context #	Train context #	Dev context #	Test context #	Unit of the context
CoQA	8399	7199	500	700	Passage
CLOTH	7131	5513	805	813	Passage
DREAM	6444	3869	1288	1287	Dialogue
Qangaroo-M	2508	1620	342	546	Passage
TQA	1076	666	200	210	Lesson
MovieQA	548	362	77	109	Movie
SQuAD1.1	536	442	48	46	Article
SQuAD2.0	505	442	35	28	Article
Short span	20,519	15,265	2770	2484	Passage
Long span	10,484	7756	1163	1565	Passage
Short cloze	58,500	40,500	9000	9000	Passage
Long cloze	58,500	40,500	9000	9000	Passage

replaced with other texts is as follows:

$$\text{Random_}N_l = 10\% \times N_l. \quad (14)$$

The number of masked samples whose text in the masked part remains unchanged is as follows:

$$\text{Remain_}N_l = 10\% \times N_l. \quad (15)$$

We use dynamic masking [14] to avoid masking the same sequences for each paragraph in every epoch. Following RoBERTa, we duplicate the input sequence 10 times so that each sequence is masked in 10 different ways.

7.2. Input Sequences. Before feeding the training data into the model, we need to preprocess the data. A preprocessed input sample is a sequence composed of both the question and the reference context. A separation token (denoted as [SEP]) is used to separate the question and context. It will be added between the question and the context, as well as the end of the context. In addition to [SEP], there are 4 special tokens in the input sequence:

[CLS]. This is used to identify the beginning of the sequence. In tasks such as classification, it is usually necessary to use the output of the [CLS] position in the last layer.

[UNK]. The out-of-vocabulary (OOV) words will be replaced by this token.

[PAD]. In the zero-padding mask, for sentences shorter than the maximum length, we will have to fill [PAD] to make up for the length.

[MASK]. In some training objectives, such as the masked language model (MLM), some input tokens are randomly replaced with the [MASK] token (being masked), and the model is required to predict the masked tokens.

After that, the question-and-context pair is tokenized. A commonly used tokenization method is the BERT tokenizer. In this baseline, we use “-vocab_path” to specify the Chinese

vocabulary path. Then, we use this vocabulary to tokenize the question-and-context pair. Finally, each token is converted into a unique index according to the index of the corresponding Chinese character in the vocabulary.

7.3. Tokenization. We use the WordPiece tokenizer. The WordPiece tokenizer follows the subword tokenization scheme. The tokenizer first checks whether the word is in the vocabulary. If so, then it will be used as a token. If the word is not in the vocabulary, then the word will be split into subwords, and the tokenizer will constantly check that the split subword appears in the vocabulary after each split. Once a subword is found in the vocabulary, we use it as a token. The WordPiece tokenizer is very effective when dealing with out-of-vocabulary (OOV) words. Because there is no subword and no space between words in Chinese, we cannot apply the WordPiece tokenizer to the Chinese text directly. Thus, when tokenizing the Chinese text with the WordPiece tokenization, following the Chinese BERT, we add spaces around all Chinese characters, and the input Chinese text will be split into Chinese characters, so all Chinese tokens (subwords) in the vocabulary are single Chinese characters.

7.4. Embeddings. In the embedding layer, the input indices are transformed into corresponding vector representations, which are usually obtained by adding three distinct representations, namely, the following:

Token embeddings (usually with shape (1, max length, hidden size)). Each input index is transformed into a multi-dimensional word embedding, which is randomly initialized from a standard normal distribution with 0 mean and unit variance.

Position embeddings (usually with shape (1, max length, hidden size)). It is used to indicate the position of the token, which is a learned embedding vector. This is different from the normal transformer in BERT, which has a preset value.

Finally, these embeddings are summed element-wise to produce a single vector representation and fed into the transformer encoders.

8. Experiments

8.1. Pretraining Setup. Using the open-source framework of UER-py [UER-py], we pretrain MLMs with different lengths on the Chinese corpus. Compared with the original BERT implementation, the main points in our implementation include the following:

- (a) The probability distribution of different masking lengths is equal to the proportional distribution of different answer lengths in the corresponding dataset
- (b) We did not use the next sentence prediction (NSP) training objective but only the masked language model (MLM)
- (c) We perform the mask replacement at the sequence level instead of performing this replacement separately for each token

TABLE 9: Analysis of each MRC dataset.

Dataset	Question style	Answer style	Corpus source	Generation method
DREAM	Natural	Free-form	Exam	Crowdsourcing
MCScript	Natural	Free-form	Narrative texts	Crowdsourcing
MovieQA	Natural	Free-form	Movie plot	Crowdsourcing
OpenBookQA	Natural	Free-form	Elementary-level science facts	Crowdsourcing
Qangaroo-M	Synthesis	Spans	Wikipedia articles	Crowdsourcing
Qangaroo-W	Synthesis	Spans	Paper abstracts	Crowdsourcing
SQuAD1.1	Natural	Spans	Wikipedia	Crowdsourcing
SQuAD2.0	Natural	Spans	Wikipedia	Crowdsourcing
WikiQA	Natural	Free-form	Relevant Wikipedia pages	Crowdsourcing
TQA	Natural	Free-form	Middle school curricula	Experts
Short span	Natural	Spans	Wikipedia	Crowdsourcing
Long span	Natural	Spans	Wikipedia	Crowdsourcing
Short cloze	Cloze	Multiple choice	Wikipedia/news	Automated
Long cloze	Cloze	Multiple choice	Wikipedia/news	Automated

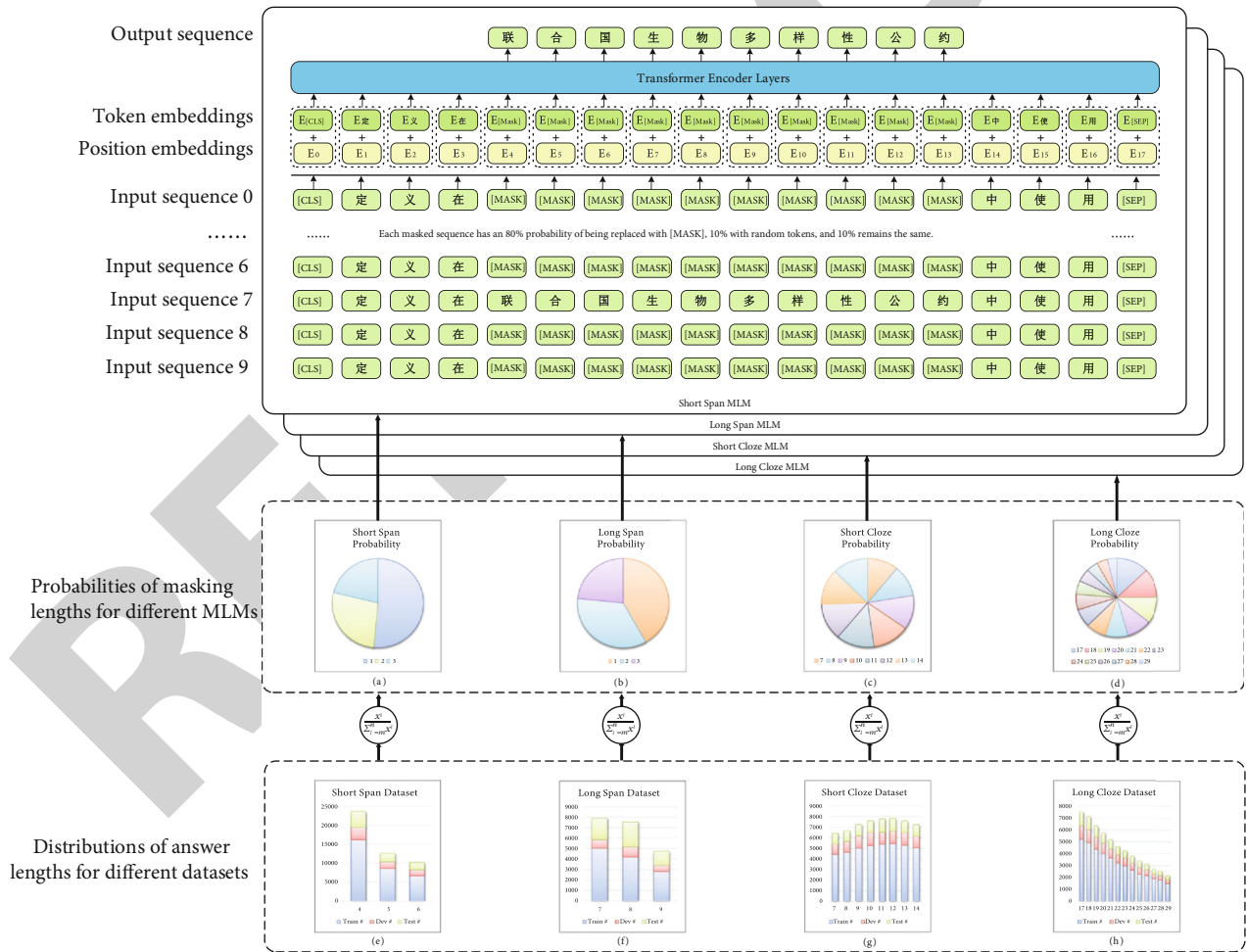


FIGURE 3: Illustration of the masked language models (MLMs) with different masking lengths according to the average distribution of answer lengths in the proposed four MRC datasets.

(d) We use dynamic masking instead of static masking

Our implementation of MLM is trained on the cloud with Nvidia V100 GPU. We use a sequence of up to 512 tokens for pretraining. The learning rate is set to $5e-5$, and the batch size is 64. The parameters of the Adam optimizer are fixed at $\beta_1 = 0.8$ and $\beta_2 = 0.9$. We use mixed precision training to reduce memory usage and accelerate pretraining.

8.2. Training Corpus. The effective pretraining of the MLM crucially relies on large-scale training data from various domains. Improving the diversity of data domains and increasing the amount of data can result in improved performance in downstream tasks [9, 30].

In this work, we collect the Chinese training data from the Internet and then cleaned the data. For example, we clean the HTML mark, remove extra empty characters, and remove the picture mark. Finally, we collect a Chinese corpus for our MLM pretraining. The corpus contains Chinese texts in the following domains:

- (1) Wikipedia that contains various Chinese Wikipedia documents
- (2) Chinese academic papers on the WanFang database
- (3) Chinese social text messages on Weibo
- (4) Chinese articles on the WeChat official accounts
- (5) Chinese news articles, including titles, keywords, descriptions, and texts. Categories include finance, real estate, stocks, home furnishing, education, technology, society, fashion, current affairs, sports, constellations, games, and entertainment

8.3. Fine-Tune and Evaluation. We fine-tune and evaluate our pretrained masked language models on four machine reading comprehension datasets, namely, the short span extraction dataset, long span extraction dataset, short multiple-choice cloze dataset, and long multiple-choice cloze dataset, and the details are given below.

8.3.1. Span Extraction. The span extraction reading comprehension task is composed of passages, questions, and answers. This task requires the computers to answer relevant questions according to the passages. The answer to the question can be found in the passage; that is, the answer is a span (fragment) in the passage.

This task can be simplified to predict a starting position and an ending position in a passage, and the answer is a text span between the start and the end.

The process of using MLM to deal with span extraction reading comprehension tasks can be divided into three layers: input layer, transformer-based encoder layer, and output layer.

(1) *Input Layer.* In the input layer, we preprocess the input passages and questions; first, we perform word piece tokenization, then splice the questions and passages; we insert [CLS] at the beginning of the input sequence and [SEP] at

the end and at the dividing point between the question and the passage so as to finally get the input sequence.

$$S = [\text{CLS}], q_1, \dots, q_m [\text{SEP}], p_1, \dots, p_n, [\text{SEP}]. \quad (16)$$

It should be noted that if the length n of the input text is less than the maximum sequence length N , the padding token [PAD] needs to be spliced after the input sequence until it reaches the maximum sequence length n . In the following example, assume that the maximum sequence length of our model is $n = 10$ and the current input sequence length is 7. Then, three padding tokens [PAD] are required after the input sequence.

$$S = [\text{CLS}], q_1, \dots, q_m [\text{SEP}], p_1, \dots, p_n, [\text{SEP}] [\text{PAD}] [\text{PAD}] [\text{PAD}]. \quad (17)$$

Conversely, if the length of the current input sequence is longer than the maximum sequence length N , the sequence needs to be sliced and divided into multiple subsequences. For example, assume that the maximum sequence length of our model is $n = 10$ and the current input sequence length is 40. Then, the model can only process input sequences with a length of 10 tokens at one time and the sequence needs to be divided into 4 subsequences.

In addition, it should be noted that we have to put the question at the beginning of the input sequence. Because if the question is divided into multiple subsequences, the question cannot be answered. If the passage is divided into multiple subsequences, the answers in the passage can be obtained through other sequences.

(2) *Encoder Layer Based on the Transformers.* The input sequence will be converted into token embeddings, position embeddings, and segment embeddings. These three embeddings will be added to obtain the input vector. The input vector will pass through 12 encoding layers. In these encoding layers, with the help of a multihead self-attention mechanism, the model will fully learn the semantic association between passages and questions.

(3) *Output Layer.* The output of the last layer of the transformer encoder passes through a full connection layer and predicts the probability PS of each position as the answer and the probability PE of the end position through Softmax.

Then, we input the prediction probabilities and the ground truth positions into the cross-entropy loss function at the same time to obtain the loss of the model. Finally, the cross-entropy loss at the starting position and the loss at the ending position are averaged to obtain the final total cross-entropy loss of the model. The training objective is to minimize the total cross-entropy loss between the prediction probability and the ground truth position.

(4) *Answer Prediction and Evaluation.* In the output layer, we select the starting position and ending position with the

highest probability as the prediction answer. Finally, F1 and EM of the predicted answer are calculated according to the standard answer.

8.3.2. Multiple-Choice Cloze. Following the method in CMRC [25], in the sentence cloze-style reading comprehension task, we select several sentences in the passages and replace them with special marks (for example, [BLANK]) to form an incomplete passage. The selected sentences will form the candidate list, and the computer is required to fill in the blanks with the right candidate sentences.

(1) Input Sequence. The input sequence is composed of an answer option and the passage (with blanks), and then the semantic representation of the context is obtained through transformer encoder layers. Finally, the probability of each blank corresponding to an option is output. It should be noted that the two components of the input sequence are an answer option and an incomplete passage with multiple blanks. Because there are 9 blanks (corresponding to 9 different options) in each passage in our dataset, therefore, we need to enter 9 different sequences, and each sequence contains an option.

For example, assume that the current answer options are as follows: $a_1, \dots, a_i, \dots, a_m$, where a_i represents the i -th word in the answer option text. Let the input paragraph with blanks be $p_1, \dots, \text{blank}_1, \dots, \text{blank}_i, \dots, p_n$, where p_n represents the n -th word of the input passage and blank_i represents the i -th masked answer. The input sequence S can be expressed as follows:

$$S = [\text{CLS}], a_1, \dots, a_m, [\text{SEP}], p_1, \dots, \text{blank}_1, \dots, \text{blank}_i, \dots, p_n, [\text{SEP}], \quad (18)$$

where [CLS] represents the special token at the beginning of the input sequence and [SEP] represents the segmentation token and the end token of the input sequence (following BERT).

It should be noted that if the length n of the input sequence is less than the maximum sequence length N , the padding token [PAD] needs to be spliced after the input sequence until it reaches the maximum sequence length N . In the following example, assume that the maximum sequence length is $n = 10$ and the input sequence length is 9. Then, one padding token [PAD] is required after the input sequence.

$$S = [\text{CLS}], a_1, \dots, a_m, [\text{SEP}], p_1, \dots, \text{blank}_1, \dots, \text{blank}_i, \dots, p_n, [\text{SEP}], [\text{PAD}]. \quad (19)$$

Conversely, if the input sequence length n is longer than the maximum length N , it needs to be truncated into multiple input sequences. Here, we usually put the answer option in the front so that the answer options will not be truncated.

(2) Embeddings. This section describes how to preprocess the input sequence to get the corresponding input representa-

tion. The input representation is composed of the sum of the token embedding, segment embedding, and position embedding. For example, assume that these three embeddings are E_{token} , E_{segment} , and E_{position} , respectively, and the input representation E corresponding to the input sequence can be calculated by the following formula:

$$E = E_{\text{token}} + E_{\text{segment}} + E_{\text{position}}. \quad (20)$$

In the formula, E_{token} represents the token embedding, E_{segment} represents the segment embedding, and E_{position} represents the position embedding; the size of the three embeddings is $M * d$, where M represents the maximum length of the sequence, which is 512 in this paper, and d represents the dimension of the word vector, which is 768 in this article.

(3) Transformer Encoders. In transformer encoders, the input embeddings pass through 12 encoder layers and use the self-attention mechanism to fully learn the semantic representation between each word in the input sequence.

$$E_i = \text{Encoder_layer}(E_{i-1}), \quad (21)$$

where E_{i-1} indicates the output vector of the i -th encoder layer, and E_0 is specified to be equal to the input embedding. Finally, after 12 encoder layers, the output vector of the encoder is as follows:

$$E_o = \text{Encoder_layer}(E_{11}), \quad (22)$$

where E_o indicates the output vector of the last encoder layer.

(4) The Pooled Layer. In this layer, the output of the encoder layer is fed into a pooled layer to get pooled output.

$$\text{Pooled_output} = E_o * W + b, \quad (23)$$

where W denotes the weight matrix of the pooled layer and b represents the bias vector.

(5) The Output Layer. In the final output result, we do not need the output of each token in the input sequence, but we only need the output sequence where the current blank is located. Therefore, for the pooled outputs of the other positions except for blanks, we will remove them from the total output and then splice the remaining pooled outputs of these blank positions to obtain the output O . Among them, for the output O_i denoting the i -th blank, we use the Softmax function to calculate the confidence probability that the current blank position matches the current option.

$$P_i = \text{Softmax}(O_i) = \frac{e^{O_i}}{\sum_j e^{O_j}}. \quad (24)$$

Finally, after obtaining the prediction probability P_i corresponding to the class label of the current sequence, the

TABLE 10: The evaluation results of pretrained models and human performance on span datasets.

Models	Short span dataset		Long span dataset	
	F1	EM	F1	EM
Human performance	93.56	85.34	90.47	82.56
PLM with short span MLM	25.03	23.93	13.09	10.79
PLM with long span MLM	24.74	23.31	13.28	11.06

TABLE 11: The evaluation results of pretrained models and human performance on cloze datasets.

Models	Short cloze dataset		Long cloze dataset	
	QAC	PAC	QAC	PAC
Human performance	97.45	92.87	95.24	90.71
PLM with short cloze MLM	64.63	17.10	65.82	17.60
PLM with long cloze MLM	63.28	15.20	67.02	18.60

cross-entropy loss between the correct answer T_i and the prediction probability P_i is calculated.

$$\text{Loss} = \text{CrossEntropyLoss}(P_i, T_i). \quad (25)$$

The training objective is to minimize the total cross-entropy loss between the prediction probability and the standard answer sequence.

(6) *Answer Prediction and Evaluation.* When predicting the answer, we choose the blank with the highest probability as the position where the answer option I should be filled. Finally, according to the standard answer, the PAC and QAC of the predicted answer are calculated.

9. Result Analysis

9.1. *Human Performance.* In order to evaluate the human performance on our datasets, we invited 10 college students to answer questions in the datasets manually. Finally, we got the answers in the test sets of the four datasets, respectively. Then, we calculated F1 and EM to roughly evaluate the human performance on the proposed long span dataset and short span dataset, and we also calculated PAC and QAC on the proposed cloze datasets.

9.2. *Model Performance.* The evaluation results on the pretrained models on different MRC datasets are presented in Table 10. For fair comparison, these models are all fine-tuned with the same hyperparameters and without any data augmentation. We fine-tuned three different runs and report the mean results. The pretrained language models based on the corresponding MLMs constantly outperform other pretrained language models on the corresponding datasets by an obvious margin.

As shown in Table 10, the pretrained language model based on the long span MLMs performs better on the long span dataset compared to the other three pretrained language models, though there still exists a large gap between this model and human performance. At the same time, the pretrained language model based on the short span MLMs performs better on the short span dataset compared to the other pretrained language models.

As shown in Table 11, pretrained with long cloze MLMs, the long pretrained model outperforms other models on the long cloze dataset. As for the short cloze dataset, the pretrained language model based on the short cloze MLMs achieves a score increase over other models, demonstrating the effectiveness of the proposed MLMs.

In summary, the experimental results demonstrate that our hypothesis is true. The length of MLM is indeed related to their performance in MRC tasks with different answer lengths. It can guide us on how to pretrain an MLM with a relatively suitable mask length distribution for various MRC tasks.

10. Conclusions

In this paper, we propose an evaluation framework to quantitatively verify whether masking schemes of different lengths will affect the results of the MLM in MRC tasks with different answer lengths. In order to address this issue, herein, (1) we propose four MRC tasks with different answer length distributions, namely, the short span extraction task, long span extraction task, short multiple-choice cloze task, and long multiple-choice cloze task; (2) four Chinese MRC datasets are created for these tasks; (3) we also have pretrained four masked language models according to the answer length distributions of these datasets; and (4) ablation experiments are conducted on the datasets to verify our hypothesis. The experimental results demonstrate that our hypothesis is true. On four different machine reading comprehension datasets, the performance of the model with correlation length distribution surpasses the model without correlation. It can guide us on how to pretrain an MLM with a relatively suitable mask length distribution for various MRC tasks. However, as a case study, we must also be conservative in the strength of our conclusions since more comprehensive future research and experiments are needed.

Data Availability

The data used to support the findings of this study are available from the corresponding author upon request.

Conflicts of Interest

The authors declare no conflict of interest.

Acknowledgments

Research reported in this publication was partially supported by the Ministry of Science and Technology of China under the project of “New Generation Artificial Intelligence” with

Retraction

Retracted: Research on Wireless Sensor Network Positioning Based on Genetic Algorithm

Wireless Communications and Mobile Computing

Received 28 November 2023; Accepted 28 November 2023; Published 29 November 2023

Copyright © 2023 Wireless Communications and Mobile Computing. This is an open access article distributed under the Creative Commons Attribution License, which permits unrestricted use, distribution, and reproduction in any medium, provided the original work is properly cited.

This article has been retracted by Hindawi, as publisher, following an investigation undertaken by the publisher [1]. This investigation has uncovered evidence of systematic manipulation of the publication and peer-review process. We cannot, therefore, vouch for the reliability or integrity of this article.

Please note that this notice is intended solely to alert readers that the peer-review process of this article has been compromised.

Wiley and Hindawi regret that the usual quality checks did not identify these issues before publication and have since put additional measures in place to safeguard research integrity.

We wish to credit our Research Integrity and Research Publishing teams and anonymous and named external researchers and research integrity experts for contributing to this investigation.

The corresponding author, as the representative of all authors, has been given the opportunity to register their agreement or disagreement to this retraction. We have kept a record of any response received.

References

- [1] J. Zhang, Y. Hu, and H. Li, "Research on Wireless Sensor Network Positioning Based on Genetic Algorithm," *Wireless Communications and Mobile Computing*, vol. 2021, Article ID 3996401, 7 pages, 2021.

Research Article

Research on Wireless Sensor Network Positioning Based on Genetic Algorithm

Jing Zhang ¹, Yajing Hu ², and Hongliang Li ¹

¹Nanjing University of Science and Technology, Nanjing 210000, China

²Beijing Institute of Technology, Beijing 100081, China

Correspondence should be addressed to Yajing Hu; n17301035@stu.ahu.edu.cn

Received 9 October 2021; Revised 24 October 2021; Accepted 1 November 2021; Published 16 November 2021

Academic Editor: Balakrishnan Nagaraj

Copyright © 2021 Jing Zhang et al. This is an open access article distributed under the Creative Commons Attribution License, which permits unrestricted use, distribution, and reproduction in any medium, provided the original work is properly cited.

For smart city wireless sensing network construction needs, a network positioning algorithm based on genetic algorithm is proposed. The genetic algorithm uses a real number encoding, and the positioning model is constructed by analyzing the communication constraint between unknown nodes and a small amount of anchor nodes and constructs the positioning model, and the model is solved. The results show that when the ranging error is 50%, the positioning error is only increased by approximately 15% compared to the nonranging error. In a more harsh environment, if the ranging error is equal to the node wireless range, the ranging error is 100%, and the positioning error and the positioning ratio are not significantly changed. The scheme obtained by this algorithm can be well approached with an ideal limit. In the case where the sensor node is given, the algorithm can obtain the maximum coverage.

1. Introduction

In the past 30 years since the reform and opening up, the prototypes of rural development have basically formed, and the urban basic construction has received more attention from the urban construction industry in my country. With the vigorous development of my country's infrastructure construction, the measurement of the quality of facilities and technology has become higher and higher, and the dynamic facility environment has also put forward higher requirements for the real-time performance of the environmental monitoring system. In urban infrastructure, traditional urban facilities have environmental factors such as soil, pressure, explosions, fire, and earthquakes, which can cause safety hazards, threatening the property and personal safety of the people. For example, in September 2012, a large area of roads in Xi'an, Shaanxi Province, collapsed causing cement tank cars to fall into the large pit, resulting in a serious natural gas pipeline rupture accident. In July 2014, the junction of Xinye Road and Fuchun Road, Hangzhou, due to the nearby river, collapsed, and river water was inverted, bringing great inconvenience to people's travel. Globally,

almost every year, a large number of urban infrastructures not only cause waste and environmental pollution but also interfere with people's normal life, but even threaten people's lives and property safety. On the other hand, traditional urban infrastructure monitoring is mostly manually monitored, and this means requires test personnel record, analysis and classification measurements, and excessive time spent. In addition, the monitoring method is often accompanied by the loss and mistiness of measurement data, high monitoring costs, and lower transmission efficiency. This will inevitably not meet real-time communication and feedback requests in infrastructure environments.

Urban infrastructure construction has the characteristics of complex structure, frequent disasters, risk aggregation, and function, which have brought serious tests on urban infrastructure monitoring. It can be seen that how to establish a real-time, effective urban infrastructure monitoring system, timely and accurate prediction of the safety hazards in the infrastructure, avoiding the occurrence of the above accidents, is one of the major challenges of urban infrastructure construction. With the rapid development of intelligent information technology, people get information in the way.

As an important representative of the IoT, wireless sensor network (WSN) is a wireless network configured by a node group that is self-organized and multi-hop-transmitted, which can process and transmit environmental information in the monitoring area. At present, the wireless sensor network has set off a new research boom in the world. Through wireless sensor networks, people can make more convenience of the perception and acquisition of objective world information, further enhancing human exploration of the world's ability. At present, the wireless sensor network has been widely used in military, environmental monitoring, traffic management, intelligent home, and other fields [1].

2. Literature Review

Wireless sensor networks can collect valuable raw data in a realistic environment, and many of the data information is dependent on geographic location information. Therefore, positioning is an important technique for wireless sensing network and has obtained extensive attention and research interest in the academic circles and research in the domestic and foreign. Due to the advancement of information technology, researchers have continuously improved urban infrastructure monitoring systems through various ways, and the urban security levels have greatly improved.

In recent years, some common smart city infrastructure, such as urban transportation monitoring system, urban environmental monitoring system, and urban waste management system, gradually applied wireless sensor network to the system's construction, truly real-time accurate science management. Rady et al. installed a large number of sensors in the Fuhu Bridge on the Beijing-Hangzhou Grand Canal, which constitutes the largest wireless sensor network detection system in the world through the sensor node and detects all kinds of information on the bridge and use wireless sensing network [2]. "Pulse" large bridge. Xiao et al. have developed a set of smart city buildings [3]. The building is an event-driven architecture that can be used to monitor the management and collaboration of heterogeneous sensors in public spaces. Experimenting on the test bench of the subway scene, the results show that the proposed building can enhance the detection of abnormal events, simplify the operator's task, and ensure the communication between the passengers in an emergency. Bhole et al. proposed an innovative mesh network architecture [4]. This structure allows WSN to collect environmental information more efficiently. In terms of future smart city concepts, it will have new technologies related to the Internet of Things to optimize environmental monitoring methods under smart cities. According to Keswani and Bhaskar for urban environmental pollution, two integer linear planning formulas based on actual pollutant proliferation models are proposed to handle minimal costs for air pollution monitoring WSN deployment [5]. They analyzed the model to actual data (i.e., Nordoham City Street Lights) and have got some effective WSN deployment to conduct air pollution monitoring. Niknamian proposed the urban waste management system based on the Internet of Things [6]. The system can confirm the monitoring of the garbage bin through the web page, and the level of gar-

bage available in the trash. This page displays the tag level of the trash and displays the garbage level collected in the trash to operate it. The system optimizes the garbage management mechanism of smart cities. Niknamian proposed a novel intelligent visual sensor for simultaneous posture estimation [6]. By enhancing tracking of vehicle attitude, it is possible to better estimate the trajectory of the vehicle, which is well solved multivehicle detection and tracking problems in smart urban traffic monitoring applications. According to Talib, deployment depends on the close resource monitoring through large-scale urban perception and designs three different atomization architectures, which will be close to sex and clouds in a valuable filtration standard. Communication is combined [7]. The results show that these three architectures can correctly identify 73% to 100% false location statement. The British Cambridge laboratory first designed and developed an Active Badge indoor positioning system. The basic principle was to communicate and position between sensor nodes to communicate and position. The American Institute of Technology (MIT) research team, in the indoor positioning, combines fingerprint recognition and inertial sensors to achieve high precision positioning. Muruganatham and El-Ocla deploy sensor nodes in the monitoring area and use radio imaging positioning techniques to track targets. The location of the target is rendered by the target motion and the received signal strength fluctuation [8].

3. Wireless Sensor Network Node Positioning Algorithm Based on Genetic Algorithm

The wireless sensor network positioning algorithm based on genetic algorithm is to establish a positioning optimization model of the unknown node position as the parameter by analyzing the communication constraint between unknown nodes and a small amount of anchor node. Estimation is unknown for unknown nodes.

The wireless sensor network has a number of nodes, wide distribution area, and more communication. The establishment of the positioning optimization model is a multiobjective multiconstraint nonlinear equation, and the genetic algorithm is a more mature evolutionary algorithm. There are simple application conditions and strong search capability, especially suitable for multiobjective, multiconstraint solution, so it is very suitable for the wireless sensor network node positioning optimization model. The node positioning problem description, node communication constraint, positioning optimization model, and genetic positioning algorithm are described in the following.

3.1. Positioning Problem Description. This paper adopts the vector $X = (x_1, x_2, \dots, x_M, y_M, x_{M+1}, y_{M+1}, \dots, x_N, y_N)$ ($m \geq 1, n \geq M + 1$) to simulate the initial position of the sensor node of the network topology area, where (x_i, y_i) ($i = 1, 2, n$) is the abscissa and ordinate of the i th node and i is a unique identifier of the node in the network. Assuming that the first m node $X = (x_1, x_2, \dots, x_M, y_M)$ is known, that is, the position of the anchor node, the post- (nm) node $X = (x_{M+1}, y_{M+1}, \dots, x_N, y_N)$ is the unknown node position of the pending node,

and the positioning problem evolves into the coordinates known to the M node, asking them the coordinates of $(N - m)$ unknown points of communication constraints [9, 10].

3.2. Node Communication Constraint. Each sensor node includes a radio frequency transmitter and receiver of a radio wave. The effective radius of the wireless connection is R (i.e., the node wireless range), the node wireless propagation model is the amphotericity of the radius of radius R . Circle model. If the distance between the two sensor network nodes is less than or equal to its wireless range R , the two nodes are regarded as communication. This article assumes that anchor nodes and unknown nodes are exactly the same on the hardware configuration. As shown in Figure 1(a), X_1 and X_2 are unknown nodes and A_i is an anchor node, and when the nodes X and X_2 are in this circle, it is considered that the anchor node A_i and the unknown nodes X_1 and X_2 can communicate with each other. Think

$$\|A_i - X_j\| \leq R, \quad j = 1, 2. \quad (1)$$

Figure 1(b) illustrates how to estimate the distance to an unknown node through the node wireless propagation model. The anchor node A_i sends radio frequency waves around it, assuming that the unknown nodes X_1 and X_2 can communicate with it. The approximate distance D_1 and D_2 , of the anchor node A_i to the unknown nodes X_1 and X_2 , is estimated by calculating the power loss based on the number of radio power received and the initial transmission power

$$\|A_i - X_j\| \approx d_j, \quad j = 1, 2. \quad (2)$$

3.3. Positioning Optimization Model. There is an n node in the WSN as shown in the WSN, where the first M is an anchor node, and then, $N - M$ is an unknown node; the wireless sensor network node positioning problem can be summarized as known anchor node A_i and anchor node communication constraints with unknown nodes X_j and both D_{ij} , looking for suitable unknown node positions, so that $\|A_i - X_j\| = d_{ij}$. However, due to the existence of ranging error, the problem is actually summarized to solve the

$$\min \sum \| \|A_i - X_j\| - d_{ij} \|. \quad (3)$$

Among them, A_i is an anchor node with communication constraints with X_j . This transforms the node positioning problem into model optimization, that is, the optimal solution of equation (3) is an estimate of unknown nodes [11, 12].

3.4. Genetic Location Algorithm. This paper increases the convergence speed of the genetic algorithm by increasing the positioning optimization model constraint conditions, setting various parameters such as genetic algorithms to accelerate the convergence speed of the genetic algorithm, and improving the efficiency of an algorithm.

- (1) Constraint conditions for positioning optimization models

It is assumed that the unknown node X_j and 3 anchor nodes can be communicated (with an anchor node which is A_i ($i = 1, 2, 3$)), respectively, the communication radius is R , and the unknown node must be in all A_i ($i = 1, 2, 3$) central, a square of a square with a side length of $2R$. The coordinates of A_i are known. If 123 represents the coordinates of the A_i , the coordinates of the three square intersecting public rectangular regions can be described as

$$\begin{cases} r_1 = (a_i)_{\min} + R, \\ r_2 = (a_i)_{\max} - R, \\ r_3 = (b_i)_{\min} + R, \\ r_4 = (b_i)_{\max} - R. \end{cases} \quad (4)$$

Among them, R_1 is the rectangular right boundary, R_2 is the rectangular left boundary, and R_3 and R_4 are rectangular on the boundary and the lower boundary. That is, for unknown nodes $X_j(x_j, y_j)$,

$$\begin{cases} r_2 \leq x_j \leq r_1, \\ r_4 \leq y_j \leq r_3. \end{cases} \quad (5)$$

Based on the constraint of X_j in equation (5), the genetic algorithm in this paper randomly generates pop positions (x_j, y_j) as the initial population, where ($j = 1, 2 \dots \text{Pop}$) [13–15].

- (2) Adaptive function settings for genetic positioning algorithms

According to the value of the parameters in formula (3), the adaptation function in the genetic algorithm is

$$f(x, y) = \sum_{i=1}^k |(x - a_i)^2 + (y - b_i)^2 - d_i^2|, \quad (6)$$

where (x, y) is the coordinate of the node and (a_i, b_i) and D_i are anchor node coordinates and distances that can communicate with them.

- (3) Individual encoding of genetic positioning algorithm is a large number of wireless sensor network nodes, and the amount of calculation is large. Considering that binary coding cannot directly reflect the individual structure, and the binary length is long, accounting for large memory, the positioning algorithm in this article is code type genetic algorithm, because of the real number encoding, easy operation, and transformation
- (4) Genetic positioning operator design genetic operator mainly includes selection, crossing, and variation operations. The selection operation adopts the

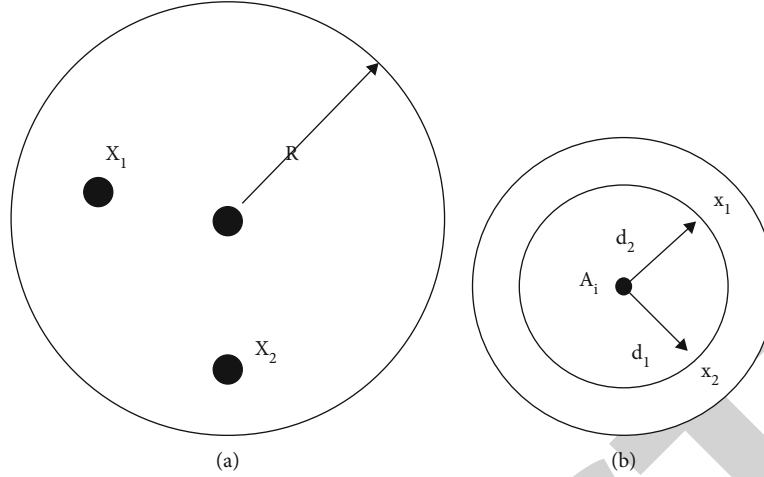


FIGURE 1: Wireless propagation model of a sensor node.

adaptive gambling selection method; the cross-adopted multipoint intersection, that is, the X -axis parameters and the Y -axis parameters, corresponds to cross; the variation operation selects the discrete single-point variant mode

- (5) Genetic positioning algorithm termination determination when the number of iterations reaches a predetermined number, or when the maturity of the group satisfies certain conditions, the iteration is stopped [16–18]

4. System Parameters and Algorithm Performance Parameters

This paper uses important system parameters in WSN and selects the position error and the positioning ratio as the algorithm performance index parameters. The performance of the algorithm can be clearly expressed by analyzing the effects of different system parameters on the performance of an algorithm.

4.1. System Parameters

- (1) Anchor node ratio λ . The number of anchors in the entire network accounts for the ratio of the total number of all nodes
- (2) Anchor node density ρ . Represents an anchor node number of anchor nodes within the wireless range of each unknown node
- (3) Network interconnection δ . The number of nodes in each unknown node wireless range
- (4) Ranging error ξ . Due to the influence of various environmental factors and the inaccurate signal propagation model, the error between the measured value and the true value of the measured distance of the node wireless communication module measures the distance. The ratio of the error value and the node wireless range is used. For example, the

ranging error of 20% indicates 20% of the ranging error equivalent to the node wireless range R [19, 20]

4.2. Performance Parameters

- (1) Positioning error ε . The estimated actual position from a size range with respect to the wireless node. The formula is

$$\varepsilon = \frac{\sum_{j=M+1}^N \|p_j - \hat{p}_j\|}{n'R}, 0 \leq n' \leq N - M, \quad (7)$$

where $j \in Mn$, $Mn = \{m + 1, \dots, n \mid m \geq 1, n \geq m + 1\}$, n' represents the number of positionable nodes, p_j indicates the estimation position of the unknown node X_j , and \hat{p}_j denotes an unknown node of the actual location of X_j

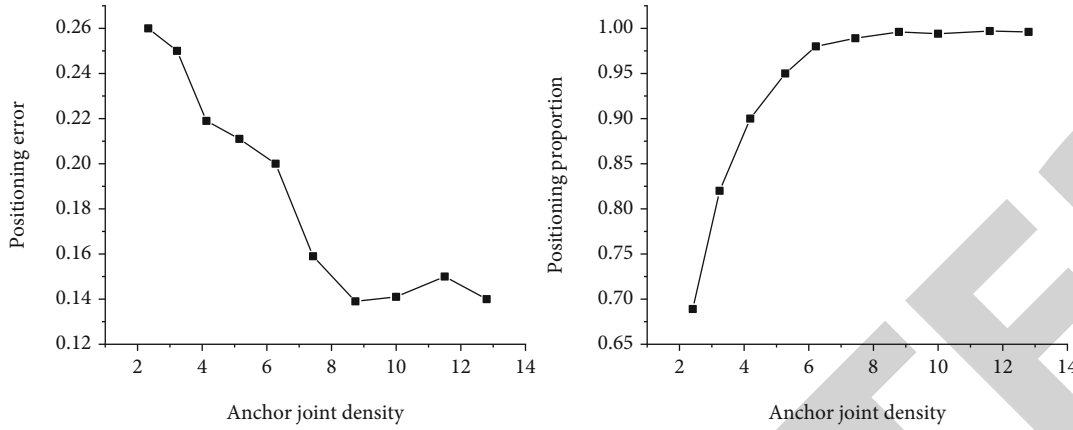
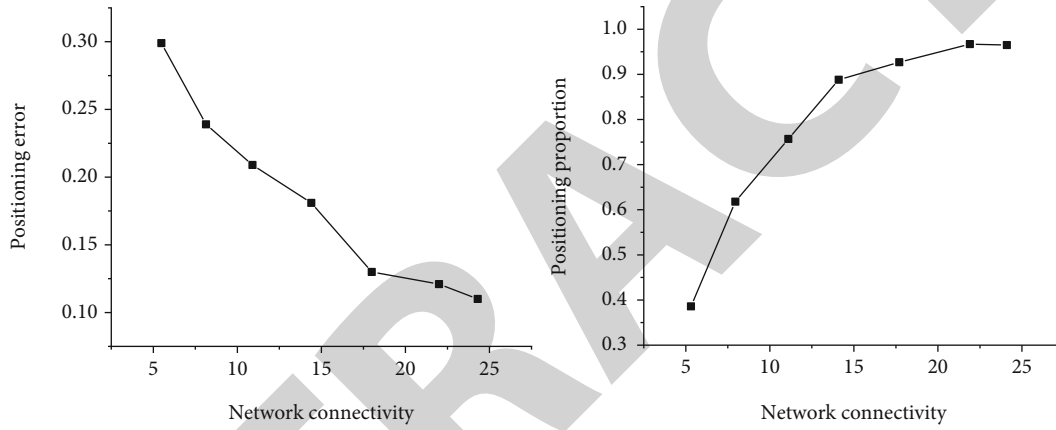
- (2) Position ratio η . Indicates that the positionable node accounts for the ratio of the number of unknown nodes, i.e.,

$$\eta = \frac{n'}{N - M} \times 100\% \quad (8)$$

5. Simulation

For the performance of the test algorithm, we conducted a series of simulation experiments. The content of this chapter mainly introduces the simulation environment and analyzes the results.

5.1. Simulation Environment. The simulation environment of the WSN in this article consists of 400 nodes, and the node is randomly distributed in the range of $10R \times 10RM^2$ and assumes that all nodes are located in the first quadrant, where r is a node wireless range. To simplify the calculation, the wireless range R is 10 meters in the experiment.

FIGURE 2: $\xi = 0.05$ and $\lambda = 0.15$.FIGURE 3: $\xi = 0.05$ and $\lambda = 0.15$.

Due to the random distribution of the sensor node, the estimation of the anchor distance has a certain random error, and the positioning results derived by the experiment have randomness that cannot be ignored. In order to obtain an accurate experimental result, the statistical method is used to simulate the algorithm. That is, 500 experiments are repeated in the same network environment; each experimentally unknown node will be renewed in the monitoring area, and statistics of 500 positional experiments [21].

5.2. Analysis of Experiment Results

- (1) Influence of anchor node density. Unlike an increase in anchor nodes, this experiment increases the network node density by increasing an anchor node communication radius. Figure 2 analyzes the relationship between anchor node density and algorithm performance. With the increase in the intercourse of the anchor node in the network, the positioning error is gradually decreased, and the positioning ratio has gradually increased. As can be seen from the figure, even if the anchor node density is only 2, the positioning error is less than 30%, and the positioning ratio is approximately equal to 70%,

and the present algorithm is suitable for an anchor node sparse

- (2) Influence of network communication. From Figure 3, increasing network connectivity can improve algorithm performance. Since network communication includes communication between anchor nodes and unknown nodes, the anchor node is related to unknown nodes. There is no effect, just communicating between unknown nodes and anchor nodes. Therefore, when the simulation changes the network communication change, the anchor node density will increase, so the improvement in algorithm performance in Figure 3 is caused by an increase in the density of the anchor node, not because of network communication variety
- (3) Effect of ranging error. For a positioning algorithm that requires a rough estimate between unknown nodes and anchor nodes, the sensitivity of the ranging error is a major factor for the evaluation algorithm. As can be seen from Figure 4, when the ranging error is 50%, the positioning error is only about 15% higher than when the ranging error is not ranging. In a more harsh environment, if the

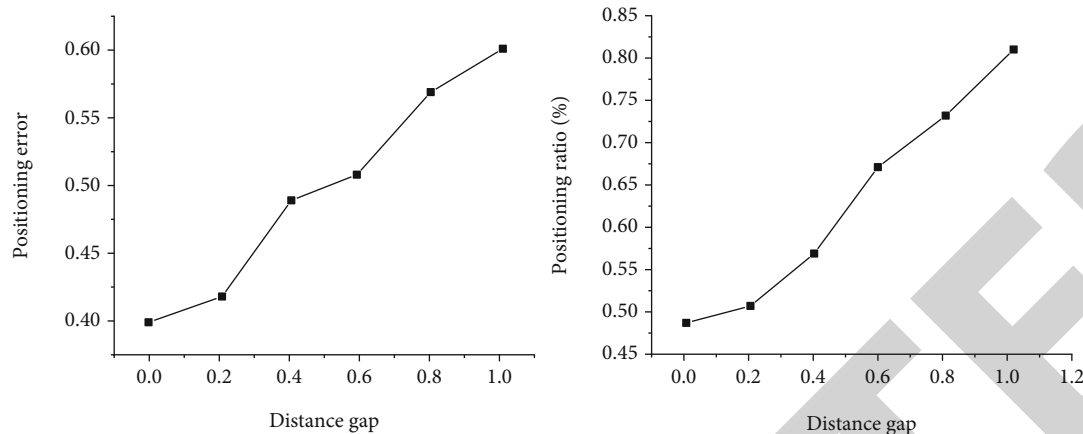


FIGURE 4: $\xi = 0.05$ and $\lambda = 0.15$.

ranging error is equal to the node wireless range, the ranging error is 100%, and the positioning error and the positioning ratio are not significantly changed. Therefore, the ranging error has little effect on the performance of the algorithm, making the algorithm have good anti-interference in a complex environment [22]

6. Conclusion

This paper is based on the construction of smart urban wireless sensing network as a background and proposes a network positioning algorithm based on genetic algorithm. The network positioning model is established. It is used to find the best solution through the genetic algorithm to implement the two anchor nodes to calculate the position of the unknown node. Simulation experiments show that the algorithm significantly increases the positioning accuracy and positioning coverage ratio compared to the traditional positioning algorithm.

Wireless sensor networks are frontier research topics belonging to multilearning cross-edge research. The progress of technology in the relevant field has promoted the continuous development of wireless sensor network positioning techniques. After each emerging technology has its shortcomings, only constantly improved, can we let technology mature. Wireless sensor network target positioning accuracy. The algorithm of this paper compares the accuracy of the model, and the parameters of the ranging model may be changed for different environments. In terms of wireless sensor network target positioning coverage, the unknown nodes of it will be upgraded into a virtual anchor node to participate in the next round of positioning, further increasing the positioning coverage.

Data Availability

The data used to support the findings of this study are available from the corresponding author upon request.

Conflicts of Interest

The authors declare no conflicts of interest.

References

- [1] P. Verde, J. Díez-González, R. Ferrero-Guillén, A. Martínez-Gutiérrez, and H. Perez, "Memetic chains for improving the local wireless sensor networks localization in urban scenarios," *Sensors*, vol. 21, no. 7, article 2458, 2021.
- [2] A. Rady, M. Shokair, S. El-Rabaie, and N. Sabor, "Efficient clustering based genetic algorithm in mobile wireless sensor networks," *Menoufia Journal of Electronic Engineering Research*, vol. 30, no. 1, pp. 1–12, 2021.
- [3] X. Xiao, H. Huang, and W. Wang, "Underwater wireless sensor networks: an energy-efficient clustering routing protocol based on data fusion and genetic algorithms," *Applied Sciences*, vol. 11, no. 1, p. 312, 2021.
- [4] J. Bhola, S. Soni, and G. K. Cheema, "Genetic algorithm based optimized leach protocol for energy efficient wireless sensor networks," *Journal of Ambient Intelligence and Humanized Computing*, vol. 11, no. 3, pp. 1281–1288, 2020.
- [5] K. Keswani and A. Bhaskar, "Flower pollination and genetic algorithm based optimization for node deployment in wireless sensor networks," *International Journal of Engineering Technologies and Management Research*, vol. 5, no. 2, pp. 281–293, 2020.
- [6] S. Niknamian, "Abnormal vehicle load identification method based on genetic algorithm and wireless sensor network," *American Journal of Traffic and Transportation Engineering*, vol. 4, no. 3, p. 82, 2019.
- [7] E. Talib, "Optimization approach to optimal power efficient based on cluster top option in wireless sensor networks," *Turkish Journal of Computer and Mathematics Education*, vol. 12, no. 4, pp. 970–979, 2021.
- [8] N. Muruganatham and H. El-Ocla, "Routing using genetic algorithm in a wireless sensor network," *Wireless Personal Communications*, vol. 111, no. 4, pp. 2703–2732, 2020.
- [9] A. Rezaeipanah, H. Nazari, and G. Ahmadi, "A hybrid approach for prolonging lifetime of wireless sensor networks using genetic algorithm and online clustering," *Journal of Computing Science and Engineering*, vol. 13, no. 4, pp. 163–174, 2019.

Research Article

Development Strategy of Internet Interactive Video under the Background of 5G Converged Media and Wireless Communication

Ruomu Miao ¹, Juan Li ² and Jiayin Gao ³

¹School of Media and Communication, Shanghai Jiaotong University, Shanghai 200240, China

²School of Arts, Shandong Management University, Jinan, Shandong 250357, China

³School of Humanities, Art and Design, Guangxi University of Science & Technology, Liuzhou, Guangxi 545000, China

Correspondence should be addressed to Jiayin Gao; gaojiayin2021@163.com

Received 8 July 2021; Accepted 21 October 2021; Published 9 November 2021

Academic Editor: Yong Deng

Copyright © 2021 Ruomu Miao et al. This is an open access article distributed under the Creative Commons Attribution License, which permits unrestricted use, distribution, and reproduction in any medium, provided the original work is properly cited.

At this stage, the promotion of 5G network has a positive basic value for the development of Internet interactive video. With the arrival of 5G era and the vigorous development of wireless communication technology, the trend of media convergence is more and more intense. The innovation of emerging technology and communication mode provides a strong support for the development of interactive video. With 5G technology as the background, Internet interactive video ushered in a blowout period of development. In recent years, video websites at home and abroad have launched interactive videos with their own characteristics. So, the imagination of integrated media evolved into the reality gradually. However, the excessively fast development speed concealed many existing shortcomings. There are still many constraints and deficiencies in the deep integration of each link of Internet interactive video. This paper discusses the development status of Internet interactive video and deeply analyzes the development characteristics of interactive video. In view of the existing problems, this paper puts forward development suggestions from the aspects of creating high-quality content and building “interactive video +” to help the better development of Internet interactive video.

1. Introduction

Under the background of the rapid advancement of information technology in recent years, the streaming media industry has also undergone tremendous changes. Traditional video gradually cannot meet the needs of the audience, and interactive video gradually enters public's field of vision. In order to better strengthen management, SARFT will officially define interactive video for the first time in 2020, emphasizing its “multitype interaction,” “nonlinear process,” and other characteristics [1]. At the same time, the development of 5G technology has provided a strong foundation for the development of interactive video. Major video platforms have launched representative interactive video products to compete for audience resources. The theoretical research and practical exploration of interactive video are also in full swing.

In terms of theoretical research, Li Siyao, from the perspective of media integration, conducts research on the integration of contemporary film and television dramas with games, analyzes interactive video in terms of aesthetics, communication methods, and audience psychology, and looks forward to the future of this field direction of development [2]. Starting with the communication characteristics of interactive video, Du Jixi sorted out and analyzed the problems existing in the development of interactive video at this stage and then gave suggestions for improvement in terms of technical production, story layout, and interactive design. Wang Yan conducted empirical analysis on specific interactive film and television dramas, selected the more influential “Love Apartment 5” as the research object, analyzed the multiple interactive nodes of the episode, especially the 13th episode, and compared the role of these nodes in breaking the “fourth

wall.” The play became an important reason for the popular video at that time [3].

In terms of practical exploration, although China’s interactive video started late, it has also recently ushered in a blowout trend. In July 2019, in order to cope with the problem of continuous loss of users, station B began to launch interactive videos, which regained the attention of a large number of users for itself. Since then, major domestic video production websites have joined the ranks of interactive video production, so 2019 can also be regarded as the “first year” of China’s interactive video development. In this year, the audience was exposed to domestic interactive film and television dramas, interactive variety shows, and short videos for the first time [4, 5]. This “novel” video method has refreshed most domestic users, and major websites have gained a high level of success, attention.

This research mainly explores the analysis of the main characteristics of Internet interactive videos, especially representative interactive video works in China, with the help of typical works analysis in a point-to-surface manner under the background of the increasingly deepening trend of 5G media convergence [6]. The characteristics of the era of the development of interactive video in our country are presented, and several suggestions for sustainable development in this field are put forward.

2. The Characteristics of the Development of Internet Interactive Video in the Context of 5G Converged Media

Although the interactive video format appeared as early as the 1960s, due to technical limitations, this interactive movie called “Kinoautomat: One Man and His House” did not attract public attention. However, with the development of information technology and the maturity of media integration, the industry development of interactive video and the appreciation experience brought to the audience have developed by leaps and bounds. See Table 1 for representative interactive video works launched by major domestic video platforms.

2.1. Inject More Vitality into the Industry. At this stage, audiences are generally tired of the linear structure of traditional film and television dramas and hope to incorporate their own wishes in the development of the plot. The popularity of online games has increased in recent years for this reason. The emergence of fusion media interactive video meets audience’s needs for psychological satisfaction of the subject status and nonlinear open ending in the current context [7]. The increase in audience’s right to speak in video works has largely got rid of the passive position when viewing traditional video programs, so that their own choices can have an important impact on the advancement of the storyline and the final outcome.

By transferring part of the initiative, the interactive video adds a sense of participation to the work similar to that of the game, and integrates the various feelings of video appreciation, game participation, and plot determination into the work, so that the relationship between the traditional work

and the user takes place. Change: such a change has injected more vitality into the development of the video industry and weakened or even reversed the unfavorable momentum of declining active members. From the financial annual reports of major video websites in recent years, it can be seen that the participation of the interactive video market has brought positive effects that cannot be ignored on company’s revenue and the growth of the number of members. Therefore, all major domestic video websites regard the production and promotion of interactive videos as one of their key targets.

Regardless of the starting point of the video website’s active involvement in interactive video, its objective effect is indeed to promote the innovation and development of the entire video industry, and at the same time, attract the attention of the audience again and further focus on user participation and other aspects as the video production [8]. One of the standards: in the era of big data led by 5G technology, the higher the user participation, the more data that can be obtained in the background, and the clearer the “individual sketch” of the user. So, the platform can more accurately grasp the real needs of users. On this basis, the introduction of interactive video has given the platform more commercialization and technical choices. In turn, let your own production also provide better conditions for the retention of users. Judging from the current situation, although various platforms generally adopt interactive video into the charging system, it has not affected the enthusiasm of users at all.

2.2. Bringing a Better Participation Experience for Users. According to media situation theory, electronic media can arrange and reorganize situations that originally belonged to various types. Judging from the reality, interactive video also conforms to this trend, fusing the two traditional scenarios of “interaction and video” together. This form brings a better participation experience to users. First of all, interactive videos help users realize the conversion of identities. Users are no longer passive viewers of video works but are able to integrate their own wishes into the work and evolve from video spectators to video participants, resulting in higher spiritual satisfaction. Although major video websites have their own interactive video products at this stage, most of the products are made by bloggers from the media groups. This diverse source of authors makes almost every work present its own unique characteristics, with both role substitution and an omnipotent God’s perspective. Let users have a variety of viewing experience.

Secondly, the current video production market is very competitive. For video sites, relying solely on the production of products such as interactive videos cannot ensure long-term maintenance of user loyalty. Therefore, the website must use high-quality products and designs to increase user retention. If you want to win a place in the video market, you must establish a sense of quality to ensure that you can attract users for a long time. Most users participate in the interaction out of a kind of curiosity, and it is an exploration of the influence of self-participation on the plot. For example, “Love Apartment 5”, which attracted the attention of the public in 2019, catered to audience’s psychology to a large extent and was a great success. Although iQiyi lags

TABLE 1: Interaction mode of main interactive products of each platform.

Platform name	Main interactive products	Interactive mode
Tencent video	Antique bureau	The plot which can choose
IQiyi	His smile	The plot which can choose
Mango TV	Star detective	Audience participation
Netflix	Black mirror: Pandas Nike	The plot which can choose

TABLE 2: Number of subscription members and payment proportion of domestic representative video platforms (as of the third quarter of 2020).

Platform name	Active member	Payment proportion
Tencent video	120 million	23.33%
IQiyi	100 million	18.03%
Station B	12.8 million	7.61%
Mango TV	36 million	15%

behind station B in the launch of interactive videos, with the strong audience base of the “Love Apartment” series and multiple interactive nodes, many episodes of the series have firmly occupied the main domestic social network once they are launched. Top of the platform rankings: with the help of the show, the iQiyi platform’s revenue in 2019 was nearly 30 billion yuan, an increase of 16% over 2018; subscription members exceeded 100 million, an increase of more than one-fifth over 2018.

It can be seen from Table 2 that in 2020, China’s top three video platforms have more than 100 million active members, and their annual revenue has also achieved substantial growth. This kind of growth rate is extremely rare in an environment where domestic video platform competition is extremely fierce.

3. Development Strategy of Internet Interactive Video under the Background of 5G Convergence Media

The reason why interactive video can quickly attract a large number of audiences on major platforms is mainly because it has interactive attributes, which have a wide range of attractiveness to audiences. Nowadays, interactive video has gradually become popular in variety shows, movies, games, and other fields and brings huge economic value. With the rapid development of 5G integrated media, interactive video will also have broad development prospects in e-commerce, medical, advertising, and other fields. However, many problems have been exposed during the development of interactive video. For example, in terms of communication channels, although there are a large number of communication channels, the communication form is relatively single, the video content lacks novelty, and the interactive form is not rich enough. If the above problems can be solved, interactive video will usher in a broader development prospect [8].

3.1. Break Platform Barriers, Win-Win Cooperation, and Broaden Communication Channels. At present, competition among major video platforms has intensified, building barriers to each other, and lack of communication and cooperation. Take IQiyi and Tencent video as examples. They each produce interactive video content with incompatible formats and cannot distribute it on the other party’s communication channels, which makes it impossible for interactive videos to establish a complete transmission chain. This situation is also common among traditional social media platforms such as WeChat, Weibo, and Toutiao. This way of doing things independently and lacking cooperation has resulted in the inability of interactive videos to reach a wider audience, and the inability of barrier-free communication and exchanges between audiences on various platforms, which makes it difficult for interactive videos to become popular.

As shown in Figure 1, although the number of interactive videos has increased on a large scale in recent years, the proportion of official production on the platform has gradually declined, which cannot effectively avoid the problems of inconsistent format and uneven content.

With the formal implementation of the “Internet Interactive Video Data Format Specification” issued by the State Administration of Radio, Film and Television, this situation has been improved, and the standard of interactive video has been unified. It has broken the barriers between various platforms and made communication channels more diversified. It has also promoted the wider dissemination of interactive videos among audiences. With the popularization of 5G wireless communication technology, network bandwidth and transmission efficiency will be further improved, which will help the efficiency and development of interactive video transmission [9].

3.2. Innovative Video Format Optimizes Video Content. Interactive video requires high professionalism and production costs from material collection and video editing to postproduction. Although there are some novel and popular interactive videos appearing on major platforms, in general, interactive videos still show uneven quality levels, lack of new ideas in content, and lack the characteristics of high-quality video content, which greatly restricts the development of interactive videos. The reason for the above-mentioned problems is that the production of interactive video requires professional technology, and the production cycle is long, and the production cost is high.

Today’s interactive video market lacks innovative video formats and high-quality video content, and a large number of similar content appears, causing aesthetic fatigue to the

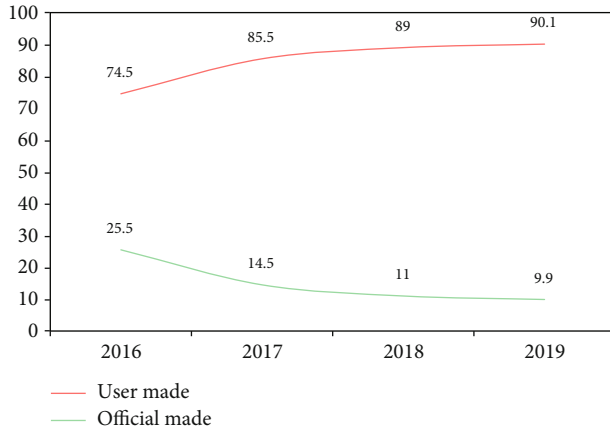


FIGURE 1: Comparison of interactive video producers in recent four years.

audience. In addition, in the process of creating interactive videos, creators either pay too much attention to interaction and lack in-depth analysis of the theme or pay too much attention to the discussion of the theme, and the interaction is insufficient to bring the audience an immersive experience in time and space. Therefore, if interactive video wants to develop rapidly, it must focus on innovative video formats and optimize video content. With the advent of the 5G era, intelligent video processing technology has brought great convenience to creators, simplifies the creation process, and saves creation costs, which can improve the production efficiency of interactive videos, innovate video formats, and optimize video content.

3.3. Build a New Business Model and Ecosystem. The main interactive form of interactive video still stays in the text interactive stage, and the interactive form is relatively single. Audiences can only watch videos through terminal devices such as computers and mobile phones, and the interactive space is limited, which makes interactive technologies still have huge development potential. The above-mentioned problems are caused mainly because the network transmission rate is not high, and new technologies such as VR and AR that rely on low latency and high transmission rate cannot be popularized, thus failing to provide users with an immersive interactive experience.

With the advent of the 5G era, the low latency and high speed characteristics of 5G communication technology will solve the above problems. The audience will also turn from viewers into real participants, elevating the form of interaction to a new level. 5G technology has promoted the change of interactive forms and will also change the traditional business form, especially in games, movies, sports, and other programs with strong interactive attributes, through the participation of audiences to achieve good interaction.

As shown in Figure 2, in 2021, interactive video is expected to focus on games, film and television integration, live broadcast, and other fields. For example, “interactive video + game” can enhance the gaming experience immer-

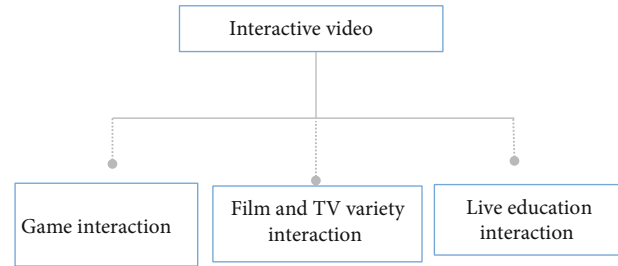


FIGURE 2: 2021 interactive video development trend analysis.

sively; “interactive video + film and television” can bring more shocking visual and auditory perception to the audience [10].

At the same time, the social attribute of interactive video also brings huge commercial value to online video outlets. For example, iQiyi added interactive form to the advertising content of the eighth issue of “China new rap” broadcast in 2019, so that popular players can directly become advertising spokesmen and help the brand realize flow cash. It also shows us the new business form brought by Internet interactive video [11]. This new business model of “interactive video +” can tap the great potential of Internet interactive video in the business field, not only in traditional games, film, and television industries but also in tourism, education, e-commerce, sports, and other fields with the trend of media convergence [12, 13]. In short, in the 5G era, more and more advanced intelligent technology will bring users a smoother interactive experience, thereby building a new business format for Internet interactive video.

4. Conclusion

The wireless communication technology represented by 5G communication technology has improved the production efficiency and spread of video content and promoted the field of interactive video to a new level. Wireless communication technology has played an important role in promoting interactive video content reconstruction, user stickiness, and marketing depth. China’s major interactive video platforms have focused on the field of interactive video, but they have not achieved the expected results in terms of economic benefits. This shows that in the context of 5G technology, how to use wireless communication technology is to promote the innovative development of interactive video to a new level. The height is still worthy of our continuous exploration. We have reason to believe that interactive video will have a broader development prospect with its unique and diverse interactive methods and high-quality video content. We must seize the opportunity and use 5G and other technological advantages to promote the rapid development of interactive video.

Data Availability

Data sharing is not applicable to this article as no datasets were generated or analyzed during the current study.

Conflicts of Interest

The authors declared no potential conflicts of interest with respect to the research, authorship, and/or publication of this article.

References

- [1] I. Hung, C. N. Kinshuk, and N.-S. Chen, "Embodied interactive video lectures for improving learning comprehension and retention," *Computers in Education*, vol. 117, pp. 116–131, 2018.
- [2] L. Zhu, "Research on the development of interactive video under the background of industrial operation," *Publishing wide angle*, vol. 11, pp. 79–81, 2020.
- [3] X. Meng, "New path of interactive video development in 5G era: a case study of station B," *Audio visual*, vol. 12, pp. 125–127, 2020.
- [4] Q. Zheng and F. Aihua, "Bottleneck and path optimization of interactive video development," *Contemporary TV*, vol. 5, pp. 87–90, 2020.
- [5] L. Chengrong, "5G network technology how to promote the construction of convergence media center," *Western radio and television*, vol. 11, pp. 247–248, 2020.
- [6] D. Shiyong and L. Xu, "Communication characteristics of interactive video works: taking invisible guardian as an example," *Young reporter*, vol. 29, pp. 96–97, 2019.
- [7] Y. Yang, Q. Liu, X. He, and Z. Liu, "Cross-view multi-lateral filter for compressed multi-view depth video," *IEEE Transactions on Image Processing*, vol. 28, no. 1, pp. 302–315, 2019.
- [8] L. Siyao, "Research on the characteristics and development of interactive video in the context of convergence media," *Television technology*, vol. 44, no. 531(2), pp. 82–84, 2020.
- [9] Z. Dewei, "Innovation path of interactive video under the background of 5G technology," *Western radio and television*, vol. 470, no. 6, pp. 34–35, 2020.
- [10] B. Gregorcic, E. Etkina, and G. Planinsic, "A new way of using the interactive whiteboard in a high school physics classroom: a case study," *Research in Science Education*, vol. 48, no. 2, pp. 465–489, 2018.
- [11] K. Schoeffmann, B. Münzer, A. Leibetseder, J. Primus, and S. Kletz, "Autopiloting feature maps: the deep interactive video exploration (diveXplore) system at VBS2019," *Conference on Multimedia Modeling*, vol. 11296, pp. 585–590, 2019.
- [12] A. T. Naman, Y. Wang, H. H. Gharakheili, V. Sivaraman, and D. Taubman, "Responsive high throughput congestion control for interactive applications over SDN-enabled networks," *Computer Networks*, vol. 134, pp. 152–166, 2018.
- [13] J. Yao, L. Wang, K. Liu et al., "Evaluation of electrical characteristics of biological tissue with electrical impedance spectroscopy," *Electrophoresis*, vol. 41, no. 16–17, pp. 1425–1432, 2020.

Retraction

Retracted: Finder-MCTS: A Cognitive Spectrum Allocation Based on Traveling State Priority and Scenario Simulation in IoV

Wireless Communications and Mobile Computing

Received 28 November 2023; Accepted 28 November 2023; Published 29 November 2023

Copyright © 2023 Wireless Communications and Mobile Computing. This is an open access article distributed under the Creative Commons Attribution License, which permits unrestricted use, distribution, and reproduction in any medium, provided the original work is properly cited.

This article has been retracted by Hindawi, as publisher, following an investigation undertaken by the publisher [1]. This investigation has uncovered evidence of systematic manipulation of the publication and peer-review process. We cannot, therefore, vouch for the reliability or integrity of this article.

Please note that this notice is intended solely to alert readers that the peer-review process of this article has been compromised.

Wiley and Hindawi regret that the usual quality checks did not identify these issues before publication and have since put additional measures in place to safeguard research integrity.

We wish to credit our Research Integrity and Research Publishing teams and anonymous and named external researchers and research integrity experts for contributing to this investigation.

The corresponding author, as the representative of all authors, has been given the opportunity to register their agreement or disagreement to this retraction. We have kept a record of any response received.

References

- [1] Z. Li and H. Shao, "Finder-MCTS: A Cognitive Spectrum Allocation Based on Traveling State Priority and Scenario Simulation in IoV," *Wireless Communications and Mobile Computing*, vol. 2021, Article ID 2270505, 18 pages, 2021.

Research Article

Finder-MCTS: A Cognitive Spectrum Allocation Based on Traveling State Priority and Scenario Simulation in IoV

Zhong Li and Hao Shao 

College of Information Science and Technology, Donghua University, Shanghai 201620, China

Correspondence should be addressed to Hao Shao; km10911@163.com

Received 1 September 2021; Accepted 12 October 2021; Published 8 November 2021

Academic Editor: Balakrishnan Nagaraj

Copyright © 2021 Zhong Li and Hao Shao. This is an open access article distributed under the Creative Commons Attribution License, which permits unrestricted use, distribution, and reproduction in any medium, provided the original work is properly cited.

With the increasing number of intelligent connected vehicles, the problem of scarcity of communication resources has become increasingly obvious. It is a practical issue with important significance to explore a real-time and reliable dynamic spectrum allocation scheme for the vehicle users, while improving the utilization of the available spectrum. However, previous studies have problems such as local optimum, complex parameter setting, learning speed, and poor convergence. Thus, in this paper, we propose a cognitive spectrum allocation method based on traveling state priority and scenario simulation in IoV, named Finder-MCTS. The proposed method integrates offline learning with online search. This method mainly consists of two stages. Initially, Finder-MCTS gives the allocation priority of different vehicle users based on the vehicle's local driving status and global communication status. Furthermore, Finder-MCTS can search for the approximate optimal allocation solutions quickly online according to the priority and the scenario simulation, while with the offline deep neural network-based environmental state predictor. In the experiment, we use SUMO to simulate the real traffic flows. Numerical results show that our proposed Finder-MCTS has 36.47%, 18.24%, and 9.00% improvement on average than other popular methods in convergence time, link capacity, and channel utilization, respectively. In addition, we verified the effectiveness and advantages of Finder-MCTS compared with two MCTS algorithms' variations.

1. Introduction

Recently, as a promising technology to serve the smart city, the internet of vehicle (IoV) has attracted the attention of governments and enterprises around the world. The moving vehicles can be regarded as mobile terminals equipped with advanced network components, such as wireless network interfaces and onboard sensors, which provide many personalized services by accessing the internet. These vehicle services (e.g., road condition broadcasts and dangerous event predictions) have high requirements for data transmission and communication quality. Although 5G technology is becoming popular and growing rapidly, the available spectrum resources have not increased simultaneously. So far, the spectrum resources of 6 GHz and below 6 GHz have almost been exhausted [1]. Moreover, the spectrum resources charged by the base stations are usually allocated to the calls and traffic services of mobile users firstly. Some up-to-date

spectrum measurements [2] have demonstrated the reality that the spectrum is vastly underutilized, while most licensed spectra have been allocated. Thus, the scarcity of spectrum resources and the low utilization of frequency bands are critical issues hindering the development of IoV.

Currently, as an effective solution to the underutilized problem of spectrum resources, cognitive radio (CR) can reuse idle spectrum resources through dynamic spectrum access technology. In CR networks, network users are divided into two types: primary users (PUs) and secondary users (SUs). PUs have a high priority to use the spectrum in the authorized frequency bands. SUs can dynamically access spectrum holes opportunistically and use available spectrum resources, which can enhance spectrum utilization. Therefore, in order to meet the spectrum demand of vehicles, we present a system model of cognitive radio-based internet of vehicle (CR-IoV) by introducing the cognitive radio function into smart vehicles.

In CR-IoV, the system includes PUs (composed of mobile phone users) and SUs (composed of vehicles equipped with CR functions). However, in reality, vehicle users with high mobility will cause frequent changes in the network topology. The availability of spectra will also change with the activation time and channel occupancy of PUs. Hence, how to meet the real-time and reliable requirements when solving the dynamic spectrum allocation problem under a time-varying environment is a significant challenge.

There are many previous studies about dynamic spectrum allocation in mobile wireless networks. The most popular studies can be mainly classified into four categories: (1) traditional optimization theory-based allocation methods [3, 4], (2) game theory-based allocation methods [5–7], (3) swarm intelligence optimization-based allocation methods [8–12], and (4) machine learning-based allocation methods [13–18]. Although the above methods can solve the spectrum allocation problem, there exist many disadvantages. First, when the constraints are complex, traditional optimization theory and game theory are not suitable for quickly solving large-scale dynamic planning problems. Second, swarm intelligence optimization is easy to fall into the local optimum [19]. Besides, the effective parameter settings and selection in the swarm intelligence optimization are also complex. Recently, deep reinforcement learning (DRL) algorithms have been proved to solve complex dynamic decision-making problems with high-dimensional state and action space. It can learn the potential regularities in the environment with the help of the idea of trial and error, thereby assisting intelligent decision-making. However, this type of machine learning-based method also exists some limitations, such as slow learning speed, poor convergence, and bad self-adaption ability. Thus, in this paper, we propose a new cognitive spectrum allocation method based on traveling state priority and different scenarios specially for IoV in this paper.

First, especially in IoV, we should consider the traveling/moving state of a vehicle. A vehicle that is about to leave the coverage area of a base station should have a relatively low spectrum allocation priority. Vehicle users with different traveling states, such as location, speed, acceleration, and communication capabilities, should have different opportunities to obtain spectrum resources. Thus, we consider the priority assignment based on vehicle state in spectrum allocation.

In addition, in this proposed new method, we choose the Monte-Carlo tree search algorithm (MCTS) to model our problem. Traditional model-free-based deep reinforcement learning algorithms (e.g., deep Q network and soft actor-critic) often require a large number of samplings and learn strategies from past experiences with the help of neural networks. However, model-based deep MCTS can not only use deep neural networks to fit the environment model from experience data but also simulate a variety of possible future trajectories for evaluation through the expansion of the tree structure, so as to choose more promising directions to explore the best policy. In this paper, through designing to simulate different scenarios, we improve the learning efficiency and reduce the searching space compared with traditional MCTS methods.

Our main contributions can be summarized as follows:

- (i) We design a priority assignment rule based on vehicle traveling states for spectrum allocation. Through defining a vehicle traveling evaluation score and a network utility score, we obtain a comprehensive priority evaluation score for each vehicle. According to the priority score, we allocate available spectrum resources from the highest priority to the lowest vehicle user, which can improve the allocation performance when doing dynamic spectrum allocation in IoV
- (ii) Combining with the above priority score, we propose a cognitive spectrum allocation method based on traveling state priority and different scenarios specially for IoV, named Finder-MCTS. We model the problem of spectrum allocation as a binary integer linear programming problem (BILP) with constraints. Meanwhile, through designing a constraint-oriented tree expansion and scenario simulation mechanism, Finder-MCTS can give an approximate optimal solution quickly and improve the link capacity of V2I (vehicle to infrastructure) communication in the network
- (iii) We conduct experiments to evaluate the performance of Finder-MCTS by using SUMO. Results show that our proposed method has 36.47%, 18.24%, and 9.00% improvements on average than other popular comparison methods in convergence time, link capacity, and channel utilization, respectively. In addition, Finder-MCTS also shows good improvements with the aid of priority evaluation and different scenarios' simulation of PUs' service durations, compared with two variations of MCTS

The remainder of this paper is organized as follows. In Section 2, a review of related work is provided. In Section 3, the system scenario and problem formalization are presented in detail. In Section 4, the priority assignment based on vehicle traveling state is described. In Section 5, the Finder-MCTS method for cognitive IoV spectrum allocation is proposed. In Section 6, simulations are carried out to demonstrate the effectiveness of the proposed Finder-MCTS method. In Section 7, conclusion and future work are given.

2. Related Work

Nowadays, there are many excellent studies on dynamic spectrum allocation in cognitive radio networks. In this section, we classify and compare them from the perspective of theoretical methods.

2.1. Spectrum Resource Allocation Based on Traditional Optimization Theory and Game Theory. In order to solve the problem of dynamic allocation of spectrum resources in wireless communications, the traditional methods mainly include the methods based on mathematical optimization [3, 4] and the methods based on game theory [5–7]. For

example, Martinovic et al. propose a cognitive radio spectrum allocation method based on integer linear programming in the work of [4], which solves the spectrum allocation problem with interference by using many complex assumptions and constraints. It is difficult or even impossible to find an optimal solution in the real cognitive radio network with the complex environment and dynamic network topology. Although the methods based on mathematical optimization have high solution accuracy, the generalization capability is insufficient.

Besides, with the goal of maximizing spectrum utilization, Yi and Cai introduce a spectrum resource allocation method based on auction in the work of [6]. Liu et al. design a dynamic spectrum access method using game theory in the work of [7]. However, these methods are not fit for IoV. The high mobility of vehicles puts forward a strict requirement for the convergence of Nash equilibrium in the game theory. It is hard to reach this equilibrium point.

2.2. Spectrum Resource Allocation Based on Swarm Intelligence Optimization. There are many related studies [8–12] based on swarm intelligence optimization in the domain of spectrum allocation. For example, Liu et al. use PSO to solve the allocation of spectrum resources in a centralized way in the work of [12]. However, the iteration of swarm intelligence optimization usually gets stuck in local optimal solutions, which can be far from the global optimal solution [19]. In addition, many swarm intelligence optimization algorithms have a large number of calculations in debugging due to complex parameters.

2.3. Spectrum Resource Allocation Based on Machine Learning. In recent years, with the development of statistical learning methods, many studies use machine learning to realize the dynamic spectrum allocation [13]. Among them, reinforcement learning can guide a system agent to learn the unknown environment by trial and error [20]. It can be applied to the spectrum allocation decision.

First, the multiarm gambling machine (MAB) not only is an important random decision-making theory in the field of operational research but also belongs to a type of online learning algorithm in reinforcement learning. The task of the agent is to select one arm to pull in each round based on the historical rewards it collected, and the goal is to collect cumulative rewards over multiple rounds as much as possible. In essence, MAB is a way to optimize the reward by balancing exploration and exploitation. Li et al. give a survey of spectrum resource allocation by using MAB in the cognitive radio network in the work of [14]. Zhang et al. formulate and study a multiuser MAB problem that exploits the idea of temporal-spatial spectrum reuse in the cognitive radio network [15]. However, the MAB modeling does not consider the cost of pulling arms in the existing allocation schemes. When MAB is utilized to solve the allocation problem in a centralized way, the scale of the arm increases exponentially with the number of users to be assigned. Therefore, the convergence of the spectrum resource scheduling algorithm based on MAB cannot be guaranteed.

In addition, model-free-based deep reinforcement learning is also applied to the research of spectrum allocation. Naparstek and Cohen propose a spectrum allocation scheme based on a deep learning framework under the wireless environment in the work of [16]. However, model-free-based deep reinforcement learning has problems of slow online learning speed and bad self-adaption ability.

Recently, another kind of model-based reinforcement learning, Monte-Carlo tree search algorithm (MCTS), is applied in the field of resource allocation [17, 18]. The MCTS-based allocation algorithm builds a decision tree to explore the possible solutions by expanding and pruning. Due to the expansion of the tree, the search space becomes tremendous gradually and the calculation scale is unacceptable. If this type of method is applied in IoV directly, the dynamic environment will further cause a large search tree. In addition, due to the neglect of environmental uncertainties, the random strategy adopted by Basic-MCTS in the simulation stage will produce a high variance, which reduces the search efficiency [21].

3. System Scenario and Problem Formalization

In this section, we introduce the system scenario of spectrum allocation in CR-IoV in Section 3.1 and give the mathematical formalization of our optimization problem in Section 3.2.

3.1. System Scenario. Figure 1 shows the system scenario of spectrum allocation in CR-IoV. PUs are the authorized mobile phone users in the current network, and SUs are vehicles equipped with CR modules. When a PU occupies a channel, there is a protection area around the PU (i.e., the red area in Figure 1). Similarly, an interference radius is also generated when the SU occupies a channel (i.e., the green area in Figure 1). Any radiation from SUs falling into the protection area would interfere with the PU.

In this scenario, our designed allocation algorithm is deployed on the base station. Vehicle nodes equipped with CR modules can sense whether there exist available idle spectrum resources. A vehicle can use the common control channel (CCC) to send a request to the base station to access the channel. The base station collects requests from vehicles centrally and learns a near-optimal policy to allocate available channel resources to cognitive vehicles within the coverage area (i.e., the black solid circle in Figure 1). Finally, the base station broadcasts the access confirmation message (i.e., the learned allocation policy) to the vehicles. The vehicle that received the access confirmation message can access the CR-IoV. Instead, the vehicle which has not received the message can continue to propose a new request to enter the next round of allocation.

Note that, because IoV is a dynamic network, our designed spectrum resource allocation algorithm must be executed within a defined allocation time window. We assume that the allocation time window for channel allocation is T . After the time window slides, we will refresh and observe the current vehicles which require to access the base station. A large time window cannot meet the real-time

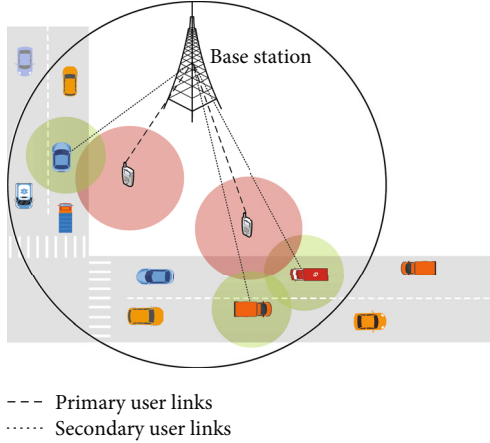


FIGURE 1: System scenario of spectrum allocation in CR-IoV.

requirement of IoV, but a time window that is too small cannot support our algorithm for well operating. In the experiment, we set the size of a time window T to 10 s to handle the dynamic network.

3.2. Definitions and Problem Formalization

3.2.1. Definitions. In this paper, we consider spectrum resource allocation in the underlay mode, i.e., each channel can support the parallel transmissions of several access users. Assume that within a base station's communication coverage, there are N SUs competing for spectrum resources of M channels at time t , and the channels are orthogonal and nonoverlapping. Meanwhile, we assume that there are K PUs as a prerequisite for spectrum allocation in the coverage area, and each PU occupies only one channel for information transmission in the current network. The spectrum resource allocation model consists of a channel availability matrix L , a SU-SU interference constraint matrix C , a channel reward matrix R , and a conflict-free channel assignment matrix A .

We define that a PU $k(1 \leq k \leq K)$ occupying a certain authorized channel $m(1 \leq m \leq M)$ in CR-IoV has a protection radius $\bar{R}(k, m)$. Meanwhile, each SU $n(1 \leq n \leq N)$ has an interference radius $\bar{R}(n, m)$ on channel m due to its transmit power. We obtain a Euclidean distance $\mathbb{D}(\bar{R}(k, m), \bar{R}(n, m))$ between a PU k and a SU n . When the inequality $\mathbb{D}(\bar{R}(k, m), \bar{R}(n, m)) - \bar{R}(k, m) \leq \bar{R}(n, m)$ holds, it means that there exists communication interference between the PU k and SU n .

Similarly, we also can obtain a Euclidean distance $\mathbb{D}(\bar{R}(n, m), \bar{R}(n', m))$ between two different SUs n and n' , where $\bar{R}(n, m)$ and $\bar{R}(n', m)$ are the interference radius values of the two SUs n and n' . When $\mathbb{D}(\bar{R}(n, m), \bar{R}(n', m)) - \bar{R}(n, m) \leq \bar{R}(n', m)$ holds, it means that there exists communication interference between the two SUs n and n' . Note that, when there is no communication interference between two users, they can use the same channel for transmissions at the same time;

otherwise, they cannot access the same channel at the same time.

Next, according to the above descriptions of communication interference between different users, we give the following definitions about our problem.

(1) *Channel Availability Matrix* L . $L = \{l_{n,m} | l_{n,m} \in \{0, 1\}\}_{N \times M}$ is an $N \times M$ -dimensional matrix used to describe the channel availability. When $l_{n,m} = 1$, it means channel m is available for SU n , and vice versa. It needs to meet the following two conditions to determine whether channel m is available for SU n . First, SU n cannot use channel m occupied by PU k under the condition $\mathbb{D}(\bar{R}(k, m), \bar{R}(n, m)) - \bar{R}(k, m) \leq \bar{R}(n, m)$. Second, SUs need to compare the interference power they received with the maximum allowable interference level γ_m on channel m . Channel m is considered to be available to SU n if the following inequality is satisfied:

$$\sum_{k=1}^K P_{m,n,k} + N_m \leq \gamma_m, \quad (1)$$

where $P_{m,n,k}$ denotes the received power at SU n of a signal transmitted from PU k on channel m and N_m denotes the level of background noise on channel m .

(2) *SU-SU Interference Matrix* C . $C = \{c_{n,n'}^{l,m} | c_{n,n'}^{l,m} \in \{0, 1\}\}_{N \times N \times M}$ is an $N \times N \times M$ -dimensional matrix used to describe the interference constraint between two different SUs n and n' on channel m , where $c_{n,n'}^{l,m} = 1$ indicates that there exists interference when SUs n and n' share the channel m for information transmission. Conversely, $c_{n,n'}^{l,m} = 0$ indicates that SUs n and n' can use channel m simultaneously. When $n = n'$, $c_{n,n'}^{l,m} = 1 - l_{n,m}$. Meanwhile, the matrix element needs to satisfy the condition $c_{n,n'}^{l,m} \leq l_{n,m} \cdot l_{n',m}$, i.e., the premise for the possibility of interference is that channel m is available to both SUs n and n' .

(3) *Channel Allocation Matrix* A . $A = \{a_{n,m} | a_{n,m} \in \{0, 1\}\}_{N \times M}$ is an $N \times M$ -dimensional matrix used to describe the conflict-free channel allocation for SUs. When $a_{n,m} = 1$ holds, it means that channel m is allocated to the SU n , and vice versa. Meanwhile, matrix A must satisfy the interference constraint given by matrix C . That is to say, for two different SUs n and n' , when $c_{n,n'}^{l,m} = 1$, the equation $a_{n,m} \cdot a_{n',m} = 0$ holds. In addition, we assume that each SU in the allocation can only occupy one channel for information transmission. Therefore, for any two different channels m and m' , the inequality $a_{n,m} + a_{n,m'} \leq 1$ should be satisfied.

(4) *Channel Reward Matrix* R . $R = \{r_{n,m} | r_{n,m} \geq 0\}_{N \times M}$ is an $N \times M$ -dimensional matrix used to describe the link rewards for different SUs. Notation $r_{n,m}$ denote the reward obtained by SU n when it occupies channel m of a base station. $r_{n,m}$

is measured by the link capacity. Link capacity is defined as follows:

$$r_{n,m} = W_m \cdot \log_2(1 + \text{SINR}_{n,m}), \quad (2)$$

where W_m is the bandwidth of channel m and $\text{SINR}_{n,m}$ is the signal-to-interference-plus-noise ratio when SU n accesses channel m . The calculation of $\text{SINR}_{n,m}$ is shown in

$$\text{SINR}_{n,m} = \frac{P_{m,n}}{N_m + \sum_{q=1, q \neq n}^{\text{Count}(A_m)} P_{m,q}}, \quad (3)$$

where we regard the SU and the base station as the transmitting-end and the receiving-end, respectively. Here, A_m represents the m th column vectors of matrices A and $\text{Count}(A_m)$ denotes the total number of allocated SUs on channel m ; $P_{m,n}$ is the power received by the receiver (base station) from the transmitter n on channel m .

3.2.2. Problem Formalization. From the above definitions, it can be seen that there are more than one channel allocation matrix satisfying the allocation constraints. Therefore, let $A_{L,C} = \{A_g\} (g \in \mathbb{N}^+)$ denote the set of all conflict-free channel allocation schemes derived from the current network conditions L and C . Because there are many possible spectrum allocation schemes, choosing different spectrum allocation schemes will generate different total system rewards. The object of spectrum allocation in this paper is to maximize the total network capacity $U(A, R)$ of the network system. We give the definition of total network capacity as follows:

$$U(A, R) = \text{SUM} \left(\sum_{m=1}^M A_m \circ R_m \right), \quad (4)$$

where R_m represents the m th column vector of matrix R . Notation \circ represents the Hadamard product, i.e., multiplication of the elements at the corresponding positions of the two vectors. A_m is a 0/1 decision vector of $N \times 1$ size, and R_m is an $N \times 1$ -dimensional reward vector with real numbers. $\sum_{m=1}^M A_m \circ R_m$ is also an $N \times 1$ -dimensional vector. Notation SUM is the operator that returns the summation of all entries of a matrix.

In the IoV, our paper is aimed at obtaining an optimal channel allocation matrix A^* (i.e., with the equation $A^* = \underset{A \in A_{L,C}}{\text{argmax}} U(A, R)$), which satisfies the above noninterference constraints and solves the problem of low utilization of spectrum resources at the base station side. The combinatorial optimization problem can be formulated as a binary integer linear programming problem (BILP) as follows:

$$*\max_{A,R} U(A, R) = *\max_{A,R} \text{SUM} \left(\sum_{m=1}^M A_m \circ R_m \right) \quad (5)$$

s.t.

$$a_{n,m} \in \{0, 1\}, r_{n,m} \geq 0, 1 \leq n \leq N, 1 \leq m \leq M \quad (5a)$$

$$a_{n,m} \leq l_{n,m} \quad (5b)$$

$$a_{n,m} \cdot a_{n,m}^{\prime} = 0 \text{ if } c_{n,n}^{\prime} = 1 \quad (5c)$$

$$a_{n,m} + a_{n,m}^{\prime} \leq 1 \quad (5d)$$

$$\bar{P}_{m,n}^{\min} \leq \bar{P}_{m,n} \leq \bar{P}_{m,n}^{\max} \text{ if } \bar{P}_{m,n} \neq 0 \quad (5e)$$

$$\sum_{i=1}^n P_{m,k,n} \leq \delta_{m,k}, 1 \leq k \leq K \quad (5f)$$

$$A_m \times R_m^T \leq \phi_m. \quad (5g)$$

Among these, constraint (5a) gives the value range of the matrix vectors A_m and R_m . Constraint (5b) ensures that an allocated channel must be an available channel for SU n . Besides, to protect the communication of each SU from interference by other SUs on channel m , the conflict-free channel allocation matrix should satisfy constraint (5c). Constraint (5d) indicates that each SU can only occupy one channel for information transmission. In constraint (5e), $\bar{P}_{m,n}$ represents the transmission power of SU n on channel m ; $\bar{P}_{m,n}^{\min}$ and $\bar{P}_{m,n}^{\max}$ represent the maximum and minimum allowable transmission power of SU n on channel m , respectively. This constraint defines the upper and lower bounds for the transmitted power of the SU. In other words, the transmission power of the SU should meet two constraints: on the one hand, it should not interfere with the normal use of the PU; on the other hand, it should meet the minimum allowable SINR required for transmissions. In the constraint (5f), $P_{m,k,n}$ represents the interference power of SU n received by PU k on channel m , and $\delta_{m,k}$ represents the maximum allowable interference power of PU k on channel m . For any PU k , the total received interference power on the channel m must be kept below the maximum allowable interference threshold, i.e., the PU is not interfered by SUs on the channel. In the constraint (5g), ϕ_m represents the available bandwidth of channel m , and R_m^T represents the transposed vector of R_m . This constraint ensures that the total network capacity of channel m should be less than or equal to its available bandwidth.

4. Priority Assignment Based on Vehicle Traveling State

In Section 4.1, we describe the problem of priority assignment. In Section 4.2, we give detailed definition of priority.

4.1. Problem Description. In CR-IoV, when the system carries out the spectrum allocation, the current state of vehicle traveling should be considered. For example, if a vehicle is about to leave the communication range of the current base station, it should be assigned to a low priority for spectrum allocation.

The traveling state of a vehicle at the current moment mainly includes direction, speed, acceleration, and GPS coordinates. Besides, the traveling state also should consider the degree of geographical dispersion among vehicles and the communication capability of a vehicle.

The current state information of each vehicle is collected by the current communicating base station. Then, we carry out priority evaluation for different cognitive vehicle users to distinguish the priority weights for spectrum allocation.

For a SU n who initiates a service request, from the perspectives of the global state and local state, a comprehensive priority evaluation score Priority score_n is constructed by defining a vehicle traveling evaluation score Traveling score_n and a network utility score Utility_n for the SU.

4.2. Priority Definition Based on Vehicle Traveling State

Definition 1 (vehicle traveling evaluation score). According to the GPS coordinates, speed, and acceleration, we define a vehicle traveling evaluation score Traveling score_n for a cognitive vehicle n as

$$\text{Traveling score}_n = \frac{1 + \cos(\theta_n)}{4} \cdot \left(\frac{v_{\max} - v_n}{v_{\max} - v_{\min}} + \frac{1}{1 + e^{a_n}} \right), \quad (6)$$

where θ_n denotes the angle between the current driving direction and the link connecting the vehicle's position with the base station's position. Notation a_n denotes the acceleration of the vehicle n . Notation v_n denotes the speed of the vehicle n . Notations v_{\max} and v_{\min} represent the maximum and minimum values of the driving speed. We assume that the vehicle speed is within the value interval $[v_{\min}, v_{\max}]$.

Obviously, a relatively large angle θ_n indicates that vehicle n will travel out of the coverage range of the base station in the future. Therefore, vehicle n with large θ_n should be given a relatively low spectrum allocation priority. We use formula $1 + \cos(\theta_n)/2$ to normalize the different weights of the angle θ_n to the value interval $[0, 1]$. In addition, a vehicle with high driving speed will quickly travel out of the coverage range of the base station in the future. Therefore, it should be given a relatively low spectrum allocation priority. The normalized formula $(v_{\max} - v_n)/(v_{\max} - v_{\min})$ is used to describe the influence of vehicle driving speed on the priority. Similarly, a vehicle with high acceleration should be given a relatively low spectrum allocation priority. To normalize the value interval to $[0, 1]$, formula $1/(1 + e^{a_n})$ is used to describe the influence of vehicle driving acceleration on the priority. Finally, to constrain the value of Traveling score_n within the value interval $[0, 1]$, we use constant coefficient $1/2$ to obtain the right side of Equation (6).

Definition 2 (network utility score). We define a network utility score to evaluate the communication capability of

cognitive vehicles. For cognitive vehicle n , its network utility score is defined as follows:

$$\text{Utility}_n = \log_2(1 + \text{SNR}_n) \cdot \frac{\sum_{1 \leq n, n' \leq N, n' \neq n} \text{Dispersion}_{n, n'}}{N - 1}, \quad (7)$$

where SNR_n denotes the signal-to-noise ratio of the user n to receive the signal from the base station. Formula $\sum_{1 \leq n, n' \leq N, n' \neq n} \text{Dispersion}_{n, n'}$ represents the global dispersion of user n within the coverage area of the base station.

For the numerator of Equation (7), we give the following detailed definition. $\text{Dispersion}_{n, n'}$ between two SUs n and n' is defined as follows:

$$\text{Dispersion}_{n, n'} = \begin{cases} 1, & D_{n, n'} > \varepsilon_n, \\ 0, & \text{others,} \end{cases} \quad (8)$$

where ε_n is a dispersion threshold and notation $D_{n, n'}$ represents the average dispersion time between two SUs n and n' . First, the threshold ε_n is obtained by taking the median value of $\{D_{n, n'} \mid 1 \leq n' \leq N, n' \neq n\}$. Second, the average dispersion time $D_{n, n'}$ is defined as

$$D_{n, n'} = \frac{\int_0^T \beta_{n, n'}(t) dt}{\tau_{n, n'}}. \quad (9)$$

In Equation (9), the communication dispersion state between two vehicles n and n' is defined as $\beta_{n, n'}(t)$. When there exists communication interference between vehicle n and n' , we let $\beta_{n, n'}(t) = 0$. It means that the two are in an "encounter" state. On the contrary, when $\beta_{n, n'}(t) = 1$, it means that the two are in a "scattered" state. Thus, in a time window T , the numerator of Equation (9) represents the total dispersion time between user n and user n' . Besides, $\tau_{n, n'}$ in the denominator denotes the total number of times that user n and user n' are in the "scattered" state in time window T . Obviously, the higher the value of $D_{n, n'}$, the longer the time that the two users n and n' are in the "scattered" state. Thus, we conclude that the higher the global dispersion $\sum_{1 \leq n, n' \leq N, n' \neq n} \text{Dispersion}_{n, n'}$, the greater the probability that vehicle n has the chance to reuse the channel, which further leads to a high network utility.

To sum up, a vehicle with a large network utility score in Equation (7) means that its global communication capability is strong, so the vehicle should be given a high spectrum allocation priority.

Definition 3 (comprehensive priority evaluation score). According to the vehicle traveling evaluation score Traveling score_n and network utility score Utility_n , we

construct a comprehensive priority evaluation score Priority score_{*n*} for the cognitive vehicle *n* below:

$$\text{Priority score}_n = \text{Traveling score}_n \cdot \text{Utility}_n. \quad (10)$$

For a cognitive vehicle who requests to access the base station, the base station calculates the priority score by collecting the vehicle's information. We rank all the scores from the largest to the smallest. Therefore, we can obtain a priority order list Priority score_list for all the cognitive vehicles in the current allocation task, which will be used in Section 5.

5. Finder-MCTS Algorithm for Cognitive IoV Spectrum Allocation

In Introduction, we mentioned that our paper will use MCTS to solve the problem of efficient spectrum allocation for CR-IoV. MCTS is a classic reinforcement learning algorithm based on tree search. To distinguish it from the method proposed in our paper, we call the classic MCTS as Basic-MCTS. The Basic-MCTS offers a concise computation framework by recursively using a tree policy to expand the search tree towards high-reward nodes and a default policy to perform the simulations for updating the estimated rewards and other statistics [22]. However, due to the continuous expansion of search actions, the search scale of Basic-MCTS is often very large, which greatly affects its search speed. In addition, due to the neglect of environmental uncertainties, the random strategy adopted by Basic-MCTS in the simulation stage will produce a high variance, which reduces the search effect of Basic-MCTS.

To improve the search speed and obtain a near-optimal solution, we propose an algorithm named Finder-MCTS in this section. First, we construct a search tree vertically according to the comprehensive priority evaluation score defined in Definition 3. Meanwhile, the constraints defined in Section 3.2 are also considered to reduce the search scale of the tree horizontally. Second, the uncertainty of the SUs' spectrum occupation activities is included in the simulation strategy. We give the bias estimation of reward in different scenarios in the simulation stage so as to approximate the real environment and accelerate the convergence of tree search.

Thus, in Finder-MCTS, the first step is to use the Markov decision process (MDP) to construct the Monte-Carlo tree computation framework (Section 5.1). Then, with respect to the state prediction, we give a DNN-based environment state predictor (ESP) (Section 5.2). Finally, we describe the detailed steps of the Finder-MCTS algorithm (Section 5.3).

5.1. Finder-MCTS' Computation Framework. The problems solved by the MCTS are commonly formalized by the Markov decision process (MDP), in which we take the base station as the spectrum scheduling agent and use the link capacity formulated in Equation (2) as the value of the reward *Q* when a SU occupies a channel. Let \mathcal{S} and \mathcal{A} denote the MDP state space and action space, respectively. $\mathcal{F} : \mathcal{S} \times \mathcal{A} \rightarrow \mathcal{S}$ denotes the MDP transition function from

a state-action pair to the next state. The state transition function f_{ESP} is given by a deep neural network (DNN) simulator in Section 5.2. The definitions of the MDP state space and action space are described as follows:

$$\mathcal{S} = \{s_v | s_v, \varphi_v, \xi_v\}, \quad (11)$$

$$\mathcal{A} = \{a_m | 1 \leq m \leq M\}. \quad (12)$$

In Equation (11), the MDP state is composed of two parts: λ_v denotes a vector of remaining bandwidth of *M* channels under the base station, with $s_v = (\lambda_v = (\bar{\lambda}_1, \dots, \bar{\lambda}_m, \dots, \bar{\lambda}_M)_v)$; $\bar{\lambda}_m$ denotes the remaining bandwidth of *m*th channel. φ_v denotes the number of service requests to be allocated. ξ_v describes the total bandwidth requests of all φ_v cognitive vehicles. In addition, in Equation (12), the action space is a set composed of whether the number of *M* channels are allocated, in which the action a_m denotes that the agent allocates the channel *m* to a vehicle that enters into the priority-based allocation sequence and is ready to be scheduled by the base station currently.

A Monte-Carlo search tree consists of nodes and edges. A node *v* is a tree node that corresponds to the MDP state s_v , and the edge connecting a parent node and a child node in the tree represents an action that causes the state transition. Each node *v* in the tree holds a *node state*, which contains three types of statistics: visit count (\bar{N}_v), MDP state (s_v), and cumulative reward (Q_v) received by node *v*.

The specific search steps are shown in Figure 2.

- (1) Create a root node of the search tree and initialize the node state. Assume that the root node is denoted by *v* and the node state is $\{\bar{N}_v, s_v, Q_v\}$
- (2) Allocate the spectrum resources for vehicles according to the priority order list Priority score_list defined in Definition 3, and extend the child node while updating the node state. Each layer's tree expansion represents the spectrum allocation for a vehicle, and each allocation process involves many iterations. Take the root node *v* in Figure 2 as an example. When the channel assignment action of vehicle ID3 is a_1 , the search tree extends down to the child node v' and update the node state through iterative calculation (i.e., $s_v' = f_{\text{ESP}}(s_v, a_1)$)
- (3) When the tree expansion reaches the termination condition of iteration (i.e., the second users or the available spectrum resources are all allocated), an optimal channel allocation matrix A^* in the current allocation period is returned. For example, assume that when reaching the node v''' in Figure 2, the iteration ends. The black arrow lines direct an allocation path $v \rightarrow v' \rightarrow v'' \rightarrow v'''$. Then, the corresponding actions constitute a feasible allocation policy set $\{a_1, a_5, a_1\}$, which can be converted to a channel allocation matrix $A_{N \times M}$ as an output

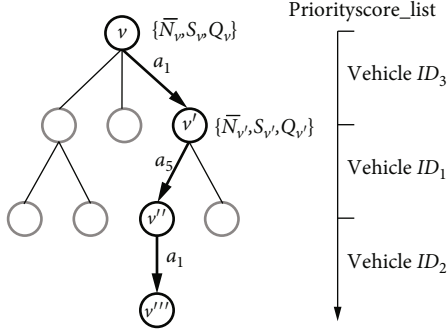


FIGURE 2: An example of search steps in Finder-MCTS.

5.2. DNN-Based Environmental State Predictor (ESP). Due to the uncertainty of the PUs' spectrum occupancy activities, when the tree is expanded from one node to the next in Section 5.1, the expansion will be not stable, i.e., given a state and an action, the next state is uncertain. This uncertainty is caused by the unknown environment of IoV. Therefore, to limit the expansion scale of the MCTS tree horizontally and speed up the search, it is necessary to gradually learn to approach the real environment of IoV when doing spectrum allocation. This section presents an offline environment state predictor (named ESP) based on a deep neural network (DNN).

Note that, to obtain the ESP, enough training data are needed. Thus, first during the cold start phase of Finder-MCTS (i.e., the algorithm just starts running), we do not rely on ESP. This does not affect the channel allocation solution of Finder-MCTS. After a period of time in the cold start phase, our base station can obtain and cumulate large numbers of "state-action transition pairs." Subsequently, we input these "state-action transition pairs" into ESP continuously as the training data to obtain a state transition function f_{ESP} , which is an offline training process. Once we have f_{ESP} , the Finder-MCTS could converge fast due to the reduction in branching. The above training is done by DNN.

The network structure of DNN consists of one input layer, three hidden layers, and one output layer. In this paper, we set the learning rate of DNN to 0.05 and the activation function of DNN is the rectified linear unit function (ReLU). To optimize the neural network parameters, we use the minibatch gradient descent method [23]. In the DNN, the training label is the state $s_{v'}$, which is the state of the corresponding expansion child node v' of node v . ESP is used to obtain the prediction state $\hat{s}_{v'}$. The loss function of ESP is

$$\text{loss}_{\text{ESP}} = \frac{1}{B} \sum_B (\|s_{v'} - \hat{s}_{v'}\|_2), \quad (13)$$

where B represents the batch size of minibatch gradient descent. In the experiment, we set $B=64$, indicating that 64 samples are selected in each iteration. Notation $\|\cdot\|_2$ represents the L2 norm. When loss_{ESP} converges, we let the DNN network parameter w_{ESP} update.

After we obtain the ESP function, based on the selected action a_m and MDP state s_v , ESP can give the MDP state of its expanded node $\hat{s}_{v'}$,

$$\hat{s}_{v'} = f_{\text{ESP}}(s_v, a_m | w_{\text{ESP}}). \quad (14)$$

5.3. Finder-MCTS Algorithm Based on Action Space Pruning and Scenario Simulation. Finder-MCTS requires to execute the following four steps: selection, expansion, simulation, and backpropagation iteratively to complete a computation process, which is shown in Figure 3. In Figure 3, the black circles indicate the nodes involved in each step and the red arrow lines indicate the actions corresponding to each step. In subfigure (c), the policy usually refers to the random selection action extended at each step of the simulation process. We usually call step (a) selection and step (b) expansion together as the tree policy. Specifically, the detailed procedures and descriptions are given in the following steps (a)–(d) and in Figure 4.

- (a) *Selection.* Each iteration starts from the root node. When the algorithm has to choose to which child node it will descend, it tries to find a good balance between exploitation and exploration. We use the upper confidence bound for tree (UCT) [24] to recursively select child nodes. The selection criterion of the optimal child node is

$$\text{argmax}_{v' \in \text{child}(v)} \left(\frac{Q_{v'}}{N_{v'}} + c \cdot \sqrt{\frac{\ln(\bar{N}_v)}{N_{v'}}} \right), \quad (15)$$

where $c \geq 0$ is a weight coefficient used to adjust the exploitation and exploration. We set $c=0.8$ in the experiment through many tests. Notation $\text{child}(v)$ represents the set of child nodes with v as the parent in the tree. $\bar{N}_{v'}$ and \bar{N}_v represent the total number of times that the child node v' and its parent node v have been visited iteratively. $Q_{v'}$ represents the cumulative reward obtained by node v' . Note that the selected child node should be expandable (i.e., have unvisited child node) and represent a nonterminal state. Next, the algorithm treats the child node with the largest value of UCT as the current node for the next expansion.

- (b) *Constraint-Oriented Expansion.* Finder-MCTS judges whether the number of visits of the current node is 0. If visit count $\bar{N}=0$, the algorithm goes to step (c) directly. If the visit count $\bar{N} \neq 0$, the algorithm enumerates the available actions. However, if it is just a simple enumeration, the number of available actions in the next layer is M . As the tree expands, a huge search tree will be built. The computational complexity grows geometrically with the number of SUs to be allocated. Thus, here, we give the constraint-oriented expansion.

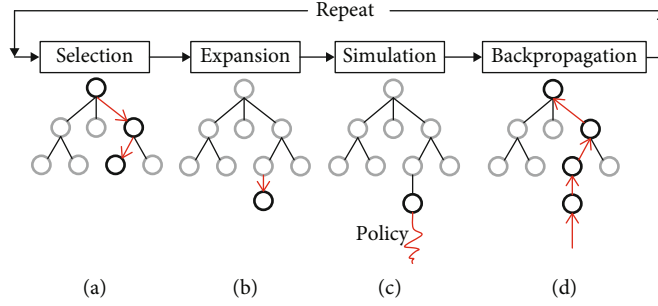


FIGURE 3: An iterative computation process of Finder-MCTS.

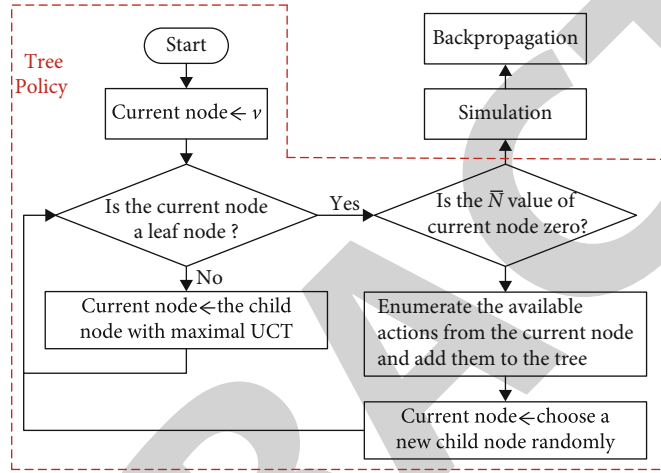


FIGURE 4: The flow chart of Finder-MCTS.

In the constraint-oriented expansion, we prune the action space according to the constraint conditions defined in Section 3.2 so as to obtain all available actions from the current node. And then, add new nodes to expand the tree and let the current node be a new child node which is randomly selected after expansion.

Specifically, we use $\mathcal{A}(n, v)$ to represent the set of available actions starting from the node v , which is used for the next round of channel allocation for the n th SU. That is to say, $\mathcal{A}(n, v)$ is an interference-free action space of a SU. The detailed implementation steps of the constraint-oriented expansion are described in Algorithm 1.

In Algorithm 1, we use three main steps to perform action pruning. First, considering the channel availability, we introduce the channel availability matrix L to prune the set of actions. We map the elements of $l_{n,m} = 1$ in the channel availability matrix for vehicle n to the available action set (Lines 2-6 in Algorithm 1). Second, considering that the vehicle ID_n currently to be allocated should not share the same channel with a vehicle having communication interference, we introduce the SU-SU interference matrix C for the tree pruning. The algorithm traverses the elements in the channel allocation matrix A and makes a judgement on whether $a_n^{l,m} = 1$ and $c_{n,n}^{l,m} = 1$ hold at the same time. If they hold at the same time, a_m is removed from the action

set (Lines 7-15 in Algorithm 1). Next, in each iteration, the algorithm needs to make a judgement on whether constraint (1) and constraints (5a)–(5g) hold. If the available channel m for the vehicle currently to be allocated does not satisfy these constraints, action a_m needs to be removed from the set of actions (Lines 16-20 in Algorithm 1). Finally, if $\mathcal{A}(n, v) = \emptyset$, the algorithm will skip the current allocation and wait for the next round of allocation (Lines 21-23 in Algorithm 1).

- (c) *Simulation Based on Different Scenarios.* From the above step (b), we know that if the visit count of the current node is zero, we will perform a simulation from the current node (i.e., the newly expanded node, denoted by \hat{v}) to the terminal node (denoted by \hat{v}_Δ). Here, the terminal node refers to the node that the descending arrives at when the SUs or the available channel resources have been all allocated. Usually, the simulation uses a random search strategy to generate a reward $Q_{\hat{v}_\Delta}$ at the final leaf node \hat{v}_Δ . However, the time-varying property of PUs' spectrum occupancy activities makes the actual available spectrum resources uncertain. This uncertainty will have potential impacts on the reward evaluation for the SU to be allocated in IoV.

Input:
 L - channel availability matrix
 C - SU-SU interference constraint matrix
 A - channel allocation matrix
 γ_m - the maximum allowable interference level of channel m
 ϕ_m - the available bandwidth of channel m
 $\delta_{m,k}$ - the maximum allowable interference power of PU k on channel m

Output:
 $\mathcal{A}(n, v)$ - the action space/set of vehicle ID_n under the current node v
Function Action (n, v)

```

1:  $\mathcal{A}(n, v) \leftarrow \emptyset$ 
2: for each  $l_{n,m}$  in the  $n$ -th row of matrix  $L$  do
3:   if  $l_{n,m} = 1$  then
4:      $\mathcal{A}(n, v) \leftarrow a_m$ 
5:   end if
6: end for
7: for each  $c_{n,n}^{l,m}$  in 1 ~  $n$  columns of the  $n$ -th row of matrix  $C$  do
8:   for each  $a_n^{l,m}$  in  $A$  do
9:     if  $c_{n,n}^{l,m} = 1$  and  $a_n^{l,m} = 1$  then
10:      if  $a_m \in \mathcal{A}(n, v)$  then
11:        remove  $a_m$  from  $\mathcal{A}(n, v)$ 
12:      end if
13:    end if
14:  end for
15: end for
16: for each  $a_m$  in  $\mathcal{A}(n, v)$  do
17:   if the available channel  $m$  for the vehicle  $ID_n$  does not satisfy the constraint (1) and constraints (5a)–(5g) then
18:     remove  $a_m$  from  $\mathcal{A}(n, v)$ 
19:   end if
20: end for
21: if  $\mathcal{A}(n, v) = \emptyset$  then
22:   the algorithm does not perform the allocation for vehicle  $ID_n$  and waits for the allocation of the next user according to the Priorityscore_list
23: end if

```

ALGORITHM 1: Constraint-oriented expansion for vehicle ID_n .

Therefore, in this paper, the duration of network service for a PU (denoted by τ) is included in the simulation when doing reward evaluation. Reference [25] pointed out that the duration of network service for PU in each channel obeys a log-normal distribution. The probability density function (PDF) is

$$f(\tau; \mu, \sigma) = \frac{1}{\tau\sigma\sqrt{2\pi}} e^{-(\ln \tau - \mu)^2 / 2\sigma^2} (\tau > 0). \quad (16)$$

The parameters (μ, σ) are in milliseconds (ms), and the values used in this paper are (2.47, 1.88) [25]. Note that the PDF model of PUs does not differentiate the location distribution of PUs (e.g., PUs on the vehicles or PUs on the pedestrians).

Through random sampling from the above distribution, we can obtain different scenarios of the service durations for the PUs at each layer in the simulation stage. Each sampling corresponds to a scenario. Since there are infinite scenarios when sampling, here, we sample the number of χ times at each layer of simulation to control the computation scale.

Thus, a scenario set is formed, denoted by $\hat{\pi} = \pi^1, \pi^2, \dots, \pi^i, \dots, \pi^\chi$. In the experiment, we set $\chi = 9$. Next, we define a stochastic bonus to adjust the reward evaluation according to different service durations, the resource supply and demand situation, and the utilities of SUs.

Definition 5 (stochastic bonus).

Assume that the channel m matches the vehicle ID_n and the tree expands from node \tilde{v} to node \tilde{v}' in the simulation stage. Then, we define a stochastic bonus for node \tilde{v} as $\mathbb{E}_{\pi} (H_{n,m}^{\tilde{v}}(i))$, in which \mathbb{E} represents the expectation of stochastic bonus obtained by vehicle ID_n in χ scenarios. We have

$$H_{n,m}^{\tilde{v}}(i) = \tanh(\text{Utility}_n) \cdot \tau_i^{-1} \cdot \left(\frac{\bar{\lambda}_m}{\text{Count}(L_m) - \text{Count}(A_m)} \right), \quad (17)$$

where $\tau_i (1 \leq i \leq \chi)$ denotes one of the samplings based on distribution $f(\tau; \mu, \sigma)$. The larger the value of τ_i , the longer

the channel occupied by the PUs in this sampling. It indicates that the bonus of vehicle ID_n when doing allocation will be low. Notation $Utility_n > 0$ represents the network utility score of vehicle ID_n (Definition 2), which reflects the communication capability of vehicle ID_n and is used as a weight coefficient here. We utilize the hyperbolic tangent function $\tanh(\cdot)$ to normalize the value of $Utility_n$ to the interval $[0, 1]$. When the $Utility_n$ is large, the weight coefficient is closer to 1, which indicates that the vehicle ID_n with strong communication ability tends to have a high bonus. Besides, $\bar{\lambda}_m / \text{Count}(L_m) - \text{Count}(A_m)$ measures the remaining minimum average bandwidth available to vehicle ID_n currently. $\text{Count}(L_m)$ records the number of elements in the m th column with value of 1 in matrix L . Thus, $\text{Count}(L_m) - \text{Count}(A_m)$ describes the maximum number of allowable access vehicles on channel m without considering the interference matrix C and the available bandwidth ϕ_m .

In summary, if a vehicle has strong communication capability, the PUs have low service durations, and the remaining resources are enough, the stochastic bonus will be high.

Based on Equation (17), we have an adjusted reward $Q_{\tilde{v}}$ for node \tilde{v} in the simulation stage:

$$Q_{\tilde{v}} = r_{(n,m)} + \mathbb{E}_{i \in \tilde{\pi}} \left(H_{n,m}^{\tilde{v}}(i) \right), \quad (18)$$

where $r_{n,m}$ refers to the immediate reward that channel m is allocated to vehicle ID_n (defined in Equation (2)). For simplicity, we use notation $Q_{\tilde{v}}$ omitting the label of n and m .

When the simulation reaches the terminal node \tilde{v}_{Δ} , we can get the simulation cumulative reward $Q_{\tilde{v}_{\Delta}}$ of all nodes on the simulation path from \tilde{v} to \tilde{v}_{Δ} . We have

$$Q_{\tilde{v}_{\Delta}} = \sum_{\tilde{v}}^{\tilde{v}_{\Delta}} \left\{ r_{n,m} + \mathbb{E}_{i \in \tilde{\pi}} \left(H_{n,m}^{\tilde{v}}(i) \right) \right\}. \quad (19)$$

- (d) *Backpropagation*. The aim of backpropagation is to update the empirical information of the prior exploration before the next iteration, which is shown in Figure 5. When an iteration reaches the terminal node \tilde{v}_{Δ} , according to Equation (19), we get the simulation cumulative reward $Q_{\tilde{v}_{\Delta}}$ for backpropagation.

In this way, the reward of backpropagation can include the reward evaluation of all expanded nodes on the simulation path, reflecting the overall spectrum allocation performance of simulation in the current iteration. Meanwhile, the algorithm updates the node state on the path from the root to the expanded node according to the following rules:

$$\begin{aligned} \bar{N}_v &\leftarrow \bar{N}_v + 1, \\ Q_v &\leftarrow Q_v + Q_{\tilde{v}_{\Delta}}. \end{aligned} \quad (20)$$

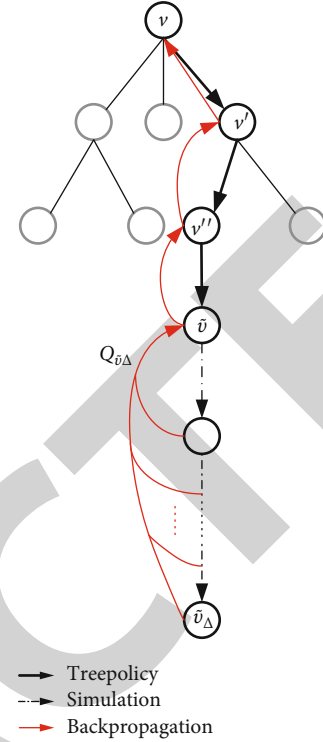


FIGURE 5: Backpropagation of Finder-MCTS.

To sum up, we provide the pseudocode of Finder-MCTS in Algorithm 2. The Finder-MCTS algorithm iteratively executes functions such as Tree policy, Simulation, and Backpropagation to explore different spectrum allocation schemes (i.e., A_m in $\Lambda_{L,C}$). It finally finds the optimal spectrum allocation scheme A^* in the current network.

6. Experimental Results and Analysis

In this section, first, we give the detailed simulation settings, including the vehicular dataset generation and some parameters in our proposed method. Second, we compare Finder-MCTS with other types of methods in terms of channel utilization ratio (CUR), average link capacity (ALC), and convergence time. Finally, we test the performance of Finder-MCTS compared with other MCTS algorithms' variations.

6.1. Simulation Settings. Our experiments are done by using the simulation of urban mobility (SUMO) simulator. All the simulations are conducted on a PC with Intel Core CPU i9-9820X 3.50 GHz processor, 64 GB RAM. We export a map of the area near Pudong Airport in Shanghai from OpenStreetMap, which is shown in Figure 6. The latitude of the experimental area is between $[31.19177, 31.19742]$. The longitude is between $[121.31134, 121.31853]$. In this area, we randomly select four base stations (depicted by red star marks). The locations of these base stations and different communication radii are listed in Table 1. Each base station can observe the traffic flows and obtain the passing vehicles' information, including the vehicle ID, location, speed, timestamp, and acceleration.

Input:
Priorityscore_List

Output:
 optimal channel allocation matrix A^*
Function Finder-MCTS ($v, \text{Priorityscore_List}$)

- 1: load network f_{ESP}
- 2: create root node v with state s_v
- 3: create channel allocation buffer $\Lambda_{L,C}$
- 4: **while** node v is a terminal node **do**
- 5: initialize a matrix $A_{N \times M}$ with all elements equaling to 0
- 6: $\tilde{v} \leftarrow \text{Treepolicy}(v)$
- 7: $Q_{\tilde{v}_\Delta} \leftarrow \text{Simulation}(s_{\tilde{v}}, \tilde{v})$
- 8: **if** $a_m = 1$ for vehicle ID_n **then**
- 9: $a_{n,m} = 1$
- 10: **else**
- 11: $a_{n,m} = 0$
- 12: **end if**
- 13: update and put $A_{N \times M}$ in $\Lambda_{L,C}$
- 14: *Backpropagation*($v, Q_{\tilde{v}_\Delta}$)
- 15: **end while**
- 16: **return** $A^* = \underset{A_{N \times M} \in \Lambda_{L,C}}{\text{argmax}} \{U(A_{N \times M}, R)\}$

Function Treepolicy(v)

- 17: **while** v is nonterminal **do**
- 18: **if** v is not a leaf node **then**
- 19: $v' \leftarrow \text{Bestchild}(v)$
- 20: *Treepolicy*(v')
- 21: **else**
- 22: **if** $\bar{N}_v = 0$ **then**
- 23: $\tilde{v} \leftarrow v$
- 24: **else**
- 25: *Expand*(v)
- 26: **end if**
- 27: **end if**
- 28: **end while**

Function Bestchild(v)

- 29: **return** $\underset{v' \in \text{child}(v)}{\text{argmax}} ((Q_{v'} / \bar{N}_{v'}) + c \cdot \sqrt{\ln(\bar{N}_v) / \bar{N}_{v'}})$

Function Expand(v)

- 30: execute *Action*(n, v)
- 31: choose $a_m \in \mathcal{A}(n, v)$ randomly
- 32: generate a new child v' of node v
- 33: initialize $Q_{v'} = 0$
- 34: $s_{v'} = f_{ESP}(s_v, a_m)$
- 35: *Treepolicy*(v')

Function Simulation(\tilde{v})

- 36: initialize $i = 0, Q_{\tilde{v}} = 0$
- 37: **while** \tilde{v} is not a terminal node \tilde{v}_Δ **do**
- 38: choose $a_m \in \mathcal{A}(n, \tilde{v})$ randomly
- 39: $s_{\tilde{v}'} \leftarrow f(s_{\tilde{v}}, a_m), \tilde{v}' \leftarrow \tilde{v}$
- 40: calculate $r_{n,m}$ according to Eq. (2)
- 41: $Q_{\tilde{v}'} \leftarrow Q_{\tilde{v}} + r_{n,m} + \text{Bonus}$ (*Bonus* is calculated based on Eq. (17), (18), (19))
- 42: $i \leftarrow i + 1$
- 43: **end while**
- 44: **return** $Q_{\tilde{v}_\Delta}$ when node \tilde{v} reaching to the terminal node \tilde{v}_Δ

Function Backpropagation($v, Q_{\tilde{v}_\Delta}$)

- 45: **while** node v is not null **do**


```

46:  $\bar{N}_v \leftarrow \bar{N}_v + 1, Q_v \leftarrow Q_v + Q_{\bar{v}_\Delta}$ 
47:  $v \leftarrow \text{parentof } v$ 
48: end while

```

ALGORITHM 2: Finder-MCTS.

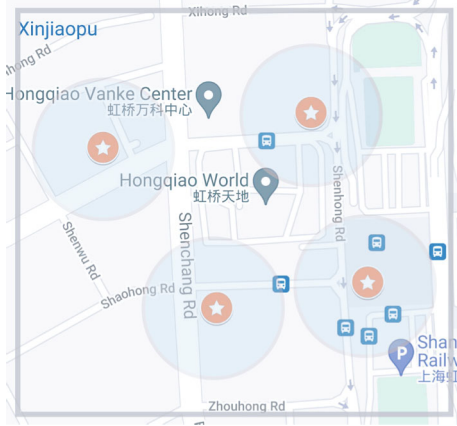


FIGURE 6: The experimental area imported from OpenStreetMap.

Assume that each base station has $M = 10$ available spectrum channels. The bandwidth of each channel is set to 20 MHz. We import 100 cognitive vehicles into the simulation scene. Each vehicle randomly proposes a service request to the base station with probability of 50% at each allocation time window. Suppose that the duration of network service for each vehicle is equal to the allocation time window. In SUMO, we set the parameters for the different types of vehicles in Table 2. Compared with the moving vehicle, a PU can be regarded as a static point in the experiment. We set a total of $K = 30$ fixed points as PUs under the four base stations. Each PU randomly occupies a part of the communication bandwidth (MHz), which is subject to $U[1, 10]$ uniform distribution. At each allocation time window, we randomly let 70% PUs occupy the nearest base station's available channels. The duration of network service for a PU is chosen according to Equation (16). The spectrum demand of each SU n is randomly selected in $[1, 3]$ MHz. The maximum allowable interference level on channel m γ_m is -114 dBm. The level of background noise on channel m N_m is 1 dB. The minimum transmission power and maximum transmission power are $\bar{P}_{m,n}^{\min} = 20$ dBm and $\bar{P}_{m,n}^{\max} = 25$ dBm, respectively. The maximum allowable interference power of PU k on channel m $\delta_{m,k}$ is 5 dB.

In the experiment, the protection radius of a PU ($\tilde{R}_{k,m}$) is set to 100 m. We let the transmit power level of SUs be generated from the set $[20 \text{ dBm}, 21 \text{ dBm}, 22 \text{ dBm}, 23 \text{ dBm}, 24 \text{ dBm}, 25 \text{ dBm}]$. Thus, the interference radius of a SU ($\bar{R}_{n,m}$) corresponding to the above power levels is 100 m, 150 m, 200 m, 250 m, 300 m, and 350 m. The transmit power of a base station is set to 46 dBm. For simplicity, assume that the transmit power is equal to the transmission power and

TABLE 1: Information of the four base stations.

Name	Latitude	Longitude	Communication radius
BS1	31.19554	121.31274	500 m
BS2	31.19604	121.31619	500 m
BS3	31.19327	121.31462	500 m
BS4	31.19363	121.31713	500 m

let the channel gain in the wireless space be constituted by the path loss. We define the path loss between SU n and base station j as $PL(n, j) = 34 + 40 \lg(d_{nj})$, where d_{nj} denotes the Euclidean distance between SU n and base station j . Besides, we define the path loss between SU n and PU k as $PL(n, k) = 40 + 24.4 \lg(d_{nk})$ [26], where d_{nk} denotes the Euclidean distance between SU n and PU k . The received signal power level is given by the product of the transmit power and the channel gain. Thus, the parameters $P_{m,n,k}$, $P_{m,k,n}$, and $P_{m,n}$ can be obtained through the above calculations.

6.2. Comparison with Other Types of Methods. Under the same simulation settings, we compare our Finder-MCTS with three other algorithms, i.e., the game theory-based method [7], particle swarm optimization-based (PSO-based) method [12], and DQN-based method [27], in terms of channel utilization ratio, convergence time, and average link capacity of SUs.

The channel utilization ratio (CUR) refers to the occupancy ratio of the available spectrum resources in the current base station. Besides, the average link capacity (ALC) is defined as follows:

$$ALC = \frac{1}{N} \cdot \sum_{n=1}^N \sum_{m=1}^M (a_{n,m} \cdot r_{n,m}). \quad (21)$$

If a method has high CUR, high ALC, and low convergence time, it means that the method can not only make full use of the spectrum resources but also enable SUs to obtain better communication service quality quickly.

First, after the simulations are all done in the four base stations, we compare the average CUR, ALC, and convergence time of the proposed Finder-MCTS with three other methods, shown in Figure 7. From the average CUR performance in Figure 7(a), we can see that Finder-MCTS performs the best, the second-best is the DQN-based method, and the worst is the PSO-based method. From the average ALC performance in Figure 7(b), we can see that Finder-MCTS performs the best, the second-best is the DQN-

TABLE 2: Parameters used in SUMO.

Parameters	Car	Bus	Truck
The maximum speed	15 (m/s)	13 (m/s)	10 (m/s)
The minimum speed	1 (m/s)	1 (m/s)	1 (m/s)
The minimum gap between vehicles	2.5 (m)	2.5 (m)	2.5 (m)
The maximum acceleration	3 (m/s ²)	1.5 (m/s ²)	1.5 (m/s ²)
The maximum deceleration	7.5 (m/s ²)	4 (m/s ²)	4 (m/s ²)
The maximum deceleration for emergency breaking	9 (m/s)	7 (m/s)	7 (m/s)

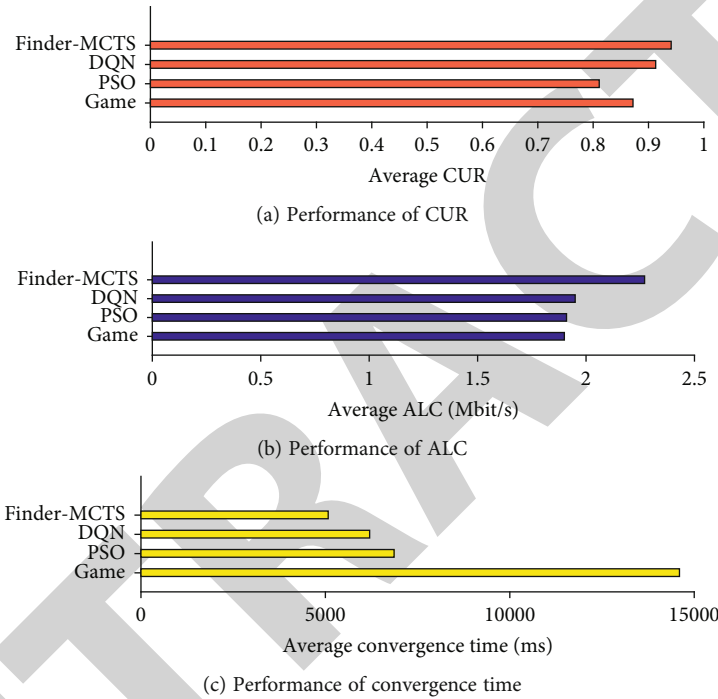


FIGURE 7: Comparison with three other methods in terms of average CUR, ALC, and convergence time.

based method, and the worst is the game theory-based method. From the average convergence time performance in Figure 7(c), we can see that Finder-MCTS performs the best, the second-best is the DQN-based method, and the worst is the game theory-based method.

Based on the above results, we give the following analysis. Because the convergence of the Nash equilibrium solution is negatively related to the size of the problem, the game theory-based method's convergence performance is poor. When the game theory-based method reaches convergence, the CUR performance of the system can be approximately optimal; however, the equilibrium of the multiuser game makes the ALC value relatively low. Besides, the PSO-based method is easy to fall into the local optimal solution; its average CUR and average ALC perform relatively poorly. Since the complicated parameters' setting of PSO, its average convergence time becomes longer as the scale of the problem becomes larger. Moreover, after the exploration of actions through reinforcement learning, the DQN-based method can obtain a higher quality spectrum allocation

solution, and the performance of average CUR and ALC is second only to Finder-MCTS. However, the convergence time of the DQN-based method is higher than that of Finder-MCTS due to the long-term exploration and value updating, although enough experience information learned through online learning can speed up the convergence time of DQN to some extent. By contrast, Finder-MCTS based on offline training and online learning has an average 36.47% improvement in convergence time than other methods. In terms of ALC, Finder-MCTS has an average advantage of 18.24% over other methods. At the same time, the channel utilization of Finder-MCTS is 9.00% higher than that of other methods on average.

Second, since the number of SUs in the coverage area of each base station is time-varying, it is necessary to observe the performance changes under different SUs' scales. The results are shown in Figure 8. Here, notice that in Figure 8, each depicted point in the curve is an averaged value statistically. For example, as to the results that distribute in the scale interval $(p_1, p_2]$ of the x -axis, we

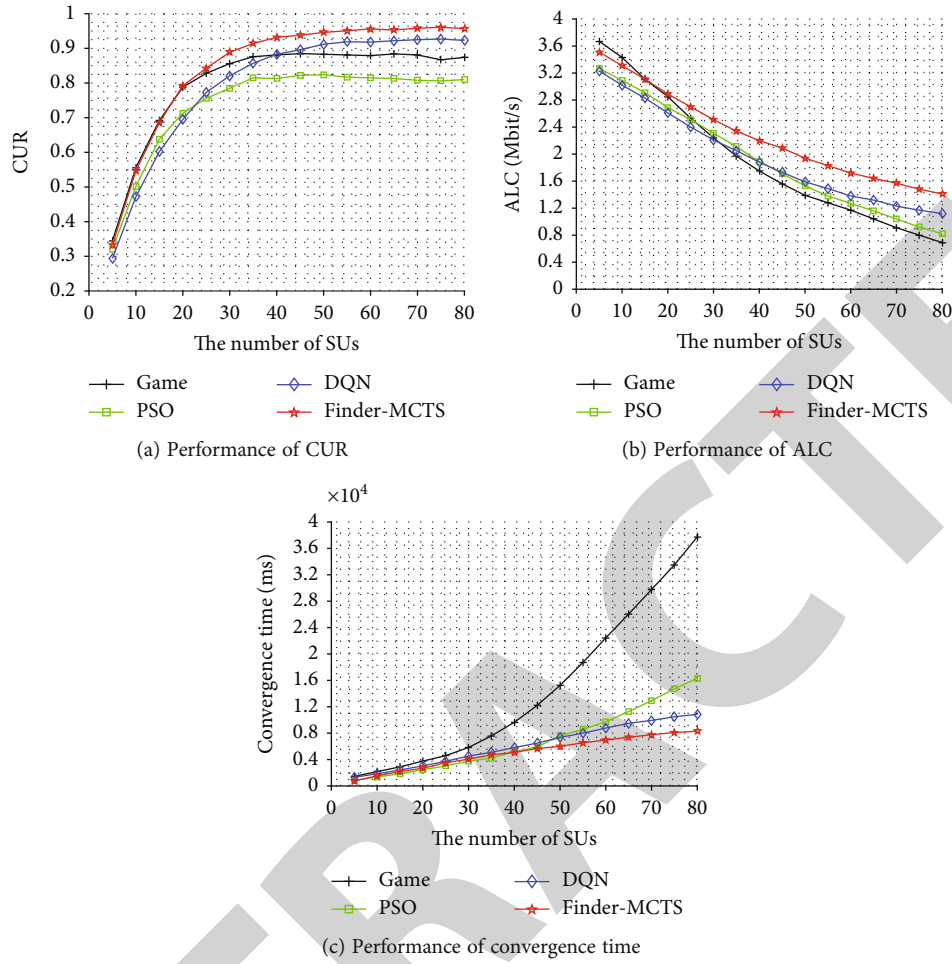


FIGURE 8: Performance comparison with varying numbers of SUs.

average these results and depict the averaged value corresponding to point p_2 .

Figure 8(a) shows the relationship between the number of SUs and CUR. In general, as the number of SUs increases, the CUR curve increases until it gradually converges. In addition, we find that when the number of SUs is small, the game theory can give a solution with high CUR. However, with the increase of SUs, the Finder-MCTS and DQN-based methods show obvious advantages in resource utilization. The reason behind that is when the scale of SU becomes large, the combination of historical experiences and online exploration can greatly improve the quality of the solution. In contrast, the game theory-based equilibrium quality for large-scale SU problems has declined. Also, the PSO-based method often converges to a local optimal solution and its CUR performance cannot be guaranteed.

Figure 8(b) depicts the relationship between the number of SUs and ALC. It is obvious that as the number of SUs increases, the ALC value decreases since the available spectrum resources of the base station side are limited. Besides, we find that when the number of SUs is small, the game-based method shows a good performance in ALC. However, as the number of SUs increases, Finder-MCTS shows an obvious advantage. This is because when the scale of SUs

becomes large, finding an optimal solution is hard for the game-based method. Moreover, since the PSO-based method is hard to reach the global convergence, the ALC performance is relatively low with the number of SUs increasing.

Figure 8(c) shows the simulation results of the relationship between the number of SUs and the convergence time. First, we can see that the convergence time of game theory-based and PSO-based methods shows an obvious growth trend as the number of SUs increases, while the convergence time based on DQN and Finder-MCTS rises moderately. The main reason is that the Finder-MCTS and DQN-based methods gradually fit the channel state model after continuous learning, thereby greatly improving the search efficiency. The convergence time of Finder-MCTS is reduced by 65.23% and 18.85% compared with the game theory-based method and the PSO-based method. In the long run, Finder-MCTS shows a short and gentle convergence time performance in the dynamic environment.

All the above phenomena verify the advantage of Finder-MCTS in solving spectrum allocation in IoV. Finder-MCTS can effectively complete the rapid learning of the approximate optimal allocation solution in a time-varying environment, which greatly improves the available spectrum utilization ratio of the current base station system.

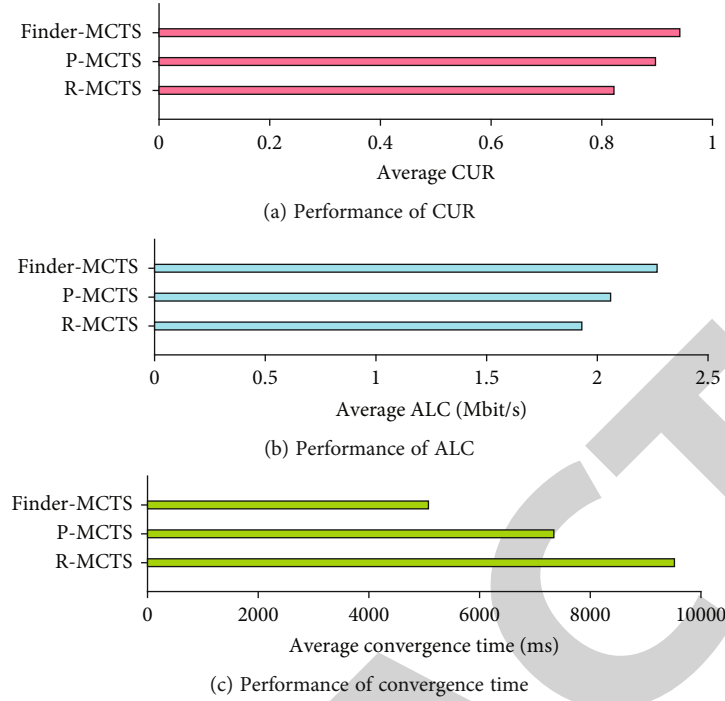


FIGURE 9: Comparison with two types of MCTS algorithms' variations in terms of average CUR, ALC, and convergence time.

6.3. Comparison with Other MCTS Algorithms' Variations. In this part, we compare Finder-MCTS with other MCTS algorithms' variations. We show why we consider the priority mechanism and simulation under different scenarios.

We set two basic types of MCTS-based spectrum allocation modes: random-order-based allocation mode and priority-based allocation mode, which are called as R-MCTS and P-MCTS, respectively. In R-MCTS, compared with Finder-MCTS, both priority and the uncertainty of PUs' service durations are not taken into consideration. In P-MCTS, compared with Finder-MCTS, only the uncertainty of PUs' service durations is not taken into consideration. The simulation results are shown in Figure 9. We can see that Finder-MCTS performs the best, the second-best is P-MCTS, and the worst is R-MCTS. According to the above results, we give the following analysis.

From Figure 9(a), we can see that the CUR performance of P-MCTS is superior than R-MCTS. This gap illustrates that the introduction of priority evaluation will improve the ratio of the spectrum utilization (about 9.12% increase). Meanwhile, Finder-MCTS has the best CUR performance. In the long run, the service duration τ of PU on each channel will give each allocated SU differentiated stochastic bonus. Hence, based on the uncertainty of the channel state occupied by the PUs, we introduce the factor τ that affects the supply-demand ratio of spectrum resources into the reward evaluation during each expansion step of the simulation process. We learn that Finder-MCTS is better (about 4.08% increase) than P-MCTS on ALC. Hence, we can conclude that the optimization of the stochastic simulation process contributes to improved spectrum usage efficiency of CR-IoV from a global perspective.

Figure 9(b) depicts the different performances of the three methods in ALC performance. With the help of priority evaluation, P-MCTS has increased by 6.73% compared with R-MCTS. The ALC performance of Finder-MCTS has increased by 10.19% compared with P-MCTS by evaluating the uncertainty of PUs' service durations.

Figure 9(c) shows the average convergence time of the three methods. Owing to the priority evaluation, P-MCTS has a 22.89% advantage over R-MCTS. This characterizes the positive impact of the differentiation priority evaluation on the algorithm convergence time. Secondly, under the same setting, with the help of reduction of action space in each descending layer, Finder-MCTS achieves a faster convergence speed (about 46.69% increase and 30.86% increase) than R-MCTS and P-MCTS.

7. Conclusion

In this paper, we investigate the spectrum allocation in CR-IoV by modeling an optimization problem to maximize the link capacity of vehicle users. What is more, we propose a method named Finder-MCTS to solve the optimization problem. We show that Finder-MCTS can learn to adapt and update allocation strategy for transmission under a dynamic network environment. The experimental results show that Finder-MCTS is more efficient in convergence speed, and it achieves good performance gain in spectrum utilization and link capacity compared with other popular strategies, especially when the number of vehicle users becomes more. Besides, we have also confirmed the effectiveness of priority evaluation and uncertainty evaluation of the PUs' service durations by comparing with two

variations of MCTS. In future work, how to achieve adaptive equilibrium between the number of sampling scenarios and the running time of uncertainty evaluation in simulation is a worthy direction to improve the convergence time of FINDER-MCTS. Besides, we will further study the cooperative spectrum allocation problem of IoV under a complex scenario with space/air/ground communications and networking.

Data Availability

The data generation method has been introduced in Section 6.1. The data can be obtained according to the configuration. We also make data available on request through sending an email to the authors.

Conflicts of Interest

The authors declare that they have no conflicts of interest.

Acknowledgments

This work was supported by the Midu Research Base Project under Grant 48093A.

References

- [1] J. Yang and H. Zhao, "Enhanced throughput of cognitive radio networks by imperfect spectrum prediction," *IEEE Communications Letters*, vol. 19, no. 10, pp. 1738–1741, 2015.
- [2] M. Höyhtyä, A. Mämmelä, M. Eskola et al., "Spectrum occupancy measurements: a survey and use of interference maps," *IEEE Communications Surveys Tutorials*, vol. 18, no. 4, pp. 2386–2414, 2016.
- [3] M. Yousefvand, N. Ansari, and S. Khorsandi, "Maximizing network capacity of cognitive radio networks by capacity-aware spectrum allocation," *IEEE Transactions on Wireless Communications*, vol. 14, no. 9, pp. 5058–5067, 2015.
- [4] J. Martinovic, E. Jorswieck, G. Scheithauer, and A. Fischer, "Integer linear programming formulations for cognitive radio resource allocation," *IEEE Wireless Communications Letters*, vol. 6, no. 4, pp. 494–497, 2017.
- [5] Z. Teng, L. Xie, H. Chen, L. Teng, and H. Li, "Application research of game theory in cognitive radio spectrum allocation," *Wireless Networks*, vol. 25, no. 7, pp. 4275–4286, 2019.
- [6] C. Yi and J. Cai, "Two-stage spectrum sharing with combinatorial auction and stackelberg game in recall-based cognitive radio networks," *IEEE Transactions on Communications*, vol. 62, no. 11, pp. 3740–3752, 2014.
- [7] X. Liu, R. Zhu, B. Jalaian, and Y. Sun, "Dynamic spectrum access algorithm based on game theory in cognitive radio networks," *Mobile Networks and Applications*, vol. 20, no. 6, pp. 817–827, 2015.
- [8] Z. Zhao, Z. Peng, S. Zheng, and J. Shang, "Cognitive radio spectrum allocation using evolutionary algorithms," *IEEE Transactions on Wireless Communications*, vol. 8, no. 9, pp. 4421–4425, 2009.
- [9] A. Y. S. Lam, V. O. K. Li, and J. J. Q. Yu, "Power-controlled cognitive radio spectrum allocation with chemical reaction optimization," *IEEE Transactions on Wireless Communications*, vol. 12, no. 7, pp. 3180–3190, 2013.
- [10] P. Bhardwaj, A. Panwar, O. Ozdemir et al., "Enhanced dynamic spectrum access in multiband cognitive radio networks via optimized resource allocation," *IEEE Transactions on Wireless Communications*, vol. 15, no. 12, pp. 8093–8106, 2016.
- [11] R. Zhang, X. Jiang, and R. Li, "Improved decomposition-based multi-objective cuckoo search algorithm for spectrum allocation in cognitive vehicular network," *Physical Communication*, vol. 34, pp. 301–309, 2019.
- [12] Q. Liu, H. Niu, W. Xu, and D. Zhang, "A service-oriented spectrum allocation algorithm using enhanced pso for cognitive wireless networks," *Computer Networks*, vol. 74, no. 12, pp. 81–91, 2014.
- [13] Q. Huang, X. Xie, H. Tang et al., "Machine-learning-based cognitive spectrum assignment for 5g urllc applications," *IEEE Network*, vol. 33, no. 4, pp. 30–35, 2019.
- [14] F. Li, D. Yu, H. Yang, J. Yu, H. Karl, and X. Cheng, "Multi-armed-bandit-based spectrum scheduling algorithms in wireless networks: a survey," *IEEE Wireless Communications*, vol. 27, no. 1, pp. 24–30, 2020.
- [15] Y. Zhang, W. P. Tay, K. H. Li, M. Esseghir, and D. Gaïti, "Learning temporal-spatial spectrum reuse," *IEEE Transactions on Communications*, vol. 64, no. 7, pp. 3092–3103, 2016.
- [16] O. Naparstek and K. Cohen, "Deep multi-user reinforcement learning for distributed dynamic spectrum access," *IEEE Transactions on Wireless Communications*, vol. 18, no. 1, pp. 310–323, 2019.
- [17] Z. Hu, T. James, and B. Li, "Spear: optimized dependency-aware task scheduling with deep reinforcement learning," in *2019 IEEE 39th International Conference on Distributed Computing Systems (ICDCS) 2019*, Dallas, TX, USA, 2019.
- [18] H. Shuai and H. He, "Online scheduling of a residential microgrid via Monte-Carlo tree search and a learned model," *IEEE Transactions on Smart Grid*, vol. 12, no. 2, pp. 1073–1087, 2021.
- [19] E. Z. Tragos, S. Zeadally, A. G. Fragkiadakis, and V. A. Siris, "Spectrum assignment in cognitive radio networks: a comprehensive survey," *IEEE Communications Surveys Tutorials*, vol. 15, no. 3, pp. 1108–1135, 2013.
- [20] R. Sutton and A. Barto, *Reinforcement Learning: An Introduction*, MIT Press, Cambridge, MA, USA, 2018.
- [21] H. Yang, S. Li, X. Xu, X. Liu, Z. Meng, and Y. Zhang, "Efficient searching with MCTS and imitation learning: a case study in Pommerman," *IEEE Access*, vol. 9, pp. 48851–48859, 2021.
- [22] Y. Shang, W. Wu, J. Liao et al., "Stochastic maintenance schedules of active distribution networks based on MonteCarlo tree search," *IEEE Transactions on Power Systems*, vol. 35, no. 5, pp. 3940–3952, 2020.
- [23] M. Li, T. Zhang, Y. Chen, and A. J. Smola, "Efficient mini-batch training for stochastic optimization," in *Proceedings of the ACM SIGKDD*, pp. 661–670, New York, NY, USA, 2014.
- [24] L. Kocsis and C. Szepesvári, "Bandit based Monte-Carlo planning," in *European Conference on Machine Learning*, pp. 282–293, Springer, 2006.
- [25] K. W. Sung, S.-L. Kim, and J. Zander, "Temporal spectrum sharing based on primary user activity prediction," *IEEE Transactions on Wireless Communications*, vol. 9, no. 12, pp. 3848–3855, 2010.

Retraction

Retracted: Information Security Situation Awareness Based on Big Data and Artificial Intelligence Technology

Wireless Communications and Mobile Computing

Received 28 November 2023; Accepted 28 November 2023; Published 29 November 2023

Copyright © 2023 Wireless Communications and Mobile Computing. This is an open access article distributed under the Creative Commons Attribution License, which permits unrestricted use, distribution, and reproduction in any medium, provided the original work is properly cited.

This article has been retracted by Hindawi, as publisher, following an investigation undertaken by the publisher [1]. This investigation has uncovered evidence of systematic manipulation of the publication and peer-review process. We cannot, therefore, vouch for the reliability or integrity of this article.

Please note that this notice is intended solely to alert readers that the peer-review process of this article has been compromised.

Wiley and Hindawi regret that the usual quality checks did not identify these issues before publication and have since put additional measures in place to safeguard research integrity.

We wish to credit our Research Integrity and Research Publishing teams and anonymous and named external researchers and research integrity experts for contributing to this investigation.

The corresponding author, as the representative of all authors, has been given the opportunity to register their agreement or disagreement to this retraction. We have kept a record of any response received.

References

- [1] F. Yao, "Information Security Situation Awareness Based on Big Data and Artificial Intelligence Technology," *Wireless Communications and Mobile Computing*, vol. 2021, Article ID 2989118, 6 pages, 2021.

Research Article

Information Security Situation Awareness Based on Big Data and Artificial Intelligence Technology

Fuguang Yao 

Chongqing University of Education, Chongqing 400065, China

Correspondence should be addressed to Fuguang Yao; yaofuguang@cque.edu.cn

Received 21 August 2021; Revised 23 September 2021; Accepted 28 September 2021; Published 22 October 2021

Academic Editor: Balakrishnan Nagaraj

Copyright © 2021 Fuguang Yao. This is an open access article distributed under the Creative Commons Attribution License, which permits unrestricted use, distribution, and reproduction in any medium, provided the original work is properly cited.

The information security threats faced by enterprises are increasing rapidly, and the technology of security attacks is also diversified and developed at a high level. The application of big data technology and artificial intelligence technology in all walks of life continues to deepen. While greatly improving social productivity, it also brings certain information security issues. Security situation awareness technology has become a new research hotspot in the field of network security. Using big data-related technologies to analyze, filter, merge, and identify known and unknown security threats is a new research discovery. This research builds a new cascaded network security situational awareness model based on the traditional and fusion decision tree algorithms. We use an induction algorithm to generate a decision tree on the preprocessed data to classify the data according to the decision rules. Research shows that a new network security situation awareness model is constructed using decision tree calculations. Compared with the traditional model, the classification effect of this model is better.

1. Introduction

The rapid development of cloud computing and the Internet has caused an explosive growth of network data. While it brings convenience to people's work and life, the massive amount of data also brings great security risks to the network. Therefore, the security situation awareness technology is designed, such as the network security situation awareness model based on the Bayesian method and the multinode network security situation prediction awareness model based on the improved G - K algorithm. These two models detect security events in the network by sensing network security threat data, but the classification effect of the security situation awareness model is not good [1]. This has led to its speedup and scale ratios being lower than expected.

For this reason, this research builds a new cascaded network security situational awareness model based on the traditional model fusion decision tree algorithm. The decision tree algorithm is a method of approximating the value of a discrete function [2]. We use an induction algorithm to generate a decision tree on the preprocessed data to classify the data according to the decision rules. The design process of the cascaded network security situational awareness model

based on the decision tree algorithm is described in detail below.

2. Design of Cascaded Cybersecurity Situational Awareness Model

2.1. Set the Category Division Module of the Perception Model. It is very important to accurately classify the types of network security elements in complex networks. Therefore, this research resets the category division module of the perception model based on traditional design.

According to the existing network attack elements, it can be seen that the current attack categories include denial of service attacks, detection attacks, remote login attacks, and access rights attacks. The abbreviations for the four types of attacks are Dos, Probe, R2L and U2R, respectively. Among them, Dos mainly paralyzes the attacked party's equipment by sending massive amounts of network data. Probe uses scanning technology to steal the privacy of other hosts. R2L then logs in to a remote computer to steal information based on potential security vulnerabilities. U2R Performs some illegal operations by obtaining the highest authority of the server. Based on experience, it can be known

that Dos attacks can pose a major threat to the security situation of cascaded networks, while Probe attacks have a lighter impact [3]. Therefore, the cascaded network elements are divided into five categories: normal online network data and four attack data. Set the identifiers of these categories to 1, 2, 3, 4, and 5. Then, we present the classification module of the perception model to the following manifestation

$$\begin{cases} G_k : \text{if } s_m \in A_m^k, \\ \text{Then, } \{(B_1, \theta_{1,k}), (B_2, \theta_{2,k}), \dots, (B_n, \theta_{n,k})\}. \end{cases} \quad (1)$$

In formula (1) G_k represents the k rule of the security situation awareness classification module. s_1, s_2, \dots, s_m represents m premise attributes. $A_1^k, A_2^k, \dots, A_m^k$ represents the reference value of m premise attributes in rule k . B_1, B_2, \dots, B_n represents the n categories of the classification problem. $\theta_{1,k}, \theta_{2,k}, \dots, \theta_{n,k}$ represents the confidence level of the n conclusion in Rule k .

We use the above formula to describe the composition rules of the model classification module and the evidence reasoning algorithm to achieve the training of the model classification to obtain the category of the input data. Therefore, a BRB classification process is established according to the classification rules given above [4]. This process uses the calculation method of the principal component analysis algorithm to reduce the dimensionality in advance and then divides the network data into two parts, the training data set and the test data set. When the training data set enters the classification module of the model, it is divided into several subsets so that each subset contains only two types of data. For example, a subset contains normal data and Dos attack data. The other subset contains normal data and Probe attack data. Therefore, the classification module of the model is only responsible for the classification of two kinds of data. According to formula (1), the calculation process of the two data classifications is obtained

$$\begin{cases} G_k : \text{if } s_m \in A_m^k, \\ \text{Then, } \{(B_1, \theta_{1,k}), (B_2, \theta_{2,k})\}. \end{cases} \quad (2)$$

We combine several BRB classifiers with building a complete network security situation classification module to achieve different data classification.

2.2. The Security Event Detection Mode of the Design Model. A security event detection model with a hierarchical structure is designed based on the set as mentioned above of category division modules of the perception model. This mode performs anomaly detection on different levels of network data and then finds the situation elements from the detection results to assess the situation overall. At the same time, the security event threat data accumulated by the model when the perception model is used to perform the network security situational awareness work provides the original data for the model perception [5]. Therefore, knowledge is formed from the detection and comparison, and then the knowledge is used to adjust the evaluation and security strat-

egy. We use the subsequent time window to detect the adjusted results to achieve a hierarchical cycle perception of the entire process. The security event detection layer is responsible for detecting abnormal behaviors of network-oriented and host-oriented data. The network-oriented data flow is the data flow that enters the cascaded network in order with data packets as the unit. The host-oriented service request flow is the data that enters the branch network or a host in the branch network in flow units. The host-oriented service response flow is the network flow data related to a host's service request and sent from the host to the outside in the flow unit. Therefore, at the security event detection level, the summary of network information is first recorded when network data flows.

We set the length of the time window to D and then use D_i to segment i network information. Then, in the time window, extract the network stream data feature (T_D) representation of the time window segmentation according to the record content of the summary information. The classification module based on the setting uses T_D as the input to detect the security status of the network traffic in the time window. The formula is

$$\begin{cases} \text{result}_N = [\text{normal}, \text{attack}_{g_N}, \text{abnormal}], \\ \text{Detect}(T_D) = \text{result}_n. \end{cases} \quad (3)$$

In formula (3) g_N represents a common attack type. Here, specifically refer to Dos, Probe, R2L and U2R. The above is the processing process facing the network data flow. When the model faces the host data stream, it also integrates the basic information of the data stream in advance. First, we use the time window D to integrate the data packets of the subnet and then organize the data records according to the inspection objects. Integrate data with the same IP when detecting service request data flow [6]. When detecting the service response data flow, the data with the same source port in the host outflow is organized together. Therefore, the tissue records of the two detection objects are denoted by flow_1 and flow_2 , respectively. For service request flow and service response flow, we use a time window D to extract the behavior characteristics of the two, which are denoted as F_1 and F_2 , respectively. Finally, the classification module is used to detect the abnormal behavior of the host-oriented data stream. The formula is

$$\begin{cases} \text{result}_1 = [\text{normal}, \text{attack}_{g_1}, \text{abnormal}], \\ \text{result}_2 = [\text{normal}, \text{abnormal}], \\ \text{Detect}(F_1) = \text{result}_1, \\ \text{Detect}(F_2) = \text{result}_2. \end{cases} \quad (4)$$

Through the above calculation process, the optimized design of the model security event detection mode is realized.

2.3. Establish a Perception Model Based on the Decision Tree Algorithm. To achieve a refined distinction between different

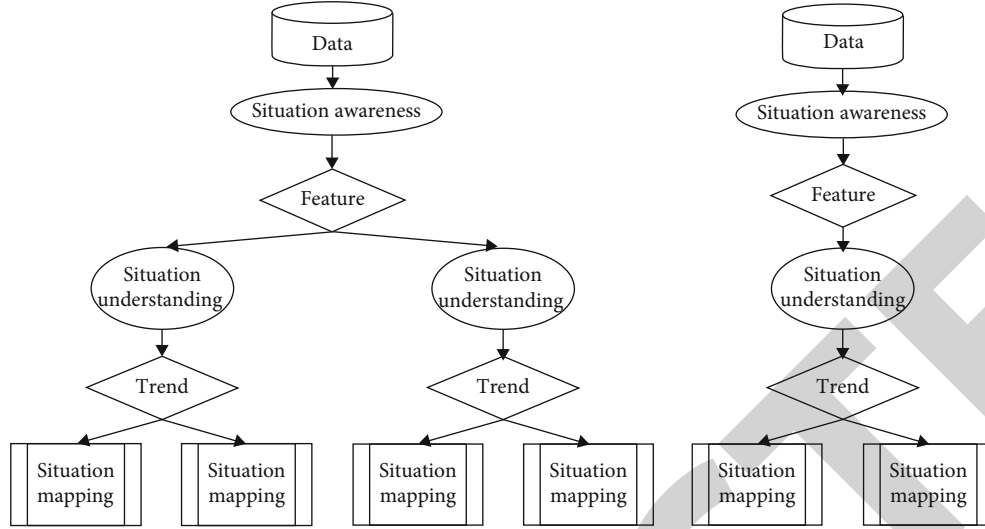


FIGURE 1: Cascade network security situation awareness model based on decision tree algorithm.

TABLE 1: Data processing process of decision tree algorithm.

Step	Algorithm execution process
1	Enter N pieces of data, generate the number of decision trees based on the data attributes, and randomly select the number of data features in the model training process
2	Process the attack data in a sampling manner to obtain the training data set
3	Select and classify the feature attributes of the training data set to generate a decision tree
4	Add decision trees to the forest
5	Judge whether all decision trees in the forest reach the initially set value
6	Traverse the decision tree in the forest, judge the records in the data set, and use the node with the most classification results as the output result.

security events, it is necessary to rely on more advanced algorithms to separate the normal data from the attack data by dividing the subset of the classification module [7]. Therefore, a cascaded network security situation awareness model based on a decision tree algorithm is constructed. The basic structure of the model is shown in Figure 1.

According to the model structure shown in Figure 1, the algorithm is a model that relies on the decision tree algorithm. The model comprises multiple decision trees, and the output result is determined by the mode of the output results of all decision trees [8]. The designed perception model has three layers, which perform security situation awareness on different data streams in top-down order. The final perception result is obtained through the posture projection of the leaf nodes. It is known that the model contains a large number of decision trees, and the decision tree algorithm is a method of dividing the space into hyperplanes. When the algorithm performs data segmentation, the space where the data is located is divided into two in advance so that each leaf node in the space is in a disjoint area. When data is separated simultaneously, it gradually decreases according to the dimensional characteristics of the input sample and finally enters any one of the M regions. Each area at this time represents a different data category. Under the control of the decision tree algorithm, each decision tree has no interrelated nature. Therefore, a large number of decision trees

TABLE 2: Classification of the sample data of the experimental group.

Training data set		Test data set	
Normal	1000 pcs	Normal	200 pcs
Dos	1000 pcs	Dos	200 pcs
Probe	310	Probe	60 pcs
R2L	120 pcs	R2L	25
U2R	200 pcs	U2R	40

form a forest. Discriminate the input new sample category through each decision tree in the forest. According to each decision tree, select the most category to confirm the attack type of the network data. The processing process of the decision tree algorithm for network attack data is shown in Table 1 below.

We use the decision tree algorithm to separate the attack data mixed with the normal data in the subset to establish a cascaded network security situational awareness model.

3. Simulation and Result Analysis

To verify the actual application performance of the cascaded network security situation awareness model based on the decision tree algorithm designed above, we design the following simulation. To avoid the singleness of the experimental

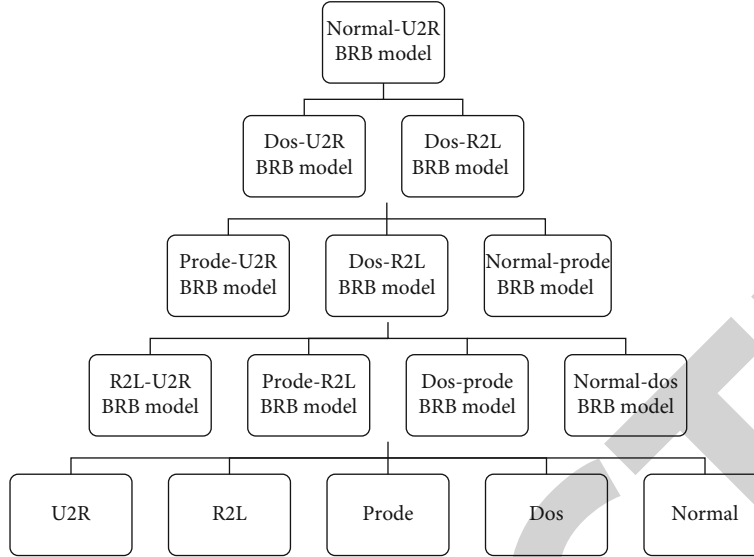


FIGURE 2: Schematic diagram of the classification structure of the confidence rule library.

TABLE 3: The initial parameters of each BRB module in the perception model.

Rule	Weights	Property reference value	Conclusion confidence
1	1	0, 0	0.5, 0.5
2	1	0, 0.5	0.5, 0.5
3	1	0, 1	0.5, 0.5
4	1	0.5, 0	0.5, 0.5
5	1	0.5, 0.5	0.5, 0.5
6	1	0.5, 1	0.5, 0.5
7	1	1, 0	0.5, 0.5
8	1	1, 0.5	0.5, 0.5
9	1	1, 1	0.5, 0.5

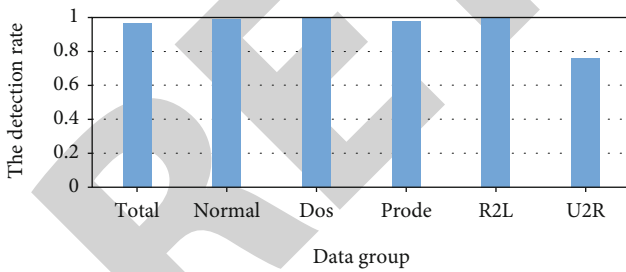


FIGURE 3: The model's security posture classification results.

results, we use the model in this paper as the test object of the experimental group [9]. We divided the subjects into control group A and control group B according to the traditional Bayes-based method and improved G - K algorithm. Compare the performance of the three sets of perception models in the process of detecting cascaded network security.

3.1. Security Situation Division. The experimental group selected 3156 samples as the basic test conditions. The distribution of the samples is shown in Table 2.

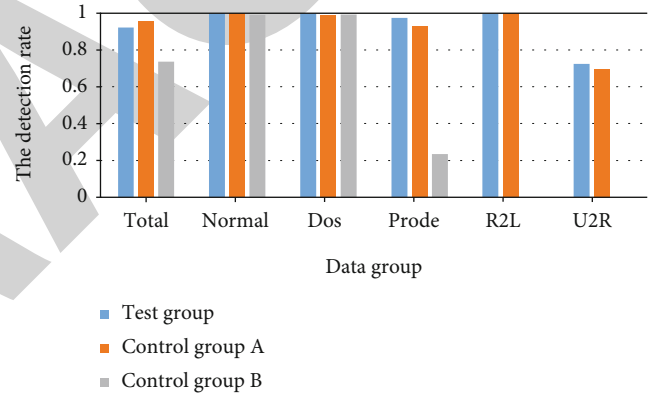


FIGURE 4: Comparison of model classification effects of different test groups.

TABLE 4: Differences in classification effects of different models.

Data set	Test group	Control group A	Control group B
Normal	99.54%	96.5%	100.00%
Dos	100.00%	100.00%	100.00%
Probe	98.82%	95.36%	25.35%
R2L	100.00%	100.00%	0.00%
U2R	74.69%	61.50%	0.00%

The model design method proposed this time uses the decision tree algorithm to reduce the dimensionality and then follows the classifier as shown in Figure 2. We divide the training data in Table 2 into ten groups, and each BRB classifier takes any of them as the source of training data.

We set up all BRB modules in Figure 2 with the same initial parameters. The initial parameters of the module are shown in Table 3.

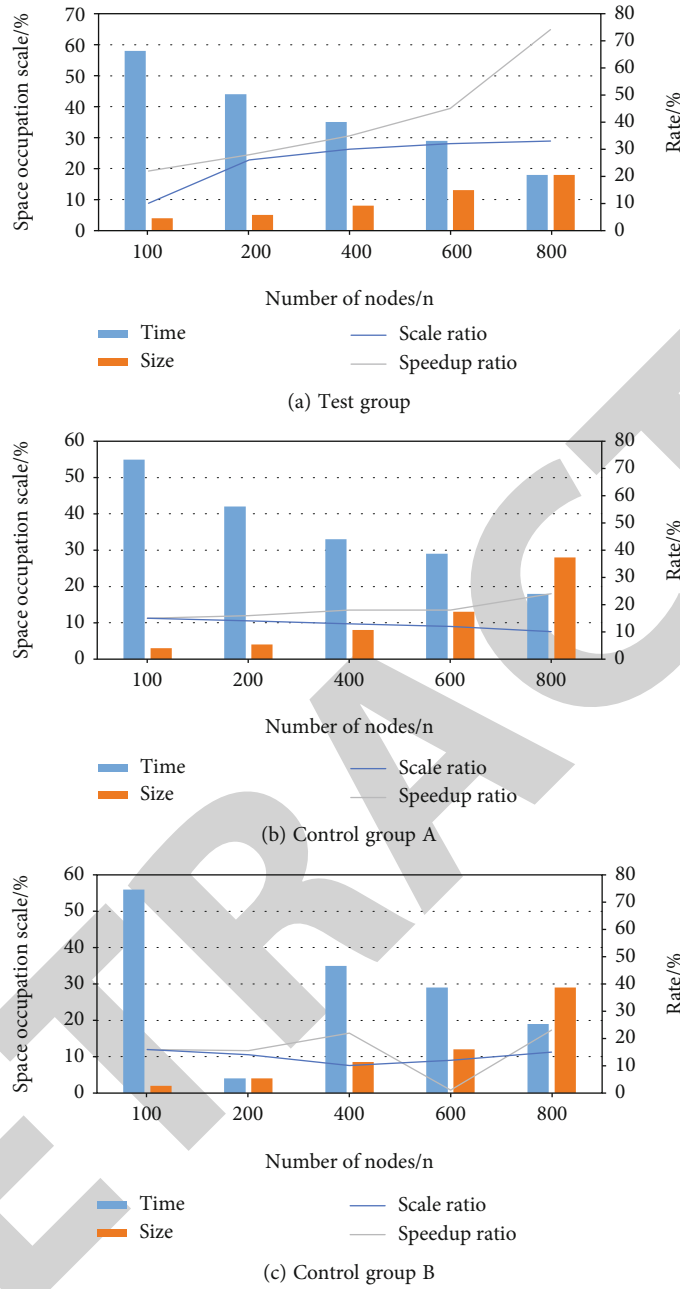


FIGURE 5: Speedup ratio and scale ratio test results.

Then, we use the model in this paper to optimize the parameters in Table 3. Figure 3 shows the classification results of the optimized BRB classifier for the network security situation [10]. The abscissa in Figure 3 represents the type of cascaded network data, and the ordinate represents the classification recognition rate of the model. According to the data in Figure 3, it can be seen that for some data sets, the classification detection output of the model in this paper has reached 100%, and the classification effect of only a few data sets is low.

3.2. Security Situation Awareness Model Classification Effect Test. To make the experimental test results more intuitive, we compare the classification effect of the model in this

paper with the classification effect of the two control models from the perspective of network security situation classification output. The result is shown in Figure 4. According to the test results in Figure 4, it can be seen that the model in this paper has a good classification effect on five different network data sets with the assistance of the decision tree algorithm [11]. The results of calculating the classification difference of the three test groups are shown in Table 4.

According to the data in Table 4, the three models' average classification effects are calculated to be 94.61%, 90.67%, and 45.07%, respectively. The classification and recognition effects of the experimental group were 3.94% and 49.54% higher than that of the two control groups, respectively. It

Research Article

Embedded Design of 3D Image Intelligent Display System Based on Virtual Reality Technology

Liang Li 

College of Art, Zhejiang Yuexiu University, Shaoxing, 312000 Zhejiang, China

Correspondence should be addressed to Liang Li; 20211032@zyufl.edu.cn

Received 5 July 2021; Revised 22 September 2021; Accepted 5 October 2021; Published 19 October 2021

Academic Editor: Fadi Al-Turjman

Copyright © 2021 Liang Li. This is an open access article distributed under the Creative Commons Attribution License, which permits unrestricted use, distribution, and reproduction in any medium, provided the original work is properly cited.

The previous 3D image intelligent display system is large in size and poor in accuracy, and the display effect and synchronization cannot meet the needs of users. Aiming at this phenomenon, a 3D image embedded intelligent display system based on virtual reality technology is designed. In recent years, with the rapid development of computer technology, three-dimensional measurement technology has become increasingly mature, and three-dimensional information technology has emerged in different fields in real life. With the development of computer science and automatic control technology, more and more intelligent robots appear in production and life. As an important subsystem of intelligent robot systems, the vision system is also receiving more and more attention. The three-dimensional imaging system projects a structured grating on the surface of the target object, uses a digital sensor to collect the deformed structured light image modulated by the surface of the object, and comprehensively uses image processing technology and precision measurement technology to achieve noncontact three-dimensional measurement of the object. This method of number of three-dimensional coordinates has the advantage of not being damaged, high efficiency, high degree of automation, low cost, etc. It has very important significance and broad application prospects for improving product quality and manufacturing efficiency and reducing production costs. Through the investigation and analysis of the existing 3D image intelligent display system embedded, this paper designs and realizes the 3D image intelligent display embedded system, which includes a high-speed structured light projection module, an embedded image acquisition and processing module, and a 3D reconstruction module. Among them, the embedded 3D imaging image acquisition and processing system is an important part of the embedded 3D measurement system, which provides a certain theoretical and practical basis for future in-depth research. The experimental results in this article show that the acquisition module takes 1.934 s to obtain the folded phase of the measured object through phase demodulation and the algorithm, while the phase demodulation and unfolding takes 2.068 s. Therefore, the algorithm needs to be further optimized to speed up the image processing speed and reflect the real-time effect of the system.

1. Introduction

With the rapid development of computer software and hardware technology, multimedia and network communication technology, and the concept of “digital earth,” more and more geographic information systems are widely used in embedded hardware platforms. Traditional imaging technology can only measure object size information, but not depth information. However, with the development of the manufacturing industry, more and more industrial measurement cases need to detect the 3D coordinate information of the object. The emergence of 3D digital imaging

technology meets this demand. 3D not only breaks the monotonous spatial information constraints on the 2D level, but also interprets and analyzes the information. This provides a better way to process size images. For example, 2D images require the most basic spatial data processing functions, such as data collection, data organization, data processing, and data analysis. Compared with 2D images, 3D images have the following advantages: (1) The display of spatial information is more intuitive. The use of 2D graphical interfaces in spatial display is very abstract, while 3D graphs are more realistic spatial display platforms and the visualization of abstract and difficult

spatial information. (2) Multidimensional spatial analysis functions are becoming more and more powerful. The process of analyzing spatial information is usually complex, dynamic, and abstract. High-tech topics with advanced achievements in different fields such as artificial intelligence and automatic control are one of the key technologies for the realization of intelligent robots and intelligent weapons. They are widely used in various fields such as military, aerospace, surveillance, biomedicine, and robotics.

For example, in the field of industrial design, it can be applied to the rapid design and testing of products and the quality control of products; in the medical industry, it can assist in the design of comfortable orthotics or prostheses and trauma care, etc.; in the cultural relics protection industry, antique restoration, and damage, the restoration and preservation of cultural relics can use three-dimensional measurement technology to quickly build models; in the consumer industry, animation production, three-dimensional advertising production, and now increasingly popular 3D movies require three-dimensional data to build animation models; in the aerospace field, three-dimensional measurement technology is helpful to complete the design and inspection of aircraft components, performance evaluation, and auxiliary aerodynamic analysis. In addition, three-dimensional measurement technology also has huge application potential in the fields of reverse engineering, biomedicine, industrial automation, and virtual reality. At the same time, the continuous improvement of personal and property safety requirements has promoted people's demand for video surveillance systems. From the security monitoring of communities and important facilities to the traffic monitoring of cities and highways, to the security monitoring of important places such as security systems, the application of video monitoring has penetrated into all aspects of society.

The vision system is a very complex system. It not only needs to collect images accurately, but also realize real-time response to changes in the outside world. At the same time, it also needs real-time tracking of external moving targets. Therefore, the vision system puts forward higher requirements on both hardware and software systems. Ohno et al. use mathematical modeling methods to reconstruct a 3D structure from a single two-dimensional (2D) training image (TI). Among many reconstruction algorithms, algorithms based on the best have been developed and have strong stability. However, this algorithm usually uses an autocorrelation function (which cannot accurately describe the morphological characteristics of porous media) as the objective function. This has a negative impact on the further study of porous media. In order to accurately reconstruct 3D porous media, they proposed a pattern density function based on random variables used to characterize image patterns. In addition, they also proposed an optimal-based original algorithm called pattern density function simulation [1]. But this algorithm still has certain flaws. Gao et al. formulate recommendations for high-risk clinical target volume (CTVHR) contours based on computed tomography (CT) for 3D image-guided brachytherapy (3D-IGBT) of cervical

cancer. At the time of his diagnosis, the CT-based CTVHR boundary was defined by each anatomical plane, regardless of whether the tumor had progressed to the cervix. Due to the current limited availability of magnetic resonance imaging (MRI) with an applicator in 3D planning, T2-weighted MRI obtained at the time of diagnosis and before brachytherapy without applicator is used for accurate assessment tumor reference [2]. Because the experiment process is not closed, there is an error in the experiment process. François et al. proposed a new design of embedded strain sensor. Based on Eshelby's inclusion model, it can be used to measure the complete 3D strain or stress tensor in any entity. Currently, ordinary embedded strain sensors can only perform one-dimensional measurements. The spherical shape of his sensor allows Eshelby's theorem (in the case of elastic behavior) to calculate the stress or strain that would exist in the structure without the sensor. They used fiber Bragg gratings to measure the deformation of the sphere, but other techniques can also be used. Their experimental test was carried out under two conditions. The first test measured the performance of the polymethyl methacrylate prototype under fluid pressure loading. In the second test, the steel prototype sensor was embedded in a standard concrete sample under axial compression and successfully used for 3D strain measurement under actual conditions [3]. After participating in this activity, learners should be better able to evaluate the literature on the effectiveness of incorporating virtual reality (VR) in the treatment of mental disorders. Maples-Keller et al. evaluate the use of exposure-based interventions for anxiety disorders. Virtual reality (VR) allows users to generate in computer experience presence in a 3D environment. This review focuses on the existing literature on the effectiveness of including VR in the treatment of various mental illnesses, with particular attention to exposure-based interventions for anxiety disorders [4]. In Jeon and Jo's research, a new noise evaluation method was proposed, in which virtual reality (VR) technology in the form of head-related transfer function (HRTF) and head-mounted display (HMD) is used to evaluate the noise inside a house building. First, before and after applying HRTF, the sound pressure level and frequency characteristics of the road traffic noise recorded in the living room were determined. Second, there are four different test environments, namely, without HRTF or HMD, with HRTF, with HMD, and with HRTF and HMD [5]. Ruiz-Moya et al.'s report discusses the basic knowledge, reconstruction techniques, practicality, and limitations of three-dimensional (3D) fusion imaging methods. The 3D fusion imaging method uses multiple modalities, but due to the limitations of computer hardware, image processing software and reconstruction methods, it is still in the early stages of development. Reconstructing standard 3D images by relatively simple processing of a kind of image data is widely used and has excellent spatial information and construction simplicity. However, due to the relatively low resolution of anatomical information, this information is not sufficient for preoperative simulation [6]. However, his experimental process is flawed, leading to discrepancies in experimental results. Computer vision has become one of the most popular competitive topics in the field of

artificial intelligence. Together with expert systems and natural language understanding, it has become the three most active areas of artificial intelligence. It is the realization of high automation of industrial production, intelligent robots, autonomous car navigation, and goals. One of the core contents of tracking and various other industrial testing, medical and military application is also a key factor for realizing machine intelligence. The purpose of computer vision is to use computers instead of human eyes and brains to perceive, interpret, and understand the environment.

The phase recovery algorithm is used to complete the design of the image acquisition and processing system, and the related circuit model is simulated according to the needs of this research, and the system research of the embedded processor of the virtual reality technology is fully utilized to design the intelligent display system such as image acquisition. The innovations of this article are (1) design and implement a digital image acquisition and processing system based on the embedded processor TMS320DM648, including system power supply design, DDR2 high-speed storage interface design, FLASH circuit design, and Gigabit Ethernet circuit design, and complete the test of each function of the hardware platform; the system has the characteristics of high degree of automation, strong processing capacity, high reliability, etc., suitable for industrial online inspection and other occasions. In order to meet the high-speed image processing system that requires high interface bandwidth and large-capacity storage, the design method of FPGA external DDR2-SDRAM is adopted, and a scheme of DDR2-SDRAM controller based on VHDL language is proposed. (2) Design and complete the CCD analog front-end circuit design based on ICX618 chip, including circuit design, FPGA programming, and imaging test. The results show that the CCD analog front-end design is reasonable, and the work is stable and reliable. (3) Based on the DSP/BIOS operating system, complete the software design of the image acquisition and processing system, including system initialization, image acquisition, phase calculation, and Gigabit Ethernet data transmission. (4) Set up an image acquisition and processing experimental system, complete the test of all modules, and realize the three-dimensional measurement of the object. After the device initialization is completed, the video image can be collected. There are two methods: one is read() to read directly; the other is mmap() memory mapping. read() reads data through the kernel buffer; mmap() bypasses the kernel buffer by mapping the device file to the memory.

This article is mainly divided into three parts. The first part is the introduction of this article by referring to relevant references, using data retrieval techniques and examples, including the description of the research background and significance of virtual reality technology and intelligent display systems. The second part is a combined analysis of the algorithms used in this research institute and the research objects of this research. These algorithms include phase recovery algorithms and four-step phase shifting methods; the third part is mainly about data acquisition and experimentation. Analyze, design the data acquisition and adjustment module, and use the image processing mod-

ule of virtual reality technology to conduct three-dimensional imaging experiments. Finally, the last part is the conclusion of this research.

2. Phase Recovery Algorithm Implementation

The phase recovery algorithm is mainly used to obtain the unfolded phase image of the measured object. In this system, the unfolded phase image is obtained by frequency conversion and phase shift [7, 8]. When the M-step phase shift is adopted, the phase shift change of each sinusoidal fringe image is $2b/M$, and the light intensity distribution received by the camera can be expressed as follows:

$$I_b(m, n) = c(m, n) + g(m, n) \cos \left(\frac{2\pi m \chi_0 + \varphi(m, n) + 2b\pi}{M} \right), \quad (1)$$

where $b = 0, 1, 2 \dots M - 1$, $I_b(m, n)$ is the light intensity distribution of the target object collected by the camera, $c(m, n)$ is the background light intensity distribution, $g(m, n)$ is the local contrast of the fringe, χ_0 is the carrier frequency, and $\varphi(m, n)$ is the phase factor containing the depth information of the object. The surface height information of the measured object can be obtained by solving $\varphi(m, n)$ in the phase function [9, 10]. From the above formula (1), the phase distribution $\varphi(m, n)$ on the surface of the measured object can be solved, namely,

$$\varphi(m, n) = \arctan \frac{\sum_{b=0}^{M-1} I_b(m, n) \sin(2\pi b/M)}{\sum_{b=0}^{M-1} I_b(m, n) \cos(2\pi b/M)}. \quad (2)$$

The phase shift method is proposed to solve the problem of measuring phase difference, so that the optical phenomenon of interference fringes is truly used for precision measurement in engineering. The idea of the interferometer is to solve the phase difference by introducing the phase shift amount and then obtain the surface shape. The design of this system adopts a 4-step phase shift method; the phase shift changes are $0, \pi/2, \pi$, and $3\pi/2$ in sequence, by formula (2).

$\Phi(m, n)$ can be obtained as follows:

$$\varphi(m, n) = \arctan \frac{I_4(m, n) - I_2(m, n)}{I_1(m, n) - I_3(m, n)}. \quad (3)$$

The phase function obtained by formula (3) cannot be distinguished in the fringe pattern of the same period, and the calculated phase value is folded, which cannot guarantee its monotonic increase. Therefore, it is necessary to unfold and recover the folded phase to solve the continuously changing phase. This process is called phase unfolding or phase reconstruction [11, 12]. This system uses generalized time phase unwrapping algorithm to solve the unwrapped phase diagram of the measured object.

The augmented virtual reality system can not only allow the user to see the real world, but also the virtual objects superimposed on the real world. It is a system that combines the real environment and the virtual environment, which

can reduce the complexity of the composition. The calculation of the real environment can also operate on the actual objects, which has truly reached the realm of reality and fantasy. According to the relationship between the phase value and the fringe frequency,

$$\frac{\varphi_t(u_1)}{u_1} = \frac{\varphi_t(u_2)}{u_2}. \quad (4)$$

In the formula, u_1 and u_2 , respectively, represent the two fringe frequencies, and $\varphi(u_1)$ and $\varphi(u_2)$, respectively, represent the unfolding phases of the two frequencies, and formula (5) is

$$\varphi_t(u_2) = b \cdot \varphi_t(u_1). \quad (5)$$

In the formula, $b = u_2/u_1$, which is the ratio of the number of two stripes.

Therefore, using the unfolding phase $\varphi_t(u_1)$ with the number of fringes u_1 , combining the above linear relationship and the folding phase $\varphi_w(u_2)$ with the number of fringes u_2 , and then unfolding,

$$\varphi_t(u_2) = \varphi_t(u_2) - 2\pi \times \text{NINT}\left(\frac{\varphi_w(u_2) - \varphi_w(u_1) \cdot b}{2\pi}\right). \quad (6)$$

In the formula, $b = u_2/u_1$, and the ratio of the number of stripes in this experimental system is 4, that is, $k = 4$.

3. Embedded Design of 3D Image Intelligent Display System

3.1. Data Acquisition and Debugging Module Design. For this experiment, it is mainly divided into three parts: preparation, experiment, and discussion. In order to ensure the accuracy and authenticity of the data, the analysis and comparison of the general three-dimensional measurement technology and the embedded processor consider multiple factors in the selection of the core processor and the image sensor. The design of the analog front end is to pave the way for the image processing module and then build the system of this research on this basis. This experiment is carried out indoors and compares and selects through the collected investigation and analysis data of core processors, front-end interfaces, and other devices.

3.1.1. Selection of Core Processor. The inside of the DSP chip adopts the Harvard structure with separate program and data, has a special hardware multiplier, widely adopts pipeline operation, and provides special DSP instructions, which can be used to quickly realize various digital signal processing algorithms. Comparing the analysis and comparison between general three-dimensional measurement technology and embedded processor, this system uses Texas Instruments (TI) Da Vinci processor series DSP chip TMS320DM648 as the core processor to construct a DSP-based image acquisition and processing system. Through the algorithm, obtain the unfolded phase map of the measured object to provide data for the next

three-dimensional reconstruction [13]. Its functional structure diagram is shown in Figure 1. Virtual reality technology is the use of a computer to generate a simulation environment; through the use of sensor equipment to make the user into the environment, the user and the environment directly interact with the technology. DM648 adopts advanced C64x+ kernel, compared with C64x kernel, the performance is increased by 20%, and the code density is increased by about 25%. The enhanced EDMA3 can realize the copy and transportation of three-dimensional data, and C64x programs can be easily transplanted to C64x+, The reuse rate is 100% [14]. In addition, DM648 integrates some common peripherals, such as I2C, PCI, and GPIO2, to help users reduce development difficulties and system costs. Comprehensive consideration, this system decided to use TMS320DM648 as the core processor of the image acquisition and processing system.

It is constructed with DM648 chip as the core, including power supply circuit, clock and reset circuit, memory circuit, and emulator circuit. The on-chip level one program cache size of DM648 is 32 K bytes, the level one data cache size is 32 K bytes, and the second-level cache size is 512 K bytes.

3.1.2. Image Sensor Selection. At present, the widely used image sensors mainly include CIS, CMOS, and CCD [15]. CIS is the contact image sensor [16]. Since this sensor is used for contact scanning, it is not suitable for non-contact measurement in this system. CMOS is the complementary metal oxide semiconductor image sensor [17]. Utilizing the semiconductor substrate doped to form negatively charged (N) and positively charged (P) semiconductors, the current generated by the photoelectric effect can be recorded by the processing wafer and converted into pictures. However, the traditional CMOS chip has a low aperture ratio, and the sensitivity is lower than that of a CCD under the same pixel size; CCD is the charge coupled device image sensor [18]. CCD is a kind of semiconductor device that uses the photoelectric effect to convert photons into signal charges. The structure of the CCD photosensitive unit is simpler than that of the CMOS. With the same area, the CCD photosensitive unit has a higher degree of integration and a higher resolution than CMOS. At the same time, in the CCD photosensitive unit, the photosensitive part occupies a larger area, and the image obtained by the sensor is also brighter. In addition, because the CCD photosensitive unit performs signal processing uniformly, the image noise is small and the signal-to-noise ratio is high. From the above analysis, we understand the advantages and disadvantages of different types of sensors. Since the main object of this system is the deformed sinusoidal fringe pattern projected on the surface of the object, it has higher requirements on the sensitivity, linearity, and signal-to-noise ratio of the sensor. Therefore, the system finally decided to use CCD sensor [19].

3.1.3. CCD Analog Front-End Design Based on ICX518. As shown in Figure 2, the CCD analog front-end circuit is

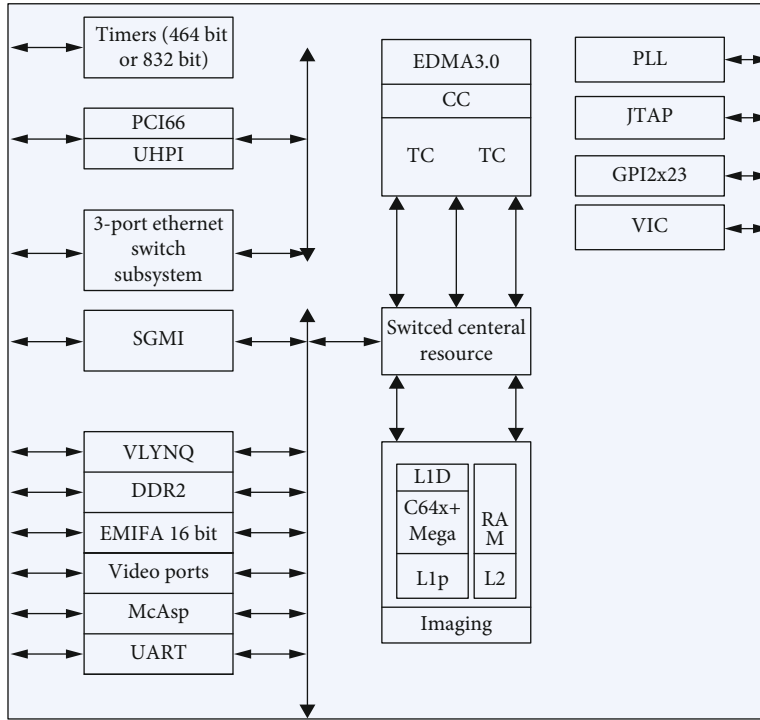


FIGURE 1: DM648 structure diagram.

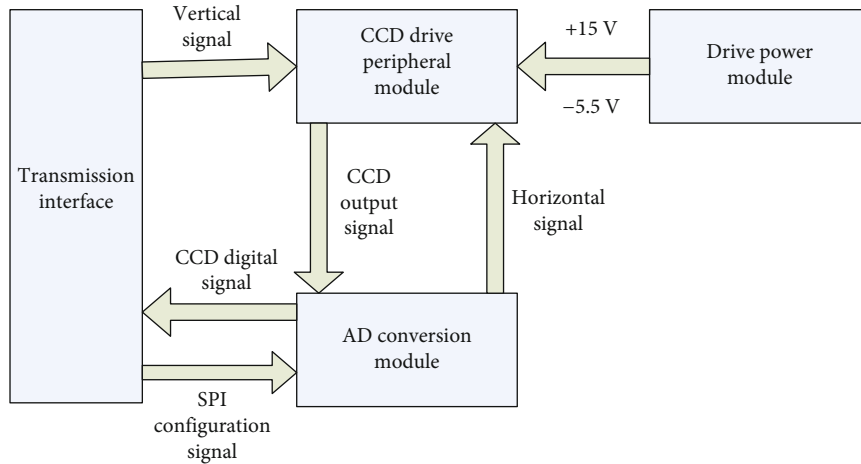


FIGURE 2: CCD analog front-end circuit composition diagram.

mainly composed of a driving power module, a CCD driving peripheral module, and an AD conversion module. With the rapid development of computer technology, there have been many high-tech based on computer technology, and the same is true for virtual reality technology (referred to as VR). This is a high-tech that is widely used in all walks of life. It is a high-end human-machine interface, including through vision, hearing, touch, smell, and taste.

The schematic diagram of the CCD drive power supply circuit designed with this chip has a built-in accurate feedback resistor, which is adjusted by modifying the resistor value—a feedback current of $25\mu A$. Finally, the feedback

current is used to adjust the positive and negative output voltages. The specific formula is as follows:

$$R_{\text{pos}} = \left(\frac{V_{\text{pos}} - 1.23}{25\mu A} \right), \quad (7)$$

$$R_{\text{neg}} = \frac{-V_{\text{neg}}}{25\mu A}. \quad (8)$$

Among them, V_{pos} is +15 V and V_{neg} is -5.5 V. According to the above formula, the resistance value of R1 is

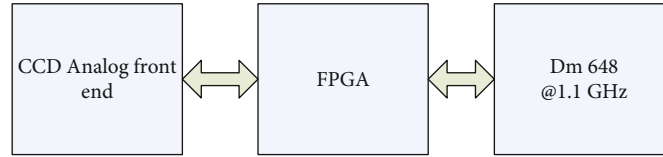


FIGURE 3: System structure block diagram.

549 K, and the resistance value of R2 is 220 K. The feedback resistors are all 1% high-precision resistors to ensure the accuracy of the output voltage [20].

3.2. Design of Image Processing Module Based on DSP. Virtual reality technology embodies the adaptation of computers to humans, and humans participate in the environment of information processing through the most ordinary means of communication to obtain an immersive experience. Virtual reality technology has three characteristics: immersion, interactivity, and conception. In order to make the system take into account the flexibility and efficiency and facilitate the upgrade of the algorithm, after detailed investigation and program comparison, this article decided to use the combination of FPGA and DSP to build a hardware processing platform. The block diagram of the system structure is shown in Figure 3.

Among them, the DM648 module is an important part of the entire system, and the image processing module is composed of the following important parts:

- (1) *FPGA Part.* Mainly realize the interconnection of various modules, which can collect the data of the ICX618-based CCD analog front end introduced in Chapter 2, and connect to the DSP through the Video Port video interface, or it can be used as a DSP coprocessor, responsible for completing the algorithms with high real-time requirements.
- (2) *Central Processing Unit TMS320DM648.* Through the video interface to achieve seamless connection with the CCD analog front end, adjust the embedded 3D imaging image acquisition and processing system design core, the chip support library to achieve the phase recovery of the measured object, and finally through the gigabit Ethernet output results.
- (3) *Storage Device.* DM648 has a dedicated DDR2 memory expansion interface, which can be connected to a DDR2 storage device that meets the JESD79D-2A standard. And in order to solidify user data and save the output result conveniently, this system connects a 512 Mbit parallel FLASH chip through the EMIF interface.
- (4) *High-Speed Data Transmission Interface.* DM648 has a three-port Gigabit Ethernet transmission module, which can realize high-speed data transmission between this system and other embedded devices or computers. This system connects the SGMII inter-

face of DM648 through the PHY chip to realize dual gigabit network port communication.

- (5) *Other Communication Interfaces.* Communication interfaces include SPI interface, I2C interface, and GPIO interface. It is very convenient to use these interfaces for data communication and interaction with external devices.

The above five parts build an embedded image processing platform with DSP as the processing core. The interconnection of various modules is realized by FPGA, which makes the hardware platform have great flexibility and real-time [21]. From a functional point of view, the hardware system consists of three parts: image acquisition module, image processing module, and data transmission module. The optical image is converted into a video data stream by the image acquisition module. The FPGA module collects and buffers the data and sends the data to the DM648 through the Video Port interface. Then, the DM648 calls the phase recovery algorithm to solve the unfolded phase of the measured object and finally passes the Gigabit Ethernet; the interface is sent to the computer.

3.3. PCB Design. In high-speed PCB design, in order to ensure the stable and reliable operation of the system, it is not enough to only consider the electrical connection. It is also necessary to consider signal integrity issues such as impedance matching, board layer design, and electromagnetic compatibility. The layout of PCB components is to place components on the PCB according to certain principles. Good component layout can reduce the difficulty of wiring during layout, which is conducive to shortening design time and reducing design costs. Therefore, it is necessary to understand some methods and principles of PCB layout [22]. First of all, the circuit board size should be moderate. Too large size not only increases the cost, but also causes the stability of the circuit board to decrease. If the size is too small, it is easy to cause the devices to be too concentrated, the signals between the devices are easy to crosstalk each other, and the heat dissipation effect is also worse [23].

The distributed virtual reality system is a product of the development and combination of virtual reality technology and network technology. It is a system in which multiple users or multiple virtual worlds located in different physical locations are connected to share information through the network in the virtual world of the network. The final physical diagram of the PCB is shown in Figures 4 and 5

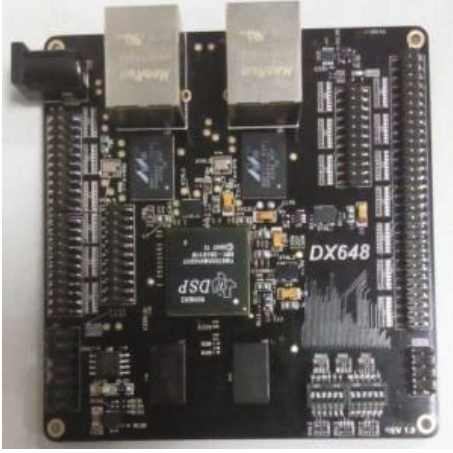


FIGURE 4: DSP circuit physical diagram.



FIGURE 5: FPGA circuit physical diagram.

(referenced to the image acquisition and processing design of embedded 3D imaging).

4. Experimental Analysis

This system adopts TMS320DM648 as the main control platform. Figure 6 is the physical map of the system. The first part is the image acquisition and processing system designed in this paper, and the second part is the high-speed structured light system environment designed by the research team.

4.1. Circuit Test. It has only been more than ten years since the concept of virtual reality was proposed, but the technology has developed by leaps and bounds. It has opened up a vast world for human-computer interaction and other aspects but also brought huge social and economic benefits.

According to the system hardware design in Chapter 3, the power consumption of this system is estimated to be 5 w, so the experiment uses 5 V, 2A power adapter as input, and it is converted into +14 V, +4.4 V, and +3.2 V which we need through various buck and boost circuits, +2.3 V and



FIGURE 6: Physical map of the test system.

TABLE 1: Actual voltage test of power supply circuit.

Theoretical voltage (V)	Test value(V)	Ripple voltage(mV)
+14	+14.32	15~49
+4.4	+4.54	25~57
+3.2	+3.23	34~65
+2.3	+2.54	35~67
-6.4	-6.43	29~69

TABLE 2: Time consumption analysis of each module of the system.

Module	Time consumption
Acquisition module	1.934
Phase demodulation and expansion	2.068

-6.4 V, and the actual voltage measured by the oscilloscope after power-on test is shown in Table 1.

It can be seen from the above table that the voltage value of the power supply part is accurate, the ripple is small, and it meets the system requirements, and the stability of the power supply is very high through long-term testing.

4.2. Three-Dimensional Imaging Test. Image tracking is an emerging technical field. It organically combines image processing, automatic control, and information science to form a real-time automatic target recognition from image signals, extract target location information, and automatically track target movement technology. In chronological order, the sinusoidal fringe pattern with 4 frequency conversion and 4-step phase shift is projected on the measured object through the DMD projector to collect a total of 16 images, the folded phase of the measured object is obtained through phase demodulation, and the generalized time phase expansion is used. The algorithm obtains the unfolded phase of the object. The system time consumption is shown in Table 2.

After the development of the image tracker is completed, the tracking performance needs to be evaluated. Through the development of the image tracker test and evaluation system, it can be evaluated in the laboratory by simulating various actual scenes and tracking the target and the interference situation.

It can be seen from Table 2 that the time consumption part of the algorithm processing and the acquisition part is basically the same, and the system can continuously collect and output and expand the phase diagram. Finally, the



FIGURE 7: Reconstruction results of 3D topography: (a) actual gypsum image and (b) reconstruction result.

existing three-dimensional reconstruction algorithm of the research group is used to reconstruct the three-dimensional topography of the measured object to verify and expand the accuracy of the phase map. The reconstruction result of the plaster image is shown in Figure 7.

The above data strongly proves that the embedded system constructed by this research institute has made great progress and improvement in image processing and tracking test evaluation, circuit correlation coefficient, data transmission, and real-time performance. By combining DSP, DM648, and high-speed PCB, a highly advantageous image intelligent display system is created.

5. Conclusions

This research is based on the analysis of the intelligent image display embedded system based on virtual reality technology. The main purpose is to design a system with high-speed image processing and as little power consumption as possible to optimize the process of 3D image imaging. With the development of 3D measurement technology, the hardware requirements of image acquisition and processing systems for 3D imaging will become higher and higher. In consideration of image acquisition quality, processor requirements, cost power consumption, and stability, the existing processing system cannot meet the requirements of portability, low power consumption, low cost, and stable operation. Based on the shortcomings of the existing system, this paper conducts research on the key technology research requirements of high-precision and high-speed 3D digital imaging and completes the construction and debugging of the entire platform. Timely testing and evaluation of image tracking on the one hand can verify the performance requirements of the image tracker; on the other hand, it can also facilitate the discovery of tracking effects and improve the performance of the tracker during the development of the image tracker. This experiment conducted strict monitoring on data acquisition and used computer technology to analyze the error of the data. In addition, the components selected for the experimental purpose of this research are all fully demonstrated feasibility components, and to maintain the authenticity of the experiment, a correspond-

ing model was constructed. Although the analysis of the details of image acquisition quality and the application of high-speed 3D digital imaging technology is not so sufficient, this research is at a complete level as a whole. In the course of the 3D imaging experiment in this study, it is necessary to rationalize the design of the parameters of the control power supply circuit, the heat dissipation effect between the devices, and the central processing unit. In order to make the error of the relevant data as small as possible, multiple experiments are required. Because the number of tests in this study is relatively small, and the parameters involved in the test are relatively large, there are some shortcomings in the research that are rough and not enough for in-depth research. For the next research direction, more are based on this research to analyze the application of the built embedded system.

Data Availability

No data were used to support this study.

Conflicts of Interest

The author states that this article has no conflict of interest.

References

- [1] T. Ohno, M. Wakatsuki, T. Toita et al., "Recommendations for high-risk clinical target volume definition with computed tomography for three-dimensional image-guided brachytherapy in cervical cancer patients," *Journal of Radiation Research*, vol. 58, no. 3, pp. 341–350, 2017.
- [2] M. Gao, Q. Teng, X. He, C. Zuo, and Z. J. Li, "Pattern density function for reconstruction of three-dimensional porous media from a single two-dimensional image," *Physical Review E, Statistical, Nonlinear, and Soft Matter Physics*, vol. 93, no. 1, article 012140, 2016.
- [3] M. L. M. François, Y. Lecieux, D. Leduc, C. Lupi, and E. Rozière, "An embedded 3D strain tensor sensor based on the Eshelby's inclusion," *Experimental Mechanics*, vol. 57, no. 5, pp. 801–811, 2017.
- [4] J. L. Maples-Keller, B. E. Bunnell, S. J. Kim, and B. O. Rothbaum, "The use of virtual reality technology in the treatment

- of anxiety and other psychiatric disorders,” *Harvard Review of Psychiatry*, vol. 25, no. 3, pp. 103–113, 2017.
- [5] J. Y. Jeon and H. I. Jo, “Three-dimensional virtual reality-based subjective evaluation of road traffic noise heard in urban high-rise residential buildings,” *Building and Environment*, vol. 148, pp. 468–477, 2019.
- [6] A. Ruiz-Moya, R. A. Lopez-Garcia, D. Sicilia-Castro, T. Gomez-Cia, and P. Infante-Cossio, “Anatomical features associated with venous congestion in DIEP flap using CT angiography with three-dimensional reconstruction,” *Plastic and Aesthetic Research*, vol. 4, no. 8, pp. 127–134, 2017.
- [7] P. Wang, J. Cheng, F. Hao, L. Wang, and W. Feng, “Embedded adaptive cross-modulation neural network for few-shot learning,” *Neural Computing and Applications*, vol. 32, no. 10, pp. 5505–5515, 2020.
- [8] G. Wang, N. Shi, Y. Shu, and D. Liu, “Embedded manifold-based kernel fisher discriminant analysis for face recognition,” *Neural Processing Letters*, vol. 43, no. 1, pp. 1–16, 2016.
- [9] S. Diamond and S. Boyd, “CVXPY: a python-embedded modeling language for convex optimization,” *Journal of Machine Learning Research*, vol. 17, no. 1, pp. 2909–2913, 2016.
- [10] S. MahdaviFar and A. A. Ghorbani, “DeNNes: deep embedded neural network expert system for detecting cyber attacks,” *Neural Computing and Applications*, vol. 32, no. 18, pp. 14753–14780, 2020.
- [11] E. Bastug, M. Bennis, M. Medard, and M. Debbah, “Toward interconnected virtual reality: opportunities, challenges, and enablers,” *IEEE Communications Magazine*, vol. 55, no. 6, pp. 110–117, 2017.
- [12] S. Baker, J. Waycott, E. Robertson et al., “Evaluating the use of interactive virtual reality technology with older adults living in residential aged care,” *Inf. Process. Manag.*, vol. 57, no. 3, p. 102105, 2020.
- [13] J. Lenoir, S. Cotin, C. Duriez et al., “Workshop on virtual reality interaction and physical simulationInteractive physically-based simulation of catheter and guidewire,” vol. 61, Tech. Rep. 13, *Journal of Preventive Medicine Information*, 2017, 2005.
- [14] A. Mirelman, L. Rochester, I. Maidan et al., “Addition of a non-immersive virtual reality component to treadmill training to reduce fall risk in older adults (V-TIME): a randomised controlled trial,” *Lancet*, vol. 388, no. 10050, pp. 1170–1182, 2016.
- [15] I. Elhenawy, S. H. Mahmoud, and A. Moustafa, “A lightweight privacy preserving keyword search over encrypted data in cloud computing,” *Journal of Cybersecurity and Information Management*, vol. 3, no. 2, pp. 29–41, 2021.
- [16] S. M. Park, Y. T. Kim, S. D. Hwang et al., “Method and apparatus for displaying two-dimensional or three-dimensional image sequence while adjusting frame rate,” *Journal of Cardiovascular Surgery*, vol. 39, no. 5, pp. 689–690, 2016.
- [17] P. Y. Chu, K. H. Lin, H. L. Kao, Y. J. Peng, and T. W. Huang, “Three-dimensional image simulation of primary diaphragmatic hemangioma: a case report,” *World Journal of Clinical Cases*, vol. 7, no. 24, pp. 4307–4313, 2019.
- [18] J. E. Schreiber, C. S. Stern, E. S. Garfein, K. E. Weichman, and O. M. Tepper, “A novel approach to surgical markings based on a topographic map and a projected three-dimensional image,” *Plastic and reconstructive surgery global open*, vol. 137, no. 5, pp. 855e–859e, 2016.
- [19] S. Hariharan and M. Gupta, “Improving cloud-based ECG monitoring, detection and classification using GAN,” *Fusion: Practice and Applications*, vol. 2, no. 2, pp. 42–49, 2020.
- [20] M. Nishi, K. Yoshikawa, J. Higashijima et al., “Utility of virtual three-dimensional image analysis for laparoscopic gastrectomy conducted by trainee surgeons,” *The Journal of Medical Investigation*, vol. 66, no. 3.4, pp. 280–284, 2019.
- [21] L. Laimeche, A. Meraoumia, and H. Bendjenna, “Enhancing LSB embedding schemes using chaotic maps systems,” *Neural Computing and Applications*, vol. 32, no. 21, pp. 16605–16623, 2020.
- [22] Y. Rivenson, Y. Wu, H. Wang, Y. Zhang, A. Feizi, and A. Ozcan, “Sparsity-based multi-height phase recovery in holographic microscopy,” *Scientific Reports*, vol. 6, no. 1, p. 37862, 2016.
- [23] Y. Qin, J. Wu, B. Xiao, T. Hojo, and Y. Y. Li, “Biogas recovery from two-phase anaerobic digestion of food waste and paper waste: optimization of paper waste addition,” *Science of The Total Environment*, vol. 634, pp. 1222–1230, 2018.

Retraction

Retracted: Facial Expression Recognition Based on Convolutional Neural Network Fusion SIFT Features of Mobile Virtual Reality

Wireless Communications and Mobile Computing

Received 28 November 2023; Accepted 28 November 2023; Published 29 November 2023

Copyright © 2023 Wireless Communications and Mobile Computing. This is an open access article distributed under the Creative Commons Attribution License, which permits unrestricted use, distribution, and reproduction in any medium, provided the original work is properly cited.

This article has been retracted by Hindawi, as publisher, following an investigation undertaken by the publisher [1]. This investigation has uncovered evidence of systematic manipulation of the publication and peer-review process. We cannot, therefore, vouch for the reliability or integrity of this article.

Please note that this notice is intended solely to alert readers that the peer-review process of this article has been compromised.

Wiley and Hindawi regret that the usual quality checks did not identify these issues before publication and have since put additional measures in place to safeguard research integrity.

We wish to credit our Research Integrity and Research Publishing teams and anonymous and named external researchers and research integrity experts for contributing to this investigation.

The corresponding author, as the representative of all authors, has been given the opportunity to register their agreement or disagreement to this retraction. We have kept a record of any response received.

References

- [1] F. Yao and L. Qiu, "Facial Expression Recognition Based on Convolutional Neural Network Fusion SIFT Features of Mobile Virtual Reality," *Wireless Communications and Mobile Computing*, vol. 2021, Article ID 5763626, 7 pages, 2021.

Research Article

Facial Expression Recognition Based on Convolutional Neural Network Fusion SIFT Features of Mobile Virtual Reality

Fuguang Yao¹ and Liudong Qiu²

¹Chongqing University of Education, Chongqing 400065, China

²Chongqing Industry Polytechnic College, Chongqing 401120, China

Correspondence should be addressed to Fuguang Yao; yaofuguang@cque.edu.cn

Received 22 August 2021; Accepted 25 September 2021; Published 14 October 2021

Academic Editor: Balakrishnan Nagaraj

Copyright © 2021 Fuguang Yao and Liudong Qiu. This is an open access article distributed under the Creative Commons Attribution License, which permits unrestricted use, distribution, and reproduction in any medium, provided the original work is properly cited.

Facial expression recognition computer technology can obtain the emotional information of the person through the expression of the person to judge the state and intention of the person. The article proposes a hybrid model that combines a convolutional neural network (CNN) and dense SIFT features. This model is used for facial expression recognition. First, the article builds a CNN model and learns the local features of the eyes, eyebrows, and mouth. Then, the article features are sent to the support vector machine (SVM) multiclassifier to obtain the posterior probabilities of various features. Finally, the output result of the model is decided and fused to obtain the final recognition result. The experimental results show that the improved convolutional neural network structure ER2013 and CK+ data sets' facial expression recognition rate increases by 0.06% and 2.25%, respectively.

1. Introduction

Facial expression recognition computer technology can obtain the emotional information of the person through the expression of the person to judge the state and intention of the person. It is of great significance in human-computer interaction, safe driving, and intelligent advertising systems. The CK+ data set is a classic facial expression library, which contains expression images of anger, disgust, fear, happiness, sadness, surprise, and contempt. The expressions are video sequences [1]. It contains a series of images with the same expression ranging from calm to violent. We can extract neutral expression images from it.

Affected by factors such as distance, the image will have the problem of blurred faces and fewer face pixels. The facial expression recognition of low-pixel facial images is to recognize facial images with low quality and inconspicuous facial features [2]. The image size obtained by sampling is 32 pixel × 32 pixel, which is in line with the low-pixel characteristics. The complexity of facial expression images is high. When the facial features are not obvious, it is difficult for us to identify by extracting specific feature information.

For facial expression images with a size of 32 pixel × 32 pixel, some scholars have proposed a facial expression recognition method based on the improved LeNetG5 convolutional neural network (CNN). Some scholars have proposed a CNN facial expression recognition method based on the local binary pattern (LBP). Research shows that CNN has a better effect on facial expression recognition in low-pixel facial images. This paper improves the CNN model on this basis. We propose an expression recognition method for low-pixel facial images and compare it with several other methods. The results show that this method has a better recognition effect.

2. Expression Recognition Method for Low-Pixel Facial Images

2.1. Facial Expression Image Reprocessing. General expression recognition methods include image reprocessing, facial feature extraction, and expression recognition. The reprocessing stage of image expression recognition performs face detection to obtain facial region images [3]. The recognition of expressions in low-pixel facial images also requires image

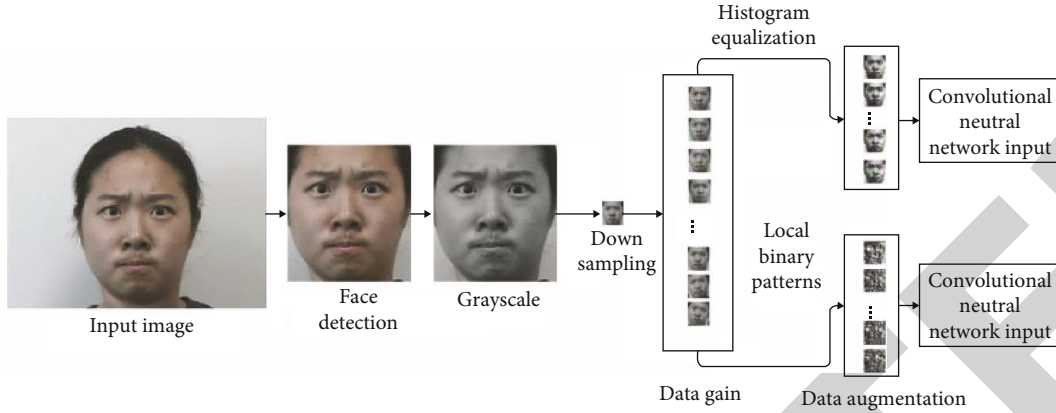


FIGURE 1: Facial expression reprocessing process.

enhancement or image superresolution during reprocessing. Image enhancement is to enhance the existing information of the image by changing the distribution of pixels, and image superresolution are to restore some missing pixel information by adding pixels.

The image reprocessing of this method includes face detection and cropping, gray processing, downsampling, data enhancement, and image enhancement. The purpose of face detection is to accurately calibrate the position and size of the face in the image. We use the D-lib model for face detection. The D-lib model can automatically estimate the coordinates of the facial feature points in the image and process the data in the OpenCV library. We use this to crop the image so that the image features are concentrated on the face. Grayscale processing is the process of converting a colour image into a gray image. Downsampling is to standardize the image size in the input CNN model. We use bilinear interpolation to ensure that the face position of the resampled image is the same as the original image. We use CNN for image recognition. The amount of training data directly affects the final recognition effect. The larger the amount of data, the better the effect [4]. Commonly used data enhancement methods include mirroring, rotating, and adding noise. These methods mirror the original data and rotate it in different angles and directions, enhancing the data to 13 times the original data. We then add different noise coefficients (salt and pepper noise, Gaussian noise, Poisson noise, and speckle noise) to the existing data, and the final data is enhanced to 130 times the original data. We perform histogram equalization on the image and use the local binary mode to obtain the enhanced image. Among them, histogram equalization is also called histogram flattening. The essence of this method is to stretch the image nonlinearly and redistribute the image pixel values. In this way, the number of pixel values in a certain grayscale range is roughly equal. The local binary mode is an operator that describes the local texture characteristics of the image. It has the advantages of rotation and gray invariance. It can be used to extract local texture features of the image. The specific reprocessing process is shown in Figure 1.

2.2. Improved Convolutional Neural Network Model. With the development of computer processing capabilities, CNN has achieved amazing results in image recognition. The efficiency of CNN-based image recognition methods has also been continuously improved and has gradually replaced the traditional facial expression image recognition methods. In the 2012 ImageNet Object-Oriented Recognition Challenge (ILSVRC), some scholars used the CNN model Alex Net to win the championship. In the 2014 ILSVRC competition, the CNN model Google Net architecture won first place in the classification. Some scholars proposed CNN-VGG Net. The second place in the classification group and the first place in the positioning project group. VGG-Net deepens the number of network layers while avoiding too many parameters, all layers use a 3×3 small convolution kernel, and the convolution layer step size is set to 1. The alternating structure of multiple convolutional and nonlinear activation layers makes extracting deeper and better features than a single convolutional layer structure. In the ILSVRC2015 competition, ResNet, proposed by scholars, won the championship [5]. A connection method called short cut connection in ResNet can theoretically keep the network in an optimal state while the network layer is constantly deepening. There is enough feature information in facial expressions to optimize model parameters to obtain a good recognition effect. Low-pixel face images need to make full use of inconspicuous feature information. On this basis, the article proposes a CNN model for expression recognition of low-pixel facial images to extract facial features better.

The image size of the input CNN model is $32 \text{ pixel} \times 32 \text{ pixel}$. We increase the number of CNN layers to increase the nonlinearity of the network model. This makes the recognition ability of the decision function stronger. To avoid gradient disappearance and gradient explosion caused by deepening the number of network layers, the network needs to have a more complex structure [6]. Some scholars have proposed a network connection structure high way networks. Some of the features in this structure can pass through certain network layers directly without processing, which makes the structure easier to optimize. Combining this structure and the short cut connection, a short method

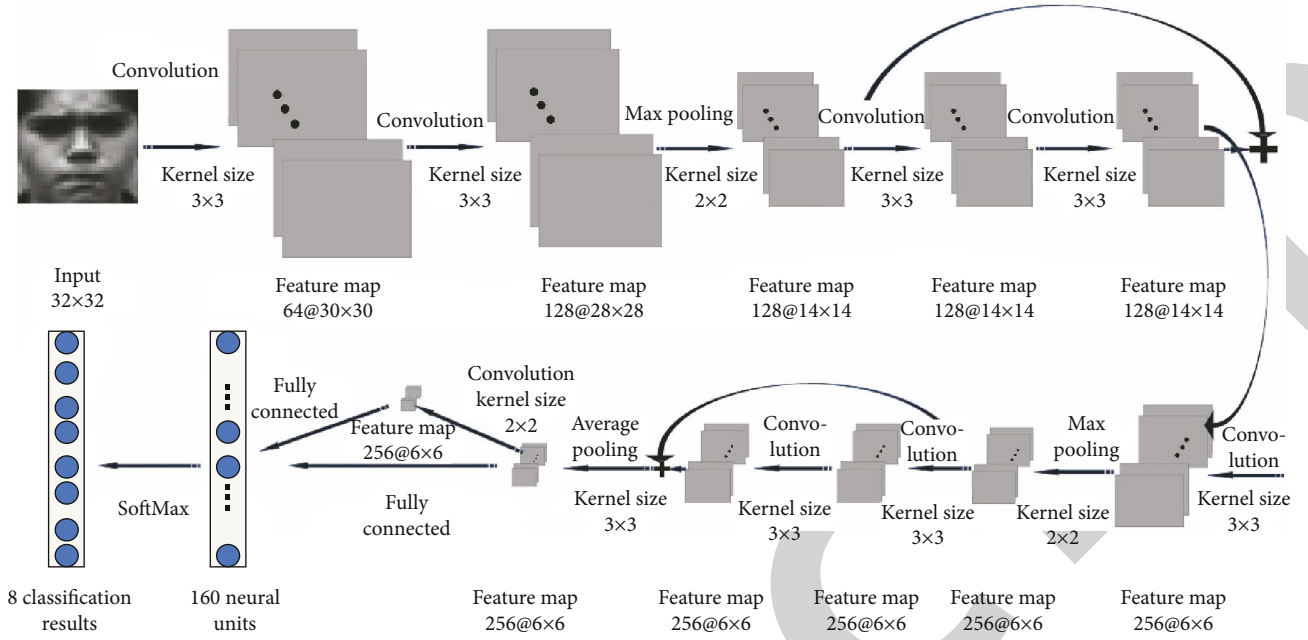


FIGURE 2: CNN model.

avoids the gradient disappearance and gradient explosion problems when using deeper networks. The experiment the CNN model used is shown in Figure 2. The number before @ is the number of feature maps, and the number after @ is the size of the feature map (pixel \times pixel).

We input the size of the feature map, the size of the kernel of the convolution and pooling operation, the step size, and the size of the output feature map in the convolution operation and the pooling operation. Its mathematical relationship is

$$\omega_2 = \frac{\omega_1 - f + 2p}{s + 1}, \quad (1)$$

where ω_2 is the feature map size after convolution or pooling operation, ω_1 is the size of the feature map before convolution or pooling, f is the size of the kernel for convolution and pooling operations, p is the number of pixels filled with zero, and s is the step size. We added the output tensor of the third layer of the model and the output tensor of the fifth layer to obtain 128 feature maps with a size of 14 pixel \times 14 pixel. Then, we pass the ReLU activation function as the input of the sixth layer. The article adds the output tensors of the seventh and ninth layers of the model to obtain 256 feature maps with a size of 6 pixel \times 6 pixel. Then, we pass the ReLU activation function as the input of the tenth layer. The twelfth layer is fully connected. We take the output of the tenth and eleventh layers through the ReLU activation function and then concatenate the obtained tensors as the input of the twelfth layer. The output is 160 neurons [7]. The last layer is the SoftMax classifier. The output is eight network nodes, representing the probability that the input image is indifferent expression states. Table 1 is the specific description of the model. The content includes the type of each layer of the model, the corresponding kernel

size and step size, and the size of the output feature map of each layer. The CNN includes three basic operations: convolution, pooling, and full connection. Among them, convolution is also divided into inner convolution and outer convolution. In other words, it is the convolution without 0 paddings and the convolution with 0 paddings. The article assumes that the input is the matrix A of $M \times N$. The convolution kernel is moment B , and $M \geq m, N \geq n$ of $m \times n$; then, the output of the inner convolution operation is $C = A * B$. The pixel c_{ij} at the corresponding position can be expressed as

$$c_{ij} = \sum_{s=1}^m \sum_{t=1}^n a_{i+m-s, j+n-t} \times b_{st}. \quad (2)$$

$1 \leq i \leq M - m + 1, 1 \leq j \leq N - n + 1$ is the corresponding multiplication with the rows and columns of matrix A . Suppose the pixel at the corresponding position of matrix B is b_{st} , and the pixel at the corresponding position of matrix A is $a_{i+m-s, j+n-t}$. Outer convolution is defined as filling A with 0, and the rows and columns of the filled matrix are related to the number of rows and columns of the B matrix. The article makes it an $(M + 2m - 2) \times (N + 2n - 2)$ matrix and then performs inner convolution with B . The formula can be expressed as

$$A \overset{\wedge}{*} B = A_B \overset{\cup}{*} B. \quad (3)$$

We pool matrix A . Suppose it is divided into nonoverlapping blocks, and the size of each block is $\lambda \times \tau$. The matrix $G_{\lambda, \tau}^A$ of block ij can be expressed as

$$G_{\lambda, \tau}^A(i, j) = (a_{st})_{\lambda \times \tau}, \quad (4)$$

TABLE 1: Convolutional network parameters.

Layer	Type	Kernel size (pixel \times pixel)	Stride	Output number	Output size (pixel \times pixel)
Layer1	Convolution	3×3	1	64	30×30
Layer2	Convolution	3×3	1	128	28×28
Layer3	Max pooling	2×2	2	128	14×14
Layer4	Convolution	3×3	1	128	14×14
Layer5	Convolution	3×3	1	128	14×14
Layer6	Convolution	3×3	1	256	12×12
Layer7	Max pooling	2×2	2	256	6×6
Layer8	Convolution	3×3	1	256	6×6
Layer9	Convolution	3×3	1	256	6×6
Layer10	Average pooling	3×3	3	256	2×2
Layer11	Convolution	2×2	1	512	1×1
Layer12	Fully connected	—	—	—	160×1
Output	SoftMax	—	—	—	8×1

where a_{st} is the element in row s and column t in matrix A , $(a_{st})_{\lambda \times \tau}$ is a matrix block composed of $\lambda \times \tau$ elements in matrix A , and $(i-1) \times \lambda + 1 \leq s \leq i \times \lambda$, $(j-1) \times \tau + 1 \leq t \leq j \times \tau$. Maximum pooling is defined as

$$d[G_{\lambda, \tau}^A(i, j)] = \max \left(\sum_{s=(i-1)\lambda+1}^{i\lambda} \sum_{t=(j-1)\tau+1}^{j\tau} a_{st} \right). \quad (5)$$

Average pooling is defined as

$$a[G_{\lambda, \tau}^A(i, j)] = \frac{1}{\lambda \times \tau} \sum_{s=(i-1)\lambda+1}^{i\lambda} \sum_{t=(j-1)\tau+1}^{j\tau} a_{st}. \quad (6)$$

We use overlapping blocks of size $\lambda \times \tau$ to downsample the maximum pooled A_{\max} and the average pooled A_{mean} , respectively. The formula can be expressed as

$$\begin{aligned} D_{\lambda, \tau}(A_{\max}) &= d[G_{\lambda, \tau}^A(i, j)], \\ D_{\lambda, \tau}(A_{\text{mean}}) &= a[G_{\lambda, \tau}^A(i, j)]. \end{aligned} \quad (7)$$

Each output A of the fully connected layer can be seen as the r node a_r in the previous layer multiplied by its weight coefficient ω_r , plus a bias value b_h . For example, the input of the fully connected layer is $256 \times 2 \times 2$ nodes. That is, the input feature map is $256@2 \times 2$, and the output has 80 nodes. A total of $256 \times 2 \times 2 \times 80 = 81920$ weight coefficients and 80 offset parameters are required. Then, a single element d_h in its output vector D can be expressed as

$$d_h = \sum_{r=1}^k \omega_r \times a_r + b_h. \quad (8)$$

In the formula, k is the number of input feature maps.

3. Expression Recognition Experiment of Low-Pixel Facial Images

3.1. Data Set Preparation. The experiment uses the CK+ data set. This data set is used to evaluate the facial expression recognition (FER) system, and it is also a relatively common data set for facial expression recognition. The content contains 593 video sequences from 123 subjects. The duration ranges from 10 to 60 frames [8]. The data set shows a series of images ranging from calm to violent. The number of original images on different expressions is unevenly distributed. The neutral expression image is the image at the beginning or end of the expression. According to the original number distribution, we select the last 1~3 expression images of each expression sequence. A total of 686 images were used for modeling. 80% is used as the training set, and 20% is used as the test set. The peak images of the same person with the same expression will not appear in the training set and the test set simultaneously.

The article adds data to the training set. We will test the data gained and ungained test sets in the same trained model. Since the research found that the difference in recognition accuracy is small, no data gain processing is done on the test set. The final image size of the training set is 71370, and the image size of the test set is 137. We perform histogram equalization and local binary mode on all images to obtain three data sets of the same size, including the original image [9]. Table 2 shows the number of images of 8 expressions in each test set and training set. The original image of the eight expressions, the image after the histogram equalization, and the image with the local binary mode are shown in Figure 3.

3.2. Evaluation Criteria. The main evaluation criteria of facial expression recognition methods are recognition accuracy and recognition speed. The recognition accuracy rate is the ratio of correctly recognized expression samples in the test set to the number of samples in all the test sets.

TABLE 2: Facial expression database.

Category	Train database	Test database
Angry	14040	27
Disgust	12220	24
Fearful	7800	15
Happy	14300	28
Sad	8970	15
Surprised	8580	16
Scorn	5460	12
Neutral	8970	15

Recognition speed is when it takes to recognize each test set sample after the recognition model is established. The time it takes is the ratio of the time it takes to identify the test set to the number of samples in the test set.

$$A = \frac{1}{p} \sum_{i=1}^p g[f(x_b) = y_b], \quad (9)$$

$$t_d = \frac{T}{p},$$

where A is the recognition accuracy rate, p is the total number of samples in the test set, g is the indicator function, x_b is the given sample, $f(x_b)$ is the output after the sample passes the model, y_b is the label of a given sample, t_d is the recognition speed [10], and T is the total time spent. We can get it by subtracting the time before the first test sample was recognized by the time after the last test sample was recognized.

3.3. Experimental Process. Because the input CNN image pixels are low, the output recognition effect will fluctuate slightly, so we introduce the decision fusion and final image recognition. In the testing phase, we use five trained network models to judge the test set data, respectively. Then, we use the SoftMax average voting (SAV) method to fuse the judgment results of the five models. Finally, we get the final result to improve the recognition effect. The test steps are shown in Figure 4.

It can be seen from Section 2.2 that the output of CNN is a 1-dimensional vector. The value of each element in the vector is the probability that the image may be a certain category. SoftMax average voting is to average the output results of five trained CNNs. Take the average of three experiments from the most likely result at the end of the article. The graphics card is NVIDIA GeForce 940MX. The main frequency is 1122 MHz, and the memory is 2.00 GB. The operating system is Linux Ubuntu 16.04. The software is Python 3.6, NVIDIA CUDA, and cuDNN libraries. We adopted the training strategy to improve the recognition accuracy is to add batch normalization (BN) and ReLU activation functions after each convolutional and pooling layer. This can overcome the disappearance of the gradient and speed up the training speed.

We selectively add L2 regularization and dropout to alleviate overfitting. The learning rate decay strategy is adopted. We choose a larger value at the beginning of the learning rate. After N rounds of iteration, the attenuation is 1/10 of the initial learning rate [11]. We use the Adam optimization algorithm during optimization, which enables the network to find the global best advantage faster. The data sets are the original image, the image with the histogram enhancement, and the local two. The CNN model is trained when the value pattern feature map is used, and at the same time, we adjust the parameters of the network.

According to the accuracy of the test, we first determine whether we need to add the L2 regularization and dropout layer and then determine which layer to place. We determine the approximate range of the learning rate according to the loss during training, training loss, and test accuracy. Two dichotomies obtain the learning rate.

3.4. Result Analysis. To find the optimal situation of the facial expression recognition system, we input the original image data set, the local binary pattern feature map data set, and the histogram equalized data set in the CNN model. The average recognition accuracy and speed obtained as a result are shown in Table 3. The experiment is the average of three experiments.

It can be found that the accuracy of the input data set after histogram equalization is better than that of the original image data set. The accuracy of the data set the input as the local binary pattern feature map is the worst. There is no obvious difference in speed between the three. The recognition speed of the data set the input as the local binary pattern feature map is slightly faster, but the speed of 0.29s has a small advantage compared with the accuracy of 3.6%. Analysing the different data sets in Figure 3, we believe that certain data enhancements will strengthen the image information and improve the recognition accuracy. Because the original pixels of the data are too low, we directly extract the feature map of its local binary mode, which will enhance the texture information while losing more information [12]. Therefore, the speed is the fastest when the accuracy is the lowest. The experiment finally selects the data set enhanced by histogram equalization to input the CNN model. We add L2 regularization and dropout after the twelfth layer. The dropout parameter is 0.7, and the initial value of the learning rate is 0.0001. After 1000 iterations, it decays to 1/10 of the initial learning rate. Table 4 shows the three experimental results of the improved CNN model on the CK+ data set for the eight-expression recognition.

It can be seen from Table 4 that the recognition rates of happy and surprised expressions are higher. Fearful's recognition rate is low and fluctuates greatly. On the one hand, it may be that the first two characteristics are more distinct, while fearful and sad have similar characteristics to some extent. On the other hand, in the CK+ data set, the amount of raw data of the first two expressions is abundant, and the amount of fearful data is small. A total of 15 images were in the fearful test set. There are only five different expression images in the original data. This leads to unequal training times. To verify the effect of the established recognition

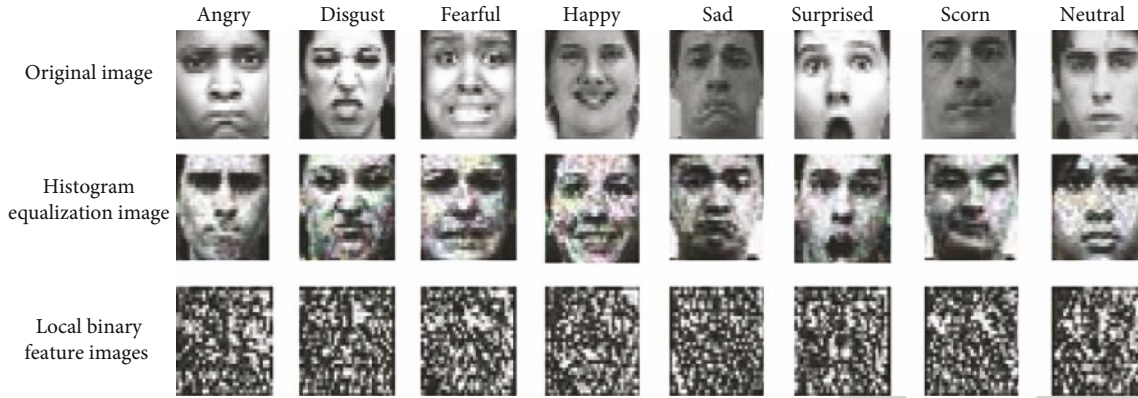


FIGURE 3: Sample images of 8 emoticons.

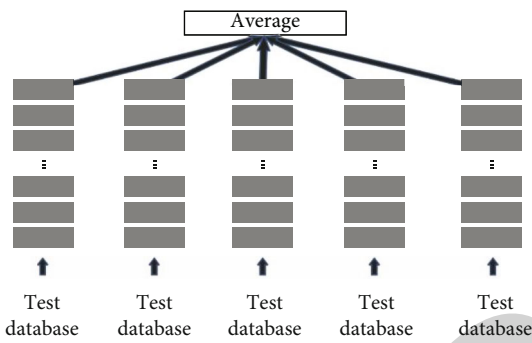


FIGURE 4: Schematic diagram of SoftMax average voting.

TABLE 3: Comparison of recognition accuracy and time.

Model	Original database	Local binary pattern database	Histogram equalization database
Accuracy (%)	89.5	86.9	90.5
Time (s)	1.54	1.27	1.56

TABLE 4: The recognition accuracy of the improved CNN model.

Category accuracy	First experiment	Second experiment	Third experiment	Total
Angry	96.3	88.9	96.3	93.8
Disgust	91.7	91.7	95.8	93.1
Fearful	60	86.7	60	68.9
Happy	100	100	100	100
Sad	86.7	80	86.7	84.5
Surprised	100	100	93.8	97.9
Scorn	83.3	83.3	75	80.5
Neutral	93.3	93.3	93.3	93.3
Total	90.5	91.2	89.8	90.5

model, we input the JAFFE data set as the test set to identify other expressions except for the contempt expression. The average recognition accuracy of the three results is 82.4%.

TABLE 5: Comparison of recognition accuracy and time between the two models.

Model	LeNet-5	Without decision level
Accuracy (%)	74.6	87.9
Time (s)	0.59	0.31

To prove that the proposed method and decision fusion method are pertinent to the expression recognition of low-pixel facial images, we conduct experiments in two cases, respectively [13]. One is to replace the improved CNN model with the classic shallow convolutional neural network LeNetG5. The second is to experiment without using decision fusion. Table 5 shows the average recognition accuracy and comparison of the three experiments in the two cases above.

It can be seen from Table 3 that the improved CNN model has an increase of 15.9% in recognition accuracy compared with the LeNetG5 network. This proves that this method is more suitable for expression recognition of low-pixel face images [14]. The recognition accuracy after decision fusion is 2.6 percentage points higher than that of the network without decision fusion. The main reason is that the experimental effects in the three experiments are unstable, and the recognition accuracy of the two experiments is about 90.0%. The result of one experiment was 83.9%. However, each experiment result of this method is obtained by averaging five trained network models, and its overall stability is relatively high. This proves that this method is effective and feasible in practice.

In recent years, facial expression recognition methods for face images with a size of 32 pixel \times 32 pixel have been proposed one after another. On the CK+ data set, some scholars have proposed a cross-connect LeNetG5 CNN. We perform seven classifications of images that do not include neutral expressions, and the recognition accuracy rate is 83.74%. Some scholars have proposed a shallow CNN to achieve a seven-class recognition accuracy of 97.38%. This is higher than the recognition accuracy of this method.

4. Conclusion

Aiming at the expression recognition of low-pixel face images, the paper proposes an improved CNN expression

Retraction

Retracted: Design and Analysis of Bridge Inspection System Based on Wireless Communication and Internet of Things Technology

Wireless Communications and Mobile Computing

Received 28 November 2023; Accepted 28 November 2023; Published 29 November 2023

Copyright © 2023 Wireless Communications and Mobile Computing. This is an open access article distributed under the Creative Commons Attribution License, which permits unrestricted use, distribution, and reproduction in any medium, provided the original work is properly cited.

This article has been retracted by Hindawi, as publisher, following an investigation undertaken by the publisher [1]. This investigation has uncovered evidence of systematic manipulation of the publication and peer-review process. We cannot, therefore, vouch for the reliability or integrity of this article.

Please note that this notice is intended solely to alert readers that the peer-review process of this article has been compromised.

Wiley and Hindawi regret that the usual quality checks did not identify these issues before publication and have since put additional measures in place to safeguard research integrity.

We wish to credit our Research Integrity and Research Publishing teams and anonymous and named external researchers and research integrity experts for contributing to this investigation.

The corresponding author, as the representative of all authors, has been given the opportunity to register their agreement or disagreement to this retraction. We have kept a record of any response received.

References

- [1] H. Sun, Z. Zhang, and P. Li, "Design and Analysis of Bridge Inspection System Based on Wireless Communication and Internet of Things Technology," *Wireless Communications and Mobile Computing*, vol. 2021, Article ID 3410844, 5 pages, 2021.

Research Article

Design and Analysis of Bridge Inspection System Based on Wireless Communication and Internet of Things Technology

Haidong Sun,¹ Zhengtao Zhang ,¹ and Peng Li²

¹Jiangsu Runyang Bridge Development Co., Ltd, Zhenjiang, Jiangsu 212000, China

²CCCC Highway Consultants Co., Ltd, Beijing 100010, China

Correspondence should be addressed to Zhengtao Zhang; zzhengtao2021@163.com

Received 8 July 2021; Accepted 16 September 2021; Published 13 October 2021

Academic Editor: Balakrishnan Nagaraj

Copyright © 2021 Haidong Sun et al. This is an open access article distributed under the Creative Commons Attribution License, which permits unrestricted use, distribution, and reproduction in any medium, provided the original work is properly cited.

The continuous development of information technology and various electronic devices has accelerated the process of informatization and digitization, enabling the development and application of the emerging technology of wireless communication and the Internet of Things. Since the continuous occurrence of vicious bridge collapse accidents in China in recent years, the problem of bridge inspection has become a hot topic among the people. At the same time, how to apply wireless communication and the Internet of Things technology to bridge inspection systems has also become a new research topic. This article mainly studies the design and analysis of bridge detection systems based on wireless communication and Internet of Things technology. In order to expand the field of bridge detection and standard management and improve the credibility and reliability of safety problem prediction and evaluation, the bridge detection system will integrate IoT sensing, internet, remote communication, digital signal analysis and processing, big data knowledge mining, big data prediction and other technologies, design and analysis of the main structure of roads and bridges, and other multifaceted knowledge fields and build a professional intelligent digital network based on bridge inspection data collection, monitoring, analysis, evaluation, and early warning. From design to use and maintenance of the bridge, a digital neural network spanning time and space throughout the life cycle is constructed to construct a digital brain with bridge sensing points as neurons. This paper uses high-power infrared sensor equipment, satellite positioning systems, sensor equipment, and other technical equipment to achieve the purpose of data communication and exchange and realize intelligent positioning, identification, supervision, tracking, and other functions, making the wireless communication and Internet of Things reliable transmission, comprehensive perception, intelligent processing, and other capabilities very effective in the field of bridge inspection. Through the research and analysis of this article, there are more and more bridge inspection systems developed by the Internet of Things and wireless communication technology in China, and the percentage of related equipment used can reach more than 90%. The functions of the bridge inspection system are becoming more and more complete, and the results of the inspection data are also increasing.

1. Introduction

As an important traffic artery, bridges are valued by all walks of life due to their complex structure, large capital requirements, and long service life, and their safety is directly related to the safety of pedestrians. The real inspection data of bridges and their safety degree are more concerned by people [1, 2]. The use of a manual mode to detect bridges cannot be directly and effectively applied to the maintenance

and inspection of some large-scale bridge projects. Therefore, it is necessary to establish an intelligent system for real-time bridge inspection to detect and evaluate the normal operation of roads and bridges in real time. During the operation period, the bearing capacity of the main structure of the bridge, the operational status, and the endurance of the main structure can be monitored in real time [3, 4]. The widespread use of network communication technology has caused great changes in the way people obtain data,

especially for some units that have high requirements for data mobility and timeliness. Bridge detection based on wireless communication and Internet of Things technology systems has also been widely used [5, 6].

To the research about the design and analysis of bridge detection systems based on the Internet of Things and wireless communication technology, many scholars have discussed it. For example, Zhang and others have proposed that the Internet of Things has strong penetration, large amount of actions, and good overall benefits. It is used in structural engineering inspection to promote the development of wireless communication and Internet of Things technology. It is conducive to the development of intelligent, refined, and networked structures; digital intelligent bridge crack detection methods can improve the efficiency of bridge safety diagnosis and reduce risk factors [7]. Mueller et al. said that bridges are fragile transport infrastructure elements and suggested that special attention should be paid to evacuation plans in the event of flood disasters [8]. According to a report issued by the American Society of Civil Engineers (ASCE), Seo and others pointed out that due to the increasing number of deteriorating bridges, a more efficient and cost-effective bridge inspection alternative is needed [9]. It plays a guiding role in the design and analysis of bridge inspection systems based on wireless communication and Internet of Things technology.

This article analyzes the reasons for the development of the bridge inspection system and the status quo at home and abroad and introduces the basic technology, functions, and software and hardware requirements of its use. Based on the analysis of the basic data requirements of the bridge, this paper studies the types of detection-related data, data collection methods, and coding methods used. At the same time, through the standard requirements of bridge construction, this paper forms a geographic location-based monitoring, tracking, assessment, and evaluation model; the unit of authenticity verification of relevant data and the progress, quality, and safety of the inspection data are in a controllable state, providing data for the decision-making of bridge engineering on the support.

2. Research on Design and Analysis of Bridge Inspection System Based on Wireless Communication and Internet of Things Technology

2.1. Research Status

2.1.1. Current Status of Research in China. In the 1950s, there were no technical conditions to support the evaluation and study of the specific conditions of a bridge. At that time, the basis of judgment was mainly based on personal experience, and the safety of the main bridge was not judged by specific and accurate data [10]. After the national major basic research project “Basic Research on the Safety and Durability of Major Civil Engineering” was put forward, a higher level of requirements was put forward in the monitoring and evaluation of structural installation. Since then, many universities and research institutions have invested

manpower and material resources to study bridge structures and other topics. They have achieved relatively satisfactory results.

2.1.2. Status of Overseas Research. Before World War II, experts had explored the health inspection of bridges, but at that time, there were only limited tests and research; the corresponding standard procedures and systems were not produced. Since the 1950s, a large number of bridge collapse accidents and global bridge structural failure accidents have occurred, making experts aware of the importance of real-time bridge inspections, and various types of bridge inspection systems have also appeared.

2.2. Module Function Design. The modules designed in this system include the data collection management module, data trend analysis module, state prediction management module, state analysis evaluation module, project supervision management module, inspection information release module, and maintenance decision management module.

The data trend analysis module will realize the five functions of data source setting, mining model establishment and training, data browsing, and result viewing. The setting of the data source is a prerequisite for other functions. The establishment of a mining model is the core function of the entire module. The training of the model is an extension of the core function and a prerequisite for viewing the results. Viewing the results makes the effect of the module displayed on the system operator. In front of it, the readability of the module is improved, and it is also easy to understand.

2.3. Module Structure Design. The bridge inspection system uses a relatively more traditional C/S software model architecture, but some B/S models are also used in some daily inspection service levels. Among them, the server side is mainly used as a container for deploying databases or multi-dimensional data sets and performing data analysis, while the client side deploys an application program interface for detecting data. The function of the application is to submit and display data information. When the data is submitted to the data access layer, the data access layer will perform a series of checksum processing on the data. If you need to explore the data in depth, it will first analyze the data, then access the data source and get the corresponding data from the data source, finally return to the application through the data access layer, and present the results to the user. If data mining is not required, but to interact with the source data, the data access layer will directly access the data source and return the obtained results to the application program and display it in front of the user.

3. Research on Design and Analysis of Bridge Inspection System Based on Wireless Communication and Internet of Things Technology

3.1. Collect User Needs. Due to the abnormality of the IoT sensor or the damage in the transmission process, the data

transmitted to the database may appear empty, zero, beyond the normal range, or the value within a certain range is constant. This paper takes the real-time monitoring data of a certain bridge as an example to extract the three main structural state parameters of the bridge, namely, temperature, vertical deflection, and suspender cable force.

3.2. Outline Design

3.2.1. Data Collection Layer. The data acquisition layer is mainly the sensor system and the data acquisition and transmission system. The purpose of the sensor system is to realize the collection and conversion of various information and data in the bridge detection process. In order to achieve this purpose, the sensor system is equipped with special bridges for environmental monitoring, geometric monitoring, load monitoring, and dynamic and static effect monitoring. The function of the data acquisition and transmission system is to collect the signals output by the sensors, regulate the working sequence and frequency of all sensors, and transmit the collected data to the data processing and analysis system through radio transmission. The sensor system uses wireless communication technology to connect with the data acquisition and transmission system.

3.2.2. Business Logic Layer. The business logic layer is the unit of responsibility for data sorting and analysis. Its main job is to classify the original data so that they can better meet the specific needs of users. With the support of sufficient data, the stress conditions of the bridge under various conditions are collected. The needs of users are different, and the central task of the business logic layer will also change accordingly. From this perspective, the business logic layer can be regarded as a collection of multiple data processing subsystems, and the logic followed by its work is the externalized expression of user demands.

4. Related Technology

4.1. Internet of Things Technology

4.1.1. RFID. RFID is composed of electronic tags, readers, and antennas. It has the characteristics of noncontact operation, no manpower, but more remote identification, and convenient application.

4.2. The Data Fusion Technology. In layman's terms, data fusion technology is like sorting equipment in a contemporary industry, responsible for classifying, summarizing, and collecting raw data. Although it originated in the military field, it has already shined in commercial and civilian fields at this stage. In the field of bridge safety monitoring, data fusion technology is mainly applied to the screening and classification of original data and intelligent assembly of related data according to attributes. It allows the user to see the desired result more intuitively.

4.3. Data Mining Technology

4.3.1. The Multidimensional Data Set. The concept of the multidimensional data sets is developed based on tables

TABLE 1: Comparison of some sensing instruments installed in bridge detection systems at home and abroad.

	Home	Overseas
Anemometer	74.83%	71.37%
Thermometer	91.62%	42.86%
Displacement meter	74.91%	71.35%
Vibrating wire strain gauge	33.29%	28.52%
Fiber optic sensor	33.28%	28.57%

and views modeled in common data source views, which are general measures (factual data) and dimensions (which can cover many aspects that we are interested in measuring, such as time, product, and customer) and pass its definition. The data measures and dimensions in the multidimensional data set are derived from the tables and views in the real data source view on which the multidimensional data set is based.

4.3.2. Data Source View. The data source view refers to a logical representation of the basic data source, which contains the model of the logical architecture used by the multidimensional data sets and dimensions as well as the data mining structure. It can be generated from one or more data sources and can also include relationships, calculated columns, and queries that do not exist in the basic data source and data independent of the basic data source. The data source view is transparent to the general client application.

4.4. Related Algorithms

4.4.1. Time Series Algorithm Based on Automatic Regression Decision Tree. In this article, the time series algorithm studied is based on decision numbers, linear regression, and Bayesian algorithm. The main functions implemented are the following: it can effectively relearn from data, it supports correct prediction, and it is easy to explain. The time series data set is transformed into data suitable for regression analysis. The transformed data set is used to obtain the target variable in the form of a decision tree. This decision tree has linear regression on its leaves. Therefore, a segmented linear model is constructed. In the automatic regression model, the structure of the decision number is determined by Bayesian technology. In the analysis process, the "predictor variable" and the "target variable" correspond to the predicted value and current value in the time series, respectively.

4.4.2. Deflection Correlation Graph (DCG). Deflection is the linear displacement of the rod axis in the direction perpendicular to the axis or the linear displacement of the plate and shell midplane in the direction perpendicular to the midplane when a force is applied or a nonuniform temperature changes.

Consider a healthy bridge system H . Making $0 \leq e, f < 1$. For $M, N \in H, M \neq N$, let $(\theta_{M,N,1-e}^V, \hat{\theta}_{M,N,1-e})$ denote the

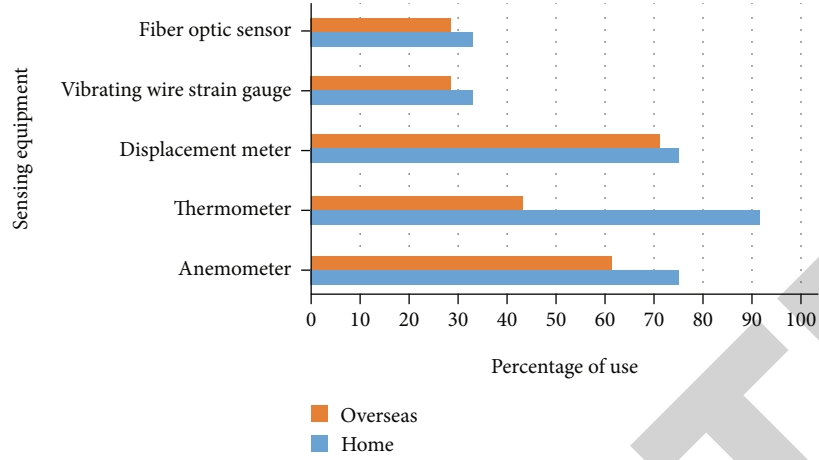


FIGURE 1: Comparison of some sensing instruments installed in bridge detection systems at home and abroad.

TABLE 2: Summary of comparison of raw and recovered data.

	Raw data	Data after recovery
2021/1/11	82	82
2021/1/25	43	84
2021/2/09	83	83
2021/2/23	81	81
2021/3/09	21	82
2021/3/23	83	83

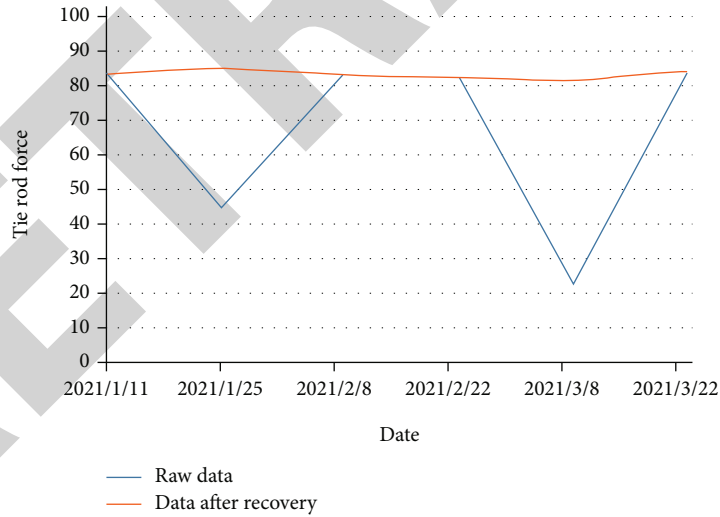


FIGURE 2: Comparison of raw and restored data.

confidence interval of $1 - e$. The $1 - e$ correlation between M and N is a random variable, which is defined as

$$cdg_{1-e}(M, N) = 1 - \frac{1}{2} * \left(\hat{\theta}_{M,N,1-e} - \theta_{M,N,1-e}^V \right). \quad (1)$$

The deflection correlation graph of the system is expressed as $ICG_{1-e,1-f}(H)$, which is a random graph with

interval labels (H, G, label) , as shown in

$$G = \{ \{M, N\} : cdg_{1-e}(M, N) \geq 1 - f \}, \quad (2)$$

$$\text{label}(\{M, N\}) = \left(\theta_{M,N,1-e}^V, \hat{\theta}_{M,N,1-e} \right). \quad (3)$$

Since then, the graph with edge labels obtained according to this definition is called a DCG.

Retraction

Retracted: Innovation and Development of University Education Management Informationization in the Environment of Wireless Communication and Big Data

Wireless Communications and Mobile Computing

Received 28 November 2023; Accepted 28 November 2023; Published 29 November 2023

Copyright © 2023 Wireless Communications and Mobile Computing. This is an open access article distributed under the Creative Commons Attribution License, which permits unrestricted use, distribution, and reproduction in any medium, provided the original work is properly cited.

This article has been retracted by Hindawi, as publisher, following an investigation undertaken by the publisher [1]. This investigation has uncovered evidence of systematic manipulation of the publication and peer-review process. We cannot, therefore, vouch for the reliability or integrity of this article.

Please note that this notice is intended solely to alert readers that the peer-review process of this article has been compromised.

Wiley and Hindawi regret that the usual quality checks did not identify these issues before publication and have since put additional measures in place to safeguard research integrity.

We wish to credit our Research Integrity and Research Publishing teams and anonymous and named external researchers and research integrity experts for contributing to this investigation.

The corresponding author, as the representative of all authors, has been given the opportunity to register their agreement or disagreement to this retraction. We have kept a record of any response received.

References

- [1] W. Li, "Innovation and Development of University Education Management Informationization in the Environment of Wireless Communication and Big Data," *Wireless Communications and Mobile Computing*, vol. 2021, Article ID 8493464, 6 pages, 2021.

Research Article

Innovation and Development of University Education Management Informationization in the Environment of Wireless Communication and Big Data

Weizhe Li 

School of Education, Communication & Society, King's College London, Strand, London, UK

Correspondence should be addressed to Weizhe Li; liweizhe_edu@163.com

Received 4 August 2021; Accepted 14 September 2021; Published 12 October 2021

Academic Editor: Balakrishnan Nagaraj

Copyright © 2021 Weizhe Li. This is an open access article distributed under the Creative Commons Attribution License, which permits unrestricted use, distribution, and reproduction in any medium, provided the original work is properly cited.

The development of information technology has spawned a new type of demand and management analysis model of big data. The value of data is vividly reflected in the contemporary era, and all walks of life have devoted great energy to the construction and use of informatization. The object of college education and management is the group of college students who are most closely connected with contemporary trends. Their thoughts are active, their state is changeable, and they are very sensitive to external stimuli. Such an educational situation has greatly increased the difficulty of educational management in colleges and universities. This article takes the big data research as the breakthrough point, focuses on the promotion and innovation of contemporary college education management informatization, and strives to improve the college education management informatization system by solving existing problems. The innovation of this research is to use big data technology as the starting point for improving the current stage of the education informatization work of colleges and universities, through the combination of data analysis and the latter, to realize the comprehensive informatization innovation of education management. The study used questionnaire surveys to investigate and interview some students and related managers in 5 universities in the province and conducted an objective assessment of the construction of educational management informatization in these universities and found that these five universities have common problems in this field. Research experiments have found that among the five representative universities in the province, the service awareness of education administrators is not above the fifth level. This shows that in the big data environment, the quality of education administrators cannot be ignored.

1. Introduction

The advent of the era of big data has profoundly affected everyone's work and life. Almost all people's behaviors can be captured by information terminals and converted into visual numbers, and then, these numbers can provide a reference for the personalized development of social services. Although it is sometimes used by illegal businesses to cause trouble to the public, its positive effect is undoubtedly dominated by the mainstream, which has been universally recognized by the public [1, 2]. It can be said that various industries and fields are actively exploring the mode of combining big data with their own work to meet the needs of the development of the times. In the context of the era of big data, how to use big data to explore objective laws to strictly

understand and master university education management and university education management innovation is undoubtedly a major topic of current and future research, and scholars in the field of education management must make theoretical and practical responses to big problems [3, 4]. This article takes the big data environment as the background and takes the innovation and informatization development of university education management as the main research goal. It is a natural, contemporary, and creative effort to this.

The research on this major subject in the educational management field includes the following: Zeng used empirical research to track and analyze the teaching practice of the space design subject in a higher vocational college in a certain place, so as to find out how information technology should be better integrated into methods in vocational

education. It turns out that the reasonable application of information technology has a very positive impact on the teaching effect and management effect of the subject [5]. Popkova believes that the modern stage of the development of the education field is characterized by the large-scale implementation of information and telecommunications technology into the activities of all members of the education process. Informatization is one of the main factors to improve the level of education, and the awareness and methods of training have been improved. The role of the teacher has changed—the teacher has changed from the translation of knowledge to the organizer of student activities in order to acquire new knowledge and skills [6]. These studies provide theoretical guidance for the creation of this article.

This article combs the latest research trends in this field domestically and internationally and finds that most experts and scholars have affirmed the positive effects of informatization construction on education management and put forward constructive predictions on the development direction of this field from many aspects [7]. At the same time, many cases also show us the shortcomings in the current stage of education management information construction, such as poor software compatibility, incomplete functions, and inability to guarantee stability, which have largely hindered the use of the advantages of the information system. In response to this phenomenon, this article puts forward targeted development ideas for the common problems embodied in the five vocational colleges [8]. It is hoped that it can effectively promote the development of information construction and make it better meet the requirements of scientific and technological progress for educational modernization.

2. Research on the Innovation and Development of University Education Management Informationization in the Big Data Environment

2.1. The Basic Connotation of Wireless Communication and Big Data. Although the term big data has been repeatedly mentioned in recent years, it has not actually been clearly defined. Many scholars have defined it from various angles according to their own research focus. In general, the more widely used definition starts from the functionality of big data. It is to classify and process the data information collected through various means, so as to extract information that is beneficial to itself. Big data is different from ordinary data. The most obvious difference is its scale and high speed; that is, it can be called big data if it meets certain requirements in terms of scale and collection time [9]. The focus of big data is to use technology and scientific knowledge as well as high-tech technology to find more valuable information about data objects [10]. It can be said that information collection is equivalent to the stage of primitive accumulation, and data analysis and application are the efficient value-added stage. In other words, collecting data is not the focus, but the development and utilization of data is the key. With the help of big data collection and analysis

to better promote the construction of the educational management information system of colleges and universities, not only can it better utilize the advantages of information equipment but also it can help to improve the overall level of college education management [11, 12].

2.2. The Innovation and Development of the Education Management Informationization of Universities in the Era of Big Data

2.2.1. Innovation of Ideas and Thinking. The era of big data is completely changing the status quo of the traditional education model, which cannot completely and truly count the effects of national education. Relying on powerful analysis capabilities, terminal equipment can quickly and accurately sort out the personalized needs of customers and adjust their management strategies in time according to this demand. What is more valuable is that the data obtained through big data analysis greatly avoids the influence of the analyst's subjective emotions on the results and fundamentally changes all the views and thinking on education management.

2.2.2. Innovation of the Education Model. In the past, college education was promoted by teachers to students, and the content and form of teaching were completely determined by the Academic Affairs Office and teachers. But in the era of big data, schools can formulate teaching priorities and teaching methods based on data analysis. At the same time, big data can also capture and analyze the content of online classrooms watched by students and reversely affect teachers' thinking and improvement of teaching. Such a more open and interactive teaching-learning cycle has been used for dozens of times. It is undoubtedly a major innovation for the university education model.

2.2.3. Innovation of the Evaluation Model. With the advent of the era of big data, the evaluation of its education is limited not only to subjective assumptions and personal experience but also to objective evaluation supported by data. Through the click statistics or activity survey of each tutor course, statistical data are provided for students on each learning platform and support is provided for all educational evaluations.

2.2.4. The Development of Informatization of College Education Management in the Era of Big Data. In the era of big data, people gradually realize that the world is composed of information rather than a series of natural or social events. In the process of digitizing the world, information has completed many very difficult tasks. Under such changes, the informatization of education management in colleges and universities must inevitably conform to the requirements of the times and establish a data-based thinking tradition and work model as soon as possible. Every day, the university itself and every teacher, student, and administrator in the university are generating this large amount of new data. In the education management work, these data are getting more and more attention, and they are beginning to be mined and used.

2.3. The Specific Situation of the Application of Big Data Technology to the Education Management of Universities

2.3.1. *Service Object.* Establish an information platform that connects students and teachers extensively, and interconnect the collected information. The information is classified and captured in a scientific manner to provide teachers and students with all-round personalized services.

2.3.2. *Campus Environment.* Accelerate the construction of school wireless networks and the Internet of Things, eliminate information blind spots, and strive to be able to grasp first-hand information changes inside and outside the campus at any time.

2.3.3. *Data Warehouse.* Only when the data reaches a certain volume can it be called big data. This requires a sufficient space for data storage and classification, which requires a data warehouse.

2.3.4. *Cloud Computing.* Cloud computing has greatly accelerated the speed of computing, enabling customers to meet their computing needs as quickly as possible and ensuring data security.

2.4. University Education Management Relies on the Development of Big Data

2.4.1. *Improve the Education Management System.* In addition to integrating the three major functions in the field of university student management, it can also effectively upgrade the student management system. However, in order to improve the quality of teaching and based on the reality of each school, a new system should be established: first, to make teaching institutionalized; second, to institutionalize and standardize the guidance; third, to pay attention to the management of examination procedures and to institutionalize; fourth, to promote employment and to establish the service system; fifth, to find specialized personnel to reasonably supervise; sixth, to innovate the teaching engineering system; seven, to evaluate the standard vocational education; and eight, the result transmission of the teaching results.

2.4.2. *The Campus Network Must Play an Important Role in Promoting Education Management.* The environment is the foundation, and the construction of the education management environment is the construction of the campus network platform. Today's teaching is inseparable from this information platform. Therefore, special attention should be paid to the role of the campus network. The construction of the campus network is not a simple signal coverage, but various information resources are interconnected under the premise of ensuring safety. This means that the university must not only increase investment in supporting software and hardware but also pay enough attention to talent training.

2.4.3. *Sufficient Investment in Teaching.* The performance of the infrastructure has a direct impact on the construction of the campus network. Without sufficient funds as a guarantee, it is difficult for universities to establish an information

management system. Nowadays, there are some ways to improve teaching: first, not only rely on government investment but also establish various investment systems, start with different entities, and find different methods; second, optimize the proportion of capital allocation, increase the efficiency of capital use, and reduce necessary loss; third, first aid relieves teachers' anxiety, is committed to teaching, and fills up the gap in the number of teachers engaged in the frontline; fourth, strengthen the essence of education and reduce the pursuit of utilitarianism.

2.4.4. *Classification Management of "Interest Clusters."* "Interest clusters" are used to manage users with different main hobbies and habits. Although there are big differences between customers, through the collection and analysis of big data, we can find out when they are generally interested in a certain topic or field, so that these customers can be classified into specific groups. It is in a common interest cluster, that is, "interest cluster." Under the guidance of this concept, the study conducted a modeling analysis on the interests and hobbies of the student group, and the main formula is

$$f(i_{p_1})|U\theta_{p_1} = M \times f(i_{p_1})|U\theta_{p_1} + (1 - M) \times f(i_{p_1})|U\theta_{p_1}. \quad (1)$$

2.5. *Improvement of the Incentive Mechanism Based on a Big Data Platform.* Regardless of the economic system, the scientific incentive mechanism plays an important role in the work enthusiasm of the workers. Similarly, in the information age, if universities want to make big data platforms play their intended role, they must also pay attention to the construction and improvement of incentive mechanisms. Colleges and universities should adopt a combination of material incentives and spiritual incentives based on their actual abilities and the needs of their workers to lay the foundation for the application of big data platforms.

Build a contribution value management system. The aspects of student management are very complicated, and this research regards these studies as nodes. Through analysis, find out the ranking of the contribution value of each node in the student management, and use it as one of the main bases for the distribution of performance. Such a distribution system can greatly stimulate the enthusiasm of various nodes, that is, the management departments of universities. In the propagation node link graph, we set P_i as the PageRank value of propagation node i , L_i is the number of propagation nodes pointed to by propagation node i , N is the total number of nodes, and q is the constant damping coefficient. The following calculation model is used as the main basis for determining the contribution value, so as to scientifically determine the precise value of each node.

- (1) Initialize all propagation nodes
- (2) For all propagation nodes, perform the calculation of

TABLE 1: Investigation and analysis on the literacy of educational managers in 5 universities in this province.

	I	II	III	IV	V
Service awareness	4.19	3.71	5.18	3.52	3.17
Professional knowledge	5.41	3.58	3.92	4.32	3.38
Information technology	3.46	4.99	2.61	2.83	4.49
Management ability	5.73	5.42	4.85	5.67	5.38

$$Q_i = \frac{1 + \mu}{N + \mu} \times \sum_{j=1}^n \frac{Q_j}{M_j}, \quad i = 1, 2, 3 \dots; j = 1, 2, 3 \dots, n. \quad (2)$$

- (3) Take the experience value in this experiment $q = 0.837$
- (4) Take the threshold x and iterate the second step until formula (3) holds for all nodes:

$$|\Delta Q_i| < \theta. \quad (3)$$

Among them, ΔQ_i is the difference between the Q_i value of the i -node last iteration and this time. After the iteration is completed, use the min-max normalization method to normalize the PageRank value of the page to obtain the final authority value.

3. Experimental Research on the Innovation and Development of University Education Management Information under the Big Data Environment

3.1. Subjects. In order to have a more comprehensive grasp of the current status of the information construction of education management in colleges and universities, this study selected 5 colleges and universities in the province to investigate and found out the common problems based on the big data analysis model. At last, this study proposed suggestions for improvement and innovation of management combined with the actual situation of the colleges and universities.

3.2. Experimental Method

(1) Field visit

Five selected colleges and universities were visited, and the teachers and students regarding the school's views on the informatization of education management in the school were interviewed.

(2) Questionnaire survey

Questionnaires were sent through the official websites of the 5 universities, and each school issued 341 questionnaires, of which the valid questionnaires returned by each school were 331, 340, 336, 337, and 330, respectively.

(3) Observation and comparison method

Observe and compare the survey results of these 5 schools, study the common problems of education management informatization in the university in the current state, and explore the informatization of education management in the big data environment that adapts to the common university.

4. Experimental Research and Analysis on the Innovation and Development of University Education Management Informatization under the Big Data Environment

4.1. Quality Analysis of Education Management Personnel. Compared with junior and senior high schools, higher education administrators have higher quality requirements, and their mastery of high and new technology must also meet the needs of the era of education informatization. This forces them to maintain a state of learning improvement; otherwise, it will be difficult to meet the ability level of matching college students, and education management is naturally quite inefficient. Table 1 is a survey and analysis table of the literacy of education administrators in 5 representative colleges and universities in the province. The level of mastery is represented by 10 numbers from 1 to 10. The higher the number, the higher the degree. The colleges are numbered in Roman alphabets (serial number).

It can be seen from Figure 1 that among the five representative colleges and universities in the province, education administrators generally have the problem of low quality. Among them, the management ability is relatively high, and the degree level is basically above 5, but there is no problem in terms of service awareness. The situation above level 5 shows that in the big data environment, the quality training of education managers cannot be ignored.

4.2. Statistical Analysis of the Subject Keywords of College Forums. At the level of interest cluster investigation and induction, the focus of this research is mainly on the campus forums of these five universities. First, collect all the data of these five college campus forums in the past six months, and comprehensively sort them according to the activity of students in the forum and the popularity of forum topics. Use this as a basis to make a portrait of each student group. It is found that in the college student forums, users' posts and replies show a certain interest bias. In order to verify the existence of this phenomenon in the whole, this paper conducts data mining on the topic keywords of forums of 5 colleges

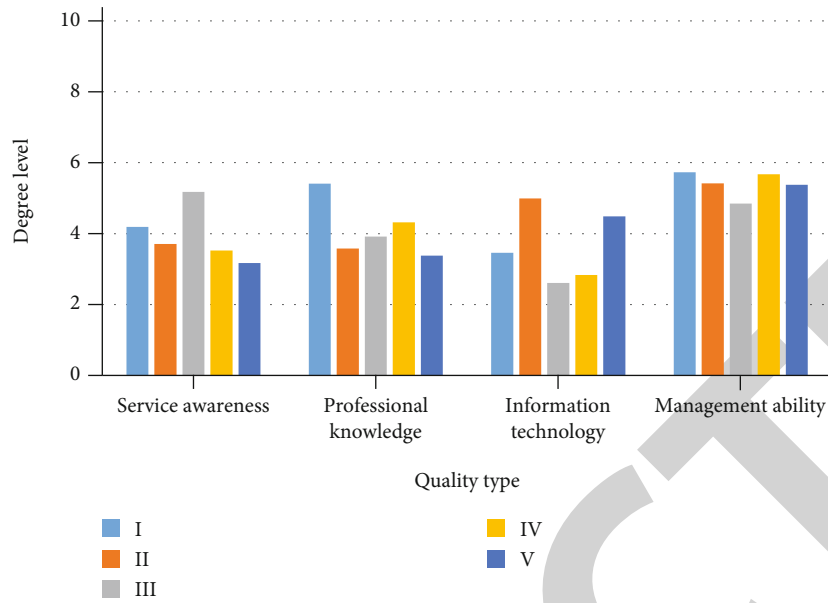


FIGURE 1: Investigation and analysis on the literacy of educational managers in 5 universities in this province.

TABLE 2: Thematic keyword statistics.

	I	II	III	IV	V
Work	1246973	452401	735925	796131	951296
Learning	1102906	590289	546127	1308503	1185598
Entertainment	441799	315653	1036002	845108	940221
Political	797891	1345623	793237	1247522	767028
Life	785725	1168416	1216118	658607	1094892

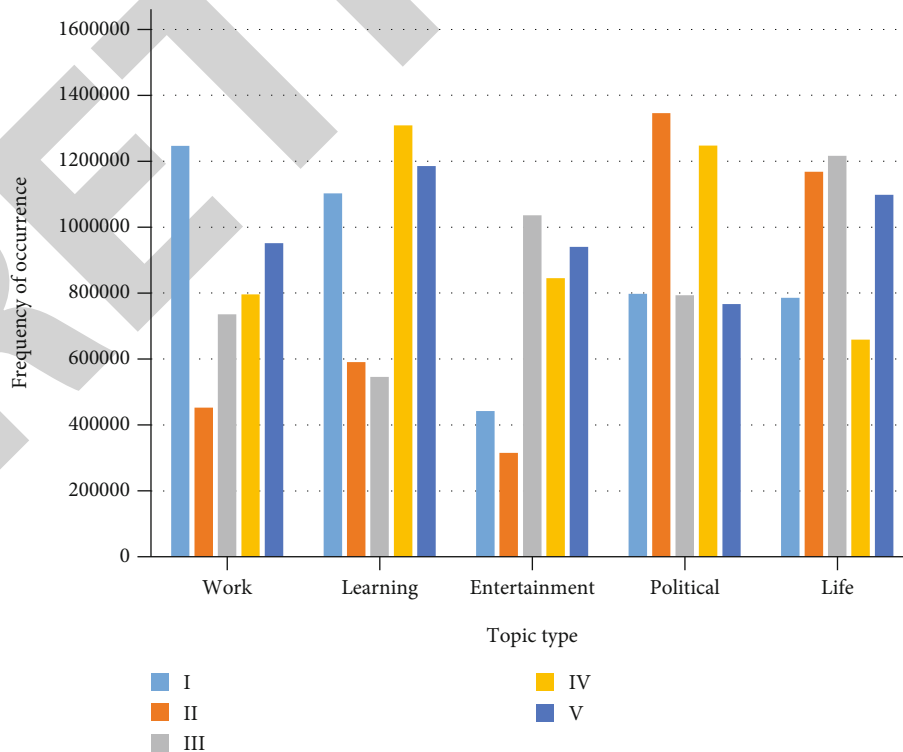


FIGURE 2: Thematic keyword statistics.

Retraction

Retracted: Conceptual Implementation of Artificial Intelligent based E-Mobility Controller in smart city Environment

Wireless Communications and Mobile Computing

Received 1 August 2023; Accepted 1 August 2023; Published 2 August 2023

Copyright © 2023 Wireless Communications and Mobile Computing. This is an open access article distributed under the Creative Commons Attribution License, which permits unrestricted use, distribution, and reproduction in any medium, provided the original work is properly cited.

This article has been retracted by Hindawi following an investigation undertaken by the publisher [1]. This investigation has uncovered evidence of one or more of the following indicators of systematic manipulation of the publication process:

- (1) Discrepancies in scope
- (2) Discrepancies in the description of the research reported
- (3) Discrepancies between the availability of data and the research described
- (4) Inappropriate citations
- (5) Incoherent, meaningless and/or irrelevant content included in the article
- (6) Peer-review manipulation

The presence of these indicators undermines our confidence in the integrity of the article's content and we cannot, therefore, vouch for its reliability. Please note that this notice is intended solely to alert readers that the content of this article is unreliable. We have not investigated whether authors were aware of or involved in the systematic manipulation of the publication process.

Wiley and Hindawi regrets that the usual quality checks did not identify these issues before publication and have since put additional measures in place to safeguard research integrity.

We wish to credit our own Research Integrity and Research Publishing teams and anonymous and named external researchers and research integrity experts for contributing to this investigation.

The corresponding author, as the representative of all authors, has been given the opportunity to register their agreement or disagreement to this retraction. We have kept a record of any response received.

References

- [1] J. Jayakumar, B. Nagaraj, S. Chacko, and P. Ajay, "Conceptual Implementation of Artificial Intelligent based E-Mobility Controller in smart city Environment," *Wireless Communications and Mobile Computing*, vol. 2021, Article ID 5325116, 8 pages, 2021.

Research Article

Conceptual Implementation of Artificial Intelligent based E-Mobility Controller in smart city Environment

Jayaraj Jayakumar ¹, Balakrishnan Nagaraj ², Shanty Chacko,¹ and P. Ajay³

¹Department of Electrical and Electronics Engineering, Karunya University, Coimbatore 641114, India

²Department of Electronics and Communication Engineering, Rathinam Technical Campus, India

³Department of Electronics and Communication Engineering, Anna University, India

Correspondence should be addressed to Jayaraj Jayakumar; emailtojayakumar@gmail.com

Received 6 July 2021; Revised 3 September 2021; Accepted 4 September 2021; Published 7 October 2021

Academic Editor: Danfeng Hong

Copyright © 2021 Jayaraj Jayakumar et al. This is an open access article distributed under the Creative Commons Attribution License, which permits unrestricted use, distribution, and reproduction in any medium, provided the original work is properly cited.

Testing and implementation of integrated and intelligent transport systems (IITS) of an electrical vehicle need many high-performance and high-precision subsystems. The existing systems confine themselves with limited features and have driving range anxiety, charging and discharging time issues, and inter- and intravehicle communication problems. The above issues are the critical barriers to the penetration of EVs with a smart grid. This paper proposes the concepts which consist of connected vehicles that exploit vehicular ad hoc network (VANET) communication, embedded system integrated with sensors which acquire the static and dynamic parameter of the electrical vehicle, and cloud integration and big data analytics tools. Vehicle control information is generated based on machine learning-based control systems. This paper also focuses on improving the overall performance (discharge time and cycle life) of a lithium ion battery, increasing the range of the electric vehicle, enhancing the safety of the battery that acquires the static and dynamic parameter and driving pattern of the electrical vehicle, establishing vehicular ad hoc network (VANET) communication, and handling and analyzing the acquired data with the help of various artificial big data analytics techniques.

1. Introduction

Testing and implementation of integrated and intelligent transport systems (IITS) of an electrical vehicle need many high-performance and high-precision subsystems. The existing systems confine themselves with limited features and have the following shortcomings.

- (i) Driving range and associated driver range anxiety
- (ii) Longer duration for charging
- (iii) Presence or frequent availability of charging stations
- (iv) Heterogeneous communication technologies between vehicle to grid (V2G) and grid to vehicle (G2V)
- (v) Data flow and cloud integration

- (vi) Handling and analysis of big data

The above issues are the critical barriers to the penetration of EVs with a smart grid. This proposed concept consists of an embedded system consisting of sensors which acquire the static and dynamic parameter of the electrical vehicle, cloud integration and big data analytics tools depicted in Figure 1, and connected vehicles that exploit vehicular ad hoc network (VANET) communication which is shown in Figure 2. Vehicle control information is generated based on machine learning-based control systems.

The capacity to organize, advance, and screen the position, steering, and well-being of vehicles is the key when looking to limit long-haul working expenses and increment in range are the important factors to be considered in electrical vehicle industries.

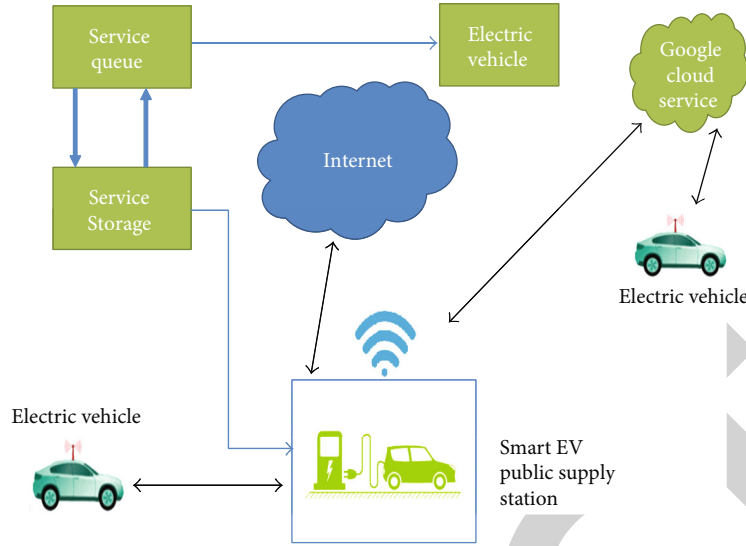


FIGURE 1: Electric vehicle grid integration.

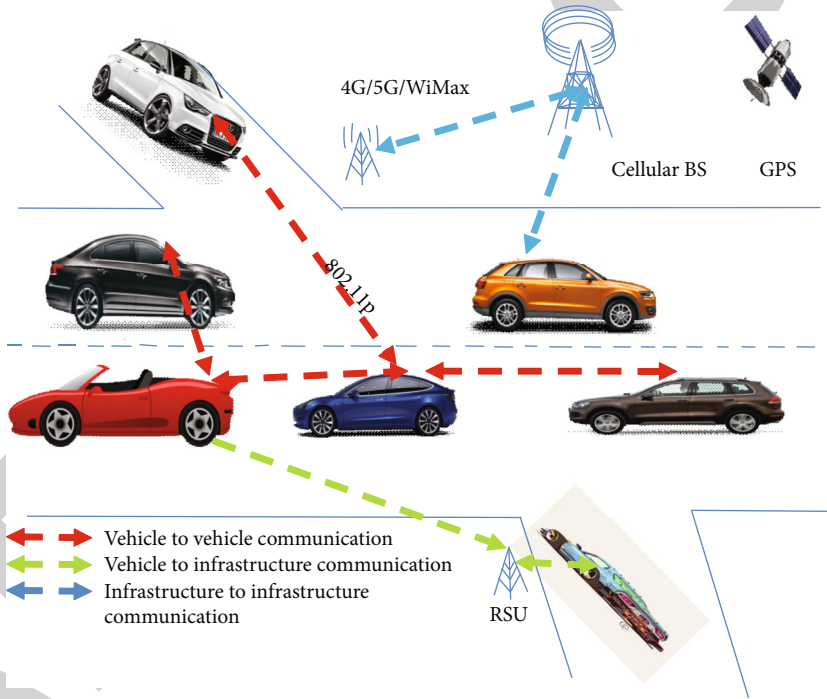


FIGURE 2: Vehicular ad hoc network.

All the electric vehicles consist of battery units, and every unit has separate estimations of cell voltages and temperatures and state of charge. Acquiring such estimations physically would require obtrusive, enormous, and complex circuits.

In this paper, a machine learning-based embedded controller is proposed. This controller screens distinctive driving procedures, energy utilization versus load conditions, the energy required for existing and important routes for future use, and battery reenergized profiles. This paper also describes the design and implementation of a data acquisition system for vehicles, with special emphasis on EVs.

2. Review of Status of Research and Development in the Smart Electrical Vehicle

The paper by Hannan et al. explains a charge equalization algorithm which gives an equal and balanced charge to all lithium ion cells in a battery pack [1, 2]. Here, a voltage method is used to find the state of the charge of a battery. Here, the voltage is compared at every instant and compared with the reference voltage so as to get voltage versus time curve which is a reference point of the state of charge. The paper by Wang et al. discusses an optimal charging method for improvement of charging efficiency of a lithium ion battery [3, 4]. It is

observed that there is no considerable improvement in the charging efficiency of a lithium ion battery.

Lithium ion batteries are not fully safeguarded from the operation problems due to several factors. So, different methods are found out to improve the performance of lithium ion batteries. These methods may be battery management system methods or their chemical constitution and manufacturing process. If we consider high-power rated battery packs, cells must be connected in parallel to improve the current and power rating. But, at that time, there are problems of loose connection and sparking in between which reduce the output and smooth operation. Also, the different cells may not behave in a uniform manner. The paper by Satyavani et al. portrays the displaying and test assessment of equal associated lithium particle cells for an electric vehicle battery framework [5]. The primary outcomes from this examination feature that huge contrasts in the current stream can happen between cells inside an equal stack that will influence how the cells age and the temperature circulation inside the battery assembly [6]. The paper by Zhang et al. clarifies an information-driven-based condition of an energy assessor of lithium particle batteries used to supply electric vehicles [7]. This paper clarifies another strategy utilizing the Kalman channel to gauge the condition of energy of a lithium particle battery. SoE or condition of energy of a lithium particle battery is the limit of a battery as far as kilowatt-hour (kWh) is concerned. The scope of an electric vehicle relies on the condition of energy of a lithium particle battery [7].

The existing intelligent transport system testbed has its own limitation in the area of wireless sensor network (WSN) research [8, 9]. These systems usually give the instructions about the design and implementation of a complex system but failed to integrate the control techniques of ITS. Already existing systems are not economically viable to take up the research for further development [10]. Certain testbeds are available for autonomous vehicles, but the results and findings need more clarity and such test system cannot be used for a wide range of systems [11]. Datta et al. propose a cloud-based service provider for ITS testbeds, but it is restricted with connected vehicles. None of the literature considers the driving range and associated driver range anxiety, longer duration for charging, presence or frequent availability of charging stations, heterogeneous communication technologies between vehicle to grid (V2G) and grid to vehicle (G2V), data flow and cloud integration, and handling and analysis of big data.

In India, lithium ion battery-based electric cars are coming into the scene. The government of India and various state governments are promoting the use of electric vehicles and provide subsidies and tax reductions on electric vehicles. But most of the electric vehicles are using a lead acid battery due to their availability and cheapness. Lithium particle batteries are not being utilized generally because of their significant expense, and furthermore, there are not many lithium particle battery makers in India which produce electric vehicle lithium particle batteries. The paper [12] clarifies the strategies and union of progress of high-rate lithium particle batteries. In this methodology, the essential concern is to improve and redesign the cathode materials. Various strate-

gies and amalgamation such as strong state techniques for LiFePO_4 powders, strong state combination, mechano-synthetic initiation, and so forth and ways to deal with work on the electrochemical execution of LiFePO_4 are being used.

In developing nations like India, the maximum population suffers from unemployment, poor education access, inferior environmental conditions, and mass death following road crashes. Hence, in this context, queries might increase about the challenges entrenched in peoples' mind, their behaviorism and skepticism regarding AVs' safety issues, and finally whether driverless vehicles would create or displace jobs [13–15]. The novelty of this study lies in exploring people's attitude towards AV and their concerns regarding challenges of AV technology in an Indian scenario with a special focus on a forward section of the society. As per Roger Everett's exemplary model, the "dissemination of innovations," among the five classes of innovators, early adopters, early majority, late majority, and laggards, the early adopters embrace the innovation faster [16, 17]. Since the forward segment of the general public with elevated places and administrative abilities has the novel attribute of innovative familiarity or on the grounds that they harbor positive perspectives towards state-of-the-art AV innovation, we guess that the respondents considered in this review will be inside the early adopters [18]. This study through adoption of an online survey objectively intends to analyze the people's mindset, attitudes, and impressions on smart car technologies and strategies. Owing to lack of adequate literature regarding AV technology emergence in India and its acknowledgement, this study would be of its initial kind to probe into the forward section user perception towards AVs in an Indian scenario [19, 20].

3. Importance of the Proposed Method in the Context of the Current Status

In the future, electric vehicles (EVs) are expected to be widely used by all kinds of people and industries. A traditional vehicle like combustion engines produces pollution into the atmosphere and causes toxic gases like SOX, NOX, and COX. When we migrate from the usage of a traditional vehicle to an electrical vehicle, the fuel consumption will be reduced by 70% which will reduce the pollution. Moreover, the operating cost, drivability, and maintenance cost will be reduced further. The usage of an electrical vehicle with IITS not only gives profit to the users but also gives more comfortable and safer journey to the users with lot of information like speed limit, nearest charging station location and charging time details, and battery parameters.

3.1. Current Issues in Our Intelligent Transport System for the Electric Vehicle. The existing electric vehicle system is facing the following problems:

- (i) Decision-making intelligence for the selection of charging stations (CSs)
- (ii) Reliable and efficient information exchanges between EVs, meters, charging stations, and the power grid

- (iii) Vehicle-to-infrastructure and vehicle-to-vehicle communication network design dynamic speed and no standard network topology
- (iv) Difficulty in collecting the vehicle parameters when the number vehicles are more with reduced distance band width limitation with a dense scenario

In order to overcome the above issues, the following suggestion is proposed in this paper. The vehicle parameters can be exchanged between nearby/peer EVs by establishing a secure ad hoc communication between EVs for a necessary action. Establishing an ad hoc communication between vehicles follows the principle of VANETs, i.e., vehicle-to-vehicle (V2V) and vehicle-to-infrastructure (V2I) communication. The location, speed, travelling distance and direction, stability loss, braking, etc. are communicated in the V2V mode with 5.9 GHz frequency and a bandwidth of 75 MHz. V2I represents a one-way hop communication between the Road Side Unit (RSU) and the vehicles. The RSU may proactively suggest fuel consumption, acceleration, velocities, and the intervehicle distance to be maintained based on the traffic conditions [21, 22]. Information to drivers may be broadcasted through the wireless connections directly. The maximum distance (limit/range) of the vehicles is set as 60 km. Usually, it is 1000 meters in simulations.

4. Proposed Methodology

Execution variety, low cycle life, and temperature affectability of a lithium particle battery stockpiling framework for electric vehicles are subject to changing driving examples. The determination of an energy stockpiling framework is vital on account of electric vehicles. It ought to have great energy thickness and extensive force thickness, and furthermore, it should be lightweight. The low-energy-thickness batteries will expand the weight needed to give the necessary energy and capacity to the vehicle. So, it will add to the complete load of the framework. This will cause the depletion of the battery without any problem. So, a lightweight battery or a battery with impressively high energy thickness should be utilized in electric vehicles. Lithium particle batteries are preferred a lot as electric vehicle batteries. They have high energy thickness, high life cycle, and smooth activity. However, there are issues related to lithium batteries; for example, they have high-temperature affectability, and their activity will be influenced by overcurrent charging and overcurrent releasing past their greatest evaluated values. It might detonate or consume on the off chance that they are fumbled.

So, for the battery, the executives and control framework are extremely fundamental in electric vehicle energy stockpiling battery packs. In these batteries, the board and control framework will control the charging current release and voltage at charging and will remove the activity if boundaries change from the permitted values. Additionally, the battery boundaries including working temperatures should be observed and controlled with the goal that the battery life or cycle life will be improved. This paper is a survey about the need of a plan of a novel battery and the board and con-

trol framework for lithium particle batteries for execution improvement in electric vehicles.

The outline is explained in Figure 3. The lithium ion battery is charged by a plug-in source. The charging and discharging according to load, driving patterns, operating temperature, state of charge, state of health, state of safety, current, etc. are monitored, and optimal operation is ensured by the intelligent controller which is represented in Figure 4. The intelligent controller consists of new algorithms which control and optimize the energy storage system for electric vehicles. The supercapacitor will support the battery while starting from rest or after braking, and the solar cell will ensure charging of the battery if the battery state of charge is less than 30%. Thus, the overall performance of the lithium ion battery and in effect the mileage of the electric vehicle are improved. Usually, electric vehicles are using a lead acid battery in India. But we are using a lithium ion battery to ensure a lightweight battery and also reduce the weight of the entire electric vehicle system.

The below objective is very useful in electric vehicles and public transport such as bus, taxi, and auto rickshaw. Based on the above objectives, an intelligent control system will be developed. This intelligent control system will utilize solar energy to charge the battery and the supercapacitor. The supercapacitor will support the vehicle while starting and climbing. The intelligent controller will take decision to power the motor from the solar cell or supercapacitor or from the battery. This decision is based on battery parameters like state of charge (SoC), battery temperature, current, and voltage stability.

The main necessity of this intelligent controller is that it will improve the performance of the battery by reducing the strain caused by different driving conditions, and so it will improve the battery cycle life. So, the operation cost of the electric vehicle will be reduced as the battery replacement frequency will be less. Because of the optimal design of the battery capacity for a particular power, the overall weight of the system can also be reduced.

4.1. Uniqueness of the Embedded Controller. The controllers available in the market are operated under an open loop. No battery parameters are considered for controller design. These kinds of controllers simply act as a switch between on and off. Because of such kind of controllers, the battery life and range of the battery vehicle are reduced. This intelligent controller is overcoming these issues, resulting in reduced processing time while taking decision. Real-time data sampling, acquiring, filtering, and processing are a real challenge. The running time and algorithm complexity are given below which are mentioned in the main manuscript as per the suggestions given by the reviewer.

- (i) Decisions cannot be taken instantaneously
- (ii) Less stable
- (iii) Frequency of changeover in switching is more
- (iv) Need a very detailed program to set the control parameters

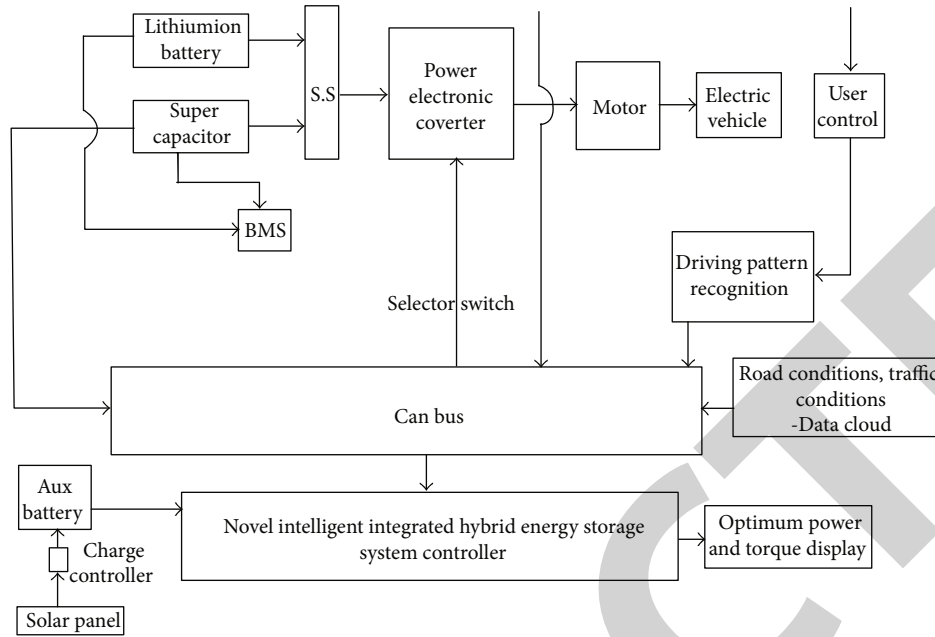


FIGURE 3: Functional block diagram of an intelligent embedded controller.

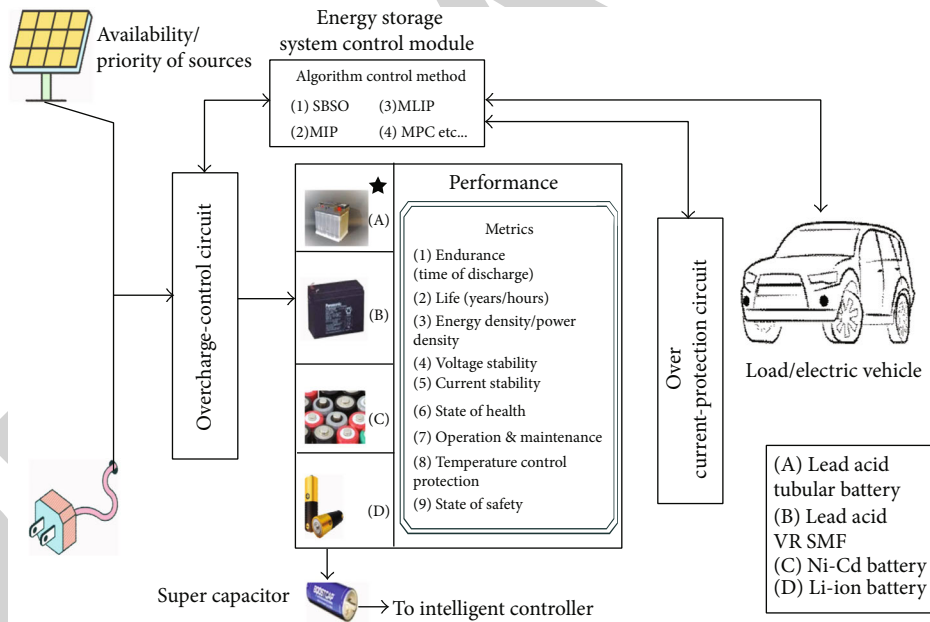


FIGURE 4: Intelligent controller-based hybrid electrical vehicle block diagram.

- (v) Predicted results may not be available always
- (vi) Error in any part affects the whole functioning of the system
- (vii) Misfiring of the system may occur due to any error in its interfacing program
- (viii) Switching between the sources causes a time lag

The above complexity has been addressed in the proposed methods. Due to the addition of all these constraints, the run time of the algorithm is increased.

The proposed embedded controller will enhance the following:

- (i) It will improve the overall performance of the lithium ion battery
- (ii) It will increase the discharge time and cycle life of the lithium ion battery
- (iii) It optimizes the battery current according to battery parameters and driving patterns
- (iv) It increases the range of the electric vehicle

TABLE 1: Specifications of the sensors used in the proposed method.

S. no.	Sensor	Features/specifications
1	MSC360 rotary position sensor	Simple & robust magnetic compact design, endless rotation, up to 360° of electrical angle, magnetic shielding, programmable linear transfer characteristics, self-diagnostic features, overvoltage protection, and reverse voltage protection Analog and PWM output
2	Steering sensors	Cast iron material, 20-22 mm diameter, hydraulic type (i) Digital angular rate sensor with the SPI interface (ii) Angular rate measurement around the z -axis (yaw) (iii) $\pm 300^\circ/\text{sec}$ input range (iv) Ultralow noise (v) Excellent bias instability (vi) 24-bit angular rate output
3	GPS-MEMS Gyroscope—GYPRO3300	(vii) Embedded temperature sensor for on-chip or external temperature compensation (viii) Built-in self-test (ix) 5 V single supply voltage (x) Low operating current consumption: 25 mA (xi) CLCC 30 package: 19.6 mm \times 11.5 mm \times 2.9 mm (xii) Weight: 2 grams
4	Low- g accelerometer LIS2DW12TR	3-axis MEMS accelerometer, ultralow power, configurable single/double-tap recognition, free fall, wakeup, portrait/landscape, 6D/4D orientation detections
5	Personal cloud-WD My Cloud Home WDBVXC0040HWT-BESN 4TB network attached storage	14 \times 5.3 \times 17.55 cm; 1.05 kilograms, 17.6 * 5.3 centimeters, model WDBVXC0040HWT-BESN, components-personal cloud storage, Ethernet cable, AC adapter and quick install guide
6	Synology DiskStation DS1621+ network attached storage drive	174% performance boost with over 110,000 4 K random read IOPS2, built-in M.2 2280 NVMe SSD slots permit cache acceleration without occupying storage drive bays, flexibly scale up to 16 drives to increase storage capacity as demand grows, back up critical data and reduce your recovery time objective (RTO) with snapshot replication, build an on premises multiuser collaboration environment with fine-grained control, 28.2 \times 24.3 \times 16.6 cm, 4.29 kg
7	MAX17843 Data acquisition interface	12-channel, high-voltage smart sensor data acquisition interface
8	IoT gateway	UTX-3117N4200 series fanless IoT gateway, supports 2 \times COM port, 1 \times HDMI, 1 \times display port, 2 \times USB3.0, TPM, and DCIN 12~24 V Built-in 1 \times M.2 expansion slot (i.e., Wi-Fi module), 1 x half size mini-PCIe expansion slot (i.e., Zigbee, module, or mSATA), and 1 \times full – size mini – PCI expansion slot (i.e., 3G/LTE module) with 5 antennas Supports 1 \times 2.5" HDD or SSD storage Wide operating temperature -20~60°C support (with E3900 series SoC) IoT SW integration: WISE-PaaS IoT software platform, AWS Greengrass, Microsoft IoT edge
9	Battery monitoring sensors	The lithium ion battery banks of an EV are monitored using a MAX17843 programmable smart data acquisition interface. Cell diagnosis, balancing, and voltage level measurements along with safe levels are addressed using this interface
10	Vehicle navigation	GPS is primarily used for tracking. To combat with the existing drawbacks of GPS such as lack of local knowledge and driving path distractions, GPS-MEMS-based gyroscopes and low- g accelerometers are used for tracking the position/path
11	Power steering sensors	The directing point sensor (SAS) figures out where the driver needs to control, coordinating with the controlling wheel with the vehicle's wheels. It is customized to decide the guiding point speed

- (v) It enhances the safety of the battery
- (vi) It acquires the static and dynamic parameter of the electrical vehicle

4.2. Steps Involved in Implementing the Concept

- (1) The static and dynamic parameters are sensed and processed. Specifications of the sensors used in the proposed method are shown in Table 1
- (2) The data can be exchanged between nearby/peer EVs by establishing a secure ad hoc communication between EVs for a necessary action. Establishing an ad hoc communication between vehicles follows the principle of VANETs, i.e., vehicle-to-vehicle (V2V) and vehicle-to-infrastructure (V2I) communication. The location, speed, travelling distance and direction, stability loss, braking, etc. are communicated in the V2V mode with 5.9GHz frequency and a bandwidth of 75 MHz. V2I represents a one-way hop communication between the Road Side Unit (RSU) and the vehicles. The RSU may proactively suggest fuel consumption, acceleration, velocities, and the intervehicle distance to be maintained based on the traffic conditions. Information to drivers may be broadcasted through the wireless connections directly
- (3) The heterogenous data can be moved to the cloud for central processing/storage exploiting the IoT gateway

5. Conclusion

A new concept of monitoring and control of the intelligent transport system has been proposed with the help of the wireless sensor network and artificial intelligence in this paper. Various modules and hardware requirement with technical specifications have also been mentioned. Guidelines to analyze the static and dynamic parameters of the electric vehicle using big data analytics are briefed in this paper. Based on the power and energy density of the battery of the electric vehicle, current and voltage stability, and state of health of the battery, a decision-making algorithm is developed and then it is integrated with AI techniques, and finally, it is implemented using an embedded controller to take intelligent decision to control and monitor the electric vehicle. Based on the proposed method, the discharge time is improved by 20 minutes and the cycle life of the lithium ion battery is increased by 200 cycles. Also, the range of the electric vehicle is increased to 2.3 km, and battery replacement cost is only 4/5 of the total cost.

Data Availability

Two sets of data will be considered to train the mode with the help of an advanced algorithm. These data have been generated during the study: (1) the discharge time extension in percentage for different conditions of driving patterns and (2) the discharge time extension in percentage for different

states of charge of the battery. The data sheet is attached in the portal as a supplementary file (available here).

Conflicts of Interest

The authors declare that there are no conflicts of interest regarding the publication of this paper

Supplementary Materials

The data are generated during the study to train the AI model with the help of an advanced algorithm: (i) the discharge time extension in percentage for different conditions of driving patterns. (*Supplementary Materials*)

References

- [1] D. Kandris, C. Nakas, D. Vomvas, and G. Koulouras, "Applications of wireless sensor networks: an up-to-date survey," *Applied system innovation*, vol. 3, no. 1, p. 14, 2020.
- [2] M. A. Hannan, M. M. Hoque, S. E. Peng, and M. N. Uddin, "Lithium-ion battery charge equalization algorithm for electric vehicle applications," *IEEE Transactions on Industry Applications*, vol. 53, no. 3, pp. 2541–2549, 2017.
- [3] K. Uddin, T. Jackson, W. D. Widanage, G. Chouchelamane, P. A. Jennings, and J. Marco, "On the possibility of extending the lifetime of lithium-ion batteries through optimal V2G facilitated by an integrated vehicle and smart-grid system," *Energy*, vol. 133, pp. 710–722, 2017.
- [4] Z. Wang, Y. Wang, L. Zhi, S. Qiang, and R. Yinan, "The optimal charging method research for lithium-ion batteries used in electric vehicles," *Energy Procedia*, vol. 104, pp. 74–79, 2016.
- [5] T. V. S. L. Satyavani, A. Srinivas Kumar, and P. S. V. Subba Rao, "Methods of synthesis and performance improvement of lithium iron phosphate for high rate Li-ion batteries: a review," *Engineering Science and Technology, an International Journal*, vol. 19, no. 1, pp. 178–188, 2016.
- [6] T. Bruen and J. Marco, "Modelling and experimental evaluation of parallel connected lithium ion cells for an electric vehicle battery system," *Journal of Power Sources*, vol. 310, pp. 91–101, 2016.
- [7] Y. Zhang, H. W. He, and R. Xiong, "A data-driven based state of energy estimator of lithium-ion batteries used to supply electric vehicles," *Energy Procedia*, vol. 75, pp. 1944–1949, 2015.
- [8] R. N. Murty, G. Mainland, I. Rose, A. R. Chowdhury, A. Gosain, and J. Bers, "CitySense: an urban-scale wireless sensor network and testbed," in *2008 IEEE Conference on Technologies for Homeland Security*, pp. 583–588, Waltham, 2008.
- [9] L. Sanchez, L. Muñoz, J. A. Galache et al., "SmartSantander: IoT experimentation over a smart city testbed," *Computer Networks*, vol. 61, pp. 217–238, 2014.
- [10] N. Hyldmar, Y. He, and A. Prorok, "A fleet of miniature cars for experiments in cooperative driving," 2019, <http://arxiv.org/abs/1902.06133>.
- [11] A. Morrisett and S. Abdelwahed, "A physical testbed for smart city research," in *2018 IEEE/ACS 15th International Conference on Computer Systems and Applications (AICCSA)*, pp. 1–2, Aqaba, Jordan, 2018.
- [12] S. K. Datta, M. I. Khan, L. Codeca, B. Denis, J. Harri, and C. Bonnet, "IoT and microservices based testbed for connected

Retraction

Retracted: FastQR: Fast Pose Estimation of Objects Based on Multiple QR Codes and Monocular Vision in Mobile Embedded Devices

Wireless Communications and Mobile Computing

Received 28 November 2023; Accepted 28 November 2023; Published 29 November 2023

Copyright © 2023 Wireless Communications and Mobile Computing. This is an open access article distributed under the Creative Commons Attribution License, which permits unrestricted use, distribution, and reproduction in any medium, provided the original work is properly cited.

This article has been retracted by Hindawi, as publisher, following an investigation undertaken by the publisher [1]. This investigation has uncovered evidence of systematic manipulation of the publication and peer-review process. We cannot, therefore, vouch for the reliability or integrity of this article.

Please note that this notice is intended solely to alert readers that the peer-review process of this article has been compromised.

Wiley and Hindawi regret that the usual quality checks did not identify these issues before publication and have since put additional measures in place to safeguard research integrity.

We wish to credit our Research Integrity and Research Publishing teams and anonymous and named external researchers and research integrity experts for contributing to this investigation.

The corresponding author, as the representative of all authors, has been given the opportunity to register their agreement or disagreement to this retraction. We have kept a record of any response received.

References

- [1] Y. Yan, Y. Liang, Z. Zhou, B. Jiang, and J. Xiao, "FastQR: Fast Pose Estimation of Objects Based on Multiple QR Codes and Monocular Vision in Mobile Embedded Devices," *Wireless Communications and Mobile Computing*, vol. 2021, Article ID 9481190, 9 pages, 2021.

Research Article

FastQR: Fast Pose Estimation of Objects Based on Multiple QR Codes and Monocular Vision in Mobile Embedded Devices

Yuheng Yan, Yiqiu Liang, Zihan Zhou, Bin Jiang, and Jian Xiao 

Nanjing University of Posts and Telecommunications, Nanjing, China

Correspondence should be addressed to Jian Xiao; xiaoj@njupt.edu.cn

Received 8 July 2021; Accepted 9 September 2021; Published 30 September 2021

Academic Editor: Balakrishnan Nagaraj

Copyright © 2021 Yuheng Yan et al. This is an open access article distributed under the Creative Commons Attribution License, which permits unrestricted use, distribution, and reproduction in any medium, provided the original work is properly cited.

In recent years, the pose estimation of objects has become a research hotspot. This technique can effectively estimate the pose changes of objects in space and is widely used in many mobile devices, such as AR/VR. At present, mainstream technologies can achieve high-precision pose estimation, but the problem of that of multiple irregular objects in mobile and embedded devices under limited resource conditions is still challenging. In this paper, we propose a FastQR algorithm that can estimate the pose of multiple irregular objects on Renesas by utilizing homography method to solve the transformation matrix of a single QR code and then establish the spatial constraint relationship between multiple QR codes to estimate the posture of irregular objects. Our algorithm obtained a competitive result in simulation and verification on the RZ/A2M development board of Renesas. Moreover, the verification results show that our method can estimate the spatial pose of the multiobject accurately and robustly in distributed embedded devices. The average frame rate calculated on the RZ/A2M can reach 28 fps, which is at least 37 times faster than that of other pose estimation methods.

1. Introduction

With the development of AR/VR and control technology, object pose estimation is needed in manifold scenes. A large number of low-cost small embedded platforms also need to carry out object spatial pose estimation, such as in the exhibition, education, and other fields [1, 2]. At present, most of the estimation of object pose depends on the binocular camera [3] or RGB-D camera [4]. This type of camera is large and requires a computing platform with a certain amount of computing power, which is not conducive to the installation on small devices. There are also inertial sensors on objects to complete pose detection [5] or the comprehensive use of IMU, binocular camera, and RGB-D camera [6], but this method has certain difficulties in data fusion and filtering. Moreover, using convolution neural network to estimate the position and pose of objects [7] has also become a research focus, which brings accuracy, but requires high computational power of the platform, and even needs to be accelerated by GPU.

In many scenarios, like AR, it is necessary to realize the fast pose estimation of objects on small portable devices, so the pose estimation of objects needs a convenient, fast, and low-cost solution. With the development and popularization of QR code technology [8] in recent years, QR code has been widely used in various aspects, such as QR code payment and QR code business cards. Most of these applications use the function of QR codes carrying text information, but at the same time, QR codes can also provide accurate pose information. At present, in the existing research, it has been possible to use QR codes as visual markers, utilizing the position, number, and other information stored in the QR code to complete the navigation [9, 10] or using the calculated position and attitude information to estimate the position and pose of the camera [11].

This paper proposes a FastQR algorithm that can estimate the pose of multiple irregular objects on Renesas by utilizing QR codes and a monocular camera and then estimate the posture of irregular objects. This method only requires low resolution camera, which reduces the amount

of computation with the characteristics of low cost, high accuracy, good robustness, low computing power requirements, fast speed, and so on, and making the multiobject pose estimation has a wider range of application scenarios. The results also verify the reliability of our method. At the same time, the highest frame rate calculated on the Renesas RZ/A2M development board can reach 45 fps, and the average frame rate can reach 28 fps.

The contributions of this paper are as follows:

- (1) It is proposed to use QR codes to realize a high frame rate and high accuracy pose estimation on equipment with limited resources
- (2) It is possible to estimate the pose of multiple objects simultaneously under the premise of ensuring the frame rate and accuracy
- (3) The proposed algorithm is tested on the simulation platform and the real object, and the result is competitive

2. The Principle of Position and Pose Estimation of Objects

2.1. Identification of QR Codes. The recognition and decoding algorithm of the QR code used in our system is AprilTag [12]. To further improve the recognition speed, the Dynamically Reconfigurable Processor (DRP) [13] on RZ/A2M is used to further accelerate the image processing steps, including adaptive binarization, Gaussian blur, and edge detection in the process of QR code recognition.

2.2. Solution of Position and Pose of QR Codes. Using the AprilTag recognition algorithm, the coordinates of the QR code in the image coordinate system can be found out.

Meanwhile, the transformation matrix $H = \begin{bmatrix} h_{00} & h_{01} & h_{02} \\ h_{10} & h_{11} & h_{12} \\ h_{20} & h_{21} & h_{22} \end{bmatrix}$ [14] from space coordinates of the QR code to plane coordinates can be obtained.

The projection matrix of the camera can be expressed as $P = K[R | T]$, which means point X in the space can be transformed into a pixel on the image through the matrix. The

rotation matrix is $R = \begin{bmatrix} r_{00} & r_{01} & r_{02} \\ r_{10} & r_{11} & r_{12} \\ r_{20} & r_{21} & r_{22} \end{bmatrix}$. The translational

vector is $T = \begin{bmatrix} t_x \\ t_y \\ t_z \end{bmatrix}$. The camera internal parameter matrix

is $K = \begin{bmatrix} f_x & 0 & c_x \\ 0 & f_y & c_y \\ 0 & 0 & 1 \end{bmatrix}$.

P is the projection matrix. In camera internal parameter matrix K , f_x and f_y represent the focal length of the camera in the x and y directions. c_x and c_y represent the position of

the intersection of the camera's principal axis on the image plane. At the same time, it is set that the plane where the QR code is located is on plane $X - Y$ ($Z = 0$), of which the center is the origin of the coordinate. Hence, the following is concluded as:

$$x = K[R | T] \begin{bmatrix} X \\ Y \\ 0 \\ 1 \end{bmatrix}. \quad (1)$$

To simplify the calculation, removing the third column of R in formula (1) can have

$$x = K[r_0 \quad r_1 \quad T] \begin{bmatrix} X \\ Y \\ 1 \end{bmatrix}. \quad (2)$$

r_0 and r_1 in formula (2) is the first and second columns of R . The homography matrix H from the point on the space plane to the point on the image is constructed.

Suppose

$$\begin{bmatrix} X \\ Y \\ 1 \end{bmatrix} = \begin{bmatrix} \lambda & 0 & 0 \\ 0 & \lambda & 0 \\ 0 & 0 & \lambda \end{bmatrix} \begin{bmatrix} X' \\ Y' \\ 1 \end{bmatrix}, \quad (3)$$

where λ represents the scaling ratio, of which $[X' \quad Y' \quad 1]^T$ is the corner of the zoom unit QR code; the following can be concluded:

$$x = K[r_0 \quad r_1 \quad T] \begin{bmatrix} \lambda & 0 & 0 \\ 0 & \lambda & 0 \\ 0 & 0 & 1 \end{bmatrix} \begin{bmatrix} X \\ Y \\ 1 \end{bmatrix}. \quad (4)$$

It is known that the internal parameter matrix of the camera is K and the single transformation matrix is H . Let $K[\lambda r_0 \quad \lambda r_1 \quad T] = K[r_0' \quad r_1' \quad T]$, the equation can be concluded as the following:

$$\begin{aligned} f_x r_{00}' + c_x r_{20}' &= h_{00}, \\ f_x r_{01}' + c_x r_{21}' &= h_{01}, \\ f_x t_x + c_x t_z &= h_{02}, \\ f_y r_{10}' + c_y r_{20}' &= h_{10}, \\ f_y r_{11}' + c_y r_{21}' &= h_{11}, \\ f_y t_y + c_y t_z &= h_{12}, \\ r_{20}' &= h_{20}, \\ r_{21}' &= h_{21}, \\ t_z &= h_{22}. \end{aligned} \quad (5)$$

$[r'_0 \ r'_1 \ T]$ can be got, and then, the unit is dealt with the following steps:

$$r_0'' = \frac{r'_0}{\sqrt{\|r'_0\| \|r'_1\|}}, r_1'' = \frac{r'_1}{\sqrt{\|r'_0\| \|r'_1\|}}, T'' = \frac{T}{\sqrt{\|r'_0\| \|r'_1\|}}. \quad (6)$$

It is shown that r_0'' and r_1'' after the dealt are the same as r_0 and r_1 , while T and T' are different from each other. For the same QR code on the camera image, T represents the translational vector of the actual size of the QR code in the direction of R , and T' represents the translational vector of the QR code whose actual size is a square in the same direction. Because of the proportional scaling of the same QR code square in the direction, the translational vector from the camera to the actual QR code can be calculated by the size of the actual one. If the width of the QR code is ω , the translational vector from the camera to the actual QR code is $T = \omega T'$. The translational vector T is also the coordinator of the QR code center in the camera coordinate system.

2.3. Position and Pose Transformation from Multiple QR Codes Coordinate System to Object Coordinate System. By pasting multiple QR codes on an object, the omnidirectional pose estimation of the object can be realized, and the QR code can be avoided being blocked from vision. Meanwhile, according to the position relation of multiple QR codes on the same object, the overall pose information of a single QR code can be obtained from one of a single QR code. The rotation matrix R and translational vector T mentioned in Section 2.2 are the rotation and shift transformation of the QR code coordinate system. In order to map the pose of the QR code to the pose of the object, it is necessary to convert the QR code into the object coordinate base vector group.

As for the pose of the object, it is assumed that the six faces of a hexahedral are affixed with QR codes, respectively, and the center of the QR code coincides with the center of each surface, as shown in Figure 1 below. Suppose the basis vectors of the object coordinate system X , Y , and Z are \vec{e}_x , \vec{e}_y , \vec{e}_z and only consider the change of the direction of the base vector of the coordinate system.

When the coordinate system of the QR code is consistent with the direction of axis X , Y , and Z of the object coordinate system, as shown in the front of the stereo in Figure 1, suppose the base vectors of the three axes under the object coordinate system are \vec{e}_{x0} , \vec{e}_{y0} , \vec{e}_{z0} , the rotation matrix can directly represent the pose of the object, that is

$$\begin{bmatrix} \vec{e}_{x0} \\ \vec{e}_{y0} \\ \vec{e}_{z0} \end{bmatrix} = \begin{bmatrix} 1 & 0 & 0 \\ 0 & 1 & 0 \\ 0 & 0 & 1 \end{bmatrix} \begin{bmatrix} \vec{e}_x \\ \vec{e}_y \\ \vec{e}_z \end{bmatrix}. \quad (7)$$

When the coordinate system of QR code is inconsistent with the direction of axis X , Y , and Z of the object coordi-

nate system, as shown on the right of the stereo in Figure 1, suppose the base vectors of the three axes under the object coordinate system are the direction of the Y -axis of the QR code coordinate system is consistent with the direction of the Y -axis of the object coordinate system; the direction of the X -axis of the QR code coordinate system is opposite to the one of the Z -axis of the object coordinate system, and the direction of the Z -axis of the QR code coordinate system is consistent with the direction of the X -axis of the object coordinate system, that is

$$\begin{bmatrix} \vec{e}_{x1} \\ \vec{e}_{y1} \\ \vec{e}_{z1} \end{bmatrix} = \begin{bmatrix} 0 & 0 & 1 \\ 0 & 1 & 0 \\ -1 & 0 & 0 \end{bmatrix} \begin{bmatrix} \vec{e}_x \\ \vec{e}_y \\ \vec{e}_z \end{bmatrix}. \quad (8)$$

Similarly, when the other surfaces of the QR code are recognized, the pose of the object can be obtained from any angle according to the relationship between the known QR code coordinate system and the object coordinate system.

As for the position of the object, suppose the coordinate of a vector in the QR code coordinate system is $(x_0, y_0, z_0)^T$, and the coordinate in the camera coordinate system is $(x'_0, y'_0, z'_0)^T$, the convert relationship can be obtained as follows:

$$\begin{bmatrix} x'_0 \\ y'_0 \\ z'_0 \end{bmatrix} = R \begin{bmatrix} x_0 \\ y_0 \\ z_0 \end{bmatrix} + T. \quad (9)$$

The convert relationship can be obtained as follows if $(x'_0, y'_0, z'_0)^T$ is transformed into $(x_0, y_0, z_0)^T$:

$$\begin{bmatrix} x_0 \\ y_0 \\ z_0 \end{bmatrix} = R^{-1} \left(\begin{bmatrix} x'_0 \\ y'_0 \\ z'_0 \end{bmatrix} - T \right). \quad (10)$$

The coordinate of the object center in the camera coordinate system can be obtained by formula (9). For example, in Figure 1, the coordinate of the object center in the QR code coordinate system can be regarded as $(0, 0, -\omega/2)^T$, of which ω stands for the edge length of the pasted QR code. The coordinate of the object center in the camera coordinate system can be acquired by the transformation of formula (11). The transformation from any point in the QR code coordinate system to the camera coordinate system can also be obtained by the transformation of formula (9), so the transformation from the base

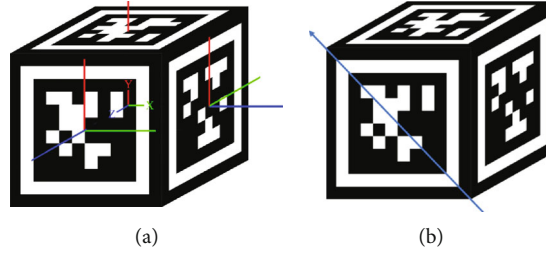


FIGURE 1: The model of tag cube. (a) Schematic diagram of the QR code and object coordinate system. (b) The model used for testing the pose measurement.

vector set of the QR code coordinate system to the camera coordinate system can be obtained.

$$\begin{bmatrix} x'_0 \\ y'_0 \\ z'_0 \end{bmatrix} = R \begin{bmatrix} 0 \\ 0 \\ -\omega/2 \end{bmatrix} + T. \quad (11)$$

From the analysis above, what is known is that the spatial pose of a three-dimensional object can be estimated through the relative position of the position and pose information of the identified QR code and multiple QR codes on the known object.

2.4. Multiple QR Code Pose Estimation of Irregular Rigid Bodies. Considering that it is difficult to get the transformation relationship from QR code coordinate system to object coordinate system on an irregular rigid body, the system can calculate the transformation relationship among QR codes according to the QR code pasted on the object, and the concrete principle is as follows.

By pasting multiple QR codes on an object, it is necessary to ensure that each QR code can be recognized along with another QR code at a certain angle of view, which is called “connection,” and that a QR code can be “connected” to all QR codes according to the above conditions, and the coordinate system of one QR code is used as the object coordinate system. The transformation relationship between the coordinate system base vector group of the QR code connected to the QR code and the base vector group of the QR code coordinate system is calculated by taking one of the QR codes in a coordinate system as the object coordinate system.

Again, taking the cube in Figure 1 as an example, remember that the QR code on the front is *A* and the QR code on the right, back, left, top, and bottom are *B*, *C*, *D*, *E*, and *F*, respectively. Firstly, the camera faces the QR code *A* on the front of the cube, where the coordinate system is regarded as the object coordinate system to rotate the cube to the left. When the camera rotates to about 45 degrees, the QR codes marked *A*, and *B* can be both recognized, and the transformation relationship from QR code *A* coordinate system to QR code *A* coordinate system can be got. To simplify the calculation, the pose and position transformations are considered separately, which means only the change of the base vector direction of the coordinate system is considered when the position transformation is carried

out, and only the change of the origin of the coordinate system is considered when the position transformation is carried out.

As for the origin of the coordinate system, the coordinate of the origin of QR code *A* coordinate system under the coordinate system of QR code *B* is $T_0 - T_1$. For the coordinate system, the following transformation formula can be obtained:

$$\begin{aligned} \vec{e}_{x0} &= R_0 R_1^{-1} \vec{e}_{x1}, \\ \vec{e}_{y0} &= R_0 R_1^{-1} \vec{e}_{y1}, \\ \vec{e}_{z0} &= R_0 R_1^{-1} \vec{e}_{z1}. \end{aligned} \quad (12)$$

R_0 and T_0 represent the rotation matrix and shift vector of QR code *A*, and \vec{e}_{x0} , \vec{e}_{y0} , \vec{e}_{z0} is the representation of the base vector group of QR code *A* coordinate system in the camera coordinate system; R_1 and T_1 represent the rotation matrix and shift vector of QR code *B*, and \vec{e}_{x1} , \vec{e}_{y1} , \vec{e}_{z1} is the representation of the base vector group of QR code *B* coordinate system in the camera coordinate system.

Keeping rotating the cube until QR code *C* and QR code *B* can be both recognized. For the origin of the coordinate system, the coordinate of the origin of the coordinate system of the QR code *B* under the coordinate system of the QR code *C* is $T'_1 - T_2$. Combined with $T_0 - T_1$, the coordinate of the origin of the coordinate system of QR code *A* under the coordinate system of the QR code *C* can be obtained: $(T'_1 - T_2) + (T_0 - T_1)$. According to formula (9), the coordinate of the QR code *A* coordinate system in the camera coordinate system can be acquired. Similarly, the transformation relationship from QR code *C* coordinate system to the QR code *B* coordinate system can be obtained from formula (13).

$$\begin{aligned} \vec{e}'_{x1} &= R'_1 R_2^{-1} \vec{e}_{x2}, \\ \vec{e}'_{y1} &= R'_1 R_2^{-1} \vec{e}_{y2}, \\ \vec{e}'_{z1} &= R'_1 R_2^{-1} \vec{e}_{z2}. \end{aligned} \quad (13)$$

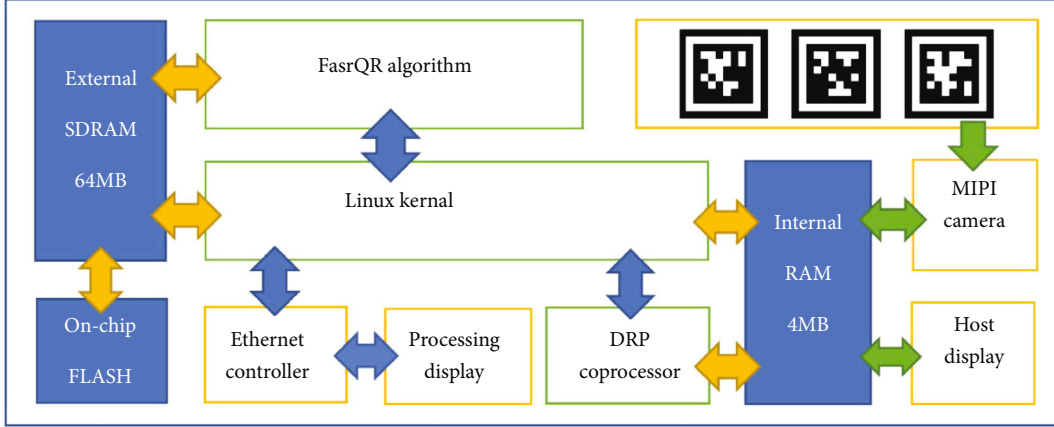


FIGURE 2: Systematic structure diagram.

R'_1 and T'_1 are the rotation matrix and shift vector of QR code B , and $\vec{e}_{x1}', \vec{e}_{y1}', \vec{e}_{z1}'$ is the representation of the base vector group of QR code B coordinate system in the camera coordinate system. Combined with formula (12), the transformation relationship from QR code C coordinate system to QR code B coordinate system can be obtained, and the rotation matrix is $R_0 R_1^{-1} R_1' R_2^{-1}$. Continue to rotate the cube, the transformation relationship from all the QR code coordinate systems on the object to QR code A coordinate system can be obtained.

The specific initialization process goes as follows: firstly, enter the number of QR codes posted on the object and the number of objects, then initialize each object one by one. Align any QR code on the first object with the camera, and the system will record the QR code coordinate system as the object coordinate system; rotate the object slowly so that the system can recognize all the QR codes posted on the object, and each new QR code needs to be recognized at the same time as an existed QR code. According to the coordinate system transformation relationship between each new QR code and the existed QR code that has been identified with it as well as the transformation relationship between the coordinate system of the existed QR code and the object coordinate system, the transformation relationship between the new QR code and the object coordinate system is obtained and recorded in the system through the principle of the above transformation relationship, and the initialization of an object is completed.

3. Verification Method and Environment

3.1. Verification Preparation. The system platform adopts Renesas RZ/A2M development board, uses rza_linux-4.19 provided by Renesas with C programming language, which connects to the RGB display through the HDM interface on the board, and sends the pose data to another PC through the network interface on the board to display the pose model. The camera has a Raspberry pi cameraV2 with a resolution of $640 * 480$. The QR code adopts Tag36H11 code in AprilTag. Camera calibration and post-data processing use Matlab2019, and the pose system

model display uses Processing3. The system structure diagram is shown in Figure 2.

The validation environment is built, as shown in Figure 3 below. The validation environment includes a Raspberry pi camera V2, Renesas RZ/A2M development board, an LCD display, Processing3 display, and the objects pasted with QR codes.

The software flow chart of the system platform is shown in Figure 4. The software mainly includes camera calibration, QR code detection, transformation matrix calculation, and object pose estimation.

3.2. Means of Verification. When checking the position measurement, the QR code is $4\text{ cm} * 4\text{ cm}$, and it is pasted on a regular hexahedral surface of $6\text{ cm} * 6\text{ cm}$. The measurement accuracy is obtained by measuring the position coordinates of the object in the camera coordinate system and comparing it with the position coordinates obtained by the system. It is also necessary to calibrate the position of the camera before testing the attitude measurement, display a QR code in the center of the display, and place the camera in the position of 1.2 m in front of the display. Adjust the angle of the camera until the angle of the measured shaft angle is 0 .

In the process of checking the pose measurement, in light of the spatial pose of the object is difficult to measure accurately, Processing3 is used to display a regular hexahedral model with 6 cm the edge length of the model. Different QR codes are displayed on the six faces of the regular hexahedral, and the axial angle of the model pose is brought out while adjusting the model. The accuracy of the measurement is obtained by comparing the pose of both the model and the measurement. The model is shown on Processing3, rotating the model around the arrow direction shown in Figure 1.

4. Results

4.1. Results and Errors of Object Pose Estimation. Considering that the edge length of QR code is 4 cm , the change range of z -axis direction is between 0.1 m and 3.0 m when $x = y = 0.0\text{ m}$, and the step size is 0.1 m with 30 groups of data. In light of the angle and view of the camera, when $z = 1.2$

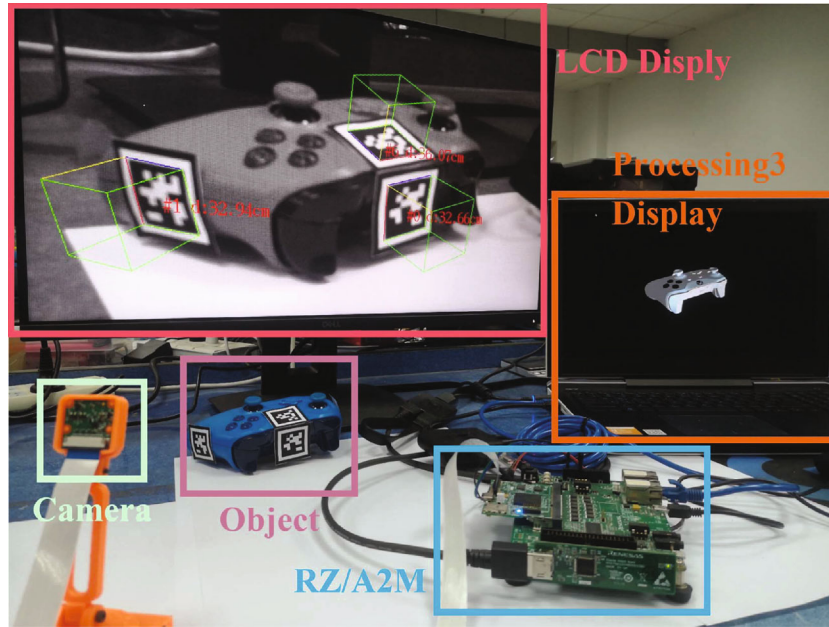


FIGURE 3: Verification environment.

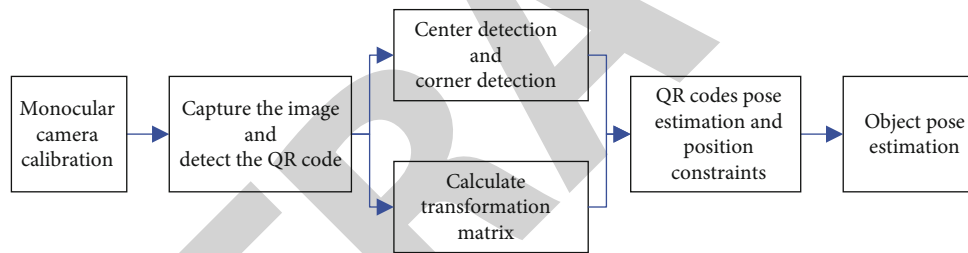


FIGURE 4: Software flow chart.

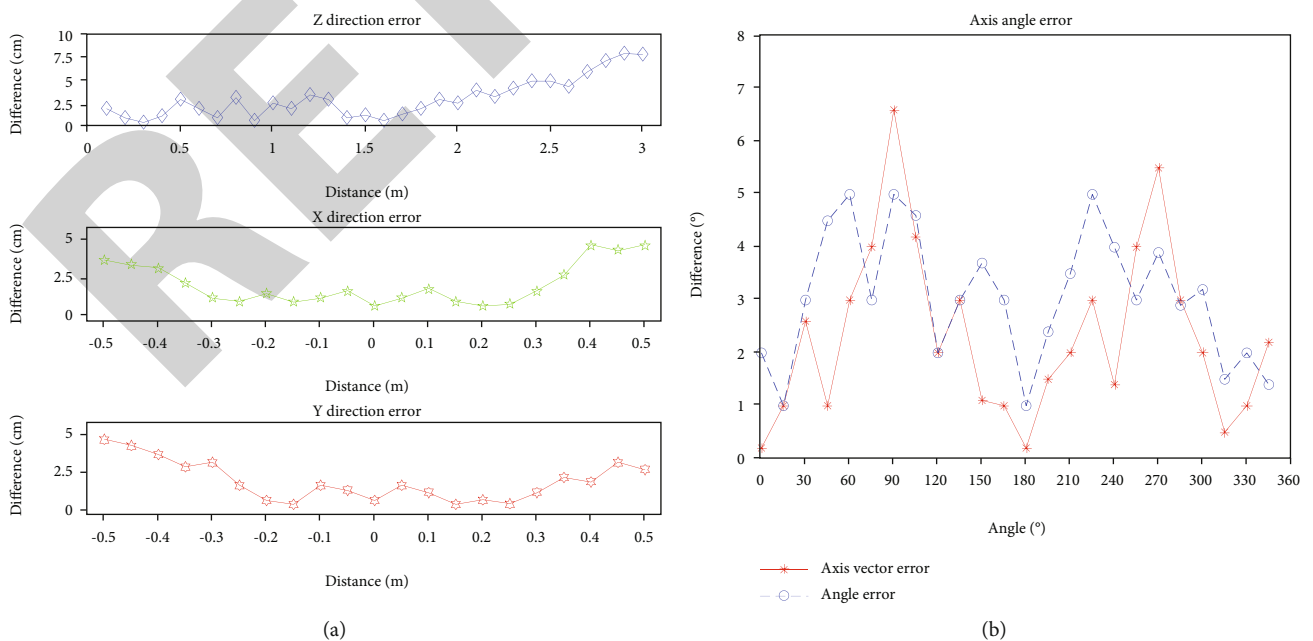


FIGURE 5: Pose estimation error. (a) The error of position estimation. (b) The error of attitude.

TABLE 1: The average time spent on object estimation.

Number of QR codes	QR code recognition time (ms)	Pose solution time (ms)	Total calculation time (ms)	Average frame rate (fps)
1	12	10	22	
2	21	15	36	28.57
3	26	21	47	

TABLE 2: Velocity comparison with other object pose estimation methods.

Number	Pose estimation method	Calculating platform	Average frame rate (fps)
1	FastQR (ours)	Renesas RZ/A2M (with the DRP)	28
2	Estimation of the 3D pose of the object by 3D model of an object [16]	A 2.83 GHz CPU (Q9550) and an NVIDIA GTX 280 GPU	4
3	Estimation of position and pose of the camera by AprilTag [17]	PC	8
4	Pose estimation of objects using fusion visual and inertial data [18]	A 3.60 GHz CPU and NVIDIA Cmadro 4000 GPU	10
5	6DoF pose estimation of objects by geometric information [19]	16-core Intel(R) Xeon(R) E5-2637 CPU and GeForce GTX 1080 GPU	30
6	Seamless single shot 6D object pose prediction [20]	Desktop with a Titan X GPU	50

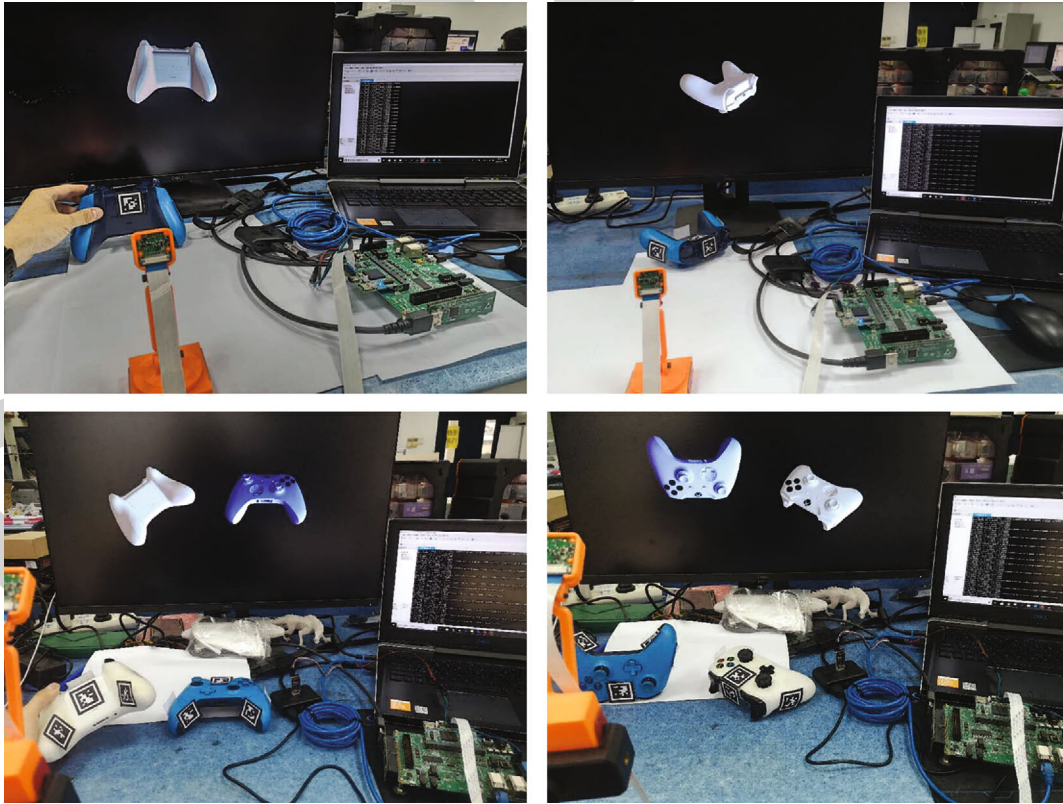


FIGURE 6: Effect diagram of the pose estimation of single and multiple irregular objects.

m, the error of the x -axis and y -axis is measured, and the range of variation is between -0.50 m and 0.50 m with 21 groups of data. The error of the angle is calculated by,

respectively, calculating the angle between the axis of the real value and the axis of the measured value and by making the difference. The results are shown in Figure 5.

From the results, it can be seen that the error between the real value and the measured one is so small that the error in the z -direction is not more than 9 cm, and the error in the x and y directions is not more than 5 cm. The angle error between the true value of the axis angle and the measured one is not more than 7° , and the angle error is not more than 5° . Due to the limitation of QR code size, camera resolution, and illumination, the accuracy of pose estimation is only more accurate, and the error will increase to a certain extent with the increase of the distance from the object to the camera.

4.2. The Estimated Velocity of Object Position. The system performance is average in terms of accuracy [15], but it can already meet the needs of 6DoF pose estimation for objects in most cases. In terms of the calculation speed, the system has very excellent performance, and its highest main frequency of the Renesas RZ/A2M development board used in this system is 528 MHz, and its captured image resolution is $640 * 480$. The average time of object estimation is shown in Table 1 below. When using DRP on RZ/A2M to accelerate some image processing steps, the fastest time for pose estimation is about 22 ms.

Compared with most of the methods that do not use visual markers to estimate the pose of objects, this method requires less calculation power and does not need to be accelerated by GPU. By using the QR code as the visual marker, the difficulty of finding feature points is avoided, and the resolution of the input image is less required. It can be implemented on MPU or CPU with low main frequency and can still maintain a smooth and available frame rate of about 28 Hz. The velocity comparison with other object pose estimation methods is shown in Table 2 below.

4.3. Position and Pose Estimation of Irregular Objects. Here, taking the XBOX handle as an example, seven QR codes are pasted on the handle to meet the requirements of Section 2.4. Note that the QR code should be pasted smoothly to avoid affecting the recognition effect, and no duplicate QR code should be pasted. The pose estimation effect for single and multiple targets is shown in Figure 6 below.

5. Conclusion

The system uses a monocular camera and multi-QR code to estimate the spatial pose of the object, which has extremely low cost, small volume, low computing power, fast speed, good robustness, and so on. This can meet the basic requirements for pose estimation. Also, at the expense of a certain precision, the calculation power requirement of object spatial pose estimation is lowered, and the calculation speed is greatly improved. It can be realized on many mobile embedded devices' cores, such as MPU or CPU with low main frequency and small memory. Compared with the one using GPU to accelerate pose estimation, the method has a higher energy efficiency ratio and greatly expands the application scene of object pose estimation. This scheme can also be further extended to complex multijoint objects in distributed embedded computing regions.

As future work, we plan to extend this method to achieve fast pose estimation on multijoint targets. By posting QR codes to each joint and connecting rod of multijoint objects, the spatial pose estimation of complex multijoint objects can be realized. We will further study to improve the accuracy of pose estimation without reducing the computing speed.

Data Availability

The datasets used and/or analyzed during the current study are available from the corresponding author on reasonable request.

Conflicts of Interest

The authors declared no potential conflicts of interest with respect to the research, authorship, and/or publication of this article.

Acknowledgments

This research was funded by the National Natural Science Foundation of China (grant number: 61974073).

References

- [1] P. Daponte, L. De Vito, F. Picariello, and M. Riccio, "State of the art and future developments of the Augmented Reality for measurement applications," *Measurement*, vol. 57, pp. 53–70, 2014.
- [2] P. Khandelwal, P. Swarnalatha, N. Bisht, and S. Prabu, "Detection of features to track objects and segmentation using Grab-Cut for application in marker-less augmented reality," *Procedia Computer Science*, vol. 58, pp. 698–705, 2015.
- [3] Z. Luo, K. Zhang, Z. Wang, J. Zheng, and Y. Chen, "3D pose estimation of large and complicated workpieces based on binocular stereo vision," *Applied Optics*, vol. 56, no. 24, pp. 6822–6836, 2017.
- [4] C. Choi and H. I. Christensen, "3D pose estimation of daily objects using an RGB-D camera," in *Proceedings of 2012 IEEE/RSJ International Conference on Intelligent Robots and Systems*, pp. 3342–3349, 2012.
- [5] M. B. Alatise and G. P. Hancke, "Pose estimation of a mobile robot based on fusion of IMU data and vision data using an extended Kalman filter," *Sensors*, vol. 17, no. 10, p. 2164, 2017.
- [6] C. X. Guo and S. I. Roumeliotis, "IMU-RGBD camera 3D pose estimation and extrinsic calibration: observability analysis and consistency improvement," in *Proceedings of 2013 IEEE International Conference on Robotics and Automation*, pp. 2935–2942, Karlsruhe, Germany, 2013.
- [7] Y. Xiang, T. Schmidt, V. Narayanan, and D. Fox, "PoseCNN: A Convolutional Neural Network for 6D Object Pose Estimation in Cluttered Scenes," 2017, <https://arxiv.org/abs/1711.00199>.
- [8] S. Tiwari, "An introduction to QR code technology," in *Proceedings of 2016 International Conference on Information Technology (ICIT)*, pp. 39–44, Bhubaneswar, India, 2016.
- [9] H. Zhang, C. Zhang, W. Yang, and C. Chen, "Localization and navigation using QR code for mobile robot in indoor environment," in *Proceedings of 2015 IEEE International Conference on Robotics and Biomimetics (ROBIO)*, pp. 2501–2506, Zhuhai, China, 2015.

Research Article

Design of Management Platform Architecture and Key Algorithm for Massive Monitoring Big Data

Wen Liu ^{1,2,3} Shanshan Li,³ Jiangru Pan,¹ Lijun Xu,^{1,2} Zheng Gu,¹ and Ling Hai¹

¹School of Control Engineering, Xinjiang Institute of Engineering, Ürümqi 830000, China

²Xinjiang Sunshine Diantong Technology Co., Ltd, Ürümqi 830000, China

³College of Computer Science and Technology, Xinjiang Normal University, Ürümqi 830000, China

Correspondence should be addressed to Wen Liu; 627952@qq.com

Received 11 August 2021; Revised 8 September 2021; Accepted 17 September 2021; Published 28 September 2021

Academic Editor: Yong Deng

Copyright © 2021 Wen Liu et al. This is an open access article distributed under the Creative Commons Attribution License, which permits unrestricted use, distribution, and reproduction in any medium, provided the original work is properly cited.

With the construction and development of industrial informatization, industrial big data has become a trend within the smart industry. To obtain valuable information on massive data, achieving the acquisition, storage, analysis, and mining is becoming an important area of research. Focusing on the application requirements for industrial fields, we propose a data acquisition and analysis system based on the NB-IoT for industrial applications. The system is an integrated system that includes sensor data acquisition, data transmission, data storage, and analysis mining. In this study, we mainly focused on the use of the NB-IoT network to collect and transmit real-time data for sensors. First, for the long time series (e.g., if we collect the data streams for one year for the sensor with a frequency of 1 Hz, the length of the series will reach 10^7). Then, we propose DSCS-LTS, a distributed storage and calculation model, and CCCA-LTS, an algorithm for the correlation coefficient of long time series in a distributed environment. Third, we propose a granularity selection algorithm and query process logic for visualization. We tested the platform in our laboratory and an automated production line for one year, and the experimental results using real data sets show that our approach is effective and scalable, can achieve efficient data management, and provide the basis for intelligent enterprise decision-making.

1. Introduction

With the rapid development of “interconnected” and “intelligent” industries, industrial big data has become the focus of current research. For all types of real-time monitoring of data in the industrial field, the technology of collection, storage, and analysis, to enable deep mining, is facing great challenges. The construction and development of the “interconnected” industry and “intelligent” industry require a large amount of basic data. These data are not only to stay in the collection stage but also to carry out deep storage, analysis, and mining, for example, real-time analysis of industrial field data, alarm of abnormal data, supervision of every process in the production process, and intelligent decision-making. This series of problems is becoming an important topic in industrial informatization research.

With the development of the Internet of Things technology, the traditional big data acquisition platforms have been

unable to adapt to the growing mass of data. However, the scheme of “centralized collection and centralized management” provides an effective solution for massive data management in the industrial field. In this paper, this specific project is an example: a large tomato sauce factory production line, collecting all kinds of monitoring data (such as sterilization temperature, tank pressure, pipeline flow rate, and motor power), real-time data through the network transmission to the data management platform, for massive data design distributed storage and analysis methods, realize data depth mining and visualization, and provide the basis for decision-making.

Based on the current situation of large tomato sauce production lines, this project designs an integrated platform for data collection, analysis, mining, and visualization. We propose a distributed storage, calculation model DSCS-LTS, correlation coefficient estimation method CCCA-LTS for massive, long time series data, and propose a data

visualization method that addresses the key problems related to the management of massive monitoring data.

2. Related Research

2.1. Related Research Work

2.1.1. Research on Time Series Data Management Platform.

In recent years, as the time series data management system (TSDB) has been developing rapidly, many time series management systems have emerged. Popular open-source time series data management systems include InfluxDB [1] and OpentsDB [2]. InfluxDB defines the field types and statistical queries for time series. However, it does not support complex queries, such as a similarity search. OpentsDB is based on the HBase-distributed time series management system, which supports simple statistical queries on time series. Recently, Tsinghua University in China developed IoTDB [3], which has become the Apache incubation project. The time series storage structure is similar to that of Parquet [4] and supports distributed computing frameworks such as MapReduce and Spark. There are also many commercial time series databases, such as the domestic T-engine. However, these systems only support basic aggregation queries but do not support association analysis, similarity queries, and other functions.

2.1.2. Similarity Query Technology for Time Series.

Time series similarity query technology has been studied for approximately 20 years. In 1993, Lomet first proposed the research problem of similarity queries for time series databases [5] and discrete Fourier transforms to reduce the dimension of time series. Second, the R-tree was used to build the index processing method. Third, the main research uses other dimension reduction technologies, which follow the routine of dimensionality reduction before index building, including discrete wavelet transform [6], APCA [7], and SAX [8]. In 2013, with respect to the complete sequence similarity query, VLDB [9] proposed a mechanism combining dimensionality reduction and index construction. In 2014, Zoumpatianos et al. proposed refining the index mechanism in the query stage, which shortened the waiting time for index construction [10]. In 2012, Rakthanmanon et al. proposed a UCR suite algorithm for subsequence similarity query [11]. Their approach supports standardized subsequence similarity queries. However, this approach cannot build an index and scan the entire sequence. In 2019, the VLDB paper proposed a variable-length standardized subsequence similarity query algorithm [12]. In 2016, the Harbin Institute Technology team proposed a set-based approximate query algorithm for time series at the SIGMOD conference [13]. The team from the University of Chinese Academy of Sciences and the State Grid Electric Power Research Institute proposed a multidimensional query system DGFIndex for smart grid data [14], and the Beihang team proposed an approximate representation and query algorithm for trajectory time series [15]. Their approach supports one-dimensional, few-dimensional time series or specific aggregate functions and cannot achieve aggregate query processing on a large-scale time series. In summary,

current scientific computing, the Internet of Things, and intelligent manufacturing have become research hotspots globally. The MengXiaofeng team of Renmin University of China proposed a scientific big data management framework, suitable for the entire life cycle of scientific data management and analyzed the key technologies in the scientific big data management system [16].

2.1.3. Correlation Coefficient Calculation of Time Series.

In the past 20 years, there have been many mining algorithms and query algorithms for time series data. Time series mining algorithms include classification, clustering, outlier detection, and motif mining [17]. Time series query algorithms include approximate queries [18], aggregate queries [19], and range queries [20, 21]. The above algorithm can only be used in a single machine environment and is not suitable for processing massive, long time series data (for example, a sensor with a frequency of 1 Hz can continuously generate 10^7 data for one year).

Computing correlation coefficients for long time series in a distributed environment has the following problems: (1) distributed calculations cannot be performed. Although the Euclidean distance can be computed in a distributed fashion, it requires the mean and standard deviation of the entire sequence to compute the correlation coefficient, so it cannot be computed in a distributed fashion; (2) when a query sequence is long, it requires extensive I/O and network costs, thus causing delays, and cannot be used in interactive query applications. To solve these problems, we propose a method to estimate the correlation coefficients of two sequences on HBase and design a fast estimation method, CCCA-LTS, for the upper and lower bounds of the correlation coefficients. The HBase algorithm iteratively estimates the correlation coefficients.

2.2. Research Contents.

This study conducts research, based on a mass monitoring data management platform, to provide an intelligent decision-making and control basis for enterprise production. The specific work is as follows: first, we designed a collection of various monitoring data collection terminals and used the NB-IoT network to transmit the data to the management platform. Second, according to the characteristics of the data, we designed the distributed storage and calculation model DSCS-LTS, which realizes the efficient storage of long-term sequences. Third, in order to calculate the correlation between the series, we designed the correlation coefficient estimation method CCCA-LTS for long-term series data; and fourth, we designed the granular selection algorithm and query process, which logically realizes the visualization of the data. The overall system architecture and data acquisition terminal design are shown in Figures 1 and 2, respectively.

The overall framework of the system is mainly composed of a collection equipment layer, a communication channel layer, and a master station layer. The acquisition device layer realizes the acquisition, processing, and real-time monitoring of monitoring data; the communication channel layer transmits the massive real-time data stream to the master station layer; the master station layer completes the data

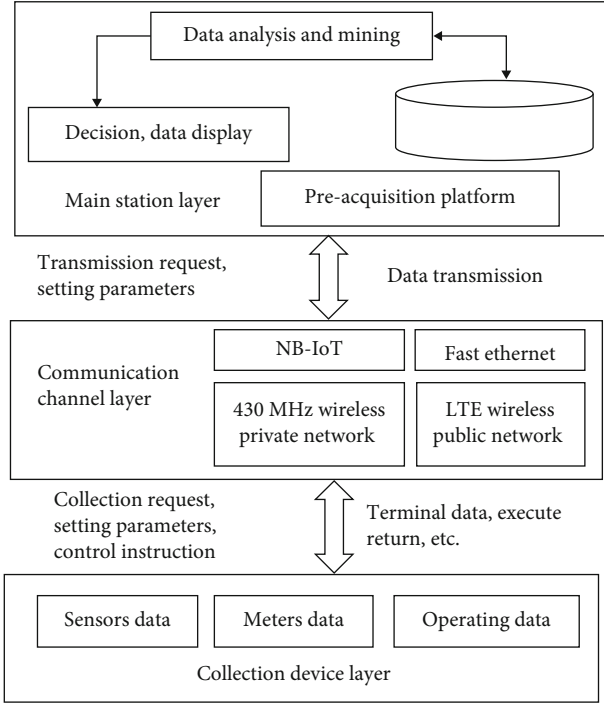


FIGURE 1: System framework diagram.

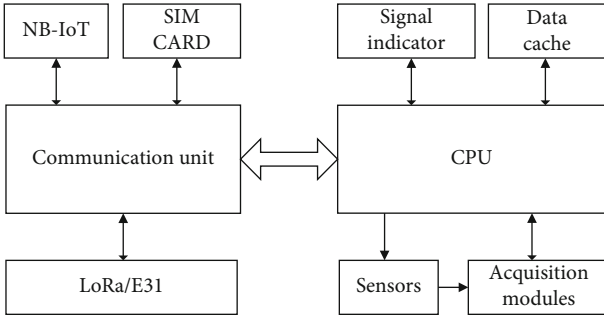


FIGURE 2: Structure diagram of acquisition terminal.

stream processing, storage, data analysis, mining, and visualization.

According to the data characteristics of sensors and instruments in the industrial field, we designed the data acquisition and data transmission terminal (including the latest NB-IoT module), as shown in Figure 2. The terminal uses an STM32 single-chip microcomputer as a processor, connects field sensors, meters, etc., through the acquisition module, and then transmits the collected data to the data management platform through the NB-IoT network.

The master station layer regards the construction of the sensor data management system as the overall goal and conducts research on actual business needs and data characteristics, as well as from platform construction, data collection, data analysis, data mining, and other levels.

2.3. Key Technology of the System

2.3.1. Prerequisite Knowledge

Definition 1 (time series). The time series can be expressed as $S = ((t_1, s_1), (t_2, s_2), \dots, (t_n, s_n))$. n is the total length of S , t_i is the timestamp, and s_i is the value of t_i and $(1 \leq i \leq n)$.

Definition 2 (equally interval time series). The equal interval time series refers to the set S that arranges the indicators of a certain phenomenon in time sequences and equal time intervals, denoted as $S = (s_1, s_2, \dots, s_n)$.

For ease of description, the time series presented in this article are all equally spaced time series, and this algorithm is also suitable for nonequally spaced time series.

Definition 3 (subsequence). $S_{i:l} = (s_i, s_{i+1}, \dots, s_{i+l-1})$ is a subsequence of S . The relationship between i and l is $1 \leq i \leq n - l$.

Definition 4 (Pearson correlation coefficient). The lengths of the time series $X = (x_1, x_2, \dots, x_n)$ and $Y = (y_1, y_2, \dots, y_n)$ are both n . The Pearson correlation coefficient was calculated as follows:

$$\rho(X, Y) = \frac{1}{n} \sum_{i=1}^n \left(\frac{x_i - \mu_x}{\sigma_x} \right) \left(\frac{y_i - \mu_y}{\sigma_y} \right). \quad (1)$$

μ_x and μ_y are the mean values of X and Y , respectively, $\mu_x = (1/n) \sum_{i=1}^n x_i$. σ_x and σ_y are the standard deviations of X and Y , respectively, $\sigma_x = \sqrt{\sum_{i=1}^n (x_i)^2 / n - (\mu_x)^2}$.

Problem definition: the time series database SS is stored in a distributed architecture HDFS or HBase. Two subsequences X and Y in database SS calculate whether the Pearson coefficient $\rho(X_{i:l}, Y_{i:l}) \geq \varepsilon$ is valid, where i is any integer, l is the subsequence length, and ε is the correlation coefficient threshold. In this study, the query window is set to $(i, i + 1, i + 2, \dots, i + l - 1)$.

2.4. Distributed Storage Scheme and Computing Model

2.4.1. Distributed Storage Solution Based on HBase. At present, many applications use the distributed storage architecture HDFS and HBase to store massive amounts of time series data. Representative platforms include OpenTSDB [1] and TempoIQ [17]. There are two schemes based on the HBase time series storage method.

Scheme 1: Figure 3 shows the first storage solution of HBase. Based on storage method 1, we can access the value of any sequence at any timestamp.

Scheme 2: Figure 4 shows the second storage solution of HBase. The scheme is based on Scheme 1, storing a subsequence consisting of a continuous period value.

This paper proposed an algorithm that satisfies the above two schemes.

2.4.2. Distributed Storage and Computing Model DSCS-LTS. To improve the generalization, we use a distributed storage model and computing model DSCS-LTS (distributed storage and calculation scheme for long time series) for the above

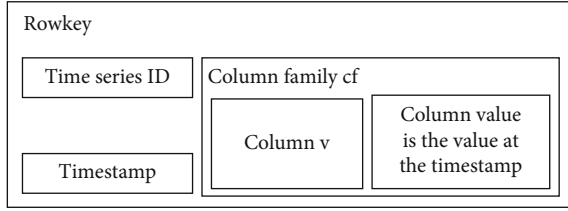


FIGURE 3: Storage method 1.

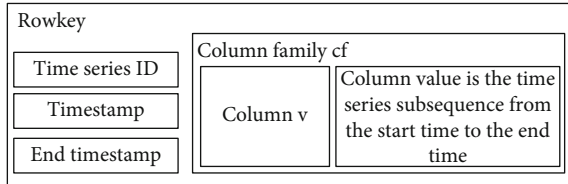


FIGURE 4: Storage method 2.

storage scheme, which is a long time series for massive monitoring distributed storage and calculation model of sequence data.

Distributed storage: L storage nodes $\{N_1, N_2, \dots, N_L\}$ in a distributed environment. Time series data in the database SS are divided into several disjoint subsequences and store them into L sequence nodes. The subsequence is $S_i = (s_{(i-1)w+1}, s_{(i-1)w+2}, \dots, s_{i-w})$, $1 \leq i \leq \lceil n/w \rceil$ where w represents the time dimension.

The subsequence database stored by node N_j is represented as SS_j , and the sequence S_i subsequence S is represented as $S_i \in SS_j$ if it is stored within a node N_j . When the length of a subsequence equals 1 ($w = 1$), only one value of a time series exists in each row, so Scheme 1 is meaningless.

Distributed computing: as shown in Figure 5, it is a distributed computing process. There are L several computing nodes $\{N_1, N_2, \dots, N_L\}$. All L nodes have storage and computing capabilities. N_0 is the query driving node, which comprehensively handles all o_i results.

2.5. CCCA-LTS Calculation Method of the Long Time Series Correlation Coefficient in a Distributed Environment

2.5.1. CCCA-LTS Algorithm. CCCA-LTS (correlation coefficient calculation algorithm for long time series) is a Pearson correlation coefficient estimation method in a distributed environment. In the correlation coefficient estimation algorithm, we assume that $X = (x_1, x_2, \dots, x_n)$ and $Y = (y_1, y_2, \dots, y_n)$ are complete subsequences, and the query window is $(1, 2, \dots, n)$. The CCCA-LTS algorithm can be directly extended to any query window.

As shown in Figure 6 (step 1 and step 2), the sequences X and Y are divided into six subsequences (step 1). Then, six subsequences are distributed to the data nodes (step 2). A simple way is to transmit all subsequences to N_0 for calculation, which will increase network transmission. To effectively reduce the cost of network transmission, this study proposes the CCCA-LTS algorithm.

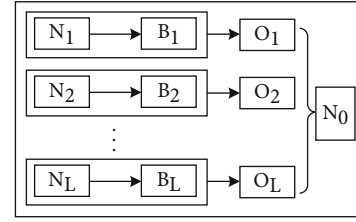


FIGURE 5: Distributed computing framework.

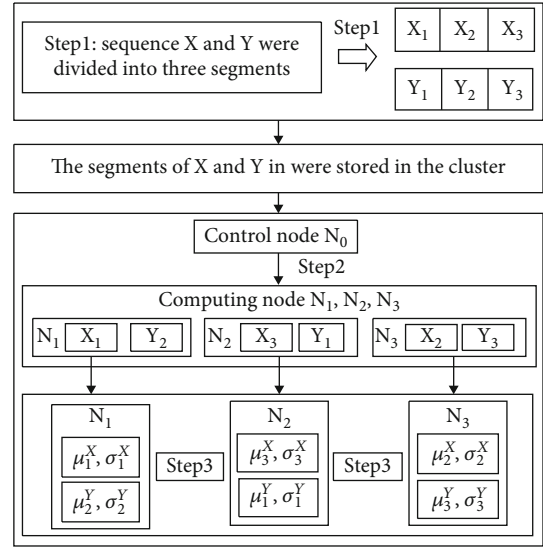


FIGURE 6: CCCA-LTS algorithm.

The core of the CCCA-LTS algorithm is illustrated in Figure 6 (step 3). All L nodes need to calculate the mean and standard deviation of the subsequence stored in the node (step 3). For example, in Figure 6, the subsequence X_1 is stored at node N_1 , and node N_1 calculates μ_1^X and σ_1^X , $\mu_1^X = (1/w) \sum_{i=1}^w x_i$, and $\sigma_1^X = \sqrt{(\sum_{i=1}^w (x_i)^2 / w) - (\mu_1^X)^2}$. Then, the values of the calculated results are transmitted to the node N_0 . N_0 estimated the correlation coefficient according to these values. Next, the CCCA-LTS algorithm was introduced in detail.

2.5.2. Relationship between Correlation Coefficient and Euclidean Distance. We first provide the estimation formulas, based on the upper and lower bounds in Figure 6 (step 3). The normalized sequences of X and Y are $\hat{X}_i = (x_i - \mu_X) / \sigma_X$ and $\hat{Y} = \{\hat{y}_i\}_{1 \leq i \leq n}$. The relationship between the correlation coefficient of X and Y and the Euclidean distance:

$$\rho(X, Y) = 1 - \frac{1}{2n} d^2(\hat{X}, \hat{Y}). \quad (2)$$

According to Equation (2), the formula $d^2(\hat{X}, \hat{Y}) \leq 2n(1 - \varepsilon)$ can be used to estimate the upper and lower bounds.

2.5.3. Correlation Coefficient Estimation Method. \hat{X} and \hat{Y} are standardized time series. We first introduce the

approximate representation method EAPCA of the time series, proposed in Reference [9]. Then, we represent $R(\hat{X})$ and $R(\hat{Y})$ according to the EAPCA of \hat{X} and \hat{Y} . Finally, we give estimates of $d(\hat{X}, \hat{Y})$.

EAPCA first divides the series S into $S = (S_1, S_2, \dots, S_m)$; the arbitrary segment is $S_j = (s_{r_{j-1}+1}, s_{r_{j-1}+2}, \dots, s_{r_j})$, ($1 \leq j \leq m$, $1 \leq r_1 < r_2 < \dots < r_m \leq n$). The EAPCA of S is denoted as $R(S) = ((\mu_1^S, \sigma_1^S, r_1), (\mu_2^S, \sigma_2^S, r_2), \dots, (\mu_m^S, \sigma_m^S, r_m))$, where X and Y are the mean and standard deviation of S_j , respectively. We denote \hat{X} and \hat{Y} as $R(\hat{X})$ and $R(\hat{Y})$, as follows:

$$\begin{aligned} R(\hat{X}) &= \left((\mu_1^{\hat{X}}, \sigma_1^{\hat{X}}, r_1), (\mu_2^{\hat{X}}, \sigma_2^{\hat{X}}, r_2), \dots, (\mu_m^{\hat{X}}, \sigma_m^{\hat{X}}, r_m) \right), \\ R(\hat{Y}) &= \left((\mu_1^{\hat{Y}}, \sigma_1^{\hat{Y}}, r_1), (\mu_2^{\hat{Y}}, \sigma_2^{\hat{Y}}, r_2), \dots, (\mu_m^{\hat{Y}}, \sigma_m^{\hat{Y}}, r_m) \right). \end{aligned} \quad (3)$$

According to [9], we obtain the boundary of the Euclidean distance of \hat{X} and \hat{Y} as follows:

$$d(\hat{x}, \hat{y}) \geq \sqrt{\sum_{i=1}^m (r_i - r_{i-1}) \left[(\mu_i^{X\wedge} - \mu_i^{Y\wedge})^2 + (\sigma_i^{X\wedge} - \sigma_i^{Y\wedge})^2 \right]}, \quad (4)$$

$$d(\hat{x}, \hat{y}) \leq \sqrt{\sum_{i=1}^m (r_i - r_{i-1}) \left[(\mu_i^{X\wedge} - \mu_i^{Y\wedge})^2 + (\sigma_i^{X\wedge} + \sigma_i^{Y\wedge})^2 \right]}. \quad (5)$$

Through the above analysis, we summarize as follows:

- (i) If $\sqrt{2n(1-\varepsilon)}$ is more than $d(\hat{X}, \hat{Y})$ (upper bond), then there must be $\rho(X, Y) > \varepsilon$
- (ii) If $\sqrt{2n(1-\varepsilon)}$ is less than $d(\hat{X}, \hat{Y})$ (lower bound), then $\rho(X, Y) < \varepsilon$ must exist
- (iii) If neither of the above two situations is true, it is impossible to judge whether $\rho(X, Y) > \varepsilon$ is true

2.5.4. Distributed Estimation Methods. In a distributed environment, as shown in Figure 6 (step 2), we cannot calculate the mean and standard deviation of the standardized subsequence \hat{X} . The calculation was the same for the standardized subsequence \hat{Y} .

This paper proposes a new method for estimating the standardized mean and standard deviation in a distributed environment. As shown in Figure 6 (step 3), each node first calculates the μ_i^X , δ_i^X , μ_i^Y , and δ_i^Y and then enters the result into N_0 . These mean and standard deviation values were used to estimate the upper and lower bounds, respectively. We provide estimation methods for $\mu_i^{\hat{X}}$ and $\sigma_i^{\hat{X}}$, $1 \leq i \leq m$. We can estimate the complete series by Equations (5)–(8), where μ_i^X and σ_i^X are the mean and standard deviation of the known subsequence; μ^X and δ^X are the overall mean

and standard deviation, respectively. The proofs of Equations (6)–(9) are given in Reference [2] and will not be repeated here.

$$\mu^X = \frac{\sum_i (r_i - r_{i-1}) \mu_i^X}{n}, \quad (6)$$

$$\sigma^X = \sqrt{\frac{\sum_{i=1}^m (r_i - r_{i-1}) \left((\mu_i^X)^2 + (\sigma_i^X)^2 \right)}{n} - (\mu^X)^2}, \quad (7)$$

$$\mu_i^{\hat{X}} = \frac{\mu_i^X}{\sigma^X} - \frac{\mu^X}{\sigma^X}, \quad (8)$$

$$\sigma_i^{\hat{X}} = \frac{\sigma_i^X}{\sigma^X}. \quad (9)$$

Using Equations (2), (4), (5), (6), (7), (8), and (9), we can calculate the correlation coefficient.

2.5.5. CCCA-LTS Algorithm. This section discusses two problems with the CCCA-LTS algorithm. The first problem is that in the previous description, we assume that the query window is the entire window, expressed as $(1, 2, \dots, n)$. The actual query window boundary does not necessarily fall on the boundary of the subsequence and may fall within the subsequence. When the query window is within the internal sequence, the query sequence is necessary to read out the window border, and there is a need to calculate the mean and standard query portion difference within the window.

The second question is whether there are three possible outcomes. When the third result appears, that is, when it is impossible to judge, we need to estimate based on the more fine-grained mean and standard deviation. At this point, we need a second or even third round of calculation. In the first round, the subsequence length is w , the mean and standard deviation are calculated, and N_0 is returned for comprehensive calculation and judgment. When the judgment result is the third type, we need to the second round of calculation; that is, we calculate the subsequence with length $w/2$ and then return N_0 for comprehensive calculation and judgment. If the judgment result is of the first or second type, it stops. Otherwise, the third round is performed, that is, e the mean and standard deviation of the subsequence with length $w/4$ are calculated. Thus, the judgment accuracy meets the needs.

CCCA-LTS algorithm analysis: the CCCA-LTS algorithm is a multiround algorithm. If only one round of calculation is required, the CCCA-LTS algorithm has the same I/O overhead as the direct calculation method. As only the mean value and standard deviation of the subsequence are transmitted, the network has a significantly reduced transmission cost. If multiple rounds of calculation are required, the query window sequence requires multiple reads, thus causing more I/O overhead.

2.6. Visualization Technology. This section focuses on two issues: granularity data visualization algorithms and query process technology. The selected size has a significant influence on the response time of the query. When the particle size is too small, a larger network transmission is required,

Algorithm 1: Select granularity (X, start time, end time, M)

Input: X time series ID, start and end time, client can display the maximum amount of data

Output: < size of granularity > Calculate the size of different granularity data of X Time Series in the historical statistics table from start time to end time;

Sort the amount of data in step 1 in descending order;

Select the first granularity that is smaller than the maximum amount of data that can be displayed on the client.

ALGORITHM 1: Granularity selection algorithm.

and the resulting query response time is too high; therefore, a large amount of data is not stored in the client memory. When the granularity is large, the amount of data transmitted to the user is small, which cannot accurately represent the trend of the original time series.

In the query process, the user sets a good time interval and a data channel. In general, a user should choose an appropriate statistical median. The statistics currently supported include mean and median. When a user requests a query data for a certain period of time, he/she can select a period of interest in the front end of the data to view more detailed data trends and other information during this period.

2.6.1. Granularity Algorithm. Select the required particle size to be determined, according to the size of the data. If the granularity is too large, the user query response time will be smaller, but the amount of data returned to the client will be smaller, thereby increasing the error. If the granularity is too small, the amount of data returned to the client will be too large. Although the error is small, the user's query response time is long.

To improve the response time of the query, we design a historical data statistics table. The historical data statistics table contains statistical data of different granularities, such as the maximum and minimum values of a certain time series within one hour. The existing granularities are day, hour, minute, and second. It is a challenge not only to find a good representation of the original time series trends in large amounts of historical data in tables but also to avoid the transmission of data to the client that is too large. The idea to solve this problem is to calculate the amount of data of different granularities according to the frequency of the time series and then sort the amount of data of different granularities from large to small. According to this order, we find the first corresponding granularity that is smaller than the maximum amount of data that can be displayed on the client. The granularity at this time can not only better represent the original time series trend but also avoid the situation in which the client data volume is too large. The granularity is jointly determined by the maximum amount of data that can be displayed by the client, the amount of data that the user queries, and the granularity in the historical data statistical table. The algorithm is illustrated in Algorithm 1.

Algorithm 1: Granularity selection algorithm. Algorithm 1: Select granularity (X, start time, end time, M)

Input: X time series ID, start and end time, client can display the maximum amount of data

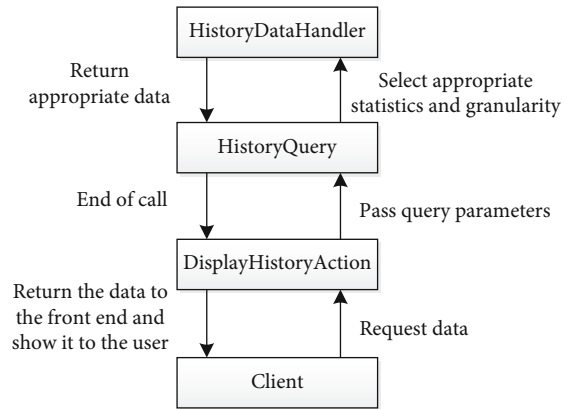


FIGURE 7: Flow chart of trend query.

Output: < size of granularity >

- (1) Calculate the size of different granularity data of X Time Series in the historical statistics table from start time to end time;
- (2) Sort the amount of data in step 1 in descending order;
- (3) Select the first granularity that is smaller than the maximum amount of data that can be displayed on the client.

2.6.2. Inquiry Process. When the user provides a channel and time interval and then selects a statistic, if the user is not given, the median is the default statistic. The statistics currently supported are mean, median, maximum, minimum, and variance. The query process is illustrated in Figure 7. DisplayHistoryAction is the front-end Servlet, which accepts user requests and passes the request parameters to the background. HistoryQuery is the core processing class in the background and is responsible for interacting with the HistoryDataHandler class in the data layer. HistoryDataHandler encapsulates HBase's API for reading and writing data and is mainly responsible for interacting with HBase.

When the user is more interested in the data in a certain period of time, the user can select a period of interest in the front end to view more detailed trend information during this period.

2.7. Experimental Data. We use experimental results to illustrate the effectiveness of the distributed storage and calculation model DSCS-LTS designed in this study and the long-term series correlation coefficient calculation method

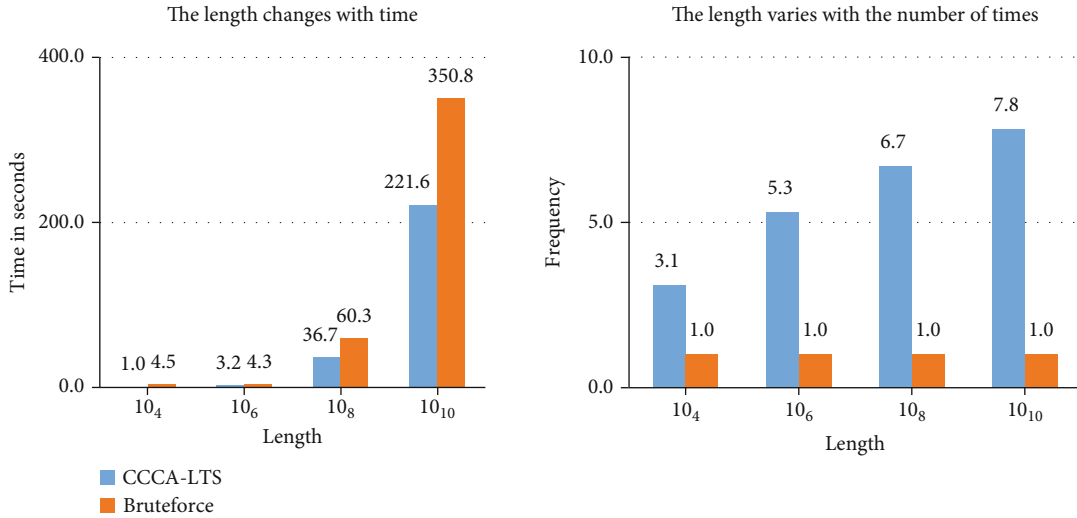


FIGURE 8: The effect of query length.

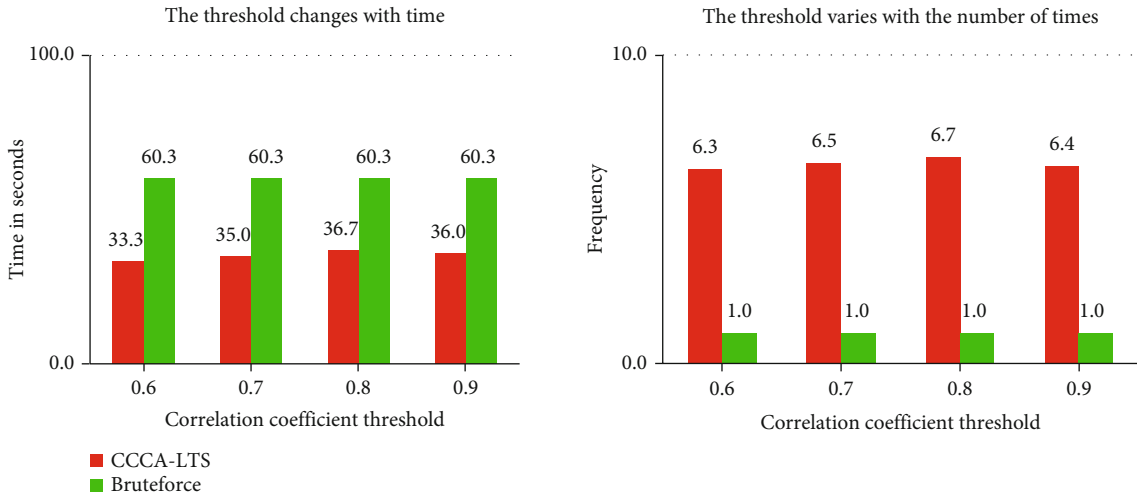


FIGURE 9: Effect of correlation coefficient threshold.

CCCA-LTS in a distributed environment. The specific test is based on the massive monitoring big data management platform, designed in this study. The main test indicators are divided into two parts: the influence of the sequence length change and the correlation coefficient threshold change of the monitoring time series on the query efficiency, and the experimental results are analyzed.

2.8. *Data Sets.* The experimental dataset comprises a large variety of sensor information collected from an industrial ketchup production line. The production line includes 100 sensors, such as thermometers, two-way/three-way accelerometers, and strain gauges. Each sensor corresponded to a time series. The sensor acquisition frequency was 1 Hz, that is, one acquisition value per second. We collected 5 years of data, which is about 250 GB.

2.9. *Experimental Environment.* The experimental cluster included five servers, and the operating system was Cen-

tOS8. Machine configuration memory to 64 GB, 8-core CPU, and 12 TB hard drive. The cluster includes 1 master node and 4 slave nodes. The Hadoop version was 2.6., and the HBase configuration was 1.0.

2.10. *Experimental Result Analysis*

2.10.1. *The Query Efficiency Changes with the Query Length.* The first experiments mainly tested the running time of CCCA-LTS and Bruteforce on the dataset and the number of algorithm iterations. The threshold was set to 0.7, and the specific test results are shown in Figure 8. Although the CCCA-LTS algorithm has more iterations, it is more efficient than the Bruteforce algorithm.

2.10.2. *The Change of Query Efficiency with Correlation Coefficient Threshold.* The second experiment mainly tests the efficiency of CCCA-LTS and Bruteforce when the threshold changes. The query length was 10^8 , and the

experimental results are shown in Figure 9. Because the Brute-force algorithm needs to take out all the data for calculation, the change in the threshold does not affect its operating efficiency, although the CCCA-LTS algorithm has many iterations, it does not need to read the entire sequence. It uses a segmented sequence to estimate the correlation coefficient of the entire sequence in an iterative manner, which is more efficient than the Brute-force algorithm.

3. Conclusion

Aiming at a massive monitoring data management platform, this study investigates the acquisition, storage, and analysis of big data monitoring. We designed a data collection terminal, collected sensor data to a distributed storage platform, through the NB-IoT network, and proposed a storage and calculation method called DSCS-LTS. According to the calculation of Pearson's correlation coefficient of a long time series, the algorithm CCCA-LTS is designed, which effectively improves the efficiency of the similarity query, by designing algorithms for particle size and query processes to solve the problem of visualization systems. In the development of the core platform to test the performance of the algorithm, the results show that the efficiency is better than that of the traditional method. Mass monitoring is an intelligent management reference for efficient time series data types.

Data Availability

The data used to support the findings of this study are available from the corresponding author upon request.

Conflicts of Interest

The authors declare that they have no competing interests.

Acknowledgments

This work is supported by NSFC under grant 61962058, Integration of Industry and Education-Joint Laboratory of Data Engineering and Digital Mine (2019QX0035), and Bayingolin Mongolian Autonomous Prefecture Science and Technology Research Program (202117).

References

- [1] "Influxdata [EB/OL]," 2021, <https://www.influxdata.com/products/influxdb/>.
- [2] W. Liu, T. Zhang, and J. Liu, "Window-based multiple continuous query algorithm for data streams," *Journal of Supercomputing*, vol. 75, no. 9, pp. 5782–5807, 2019.
- [3] "IoTDB [EB/OL]," 2021, <http://iotdb.incubator.apache.org/UserGuide/Master/IoTDB-Introduction/>.
- [4] "Parquet [EB/OL]," 2021, <http://parquet.apache.org/documentation/latest/>.
- [5] D. B. Lomet, "Data series management: the road to big sequence analytics," in *Proceedings of the 4th International Conference on Foundations of Data Organization and Algorithms//International Conference on Foundations of Data Organization & Algorithms*, Chicago, Illinois, USA, 1993.
- [6] T. Palpanas, "Data series management," *ACM SIGMOD Record*, vol. 44, no. 2, pp. 47–52, 2015.
- [7] K. Chakrabarti, E. Keogh, S. Mehrotra, and M. Pazzani, "Locally adaptive dimensionality reduction for indexing large time series databases," *ACM Transactions on Database Systems*, vol. 27, no. 2, pp. 188–228, 2002.
- [8] A. Camerra, T. Palpanas, J. Shieh, and E. Keogh, "iSAX 2.0: indexing and mining one billion time series," in *ICDM 2010, The 10th IEEE International Conference on Data Mining*, Sydney, Australia, 2010.
- [9] Y. Wang, P. Wang, J. Pei, W. Wang, and S. Huang, "A data-adaptive and dynamic segmentation index for whole matching on time series," *Proceedings of the VLDB Endowment*, vol. 6, no. 10, pp. 793–804, 2013.
- [10] K. Zoumpatianos, S. Idreos, and T. Palpanas, "Indexing for interactive exploration of big data series," in *Proceedings of the 2014 ACM SIGMOD International Conference on Management of Data*, pp. 1555–1566, Snowbird Utah USA, 2014.
- [11] T. Rakthanmanon, B. Campana, A. Mueen et al., "Searching and mining trillions of time series subsequences under dynamic time warping," in *KDD '12: Proceedings of the 18th ACM SIGKDD international conference on Knowledge discovery and data mining*, Beijing China, 2012.
- [12] M. Linardi and T. Palpanas, "Scalable, variable-length similarity search in data series," *Proceedings of the VLDB Endowment*, vol. 11, no. 13, pp. 2236–2248, 2018.
- [13] J. Peng, H. Wang, J. Li, and H. Gao, "Set-based similarity search for time series," in *SIGMOD '16: Proceedings of the 2016 International Conference on Management of Data*, San Francisco California USA, 2016.
- [14] Y. Liu, S. Hu, T. Rabl et al., "DGFIndex for smart grid," *Proceedings of the VLDB Endowment*, vol. 7, no. 13, pp. 1496–1507, 2014.
- [15] X. Lin, S. Ma, H. Zhang, T. Wo, and J. Huai, "One-pass error bounded trajectory simplification," *Proceedings of the VLDB Endowment*, vol. 10, no. 7, pp. 841–852, 2017.
- [16] J. Li, Z. Shen, and X. Meng, "Scientific big data management: concepts, technologies and system," *Journal of Computer Research and Development*, vol. 54, 2017.
- [17] C. Faloutsos, M. Ranganathan, and Y. Manolopoulos, "Fast subsequence matching in time-series databases," in *International Conference on Data Engineering*, Minneapolis Minnesota USA, 2001.
- [18] E. Soroush, M. Balazinska, and D. L. Wang, "Array Store: a storage manager for complex parallel array processing," in *ACM Sigmod International Conference on Management of Data*, Athens Greece, 2011.
- [19] X. P. Yuan, "Estimation of three-way similarities based on connected bit minwise hash," *Journal of Shanghai Jiaotong University*, vol. 48, no. 7, pp. 936–941, 2014.
- [20] Y. Tao, K. Yi, C. Sheng, J. Pei, and F. Li, "Logging every footstep: quantile summaries for the entire history," in *ACM Sigmod International Conference on Management of Data*, Indianapolis Indiana USA, 2010.
- [21] W. Liu, T. Zhang, Y. Shen, and P. Wang, "Fast correlation coefficient estimation algorithm for HBase-based massive time series data," *Frontiers of Computer Science*, vol. 13, no. 4, pp. 864–878, 2019.

Retraction

Retracted: Malicious Intrusion Data Mining Algorithm of Wireless Personal Communication Network Supported by Legal Big Data

Wireless Communications and Mobile Computing

Received 28 November 2023; Accepted 28 November 2023; Published 29 November 2023

Copyright © 2023 Wireless Communications and Mobile Computing. This is an open access article distributed under the Creative Commons Attribution License, which permits unrestricted use, distribution, and reproduction in any medium, provided the original work is properly cited.

This article has been retracted by Hindawi, as publisher, following an investigation undertaken by the publisher [1]. This investigation has uncovered evidence of systematic manipulation of the publication and peer-review process. We cannot, therefore, vouch for the reliability or integrity of this article.

Please note that this notice is intended solely to alert readers that the peer-review process of this article has been compromised.

Wiley and Hindawi regret that the usual quality checks did not identify these issues before publication and have since put additional measures in place to safeguard research integrity.

We wish to credit our Research Integrity and Research Publishing teams and anonymous and named external researchers and research integrity experts for contributing to this investigation.

The corresponding author, as the representative of all authors, has been given the opportunity to register their agreement or disagreement to this retraction. We have kept a record of any response received.

References

- [1] K. Ji, "Malicious Intrusion Data Mining Algorithm of Wireless Personal Communication Network Supported by Legal Big Data," *Wireless Communications and Mobile Computing*, vol. 2021, Article ID 8321636, 7 pages, 2021.

Research Article

Malicious Intrusion Data Mining Algorithm of Wireless Personal Communication Network Supported by Legal Big Data

Kai Ji 

China People's Police University, 065000 Langfang, China

Correspondence should be addressed to Kai Ji; dr.qya@qq.com

Received 23 July 2021; Accepted 4 September 2021; Published 25 September 2021

Academic Editor: Balakrishnan Nagaraj

Copyright © 2021 Kai Ji. This is an open access article distributed under the Creative Commons Attribution License, which permits unrestricted use, distribution, and reproduction in any medium, provided the original work is properly cited.

Wireless personal communication network is easily affected by intrusion data in the communication process, resulting in the inability to ensure the security of personal information in wireless communication. Therefore, this paper proposes a malicious intrusion data mining algorithm based on legitimate big data in wireless personal communication networks. The clustering algorithm is used to iteratively obtain the central point of malicious intrusion data and determine its expected membership. The noise in malicious intrusion data is denoised by objective function, and the membership degree of communication data is calculated. The change factor of the neighborhood center of gravity of malicious intrusion data in wireless personal communication network is determined, the similarity between the characteristics of malicious intrusion data by using the Markov distance was determined, and the malicious intrusion data mining of wireless personal communication network supported by legal big data was completed. The experimental results show that the accuracy of mining malicious data is high and the mining time is short.

1. Introduction

With the rapid development of electronic information technology, wireless communication technology has become the most critical technology in current communication. As the rapid development of wireless communication network, personal rapid communication has become a more pillar industry [1]. Personal and external real-time communication and understanding of information need to be through wireless communication network. At present, with the explosive growth of many kinds of big data in the society, the pressure of wireless communication network is increasing. At the same time, a large number of uncertain data in the personal communication network have a certain virus, which has a great impact on personal wireless communication security [2]. Wireless communication network ensures the normal transmission and exchange of a large amount of data but also ensures the security of data. At this time, the deep mining of large quantities of data in wireless communication becomes an indispensable link. Among them, in personal communication, the interference of some unknown information leads to the intrusion of personal privacy communication data, result-

ing in the security of personal communication information cannot be guaranteed [3]. At present, China's network security legal system is still in the process of step-by-step construction, but now, the network security has laws to follow [4]. Therefore, with the support of legal big data, researchers in this field have done a lot of mining for malicious intrusion data in wireless personal communication network to ensure the security of personal communication information.

In reference [5], a new malicious intrusion detection data method is proposed. This method can effectively filter the malicious intrusion data according to the set communication data white list, and the operation process is relatively simple. However, the type of communication data in the white list set by this method is less, and the accuracy of malicious intrusion data mining is low. In reference [6], a distributed intrusion data detection model based on deep forest algorithm is proposed. This method has high detection accuracy for intrusion data, but it is easy to be interfered by high noise data in the process of classification, resulting in poor detection results. In reference [7], a data mining-based abnormal data detection method for optical fiber communication network is proposed. The operation process of this

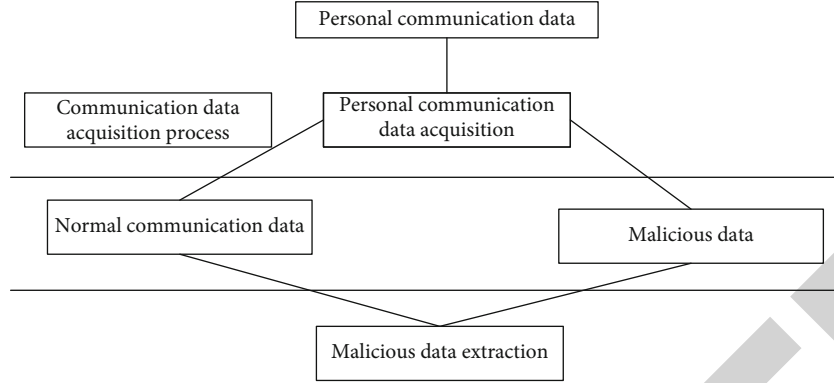


FIGURE 1: Acquisition process of malicious intrusion data.

method is relatively simple, and the clustering accuracy of feature attributes in classification is high, but the amount of data after attribute fusion is less, so it cannot be widely used.

In order to solve the shortcomings of the above methods, this paper proposes a malicious intrusion data mining algorithm for wireless personal communication networks supported by legal big data. With the help of clustering algorithm, the central point of malicious intrusion data is obtained iteratively, and the expected membership degree is determined to complete the malicious data acquisition in wireless personal communication. The noise in the malicious intrusion data is reduced by the objective function, and the membership degree of the communication data is calculated to complete the preprocessing of the intrusion data of the wireless personal communication network. The neighborhood center of gravity change factor of malicious intrusion data in wireless personal communication network is determined, the similarity degree between the features of malicious intrusion data is determined by the Markov distance, and the data features are normalized in the form of covariance matrix. The interference between malicious intrusion data was eliminated. With the help of sliding window calculation, the correlation between the features of malicious intrusion data is determined, and the nonlinear features of malicious data in different dimensions are calculated. The malicious intrusion data mining model of wireless personal communication network is constructed. The malicious intrusion data mining of wireless personal communication network supported by legal big data is completed.

2. Data Acquisition and Preprocessing of Malicious Intrusion in Wireless Personal Communication Network

2.1. Malicious Intrusion Data Collection in Wireless Personal Communication Network. China's network industry continues to develop, and there are many types of data in the network, easy to affect the values of the masses. Accordingly, our country has carried on the legislation management to some behavior in the network, manages the network environment unceasingly, and strives to provide the more comfortable and secure network communication space for the

people [8]. Therefore, before the advanced processing of malicious intrusion data in wireless personal communication network, it is necessary to collect malicious intrusion data in wireless personal communication network. In the process of personal wireless communication, the content data and virus data including communication are generated, which is malicious intrusion data. Therefore, this paper first designs a malicious intrusion data collection process, as shown in Figure 1.

In the malicious intrusion data acquisition of the wireless personal communication network, all the personal communication data is first collected and extracted from the wireless personal communication network environment to provide the basis for the subsequent data intrusion processing. The reasonable communication data in communication data acquisition and the different data are detected accordingly, and the data determined as malicious invasion will be processed, so as to reduce the insecurity of personal communication. In order to process the malicious data, this paper first gathers the wireless personal communication network data with the help of the clustering algorithm. Malicious data acquisition was completed in wireless personal communication by continuously iterating acquiring the central point of malicious intrusion data and determining the expected relevant membership of the [9].

Suppose the data set of wireless personal communication is

$$Q = \{q_1, q_2, \dots, q_n\}. \quad (1)$$

All the data in formula (1) are divided into clusters, and the central data of wireless personal communication data are set as follows:

$$P = \{p_1, p_2, \dots, p_n\}. \quad (2)$$

The data point center in formula (2) is randomly generated in the wireless personal communication data, and because it cannot be strictly restricted, its membership should be calculated, namely

$$W = P \left(\sum U_i \right). \quad (3)$$

In the formula, W represents the degree of affiliation of data point center data, and U_i represents a cluster of wireless personal communication data.

All communication data are classified according to the membership degree between the above wireless personal communication data. Because wireless personal communication data mainly includes two kinds of data, one is normal data and the other is malicious intrusion data [10], it is necessary to separate malicious intrusion data from all data. That is to become the focus of this study data. Through formula (4), the analysis is as follows:

$$E(X) = \sum_{i=1}^n U_i W V_j. \quad (4)$$

In the formula, V_j represents fuzzy weights, and it is a constant greater than 0.

According to the above analysis, the acquisition of malicious intrusion data in the wireless personal communication network is realized. Basic data support for subsequent mining is provided.

2.2. Preprocessing of Malicious Intrusion Data in Wireless Personal Communication Network. Because there is some noise and indistinguishable normal communication data in the malicious intrusion data of wireless personal communication network obtained above, it is necessary to preprocess the malicious intrusion data of wireless personal communication network. First, the noise in the malicious intrusion data is reduced by the objective function, that is

$$G = \sum_{i=1}^n \sum_{j=1}^m d_{ij} h_{ij} U_i + \beta \left(1 - \sum_{i=1}^n d_{ij} \right). \quad (5)$$

In the formula, G represents the target function, d_{ij} represents the Gaussian noise data of the malicious intrusion data, h_{ij} represents the white noise data of the malicious intrusion data, and β represents the noise reduction factor.

In the process of noise reduction of malicious intrusion data in wireless personal communication network, secondary noise reduction is needed to ensure the accurate extraction of malicious intrusion data, that is

$$U(t) = \mu \frac{1}{\sum_{i=1}^n (h_{ij}/d_{ij})}. \quad (6)$$

In the formula, μ describes the central point of malicious intrusion data.

After noise reduction of the above wireless personal communication data, we should further distinguish the non-malicious intrusion data doped in the malicious intrusion data and delete it effectively [11]. First, this type of data is set to

$$Y = \{y_1, y_2, \dots, y_n\}. \quad (7)$$

If the membership degree is 0 or less than 0, this part of the data is deleted. If the communication data is greater than 0, the communication data is considered malicious intrusion data [12], that is

$$R = \begin{cases} \sum_{i=1}^n d_{ij} > 0 \\ \sum_{i=1}^n d_{ij} < 0. \end{cases} \quad (8)$$

By judging the membership degree of nonmalicious data in malicious data, the set of malicious intrusion data is determined, and the preprocessing of wireless personal communication intrusion data is completed.

3. Construction of Malicious Intrusion Data Mining Model for Wireless Personal Communication Network

According to the above obtained malicious intrusion data of wireless personal communication network, in order to ensure the security of wireless personal communication, the influence of malicious intrusion data is deeply processed, through the construction of wireless personal communication network.

First, the neighborhood center of gravity change factor of the malicious intrusion data of the wireless personal communication network is determined to obtain the main feature of the malicious intrusion data [13].

Suppose ρ_i describes the length between the center of gravity $a(\rho)$ and $a+1(\rho)$ of malicious intrusion data in a wireless personal communication network; then, there is

$$\rho_i = D[a(\rho) + a - 1(\rho)]. \quad (9)$$

At this time, the malicious data center of gravity in wireless personal communication is the largest, but because of the fluctuation of its peripheral data, the data center of gravity cannot always be kept as the maximum value [14], and the absolute difference between $a(\rho)$ and $a+1(\rho)$ therefore needs to be calculated to obtain

$$\Delta\rho_i = D[a(\rho) - a + 1(\rho)]. \quad (10)$$

At this time, it can guarantee the maximum value of malicious data center of gravity in wireless personal communication. The maximum value is quantized, and the change factor of its neighborhood center of gravity is as follows:

$$IN(\rho) = \sum_{i=1}^m \Delta\rho_i. \quad (11)$$

The larger the value of formula (11), the more obvious the abnormal characteristics of malicious data in wireless personal communication.

After determining the abnormal characteristics of malicious data in wireless personal communication, the Mahalanobis distance is used to determine the similarity between the features of malicious intrusion data, which provides more powerful evidence for its mining [15]. The Markov distance is normalized to the data features in the form of covariance matrix to eliminate the interference between malicious intrusion data [16].

The time period of wireless personal communication was set as t . At this time, the feature vector of malicious intrusion data is h , its dimension is set to b , and the feature vector matrix of malicious intrusion data is determined in $t-1$ period as follows:

$$H_{(t-1)} = [h_{t-1}, h_{t-2}, \dots, h_{t-n}]^T. \quad (12)$$

By calculating the covariance matrix, the following results are obtained:

$$K(P) = \sqrt{(h_{t-1} - h)^{T-1}}. \quad (13)$$

According to formula (13), the minimum value of the eigenvector is determined [17], namely

$$\min K(P) = \text{dis} \sqrt{(h_{t-1} - h)^{T-1}}. \quad (14)$$

Based on the above calculation of abnormal malicious intrusion data characteristic vector of personal wireless communication, we analyze the characteristics of malicious intrusion data feature vector distribution and set the amount of malicious intrusion data in a certain communication as follows:

$$S_{ir} = [z_1, z_2, \dots, z_i, \dots, z_{i+1}]. \quad (15)$$

According to the amount of data, the sliding window is calculated to determine the correlation between the characteristics of malicious intrusion data [18], that is

$$Z(t) = \frac{\sum_{a=1}^m (z - z_i)}{\sqrt{\sum_{a=1}^m (z - z_i)} \sqrt{\sum_{a=1}^m (z_i - z_{i+1})}}. \quad (16)$$

According to the characteristic correlation between the above malicious intrusion data, the malicious data is regarded as different characteristics in each dimension, and the final amount of each malicious data is determined according to the calculation of its high and low dimensions [19, 20].

Based on the above analysis, the nonlinearity of malicious intrusion data is determined, and the nonlinear characteristics of malicious intrusion data are constructed by

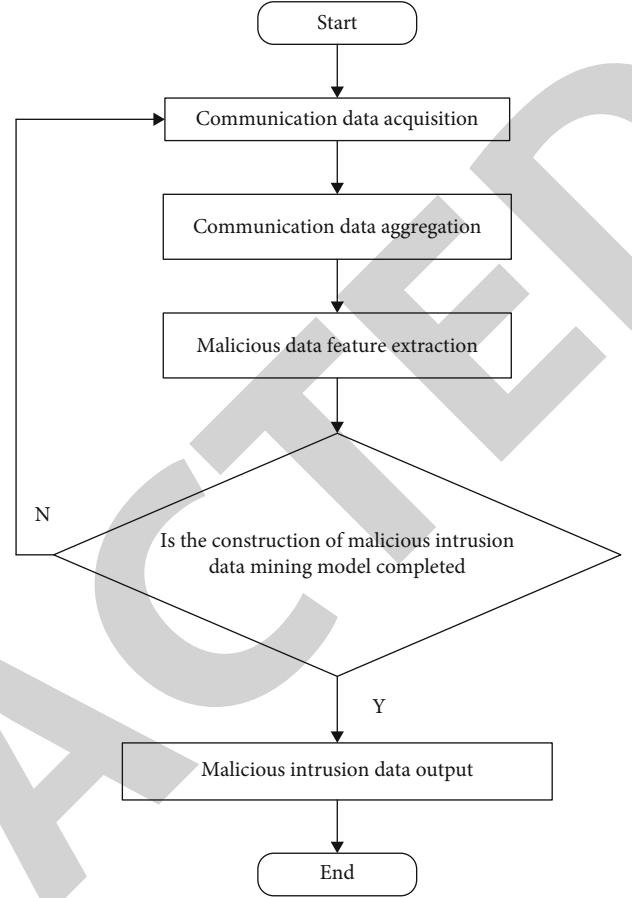


FIGURE 2: Flow chart of malicious intrusion data mining of wireless personal communication network.

the kernel function, that is

$$s = \frac{1}{m} \sum \sigma(x) \theta(xx^t). \quad (17)$$

In the formula, σ and θ represent the nonlinear feature of malicious data in different dimensions, respectively.

On this basis, the construction of malicious intrusion data mining model of wireless personal communication network is completed, that is

$$\aleph = K_i \left(\sum_{i=1}^m K_i + s \sum_{j=1}^m z(t) + \frac{1}{N} K_i \right). \quad (18)$$

In the formula, K_i represents the K primary component of malicious intrusion data for wireless personal communications networks.

The malicious intrusion data mining of the wireless personal communication network was completed by formula (18), and the implementation process is as shown in Figure 2.

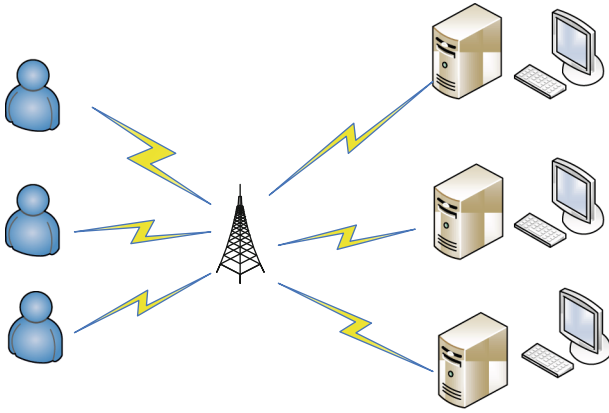


FIGURE 3: Experimental environment.

TABLE 1: Experimental parameters.

Parameter	Data
Sample communication data (GB)	2
Normal communication data (bar)	1000
Malicious communication data (bar)	1000
Data mining interval (s)	2
Data interference noise (dB)	0-2
Number of iterations (times)	100

4. Experimental Analysis

4.1. Experimental Environment. To verify the effectiveness of the mining algorithm, the experiment is realized by the simulation software, the Apple system, and the memory of 16 GB; experimental data are processed through the SPSS 13.0 software. The specific experimental environment is shown in Figure 3.

4.2. Design of Experimental Parameters. In order to ensure the effectiveness of the experiment, the relevant parameters used in the experiment are set up, as shown in Table 1.

4.3. Experimental Index Design. On the basis of the above experimental environment and parameter design, the experiment is carried out by comparing the methods of this paper, reference [5], reference [6], and reference [7]. The experimental indexes are the precision of malicious intrusion data mining in wireless personal communication network, the time consumption of mining, and the error of malicious intrusion data extraction. In order to ensure the credibility of the experimental data, the experimental results are iterative 100 times, and the results are verified many times.

4.4. Result

4.4.1. Accuracy Analysis of Different Methods of Malicious Intrusion Data Mining. The accuracy of malicious intrusion data mining in wireless personal communication network is the key index to measure the mining algorithm. The higher the value, the better the effect of mining. Therefore, results of the experimental comparison of this method and the

methods from references [5], [6], and [7], to sample wireless personal communication network malicious intrusion data mining accuracy, are shown in Figure 4.

The analysis of the experimental results in Figure 4 shows that as the sample intrusion data increases, four methods have changed the accuracy of malicious intrusion data mining. When the malicious data is 800, the accuracy of this method is about 98%, about 79% of the accuracy of the method in reference [5], about 82% of the accuracy of the method in reference [6], and about 75% of the accuracy of the method in reference [7]. When the malicious data is 1600, the accuracy of this method is about 99%, about 71% of the accuracy of the method in reference [5], about 80% of the accuracy of the method in reference [6], and about 65% of the accuracy of the method in reference [7]. By comparing these four methods, we can see that the accuracy of this method is the highest. The practical effectiveness of this method is verified.

4.4.2. Time-Consuming Analysis of Malicious Intrusion Data Mining by Different Methods. Based on the basis of the mining accuracy, the time consumption of malicious intrusion data mining of this method and the methods in references [5], [6], and [7] is analyzed. The results are shown in Table 2.

As can be seen from the data in Table 2, with the increase of sample data, the four methods have changed the mining time of malicious intrusion data. When the sample data is 600, about 2.3 s is consumed by the mining time in this method. The mining time of the method in reference [5] is about 3.2 s. The mining time of the method in reference [6] is about 3.3 s. The mining time of the method in reference [7] is about 3.1 s. When the sample data is 1200, about 2.4 s of the mining time is taken. The mining time of the method in reference [5] is about 4.0 s. The mining time of the method in reference [6] is about 4.2 s. The mining time of the method in reference [7] method is 3.9 s. When the sample data is 2000, about 2.3 s of mining time is consumed in this method. The mining time of the method in reference [5] is about 6.1 s. The mining time of the method in reference [6] is 5.6 s. The mining time of the method in reference [7] is about 5.2 s. The analysis of the data shows that in the four methods of sample data mining, the time-use change of this method is stable, and the other three methods of mining time are on the rise. The effectiveness of this method is verified.

4.4.3. Error Analysis of Malicious Intrusion Data Extraction by Different Methods. In order to further reflect the reliability of the proposed method, the error analysis of the present method and the methods in references [5] and [6] and sample malicious intrusion data extraction in the method in reference [7] are analyzed. The results are shown in Figure 5.

According to the experimental results in Figure 5, there are some differences in the error of extracting malicious intrusion data by four methods. With the increase of sample data, the extraction errors of the four methods show a downward trend. And convergence is also increasing. Among them, the minimum error of this method is about 0.2%

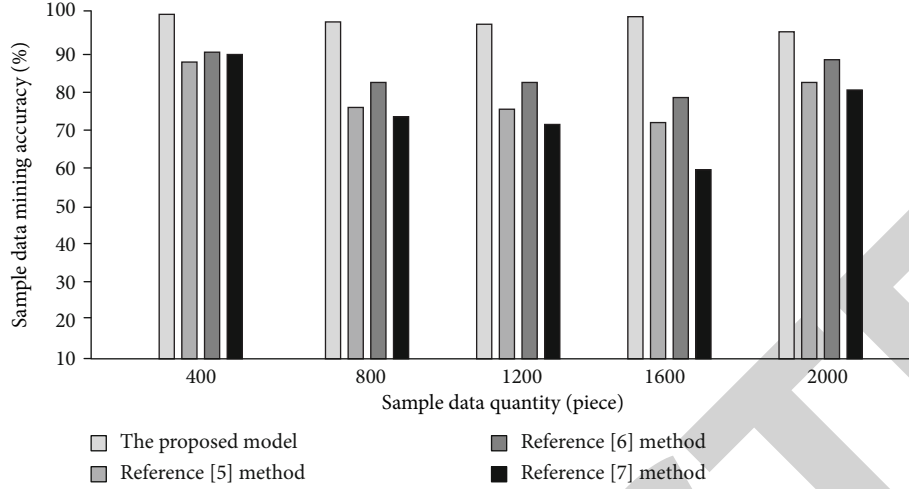


FIGURE 4: Accuracy analysis of malicious intrusion data mining with different methods.

TABLE 2: Time-consuming comparison of malicious intrusion data mining (s).

Sample data/bar	Methods of this paper	Method in reference [5]	Method in reference [6]	Method in reference [7]
200	2.3	2.8	2.5	2.3
400	2.2	3.1	2.8	2.8
600	2.3	3.2	3.3	3.1
800	2.4	3.5	3.5	3.5
1000	2.5	3.7	3.8	3.7
1200	2.4	4.0	4.2	3.9
1400	2.2	5.1	4.5	4.2
1600	2.3	5.6	4.7	4.5
1800	2.4	5.7	5.1	4.8
2000	2.3	6.1	5.6	5.2

[5], the minimum error in extracting malicious intrusion data is about 1.6% [6], the minimum error in extracting malicious intrusion data is about 0.8% [7], and the minimum error in extracting malicious intrusion data is about 0.6%. Compared with the other four methods, this method has increased by about 1.4%, 0.6%, and 0.4%, respectively. The proposed method is more effective. It is verified that the effectiveness of this method is better in these four methods. The control of malicious intrusion data in personal communication will be better and more advantageous.

5. Conclusion

This paper proposes a malicious intrusion data mining algorithm for wireless personal communication network supported by legal big data. With the help of the calculation of the sliding window to determine the correlation between the characteristics of malicious intrusion data and to calculate the nonlinear characteristics of malicious data in different dimensions, the malicious intrusion data mining model of wireless personal communication network was built, and the malicious intrusion data mining of wireless personal communication network supported by legal big data was completed. This method has the following advantages:

- (1) The highest accuracy of mining malicious data using the proposed method is about 98%, with a certain reliability
- (2) The proposed method is the shortest time-consuming to mining malicious data and improves the efficiency of the algorithm
- (3) The proposed method shows the low extraction error of malicious data.

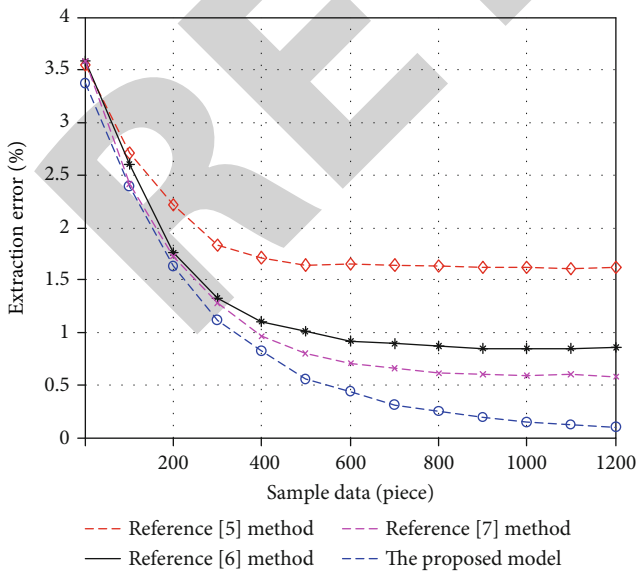


FIGURE 5: Error analysis of malicious intrusion data extraction by different methods.

Data Availability

Data sharing is not applicable to this article as no datasets were generated or analyzed during the current study.

Retraction

Retracted: Research on the Development Path of a Cross-European e-Commerce Logistics Mode under the Background of “Internet Plus”

Wireless Communications and Mobile Computing

Received 1 August 2023; Accepted 1 August 2023; Published 2 August 2023

Copyright © 2023 Wireless Communications and Mobile Computing. This is an open access article distributed under the Creative Commons Attribution License, which permits unrestricted use, distribution, and reproduction in any medium, provided the original work is properly cited.

This article has been retracted by Hindawi following an investigation undertaken by the publisher [1]. This investigation has uncovered evidence of one or more of the following indicators of systematic manipulation of the publication process:

- (1) Discrepancies in scope
- (2) Discrepancies in the description of the research reported
- (3) Discrepancies between the availability of data and the research described
- (4) Inappropriate citations
- (5) Incoherent, meaningless and/or irrelevant content included in the article
- (6) Peer-review manipulation

The presence of these indicators undermines our confidence in the integrity of the article’s content and we cannot, therefore, vouch for its reliability. Please note that this notice is intended solely to alert readers that the content of this article is unreliable. We have not investigated whether authors were aware of or involved in the systematic manipulation of the publication process.

Wiley and Hindawi regrets that the usual quality checks did not identify these issues before publication and have since put additional measures in place to safeguard research integrity.

We wish to credit our own Research Integrity and Research Publishing teams and anonymous and named external researchers and research integrity experts for contributing to this investigation.

The corresponding author, as the representative of all authors, has been given the opportunity to register their

agreement or disagreement to this retraction. We have kept a record of any response received.

References

- [1] W. Zhu and M. Shi, “Research on the Development Path of a Cross-European e-Commerce Logistics Mode under the Background of “Internet Plus,”” *Wireless Communications and Mobile Computing*, vol. 2021, Article ID 6964302, 7 pages, 2021.

Research Article

Research on the Development Path of a Cross-European e-Commerce Logistics Mode under the Background of “Internet Plus”

Wangli Zhu  and Meixia Shi 

School of Economics and Management, Beijing Jiaotong University, Beijing, China

Correspondence should be addressed to Wangli Zhu; 15113183@bjtu.edu.cn

Received 5 August 2021; Accepted 30 August 2021; Published 21 September 2021

Academic Editor: Balakrishnan Nagaraj

Copyright © 2021 Wangli Zhu and Meixia Shi. This is an open access article distributed under the Creative Commons Attribution License, which permits unrestricted use, distribution, and reproduction in any medium, provided the original work is properly cited.

Cross-border e-commerce and the logistics industry are interrelated in specific economic and circulation fields. Based on the development of cross-border e-commerce in China and Europe, this paper analyzes the economic development of China's cross-border e-business logistics providers in the context of Internet plus and analyzes the development trend of cross-border e-commerce in China and gives suggestions for optimization, with a view to providing cross-border e-commerce for the future. In-depth cooperation provides reference.

1. Introduction

The rapid development of transnational E-commerce needs not only the innovation of the e-commerce mode but also the perfection of the logistics mode and logistics system. At the same time, the development speed of cross-border logistics is closely related to the openness of policies. Cross-border e-commerce is an advanced application of e-commerce [1]. Different countries and regions can realize the digitization of traditional trade display, negotiation, and transaction through the Internet and realize the new mode of product import and export trade through network mail and express declaration [2]. In the modern society, e-commerce is one of the indispensable means of computer processing information and is a new way of information processing; it and logistics promote each other, for common development. It will greatly improve the efficiency of logistics services, meet the needs of the market at a higher level, and meet the needs of consumers. European cross-border e-commerce logistics management is a new trend of economic and social development since the 21st century,

which is highly recognized and supported by domestic and foreign counterparts.

At present, China has basically realized cross-border trade e-commerce. The traditional foreign trade “container” type of large transactions gradually reduced, and most of the small-batch, multibatch, and fast delivery foreign trade orders appeared. In people's daily life, more and more consumers choose to collect foreign high-quality products and services through the Internet. The new mode of overseas direct shopping without foreign trade agents is gradually accepted by more and more people [3]. The change of consumers' concept promotes the development of cross-border e-commerce. Whether the goods can arrive on time, whether the safety is achieved, and whether the quality is guaranteed are very important factors that consumers need to consider when shopping, which also involves the e-commerce logistics. Logistics plays a key role in cross-border e-commerce [4]. First of all, any transaction of cross-border e-commerce involves information flow, capital flow, business flow, and logistics flow. As the last part of the transaction, logistics is related to the success or failure of

cross-border e-commerce transactions. Secondly, because cross-border e-commerce transactions involve many countries and the distance is long, the logistics cost is high. Therefore, this paper studies the logistics mode selection under the background of cross-border e-commerce.

2. Research on the Development Path of the Cross-Border e-Commerce Logistics Mode

2.1. Survey on the Development of the Cross-Border e-Commerce Logistics Mode between China and Europe. Europe is China's third largest trading partner. With the continuous expansion of bilateral investment between China and the EU, the sales volume of the bilateral trade has increased by more than 15%. Since the cooperation of China EU free trade area, bilateral cooperation has been deepened [5]. The growth of China's domestic demand has driven the development of European countries. It has also strengthened the industrial chain cooperation with European countries, improving the economic and technological levels of both sides and increasing the demand for mutual cooperation. In recent years, with the advancement of the "Belt and Road" Initiative, economic cooperation between China and Europe has become more extensive and China's investment in Europe has increased. By the end of 2018, China's total investment in Europe was 318.0 billion US dollars [6]. Due to the different degree of e-commerce development in European countries, the development of the logistics distribution system is also different. Generally speaking, the cross-border e-commerce logistics distribution system of China and Europe is relatively weak, because the cross-border logistics system is controlled by transnational e-commerce companies, so it is difficult to use it to distribute third-party goods [7]. Generally speaking, compared with some European and American countries that develop e-commerce, the construction of e-commerce laws and regulations in European countries needs to be strengthened. At the same time, the rapid development of e-commerce and expanding the scale of European countries have also formulated corresponding e-commerce policies and regulations.

According to the survey, from 2008 to 2012, the volume of export and cross-border e-commerce transactions exceeded 90%. In recent years, with the advancement of the "Belt and Road" Initiative and the development of the digital economy, the proportion of cross-border e-commerce import transactions has continued to increase. In 2013, the scale of cross-border e-commerce import transactions accounted for 14.3%, and by 2018, it exceeded 20%. From the perspective of the distribution of import and export structures, China's import and export proportion is relatively low but it shows an upward trend year by year. With the gradual opening of the cross-border e-commerce market, the proportion of import and export will gradually increase [8]. With the implementation of the "14th Five-Year Plan", the high-quality construction of the "Belt and Road" will be promoted. At present, China has carried out extensive cooperation with European countries in the fields of open trade, service, and investment. China's cross-border e-commerce market is still in the early stage of development, mainly to provide information services. However, with the development of the industry, cross-border

e-commerce effectively reduces the intermediate links and promotes the development of import trade. In the multilevel and multilink supply chain cooperation, cross-border small e-commerce transactions will also get rapid development [9]. In the early years, <http://JD.com> regarded cross-border e-commerce as a vital strategic development goal. In these years, it has indeed done so. At present, JD Global Shopping has successfully entered the international stage and occupies an extremely important position. In order to better promote the healthy development of accounting e-commerce logistics mode, the integration mode of cross-border e-commerce logistics supply chain service platform is optimized and the specific structure is shown in Figure 1.

The figure includes warehousing, logistics, and other links. Through integration, the global resource allocation is optimized, the enterprise cost is reduced, and the import and export trade is promoted, to provide better service for consumers [10]. For cross-border e-commerce transactions, cross-border logistics is the key factor restricting the development of the entire cross-border e-commerce industry and the delivery speed directly affects the shopping experience of consumers. The rapid rise of international e-commerce provides opportunities for cross-border logistics [11]. The cross-border logistics transportation has developed from single package transportation to the coexistence of multiple transportation modes, mainly package transportation. It is found that reducing transportation costs, ensuring the safety of goods, and realizing the traceability of logistics information are the future development direction [12]. The distribution mode needs innovation. Therefore, exploring and innovating the third-party logistics mode to adapt to the development needs of cross-border e-commerce in China have become the key to the development of cross-border e-commerce in China.

2.2. Comparative Analysis of Existing Cross-Border e-Commerce Logistics Modes. International packets mainly refer to China Post, Hongkong Post, and Singapore Post. International express usually refers to the four giants, such as FedEx, DHL, TNT, and UPS. These two ways are the most traditional and the simplest way of logistics [13]. For most small- and medium-sized enterprises, they are the only alternative way of logistics. Postal has almost global coverage of the network, it can be said that the degree of network coverage is wider than any other logistics channels. Of course, this is due to two organizations: the Universal Postal Union and the Kahala postal Organization (KPG). International parcel and international express are relatively simple and direct logistics modes [14]. There are two characteristics of international small bags: first, the price is cheap, and second, the delivery time is long. The time limit for transportation is about 5–10 days for Asian neighbors, 7–15 days for major European and American countries, and 7–30 days for other regions and countries [15]. Compared with the international package, the international express delivery time is shorter but its cost is higher. Although the way of international small package is convenient and flexible, it is risky. There are still some problems in postal packets, such as high-packet loss rate and no way to track if the items are not registered. But even so, for small-scale foreign trade enterprises,

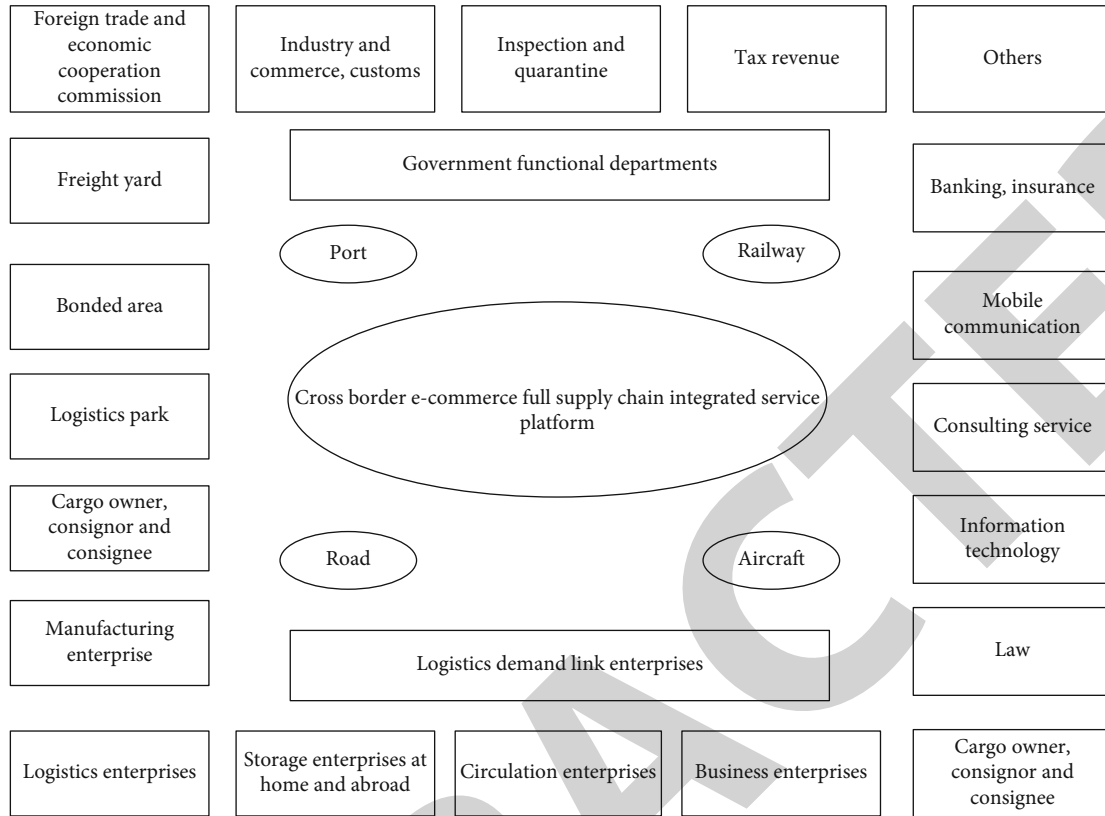


FIGURE 1: Cross border e-commerce logistics supply chain service platform.

international small bags and express delivery are still the most common choice of logistics. Postal service has almost a global network, and postal packets can reach any place with a post office, which can also greatly expand the trade market of the cross-border e-commerce platform. Moreover, the application scope of postal packets is wide and platforms such as eBay and Dunhuang can be used without special mailing restrictions.

Here, Table 1 is a set of statistical data from Sifang Express Company on the service level of postal parcels. In Table 1, we can see that the logistics in Singapore and Malaysia has the highest success rate to arrive in 15 days. And Brazil has the lowest; it is almost impossible to complete within 15 days; even for 20 days, it is almost impossible. Singapore has the highest logistics efficiency, while at the same time, Brazil has the lowest logistics efficiency.

About international express, as shown in Table 1, its biggest advantage is stable and fast and the information is very transparent. Consumers can obtain the transportation route and transportation time of goods by querying the logistics information and the phenomenon of packet loss is rare, which is relatively stable [16]. The time limit is basically maintained at about 3–5 days, and there is no great restriction on the weight of goods, so it is also a logistics mode that many cross-border e-commerce enterprises are willing to choose. Express giants also have their own unique characteristics; especially when different weights of express are sent to different continents, there are obvious differences. For example, when it is sent to Western European countries, TNT's

customs clearance speed is the fastest, while UPS's speed is extremely fast when it is sent to the United States.

But it also has its own disadvantages, mainly in the following two aspects. First, the price is more expensive. Under the same weight, the charge standard of international express is almost twice that of the international small package. Therefore, if you are not so eager for the goods you are shopping for, you will not be willing to choose the international express mode. Second, there are surcharges in remote areas. International express has not covered its distribution network all over the world. Therefore, compared with the small package, there are many places that cannot be covered. There will be such a situation when the customer has paid the express fee, but when the goods are transported to your hands, the relevant express company will charge a surcharge of 100–300 yuan in remote areas.

3. China EU Cross-Border e-Commerce Logistics Path Selection

There are two logistics modes available for cross-border enterprises in the past, one is mail express and the other is to deposit goods in overseas warehouses. On this basis, the logistics model is divided into parcel express and overseas warehouse, among which overseas warehouse can be divided into the self-supporting mode and outsourcing mode [17]. The effective cross-border e-commerce logistics mode is selected reasonably for comparative analysis, as shown in Table 2.

TABLE 1: Performance of postal parcel service level.

Main destinations	Arrived within 15 days	Arrived in 20 days	Main prescription
Brazil	0.1%	7.0%	19~28 days
Germany	32.3%	54.8%	12~15 days
The United Kingdom	51.8%	53.7%	5~17 days
Malaysia	82.2%	87.4%	10~15 days
Russia	12.1%	19.8%	15~23 days
Singapore	96%	98.9%	5~9 days
Thailand	41.3%	44.8%	5~16 days
U.S.A	48.8%	67.3%	14~22 days

From the analysis of Table 2, it can be seen that the external factors have the greatest influence and the internal factors have the least influence. Its function mode is certain economic, and the institutional environment is the basis of restricting the formation of a cross-border e-commerce logistics mode [18]. Technological progress improves management efficiency and reduces transaction cost, which is the economic portrayal of logistics mode transformation. Under the joint action of the economic system environment, consumer behavior preference, and technological progress, transaction cost has a direct impact on the choice of the enterprise logistics mode, so as to obtain the maximum benefits. Based on this, the selection conditions of the logistics mode are standardized, as shown in Figure 2.

Among them, logistics cost is the first link of enterprise logistics decision. When multinational e-commerce enterprises choose the logistics mode, they must consider the total cost of the logistics system. According to the different links of logistics, the total logistics cost can be divided into inventory maintenance costs, transportation costs, customer maintenance costs, etc [19]. If T_c represents the total logistics cost, the total logistics cost is shown as formula (1) as follows:

$$T_c = S + T + L + C + P + F. \quad (1)$$

In formula (1), S represents the cost of inventory maintenance, which includes the cost of inventory management, packaging, and rework. T is all expenses incurred in transportation; L is the batch cost, i.e., material processing and purchasing cost; C is customer cost, i.e., shortage and customer loss cost; P is order processing and information cost; F is fixed and warehouse variable cost. There are contradictions and conflicts in the composition of logistics cost. For the choice of the logistics mode, we should first consider the logistics cost and then make a reasonable choice.

4. Constraint Algorithm for Logistics Mode Selection of Cross-Border e-Commerce

When cross-border e-commerce logistics services are provided, the demand function is set as $f(t) = kt$ and the seller chooses to deliver the goods at T_1 time and store the goods to the overseas warehouse. The change rate of the demand is

$Q_1(t)$, in which $f_1(t) = K_1 t$, $K_1 > k$; if the initial investment profit of logistics express is p , the transportation cost allocated to each cargo is CF , the monetary unit of the discount rate. Based on the general dynamic equilibrium model, the discount value of the long-term profit maximization function is given.

$$\max E_0 = TC \int_0^T e^{-n} [Q_1 z(t) \times f(t)] dt - c_j e^{-\gamma T} + \int_T^{+\infty} e^{-n} [(p - c_f) \times f_1(t)] dt. \quad (2)$$

Firstly, the weight of each index is determined and each index is analyzed and decomposed. The highest level is the target level, the middle level is the index level, and the lowest level is the scheme level. The priority judgment matrix is established. According to the relative importance of the elements of this layer to the elements of the upper layer, the fuzzy consistent judgment matrix is established. In the process of actual decision-making analysis, due to the complexity of the problem and the one sidedness of people's cognition of the problem, the constructed judgment matrix is often lacking of consistency, which needs to be transformed into the fuzzy consistent judgment matrix by using the transformation formula. The transformation formula is shown in formula (3).

$$r_{ij} = 0.5 + \frac{r_i - r_j}{2n}. \quad (3)$$

In formula (3), $r_i \sum_{j=1}^n f_{ij}$ and the priority judgment matrix $F = (f_{ij})_{n \times n}$ is transformed into a fuzzy consistent judgment matrix.

$$R = (r_{ij})_{n \times n} = \begin{bmatrix} r_{11} & r_{12} & \cdots & r_{1n} \\ r_{21} & r_{22} & \cdots & r_{2n} \\ \vdots & \vdots & \ddots & \vdots \\ r_{n1} & r_{n2} & \cdots & r_{nn} \end{bmatrix}. \quad (4)$$

In terms of logistics mode, there are three main logistics strategies of enterprises: always choose the parcel express mode and directly the choose overseas warehousing and distribution mode and the overseas distribution mode within a certain period of time from parcel express to the destination. According to the fuzzy consistent judgment matrix, formula (2) is differentiated and simplified and the basic conditions are obtained, as shown in formula (3).

$$rc_F \max E_0 + [pk - k_1(p - c_f)] T = 1. \quad (5)$$

In formula (5), according to the above formula, when $p - k_1(p - c_f) \geq 0$, the value range of E is $T = +\infty$; if $pk - k_1(p - c_f)$ is less than 0, then,

TABLE 2: Selection of cross border e-commerce logistics mode.

	International bag	International express service	Overseas warehouse
Delivery time	Slow	Fast	Fast
Delivery efficiency	Low	High	High
Logistics cost	Low	High	According to the turnover rate of goods
Initial investment risk	Nothing	Nothing	Certain investment
Cargo restrictions	Weight, volume	Weight, volume	Nothing

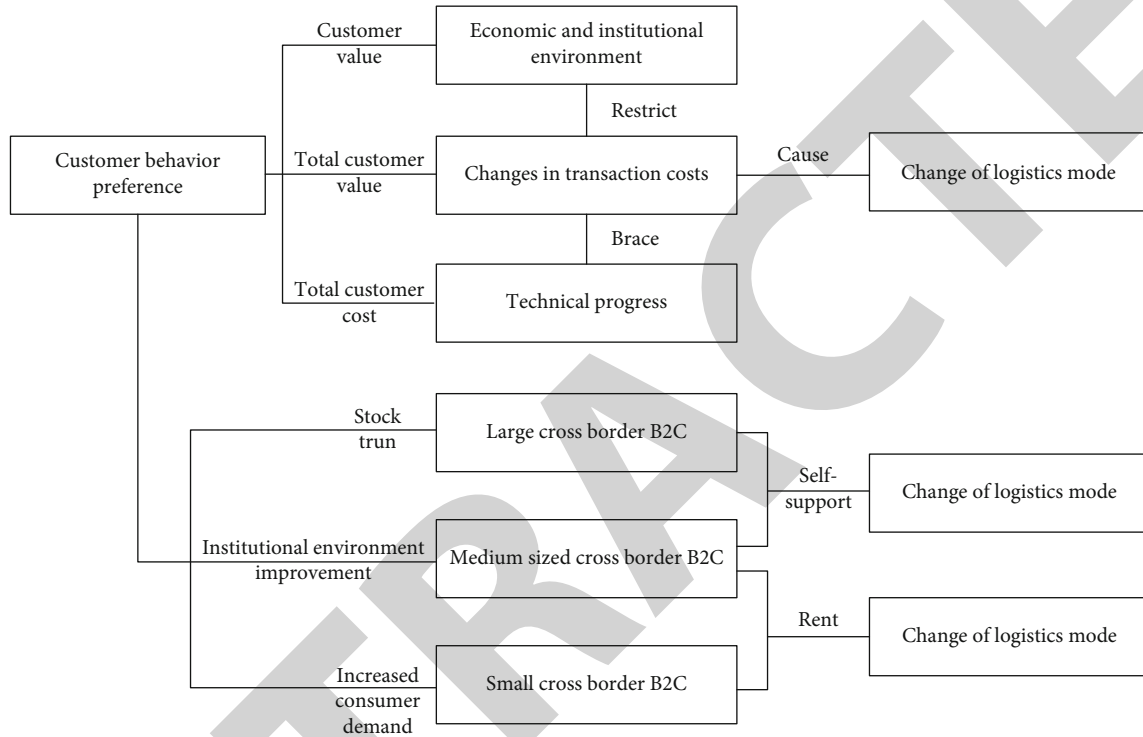


FIGURE 2: Logistics mode selection conditions.

$$T + \frac{rc_F}{k_1(p - c_f)} - pk. \quad (6)$$

Through formula (6), it can be seen that in the calculation process, the higher the value of p , the higher the profit margin of using high-value products, the easier it is to maximize the profit of overseas warehouses by using overseas warehouses, the more sensitive transaction costs are, and the easier it is for k_1 to maximize the operation of overseas warehouses in this region; the more the capital investment of enterprises, the later the use of overseas warehouses will be. It can be seen that the higher the commodity price, the stronger the logistics cost bearing capacity and the stronger the market sales ability [20]. The use of overseas warehouses can increase profits. On this basis, from the current opening strategy of cross-border e-commerce, developed countries have basically formed the export of warehousing goods to Europe and the United States. The main reasons for this phenomenon are that the relevant legal system is not sound, the policy is not transparent, and enterprises are more suspicious of investing in overseas warehouses, because these

countries have too much foreign exchange reserves, which makes it difficult to recover the investment. Put forward the important role of policy threshold in the choice of the logistics mode. Labor costs are also an important part of the cost. There is a huge gap between China and European countries. European countries have higher social security costs, minimum wage levels, working hours, and rest and vacation standards than China, so labor costs are also higher. In addition, the General Data Protection Regulations (GDPR) issued by the European Union may be a challenge for China-EU cross-border e-commerce logistics. As China's awareness of personal information data protection increases, China-EU cross-border e-commerce logistics will become more standardized.

5. Suggestions on the Development of Cross-Border e-Commerce Logistics between China and Europe

With the development of the economy, consumers' shopping demand is also growing. When the domestic market

cannot meet the demand, consumers will turn their attention to foreign countries. From China's per capita consumption data, cross-border e-commerce provides a huge growth opportunity for per capita consumption [21]. At the same time, with the development of economy, the logistics mode of cross-border e-commerce has changed from the traditional "container-type" transportation to the current multiple transportation modes, enabling enterprises to set up warehouses overseas and choose the third-party logistics, so as to better provide logistics services for customers. With the rapid development of China's economy, consumers' demand for purchased goods and logistics is growing and the cross-border e-commerce logistics mode is constantly emerging. The main reason for overseas shopping is the uneven distribution of resources, which can bring about user experience. It should be the focus of cross-border e-commerce enterprises, and economic development will inevitably affect the scale of cross-border e-commerce and the choice of the logistics mode.

The freight industry is a very complex industry. The global development of network makes freight transportation an indispensable part of people's life, helping customers understand the international logistics system and promoting cross-border trade [22]. When choosing logistics for different goods purchased by foreign consumers, we should pay attention to the return information of customers at any time and update the logistics information of commodity distribution in time, so as to promote the coordinated development of online and offline and better carry out cross-border logistics. In the network era, the cross-border logistics testing industry has developed rapidly. In the face of global customers, the logistics workload is increasing and the pressure of supervision is increasing [23–25]. Therefore, it is necessary to strengthen logistics supervision to ensure the normal operation of cross-border logistics in a certain period of time and it cannot be stagnated due to regulatory problems in a certain link. It is the ultimate goal of logistics enterprises to deliver goods to consumers within the specified time. In order to carry out international e-commerce logistics, we should not only pay attention to the cooperation between logistics but also attach importance to the integration of enterprise advantages, so as to shorten the transaction time and reduce the logistics cost.

The outbreak of the new crown epidemic has had a serious impact on the global economy. As an export-oriented country, China is an importer of basic daily necessities in most countries. The epidemic may promote the development of e-commerce and at the same time have a certain reform and promotion effect on the logistics model. The integration of digitization and intelligence may become an important direction of the cross-border e-commerce logistics reform model, and it is also an opportunity for Chinese-funded enterprises. The current cross-border logistics cannot meet the needs of the rapid development of cross-border e-commerce. The development direction of cross-border logistics is to shorten the logistics cycle, reduce transportation costs, ensure the safety of goods, and realize the traceability of logistics information. Modern logistics mode needs innovation. On this basis, we will explore and innovate the third-party logistics mode

to better meet the needs of cross-border e-commerce development in China. Cross-border e-commerce logistics will continuously improve the efficiency of warehousing, inventory, ordering, distribution, and other links and provide more convenient services for cross-border e-commerce.

6. Conclusion

Under the environment of e-commerce, whether the digital management of logistics transportation can be realized is an important symbol to measure the development level of a country. In today's world, the development of the economy and market is increasingly integrated. With the advancement of the "Belt and Road" Initiative and the rise of the digital economy, China-Europe cross-border e-commerce will move to a new level and the logistics industry will also develop rapidly. How to effectively apply e-commerce to data processing, so as to realize the transformation from logistics reexport to transportation management, is also a powerful means to further improve the efficiency of logistics services. Through the analysis of the current situation of logistics and transportation management in China, the development and development path of the logistics mode of cross-border e-commerce in China and Europe under the background of "Internet plus" are studied. The optimization suggestions are put forward accordingly to maximize the economic benefits. The international community should pay attention to the development of logistics transportation, face up to, and solve the existing problems from the reality, so as to provide more innovative models for the development of cross-border logistics transportation in China.

Data Availability

Data sharing is not applicable to this article as no datasets were generated or analyzed during the current study.

Conflicts of Interest

The authors declare that they have no conflicts of interest.

References

- [1] Á. Valarezo, T. Pérez-Amaral, T. Garín-Muñoz, I. H. García, and R. López, "Drivers and barriers to cross-border e-commerce: evidence from Spanish individual behavior," *Telecommunications Policy*, vol. 42, no. 6, pp. 464–473, 2018.
- [2] S. Ji, X. Wang, W. Zhao, and D. Guo, "An application of a three-stage XGBoost-based model to sales forecasting of a cross-border E-commerce enterprise," *Mathematical Problems in Engineering*, vol. 2019, 15 pages, 2019.
- [3] Y. Liu, X. Zhang, and Q. Zhou, "VR technology online classroom mode in cross border E-commerce teaching in colleges and universities," *IEEE Access*, 2020.
- [4] B. Song, W. Yan, and T. Zhang, "Cross-border e-commerce commodity risk assessment using text mining and fuzzy rule-based reasoning," *Advanced Engineering Informatics*, vol. 40, pp. 69–80, 2019.

Retraction

Retracted: Mobile Communication Network Optimization System Based on Artificial Intelligence

Wireless Communications and Mobile Computing

Received 28 November 2023; Accepted 28 November 2023; Published 29 November 2023

Copyright © 2023 Wireless Communications and Mobile Computing. This is an open access article distributed under the Creative Commons Attribution License, which permits unrestricted use, distribution, and reproduction in any medium, provided the original work is properly cited.

This article has been retracted by Hindawi, as publisher, following an investigation undertaken by the publisher [1]. This investigation has uncovered evidence of systematic manipulation of the publication and peer-review process. We cannot, therefore, vouch for the reliability or integrity of this article.

Please note that this notice is intended solely to alert readers that the peer-review process of this article has been compromised.

Wiley and Hindawi regret that the usual quality checks did not identify these issues before publication and have since put additional measures in place to safeguard research integrity.

We wish to credit our Research Integrity and Research Publishing teams and anonymous and named external researchers and research integrity experts for contributing to this investigation.

The corresponding author, as the representative of all authors, has been given the opportunity to register their agreement or disagreement to this retraction. We have kept a record of any response received.

References

- [1] C. Duan and J. Luo, "Mobile Communication Network Optimization System Based on Artificial Intelligence," *Wireless Communications and Mobile Computing*, vol. 2021, Article ID 9999873, 5 pages, 2021.

Research Article

Mobile Communication Network Optimization System Based on Artificial Intelligence

Chao Duan  and Jun Luo

School of Engineering, Guangzhou College of Technology and Business, Foshan, Guangdong Province, China 528100

Correspondence should be addressed to Chao Duan; 17742417090@mail.nwpu.edu.cn

Received 16 July 2021; Revised 13 August 2021; Accepted 17 August 2021; Published 20 September 2021

Academic Editor: Balakrishnan Nagaraj

Copyright © 2021 Chao Duan and Jun Luo. This is an open access article distributed under the Creative Commons Attribution License, which permits unrestricted use, distribution, and reproduction in any medium, provided the original work is properly cited.

The objective of this paper is to study the key technology of the mobile communication network optimization system based on artificial intelligence technology. *Specific Content.* This paper designs the artificial intelligence agent- (IA-) type mobile communication network optimization tool iOS2CMCN, analyzes the relevant intelligent technology introduced into the system, and analyzes the feasibility and practicability of iOS2CMCN through application examples. The results show that the optimization of mobile communication networks is one of the important links in the construction of communication networks and ensuring the quality of network service. In the form of an artificial intelligence agent, iOS2CMCN absorbs the experience and knowledge of a large number of network optimization engineers and experts and realizes the intelligence and automation of mobile communication network optimization. It is proven that the fuzzy technology is introduced in theory, the practical problem is reasonably modeled, and the rule and case reasoning are used to simulate the thinking mode of a human being when solving the problem. It reduces the dependence of network optimization on humans, improves the efficiency of network optimization, and provides a new idea for practical mobile communication network optimization.

1. Introduction

Artificial intelligence (AI) was first proposed at the Dartmouth Society in 1956. At this conference, McCarthy, Minsky, Rochester, and Shannon created the discipline of artificial intelligence by using machines to simulate human intelligence. Since then, artificial intelligence technology has had a spiraling development, has become a hot field of computer science many times, and has produced many schools, such as reasoning and knowledge-centered symbolism, bionics-based connectionism, and data-centered machine learning science. At the beginning of the 21st century, with the emergence of big data technology, the existing data analysis ability has been greatly improved. The rich data resources accumulated in social production and life have further promoted the breakthrough of artificial intelligence technology. The AI craze is here again. To date, artificial intelligence has achieved great success in many fields.

The optimization of the mobile communication network requires “intelligence” of the optimization tools of the

mobile communication network, and expert system theory makes the domain tools that allow them to have the ability of domain experts—“intelligence.” Guo summarized the Internet technology under 5G mobile communication, analyzed the connotation of the Internet of Things, studied the integration of 5G mobile communication and the Internet of Things technology, and analyzed and discussed the new possibilities of the Internet of Things era under 5G mobile communication technology [1]. Chu et al. gave a general overview of AI algorithms based on artificial intelligence technology, mainly focusing on their use in network intrusion detection [2]. Das et al. help information and communication technology (ICT) practitioners use AI tools and methods to effectively manage their platforms and provide them with sufficient AI background to deal with real-life problems [3]. The combination of the two, that is, applying the expert system theory to the optimization of the mobile communication network, is an effective way to realize the “intellectualization” of the optimization of the mobile communication network. There are many existing network

optimization tools, but they have a common feature of strong pertinence. These types of software all focus on completing certain functions, but lack the thinking mode of “why do you do this?” Due to the “mobile” characteristics of the mobile communication network, the structure and operation process of the whole network are very complex, and problems arising in the maintenance process also involve many aspects, requiring a large number of personnel with specialized knowledge to carry out maintenance and optimization [4, 5].

2. Materials and Methods

2.1. BP Neural Network. Assume that the input data of BP neural network is $X = (X_1, X_2, \dots, X_n)^T$, n represents the number of nodes of neurons in the input layer, the corresponding output data is $O = (O_1, O_2, \dots, O_m)^T$, m represents the number of nodes of neurons in the output layer, and W_{ij} and W_{ik} are the connection weights of the hidden layer and the output layer, respectively, for input component X_i in layer i ; the corresponding output of the hidden layer and the output layer can be expressed as shown in formula (1).

The training steps of BP neural network are as follows:

Randomly initialize weights W_{ij} and W_{ik} , their values must not be the same, the usual range is (-1.0, 1.0), and for the sample (X_p, Y_p) , its output value is O_p .

Calculate the error between O_p and Y_p and adjust the weight matrix according to the error; for the p sample, we can get as shown in formula (2).

The neural network error calculation formula of all samples is as shown in formula (3), where s is the number of samples.

The process of minimizing E can be regarded as an optimization problem. The steepest descent method is adopted to adjust the weight matrix, namely, as shown in formulas (4) and (5).

In the formula, α represents the learning rate.

The initial values of W_{ij} and W_{ik} of a traditional BP neural network are determined by the random method, which makes the performance of the BP neural network unstable; the solution of the problem cannot get the optimal result, so the particle swarm optimization algorithm of artificial intelligence algorithm is introduced to optimize the initial values of W_{ij} and W_{ik} .

2.2. Artificial Intelligence Algorithm. The position vector of the particle is $x_i = (x_{i1}, x_{i2}, \dots, x_{iD})$; it represents a set of initial values of W_{ij} and W_{ik} , and we also have a velocity vector $v_i = (v_{i1}, v_{i2}, \dots, v_{iD})$. Particles adjust their flight direction by tracking the optimal positions of individuals and groups, as shown in formulas (6) and (7), where t is the number of iterations and ω is the inertia weight.

2.3. Intelligent Optimization Agent. Mobile communication network optimization has a high level of maintenance work, is involved in the process of optimization of network software and hardware components, and is applied to various knowledge and skills, such as the redistribution of the net-

work resources and network parameters for readjustment, including antenna position, antenna pitching angle, frequency, handoff parameters, and base stations receiving the threshold adjustment. Since the equipment parameters provided by different manufacturers and the network element performance data collected are different, the characteristics of equipment and system of different manufacturers should be taken into account in network optimization work [6]. The complexity of the mobile communication network determines the specific network optimization work with no fixed rules to follow, in order to improve network performance in time, improve the quality of network services, and avoid a lot of unnecessary repetitive work; making full use of network optimization engineers' and experts' experience knowledge is an effective method to realize network optimization. Using IA technology which takes knowledge utilization as the core and combining with actual network optimization work, an intelligent optimization system of mobile communication network is designed. iOS2CMCN is a self-learning closed-loop intelligent system. The system is driven by network performance monitoring and user reporting information data, using four kinds of intelligent technologies: data analysis tools, fuzzy quantification rules, model analysis, and information reasoning. Using the optimized log base and the comprehensive knowledge base of historical events and experience knowledge, supplemented by man-machine information interaction, the optimization agent provides the corresponding optimization scheme and suggestion for the network optimizer. The network operation proves that the reasonable optimization scheme is kept as the optimization log. If the scheme cannot effectively improve the network performance, after the network model is modified, the intelligent optimization will be carried out again in the form of self-learning until an effective optimization scheme or suggestion is found. For some recurring problems in the network, the system can directly extract the optimization scheme from the optimization log database memory to improve the network optimization efficiency of the system [7, 8].

2.4. Artificial Intelligence Technology. The intelligence of iOS2CMCN runs through the whole process of network optimization, which is mainly embodied in three aspects: the establishment of the network model, the analysis of the network model, and the information reasoning of obtaining the network optimization scheme. Combined with fuzzy quantization, fuzzy evaluation matrix, and fuzzy reasoning in artificial intelligence technology, the intelligent optimization of the mobile communication network is realized by using the knowledge base including wireless network theory [9, 10] and the experience of network optimization experts, as well as the optimization log database containing a large number of network events and optimization schemes.

2.4.1. Intelligent Modeling. The characteristics of the mobile communication network are characterized by a large number of data collected from the manufacturer OMC. In order to realize network optimization based on network performance evaluation, it is necessary to analyze these data and

TABLE 1: Network performance statistics.

Parameter	Plot no.	Number of carrier frequency	Traffic	SD congestion	TCH congestion rate	TCH dropped	Handover success rate	The RF dropped	RF switch drop rate
The original data	86	4	20.67	0.07	11.88	10.78	80	8.23	2.1
	87	4	3.97	70.25	0	87.88	53	1.5	85.22
Quantitative model	86	Quantitative values	0.8	0	0.75	0.72	0.7	0.72	0.17
		The fuzzy degree	Normal	No	High	High	High	High	High
		Quantitative values	0.9	0.85	0	0.87	0.7	0.1	0.8
	87	The fuzzy degree	Low	High	No	Very high	Low	High	Very high

judge network operation conditions (such as congestion of SDCCH and high drop rate of TCH). iOS2CMCN, quoting the fuzzy membership degree method, the fuzzy network performance data, including SDCCH congestion rate, each channel traffic and dropped, described it as like “village high traffic,” “residential dropped the high,” and “village TCH congestion” natural language, establish reasonable quantitative network model for describing the network operation status [11]. Based on the communication with network optimization experts and the fuzzy function theory, the network performance parameters can be described by the adaptive Gaussian function network, in which each fuzzy subset has adaptive factors.

2.4.2. Fuzzy Knowledge Base. Mobile communication network integrates complex systems by collecting various communication technologies and multivendor equipment. The key to network optimization is the factors affecting network performance, diversity, uncertain knowledge, technology, and application experience. Knowledge is an important part of developing an intelligent network optimization system. In iOS2CMCN, fuzzy knowledge expression based on rules and cases is adopted. The rule expression is to summarize the experience of network excellence into the form of “premise and conclusion” and introduce fuzzy factors to reflect the fuzzy uncertainty of knowledge. This expression is suitable for the knowledge used in human brain logical thinking. Rule expression is a “case attribute” event, which uses a fuzzy quantity to describe the network optimization case in the form of synthesis. This fuzzification quantity includes, for example, the description of each state attribute in the language set after entering the numerical set and the weight of the given factor of each attribute. From the practical application point of view, the fuzzy knowledge representation in iOS2CMCN can effectively describe the network optimization knowledge used by network optimization engineers in specific network optimization work.

3. Results and Discussion

3.1. Information Reasoning. Information reasoning is the process of using real-time information and empirical knowledge to solve problems. In the optimization of mobile communication network, network optimization experts use real-time network performance statistics data, the operation status of hardware equipment, and rich experience and

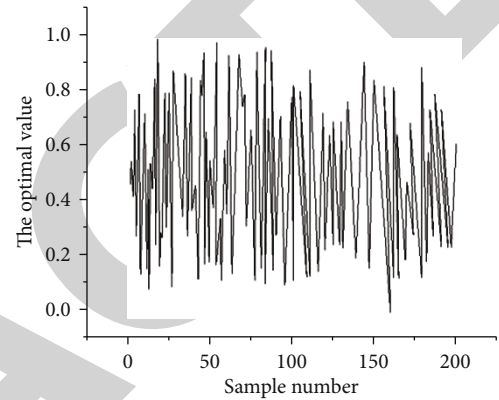


FIGURE 1: Optimized risk value of wireless mobile communication system. In this figure, the original value of the wireless mobile communication system optimization analysis can clearly show that the uncertainty of the wireless mobile communication system has strong randomness but also has certain regularity change characteristics; choosing a village as the validation sample, the optimized plan for the 86 other districts as a wireless mobile communication system optimizes the training sample.

knowledge of network optimization to come up with reasonable and effective optimization schemes. After automatically identifying the network optimization event model, the inference machine enters rule or case reasoning. When rule reasoning is adopted to solve problems, the information inference machine is driven by current network operation events and uses fuzzy rules in fuzzy knowledge base to simulate and realize the logical thinking process of network optimization experts [12]. The characteristics of network events are analyzed by case-based reasoning. According to the typical examples of fuzzy knowledge base, the network optimization is carried out on the basis of correlation and analogy event processing. At the same time, new events are saved and modified in case to simulate the analogy learning ideas of network optimization experts in the form of real-time analysis and memory.

3.2. Simulation Test. The author studies and analyzes the practicability of iOS2CMCN based on the work and experience of mobile communication network optimization in a city. Table 1 shows the fuzzy quantization model of the performance statistics of the two cells collected by OMC and the corresponding network optimization events. Under the function of the above information on the inference machine, the

fuzzy knowledge is used to optimize the two plots. Using the fuzzy rule reasoning method, according to rules A2, A4, B3, and B4, the optimization scheme of cell 87 is obtained. Using the fuzzy case reasoning method, the events of plot 86 are compared with the related cases in the fuzzy case database. According to the calculation method of similarity between the related cases, plot 86 is similar to the fuzzy case D015.

In order to test the design of wireless mobile communication system optimization based on artificial intelligence algorithm, the risk historical data of wireless mobile communication system in a period of time is selected as the research object. Firstly, the data of wireless mobile communication system optimization is collected, and some preprocessing is carried out. Then, the corresponding optimization level value of wireless mobile communication system is obtained. Due to the limited space, only the optimization value of wireless mobile communication is displayed, as shown in Figure 1. In Figure 1, the original value of the wireless mobile communication system optimization analysis can clearly show that the uncertainty of the wireless mobile communication system has strong randomness but also has certain regularity change characteristics; choosing a village as the validation sample, the optimized plan for the 86 other districts as a wireless mobile communication system optimizes the training sample.

3.3. Analysis of Optimization Results of Wireless Mobile Communication System Based on the Model in This Paper. The optimization results of the wireless mobile communication system of the model are divided into a particle swarm optimization algorithm to determine the initial connection weight of the BP neural network, and then, the optimization results of the wireless mobile communication system of the model in this paper are obtained as shown in Figure 2. It can be seen from the analysis of the optimization results of the wireless mobile communication system in Figure 2 that the optimization deviation of the wireless mobile communication system in this model is quite small and can be ignored. The optimization accuracy of the wireless mobile communication system is high, and the reliability of the evaluation results is high. It is a feasible wireless mobile communication system optimization model.

In order to test the superiority of the optimization model of wireless mobile communication system based on artificial intelligence algorithm, gray model, cluster analysis, and standard BP neural network were used to carry out comparative experiments on the same data set in the same simulation environment, and the optimization accuracy and training time of wireless mobile communication system were calculated, as shown in Table 2. It can be found from Table 2, in this paper, that the wireless mobile communication system based on artificial intelligence algorithm optimization model of efficiency is more than 95%, the classic efficiency of the wireless mobile communication system optimization model is less than 95%, and the model of short training time in classical optimization model for wireless mobile communication system, to speed up the wireless mobile communication system optimization, is presented. Therefore, the optimization result of the wireless mobile

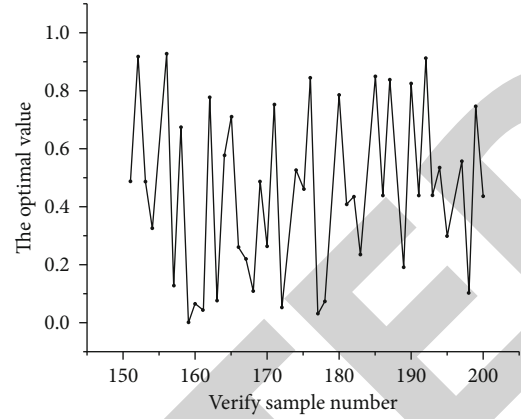


FIGURE 2: The optimization results of the wireless mobile communication system of this model. It can be seen from the analysis of the optimization results of the wireless mobile communication system in this figure that the optimization deviation of the wireless mobile communication system in this model is quite small and can be ignored.

TABLE 2: Comparison of the optimization results of wireless mobile communication system with the classical model.

Optimization model of wireless mobile communication system	Optimize the efficiency	Optimization of time
Grey model	89.95	11.61
Clustering analysis	87.73	12.38
Standard BP neural network	93.26	7.83
Model	96.78	4.49

communication system based on the model in this paper is more ideal.

$$Y_o = f(X_i W), \quad (1)$$

$$E_p = \frac{1}{2} \sum_{j=1}^m (y_{pj} - o_{pj})^2, \quad (2)$$

$$E = \sum_{l=1}^s E_{pl}, \quad (3)$$

$$W_{jk} = W_{jk} + \Delta W_{jk} = W_{jk} + \alpha O_j (1 - O_k) (Y_k - O_k) O_j, \quad (4)$$

$$W_{ij} = W_{ij} + \Delta W_{ij} = W_{ij} + \alpha O_j (1 - O_j) O_i \cdot \sum_{k_1=1}^h \sum_{k_2=1}^m W_{k_1 k_2} O_{j+1, k_2} (1 - O_{j+1, k_2}) (Y_{j+1, k_2} - O_{j+1, k_2}), \quad (5)$$

$$v_{id}(t+1) = \omega v_{id}(t) + c_1 r_1 (p_{id} - x_{id}(t)) + c_2 r_2 (p_{gd} - x_{id}(t)), \quad (6)$$

$$x_{id}(t+1) = x_{id}(t) + v_{id}(t+1). \quad (7)$$

4. Conclusions

The key technology research and implementation of a mobile communication network optimization system based on artificial intelligence technology are presented. The

Retraction

Retracted: Analysis of the Needs of English-Chinese Translation Courses and Research on Teaching Strategies under the Background of Wireless Communication and Big Data

Wireless Communications and Mobile Computing

Received 28 November 2023; Accepted 28 November 2023; Published 29 November 2023

Copyright © 2023 Wireless Communications and Mobile Computing. This is an open access article distributed under the Creative Commons Attribution License, which permits unrestricted use, distribution, and reproduction in any medium, provided the original work is properly cited.

This article has been retracted by Hindawi, as publisher, following an investigation undertaken by the publisher [1]. This investigation has uncovered evidence of systematic manipulation of the publication and peer-review process. We cannot, therefore, vouch for the reliability or integrity of this article.

Please note that this notice is intended solely to alert readers that the peer-review process of this article has been compromised.

Wiley and Hindawi regret that the usual quality checks did not identify these issues before publication and have since put additional measures in place to safeguard research integrity.

We wish to credit our Research Integrity and Research Publishing teams and anonymous and named external researchers and research integrity experts for contributing to this investigation.

The corresponding author, as the representative of all authors, has been given the opportunity to register their agreement or disagreement to this retraction. We have kept a record of any response received.

References

- [1] B. Gao, "Analysis of the Needs of English-Chinese Translation Courses and Research on Teaching Strategies under the Background of Wireless Communication and Big Data," *Wireless Communications and Mobile Computing*, vol. 2021, Article ID 3424658, 5 pages, 2021.

Research Article

Analysis of the Needs of English-Chinese Translation Courses and Research on Teaching Strategies under the Background of Wireless Communication and Big Data

Bei Gao 

School of Foreign Languages, Xuzhou University of Technology, Xuzhou, Jiangsu 221000, China

Correspondence should be addressed to Bei Gao; gaobei_vip@163.com

Received 4 August 2021; Accepted 31 August 2021; Published 17 September 2021

Academic Editor: Balakrishnan Nagaraj

Copyright © 2021 Bei Gao. This is an open access article distributed under the Creative Commons Attribution License, which permits unrestricted use, distribution, and reproduction in any medium, provided the original work is properly cited.

The development of wireless communication technology and the widespread application of big data has accelerated the degree of globalization. Both English and Chinese are widely used languages internationally, and the cultural exchanges between the two occupy a very important proportion in the world. The society's demand for English-Chinese translation talents has increased, and colleges and universities have also taken measures to improve students' English-Chinese translation ability. This article analyzes the English-Chinese translation course under the environment of wireless communication and big data, discusses the influence of the development of wireless communication and big data on the teaching of English-Chinese translation, the problems existing in the teaching of English-Chinese translation in colleges and universities, and gives solutions to the existing problems. Finally, using the method of online survey to investigate the current situation of English-Chinese translation teaching in colleges and universities in the province, 245 valid questionnaires were recovered, only 87 of which indicated that their majors offered separate English translation courses, accounting for 35.51% of the total; 158 indicated their majors. There are no English translation courses, accounting for 64.49% of the total. Such a ratio does not match the overall demand for cultural exchanges in the context of the rapid development of wireless technology and big data. Therefore, the convenience brought by new technologies should be actively used to promote the development of the English-Chinese translation teaching system in colleges and universities.

1. Introduction

Traditional English teaching has been unable to meet the current situation. It is inevitable to introduce new teaching models into English teaching. English-Chinese translation teaching has always been the shortcoming of many universities. English-Chinese translation ability is a major indicator to measure English proficiency, and it occupies an important position in many English exams. The network learning platform, smart campus, and flipped classroom have pointed out new directions for education reform. Rethinking positioning of translation education in a wireless communication and big data environment, finding out the shortcomings, breaking the convention, and using wireless communication and big data technology to reform English-Chinese teaching is

an effective strategy to improve students' English-Chinese translation level and overall English level.

Soang found that many students are accustomed to using spoken language to write text when translating but ignore the importance of mother tongue knowledge and cultural factors, resulting in improper translation. Therefore, he designed a new teaching model that can practice translation in class. After evaluating the translation process through multidisciplinary evaluation methods, it can help students understand the working principles of translation and use reasonable methods to solve translation problems [1]. Qiao and Wang analyzed the characteristics of mobile teaching from the perspective of constructivism and constructed a new mobile interactive translation teaching model. Then, they verified the model with WeChat, QQ, and Weibo as examples and

pointed out that the Internet translation teaching is about to become the norm [2]. Lin and Yip found corpus-assisted translation education can accomplish teaching goals. They proposed an application improvement plan for the corpus in view of its goals, data alignment methods, data annotation systems, and function keys [3].

English-Chinese translation is a way to promote cultural exchange. As the main force of country's modernization, young college students should have the ability to read foreign language documents without barriers and fluent English communication. Today, English-Chinese translation teaching is only the reading comprehension and English level test. This article mainly analyzes the points of English-Chinese translation education and puts forward corresponding suggestions.

2. Demand Analysis of English-Chinese Translation Courses and Research on Teaching Countermeasures

2.1. English-Chinese Translation Teaching in a Wireless Communication and Big Data Environment. Under Internet technology constantly developing, my country's education has undergone tremendous changes due to its influence. Wireless communication and big data can provide personalized, collection, mining, management, analysis, and other services, and it has achieved the ultimate in information integration and resource sharing. It can not only provide a comfortable and convenient teaching environment but also collect online teaching resources for use in English-Chinese translation teaching and cultivate students' good learning. Get used to a comprehensive level of students' English ability. The smart learning platform can provide a wealth of teaching services, including teacher preparation and teaching and tutoring, as well as students' preclass preparation and after-class review.

2.2. The Necessity of English-Chinese Translation Teaching. Translation of English-Chinese is an important part of College English Test Four and Six, and research is an important part of the entrance examination, and it is a prerequisite for cultivating students' listening, speaking, reading, and writing skills. English-Chinese translation mainly tests the students' English reading comprehension ability and Chinese language expression ability [4]. The basic premise of expressing one's thoughts in written language is reading comprehension ability, that is, obtaining information through reading the original text and understanding it. Translation is a common means to check whether the obtained information is correct. If the knowledge level of the foreign language is poor, the correct information to be expressed in the original text cannot be obtained, and the translation will inevitably be wrong. In addition. If the meaning of the original text is understood, but the language expression ability of Chinese is not good or the translation skill is lacking, such translations are often prone to ambiguity or language expression does not conform to the Chinese standard [5]. Therefore, it is particularly important to improve students' English-Chinese translation ability. This will not only help improve students' translation level and mas-

ter the basic knowledge of Chinese but also promote students' open thinking and correct language learning from different language perspectives.

2.3. Problems in College English-Chinese Translation Teaching

2.3.1. The School Does Not Pay Enough Attention to College English Translation Teaching. In undergraduate English teaching, most of the guidance focus is still oriented to passing the course test and English level. In addition, traditional English teaching mainly focuses on vocabulary, grammar, and listening teaching. It usually leads to that the students are good at answering the test papers correctly but are not fluent. Translation teaching in university classrooms is relatively small, and teachers seldom use translation as a main content for teaching. Even if it involves translation, it requires the general meaning of the original text to be summarized completely, and students are allowed to practice translation sentence by sentence and paragraph by paragraph. In the selected English textbooks, the theories and space involved in translation are also relatively small [6, 7]. Therefore, many students can understand the general idea of the article when doing reading comprehension but will get entangled when doing the question. This is because there is no systematic translation training that leads to students' incomplete grasp of the original content.

2.3.2. Pay Attention to Knowledge Mastering and Neglect the Cultivation of Language Communication Ability. Language is an important tool for humans to express their thoughts and emotions. If language learning is only included in textbooks and exams, it will have no practical meaning. The most important thing in learning English is to be able to understand what is meant to be expressed in English and to be able to relay it in English or mother tongue in your own words. English teaching in many domestic universities only requires students to master the textbooks and test content, and English translation only needs to look at the general idea and sentence structure. The English test scores are used to measure students' English level, which makes students fall into a misunderstanding in English learning-rote memorization, but they are confused when they speak [8].

2.3.3. Lack of Cultural Theory Teaching. Translation is not a simple paraphrase, but a linguistic creative activity of cross-cultural awareness. English represents Western culture, and Chinese represents Chinese national culture. They are two different social ideologies. Specifically, culture includes content such as religious beliefs, geographic customs, and academic thoughts. It is often just a direct translation, and no time is spent comparing and exploring the Eastern and Western cultures involved. Such translation is also relatively rigid and lacks charm [9, 10].

2.4. Teaching Strategies of College English-Chinese Translation

2.4.1. Optimize the Teaching System of College English Courses. It is very important to cultivate high-quality

comprehensive talents. Globalization has long been a reality, and mastering an international common language is one of the talent standards in the new era. Today, society has more diverse requirements for language talents, and college English teaching concepts and teaching methods should also be changed as soon as possible. Establish a complete English teaching system and carry out teaching from all aspects of language learning. We should ensure that students can improve their translation ability after acquiring English knowledge. Organize English translation competitions and offer English translation elective courses to increase students' interest. Improve proportion of English translation, including sentence translation and paragraph translation [11].

2.4.2. Strengthen the Cultivation of Cultural Awareness. Translation is an effective way to promote the exchange and integration of different cultures, and the conversion between languages needs to include the change of different cultural consciousness. Therefore, in college English translation teaching, teachers should popularize language and culture involved in English and Chinese, analyze differences in language expression and cultural differences between them, then use translation skills to minimize the differences, and improve the quality of translation [12].

2.4.3. Cultivate Students' Self-Learning Ability. Students need to have a proactive thirst for knowledge and the ability to learn independently. English teaching resources available to students are at your fingertips, including not only literature but also explanation videos by teachers and experts. Students can learn English knowledge in advance in many ways with better classroom learning results. Therefore, guiding students to develop study habits after class on English-Chinese translation is important.

2.4.4. Fully Explore Wireless Communication and Big Data Teaching Technology and Resources. College English translation teaching ushered in a key opportunity for transformation. However, there are large amount of fragmentation of information in wireless communication and big data, there are many problems in building a teaching environment and grasping teaching content. Therefore, when constructing an English translation teaching model, we should focus on teaching situation, role transformation and communication. Use modern information technology to fully integrate teaching resources, innovate English-Chinese teaching methods, change traditional English-Chinese teaching concepts, and use intelligent teaching equipment to create efficient and vivid English-Chinese translation classrooms.

3. Explore the Teaching Experiment of English-Chinese Translation Course under the Background of Wireless Communication and Big Data

3.1. Experimental Content. In order to understand the teaching status of English-Chinese translation courses in English classrooms in the province, this paper designs a question-

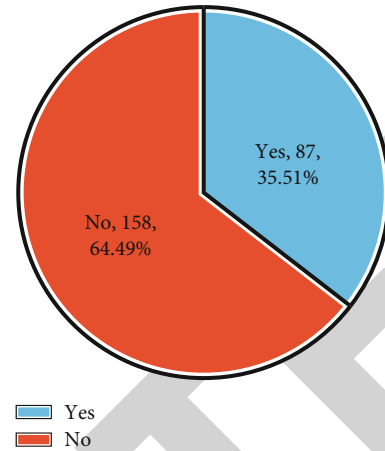


FIGURE 1: Whether to offer a separate English translation course.

naire about English-Chinese translation classrooms based on the background of wireless communication and big data. The main content of the questionnaire includes the teaching methods and teaching effects of the English-Chinese translation classroom in the school, and the students' needs for the English-Chinese translation classroom.

3.2. Experimental Process. According to the experimental content and referring to the questionnaire design specifications, the specific content of the questionnaire was designed. Distributed in the form of an online questionnaire. A total of 245 questionnaires were collected, and the collected questionnaires were collected for data statistics and then analyzed. Finally, summarize the results of the questionnaire survey and give corresponding suggestions based on the results. In the process of data collection and processing, the experiment used the following Formula (1) and (2):

Sample variance formula:

$$k^2 = \frac{\sum_{i=1}^m (r_i - r)}{m - 1}. \quad (1)$$

Sample standard deviation formula:

$$k = \sqrt{k^2} = \sqrt{\frac{\sum_{i=1}^m (r_i - r)}{m - 1}}. \quad (2)$$

4. Analysis of English-Chinese Translation Course Teaching

4.1. Analysis of Teaching Methods of English-Chinese Translation Course. The questionnaire designed "Does your major offer a separate English translation course?" and "How does the teacher teach English-Chinese translation knowledge in class?" Some relevant data and statistical results are as follows.

From Figure 1, we can see that 87 of the surveyed persons indicated that their majors have opened an English translation course alone, accounting for 35.51% of the total; 158 of them said that their majors did not provide additional English translation courses, accounting for the total 64.49%.

TABLE 1: How does the teacher teach English-Chinese translation knowledge in class.

	Practical teaching	Theory teaching	Interpretation teaching	Translation detection
Offering English-Chinese translation course	84%	32%	45%	83%
No English-Chinese translation courses are offered	87%	59%	47%	50%

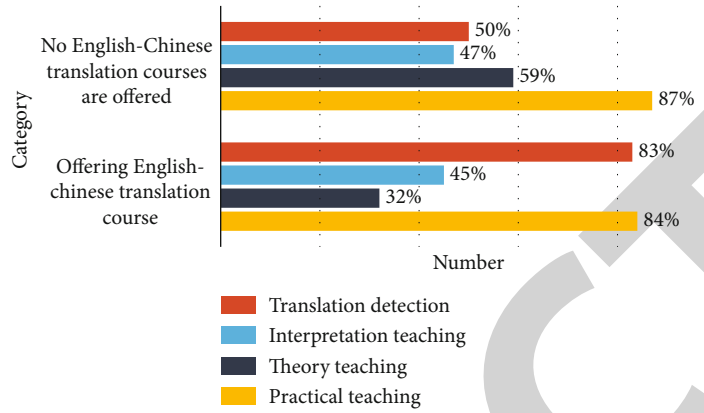


FIGURE 2: English classroom teaching methods.

According to the conclusions drawn in Figure 1, it can be seen from Table 1 and Figure 2 that the majors that have opened English translation courses are still based on practical teaching and theory teaching, and the interpretation teaching is relatively small. For the majors that do not have English translation courses, practical teaching is the main English translation teaching method, and the other three teaching methods are rarely used. Regardless of whether English translation courses are offered, English-Chinese translation teaching is lacking in cultural background comparison and interpretation teaching. Both English and Chinese have a particularly important position in the world, and both represent excellent national culture. If there is a lack of theoretical teaching, the English-Chinese translation teaching will also lose its soul. It will not expand the students' cognition but also make the English-Chinese translation only stay in surface.

4.2. Analysis of the Teaching Effect of English-Chinese Translation. In order to improve the level of English-Chinese translation teaching, an English-Chinese translation question was designed in the questionnaire. The content of the question is an English paragraph. The results are scored from the main idea of the paragraph, sentence structure, detail processing, word and sentence application, and connotation. The statistical score is calculated as an average.

In Figure 3, we can see that the average score of English-Chinese translation is 87.82 for majors that have opened an English-Chinese translation course. In the statistical process, it is found that there is basically no problem in their translation, but the translated sentences need emotional expression. The average score of majors that did not offer an English translation course was 63.54 points. They only managed to express the paragraphs in a clear way without paying attention to details and emotional connotations.

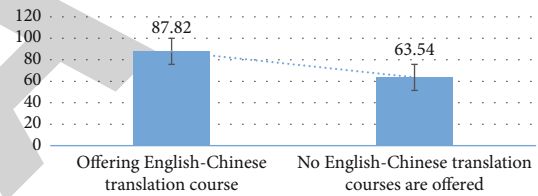


FIGURE 3: English-Chinese translation results.

The development of technologies such as wireless communication and big data analysis has provided strong support for us to better promote the progress of English-Chinese translation courses. First of all, we can actively develop various learning apps, so that students can make full use of the fragmented time for learning. Secondly, the school has made it into an auxiliary resource in line with its own teaching characteristics through the collection and editing of network resources. The third is to provide students with a more open space for communication, so that they can improve their English-Chinese translation skills by listening and using more.

5. Conclusions

In the background of wireless communication and big data, society has more stringent requirements for language talents. College English teaching must keep up with the trend of the times, change teaching methods. English-Chinese translation teaching should be treated as the focus of College English teaching, establish a systematic English-Chinese translation teaching system, and use English-Chinese translation materials and advanced experience on the Internet to improve students' translation level. Traditional English-Chinese translation teaching modes need reform and innovation, formulate personalized teaching plans based on students' actual English-Chinese translation level, and provide qualified translators to the society.

Retraction

Retracted: Research on Cultural Communication in College English Teaching Based on Wireless Communication and Multimedia Network Technology

Wireless Communications and Mobile Computing

Received 28 November 2023; Accepted 28 November 2023; Published 29 November 2023

Copyright © 2023 Wireless Communications and Mobile Computing. This is an open access article distributed under the Creative Commons Attribution License, which permits unrestricted use, distribution, and reproduction in any medium, provided the original work is properly cited.

This article has been retracted by Hindawi, as publisher, following an investigation undertaken by the publisher [1]. This investigation has uncovered evidence of systematic manipulation of the publication and peer-review process. We cannot, therefore, vouch for the reliability or integrity of this article.

Please note that this notice is intended solely to alert readers that the peer-review process of this article has been compromised.

Wiley and Hindawi regret that the usual quality checks did not identify these issues before publication and have since put additional measures in place to safeguard research integrity.

We wish to credit our Research Integrity and Research Publishing teams and anonymous and named external researchers and research integrity experts for contributing to this investigation.

The corresponding author, as the representative of all authors, has been given the opportunity to register their agreement or disagreement to this retraction. We have kept a record of any response received.

References

- [1] Y. Li, "Research on Cultural Communication in College English Teaching Based on Wireless Communication and Multimedia Network Technology," *Wireless Communications and Mobile Computing*, vol. 2021, Article ID 5123421, 5 pages, 2021.

Research Article

Research on Cultural Communication in College English Teaching Based on Wireless Communication and Multimedia Network Technology

Yun Li 

School of Foreign Studies, Xi'an University, Xi'an, Shaanxi 710065, China

Correspondence should be addressed to Yun Li; liyun_edu@163.com

Received 4 August 2021; Accepted 1 September 2021; Published 17 September 2021

Academic Editor: Balakrishnan Nagaraj

Copyright © 2021 Yun Li. This is an open access article distributed under the Creative Commons Attribution License, which permits unrestricted use, distribution, and reproduction in any medium, provided the original work is properly cited.

In the context of the rapid development of wireless communication and information technology, the network has greatly shortened the actual spatial distances around the world. Multimedia technology and wireless communication, as an important branch of information technology, can better connect people and the network, exploding very powerful energy in the field of education. This research analyzes the cultural communication function of wireless communication and multimedia network technology in university teaching, especially English teaching. At this stage, almost all universities in our country are using multimedia technology to assist teaching, and even many teachers believe that multimedia has become a necessary foundation for the in-depth development of the “teaching-learning” interaction in colleges and universities in the information age. The demand for English talents in the Chinese labor market is dominated by application-oriented talents, but the purpose of English teaching in many schools is still in the reality of traditional research-based teaching. It is concluded that the root of this contradiction lies in the disconnection between the cultivation of talents in universities and the needs of society. The experimental results show that if the advantages of wireless communication and multimedia network technology can be fully utilized, the teaching efficiency of cultural communication in college English teaching can be increased by 22%. This article also analyzes, discusses, and summarizes the methods and approaches of cultural dissemination to enrich academic research results.

1. Introduction

The most remarkable is the highlight of the cross-cultural attribute of English teaching [1, 2]. In the course of teaching, the differences between English culture and local culture and the improvement of this kind of teaching are increasingly emphasized. Meanwhile, the teaching mode of English is becoming more and more diversified. This requires that we choose and develop English teaching types and gradually take cultural differences as one of the core elements [3, 4]. Because of the many research results on English teaching, most of them come from overseas. In other words, most of the mainstream linguistics theory, psychology theory, and pedagogy theory in the world are based on English teaching. Therefore, we must combine the cultural background and relevant linguistic context of literary works when we teach

English in colleges and universities [5–7]. The tradition of isolating literary works has lagged behind the times.

As one of the most widely used languages in the world, English teaching has become a common concern in the world. Bhattacharyya and Raj believe that English teaching is closely related to cultural communication. In recent years, English has been trained since primary school [8, 9]. Liu et al. propose that the influence of intercultural communication on human society is becoming more and more profound, and the significance of intercultural communication in English teaching is becoming more and more important. As an important part of English culture teaching, the cultivation of language view has been put in the first place [10, 11]. But the results of the two studies are not accurate because of the error in their experimental process. By combining many monographs of linguistics, we find that at present, it is mainly

from the perspective of system, tool, and national culture. The different angle of development also causes the changes of English teaching in the content and purpose. In particular, the importance of the establishment of language learning concept is undoubted. Similar to the development of linguistics, different learning paradigms should be adopted, and the matching of learning methods should be emphasized. Only in this way can students' investment be strengthened, and passive learning can be changed into active learning.

Combined with the new characteristics of the times reflected in English cross-cultural communication, this study adopts to a new perspective. Students can build their own knowledge system, culture system, and value system by absorbing different languages and cultures and master the ability of correct application of English through simulation teaching of different real situations. In order to enhance students' comprehensive quality in foreign language learning and achieve the purpose of foreign language learning, it is necessary to carry out the teaching of cultural communication.

2. English Teaching on Wireless Communication and Multimedia Network

2.1. English Teaching Background. In the new era, the cultivation of students' communicative competence has become one of the most important goals of English teaching. Teaching is no longer concerned with the mastery of knowledge, but with the improvement of practical ability. English is more of a communicative tool but also serves as a bridge between English culture and non-English culture. As we all know, intercultural communication must be based on mutual respect for each other's cultural traditions. In other words, in order to achieve effective communication, people in two cultural contexts should not only have equal cultural literacy, but also have a certain understanding of each other's cultural system. In this context, intercultural communication ability has become an indispensable part of foreign language teaching system all over the world. This puts forward higher requirements for foreign language teachers. Among them, whether teachers have cultural consciousness and can scientifically convey it to students in teaching, respect students' personality development in the dynamic teaching environment and actively choose appropriate teaching methods according to the changes of external factors have become the important yardsticks to measure excellent teachers. Supported by information technology, contemporary college English classrooms generally introduce multimedia devices, and through MOOCs and rain classrooms, the way for students to acquire English knowledge is expanded, and students can choose a learning method that is more suitable for them.

Although the cross-cultural conscious English paradigm has been paid more and more attention, its practice is not close. Its success and popularization cannot be separated from the corresponding theoretical guidance and practice path exploration. For English teachers, the following points must be done to clear the way for the development of cross-cultural conscious English teaching paradigm. First, we must insist on the attitude of cultural consciousness to

English teaching; secondly, realize the unified development of knowledge teaching and ability improvement in English teaching; thirdly, practice English teaching with scientific values; fourthly, adhere to the cultural and ability objectives of English teaching; fifth, we should adhere to the integration of knowledge and culture of English teaching content; sixth, adhere to the diversity of forms and methods in the process of English teaching; seventh, ensure the diversity and three-dimensional evaluation of English teaching. This function can be used to design an effective algorithm in the cultural communication of English teaching, as shown in the following Formulas (1)–(3).

$$P = (U, A, K, Q). \quad (1)$$

The calculated value of the cultural transmission efficiency of English teaching is as follows:

$$3H_{01} = H_{A1} + H_{B1} + H_{C1} = 3U_{0j}\omega C_{01}. \quad (2)$$

The test shall use the following formula:

$$C(M, N) = 1 - |M \oplus N|/|M|. \quad (3)$$

2.2. College English Application. This is the dilemma of our English teaching, but this situation also provides us with an opportunity to carry out bold reform. Teaching mode is approaching the front of the times. More and more teachers and scholars are also involved in the theoretical research and practical exploration of teaching reform.

Generally speaking, the attempt to reform the new teaching mode has some characteristics and trends. The most striking of them is the constructivism teaching concept as the leading. It emphasizes the instrumental nature of English and advocates that the meaning of language is more than the form of language. Instead of taking English as a narrow perspective of subject, in fact, it is regarded as a powerful communication tool, which can cultivate students' ability to use language appropriately and restore the essence of English communication tools. To achieve this goal, English teaching should take "use" as one of the core, from sentence teaching to the transmission of cultural beauty, and we should strive to achieve the unity of teaching content and teaching objectives in the context. Since English is a tool language, students should have the ability to communicate and communicate with them and even work after learning.

3. Teaching Paradigm of Wireless Communication and Multimedia Network

3.1. English Teaching Paradigm. Since the research of English teaching paradigm has been approved by the industry, it has been playing an important guiding role in specific English teaching. It not only provides the development goal for English teaching, but also brings the methods and models of English education into its own orbit. Because of this, the change of English teaching method as the guiding ideology will inevitably lead to the corresponding deviation of teaching objectives and teaching methods. This shows

TABLE 1: Byram's category of cultural themes.

No.	Category	Range
1	Social identity and social group	Social class, regional identity
2	Social interaction	Differing levels of formality
3	Belief and behavior	As outsider and moral, religious beliefs
4	Social and political institutions	Daily routines state institutions

that English teaching cannot be conducive to social development stage. From the perspective of China's English education function, it is carried out with new ways for teenagers' English application ability and lays the foundation for their future social work. As the basic way of school education, school teaching naturally comes into being for the purpose of education.

3.2. Teaching Paradigm under Wireless Communication and Multimedia Technology. From the spontaneity of cultural communication to the awakening of cultural communication: the rise of online social communication has caused great changes in traditional social communication. A person who is silent in reality may talk aloud and endlessly on the Internet. Because in the network communication, there is no traditional social must abide by the concerns and rigorous, and optional space is also very broad. On this ground, more and more students join the ranks of online communication. However, the biggest drawback of this "double-edged sword" is that it may weaken students' oral ability and cause students' confusion in English grammar. This is contrary to the strict grammar teaching that we have always emphasized in the past. At present, some English paragraphs appearing on the Internet often use English which is similar to Chinese expression habit in order to express clearly and easily. This situation will cause great trouble to students' English learning. If we want to guide students to understand these problems correctly, we cannot solve them by simple preaching.

Interview method. Through structural interviews with teachers and students of English teaching and education major, this paper is aimed at understanding the relevant information such as the ability training program of English teaching and education major, as well as their opinions and suggestions. With the emergence of daily learning, the research on teaching ability emerges as the times require. It is considered to be the product of the mutual penetration of humanistic quality and English. English learning is not limited to a certain subject or field, but open. The specific results are shown in Table 1.

Through the application of multimedia in college English classrooms, teachers have constructed a more open and interactive teaching system, using multimedia technology to create teaching situations and achieve immersive teaching. At the same time, the application of multimedia has also enhanced the appeal of teaching materials, breaking through the rigidities and limitations of traditional paper teaching materials, giving students more choices.

4. Cultural Communication on Wireless Communication and Multimedia Network

4.1. Cultural Communication Background. The background of cultural communication research in today's increasingly developed science and technology, the development of "science and technology development, economic globalization, the development of the border culture of immigrants worldwide, and the end of supranational and affiliated national identity" has brought us into the era of cultural communication and communication. The development of science, technology, and information technology has promoted the progress of transportation and information. People can learn about the conditions and changes in all parts of the world without leaving their homes, and they can also travel across the east and west of the earth or the northern and southern hemispheres in one day; thoughts and information of the spread has also crossed national borders. The cultural communication exchange itself requires two-way cultural communication, and language itself is produced and developed in the exchange. Therefore, the process of cultural communication foreign language teaching should be an interactive process, and students' enthusiasm for learning and participation must be fully brought into play. The specific results are shown in Figure 1. English-teaching schools generally have a higher level of education than ordinary colleges and universities and can reasonably arrange the progress of foreign language teaching.

4.2. Cultural Communication under Wireless Communication and Multimedia. Multimedia network technology enables more and more face-to-face communication between people from different cultures. The development of science and technology has connected businesses and markets around the world and has become increasingly international; the economic development of a region requires economic cooperation in other regions of the world. The interdependence of world economic development reflects the importance of cultural communication. Learning to understand mutual understanding between cultures is becoming an essential factor in global business. Communication in cultural communication requires knowledge and ability in both language and cultural communication. The development of cultural communication ability needs to be investigated from both aspects of language and cultural communication, but without exception, and cultural communicationists usually neglect to develop language skills, while language teachers often ignore the task of developing cultural communication capabilities. The specific results are shown in Table 2.

Computer multimedia teaching has its unique advantages: optimizing the structure of English classroom teaching; it is beneficial to mobilize students' diverse senses, emotional participation in the teaching process, and improve students' attention. The Internet can connect the world together, shorten the distance between people and culture, allow English learners to roam the online English world, and even participate in activities in English-speaking countries through the Internet, so as to feel the real language environment and get the real cultural materials and practice the

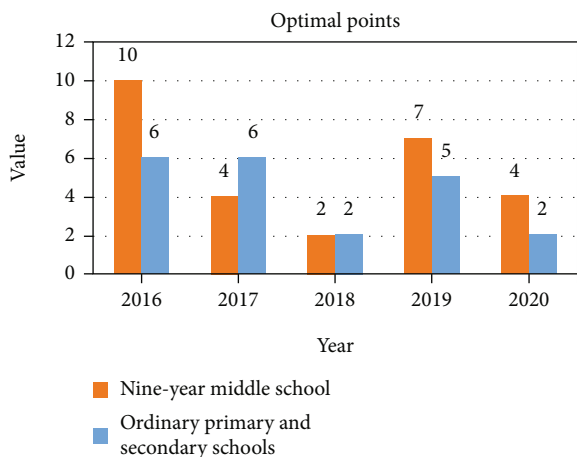


FIGURE 1: Mental model work.

TABLE 2: Statistical table of sample library.

Major-grade	Distribution	Collection	Validity
Law Japanese-1	54	52	96.30%
Law Japanese-2	47	43	91.49%
Mathematics-1	53	52	98.11%
Biology-2	48	47	97.92%

ability to apply language in a real language environment. This is an advantage that any other classroom can match. The specific results are shown in Figure 2. Most of the students in both schools A and B chose to focus on English, accounting for 78.49% and 54.98%, respectively. In addition, 17.16% of the students in school B chose the whole English language.

4.3. Analysis of Communication Strategy under Wireless Communication and Multimedia. As an important symbol of culture, language is an integral part of it. From the use of language, we can observe the characteristics and many attributes of this culture. On the contrary, language cannot survive independently without its culture; otherwise, it will become rootless duckweed. Multimedia technology provides a strong support for our traditional cultural behavior in English teaching. But it does not mean that everything is going well. We must follow the law of education and teaching step by step.

The first is to use multimedia technology to retrieve information and make courseware to help students establish intuitive feelings, that is, to “reproduce” the relevant cultural scenes in front of students’ eyes. This model greatly expands the students’ horizons and makes the boring English teaching become a vivid cultural appreciation. It contains the characteristics of inclusiveness. With the blessing of multimedia technology, every student has become a connoisseur and disseminator of culture. This change of identity makes the whole classroom a real English cultural scene, and the cultural stimulation students receive is particularly strong. It will make students have a deep memory of this part of

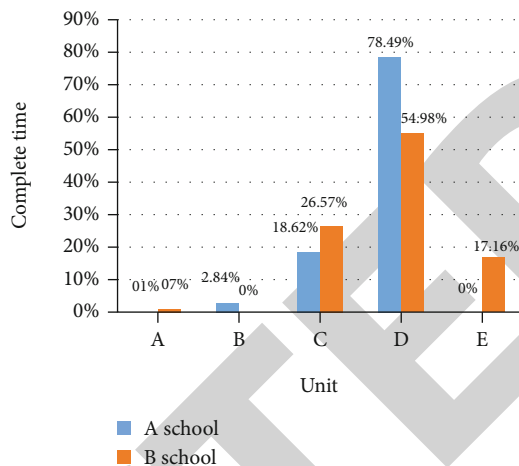


FIGURE 2: Questionnaire.

the relevant content, so as to help us better complete the teaching objectives.

The second is teachers’ rational use of multimedia technology in classroom teaching, which is one of the biggest challenges for teachers. In the process of cultural communication, the bridge role of college English teachers is particularly obvious, how to combine the mission of cultural communication in classroom teaching with the knowledge teaching required by the syllabus, so that the two can complement each other, how to strive to upgrade their knowledge system, so that classroom teaching can keep pace with the development of the times, and so on.

The third is to ingeniously combine the knowledge learned with the cultural background and use multimedia to form a novel and effective review system to help students better master the knowledge they have learned. One of the biggest difficulties faced by Chinese students in learning English is the differences between cultures. Facing some knowledge points, they can only adopt hard memory methods. This method consolidates the knowledge level of students and has very limited help in improving their English proficiency. With the help of multimedia, students can compare the cultural differences between the two sides more intuitively, thus forming an image memory.

5. Conclusions

The main objective of this study is how to adjust the intercultural communication of college English in the context of multimedia development. Firstly, it systematically analyzes the evolution of cultural communication teaching in college English teaching from two aspects of English education and cultural communication. Second, the demand for English talents in China’s labor market focuses on application-oriented talents, but the purpose of English teaching in many schools remains in the reality of traditional research-oriented teaching. The experimental results show that the teaching efficiency of cultural communication in college English teaching can be greatly improved. But there are also some shortcomings. For example, the updating of college

Retraction

Retracted: Research on Webcast Supervision Based on Convolutional Neural Network and Wireless Communication

Wireless Communications and Mobile Computing

Received 28 November 2023; Accepted 28 November 2023; Published 29 November 2023

Copyright © 2023 Wireless Communications and Mobile Computing. This is an open access article distributed under the Creative Commons Attribution License, which permits unrestricted use, distribution, and reproduction in any medium, provided the original work is properly cited.

This article has been retracted by Hindawi, as publisher, following an investigation undertaken by the publisher [1]. This investigation has uncovered evidence of systematic manipulation of the publication and peer-review process. We cannot, therefore, vouch for the reliability or integrity of this article.

Please note that this notice is intended solely to alert readers that the peer-review process of this article has been compromised.

Wiley and Hindawi regret that the usual quality checks did not identify these issues before publication and have since put additional measures in place to safeguard research integrity.

We wish to credit our Research Integrity and Research Publishing teams and anonymous and named external researchers and research integrity experts for contributing to this investigation.

The corresponding author, as the representative of all authors, has been given the opportunity to register their agreement or disagreement to this retraction. We have kept a record of any response received.

References

- [1] Z. Sun, J. Sun, and X. Li, "Research on Webcast Supervision Based on Convolutional Neural Network and Wireless Communication," *Wireless Communications and Mobile Computing*, vol. 2021, Article ID 1191641, 7 pages, 2021.

Research Article

Research on Webcast Supervision Based on Convolutional Neural Network and Wireless Communication

Zhidong Sun ¹, Jie Sun ², and Xueqing Li ¹

¹School of Software, Shandong University, Shandong, China

²Affiliated Hospital of Qingdao Binhai University, Shandong, China

Correspondence should be addressed to Xueqing Li; xqli@sdu.edu.cn

Received 3 August 2021; Accepted 24 August 2021; Published 16 September 2021

Academic Editor: Balakrishnan Nagaraj

Copyright © 2021 Zhidong Sun et al. This is an open access article distributed under the Creative Commons Attribution License, which permits unrestricted use, distribution, and reproduction in any medium, provided the original work is properly cited.

Action recognition is the technology of understanding people's behavior and classification from video or image sequences. This thesis uses the deep learning approach for action recognition to realize webcast supervision. This paper uses the convolutional neural network (CNN) and the Gaussian Mixture Model (GMM) to establish the webcast supervision system. At the same time, streaming-based wireless communication network technology is adopted to ensure video transmission speed and quality. Results show that the average detection speed of the system can reach 11.86 frame/s, and the average recognition accuracy is 92.16%, and the missed detection rate is lower than 5%. The design of this system can fully meet the requirements of webcast supervision.

1. Introduction

As a new internet entertainment business model, the webcast is the product of the rapid development of the information age. The spread and rapid growth of this are mainly based on the progress of Internet technology and the rise of various live broadcast platforms. As a new product of the Internet age, there is nothing wrong with bringing social entertainment. However, if it challenges social value and standard social order, it must be effectively regulated. For example, in the current major live broadcast platforms on the market, there are often problems in the operation of the broadcast, like being vulgar and low threshold access of the host broadcast. These problems affect the development of the live broadcast platform and affect the environment of the Internet. However, current live broadcast supervision is mostly manual, which is far from efficient and also vulnerable to loopholes by illegal personnel. Therefore, it is urgent to establish an automatic live broadcast supervision system.

At present, there is relatively little research on the supervision of webcast, but there are more researches on video monitoring system [1, 2], which two share the same charac-

teristics in some way. The so-called video monitoring system is the product of the comprehensive application of multimedia technology, computer network, industrial control, and artificial intelligence. It is developing towards the direction of video digitization, system network, and intelligent management. In the simulation era, video monitoring is mainly represented by an analog tape recorder. The system comprises an analog camera, special cable, video switching matrix, analog monitor, analog video equipment, and videocassette. In the digital era, digital video recorder has begun to appear due to the development of digital video compression and coding technology. DVR enables users to digitize analog video signals and store them on a computer hard disk instead of a videocassette. Digital storage greatly improves the user's ability to process video information. In the network era, with the further development of the whole digital and networked video monitoring system, the role of video monitoring is becoming more and more important. However, it is weighty work for the staff who continuously monitor activities in the monitoring scene, day and night. Therefore, video monitoring needs to be more intelligent, active, and effective, so computer vision and application

researchers timely put forward the concept of a video monitoring of new generation.

Intelligent video monitoring is a new subject direction and application field by combining computer vision technology with multimedia communication technology, which is also a new challenging research content in the field of computer vision. By applying the method of computer vision and video analysis, it realizes the positioning, identification, and tracking of the target in the monitored scene by automatic analysis of the image sequence recorded by the camera without human intervention. On this basis, it will analyze and judge the related targets' behavior to realize 24-hour all-weather monitoring, accurate alarm, and high response speed. The introduction of intelligent video monitoring technology into the supervision of live broadcast networks can monitor the environment of live broadcasts and alarm the bad behavior of the host in time, which significantly improves the working efficiency of the staff.

In recent years, CNN has been widely used in human behavior recognition. As a representative deep learning network, CNN has a great improvement over the traditional neural network recognition effect [3–9]. Moreover, this method is an end-to-end recognition method, which does not need to be designed manually, and is of translation invariance and scale invariance. Its calculation way is very similar with the mammal visual system.

In this paper, the supervision of network live broadcast is a security supervision system which is established based on CNN. It can monitor the behavior of anchors in real time so as to guarantee the safety and health of network live broadcast.

2. Methods

2.1. Neural Network. A neural network is a kind of machine learning model employed for data classification or data prediction. The model structure is constructed based on data and learning rules. A neural network regression model is trained with data based on a training algorithm to predict a subsequent set of data.

As shown in Figure 1, a neural network model consists of some nodes/neurons, set at multiple layers: the input layer, one or more hidden layers, and the output layer. Each node/neuron has an activation function, which calculates how much neuron is “stimulated.” At each layer, the collections of nodes/neurons transform the input parameters; these parameters are distributed to the next layer, which is described as

$$z_j^n = \sum (w_{ji}^{(1)} x^{n-1} i + w_{j0}^{(1)}), \quad (1)$$

$$a_1^n = \sum (w_{ij}^{(2)} z^{n-1} i + w_{i0}^{(2)}), \quad (2)$$

$$y_1^n = F(a_1^n), \quad (3)$$

where x represents the input to the first layer; z represents the first layer's output; i, j represents the neural network node index; $w_{ji}^{(1)}$ represents the weight between the j

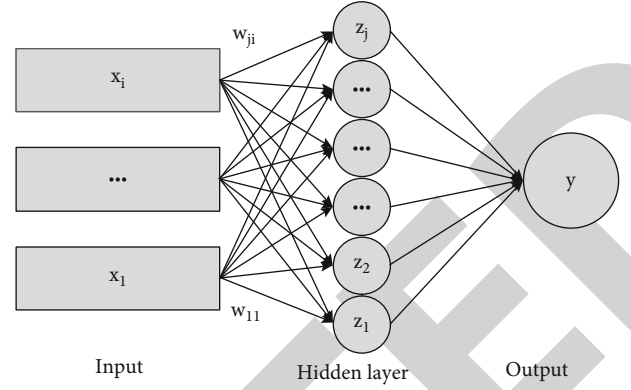


FIGURE 1: Scheme of neural network.

th node in the i th layer and the i th node in the $(i + 1)$ th layer; $F(a_i^n)$ represents the output value of the i th node in the $(n + 1)$ th layer after being activated by the activation function; w and w_0 represent the weight and bias between the neurons, which measures the significance of the data passed along the link (synapse). $F(a)$ employs the activation function, which employs the hidden layer's aggregated output to calculate output y .

The initial weights and biases are randomly assigned, and the training process continues until the desired output is obtained, which is evaluated by the cost function

$$E(w) = \frac{1}{2} \sum_{k=1}^K y(x_k, w_k) - t_k^2, \quad (4)$$

where y represents the output; t represents the desired output. The Levenberg-Marquardt (LM) algorithm is utilized in the neural network training process, which is a variation of gradient descent. The weight and bias of the neural network model are changed during the training process to minimize the error, which is described as

$$w^n = w^{n-1} - (J^T J + \mu I)^{-1} J e^{n-1}, \quad (5)$$

where $J = \partial E / \partial w$ represents the full-scale Jacobian matrix related to w ; I represents the identity matrix; μ represents a combination coefficient; e represents the prediction error.

The Levenberg-Marquardt algorithm starts with a forward computation by (1), (2), and (3). The prediction errors of the output layer and the hidden layer are calculated by

$$\begin{aligned} e^{(3)} &= y_1 - t, \\ \delta_1^{(3)} &= e_1^{(3)}, \\ \delta_j^{(2)} &= w_{1j} \delta_1^{(3)}. \end{aligned} \quad (6)$$

As shown in Equations (7) and (8), the Jacobian is calculated by a back-propagation process:

$$\frac{\partial E}{\partial w_{ji}} = \delta_j^{(2)} x_i, \quad (7)$$

$$\frac{\partial E}{\partial w_{1j}} = \delta_1^{(3)} z_j. \quad (8)$$

In the training process of the sample, the learning sample should be processed to make it fluctuate in a certain range. The normalization method is adopted in this paper to process the data to ensure that the data is between 0 and 1, which is written as

$$x_i = \frac{x_i - x_{\min}}{x_{\max} - x_{\min}}, \quad (9)$$

where x_i represents the average value, x_{\max} represents the maximum value, and x_{\min} represents the minimum value.

2.2. Convolutional Neural Network. Figure 2 is the structure of a typical CNN, which consists of an input layer, a convolution layer, a downsampling layer (pooling layer), a fully connected layer, and an output layer.

The input of a CNN is usually the raw image X . If H_i is the characteristic graph of the convolutional neural network layer i ($H_0 = X$), the production process of H_i is as follows:

$$H_i = f(H_{i-1} \otimes W_i + b_i), \quad (10)$$

where W_i is the weight vector of the convolution kernel at the first level i . The sign \otimes represents the convolution kernel to convolve with the image of layer $i - 1$ or feature graph, and the output of the convolution is added to the offset vector b_i at level i . Finally, the characteristic graph H_i of the layer i is obtained through the nonlinear excitation function $f(x)$.

The subsampling layer is usually behind the convolution layer, and the subsampling rule is as follows:

$$L_i = \text{subsampling}(H_{i-1}). \quad (11)$$

The CNN classifies the extracted features through the alternating transfer of multiple convolutional layers and lower sampling layer, and then, the probability distribution Y based on the input is got.

$$Y(i) = P(L = l_i | H_0; (W, b)). \quad (12)$$

The training objective of CNN is to minimize the loss function $L(W, b)$ of the network. The difference of the input H_0 and the value of expectation (residual error) is calculated by the loss function after the forward conduction. In this paper, the Levenberg-Marquardt is used. The Levenberg-Marquardt back propagation is employed to enhance the model training rate related to pure error back propagation or steepest descent, and this algorithm maintains the accuracy of the trained model. The neural network regression model is trained with the designed model structure, input parameters, and the number of nodes. The accuracy of both the training and the prediction/estimation is evaluated by mean absolute error (MSE), which is written as

$$e_{\text{avg}} = \frac{1}{n} \sum_{k=1}^n |\text{Output}_k - \text{Output}_{r,k}|, \quad (13)$$

where e_{avg} represents the average absolute error; n represents the number of data points, Output_k represents the k th estimated output parameter, and $\text{Output}_{r,k}$ represents the k th reference output parameter.

In the training process, the CNN is a commonly used gradient descent method. The residual error is propagated back through gradient descent, and the trainable parameters of each layer of CNN are updated layer by layer (W and b). The learning rate parameter η is used to control the intensity of the normal propagation of residuals:

$$\begin{aligned} W_i &= W_i - \eta \frac{\partial E(W, b)}{\partial W_i}, \\ b_i &= b_i - \eta \frac{\partial E(W, b)}{\partial b_i}. \end{aligned} \quad (14)$$

2.3. Extracting the Foreground of the Person Video. The common character behavior video foreground extraction tools are mixed Gaussian background modeling (GMM) [10], codebook algorithm [11], self-organizing background checks [12], vibe algorithm [13], and so on. In this paper, the GMM method is used to extract anchors' behaviors. The GMM is used to conduct statistics on pixel sample information, and statistical information such as probability density of a large number of sample values of pixel points over a long period of time is used to represent the background. Generally, this statistical information includes the number of patterns, the mean of each pattern, and standard deviations. Then, the method of statistical difference (such as 3σ principle) is used to distinguish the target pixel, which also has a good modeling effect on the more complex dynamic background. In the GMM, 3 to 5 Gaussian models are generally used to represent each pixel's features in the image. Moreover, each pixel in the current image is matched with the mixed Gaussian model so as to update the model after a new frame is obtained. In addition, if the match is successful, it is the background point; otherwise, it is the foreground point.

In this model, it is general that the color information between pixels is not related. Therefore, the pixels are handled independently of each other. For each pixel on the video frame image, the change of the pixel value on the sequence image is treated as a random process that continuously generates the pixel value. It means that the Gaussian distribution is used to describe the color rules of each pixel.

For the multimodal (multimodal Gaussian distribution) models, each pixel on an image frame is viewed as a superposition of multiple Gaussian distributions with different weights. The weights and distribution parameters of each Gaussian distribution are updated over time, and each Gaussian distribution corresponds to a state that may produce the color of the pixel. In the process of color image processing, it is assumed that the three color channels of pixel point are independent of each other and have the same variance. For

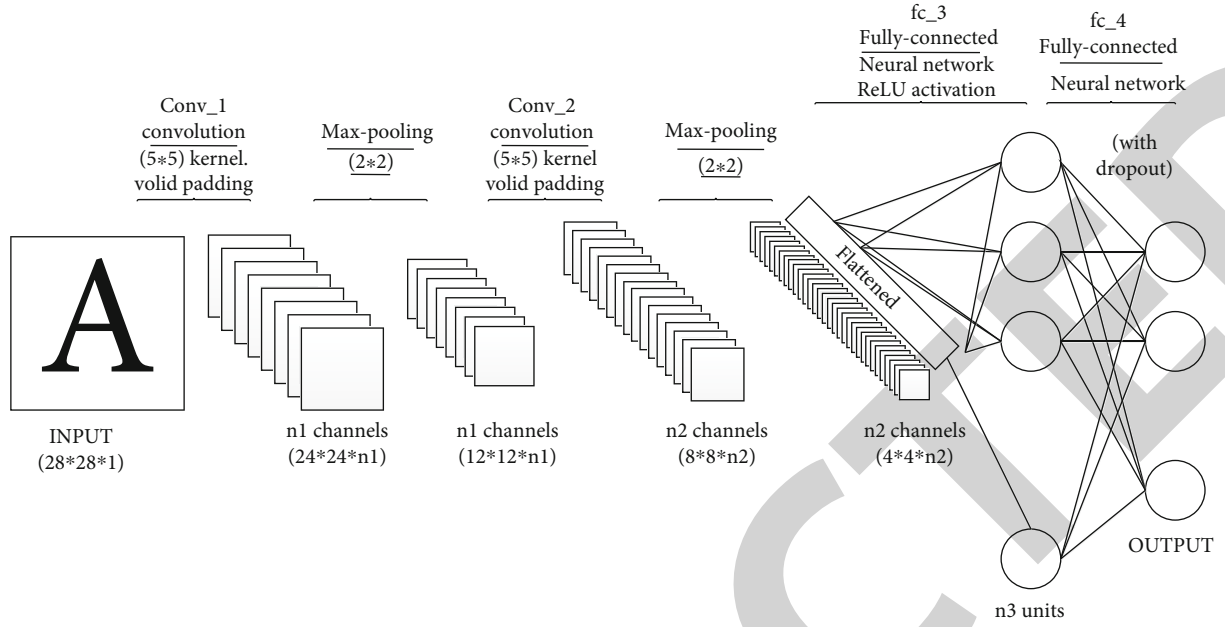


FIGURE 2: Fundamentals of CNN.

the observation dataset $\{x_1, x_2, \dots, x_N\}$ of the random variable X , $x_t = (r_t, g_t, b_t)$ is the sample of the pixel in the t moment, so the single sampling point x_t obeys the probability density function of the mixed Gaussian distribution:

$$p(x_t) = \sum_{i=1}^k w_{i,t} \times \eta(x_t, \mu_{i,t}, \tau_{i,t}), \eta(x_t, \mu_{i,t}, \tau_{i,t}) = \frac{1}{|\tau_{i,t}|^{1/2}} e^{-(1/2)(x_t - \mu_{i,t})^T \tau_{i,t}^{-1} (x_t - \mu_{i,t})}, \tau_{i,t} = \delta_{i,t}^2 I, \quad (15)$$

where k is the total number of distribution patterns, $\eta(x_t, \mu_{i,t}, \tau_{i,t})$ is the i Gaussian distribution at t moment, $\mu_{i,t}$ is the average of the Gaussian distribution, $\tau_{i,t}$ is the covariance matrix for it, $\delta_{i,t}$ is the variance, I is the three-digit identity matrix, and $w_{i,t}$ is the weight of the i Gaussian distribution at the t moment.

2.4. Extraction of Character Features. Feature extraction is an important part of character behavior detection. For network broadcast, sample selection plays an important role in the detection of character behavior. Currently, there are many methods of character feature extraction, such as SIFT [14], Haar [15], HOG [16], and LBP [17]. HOG feature extraction method is used in this paper. The specific steps of HOG are as follows.

2.4.1. Graying. In view of the fact that the color information of the image does not play a significant role in the live broadcast monitoring, it is necessary to convert the image to grayscale first in order to facilitate the later operation.

2.4.2. Standardize the Gamma Space and Color Space. This step mainly reduces the impact of illumination on the recog-

nition effect and normalizes the image before the subsequent steps. The gamma compression formula is shown in

$$I(x, y) = I(x, y)^{\text{gamma}} \left(\text{gamma} = \frac{1}{2} \right). \quad (16)$$

2.4.3. Calculating Image Gradient. In this step, it needs to calculate the horizontal gradient and vertical gradient of the image and calculate the gradient direction value of each pixel. The main effect of this step is to further reduce the effect of illumination (light). The computing method of the gradient is shown in

$$G_x(x, y) = H(x+1, y) - H(x-1, y), G_y(x, y) = H(x, y+1) - H(x, y-1), \quad (17)$$

where $G_x(x, y)$, $G_y(x, y)$, $H(x, y)$ is the horizontal and vertical gradients and pixel values at pixel points, respectively; furthermore, the gradient value and the gradient direction of the pixel (x, y) can be written by

$$G(x, y) = \sqrt{G_x(x, y)^2 + G_y(x, y)^2}, \alpha(x, y) = \tan^{-1} \left(\frac{G_y(x, y)}{G_x(x, y)} \right). \quad (18)$$

2.4.4. Component Gradient Histogram. In this step, the image is divided into a number of cell units ($a \times a$). The histogram of n bins is used to calculate the gradient information of the $a \times a$ pixels. As is shown in Figure 3, if the gradient of a pixel is within a^2 degrees, the $i+1$ bin count in the histogram is incremented by 1. In this way, the histogram of the cell's gradient direction can be obtained.

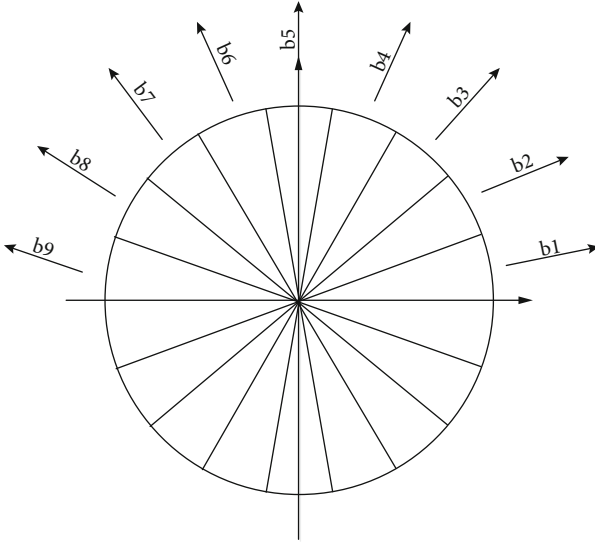


FIGURE 3: Graph of gradient direction projection.

2.4.5. *Combination of Block.* Variations in the foreground-background contrast and local illumination greatly increase the range of gradient intensity. In order to avoid this effect, it is usually necessary to do a local normalization of the gradient intensity. Normalization can compress the shadows, lighting, and edges. A common approach is to combine individual cell units into a block to get the HOG feature of this block by connecting the eigenvectors for all cell units in a partnership. Consequently, the overlap between the different blocks can effectively improve the problems such as local lighting.

3. Results and Discussions

3.1. *Design of Webcast Supervision System.* As is shown in Figure 4, the framework of the webcast supervision system is based on the GMM and the CNN; the specific process is as follows:

Firstly, a dataset is established to collect a large number of anchors' behavior samples and the size unified to the height is 100 and the width is 50. Then, the training set and the test set are found, respectively. Before the neural network model training, a large-scale training set should be established first. In order to detect the effect of the network, a test set should be built to consider the effect of the neural network model. 1241 images of anchors' behavior are collected in this paper, of which the training set and the test set were 80% and 20%, respectively. In terms of data sources, live-broadcast shots of anchors on various live broadcast platforms were selected, including waving, clapping, walking, and running. In order to monitor anchors' behaviors, this paper selected bad behaviors (smoking) as cases of violations.

Secondly, the classifier was trained and the CNN structure was built, and the dataset was trained to obtain the model.

In this paper, the structure of the CNN network includes 5 layers.

- (1) Convolutional layer C1: the input is the 3-channel RGB image with a size of $100 * 5$, which is convolved

with a $5 * 5$ convolution check to get 16 feature maps of $96 * 46$

- (2) Sampling layer S2: S2 is a lower sampling layer, which uses the principle of local correlation of images to sample images. This method can reduce the amount of data processing when retaining effective information. The subsampling is carried out for the data of the C1 layer. For the $3 * 3$ region of each C1 feature map, we sum and add bias to the 9 pixels and then store the results calculated by using the Sigmoid activation function in the new feature map. Finally, we get a feature diagram of $16 * 32 * 16$ in S2 layer S2
- (3) Convolutional layer C3: after step 2, the S2 layer is convolved by the $16 * 3 * 3$ convolution checks and a $30 * 14$ feature map is got
- (4) Sampling layer S4: the function of S4 is the same as the S2; it has $16 * 15 * 7$ feature maps, which are connected with the feature maps of the C3 layer
- (5) F5: the connection between the F5 layer and the S4 layer is the standard full connection, which is a standard MLP neural network transfer mode. Finally, F5 is connected to the classifier to complete the last part of the training

Thirdly, enter the video stream. In the paper, we used the HikVision webcam and input the video stream in the RTSP format.

Fourthly, Gaussian background was mixed for modeling, and foreground pixels were extracted after modeling. The process of the Gaussian background modeling algorithm is as follows:

- (1) Each new image's prime value x_t is kept comparing (15) until a distribution model matches the new pixel values. In other words, the mean deviation of the same model is below 2.5σ :

$$|X_t - u_{i,t-1}| \leq 2.5\sigma_{i,t-1} \quad (19)$$

- (2) The weight of each pattern is updated according to Equation (20), where α is the learning rate. For the matched pattern, $M_{k,t} = 1$; otherwise, however, $M_{k,t} = 0$. Then, the weight of each pattern is normalized:

$$\omega_{k,t} = (1 - \alpha) \times \omega_{k,t-1} + \alpha \times M_{k,t} \quad (20)$$

- (3) The mean value and variance of the unmatched pattern remain unchanged, and the parameters of the matched pattern are updated according to

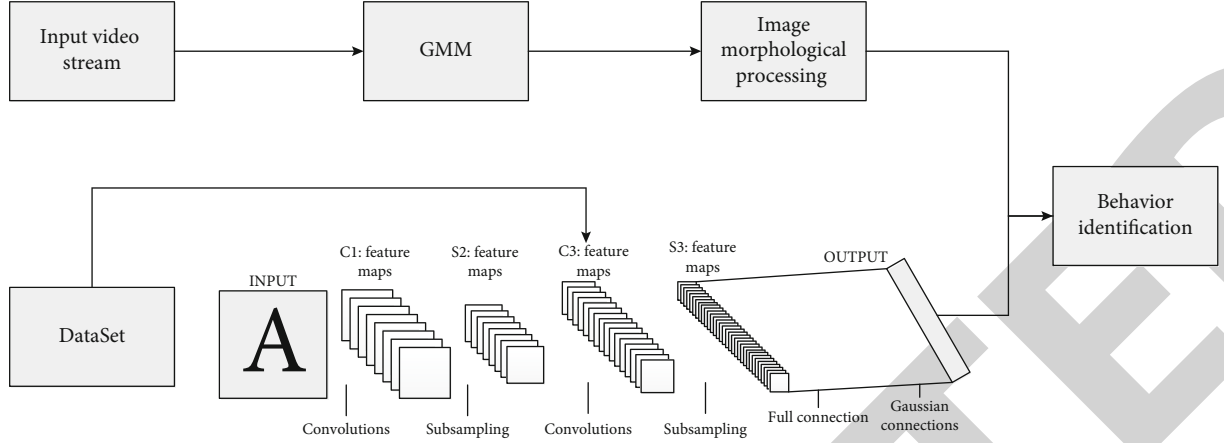


FIGURE 4: Webcast supervision system.

TABLE 1: The accuracy of identification.

Category		Accuracy (%)	Detection speed (frame/s)	Missed detection rate (%)
Waving		91.7	12.2	4.3
Clapping		92.6	11.7	5.4
Walking		97.2	10.9	3.8
Running		85.9	13.4	3.7
Smoking		93.4	11.1	4.7
Average	GMM+CNN	92.16	11.86	4.38
	Faster+R-CNN	88.71	0.87	41.56
	HOG+SVM	90.70	4.72	24.51

$$\begin{aligned} \sigma_t^2 &= (1 - \rho) \times \sigma_{t-1}^2 + \rho \times (X_t - \mu_t)^{T+1}, \rho = \alpha \times \eta \times (X_t | \mu_k, \sigma_k), \mu_t \\ &= (1 - \rho) \times \mu_{t-1} + \rho \times X_t \end{aligned} \quad (21)$$

- (4) If no relevant patterns are matched in step 1, the pattern with the least weight will be replaced. The mean value of this pattern is the current pixel value, the standard deviation is the initial larger value, and the weight is the smaller value
- (5) Each pattern is arranged in descending order according to the value of ω/α^2
- (6) The B module is the back view according to (22), where T representation of the proportion:

$$B = \arg \left(\min \left(\sum_{k=1}^b w_k > T \right) \right) \quad (22)$$

Fifthly, the extracted foreground point is binarized, and the image morphology is processed, including filtering, expansion, and etching, and the edge contour is extracted to get the processed image.

Finally, the processed graphics and the model trained by CNN were compared and analyzed to judge the anchor's behavior.

3.2. The Accuracy of Identification. Each test sample will be tested in the testing stage for each kind of behavior, and then, the classification result will be obtained. The classification result will be compared with the label of the test sample. In Table 1, the accuracy rate of each class is, respectively, counted. Finally, the average accuracy rate is obtained by using the accuracy rate of each class. In addition, the detection speed and missed detection rate are also given in Table 1. Furthermore, comparing with the recognition accuracy of different methods, it is seen that the recognition method of GMM+CNN is higher than the other algorithms, reflecting its accuracy in live broadcast behavior detection.

4. Conclusion

In this paper, an anchor behavior monitoring system based on a CNN+GMM is designed. The deep neural network can autonomously and fully learn behavior features, which avoids explicit feature extraction and makes the algorithm more robust, by effectively eliminating the influence of illumination, angle, form, and other factors on the final detection results.

The system can meet the requirements of real-time performance. There is no lag phenomenon in visual measurement in

Research Article

Visual Fatigue Alleviating in Stereo Imaging of Anaglyphs by Reducing Retinal Rivalry and Color Distortion Based on Mobile Virtual Reality Technology

Min Qi ^{1,2}, Shanshan Cui ¹, Qianmin Du ³, Yuelei Xu ⁴, and David F. McAllister ⁵

¹School of Electronics and Information, Northwestern Polytechnical University, Xi'an, China

²National Engineering Laboratory for Integrated Aero-Space-Ground-Ocean Big Data Application Technology, Xi'an, China

³Patent Examination Cooperation Hubei Center of Patent Office, Wuhan, China

⁴Unmanned System Research Institute, Northwestern Polytechnical University, Xi'an, China

⁵Department of Computer Science, North Carolina State University, Raleigh, USA

Correspondence should be addressed to Min Qi; drqimin@nwpu.edu.cn

Received 1 July 2021; Accepted 13 August 2021; Published 16 September 2021

Academic Editor: Raffaele Mascella

Copyright © 2021 Min Qi et al. This is an open access article distributed under the Creative Commons Attribution License, which permits unrestricted use, distribution, and reproduction in any medium, provided the original work is properly cited.

Stereoscopic display is the means of showing scenes in Virtual Reality (VR). As a type of stereo images, anaglyphs can be displayed not only on the screen, but are currently the only solution of stereo images that can be displayed on paper. However, its deficiencies, like retinal rivalry and color distortion, could cause visual fatigue. To address this issue, an algorithm is proposed for anaglyph generation. Unlike previous studies only considering one aspect, it considers both retinal rivalry and color distortion at the same time. The algorithm works in the CIE $L^*a^*b^*$ color space and focuses on matching the perceptual color attributes especially the hue, rather than directly minimizing the sum of the distances between the perceived anaglyph color and the stereo image pair. In addition, the paper builds a relatively complete framework to generate anaglyphs so that it is more controllable to adjust the parameters and choose the appropriate process. The subjective tests are conducted to compare the results with several techniques which generate anaglyphs including empirical methods and computing methods. Results show that the proposed algorithm has a good performance.

1. Introduction

Through the stereoscopic display technology, VR can show various scenes by vivid realistic visual effects and provide more information. The technology can be used in education, training, and many different application fields. The mechanism of stereo imaging is so-called the binocular vision. The image received by the left eye is slightly different from that received by the right eye of the same scene. Based on these two images, the human brain calculates the depth information of the scene [1]. A binocular vision system includes two cameras placed in parallel using different views to capture two images in order to obtain the depth information [2, 3]. There are three kinds of stereoscopic display

technology based on the principle of binocular parallax. They are autostereoscopic display, helmet-mounted display (HMD), and stereo glass display. Autostereoscopic display can realize the stereoscopic effect viewed by naked eyes. It is currently very limited and needs much further researches. HMD has developed rapidly in recent years, and the device becomes much lighter than before. It completely blocks people's vision from the outside world, so that people are immersed in the stereoscopic virtual world. HMD uses two channel videos of stereo image pairs as input signals of each small screen which is close in front of each eye. Stereo glasses are the most used stereo display devices in public where the stereo image pairs or two channel videos are projected onto a large curtain, displayed on computer screens or prints.

Colored-filter glasses are a type of stereo glasses with anaglyphs as input stereo image pairs, by which the stereoscopic visual effect can be perceived.

Anaglyphs have some unique advantages which are not available from other stereoscopic display technology:

- (1) Compared with full-color stereo image pairs, the image compression ratio of anaglyphs reaches more than 79% for the same scene. This is an outstanding advantage for data transmission
- (2) Users can perceive the stereo effect not only on screen, but also even on prints [4, 5]. Anaglyphs are the only way that can display stereo objects on prints. It just needs ordinary paper without using any special ink or special printer. This obviously provides an attractive way of conveying stereo information to users, because the stereo objects in papers can be taken anywhere to provide a vivid visual experience when people communicate
- (3) Compared with the polarized glasses which need to use expensive displaying devices and compared with the shutter glasses which need to strictly control the high refresh rate, anaglyphs just need an inexpensive colored-filter glasses instead to form an specific stereoscopic display system. The stereo effect is achieved by allowing different light waves of anaglyph images to reach each eye using different colored-filter glasses. The colored-filter glasses are the most inexpensive hardware among the stereoscopic display devices. This characteristic removes an economic obstacle, especially for underdeveloped areas
- (4) Only anaglyphs can be used as the input signals for all the other display devices. That means anaglyphs have the strongest commonality

However, anaglyphs are also riddled with problems. A problem needs to be considered for generating anaglyphs is retinal or binocular rivalry. If the difference of color or luminance between the perceived left and right images exceeds a certain level, it will cause one of the two images to dominate to be seen at some point in turn [6, 7]. Thus, the eyes will perceive two slightly different images alternatively, instead of fusing them into a single and stable stereoscopic perception. Retinal rivalry is of great concern in anaglyphs because it often leads to visual fatigue and other side effects. Fortunately, the adverse consequences of retinal rivalry can be effectively reduced by manipulating the luminance.

When generating anaglyphs, color distortion is also an intractable problem which will cause degradation in the stereoscopic effect. Color distortion can also be understood as a limited color reproduction. It may lead to the perceived color through the colored-filter glasses to be very different from the original view and directly determines the color fidelity of the perceived stereo scene.

In this paper, a novel method is proposed for anaglyph generation, which considering the retinal rivalry and color

distortion together instead of some studies which only consider one aspect in a one-sided way. We choose LCD as the displaying device and colored-filter glasses as viewing device. For colored-filter glasses, red-cyan glasses are most common nowadays. It can be bought for just a few cents, and most books with anaglyphs are also sold with red-cyan glasses together. So we choose red-cyan glasses to do this study. The principle may also be applied to the other colored-filter glasses but some parameters may need to be manipulated renewedly, which are beyond the scope of this paper.

Then, we will introduce the outline of this paper. Section 2 gives the brief review of existing studies on anaglyph generation. Section 3 gives the mathematical framework of the proposed algorithm and its motivation and novelty. Section 4 introduces a detailed implementation of the proposed method. Section 5 compares the results of our method with other methods and gives the research results of the experiment. At last, conclusions are given in Section 6.

2. Related Work

The anaglyph method was patented in 1891 by Louis Ducos du Hauron, but similar methods had been demonstrated previously by W. Rollmann in 1853 and J.C.D'Almeida in 1858. Since the conception of anaglyphs in the 1850s, not many anaglyph generation techniques have been developed and most of them are empirically designed until a mathematical analysis by Dubois [8] in 2001. The remarkable advantages of anaglyphs are low-budget viewing devices, efficiency transmission, and being the only solution that can be printed on paper and perceived stereoscopic effects for arbitrary angles without reducing brightness of images. The improved algorithms based on Eric Dubois' method are constantly emerging, which make anaglyphs viewed more comfortable to some extent. They can be summarized as computed method.

Computed method takes into account the spectral parameters of the display device and the absorption curve function of colored-filter glasses for different bands. Dubois' method of generating anaglyphs begins with an understanding of the visual pathway from the digital image values until it is perceived by the viewer. The core idea of McAllister's method [9] is transforming the calculation of the color distance between the perceived anaglyph and the stereo image pairs into CIE $L^*a^*b^*$ color space which is a uniform color space. The whole processing is similar to the procedures of Dubois's method. Midpoint algorithm [10] is also worked in CIE $L^*a^*b^*$ color space. It directly use the midpoint of the perceived left image and perceived right image in CIE $L^*a^*b^*$ color space as the information of the anaglyph. In contrast to the above methods, Songnan Li's method [11] is trying to match the perceptual color appearance attributes instead of minimizing the error matrix of color distance in CIE $L^*a^*b^*$ color space. It presents a new train of thought. The method is aimed at minimizing the perceptual differences between the original and perceived colors based on matching the meaningful color appearance attributes instead of different color spaces, which is also the inspiration of our proposed algorithm.

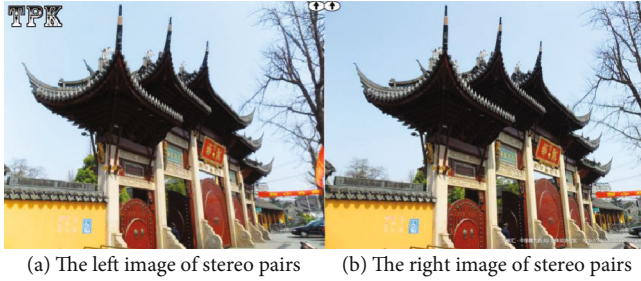


FIGURE 1: Stereo pairs named gate.

From Figure 1 of gate, stereo image pairs were taken by the stereoscopic camera, and the anaglyphs of four computed methods are shown in Figure 2. The anaglyphs in upper line are generated, respectively, by Dubois' method and McAllister's method, and the anaglyphs in lower line are generated, respectively, by Midpoint algorithm and Songnan Li's method.

3. Framework of Anaglyph Designing

3.1. Systematic Framework. For the convenience of presentation, we denote the left image of the stereo pairs as $I_{L,RGB}$, the right image as $I_{R,RGB}$, and the final anaglyph as $I_{A,RGB}$ in RGB color space. The systematic framework of our method for generating anaglyphs is shown in Figure 3.

As the frame figure shows, we need to convert the stereo pairs into CIE $L^*a^*b^*$ color space firstly and then take different operations for the left and right images. Our objective is to obtain the G and B channels from the processed right image and the R channel from the processed left image. Instead of using the R channel of left image to be the R channel of the final anaglyph and the G and B channels of right image to be the final anaglyph's G and B channels directly, our algorithm will do a series of operations for the stereo pairs in CIE $L^*a^*b^*$ color space before this procedure. CIE $L^*a^*b^*$ color space is based on the physiological characteristics of human beings. It is a digital way of describing persons' visual perception. In the CIE $L^*a^*b^*$ color space, the change value of the color is consistent with the change amount of the eye perception of the color. So in the second step, a matching process based on the color attributes for the right image is implemented in CIE $L^*a^*b^*$ color space. In addition to the matching principles in Songnan Li's method, our method is more focused on the matching of hue as well so that we can get a better color reproduction. Next, we will give a delightness operation for the left and right images simultaneously to reduce the effect of retinal rivalry caused by the nonuniform brightness between them, which is also conducted in CIE $L^*a^*b^*$ color space. At last, we need to calculate the L^* , a^* , and b^* component values of the processed right image and processed left image and then convert them into RGB color space. Combining R channel derived from the processed left image and G and B channels derived from the processed right image, the anaglyph is completed by this time.

This systematic framework just shows the simple process of generating anaglyphs which is used to help the readers to form a preliminary understanding. The specific implementations will be shown in Section 4.

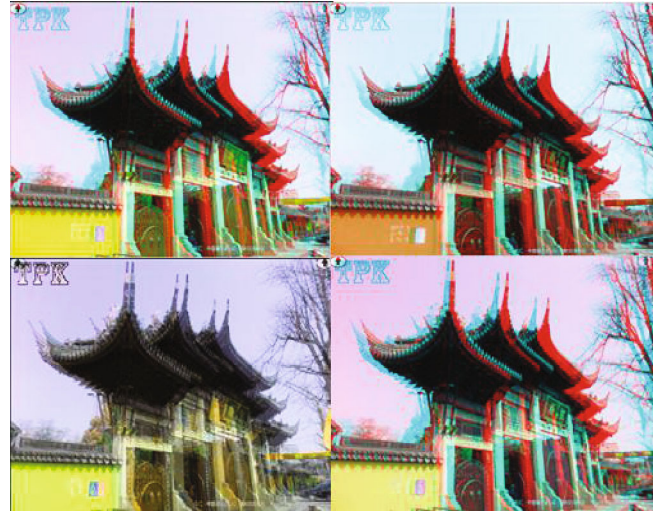


FIGURE 2: The anaglyphs of four computed methods.

3.2. Inspiration and Advantages. This method is inspired by Professor McAllister's method and Songnan Li's method. The anaglyph generated by McAllister's method has a great improvement in color reproduction but with a heavy retinal rivalry especially in the red-like region, and the anaglyph generated by Songnan Li's method does have a better visual comfort but it has a heavy color distortion. Through the analysis of this phenomenon, we make an improvement on Songnan Li's method to gain a better color reproduction by adding another matching principle which is the matching process of hue in CIE $L^*a^*b^*$ color space as well. In order to ensure the hue of matched image as close to the hue of original image as possible during the matching processing, we can get a more accurate color reproduction.

In terms of computation complexity and time complexity, our algorithm has obvious advantages compared to McAllister's method which needs iterative optimization. At the same time, because the matching processing based on color attributes need to be conducted in CIE $L^*a^*b^*$ color space, we can adjust the saturation and lightness more flexible according to different stereo pairs.

In summary, our method can dynamically adjust the balance between the retinal rivalry and color reproduction.

4. Detailed Information of Generating Anaglyphs

As the systematic framework in Section 3 described above, we need to do different treatments for the left and right images. Detailed information on each processing step of the systematic framework will be given below.

4.1. Converting the Stereo Pairs to CIE $L^*a^*b^*$ Color Space. For the convenience of description, we denote the left image in CIE XYZ color space as $I_{L,XYZ}$ and the right image in CIE XYZ color space as $I_{R,XYZ}$. Accordingly, $I_{L,Lab}$ can represent the left image, and $I_{R,Lab}$ can represent the right image in CIE $L^*a^*b^*$ color space. In the first step, we need to chip the elements of the stereo pairs in the range 0-1 and then

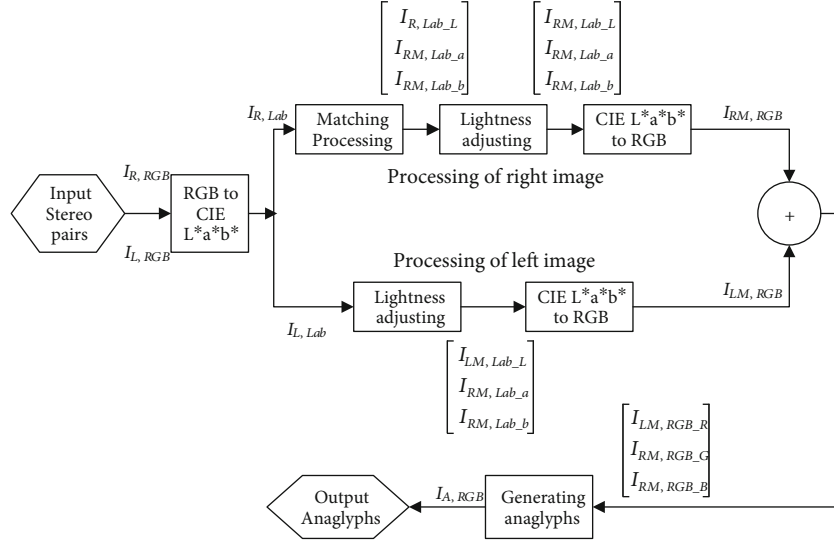


FIGURE 3: Systematic framework of generating anaglyphs.

convert the stereo pairs to CIE $L^*a^*b^*$ color space, which requires the CIE XYZ color space as the intermedium. So we can separate this conversion into two steps, and the first step is to map the stereo pairs from RGB color space to CIE XYZ color space:

$$\begin{bmatrix} I_{L,XYZ-X} \\ I_{L,XYZ-Y} \\ I_{L,XYZ-Z} \end{bmatrix} = Cs \times \begin{bmatrix} I_{L,RGB-R} \\ I_{L,RGB-G} \\ I_{L,RGB-B} \end{bmatrix} \begin{bmatrix} I_{R,XYZ-X} \\ I_{R,XYZ-Y} \\ I_{R,XYZ-Z} \end{bmatrix} = Cs \times \begin{bmatrix} I_{R,RGB-R} \\ I_{R,RGB-G} \\ I_{R,RGB-B} \end{bmatrix}, \quad (1)$$

where $I_{L,XYZ-X}$, $I_{L,XYZ-Y}$, and $I_{L,XYZ-Z}$ represent, respectively, the X, Y, and Z component values of left image in CIE XYZ color space, and $I_{R,XYZ-X}$, $I_{R,XYZ-Y}$, and $I_{R,XYZ-Z}$ represent, respectively, the X, Y, and Z component values of right image in CIE XYZ color space. The values of conversion matrix Cs are given in formula (2) which refers to [9]. At the same time, we give the values of A_L and A_R by formula (3). These values were calculated by Professor McAllister, who made an improvement based on Dubois' computing method so that these values are also used for LCD displaying which is exactly what we need.

$$Cs = \begin{bmatrix} 0.4243 & 0.3105 & 0.1657 \\ 0.2492 & 0.6419 & 0.1089 \\ 0.0265 & 0.1225 & 0.8614 \end{bmatrix}, \quad (2)$$

$$A_L = \begin{bmatrix} 0.1840 & 0.0179 & 0.0048 \\ 0.0876 & 0.0118 & 0.0018 \\ 0.0005 & 0.0012 & 0.0159 \end{bmatrix} A_R = \begin{bmatrix} 0.0153 & 0.1092 & 0.1171 \\ 0.0176 & 0.3088 & 0.0777 \\ 0.0201 & 0.1016 & 0.6546 \end{bmatrix}. \quad (3)$$

In the second step, we need convert the left image $I_{L,XYZ}$

and right image $I_{R,XYZ}$ to CIE $L^*a^*b^*$ color space, respectively, by the formulas below:

$$\begin{cases} I_{L,Lab-L} = 116 \cdot f\left(\frac{I_{L,XYZ-Y}}{Y_{white}}\right) - 16 \\ I_{L,Lab-a} = 500 \cdot \left[f\left(\frac{I_{L,XYZ-X}}{X_{white}}\right) - f\left(\frac{I_{L,XYZ-Y}}{Y_{white}}\right) \right] \\ I_{L,Lab-b} = 200 \cdot \left[f\left(\frac{I_{L,XYZ-Y}}{Y_{white}}\right) - f\left(\frac{I_{L,XYZ-Z}}{Z_{white}}\right) \right] \end{cases}, \quad (4)$$

$$\begin{cases} I_{R,Lab-L} = 116 \cdot f\left(\frac{I_{R,XYZ-Y}}{Y_{white}}\right) - 16 \\ I_{R,Lab-a} = 500 \cdot \left[f\left(\frac{I_{R,XYZ-X}}{X_{white}}\right) - f\left(\frac{I_{R,XYZ-Y}}{Y_{white}}\right) \right] \\ I_{R,Lab-b} = 200 \cdot \left[f\left(\frac{I_{R,XYZ-Y}}{Y_{white}}\right) - f\left(\frac{I_{R,XYZ-Z}}{Z_{white}}\right) \right] \end{cases}, \quad (5)$$

where $I_{L,Lab-L}$, $I_{L,Lab-a}$, and $I_{L,Lab-b}$ represent, respectively, the L^* , a^* , and b^* component values of left image in CIE $L^*a^*b^*$ color space, and $I_{R,Lab-L}$, $I_{R,Lab-a}$, and $I_{R,Lab-b}$ represent, respectively, the L^* , a^* , and b^* component values of right image in CIE $L^*a^*b^*$ color space. $[X_{white} Y_{white} Z_{white}]$ is X, Y, and Z values of white point, and we can get its values by

$$[X_{white} Y_{white} Z_{white}]^T = Cs \times [111]^T. \quad (6)$$

The specific expression of function $f(\bullet)$ is

$$f(s) = \begin{cases} s^{1/3} & \text{if } s > \left(\frac{6}{29}\right)^3 \\ \frac{1}{3} \left(\frac{29}{6}\right)^2 s + \frac{4}{29} & \text{otherwise.} \end{cases} \quad (7)$$

4.2. Matching Color Attributes in CIE $L^*a^*b^*$ Color Space.

According to [11], color attributes are deemed to be the color representation in the late stage of HVS. Therefore, similar to Songnan Li's method, our designing method is also matching the meaningful color attributes. But in addition to its matching principles which require the matched right image can generate lightness, hue, and saturation values as close to its original perceived right image and require the matched image can be represented by $\{R, G, B\}$ with $R = 0$, our method is more focused on the matching of hue as well. Thus, we can get a better color reproduction. For the stereo pairs which have been converted to CIE $L^*a^*b^*$ color space, we need to deal with them, respectively, as follows.

4.2.1. Preprocessing for the Right Image. In CIE $L^*a^*b^*$ color space, the meaning of saturation is the same as the chroma under the condition of describing the psychological attributes of one color. So, in terms of right image, we can get its corresponding saturation H_R and S_R hue by

$$H_R = \arctan\left(\frac{I_{R,Lab-b}}{I_{R,Lab-a}}\right), \quad (8)$$

$$S_R = \sqrt{(I_{R,Lab-a})^2 + (I_{R,Lab-b})^2}. \quad (9)$$

4.2.2. Matching the Right Image. For the matching principles we have mentioned above, two of the most important are as follows:

- (1) In CIE $L^*a^*b^*$ color space, $I_{RM,Lab-L}$, $I_{RM,Lab-a}$, and $I_{RM,Lab-b}$ are corresponding to L^* , a^* , and b^* component values of the matched right image which should be close to the perceived right image filtered by the colored glasses as possible. We can regard this principle as a projection, i.e., we need to ensure that the distribution of the matched image in CIE $L^*a^*b^*$ color space is in the scope of the distribution of the perceived right image in CIE $L^*a^*b^*$ color space
- (2) Utilize the immutability of hue to assure the hue of the matched right image is equal to the hue of the original right image. We can regard this principle as the rule of projection, i.e., we must ensure the hue of matched right image as close to the hue of original right image as possible during the projection

Therefore, according to the first principle, we can use a matrix $C = [R = 0, 1, \dots, 255, G = 0, 1, \dots, 255, B = 0, 1, \dots, 255]$ which could represent every color in RGB color space as the right image to calculate its corresponding perceived L^* , a^* , and b^* component values which can be denoted by $I_{RP,Lab-L}$, $I_{RP,Lab-a}$, and $I_{RP,Lab-b}$ in CIE $L^*a^*b^*$ color space and draw the $L^*a^*b^*$ 3D figure. Thus, the distribution range in the 3D figure is the range of any perceived color filtered by the colored glasses in CIE $L^*a^*b^*$ color space, which is called the perceived field. However, the computational complexity and time complexity of drawing the target 3D figure are considerable, which is a big burden for the computer's memory.

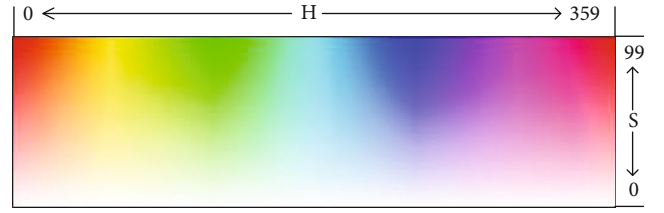


FIGURE 4: HS figure with $V = 100$.

Instead of drawing the perceived field directly using the above means, we choose to utilize the relationship between RGB color space and HSV color space to convert the matrix C which has $256 \times 256 \times 256$ elements that can represent every color in RGB color space into 100 HS figures whose V is an integral ranges from 1 to 100. Here, V is the brightness of HSV color space, HS figure is a 2D plane whose horizontal axis is the hue, and vertical axis is the saturation. Figure 4 shows a HS figure with $V = 100$.

Based on the above analysis, we can get down to the 100 HS figures in turn. If R , G , and B channels of HS figure in RGB color space can be denoted by I_{HS-R} , I_{HS-G} , and I_{HS-B} , and $I_{RP,XYZ-X}$, $I_{RP,XYZ-Y}$, and $I_{RP,XYZ-Z}$ can represent its corresponding X , Y , and Z values, thus they can be calculated by

$$\begin{bmatrix} I_{RP,XYZ-X} \\ I_{RP,XYZ-Y} \\ I_{RP,XYZ-Z} \end{bmatrix} = A_R \times \begin{bmatrix} I_{HS-R} \\ I_{HS-G} \\ I_{HS-B} \end{bmatrix}. \quad (10)$$

Then the perceived L^* , a^* , and b^* can be calculated by

$$\begin{cases} I_{RP,Lab-L} = 116 \cdot f\left(\frac{I_{RP,XYZ-Y}}{Y_{R_white}}\right) - 16, \\ I_{RP,Lab-a} = 500 \cdot \left[f\left(\frac{I_{RP,XYZ-X}}{X_{R_white}}\right) - f\left(\frac{I_{RP,XYZ-Y}}{Y_{R_white}}\right) \right], \\ I_{RP,Lab-b} = 200 \cdot \left[f\left(\frac{I_{RP,XYZ-Y}}{Y_{R_white}}\right) - f\left(\frac{I_{RP,XYZ-Z}}{Z_{R_white}}\right) \right], \end{cases} \quad (11)$$

where the values of conversion matrix A_R have been given above, which is calculated by taking the spectral absorption curve of cyan glass and the primaries of the display devices together into consideration. $[X_{R_white} \ Y_{R_white} \ Z_{R_white}]$ is the reference white point in CIE XYZ color space, which can be computed by

$$[X_{R_white} \ Y_{R_white} \ Z_{R_white}]^T = A_R \times [111]^T. \quad (12)$$

After calculating $I_{RP,Lab-L}$, $I_{RP,Lab-a}$, and $I_{RP,Lab-b}$ of these 100 HS figures in CIE $L^*a^*b^*$ color space, we can draw the $L^*a^*b^*$ 3D figure. The distribution range of this figure is a series of point cluster, which means the range of most perceived colors filtered by cyan glass and can be regarded

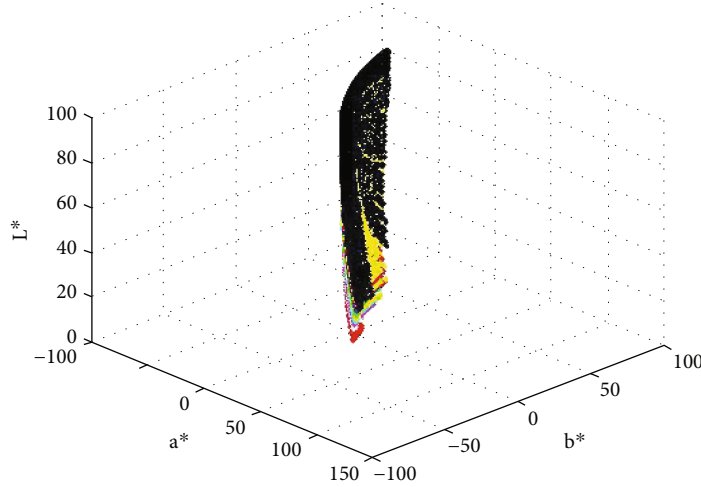


FIGURE 5: Distribution ranges of the 10 HS figures in CIE $L^*a^*b^*$ color space.

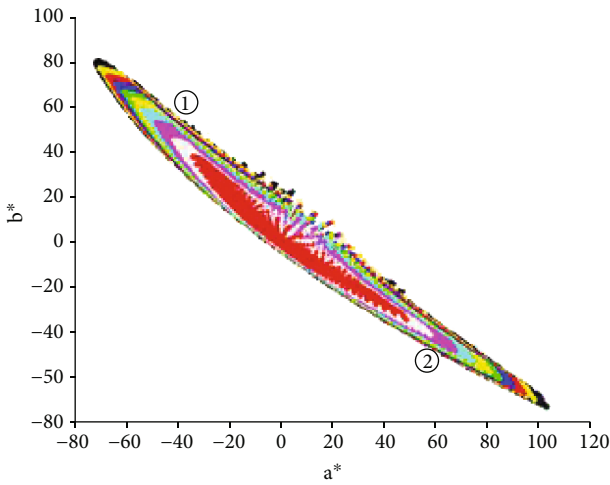


FIGURE 6: Projection of the 3D point cluster in $a^* - b^*$ 2D plane.

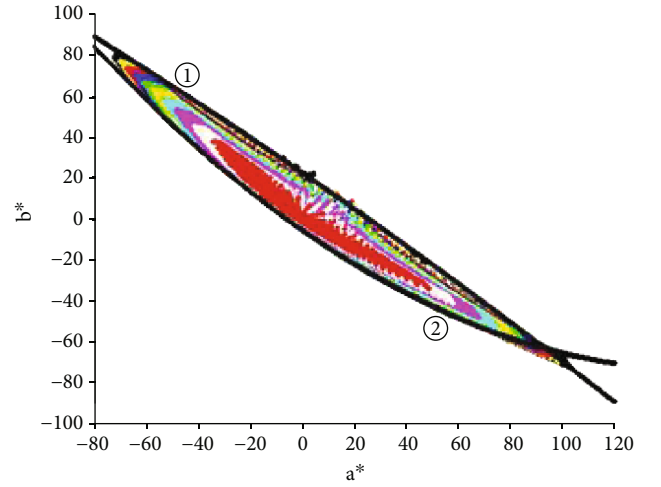


FIGURE 7: The fitting curves of the projected point cluster boundary in $a^* - b^*$ 2D plane.

equivalent to the perceived field. In fact, the purpose of the matching processing is aimed at mapping the distribution range of the original right image into this perceived field, so it is necessary to solve the function of the surface of the point cluster. Fortunately, we have conducted a number of experiments based on the relationship between HSV color space and RGB color space to find that there is a lot of overlap in the distribution range of the 100 HS figures converted into the CIE $L^*a^*b^*$ color space. In order to further reduce the calculation amount, we decide to choose convert 10 HS figures with $V = 10, 20 \dots 100$ to CIE $L^*a^*b^*$ color space to draw the $L^*a^*b^*$ 3D figure. As for the other HS figures, they must also be mapped into this distribution range based on the transformational rules. Figure 5 shows the $L^*a^*b^*$ 3D figure drawn by the 10 HS figures, which is proved to be approximate to the perceived field as well.

From Figure 5, we can see that the original surface is nearly perpendicular to $a^* - b^*$ 2D plane. Therefore, according to the first principle of matching, we can set the component of L^* aside temporarily and do the matching

procedure based on the color attributes in $a^* - b^*$ 2D plane. Figure 6 shows the projection of the 3D point cluster in $a^* - b^*$ 2D plane, and 10 different colors represent, respectively, the different distribution range of 10 different HS figures when they converted into CIE $L^*a^*b^*$ color space.

To satisfy the first matching rule, we need to make a nice curve fitting for the boundary of the distribution range in 2D plane. Defined the fitting curve composed by the boundary points in the top-right corner as the curve ① and the fitting curve composed by the boundary points in the below-left corner as the curve ②, which have signed in Figure 6. Considering the distribution of point cluster and the efficiency of curve fitting, we adopt the quadratic polynomial curve fitting to calculate the curves ① and ②, and their functions of the fitting curve are as follows:

$$b1 = -5.1146 \times 10^{-4} \cdot (a1)^2 - 0.8724 \cdot (a1) + 22.5848, \quad (13)$$

$$b2 = 0.0029 \cdot (a2)^2 - 0.89 \cdot (a2) - 5.5028, \quad (14)$$

where $b1$ and $a1$ are the b and a components of curve ① and $b2$ and $a2$ are the b and a components of curve ②. After the fitting processing, we can get the perceived filed shown in Figure 7 which is composed by the curves ① and ② and their internal zone. For the right image of any stereo pairs, the distribution range of the perceived right image filtered by the cyan glass in CIE $L^*a^*b^*$ color space will be on the inside of the perceived filed.

According to the second principle of matching, we need to assure the hue of the matched right image is equal to the hue of the original right image, which can be described by the following formula:

$$\frac{180}{\pi} \cdot \arctan \left(\frac{I_{RM,Lab-b}}{I_{RM,Lab-a}} \right) = H_{RM} = H_R = \frac{180}{\pi} \cdot \arctan \left(\frac{I_{R,Lab-b}}{I_{R,Lab-a}} \right). \quad (15)$$

Thus, what we need to do next is map the points outside the perceived filed into the boundary of perceived filed with minimum distortion and the points inside the perceived filed remain the same in CIE $L^*a^*b^*$ color space to make the $I_{RM,Lab-L}$, $I_{RM,Lab-a}$, and $I_{RM,Lab-b}$ of matched right image as close to $I_{RP,Lab-L}$, $I_{RP,Lab-a}$, and $I_{RP,Lab-b}$ of the perceived right image as possible which also is the first principle of matching rules. At the same time, keeping the hue of the right image unchanged after the matching processing, i.e., for the points located outside the top-right of the perceived filed, we need to use formula (16) to project them into the curve ①.

$$\begin{cases} \frac{180}{\pi} \cdot \arctan \left(\frac{I_{RM,Lab-b}}{I_{RM,Lab-a}} \right) = \frac{180}{\pi} \cdot \arctan \left(\frac{I_{R,Lab-b}}{I_{R,Lab-a}} \right), \\ I_{RM,Lab-b} = -5.1146 \times 10^{-4} \cdot (I_{RM,Lab-a})^2 - 0.8724 \cdot (I_{RM,Lab-a}) + 22.5848. \end{cases} \quad (16)$$

Simplifying this equation set, we can get the following:

$$\begin{cases} \frac{I_{RM,Lab-b}}{I_{RM,Lab-a}} = \frac{I_{R,Lab-b}}{I_{R,Lab-a}}, \\ I_{RM,Lab-b} = -5.1146 \times 10^{-4} \cdot (I_{RM,Lab-a})^2 - 0.8724 \cdot I_{RM,Lab-a} + 22.5848. \end{cases} \quad (17)$$

Similarly, for the points located outside the below-left of the perceived filed, we need to use formula (18) which has been simplified to project them into the curve ②.

$$\begin{cases} \frac{I_{RM,Lab-b}}{I_{RM,Lab-a}} = \frac{I_{R,Lab-b}}{I_{R,Lab-a}}, \\ I_{RM,Lab-b} = 0.0029 \cdot (I_{RM,Lab-a})^2 - 0.89 \cdot I_{RM,Lab-a} - 5.50288. \end{cases} \quad (18)$$

With this, the matching processing based on the color attributes for the right image has been completed, and we can get the components of $I_{RM,Lab-a}$ and $I_{RM,Lab-b}$ in CIE $L^*a^*b^*$ color space by above calculations.

4.3. Lightness Adjustment for the Stereo Pairs. During the processes of generating anaglyphs, the phenomenon of reti-

nal rivalry will be quite obvious if saturation and lightness of the red-like color are very bright simultaneously, which will lead to visual fatigue easily. Therefore, it is necessary to adjust the lightness properly to reduce the effect of the retinal rivalry.

In RGB color space, the R , G , and B values of red point can be denoted as $Red = (1, 0, 0)$. We can utilize the conversion procedure to convert this point into CIE $L^*a^*b^*$ color space to calculate its corresponding hue, i.e., $H_{Red} = 41.7515$ and then adjust the hue which is in this range ($H_{Red} - T$ and $H_{Red} + T$). According to a number of experiments (refer to Songnan Li's method), we determine the threshold $T = 14$. So that the processed lightness of the right image is

$$I_{RM,Lab-L} = \begin{cases} I_{R,Lab-L} \cdot \left(1 - Wr \cdot \frac{T - |H_R - H_{Red}|}{T} \right) & H_R \in (H_{Red} - T, H_{Red} + T), \\ I_{R,Lab-L} & \text{otherwise,} \end{cases} \quad (19)$$

where Wr is a weight parameter; its values can be changed by its corresponding saturation, and its specific expression is

$$Wr = \begin{cases} W_{max} & \text{if } Sr > S_{max}, \\ W_{max} \cdot \frac{Sr - S_{min}}{S_{max} - S_{min}} & \text{if } S_{min} < Sr < S_{max}, \\ 0 & \text{otherwise,} \end{cases} \quad (20)$$

where $W_{max} = 0.4$, $S_{max} = 50$, and $S_{min} = 40$, which refer to the Songnan Li's method. It means that Wr will be increased if the saturation is higher, which will lead to the values of $I_{RM,Lab-L}$ which has to be reduced to avoid the effect of retinal rivalry. On the contrary, if the $I_{RM,Lab-L}$ only changes a little, which means that the effect of retinal rivalry cause by its own lightness is not too much, so the matched lightness has not a big change.

Similarly, the lightness adjustment of the left image will be implemented by

$$I_{LM,Lab-L} = \begin{cases} I_{L,Lab-L} \cdot \left(1 - Wl \cdot \frac{T - |H_L - H_{Red}|}{T} \right) & H_L \in (H_{Red} - T, H_{Red} + T), \\ I_{L,Lab-L} & \text{otherwise,} \end{cases} \quad (21)$$

where $I_{LM,Lab-L}$ is the processed lightness of left image. Wl also is a weight coefficient, which plays a role similar to the Wr . Its specific expression is

$$Wl = \begin{cases} W_{max} & \text{if } Sl > S_{max}, \\ W_{max} \cdot \frac{Sl - S_{min}}{S_{max} - S_{min}} & \text{if } S_{min} < Sl < S_{max}, \\ 0 & \text{otherwise.} \end{cases} \quad (22)$$

H_L and Sl are the hue and saturation of the left image, which can be calculated by



FIGURE 8: Processed stereo pairs for generating anaglyphs.

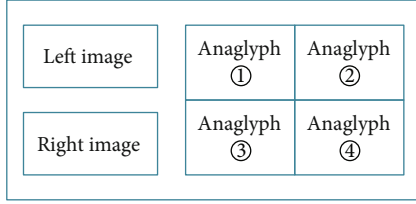


FIGURE 9: The layout of four anaglyphs on the screen for subjective tests.

$$H_L = \arctan \left(\frac{I_{L,Lab-b}}{I_{L,Lab-a}} \right), \quad (23)$$

$$S_L = \sqrt{(I_{L,Lab-a})^2 + (I_{L,Lab-b})^2}. \quad (24)$$

With this, we have completed the lightness adjustment for the stereo pairs. On one hand, this empirical operation is helpful to improve the chrominance accuracy of red-like colors to avoid the heavy color distortion. On the other hand, this operation can keep the balance of the lightness between the processed left image and processed right image to reduce the retinal rivalry caused by the different perceived lightness.

4.4. Converting the Processed Stereo Pairs into RGB Color Space. Through the above processes, we can calculate the $I_{RM,Lab-L}$, $I_{RM,Lab-a}$, and $I_{RM,Lab-b}$ of the processed right image and $I_{LM,Lab-L}$ of the processed left image. Firstly, for the processed right image, we need to convert it into the RGB color space. Undoubtedly, this conversion needs the CIE XYZ color space as the intermedium. We denote the $I_{RM,XYZ-X}$, $I_{RM,XYZ-Y}$, and $I_{RM,XYZ-Z}$ as the X, Y, and Z components of the processed right image in CIE XYZ color space, which can be calculated by

$$\begin{cases} I_{RM,XYZ-X} = X_{R_white} \cdot f^{-1} \left(\frac{I_{RM,Lab-L} + 16}{116} + \frac{I_{RM,Lab-a}}{500} \right), \\ I_{RM,XYZ-Y} = Y_{R_white} \cdot f^{-1} \left(\frac{I_{RM,Lab-L} + 16}{116} \right), \\ I_{RM,XYZ-Z} = Z_{R_white} \cdot f^{-1} \left(\frac{I_{RM,Lab-L} + 16}{116} - \frac{I_{RM,Lab-b}}{200} \right), \end{cases} \quad (25)$$

where $f^{-1}(\bullet)$ is the inverse function of the function $f(\bullet)$, and its specific expression is

$$f(s)^{-1} = \begin{cases} s^3 & \text{if } s > \frac{6}{29}, \\ \left(\frac{6}{29}\right)^2 \cdot \left(3t - \frac{12}{29}\right) & \text{otherwise.} \end{cases} \quad (26)$$

Then, utilize the matrix A_R^{-1} which is the inverse matrix of A_R to convert the $I_{RM,XYZ-X}$, $I_{RM,XYZ-Y}$, and $I_{RM,XYZ-Z}$ to RGB color space by the following formula:

$$\begin{bmatrix} I_{RM,RGB-R} \\ I_{RM,RGB-G} \\ I_{RM,RGB-B} \end{bmatrix} = A_R^{-1} \times \begin{bmatrix} I_{RM,XYZ-X} \\ I_{RM,XYZ-Y} \\ I_{RM,XYZ-Z} \end{bmatrix}. \quad (27)$$

For the processed left image, we have already known the lightness component $I_{LM,Lab-L}$. Here, we keep its a and b components unchanged, i.e., $I_{LM,Lab-a} = I_{L,Lab-a}$ and $I_{LM,Lab-b} = I_{L,Lab-b}$. Similarly to the inverse conversion of the processed right image, we denote the $I_{LM,XYZ-X}$, $I_{LM,XYZ-Y}$, and $I_{LM,XYZ-Z}$ as the X, Y, and Z components of the processed right image in CIE XYZ color space, which can be calculated by

$$\begin{cases} I_{LM,XYZ-X} = X_{L_white} \cdot f^{-1} \left(\frac{I_{LM,Lab-L} + 16}{116} + \frac{I_{LM,Lab-a}}{500} \right), \\ I_{LM,XYZ-Y} = Y_{L_white} \cdot f^{-1} \left(\frac{I_{LM,Lab-L} + 16}{116} \right), \\ I_{LM,XYZ-Z} = Z_{L_white} \cdot f^{-1} \left(\frac{I_{LM,Lab-L} + 16}{116} - \frac{I_{LM,Lab-b}}{200} \right), \end{cases} \quad (28)$$

where $[X_{L_white} \ Y_{L_white} \ Z_{L_white}]$ is the reference white point relative to A_L in CIE XYZ color space, which can be computed by

$$[X_{L_white} \ Y_{L_white} \ Z_{L_white}]^T = A_L \times [111]^T. \quad (29)$$

Then, utilize the matrix A_L^{-1} which is the inverse matrix of A_L to convert the $I_{LM,XYZ-X}$, $I_{LM,XYZ-Y}$, and $I_{LM,XYZ-Z}$ to RGB color space by the following formula:

TABLE 1: Subjective test results for different computed methods for generating anaglyphs.

Methods	Color fidelity			Visual quality			
	3: no distortion	2: a little distortion	1: severe distortion	4: comfortable	3: fair	2: a little uncomfortable	1: uncomfortable
Dubois' method	2	3	10	3	7	2	3
McAllister's method	9	4	2	4	5	3	3
Songnan Li's method	2	3	10	5	7	1	2
Our method	10	3	2	4	7	2	2

$$\begin{bmatrix} I_{LM,RGB_R} \\ I_{LM,RGB_G} \\ I_{LM,RGB_B} \end{bmatrix} = A_L^{-1} \times \begin{bmatrix} I_{LM,XYZ_X} \\ I_{LM,XYZ_Y} \\ I_{LM,XYZ_Z} \end{bmatrix}. \quad (30)$$

At last, we need combine the processed left and right RGB values together, using the values of I_{RM,RGB_G} and I_{RM,RGB_B} as the G and B channels of the final anaglyph and the I_{LM,RGB_R} as the R channel. Denote the I_{A,RGB_R} , I_{A,RGB_G} , and I_{A,RGB_B} as the R , G , and B values of the final anaglyph; then, this procedure can be represented by

$$[I_{A,RGB_R} I_{A,RGB_G} I_{A,RGB_B}] = [I_{LM,RGB_R} I_{RM,RGB_G} I_{RM,RGB_B}]. \quad (31)$$

Then, an anaglyph $I_{A,RGB}$ is performed when they scaled by multiplying 255. The above operations are performed on each pixel of the anaglyph, and finally, the anaglyphs are obtained which is shown in Figure 8.

5. Evaluation

In this section, we conduct subjective tests to evaluate the performance of our algorithm by comparing it to the other computed methods mentioned in Section 2, i.e., Dubois' method, McAllister's method, and Songnan Li's method. We do not put the Midpoint method into the comparison because it destroys the 3D perception heavily and makes no sense to compare.

5.1. The Scheme of Subjective Test. We use 15 stereo pairs with diversified colors as the input and then downscale them to a proper size while keeping their aspect ratios unchanged. For every stereo pair, we need to generate 4 anaglyphs by 4 different methods and their relative positions on the screen are shown in Figure 9. We put the input stereo pairs on the left of the screen is to make convenience for comparing the color reproduction of 4 anaglyphs simultaneously while the color of the stereo pairs is the reference standard. On the right of the screen, we set anaglyphs side-by-side to speed up the comparison processing to alleviate the visual fatigue of subjects instead of presenting each anaglyph sequentially, and this layout can achieve more intuitive comparison about the retinal rivalry of 4 anaglyphs at the same time. In addition, both the positions of the anaglyphs which

are denoted as ①-④ and the orders of the 15 experimental images are set casually to avoid the subjects' inertial choice and evaluation.

This experiment is conducted in a room with fluorescent lights. We choose the 20" 1600 × 900 HP LCD display as the displaying devices and Bertha red-cyan glass as the colored-filter glasses in the subjective test. Viewing distance is about 3 times the screen height, and the time of the subjective tests with 15 stereo pairs is controlled in 10 minutes to avoid fatigue test. For the 10 subjects who have normal vision and have passed the color blindness test, a training process can be implemented to familiarize the subjects with the anaglyph 3D viewing. Then, they need to complete two tasks when the 15 experimental images displayed in sequence on the screen. One task is to give the assessment of color fidelity which is divided into three grades, i.e., 3: no distortion, 2: a little distortion, and 1: severe distortion. Another task is to give the visual quality which can assess the anaglyph fully, and it also can be divided into 4 grades, i.e., 4: comfortable (with no visual fatigue), 3: fair, 2: a little uncomfortable, and 1: uncomfortable (with heavy visual fatigue). Of course, in order to get a better feedback from subjects, we can encourage these subjects to express their feelings about the anaglyphs and point out the reasons of their assessment, and another person will record the corresponding grades and evaluations meanwhile.

5.2. Evaluating Result. Through the subjective tests described above, we can get the evaluating result which is shown in Table 1. The data in this table represents how many subjects choose the corresponding grade by conducting the subjective test. The data indicates that our method does have a better color reproduction compared to Dubois' method and Songnan Li's method. And in terms of the visual quality, our method is no less than the other three methods. Of course, the result may be a little different by different subjects, but it also is able to explain that our method is effective especially in the excellent balance between the color distortion and retinal rivalry to some extent.

6. Conclusion

With the development of stereoscopic display technology, VR is becoming more and more mature. Anaglyphs have some irreplaceable values including high data compressibility, low cost of use, and input sources for all display devices.

In this paper, we have concluded the predecessors' methods for generating anaglyphs at first. Then, we proposed a new algorithm for generating anaglyphs based on matching color attributes especially the hue in CIE $L^*a^*b^*$ color space, which can achieve a better color reproduction and can dynamically adjust the balance between retinal rivalry and color distortion. In order to compare the results of different methods, we built a scheme for subjective test, which turns out that our method does demonstrate a good performance to some extent. It is also worth mentioning that the process of matching color attributes is not the only solution to improve the stereoscopic visual effect of anaglyphs. Some literatures have been pointed out that gamma correction and ghosting phenomenon elimination also can be used to improve the stereoscopic effect [12, 13], but the specific reasons and parameters need to be researched further.

Data Availability

Data sharing is not applicable to this article as no datasets were generated or analysed during the current study.

Conflicts of Interest

The authors declare that they have no conflicts of interest.

Acknowledgments

The authors acknowledge the funding of the Key Project of Shaanxi Province Innovation Program, China (2017ZDCXL-GY-11-02-02).

References

- [1] M. Wu and Z. Hong, "Subjective quality assessment of stereo image compression based on stereoscopic fusion in binocular vision," *Journal of Ambient Intelligence and Humanized Computing*, vol. 10, no. 8, pp. 3307–3314, 2019.
- [2] G. L. McCormack and K. M. Hogan, "Clear and single binocular vision in near 3D displays," *Optometry and Vision Science*, vol. 96, no. 11, pp. 850–859, 2019.
- [3] Q. Wang, Y. Yin, W. Zou, and D. Xu, "Measurement error analysis of binocular stereo vision: effective guidelines for bionic eyes," *IET Science, Measurement & Technology*, vol. 11, no. 7, pp. 829–838, 2017.
- [4] I. V. Safonov and I. V. Kurilin, *Anaglyph Printing*, Springer, Singapore, 2018.
- [5] A. J. Woods, C. R. Harris, D. B. Leggo, and T. M. Rourke, "Characterizing and reducing crosstalk in printed anaglyph stereoscopic 3D images," *Optical Engineering*, vol. 52, no. 4, pp. 1–19, 2013.
- [6] S. X. Qiu, C. L. Caldwell, J. Y. You, and J. D. Mendola, "Binocular rivalry from luminance and contrast," *Vision Research*, vol. 175, pp. 41–50, 2020.
- [7] K. C. Dieter, J. L. Sy, and R. Blake, "Persistent biases in binocular rivalry dynamics within the visual field," *Vision*, vol. 1, no. 3, pp. 18–39, 2017.
- [8] E. Dubois, "A projection method to generate anaglyph stereo images," in *International Conference on Acoustics, Speech and Signal Processing*, pp. 1661–1664, Salt Lake City, 2001.
- [9] D. F. McAllister, Y. Zhou, and S. Sullivan, "Methods for computing color anaglyphs," *Stereoscopic displays and applications XXI*, vol. 75240S, no. 12, pp. 1–75240S, 2010.
- [10] V. M. Tran, *New Methods for Rendering of Anaglyph Stereoscopic Images on CRT Displays and Photo-Quality Ink-Jet Printers*, Ottawa-Carleton Institute for Electrical and Computer Engineering, 2005.
- [11] S. Li, L. Ma, and K. Ngi Ngan, "Anaglyph image generation by matching color appearance attributes," *Signal Processing Image Communication*, vol. 28, no. 6, pp. 597–607, 2013.
- [12] T. Fukiage, T. Kawabe, and S. Nishida, "Hiding of phase-based stereo disparity for ghost-free viewing without glasses," *ACM Transactions on Graphics*, vol. 36, no. 4, pp. 1–17, 2017.
- [13] J. Kim, T. Kim, S. Lee, and A. C. Bovik, "Quality assessment of perceptual crosstalk on two-view auto-stereoscopic displays," *IEEE Transactions on Image Processing*, vol. 26, no. 10, pp. 4885–4899, 2017.

Retraction

Retracted: Construction of Live Broadcast Training Platform Based on “Cloud Computing” and “Big Data” and “Wireless Communication Technology”

Wireless Communications and Mobile Computing

Received 28 November 2023; Accepted 28 November 2023; Published 29 November 2023

Copyright © 2023 Wireless Communications and Mobile Computing. This is an open access article distributed under the Creative Commons Attribution License, which permits unrestricted use, distribution, and reproduction in any medium, provided the original work is properly cited.

This article has been retracted by Hindawi, as publisher, following an investigation undertaken by the publisher [1]. This investigation has uncovered evidence of systematic manipulation of the publication and peer-review process. We cannot, therefore, vouch for the reliability or integrity of this article.

Please note that this notice is intended solely to alert readers that the peer-review process of this article has been compromised.

Wiley and Hindawi regret that the usual quality checks did not identify these issues before publication and have since put additional measures in place to safeguard research integrity.

We wish to credit our Research Integrity and Research Publishing teams and anonymous and named external researchers and research integrity experts for contributing to this investigation.

The corresponding author, as the representative of all authors, has been given the opportunity to register their agreement or disagreement to this retraction. We have kept a record of any response received.

References

- [1] Z. Sun and X. Li, “Construction of Live Broadcast Training Platform Based on “Cloud Computing” and “Big Data” and “Wireless Communication Technology,” *Wireless Communications and Mobile Computing*, vol. 2021, Article ID 8971195, 9 pages, 2021.

Research Article

Construction of Live Broadcast Training Platform Based on “Cloud Computing” and “Big Data” and “Wireless Communication Technology”

Zhidong Sun  and Xueqing Li 

School of Software, Shandong University, Shandong, China

Correspondence should be addressed to Xueqing Li; xqli@sdu.edu.cn

Received 22 July 2021; Accepted 24 August 2021; Published 14 September 2021

Academic Editor: Balakrishnan Nagaraj

Copyright © 2021 Zhidong Sun and Xueqing Li. This is an open access article distributed under the Creative Commons Attribution License, which permits unrestricted use, distribution, and reproduction in any medium, provided the original work is properly cited.

With the rapid development of information technology, a scientific theory is brought by the rapid progress of science and technology. The advancement of science and technology of the impact on every field, changing the mode of transmission of information, the advent of big data for promotion and dissemination of resources played their part, let more and more people benefit. In the context of cloud computing, big data ushered in another upsurge of development and growth. Given this, the live broadcast training platform, which focuses on enterprise staff training and network education, arises at the right moment. People favor its convenience, real-time performance, and high efficiency. However, the low-value density of big data and cloud computing's security problem has difficulties constructing a live broadcast training platform. In this paper, the live broadcast training platform's structure is improved by constructing three modules: the live training module based on cloud computing, the user recommendation module based on big data, and the security policy guarantee module. In addition, to ensure that the trainees can receive training anytime and anywhere, this paper uses wireless communication technology to ensure the quality and speed of all users' live video sources.

1. Introduction

In 2020, affected by the COVID-19, people have to shift their working mode from the company to their home. Powerful live broadcast training platforms will take this opportunity to stand out. The live broadcast training platforms represented by education and staff training will develop particularly rapidly. At present, although the COVID-19 situation has been stabilized, the way of webcast training makes people see its convenience. The webcast training will become the future development trend of education departments and significant enterprises.

The recent development in information technology, such as big data, cloud computing, and communication technologies, plays a vital role in making the world brighter [1–3]. With these intelligent technologies' immense power, we can connect, generate, retrieve, and process data anytime and anywhere. Meanwhile, we can also share data in real-time through the network broadcast.

The cloud computing paradigm has been designed for solving storage capacity and related computational issues. It enables high-performance computation with secure and robust storage capability [4, 5]. In modern computing paradigms, a massive amount of data is stored and processed at various clouds rather than the centralized cloud. Thus, all data requests coming from multiple sources have been directly transmitted to the centralized cloud. Therefore, large increments have been seen in the processing speed as compared to network bandwidth. Consequently, this provides a strong guarantee for the stability and fluency of network broadcast.

In Figure 1, network big data refers to the massive data generated by interaction and fusion of the ternary human-machine-thing universe in Cyberspace and available on the Internet. As a data technology developed under the Internet environment, big data has many prominent characteristics such as large data volume, multiple data types, low-value density, and fast processing speed. The online training

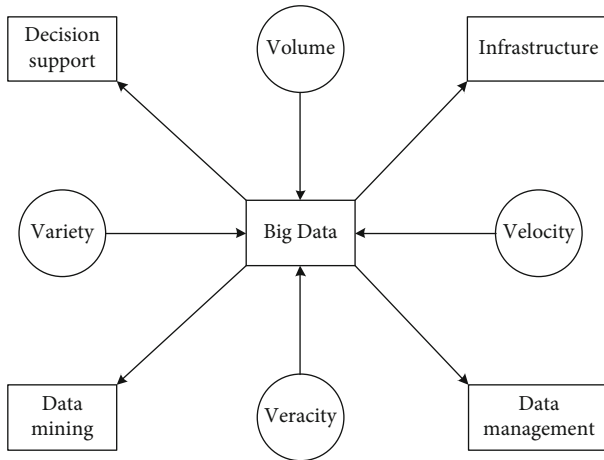


FIGURE 1: Big data features.

platform can realize a reasonable allocation of resources and more targeted training content based on big data.

At present, there are much researches on cloud computing and big data. Cloud computing is widely used in e-commerce, enterprise management, and information security. Explicitly speaking, cloud computing can provide information sharing and business collaboration for e-commerce [6], reduce the operating costs for enterprises [7], and ensure the security of data transmission and data storage [8]. Moreover, big data is mainly used in business, finance, healthcare, and manufacturing. Business is the most extensive application field for big data. Merchants can understand customers' shopping habits and create value by analyzing the unstructured data of consumers' shopping behavior [9]. In the financial field, consumers' credit scores can be obtained to infer customers' payment intentions and ability and to discover potential frauds through big data [10]. In the manufacturing industry, enterprises need to dig out the required information from the stored mass of information to promote decision-making and avoid risks [11]. However, at present, there are relatively few applications of big data and cloud computing on live broadcast platforms.

To sum up, it can be seen that the use of big data technology can systematically establish a live broadcast training platform and make full use of big Internet data to train trainees. However, big data's low-value density disadvantage requires cloud computing to make up through deep data mining. Besides, cloud computing's security problem will also make big data face the risk of leakage in the cloud environment. In this paper, cloud computing is used to deep excavate big data. The extensive data recommendation system is used to improve the precise positioning of live training. A security assurance strategy is used to enhance big data of the activity in the cloud environment. Consequently, the impeccable live broadcast training platform is founded.

2. Overall Framework Design of the Live Broadcast Training Platform

As is shown in Figure 2, the live broadcast training platform comprises three modules: the live training module based on

cloud computing, the user recommendation module based on big data, and the security policy guarantee module.

The functions such as authority authentication, platform data management, live broadcast content management, and user management need to be realized in the live training module.

The user recommendation module mainly includes the user characteristic data generation module, information matching module, and recommendation module.

In the security policy guarantee module, data storage security, user identity authentication, authentication of access, protection of data privacy, and construction of virtual security need to be realized.

3. Design of the Live Training Module

3.1. Authority Authentication. This section realizes the authority authentication for users of the background management system of the live broadcast training platform and prevent illegal user to call the system interface behavior. It is mainly composed of three functions: system administrator authentication, institution administrator authentication, and anchor authentication are shown in Figure 3.

3.1.1. System Administrator Authentication. The key to this step is the identity token recognition and the timing of authority authentication. The token has six categories:

- (1) AuthController is the control class for permission authentication. When a system user logs in, the AuthController will invoke concrete methods to verify the user's identity. Then, the role encapsulates the user's identity information as an identity plate and returns it to the user. The identifying label is used as the user's passport to the system
- (2) SysUserService is the service class that the system user operates. It can interact with the database through different requests sent by the front end and includes query system user, update system user information, login verification, and other methods
- (3) CusPncipalService is the service class that the system consumer operates on. After the management end of the system login user, the vital information such as username and password will be separately encapsulated as CusPrincipalEntity entity
- (4) CusHostService is the service class of anchor information operation. After receiving the front-end request, the permission authentication control class can complete the anchor's process through this interface. It includes adding anchor, inquiring anchor information, updating anchor information, and other methods
- (5) AuthenticationManager is the interface provided to validate user information in Spring Security. In this system, judging the user's identity and matching the user's password are mainly accomplished through the instance of this interface

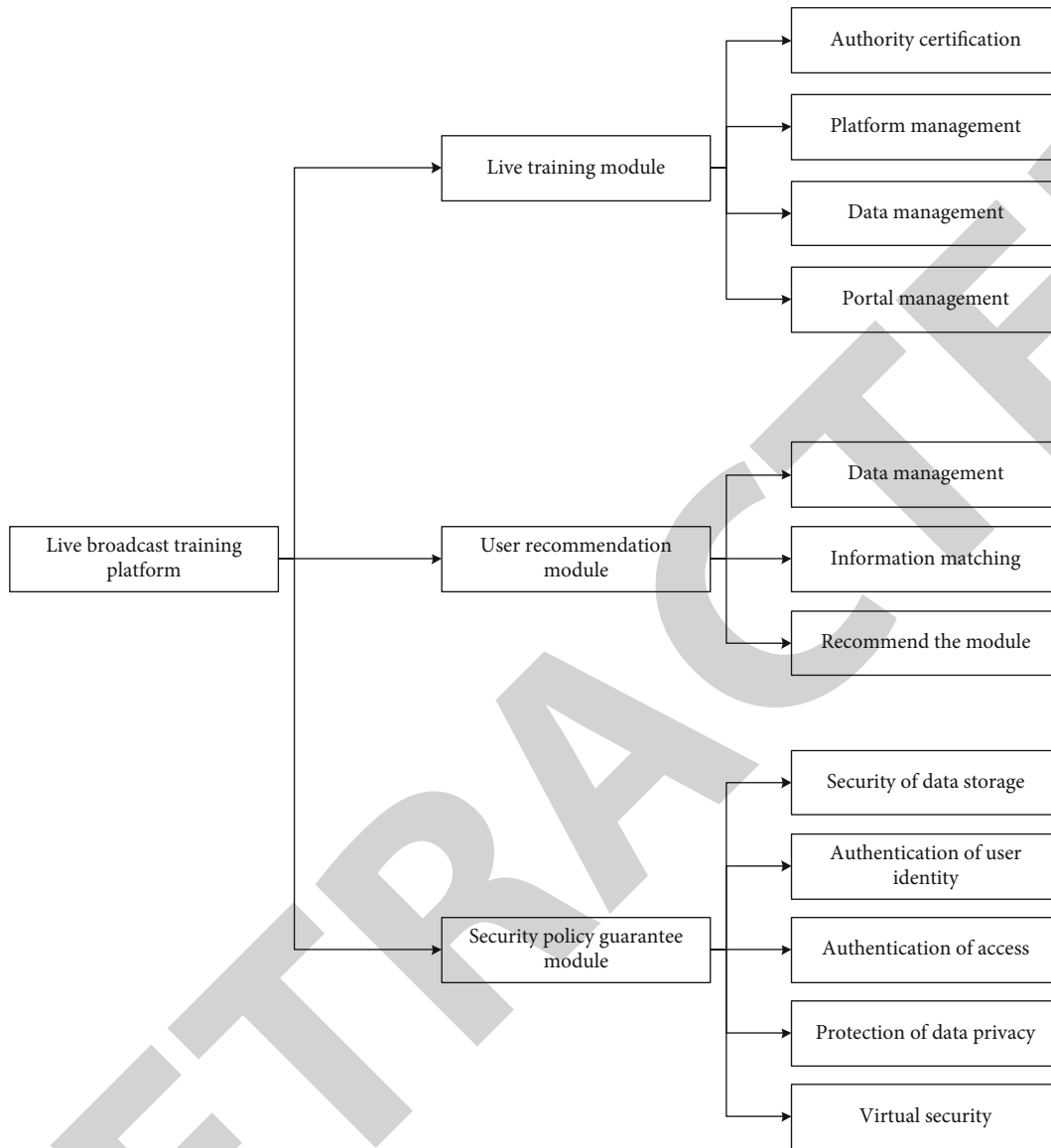


FIGURE 2: Overall framework design of the live broadcast training platform.

(6) JwtTokenUtil is mainly used to generate identity for the system users through the user's information. This identity plate is included in every request after the administrator or anchor successfully logs into the live training platform's background management system

The timing diagram of system administrator authority authentication is shown in Figure 4.

3.1.2. *Institution Administrator Authentication.* When the system administrator logs into the background management system of the live training platform, it can call the login method of or user service and reach the authenticate method of AuthenticationManager to validate the user's input information. After verification, the security context is established, and the user role is obtained to encapsulate its permission information. Consequently, the generated token method of

the jwtTokenUtils will generate the token and return it to the user.

3.1.3. *Anchor Authentication.* When the anchor logs into the live training platform's background management system, it can call the login method of HostService. Then, it calls the authenticate method of AuthenticationManager to validate the input information of the user. After verification, the security context is established, and the user role is obtained to encapsulate its permission information. Consequently, the generated token method of thejwtTokenUtils will generate the token and return it to the user.

3.2. *Platform Data Management.* The main data management module of the live training platform is mainly for the system administrators to manage all the administrators of the live broadcast platform and the anchors of the

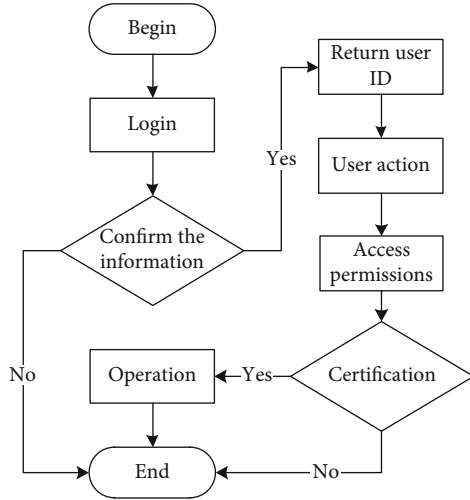


FIGURE 3: Flowchart of authority certification.

organization. The class diagram of broadcast room management is shown in Figure 5.

LiveRoomController is the control class of broadcast room management. It is mainly used to create a broadcast room and accept front-end requests and data. The creatLiveRoom method is primarily used to create a broadcast room through the broadcast room information's front-end submission.

LiveRoomService is the service class of broadcast room management. CreateLiveRoom, update, delete, and delete batch are used to create, update, delete, and batch remove the broadcast room.

LiveAdPageService is a service class that sets the guide page of the live room. The queryObject method is used to query the guide page information; the queryByLiveRoomId method is used to find the guide page by the ID of the live room, the queryList method is used to obtain the list of guide pages, save is used to add the guide page, update is used to modify the attributes of the guide page, and delete is used to delete the guide page.

LiveTypeService is a service class that sets the type of live broadcast room. The queryObject method is used to query the live category entity, the queryByOrgId method is used to query the live category set by an institution through the institution ID, the queryList method is used to obtain the live category list, the queryTotal method is used to query the total number of live categories, save is used to add live classes, the update is used to modify live types, delete is used to delete live categories, and delete batch is used to delete live categories in batches.

LiveRoomTabService is a service class that sets the menu of the live room and is mainly used to view, add, and delete the menu bar of the live room.

LiveRoomViewCodeService is a service class for setting the viewing code in the live room, which is mainly used to view, modify, and delete the viewing code in the live room.

3.3. Live Broadcast Content Management. The live content management module is mainly for system administrators and institutional administrators to manage sensitive content, live video, message, live data, and other content. Administra-

tors can view sensitive content screenshots, delete sensitive content, view recording, delete a recording, and view, retrieve, and reset messages in the live room. Here, we focus on sensitive content. When the Tencent cloud server identifies that the live video screenshot is suspected of violation, it will send a message notification in JSON format to the live platform's management end. When the type value is 200, it means that a sharp picture is detected. The notification message will continue to read the link address, picture size, screenshot time, and other information. Then, it encapsulates them into the LiveShotEntity, calls the save method in the LiveShotService, passes in the LiveShotEntity, and then continues to call the save method in the LiveShotDao to save the attribute information in the LiveShotEntity to the data and returns the message of successful saving.

3.4. User Management

3.4.1. Third-Party Login. Users can chat or comment only after they log in with a third-party account. When users choose third-party login of QQ, they will generate URL through appId, callback address, and random code. When users log in successfully, they will return the code through a callback address. They can get the user's accessToken by calling the qqoauth method in OAuthController by code. Use an access token to call the third-party interface to obtain the user's head image, gender, and other identifying information encapsulates it in the map, and return it to the front end.

3.4.2. Watching Live and Recorded Broadcasting. When the anchor creates a live room in the background, the streaming software can push the live stream to the cloud server through the streaming address. When the cloud server detects the change of a particular streaming stream's status, it will send the new event to our server in JSON format through a callback address. When the event type in the notification message is 1, a particular multicast stream begins to push the stream to the server. At this time, users can start to watch the live broadcast when they click to enter the live room.

3.4.3. Online Chatting. When the user successfully logs in with a third-party account, the browser will call the getRongYunToken method in RongCloudController and pass in the user ID. This method will generate a digital signature through the key and timestamp t assigned by the developer platform and then send a request to the RongCloud server to obtain the token. When the user obtains the token, it will call connect in the class library provided by RongCloud at the front end. When the user enters the chat message and clicks send, the TextMessage method will push the chat content to the server.

4. Design of the User Recommendation Module

The recommender system consists of three parts. The first part generates user characteristic data, the second part is to match data information, and the third part gives recommendation results. Among them, generating user data is the premise, matching is the foundation, and giving recommendation results is the focus. All three are indispensable.

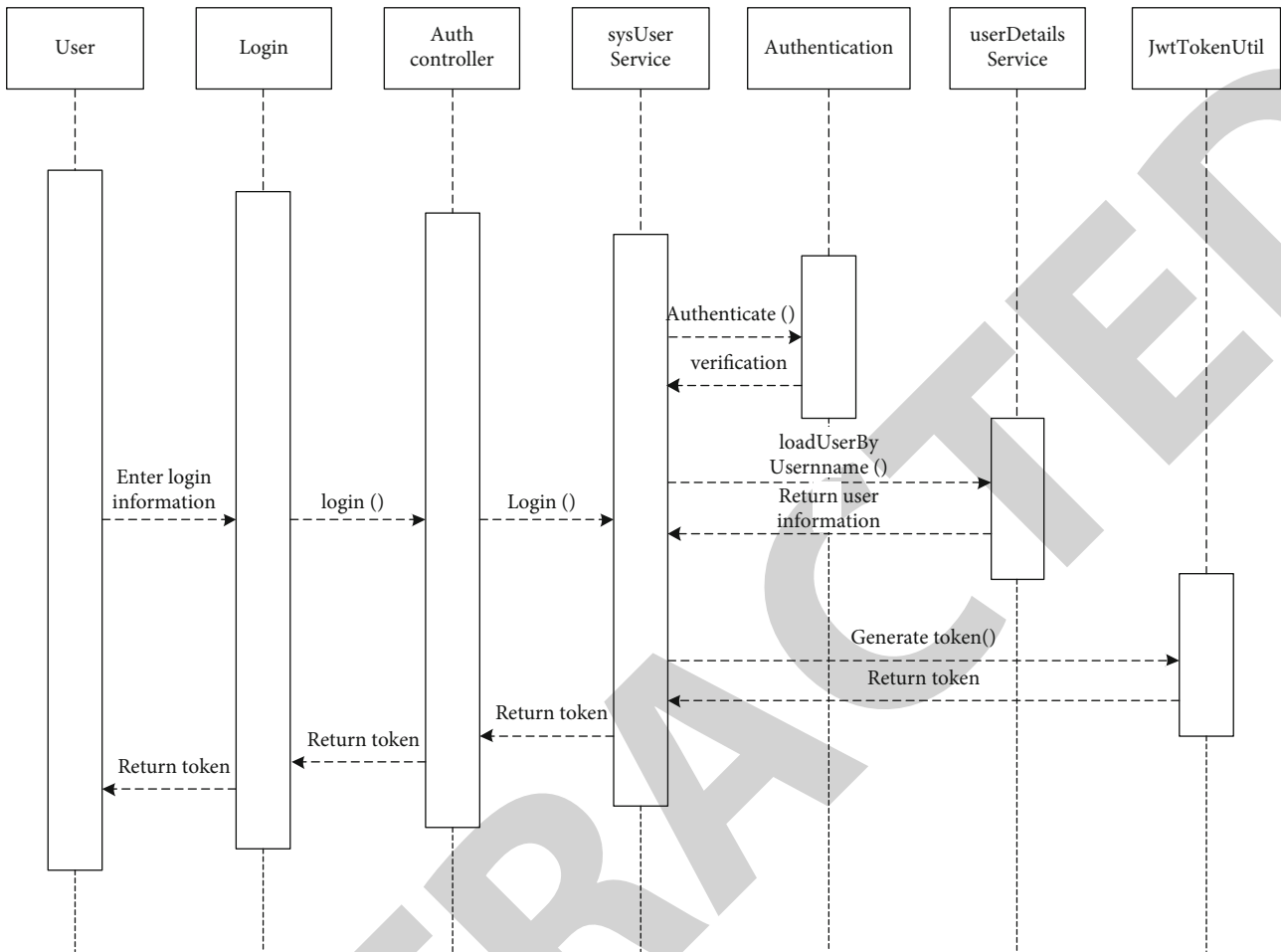


FIGURE 4: Sequence diagram of authentication.

It is necessary to collect many user needs and interests, filter and calculate according to relevant algorithms, extract scores, and make statistics to extract user characteristic data. The general architecture of the recommendation engine system is shown in Figure 6.

Recommendation engine consists of three essential elements:

- (1) *User Eigenvector*. The feature vector here refers to the user data. The computer analyzes and extracts the user's behavior (interests, needs) and then converts this behavior into data to generate the user feature vector
- (2) *Initial Recommendation Results*. According to the data classification, the data that accord with the user feature vector is preliminarily screened, and the data table is generated
- (3) *The Final Recommendation Results*. According to the initial recommendation data table, the final recommendation results are formed after statistical sorting

Here, in particular, the feature extraction of users is based on personal preferences. The data value of personal

preferences can be extracted from the primary operation behavior of users, for example, the length of time users browse a web page, evaluate and collect the item, and the number and frequency of browsing an item. The system's design is mainly based on Hadoop, which is a very reliable, scalable, low-cost distributed computing platform.

This paper uses the Hadoop distributed computing platform to realize the design of the user recommendation engine. The system design is shown in Figure 7.

Additionally, system security is an essential guarantee for the successful operation of the system, so the design and management of system security are crucial in system development. This paper adopts security management, firewall, agent strategy, and secure transmission strategy to secure the system.

(1) Security management strategy

The system will generally have security management settings. For example, during the live broadcast, users can set a multilevel password and access rights to the users participating in the live broadcast. Access is linked to the database and cannot be accessed without the appropriate privileges.

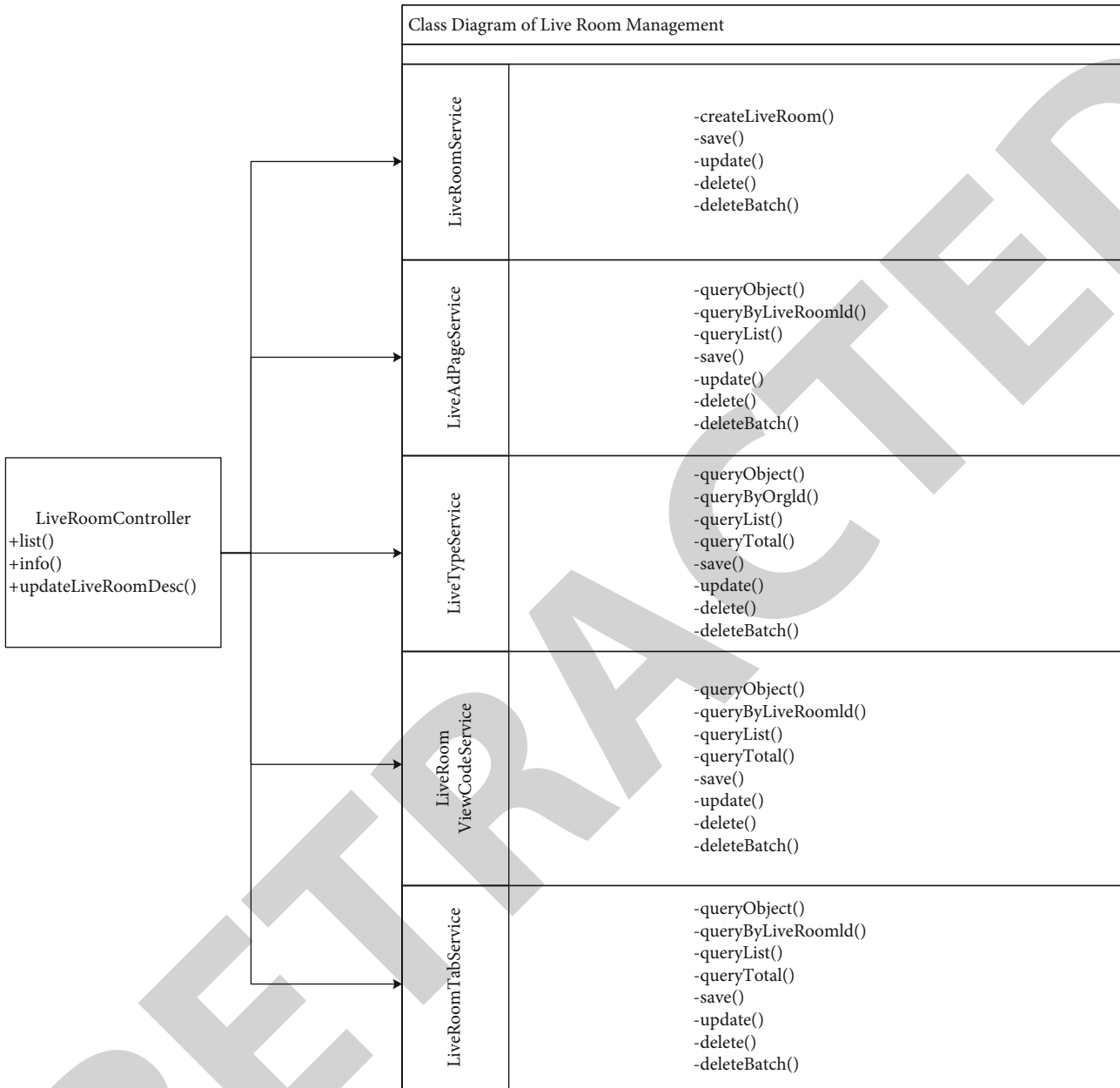


FIGURE 5: Class diagram of live room management.

(2) Firewall and proxy policies

A firewall is the most basic system security; it can have a hardware firewall and software firewall. All the data streams that can access the system are filtered by the firewall first, and only secure data streams can pass so that users can operate the system at ease. Adding a proxy policy can also work as a firewall.

(3) Safe transmission policy

When the system transmits the data, it can be dynamically encrypted in the client. When the server receives a dynamic password request from the client, the server will

be verified and returns the generated password to the client—this way, the data is transmitted in absolute security.

5. Design of the Security Policy Guarantee Module

When users operate on cloud training big data, security measures including data storage security, identity authentication security, trusted access control security, and virtual security begins to work. A complete set of solutions ensure that legitimate users operate on cloud training big data. The security of training big data has also been improved, and the security strategy is shown in Figure 8.

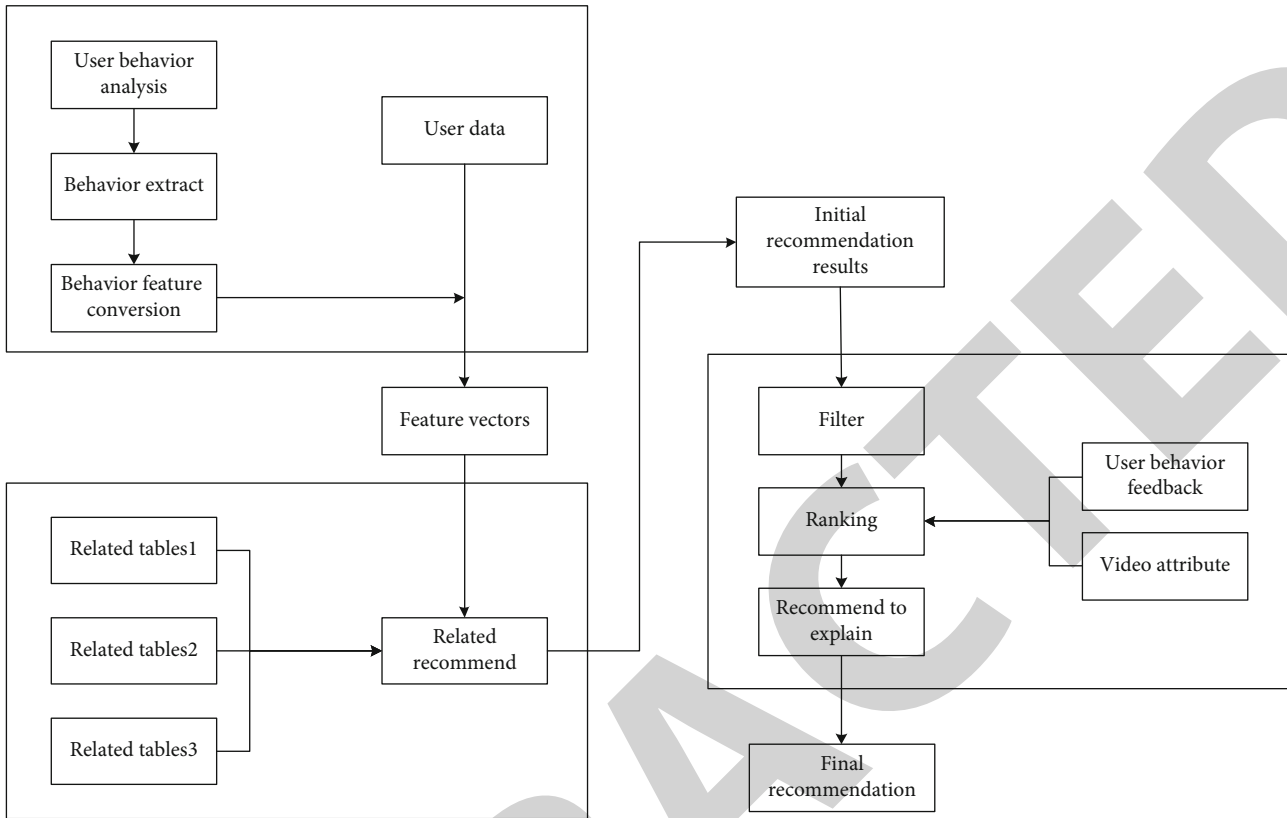


FIGURE 6: Recommended engine.

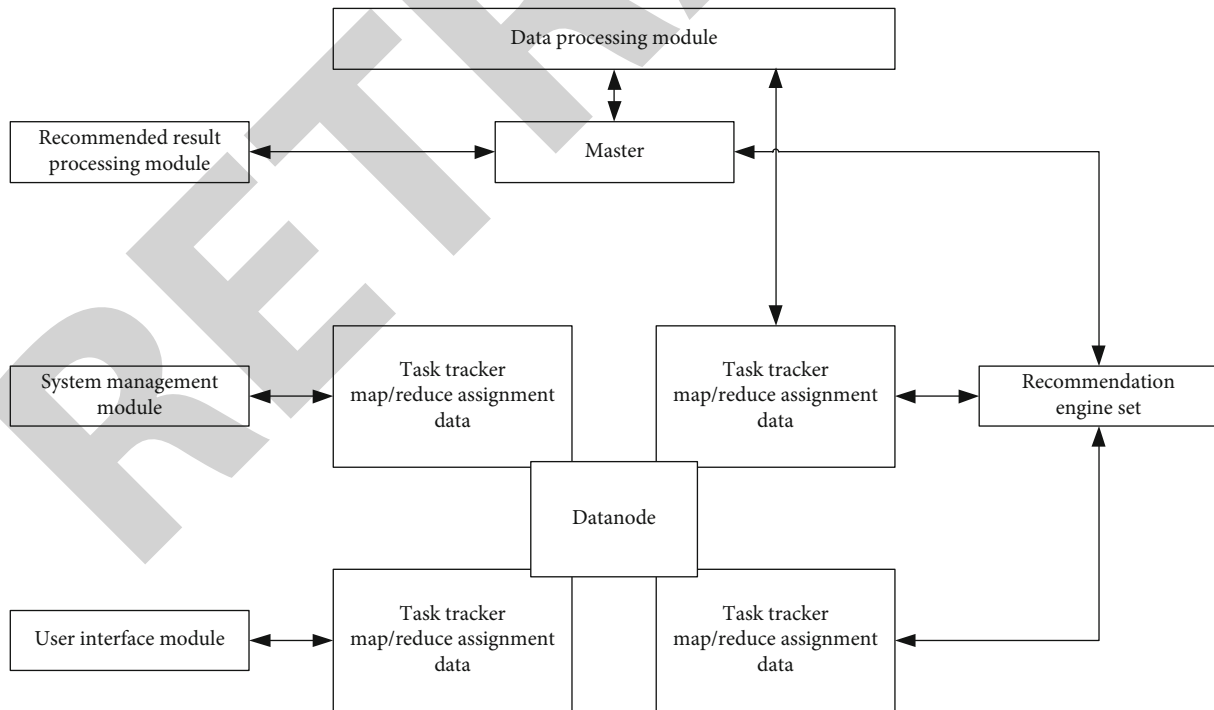


FIGURE 7: System design based on Hadoop.

Users log in with personal login information at the single sign-on entrance and can access the big training data after the application system confirms the identity. The trusted

access control based on cryptography effectively restricts the user's behavior to only operate on the data conforming to their permissions.

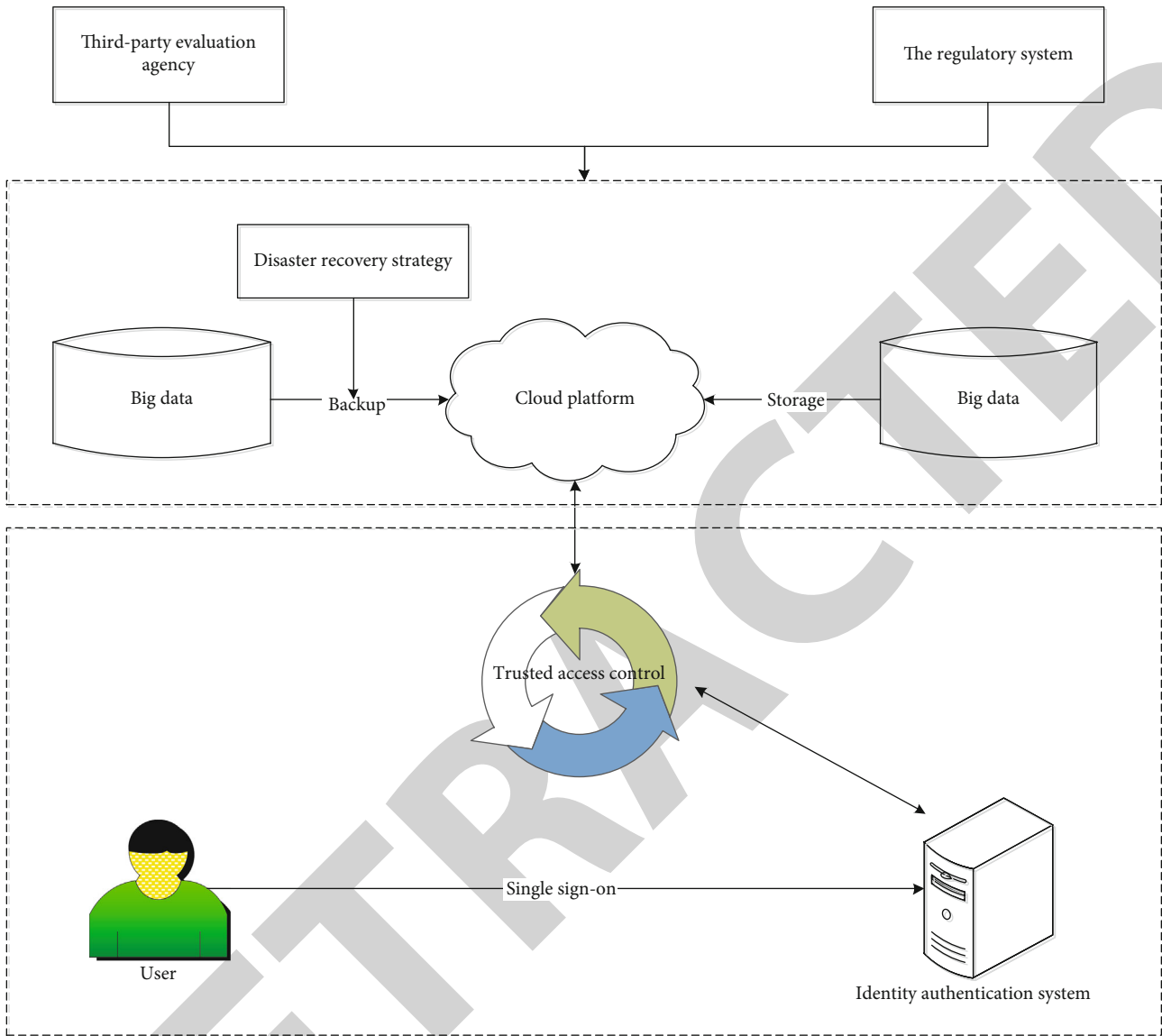


FIGURE 8: Security policy.

The extensive training data stored in the cloud environment is backed up at different levels according to different security levels, and a targeted disaster recovery strategy is established. The file management log will record the operation for each data.

According to the cloud platform’s security performance indicators, the third-party evaluation organization evaluates the services provided by cloud service providers and submits the evaluation results to users. The regulatory system supervises cloud service providers’ behavior to ensure the security of cloud data and the legitimate rights and interests of users.

The security policy guarantee module protects the big data in the following three ways:

(1) Data backup

Network training big data uploaded to the cloud platform needs to be backed up and a more targeted lattice for

data at different levels of confidentiality. Depending on the density level of big data, different backup strategies can be used for public, general, necessary, essential, and core data.

(2) Disaster recovery

Cloud platform service providers for the specific services rented by training institutions formulate specific data disaster recovery strategies. When the cloud environment is attacked or due to power failure, fire, other accidents, and other natural disasters, it can maximize the recovery system, ensure the continuous availability of the cloud platform, and ensure the ample data security of the organization.

(3) Document management log

The establishment of a file management log system for the training data of the institution is another important

Retraction

Retracted: Research on the Integration and Development of Culture and Tourism Based on Wireless Communication and Virtual Reality Technology

Wireless Communications and Mobile Computing

Received 28 November 2023; Accepted 28 November 2023; Published 29 November 2023

Copyright © 2023 Wireless Communications and Mobile Computing. This is an open access article distributed under the Creative Commons Attribution License, which permits unrestricted use, distribution, and reproduction in any medium, provided the original work is properly cited.

This article has been retracted by Hindawi, as publisher, following an investigation undertaken by the publisher [1]. This investigation has uncovered evidence of systematic manipulation of the publication and peer-review process. We cannot, therefore, vouch for the reliability or integrity of this article.

Please note that this notice is intended solely to alert readers that the peer-review process of this article has been compromised.

Wiley and Hindawi regret that the usual quality checks did not identify these issues before publication and have since put additional measures in place to safeguard research integrity.

We wish to credit our Research Integrity and Research Publishing teams and anonymous and named external researchers and research integrity experts for contributing to this investigation.

The corresponding author, as the representative of all authors, has been given the opportunity to register their agreement or disagreement to this retraction. We have kept a record of any response received.

References

- [1] H. Gan, Y. Li, and Y. Song, "Research on the Integration and Development of Culture and Tourism Based on Wireless Communication and Virtual Reality Technology," *Wireless Communications and Mobile Computing*, vol. 2021, Article ID 8322092, 6 pages, 2021.

Research Article

Research on the Integration and Development of Culture and Tourism Based on Wireless Communication and Virtual Reality Technology

HeChi Gan , YaoGuang Li , and YaNan Song 

College of Culture and Tourism, Jeonju University, Jeonju, Jeollabub-do, 55069, Republic of Korea

Correspondence should be addressed to YaoGuang Li; yaoguang_edu@outlook.com

Received 28 July 2021; Accepted 24 August 2021; Published 11 September 2021

Academic Editor: Balakrishnan Nagaraj

Copyright © 2021 HeChi Gan et al. This is an open access article distributed under the Creative Commons Attribution License, which permits unrestricted use, distribution, and reproduction in any medium, provided the original work is properly cited.

The interconnection of all things and industrial integration is the current trend of the times. Among them, the interconnection of all things is the demand of informationization of the times, and the industrial integration is the demand of industrial development. The interconnection of all things is realized based on wireless communication technology. It is necessary to combine the development of the tourist area and the surrounding culture. The relationship between tourist attractions and culture needs to be fully and effectively developed. In order to fully explore the advantages of the cooperation between the two, it is necessary to combine modern technology to package the tour process of each characteristic culture of the scenic spot. Virtual reality is a modern technology that can combine culture and tourism. Wireless communication and VR technology are applied to the development of integration of culture and tourism. The process of tourism will promote profound changes in the tourism model. Under the demand for informatization in various industries, the tourism industry is gradually developing in this direction. The integration of culture and tourism will also be driven by informatization and technology. This paper analyzes the current situation of culture and tourism, summarizes the problems existing in the current process of integration of culture and tourism, and finally puts forward targeted solutions. Mainly in the process of the integration and development of tourism and cultural industries, the traditional culture and scenic spots are the basic factors, combined with wireless communication and virtual reality technology, to develop a tourism industry with technological characteristics of the new era.

1. Introduction

1.1. The Integration of Culture and Tourism. Mainly refers to the characteristic tourism that tourists feel the combination of culture and tourism during the process of visiting the scenic spot. In the mutual penetration of the two, a tourism style is formed, which allows tourists to have a better tour experience when entering the scenic spot. It can also be understood as the sum of various materials and services. The combined development of culture and the characteristics of the scenic spot can effectively promote the increase in the number of tourists in the scenic spot, and it can also promote the employment and economic development of various local industries [1]. The combination of culture and scenic spots can also enhance the local attractiveness. Tourism management departments can also more accurately divide and man-

age special scenic spots. The various cultural characteristics of scenic spots can also drive local resource utilization, such as for scenic areas that need to climb mountains, it is necessary to wear corresponding mountain climbing equipment in combination with cultural characteristics, thereby promoting the exchange and use of local resources. It can be seen that the integration of culture and tourism has occurred in a subtle way. [2].

1.2. Wireless Communication Technology. It is a technology for wireless information transmission in accordance with the standards set by the International Communication Organization. It can realize signal transmission without cables and other conduction. The current mainstream wireless communication technologies include Bluetooth, RFID, WIFI, and ZigBee [3].

Apply wireless communication technology to the traditional tourism industry, use the strategy of combining communication and cloud computing platform to collect a large amount of tourism data [4], and fully efficient use Internet information technology to transform the low-efficiency links of the traditional tourism industry and improve the efficiency of tourism marketing [5]. The use of wireless communication technology can also better protect the personal safety of tourists. At present, there are still many scenic spots that will cause tourists to get lost due to overly complex terrain and bad weather [6]. Using wireless communication technology, not only tourists can report their own address information. Scenic staff can also directly find tourists through drones and other measures [7].

1.3. Virtual Reality Technology. This technology refers to the projection of virtual objects into the vision of the user of the virtual reality device through visual simulation and other technologies [8]. Its main technical points are eye movement tracking and user motion capture, which can realize the processing of user perception, through the built-in processor and corresponding algorithm to complete the simulation processing of the user's actual experience data. Using virtual reality technology to optimize the integration and development of culture and tourism will have many advantages [9]. For example, many historically beautiful scenic spots no longer exist, and VR technology can restore the destroyed scenic spots based on animation, such as the Old Summer Palace. As an example, if the programmer configures in advance the corresponding scenes of the historical prosperity of the Old Summer Palace and the scenes of destruction and plundering during the invasion of the Eight-Power Allied Forces, visitors will be able to relive the beauty of the scenery of the Old Summer Palace through VR and understand the source of the current state of tourist attractions [10]. At present, a method called virtual tourism is gradually appearing in the public's field of vision through VR technology, which represents that real people can travel without going to the scene and get the same travel experience. Technically, it is mainly realized by external hardware devices [11].

From the perspective of the development of the integration of culture and tourism, scenic spots need to properly arrange the corresponding hardware facilities required for the integration of culture and tourism. These hardware facilities include wireless communication base stations and virtual reality wearable devices, as well as transportation and sanitation. Ensure that wireless communication services and entertainment services can make tourists feel the cultural characteristics of the scenic area, so that tourists can rely on the scenic area and pave the way for the development of the scenic spot [12].

2. The Current Status of the Integration of Culture and Tourism

The integrated development of culture and tourism is a new product of this era. Before the 21st century, people paid less

attention to the quality of tourism. However, in recent years, the combination of tourism and local culture has gradually been accepted by the public. Culture and tourism fusion are currently in the experimental stage in each scenic area, there is no unified reference standard, and the degree of integration and development of each scenic area is also different [13].

Through the questionnaire star, the author issued a questionnaire survey to 500 people who are responsible for long-term tourism in various industries and the management of surrounding affairs in the tourist area. The statistical results found that factors affecting the integrated development of culture and tourism around the scenic spot are shown in Table 1.

It can be seen from Table 1 that the main factors affecting the culture and tourism of scenic spots include income and the number of people in the industry. Among them, the entertainment and tourism incomes of scenic spots have the greatest influence on the integrated development of culture and tourism, with the highest degree of influence. At present, all scenic spots have similar operations. Mode, but there are also scenic spots that have arranged special product trails, snack areas, wine towns, and handicraft workshops to integrate culture and tourism. However, the scenic spots are not empowered by smart technology. Most scenic spots are operated according to the traditional mode of tourists paying to enter the venue on their own. A few scenic spots are equipped with advanced temperature monitoring, intelligent robot security inspection, and other equipment at the entrance. However, the technologies that have been maturely used in other industries have not been applied to tourism scenes. From a creative point of view, the current feature technology of tourist attractions always takes a long time to replace and will not be used as soon as the technology appears. The degree of innovation is not high, but it can basically express the cultural characteristics of the scenic spot. The integration of culture and tourism requires the use of more new technologies to keep up with technological leapfrogging in order to attract more tourists. Integrating various historical data of culture and tourism, the analysis of the surrounding culture and tourism of the scenic spot is shown in Figure 1.

It can be found from Figure 1 that the culture of scenic spots and tourism is highly related, but in reality, there are basically no large-scale cultural industry enterprises involved in the operation of the current tourist areas. Only the government and individual merchants are more concerned about the integration of culture and tourism in each scenic spot, and there is no large-scale culture industry enterprises. The main reason is that the scenic spots did not arrange professional technology and resource research and development institutions to participate. For example, most of the merchants in the hotel did not understand other network technologies other than mobile payment, did not realize the importance of wireless communication and virtual reality technology to their development, and cannot effectively use this resource to promote local culture and tourism. This is a waste of resources [14].

TABLE 1: Factors affecting the integrated development of culture and tourism around the scenic spot.

Judge Factor	Culture	Tourism	Impact factor
Income	Culture income	Tourism income	0.318
Scale	Art show	Passenger volume	0.239
Number of industry	Number of art	Number of people served	0.287
Acceptance	Number of libraries	Number of scenic spots	0.106

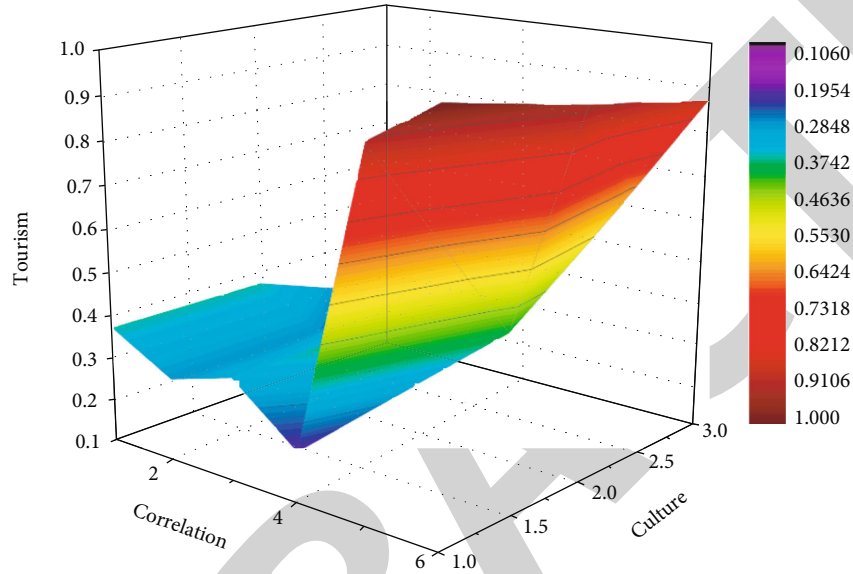


FIGURE 1: The relevance of culture and tourism around the scenic spot.

3. The Main Problems That Still Exist in the Integrated Development of Culture and Tourism

3.1. Lack of Platform. The integrated development of culture and tourism lacks a unified tourism management platform for information release and update management. Moreover, the travel patterns of various places are similar, there is no personalized travel characteristics, and many scenic spots do not even give a detailed introduction to their cultural background. Tourists use the intelligent network to search and understand the situation.

3.2. Incomplete Service. Most of the current tourist attractions do not arrange the itinerary of tourists according to the chronological order of the cultural and historical event background of the attraction. After visiting the attractions, tourists may only watch the corresponding scenic spots without clarifying the cultural connotation behind them. Most tourists go to various attractions and want to leave some memorable memories. Some tourists will buy figures related to the cultural background of the attraction, and some tourists will take photos with exaggerated actions, but in fact, many tourists will forget to take pictures during the tour, or the mobile device does not have a power reserve and miss the opportunity to take pictures, leaving regrets.

3.3. Not Smart. With the overall trend of tourism developing towards intelligence, most of the domestic tourism process is still not smart enough, tourists cannot experience the feeling described by smart tourism, and most tourist attractions fail to explain clearly the cultural connotation of the attractions, only allowing tourists explore and understand while playing. Moreover, the experience of the play process is not smooth, such as May Day and National Day. There are many tourists in some famous scenic spots in China, and there are other tourists every few meters. Even the tourism experience under the integration of culture and tourism is relatively poor. In addition, there are also problems that most tourists do not have navigation work after entering the scenic area.

4. Cultural and Tourism Integrated Development Solutions Based on Wireless Communication and Virtual Reality Technology

4.1. Measures to Solve the Lack of Platform Problem. In response to the lack of a unified tourism management platform, personalized custom development of the corresponding cultural, and tourism integration development APP, the rapid development of new technologies such as wireless communication technology and virtual reality terminal equipment has promoted the deep development of smart

TABLE 2: Statistics on changes in technology input and tourists' expectations for culture and tourism.

Expectations Tech input	Culture	Tourism
0.2	0.42	0.58
0.3	0.35	0.43
0.9	0.38	0.65
1.0	0.91	0.85

tourism and the rapid development of new media. The development and all-round network marketing have made more and more tourists get used to obtaining necessary travel information from the Internet, travel apps, and official accounts. Although tourists can obtain the multidirectional and multilevel travel information they need from the official account and travel APP; but the truth of this information is mixed, the data is complicated, and the timeliness and effectiveness cannot be guaranteed, so tourists cannot be fully and make effective use of the above tourism information to make scientific and intelligent tourism decisions. Therefore, the relevant tourism administrative department (government) should actively build and improve the smart tourism platform; release the latest tourism news through the audit system; conduct an orderly processing of the tourism information; and modular presentation of tourism information such as food, housing, transportation, travel, shopping, and entertainment that tourists care about. The most important thing is to ensure that the information is true, timely, and effective. At the same time, it pays attention to multichannel online marketing, with the help of the combination of APP and website, to truly promote the smart travel platform to the hands of tourists, and tourists can truly rely on the platform to make all-round smart decisions. In this paper, the relationship between the changes in technology input and the changes in tourists' expectations of culture and tourism through visits and surveys is as shown in Table 2.

In view of the unexplained connotation of tourist attractions, wireless communication technology can be considered to optimize various communication facilities and equipment in the scenic area. For example, driven by the high speed of 5G, there will be no network delay problems when tourists search and understand the cultural background of the scenic area. Wireless communication technology can also be used in unmanned vehicles for sightseeing in scenic spots. Only the high-speed network transmission load drives the unmannedness of unmanned vehicles. When the unmanned vehicles experience abnormalities on the way, wireless communication can also be used. Even if the information is sent back to the monitoring station of the tourism management department immediately, the safety of tourists is guaranteed. Figure 2 shows the changes of tourists' expectations of scenic area culture and scenic tourism under the condition that the input volume of VR and wireless communication technology increases.

4.2. Measures to Solve the Problem of Incomplete Service. In view of the order of the tour and the photo commemoration of tourists, a small travel smart eye should be developed that

tourists carry when they enter the scenic spot. It is similar to the VR eye that needs to be equipped to watch a 3D movie. The tour process that combines culture and tourism must be equipped with this eyes, which are worn when entering the attraction site. The eyes can be set to remind visitors to follow the time sequence of cultural and historical events and take into account the characteristics that most tourists are not familiar with the cultural connotation behind the attraction. The special address in the scenic spot directly broadcasts its historical retrospective scene through the travel smart eyes, allowing visitors to experience the culture at the scene of historical event restoration through virtual reality technology. After returning to reality, visitors will have a better understanding of the culture of the scenic spot. Smart eyes can be equipped with a camera function. If tourists keep their eyes closed for more than 5 seconds, it means that they confirm the photo. Using wireless communication technology can realize the travel smart eyes directly take photos and send them to other platform accounts that are logged in or bound, or they can be sent to the cloud and wait. Download the corresponding photos the next time you log in to the cloud. This method can effectively avoid problems caused by tourists forgetting to take pictures and insufficient mobile phone battery power during travel. If tourists do not need photos in the short term, they can also download them from the cloud when they are needed later; this method greatly facilitates the travel of tourists [15].

4.3. Measures to Solve the Problem of Unintelligence. Aiming at the problem that the travel process is not smart enough, a smart travel system can be established, and the system function interface can be opened before tourists visit the scenic spot. The functional interface includes one-click VR to understand the cultural history of the scenic spot and the different cultural representatives in the scenic spot. Explain the prompt sound and cloud map-style online cultural tourism coordinate point explanation, in which tourists use VR eyes to directly restore the historical scene and truly experience the real cultural and historical events behind the tourist attraction. For example, the tour of Baidi City can be combined with Liu Bei. The historical scene of Baidi Tuogu is restored in VR. In view of the fact that there are many tourists in the scenic spot at a specific time, wireless communication technology can be used to optimize the network in the key areas of the cultural connotation of the scenic spot and the most frequently parked area of tourists to enhance the tourists' mobile phone signal transmission experience, and the scenic spot itself can also be based on wireless communication. According to technical statistics, the number and density of tourists entering the scenic spot intelligently push information to the intentional tourists who have not entered the scenic spot that day, directly avoiding the occurrence of congestion. The latest wireless communication technology can also respond in real time, quickly, efficiently, and accurately according to the various weather, traffic, hotel, and scenic information required by tourists. The gradual development and maturity of the combination of culture and tourism have made tourists put forward higher requirements for the authenticity of the information on the virtual

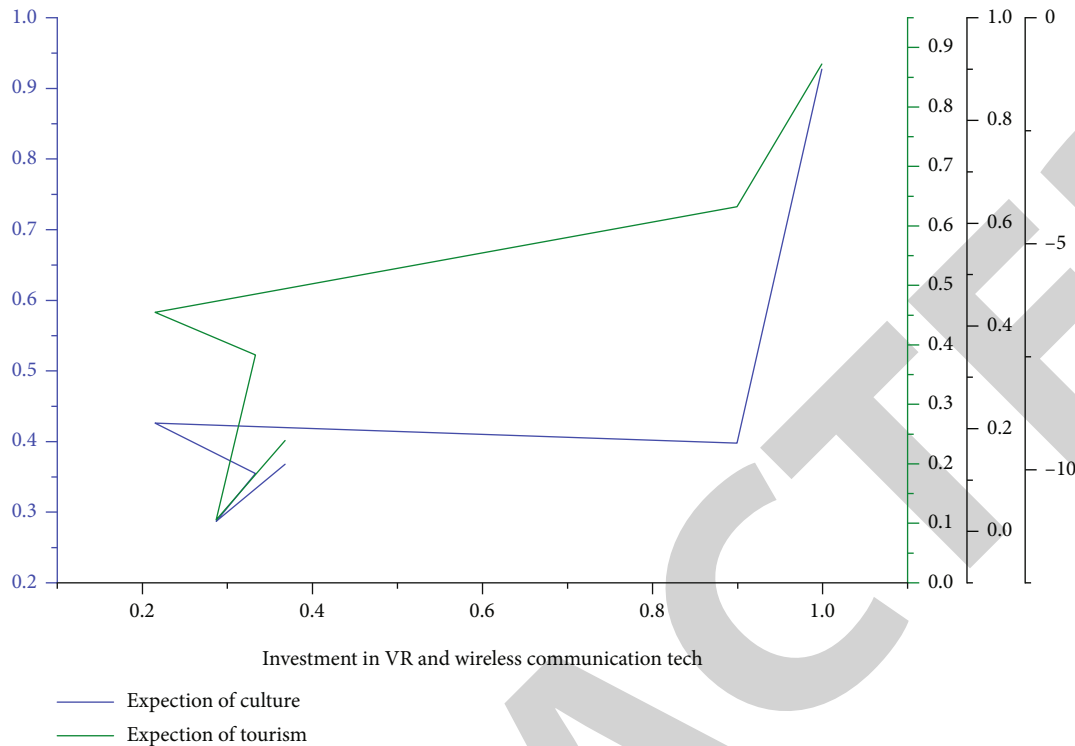


FIGURE 2: The relationship between the changes in the input of VR and wireless communication technologies and the changes in tourists' expectations of culture and tourism.

platform and the security of the network. It is necessary for the tourism administration department to establish a regulatory feedback mechanism platform to incorporate all aspects involved into the regulatory system. Only when the supervision and management are done can the integration of culture and tourism be truly sustainable. Aiming at the problem of navigation and cultural attraction, this, first of all, we must do a good job in road guidance, using wireless communication technology, when tourists enter the coverage area of the scenic area, automatically send text messages or APP ringing reminders to carry out road guidance work. After that, the culture of the scenic spot is spread through wireless communication technology, such as setting the free WIFI name of the scenic spot as a cultural background-related name, and the WIFI password can also be a content point for cultural promotion, so that tourists can already experience the scenic spot before they start visiting. Culture, this method can introduce and improve the attraction of culture to tourists. In addition, tourists like to stay in a homestay at a scenic spot, because the homestay is closer to the cultural characteristics of this scenic spot. The administrator of the scenic spot can arrange more cultural elements in the homestay to enhance tourists' interest in visiting, such as arranging VR preemptive travel experience directly in the homestay allow tourists to experience the features of scenic spots that they have not experienced for free, so as to fully display the cultural features of the scenic spots and attract tourists and increase the income of scenic spots.

5. Conclusion

The purpose of tourism itself is to relax the body and mind, but in addition, if it can also enable tourists to learn some new knowledge and gain some new experiences, then, tourism can become more meaningful. The development strategy of cultural and tourism integration based on wireless communication technology and VR technology will adopt new technologies to strengthen the historical and cultural influence on tourists. Using wireless communication technology to integrate the historical and cultural resources contained in each scenic spot, leading tourists to visit the historical and cultural background of the scenic spot and the current scenic spot through VR eyes, understand the whole ins and outs of the scenic spot and feel the culture precipitated by the scenic spot in the historical development. In turn, tourists are driven to have a deeper understanding of the scenic spot from the ideological point of view, also have a real experience of the cultural life of the scenic spot, increase the income of scenic spots, and achieve a win-win situation for tourists and scenic spots.

Data Availability

Data sharing not applicable to this article as no datasets were generated or analysed during the current study.

Retraction

Retracted: Application of Wireless Communication in Experimental Research of the Interface Bonding Condition between Asphalt Layers by Tensile Testing

Wireless Communications and Mobile Computing

Received 28 November 2023; Accepted 28 November 2023; Published 29 November 2023

Copyright © 2023 Wireless Communications and Mobile Computing. This is an open access article distributed under the Creative Commons Attribution License, which permits unrestricted use, distribution, and reproduction in any medium, provided the original work is properly cited.

This article has been retracted by Hindawi, as publisher, following an investigation undertaken by the publisher [1]. This investigation has uncovered evidence of systematic manipulation of the publication and peer-review process. We cannot, therefore, vouch for the reliability or integrity of this article.

Please note that this notice is intended solely to alert readers that the peer-review process of this article has been compromised.

Wiley and Hindawi regret that the usual quality checks did not identify these issues before publication and have since put additional measures in place to safeguard research integrity.

We wish to credit our Research Integrity and Research Publishing teams and anonymous and named external researchers and research integrity experts for contributing to this investigation.

The corresponding author, as the representative of all authors, has been given the opportunity to register their agreement or disagreement to this retraction. We have kept a record of any response received.

References

- [1] H. Yin, D. Wang, J. Zou, and Y. Zhu, "Application of Wireless Communication in Experimental Research of the Interface Bonding Condition between Asphalt Layers by Tensile Testing," *Wireless Communications and Mobile Computing*, vol. 2021, Article ID 2488947, 5 pages, 2021.

Research Article

Application of Wireless Communication in Experimental Research of the Interface Bonding Condition between Asphalt Layers by Tensile Testing

Hua Yin ¹, Daming Wang,² Jianwei Zou,¹ and Yaoting Zhu³

¹Transportation Institute, Inner Mongolia University, Bridge Detection and Maintenance Engineering Technology Research Centre of Inner Mongolia Autonomous Region, Hohhot, China

²Civil Engineering College, Nanjing Forestry University, Nanjing, China

³Jiangxi Research Institute of Transportation, Nanchang, China

Correspondence should be addressed to Hua Yin; 311976327@imu.edu.cn

Received 3 July 2021; Accepted 19 August 2021; Published 7 September 2021

Academic Editor: Balakrishnan Nagaraj

Copyright © 2021 Hua Yin et al. This is an open access article distributed under the Creative Commons Attribution License, which permits unrestricted use, distribution, and reproduction in any medium, provided the original work is properly cited.

The vigorous development of communication technology, especially the development of wireless network communication technology, has accelerated its informatization process in more and more industrial applications. In the field of monitoring and detection applications, the many advantages of wireless network transmission technology provide an important reference for high-quality compaction monitoring. Engineering practice shows that the construction technology of asphalt pavement is the ultimate guarantee of engineering quality. It is important to recognize that pavement performance is greatly influenced by interface bonding condition and interface failure can reduce the serviceability of pavements rather than their overall structural lifetime. This paper presents a laboratory test to investigate the bonding tensile performance between asphalt layers by tensile testing. The test methods and devices for determining the bond regarding tensile testing are summarized as follows. Different interface conditions have been analyzed herein: 0.2, 0.4, and 0.6 kg/m² with corresponding emulsified asphalt (MA) and SBS-modified MA. It is found that the stress-strain relationship of tensile testing for interface bonding is similar with low-carbon steels and it can be categorized into four zones. The results of tensile strength and damage displacement are discussed which are key parameters in describing the interface bonding condition and evaluating pavement performance.

1. Introduction

The interface bonding condition between asphalt layers is one of the most important factors that affect the performance of the pavement structure and have attracted more and more attention to study the bonding testing during recent years. This leads to the development of different test devices and corresponding parameters to characterize the bonding properties in numerous papers and scientific contribution, such as layer parallel direct shear test, wedge splitting test, torque test, and pull-off test [1–4]. In China, extensive technical specifications and rules of tack coat for asphalt layers have been set up but the standard test method for evaluating the quality of layer bonding does not exist. In general, in order to investigate the interfacial strength of

layer bonding, two different laboratory tests are widely considered, namely, shear testing and tensile testing. Samples can be made in the laboratory or cored sampling on the pavement. Although shear-type tests are popular to being applied, there are some limitations to assess the interface bonding condition [5–8]. It is well recognized that shear stress is not the unique factor to result in poor bonding or loss of bonding and tensile stress is also a major factor contributing to the distresses of interface bonding [9].

The aim of this paper is the investigation of the bonding properties for asphalt layers and to assess interface tensile characteristics between layers of asphalt concrete. In this paper, the results of an improved direct tensile testing are presented and compared with the different materials for interface bonding by laboratory-prepared specimens.

TABLE 1: The asphalt binder performance.

Test	AH-50	
Penetration (25°C, 100 g, 5 s) (0.1 mm)	53	
Ductility (15°C, 5 cm/min) (cm)	>100	
Softening point (°C)	50.5	
Density (15°C) (g/cm ³)	1.040	
Thin film oven test (TFOT) (163°C, 5 h)		
	Mass loss (%)	1
	Penetration (%)	64.2
	Ductility 10°C (cm)	4.3

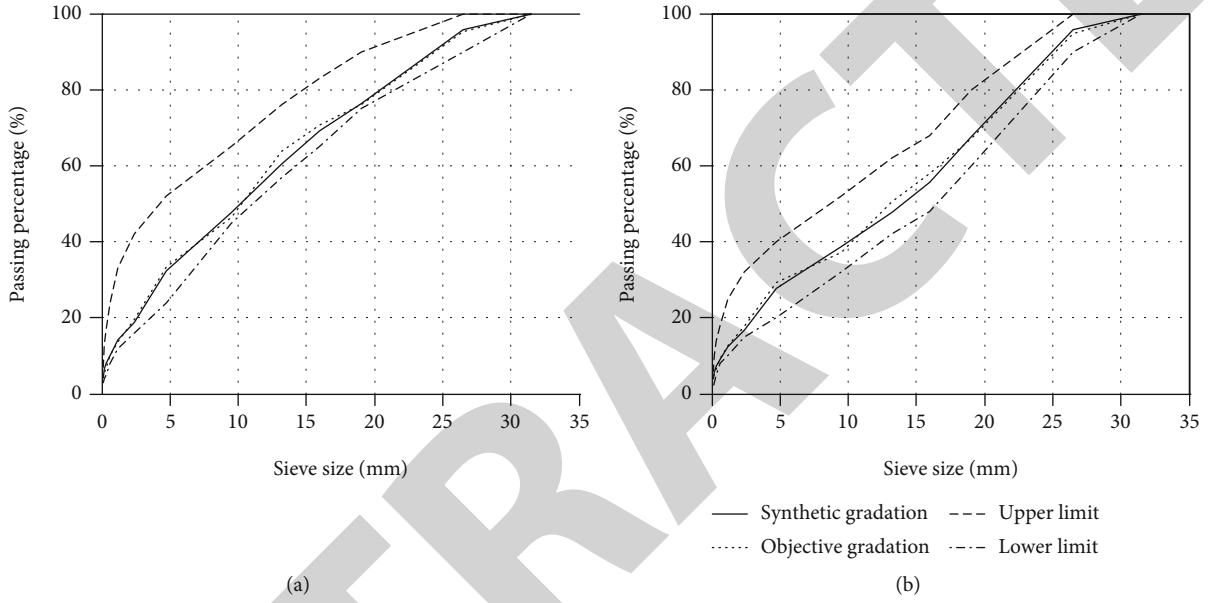


FIGURE 1: The graded curve of AC-25 (a) and ATB-25 (b) [9].

2. Experimental Details

During the tensile testing of the interlayer bonding condition of asphalt, we followed the operating instruction for the materials and test methods of the “Study on the mechanical properties of tack coat between asphalt layers by interlaminar shear tests,” Applied Mechanics and Materials, <https://www.scientific.net/AMM.361-363.1490> [10–13]. Beyond that, interlaminar shear test and tensile test were all experienced by this manuscript’s author. There are two kinds of experiments for raw materials and gradation of the same two asphalt mixtures. Specific materials and methods will be introduced and explained below. Relative data along with the manuscript of the “Study on the mechanical properties of tack coat between asphalt layers by interlaminar shear tests” are offered in information file.

The asphalt used in this test was AH-50 Asphalt produced by the Esso Asphalt Company. Limestone from Jiangxi province, China, was selected as aggregate according to relevant design standards. Two typical hot mix asphalt mixtures (AC-25 and ATB-25) were prepared to study the bonding performance between layers of asphalt concrete. The asphalt binder performance is given in Table 1.

TABLE 2: The emulsified asphalt performance [9].

Test	Ordinary MA	SBS-modified MA
Demulsification rate	Quick	Quick
Charge	Positive	Positive
Engler viscosity	7.0	7.5
Sieve residue (%)	0.02	0.02
Storage stability (%)	0.7	0.5
Residue		
Distillation residue (%)	60.7	61.2
Penetration at 25°C (0.1 mm)	55	63
Ductility at 25°C (cm)	>100	>100

According to the Marshall test, the optimal asphalt content of AC-25 is 3.9% and the optimal asphalt content of ATB-25 is 3.5%. The distribution of the graded aggregate is shown in Figure 1.

The asphalt mixture used in the test are divided into three parts: AC-25 HMA, cemented layer material and ATB-25 HMA from top to bottom. Firstly, the ATB-25

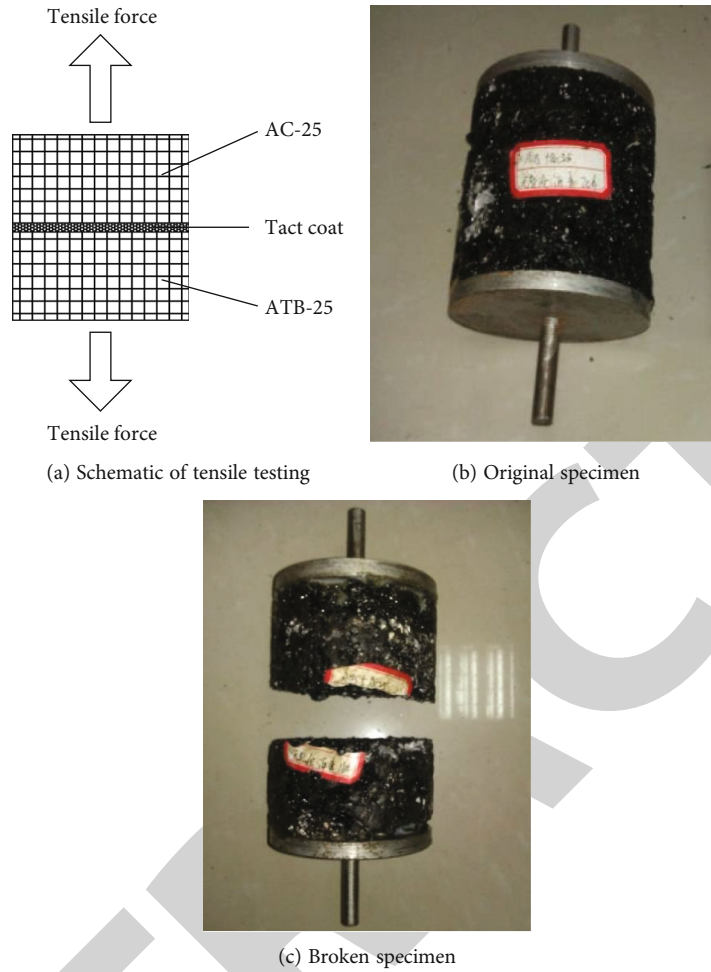


FIGURE 2: Schematic of direct tensile testing and the specimen.

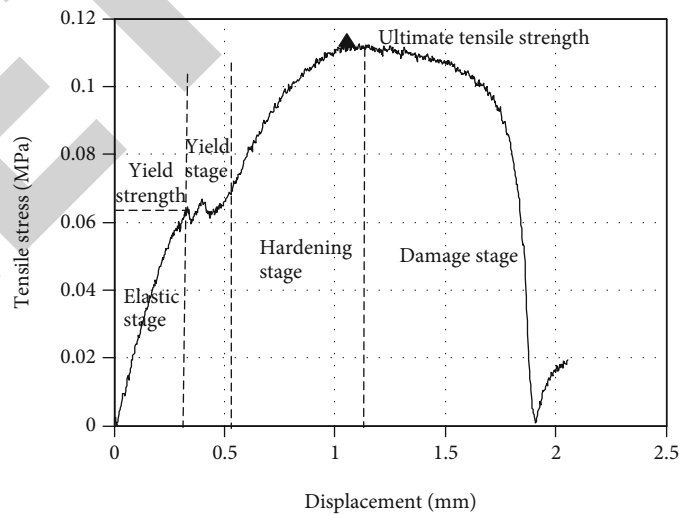


FIGURE 3: Typical curve for tensile stress vs. displacement.

and AC-25 samples with diameter of 101.5 mm and height of 50 mm were made by Marshall principle. After cooling for two hours, apply the cementing layer material on the upper surface of ATB-25 sample and bond with the lower

surface of AC-25 sample. The asphalt binders used are ordinary MA and SBS modified MA with three different asphalt dosages (0.2, 0.4, and 0.6 kg/m²). The related performance indicators are shown in Table 2.

TABLE 3: Laboratory tensile test results.

Test	Bond content (kg/m ²)	Ultimate tensile strength (MPa)	Damage displacement (mm)
MA	0.2	0.11	0.98
	0.4	0.15	1.49
	0.6	0.13	1.07
SBS modified MA	0.2	0.18	1.48
	0.4	0.08	0.62
3% cement + SBS – modified MA	0.4	0.14	1.23
5% cement + SBS – modified MA	0.4	0.11	0.98

Figure 2 is the configuration diagram of the direct tensile test in this study. A 50 kN Universal Servo-Hydraulic Testing Machine and a linear variable differential transformer (LVDT) are used to apply tensile force to the specimen under static or cyclic load conditions. The Universal Servo-Hydraulic Universal Testing Machine stretches the test sample at a constant rate of 5 mm/min, which makes the boundary between the two layers of the specimen produce tension and destroy. The test temperature of 25°C was selected. The corresponding tensile stress and displacement are recorded by the software of the equipment until the specimen failure. The load-extension relationship and the stress-strain relationship are shown in Figure 3.

3. Results and Discussion

During the tensile test programme, 28 specimens were tested using the tensile test equipment as mentioned above. Figure 3 illustrates the relationship between tensile stress and displacement. It is found that the stress-strain relationship of interface bonding is similar with low-carbon steels. Four stages can be used to represent this figure: (i) elastic stage, (ii) yield stage, (iii) hardening stage, and (iv) damage stage. At the beginning of the test, the tensile stress increases linearly and then reaches the yield strength.

- (1) The linear growth of tensile stress in the elastic stage satisfies Hooke's law and has an initial slope expressed as elastic modulus which is important and applied in the engineering
- (2) If the loading continues to be applied after the elastic stage, the material will enter the yield stage and produce irreversible deformation. When the yield strength reaches and the specimen continues to extend, the stress fluctuates near the yield strength and strain increase
- (3) Beyond the yield stage, stress increases continuously in the hardening stage due to the continuous loading. The material has the ability to resist further deformation. The specimen shows strain hardening, and the degree of hardening is related to the performance and content of the interface binder
- (4) When the load is continued, the stress of the tensile curve reaches the maximum value, that is, the ultimate

tensile strength, and the material loses its resistance to deformation and begins to get destroyed

Table 3 lists all the cemented layer materials used in the tensile test and the test results. The minimum tensile strength is 0.08 MPa and the maximum tensile strength is 0.18 MPa and the damage displacement range from 0.62 to 1.49 mm. It can be also found that the larger damage displacement generally indicates a higher level of interface bonding. The results show that the optimal amount of the binder is 0.4 kg/m²; SBS-modified MA can significantly improve the interfacial bonding strength of asphalt concrete. When cement is added to the interface material, the tensile strength is also improved, showing good tensile ductility.

4. Conclusion

Based on the laboratory test, the following conclusions can be drawn from the analysis of the interface bonding conditions between layers of asphalt concrete.

- (1) The stress-strain relationship of tensile testing for interface bonding is similar with low-carbon steels and four stages can be used to represent: (i) elastic stage, (ii) yield stage, (iii) hardening stage, and (iv) damage stage
- (2) The optimal amount of the binder for tensile strength is 0.4 kg/m²; SBS-modified MA can significantly improve the interfacial bonding strength of asphalt concrete. When cement is added to the interface material, the tensile strength is also improved, showing good tensile ductility

Data Availability

Data sharing is not applicable to this article as no datasets were generated or analyzed during the current study.

Conflicts of Interest

The authors declare that they have no conflicts of interest.

Acknowledgments

This research was supported by the Natural Science Foundation of China's Inner Mongolia Autonomous Region (Grant:

Retraction

Retracted: Research on the Detection and Tracking Algorithm of Moving Object in Image Based on Computer Vision Technology

Wireless Communications and Mobile Computing

Received 28 November 2023; Accepted 28 November 2023; Published 29 November 2023

Copyright © 2023 Wireless Communications and Mobile Computing. This is an open access article distributed under the Creative Commons Attribution License, which permits unrestricted use, distribution, and reproduction in any medium, provided the original work is properly cited.

This article has been retracted by Hindawi, as publisher, following an investigation undertaken by the publisher [1]. This investigation has uncovered evidence of systematic manipulation of the publication and peer-review process. We cannot, therefore, vouch for the reliability or integrity of this article.

Please note that this notice is intended solely to alert readers that the peer-review process of this article has been compromised.

Wiley and Hindawi regret that the usual quality checks did not identify these issues before publication and have since put additional measures in place to safeguard research integrity.

We wish to credit our Research Integrity and Research Publishing teams and anonymous and named external researchers and research integrity experts for contributing to this investigation.

The corresponding author, as the representative of all authors, has been given the opportunity to register their agreement or disagreement to this retraction. We have kept a record of any response received.

References

- [1] C. Chen and D. Li, "Research on the Detection and Tracking Algorithm of Moving Object in Image Based on Computer Vision Technology," *Wireless Communications and Mobile Computing*, vol. 2021, Article ID 1127017, 7 pages, 2021.

Research Article

Research on the Detection and Tracking Algorithm of Moving Object in Image Based on Computer Vision Technology

Chunsheng Chen  and Din Li

Anqing Normal University, Anqing 246000, China

Correspondence should be addressed to Chunsheng Chen; chenchunsheng@aqnu.edu.cn

Received 7 July 2021; Accepted 9 August 2021; Published 6 September 2021

Academic Editor: Balakrishnan Nagaraj

Copyright © 2021 Chunsheng Chen and Din Li. This is an open access article distributed under the Creative Commons Attribution License, which permits unrestricted use, distribution, and reproduction in any medium, provided the original work is properly cited.

In order to improve the video image processing technology, this paper presents a moving object detection and tracking algorithm based on computer vision technology. Firstly, the detection performance of the interframe difference method and the background difference model method is compared comprehensively from both theoretical and experimental aspects, and then the Robert edge detection operator is selected to carry out edge detection of the vehicle. The research results show that the algorithm proposed in this paper has the longest running time per frame when tracking a moving target, which is about 2.3 times that of the single frame running time of the CamShift algorithm. The algorithm has high running efficiency and can meet the requirements of real-time tracking of a foreground target. The algorithm has the highest tracking accuracy, the time consumption is reduced, and the error of the tracking frame deviating from the real position of the target is the least.

1. Introduction

Before computers and the appearance of modern science and technology, people tend to rely mainly on vision when accessing outside information. However, in our country, under the background of computer technology development promotion, the emergence of computer vision technology has made developments to further extend the human eye vision, especially under the help of all kinds of sensor technology. In this way, people can track moving targets in real time so as to accurately grasp the specific morphological attributes of the target [1]. Under the background of the continuous enhancement of China's economic strength, the process of socialist modernization is also gradually advancing, and computer information technology has made great progress, which makes a lot of reform and innovation in the related image engineering and artificial intelligence technology. The detection of moving targets in video images has always been an important problem in the field of computers. Its application to urban management is of vital significance in combating illegal crimes, maintaining people's safety, and promoting social stability and harmony [2]. To solve

many practical problems in real life, people need to be able to accurately capture the moving information. Therefore, it is very urgent to study the way and algorithm of moving target detection at present. Detecting moving targets is the most important content in video sequence images; to observe the whole scene image and find out the moving object involves many contents, such as computer image analysis, image processing, and artificial intelligence. To detect a moving target is too late for target tracking, and to understand behavior and the important basis of classification belongs to the bottom of the video monitoring system. To a large extent, it affects the function of the video surveillance system [3].

Object tracking is an important branch in the field of computer vision, and in order for computers to better understand the real world and carry out efficient human-computer interaction, research on the related technology of object tracking is the top priority. The main task of target tracking is to extract the target of interest from the video image and obtain its characteristic information such as position, size, moving speed, and angle in space continuously. At present, few algorithms can accurately track any scene in

real life, especially when the target is occluded and deformed, and the color features change; the tracking frame will more or less shift the real target position, or even completely lose track of the target. At present, visual target tracking-related technology has been integrated more closely with modern people's life, so that computers can assist or completely replace humans to efficiently complete many types tedious and dangerous work. For example, monitoring equipment in a complex traffic area, video monitoring in coal mine safety operations, and visual navigation technology in the military neighborhood are all typical applications of target tracking technology in real life. Sergio et al. [4]. investigated how visual context affects motion's glasses, whether consistent or independent of natural gravity. To do this, 28 subjects followed a computer-simulated trajectory that was disturbed in the descent section, its gravitational effect ($0g/2g$) or fixed natural motion ($1g$). Shortly after the disturbance (550 ms), the target disappears for 450 or 650 ms and becomes visible again until landing. Target movements occur in quasirealistic graphical cues such as balance sequences or unified backgrounds. We analyzed the saccade and pursuit motions after 0G and 2G target-motion perturbations, and we also analyzed the corresponding intervals for undisturbed 1G trajectories after the corresponding occlusion. Furthermore, we consider the target to reappear at eye distance to the target. Tracking parameters differ significantly between scenes: through a neutral background, eye movements do not correspond to target movements, while under a patterned background, they show a significant dependency, indicating better tracking of accelerated targets. These results indicate that the motor control is adjusted to the realistic attributes of the visual scene [5]. Sudha et al. [6] proposed an advanced deep learning method called "enhanced," a V3 and improved visual background extractor algorithm for detecting multiple types and multiple vehicles in the input video. More precisely, tracking is done using a combination of the Kalman filter algorithm and particle filter technology to find the trajectory of the incoming vehicle. In order to improve the tracking results, the technology named the multicarrier tracking algorithm is further proposed and tested with different weather conditions, such as sunshine, rain, night, and fog, with input video at 30 frames per second. Major research issues found in its department's recent literature are closely related to real-time traffic environment issues such as occlusion, camera oscillations, background changes, sensors, clutter, camouflage, and different lighting variations during the day—sunny and night vision. The experimental results were tested with ten different input videos and two benchmark datasets, KITTI and DETRAC. Up to eight advanced features have been considered for automatic feature extraction and annotation. The attributes are length, width, height, number of mirrors, and wheels as well as windshield shielding glass to detect the target area (vehicle) on the road. In addition, further experiments were carried out using a high-definition multi-input video with a monocular camera, with an average accuracy of 98.6%. The time complexity of the algorithm was 0, and the tracking result reached 96.6% [7].

Based on this, this paper proposes an algorithm for detecting and tracking moving objects in images based on computer vision technology. Firstly, the detection performance of the interframe difference method and that of the background difference model method are compared comprehensively from both theoretical and experimental aspects, and then the Robert edge detection operator is selected to carry out the edge detection of the vehicle. In the problem of vehicle target segmentation, the algorithm can clearly distinguish the interference between each target and accurately describe the moving face target, so as to track the moving target better. Combined with the edge detection of the gray vehicle image, the maximum interclass variance can be obtained, and the accuracy and real-time performance of segmentation can be improved. It is proven that the modified algorithm has a better tracking effect [8].

2. Materials and Methods

2.1. Theoretical Framework of Visual Computing. The theoretical framework of computer vision affects the development of computer vision and is a guiding ideology in the field of computer vision. Marr's vision theory is a view of information processing that combines physics, neurophysiology, and image processing. Under this theoretical framework, the generation of visual images can be divided into three stages:

- (1) Two-dimensional schematic diagram: the initial schematic diagram uses edge segments, lines, spots, and endpoints to describe the brightness changes in the image, and then it uses virtual lines to completely and explicitly represent the geometric relationship. Finally, the initial schematic diagram whose description level can cover a certain scale range is obtained
- (2) 2.5-dimensional diagram: by performing a series of manipulations on the initial diagram, a representation of the geometrical features of the visible surface is derived, including surface orientation, observer distance, discontinuity between orientation and distance, surface reflection, and some rough description of the predominant illumination
- (3) 3D model: realize the representation of the three-dimensional structure of the observed object in the object-centered coordinate system and some description of the surface properties of the object, so as to obtain the spatial structure of the image

There are two main approaches to the visual tracking problem. One is a bottom-up approach, and the other is a top-down approach. The method in this paper can be divided into three stages by using the bottom-up method and combining with the visual computing theory of the Marr visual process: layer vision, middle-layer vision, and high-level vision. From the low-level vision to the middle-level vision is the image feature description, from the middle-level vision to the high-level vision is the 2.5D description, and from the high-level vision is the 3D

description. The bottom-up tracking process is obviously able to get the position, speed, and acceleration of the scene. Therefore, we first need to detect the moving target and then determine whether the target is a tracking target. Finally, the target position, trajectory, and other information are obtained. We are now going to track a moving vehicle, and with the help of Marr's theory, the visual tracking framework is easy to implement. There are mainly the following three stages: vehicle detection is in an early stage; target extraction and recognition to determine whether there is tracking is in the middle stage; obtaining the target position and trajectory information is in the later stage [9].

2.2. Video Image Moving Target Detection Method

2.2.1. Interframe Difference Method. As one of the most commonly used methods for moving object detection, the interframe difference method can effectively detect dynamically changing images, and more than between adjacent frames or between three frames. Therefore, it is called the frame difference method, which is mainly based on the principle of strong correlation between adjacent frames of a sequence of images and can realize the change detection of moving targets. Under the effect of filtering, the range and area of the moving target are determined, and the calculation formula can be described as follows: $d_k(x, y) = |f_k(x, y) - f_{k-1}(x, y)|$. Among them, $f_k(x, y)$ and $f_{k-1}(x, y)$ represent two successive frames of moving images and $d_k(x, y)$ represents the absolute difference image; this calculation formula only includes subtraction calculation of pixel intensity, and the whole calculation process is relatively simple, feasible, and easy to implement. This detection method also has some defects. It is easily affected by noise interference. When the occluded background appears under the influence of motion, the new background will be misdetected as a moving object; in order to effectively avoid the influence of a "ghost" on moving targets, a new improvement was made to the frame search method. By verifying the difference intersection of multiple frames of images, moving targets were detected, and symmetric difference detection was commonly used, as shown in Figure 1 [10].

2.2.2. Background Difference Method. The so-called background difference method mainly refers to subtracting the current frame image presented in the video sequence from the prestored background image to detect and extract the target. The specific process is shown in Figure 2. The background difference method can be described as follows: $d_k(x, y) = |f_k(x, y) - B(x, y)|$. Among them, the difference image is represented by $d_k(x, y)$, the background is represented by $B(x, y)$, and the current frame image is $f_k(x, y)$. When detecting the target, the K -frame image is subtracted from the background image, and then the difference image is extracted, and then the threshold is selected, The obtained difference image is transformed into a binary difference image, in which the pixel of 0 is determined as the background region, and the pixel of 1 is determined as the moving target region. As a very important part of the background difference method, preprocessing refers to the

simple filtering of video images to avoid camera noise and instantaneous noise of external links. If the camera shakes, then, before background modeling, the acquired continuous video frames must be integrated into image processing [11].

2.3. Algorithm Analysis of Moving Objects in Video Images

2.3.1. Multiframe Image Average Method. The so-called multiframe image average method mainly implies that when detecting and analyzing the moving target, it is taken as the noise source, and the accumulated average method is adopted to gradually eliminate the noise, and the sequence image of the running target is taken as the key analysis object. The background image can be expressed as follows:

$$B(x, y) = \frac{1}{N} \sum_{i=1}^N f_k(x, y). \quad (1)$$

Using this algorithm, the corresponding background image can be obtained, and the image is affected by the average frame number. The larger the average frame number is, the better the noise elimination effect will be.

2.3.2. Continuous Frame Difference Method. The so-called continuous frame difference method mainly refers to the calculation of the difference between the current frame image and the previous frame image in the process of extracting and calculating the moving object of the video image, and determines the moving region based on it; it can keep the background in the moving region unchanged, while for the background in the nonmoving region, the current frame can be used to realize dynamic update. Under the action of iteration, the background can be extracted. First, the original image B_0 can be represented by the first frame image I_0 ; then, we set the iteration parameter as $I = 1$ and obtain the difference of the binary image between the current frame and the previous frame, namely, BW_1 . The specific calculation method is as follows:

$$BW_i \begin{cases} 1 & \text{ads}(I_k - I_{i-1}) \geq T, \\ 0 & \text{ads}(I_k - I_{i-1}) < T, \end{cases} \quad (2)$$

where the images of the current frame and the previous frame are represented by I_i and I_{i-1} , respectively, the difference between frames is $\text{ads}(I_i - I_{i-1})$, the grayscale histogram of interframe difference images is represented by T , that is, the gray value corresponding to 1/10 of the right side of the maximum peak value. Then, the background is updated through a binary image, and the specific calculation method is as follows:

$$B_i(x, y) \begin{cases} B_{i-1}(x, y) BW_i(x, y) = 1 \\ aI_i + (I - a)B_{i-1}(x, y) BW_i(x, y) = 0 \end{cases}, \quad (3)$$

where $B_i(x, y)$ and $BW_i(x, y)$ represent the positions of the two images in the coordinates, and the updating speed coefficient is set as 0.1. Set the condition $I = I + 1$, and then substitute it with BW_i for iterative calculation; when a certain number is

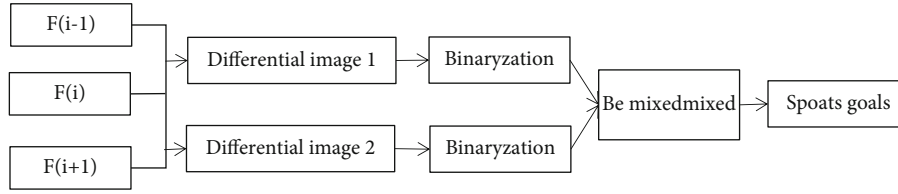


FIGURE 1: Symmetric difference method. By verifying the difference intersection of multiple frames of images, moving targets were detected, and symmetric difference detection was commonly used.

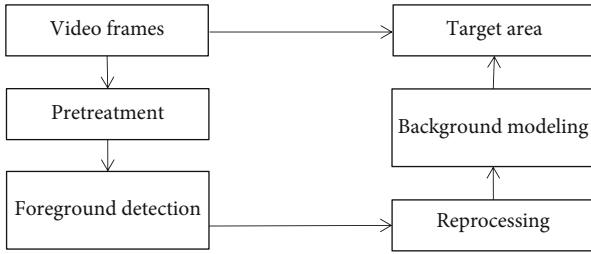


FIGURE 2: Detection flow. The so-called background difference method mainly refers to subtracting the current frame image presented in the video sequence from the prestored background image to detect and extract the target.

reached, the iteration ends and AA is set to extract the background.

2.3.3. Maximum Threshold Segmentation. Usually, high-quality moving images are often needed in practical work. In order to meet the needs of high-quality moving objects in various fields, the threshold can be determined to segment the image, so that the binary image can accurately reflect the moving objects of the image. In general, the histogram of the image is in a bimodal state, and the optimal threshold is the valley of the bimodal histogram. But for multipeak histograms, the threshold true rule is faced with difficulties. After research, the probability distribution method can be used to represent the information. Generally, when the threshold is different, the amount of information in the target area and the background area is obviously different, so the total amount of information threshold T is the optimal segmentation value, that is, the optimal threshold.

2.4. Performance Analysis of Moving Target Segmentation Algorithm. Image segmentation is an important method in computer moving object tracking. To solve the vehicle-tracking problem, the Robert edge detection operator is used to detect the edge of the target vehicle, which greatly improves the segmentation accuracy. In addition, we also propose a vehicle target segmentation strategy with maximum interclass variance, and the experimental results show that the algorithm has good segmentation effect. The OTSU method is a threshold segmentation method, which is based on the principle of discriminant analysis and least square method. In this method, the pixel threshold is divided into two parts, target C_0 and background C_1 , and then the inter-class variance is obtained:

Assume that the image gray value in a certain range is $\{0, 1, \dots, l-1\}$, the gray level I of pixel is expressed as n_i ,

and the whole pixel is expressed as $N = \sum_{i=0}^{l-1} n_i$. The occurrence probability of gray level I is shown in formula (4).

Select the threshold T to distinguish between the target and the background area, $C_0 = \{0, 1, \dots, t\}$; $C_1 = \{t+1, t+2, \dots, l-1\}$. The probability of the possible occurrence of target C_0 and background C_1 is shown in formula (5).

The mean is shown in formula (6).

The average gray level of the image is shown in formula (7).

According to equation (5), equation (6), and equation (7), the interclass variance is calculated and shown in formula (8).

Next, we define the in-class variance as shown in formula (9).

The total variance is defined as shown in formula (10).

For second order statistics $0_w^2(t)$ and 0_r^2 independent of t , we made a simple judgment as shown in formula (11).

Under such a criterion, both types of t values belong to the optimal threshold, so $\eta(t)$ is the maximum criterion, as shown in formula (12).

2.5. Performance Analysis of Target Tracking Algorithm. In many visual tracking algorithms, there are basically two categories: one is based on motion, and the other is based on a specific model. It is mainly based on the model tracking method, through mutual matching to achieve tracking. Template matching can be divided into two types based on target and target region. The target-based method matches by angle, color, etc. In a complex environment, its matching effect is better than the boundary matching method. In fact, due to the movement of the target itself, for the fixed target model that cannot be stable for a long time, it is necessary to update the target features in real time to adapt to the change of the target. If the target model of the current frame cannot accurately describe the current target, it will lead to wrong model update. To solve this problem, we proposed an image matching and tracking algorithm based on multiassociated templates. The algorithm flow is shown in Figure 3:

In the target tracking problem, the target tracking information is determined by the matching of the image relative to the original image. In fact, there is a certain degree of difference between the template involved in the image matching and the potential matching factors. Therefore, detecting a matching object on an unknown image is a complex task. The relationship between template T and the potential match object P is shown in formula (13).

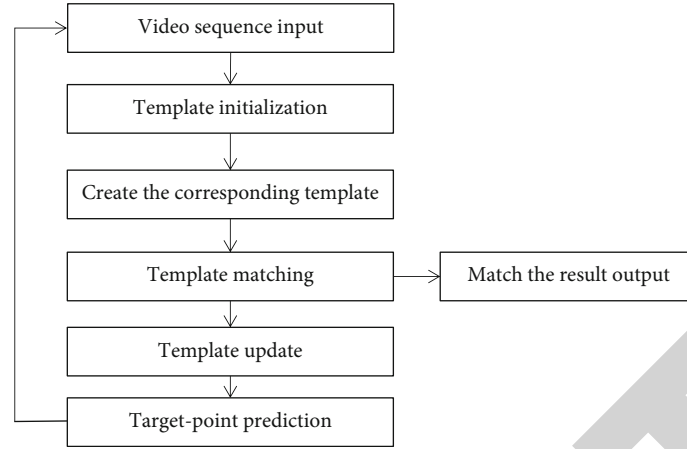


FIGURE 3: Tracking algorithm flow chart. To solve this problem, we proposed an image matching and tracking algorithm based on multiassociated templates.

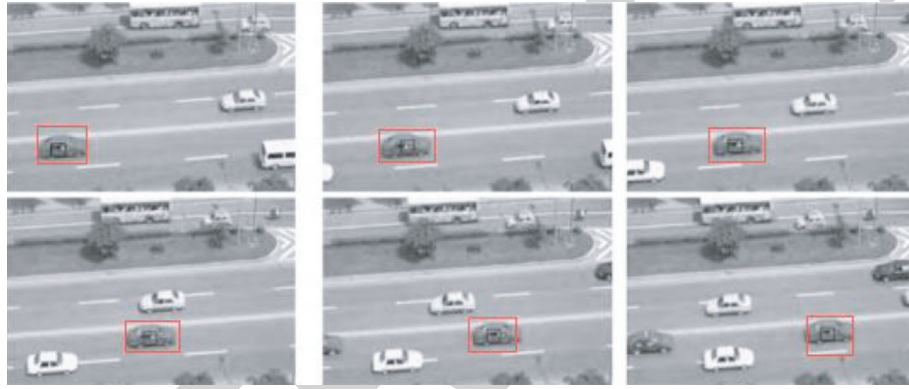


FIGURE 4: Tracking experiment results: tracking effect of black cars. In order to verify the accuracy of the algorithm, the experiment selected a PC configured with Intel core i5 2 GB memory.

Among them, $(x, y) \in T, (x', y') \in p$, and β_{ij}, α_i are constants. By combining the similarity criterion, mean absolute difference method, and mean square error method, the similarity measure of the mean absolute error is obtained as shown in formula (14).

Here, the size of the reference image $f_1(x, y)$ is $m \times n$, the size of the real-time image $f_2(x, y)$ is also $m \times n$, and the mean square error similarity measure can be expressed as shown in formula (15).

In equation (14) and equation (15), the offset (x_0, y_0) that satisfies $D(x_0, y_0)$ is called the matching point, but when the target is heavily affected by illumination, the tracking effect will not be very ideal. The linear change of the image can be tracked by the normalization algorithm. The similarity measure of the normalized algorithm can be expressed as shown in formula (16).

Here, \bar{f}_1 and \bar{f}_2 , respectively, correspond to the grayscale value of the template and the sample image [12].

3. Results and Discussion

In order to verify the accuracy of the algorithm, the experiment selected a PC configured with Intel core i5 and 2 GB

memory, and carried out experiments under two videos, respectively. The tracking results are shown in Figures 4 and 5.

Figure 6 is the tracking performance analysis of the above algorithm during the whole tracking period. As can be seen from the above table, the algorithm proposed in this paper has the longest running time of a single frame when tracking moving targets, which is about 2.3 times that of the CamShift algorithm. The algorithm has high running efficiency and can meet the requirements of real-time tracking of foreground targets. In terms of the tracking accuracy of the target, the algorithm in this paper has the highest tracking accuracy, reduced time consumption, and minimized error of the tracking box deviating from the real position of the target.

3.1. Advice on Equations.

$$\begin{aligned}
 p_i &= \frac{n_i}{N}, \\
 p_i &\geq 0, \\
 \sum_{i=0}^{1-1} p_i &= 1,
 \end{aligned} \tag{4}$$



FIGURE 5: Tracking experiment results: tracking effect of white cars. In order to verify the accuracy of the algorithm, the experiment selected a PC configured with Intel core i5 2 GB memory.

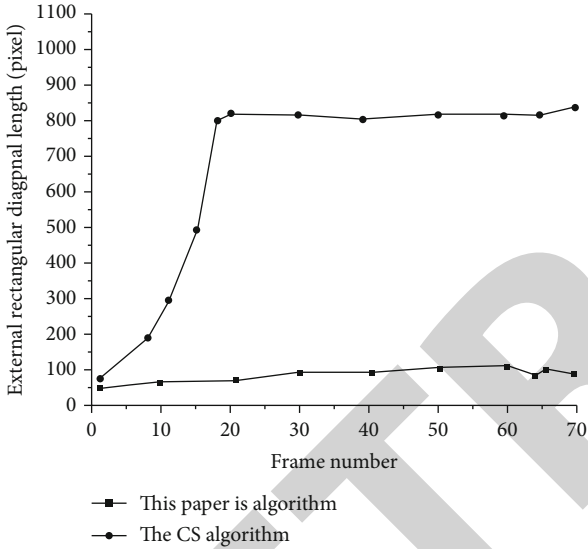


FIGURE 6: Dynamic changes of tracking box size under the complex background of two algorithms. The tracking performance analysis of the above algorithm during the whole tracking period is shown.

$$P_0(t) = \sum_{i=1}^t p_i, \quad (5)$$

$$P_1(t) = \sum_{i=t+1}^{1-1} P_i,$$

$$\mu_0(t) = \sum_{i=1}^t \frac{ip_i}{P_0(t)}, \quad (6)$$

$$\mu_1(t) = \sum_{i=t+1}^{1-1} \frac{ip_i}{P_1(t)},$$

$$\mu_T = \sum_{i=0}^{1-1} ip_i, \quad (7)$$

$$O_B^2(t) = P_0(t)[\mu_0(t) - \mu_T]^2 + P_1(t)[\mu_1(t) - \mu_T]^2, \quad (8)$$

$$O_w^2(t) = P_0(t) \sum_{i=0}^t \left[(i - U_0)^2 * \frac{P_i}{P_0(t)} \right] \quad (9)$$

$$+ P_1(t) \sum_{i=t+1}^{1-1} \left[(i - U_1)^2 * \frac{P_i}{P_1(t)} \right],$$

$$O_r^2 = O_B^2 + O_w^2, \quad (10)$$

$$\eta(t) = \frac{\sigma_B^2}{\sigma_T^2}, \quad (11)$$

$$\max_{0 < t < 1-1} \eta(t) = \max \eta(t^*), \quad (12)$$

$$\begin{bmatrix} x' \\ y' \end{bmatrix} \approx \begin{bmatrix} \beta_{11} & \beta_{12} \\ \beta_{21} & \beta_{22} \end{bmatrix} \begin{bmatrix} x \\ y \end{bmatrix} + \begin{bmatrix} \alpha_1 \\ \alpha_2 \end{bmatrix}, \quad (13)$$

$$D(x_0, y_0) = \frac{1}{mn} \sum_{x=0}^{m-1} \sum_{y=0}^{n-1} |f_1(x, y) - f_2(x + x_0, y + y_0)|, \quad (14)$$

$$ID(x_0, y_0) = \frac{1}{mn} \sum_{x=0}^{m-1} \sum_{y=0}^{n-1} |f_1(x, y) - f_2(x + x_0, y + y_0)|^2, \quad (15)$$

$$R(x_0, y_0) = \frac{\sum_{x=0}^{m-1} \sum_{y=0}^{n-1} [f_1(x, y) - \bar{f}_1] [f_2(x + x_0, y + y_0) - \bar{f}_2]}{\sqrt{\sum_{x=0}^{m-1} \sum_{y=0}^{n-1} [f_1(x, y) - \bar{f}_1]^2} \sqrt{\sum_{x=0}^{m-1} \sum_{y=0}^{n-1} [f_2(x + x_0, y + y_0) - \bar{f}_2]^2}}. \quad (16)$$

3.2. Advice on Figures. Figures 1, 2, 3, 4, 5, and 6 are provided.

4. Conclusions

In recent years, the way to detect moving objects and the specific detection algorithm are two of the hot issues in the field of computers. It is an important practice of video image processing technology, and its application prospect is very broad. The detection and tracking algorithm of moving objects in images based on computer vision technology is studied. This algorithm improves the image processing

Retraction

Retracted: High-Precision 3D Reconstruction of Cooperative Markers under Motion Blur

Wireless Communications and Mobile Computing

Received 28 November 2023; Accepted 28 November 2023; Published 29 November 2023

Copyright © 2023 Wireless Communications and Mobile Computing. This is an open access article distributed under the Creative Commons Attribution License, which permits unrestricted use, distribution, and reproduction in any medium, provided the original work is properly cited.

This article has been retracted by Hindawi, as publisher, following an investigation undertaken by the publisher [1]. This investigation has uncovered evidence of systematic manipulation of the publication and peer-review process. We cannot, therefore, vouch for the reliability or integrity of this article.

Please note that this notice is intended solely to alert readers that the peer-review process of this article has been compromised.

Wiley and Hindawi regret that the usual quality checks did not identify these issues before publication and have since put additional measures in place to safeguard research integrity.

We wish to credit our Research Integrity and Research Publishing teams and anonymous and named external researchers and research integrity experts for contributing to this investigation.

The corresponding author, as the representative of all authors, has been given the opportunity to register their agreement or disagreement to this retraction. We have kept a record of any response received.

References

- [1] Y. Shi, C. Tao, X. Wang, and L. Zhang, "High-Precision 3D Reconstruction of Cooperative Markers under Motion Blur," *Wireless Communications and Mobile Computing*, vol. 2021, Article ID 6467337, 9 pages, 2021.

Research Article

High-Precision 3D Reconstruction of Cooperative Markers under Motion Blur

Yun Shi, Cong Tao, Xiaoping Wang, and Liyan Zhang 

College of Mechanical and Electrical Engineering, Nanjing University of Aeronautics and Astronautics, Nanjing, CO 210016, China

Correspondence should be addressed to Liyan Zhang; 870751547@qq.com

Received 21 June 2021; Revised 31 July 2021; Accepted 12 August 2021; Published 6 September 2021

Academic Editor: Balakrishnan Nagaraj

Copyright © 2021 Yun Shi et al. This is an open access article distributed under the Creative Commons Attribution License, which permits unrestricted use, distribution, and reproduction in any medium, provided the original work is properly cited.

The application of artificial intelligence and deep learning in the fields of wireless communication, image and speech recognition, and 3D reconstruction has successfully solved some difficult modeling problems. This paper focuses on the high-precision 3D reconstruction of the motion-blurred cooperative markers, including the Chinese character coded targets (CCTs) and the noncoded circular markers. A simulation-based motion-blurred image generation model is constructed to provide sufficient samples for training the convolutional neural network to identify and match the motion-blurred CCTs on the moving object. The blurred noncoded marker matching is performed through homography. The 3D reconstruction of the markers is realized via the optimization of the spatial moving path within the exposure period. The midpoint of the moving path of the markers is taken as the final reconstruction result. The experimental results show that the 3D reconstruction accuracy of the markers with a certain motion blur effect is about 0.08 mm.

1. Introduction

Machine vision has been widely used in object positioning, pose detection, motion tracking, and 3D shape reconstruction [1–5]. However, the imaging blur effect of moving targets makes these tasks difficult.

There are two potential ways to the 3D reconstruction of motion-blurred targets: one is the reconstruction after deblurring, and the other is the reconstruction directly from the blurred images. Image deblurring is a typical inverse problem. The classic nonblind deconvolution algorithms alleviate the motion blur effect with given blur kernels such as point spread function [6] and Richardson and Lucy [7, 8]. For blind deconvolution with unknown blur kernel, Ref. [9] first used Radon transformation to estimate the blur parameters based on the spectrum information. The nonblind deconvolution is then used to recover the clear image. In [10], the gradient information of the motion-blurred image was used to determine the length and angle of the blur path. In [11], the unsaturated region

was selected to estimate the blur kernel by using prior knowledge. The regularization equation was established, and the variation Bayesian was used to solve the optimal problem. In [12], the sharp boundary template was extracted from the downsampled image of the blurred image, and then, the blurred and the predicted value images were used to calculate the blur kernel. Although the above-mentioned methods can restore the motion-blurred images to some extent, the algorithms still need to make assumptions about the motion of the target or the camera. These assumptions implied the uniformity of the blur, which is usually not the case in practice.

For reducing spatially varying motion blur, Tai et al. [13] used a hybrid camera system that simultaneously captures high-resolution video at a low-frame rate together with low-resolution video at a high-frame rate. Extra information available in the hybrid camera is utilized to reformulate the correction process to achieve better deblurring effect. The optical flow method proposed in [14] calculated the spatial change. The pose data output by the gyroscope attached to

the camera was used by [15, 16] to determine the path of camera shaking and calculate the blur kernel caused by the shake. Tai et al. [17] used the coded exposure method to collect motion-blurred images, where the user estimated the homography matrix of the intermittent motion through multiple interventions.

The different depths of the image points lead to the different motion blur kernel functions, which reveal that the blurring effect is inherently related to the 3D geometry of the scene. In [18], Xu and Jia used the depth information generated by the binocular stereo image to deblur the image in any form of motion. However, this was essentially a quasi-uniform blur model with obvious ring artifacts. In [19], Lee and Lee developed a depth reconstruction method based on blur perception. Although the deblurring effect was good, the premise of the reconstruction was to know the motion path of the camera, which made it unsuitable for the 3D reconstruction of an object with unknown motion path. Hong et al. [20] achieved better motion blur removal effect in multiview images. However, they did not provide 3D reconstruction result.

Several researchers have tried to extract useful information directly from the blurred images without deblurring. In [21], a segmentation-based symmetrical stereo vision matching method was proposed to address the high matching error rates of the images with motion blur. Although this method effectively reduced the false matching rates, it was only suitable for images with slight local blurring. In [22], a motion model based on the affine transformation principle was established. This method estimated the motion blur parameters of each subregion, but it was only suitable for problems tolerating relative low accuracy. In [23], the circular coded target under the effect of motion blur was 3D reconstructed. However, the circular coded targets have a simple structure and relatively low distinguishability; therefore, they are difficult to be correctly recognized under motion blur effect. Ref. [24] proposed a set of cooperative markers which used Chinese characters as the feature target and achieved better recognition performance under motion blur effect.

For the 3D reconstruction of a high-speed moving target, the movement of the target within the exposure time cannot be ignored. The trajectory of the target during the exposure period will result in superimposed imaging, forming a certain degree of motion blur effect. Taking multiview images with motion blur effect as input, we propose an approach to 3D reconstruction of cooperative markers, including both coded and noncoded ones. The remaining sections are organized as follows. Section 2 introduces the structure and the segmentation algorithm of the marker points and establishes a simulation model for the motion-blurred marker targets. Section 3 uses convolutional neural network (CNN) to match the Chinese character coded targets (CCTs) with motion blur effect. Section 4 establishes the objective function of the marker targets and provides the initial values of the parameters. Section 5 designs an experimental procedure to reconstruct the marked targets in motion. Finally, Section 6 summarizes the article.

2. The Marker Targets

The cooperative markers in this paper include the CCTs [24] and noncoded circular markers. Each of the CCTs has a unique identity and is relatively easy for establishing correspondences among the multiview images. However, the CCTs are too large to be employed for all interest points on the object. Therefore, the relative small noncoded circular markers are also utilized. The correspondences between the noncoded markers are established based on the correspondences of the CCTs.

2.1. Structure of the Markers. The structure of each Chinese character is unique. Even if a motion blur occurs, they still possess certain characteristic information. The CCTs proposed in [24] are shown in Figure 1(a), which are composed of three concentric black/white/black circles (the center of the circles is also the center of the CCTs) and a combination of different Chinese characters. The diameter of the three circles and the size of the Chinese characters are in the ratio of 1:2:3:6. We choose 100 Chinese characters as the target to be coded and use numbers 0-99 as the encoding value of the corresponding CCTs. The Chinese characters in the coded targets are different. Thus, they can be used as the target point of the unique identity characterization. The noncoded target, shown in Figure 1(b), is a square, where the positioning area is composed of a white auxiliary circle concentric with a black positioning circle. The diameter of the two circles and the square is in the ratio of 1:2:3. In different applications, the size of the markers, including the CCTs and the noncoded markers, can be scaled to fit in the range of the scene. In our experiment, the size of the marker point is set to $x = 4$ mm.

2.2. Simulation of the Motion-Blurred CCTs. We generate a large number of CCT images via soft program to provide sufficient samples for training the recognition network.

2.2.1. The Virtual Camera Method. Figure 2 illustrates a schematic diagram that defines the blur degree (intensity) σ , which can be expressed as

$$\sigma = \left| \mathbf{O}_{\text{obj}}^e - \mathbf{O}_{\text{obj}}^s \right| / \left| \mathbf{D}'_2 - \mathbf{D}'_1 \right|, \quad (1)$$

where $\mathbf{O}_{\text{obj}}^s$ and $\mathbf{O}_{\text{obj}}^e$ are the starting and ending points of the marker's center on the imaging plane, respectively, and \mathbf{D}'_1 and \mathbf{D}'_2 are the two intersection points.

Figure 3 shows the simulation steps of motion blur imaging. uvo_2 and xvo_1 , respectively, represent the pixel coordinate system and the image coordinate system. The camera coordinate system $O_c X_c Y_c Z_c$ and the marker coordinate system $O_{\text{obj}} X_{\text{obj}} Y_{\text{obj}} Z_{\text{obj}}$ are described by the rotation matrix \mathbf{R}_{oc}^1 and the translation vector \mathbf{t}_{oc}^1 . The point O_{obj} is translated to the point O'_{obj} , where the spatial displacement is $\Delta \mathbf{t}_{\text{oc}}$. The new camera coordinate system $O'_{\text{obj}} X'_{\text{obj}} Y'_{\text{obj}} Z'_{\text{obj}}$ and the translated coordinate system of the marker

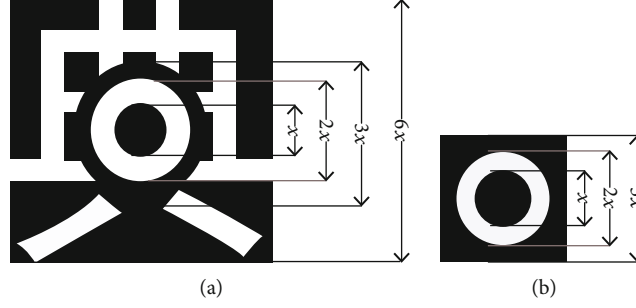


FIGURE 1: Marker structure diagram.

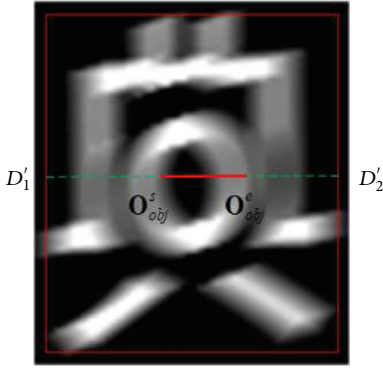


FIGURE 2: The schematic diagram defining the degree of blur.

targets are described by the rotation matrix \mathbf{R}_{oc}^e and the translation vector \mathbf{t}_{oc}^e , which satisfy

$$\begin{cases} \mathbf{R}_{oc}^e = \mathbf{R}_{oc}^1, \\ \mathbf{t}_{oc}^e = \mathbf{t}_{oc}^1 + \Delta\mathbf{t}_{oc}. \end{cases} \quad (2)$$

The displacement of the marker targets is evenly discretized into N points. The rotation matrix \mathbf{R}_{oc} and the translation vector \mathbf{t}_{oc} between the camera and the marker targets' coordinate systems with the i th point used as the origin can be expressed as

$$\begin{cases} \mathbf{R}_{oc} = \mathbf{R}_{oc}^1, \\ \mathbf{t}_{oc} = \mathbf{t}_{oc}^1 + \frac{i-1}{N-1} \Delta\mathbf{t}_{oc}. \end{cases} \quad (3)$$

The process of generating the dynamic simulation segmentation image \mathbf{I}_b from the original image \mathbf{I}_{obj} of the marker point can be expressed as

$$\mathbf{I}_b(\mathbf{D}'_d) = \left\langle \frac{1}{N} \sum_{i=1}^N f(\mathbf{A}_C, \mathbf{k}_{C1}, \mathbf{k}_{C2}, \mathbf{p}_{C1}, \mathbf{p}_{C2}, \mathbf{R}_{oc}^1, \mathbf{t}_{oc}^1 + \frac{i-1}{N-1} \Delta\mathbf{t}_{oc}, \mathbf{D}_{obj}, \mathbf{I}_{obj}(\mathbf{D}_{obj})) \right\rangle, \quad (4)$$

where $\mathbf{I}_b(\mathbf{D}'_d)$ is the gray value at \mathbf{D}'_d in \mathbf{I}_b , and $\langle \rangle$ refers to the smallest bounding box of the simulated images.

The rotation matrix \mathbf{R}_{oc} is not intuitive enough. In this paper, the rotation vector $\mathbf{r}_{oc} = [r_x, r_y, r_z]^T$ is used to represent the spatial orientation of the markers, where r_x , r_y , and r_z represent the angles of the marker coordinate system rotating around the axes $O_{obj}X_{obj}$, $O_{obj}Y_{obj}$, and $O_{obj}Z_{obj}$ in turn. In the actual measurements, the range of \mathbf{r}_{oc} is set as

$$\mathbf{r}_{oc} = \left\{ [r_x, r_y, r_z]^T \mid r_x, r_y \in \left[-\frac{\pi}{3}, \frac{\pi}{3}\right], r_z \in [-\pi, \pi] \right\}. \quad (5)$$

2.2.2. The Perturbation Model. The real images are affected by noise, light distribution, and light intensity. The perturbation model adds noise η , gray contrast φ , and gray increment β to simulate these imaging factors. Hence, we assume the relationship between $\mathbf{I}_{obj}(\mathbf{D}_{obj})$ and the gray value $\mathbf{I}_{img}(\mathbf{D}'_d)$ at the corresponding point \mathbf{D}'_d on the simulated image \mathbf{I}_{img} satisfying

$$\mathbf{I}_{img}(\mathbf{D}'_d) = \{ \varphi \mathbf{I}_{obj}(\mathbf{D}_{obj}) + \beta \mid \varphi \in [0.3, 1], \beta \in [0, 25] \}. \quad (6)$$

By combining with the perturbation model (6), the virtual camera method (4) is modified to generate the CCT simulation segmentation image as

$$\mathbf{I}_b(\mathbf{D}'_d) = \left\langle \frac{1}{N} \sum_{i=1}^N f(\mathbf{A}_C, k_{C1}, k_{C2}, p_{C1}, p_{C2}, \mathbf{R}_{oc}^1, \mathbf{t}_{oc}^1 + \frac{i-1}{N-1} \Delta\mathbf{t}_{oc}, \mathbf{D}_{obj}, \mathbf{I}_{obj}(\mathbf{D}_{obj}), \varphi, \beta) \right\rangle + \eta, \quad (7)$$

where η refers to the noise. Then, the parameters of the simulation model are determined to generate various motion-blurred CCTs. Figure 4 shows the simulated motion-blurred image examples with various spatial positions, directions, motion paths, blur levels, and noise levels.

3. Recognition of the Motion-Blurred CCTs

The CNN utilized for motion-blurred CCT recognition is composed of five layers: the input layer, convolutional layer (C), pooling layer (P), fully connected layer (F), and the output layer.

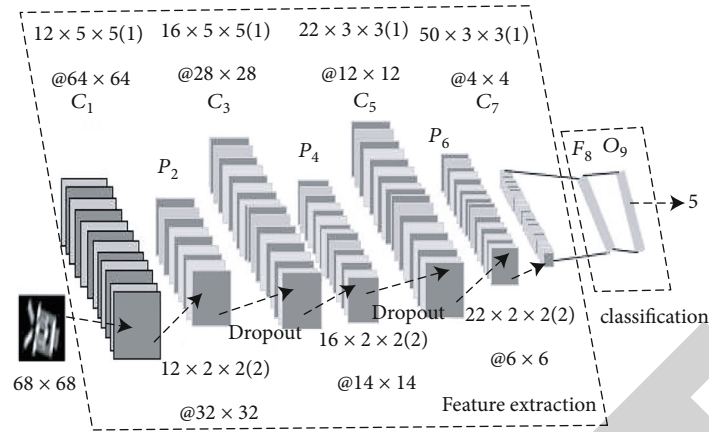


FIGURE 5: The CNN's structure diagrams of the CCT "典."



FIGURE 6: Recognition result of the CCTs.

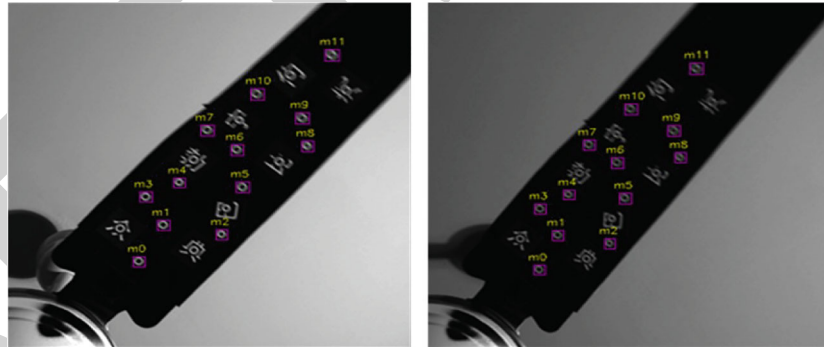


FIGURE 7: The matching results of the noncoded targets.

right image. We then calculate the pixel distance between D'_{IHR} and the center coordinates of the bounding box of all noncoded targets in the right picture. Finally, we take D'_{uinitr} , which is nearest to D'_{IHR} , as the matching point of D'_{uinitl} .

Figure 7 shows the matching results of the noncoded targets, in which the box is the division rectangle, and the same number represents the corresponding noncoded targets after matching. When the noncoded target matching is completed, D'_{uinitl} and D'_{uinitr} are taken as the initial values of the pixel coordinate of the noncoded targets' positioning

center, and hence, the initial 3D coordinates of the positioning center D_{uinit} is obtained.

4.2. Establishment of the Objective Function. In the motion-blurred images, the markers are imaged along a 3D moving path instead of at a certain spatial point during the exposure period. Therefore, the optimization parameters in our method concern the spatial moving path of the markers.

4.2.1. Binocular System Virtual Camera Method. The virtual camera method of the binocular system is used to simulate the motion-blurred images of the CCTs on the camera-

imaging plane under high-speed motion. The process of generating the dynamic simulation segmentation images \mathbf{I}_{bl} and \mathbf{I}_{br} of the original image \mathbf{I}_{obj} of the CCT in the left and right cameras can be expressed as

$$\mathbf{I}_{bl}(\mathbf{D}'_d) = \left\langle \frac{1}{N} \sum_{i=1}^N f(\mathbf{A}_{Cl}, k_{C1l}, k_{C2l}, p_{C1l}, p_{C2l}, \mathbf{R}_{oc}^1, \mathbf{t}_{oc}^1 + \frac{i-1}{N-1} \Delta \mathbf{t}_{oc}, \mathbf{D}_{obj}, \mathbf{I}_{obj}(\mathbf{D}_{obj}), \varphi, \beta) \right\rangle, \quad (11)$$

$$\mathbf{I}_{br}(\mathbf{D}'_d) = \left\langle \frac{1}{N} \sum_{i=1}^N f(\mathbf{A}_{Cr}, k_{C1r}, k_{C2r}, p_{C1r}, p_{C2r}, \mathbf{R}_{rl}^{-1} \mathbf{R}_{oc}^1, \mathbf{R}_{rl}^{-1}(\mathbf{t}_{oc}^1 - \mathbf{t}_{rl}) + \frac{i-1}{N-1} \Delta \mathbf{t}_{oc}, \mathbf{D}_{obj}, \mathbf{I}_{obj}(\mathbf{D}_{obj}), \varphi, \beta) \right\rangle, \quad (12)$$

where the noise is removed as it is not a suitable optimization parameter.

4.2.2. Optimization Goal Based on Differential Images. As in [23], we also minimize the difference between the dynamic analog segmented images and the real-shot segmented images of the markers in the left and right cameras, namely, $\mathbf{I}_{\Delta l}$ and $\mathbf{I}_{\Delta r}$, to fine tune the 3D reconstruction. The process is as follows:

$$\begin{cases} \mathbf{I}_{\Delta l} = |\mathbf{I}_{rl} - \mathbf{I}_{bl}|, \\ \mathbf{I}_{\Delta r} = |\mathbf{I}_{rr} - \mathbf{I}_{br}|, \end{cases} \quad (13)$$

where $|\bullet|$ ensures that the gray values of all pixels in differential images are nonnegative numbers. Here, firstly, the sizes of \mathbf{I}_{bl} , \mathbf{I}_{br} , \mathbf{I}_{rl} , and \mathbf{I}_{rr} have been unified to $U \times V$. Next, the optimized function F_{Δ} that minimizes the average gray value of the difference image is set as the optimization goal, which can be expressed as

$$F_{\Delta} = \frac{\left(\sum_{u=0}^{U-1} \sum_{v=0}^{V-1} \mathbf{I}_{\Delta l}((u, v)) + \sum_{u=0}^{U-1} \sum_{v=0}^{V-1} \mathbf{I}_{\Delta r}((u, v)) \right)}{2UV}, \quad (14)$$

where $\mathbf{I}_{\Delta l}((u, v))$ and $\mathbf{I}_{\Delta r}((u, v))$ represent the gray value at (u, v) of the differential image. The optimization function F_{Δ} can be expressed in terms of \mathbf{R}_{oc}^1 , \mathbf{t}_{oc}^1 , $\Delta \mathbf{t}_{oc}$, φ , and β as

$$F_{\Delta} = \text{opt}(\mathbf{R}_{oc}^1, \mathbf{t}_{oc}^1, \Delta \mathbf{t}_{oc}, \varphi, \beta). \quad (15)$$

4.3. Estimation of the Initial Values of the Parameters. This subsection describes how the initial values of the optimized parameters are obtained for both CCTs and the noncoded targets. The initial values of the CCTs are obtained by improving the method in [23]. An effective method for determining the initial value of the noncoded targets is independently proposed.

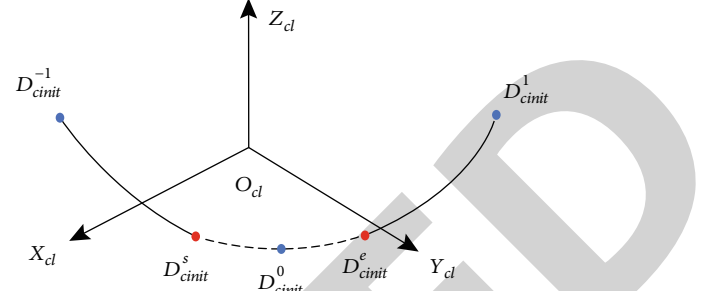


FIGURE 8: The diagram showing the motion relationships of the CCTs.

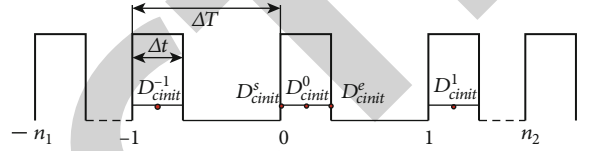


FIGURE 9: The relationship between Δt and ΔT .

4.3.1. Initial Values of the CCTs

(1) *Determination of the Initial Values \mathbf{t}_{oc}^1 and $\Delta \mathbf{t}_{oc}$ of the Space Position.* Figure 8 shows the motion relationship diagram of the CCTs, while the relationship between the camera exposure time Δt and ΔT is shown in Figure 9. Three sets of images with motion blur effect are shot under high-speed motion at equal time intervals of ΔT , where -1, 0, and 1 represent the previous frame, current frame, and the next frame in the shooting process, respectively.

For a CCT, the initial values of the 3D coordinates of the midpoint of the path within the previous, current, and the next frames are \mathbf{D}_{cinit}^{-1} , \mathbf{D}_{cinit}^0 , and \mathbf{D}_{cinit}^1 , which are shown by the points D_{cinit}^{-1} , D_{cinit}^0 , and D_{cinit}^1 in Figure 8. Take points D_{cinit}^s and D_{cinit}^e and the midpoint D_{cinit}^0 on the fitted curve. If the arc length $D_{cinit}^s D_{cinit}^e$ is used to represent the intraframe path of the current frame, the relationship can be given as

$$\frac{l_s}{L_s} = \frac{\Delta t}{2\Delta T}, \quad (16)$$

where L_s represents the arc length of the curve and l_s represents the arc length of $D_{cinit}^s D_{cinit}^e$. After calculating l_s , the spatial coordinates \mathbf{D}_{cinit}^s and \mathbf{D}_{cinit}^e of the points D_{cinit}^s and D_{cinit}^e can be solved. The relationships between \mathbf{D}_{cinit}^s and \mathbf{D}_{cinit}^e and \mathbf{t}_{oc}^1 and $\Delta \mathbf{t}_{oc}$ are as follows:

$$\begin{cases} \mathbf{t}_{oc}^1 = \mathbf{D}_{cinit}^s, \\ \Delta \mathbf{t}_{oc} = \mathbf{D}_{cinit}^e - \mathbf{D}_{cinit}^s. \end{cases} \quad (17)$$

(2) *Determination of the Initial Gray Image Values φ and β .* To improve the initial value setting of β provided in [23], we distinguish the black background of the dynamic real-

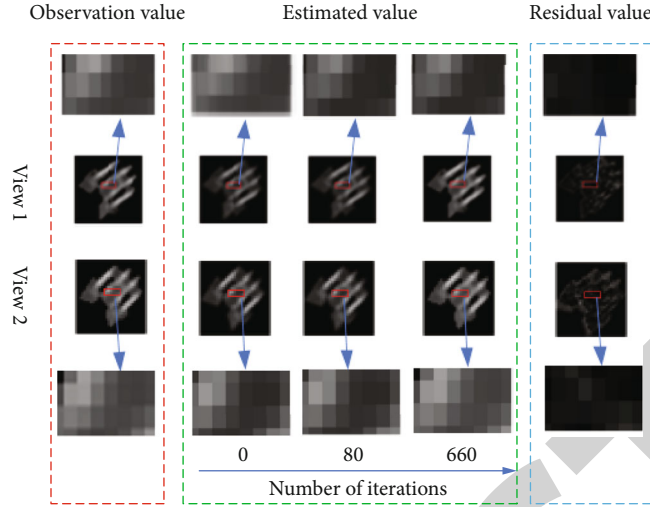


FIGURE 10: The difference image at different stages of the optimization process.

TABLE 1: The mean time-consuming of different types of markers.

Time-consuming steps	The initial search of the spatial attitude	Minimization
CCTs	647.4 s	523.9 s
Noncoded targets	12.6 s	494.5 s

shot segmented image and take its gray average value as β to generate the dynamic analog-segmented image. Hence, the initial value of φ can be calculated as

$$\varphi = \frac{\sum_{u=0}^{U-1} \sum_{v=0}^{V-1} (\mathbf{I}_r((u, v)) - \beta)}{\sum_{u=0}^{U-1} \sum_{v=0}^{V-1} \mathbf{I}_{obj}((u, v))}, \quad (18)$$

where \mathbf{I}_r represents the dynamic real shot segmented image and $\mathbf{I}_{obj}((u, v))$ and $\mathbf{I}_r((u, v))$ represent the gray value of \mathbf{I}_{obj} and \mathbf{I}_r at the pixel coordinate (u, v) .

(3) *Determination of the Initial Space Attitude \mathbf{R}_{oc}^1* . We first divided r_x and r_y in \mathbf{r}_{oc} into 10 equal parts and r_z into 50 equal parts; hence, a total of $10 \times 10 \times 50 = 5000$ combinations were obtained. We then calculated the initial value of \mathbf{r}_{oc} using r_x , r_y , and r_z when F_Δ is the smallest and hence determined the initial value of \mathbf{R}_{oc}^1 .

4.3.2. Initial Values of the Noncoded Targets

(1) *Determination of the Initial Values of \mathbf{t}_{oc}^1 and $\Delta \mathbf{t}_{oc}$* . For a rigid body moving in the 3D space, its relative pose between the beginning and the end of the motion can be described by a rotation and a translation transformation. If the rotation matrix \mathbf{R}_{obj} represents its rotation transformation and the translation vector \mathbf{t}_{obj} represents its translation transforma-

tion, the coordinate transformation of any point on the rigid body can be expressed as

$$\mathbf{P}'_{obj} = \mathbf{R}_{obj} \mathbf{P}_{obj} + \mathbf{t}_{obj}, \quad (19)$$

where \mathbf{P}_{obj} and \mathbf{P}'_{obj} are the 3D coordinates of the point on the rigid body before and after the movement. If the midpoint and the endpoint of the intraframe path after the optimization of the CCTs are marked as \mathbf{D}_{copt}^m and \mathbf{D}_{copt}^e , their relation can be given as

$$\mathbf{D}_{copt}^e = \mathbf{R}_{obj} \mathbf{D}_{copt}^m + \mathbf{t}_{obj}, \quad (20)$$

where \mathbf{R}_{obj} and \mathbf{t}_{obj} , respectively, represent the rotation matrix and the translation vector of the movement of the marker targets from the midpoint of the camera exposure time to the end of the camera exposure. In this paper, \mathbf{R}_{obj} and \mathbf{t}_{obj} are obtained by parameter fitting through the intraframe path relations of more than five CCTs. Regarding the center of the reconstructed noncoded targets, the midpoint and endpoint of the nonoptimized intraframe path are denoted as \mathbf{D}_{uinit}^m and \mathbf{D}_{uinit}^e , respectively. Their relation can be expressed as

$$\mathbf{D}_{uinit}^e = \mathbf{R}_{obj} \mathbf{D}_{uinit}^m + \mathbf{t}_{obj}. \quad (21)$$

The starting point \mathbf{D}_{uinit}^s of the noncoded intraframe path without optimization is $\mathbf{D}_{uinit}^s = 2\mathbf{D}_{uinit}^m - \mathbf{D}_{uinit}^e$. Here, \mathbf{t}_{oc}^1 and $\Delta \mathbf{t}_{oc}$ between the marker point coordinate system of the noncoded targets and the left camera coordinate system can be expressed as

$$\begin{cases} \mathbf{t}_{oc}^1 = \mathbf{D}_{uinit}^s, \\ \Delta \mathbf{t}_{oc} = \mathbf{D}_{uinit}^e - \mathbf{D}_{uinit}^s. \end{cases} \quad (22)$$

TABLE 2: The 3D coordinate reconstruction error of the markers.

Fan blade state	Static			Rotate at a fixed speed				
Exposure time (ms)	1.0	0.6	0.8	1.0	1.2	1.4	1.6	1.8
Before optimization (mm)	0.195	0.914	1.225	1.251	1.451	1.492	1.598	1.655
After optimization (mm)	0.036	0.075	0.088	0.086	0.088	0.091	0.095	0.136

(2) *Determination of the Initial Values of φ and β .* The method for determining the initial values of φ and β of the noncoded targets is the same as that of the CCTs.

(3) *Determination of the Initial Value \mathbf{R}_{oc}^1 .* When determining \mathbf{R}_{oc}^1 of the noncoded targets, r_x and r_y of \mathbf{r}_{oc} need to be sampled at equal intervals within their value range. The parameter r_z is set to zero for the circular symmetry property of the noncoded targets. Hence, \mathbf{r}_{oc} of the noncoded targets has only $10 \times 10 = 100$ combinations.

4.4. Optimization Method and Results. We used Powell optimization to minimize F_{Δ} . Figure 10 shows the difference image during the optimization process for various iterations of the CCT “典.” The first row and the fourth row in Figure 10, respectively, represent the enlarged results of the red rectangular boxes in the second and the third rows. When the optimization is over, the difference image is nearly black, which indicates that the simulated segmented image is very close to the real segmented image. In other words, the optimization achieves good convergence.

In the final error calculation, the space coordinates of the static marker targets reconstructed by a commercial structured-light device ATOS® are assumed as the true values. Accordingly, the midpoints of the 3D moving paths of the markers are taken as the final 3D reconstruction result for the error evaluation. So far, the whole 3D reconstruction procedure of the two types of the cooperative markers with motion blur effect is completed.

5. Experiments

To validate the effectiveness of the 3D reconstruction algorithm, the multiview images of the motion target under different exposure times are captured, and the intraframe motion paths of the motion blur markers are reconstructed.

5.1. Experimental Setup. We select the rotating ceiling fan blades as the experimental object. A synchronous controller is used to control the left and right cameras to obtain the multiview images of the moving blade at 19 Hz frequency. The image resolution is 1392×1040 , obtained by a Basler A102f camera.

When the fan blades are in a static state, the camera exposure time is set to 1 ms, and the binocular stereo vision system is used to obtain clear images. When the fan blade rotates at a fixed speed, the camera exposure time is set to 0.6 ms, 0.8 ms, 1.0 ms, 1.2 ms, 1.4 ms, 1.6 ms, and 1.8 ms, respectively. Then, we shoot three sets of images with

motion blur effect under high-speed motion at each exposure time.

5.2. Reconstruction Results. We perform 3D reconstruction and optimization on the markers in all the images and acquired the 3D coordinates of the marker points before and after the optimization. The time-consuming steps in the optimization process mainly include the initial value search of the marker space attitude and the minimization. The average time-consuming statistics are provided in Table 1.

It can be seen from Table 1 that the average times of the two types of markers are very close for the minimization optimization. In the process of searching for the initial value of the spatial pose, the time of noncoded targets to be searched is about 1/50 of the time of the CCTs to be searched. Therefore, using the noncoded targets as the 3D reconstruction target can greatly improve the optimization efficiency.

We take the 3D coordinates of the markers reconstructed by the commercial ATOS system as the true values to measure the reconstruction accuracy. Due to the inconsistent coordinate systems between the two results, it is necessary to align the 3D points in a unique coordinate system through the best fitting function. Then, the errors of the reconstructed 3D coordinates of the markers are calculated. To validate the optimization algorithm based on the image difference minimization, the errors before and after the optimization are calculated. The results are shown in Table 2.

6. Conclusions

The 3D reconstruction error after the optimization is at least one order of magnitude lower than that of before optimization. This indicates that the optimization algorithm based on the differential image has an obvious effect on improving the accuracy of the reconstructed 3D spatial coordinates of the cooperative markers.

In the experiments, the rotating fan blade is not a rigid body due to the air perturbation, resulting in small changes in the relative position between the markers. Therefore, the actual errors of the reconstructed 3D coordinates of the markers might be smaller than the results provided in Table 2.

Data Availability

The authors declared no underlying data of this article.

Retraction

Retracted: MEC-Driven Fast Deformation Monitoring Based on GNSS Signal

Wireless Communications and Mobile Computing

Received 28 November 2023; Accepted 28 November 2023; Published 29 November 2023

Copyright © 2023 Wireless Communications and Mobile Computing. This is an open access article distributed under the Creative Commons Attribution License, which permits unrestricted use, distribution, and reproduction in any medium, provided the original work is properly cited.

This article has been retracted by Hindawi, as publisher, following an investigation undertaken by the publisher [1]. This investigation has uncovered evidence of systematic manipulation of the publication and peer-review process. We cannot, therefore, vouch for the reliability or integrity of this article.

Please note that this notice is intended solely to alert readers that the peer-review process of this article has been compromised.

Wiley and Hindawi regret that the usual quality checks did not identify these issues before publication and have since put additional measures in place to safeguard research integrity.

We wish to credit our Research Integrity and Research Publishing teams and anonymous and named external researchers and research integrity experts for contributing to this investigation.

The corresponding author, as the representative of all authors, has been given the opportunity to register their agreement or disagreement to this retraction. We have kept a record of any response received.

References

- [1] B. Li, S. Chen, Y. Liu, K. Xie, and S. Xie, "MEC-Driven Fast Deformation Monitoring Based on GNSS Signal," *Wireless Communications and Mobile Computing*, vol. 2021, Article ID 9517133, 9 pages, 2021.

Research Article

MEC-Driven Fast Deformation Monitoring Based on GNSS Signal

Bo Li,¹ Shangwei Chen,^{1,2} Yi Liu ,^{1,3} Kan Xie ,^{1,4} and Shengli Xie ,^{1,5}

¹School of Automation, Guangdong University of Technology, Guangzhou, China

²Guangdong Key Laboratory of IoT Information Technology (GDUT), Guangzhou, China

³Key Laboratory of Intelligent Detection and the Internet of Things in Manufacturing, Ministry of Education (GDUT), Guangzhou, China

⁴Guangdong-HongKong-Macao Joint Laboratory for Smart Discrete Manufacturing (GDUT), Guangzhou, China

⁵111 Center for Intelligent Batch Manufacturing Based on IoT Technology (GDUT), Guangzhou, China

Correspondence should be addressed to Kan Xie; kxie@gdut.edu.cn

Received 9 July 2021; Accepted 17 August 2021; Published 2 September 2021

Academic Editor: Balakrishnan Nagaraj

Copyright © 2021 Bo Li et al. This is an open access article distributed under the Creative Commons Attribution License, which permits unrestricted use, distribution, and reproduction in any medium, provided the original work is properly cited.

In the deformation monitoring based on satellite positioning, the extraction of the effective deformation signal which needs plenty of computing resources is very important. Mobile-edge computing can provide low latency and near-edge computing agility for the deformation monitoring process. In this paper, we propose an edge computing network architecture to reduce the satellite observation time while maintaining a certain positioning accuracy. In such architecture, the state transition equation is established for monitoring, and the Kalman filter is used to reduce the error caused by the reduction of the observation time. At the same time, the method of determining the initial filter value and the filtering process are given. Through the actual monitoring of a certain section of railway track, the feasibility of the proposed method is proved.

1. Introduction

Deformation is a common phenomenon in nature. The deformation body's shape, size, and location are changed in space and time domain by a variety of loads. The so-called deformation monitoring is the monitoring to the deformation phenomena of the deformation body by the use of special instruments and methods of measurement and deformation monitoring. Its task is to determine space state and time feature of the deformation body's shape, size, and location changes in the effects of various loads and external force [1]. As we all know, engineering buildings during construction and operation, due to the influence of a variety of subjective and objective factors, will cause deformation. If the deformation exceeds the prescribed limit, it will endanger the safety of the building and bring huge losses to the society and people. Therefore, the study of collecting accurate deformation data of objects has important engineering application value.

Currently, the primary techniques for monitoring convergence deformation are automatic tracking total-station technique, automatic close-range photogrammetry, and convergence gauge [2]. They have been widely used in engineering, such as References [3–5]. However, these monitoring technologies cannot be used on a large scale area because of their high cost. Meanwhile, due to the limitation of the precision of equipment, these technologies cannot be applied to the harsh environment for a long time. In addition to GPS, the global navigation satellite system (GNSS) includes Russia's GLONASS, China's Beidou satellite navigation system, and the European Union's Galileo system, which are under formation. Conventional GNSS positioning technology usually requires a long time of synchronous observation to ensure the accuracy and reliability of positioning results. With the establishment of global positioning system and the rapid popularization of GPS positioning technology, its application has been more and more wide, such as geodetic survey, engineering survey, and deformation monitoring.

However, the long-term positioning technique is not suitable for these new applications (because the positioning time is too long, there are other options). Therefore, in recent years, researchers have been looking for fast GNSS positioning techniques that can obtain the required accuracy only by short observation time, in order to greatly improve the operation efficiency. Thus, it can make GNSS positioning technology more competitive in these applications. With technological developments, the global positioning system has been widely used for the real-time deformation monitoring of natural hazards and structures such as landslides and bridges. It helps us better understand the tendency of deformations and prevent disasters [6]. In [7], a large-section shallow buried tunnel deformation monitoring method based on GNSS technology was proposed. The GNSS automation equipment and its technology are combined to realize the real-time acquisition of monitoring data, and the displacement trend diagram of monitoring points is displayed. By designing high-precision GNSS data processing strategy, the authors facilitate the extraction and analysis of vertical deformation of suspension bridge pylon and explain its deformation mechanism [8]. In the South-to-North Water Transfer Project in China, GNSS is used to monitor the deformation of dams [9].

Moving edge computing is an effective method to deal with massive data [10, 11]. With the increase of the number of observations and the number of monitoring stations, the number of signals (navigation messages, etc.) received by the monitoring stations from satellites will become very large. The requirement of the processor for solving in the monitoring station will increase accordingly. The data processing power of the system can be significantly improved by moving the data to the adjacent MEC server [12]. In [12], it investigates the system of unmanned aerial vehicle (UAV) daily routine inspection in a wind farm, where UAV performs detection and sensory data processing with the aid of edge server and satellite. In [13], it proposed a collaborative UAV-enabled edge computing network for the power Internet of Things (IoT) system. In [14], the computation efficiency is studied for the UAV-enabled MEC network by jointly optimizing the offloading times, the trajectory of the UAV, etc. The UAV-enabled MEC network in which the UAV servers are powered by microwave power station is introduced in [15]. However, when GNSS is used for positioning, a relatively accurate coordinate value needs to be solved through a certain observation duration. In the case of shortening observation time, some multipath errors cannot be eliminated due to the reduction of observation data, so that the positioning accuracy cannot be guaranteed.

In this paper, we propose an edge computing network architecture to reduce the satellite observation time while maintaining a certain positioning accuracy. That is, the Kalman filter model is used to establish the state space of the monitoring points, and the optimal estimated state of the observation points is obtained by combining GNSS observation values. In this way, the problem of accuracy decline caused by the decrease of observation time can be reduced to a certain extent. The feasibility of this method is proved in the real monitoring of high-speed railway tracks.

2. Deformation Monitoring Based on GNSS System

2.1. Preliminary. The GNSS monitoring system can be used to measure the monitoring area in all-weather, continuous, and full coverage. And the three-dimensional space position of the monitoring point can be obtained by it in real time. It is mainly composed of three parts: data acquisition subsystem, data transmission subsystem, and data processing and analysis subsystem. In order to improve the accuracy and reliability of the monitoring data, we use reference stations and monitoring stations as the reference basis for the data acquisition subsystem. The reference station is the frame of reference for the whole subsystem to collect displacement data. This monitoring system was installed with a stable monitoring reference station, and it can meet the observation conditions of GNSS satellites. The monitoring station is the main basis for the subsystem to collect surface displacement. Representative points are selected for monitoring stations which can reflect the deformation state of the rail in real time and also can meet the conditions of GNSS satellite observation. With long-term continuous tracking and observation of satellite signals, each monitoring point combined with the observation data and the original coordinates of base station to obtain the real-time three-dimensional coordinates of the monitoring point in the center of the control system. The GNSS displacement data collected by the monitoring point relies on the data transmission subsystem to transmit it to the disk through the Internet communication technology and computer system integration technology. Finally, the server of data processing and analysis subsystem control center processes, analyzes, stores, and manages monitoring data which come from monitoring point.

2.2. GNSS Monitoring System for Guangshan Railway. Aiming at the wide distribution, large number, and huge satellite observation data of Guangshan Railway track monitoring points, this paper combines mobile-edge computing with traditional GNSS automated online monitoring systems to provide low latency and near-edge computing agility for the deformation monitoring process. Its overall structure is similar to the traditional monitoring system, as shown in Figure 1.

But at the reference stations, the processor is replaced with edge devices with more powerful computing capabilities. It is different from the traditional positioning monitoring station solution, and the solution task of the system is carried out on the edge device, as shown in Figure 2.

By installing a GNSS antenna and a GNSS receiver on the edge device, it not only serves as a computing node but also has the function of a reference station. Therefore, the monitoring station only needs to perform simple data forwarding work. It sends satellite signals such as navigation messages received from satellites to edge devices. On the edge device, the satellite signal from the monitoring station and the satellite signal from the reference station are differentially calculated to eliminate the error caused by the signal propagation in space, and finally, the three-dimensional coordinates of the monitoring station are obtained. Therefore, it reduces the hardware performance requirements of

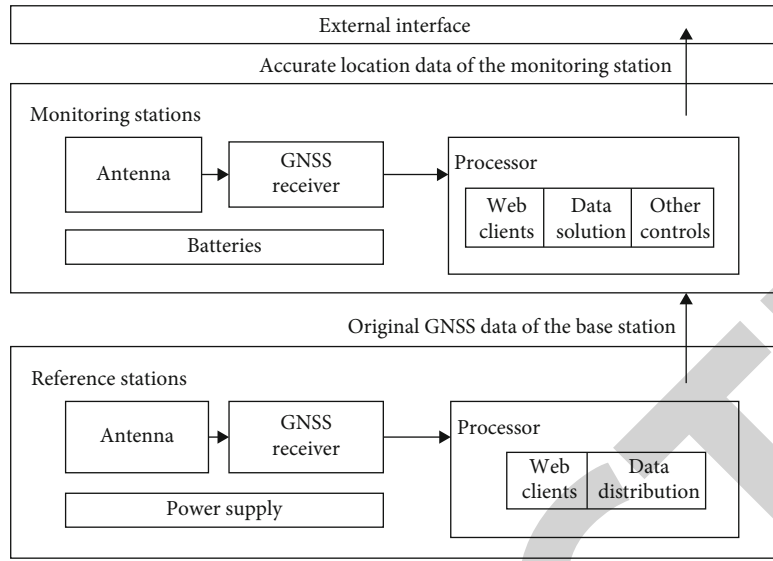


FIGURE 1: Traditional system architecture.

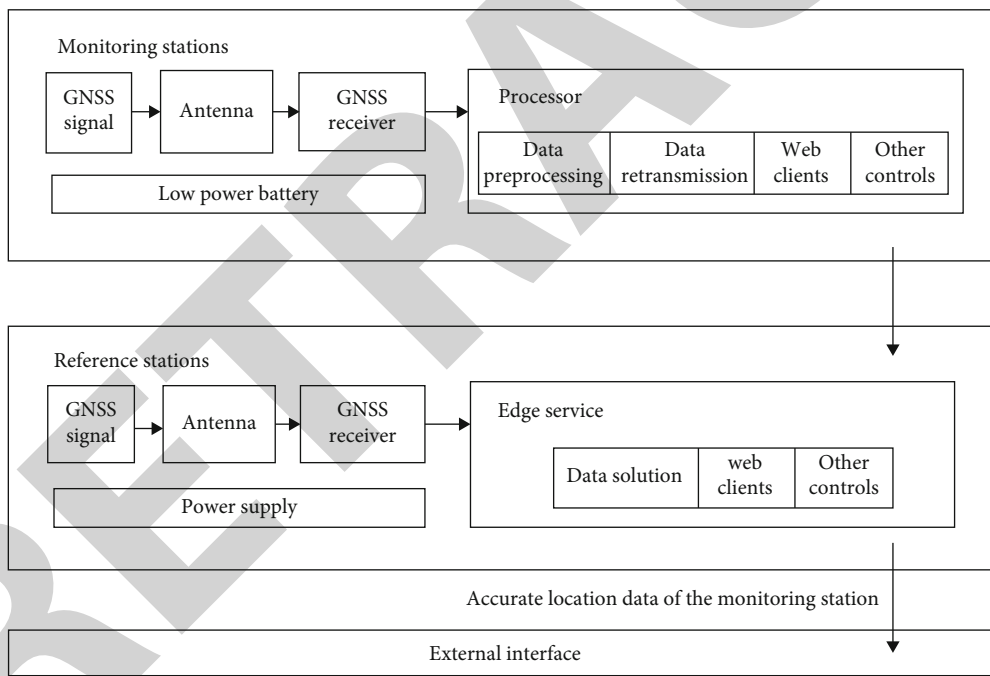


FIGURE 2: System architecture based on edge computation.

the monitoring station. The traditional positioning method forwards the satellite signal received by the reference station to the monitoring station and performs differential calculations in the monitoring station. From the perspective of the overall structure of the system, the flow of data has changed from the base station to the monitoring station to from the monitoring station to the base station, but the process of data transmission has not become complicated, and it is still a one-way single transmission. Therefore, the data processing capabilities of edge computing can provide low latency and near-edge computing agility for the deformation moni-

toring process. The general positioning process is shown in Figure 3.

This system realizes the centralization of computing tasks, enabling monitoring stations to be manufactured with lower-performance and inexpensive processors. However, the demand for computing power of edge devices will increase, but it can provide solution services for multiple monitoring stations at the same time, and the overall cost will be lower than that of traditional monitoring systems. At the same time, the power environment of the edge device is better than the power environment of the monitoring

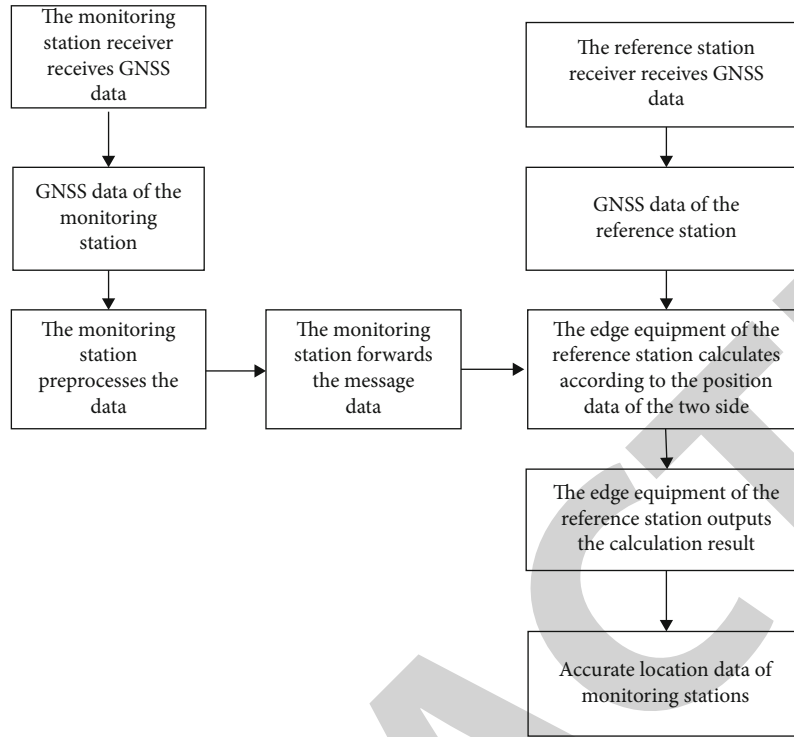


FIGURE 3: Positioning process.

station, which can give full play to the system hardware performance, and can greatly improve the endurance of the monitoring station. To a certain extent, the expansion cost of the traditional positioning network is reduced, which is conducive to its further popularization in the field of deformation monitoring.

2.3. Monitoring and Reference Point Placement. The selection of deformation monitoring reference station and monitoring station position is very important to the monitoring results, and the accuracy and reliability of monitoring are directly affected by it. Therefore, when we select monitoring stations and reference stations, it is necessary to avoid radar stations, substations, tall buildings, and large water areas around the observation point to ensure that the observation point is empty and free of obstructions and eliminate all interference from external factors. At the same time, the position of the reference point should be set to meet the convenience of observation and not be affected by factors such as construction. And the reference station should be closely integrated with the bedrock to ensure that the base point does not produce displacement. With consideration of the convenience of measurement and the safety of monitoring personnel, the monitoring point is set in a representative, deformation-sensitive, and relatively stable place to reflect the true deformation of the rail. After analyzing the actual geographical conditions of the Guangshan Railway and the deformation requirements of the rails, the monitoring point has mainly been placed in a location which is prone to deformation of the Guangshan Railway. The monitoring point is mainly set at the tortuous part of the Guangshan Railway, because it is under greater pressure and has a higher proba-

bility of deformation. In this paper, the GNSS real-time online monitoring system has successively established a reference point and 6 monitoring points and the measuring stations are mainly distributed on two monitoring baselines. The distribution of monitoring points is shown in Figure 4.

The Guangshan Railway focuses on stability control to achieve the purpose of early warning. It is necessary to ensure a certain monitoring density to be able to continuously observe the dynamic displacement of the railway. The monitoring period is 12 months, and the monitoring frequency is once a day. However, in order to further grasp the dynamic displacement of this section of the Guangzhou-Shantou Railway, it needs to reduce the duration of satellite observation, that is, to increase the frequency of monitoring—from once a day to once every 30 minutes. Due to the reduction of observation time, some short-term multipath errors cannot be eliminated, thus resulting in lower positioning accuracy. In order to solve this problem, this paper proposes a strategy of using the Kalman algorithm to solve the decrease of the positioning accuracy caused by the decrease of the observation time to ensure the positioning accuracy.

3. Fast Deformation Monitoring of Guangshan Railway with Kalman Filtering

3.1. Kalman Filtering Model. For the railway deformation monitoring system in this article, for the monitoring points, its deformation process is gradual, it takes time, and it is also irreversible (except for extreme conditions such as earthquakes). Therefore, the recursive Kalman filter technology is used to establish its state transition equation for the monitoring point and combined with the GNSS observations to



FIGURE 4: Distribution of monitoring stations.

obtain the optimal estimation value of the current state of the monitoring point. At the same time, it occupies a small amount of memory (except for the previous state, there is no need to keep other historical data), and the calculation speed is fast. Therefore, it is more suitable to be applied to this system. So Kalman filtering can solve the problem of reduced positioning accuracy due to the reduction of GNSS observation time to a certain extent.

The mathematical model of the Kalman filtering algorithm includes two parts: state equation (also known as dynamic equation) and observation equation, and its discretization form is as follows:

$$\begin{aligned} X_t &= FX_{t-1} + Q, \\ Z_t &= HX_t + R. \end{aligned} \quad (1)$$

X_t is the state vector of the system at time t ; Z_t is the observation vector of the system at time t ; F is the system state transition matrix from $t-1$ to t ; H is the observation matrix; Q and R are dynamic noise and observation noise, respectively.

Assuming that both the dynamic noise and the observed noise meet the Gaussian distribution, the recursive formula of Kalman filtering can be obtained as follows:

State prediction equation:

$$X_t^- = FX_{t-1}. \quad (2)$$

State covariance matrix prediction:

$$P_t^- = FP_{t-1}F^T. \quad (3)$$

State estimation:

$$X_t = X_t^- + K_t(Z_t - HX_t^-). \quad (4)$$

State covariance matrix estimation:

$$P_t = (I - K_tH)P_t^-. \quad (5)$$

In this, K is the filtering gain matrix, whose specific form is as follows:

$$K_t = P_t^-H^T(HP_t^-H^T + R)^{-1}. \quad (6)$$

It can be seen from the above formula that when the system is observed Z_t at time t , the observed value can be used to modify the forecast value and obtain the optimal state estimate X_t of the system at time t . In this way, the recursive prediction and filtering are repeated to solve the problem that the positioning accuracy of GNSS is reduced due to the reduction of observation time. The specific process is shown in Figure 5.

3.2. Determination of State Equation and Observation Equation.

In this paper, GNSS is used as the tool of the automatic system of three-dimensional track deformation monitoring. When GNSS is used to monitor the track deformation, the position of the monitoring point is the coordinate (x, y, z) in the independent coordinate system of the project itself. The position of the monitoring point $X = (x, y, z)$, the deformation rate $\dot{X} = (\dot{x}, \dot{y}, \dot{z})^T$, and the acceleration $\ddot{X} = (\ddot{x}, \ddot{y}, \ddot{z})^T$ of the monitoring point are selected as the state vectors. The change rate of the acceleration of the monitoring point is regarded as random interference, and the state equation can be established as

$$\begin{bmatrix} X \\ \dot{X} \\ \ddot{X} \end{bmatrix}_k = \begin{bmatrix} I & \Delta t I & \frac{1}{2} \Delta t^2 I \\ 0 & I & \Delta t I \\ 0 & 0 & I \end{bmatrix} \begin{bmatrix} X \\ \dot{X} \\ \ddot{X} \end{bmatrix}_{k-1} + Q. \quad (7)$$

In this formula, 0 and I are third-order zero matrices and

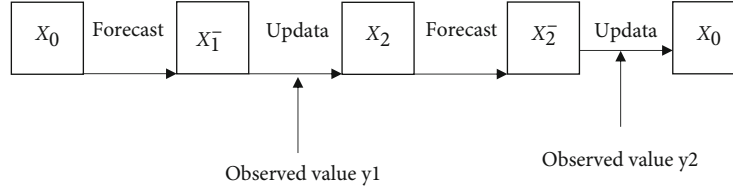
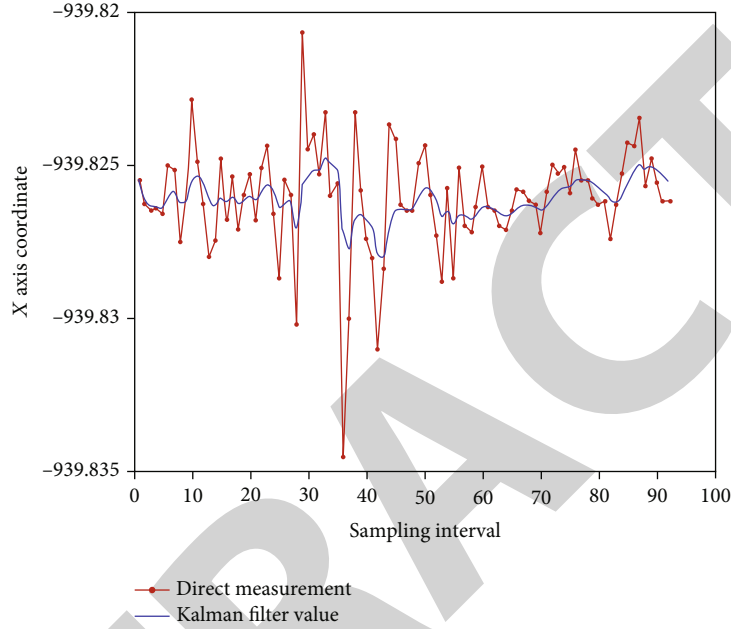


FIGURE 5: Recursive process.

FIGURE 6: x axis coordinate raw data and Kalman filter data.

third-order identity matrices, respectively. $\Delta t = t_k - t_{k-1}$ is the difference between adjacent observation moments.

Since the measurement result of GNSS is the three-dimensional coordinate of the monitoring point, the three-dimensional coordinate result is taken as the observation measurement, and the observation equation is established as follows:

$$\begin{bmatrix} x \\ y \\ z \end{bmatrix}_k = [I \ 0 \ 0] \begin{bmatrix} \dot{X} \\ \ddot{X} \end{bmatrix}_{k-1} + R. \quad (8)$$

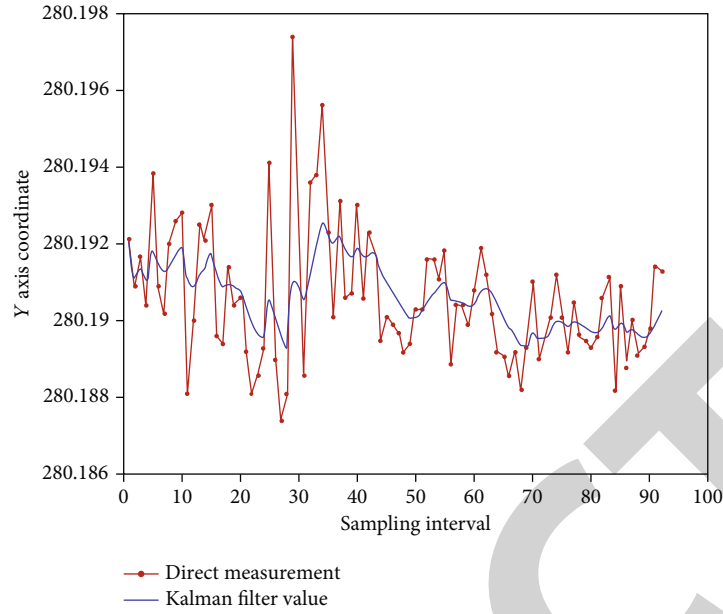
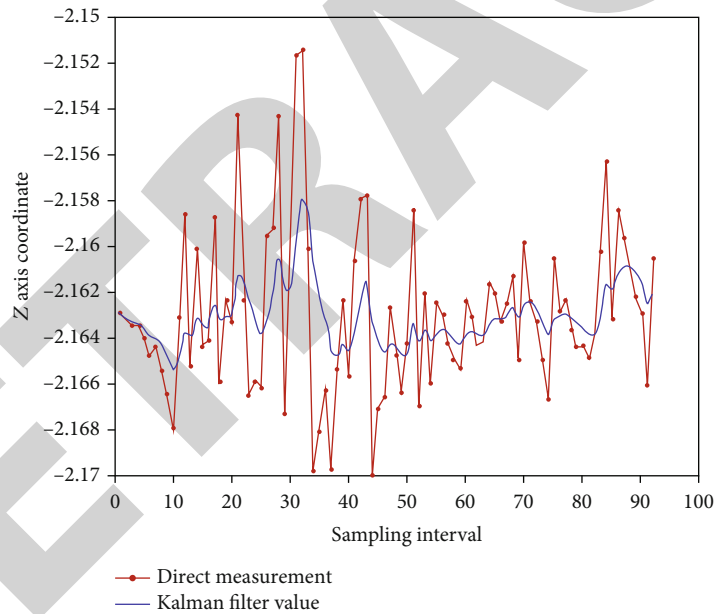
3.3. Determination of Initial Filtering Value. It can be seen from the Kalman filter equation that to determine the state of the system at the time of t , the initial state of the system must be known first. That is, the initial value of the system should be understood. In general, the initial state of the system before filtering is difficult to be determined accurately. However, if the selection of the initial value does not meet certain requirements, it may cause a large error in the filtering result, and the deformation of the GNSS point according to the filtering result will be distorted. Therefore, when the observation time is reduced, a correct and appropriate initial

value is one of the prerequisites for obtaining correct results. The initial value of system filtering includes initial state vector X_0 , process covariance matrix P_0 , the dynamic noise covariance matrix Q , and the observation noise covariance matrix R .

When the position, speed, and acceleration of the monitoring point are used as the state vectors, it can be obtained according to the previous two periods of monitoring data. Their initial values are selected as follows:

$$\begin{aligned} X_0 &= \frac{X_I + X_{II}}{2}, \\ \dot{X}_0 &= \frac{X_I - X_{II}}{\Delta t}, \\ \ddot{X}_0 &= \frac{X_I - X_{II}}{\Delta t^2}. \end{aligned} \quad (9)$$

In this, the variance R of the observed noise can be directly determined by the observation data processing method. That is, the positioning accuracy after reducing the observation time is directly used as the variance of the observation noise. At the same time, it is also used as the initial position variance in the initial variance matrix P of the position state vector parameter. The initial velocity variance and the initial

FIGURE 7: y axis coordinate raw data and Kalman filter data.FIGURE 8: z axis coordinate raw data and Kalman filter data.

acceleration variance can be obtained by the law of covariance propagation. In the dynamic noise covariance matrix, the position variance is R , the corresponding instantaneous rate variance is $4\Delta t^{-4}R$, and the instantaneous acceleration rate variance can be a smaller number.

After determining the state equation, observation equation, and filtering, the entire Kalman filtering process is as follows:

- (1) Determining the system state transition matrix F , the dynamic noise matrix Q , and the observation matrix H from the mathematical model relations of the deformed system
- (2) Using the first set of data in the m sets of observation data to determine the initial value of the filter
- (3) Reading m groups of observation data and implement Kalman filtering
- (4) Storing the state vector estimate X and the corresponding covariance matrix P of the last group in the filtering result
- (5) Waiting for the data of the current observation period
- (6) Remove the first set of observation data from the above m sets of observation data, put the current

new set of observation data at its rearmost position, reconstitute the m sets of observation data, go back to the first step, and perform Kalman filtering again

4. Evaluation Results

The data in this paper is taken from the monitoring data of Guangshan Railway Monitoring Station M005. The observation time is May 30, 2018 (it can be considered that the point is still and there is no deformation on that day). After reducing the observation time from 6 hours per solution to 15 minutes per solution, there are 92 sets of valid data. The data result contains the three-dimensional position information of the monitoring point: radial direction (x), tangential direction (y), and vertical direction (z). The recursive Kalman filtering method is used to process it, and the optimal estimation value of the state vector $X = (x, y, z)$ of the data sequence can be obtained. We show the comparison between the observation data and the Kalman filtering result of the monitoring points on the x, y , and h directions in Figures 6, 7, and 8, respectively.

It can be seen from the above figure that the Kalman filter model established is reasonable and reliable. According to the calculation, the variance of the original observation sequence in x, y, z three directions is 1.782 mm, 1.708 mm, and 3.486 mm. The values are reduced to 0.625 mm, 0.829 mm, and 1.320 mm after Kalman filtering. Meanwhile, the fluctuation range of the filtered curve is obviously smaller than that of the original observation series curve. It is shown that the Kalman filter can effectively reduce the multipath error and better reflect the real state of the track. Therefore, it can be clearly seen from the above three pictures that the accuracy of the filtering value is higher than the original observation value. Therefore, Kalman filtering technology can effectively solve the problem of positioning accuracy decline due to the shortening of observation time.

5. Conclusion

This paper proposed a deformation monitoring scheme driven by mobile-edge computing. It applied mobile-edge computing technology to the traditional GNSS automated online monitoring system, providing low latency and near-edge computing agility for the deformation monitoring process. And it is suitable for general dam deformation monitoring, roadbed settlement, bridge deformation, and other open-air and open-view occasions. At the same time, Kalman filter technology was applied on this basis. It solved the problem of positioning accuracy caused by the reduction of observation time. With the combination of the state transition equation of the monitoring point and the GNSS observation value, it gave the optimal estimation of the state of the monitoring point and eliminates the influence of part of the periodic error to improve the positioning accuracy. The feasibility of this method was verified by analyzing the measured data of Guangshan Railway.

Data Availability

Data sharing is not applicable to this article as no datasets were generated or analyzed during the current study.

Conflicts of Interest

The authors declared no potential conflicts of interest with respect to the research, authorship, and/or publication of this article.

References

- [1] D. Yuan, X. Cui, D. Fan, W. Feng, and Y. Yu, "Application of Kalman filter method to the date processing of GPS deformation monitoring," in *2010 Second International Workshop on Education Technology and Computer Science*, Wuhan, China, 2010.
- [2] T. Wang, Y. Tang, H. Yang, X. Xu, W. Liu, and X. Li, "Convergence deformation monitoring of a shield tunnel based on flexible long-gauge FBG sensors," *Mechanics of Advanced Materials and Structures*, vol. 3, pp. 1–11, 2021.
- [3] E. Tang, V. Lui, and A. Wong, *Application of Automatic Deformation Monitoring System for Hong Kong Railway Monitoring* https://xueshu.baidu.com/usercenter/paper/show?paperid=4f5225c64f4d4089e5391a3dfd1ae09a&site=xueshu_se.
- [4] Q. B. Zhang, L. He, and W. S. Zhu, "Displacement measurement techniques and numerical verification in 3D geomechanical model tests of an underground cavern group," *Tunnelling and Underground Space Technology*, vol. 56, pp. 54–64, 2016.
- [5] F. Ariznavarreta-Fernández, C. González-Palacio, A. Menéndez-Díaz, and C. Ordoñez, "Measurement system with angular encoders for continuous monitoring of tunnel convergence," *Tunnelling and Underground Space Technology incorporating Trenchless Technology Research*, vol. 56, pp. 176–185, 2016.
- [6] L. Li and H. Kuhlmann, "Real-time deformation measurements using time series of GPS coordinates processed by Kalman filter with shaping filter," *Survey Review*, vol. 44, no. 326, pp. 189–197, 2013.
- [7] N. Li, "Deformation monitoring method of large section shallow buried tunnel based on GNSS technology," in *2020 IEEE International Conference on Industrial Application of Artificial Intelligence (IAAI)*, pp. 100–105, Harbin, China, 2020.
- [8] Q. Chen, W. Jiang, X. Meng et al., "Vertical deformation monitoring of the suspension bridge tower using GNSS: a case study of the forth road bridge in the UK," *Remote Sensing*, vol. 10, no. 3, p. 364, 2018.
- [9] R. Xiao, L. Wei, D. Fu, J. Yan, and H. Wang, "Noise-suppressing Newton algorithm for kinematic control of robots," *IEEE Access*, pp. 1–1, 2019.
- [10] Y. Liu, H. Yu, S. Xie, and Y. Zhang, "Deep reinforcement learning for offloading and resource allocation in vehicle edge computing and networks," *IEEE Transactions on Vehicular Technology*, vol. 68, no. 11, pp. 11158–11168, 2019.
- [11] Z. Li, Z. Yang, and S. Xie, "Computing resource trading for edge-cloud-assisted internet of things," *IEEE Transactions on Industrial Informatics*, vol. 156, no. 6, pp. 3661–3669, 2019.

Retraction

Retracted: SLAM of Mobile Robot for Wireless Communication Based on Improved Particle Filter

Wireless Communications and Mobile Computing

Received 28 November 2023; Accepted 28 November 2023; Published 29 November 2023

Copyright © 2023 Wireless Communications and Mobile Computing. This is an open access article distributed under the Creative Commons Attribution License, which permits unrestricted use, distribution, and reproduction in any medium, provided the original work is properly cited.

This article has been retracted by Hindawi, as publisher, following an investigation undertaken by the publisher [1]. This investigation has uncovered evidence of systematic manipulation of the publication and peer-review process. We cannot, therefore, vouch for the reliability or integrity of this article.

Please note that this notice is intended solely to alert readers that the peer-review process of this article has been compromised.

Wiley and Hindawi regret that the usual quality checks did not identify these issues before publication and have since put additional measures in place to safeguard research integrity.

We wish to credit our Research Integrity and Research Publishing teams and anonymous and named external researchers and research integrity experts for contributing to this investigation.

The corresponding author, as the representative of all authors, has been given the opportunity to register their agreement or disagreement to this retraction. We have kept a record of any response received.

References

- [1] D. Zhu, M. Wang, M. Su, S. Liu, and P. Guo, "SLAM of Mobile Robot for Wireless Communication Based on Improved Particle Filter," *Wireless Communications and Mobile Computing*, vol. 2021, Article ID 9263277, 14 pages, 2021.

Research Article

SLAM of Mobile Robot for Wireless Communication Based on Improved Particle Filter

Daixian Zhu¹, Mingbo Wang¹, Mengyao Su¹, Shulin Liu², and Ping Guo¹

¹College of Communication and Information Engineering, Xi'an University of Science and Technology, Xi'an 710054, China

²College of Electrical and Control Engineering, Xi'an University of Science and Technology, Xi'an 710054, China

Correspondence should be addressed to Daixian Zhu; zhudaixian@xust.edu.cn

Received 3 July 2021; Revised 23 July 2021; Accepted 9 August 2021; Published 30 August 2021

Academic Editor: Balakrishnan Nagaraj

Copyright © 2021 Daixian Zhu et al. This is an open access article distributed under the Creative Commons Attribution License, which permits unrestricted use, distribution, and reproduction in any medium, provided the original work is properly cited.

The mobile robot is moved by receiving instructions through wireless communication, and the particle filter is used to simultaneous localization and mapping. Aiming at the problem of the degradation of particle filter weights and loss of particle diversity, which leads to the decrease of filter accuracy, this paper uses the plant cell swarm algorithm to optimize the particle filter. First of all, combining the characteristics of plant cells that affect the growth rate of cells when the auxin content changes due to light stimulation realizes the optimization of the particles after importance sampling, so that they are concentrated in the high-likelihood area, and the problem of particle weight degradation is solved. Secondly, in the process of optimizing particle distribution, the auxin content of each particle is different, which makes the optimization effect on each particle different, so it effectively solves the problem of particle diversity loss. Finally, a simulation experiment is carried out. During the experiment, the robot moves by receiving control commands through wireless communication. The experimental results show that the algorithm effectively solves the problem of particle weight degradation and particle diversity loss and improves the filtering accuracy. The improved algorithm is verified in the simultaneous localization and mapping of the robot, which effectively improves the robot's performance at the same time positioning accuracy. Compared with the classic algorithm, the robot positioning accuracy is increased by 49.2%. Moreover, the operational stability of the algorithm has also been improved after the improvement.

1. Introduction

The particle filter (PF) algorithm is a filtering method based on Monte Carlo and Bayesian estimation. The basic idea is to use a set of weighted samples randomly drawn from the probability density to approximate the posterior probability density. Since the proposed particle filter algorithm, it has been widely used in the field of nonlinear system parameter estimation, such as target tracking [1], system state detection [2], and simultaneous localization and mapping (SLAM) of robots [3].

Although the classical particle filter algorithm has achieved good filtering effect in practical application, it uses the prior probability density function as the important density function, which will lead to the increase of important weight variance with the increase of time. The phenomenon that the weights are concentrated on a few particles occurs,

that is, the degradation of particle weights. In order to solve the problem of particle weight degradation, the resampling strategy is introduced in the classical particle filter algorithm, and the corresponding algorithm is called Rao-Blackwellized particle filters (RBPF); Rao-Blackwellized particle filter is applied to robotic SLAM and is named FastSLAM1.0 algorithm [4]. The FastSLAM2.0 algorithm [5] fuses the noise of the sensor on the sampling function of the predicted pose to improve the positioning accuracy caused by the reduction of particle diversity.

Frequent resampling steps lead to gradual dissipation of particles; the current popular solution is to solve the problem of particle weight degradation and particle diversity loss through the efficient combination of one or several meta-heuristic algorithms [6] and particle filtering. Shiming and others [7] use the rules of planet formation in the universe to take the particles sampled from the importance function

as the dust in the universe and the global optimal value as the central dust. Through, the attraction and repulsion of the central dust, the particle set is distributed near the high-likelihood region, which alleviated the weight degradation and improved the diversity of particles [8]. This improved algorithm has also been successfully applied to SLAM and achieved a good positioning effect. However, due to the strong optimization ability of the gravitational field algorithm, there is a risk of premature maturity in the iterative process of the algorithm. The literature [9–11] optimizes the original particle filter improvement algorithm and improves the particle weight degradation and diversity loss jointly through the efficient combination of several algorithms, so as to improve the filtering performance of the algorithm. Although the above algorithm improves the performance of particle filtering, a large number of particles are needed to realize state estimation in the scene with complex environment and strong noise. The fusion of multiple algorithms will inevitably cause the problems of long running time and low operating efficiency.

In this paper, an improved plant cell swarm algorithm (PCSA) improves PF by optimizing the particle distribution after importance sampling and omit the resampling process in particle filter algorithm, by initializing the plant cell swarm, determining the position of the strongest light, calculating the growth rate, and updating the plant cell swarm, and the PCSA-PF method is obtained. The PCSA-PF is applied to FastSLAM 2.0 framework, which can be called PCSA-FastSLAM. Experimental results show that the improved algorithm can effectively improve the particle degradation and particle diversity loss in FastSLAM 2.0 algorithm and improve the accuracy of robot positioning mapping.

The rest of the paper is organized as follows. Section 1 introduces briefly the PF and FastSLAM. Section 2 introduces the principle of plant cell swarm algorithm. Section 3 discusses the proposed PCSA-PF and PCSA-FastSLAM in detail. Section 4 gives the simulation results and analyzes the performance of the PCSA-PF and PCSA-FastSLAM in detail. Finally, Section 5 concludes the paper and gives some orientations for future work.

2. Particle Filter Algorithm and Its Application in Robot Autonomous Mobile Mapping

2.1. Particle Filter Algorithm. Particle filtering is a method to realize recursive Bayesian filtering through Monte Carlo thought [12], which uses Monte Carlo method to solve the integral problem in Bayesian estimation.

The main steps of the classical PF algorithm are as follows: initialization particle set, importance sampling, importance weight calculation, resampling, and state estimation.

Initialization: at $k=0$, sample N particles are from the prior distribution $p(x_0)$, the set weight of each particle is $1/N$, and the sampled particle set is $\{x_0^i, 1/N\}_{i=1}^N$.

Importance sampling: at $k \geq 1$, the particles are sampled from the importance density function. The importance density function is

$$q(x_k^i | x_{k-1}^i, z_k) = p(x_k^i | x_{k-1}^i). \quad (1)$$

Calculation of importance weight: calculate the weight of each particle for the sampled particles. The weight calculation formula is

$$\tilde{w}_t^i = \tilde{w}_{t-1}^i \frac{p(z_t | \tilde{x}_t^i) p(\tilde{x}_t^i | \tilde{x}_{t-1}^i)}{q(\tilde{x}_t^i | x_{t-1}^i)}. \quad (2)$$

Weight normalization: normalize weights for particles with different weights:

$$w_t^i = \frac{\tilde{w}_t^i}{\sum_{i=1}^N \tilde{w}_t^i}. \quad (3)$$

Resampling: in order to solve the problem of particle weight degradation, the resampling strategy is introduced. For the evaluation of the degree of particle weight degradation, the effective particle number is adopted as the criteria:

$$\tilde{N}_{\text{eff}} = \frac{1}{\sum_{i=1}^N (\tilde{w}_t^i)^2}, \quad (4)$$

by comparing the effective particle number \tilde{N}_{eff} with the set threshold N_{thres} . If $\tilde{N}_{\text{eff}} \leq N_{\text{thres}}$, the resampling strategy is carried out: that is, the particles with heavier weight are copied multiple times, and the particles with lower weight are copied to reduce the number of times or even without copying. The number of particles after resampling is equal to the original particles, and the weight is the same as $1/N$. If not, continue to perform the state estimation operation.

State estimation:

$$\tilde{x}_t = \sum_{i=1}^N w_t^i x_t^i. \quad (5)$$

2.2. FastSLAM2.0 Algorithm. PF algorithm is applied to SLAM of robots. The core idea is to decompose the system state estimation through the Rao-Blackwellized decomposition method and decompose it into path estimation and environment map estimation. The decomposition formula is

$$\begin{aligned} p(x_{1:k}, m | z_{1:k}, u_{0:k-1}) \\ = p(x_{1:k} | z_{1:k}, u_{0:k-1}) \prod_{i=1}^M p(m_i | x_{1:k}, z_{1:k}, u_{0:k-1}). \end{aligned} \quad (6)$$

In the above formula, $p(x_{1:k}, m | z_{1:k}, u_{0:k-1})$ represents the mathematical formula expression of the SLAM problem, $p(x_{1:k} | z_{1:k}, u_{0:k-1})$ represents the robot path estimation, and $\prod_{i=1}^M p(m_i | x_{1:k}, z_{1:k}, u_{0:k-1})$ represents the robot environment map estimation.

Due to the different selection methods of the proposed distribution function, the FastSLAM algorithm can be divided into the FastSLAM1.0 algorithm and the FastSLAM2.0 algorithm. Compared with the FastSLAM1.0

algorithm that uses the prior distribution $p(x_{k+1}|x_k^i, u_k)$ as the proposal distribution function, the proposal distribution function of the FastSLAM2.0 algorithm is updated by EKF from $p(x_{k+1}|x_k^i, u_k)$. This improvement makes the proposal distribution function contain historical information and observation information at the current moment. Therefore, it will effectively alleviate the problem of algorithm degradation and improve the filtering accuracy of the algorithm [13].

In order to solve the problem of particle weight degradation, the FastSLAM2.0 algorithm adopts a resampling strategy, which will cause the loss of particle diversity and reduce robot positioning accuracy. Therefore, the key to improving the accuracy of robot positioning and mapping is to effectively solve the particle weight degradation and loss of particle diversity [14].

3. Plant Cell Swarm Algorithm

On the basis of studying the process of plant positive growth, plant positive cell swarm algorithm is proposed, hereinafter referred to as plant cell swarm algorithm (PCSA) [15].

3.1. Growth Mechanism of Positive Plants. Positivity is the result of long-term evolution of plants, which helps them absorb more light energy. Under the stimulation of light, the distribution of auxin in the plant changes. The auxin is transported from the strong light side to the backlight side. The auxin concentration on the backlight side is higher than the strong light side, so the growth rate of plant cells on the backlight side is faster than the strong light side and makes the plant body bend toward the sun, so the plant grows toward the sun.

Auxin plays a crucial role in plant growth, which is manifested in duality: auxin can not only promote cell growth but also inhibit cell growth. The effect of auxin on plant cells is shown in Figure 1.

3.2. Plant Cell Swarm Algorithm. The plant cell swarm algorithm simulates the growth behavior of sunny plants, takes the location of plant cells with the highest light intensity and the distance from other cells as the standard of auxin concentration distribution, determines the growth rate of different plant cells based on auxin concentration, and finds the maximum location of light intensity through multiple iterations.

The plant cell swarm algorithm is mainly divided into the following five steps: initializing the plant cell swarm, determining the position of the strongest light, allocating auxin, calculating the growth rate, and updating the plant cell swarm.

Step 1. Initialize the plant cell swarm.

Randomly generate a plant cell swarm with a population of N . In the process of generating, keep the cell swarm covering all feasible solutions. Assuming the search in the D -dimensional search space, the k -dimensional coordinate is x_k , the position of the m th cell is $X_m = (x_{m1}, x_{m2}, \dots, x_{mk}, \dots, x_{md})$, and there are

$$x_{mk} = x_{k \min} + \text{rand} (x_{k \max} - x_{k \min}). \quad (7)$$

In formula (1), $x_{k \min}$ is the minimum value of the k -dimension coordinate in the domain of definition, $x_{k \max}$ is the maximum value of the k -dimension coordinate, and rand is a random number in the interval $[0,1]$.

Step 2. Determine the location of the strongest light.

Assuming the function is $P_i = f(X_i) (i = 1, 2, \dots, d)$, p_i represents the total amount of sunlight that each plant cell is exposed to in the D -dimensional space, and f represents the mapping of the plant cell in the D -dimensional space and the total amount of light intensity. By calculating the total amount of light exposed to each cell in the plant cell swarm and comparing it, the maximum light intensity in a cell is recorded as sun ; the position of the plant cell with the maximum light intensity is X_{sun} ; that is, the formula is expressed as

$$\text{sun} = \max \{f(X_1), f(X_2) \dots f(X_D)\}. \quad (8)$$

Step 3. Allocate auxin.

First, calculate the distance between the position of each cell in the plant cell swarm and the maximum light intensity of X_{sun} . The distance was calculated using the European formula, and the calculation formula is

$$L(X_i, X_{\text{sun}}) = \left[\sum_{k=1}^d (X_i - X_{\text{sun}})^2 \right]^{1/2}. \quad (9)$$

In the above formula, X_i represents the position of the i th cell, d represents the dimension of the plant cell, and $L(X_i, X_{\text{sun}})$ represents the distance between the i th cell and maximum light intensity.

The distance value calculated by the above formula is used to calculate the auxin content of each cell location. The calculation formula is

$$Q_i = 1 + \frac{L(x_i, X_{\text{sun}})}{(1 + P_i)}. \quad (10)$$

Step 4. Calculate the growth rate.

From the above biological mechanism of the effect of auxin on the growth of plant cells, it can be seen that for positive organisms, auxin will move when it receives light stimulation. The farther the plant cell is from the maximum light intensity, the higher the auxin content is. In addition, the different content of auxin has different promoting effects on plant cell growth. The mechanism of action is as follows:

- (1) $0 < Q_i \leq \alpha$, with the increase of auxin, the growth promotion effect on plant cells gradually increases
- (2) $\alpha < Q_i \leq \beta$, with the increase of auxin, the growth promotion effect on plant cells gradually weakens
- (3) $\beta < Q_i \leq \gamma$, with the increase of auxin, it has an inhibitory effect on the growth of plant cells

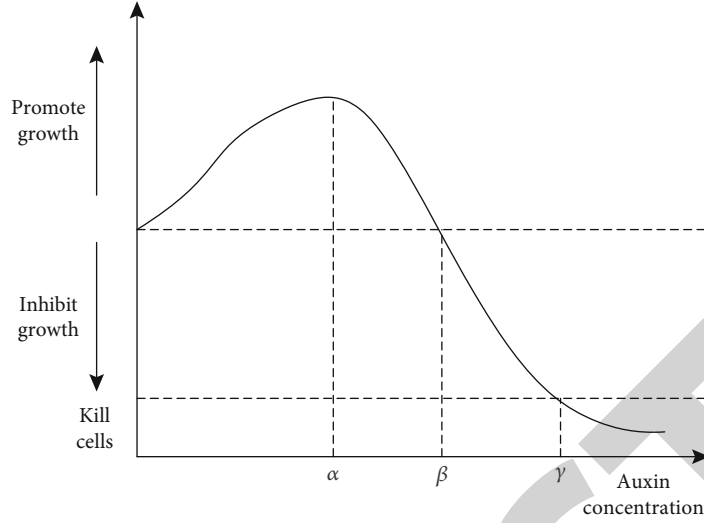


FIGURE 1: The effect of auxin concentration on plant cells.

(4) $\gamma < Q_i$, auxin kills cells

In summary, auxin with different contents has different effects on the growth of plant cells. When the plant receives light stimulation and completes auxin distribution, the calculation formula for the growth rate of each plant cell V_i is

$$V_i = \begin{cases} \frac{aQ_i}{b} L(X_i, X_{\text{sun}}), & Q_i \leq \alpha, \\ \frac{-aQ_i + 2a\alpha}{c} L(X_i, X_{\text{sun}}), & \alpha < Q_i \leq \gamma, \\ 0, & Q_i > \gamma. \end{cases} \quad (11)$$

In the above formula, the $a > 0, b > 0, c > 0$ value is large enough to make $V_i < L(X_i, X_{\text{sun}})$; that is, the growth distance of plant cells under the action of auxin is less than the distance between plant cells and the maximum light intensity before they move.

The direction of V_i is the vector direction from the position of the i cell to the position of the strongest light.

Step 5. Update the plant cell swarm.

Calculate the position X_i^* of each cell in the plant cell group after growth; the calculation formula is

$$X_i^* = X_i + V_i. \quad (12)$$

Calculate the total amount of sunlight P_i^* received by the i cell after its position update in the d space:

$$P_i^* = f(x_{i1}^*, x_{i2}^*, \dots, x_{ik}^*, \dots, x_{id}^*). \quad (13)$$

If $P_i^* > P_i$, then $P_i^* = P_i$, and $X_i = X_i^*$; otherwise, the growth is considered invalid.

When the auxin concentration of the i cell is greater than γ , the cell does not grow. At this point, a new cell is generated according to formula (1), and let $P_i^* = P_i$ and $X_i = X_i^*$.

When all cells are updated, calculate the amount of sunlight at the location of each cell to find the maximum light value sun^* , $\text{sun}^* > \text{sun}$, and $X_{\text{sun}} = X_{\text{sun}^*}$.

4. Optimized Particle Filter Based on Plant Cell Swarm Algorithm (PCSA-PF)

The detailed process of plant cell swarm algorithm is introduced above. Regarding the process of iteration to find the optimal solution among all feasible solutions in PCSA, it is based on the research of the sunny plant growth process. When the sunny plants receive light stimulation, the auxin moves from the backlight side to the strong light side. The auxin concentration on the backlight side is higher than the strong light side, so the plants bend to the strong light side. In this process, the plant cells move toward the maximum light intensity; that is, the feasible solution of the algorithm gradually approaches the optimal solution in the iterative process. Therefore, particle distribution after importance sampling is optimized by PCSA. PCSA optimizes the particle distribution after importance sampling and uses the PCSA's strong optimization ability to distribute the particle set in the high likelihood region, thus alleviating the particle degradation problem. At the same time, the distribution of plant cells is determined by the concentration of auxin. Different concentrations of auxin have different effects on the growth of plant cells, which will enhance the diversity of particles.

In summary, it can be considered to apply the PCSA to the improvement of PF algorithm.

4.1. Particle Weight Is Used as the Light Intensity Value in the PCSA. It can be seen from the above that after initializing the plant cell swarm, the PCSA evaluates the light intensity of the location of each plant cell through the correlation function. In the PF algorithm, the particle weight after importance sampling is used as the standard to evaluate the performance of each particle filter. Therefore, in this paper, the particle weight is taken as the light intensity value in

the PCSA. This step not only completes the PF performance evaluation but also establishes the relationship between the PCSA and the PF. This process is the basis for improving the particle filter of the PCSA.

4.2. Choose the Appropriate Growth Rate Formula. In the PCSA, the growth rate depends on the concentration of auxin. Under different auxin concentrations, the growth rate of plant cells is different, which is manifested as follows: as the auxin increases, the growth rate of plant cells is accelerated, the growth rate of plant cells is inhibited, or plant cells are killed. The PF is improved by the PCSA. For the important sampled particles, the particle set should move to the high-likelihood region under the optimization of the PCSA. Therefore, this article selects the $Q_i \leq \alpha$ section; that is, with the increase of auxin, the growth promotion effect on plant cells gradually increases. Since the particles sampled from the importance function are not distributed near the global optimal value. Improving by this method, the farther the particles are, the more effective the optimization is. In this paper, the plant cell growth formula used in the process of optimizing particle filtering is

$$V_i = a \frac{Q_i}{b} L(X_i, X_{\text{sun}}). \quad (14)$$

The PCSA-PF process is as follows.

Step 1. At $k = 0$, N particles were sampled from the prior distribution, and the weight of each particle was set as $1/N$, the particle set after sampling was set as $\{x_0^i, 1/N\}_{i=1}^N$, and the number of population in the PCSA was set as N .

Step 2. When $k \geq 1$, particles are sampled from the importance density function, the weight of each particle is calculated, and the weight is normalized.

Step 3. PCSA optimized particle distribution:

- (1) The weight of the sampled particles was taken as the light intensity of the plant cell population algorithm to determine the maximum point of the current light intensity, that is, the position of the global optimal value
- (2) The auxin content of each particle was calculated
- (3) Cell growth
- (4) Update the plant cell population to determine whether the iteration is over. If the iteration is over, go to Step 4; otherwise, recalculate the weight of each particle after optimization and return to (1).

Step 4. Particle weights are normalized.

Step 5. The state estimation is realized by formula (5).

5. Experimental Results and Analysis

The hardware environment of the experiment is a desktop computer (IntelCorei5 processor, 4GB memory), and the experiment environment is MATLAB 2016b.

5.1. Analysis of Particle Filter Simulation Experiment. The improved algorithm is compared and analyzed by experiments to verify its filtering performance and whether the improved algorithm can effectively alleviate the problem of particle weight reduction and diversity loss. This experiment is based on a univariate dynamic change filter model. When the particle number is 100, the classical PF algorithm, the gravitational field-based optimization PF algorithm (GFA-PF) [8], and the improved algorithm proposed in this paper (PCSA-PF) are compared.

The system equations and state equations used in PF simulation are

$$\begin{aligned} x(t) &= 0.5x(t-1) + \frac{2.5x(t-1)}{1+x(t-1)^2} + 8 \cos [1.2x(t-1)] + w(t-1), \\ z(t) &= \frac{x(t)^2}{20} + v(t). \end{aligned} \quad (15)$$

This model is a typical nonlinear non-Gaussian system model; $w(t)$, $v(t)$ is a zero mean Gaussian noise.

The performance of the filtering algorithm is expressed by the root mean square error (RMSE), and the formula is

$$\text{RMSE} = \left[\frac{1}{T} \sum_{i=1}^T (x_k - \tilde{x}_k)^2 \right]^{1/2}, \quad (16)$$

where k is the number of iterations, \tilde{x}_k is the state true value, and x_k is the filtering estimate.

K is the filtering estimate.

5.1.1. Algorithm Convergence Analysis. The PCSA-PF is improved on the classic PF algorithm. So the improved algorithm theoretically has similar convergence properties to the classic algorithm. Therefore, the RMSE comparison is performed under the condition of different numbers of particles. The simulation results are shown in Figure 2.

Figure 2 shows that as the number of particles gradually increases, the RMSE of both the PCSA-PF and classic PF algorithm gradually decreases, and when the number of particles reaches 200, the RMSE value tends to stabilize. It indicates that the PCSA-PF and PF algorithm has the same convergence characteristics; that is, as the number of particles continues to increase, and the filtering accuracy of the algorithm gradually stabilizes while improving the algorithm convergence.

5.1.2. Comparison of Filtering Accuracy. In order to verify the filtering accuracy of the PCSA-PF, the sampling points were set to 100 and the sampling period was $T = 100$. Then, the GFA-PF-related parameters are set by reference [8], the iteration number of the PCSA-PF is 8, and the ratio between

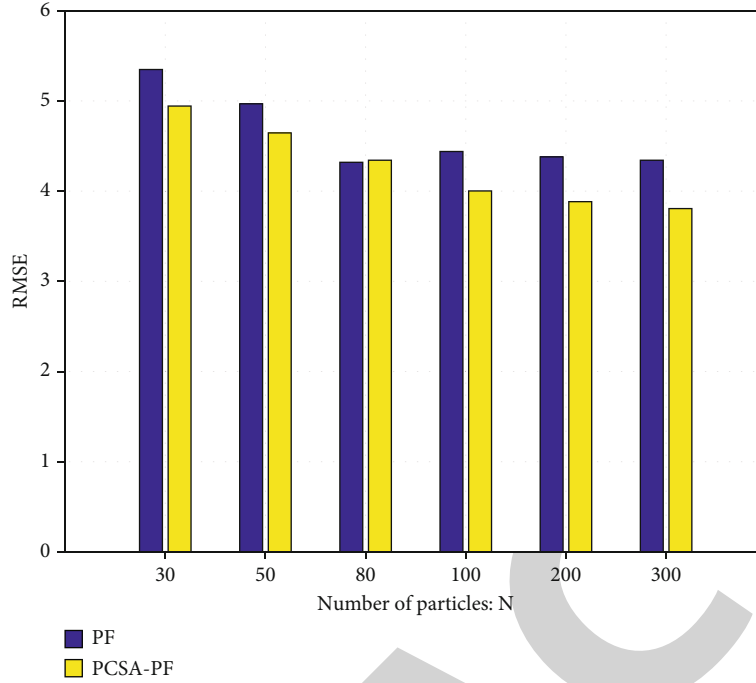


FIGURE 2: Algorithm convergence comparison.

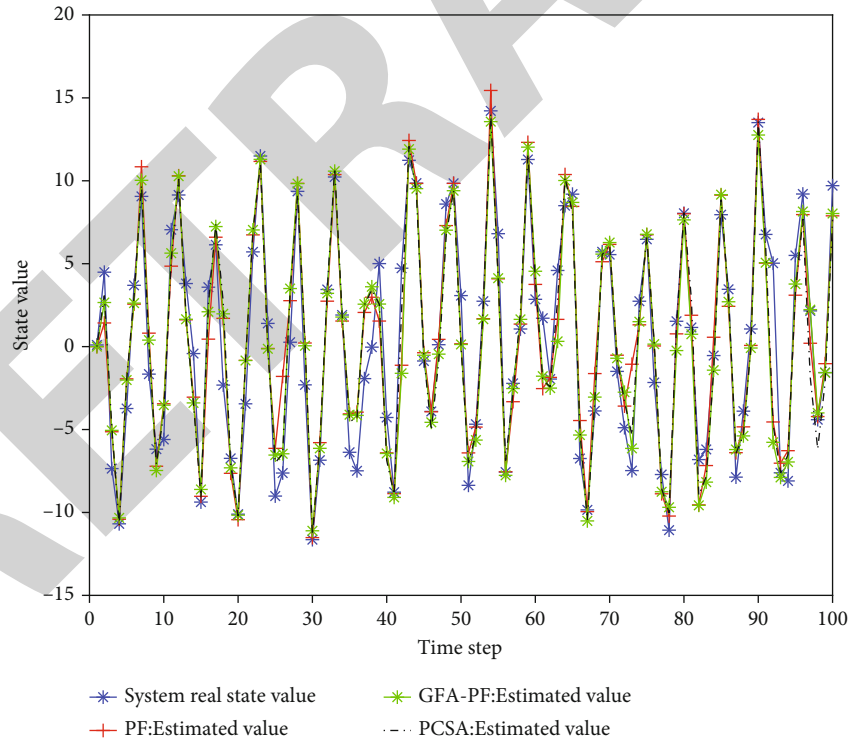


FIGURE 3: System state estimation.

a and b in the above equation (11) was set to 0.002. Set the noise variance of the system state equation as 10 and the noise variance of the system observation equation as 1. Then, compare among the PF, GFA-PF, and PCSA-PF algorithm. The experimental results are shown in Figures 3 and 4.

From Figures 3 and 4, it can be seen that the PCSA-PF proposed in this paper and the GFA-PF proposed in [8] have better filtering accuracy than the classical PF algorithm, and the PCSA-PF has better filtering accuracy than the GFA-PF. This is because after the unique optimization mechanism of

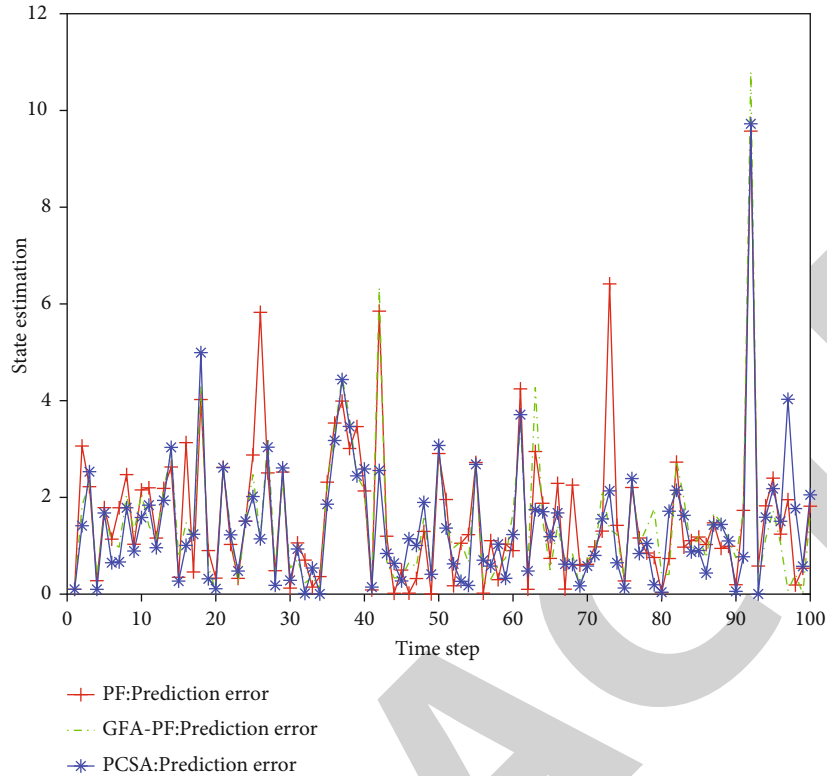


FIGURE 4: Absolute value of estimated error.

PCSA-PF is combined with PF; the particle set will move to the high likelihood area under the effect of the global optimal value, which makes the filtering accuracy improve; and the PCSA has a more obvious promotion effect on particles farther from the global optimal value, which is also the reason for the improved filtering accuracy.

From Tables 1 and 2, it can be seen that under the same number of particles, the filtering accuracy of GPA-PF and PCSA-PF is higher, and the PCSA-PF has higher filtering accuracy when there is less number of particles $N = 50$. It is proved that the PCSA and PF algorithm are efficiently combined. The PCSA plays a vital role in optimizing the particles after the importance sampling and effectively optimizes the distribution of the particles to make them concentrated in the high likelihood region. The PCSA-PF achieves higher filtering accuracy through a smaller number of particles in a strong noisy environment. In addition, compared with the GFA-PF algorithm, the PCSA-PF algorithm efficiency is high; the reason for this phenomenon is that the proposed algorithm's time complexity is $O(N)$, namely, complete particle through a loop optimization, the GFA-PF algorithm firstly by the global optimal value to attract the operations of particles, and then throw, partly to increase the time complexity of the algorithm.

5.1.3. Spatial Distribution Characteristics of Particle Samples.

For the evaluation of the degradation degree of particle weights, adopt effective particle number on the measurement. The experiment set the particle number is 100. In order to avoid contingency, 10 experiments were compared.

TABLE 1: Comparison of mean square error of three algorithms.

Algorithm	$N = 30$	$N = 50$	$N = 80$	$N = 100$
PF	6.565690	5.201521	4.724141	4.442274
GFA-PF	5.069986	4.389173	4.183473	4.005711
PCSA-PF	4.820985	4.116689	4.062849	3.838158

TABLE 2: Comparison of running time of three algorithms.

Algorithm	$N = 30$	$N = 50$	$N = 80$	$N = 100$
PF time/s	0.002856	0.003664	0.004355	0.004355
GFA-PF time/s	0.006497	0.009463	0.014663	0.016842
PCSA-PF time/s	0.007014	0.009079	0.011923	0.014418

According to the Table 3, we can find that the PCSA-PF has greatly improved the degradation degree of particle weights compared with the classic PF. Therefore, it can be concluded that the PCSA-PF effectively solves the problem of particle weight degradation.

In order to verify the impact of PCSA-PF on the diversity of particles, when the number of particles is 80, take $t = 10$, $t = 40$, and $t = 75$, that is, compare the results of three experiments in the initial, middle, and final stages of the algorithm. The experimental results are shown in Figure 5.

From Figure 5, it can be seen that the particles are concentrated in the high likelihood area at the end of the PF algorithm, which loses the diversity of particles to a certain

TABLE 3: Comparison of effective particle number.

Time	1	2	3	4	5	6	7	8	9	10
PF	51.44	51.69	51.19	51.76	51.78	51.07	51.56	51.81	51.38	51.64
PCSA-PF	71.05	71.13	70.74	70.73	70.63	70.40	70.23	70.30	70.95	70.30

extent, thus leading to a decrease in filtering accuracy. In the later stage of the PCSA-PF, while most of the particles are concentrated in the high-likelihood area, some particles are distributed around the true value of the particles. This shows that PCSA-PF has improved the diversity of particles to a certain extent which is also the reason of PCSA-PF precision promotion.

5.2. Experiment of Robot Localization and Mapping. Experiments are performed in order to verify the effectiveness of the algorithm proposed in this paper, thus, comparing the classic FastSLAM2.0, GFA-FastSLAM2.0, and the PCSA-FastSLAM2.0.

Firstly, establish the mobile robot simulation model. The model is a mobile robot motion model:

$$\begin{bmatrix} x_k^v \\ y_k^v \\ \Phi_k^v \end{bmatrix} = \begin{bmatrix} x_{k-1}^v + \Delta T \cdot \cos(\Phi_{k-1}^v + \alpha_k) \\ y_{k-1}^v + \Delta T \cdot \sin(\Phi_{k-1}^v + \alpha_k) \\ \Phi_{k-1}^v + \frac{(\Delta T \cdot v_k \cdot \sin(\alpha_k))}{D} \end{bmatrix} + \begin{bmatrix} v_x \\ v_y \\ v_\phi \end{bmatrix}. \quad (17)$$

In the formula, (x_k^v, y_k^v) represents the position posture state of the robot in the two-dimensional environment at the k moment; Φ_k^v represents the heading angle, and the value range is $[-180^\circ, 180^\circ]$; v_k represents the movement speed of the robot; α_k represents its steering angle; α_k is the robot odometer sampling time; v_x, v_y, v_ϕ is the noise during the robot movement; and D is the distance between the drive shafts. The mobile robot observation model is

$$\begin{bmatrix} r_k \\ \theta_k \end{bmatrix} = \begin{bmatrix} \sqrt{(x_i - x_k^v)^2 + (y_i - y_k^v)^2} \\ \arctan \frac{y_i - y_k^v}{x_i - x_k^v} - \Phi_k^v \end{bmatrix} + \omega_k. \quad (18)$$

In the formula, r_k, θ_k , respectively, represents the distance between the detected environmental feature and the mobile robot, and the angle of movement direction; ω_k is the observation noise.

First, simulate the robot localization and mapping; establish the working environment and mobile robot motion parameters and noise parameters, as shown in Figure 6 and in Table 4; set the 17 heading points and 35 road marking points; and the mobile robot movement range is 100 m \times 80m. The mobile robot starts from the coordinate origin (red point in Figure 6) and moves counterclockwise by the movement command obtained through wireless communication, the green * represents the road marking point, red* represents the heading point, and cyan line represents the prescribed robot path.

Figures 7–9, respectively, show the robot localization mapping effects of the three algorithms. The robot is set to move for two circles and compare the predicted trajectory with the actual trajectory during the second circle. Compared to the classic FastSLAM2.0 algorithm, the predicted trajectory of GFA-FastSLAM2.0 and PCSA-FastSLAM2.0 overlaps with the real trajectory in many parts, and the PCSA-FastSLAM2.0 has the most overlapped part; that is, the PCSA-FastSLAM2.0 algorithm has the good prediction effect. The reason is that compared to the particle adjustment way of GFA-FastSLAM2.0 after importance sampling, the PCSA-FastSLAM2.0 has the higher degree of attraction for particles far from the global optimal value; thus, the PCSA-FastSLAM2.0 for the robot localization accuracy has been significantly improved. And it is through the prediction of road signs in Figures 8–10 (the red dot represents the predicted location of the road signs). In Figure 8, the predicted road sign accuracy of FastSLAM2.0 gradually decreases as the running time increases. This is due to the degradation of particle weights and loss of particle diversity, resulting in a decrease in localization accuracy, which in turn affects the estimation of road signs. As illustrated in the PCSA-FastSLAM2.0 shown in Figure 10, it can be seen that the predicted value of the road sign and the actual value have a higher degree of coincidence, which indicates that the PCSA-FastSLAM2.0 improves the degradation of particle weight, loss of particle diversity, and other problems and further illustrates the superiority of the PCSA-FastSLAM2.0.

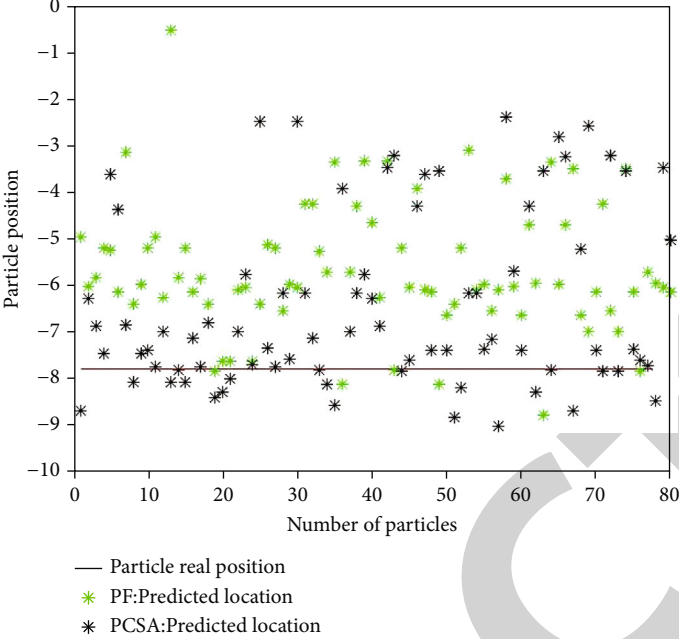
In order to further verify the optimization effect of the PCSA-FastSLAM2.0 on robot localization and mapping, at 8000 sampling moments, respectively, compare the Euclidean distance between the predicted value and the estimated value of the three algorithms, namely, the localization error. The formula is:

$$\rho = \sqrt{(x_1 - x_2)^2 + (y_1 - y_2)^2}. \quad (19)$$

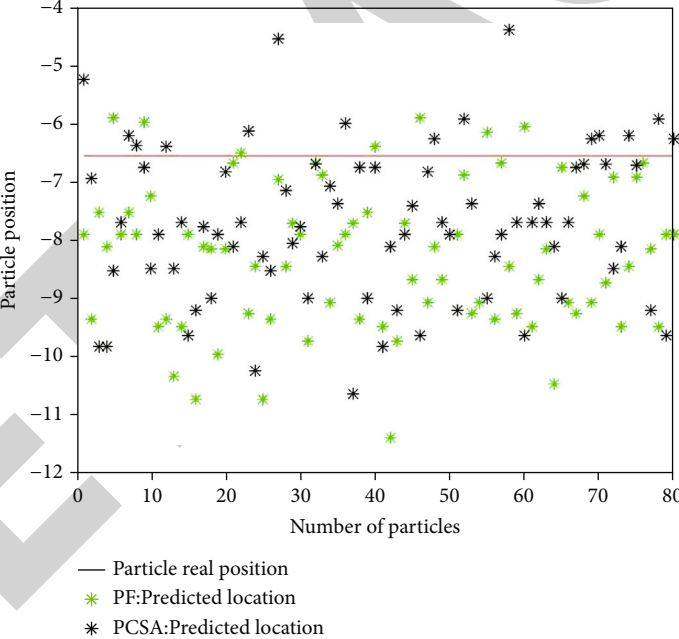
In the formula, $(x_1, y_1), (x_2, y_2)$ represents the coordinates of the predicted position and actual position.

The comparison of the robot localization accuracy errors of the three algorithms is shown in Figure 10.

From the above Figure 10, it can be seen the PCSA-FastSLAM2.0 has the highest localization accuracy and is relatively stable compared to FastSLAM2.0 and GFA-FastSLAM2.0. While the localization accuracy of the classic FastSLAM2.0 increases, the running time gradually increases, and the localization accuracy error also gradually increases. This is because in the later iterations of the algorithm, the particles are severely degraded and the diversity is lost, resulting in lower localization accuracy. The PCSA-FastSLAM2.0 solves this problem effectively and increases



(a) Particle distribution ($t = 10, N = 80$)



(b) Particle distribution ($t = 40, N = 80$)

FIGURE 5: Continued.

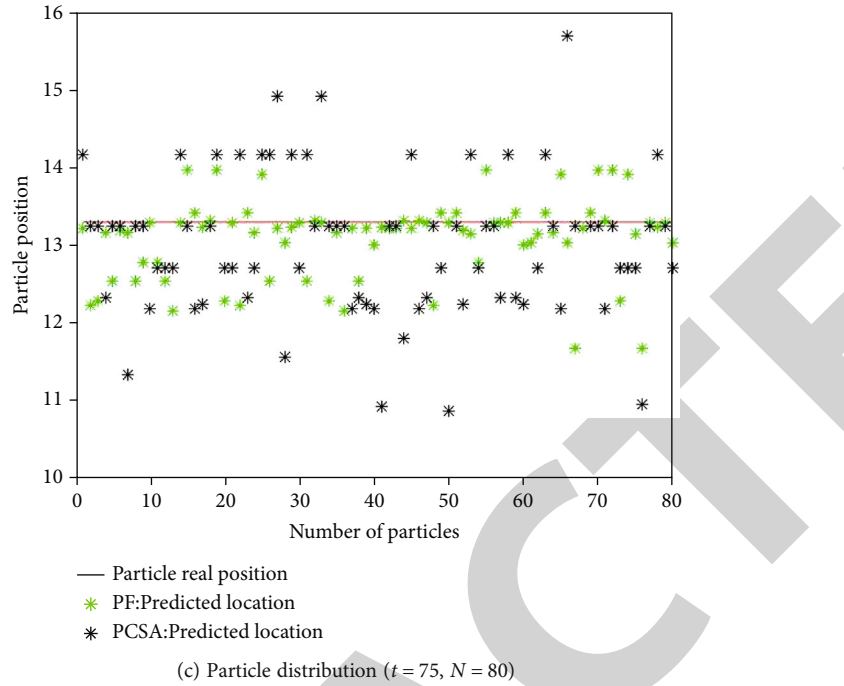


FIGURE 5: Particle diversity experiment.

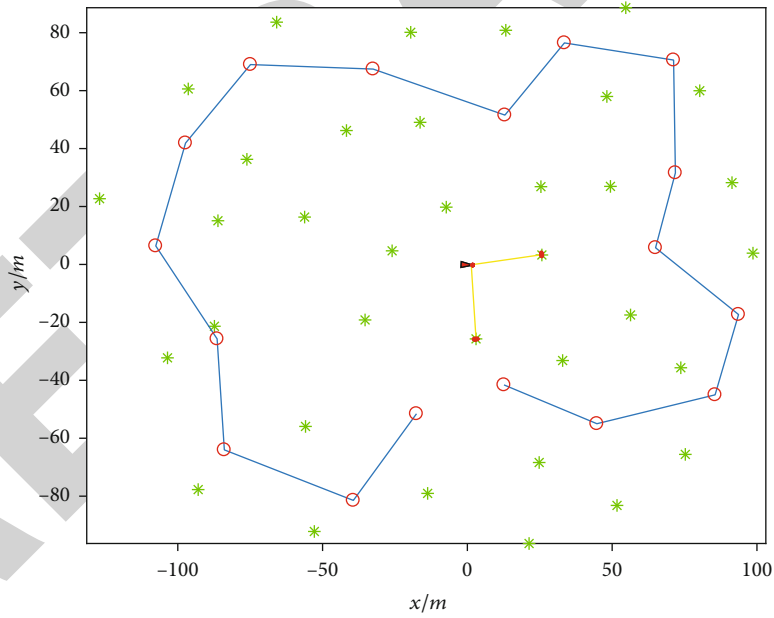


FIGURE 6: Simulation environment.

TABLE 4: Mobile robot motion parameters and noise parameters.

Motion parameters	Value	Noise parameters	Value
Speed	3 m/s	Motion noise	0.3 m/s
Maximum steering angle	10°		1.5°
Maximum steering angle speed	15°/s	Observation noise	0.1 m/s
Wheel spacing	4 m		1°
Sampling interval	0.025 s		

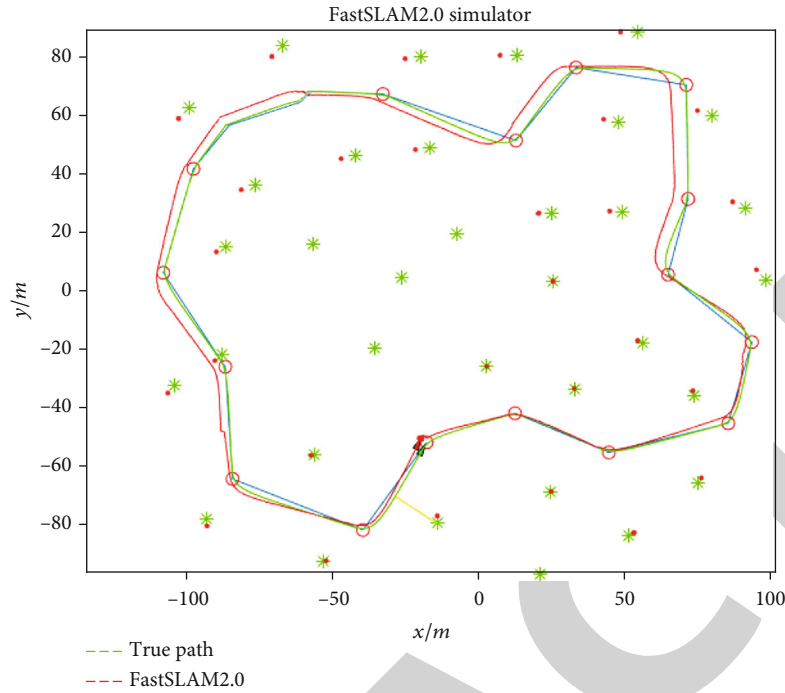


FIGURE 7: FastSLAM2.0 simulation result.

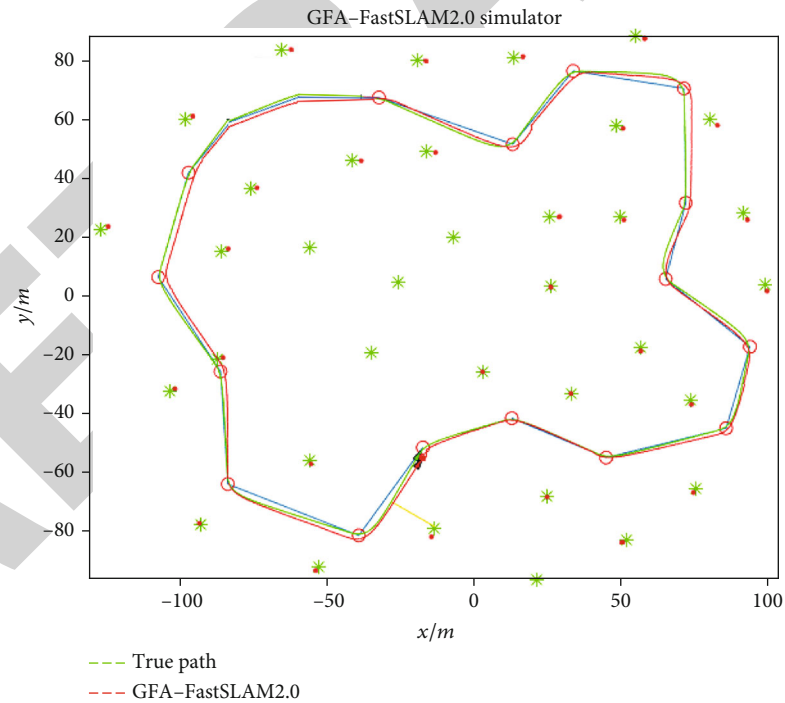


FIGURE 8: GFA-FastSLAM2.0 simulation result.

the localization accuracy. For the GFA-FastSLAM2.0, its positioning accuracy is lower than the PCSA-FastSLAM2.0, but better than the classic FastSLAM2.0. This is because the GFA has a certain degree of optimization effect on importance sampled particles, and GFA-PF has improved the diversity of particles to a certain extent. Therefore, the

GFA-FastSLAM2.0 has a certain degree of improvement on the robot localization accuracy. But compared with the idea of PCSA-FastSLAM2.0, the PCSA has a strong degree of optimization for particles far from the global optimal value; thus, the PCSA-FastSLAM2.0 is better than GFA-FastSLAM2.0 in the robot localization accuracy improvement.

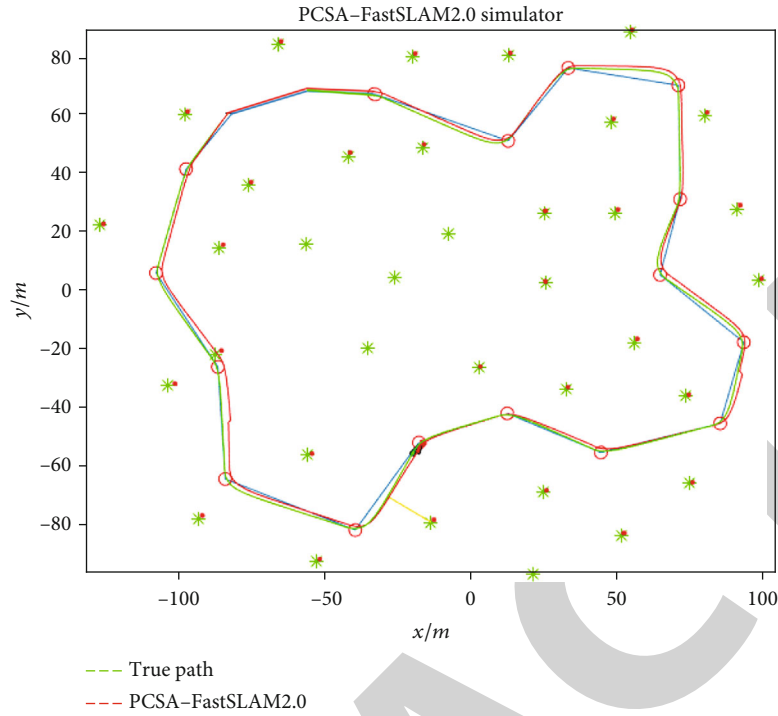


FIGURE 9: PCSA-FastSLAM2.0 simulation result.

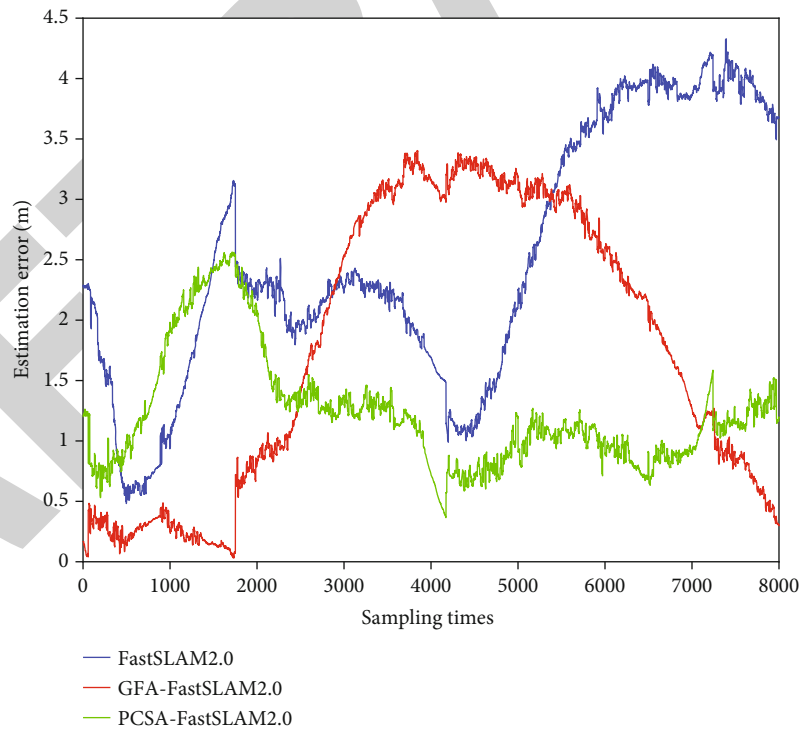


FIGURE 10: Comparison chart of robot localization accuracy error.

In order to verify the improvement effect of the improved algorithm on the robot localization accuracy, compare the mean error and variance of the localization accuracy of the three algorithms, as shown in Table 5.

In the above table, the PCSA-FastSLAM2.0 has the lowest mean error value and the smallest variance of positioning accuracy, which indicates that the PCSA-FastSLAM2.0 improves the localization accuracy, also improving the

TABLE 5: Comparison of mean error and variance of localization accuracy of three algorithms.

Algorithm	Mean localization accuracy error (m)	Variance of localization accuracy error	Improvement rate of localization accuracy (%)	Improvement rate of stability (%)
FastSLAM2.0	2.5479	1.0754		
GFA-FastSLAM2.0	1.6728	1.3949	35%	-29%
PCSA-FastSLAM2.0	1.2309	0.2101	62%	81%

TABLE 6: Comparison of x -axis, y -axis and road sign RMSE estimation of three algorithms.

Algorithm	RMSE of x -axis (m)	RMSE of y -axis (m)	RMSE of road sign estimation (m)
FastSLAM2.0	1.9634	2.2563	2.8910
GFA-FastSLAM2.0	1.3695	0.9363	1.6485
PCSA-FastSLAM2.0	0.8036	0.7235	1.0415

stability at the same time, while in the strategy of adjusting the sampled particles in GFA-FastSLAM2.0, it makes the sampled particles centrally distributed near the global optimal value, because of the unique strategy of simulating the gravitational field; that is, the central dust attracts and repels the surrounding dust and adjusts the particle distribution. This is the reason why the accuracy of the GFA-FastSLAM2.0 is improved. At the same time, the stability of the algorithm decreases due to the unique optimization mechanism.

In order to verify the degree of improvement in the accuracy of robot localization and mapping, respectively, compare the RMSE of the x -axis, y -axis, and road signs, as shown in Table 6.

From Table 6, it can be seen that the PCSA-FastSLAM2.0 is better than FastSLAM2.0 and GFA-FastSLAM2.0 algorithms in the x -axis, y -axis, and road sign estimation. This is because the improved algorithm efficiently optimizes the particles after importance sampling and produces the best effect, and this also shows that the optimization of particles in PCSA-FastSLAM2.0 is better than GFA-FastSLAM2.0. The main reason is that the unique particle optimization method in PCSA-FastSLAM2.0 simulates the stimulation of auxin on plant cells, and the more distant the particle is from the global optimal value, the more obvious the optimization effect is. Therefore, PCSA-FastSLAM2.0 has the highest prediction accuracy.

6. Conclusion

This paper proposes an improved particle filter algorithm based on the plant cell swarm algorithm (PCSA-PF) and applies it to the robot autonomous mobile mapping. By improving the particle distribution after importance sampling, this algorithm guides the particle set to be distributed in the high-likelihood area, and the farther the particle is from the global optimal value, the stronger the optimization effect of the algorithm. In the experimental verification of particle filtering, the improved algorithm effectively allevi-

ates the problem of particle weight degradation and improves the particle diversity, so as to improve the filtering accuracy and achieve a higher filtering accuracy through a small number of particles in the strong noise scene. In the experiment of SLAM, the robot receives the wireless communication command and moves; the localization accuracy and the stability greatly are improved. However, in the simulator used in this paper, the environment of the robot is a static environment, which is different from the actual working environment of the robot. In the future, the feasibility of the algorithm proposed in this paper will be further verified through robot experiments.

Data Availability

The datasets used and analyzed during the current study are available from the corresponding author on reasonable request.

Conflicts of Interest

The authors declare that they have no conflicts of interest.

Acknowledgments

This work is partially supported by the National Natural Science Foundation of China (No. 61302133), Key Research and Development Program of Shaanxi Province of China (No. 2021GY-338), and Xi'an Beilin District Science and Technology plan project (No. GX1930).

References

- [1] S. S. Moghaddasi and N. Faraji, "A hybrid algorithm based on particle filter and genetic algorithm for target tracking," *Expert Systems with Applications*, vol. 147, article 113188, 2020.
- [2] J. A. Nunez, D. I. Singham, and M. P. Atkinson, "A particle filter approach to estimating target location using Brownian bridges," *Journal of the Operational Research Society*, vol. 71, no. 4, pp. 589–605, 2020.
- [3] A. Stentz, D. Fox, M. Montemerlo et al., "FastSLAM: a factored solution to the Simultaneous localization and mapping problem with unknown data association," in *Proceedings of AAAI National Conference on Artificial Intelligence*, pp. 240–248, Edmonton, AB, USA, 2002.
- [4] D. Jiahui, X. Pengcheng, and L. Xiaobo, "FastSLAM algorithm of second-order central difference particle filter," *Control Theory and Applications*, vol. 35, no. 9, pp. 1382–1390, 2018.
- [5] M. Montemerlo, S. Thrun, D. Koller, and B. Wegbreit, "FastSLAM2.0: an improved particle filtering algorithm for simultaneous localization and mapping that provably converges," in

Retraction

Retracted: Application of Wireless Communication Technology in Construction Project Information Management

Wireless Communications and Mobile Computing

Received 28 November 2023; Accepted 28 November 2023; Published 29 November 2023

Copyright © 2023 Wireless Communications and Mobile Computing. This is an open access article distributed under the Creative Commons Attribution License, which permits unrestricted use, distribution, and reproduction in any medium, provided the original work is properly cited.

This article has been retracted by Hindawi, as publisher, following an investigation undertaken by the publisher [1]. This investigation has uncovered evidence of systematic manipulation of the publication and peer-review process. We cannot, therefore, vouch for the reliability or integrity of this article.

Please note that this notice is intended solely to alert readers that the peer-review process of this article has been compromised.

Wiley and Hindawi regret that the usual quality checks did not identify these issues before publication and have since put additional measures in place to safeguard research integrity.

We wish to credit our Research Integrity and Research Publishing teams and anonymous and named external researchers and research integrity experts for contributing to this investigation.

The corresponding author, as the representative of all authors, has been given the opportunity to register their agreement or disagreement to this retraction. We have kept a record of any response received.

References

- [1] J. Zhang, X. Guo, and Y. Xu, "Application of Wireless Communication Technology in Construction Project Information Management," *Wireless Communications and Mobile Computing*, vol. 2021, Article ID 8174600, 7 pages, 2021.

Research Article

Application of Wireless Communication Technology in Construction Project Information Management

Jie Zhang ¹, Xin Guo ², and Ying Xu ³

¹School of Civil and Environmental Engineering, The University of New South Wales, Sydney, Australia 430071

²School of Economics and Management, Jinzhong University, Jinzhong, Shanxi, China 030619

³Shanxi Professional College of Finance, Taiyuan, Shanxi, China 030008

Correspondence should be addressed to Jie Zhang; z5123256@zmail.unsw.edu.au

Received 28 July 2021; Accepted 11 August 2021; Published 29 August 2021

Academic Editor: Balakrishnan Nagaraj

Copyright © 2021 Jie Zhang et al. This is an open access article distributed under the Creative Commons Attribution License, which permits unrestricted use, distribution, and reproduction in any medium, provided the original work is properly cited.

With the replacement of the times, the electronic information technology of all countries in the world has developed rapidly, and 4G mobile communication technology has also obtained the opportunity of development, which has improved the transmission speed of 5G mobile communication technology, which has been widely used in intelligent information management of construction engineering. Under this background, this paper selects the research methods of theory guiding practice and practice updating theory to guide the application of information technology. Based on the actual engineering cases, this paper discusses the scientific process of information management construction of construction projects from the perspective of BIM Technology by taking the specific construction details as the starting point. Firstly, this paper systematically introduces the key technologies of BIM and the related concepts and basic contents of construction project management informatization, expounds and analyzes the three construction modes that should be followed by construction project collaborative management informatization, and puts forward the key and main contents of standardization construction. Then, taking New York freedom building as an engineering case, this paper analyzes the application of building information modeling (BIM) in the architectural design of New York freedom building. Relevant research can provide theoretical and practical references for realizing and ensuring the combination of project management and information technology.

1. Background

In recent years, in order to accelerate the process of informatization management of construction projects, my country has successively issued the “Twelfth Five-Year Development Plan for the Construction Industry” and the “2011-2015 Outline for the Development of the Construction Industry Informatization,” both of which clearly pointed out the following: emerging intelligent management tools, such as BIM Technology, Internet of Things technology, 5G mobile communication technology, and 4D smart vision have greatly strengthened the intelligent control and management of engineering construction [1], so it is very necessary to further develop and construct information intelligent management tools. In mid-2016, the Party Central Committee issued the “2016-2020 Construction Industry Information Development Outline,” further planning the overall develop-

ment of the construction industry, which emphasized the importance of information technology such as building information modeling and construction management information systems [2]. In addition, the document also pointed out that the current society’s construction information management technology is far from reaching the expected goal, and the entire construction industry alone has generated huge technical needs for it, especially construction engineering information management and modern emerging mobile communications. The integration of technology will greatly promote the efficiency of construction engineering information management.

“Internet+” brings new opportunities to the development of the times and leads all fields into the era of information management. As a leader in the field of construction engineering, project management must adapt to the changes in the new era. In addition, with the rapid development of

science and technology, mobile communication technology has also made a qualitative leap [3, 4]. As a result, 5G wireless communication technology, which not only covers a wide range but also has high-speed transmission speed, is on the stage, which brings good development opportunities for the development of construction project management information [5]. The analysis of hot topics in domestic and foreign research shows that the life cycle management of construction projects is currently a hot topic in the construction industry. The key to achieving this goal is to establish an information model, which is now called BIM (building information modeling) technology.

The monitoring and control of construction progress is a long-term and dynamic development process, which requires the continuous update of on-site data and the generation of a large amount of information. With the continuous development of the construction progress of the project, the progress information of the project will continue to increase dynamically. And some information in the construction process can be used in the later stages of the building, such as the operation and maintenance stage, thereby contributing to the life cycle of the building [6, 7].

The information generated in the process of building construction monitoring and control is dynamic and real-time development, so it is necessary to keep, share, and manage the information generated in the construction process, so as to facilitate all parties involved in the construction project to obtain the information in a time when the construction project information changes and avoid unnecessary rework due to information errors in the later stage. As a comprehensive and coordinated information database, BIM has incomparable speed and portability in obtaining the required information and realizing information sharing [8]. Based on this advantage, the application of BIM Technology in practical engineering projects has become the common expectation of all participants and also promotes all parties to make better use of information for their own adjustment, so as to promote the better realization of construction projects.

BIM Technology can be applied to the storage and query of information in the whole life cycle of construction projects. It can effectively sort out and track the transmission and change of construction information from one stage to another, avoiding "information interruption" and information loss. Another function of BIM Technology is to reduce information fuzziness and unconformity. The research on BIM by many scholars at home and abroad also fully reflects the feasibility and value of the application measures taken by BIM Technology in the design and implementation of construction projects. Therefore, BIM Technology is widely applied to the dynamic real-time construction monitoring and management system of the construction industry, which can effectively provide excellent solutions for the fields of dynamic monitoring data information integration and analysis of the construction industry and resource sharing.

For the practical application value of BIM Technology, this paper will select an engineering example to show the working path of project management. At the same time, in order to promote the technology to comply with the require-

ments of the development of the times and meet the development needs of modern architecture, it is also necessary to point out the limitations and defects of existing models in the process of practical case application, promote the technology to keep pace with the times, and give full play to the characteristics and advantages of BIM Technology in the practical application of the construction industry. By analyzing the improvement and upgrading of traditional project management by BIM Technology, this paper obtains the advantages of project management based on BIM Technology compared with traditional project management.

2. BIM Key Technology and Construction Project Information Construction

2.1. BIM Key Technology. Based on the realization of the 3D building model, BIM Technology realizes the sharing of information generated by the 3D building model among all participating departments of the building. By connecting all stages of the whole construction life cycle of the construction project with each department one by one, it truly realizes the unified application and management of information. For each stage, each department forms a complete, comprehensive interpretation of guidance. All departments of the construction project have access to the same 3D building model, and all the building information is added to the model to facilitate the extraction of the necessary information. Through such analysis, we can know that BIM Technology has the advantages of integrating, managing, and sharing all information in the whole life cycle of buildings. It can not only achieve certain coordination and consistency in the transmission and use of drawings, data, and other information in the profession. More importantly, it can also easily realize the information sharing, extraction, and use of timeliness and accuracy of information in different majors.

In order to perfectly realize the functional benefits brought by BIM Technology, it is also necessary to create an information application platform, which can uniformly manage the project construction information of all participants in the project and, based on the information application platform, create an open information model that can exchange and communicate, namely, IFC; thus, a 3D building information exchange application model is established.

Tracing the development process of BIM Technology, it can be seen that it originated in the United States, but it has developed rapidly. In just a few years, it has been applied and promoted by many countries, such as Britain, Switzerland and other European countries, Japan, Singapore, and other developed countries. The application of BIM Technology in China started late, and it began to talk about BIM Technology after 2002 at the earliest. He Guanpei, a famous research scholar in China, proposed that since the BIM model is the basis for supporting the whole BIM process, the core of the BIM software also lies in the BIM modeling software (see Figure 1).

2.2. Application Value of BIM Technology. Through practical application, it can be seen that BIM Technology is more or less applied in different stages of the whole life cycle of

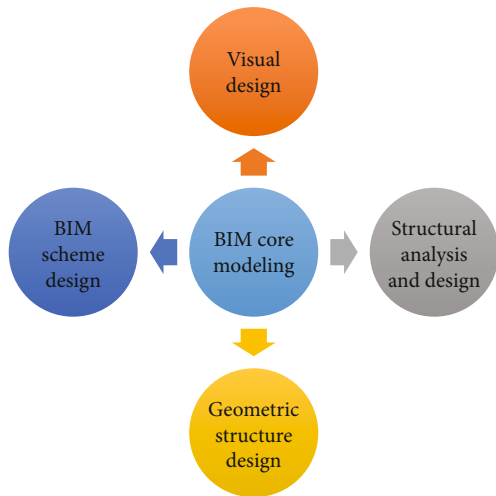


FIGURE 1: BIM software category summary.

construction projects. The following is mainly explained from two aspects: engineering design and project management.

2.2.1. Intelligent Engineering Design. When the collaborative management application of construction projects is realized in the actual project, the designers of the company can make full use of the 3D rendering function of BIM Technology to carry out relevant operations on the mode of construction projects, simulate the actual scene of buildings, and render the documents and images of buildings and scenes through the change of data and mode. When there are changes related to the 3D model, the corresponding files and drawings can be automatically updated. After that, construction management such as joint design can be carried out.

2.2.2. Information-Based Project Management. In the previous construction project information collaborative management, paper is often used. This paper method is greatly affected by human subjective factors. If there is improper storage or loss in the process of mutual transmission, all kinds of data and information on this paper will be distorted and produce wrong information, which will affect the information of construction projects and the management quality of a large number of data. Therefore, in the information management of construction projects, the use of BIM Technology effectively overcomes the defects existing in the information management of existing construction projects and avoids the problems of confusion or lack of information. On this basis, participants can also use the information query service function provided by the information management system and database to quickly obtain the necessary construction project data, so as to more efficiently optimize the work efficiency and quality of project data management.

2.3. Application Outline of Civil Engineering Information Management Technology. First, construction enterprises should pay attention to the comprehensive application of information technology. There are a lot of manual operations in the management process, which has a certain nega-

tive impact on the reliability, integrity, and quality of construction enterprise information.

Second, construction engineering enterprises need to constantly absorb experts with professional information management talents and strengthen their own talent management team. At present, the level of hardware equipment of many construction companies has been greatly improved, but the informatization of enterprise internal management is still at a low level. Some new procurement information management software has not been fully developed, so it is necessary to further improve the informatization management level.

Third, construction engineering enterprises must pay attention to the phased development process of information management and replan the construction of enterprise information management in the heyday of strategic development. At the same time, we should also pay attention to the system planning process and put forward practical information management solutions according to the current financial situation, personnel, equipment, technical situation, and market situation of the enterprise, so as to reduce the resistance of information management in the application process.

3. Construction Enterprise Project Management Information Construction

In the whole process of the implementation of construction project management, in order to realize the informatization of construction, we must not only need mature software system products and stable hardware operating environment but also establish a set of the corresponding management system, management framework, and good cultural atmosphere. These are the necessary conditions for the construction industry to implement project management informatization. As shown in Figure 2, the basic preparation for project management informatization in the construction industry is mainly carried out in four steps.

For the buzzsaw platform, project participants provide leasing services through the approved project management platform, and all participants save project shared information through the central database of the network. The comparison of the characteristics of the three methods is shown in Figure 3.

It can be seen from Figure 3 that among the three informatization management methods, each has its own advantages. Therefore, the author establishes the project management informatization standard system according to its advantages, and the overall block diagram is shown in Figure 4.

The overall block diagram is composed of standard content, standard level, and professional categories. The standard system table is shown in Tables 1 and 2.

4. Application of BIM Key Technology in Construction Project Management

The freedom building in New York is the first building built on the former site of the world trade building. The freedom



FIGURE 2: Project information construction preparation.

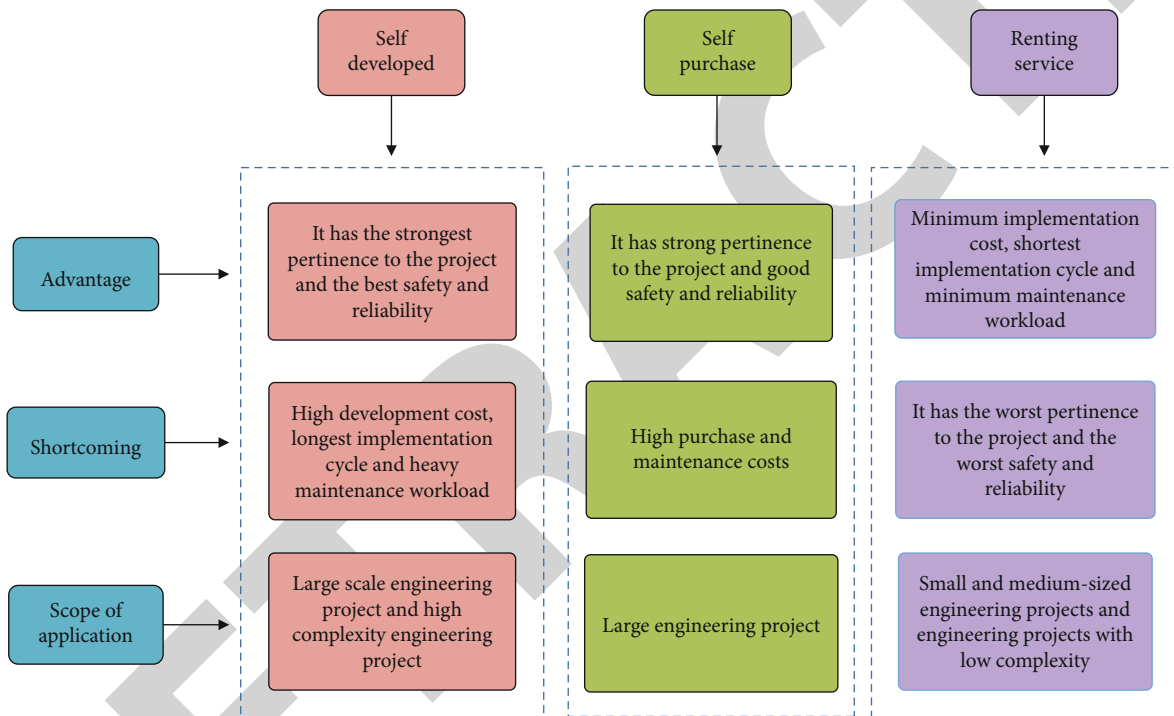


FIGURE 3: Comparison of three construction project information management methods.

building is equipped with world-class restaurants, viewing platforms, and the most advanced news broadcasting facilities. In addition, other interior design places of the building adopt the highest level of design technology to achieve the purpose of building safety, sustainability, and quality. The project is of great significance to the United States. Its completion will mark the development of a new generation of buildings. SOM and other companies have established cooperation with Autodesk consulting company to realize the Autodesk Revit architectural information modeling platform, so as to successfully complete this innovative architectural design.

The freedom building project in the United States is a complex building with a height of about 450 meters and a rotation of 40 degrees. The building is designed to reduce the wind power of the Hudson River and realize the purpose of dispersing wind power. In other words, the layout of each

floor of the building is different. In addition, the broadcast antenna on the top of the freedom building is a steel cable, which plays a role as a wind turbine to generate building power. The design style of the freedom building corresponds to the design style of the Brooklyn Bridge.

Any complex design needs to rely on advanced computer technology, because as long as there is a small error, it may cause high cost and construction delay during the construction period. After screening various industry software, SOM selects Autodesk Revit as the priority architecture design tool of the project to realize the seamless integration of the other two components of the building information modeling platform and generate the proposed structural solution in real time. In the design process, when the model data is updated, all project participants in other fields can display the latest and complete information of the whole project in real time. In addition, the software also

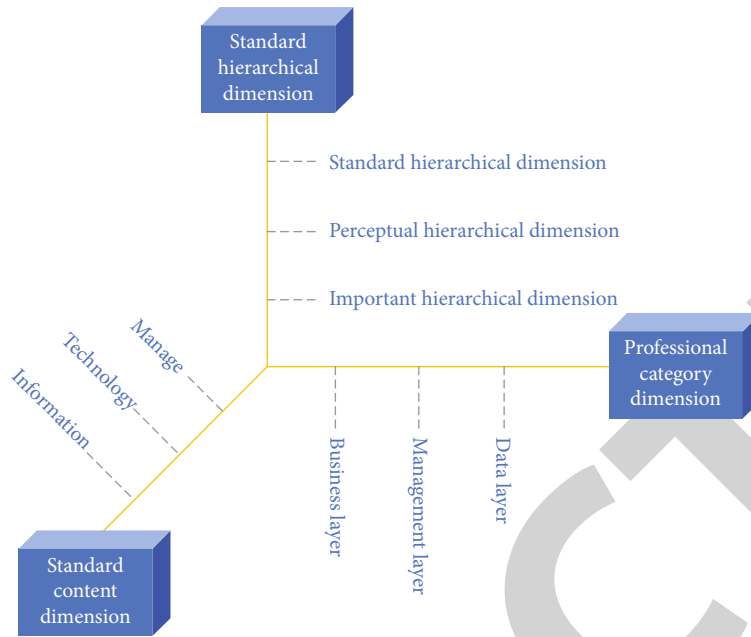


FIGURE 4: Project management informatization standard system.

TABLE 1: Basic standard system.

System coding	Standard name
1.1	Terminology standard
1.1.1	Standard for basic terms of engineering management informatization
1.2	Text graphic symbol standard
1.2.1	Standard for text and graphic symbols of engineering management information system
1.2.2	Unified standard for electronic documents of engineering management
1.3	Information classification and coding standard
1.3.1	Classification and coding standard of engineering management information
1.3.2	Application data classification and coding standard in the field of engineering management informatization

TABLE 2: Special standard system.

System coding	Standard name
2	Application system specific standards
2.1	Technical specification for collaborative construction information system
2.2	Technical specification for supervision behavior system
2.3	Technical specification for on-site real-time monitoring
2.4	Technical specification for construction quality management system
2.5	Site safety and health management standards

facilitates extensive design cooperation. In the original design process, when the designer changes the very complex part, it is often discussed around the design drawing. With the help of the Revit platform, the architect only needs to open the model on the screen and change the area to be adjusted.

Taking freedom tower as an example, Autodesk Revit structure software can help architects effectively improve the integrity and coordination of the project in the field of engineering construction. This is because the building information modeling can adjust its own model according to needs, so it can greatly save design time and design change time. Instead of marking the problem in red, the project leader waited a week to obtain the image of the building column in real time. Using Autodesk consulting software, SOM divides the project into five parts: foundation, core structure,

around the foundation, around the main tower, and spire. It can be seen that the Revit platform is a technological revolution, which has made outstanding contributions to the construction of freedom building.

5. Countermeasures for Information Technology to Improve the Effect of Collaborative Management of Construction Projects

5.1. Make Full Use of Big Data Technology to Strengthen the Information Management Awareness of Senior Managers. In order to improve the effectiveness of collaborative management of construction projects, construction enterprises must make maximum use of big data technology. After nearly 10 years of development, China's construction industry continues to expand, and construction technology and equipment are constantly updated. The application of big data technology to the construction of information in the

construction industry can significantly improve the practical application level of project collaborative management.

5.2. Make Efficient Use of Cloud Technology to Build a Comprehensive Information Management Platform. Facing the development of modern technology, China's construction industry needs to make maximum use of cloud computing technology, build an information collaborative management platform, and promote the all-round promotion of the information management mode. Construction engineering companies can make full use of this good market environment to build their own companies, promote the development of the company, improve the level of construction technology, and improve the efficiency of management.

5.3. Improve the Informatization Management Level of Project Managers. The engineering company can implement special technical training for information technology implementers, actual operators, and persons in charge of later maintenance. Finally, the construction engineering company forms standardized measurement standards by holding lectures and training, checks the learning achievements of employees, and regularly checks the status of employees using information technology to guide their work.

5.4. Make Efficient Use of Mobile Communication Technology to Speed Up the Project Informatization Audit. The engineering construction company should not only further improve the quality level of project information construction and improve the scientific effectiveness of project quality supervision and management but also make full use of wireless communication technology to speed up the audit of project information construction. Because the project management of a construction enterprise often has obvious timeliness and periodicity, in the progress and development of modern construction enterprises, wireless communication technology can establish an effective wireless communication conveyor belt for the financial management, design department, construction management, human resources, and management of the whole construction enterprise. With this frequent communication from the construction site and project management process, effective communication with the project manager can be effectively improved. The wide application of mobile communication technology will greatly change the specific operation and management mode of construction engineering enterprises. Through the research and development of wireless communication technology, architectural designers can transfer the special conditions of the construction site under certain conditions to the actual application design drawings of construction engineering construction in real time. In addition to the above means, construction engineering enterprises can also use the development of remote control technology and remote supervision technology to strengthen the effective supervision and management of construction sites.

To sum up, the use of information management technology can reduce the waste of resources in construction project management and improve the integrity of management. From the analysis of this paper, it can be seen that the

research on the application of informatization in construction engineering management will help construction engineering enterprises to see the shortcomings in the current enterprise engineering management process from the perspective of problems and upgrade the management scheme pertinently. Therefore, construction enterprises should pay more attention to information technology and explore countermeasures to improve the effectiveness of management in management practice.

6. Conclusion

Modern construction projects are gradually driven in the direction of complexity and large scale. The complex building structure has brought unprecedented challenges to the engineering construction management industry. The traditional project management model can no longer meet today's complex project management needs. Therefore, BIM Technology appears in people's vision without solving the problems. BIM Technology uses the latest information collection, processing, analysis, and sharing technology to integrate a large number of complex engineering information into a unified work platform according to the unified IFC standard. All relevant personnel related to the project can retrieve and query data and information related to the project. Therefore, BIM Technology provides a rapid and convenient communication method for all participants in engineering construction. At the same time, it ensures the real-time update of project information and the synchronization of information of all relevant personnel after information change.

Data Availability

Data sharing is not applicable to this article as no datasets were generated or analyzed during the current study.

Conflicts of Interest

The authors declared no potential conflicts of interest with respect to the research, authorship, and/or publication of this article.

References

- [1] J. Wang, J. Tang, Z. Xu et al., "Spatiotemporal modeling and prediction in cellular networks: a big data enabled deep learning approach," in *IEEE INFOCOM 2017-IEEE Conference on Computer Communications*, pp. 1–9, Atlanta, GA, USA, May 2017.
- [2] B. Ai, K. Guan, M. Rupp et al., "Future railway services-oriented mobile communications network," *IEEE Communications Magazine*, vol. 53, no. 10, pp. 78–85, 2015.
- [3] Z. Henrique and C. Luiz, "Designing the Car2X-Communication infrastructure based on the Internet of Things for the Curitiba public transport system," *IFAC-Papers on Line*, vol. 49, no. 30, pp. 239–244, 2016.
- [4] E. Ndashimye, S. K. Ray, N. I. Sarkar, and J. A. Gutiérrez, "Vehicle-to-infrastructure communication over multi-tier heterogeneous networks: a survey," *Computer Networks*, vol. 112, pp. 144–166, 2017.

Retraction

Retracted: The Development of Data Acquisition System of Formula SAE Race Car Based on CAN Bus Communication Interface and Closed-Loop Design of Racing Car

Wireless Communications and Mobile Computing

Received 28 November 2023; Accepted 28 November 2023; Published 29 November 2023

Copyright © 2023 Wireless Communications and Mobile Computing. This is an open access article distributed under the Creative Commons Attribution License, which permits unrestricted use, distribution, and reproduction in any medium, provided the original work is properly cited.

This article has been retracted by Hindawi, as publisher, following an investigation undertaken by the publisher [1]. This investigation has uncovered evidence of systematic manipulation of the publication and peer-review process. We cannot, therefore, vouch for the reliability or integrity of this article.

Please note that this notice is intended solely to alert readers that the peer-review process of this article has been compromised.

Wiley and Hindawi regret that the usual quality checks did not identify these issues before publication and have since put additional measures in place to safeguard research integrity.

We wish to credit our Research Integrity and Research Publishing teams and anonymous and named external researchers and research integrity experts for contributing to this investigation.

The corresponding author, as the representative of all authors, has been given the opportunity to register their agreement or disagreement to this retraction. We have kept a record of any response received.

References

- [1] Z. Li, D. Wang, and Q. Kang, "The Development of Data Acquisition System of Formula SAE Race Car Based on CAN Bus Communication Interface and Closed-Loop Design of Racing Car," *Wireless Communications and Mobile Computing*, vol. 2021, Article ID 4211010, 18 pages, 2021.

Research Article

The Development of Data Acquisition System of Formula SAE Race Car Based on CAN Bus Communication Interface and Closed-Loop Design of Racing Car

Zhonghao Li , Da Wang , and Qiao Kang

Jilin University, College of Automotive Engineering, Jilin University, Changchun, China

Correspondence should be addressed to Da Wang; wangda_gspeed@jlu.edu.cn

Received 21 June 2021; Revised 13 July 2021; Accepted 23 July 2021; Published 26 August 2021

Academic Editor: Balakrishnan Nagaraj

Copyright © 2021 Zhonghao Li et al. This is an open access article distributed under the Creative Commons Attribution License, which permits unrestricted use, distribution, and reproduction in any medium, provided the original work is properly cited.

This paper is mainly based on the college formula race car, through the application of CAN bus communication interface settings, the layout and adjustment of the car sensors, and then carry out the data collection and analysis of the car. CAN bus is the local area network of controller and is one of the field bus which is put forward by German Bosch company and applied most widely in the world. The development of the data analysis system is mainly based on the MoTeC i2 data analysis software. MoTeC i2 data analysis software has been developed for many years under the continuous research of professional teams all over the world. According to the data analysis requirement of FSAE undergraduate Formula 1 teams, this paper introduces a series of data analysis methods closely related to FSAE, mainly including data channel research. This paper expounds the reliability, suspension, tire temperature, steering, and braking data analysis, respectively. Based on the data analysis template created by Motec i2, this paper conducts analysis and basic application according to the data of the real car, so as to meet the requirements of verifying design made by simulation model and tuning the real car scientifically. By means of wheel speed sensor, acceleration sensor, displacement sensor, multichannel temperature sensor, and so on, we conduct a series of tests on 2020 season car, including endurance test, linear acceleration experiment, steady rotation, etc., evaluate the data collected, and then carry on a reasonable set-up of racing, ultimately improving lap speed.

1. Introduction

Formula SAE (FSAE) was first proposed by an American factory in 1978. This race is held for college students to collect small formula cars with creative design and scientific ideas. These cars are stable and durable in all aspects of performance. Compared with foreign countries, our domestic college student formula racing started late. The first Formula Student China (FSC) competition was held at the Shanghai International Circuit in 2010. Formula Student of China ("China FSC") is a car design and manufacturing competition organized by students majoring in automotive engineering or automotive related in universities. Each participating team in accordance with the rules of the race and racing car manufacturing standards, in one year's time to design and manufacture a small single-seat recreational racing car in the acceleration, braking, handling, and other aspects of

excellent performance, can successfully complete all or part of the race links. China FSC is committed to building a public platform for the training and selection of outstanding domestic automotive talents, and through general assessments to improve students' comprehensive capabilities in five aspects, including design, manufacturing, cost control, commercial marketing, communication, and coordination. In order to improve the comprehensive quality of automotive students, make long-term talent accumulation for the development of China's automotive industry, and promote the strategic direction of China's automotive industry from a "manufacturing country" to an "industrial power" [1]. Gspeed Electric Racing Team of Jilin University has participated in the FSC series for 5 consecutive years. In 2019, it went to Japan to participate in the Formula Student Japan and won the second prize of design project many times. In 2018, it won the first prize of the FSC. GspeedE-2019 and

GspeedE-2020 race cars are shown in Figures 1 and 2, respectively. When we design a racing car, we often fail to make a reasonable design for some parameters of each system, and the rough design fails to support and prove the completed design with data. Therefore, we installed a data acquisition system on our race car, that is, the sensors we need and the wiring harnesses which connect them to a low-voltage electrical system and panel. Then, we used MoTec i2 to deal with the data we collected. Due to the large proportion of engineering design events and dynamic events in Formula Student [2], data analysis of race cars, which plays an important role in verifying design, guiding tuning, and further contributing to future design, do show its important value. Therefore, we do research on analysis methods of race cars and put it into practice by using MoTec i2 templates and math channels, which quickly analyze the large amount of data generated by each test. In this way, we obtain the direction of tuning and improve the performance of our car.

At the same time, the data acquisition and analysis system of the whole car is a feedback system for driver training and making suggestions for tuning [3]. Through scientific road test and data analysis, the whole process can form a closed-loop design. In addition, the driving habits and styles of different drivers can be summed up by recording and analyzing the same project they conduct. In this way, different car set-up methods can be matched for different drivers. Figure 3 shows the flow chart of data collection and analysis of the race car.

The sensor interface setup and connection of the vehicle are based on CAN bus communication protocol, among which, the car has three CAN communication networks:

- (1) Motor control network, connecting the vehicle controller with the motor controller, to realize the function of sending the torque instruction of the drive system and obtaining the working state of the motor of the drive system
- (2) The conventional information communication network realizes the information transmission between the vehicle controller and the battery management system, instrument panel, sensors, and other equipment
- (3) In order to charge the communication network, the experimental information transmission between the battery management system and the charger

Using the MoTeC C125 racing digital instrument, ECU uses CAN-B to collect and record training data for improved vehicle performance.

Figure 4 shows the CAN bus network of the whole vehicle.

2. Reliability Data Analysis

As we know, one of the most important functions of the data acquisition system is to find the potential faults of race car by monitoring the reliability data, which determines whether the car can run normally or not. So we should make obtaining and checking reliability data a top priority. Once anything abnormal is found, stop the car immediately and



FIGURE 1: GspeedE-2019 racecar.



FIGURE 2: GspeedE-2020 racecar.

troubleshoot the fault. For Formula E racing, the important reliability data consist of high voltage battery voltage, high voltage battery temperature, motor output power, low voltage battery voltage, etc. Second, there are some reliability indicators, such as tire pressure, and brake pressure. Figure 5 is the reliability data template.

To check the reliability data, the first step is to observe the maximum and average values of each channel, and the second step is to examine its changing trend. The observation of maximum value can determine whether the data is within safe range, while the observation of variation trend can determine whether the car is running normally during the whole process and can predict the state of the car when running continuously. Especially in endurance test, the data of battery temperature and power usually change linearly.

In order to know the condition of reliability parameters during each run, we set up an alarm mechanism on the car instrument panel. In the endurance race, it is one of the key factors to detect abnormal reliability parameters in advance and make a right decision.

Similarly, an alarm mechanism can be set in the data analysis software to find out the problematic channel data in the first time.

If the voltage provided by the power battery is found to be too low, it is considered that the power supply system of the battery box body has poor contact and the battery module bolts have loosened. At this time, the battery box should be inspected and the battery management system (BMS) should be used for fault detection.

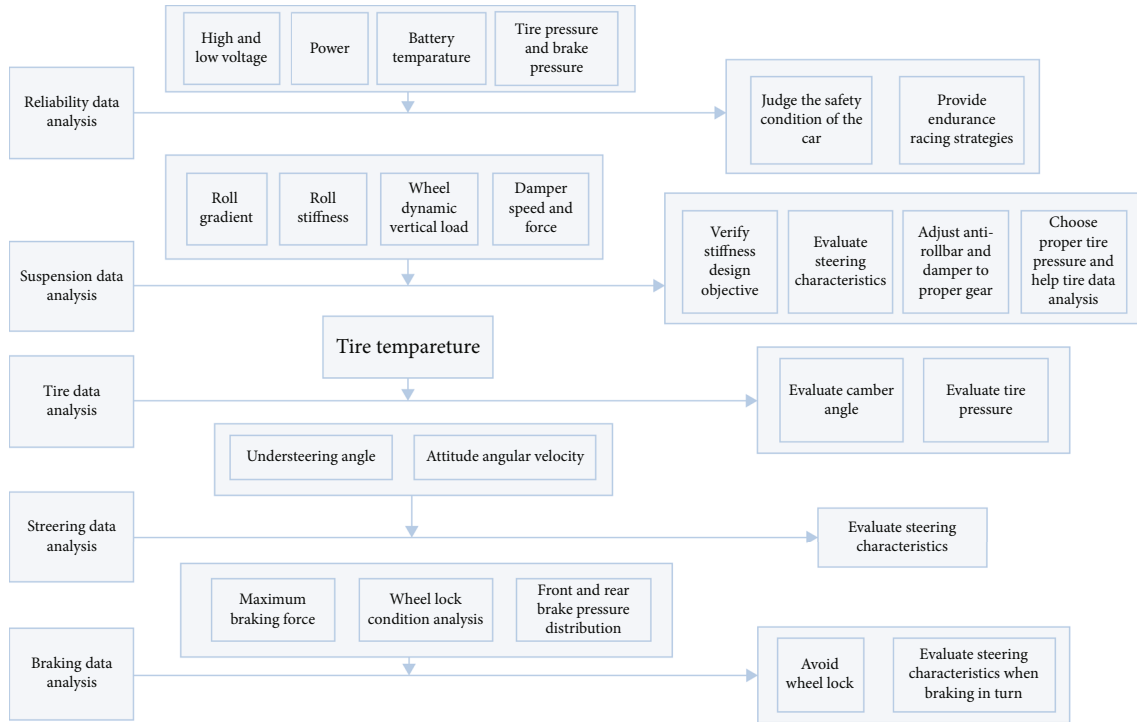


FIGURE 3: Flow chart of data collection and analysis for racing car.

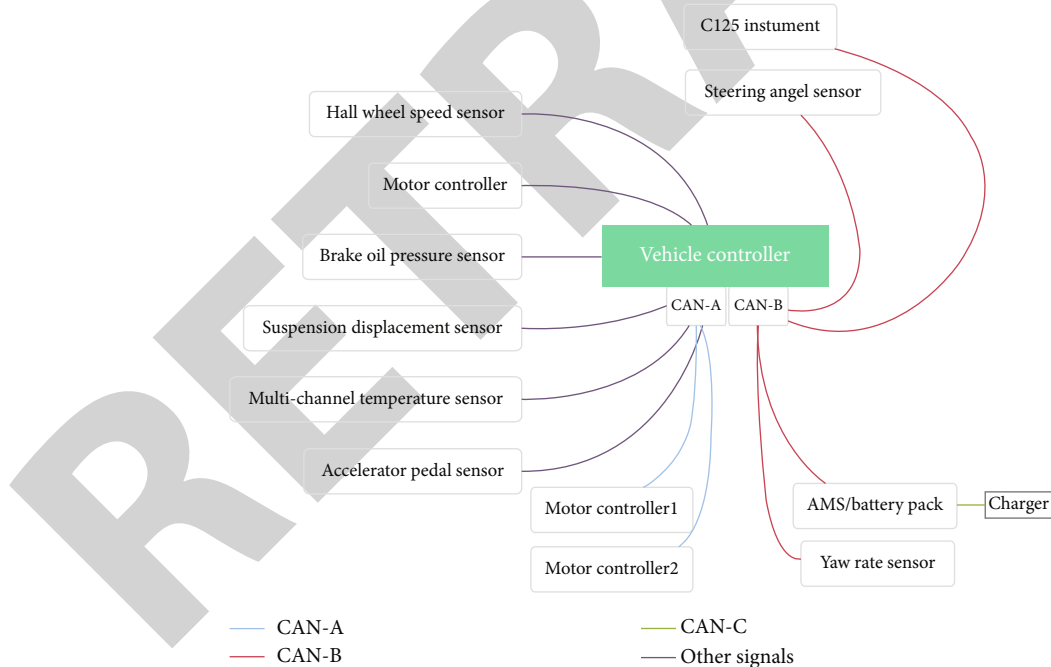


FIGURE 4: Vehicle CAN network.

3. Suspension System Data Analysis

The suspension system of this season’s Gspeed formula E racing car is an independent suspension of unequal length, with a third spring system and a T-shaped anti-roll bar.

This part includes the calculation of roll gradient and roll stiffness, load transfer, and the analysis of shock absorber.

The purpose of suspension data analysis is to verify the design and guide the adjustment through the compilation and processing of the data. Detailed tuning projects consist of tire pressure, shock absorber gear, antiroll bar stiffness, load distribution of front and rear tires, adjusting four-wheel positioning parameters, and carrying out the corresponding fault troubleshooting.

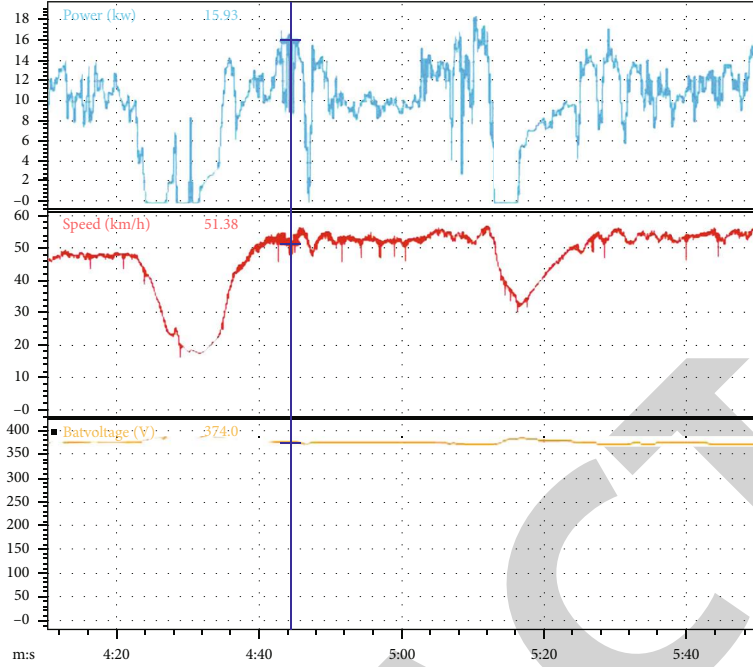


FIGURE 5: Reliability data template.

3.1. Roll Gradient (RG) Analysis. In vehicle dynamics, roll gradient refers to the roll angle of a vehicle per unit lateral acceleration.

Equation (1) is the definition formula of roll gradient RG.

$$RG = \frac{\alpha_{\text{roll}}}{G_{\text{lat}}}. \quad (1)$$

In the above formula, α_{roll} is roll angle (deg); G_{lat} is lateral acceleration (g).

Therefore, in order to calculate the roll gradient, the first parameter we need to get is the roll angle. The following is the mathematical channel formula of the front and rear suspension roll angle α_F and α_R and the total suspension roll angle α . In order to get the roll angle of the vehicle, the left and right suspension displacements should be calculated, and the trigonometric function formula should be used to solve the problem. Table 1 shows the vehicle parameters required by formulas (2)–(4).

$$\alpha_F = \text{ArcTan} \left[\frac{(x_{\text{SuspLF}} - x_{\text{SuspRF}})MR_F}{T_F} \right] \cdot \frac{180}{\pi}, \quad (2)$$

$$\alpha_R = \text{ArcTan} \left[\frac{(x_{\text{SuspLR}} - x_{\text{SuspRR}})MR_R}{T_R} \right] \cdot \frac{180}{\pi}, \quad (3)$$

$$\alpha = \text{ArcTan} \left[\frac{(x_{\text{SuspLF}} - x_{\text{SuspRF}})MR_F + (x_{\text{SuspLR}} - x_{\text{SuspRR}})MR_R}{T_F + T_R} \right] \cdot \frac{180}{\pi}. \quad (4)$$

Among these parameters, suspension displacement is what we should detect. It can be obtained by measuring the

displacement of the shock absorber with the traditional linear displacement sensor. And when the suspension arrangement style is not suitable for using displacement sensor (for instance, a decoupling suspension with single spring mounted between two rockarms), we can use angular displacement sensor to get suspension displacement indirectly by measuring rockarm rotation angle. The angle and the suspension displacement usually have high linearity, whose linear coefficient can be fitted by means of parallel wheel jump simulation in Adams-Car [2]. After this work, what we need to do is to set up math channel in MoTec i2. Figure 6 shows the template of suspension system roll angle data.

It should be noted that the roll angle calculated from the suspension displacement is only the roll angle caused by the lateral transfer of sprung mass, that is, the suspension roll angle. Therefore, the following calculation is also the roll gradient of the suspension system using the roll angle of the suspension.

Then, we create a scatter graph with the vertical axis as roll angle and the horizontal axis as lateral acceleration and obtain the trend line equation, whose slope is the roll gradient of the suspension system. Figure 7 is the roll gradient diagram of GspeedE-2019 in a test. From the equations in the lower left corner of each template in the figure, it can be seen that the roll gradients of front suspension, rear suspension, and total suspension are $0.552^\circ/\text{G}$, $0.557^\circ/\text{G}$, and $0.555^\circ/\text{G}$, respectively.

3.2. Roll Stiffness. The roll stiffness of suspension refers to the total elastic recovery couple moment given by the suspension system to the carriage under the unit carriage rotation angle when the vehicle rolls (the wheels remain on the ground). The roll stiffness of the suspension will affect the lateral load transfer of the car during steering and then affect the wheel

TABLE 1: Parameters in formulas (2)–(4).

Parameter	Description
x_{SuspLF}	Left front suspension displacement
x_{SuspRF}	Right front suspension displacement
x_{SuspLR}	Left rear suspension displacement
x_{SuspRR}	Right rear suspension displacement
MR_F	Front suspension motion ratio
MR_R	Rear suspension motion ratio
T_F	Front track width
T_R	Rear track width

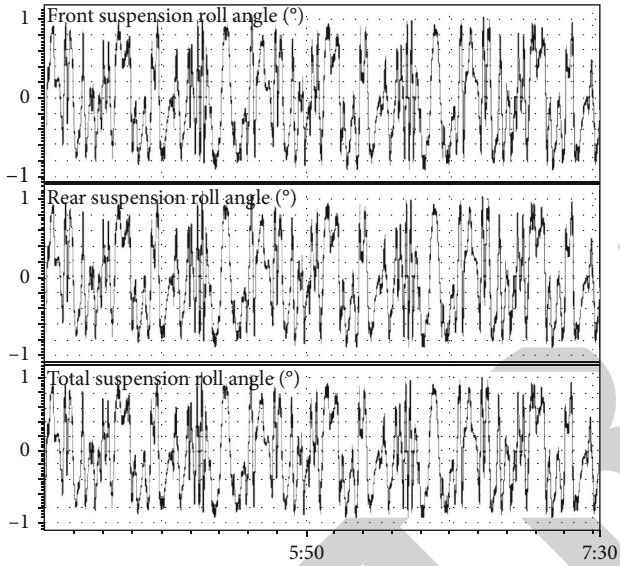


FIGURE 6: Template of suspension system roll angle data.

load of the inside and outside wheels as well as the front and rear wheels. The difference of wheel load will lead to the difference of the slip angle of the tires and then affect the steering characteristics [4]. According to the above roll gradient analyzed by MoTec i2 software and the vehicle parameters provided in Table 2, the roll stiffness of the suspension system and its components can be further calculated. Among them, the collection and analysis result of the roll gradient is $RG_F = 0.552^\circ/G$, $RG_R = 0.557^\circ/G$, $RG = 0.555^\circ/G$.

We can obtain the following parameters by taking the torque on the ground:

Height of sprung mass center h_S :

$$h_S = \frac{W_T h - W_{UF} R_F - W_{UR} R_R}{W_S}. \quad (5)$$

Roll moment lever arm h_{RM} :

$$h_{RM} \cong h_S - [Z_F + (Z_R - Z_F)(1 - a_S)] = 0.252\text{m}. \quad (6)$$

Roll moment per lateral acceleration M_ϕ :

$$M_\phi = W_S h_{RM}. \quad (7)$$

Then, the total suspension roll stiffness K_ϕ is

$$K_\phi = \frac{M_\phi}{RG} = 1161.379\text{N} \cdot \text{m}/^\circ. \quad (8)$$

According to the distribution of front and rear roll stiffness, the front and rear suspension roll stiffness $K_{\phi F}$ and $K_{\phi R}$ can be calculated as follows:

$$K_{\phi F} = K_\phi \cdot \frac{RG_R}{RG_F + RG_R} = 583.308\text{N} \cdot \text{m}/^\circ, \quad (9)$$

$$K_{\phi R} = K_\phi - K_{\phi F} = 578.072\text{N} \cdot \text{m}/^\circ. \quad (10)$$

Because in many cases, the roll stiffness provided by the spring cannot meet the requirement, so the antiroll bar mechanism is added. Therefore, suspension roll stiffness is the sum of the roll stiffness provided by spring and antiroll bar. Table 3 shows the vehicle parameters required by formulas (11) and (12).

$$K_{\phi F} = K_{\text{SpringF}} + K_{\text{ARBFF}}, \quad (11)$$

$$K_{\phi R} = K_{\text{SpringR}} + K_{\text{ARBRR}}. \quad (12)$$

In the above formula, K_{SpringF} ($\text{N} \cdot \text{m}/^\circ$) is the roll rate of the front spring; K_{SpringR} ($\text{N} \cdot \text{m}/^\circ$) is the roll rate of the rear spring; K_{ARBFF} ($\text{N} \cdot \text{m}/^\circ$) is the roll rate of the front antiroll bar; K_{ARBRR} ($\text{N} \cdot \text{m}/^\circ$) is the roll rate of the rear antiroll bar.

After calculating the roll stiffness of the spring through the known number of spring pounds, the roll stiffness of the antiroll bar can be further calculated [5].

By comparing the roll gradient and roll stiffness with the design objective, the gap between the actual race car and the simulation design can be obtained. If there is a large error, it is necessary to examine the specific cause of the error (for example, processing or assembly problem of parts) and solve it in time. In the test and tuning of real vehicle, after the ideal tuning strategy is obtained, the corresponding roll gradient can be used as the reference aim of the next season.

3.3. Dynamic Vertical Load of Tires. The vertical load directly affects the grip performance of the tire, while the load distribution between front and rear affects the steering characteristics of the car. In addition, the amount of tire load transfer can also affect the aerodynamic performance of the car. Therefore, knowing the tire dynamic vertical load is beneficial to evaluating the balance of a racing car, as well as the choice of tire pressure and analysis of tire surface temperature. By optimizing the four-wheel positioning parameters and other tuning methods, the tire load transfer of the racing car can be reduced

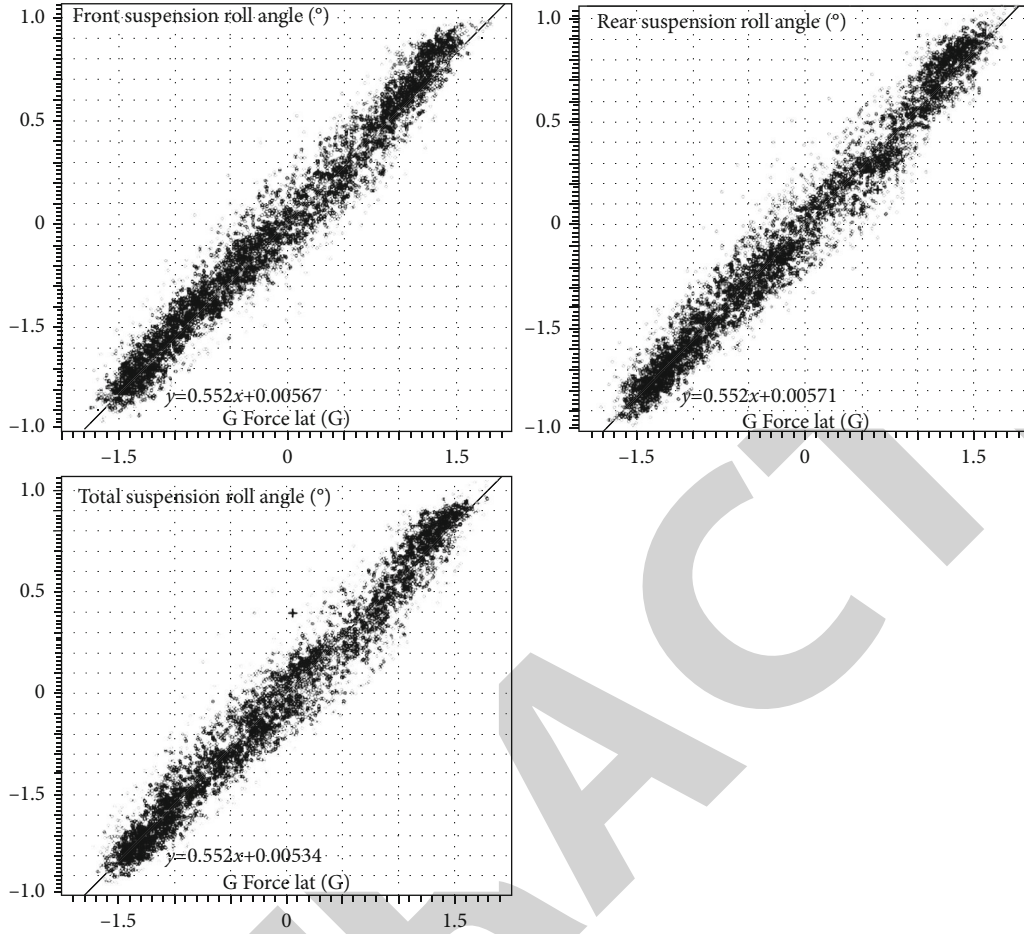


FIGURE 7: Roll gradient data template.

TABLE 2: Basic parameters of racing car.

Parameter	Description	Value : front	Rear	Total
W_T	Total mass (kg)	134.2	170.8	305
W_U	Unsprung mass (kg)	21	23	44
W_S	Sprung mass (kg)	113.2	147.8	261
h	Height of mass center (m)		0.28	
Z	Height of roll center (m)	0.03	0.04	
R	Tire load radius (m)	0.235	0.235	
T	Track width (m)	1.266	1.241	
L	Wheel base (m)		1.575	
a_S	Sprung mass distribution on the front suspension (%)		45	

TABLE 3: Parameters in formulas (11) and (12).

Parameter	Description
$K_{SpringF}$	Roll rate of the front spring
$K_{SpringR}$	Roll rate of the rear spring
K_{ARBF}	Roll rate of the front antiroll bar
K_{ARBR}	Roll rate of the rear antiroll bar

and balanced as far as possible, and the ultimate performance of race car can be further improved.

In order to calculate the dynamic vertical load of each wheel, it is necessary to understand the various parameters and influencing factors involved. And Figure 8 shows each component of wheel load.

The vertical load on each wheel is the sum of the components listed above. The detailed analysis and calculation are as follows.

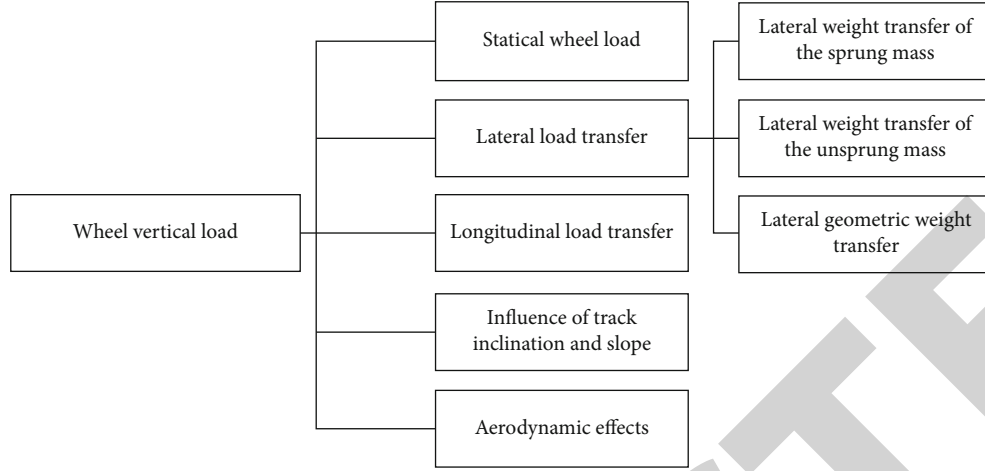


FIGURE 8: Each component of wheel load.



FIGURE 9: Static wheel load measurement.

3.3.1. *Static Wheel Load.* We can measure the static load of each wheel when the car is in the ready state (that is, the car with fully equipped driver). Figure 9 shows static wheel load measured by loadometer.

3.3.2. *Lateral Load Transfer.* We can measure the force of the suspension push rod through the pull pressure sensor, and then we can get the curve of tire load change with time. After that, by using the mechanical formula to calculate the other force elements of the suspension system, we can get the value of the downward pressure produced by the aerodynamic package on the race car, which is conducive to the design of the aerodynamic package on the racing car. Figure 10 shows the data collected by the pressure sensor.

(i) Lateral load transfer of the unsprung mass ΔW_u

$$\Delta W_{uF} = \frac{W_{uF} \cdot G_{lat} \cdot R_F}{T_F}, \quad (13)$$

$$\Delta W_{uR} = \frac{W_{uR} \cdot G_{lat} \cdot R_R}{T_R}. \quad (14)$$

It should be noted that in the early design, we used the tire load radius as an approximate value of unsprung mass center height. After the design work is completed, the height of wheel carrier mass center can be calculated in the 3D modeling software, which can be used as a more accurate value of unsprung mass center height.

(ii) Lateral geometric load transfer ΔW_g

$$\Delta W_{gF} = \frac{W_{sF} \cdot G_{lat} \cdot Z_F \cdot (S/L)}{T_F}, \quad (15)$$

$$\Delta W_{gR} = \frac{W_{sR} \cdot G_{lat} \cdot Z_R \cdot (1 - S/L)}{T_R}. \quad (16)$$

In the above formula, S is the distance (m) from the geometric center of rear axle to the sprung mass center in the side view. The calculation formula is as follows:

$$S = L \cdot \frac{W_{SF}}{W_S}. \quad (17)$$

It should be noted that the unsprung mass and the geometric load transfer cannot be measured by pull pressure sensor and displacement sensor. Except lateral acceleration, other parameters are in Table 1, considered as theoretical value.

(iii) Lateral load transfer of the sprung mass ΔW_s

$$\Delta W_{sF} = \frac{W_s \cdot G_{lat} \cdot h_{RM}}{T_F} \cdot q, \quad (18)$$

$$\Delta W_{sR} = \frac{W_s \cdot G_{lat} \cdot h_{RM}}{T_R} \cdot (1 - q). \quad (19)$$

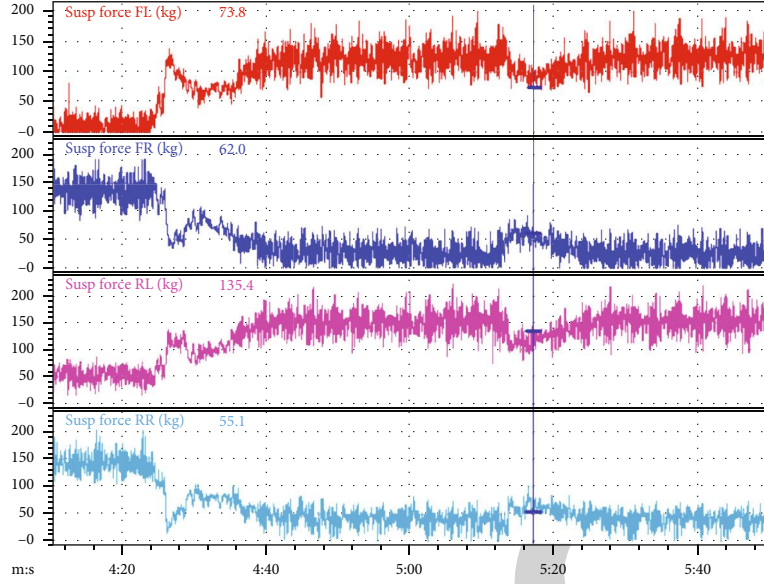


FIGURE 10: Data acquisition by pressure sensor.

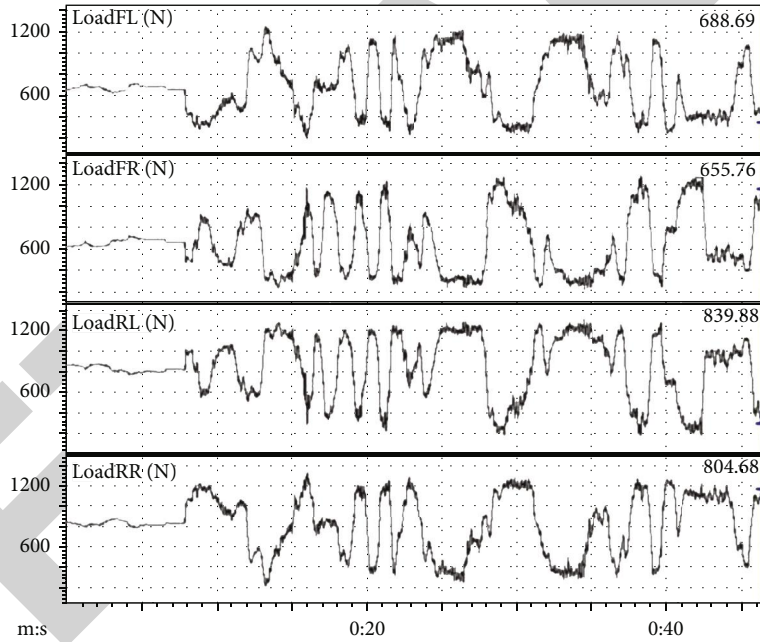


FIGURE 11: Tire dynamic load template.

The definition of q is

$$q = \frac{K_{\varnothing F}}{K_{\varnothing F} + K_{\varnothing R}} = \frac{RG_R}{RG_F + RG_R}. \quad (20)$$

From the above equations, we can see the importance of calculating roll gradient. The roll gradient can not only be used to further calculate the roll stiffness, verify whether the real car reaches the preliminary design expectation, and guide the adjustment of spring pounds and antiroll bar stiffness but also reflect the proportion of the lateral sprung mass

transfer on front and rear suspension compared with total amount and then calculate respective values.

3.3.3. Total Longitudinal Load Transfer ΔW_{Long}

$$\Delta W_{Long} = \frac{W \cdot G_{Long} \cdot h}{L}. \quad (21)$$

To sum up, we can find that a large part of the calculation of load transfer is to calculate the value of mechanical concepts such as the mass center height, the roll center height, and the roll moment lever arm, while the lateral and

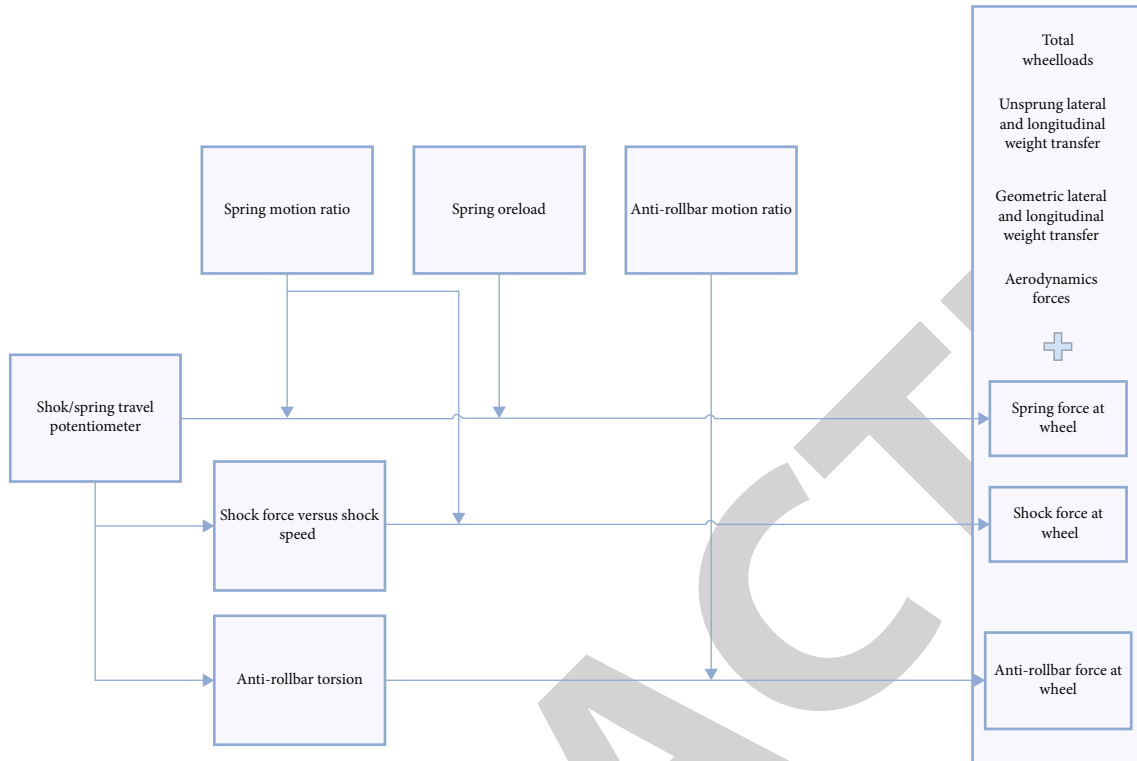


FIGURE 12: Tire load collection and calculation process.

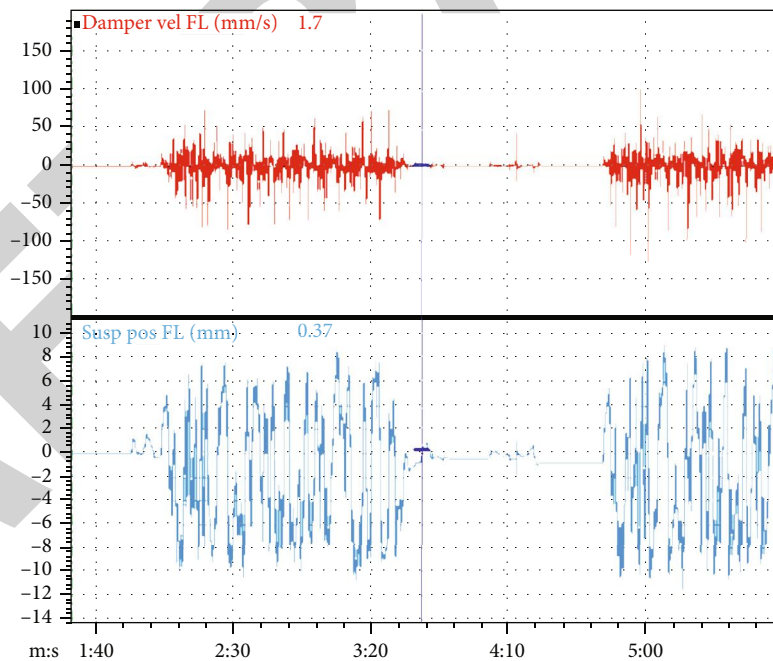


FIGURE 13: Displacement and velocity data acquisition diagram of shock absorber.

longitudinal accelerations are obtained by the digital acquisition equipment.

3.3.4. *Influence of Track Slope.* Since FSAE racing venues are usually well paved, this effect is ignored here. For example, the 2020 season was held at the Da'an Automotive Testing

Center in Xiangyang, Hubei Province, which is authorized by the National Automobile Testing Ground. As a result, road conditions can be guaranteed.

3.3.5. *Aerodynamic Effect.* The aerodynamic effect on car can be measured with relevant sensors. When all components are

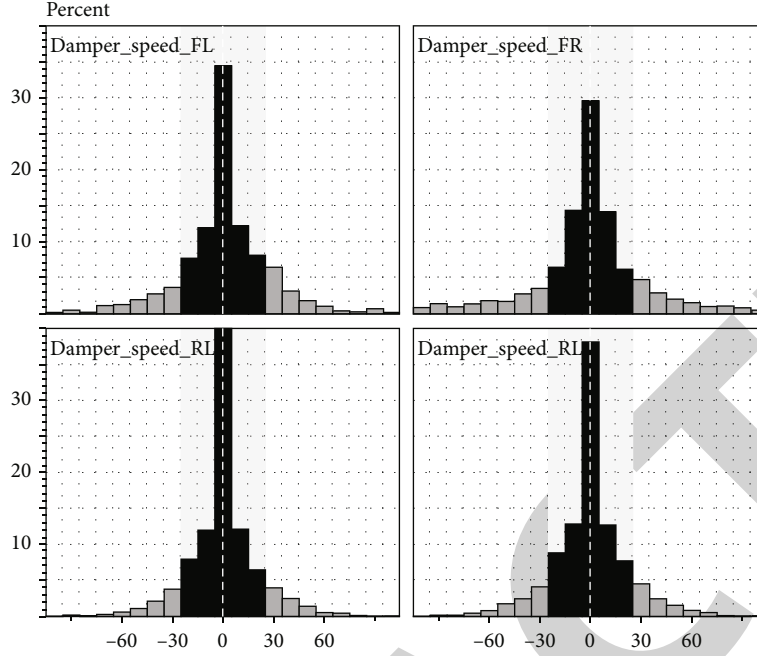


FIGURE 14: Damping velocity histogram data acquisition graph.

known, the total vertical load on each wheel can be calculated. Figure 11 is the dynamic load data of the tire in a skidpad track event (the skidpad track consists of two pairs of concentric circles in a figure of eight pattern) [3].

According to the average value in the upper right corner of the tire load graph above, the load transfer in the skidpad test is distributed as the front 48% and the rear 52%. Theoretically, neutral steering occurs when the distribution of load transfer is equal to the distribution of axle load [1]. Since the axle load distribution of the real car is the front 45% and the rear 55%, it can be concluded that the steering characteristics of the car are very close to the neutral steering.

According to the tire dynamic load, we can also choose more appropriate tire pressure according to the tire file provided by manufacturer. In FSAE, the straight line acceleration, skidpad event, and autocross event are performed in cold tire conditions [3], so in these events, the tire pressure can be directly selected according to the tire load that required lateral and longitudinal acceleration determine, without extra consideration of the tire temperature influence. The collection and calculation processes of tire load are shown in Figure 12.

3.4. Damper Analysis Study. For the data acquisition and analysis system, the analysis of the shock absorber is mainly to analyze its velocity through the displacement sensor. Equation (22) is the relation between the damper force and its velocity.

$$F_{\text{dam}} = C \cdot v_{\text{dam}} \quad (22)$$

In the above formula, F_{dam} is the force generated by shock absorber, C is the damper coefficient, and v_{dam} is the velocity of the shock absorber.



FIGURE 15: Position of tire temperature sensor.

To get the velocity, we can take derivative of the shock absorber displacement signal.

$$v_{\text{dam}} = \frac{d}{dt} s_{\text{dam}} \quad (23)$$

And Figure 13 shows the displacement and velocity data acquisition diagram of shock absorber.

In part 2.1 we have discussed, the shock absorber can be measured by linear displacement sensor directly or calculated through rockarm rotation angle.

The velocity interval of the shock absorber is mainly divided into three parts:

- (i) *The First Interval* (<5 mm/s). The velocity in this area is mainly caused by friction in the suspension system

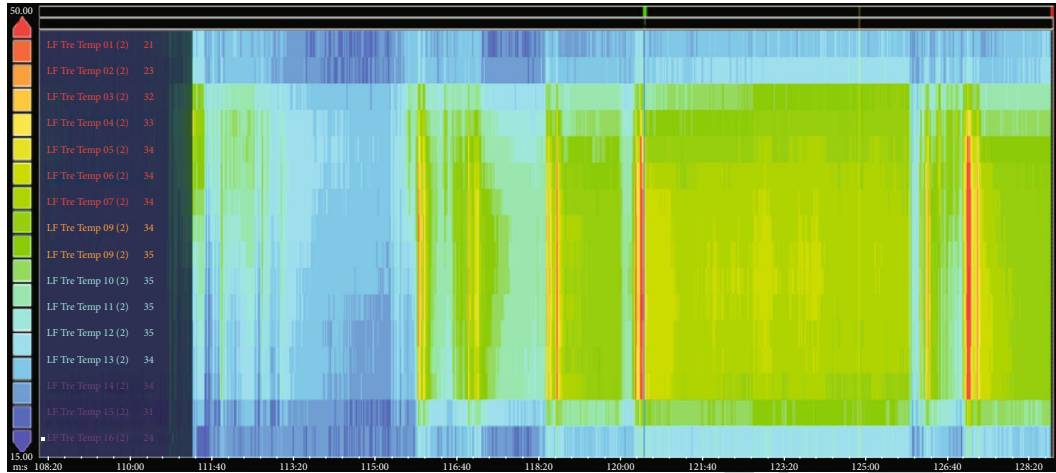


FIGURE 16: Tire temperature data acquisition graph.

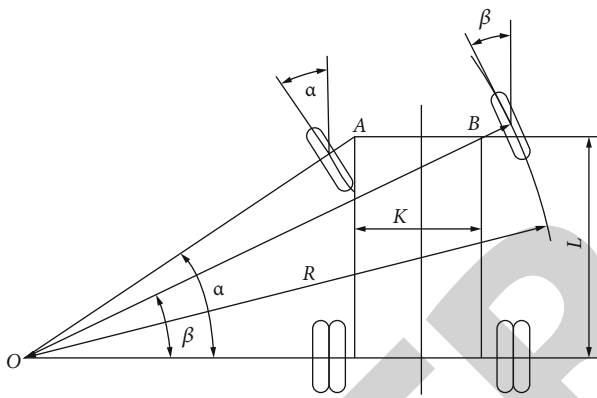


FIGURE 17: Ideal Ackermann angle.

- (ii) *The Second Interval (5-25 mm/s) (Low-Speed Damping Interval)*. This area is the main area where the shock absorber responds to chassis motion of the car and is also an important area for driver to perceive the car
- (iii) *The Third Interval (25-200 mm/s) (High Speed Damping Interval)*. The velocity of shock absorber in this area is mainly caused by road excitation. The impact of road shoulder usually allows the velocity to exceed 200 mm/s

In order to make the time ratio of shock absorber velocity in each interval more intuitive, damping velocity histogram, an important tool for damper analysis and adjustment, is presented here. The damping velocity histogram is a graph that describes the time proportion of damping in each velocity interval [6]. By observing the shape of the histogram, we can roughly analyze the “soft” and “hard” of the suspension. The establishment method of this histogram template is as follows: create a new workbench in MoTec i2, select the histogram template, and choose the time and proportion in horizontal and vertical coordinates, respectively. Finally, add the digital channel of the linear displacement sensor of the shock

absorber, import the data, and then generate the template [7]. Figure 14 shows the damping velocity histogram of the car after an endurance test.

In order to improve the tire grip performance and maintain a certain contact between tire and ground, the damping adjustment should make the histogram conform to the normal distribution as far as possible, and the histogram shape of the four wheels should be consistent with each other, as well as the difference between peak values should be as small as possible [2].

4. Tire Temperature Analysis

As we know, tire surface temperature is an external indication of how well the tire works during testing. By analyzing the tire surface temperature and considering various factors of suspension kinematics and dynamics, the ideal working temperature range of the tire can be obtained, and the adjustment trend of tire camber can be deduced, as well as the real-time state of tire pressure in the test. By adding a tire temperature sensor, real-time tire temperature distribution and temperature rise data during running can be obtained conveniently, and the relationship between tire temperature and damping ratio can be established to guide the racing car set-up [8].

4.1. Evaluate Wheel Camber from Tire Temperature. As the car runs, the camber of wheels determines the position in which the tires are in contact with the ground, and the surface temperature of tires provides the desired position. When the car corners, for the outside wheels, by observing the color contrast diagram of tire temperature distribution, we can conclude that if the temperature distribution is uniform, then the camber angle is appropriate [9]. If the outer temperature of the outside wheel is significantly higher than that of the inner, it means that the camber angle is too small, otherwise, the camber angle is too large. For the inside wheel, if the temperature in the inner or middle of the wheel rises too fast, it means that the camber angle is too large; otherwise, it is too small. Since the outside wheels provide most of the lateral

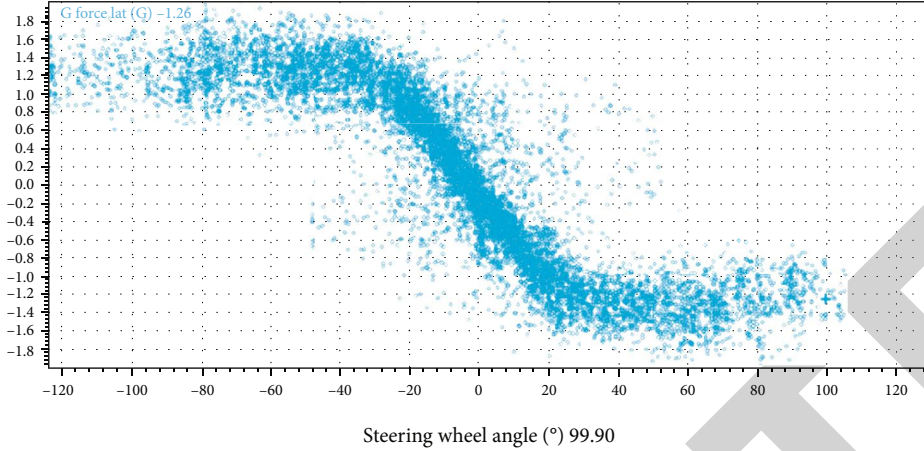


FIGURE 18: Data acquisition of steering wheel angle and lateral acceleration data scatter diagram.

TABLE 4: Parameters in formulas (26)–(28).

Parameter	Description
θ_{sw}	Actual steering angle
i	Steering ratio
L	Lateral acceleration
G_{la}	Roll rate of the rear antiroll bar
V	Vehicle speed

force when cornering, the camber of the outside wheels is of more concern. We can characterize the camber state by the temperature difference between the inside and outside of the tire [10]. Equation (24) is the calculation formula of temperature difference between inside and outside tire surface:

$$\Delta T_{t_i} = T_{t_i}(\text{in}) - T_{t_i}(\text{out}). \quad (24)$$

In the above formula, i is LF (left front wheel), RF (right front wheel), LR (left rear wheel), RR (right rear wheel), $T_{t_i}(\text{in})$ is the temperature of the inside of the tire ($^{\circ}\text{C}$), and $T_{t_i}(\text{out})$ is the temperature of the outside of the tire ($^{\circ}\text{C}$).

However, it is not in line with scientific principles to make a final judgment on the data of a few specific corners, so it is necessary to evaluate the data of the whole lap comprehensively [11]. By equipping multichannel tire temperature sensors, we can obtain real-time tire temperature distribution and temperature rise data during running conveniently. Therefore, the proper camber angle can be determined by observing the average tire surface temperature difference throughout the lap [12]. Figure 15 shows the layout of tire temperature sensor on our car.

4.2. Examine Tire Pressure from Temperature Analysis. Except evaluating whether the camber angle is appropriate, we also use the tire temperature to analyze the tire pressure when the car is running [13]. Comparing the temperature of the inner and outer part of the tire with the middle, we can find that when the tire pressure is too low, the inner

and outer tire temperature will be higher than that of the middle part, while when the tire pressure is too high, the situation will be opposite. Therefore, the tire pressure can be evaluated by the difference between the middle and the average inner and outer tire temperature [14]. This difference is denoted as $\Delta T p_i$.

$$\Delta T p_i = T_{t_i}(\text{mid}) - \frac{T_{t_i}(\text{in}) + T_{t_i}(\text{out})}{2}. \quad (25)$$

In the above formula, $T_{t_i}(\text{mid})$ is the tire middle temperature ($^{\circ}\text{C}$), $T_{t_i}(\text{in})$ is the tire inside temperature ($^{\circ}\text{C}$), and $T_{t_i}(\text{out})$ is the tire outside temperature ($^{\circ}\text{C}$). When the result $\Delta T p_i$ is positive, it indicates that the tire pressure is too high, vice versa. The following figure shows the tire temperature data collected in the first 20 seconds of a linear acceleration event. Through observation, it can be seen that the temperature in the middle part of the tire is higher and the temperature on both sides is lower. It can be preliminarily concluded that the tire pressure is too high and should be lowered. Figure 16 shows the tire temperature data acquisition graph.

5. Steering System Data Analysis

The design of the steering system is based on Ackerman steering geometry and takes the slip angle of tire into account. In the analysis of steering data, the steering characteristic of the race car is mainly studied. In addition, the steering design of Formula One should not only reduce tire wear and prolong the service life of tires but also have good steering stability [7]. The racing car mostly uses the broken steering trapezoid, the steering torque on the steering wheel from the transmission mechanism to the gear of the steering machine, and then driven by the gear and rack movement. Both ends of the steering rod are, respectively, connected with the steering rack and the steering knuckle arm. Under the action of the pull rod thrust and tension, the steering knuckle arm drives the tire to rotate, so as to achieve steering. A reasonable steering trapezoid structure should make the four steering wheels roll as far as possible without

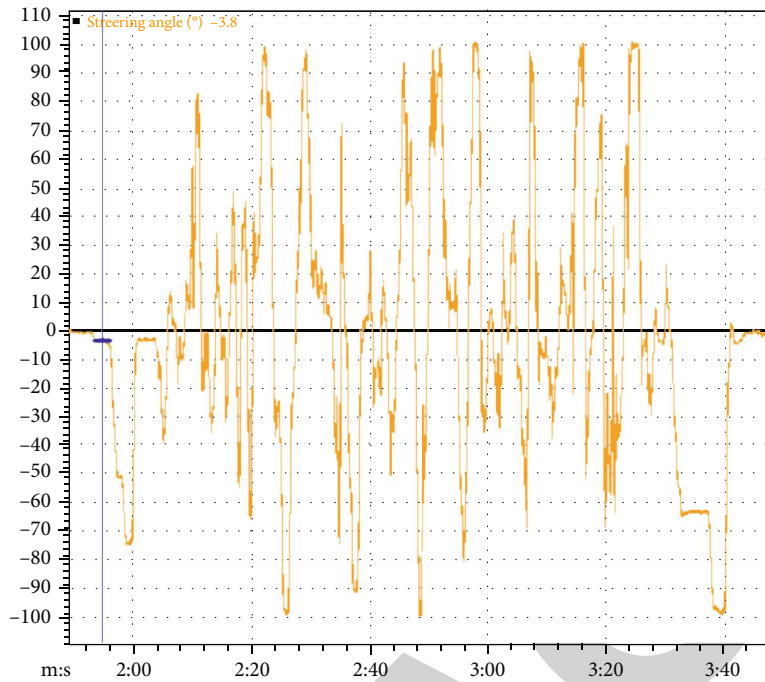


FIGURE 19: Actual steering angle data acquisition chart.

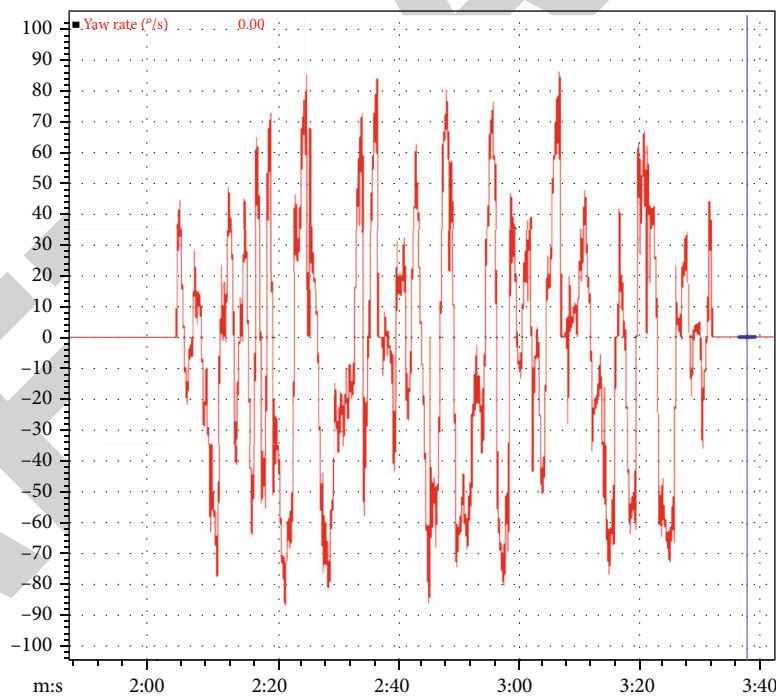


FIGURE 20: Yaw rate data acquisition graph.

sideslipping, that is, the instant center of the four steering wheels' speed intersects at the same point. When the rear wheels of the race car do not steer, the steering center of the race car should be on the rear wheel axle line. This steering relationship is the ideal Ackermann turning angle relationship, as shown in Figure 17. For this reason, the concepts of understeer angle and attitude angular velocity

are presented in this section to evaluate the steering characteristic of race cars [4]. Figure 18 shows the data acquisition of steering wheel angle and lateral acceleration data scatter diagram [15].

5.1. Understeering Angle. According to the definition of steering characteristic in Race Car Vehicle Dynamics [5], when

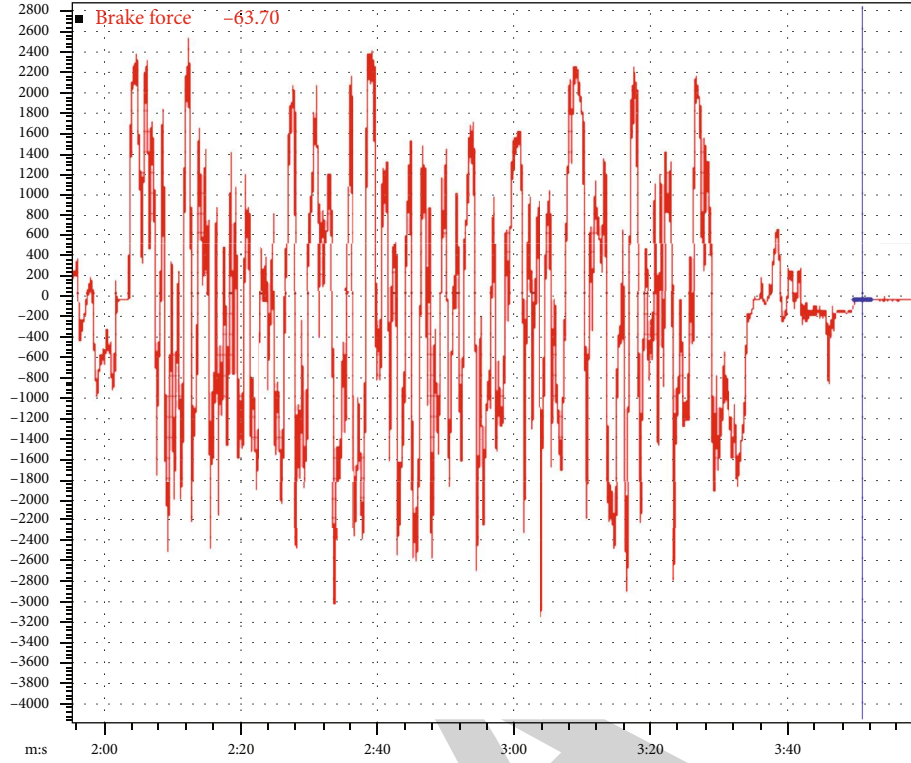


FIGURE 21: Braking force data collection in race car running test.

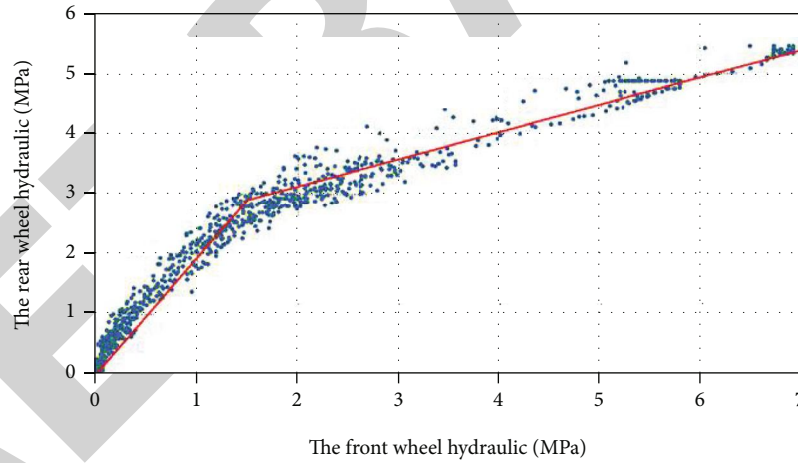


FIGURE 22: Actual braking force distribution obtained from data collection.

the actual wheel steering angle is equal to Ackerman steering angle, the vehicle will have neutral steering. When the steering angle is larger than Ackerman steering angle, the vehicle understeers. Oversteer on the other hand. Therefore, the difference between the absolute value of the actual wheel steering angle θ and Ackerman steering angle θ_{Ack} can be defined as the understeering angle θ_u . The formula is as follows

$$\theta_u = |\theta| - |\theta_{Ack}|, \quad (26)$$

$$\theta = \frac{\theta_{sw}}{i}, \quad (27)$$



FIGURE 23: Race car running test.

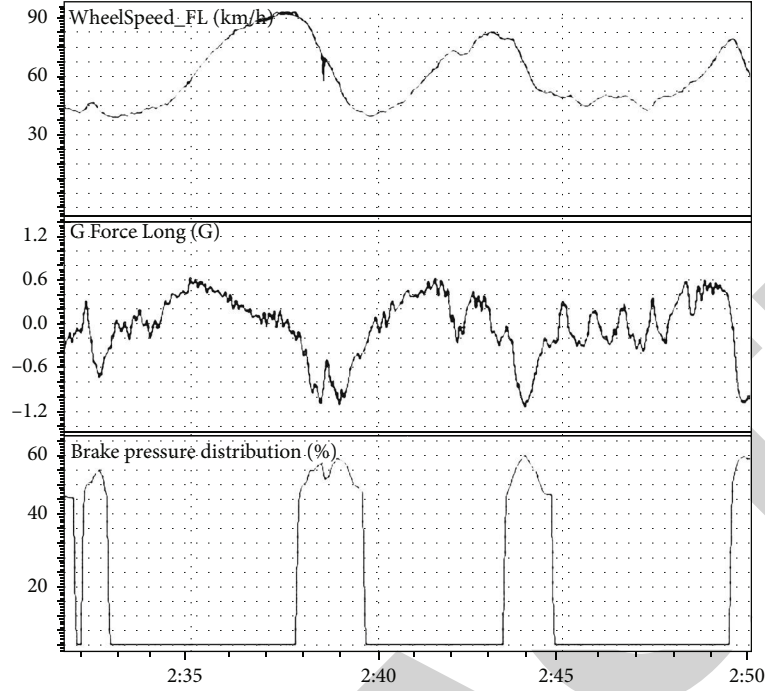


FIGURE 24: Brake data analysis template.

$$\theta_{Ack} = \frac{L \cdot G_{la}}{V^2}. \quad (28)$$

Table 4 shows the vehicle parameters required by formulas (26)–(28).

According to formula (26), the following conclusions can be drawn:

$$\theta_u \begin{cases} < 0, \text{ oversteer,} \\ = 0, \text{ neutral steer,} \\ > 0, \text{ understeer.} \end{cases} \quad (29)$$

By calculating the understeering angle, we can understand the steering characteristics at various stages of the corner. In order to study the overall steering characteristics of the car, the average understeering angle of the car can be obtained through the steady-state rotation test, and the overall steering characteristic of the car can be evaluated [13]. Figure 19 shows the actual steering angles of the car collected by MoTec i2 analysis.

5.2. Attitude Velocity Analysis. In addition to the understeering angle, the vehicle steering characteristics can be characterized by the difference between the absolute value of the actual yaw rate and the theoretical yaw rate, that is, the attitude angular velocity [16]. The following is the definition formula of attitude angular velocity ω_a .

$$\omega_a = |\omega_{yaw}| - |\omega_t|, \quad (30)$$

$$\omega = \frac{G_{lat}}{V}. \quad (31)$$

In the above formula, ω_{yaw} is the actual yaw rate of the vehicle ($^\circ/s$), and ω_t is the theoretical yaw rate of the vehicle ($^\circ/s$). Figure 20 shows the yaw rate data collected.

Through the analysis, the following conclusions can be drawn:

$$\omega_a \begin{cases} < 0, \text{ oversteer,} \\ = 0, \text{ neutral steer,} \\ > 0, \text{ understeer.} \end{cases} \quad (32)$$

6. Braking System Data Analysis

In race car competition, we know that if you spend less time slowing down, you spend more time accelerating and you can improve your lap speed. As for the braking system, the important analysis data include vehicle speed, wheel speed, longitudinal acceleration, front and rear brake pressure, and front brake ratio.

6.1. Braking Force. The real braking force data can be collected through the brake oil pressure sensor, and the maximum longitudinal deceleration obtained in the running test corresponds to the maximum braking force of the car. The maximum braking force is one of the evaluation parameters of car braking performance, and usually, the maximum longitudinal deceleration of the car should be about 95% of the maximum lateral acceleration [5]. Figure 21 shows the braking force data collected in a race car running test, and Figure 22 shows the actual braking force distribution obtained from data collection. We performed a dynamic test on the car. Figure 23 shows the picture taken during the test [17].

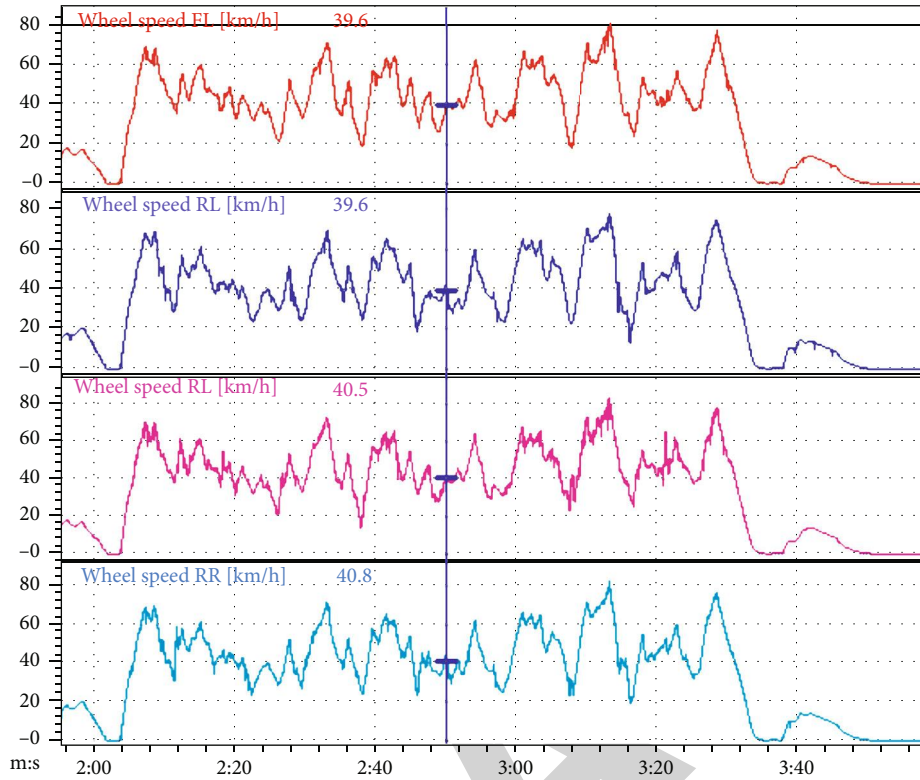


FIGURE 25: Wheel speed data.

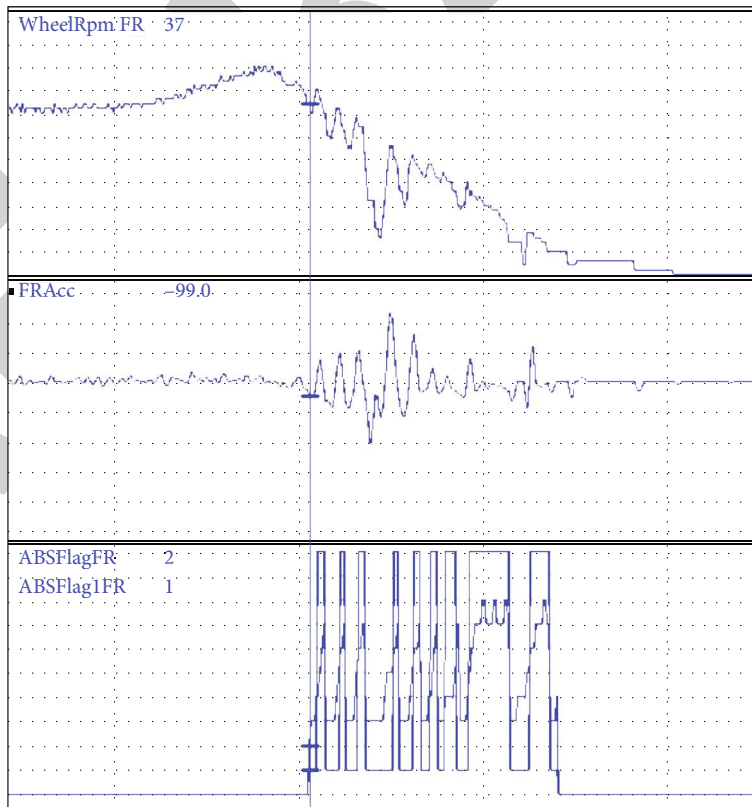


FIGURE 26: ABS simulation result.

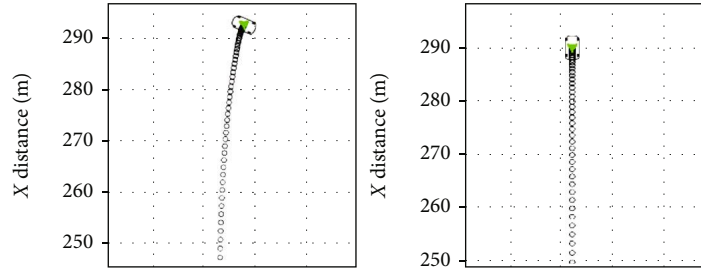


FIGURE 27: Comparison of simulation under open road conditions (the figure on the left does not include ABS braking, and the figure on the right includes ABS braking).

6.2. Braking Lock. The braking lock can be directly observed through the curve of wheel speed data. When decelerating, the wheel speed will drop in a straight line, when the tire is locked, the wheel speed will drop rapidly; when the driver senses that the tire is locked, he releases the brake slightly, and the wheel speed returns to its original straight line, forming a small trough, as shown in the wheel speed curve in Figure 24. The braking lock will cause the tire to lose grip performance, which should be avoided as far as possible.

6.3. Braking Pressure Distribution. Braking pressure distribution is the ratio of the front braking pressure to the total braking pressure, and equation (30) is the math channel formula of it:

$$B_F = \frac{\text{Brake}P_F}{\text{Brake}P_F + \text{Brake}P_R} \cdot 100\%. \quad (33)$$

In the equation, $\text{Brake}P_F$ is the front brake pressure (MPa), $\text{Brake}P_R$ is the rear brake pressure (MPa). Figure 25 shows the wheel speed data.

Braking pressure distribution affects the maximum braking force in the pure braking condition and the steering characteristics in the cornering condition with braking. Too much distribution of brake pressure on one axle will result in the corresponding tire lock. In the corner with braking, too much braking pressure to the front axle will lead to understeer, and too much to the rear axle will lead to oversteer. Therefore, according to the track characteristics and driver's feedback, and combined with data collection, we can improve the performance of our car by tuning braking pressure distribution properly.

6.4. Set the ABS. We analyze information obtained by data acquisition, concluding that in the process of race, the braking intensity is usually small and medium-sized. In the traditional brake system design, in order to make the front wheel lock first and achieve stable condition, the traditional design always matches a large synchronous adhesion coefficient to achieve this goal, so that will make the rear wheels have larger attachment loss. The inability to provide greater longitudinal adhesion of rear wheels results in the lack of lateral adhesion of the front wheels, which is very detrimental in the process of cornering and cannot guarantee the speed and stability of the car. Therefore, the ABS system is set to ensure that the front and rear wheels do not lock, lose steering ability,

or slip, and at the same time, the braking force distribution of the rear wheels is improved then the speed of cornering is improved. At the beginning of design, we use Simulink and Carsim cosimulation to establish the corresponding model, to judge its feasibility, and whether it can reduce the braking distance. Figure 26 shows the ABS/EBD simulation result, and Figure 27 shows the comparison of simulation under open road conditions [18].

7. Conclusion

This paper introduces the important mathematical channels for FSAE racecar data collection of the five types: reliability, suspension, tire, steering, and braking, as well as the corresponding calculation formula and the analysis template used in data analysis. Based on the MoTec i2 data processing platform, the paper carries out data analysis and post-processing for formula student. In addition, we use CAN bus communication to layout and design the vehicle sensor and wiring harness system.

In the sensor fault diagnosis, for CAN bus signal, we use interrupt counter counting method to diagnose the loss of signal frame or signal line disconnection and other faults.

As for reliability data, we analyze the safety and reliability of race cars by collecting battery voltage, battery temperature and motor power, so as to troubleshoot potential faults.

As for suspension system, we mainly analyzed the data collected by linear displacement sensor and studied the roll gradient, roll stiffness, tire load transfer, and shock absorber, so as to verify our design and tune the suspension to an appropriate state.

As for tires, we studied whether the corresponding four-wheel positioning parameters and tire pressure were appropriate and whether the utmost performance of tires could be exerted through the data collected from the multichannel tire temperature sensor.

As for the steering system, we obtained steering angle and lateral acceleration scatter diagram and change rate of steering angle and yaw velocity, to judge the steering characteristics of race car and make corresponding adjustments.

As for the braking system, we analyzed maximum braking force, braking pressure distribution, and checked wheel speed data to deal with brake lock. Furthermore, we do some research on the ABS/EBD system.

Due to our limited knowledge, the data analysis we have done is relatively basic, but for FSAE teams, it has been an

Retraction

Retracted: Multimodal Emotion Recognition Model Based on a Deep Neural Network with Multiobjective Optimization

Wireless Communications and Mobile Computing

Received 28 November 2023; Accepted 28 November 2023; Published 29 November 2023

Copyright © 2023 Wireless Communications and Mobile Computing. This is an open access article distributed under the Creative Commons Attribution License, which permits unrestricted use, distribution, and reproduction in any medium, provided the original work is properly cited.

This article has been retracted by Hindawi, as publisher, following an investigation undertaken by the publisher [1]. This investigation has uncovered evidence of systematic manipulation of the publication and peer-review process. We cannot, therefore, vouch for the reliability or integrity of this article.

Please note that this notice is intended solely to alert readers that the peer-review process of this article has been compromised.

Wiley and Hindawi regret that the usual quality checks did not identify these issues before publication and have since put additional measures in place to safeguard research integrity.

We wish to credit our Research Integrity and Research Publishing teams and anonymous and named external researchers and research integrity experts for contributing to this investigation.

The corresponding author, as the representative of all authors, has been given the opportunity to register their agreement or disagreement to this retraction. We have kept a record of any response received.

References

- [1] M. Li, X. Qiu, S. Peng et al., "Multimodal Emotion Recognition Model Based on a Deep Neural Network with Multiobjective Optimization," *Wireless Communications and Mobile Computing*, vol. 2021, Article ID 6971100, 10 pages, 2021.

Research Article

Multimodal Emotion Recognition Model Based on a Deep Neural Network with Multiobjective Optimization

Mingyong Li , Xue Qiu , Shuang Peng, Lirong Tang, Qiqi Li, Wenhui Yang, and Yan Ma 

College of Computer and Information Science, Chongqing Normal University, Chongqing 401331, China

Correspondence should be addressed to Yan Ma; 20130939@cqnu.edu.cn

Received 8 July 2021; Accepted 7 August 2021; Published 26 August 2021

Academic Editor: Balakrishnan Nagaraj

Copyright © 2021 Mingyong Li et al. This is an open access article distributed under the Creative Commons Attribution License, which permits unrestricted use, distribution, and reproduction in any medium, provided the original work is properly cited.

With the rapid development of deep learning and wireless communication technology, emotion recognition has received more and more attention from researchers. Computers can only be truly intelligent when they have human emotions, and emotion recognition is its primary consideration. This paper proposes a multimodal emotion recognition model based on a multiobjective optimization algorithm. The model combines voice information and facial information and can optimize the accuracy and uniformity of recognition at the same time. The speech modal is based on an improved deep convolutional neural network (DCNN); the video image modal is based on an improved deep separation convolution network (DSCNN). After single mode recognition, a multiobjective optimization algorithm is used to fuse the two modalities at the decision level. The experimental results show that the proposed model has a large improvement in each evaluation index, and the accuracy of emotion recognition is 2.88% higher than that of the ISMS_ALA model. The results show that the multiobjective optimization algorithm can effectively improve the performance of the multimodal emotion recognition model.

1. Introduction

The concept of “emotional computing” was first proposed by professor Picard of the Massachusetts Institute of Technology in the book *Affective Computing* published in 1997. She defined “affective computing” as the calculation of factors related to human emotion, triggered by human emotion or able to affect emotion [1]. The research of affective computing is aimed at achieving harmonious and efficient human-computer interaction, so that computers have higher and more comprehensive intelligence [2, 3].

The external expression of human emotion mainly includes voice, facial expression, posture, and so on. Human speech contains not only linguistic information but also non-linguistic information such as people’s emotional state. For example, the same sentence often feels different to the listener because of the different emotional states of the speaker. Human speech can express emotion because it contains parameters that can reflect the characteristics of emotion. Facial expression is also an important external form of emotion, which contains certain emotional information. The research of facial expres-

sion recognition can effectively promote the development of emotion recognition research and the research of automatic understanding of computer images [4–6].

Since the performance of speech emotion recognition is easily disturbed by the noise of the surrounding environment, facial expressions are also easily affected by problems such as dark lighting, different angles, and blocked areas. Therefore, single-modal emotion recognition has some limitations. In order to improve the overall recognition performance and learn from each other in different emotional features, researchers propose a multimodal emotion recognition method based on the fusion of speech and facial expression, which has important research significance in the practical application of emotion recognition. According to the processing of different modal signals in different stages, it can be divided into signal-level fusion, feature-level fusion, decision-level fusion, and hybrid fusion. In this paper, the decision-level fusion method is used to independently inspect and classify the features of each modal and merge the results into a decision vector. The schematic diagram of multimodal emotion recognition is shown in Figure 1.

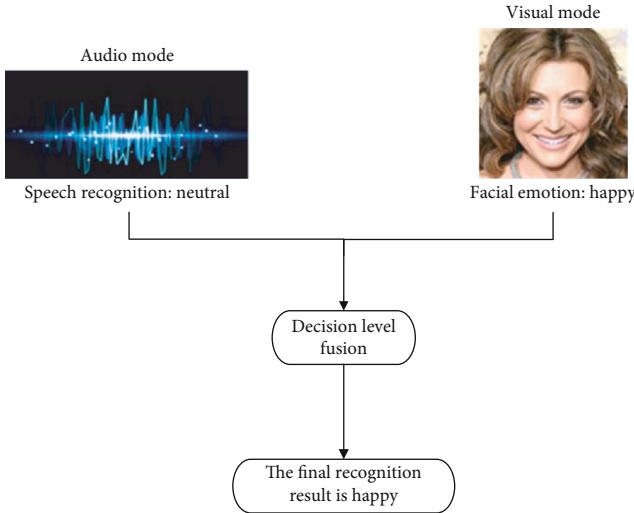


FIGURE 1: Speech emotion recognition based on a deep convolution neural network.

In many optimization fields, such as production scheduling, artificial intelligence, combinatorial optimization, large-scale data processing, and data mining, we often encounter many complex optimization problems closer to real life [7–11]. In the real world, the optimization problem is usually multiattribute, which is usually the simultaneous optimization of multiple objectives. In order to achieve the optimization of the overall goal, it is usually necessary to consider the conflicting subgoals comprehensively. Therefore, a multiobjective optimization (MOO) algorithm is proposed. This article uses two evaluation indicators, accuracy and emotion recognition uniformity, to evaluate the performance of emotion recognition models. In order to improve the two evaluation indexes at the same time, the multiobjective optimization algorithm is used to optimize the emotion recognition model.

- (1) The first time, the multiobjective optimization algorithm is combined with multimodal emotion recognition, and the performance of multimodal emotion recognition is effectively improved by optimizing the accuracy and uniformity of the model at the same time in the decision level
- (2) In this paper, a deep convolutional neural network (DCNN) and a deep separable convolutional neural network (DSCNN) are proposed for speech recognition and face recognition, respectively, and good experimental results are obtained
- (3) The proposed multimodal emotion recognition model based on multiobjective optimization has a better recognition effect, and the accuracy of emotion recognition is 2.88% higher than that of the ISMS_ALA model

The rest of this paper is organized as follows. Section 2 reviews the related research work of the multiobjective optimization algorithm and multimodal emotion recognition.

In Section 3, we introduce the framework and model of two basic techniques used in multimodal emotion recognition. In Section 4, we test the proposed model. Finally, the conclusion of this paper is given in Section 5.

2. Related Work

At present, the research on multimodal emotion recognition is a hot topic in the interdisciplinary research of cognitive science, physiology, psychology, linguistics, computer science, and so on. Multimodal emotion recognition has attracted more and more attention from scientific research institutions and researchers domestically and internationally.

In 1997, Duc et al. [12] proposed “multimodality” for the first time, using facial expression and speech fusion to recognize human identity and behavior. Professor Chen et al. of the Beckman College of the University of Illinois jointly [13] proposed the research of multimodal emotion recognition, which mainly involves the emotion recognition of speech and facial expression information. The experimental results show that the recognition rate of a single mode is lower than that of a multimodal one. For the feature contribution of emotion recognition, there is a big difference between speech and expression. Normally, the feature of expression makes a greater contribution to emotion recognition. Busso and Narayanan [14] of the Viterbi School of Engineering at the University of Southern California are working together on emotion recognition. Wang and Guan [15] proposed a vision-based emotion recognition method, which extracts visual features from Gabor wavelet key frames and then uses a feature-level data fusion scheme to combine audio features with visual features; Ding et al. [16] combined convolutional neural network (CNN) and Directional Gradient Histogram (HOG) methods to extract more expression features and achieved 90% recognition accuracy in happy emotion categories; Lan and Zhang [17] proposed a joint strategy (FRN+BN) to recognize facial expressions and improve the recognition accuracy of 5.6% on the CK + dataset.

When the accuracy of emotion recognition based on single-modal speech or facial expressions is not optimistic, it is jointly proposed to integrate speech and facial expression information for emotion recognition. With the deepening of fusion algorithm research, multimodal emotion recognition has achieved rapid development. Multimodal fusion can improve the recognition rate and has better robustness [18]. At present, the common multimodal emotion detection methods mainly include physiological signal+emotional behavior combination and the combination between different emotional modalities. Multimodal fusion methods include feature-level fusion (early stage), decision-level fusion (late stage), and hybrid fusion. The typical early fusion model is EF-LSTM [19], which stitches the feature representations of the three modalities of text, speech, and image to obtain a multimodal representation, which is then input into LSTM for encoding. Late fusion [20] occurs after decoding; it is a fusion at the decision level, which can extract interactive information within modalities but cannot extract interactive information between modalities. Hybrid fusion combines the first two fusion methods.

Because the two modalities of facial expression and voice can be directly extracted in the video, they have the advantages of convenient data collection, obvious features, and high precision. They are the most widely used emotion recognition methods in practical applications. Lu and Zhang [21] proposed a neural network-based audio and video emotion recognition model. The model uses data from three aspects: frontal facial expressions, side facial expressions, and audio. It belongs to a model layer fusion method and has achieved good classification results; Sahoo and Routray [22] proposed a multimodal emotion recognition method using facial image and voice data, which uses a rule-based decision-level fusion method. The M-BERT model proposed by Rahman et al. [23] applies the pretraining model to multimodal emotion recognition tasks. M-BERT adds a modal fusion layer between the input layer and the coding layer to achieve the fusion of three modalities.

In this study, the Mel Frequency Bank (MFB) method is used to extract the emotional features of speech signals, and the hidden Markov model (HMM) method is used to train these features. At the same time, these speech emotional features are optimized appropriately. For expression images, the method of dividing regions is used in the research, and different weights are assigned to each region to extract features. Then, the speech and facial expression features are fused, and the speech features of each expression in each region of the face are used to classify. The experimental results show that after using the feature fusion of speech and expression, the effect is obviously better than that of only speech or expression.

Many scientific and engineering problems in industry, agriculture, national defense, transportation, information, economy, and management can be transformed into optimization problems. A multiobjective optimization problem (MOP) is a kind of challenging and complex optimization problem. Because the optimization goals conflict with each other, it is extremely difficult to obtain a single global optimal solution, so it is a set of compromise Pareto optimal solutions [24, 25]. In recent decades, many similar optimization algorithms have appeared, such as PEAS [26], SPEA2 [27], NSGAI2 [28], MOEA [29], MOEA/D [30], IBEA [31], and HypE [32]. These algorithms have achieved better optimization results. However, affected by the background of various algorithms, there is no algorithm that can obtain the optimal solution set when solving all multiobjective optimization problems.

In this paper, we propose a new multimodal emotion recognition technology, which uses a multiobjective optimization algorithm to perform fusion operation at the decision level. The final decision is obtained by the linear weighted sum of all single-modal classification results. In this way, different modalities can be identified cooperatively, so as to give full play to their respective advantages.

3. Proposed Method

3.1. Speech Emotion Recognition Based on DCNN. Audio also contains emotional information about people. Generally speaking, multimodal emotion recognition is more reliable than single-modal recognition. Traditional speech emotion recognition algorithms use LLDs or HSFs for feature extrac-

tion and then use statistical classification models such as HMM for emotion classification, but the performance of these algorithms is not particularly satisfactory. With the continuous development of deep learning, people use deep neural networks for speech emotion recognition, and many speech emotion recognition algorithms based on deep neural networks have been proposed.

The process of speech emotion recognition is divided into three parts: signal processing, feature extraction, and classification. Signal processing applies acoustic filters to the original audio signal and divides it into meaningful units. In this study, we first use the OpenSmile toolbox to extract frame-level acoustic features from speech signals. The extracted features are eighty-eight feature sets of eGeMAPS. After feature extraction, a 256-dimensional feature vector can be obtained for each frame. In order to further prepare a fixed-length feature map suitable for model input, it is necessary to perform a length normalization operation on the obtained feature sequence of variable length. Because only a few of the speech in IEMOCAP dataset are longer than one thousand frames, the algorithm abandons the features of those speech that are longer than one thousand frames. For the voice whose length is less than one thousand frames, zero filling operation is carried out to make its length reach one thousand frames. After feature extraction, the feature vector sequence with a length of one thousand and a dimension of 256 can be obtained. In the speech emotion classification stage, the speech emotion recognition algorithm based on the deep convolutional neural network proposed in this paper is used to predict. The speech emotion recognition model based on DCNN is shown in Figure 2.

Figure 2 shows the voice emotion recognition model based on CNN. The input of the model is a $256 * 1000$ feature map. The model uses four convolution layers to extract features, and the number of convolution kernels in the convolution layer is 4, 8, 16, and 32 in turn. The convolution kernel of the first convolution layer has a step size of one, a width of one, and a length of five, using the same convolution method. Therefore, the size of the feature map obtained through the first layer of convolution is $238 * 1000 * 4$. Then, global k -Max Pooling (GKMP) is used, and the k value of the first pooling layer is 512. Therefore, a feature map with a size of $238 * 512 * 4$ is obtained. The step size and width of the convolution kernel of the second convolution layer are 1, and the length is 3, and the same convolution in the same mode is used. The k value of this layer is 256. The feature map is obtained by the second convolution. The size is $238 * 256 * 8$. The next two layers use the same step size and convolution kernel size as the second layer of convolution. The k value is 128 and 1, respectively. Then, after 4 layers of full connection, the number of hidden layer neurons is 512, 256, 128, and 4, respectively. Finally, a feature vector of length of 4 can be obtained, and then, through the softmax layer, the prediction of the model can be obtained.

3.2. Facial Expression Recognition Based on DSCNN. Facial expression is the main form of emotional expression, and the emotional information conveyed by facial expression is common in different countries, nationalities, and cultures.

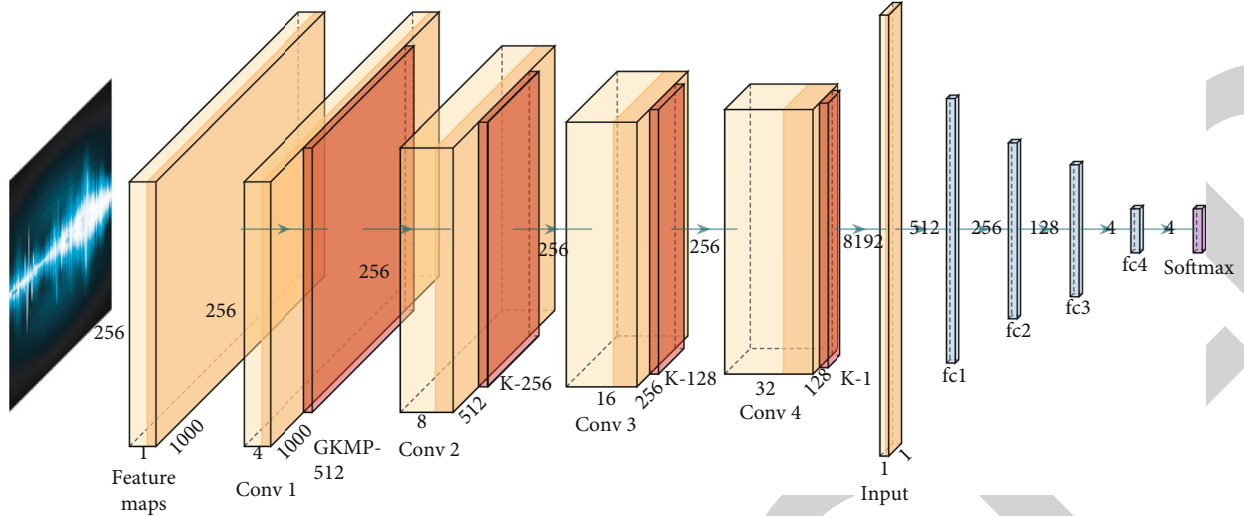


FIGURE 2: Speech emotion recognition based on a deep convolution neural network.

This paper constructs a deep learning algorithm based on deep separation convolution for facial expression.

Szegedy et al. [33] proposed the Inception structure. The main idea is to first use a $1 * 1$ convolution kernel to map each channel of the feature map to a new space. In this process, the correlation between channels can be learned, and then, convolution can be carried out through the conventional $3 * 3$ or $5 * 5$ convolution kernel. At the same time, the spatial correlation and the correlation between channels can be learned. Chollet [34] proposed “extremely” this idea, using a two-dimensional depthwise separable convolution (Separableconv2D) method and the channel correlation and spatial correlation to achieve a complete separation effect. This operation increases the width of the network and plays a great role in improving the accuracy of classification.

Deep separation convolution [35, 36] consists of two processes: layer-by-layer convolution and pixel-by-pixel convolution. This paper constructs an algorithm model based on deep separation convolution, as shown in Figure 3.

3.3. Multiobjective Optimization. For the mathematical description of the multiobjective problem, we take the minimum value problem as an example:

$$\begin{aligned}
 &\text{Minimize} && f(\mathbf{x}) = f_1(\mathbf{x}), f_2(\mathbf{x}), \dots, f_l(\mathbf{x}) \\
 &&& g_i(x) \geq 0, i = 1, 2, \dots, m \\
 &\text{Subject to :} && h_i(x) = 0, i = 1, 2, \dots, p \\
 &&& L_i \leq x_i \leq U_i, i = 1, 2, \dots, n,
 \end{aligned} \tag{1}$$

where n , l , m , and p are the number of variables, objective functions, inequality constraints, and equality constraints, respectively. g_i and h_i represent the i -th inequality and equality constraint, respectively, and $[O_i, U_i]$ is the boundary of the i -th variable.

Obviously, solutions to the multiobjective problem cannot be compared by using the above relational operators. There-

fore, for the multiobjective problem, the relational operator must be extended. Four key definitions in MOO are as follows.

(1) Pareto dominance

Assume two vectors such as $\mathbf{x} = (x_1, x_2, \dots, x_k)$ and $\mathbf{y} = (y_1, y_2, \dots, y_k)$. Vector x is said to dominate vector y (denoted as $x < y$) if and only if

$$\forall i \in \{1, 2, \dots, k\}: f(x_i) \leq f(y_i). \tag{2}$$

(2) Pareto optimality

A solution $x \in X$ is called Pareto-optimal if and only if

$$\exists y \in X | f(y) < f(x). \tag{3}$$

(3) Pareto-optimal set

The set of all Pareto-optimal solutions is called the Pareto set as follows:

$$P_s = \{\mathbf{x}, \mathbf{y} \in \mathbf{X} | \exists f(\mathbf{y}) > f(\mathbf{x})\}. \tag{4}$$

(4) Pareto-optimal front

A set containing the value of objective functions for the Pareto solution set is

$$P_f = \{f(\mathbf{x}) | \mathbf{x} \in P_s\}. \tag{5}$$

For solving a MOP, we have to find the Pareto-optimal set, which is the set of solutions representing the best trade-offs between different objectives.

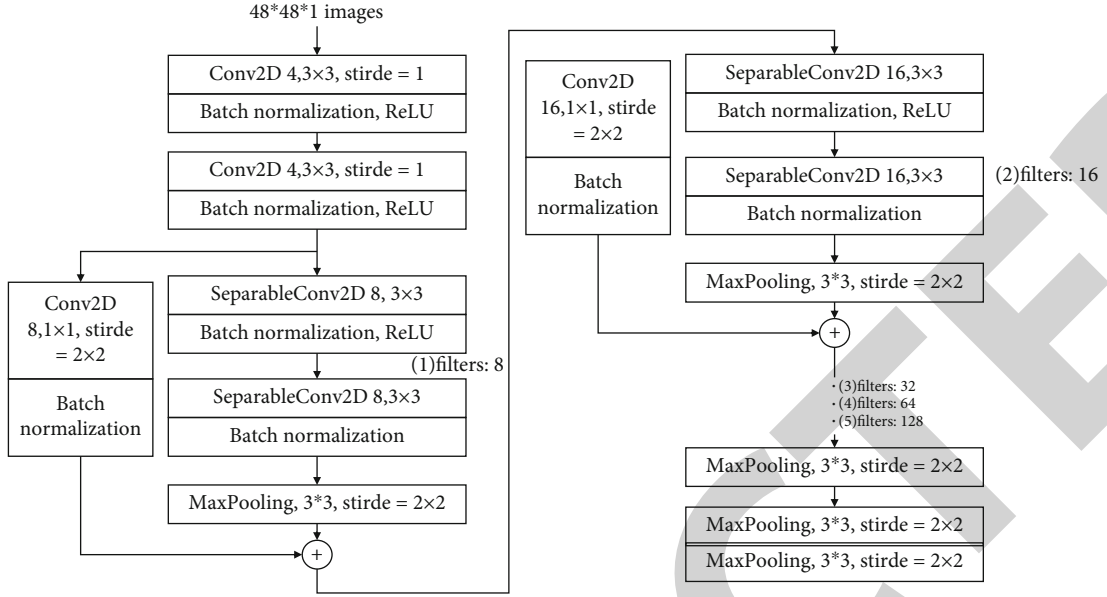


FIGURE 3: Facial expression recognition based on deep separation convolution.

3.4. *Decision-Level Fusion Based on a Multiobjective Optimization Algorithm.* The same dataset often produces different prediction results in speech and face recognition. In order to improve the recognition accuracy and balance of different expressions after fusion, the multiobjective optimization algorithm is used to fuse the two modalities, so that the recognition results of their different modalities can make up for each other.

In this article, we use two coefficients to linearly combine two basic emotion recognition technologies (based on deep separation convolutional facial emotion recognition and deep convolutional neural network-based voice emotion recognition). And use a multiobjective optimization algorithm to simultaneously optimize accuracy (precision) and the evaluation model of emotion recognition uniformity, as shown in

$$R = w_1 \times R_1 + w_2 \times R_2, \quad (6)$$

where R_1 and R_2 are the final prediction results of speech emotion recognition based on a deep convolution neural network and deep separation convolution facial emotion recognition, respectively. In addition, w_1 and w_2 are coefficients that need to be optimized. According to the actual meaning of the model, the constraints of the two coefficients are as follows:

$$w_1 + w_2 = 1. \quad (7)$$

The function of the multiobjective optimization algorithm is to optimize the two coefficients, so that the two recognition techniques can be effectively combined. The accuracy of the optimization coefficient will directly affect the final recognition result of the model and then affect the accuracy of facial expression recognition.

After obtaining the facial and voice results, the decision-level fusion method is adopted to fuse the two to obtain the final recognition result. For the first time in this article, a multiobjective optimization algorithm is used to optimize the emotion recognition model to achieve the best results. Its framework is shown in Figure 4.

R_1 and R_2 show the emotion recognition results using the two recognition techniques, respectively, in Figure 4. At the same time, w_1 and w_2 represent the coefficients of combining the two recognition techniques.

4. Experiments

4.1. *Experimental Setup.* In order to prove the effectiveness of the multiobjective optimization algorithm for improving the effect of multimodal emotion recognition, this article compares the effect of emotion recognition using the multiobjective optimization algorithm with the model effect without using the multiobjective optimization algorithm. This paper uses the IEMOCAP multimodal emotion database. In addition to the comparison test with the single-modal model proposed in this paper, the comparison experiment is also compared with the multimodal emotion recognition ISMS_ALA [37] model that has not been optimized by the multiobjective optimization algorithm.

4.2. *Evaluation Method.* The multiobjective optimization algorithm is used to optimize the accuracy of model recognition and the uniformity of emotion recognition at the same time. The confusion matrix of seven categories of emotion recognition is shown in Table 1.

In the first evaluation, the standard accuracy is defined as the ratio of the number of correctly predicted classified emotions to the total number of all data. The accuracy formula is as follows:

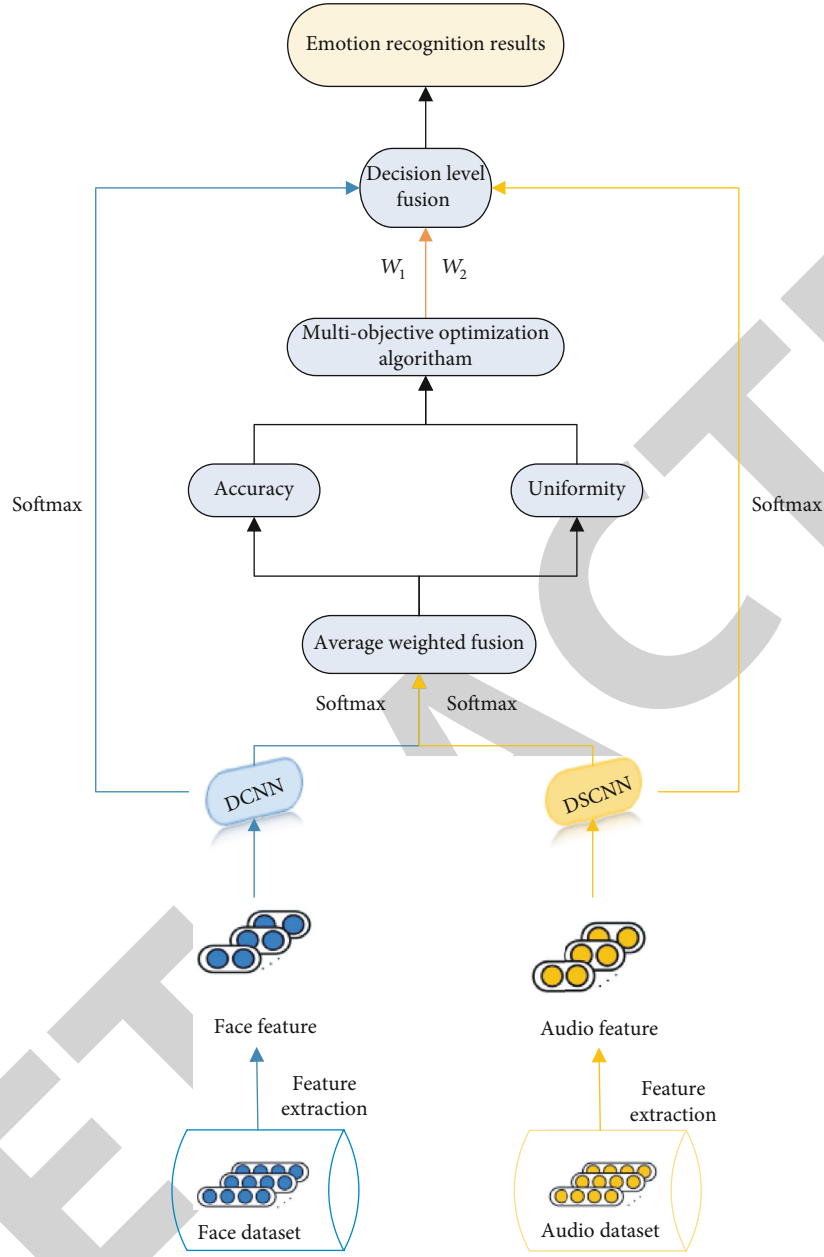


FIGURE 4: The framework of the multimodal emotion recognition model with many objectives.

$$\text{Accuracy} = \frac{T}{T + F}, \quad (8)$$

where T represents the number of samples that predict the correct sentiment and F represents the number of samples that predict the wrong sentiment.

Because of this research, emotion recognition belongs to seven categories. Different emotions have corresponding prediction accuracy results. In the traditional research of multimodal emotion recognition, the accuracy of different emotion recognition often differs greatly. Therefore, in order to balance and improve the recognition accuracy of different emotions, the evaluation index of emotion recognition uniformity is proposed.

TABLE 1: Confusion matrix of the evaluation indicators.

		Predicted result			
		1	2	3	4
Actual result	1	TP_{11}	FP_{21}	FP_{31}	FP_{41}
	2	FP_{12}	TP_{22}	FP_{32}	FP_{42}
	3	FP_{13}	FP_{23}	TP_{33}	FP_{43}
	4	FP_{14}	FP_{24}	FP_{34}	TP_{44}

In order to define the second evaluation index, the uniformity of emotion recognition, we first introduce the concept of recall rate. The recall rate refers to the number of correct predictions of each different emotion in the

prediction results and the total number of corresponding emotions in all data.

$$\text{Recall}_i = \frac{T_{ii}}{\sum_{j=1, j \neq k}^N F_{ji} + T_{ii}}. \quad (9)$$

Recall_i represents the recall rate predicted by the current i class emotion algorithm. In order to balance and improve the recognition accuracy of different emotions, the evaluation index of emotion recognition uniformity is proposed.

$$U = \frac{\sum_{i=1}^N |\text{Recall}_i - \text{Recall}_{\text{aver}}|}{N}. \quad (10)$$

$\text{Recall}_{\text{aver}}$ represents the average recall rate of seven emotion categories.

4.3. Experimental Result. As shown in Tables 2 and 3, the single-modal emotion recognition accuracy of the facial emotion recognition model based on the deep separation convolution and speech emotion recognition model based on the deep convolution neural network are, respectively, shown.

According to the analysis of the above table, the accuracy of facial emotion recognition is higher than that of speech emotion recognition. The calculation shows that the average recognition accuracy of facial emotion recognition using deep separation convolution is 71.2%. The average accuracy of speech emotion recognition based on deep convolutional neural networks is 69.1%. At the same time, through observation, we also found that there is a big gap in the uniformity of different emotion recognition of facial and voice emotion recognition. Among them, the recognition accuracy of facial and voice neutral emotions are only 64.1% and 61.3%, respectively. However, the recognition accuracy of happy emotion reached 81.3% and 76.7%, respectively. Therefore, we use the multiobjective optimization algorithm to optimize the accuracy and uniformity of emotion recognition at the same time.

In the model training stage, NSGA-III [38], MOEA/DD [39], HypE [32], and PEAS [26] were used to optimize coefficients w_1 and w_2 , respectively. Each time the algorithm runs once, pop_size individuals will be generated. Different individual experiences are fused into different recognition results. Common parameter settings in MOEA are shown in Table 4.

As shown in Figures 5(a) and 5(b), the results of the four algorithms optimized multimodal emotion recognition model in the two evaluation indicators which are drawn into a box plot. In these figures, each box represents all individuals except discrete individuals in the group (discrete individuals are represented by small circles). Each line represents the performance of a basic monomodal emotion recognition technology on the evaluation index. The green dotted line represents the performance of the ISMS_ALA model on the IEMOCAP test set.

From the analysis in Figures 5(a) and 5(b), we can conclude that compared with the other three algorithms, the model optimized by the PEAS algorithm has the shortest box line graph length on three different optimization objec-

TABLE 2: Speech emotion recognition results based on a deep convolution neural network.

		Predicted result			
		Anger	Happy	Neutral	Sad
Actual result	Anger	70.6%	5.6%	11.3%	12.5%
	Happy	4.5%	81.3%	6.7%	7.5%
	Neutral	8.7%	9.3%	64.1%	17.9%
	Sad	12.7%	5.8%	12.3%	69.2%

TABLE 3: Facial expression recognition results based on deep separation convolution.

		Predicted result			
		Anger	Happy	Neutral	Sad
Actual result	Anger	72.2%	7.8%	5.1%	14.9%
	Happy	13.4%	76.7%	5.8%	4.1%
	Neutral	9.2%	8.2%	61.3%	21.3%
	Sad	7.7%	8.9%	17.2%	66.2%

TABLE 4: The setting of common parameters.

Parameter	Meaning	Value
Iter	Number of iterations	500
POP _{size}	The population size	100
D	Dimensions of decision variables	2
M	The number of optimization objectives	2
P_m	The mutation probability	0.2
P_c	The crossover probability	1

tives, and there is no discrete individual. This shows that PEAS has better convergence than other algorithms when solving this model. At the same time, it can be seen that the model optimized based on the NSGA-III, HypE, and MOEA/DD algorithm has a small number of scattered individuals and the length of the box plot is too long, indicating that the convergence of the population is insufficient. At the same time, we can see that the optimal model optimized by the multiobjective optimization algorithm is better than the technology only using single modal for emotion recognition and ISMS_ALA model without the multiobjective optimization algorithm. Next, compare the performance of the four algorithms in solving the model, and the results are shown in Table 5.

From the analysis of Table 5, it can be concluded that the results of the PEAS optimization model are the best in accuracy and uniformity. The highest accuracy is 75.38%. The accuracy of the model is improved by 2.88% compared with that of the ISMS_ALA model, and the uniformity evaluation index is reduced by 0.0211. In terms of the worst value and average value of the evaluation index, PEAS is also better than the other three optimization algorithms. At the same time, compared to the single-modal emotion recognition model that uses multiobjective optimization algorithms, the

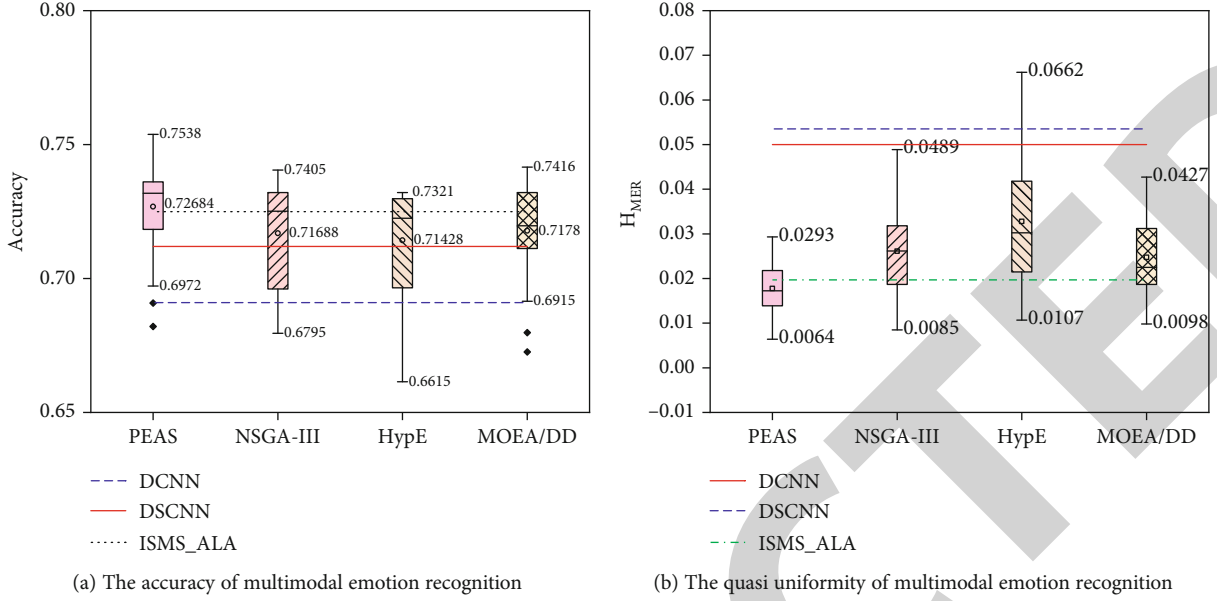


FIGURE 5: Four multiobjective optimization algorithms for multimodal emotion recognition.

TABLE 5: Algorithm performance comparison.

	Algorithm	Accuracy	H_{MER}
Single modal emotion recognition technology	DCNN	0.712	0.05
	DSCNN	0.691	0.0535
	ISMS_ALA	0.725	0.0245
Best value	NSGA-III	0.7405	0.0085
	HypE	0.7321	0.0107
	PEAS	0.7538	0.0034
	MOEA/DD	0.7416	0.0098
Worst value	NSGA-III	0.6795	0.0489
	HypE	0.6615	0.0662
	PEAS	0.6972	0.0261
	MOEA/DD	0.6726	0.0427
Mean value	NSGA-III	0.7169	0.0261
	HypE	0.7143	0.0328
	PEAS	0.7268	0.0178
	MOEA/DD	0.7178	0.0247

accuracy and uniformity indicators are greatly improved. Experiments show that the multiobjective optimization algorithm effectively improves the performance of the multimodal emotion recognition model.

5. Conclusions

This paper presents a multimodal emotion recognition model based on the multiobjective optimization algorithm. The model can optimize the accuracy and uniformity of recognition results at the same time. Through the model optimization experiments of four multiobjective optimization algorithms, it is found that the model optimized by the algo-

gorithm has a great improvement compared with the single-modal emotion recognition model. At the same time, compared with the traditional multimodal emotion recognition ISMS_ALA model, the accuracy is improved by 2.88%, and the uniformity is also significantly improved. To sum up, the proposed multiobjective optimization algorithm effectively improves the performance of the multimodal emotion recognition model.

Data Availability

For the data used to support the results of this study, please contact the corresponding author.

Conflicts of Interest

The authors declare that they have no conflicts of interest.

Acknowledgments

The work reported in this paper is partially supported by the science and technology project of the Chongqing Education Commission of China (No. KJQN201900520), humanities and social sciences project of Chongqing Education Commission (No. 19SKGH035), graduate education reform project of Chongqing Education Commission (No. yjg193093), and Chongqing Normal University Graduate Scientific Research Innovation Project (Grant YZH21014 and YZH21010).

References

- [1] R. W. Picard, *Affective Computing*, MIT press, 2000.
- [2] R. W. Picard, "Affective computing: challenges," *International Journal of Human-Computer Studies*, vol. 59, no. 1-2, pp. 55–64, 2003.
- [3] J. Tao and T. Tan, "Affective computing: a review," in *International Conference on Affective Computing and Intelligent Interaction*, pp. 981–995, Beijing, China, 2005.
- [4] S. Li and W. Deng, "Deep facial expression recognition: a survey," *IEEE Transactions on Affective Computing*, 2020.
- [5] Y. Li, J. Zeng, S. Shan, and X. Chen, "Occlusion aware facial expression recognition using CNN with attention mechanism," *IEEE Transactions on Image Processing*, vol. 28, pp. 2439–2450, 2018.
- [6] Z. Meng, P. Liu, J. Cai, S. Han, and Y. Tong, "Identity-aware convolutional neural network for facial expression recognition," in *2017 12th IEEE International Conference on Automatic Face & Gesture Recognition (FG 2017)*, pp. 558–565, Washington, DC, USA, 2017.
- [7] R. Tanabe and H. Ishibuchi, "An easy-to-use real-world multi-objective optimization problem suite," *Applied Soft Computing*, vol. 89, article 106078, 2020.
- [8] M. J. Mayer, A. Szilágyi, and G. Gróf, "Environmental and economic multi-objective optimization of a household level hybrid renewable energy system by genetic algorithm," *Applied Energy*, vol. 269, article 115058, 2020.
- [9] J. Zhang, Y. Huang, Y. Wang, and G. Ma, "Multi-objective optimization of concrete mixture proportions using machine learning and metaheuristic algorithms," *Construction and Building Materials*, vol. 253, article 119208, 2020.
- [10] F. Wang, Y. Li, F. Liao, and H. Yan, "An ensemble learning based prediction strategy for dynamic multi-objective optimization," *Applied Soft Computing*, vol. 96, article 106592, 2020.
- [11] M. Abdel-Basset, R. Mohamed, and S. Mirjalili, "A novel whale optimization algorithm integrated with Nelder-Mead simplex for multi-objective optimization problems," *Knowledge-Based Systems*, vol. 212, p. 106619, 2021.
- [12] B. Duc, E. S. Bigün, J. Bigün, G. Maître, and S. Fischer, "Fusion of audio and video information for multi modal person authentication," *Pattern Recognition Letters*, vol. 18, no. 9, pp. 835–843, 1997.
- [13] L. S. Chen, T. S. Huang, T. Miyasato, and R. Nakatsu, "Multi-modal human emotion/expression recognition," in *Proceedings Third IEEE International Conference on Automatic Face and Gesture Recognition*, pp. 366–371, Nara, Japan, 1998.
- [14] C. Busso and S. S. Narayanan, "Joint analysis of the emotional fingerprint in the face and speech: a single subject study," in *2007 IEEE 9th Workshop on Multimedia Signal Processing*, pp. 43–47, Chania, Greece, 2007.
- [15] Y. Wang and L. Guan, "Recognizing human emotional state from audiovisual signals," *IEEE Transactions on Multimedia*, vol. 10, no. 4, pp. 659–668, 2008.
- [16] M. D. Ding and L. Li, "CNN and HOG dual-path feature fusion for face expression recognition," *Information and Control*, vol. 49, no. 1, pp. 47–54, 2020.
- [17] L. Q. Lan and X. Zhang, "Facial expression recognition method based on a joint normalization strategy," *Journal of Beijing University of Aeronautics and Astronautics*, vol. 46, no. 9, pp. 1797–1806, 2020.
- [18] A. A. Muhammad and J. K. Muhammad, "EEG-based multi-modal emotion recognition using bag of deep features: an optimal feature selection approach," *Sensors*, vol. 19, no. 23, 2019.
- [19] A. Zadeh, P. P. Liang, and S. Poria, "Multi-attention recurrent network for human communication comprehension," in *Proceedings of the 32th AAAI Conference on Artificial Intelligence*, pp. 5642–5649, New Orleans, USA, 2018.
- [20] C. G. M. Snoek, M. Worring, and A. W. M. Smeulders, "Early versus late fusion in semantic video analysis," in *Proceedings of the 13th annual ACM international conference on Multimedia - MULTIMEDIA '05*, pp. 399–402, Singapore, 2005.
- [21] K. Lu and X. Zhang, "Audio-visual emotion recognition using neural networks learned with hints," in *2013 seventh international conference on image and graphics (ICIG)*, pp. 515–519, Qingdao, China, 2013.
- [22] S. Sahoo and A. Routray, "Emotion recognition from audio-visual data using rule based decision level fusion," in *2016 IEEE Students' Technology Symposium (TechSym)*, pp. 7–12, Kharagpur, India, 2016.
- [23] W. Rahman, M. K. Hasan, and A. Zadeh, "M-BERT: injecting multimodal information in the BERT structure," in *Proceedings of the 58th Annual Meeting of the Association for Computational Linguistics*, pp. 2359–2369, 2020.
- [24] X. Chen, B. Wu, and P. Sheng, "A multiobjective evolutionary algorithm based on surrogate individual selection mechanism," *Personal and Ubiquitous Computing*, vol. 23, no. 3-4, pp. 421–434, 2019.
- [25] Y. Hou, H. Han, and J. Qiao, "Adaptive multi-objective differential evolution algorithm based on the dynamic parameters adjustment," *Control & Decision*, vol. 32, 2017.
- [26] H. P. Ren, X. N. Huang, and J. X. Hao, "Finding robust adaptation gene regulatory networks using multi-objective genetic algorithm," *IEEE/ACM Transactions on Computational Biology and Bioinformatics*, vol. 13, pp. 571–577, 2015.
- [27] B. A. al Jassani, N. Urquhart, and A. Almaini, "State assignment for sequential circuits using multi-objective genetic algorithm," *IET Computers & Digital Techniques*, vol. 5, no. 4, pp. 296–305, 2011.
- [28] Y. F. Cheng, W. Shao, S. J. Zhang, and Y. P. Li, "An improved multi-objective genetic algorithm for large planar array thinning," *IEEE Transactions on Magnetics*, vol. 52, pp. 1–4, 2015.
- [29] A. Zhou, B. Y. Qu, H. Li, S. Z. Zhao, P. N. Suganthan, and Q. Zhang, "Multiobjective evolutionary algorithms: a survey of the state of the art," *Swarm and Evolutionary Computation*, vol. 1, no. 1, pp. 32–49, 2011.

Retraction

Retracted: Research and Application of Multifeature Gesture Recognition in Human-Computer Interaction Based on Virtual Reality Technology

Wireless Communications and Mobile Computing

Received 1 August 2023; Accepted 1 August 2023; Published 2 August 2023

Copyright © 2023 Wireless Communications and Mobile Computing. This is an open access article distributed under the Creative Commons Attribution License, which permits unrestricted use, distribution, and reproduction in any medium, provided the original work is properly cited.

This article has been retracted by Hindawi following an investigation undertaken by the publisher [1]. This investigation has uncovered evidence of one or more of the following indicators of systematic manipulation of the publication process:

- (1) Discrepancies in scope
- (2) Discrepancies in the description of the research reported
- (3) Discrepancies between the availability of data and the research described
- (4) Inappropriate citations
- (5) Incoherent, meaningless and/or irrelevant content included in the article
- (6) Peer-review manipulation

The presence of these indicators undermines our confidence in the integrity of the article's content and we cannot, therefore, vouch for its reliability. Please note that this notice is intended solely to alert readers that the content of this article is unreliable. We have not investigated whether authors were aware of or involved in the systematic manipulation of the publication process.

Wiley and Hindawi regrets that the usual quality checks did not identify these issues before publication and have since put additional measures in place to safeguard research integrity.

We wish to credit our own Research Integrity and Research Publishing teams and anonymous and named external researchers and research integrity experts for contributing to this investigation.

The corresponding author, as the representative of all authors, has been given the opportunity to register their

agreement or disagreement to this retraction. We have kept a record of any response received.

References

- [1] Z. Feng, J. Wu, and T. Ni, "Research and Application of Multifeature Gesture Recognition in Human-Computer Interaction Based on Virtual Reality Technology," *Wireless Communications and Mobile Computing*, vol. 2021, Article ID 3603693, 5 pages, 2021.

Research Article

Research and Application of Multifeature Gesture Recognition in Human-Computer Interaction Based on Virtual Reality Technology

Zhao Feng,¹ Jinlong Wu,² and Taile Ni ¹

¹School of Literature, Journalism & Communication, Xihua University, Chengdu, Sichuan 61000, China

²Nanjing Normal University Taizhou College, Taizhou, Jiangsu 225300, China

Correspondence should be addressed to Taile Ni; nitaile@mail.xhu.edu.cn

Received 6 July 2021; Revised 27 July 2021; Accepted 9 August 2021; Published 20 August 2021

Academic Editor: Balakrishnan Nagaraj

Copyright © 2021 Zhao Feng et al. This is an open access article distributed under the Creative Commons Attribution License, which permits unrestricted use, distribution, and reproduction in any medium, provided the original work is properly cited.

Objective. To explore the research and application of multifeature gesture recognition in virtual reality human-computer interaction and to explore the gesture recognition technology scheme to achieve better human-computer interaction experience. **Methods.** Through the study of the technical difficulties of gesture recognition, comparative static gesture feature recognition and feature fusion algorithms are applied, in the process of research on gesture partition, and adjust the contrast of characteristic parameters, combined with the feature of space-time dynamic gesture tracking trajectory and dynamic gesture recognition and gesture recognition effect under different scheme. **Results.** The central region was divided into 0 regions, and the central region was divided into 1-4 regions in counterclockwise direction. Compared with the traditional gesture changes, the overlapping problem in the four partition modes was reduced, the gesture was better displayed, and the operation and use of gesture processing were realized more efficiently. **Conclusion.** Gesture recognition requires the combination of static gesture feature information recognition, gesture feature fusion, spatiotemporal trajectory feature, and dynamic gesture trajectory feature to achieve a better human-computer interaction experience.

1. Introduction

With the wide use of computer and Internet in people's daily life, it is generally believed that the human-computer interaction technology, which is widely used at present with the mouse, keyboard, or touch screen as the interactive means, will become the bottleneck for the further effective utilization of information flow. With the continuous popularization of intelligent concepts and the rapid development of related technologies, people begin to explore more natural, more friendly, and more effective human-computer interaction methods [1, 2]. As a result, a variety of new human-computer interaction technologies continue to emerge, such as speech recognition, facial recognition, gesture recognition, and human movement recognition. Among these numerous technologies, gesture interaction technology has a wide range of application fields and broad application prospects because of its natural, intuitive, and easy to learn characteristics.

Multifeature gesture recognition is carried out by using the virtual reality human-computer interaction software. Line of sight selection directly affects the final gesture recognition function [3]. Only by selecting the correct sight gesture recognition can it proceed smoothly, so as to meet the recognition and tracking requirements in the virtual reality human-computer interaction system [4]. Gesture recognition belongs to the dynamic information capture, tracking accuracy in information and update on time to achieve defined standards; implementation choice first needs to determine the control points, which is the line of sight in the process of exchange center, determined by the center for visual direction judgment, users in the process of watching interaction point, to achieve the transformation on the vision. And the multifeature gesture is recognized into the computer software [5]. In the tracking algorithm of multifeature gesture recognition, line of sight selection can also be understood as the control of gesture capture points. The

basic anchor points of each gesture are captured to more accurately integrate multifeature dynamic gesture recognition into the human-computer interaction system.

Virtual reality (VR for short) refers to the use of computer-related technology to simulate the real scene and experience, trying to create an immersive feeling. Among them, the word “virtual” means that it does not exist in the actual physical space but exists in the virtual/cyberspace of the image made by the computer. Virtual reality technology is an upgrade of display technology and a combination of highly developed computer technology in various fields. Virtual reality technology was mainly applied to the desktop in the early stage. Due to the large size and high price of immersive virtual reality display helmet, exists only in some research institutions and laboratories, but with the development of smart hardware technology, such as gyroscopes, small high-definition screens, and lightweight processors, it reduces the development cost of virtual reality equipment and improves related performance, which makes the Oculus Rift prototype appear in 2012 and immersive virtual reality technology enter the consumer level. Thus, virtual reality begins to transform from desktop to immersive [6].

At present, the characteristics of virtual reality technology can be summarized into three points: immersion, interaction, and imagination, referred to as 3I characteristics [7]. In recent years, the development of virtual reality technology is mainly to solve the first attribute, namely, immersion. By improving the performance of related hardware, it tries to make users in the virtual environment reach the degree that it is difficult to distinguish the real from the fake. However, it should be noted that interaction is also a very important attribute, which is the core link for virtual reality to provide users with experience and move towards application.

Real-time dynamic gesture recognition technology is based on computer vision, and using OpenTV computer vision library on the platform to design an application is based on this technology in multimedia teaching control. The main content is divided into four parts: gesture detection, gesture tracking, gesture recognition, and the final application implementation. In the part of gesture detection, first of all, the method is used to collect real-time video images, and then, the motion detection method combining background difference and color histogram information is used to complete gesture detection. In the experiment, the brightness values of the pixels in the moving skin region were specially adjusted to eliminate interference from the stationary face region.

At present, gesture interaction generally uses computer vision algorithm to capture the user’s hand movement and convert it into human-computer interaction commands. Compared with traditional interaction methods, gesture interaction based on vision can enable the user to get rid of the constraints of input devices. It has the advantages of low attachment, weak invasion, and more natural interaction experience [8]. However, due to the excessive flexibility of gestures and the accuracy of the sensor itself, the existing gesture interaction accuracy still needs to be improved. In order to solve the above problems, there is an urgent need to develop new theories and methods of gesture interaction,

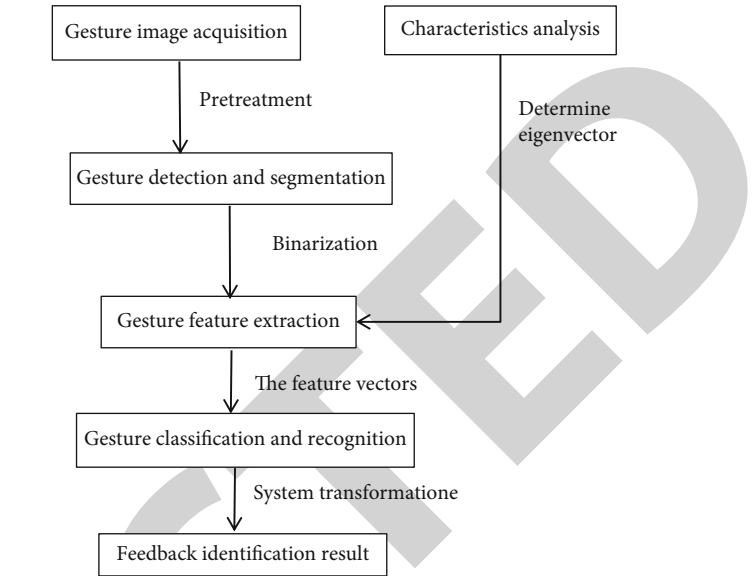


FIGURE 1: Basic steps for static gesture recognition.

so as to improve users’ interactive experience in the immersive virtual reality environment.

2. Research Methods

Gesture recognition research mainly includes two aspects: static gesture recognition and dynamic gesture recognition. The essence of static gesture recognition is to classify different static gestures, that is, to extract the features of the acquired gestures first, and then to use the classification algorithm to determine. Static gesture recognition is the foundation of dynamic gesture recognition, which is more complicated.

2.1. Static Gesture Recognition. The basic steps of static gesture recognition mainly include the acquisition of gesture image, gesture detection and segmentation, gesture feature analysis and feature extraction, gesture classification and recognition, and feedback of the final result. The basic steps of static gesture recognition are shown in Figure 1.

Gesture model construction is the key of gesture feature analysis. The essence of gesture model construction is to propose a practical and effective discriminator for gesture recognition through in-depth analysis of all valid features of gestures in practical application situations. The specific process includes two main steps: first, for the extracted gesture image, analysis and extraction of its main features. Second, the feature pattern library of different gestures is constructed according to the extracted gesture features [9]. Among them, the first step is the foundation, and the quality of the pattern library constructed in the second step will directly affect the recognition result. At present, static gesture modeling is divided into two categories: epigenement-based gesture modeling and 3D-based gesture modeling. The main difference lies in the perspective from which the model is modeled, 2D and 3D, respectively. In different

application scenarios, different gesture modeling methods should be selected according to the conditions.

Gesture modeling based on appearance analyzes and extracts the gesture feature information from the two-dimensional plane image of the gesture, and the commonly used information includes color information, contour information, and texture information. The color information of gesture is modeled by building skin color model. Gesture contour information is extracted after edge detection, which belongs to the whole geometric feature of gesture. Gesture texture information is the texture feature that describes the details of gesture image. In comparison, gesture modeling based on 3D model pays more attention to 3D characterization of the whole gesture, and the gesture information described is more accurate, and the model contains a lot of parameters. The construction of 3D model requires multiple cameras to collect gesture images from different perspectives, and the amount of data acquired is usually large, and the processing is complex. At the same time, in the real application environment, a single ordinary camera is relatively common. It can only obtain the user's gesture image from a two-dimensional plane, extract the color, contour and texture information of the gesture, and construct the appearance model of the gesture [10].

2.2. Dynamic Gesture Tracking. Compared with static gesture recognition, the process of dynamic gesture recognition is more complicated and has more problems. Because dynamic gesture is composed of a series of continuous static gesture sequences, it not only contains all the characteristic information of a single static gesture, but also contains the shape change and position change of the gesture in space. Therefore, according to different recognition scenarios, different feature information should be selected to describe dynamic gestures.

Gesture tracking is a key step in the process of visual dynamic gesture recognition. Gesture tracking refers to the real-time positioning and tracking of moving gestures in video sequence images by using certain characteristics of gestures, which is used to establish a time-domain model of dynamic gestures. The efficiency of gesture tracking will seriously affect the real-time performance of the whole interactive system, and the accuracy of tracking will directly affect the accuracy of subsequent gesture recognition results [11]. It is of great significance to build a robust gesture recognition interactive system through in-depth study of gesture tracking. Because gestures are nonrigid and highly flexible, and dynamic gestures may have random deformation, illumination intensity change, complex environment interference in real time (such as the interference of skin color objects), object blocking, and other situations during the movement, it is very challenging to solve these problems.

In a complex environment, it is still a big challenge to be able to efficiently and accurately implement a realistic visual-based gesture tracking algorithm. Researchers often sacrifice the real-time requirement of the system by integrating the accuracy and robustness of multifeature reality tracking. There are various factors in the real environment, such as gesture deformation, motion speed, gesture scale, light

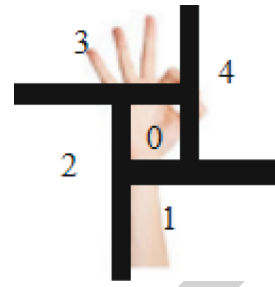


FIGURE 2: Area map of gesture. After applying the HOG feature region method, there is also a breakthrough innovation in the partitioning processing of gesture changes.

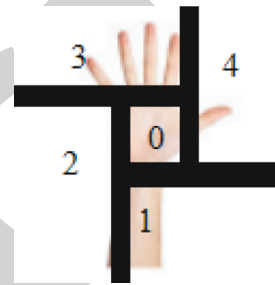


FIGURE 3: Area map of gesture. After applying the HOG feature region method, there is also a breakthrough innovation in the partitioning processing of gesture changes.

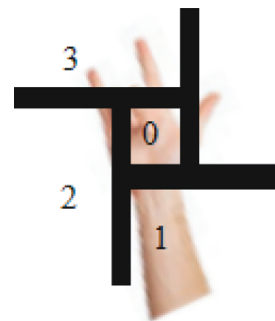


FIGURE 4: Area map of gesture. After applying the HOG feature region method, there is also a breakthrough innovation in the partitioning processing of gesture changes.

intensity, and target occlusion, which affect the accuracy and real-time performance of visual gesture tracking.

2.3. Research and Application of Multifeature Gesture Recognition

2.3.1. Gesture Recognition Feature Extraction. HOG feature extraction. In this feature extraction algorithm, image description is used to construct the scene. In the face of multifeature gestures, the first step in the extraction process is to determine the appearance, extract the features of the external contour, depict the virtual scene consistent with the gesture, and continue to enhance the accuracy of multifeature gestures through the construction of this virtual scene. This feature extraction algorithm is often used in security identification. The multifeature gesture changes a lot, and the final control efficiency will be significantly

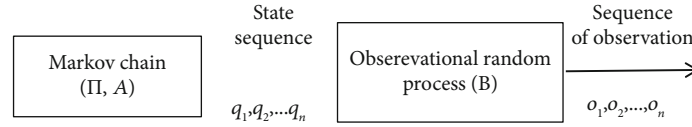


FIGURE 5: Composition of the HMM trajectory identification system. During recognition, relevant sequences will be established, and the edge area of gesture action will be formed through random generation inside the system to achieve the best simulation effect.

enhanced after the application of this tracking method. Using the HOG extraction method in multifeature gesture tracking, the gesture image will be subdivided into multiple units, and each unit has different features, so as to describe the edge image in the change of gesture [12]. And these subdivided cells are uniformly divided into the same area, so that the extracted gradient edge map is also connected together.

Dynamic gesture image partition processing. After applying the HOG feature region method, there is also a breakthrough innovation in the partitioning processing of gesture changes. According to the gesture changes under different circumstances, it is divided into 5 regions, as shown in Figures 2–4.

The central region of the palm was divided into 0 regions, and along the central region, 1-4 regions were divided in a counterclockwise direction. Compared with the traditional gesture change, this kind of gesture change reduces the overlapping problem in the four partition modes and presents the gesture better. In capturing gestures in different regions, error control should be kept consistent. After the overlap problem is solved, the details of gesture actions are also displayed, and the captured actions can be reflected in real time in the virtual reality human-computer interaction system, so as to realize more efficient operation and use of gesture processing. After the task of gesture capture, it can enter the following algorithm fusion. The field control is carried out through the cooperation between algorithms, and the specific changes of gestures are shown through the transformation between algorithms.

HOG feature extraction and tracking algorithm. The Gaussian function calculation method was used to construct the field calculation and smooth processing of the grayscale image captured by the gesture edge. The calculation formula is as follows:

$$\frac{\delta f}{\delta x} = f(x+1) - f(x), \quad (1)$$

where it represents the position of captured dynamic points in coordinates, establishes a subset of captured dynamic recognition points of multifeature gestures, and improves the final capture effect in its own interactive processing. The gradient value of the edge part is also affected by the pixels in the process of gesture dynamic capture, and the influence of edge jitter is more serious in the process of gesture dynamic capture. In this case, the range of coordinate value subset can be designed in the process of pixel capture control. The system makes automatic error compensation according to the parameter results in the operation process.

After adjusting the data, the captured edge of the gesture is more rounded.

2.3.2. HOG Gesture Feature Fusion. Gesture feature fusion needs to be based on the weighted matrix, and interactive processing can be carried out through the default feature fusion within the system [13]. The mark points in the changes of different gestures are tracked and captured. In the process of feature fusion, it is only carried out for the changes of gesture movements. Therefore, in the primary processing stage, the grayscale processing is carried out on the image to avoid the influence of image color on feature fusion. The feature fusion adopts the mutual fusion between vector and matrix. The feature vector set of gesture image is $FHOG=[FH1OG\ FH2OG\dots\ FHN OG]$, and the global feature is represented by the vector $FHU=[FH1\ FH2\ FH3\dots\ FH8\ FH9]$. The influence degree of different features varies greatly. If the influence degree is directly applied to feature fusion, the interaction between different influences will result in the final gesture recognition error. Before feature fusion, one of the vectors will be normalized to determine that the subset can maintain the influence of the same vector in the mutual influence mode, so as to help improve the final extraction of virtual reality human-computer interaction algorithm and determine the required data subset range through this method.

2.3.3. Dynamic Gesture Characteristics of Spatial-Temporal Trajectory. Gesture feature extraction based on spatiotemporal trajectory should first determine its position, observe the position of the gesture in the spatiotemporal trajectory, and then magnify the key part to facilitate the capture and recognition of the changes of the gesture. The description of position trajectory also needs to be carried out with the help of vector to determine the angle in the process of gesture change. Establish the following formula: $\theta = \arctan [(yt+1 - yt)/(xt+1 - xt)]$. Different angle coordinates in the process of gesture change can be brought into it, and more detailed results and values can be obtained through calculation, so as to capture dynamic gesture features under the spatiotemporal trajectory. At the same time, there may be interference factors in the picture entered into the virtual reality human-computer interaction mode. The purpose of determining the position through angle calculation is to screen out such interference data and realize more accurate multifeature gesture recognition and tracking.

2.3.4. HMM Dynamic Gesture Track Recognition. Trajectory recognition is an important basis of gesture authentication. When the gesture to be recognized is in the dynamic mode, the trajectory of the whole movement process needs to be

Retraction

Retracted: Study of Node Distribution and Density Optimization in Mobile Sensor Network 3D Space

Wireless Communications and Mobile Computing

Received 28 November 2023; Accepted 28 November 2023; Published 29 November 2023

Copyright © 2023 Wireless Communications and Mobile Computing. This is an open access article distributed under the Creative Commons Attribution License, which permits unrestricted use, distribution, and reproduction in any medium, provided the original work is properly cited.

This article has been retracted by Hindawi, as publisher, following an investigation undertaken by the publisher [1]. This investigation has uncovered evidence of systematic manipulation of the publication and peer-review process. We cannot, therefore, vouch for the reliability or integrity of this article.

Please note that this notice is intended solely to alert readers that the peer-review process of this article has been compromised.

Wiley and Hindawi regret that the usual quality checks did not identify these issues before publication and have since put additional measures in place to safeguard research integrity.

We wish to credit our Research Integrity and Research Publishing teams and anonymous and named external researchers and research integrity experts for contributing to this investigation.

The corresponding author, as the representative of all authors, has been given the opportunity to register their agreement or disagreement to this retraction. We have kept a record of any response received.

References

- [1] M. Gu, C. Gao, J. Lyu, W. Fan, and L. You, "Study of Node Distribution and Density Optimization in Mobile Sensor Network 3D Space," *Wireless Communications and Mobile Computing*, vol. 2021, Article ID 6978812, 7 pages, 2021.

Research Article

Study of Node Distribution and Density Optimization in Mobile Sensor Network 3D Space

Musong Gu ^{1,2,3}, Chaobang Gao ¹, Jingjing Lyu ^{1,3}, Wenjie Fan ¹ and Lei You ¹

¹College of Computer Science, Chengdu University, Chengdu, China

²School of Information and Communication Engineering, University of Electronic Science and Technology of China, Chengdu, China

³Key Laboratory of Pattern Recognition and Intelligent Information Processing, Institutions of Higher Education of Sichuan Province, Chengdu University, Chengdu, China

Correspondence should be addressed to Jingjing Lyu; lvjingjing@cdu.edu.cn

Received 28 June 2021; Accepted 3 August 2021; Published 20 August 2021

Academic Editor: Balakrishnan Nagaraj

Copyright © 2021 Musong Gu et al. This is an open access article distributed under the Creative Commons Attribution License, which permits unrestricted use, distribution, and reproduction in any medium, provided the original work is properly cited.

Mobile sensor network is applied in information collection in emergencies. As the mobile sensor network in real environment is widely deployed with different height and the redundancy of the sensor node needs to be as low as possible, therefore, it is necessary to effectively deploy mobile sensor nodes in the 3D space to have reasonable layout and optimized density. To this end, we established the optimization model of mobile sensor network deployment and solved the model with chemical reaction optimization (CRO). The experimental results have shown that compared with traditional particle swarm optimization (PSO), CRO algorithm can achieve reasonable deployment more rapidly and enhance the network performance evaluation value effectively. The reasonable deployment of mobile sensor network node is very significant to information collecting, postperiod decision-making, and rapid rescuing work in emergencies.

1. Introduction

In recent years, advances in technology have made it possible to achieve compact and low-cost mobile sensors, and more and more people are beginning to focus on mobile sensor networks. In this chapter, we study a wireless sensor network in which each mobile node has some maneuvering capabilities of traditional static nodes; besides, it is composed of all the enhanced nodes with controllable mobility. For some traditional, wireless sensor network deployment methods will be very difficult or even invalid if they are used in hazardous areas and dynamic environmental objects such as disaster sites and emergency rescue. With the mobile sensor network composed of mobile sensor nodes, the problem can be solved. Related sensor's mobile node can be automatically deployed on site, according to predetermined procedure to obtain an appropriate node distribution density and then network coverage timely return real-time monitoring data. The issue of wireless sensor network node distribution and density optimization is one of focuses of

the wireless sensor network study [1], mainly concerning deployment environment, node sense model and deployment algorithm [2], etc.; full coverage of sensor network can be achieved after comprehensive consideration of many factors. Compared with the deployment of conventional 2D plane environment, it is more complex to achieve the deployment of 3D plane environment, which is much closer to practical application environment; therefore, the research work is more of practical meaning.

Due to the limited energy of sensor node and inaccessibility of its application area, in order to improve the surveillance quality and network reliability of the wireless sensor network, generally, the sensor nodes are deployed in the target area of interest extensively and densely, causing the coverage area of large amounts of nodes in the network to overlap with each other. This coverage redundancy directly leads to redundancy of collecting and transmitting data, thus resulting in unnecessary energy consumption. To address the coverage redundancy of the sensor network node, we study the density optimization of node distribution in the 3D space of mobile

sensor network in this paper. The model is built in 3D space, considering the coverage and connectivity of wireless sensor network and forming a composite evaluation function. In order to reduce the difficulty of solving this function, we use geometric weighting method to transform the multiobjective constraint optimization function into an equivalent single constraint optimization function and use a relatively new chemical reaction optimization (CRO) algorithm to solve this function.

In the study of mobile sensor network, the deployment of mobile node is an important research branch, which concerns how to put limited node into the surveillance area reasonably to achieve maximum network surveillance performance. Many scholars discussed the self-organizing of mobile sensor network node; literature [3] proposed a 3D self-deployment (3DSD) algorithm, which maintains the connectivity of the network by adopting the negotiation strategy and used the density control method to balance the distribution of nodes.

The algorithm can achieve more rapid and more uniform node automatic deployment in a 3D space with obstacles. Literature [4] holds that although the full coverage is very important to the surveillance and control of wireless sensor network, however, as it is inevitable to cover voids for various reasons, the paper applies hollow circle attribute evaluation method to identify the covered voids that occurred. Based on the node density, literature [5] applies distributive coverage blind area repair algorithm to solve the deployment issue caused by node death in the directed sensor network. Literature [6] proposed the node deployment reinforced algorithm based on constraint artificial fish swarm in the directed sensor network; in this algorithm, we set up 2D plane node model, introduced “perceptual centroid” as artificial fish, and simulated consistent foraging of fish swarm to find the optimal solution in the solution space. In literature [7], genetic algorithm and simulated annealing algorithm are used to improve the coverage algorithm, and a deployment enhancement algorithm for multimedia directed sensor network is proposed, which can improve the coverage and reduce the number of iteration calculation.

This paper focuses on the study of mobile sensor network node deployment and density optimization used for information collection in emergencies. In the detailed application above, in general cases, in order to guarantee the surveillance quality of the network, the sensor nodes need to be randomly deployed with high density in the target surveillance area. The network model used in this paper is based on the following assumption:

- (1) The sensor network consists of one base station and large amounts of sensor nodes in the 3D space; each of the nodes has unique identification
- (2) All sensor nodes stay still after optimal deployment
- (3) The energy of sensor node is limited, while the energy of base station is infinite
- (4) By means of satellite positioning technology, all sensor nodes can obtain their own position information

- (5) Time synchronization technology can be applied to achieve synchronization of sensor node and base station

The sensor node monitors the target periodically; in every monitoring period, all nodes can directly communicate with one another, sending the collected data information to the node of base station.

2. Problem Description

In building up the wireless sensor network, the network coverage is one of standard issues of the wireless sensor network, which is how to deploy sensor network node. Under the condition of ensuring certain service quality (QOS), the network node should be used as few as possible to achieve maximum network coverage scope. In the optimization of network coverage [8–12] for mobile sensor networks, we need to consider both node coverage and regional coverage.

Suppose the monitoring 3D region A is digitally discretized into $m \times n \times h$ pixels, and the number of mobile sensor nodes with the same parameters is n , the coordinates of each node are known, and the sensing radius is r , and the communication radius is R . The equation $S_i = (x_i, y_i, z_i, r)$ represents the sensor node i , whose coordinate is $\{x_i, y_i, z_i\}$, and its monitoring radius is r . Suppose the coordinates of the target pixel are (x, y, z) , then the distance between the target pixel and the sensor node is

$$d(s_i, p) = \sqrt{(x_i - x)^2 + (y_i - y)^2 + (z_i - z)^2}. \quad (1)$$

The node coverage can be defined as the event that the target pixel is covered by the mobile sensor node i is defined as r_i ; then, the probability $P_{\text{cov}}(x, y, z, s_i)$ of the event is the probability that the coordinate point (x, y, z) is covered by the sensor node s_i . The sensor node coverage model presents a probability distribution of certain characteristics in practical application, that is

$$P_{\text{cov}}(x, y, z, s_i) = \begin{cases} 1 & d(s_i, p) \leq r \\ 0 & \text{otherwise} \end{cases}. \quad (2)$$

The average probability of all points on the road being detected is taken to represent the coverage performance of the sensor network. As long as there is one node coverage point (x, y, z) , the coordinate (x, y, z) is regarded to be covered by node set. The coverage of the node set can be calculated with the formula (3):

$$P_{\text{cov}}S = 1 - \prod_{i=1}^N (1 - P_{\text{cov}}(x, y, z, s_i)). \quad (3)$$

There are $m \times n \times h$ pixels in the monitoring area A and whether each pixel is covered can be represented by the joint measurement probability $P_{\text{cov}}(S)$. Area coverage $R_{\text{area}}(S)$ can

be defined as the ratio of the coverage area $A_{\text{area}}(S)$ of node set S to the total area A_s of monitoring area A , as shown in formula (4) below:

$$R_{\text{area}}(S) = \frac{A_{\text{area}}(S)}{A_s} = \frac{\sum P_{\text{cov}}(S)}{m \times n \times h}. \quad (4)$$

In order to analyze network performance, the probability model is used as the communication model of wireless sensor node S_i , reflecting the communication quality of internode in practical network environment.

$$T(s_i, s_j) = \begin{cases} 1 & 0 \leq d(s_i, s_j) \\ 0 & d(s_i, s_j) > R \end{cases}. \quad (5)$$

In the formula, $T(s_i, s_j)$ is the communication strength of sensor node s_i and s_j . R is effective communication scope, supposing $R = 50$ m.

The communication intensity of the network is used to indicate the communication performance of the network. This value can be obtained by calculating the average communication intensity of all mobile sensor nodes. According to the node communication model formula in formula (5), we can conclude that the network communication intensity is

$$\text{Trans} = \frac{\sum_{i=1}^N T(s_i, s_j)}{2N}. \quad (6)$$

3. Methodology

3.1. Optimization Model of Mobile Sensor Network Deployment. By optimizing the position of each mobile sensor node, the coverage and connectivity of the network are optimized. In order to achieve the optimal coverage and connectivity at the same time, it is necessary to solve the multiobjective constraint optimization problem. We transform the multiobjective optimization problem into an equivalent single constraint optimization problem by geometric weighting method.

The nonconstraint optimization issue equivalent to the constraint optimization issue above is

$$f = \min \left[\max \left(\frac{1 - \prod_{i=1}^N (1 - P_{\text{cov}}(x, y, z s_i))}{m \times n \times h} \right) \omega_1 \times \max \left(\frac{\sum_{i=1}^N T(s_i, s_j)}{N} \right) \omega_2 \right]. \quad (7)$$

ω_1 and ω_2 represent the weights of their respective functions in the overall function.

The constraint conditions are

$$s.t. R_{\text{area}}(S) \geq 0.95. \quad (8)$$

Firstly, according to the usual coverage standard, the network coverage $R_{\text{area}}(s)$ needs to be greater than or equal to 95% to ensure that the entire network is effectively covered by the sensor node set.

$$\begin{aligned} g_i(X) &\leq 0, i = 1, 2, \dots, n, \\ h_j(X) &\leq 0, j = 1, 2, \dots, m. \end{aligned} \quad (9)$$

In the formula, $g_i(X)$ and $h_j(X)$ represent the connectivity of the network and the constraint conditions determined by the need of network coverage and connection.

Secondly, in the connectivity requirement, the following conditions should be met: the number of adjacent nodes of any mobile sensor node is not 0, and the network island is not formed.

Due to the complexity of the problem model, we adopted a relatively new intelligent optimization algorithm—chemical reaction optimization algorithm (CRO) [13–15] to solve it. This algorithm is a swarm intelligence algorithm based on the collision and energy conversion of molecules in the process of chemical reaction. It is searched by the collision of molecules and the chemical reaction after the collision to lead the molecules to the lowest possible energy state.

3.2. Chemical Reaction Optimization Algorithm. The CRO algorithm simulates the change and migration of molecules in a chemical reaction system. In the chemical reaction, each molecule has kinetic energy KE and potential energy PE. After the invalid collision of single molecule, a new molecular structure ω' is obtained, which satisfies the inequality:

$$\begin{aligned} PE_{\omega} + KE_{\omega} &\geq PE_{\omega'}, \\ KE_{\omega}' &= (PE_{\omega} - PE_{\omega}' + KE_{\omega}) \times \alpha. \end{aligned} \quad (10)$$

α represents the kinetic energy KE loss rate. The kinetic energy KE_{ω}' is stored in the central energy buffer to support the Decomposition and Synthesis of molecules, which is also a feature of the CRO, while the other part of the kinetic energy $(PE_{\omega} - PE_{\omega}' + KE_{\omega}) \times (1 - \alpha)$ is consumed in the reaction system.

Basic chemical reactions can be broken down into four categories: On-wall Ineffective Collision, Decomposition, Intermolecular Ineffective Collision, and Synthesis. The specific principle of each basic chemical reaction is as follows:

- (1) *Intermolecular Ineffective Collision.* The Intermolecular Ineffective Collision can be regarded as the collision reaction of two molecules, because the energy conversion involved in the exchange reaction is small; the two molecules exchanged a small amount of energy during the collision, and the energy loss can be ignored. So ω_1 and ω_2 are the two molecules that are involved in the collision, and you can get two new molecules by the collision reaction, and the molecular structure is ω'_1 and ω'_2 .
- (2) *On-Wall Ineffective Collision.* In the process, the properties of the molecule change, the structure of the molecule changes, and a new molecule are created. Because the impact force is not large, the structure of the new molecule is similar to the structure of

the original molecule. The original molecular structure is ω , and the new molecular structure is ω'

- (3) *Synthesis*. When two molecules collide with each other, the two molecules combine into one molecule due to the fierce and powerful impact, and the energy is transferred. So the two molecules before the collision are ω_1 and ω_2 , and the new molecules after the collision are ω' . In the synthesis reaction, molecules collide with each other with great strength and energy conversion, resulting in two molecules combining into one molecule. This new molecular structure ω' is greatly different from that of the two original molecules
- (4) *Decomposition*. The collision force in the decomposition reaction is very large; one molecule ω is decomposed into two new molecules ω'_1 and ω'_2 ; the new molecules are greatly different from the original molecule. This mechanism enables CRO algorithm to jump out of local minimum value

The flow diagram of CRO algorithm is shown in Figure 1. The main steps of the algorithm are:

Step 1. In the initialization phase, we initialized the molecular set; the target function is set to be PE of molecule. Initialized KE of every molecule is set to be InitialKE value.

Step 2. In every iteration, different molecular combination types are chosen based on whether it is uni-molecular reaction or intermolecular reaction. When it is uni-molecular, we choose On-wall Ineffective Collision or Decomposition. When it is an intermolecular reaction, we choose the Intermolecular Ineffective Collisions or Synthesis.

Step 3. Calculate the value of target function and test whether it is new minimum value.

Step 4. When the termination condition is met, the iteration process is stopped. We output the present optimal solution.

Condition of termination. The program will be stopped when the iteration number reaches the predetermined maximum iteration number.

4. Results and Discussion

4.1. Experimental Environment and Parameter Setting. In order to verify the effect of the algorithm designed in this paper on the sensor network deployment optimization problem, the experimental platform is Win10/MATLAB (R 2012a); the computer hardware is Inter(R) Core (TM) i5-3230m CPU, 8 GB RAM. The CRO algorithm is designed, and the simulation results are compared with those of particle swarm optimization (PSO) [16, 17] intelligent algorithm.

In order to simulate the three-dimensional deployment environment, the sensor node is randomly deployed in the $500\text{ m} \times 500\text{ m} \times 500\text{ m}$ space, as shown in Figure 2. The main test criterion is the adaptive value of the optimization

function. In this space, the number of sensor nodes is 200. After repeated experiments, the control parameters are set to be the communication distance of node is $R_1 = 50\text{ m}$, the sensing radius of node is $r = 50\text{ m}$, the weight value of network coverage is $\omega_1 = 0.5$, and the weight value of network communication intensity is $\omega_2 = 0.3$.

4.2. Network Connectivity and Deployment Testing. Figure 3 is the neighbor relation diagram between nodes, which is mainly used to test the connectivity of the network to see whether there is a network island. In the figure, the red circle is the sensor node, and the blue line is the analog communication connection between nodes. If two nodes can communicate with each other, a blue line is established between them and their neighbors. As can be seen from the following figure, all nodes can interconnect with each other and communicate with each other, so there are no isolated nodes and information islands.

Figure 4 shows the regional deployment coverage diagram of the node. We should try our best to make each node strengthen the coverage, but no information island can appear. In the figure below, the red asterisk is the sensor node, the blue sphere is the monitoring coverage of the node, and the area inside the blue sphere is the area that the node can perceive and detect. We will use the CRO algorithm to enable the node to be better deployed to cover the vast majority of the area without having an information island.

Figure 5 is a schematic diagram of CRO algorithm. The energy change process of chemical reaction can be reflected from the change of potential energy. It is inspired by the interaction between molecules in chemical reactions to find the lowest potential energy phenomena in the potential energy surface. The four primary reactions are Intermolecular Ineffective Collision, Decomposition, On-wall Ineffective Collision, and Synthesis. The result of a chemical reaction is the product of a chemical reaction. The change of the chemical reaction product is expressed by the system potential energy. The whole reaction process is a process in which the reaction potential energy gradually decreases. At the end of the reaction process, the system potential energy reaches the minimum, and the state tends to be stable. It can be seen that CRO algorithm is an optimization process to seek the minimum system potential energy.

4.3. Comparison between CRO Algorithm and PSO Algorithm. Figure 6 is the relation schema of iteration number-perception radius; in the simulation experiment, we applied CRO algorithm and PSO algorithm to make comparison. The perception radius of node is from 8 m to 10 m; the step length is 0.05 m; when the constraint conditions of formula (8) are met, record the number of iterations taken. The program will continue to run until the preset conditions are met or the number of iterations reaches the preset number. To prevent the program from running invalid for a long time, we set the maximum number of iterations to 700. Through Figure 5, we can discover that CRO algorithm can reach the constraint condition of the system with different perception radius and small number of iteration, which means that the regional coverage is higher than 95%, and

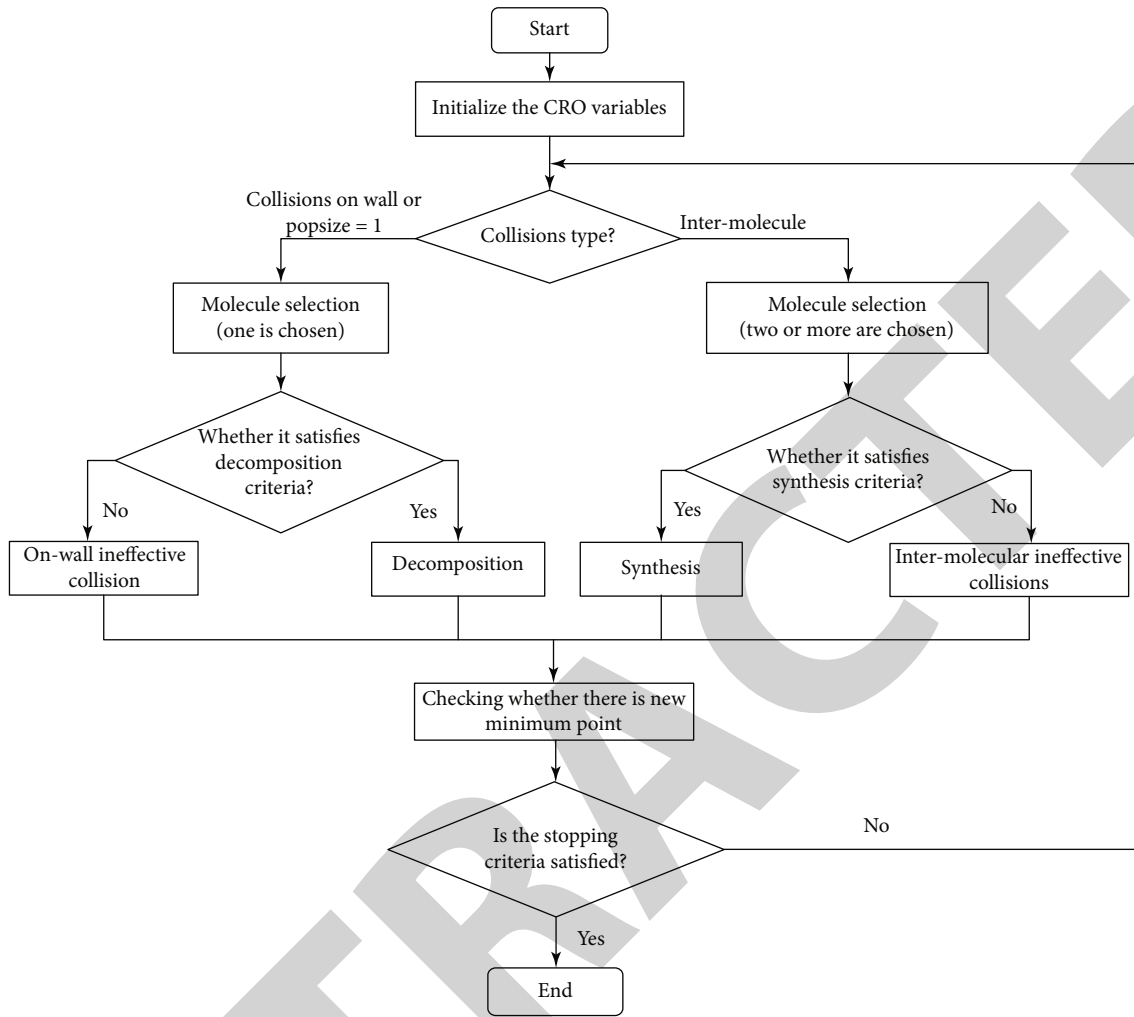


FIGURE 1: The flow diagram of CRO algorithm.

The distribution diagram of sensor nodes

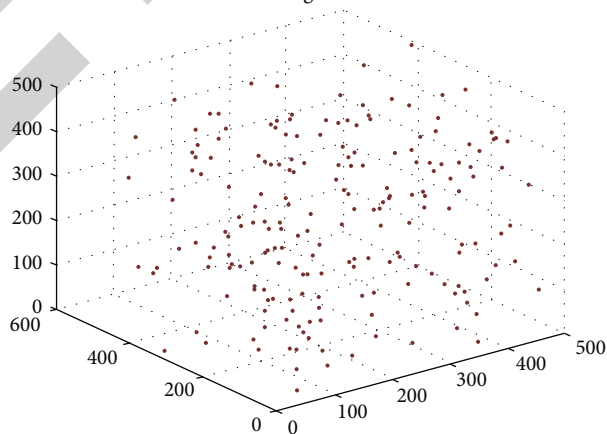


FIGURE 2: The distribution diagram of sensor nodes.

communication can be made between any two nodes, and no island occurred. From this, we know that CRO algorithm is more effective than PSO algorithm.

Table 1 is the comparison table of the optimal value of fitness function. CRO algorithm and PSO algorithm are used to solve the function model, and the final value of the fitness

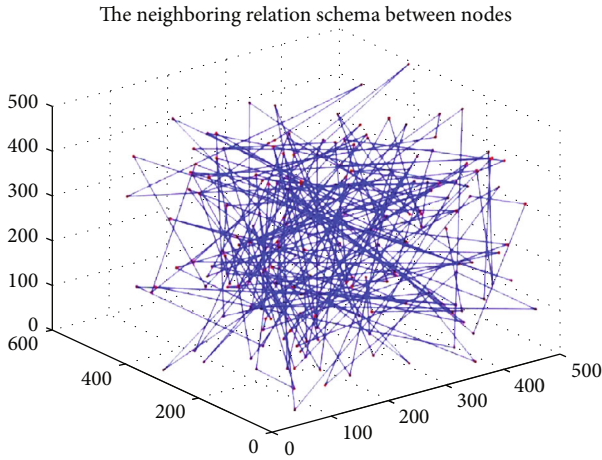


FIGURE 3: The neighboring relation schema between nodes.

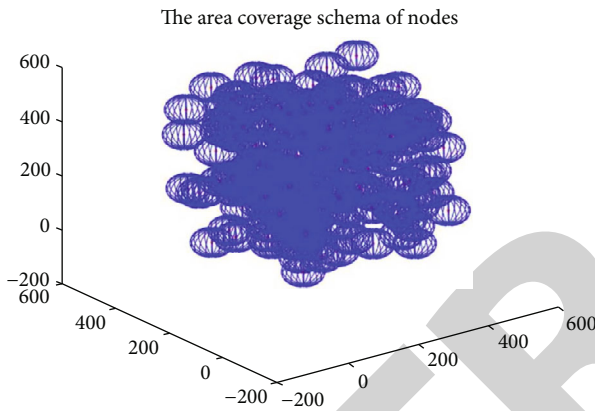


FIGURE 4: The area coverage schema of nodes.

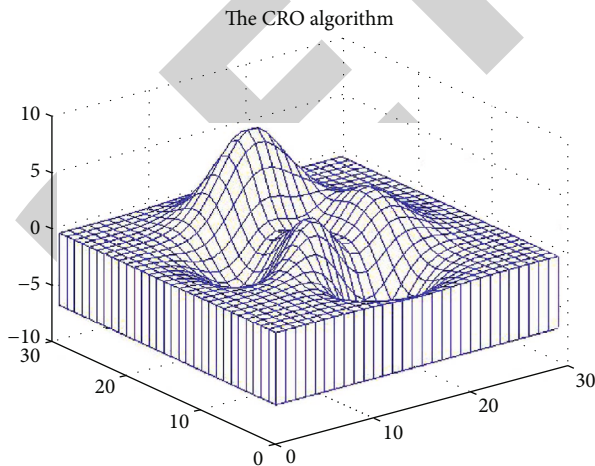


FIGURE 5: Sketch map of chemical reaction optimization algorithm.

function obtained in 5 simulation experiments is recorded. According to the following table, the average value of the function obtained by CRO algorithm is 11.24, while the average value of the function obtained by PSO algorithm is 9.864. Through comparison, it is found that the average value of the

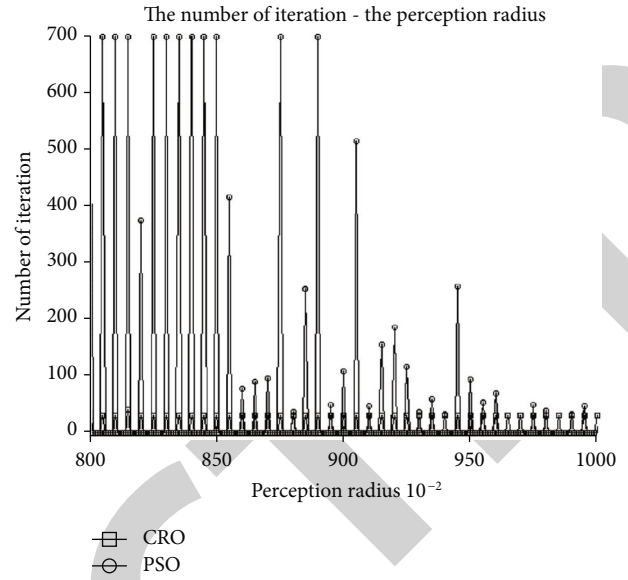


FIGURE 6: Relation schema of number of iteration-perception radius.

TABLE 1: Comparison table of optimal value of fitness function.

Experiment no.	PSO	CRO
Experiment 1	9.94	11.19
Experiment 2	9.85	11.26
Experiment 3	10.01	11.17
Experiment 4	9.77	11.27
Experiment 5	9.75	11.31

function obtained by CRO algorithm is 1.376 higher than that obtained by PSO algorithm. The reason for this phenomenon is that CRO algorithm is a comprehensive algorithm, which has a variety of operators such as Decomposition and Synthesis, which can help the program to change the position of node coordinates greatly, so as to better and faster jump out of the local optimal solution and find the global optimal value.

5. Conclusion

To address the reasonable deployment of mobile sensor, the mobile sensor network deployment optimization model is established for information collecting of emergencies and solved with CRO algorithm. The experimental results have shown that CRO algorithm is more suitable for solving the mobile sensor network deployment optimization of information collecting in emergencies than PSO algorithm, which can effectively optimize network layout, enabling the comprehensive evaluation value of network performance to improve by 13.95%; CRO algorithm can obtain better mobile sensor network deployment by improving the disadvantage of PSO algorithm easily engaged in optimal local value.

Retraction

Retracted: Microcomputer Control System of Bridge Dehumidification Based on Energy Consumption Optimization and Wireless Communication

Wireless Communications and Mobile Computing

Received 28 November 2023; Accepted 28 November 2023; Published 29 November 2023

Copyright © 2023 Wireless Communications and Mobile Computing. This is an open access article distributed under the Creative Commons Attribution License, which permits unrestricted use, distribution, and reproduction in any medium, provided the original work is properly cited.

This article has been retracted by Hindawi, as publisher, following an investigation undertaken by the publisher [1]. This investigation has uncovered evidence of systematic manipulation of the publication and peer-review process. We cannot, therefore, vouch for the reliability or integrity of this article.

Please note that this notice is intended solely to alert readers that the peer-review process of this article has been compromised.

Wiley and Hindawi regret that the usual quality checks did not identify these issues before publication and have since put additional measures in place to safeguard research integrity.

We wish to credit our Research Integrity and Research Publishing teams and anonymous and named external researchers and research integrity experts for contributing to this investigation.

The corresponding author, as the representative of all authors, has been given the opportunity to register their agreement or disagreement to this retraction. We have kept a record of any response received.

References

- [1] X. Zhou, F. Xiong, P. Li, and Q. Yu, "Microcomputer Control System of Bridge Dehumidification Based on Energy Consumption Optimization and Wireless Communication," *Wireless Communications and Mobile Computing*, vol. 2021, Article ID 2689878, 5 pages, 2021.

Research Article

Microcomputer Control System of Bridge Dehumidification Based on Energy Consumption Optimization and Wireless Communication

Xudong Zhou ¹, Feng Xiong ², Peng Li ³, and Qi Yu ³

¹Guangdong Highway Construction Co., Ltd., Guangzhou, Guangdong 510623, China

²Guangdong Humen Bridge Co., Ltd., Dongguan, Guangdong 523910, China

³CCCC Highway Consultants Co., Ltd., Beijing 100088, China

Correspondence should be addressed to Xudong Zhou; zxudong2021@163.com

Received 8 July 2021; Accepted 10 August 2021; Published 20 August 2021

Academic Editor: Balakrishnan Nagaraj

Copyright © 2021 Xudong Zhou et al. This is an open access article distributed under the Creative Commons Attribution License, which permits unrestricted use, distribution, and reproduction in any medium, provided the original work is properly cited.

At present, with the development of wireless communication and microcomputer control system, the design and construction level of long-span bridges in China are also improving. How to improve the durability of bridge structure has become a major scientific and technological problem in bridge design and construction. This paper studies a microcomputer control system of bridge dehumidification based on energy consumption optimization and wireless communication. It compares three kinds of dehumidification and anticorrosion methods of bridge engineering, namely, freezing dehumidification system, rotary dehumidification system, and hybrid dehumidification system. In the hardware design of microcomputer control system of dehumidification system, ATmega128 bit main control chip and aluminum designer are used to draw the power circuit. Then, the MCU program of the air dehumidifier is written, and the power of the air dehumidifier is controlled by the PWM signal generated by the timer 0 of the MCU. The air dehumidifier is divided into three tap positions corresponding to three duty cycles, and the power of the air dehumidifier is changed according to the input tap position.

1. Introduction

In the long history of development, all kinds of bridges have emerged, such as arch bridge, beam bridge, and suspension bridge [1]. In the early days, people used bamboo strips, vines, and other natural materials to build simple suspension bridges. This kind of small pedestrian suspension bridge is considered to be the prototype of modern suspension bridge. The main cable of the suspension bridge mainly bears the tension from the action of load and at the same time produces the transverse and longitudinal forces at the anchorage so that the tensile performance of the steel material can be best exerted, which is also the reason why the suspension bridge can have a large span. The general environment of suspension bridges is very harsh. It not only has to withstand wind load, vehicle load, and dynamic load but also be affected by corrosive media such as temperature and humidity. The main cable of suspension bridge is the main load-bearing sys-

tem. The suspension system is based on current technology. The main cable system is a one-time system that can only be repaired but cannot be replaced. The main cable corrosion seriously affects the safety of the bridge. Examples of accidents occurring due to the corrosion of the cable system in the use of bridges abound [2, 3]. Corrosion of the bridge main cable is a common engineering phenomenon and a worldwide problem. Because the main cable is wrapped, it is difficult to detect this phenomenon, which brings serious hidden danger to the bridge safety and high maintenance costs [4].

The purpose of main cable protection is to prevent water from entering the main cable and keep the main cable in a relatively closed, dry environment. However, due to the existence of a series of problems mentioned above, it is difficult to achieve this goal. This paper explains and discusses the case from the main cable and cable-stayed bridge as well as points out the way of water intake and the reasons for the

two structures. On this basis, Jensen et al. discuss the disadvantages of different wire rope concepts and then make the different mitigation measures [5].

This paper mainly studies the microcomputer control system of the dehumidification system, selects the appropriate type of single-chip microcomputer as the control core, designs the corresponding control circuit, and produces a device that can detect the relative humidity of the air according to a set of expected humidity and humidity values. The controller is able to communicate with the single-chip microcomputer connected to the Internet.

2. Bridge Main Cable Dehumidification System

2.1. Overview of Dehumidification Systems

2.1.1. Refrigeration and Dehumidification System. The principle of the refrigeration and dehumidification system is to filter the outside air through a set of filtering device. Firstly, the impurities contained in the gas itself are removed. The filtered gas enters the refrigerator to cool the air and remove moisture. Then, it is heated to a similar temperature and low humidity by a heater. At last, dry gas is delivered to the bridge cable [6].

2.1.2. Wheel Dehumidification System. The working principle of the rotary dehumidifier: the outside air is filtered through the filter, and the fresh air passes through the desiccant wheel to remove part of the moisture and gas and then passes through the filter again to remove the desiccant residue in the air, and the filter is filtered again to cool air. Then, cool to a similar temperature and low humidity environment to bridge the cables. On the other side of the dehumidification wheel, the air passes through the filter and then is heated by the heater. The heated gas will dry the residual moisture of the dehumidification wheel during the dehumidification process to ensure that the dehumidification wheel is in a relatively dry state when it enters the working area [7]. In this way, the drying and dehumidification process and the regeneration process are performed at the same time, and the continuous drying process of moisture is realized.

2.1.3. Mixed Dehumidification System. The working principle of the hybrid dehumidification system is that the outside air is first filtered through a filter. The filtered air enters a refrigerator to cool the air to remove the moisture. The cooled low-temperature and high-humidity air passes through the dehumidification wheel to remove part of the moisture. The outgoing air is filtered through a filter and then frozen to remove the desiccant residue in the air. The filtered air is heated to a low humidity and similar temperature to the environment through a heater and then sent to the bridge cable [8]. On the other side of the dehumidification wheel, the air is heated by a heater, and the heated gas blows off the residual moisture in the dehumidification wheel to ensure that the dehumidification wheel is relatively dry when it enters the working area.

2.2. Hardware Design of the Dehumidification System. The whole dehumidification system uses ATmega128 as the con-

trol core. A series of low-voltage pulses are generated by controlling the output of the signal, which is used as the source circuit of the dehumidifier. In addition, the microcontroller will output another PWM signal to control the dehumidification power. The temperature and humidity sensor will measure the temperature and humidity of the bridge cable and collect the data and transmit it to the MCU control unit through the network. The display unit, which is mainly based on touch screen, is connected with MCU to display the temperature and humidity of bridge cable and various parameters representing the operation status of dehumidification system. Wi-Fi module is the bridge between MCU control unit and Internet, which plays an important role in the remote control process of the dehumidification system.

ATmega128 MCU is an AVR MCU produced by ATMEL company. ATmega128 MCU has rich I/O pin resources, including two 8-bit timers/counters, two 16-bit extended timers/counters, one real-time clock counter, two 8-bit PWM channels, six 2–16-bit PWM channels, and programmable continuous serial port UART 2, which fully meet the needs of each function of the dehumidification system [9, 10].

The 17V DC output from the bridge rectifier is connected with a set of three terminal voltage-stabilizing integrated circuit lm7812 and an NPN triode. lm7812 stabilizes the unstable 17V voltage to 12V and uses three grounding capacitors for filtering.

3. Energy Consumption Analysis of the Dehumidification System

The dehumidification process of the main cable of a suspension bridge is to pass cold and dry air through the main cable. The cold and dry air takes away the hot and humid air in the main cable and then exits from the exhaust point [10, 11]. During the dehumidification process, the air in the main cable is not circulating, that is, the main cable dehumidification system is an open design; dry air enters through the air inlet and flows along the main cable, gradually leaking into the atmosphere along the way. Condensation along the main cable is avoided by relying on dry air from inside the main cable. Therefore, the return air does not need to be considered in the calculation of enthalpy and humidity relationship of the system. According to the construction drawing in the design stage, it can be known that the design parameters of the dehumidification of the main cable of the bridge are dry bulb temperature $T_n = 20^\circ\text{C}$, relative humidity $\phi_n = 10\%$, ambient dry bulb temperature $T_w = 20^\circ\text{C}$, and relative humidity $\phi_n = 70\%$. If the air supply temperature difference is 5°C and the moisture content of the air remains unchanged, then the temperature of the air supply point is $T_n = 15^\circ\text{C}$, $\phi_n = 54.86\%$, and the enthalpy value of the corresponding air supply point is 29.8 kJ/kg . By referring to the construction drawings at the design stage, one 1100CMH process air volume dehumidifier is selected for the main cable dehumidification of one suspension bridge in the Pearl River Delta of China, with a

power of 11.1 kW. The air supply to the main cable dehumidification system is $G = 2500 \text{ m}^3/\text{h}$. The following is a detailed calculation and design for the three systems.

4. Energy Consumption Results of Different Dehumidification Systems and Computer Control Program Design

4.1. Energy Consumption Results of the Dehumidification System

4.1.1. Refrigeration Dehumidification System. Figure 1 shows the dehumidification process of freezing dehumidification. The external air state point W is processed by the freezer to reach the state point O and then heated by the heater to reach the state point N , which is then fed into the main cable of the suspension bridge. Through the enthalpy humidity chart, the enthalpy humidity of each state point of the dehumidification system can be calculated as follows: dry bulb temperature of O point $t_o = 6.01^\circ\text{C}$, humidity content $d_o = 5.8 \text{ g/kg}$, enthalpy value $i_o = 20.63 \text{ kJ/kg}$, this point is the dew point temperature of N point, relative humidity $\phi_o = 100\%$, and this point is the same as the humidity content of N point. The dry bulb temperature at W point $t_w = 30^\circ\text{C}$, moisture content $d_w = 18.79 \text{ g/kg}$, and enthalpy $i_w = 78.34 \text{ kJ/kg}$.

The calculation formula of energy consumption of refrigerating dehumidification system is shown in

$$Q = \frac{1.2 \cdot G \cdot \Delta i}{3600}, \quad (1)$$

where Q is the cooling load at each state point; G is air supply volume, unit m^3/h ; and 1.2 is the density of the treated gas in kg/m^3 .

The cooling load of the refrigerating dehumidification system can be calculated as shown in

$$Q_{\text{cold}} = \frac{1.2 \cdot 2500 \cdot (78.343 - 20.63)}{3600} = 48.09 \text{ kW}. \quad (2)$$

The heat load of the refrigerating dehumidification system is shown in

$$Q_{\text{hot}} = \frac{1.2 \cdot 2500 \cdot (29.807 - 20.63)}{3600} = 7.65 \text{ kW}. \quad (3)$$

It can be obtained that the total energy consumption of the refrigerating dehumidification system is shown in

$$Q_{\text{total}} = Q_{\text{cold}} + Q_{\text{hot}} = 56.74 \text{ kW}. \quad (4)$$

Feasibility analysis of freezing dehumidification system: in order to meet the dehumidification requirements, the dew point temperature of the air supply outlet can be obtained by calculation as 6°C , and the moisture content of the air outlet is 5.8 g/kg . When the air moisture content of the freezer dehumidifier is lower than 6.5 g/kg , the surface of the evaporator of the freezer is prone to frosting, which

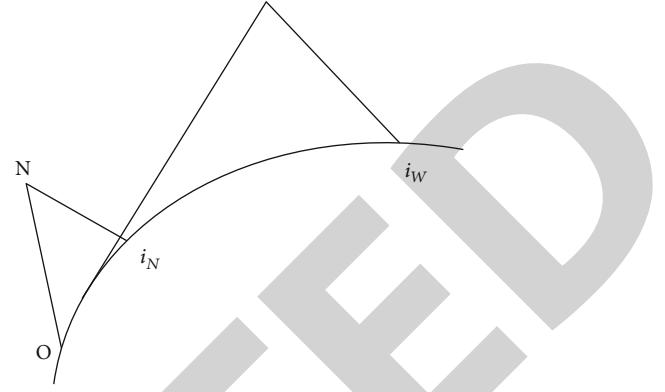


FIGURE 1: Refrigeration dehumidification system.

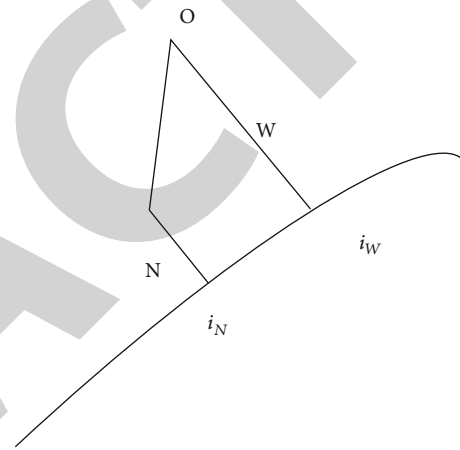


FIGURE 2: Wheel dehumidification system.

affects the dehumidification efficiency of the dehumidifier. Therefore, for the feasibility of the dehumidification system, freezing dehumidification is difficult to meet the demand.

Therefore, for the dehumidification system, the effect of freezing dehumidification is not very ideal or cannot fully meet the design requirements. In this case, it is unreasonable to select freezing dehumidification alone.

4.1.2. Wheel Dehumidification System. As shown in Figure 2, the external air state point is dehumidified by the runner W to reach the state point O , and then by surface cooling, the hot and dry gas reaches the point N and finally is sent into the main cable of the suspension bridge. Through the enthalpy humidity chart, the enthalpy humidity of each state point of the dehumidification system can be calculated as follows: dry bulb temperature of O point $t_o = 62.55^\circ\text{C}$, moisture content $t_o = 5.8 \text{ g/kg}$, enthalpy $i_o = 78.343 \text{ g/kg}$, and relative humidity $\phi_o = 4.17\%$.

Similarly, according to Equation (1), the cooling load of the refrigerating dehumidification system can be calculated as shown in

$$Q_{\text{cold}} = \frac{1.2 \cdot 2500 \cdot (78.343 - 29.807)}{3600} = 40.45 \text{ kW}. \quad (5)$$

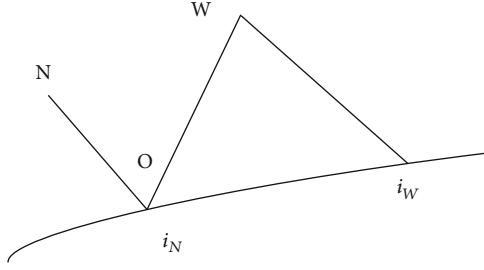


FIGURE 3: Hybrid dehumidification system.

For the same moisture content method (runner dehumidifier), directly take the runner dehumidifier rated power 11.1 kW, as shown in

$$Q_{\text{cold}} = 40.45 + 11.1 = 51.55 \text{ kW}. \quad (6)$$

Runner dehumidification system feasibility analysis: according to the requirements of dehumidification, if the runner is used alone to dehumidify, the temperature of the runner treatment will reach more than 60°C, which will undoubtedly damage the drying wheel of the runner dehumidification system and will greatly reduce the life of the runner dehumidifier.

4.1.3. Mixed Dehumidification System. As shown in Figure 3, the external air state point W is cooled and dehumidified by the freezer to reach state point O , and then, the dry and cold air reached point N through the runner and finally sent into the main cable of the suspension bridge. Through the enthalpy humidity chart, the enthalpy humidity of each state point of the dehumidification system can be calculated as follows: dry bulb temperature of O point $t_o = 10.207^\circ\text{C}$, moisture content $d_o = 7.738 \text{ g/kg}$, enthalpy $i_o = 29.807 \text{ kJ/kg}$, and relative humidity $\phi_o = 100\%$.

Feasibility analysis of the wheel dehumidification system: for the mixed dehumidification system, the cooler will preprocess the hot and humid air, and the dry air will be dehumidified by the wheel, which can both take into account the dehumidification advantage of the freezing dehumidification on the hot and humid air and the dehumidification advantage of the wheel on the low-temperature air. According to the calculation results of the moisture content of the outlet air, the evaporator of the refrigerator will not frost, and according to the calculation results of the temperature, the dehumidifier will not overheat, so it is the best choice in terms of the feasibility of the scheme.

4.2. MCU Subroutine Design. The two fans of dehumidifier are parallel with the semiconductor refrigeration plate. Changing the duty cycle of PWM signal can change the fan speed and cooling power of the cooling plate at the same time, thus changing the dehumidification rate. According to PWM signal duty score, the dehumidifier is three working gears, and the corresponding working voltage is 100%, 60%, and 30% of the maximum working voltage, respectively. The gear can be determined according to the difference between the expected air humidity and the actual

TABLE 1: The parameters of the three working gears of the dehumidifier.

Work gear	Umax percentage	PWM duty cycle	OCr0
1	45%	55%	164
2	75%	25%	82
3	100%	0	0

measured value and the size of dehumidification space. The gear is set by the touch screen.

The timer T0 of ATmega128 microcontroller is used to generate the PWM control signal of the air dehumidifier. The timer T0 is 8-bit. TCNT0 counts from 0 to 255, and then, 1 is added to return 0, as shown in

$$k = \frac{k \alpha \beta}{m \times 255} = 1961 \text{ Hz}, \quad (7)$$

where $n = 8$ (8 frequency divider), the size of the output comparison register OCr0 determines the duty cycle and changes the duty cycle by changing the value of OCr0. The corresponding relations of working gear, maximum working voltage percentage, PWM duty cycle, and OCr0 are shown in Table 1.

5. Conclusions

This paper first introduces the working principles of refrigeration dehumidification system, rotary dehumidification system, and hybrid dehumidification system, then analyzes the feasibility, and points out the advantages and disadvantages of these three dehumidification systems. The analysis shows that the hybrid dehumidification system can effectively dehumidify both the cold air and the hot and humid air and is the best choice in the feasibility. In addition, this paper focuses on the design of single-chip microcomputer program of dehumidification system. MCU program mainly includes pulse generation subroutine, which generates two PWM signals by timer. Dehumidifier subroutine uses PWM signal produced by timer T0 to drive the semiconductor chip. Because the difference between the actual humidity measured by dht1 temperature and humidity sensor and the expected humidity is different, the air dehumidifier is divided into three tap levels, corresponding to the three values of OCr0. Using ADC subroutine of single-chip microcomputer to measure the Outv in current sampling circuit, the analog quantity is converted into digital quantity, and the current of MPS multipulse electro osmotic dehumidification circuit is obtained. Through this set of intelligent microcomputer control system, the dehumidification efficiency of the bridge can be greatly enhanced, the cost can be saved, and the temperature can be accurately controlled according to different climate environments, which has important promotion and practical significance. However, this system also has some shortcomings, such as high dependence on the network environment, requiring professional technical personnel to operate, and not being practical in some extreme environments. However, with the popularization of 5G networks, I believe this system will be widely promoted and used.

Retraction

Retracted: Mobile Communication Procurement Platform Optimization Decision Based on Overseas Retailer Investment under Supply and Demand Disruption Risk

Wireless Communications and Mobile Computing

Received 28 November 2023; Accepted 28 November 2023; Published 29 November 2023

Copyright © 2023 Wireless Communications and Mobile Computing. This is an open access article distributed under the Creative Commons Attribution License, which permits unrestricted use, distribution, and reproduction in any medium, provided the original work is properly cited.

This article has been retracted by Hindawi, as publisher, following an investigation undertaken by the publisher [1]. This investigation has uncovered evidence of systematic manipulation of the publication and peer-review process. We cannot, therefore, vouch for the reliability or integrity of this article.

Please note that this notice is intended solely to alert readers that the peer-review process of this article has been compromised.

Wiley and Hindawi regret that the usual quality checks did not identify these issues before publication and have since put additional measures in place to safeguard research integrity.

We wish to credit our Research Integrity and Research Publishing teams and anonymous and named external researchers and research integrity experts for contributing to this investigation.

The corresponding author, as the representative of all authors, has been given the opportunity to register their agreement or disagreement to this retraction. We have kept a record of any response received.

References

- [1] D. Wang and W. Li, "Mobile Communication Procurement Platform Optimization Decision Based on Overseas Retailer Investment under Supply and Demand Disruption Risk," *Wireless Communications and Mobile Computing*, vol. 2021, Article ID 2630814, 12 pages, 2021.

Research Article

Mobile Communication Procurement Platform Optimization Decision Based on Overseas Retailer Investment under Supply and Demand Disruption Risk

Deli Wang  and Wuwei Li 

Glorious Sun School of Business and Management, Donghua University, Shanghai 200051, China

Correspondence should be addressed to Wuwei Li; m030120227@sues.edu.cn

Received 25 May 2021; Revised 6 July 2021; Accepted 7 August 2021; Published 18 August 2021

Academic Editor: Balakrishnan Nagaraj

Copyright © 2021 Deli Wang and Wuwei Li. This is an open access article distributed under the Creative Commons Attribution License, which permits unrestricted use, distribution, and reproduction in any medium, provided the original work is properly cited.

With the rapid development of mobile communication procurement platform, it is faced with many risks, such as national policy differences, regional market differentiation, trade control, and technical barriers. Among them, the risk of supply and demand interruption will lead to the disconnection between upstream and downstream enterprises and consumers in the crossborder supply chain, making it difficult for them to achieve the profit target of the supply chain and meet the market demand. In order to reduce the risk of supply and demand disruption in mobile communication procurement platform and improve the ability to prevent and deal with disruption emergencies, a two-level supply chain composed of crossborder suppliers, overseas suppliers, and overseas retailers is established, and the procurement decision optimization of crossborder supply chain under the condition of single channel procurement and dual channel procurement before and after investment is studied. The research show that when overseas retailers invest in crossborder suppliers and choose a dual-source ordering strategy, it is more conducive to overseas retailers to reduce the risk of crossborder supply chain interruption and obtain higher expected profits.

1. Introduction

Under the background of economic globalization, information technology, and international division of labor, the international supply network is more and more closely linked. At the same time, the traditional decentralized procurement mode is gradually replaced by the new platform procurement mode. Through the intensive platform, the smooth and efficient operation of the procurement process can be realized. For mobile communication procurement platforms, scholars have combined with the transformation of procurement organizations to study how to organize the design of platform procurement; improve VCG payment rules and propose a new platform-based logistic procurement two-way bidding transaction model, and build a duopoly competition enterprise and government-led the bilateral Nash bargaining game model between centralized procurement platforms promotes the collaboration between enterprises and centralized procurement platforms [1–3].

However, there is little research on the supply chain disruption problem of the procurement platform. The mobile communication procurement platform will select multiple suppliers from all over the world, when a certain supplier cannot satisfy the retailer due to complex procedures, machine failures, insufficient human resources, etc. Procurement requirements are prone to supply disruption risks, which will result in the stagnation of production and logistic transportation for companies that place orders on the procurement platform for a long period of time, and the liquidity cannot be returned to the circulation. Supply interruption will stimulate market demand, and the demand will increase rapidly but it is difficult to meet, forming a vicious circle, endangering the stability of supply chain system, and bringing disaster damage to upstream and downstream enterprises and the whole supply chain. Based on the above problems, this article reduces the uncertainty risk of the crossborder supply chain, stabilizes the market demand share, and realizes the overall profit increase of the supply chain of the

crossborder communication procurement platform by means of dual-source procurement and retailer's financial support to suppliers.

From the perspective of supply disruption, we can improve the risk response capability of the supply chain by selecting suitable suppliers, determining the number of suppliers, and formulating procurement and inventory strategies [4]. Ivanov et al. tried to integrate digital technology into risk management from the perspective of digitalization and Industry 4.0 and studied the control strategy of supply chain reaction and interruption risk [5]. Li et al. combined with the real option theory, focused on the analysis of two emergency ordering modes of purchasing from backup suppliers in the case of supply interruption [6]. Kong et al. established a multivariable coupling control model and proposed that when supply disruptions occur, deep learning algorithms can effectively improve the resilience of OEM supply chains [7]. From the perspective of demand disruption, different from the more mature supply system of autoparts manufacturing industry, retailers represented by fresh and cold chain are faced with social responsibilities such as emission reduction; so, the market risk is increasing [8, 9]. Zhang et al. introduced the system dynamic model to model and simulate the two-level supply chain composed of raw material suppliers, manufacturers, and product subcontracting emergency suppliers and obtained the optimal emergency strategy of the production inventory system when the demand drops [10]. Based on the background of demand interruption, Shi et al. compare the coordination mechanism under the situation of no demand interruption and no overconfidence and construct the mobilization chain model of government emergency materials by using the quantitative elastic contract [11].

From the perspective of dual-source procurement, it refers to the design of coordination mechanisms that can reduce the risk of supply chain disruptions by selecting multiple backup suppliers or emergency suppliers in the absence of significant differences in raw materials, products, and services. Xin and Goldberg used the TBS strategy to try to solve the inventory optimality problem for purchasing from two suppliers and proved its applicability to be asymptotically optimal [12]. Lucker et al. conducted a joint analysis of inventory risk inventory (RMI), dual-source sourcing, and agility capabilities in pharmaceutical supply chains to introduce metric parameters modeling to quantify supply chain resilience and reduce supply and inventory risk [13]. Hu et al. discussed the impact of disaster event probability, government reserves, and spot market price on the government enterprise dual-source joint emergency material procurement mode based on the scenario of rapid growth of emergency material demand after disaster [14]. Chen constructed a game model between a manufacturer and two suppliers under two scenarios of random supplier output and supply disruption and found that the manufacturer's profit level can be increased by reducing the probability of disruption through dual-source purchasing decisions [15]. Liu et al., based on passengers' personality, route, and waiting time, used the historical data of the bus to simulate and customize the price for passengers [16]. Han et al. studied the dual-source procurement strategy based on the

update of demand forecasts under the background of two-period demand under the double uncertain information. In this case, the retailer made the most profit [17].

Through the literature review of supply disruption, demand disruption, and dual-source procurement, it is found that dual-source procurement, option contract, and other methods can reduce the risk of supply disruption and effectively deal with the uncertainty of market demand, especially in the process of crossborder e-commerce supply chain operation. However, dual-source procurement mostly focuses on the optimal profit of manufacturers or retailers and transfers risk cost to suppliers through zero inventory or buy back strategy, which is not conducive to the coordinated development of the whole supply chain. Therefore, we can choose to invest in suppliers from the perspective of retailer investment, which can not only strengthen supply chain communication and cooperation but also expand capacity advantage, reduce purchase price, and improve order fulfillment rate [18]. Liu et al. compare the different cooperation strategies among supply chain members in the context of carbon tax constraints and select the optimal decision-making method to reduce carbon emissions and ensure the benefits of enterprises [19]. Krause et al. showed that improvements in sourcing product quality, speed of delivery, and flexibility relied more on direct investments in suppliers [20]. Yang et al. discuss the problem of which investment strategy to adopt when the competitive intensity of two retailers increases, obtain a financing evolution model for the equilibrium scenario, and perform a sensitivity analysis of the capital structure and competitive intensity of the retailers [21]. Niu et al. combined product quality with investment output spillover effect and considered that the manufacturer's optimal strategy was to invest in supplier's quality [22]. Liu et al. found that retailers investing in manufacturers can help the supply chain reduce carbon emissions [23]. In view of the actual operation of crossborder procurement platform supply chain and the research basis of previous scholars, it is of theoretical and practical significance to incorporate retailer investment into crossborder supply chain procurement model [24–26]. Therefore, in the case of supply and demand disruption risk, this paper considers the optimal procurement decision under single source procurement, dual-source procurement, and overseas retailer investment; clarifies the relationship between crossborder supply chain disruption probability, overseas retailer procurement volume, and overseas retailer expected profit under different procurement situations; selects the optimal procurement mode; improves overseas retailer expected profit; and ensures supply the stability of the chain.

2. Methods

2.1. Model Assumptions. This paper takes the crossborder e-commerce supply chain as the research object and constructs a two-level supply chain composed of cross-border suppliers, overseas suppliers, and overseas retailers, as shown in Figure 1. This paper studies the optimal purchasing decisions of the supply chain under four conditions: retailers purchase only from crossborder suppliers, only from overseas

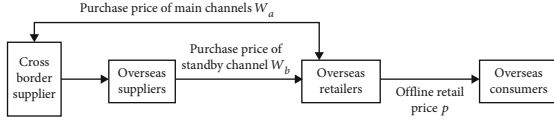


FIGURE 1: Mobile communication procurement platform supply chain procurement flow chart.

suppliers, purchase from both crossborder and overseas suppliers, and purchase from both crossborder and overseas suppliers after retailers invest [27, 28]. This paper mainly solves the following problems:

- (1) Establish a supply chain newsboy model under single-source procurement, dual-source procurement, and dual-source procurement after retailer investment and compare the optimal procurement decisions in each situation to select the optimal procurement method and procurement volume
- (2) Looking for approach to improve the competitiveness of the crossborder e-commerce supply chain, the lower the probability of supply and demand disruption and the higher the stability of the supply chain, the more able it is to stand out among many crossborder retail platforms and win the trust of consumers
- (3) One of the purposes of optimizing the procurement decision of crossborder e-commerce supply chain is to improve the overall profit of the supply chain and to select the most suitable supply chain optimization method by comparing the profit of retailers under different procurement decisions

2.2. Model Description. Overseas retailers purchase products from crossborder suppliers or overseas suppliers with the same quality and sell them to overseas consumers to meet market demand [29, 30]. Assuming D is the entire market demand $D = m \cdot \lambda$, m is the deterministic demand (related to product prices, etc.), and λ is the uncertain market demand. Suppose λ is a random variable defined on (a, b) , the probability density function and probability distribution function are $f(\lambda)$ and $F(\lambda)$, respectively, and $F(a) = 0$, $F(b) = 1$. Assume that all participants in the supply chain are completely rational, they all have a risk-neutral attitude. As the main supplier, crossborder suppliers are affected by factors such as distance and policies. They have low stability and high possibility of supply interruption, but they have price advantages, and the purchase price provided by crossborder suppliers is w_a . The products of overseas suppliers are provided by crossborder suppliers and then sold to overseas retailers. Therefore, they have high stability and no risk of interruption, but the prices are higher. The purchase price provided by overseas suppliers is w_b . The overseas retailer sells the product to the consumer at a price p , and $w_a < w_b < p$. Assume that the probability of disruption of the main supplier is r , and that the product cannot be supplied after the disruption, the deterministic demand of the consumer increases from m to $m + \Delta m$ after the supply disruption of

the main supplier. If the retailer invests in the main supplier and the amount of investment is I , the probability of interruption risk of the main supplier is reduced to $r^* = r - \alpha I$ ($r^* > 0$), and the supply price of the crossborder supplier is reduced to $w_a^* = w_a - \beta I$ ($w_a^* > 0$), α , and β and ($\alpha < \beta$) are the influence coefficients of investment on the risk and supply price, respectively [31–33]. The parameters used in the article are shown in Table 1.

2.3. Crossborder Suppliers as the Sole Source of Procurement. When an overseas retailer only purchases from a crossborder supplier, if the crossborder supplier does not experience supply interruption, then the profit function π_{kn}^s of the overseas retailer can be obtained at this time [34, 35].

$$\pi_{kn}^s = p \min(Q_k^s, D) - w_a Q_k^s - c[D - Q_k^s]^+ + u[Q_k^s - D]^+. \quad (1)$$

In which, the expected profit function $E(\pi_{kn}^s)$ of overseas retailers can be obtained:

$$\begin{aligned} E(\pi_{kn}^s) = & p \left[\int_A^{Q_k^s} Df(D)dD + \int_{Q_k^s}^B Q_k^s f(D)dD \right] \\ & - c \int_{Q_k^s}^B (D - Q_k^s)Df(D)dD - w_a Q_k^s \\ & + u \int_A^{Q_k^s} (Q_k^s - D)f(D)dD. \end{aligned} \quad (2)$$

Using the partial integration method to further simplify, we can get

$$\begin{aligned} E(\pi_{kn}^s) = & (p + c - w_a)Q_k^s - (p + c - u)m \int_A^{Q_k^s/m} F(\lambda)d\lambda - cm\mu, \mu \\ = & \int_A^B \lambda f(\lambda)d\lambda. \end{aligned} \quad (3)$$

According to the derivation of the expected profit function based on the newsboy model, the optimal purchase volume and optimal expected profit of overseas retailers can be obtained under the condition that crossborder suppliers are not interrupted [36, 37]:

$$Q_k^s = mF^{-1}\left(\frac{p + c - w_a}{p + c - u}\right), \quad (4)$$

$$\begin{aligned} E(\pi_{kn}^s) = & (p + c - w_a)mF^{-1}\left(\frac{p + c - w_a}{p + c - u}\right) \\ & - (p + c - u)m \int_A^{F^{-1}\left(\frac{p+c-w_a}{p+c-u}\right)} F(\lambda)d\lambda - cm\mu. \end{aligned} \quad (5)$$

When the overseas retailer only purchases from the crossborder supplier, if the crossborder supplier has supply interruption, then the crossborder supplier cannot provide products to the overseas retailer at all, and the purchase

TABLE 1: Parameter description and explanation.

Parameter	Definition
w_a	Unit purchase price provided by crossborder suppliers
w_b	Unit purchase price provided by overseas suppliers
p	Retail price of crossborder e-commerce products
D	Random market demand of crossborder e-commerce products
m	The deterministic part of stochastic market demand for cross border e-commerce products
λ	The uncertain part of the random market demand for crossborder e-commerce products, the mean is μ
Δm	Increased demand due to supply disruption
r	Probability of supply disruption for cross-border suppliers
c	Unit shortage cost of overseas retailers
u	Residual value of unsold products of overseas retailers
Q_k^s	The optimal purchase quantity of overseas retailers under the condition that crossborder suppliers are the only source of purchase without interruption
Q_h^s	The optimal purchasing quantity of overseas retailers with overseas suppliers as the sole purchasing source
Q_k^d	The purchase quantity of overseas retailers ordering from crossborder suppliers under dual-source procurement
Q_h^d	The purchase quantity of overseas retailers ordering from overseas suppliers under dual-source procurement
Q_k^{d*}	After the retailer invests, the purchase quantity of overseas retailers ordering from crossborder suppliers under dual-source purchasing
Q_h^{d*}	After the retailer invests, the purchase quantity of overseas retailers ordering from overseas suppliers under dual-source procurement
I	Investment amount of overseas retailers in crossborder suppliers
r^*	Probability of supply disruption for crossborder suppliers after investment
w_a^*	Supply price of crossborder suppliers after investment
π	Profits of overseas retailers

quantity is 0, and then the expected profit function of the overseas retailer is $E(\pi_{ky}^s)$ [38–40].

$$E(\pi_{ky}^s) = -c(m + \Delta m)\mu, \mu = \int_A^B \lambda f(\lambda) d\lambda. \quad (6)$$

Combining equations (5) and (6), we can obtain that with crossborder suppliers as the sole source of procurement, the expected profit of overseas retailers is

$$\begin{aligned} E(\pi_k^s) &= rE(\pi_{ky}^s) + (1-r)E(\pi_{kn}^s) \\ &= (1-r) \left[(p+c-w_a)mF^{-1}\left(\frac{p+c-w_a}{p+c-u}\right) \right. \\ &\quad \left. - (p+c-u)m \int_A^{F^{-1}\left(\frac{p+c-w_a}{p+c-u}\right)} F(\lambda) d\lambda \right] - c\mu(m+r\Delta m). \end{aligned} \quad (7)$$

2.4. Overseas Suppliers as the Sole Source of Procurement. When overseas retailers only purchase from overseas suppliers, since overseas suppliers do not have the risk of supply interruption, the profit function π_h^s of overseas retailers at this time can be obtained [41, 42].

$$\pi_h^s = p \min(Q_h^s, D) - w_b Q_h^s - c[D - Q_h^s]^+ + u[Q_h^s - D]^+. \quad (8)$$

Lemma 1. When overseas suppliers are the sole source of retail purchases, the optimal purchase volume and optimal expected profit of overseas retailers are Q_h^s and $E(\pi_h^s)$, respectively.

Proof. First of all, the expected profit function of overseas retailers can be obtained by calculation as $E(\pi_h^s) = p[\int_A^{Q_h^s} D f(D) dD + \int_{Q_h^s}^B Q_h^s f(D) dD] - c \int_{Q_h^s}^B (D - Q_h^s) D f(D) dD - w_b Q_h^s + u \int_A^{Q_h^s} (Q_h^s - D) f(D) dD$. \square

Further simplification with the method of integration by parts

$$\begin{aligned} E(\pi_h^s) &= (p+c-w_b)Q_h^s - (p+c-u)m \int_A^{Q_h^s} F(\lambda) d\lambda - cm\mu, \mu \\ &= \int_A^B \lambda f(\lambda) d\lambda. \end{aligned} \quad (9)$$

By deriving the expected profit function from the newsboy model, the optimal purchase quantity and the optimal expected profit of the overseas retailer can be obtained under the condition that the supply of the overseas supplier is not interrupted [43, 44].

$$Q_h^s = mF^{-1}\left(\frac{p+c-w_b}{p+c-u}\right),$$

$$E(\pi_h^s) = (p+c-w_b)mF^{-1}\left(\frac{p+c-w_b}{p+c-u}\right) - (p+c-u)m \int_A^{F^{-1}\left(\frac{p+c-w_b}{p+c-u}\right)} F(\lambda)d\lambda - cm\mu. \quad (10)$$

2.5. Both Crossborder and Overseas Suppliers Are Used as Procurement Sources. When overseas retailers purchase products from crossborder suppliers and overseas suppliers at the same time, the final purchase volume is the sum of the purchase volume of the two channels, and then the profit function of the overseas retailer at this time is

$$\begin{aligned} \pi^d = (1-r) & \left\{ p \min(Q_k^d + Q_h^d, D) - w_a Q_k^d - w_b Q_h^d \right. \\ & \left. - c [D - Q_k^d - Q_h^d]^+ + u [Q_k^d + Q_h^d - D]^+ \right\} \\ & + r \left\{ p \min(Q_h^d, D^*) - w_b Q_h^d - c [D^* - Q_h^d]^+ \right. \\ & \left. + u [Q_h^d - D^*]^+ \right\}, D^* = (m + \Delta m)\lambda. \end{aligned} \quad (11)$$

Lemma 2. When the overseas supplier makes dual-source procurement and the probability of supply interruption of the overseas supplier is $r \geq w_b - w_a/p + c - w_a$, the purchase volume of the overseas retailer from the crossborder supplier and the overseas supplier is Q_k^d and Q_h^d , respectively, and $Q_k^d + Q_h^d = Q_k^s$ [45, 46].

Proof. First of all, the expected profit function of overseas retailers can be obtained by calculation

$$\begin{aligned} E(\pi^d) = (1-r) & \left\{ p \left[\int_A^{Q_k^d + Q_h^d} Df(D)dD \right. \right. \\ & \left. \left. + \int_{Q_k^d + Q_h^d}^B (Q_k^d + Q_h^d)f(D)dD \right] - w_a Q_k^d - w_b Q_h^d \right. \\ & \left. - c \int_{Q_k^d + Q_h^d}^B [D - (Q_k^d + Q_h^d)]Df(D)dD \right. \\ & \left. + u \int_A^{Q_k^d + Q_h^d} (Q_k^d + Q_h^d - D)f(D)dD \right\} \\ & + r \left\{ p \left[\int_A^{Q_h^d} D^*f(D^*)dD^* + \int_{Q_h^d}^B Q_h^d f(D^*)dD^* \right] \right. \\ & \left. - c \int_{Q_h^d}^B (D^* - Q_h^d)D^*f(D^*)dD^* - w_b Q_h^d \right. \\ & \left. + u \int_A^{Q_h^d} (Q_h^d - D^*)f(D^*)dD^* \right\}. \end{aligned} \quad (12)$$

Simplify the above equation using the method of integration by parts

$$\begin{aligned} E(\pi^d) = (1-r) & \left[(p+c-w_a)Q_k^d + (p+c-w_b)Q_h^d \right. \\ & \left. - m(p-u+c) \int_A^{\frac{Q_k^d + Q_h^d}{m}} F(\lambda)d\lambda - cm\mu \right] \\ & + r \left[(p+c-w_b)Q_h^d - (m+\Delta m)(p-u+c) \int_A^{\frac{Q_h^d}{m+\Delta m}} F(\lambda)d\lambda \right. \\ & \left. - c(m+\Delta m)\mu \right]. \end{aligned} \quad (13)$$

Finding the first derivative of $E(\pi^d)$ with respect to Q_k^d and Q_h^d , respectively, we can get

$$\frac{\partial E(\pi^d)}{\partial Q_k^d} = (1-r) \left[(p+c-w_a) - (p-u+c)F\left(\frac{Q_k^d + Q_h^d}{m}\right) \right], \quad (14)$$

$$\begin{aligned} \frac{\partial E(\pi^d)}{\partial Q_h^d} = (1-r) & \left[(p+c-w_b) - (p-u+c)F\left(\frac{Q_k^d + Q_h^d}{m}\right) \right] \\ & + r \left[(p+c-w_b) - (p-u+c)F\left(\frac{Q_h^d}{m+\Delta m}\right) \right]. \end{aligned} \quad (15)$$

Assign the value of 0 to formulae (14) and (15) and solve the system of equations to obtain

$$Q_k^d = mF^{-1}\left(\frac{p+c-w_a}{p+c-u}\right) - (m+\Delta m)F^{-1}\left[\frac{(1-r)w_a - w_b + r(p+c)}{r(p+c-u)}\right]. \quad (16)$$

$$Q_h^d = (m+\Delta m)F^{-1}\left[\frac{(1-r)w_a - w_b + r(p+c)}{r(p+c-u)}\right]. \quad (17)$$

According to the solution result, it can be found that in $F^{-1}[(1-r)w_a - w_b + r(p+c)/r(p+c-u)]$, only when $(1-r)w_a - w_b + r(p+c) \geq 0$, Q_k^d will be greater than 0, overseas retailers will purchase from overseas suppliers, and the phenomenon of dual-source procurement will appear; so, $r \geq w_b - w_a/p + c - w_a$. Then, $Q_k^d + Q_h^d = mF^{-1}(p+c-w_a/p+c-u) = Q_k^s$ is obtained by adding the quantity of crossborder suppliers and overseas suppliers under dual-source procurement, and the proof is complete [47]. \square

Lemma 3. Under dual-source procurement, with the increase of the interruption probability of crossborder suppliers, the quantity of products purchased by overseas retailers from crossborder suppliers will decrease, while the quantity of products purchased from overseas suppliers will increase. And when the crossborder supplier interruption probability

$r > (w_b - w_a)Q_h^d / (p + c - w_a)Q_h^d - (m + \Delta m)(p - u + c) \int_A^{Q_h^d / m + \Delta m} F(\lambda) d\lambda$, the dual-source procurement decision of overseas retailers will be better than the decision of using crossborder suppliers as the sole source of procurement.

Proof. $\partial Q_k^d / \partial r = -((m + \Delta m)(w_b - w_a) / r^2 (p + c - u)) f^{-1}[(1 - r)w_a - w_b + r(p + c) / r(p + c - u)] < 0$, and $\partial Q_h^d / \partial r = ((m + \Delta m)(w_b - w_a) / r^2 (p + c - u)) f^{-1}[(1 - r)w_a - w_b + r(p + c) / r(p + c - u)] > 0$. Therefore, the higher the probability of supply interruption of crossborder suppliers, the less the quantity of products purchased from crossborder suppliers, so as to reduce the loss caused by interruption risk to overseas retailers. If the expected profit of the dual-source purchasing decision is better than the expected profit of the crossborder supplier as the only source, overseas retailers will tend to choose dual-source purchasing, and at this point, there is inequality $E(\pi^d) > E(\pi_k^s)$. According equation $Q_k^d + Q_h^d = Q_k^s$ derived from Lemma 2, the expected profit of overseas retailers' dual-source procurement is transformed into

$$E(\pi^d) = (1 - r) \left[(p + c)Q_k^s - w_a Q_k^d - w_b Q_h^d - m(p - u + c) \int_A^{Q_k^s} F(\lambda) d\lambda - cm\mu \right] + r \left[(p + c - w_b)Q_h^d - (m + \Delta m)(p - u + c) \int_A^{Q_h^d} F(\lambda) d\lambda - c(m + \Delta m)\mu \right]. \quad (18)$$

Due to $E(\pi^d) - E(\pi_k^s) = (1 - r)(w_a - w_b)Q_h^d + r[(p + c - w_b)Q_h^d - (m + \Delta m)(p - u + c) \int_A^{Q_h^d} F(\lambda) d\lambda]$, the solution is available $r > (w_b - w_a)Q_h^d / (p + c - w_a)Q_h^d - (m + \Delta m)(p - u + c) \int_A^{Q_h^d} F(\lambda) d\lambda$. \square

If an overseas retailer cooperates with a crossborder supplier, and the overseas retailer invests in the crossborder supplier, the amount is I , and the crossborder supplier will provide products to the overseas retailer at a lower supply price w_a^* . After the investment, affected by factors such as the speed of logistics and the quality of transportation equipment, the risk of supply interruption is reduced to r^* . At this time, the profit function π_d^* for overseas retailers' dual-source procurement is

$$\begin{aligned} \pi_d^* = & (1 - r^*) \left\{ p \min(Q_k^{d*} + Q_h^{d*}, D) - w_a^* Q_k^{d*} - w_b Q_h^{d*} \right. \\ & \left. - c[D - Q_k^{d*} - Q_h^{d*}]^+ + u[Q_k^{d*} + Q_h^{d*} - D]^+ \right\} \\ & + r^* \left\{ p \min(Q_h^{d*}, D^*) - w_b Q_h^{d*} - c[D^* - Q_h^{d*}]^+ \right. \\ & \left. + u[Q_h^{d*} - D^*]^+ \right\} - I, D^* = (m + \Delta m)\lambda. \end{aligned} \quad (19)$$

Lemma 4. After the overseas retailers' investment, when the supply interruption risk and investment amount meet the conditions $r \geq \alpha I + (w_b - w_a + \beta I) / (p + c - w_a + \beta I)$, the purchasing volumes of overseas retailers from crossborder suppliers and overseas suppliers are Q_k^{d*} and Q_h^{d*} , respectively.

Proof. After the investment behavior, the expected profit function of the overseas retailer is $E(\pi^{d*}) = [1 - (r - \alpha I)] \{ p [\int_A^{Q_k^{d*} + Q_h^{d*}} Df(D) dD + \int_{Q_k^{d*} + Q_h^{d*}}^B (Q_k^{d*} + Q_h^{d*}) f(D) dD] - (w_a - \beta I) Q_k^{d*} - c \int_{Q_k^{d*} + Q_h^{d*}}^B [D - (Q_k^{d*} + Q_h^{d*})] Df(D) dD + u \int_A^{Q_k^{d*} + Q_h^{d*}} (Q_k^{d*} + Q_h^{d*} - D) f(D) dD - w_b Q_h^{d*} \} + (r - \alpha I) \{ p [\int_A^{Q_h^{d*}} D^* f(D^*) dD^* + \int_{Q_h^{d*}}^B Q_h^{d*} f(D^*) dD^*] - c \int_{Q_h^{d*}}^B (D^* - Q_h^{d*}) D^* f(D^*) dD^* - w_b Q_h^{d*} + u \int_A^{Q_h^{d*}} (Q_h^{d*} - D^*) f(D^*) dD^* \} - I$. \square

Simplify by using the method of integration by parts

$$E(\pi^{d*}) = [1 - (r - \alpha I)] \left[(p + c - w_a + \beta I) Q_k^{d*} + (p + c - w_b) Q_h^{d*} - m(p - u + c) \int_A^{Q_k^{d*} + Q_h^{d*}} F(\lambda) d\lambda - cm\mu \right] + (r - \alpha I) \cdot \left[(p + c - w_b) Q_h^{d*} - (m + \Delta m)(p - u + c) \int_A^{Q_h^{d*}} F(\lambda) d\lambda - c(m + \Delta m)\mu \right] - I. \quad (20)$$

By finding the derivatives of $E(\pi^{d*})$ with respect to Q_k^{d*} and Q_h^{d*} , we can obtain

$$\frac{\partial E(\pi^{d*})}{\partial Q_k^{d*}} = (1 - r + \alpha I) [(p + c - w_a + \beta I) - (p - u + c) F\left(\frac{Q_k^{d*} + Q_h^{d*}}{m}\right)], \quad (21)$$

$$\begin{aligned} \frac{\partial E(\pi^{d*})}{\partial Q_h^{d*}} = & (1 - r + \alpha I) \left[(p + c - w_b) - (p - u + c) F\left(\frac{Q_k^{d*} + Q_h^{d*}}{m}\right) \right] \\ & + (r - \alpha I) \left[(p + c - w_b) - (p - u + c) F\left(\frac{Q_h^{d*}}{m + \Delta m}\right) \right]. \end{aligned} \quad (22)$$

Assigning formulae (21) and (22) to 0, solving the system of equations can be obtained

$$Q_k^{d*} = mF^{-1}\left(\frac{p + c - w_a + \beta I}{p + c - u}\right) - (m + \Delta m)F^{-1}\left[\frac{(1 - r + \alpha I)(w_a - \beta I) - w_b + (r - \alpha I)(p + c)}{(r - \alpha I)(p + c - u)}\right]. \quad (23)$$

$$Q_h^{d*} = (m + \Delta m)F^{-1} \left[\frac{(1-r+\alpha I)(w_a - \beta I) - w_b + (r-\alpha I)(p+c)}{(r-\alpha I)(p+c-u)} \right]. \quad (24)$$

To make a meaningful solution of equations that must satisfy the condition $(1-r+\alpha I)(w_a - \beta I) - w_b + (r-\alpha I)(p+c) \geq 0$, in this time, there will exist $Q_h^{d*} > 0$, which is the case of dual-source procurement. So, $r \geq \alpha I + (w_b - w_a + \beta I)/p + c - w_a + \beta I$ and complete the proof of the lemma.

Lemma 5. *After overseas retailers have invested, under the dual-source procurement situation, overseas retailers have increased their purchases of products supplied by crossborder suppliers and have reduced their purchases of products supplied by overseas suppliers. The overall purchase volume has increased.*

Proof. According to equations (17) and (24), we can get the purchase quantity of overseas retailers from overseas suppliers before and after investment; so,

$$Q_h^d - Q_h^{d*} = (m + \Delta m) \left\{ F^{-1} \left[\frac{(1-r)w_a - w_b + r(p+c)}{r(p+c-u)} \right] - F^{-1} \left[\frac{(1-r+\alpha I)(w_a - \beta I) - w_b + (r-\alpha I)(p+c)}{(r-\alpha I)(p+c-u)} \right] \right\}. \quad (25)$$

$F^{-1}(x)$ is the inverse function of $F(x)$, which has the same monotonicity, while as a continuous probability distribution function, function $F(x)$ is monotonous increasing with the increase of x , due to

$$\begin{aligned} & \frac{(1-r)w_a - w_b + r(p+c)}{r(p+c-u)} \\ & - \frac{(1-r+\alpha I)(w_a - \beta I) - w_b + (r-\alpha I)(p+c)}{(r-\alpha I)(p+c-u)} \\ & = \frac{I[\beta r(1-r) + \alpha(w_b - w_a) + I\alpha\beta r]}{r(r-\alpha I)(p+c-u)} \\ & > 0 F^{-1} \left[\frac{(1-r)w_a - w_b + r(p+c)}{r(p+c-u)} \right] \\ & > F^{-1} \left[\frac{(1-r+\alpha I)(w_a - \beta I) - w_b + (r-\alpha I)(p+c)}{(r-\alpha I)(p+c-u)} \right]. \end{aligned} \quad (26)$$

So, $Q_h^d > Q_h^{d*}$, and the purchase volume of this channel from overseas suppliers has decreased. It is the same because of

$Q_k^d + Q_h^d = mF^{-1}(p+c-w_a/p+c-u)$, $Q_k^{d*} + Q_h^{d*} = mF^{-1}(p+c-w_a+\beta I/p+c-u)$, while $p+c-w_a/p+c-u \leq p+c-w_a+\beta I/p+c-u$; so, we can get, $F^{-1}(p+c-w_a/p+c-u) \leq F^{-1}(p+c-w_a+\beta I/p+c-u)$, $Q_k^d + Q_h^d \leq Q_k^{d*} + Q_h^{d*}$, and the overall purchase volume of retailers has increased. Through the overall procurement volume and

the procurement volume from overseas suppliers, it can be found that the volume of products purchased by overseas retailers from crossborder suppliers has increased, and the increase is more than the reduction from overseas suppliers. This is because after the investment, the prices of crossborder suppliers have advantages, the instability is reduced, and overseas retailers can obtain more profits. \square

3. Results and Discussion

In order to verify the rationality of the model and reveal the changes in the expected profit and purchase volume of overseas retailers under different purchasing methods, this section verifies the conclusions reached above. In the two-tier supply chain composed of crossborder suppliers, overseas suppliers, overseas retailers, and consumers, according to the parameter range set above, select parameter values, random market demand $\lambda \in (100, 200)$ is evenly distributed, crossborder suppliers and overseas suppliers supply prices that are $w_a = 6$ and $w_b = 10$, respectively, overseas retailers sell products at retail prices of $p = 15$, market demand determination part is $m = 18$, if supply interruption, demand increase is $\Delta m = 2$, out-of-stock cost is $c = 4$, the residual value of the product is $u = 1$, and the impact factors of investment on supply disruptions and crossborder supplier supply prices were $\alpha = 0.005$ and $\beta = 0.1$, respectively.

3.1. The Impact of Supply Disruption Probability on Purchase Volume. In the case of single source procurement and dual-source procurement, if the disruption probability of crossborder suppliers changes, the purchase volume of overseas retailers in each channel will also change. According to Lemma 4, when $r \geq w_b - w_a/p + c - w_a$, that is $r \geq 0.3077$, there will cause double source procurement. Assuming that r rises from 0.4 to 0.7, we will get the change of procurement quantity in two cases, as shown in Figure 2.

It can be seen from Figure 2 that if the crossborder suppliers do not experience disruption under single-source procurement, then the purchase volume of overseas retailers from crossborder suppliers is equal to the total purchase volume under dual-source procurement. If overseas retailers choose to purchase from single source, the purchase volume of overseas retailers from crossborder suppliers is more than that from overseas suppliers. If overseas retailers choose dual-source procurement, with the increase of supply interruption probability of crossborder suppliers, overseas retailers will reduce the procurement of goods provided by crossborder suppliers and increase the procurement of goods provided by overseas suppliers, so as to avoid risks and reduce losses.

3.2. The Impact of Supply Disruption Probability on Expected Profit. In the case of single-source procurement and dual-source procurement, if the disruption probability of crossborder suppliers changes, the expected profits of overseas retailers in various channels will also change. Suppose r goes up from 0.1 to 0.6, the change of expected profit under these two conditions is obtained, as shown in Figure 3.

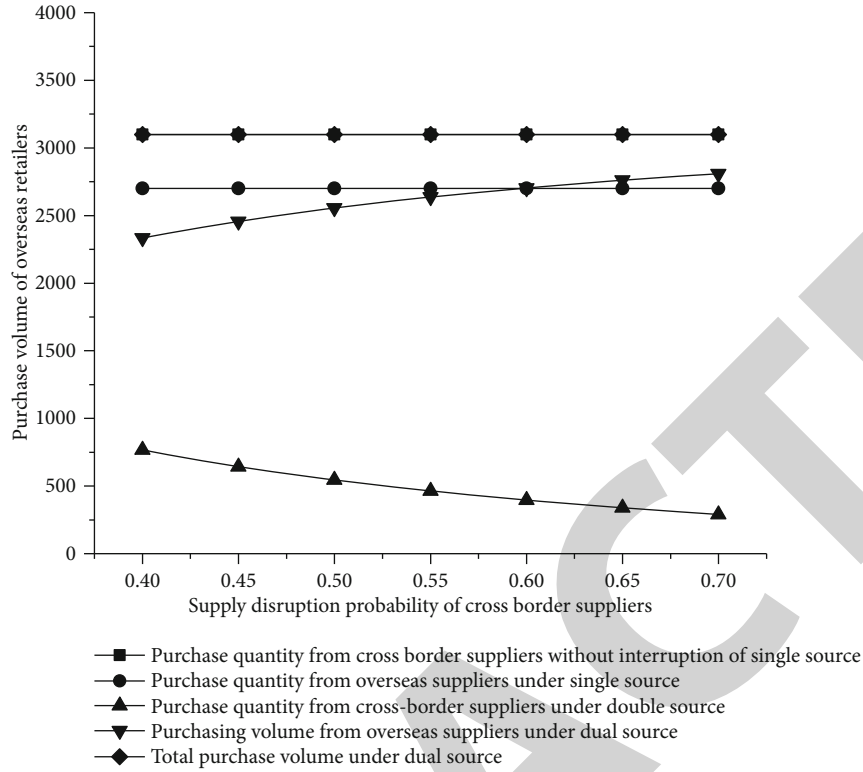


FIGURE 2: The relationship between retailer procurement volume and crossborder supplier supply disruption probability under single-source and dual-source procurement.

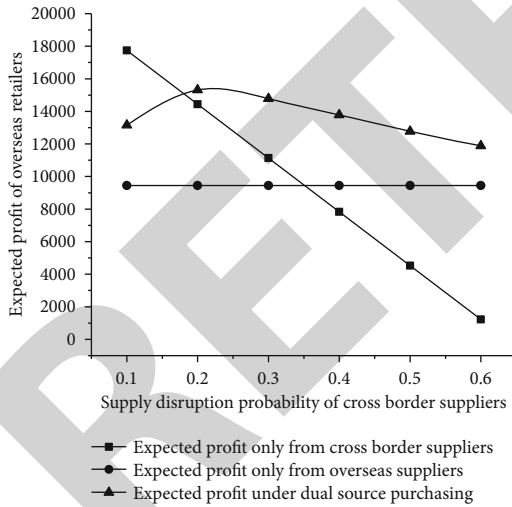


FIGURE 3: The relationship between retailer’s expected profit and crossborder supplier supply disruption probability under single-source and dual-source procurement.

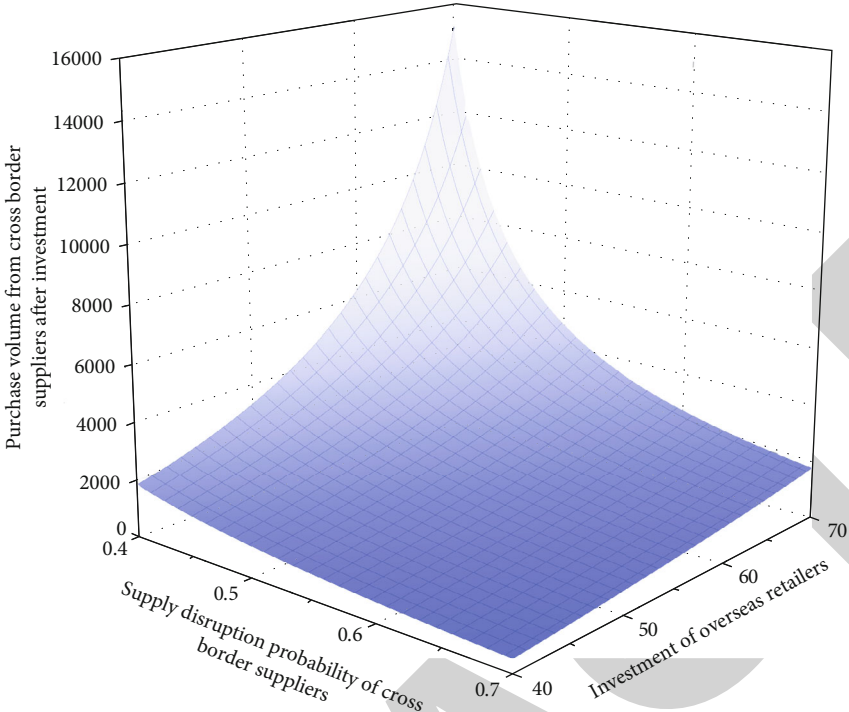
It can be seen from Figure 3 that the expected profit of overseas retailers is not affected by the disruption probability when they only purchase from overseas suppliers. With the increase of interruption probability of crossborder suppliers, the expected profit will decrease rapidly and face huge losses if only purchasing from crossborder suppliers. When overseas retailers choose dual-source procurement, it will not only achieve the maximum expected profit within a certain

risk but also effectively curb the decline of expected profit. When the disruption risk is greater than 0.1761, the expected profit from crossborder suppliers is lower than that from dual-source suppliers, and the decision of dual-source suppliers is better than that of single source suppliers.

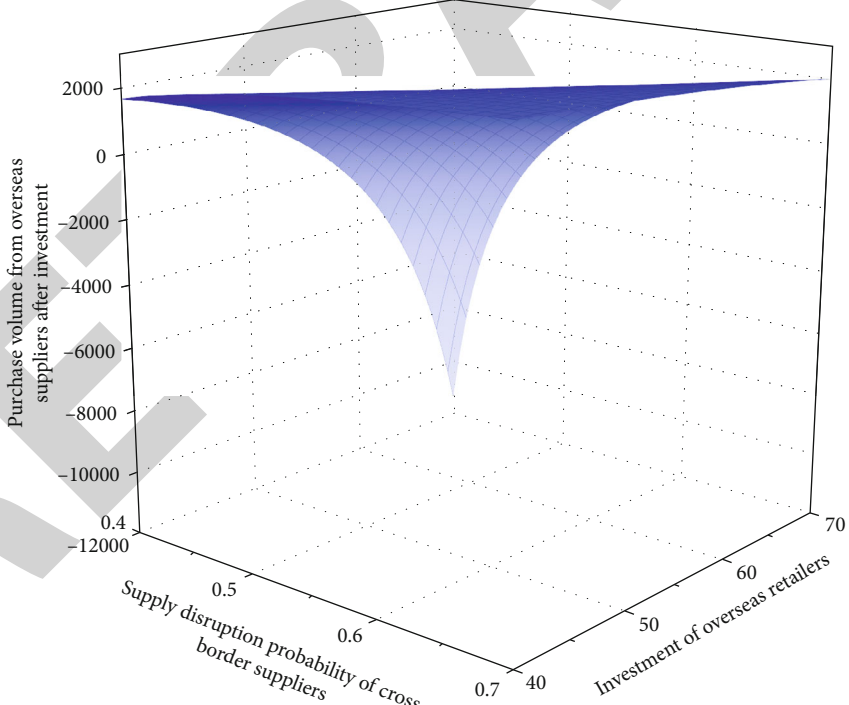
In combination with Figures 3 and 4, it can be found that under dual-source procurement, overseas retailers will not be too passively affected by the probability of disruption of crossborder supplier supply and will be able to ensure to some extent the expected profits of overseas retailers.

3.3. *The Impact of Supply Disruption Probability and Investment Amount on Expected Profit.* When the overseas retailer invests in the crossborder supplier, the expected profit of the overseas retailer will be affected by both the supply interruption probability of the crossborder supplier and the investment amount of the overseas retailer. According to Lemma 4, when the supply interruption probability of the crossborder supplier r and the investment amount of the overseas retailer I meet $r \geq \alpha I + (w_b - w_a + \beta I / p + c - w_a + \beta I)$, the situation of dual-source procurement will appear. Thus, suppose r rises from 0.4 to 0.7 and corresponding I rises from 40 to 70. The change of purchasing volume and expected profit after investment of overseas retailers under dual-source procurement is shown in Figure 4.

It can be seen from Figure 4 that after overseas retailers invest, if the probability of crossborder supplier interruption is low, and at the same time they have made large

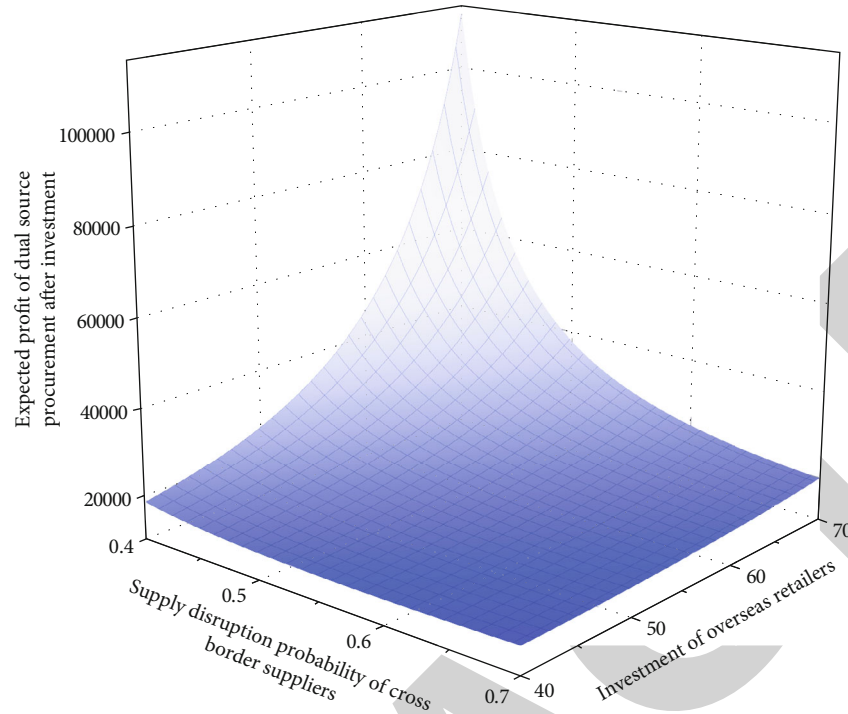


(a) Purchase volume from crossborder suppliers after investment



(b) Purchase volume from overseas suppliers after Investment

FIGURE 4: Continued.



(c) Expected profit of dual-source procurement after investment

FIGURE 4: Changes of various parameters under the dual influence of supply disruption probability and investment amount.

investments in crossborder suppliers, then overseas retailers will purchase a large number of crossborder suppliers' products and greatly reduce the products of overseas suppliers, and the expected profits of overseas retailers will also be very high. In addition, when the risk of supply interruption of crossborder suppliers is large, the higher investment number of overseas retailers, the higher expected profit of dual-source procurement will be received, and the investment behavior of overseas retailers can effectively restrain the risk of crossborder supplier disruption. Therefore, the risk stability of dual-source procurement can be further strengthened through investment by overseas retailers, and the expected profits of retailers can be improved.

4. Conclusion

This paper takes the mobile communication procurement platform supply chain as the research object and constructs a two-level supply chain composed of crossborder suppliers, overseas suppliers, and overseas retailers. Study the optimal purchasing decision problem of the supply chain in four situations: only purchasing from crossborder suppliers, purchasing only from overseas suppliers, purchasing from crossborder and overseas suppliers at the same time, and purchasing from crossborder and overseas suppliers at the same time after retailer investment. The analysis found that compared with single-source procurement, dual-source procurement can make overseas retailers not passively affected by the probability of supply disruption by crossborder suppliers and can also ensure the expected profits of overseas

retailers to a certain extent. At the same time, the investment behavior of overseas retailers in crossborder suppliers can effectively curb the possible negative impact of crossborder supplier disruption risk under dual-source procurement. As a result, overseas retailers may consider investing in crossborder suppliers and opting for a two-channel approach to procurement to achieve higher expected profits with stable risk. Of course, the above model has certain limitations. For example, it only considers the risk neutral conditions of each enterprise and does not consider issues such as the risk preference of decision makers and retailer price decisions. In the future, research on supply chain coordination can be carried out from the perspective of supplier risk preference.

Data Availability

The data used to support the findings of this study are available from the corresponding author upon request.

Conflicts of Interest

The authors declare that they have no conflicts of interest.

Acknowledgments

The finding is sponsored by the Key Lab of Information Network Security of Ministry of Public Security (Grant No. C20609) and Municipal Key Curriculum Construction Project of University in Shanghai (Grant No. S202003002).

References

- [1] Y. Zhou, F. Jia, F. Wang, and Y. Jiang, "A platform-based procurement organization that guides suppliers to participate in the development of new products in the early stage: a single case study based on Haier procurement organization," *Chinese Journal of Management*, vol. 16, no. 9, pp. 1290–1300, 2019.
- [2] L. Zhou, K. Teng, and F. Lu, "Research on the innovation of two-way bidding transaction mode of platform logistics procurement," *Chinese Journal of Management*, vol. 16, no. 4, pp. 624–632, 2019.
- [3] X. Zhang, W. Hou, C. Shen, and Q. He, "Willingness to participate in centralized procurement, bargaining power of pharmaceutical enterprises and drug market performance," *Chinese Journal of Management Science*, vol. 25, no. 7, pp. 113–122, 2017.
- [4] S. K. Paul, R. A. Sarker, and D. L. Essam, "A reactive mitigation approach for managing supply disruption in a three-tier supply chain," *Journal of Intelligent Manufacturing*, vol. 29, no. 7, pp. 1581–1597, 2018.
- [5] D. Ivanov, A. Dolgui, and B. Sokolov, "The impact of digital technology and industry 4.0 on the ripple effect and supply chain risk analytics," *International Journal of Production Research*, vol. 57, no. 3, pp. 829–846, 2019.
- [6] X. Li, J. Wang, and Q. Da, "Emergency decision analysis based on backup supplier in case of supply interruption," *Chinese Journal of Management Science*, vol. 24, no. 7, pp. 63–71, 2016.
- [7] F. Kong and J. Li, "OEM supply chain resilient operation and promotion strategy under the risk of supply interruption," *Chinese Journal of Management Science*, vol. 26, no. 2, pp. 152–159, 2018.
- [8] Z. Liu, B. Hu, B. Huang, L. Lang, H. Guo, and Y. Zhao, "Decision optimization of low-carbon dual-channel supply chain of auto parts based on smart city architecture," *Complexity*, vol. 2020, Article ID 2145951, 14 pages, 2020.
- [9] Z. Liu, H. Guo, Y. Zhao et al., "Research on the optimized route of cold chain logistics transportation of fresh products in context of energy-saving and emission reduction," *Mathematical Biosciences and Engineering*, vol. 18, no. 2, pp. 1926–1940, 2021.
- [10] Y. Zhang, J. Long, and Y. Chen, "Emergency strategy and operation simulation of supply chain interruption with variable market demand," *Journal of Systems & Management*, vol. 28, no. 6, pp. 1202–1210, 2019.
- [11] W. Shi, Z. Kong, and M. Wang, "Coordination of emergency supplies mobilization chain that takes into account interruption of demand and overconfidence of buyers," *Control Theory & Applications*, vol. 37, no. 10, pp. 2163–2177, 2020.
- [12] L. Xin and D. A. Goldberg, "Asymptotic optimality of tailored base-surge policies in dual-sourcing inventory systems," *Management Science Journal of the Institute of Management Sciences*, vol. 64, no. 1, pp. 437–452, 2018.
- [13] F. Lucker and R. W. Seifert, "Building up resilience in a pharmaceutical supply chain through inventory, dual sourcing and agility capacity," *Omega*, vol. 73, no. 12, pp. 114–124, 2017.
- [14] Z. Hu, J. Tian, and G. Feng, "Pricing model of dual-source emergency material purchase based on quantity flexible contract," *Chinese Journal of Management Science*, vol. 27, no. 12, pp. 100–112, 2019.
- [15] C. Chen and Z. Chen, "Dual source procurement decision under supplier output stochastic and supply disruption," *Chinese Journal of Management Science*, vol. 27, no. 6, pp. 113–122, 2019.
- [16] Z. Liu, S. Chen, B. Hu, M. Zhou, and Y. Zhao, "Research on staged pricing model and simulation of intelligent urban transportation," *IEEE Access*, vol. 7, no. 9, pp. 141404–141413, 2019.
- [17] S. Han and H. Song, "Research on dual source purchasing strategy under dual uncertain information," *Management Review*, vol. 32, no. 2, pp. 299–307, 2020.
- [18] A. Arya, B. Mittendorf, and D. E. Sappington, "The bright side of supplier encroachment," *Marketing Science*, vol. 26, no. 5, pp. 651–659, 2007.
- [19] Z. Liu, B. Hu, Y. J. Zhao et al., "Research on intelligent decision of low carbon supply chain based on carbon tax constraints in human-driven edge computing," *IEEE Access*, vol. 8, no. 3, pp. 48264–48273, 2020.
- [20] D. Krause, R. Handfield, and B. Tyler, "The relationships between supplier development, commitment, social capital accumulation and performance improvement," *Journal of Operations Management*, vol. 25, no. 2, pp. 528–545, 2007.
- [21] H. Yang, W. Zhuo, and L. Shao, "Equilibrium evolution in a two-echelon supply chain with financially constrained retailers: the impact of equity financing," *International Journal of Production Economics*, vol. 185, no. 3, pp. 139–149, 2017.
- [22] W. Niu, J. Xia, and W. Tang, "Co-supplier quality investment strategy with spillover effect in market competition," *Journal of Industrial Engineering and Engineering Management*, vol. 31, no. 2, pp. 222–232, 2017.
- [23] Z. Liu, L. L. Lang, B. Hu, L. H. Shi, B. T. Huang, and Y. J. Zhao, "Emission reduction decision of agricultural supply chain considering carbon tax and investment cooperation," *Journal of Cleaner Production*, vol. 294, article 126305, 2021.
- [24] B. H. Li, Y. Liu, A. M. Zhang, W. H. Wang, and S. Wan, "A survey on blocking technology of entity resolution," *Journal of Computer Science and Technology*, vol. 35, no. 4, pp. 769–793, 2020.
- [25] A. Li, D. Spano, J. Krivochiza et al., "A tutorial on interference exploitation via symbol-level precoding: overview, state-of-the-art and future directions," *IEEE Communications Surveys and Tutorials*, vol. 22, no. 2, pp. 796–839, 2020.
- [26] Z. Niu, B. Zhang, J. Wang et al., "The research on 220GHz multicarrier high-speed communication system," *China Communications*, vol. 17, no. 3, pp. 131–139, 2020.
- [27] B. Li, R. Liang, W. Zhou, H. Yin, H. Gao, and K. Cai, "LBS meets blockchain: an efficient method with security preserving trust in SAGIN," *IEEE Internet of Things Journal*, 2021.
- [28] J. Zhang, C. Shen, H. Su, M. T. Arafin, and G. Qu, "Voltage over-scaling-based lightweight authentication for IoT security," *IEEE Transactions on Computers*, 2021.
- [29] J. Zhang and G. Qu, "Physical unclonable function-based key sharing via machine learning for IoT security," *IEEE Transactions on Industrial Electronics*, vol. 67, no. 8, pp. 7025–7033, 2020.
- [30] X. Zhang, Y. Wang, C. Wang, C. Y. Su, Z. Li, and X. Chen, "Adaptive estimated inverse output-feedback quantized control for piezoelectric positioning stage," *IEEE Transactions on Cybernetics*, vol. 49, no. 6, pp. 2106–2118, 2019.
- [31] Z. Xiong, N. Xiao, F. Xu et al., "An equivalent exchange based data forwarding incentive scheme for socially aware networks," *Journal of Signal Processing Systems*, vol. 93, no. 2–3, pp. 249–263, 2021.

Retraction

Retracted: The Construction of Immersive Learning System Based on Virtual Testing Technology of Virtual Reality

Wireless Communications and Mobile Computing

Received 28 November 2023; Accepted 28 November 2023; Published 29 November 2023

Copyright © 2023 Wireless Communications and Mobile Computing. This is an open access article distributed under the Creative Commons Attribution License, which permits unrestricted use, distribution, and reproduction in any medium, provided the original work is properly cited.

This article has been retracted by Hindawi, as publisher, following an investigation undertaken by the publisher [1]. This investigation has uncovered evidence of systematic manipulation of the publication and peer-review process. We cannot, therefore, vouch for the reliability or integrity of this article.

Please note that this notice is intended solely to alert readers that the peer-review process of this article has been compromised.

Wiley and Hindawi regret that the usual quality checks did not identify these issues before publication and have since put additional measures in place to safeguard research integrity.

We wish to credit our Research Integrity and Research Publishing teams and anonymous and named external researchers and research integrity experts for contributing to this investigation.

The corresponding author, as the representative of all authors, has been given the opportunity to register their agreement or disagreement to this retraction. We have kept a record of any response received.

References

- [1] S. Li and D. Zhou, "The Construction of Immersive Learning System Based on Virtual Testing Technology of Virtual Reality," *Wireless Communications and Mobile Computing*, vol. 2021, Article ID 9656578, 6 pages, 2021.

Research Article

The Construction of Immersive Learning System Based on Virtual Testing Technology of Virtual Reality

Sansan Li¹ and Dongxian Zhou² 

¹School of Engineering, Guangzhou College of Technology and Business, Guangzhou, Guangdong 510850, China

²School of Business, Guangzhou College of Technology and Business, Guangzhou, Guangdong 510850, China

Correspondence should be addressed to Dongxian Zhou; zhdongx@mail3.sysu.edu.cn

Received 6 July 2021; Revised 27 July 2021; Accepted 7 August 2021; Published 18 August 2021

Academic Editor: Balakrishnan Nagaraj

Copyright © 2021 Sansan Li and Dongxian Zhou. This is an open access article distributed under the Creative Commons Attribution License, which permits unrestricted use, distribution, and reproduction in any medium, provided the original work is properly cited.

Objective. To explore the construction of immersive learning system based on virtual reality (VR) and test its learning effect. **Methods.** 20 qualified subjects were divided into two groups, each tending to agree, each with 5 boys and 5 girls. Experimental group 1 is in the real operating environment, and experimental group 2 is in the VR virtual disassembly experimental environment. The task process errors, knowledge questionnaire scores and user subjective satisfaction were analyzed statistically. **Results.** The significance probability P of knowledge questionnaire in the Levene test was 0.777, greater than 0.05, and the variance homogeneous, so the final P of independent sample t -test was subject to “assumed variance equal”; the significance probability was 0.613, greater than 0.05; the questionnaire scores of two groups showed no significant difference, so VR virtual environment can achieve the learning effect of the real environment. The number of errors in a VR virtual situation is significantly lower than the number of errors in the real environment, the VR virtual environment can achieve the learning effect of the real environment, and the VR virtual environment can achieve more interaction, with good interaction. **Conclusion.** The immersive learning system based on VR detection technology can realize the cognition of three-dimensional model structure and has a certain learning effect.

1. Introduction

At present, in the field of education, more and more scholars have seen the importance of VR technology in classroom learning environment. For example, one of the characteristics of intelligent learning environment proposed by Professor Huang Ronghuai is that intelligent learning environment should realize the integration of physical environment and virtual environment; in the intelligent environment, the perception, monitoring, and adjustment functions of the physical environment are further enhanced; and the application of augmented reality technology makes the virtual environment and the physical environment seamlessly integrated [1]. VR virtual learning environment provides a large number of construction tool systems and performance areas, which can improve the subjective initiative of learners, which is consistent with Piaget’s conception and practice of “mov-

ing the laboratory into the classroom” and his constructivist view of “learning is the experience of a real situation” [2].

The biggest difference between “VR-based virtual testing technology” and the virtual instrument-based virtual testing technology that has been widely used at present lies in the introduction of VR technology into the testing field and the realization of the simulation of the testing process and visualization of the test results by the virtual testing system including operators [3]. Virtual testing technology based on VR has the following characteristics.

Nakayama et al. [4] proposed a simulated environment learning support system, based on Kinect sensor, systematic animation, and student action synchronous display on ancient biological animals and its habitat, soaking learners in real life, through record. The real-time measurement of the learner’s movement is evaluated system and controls the animation based on the sensor output, followed by an

interview to assess their immersion. The learner feels immersive and experiences an enhanced interest.

Fang [5] Focusing on the design of the teaching quality evaluation model based on machine learning theory, an in-depth study is conducted on the pretreatment and support vector machine teaching quality assessment model of assessment indicators. In addition, the study uses improved main component analysis to reduce the dimension of evaluation indicators, thereby avoiding the impact of too complex network model on prediction effects.

This paper mainly studied the immersive learning system based on VR virtual testing technology. We conducted experimental research on the construction of VR immersive learning system and concluded that the questionnaire scores of the two groups of experimenters generally did not differ significantly, which shows that the VR virtual environment can achieve the learning effect of the real environment. The number of errors in a VR virtual situation is significantly lower than the number of errors in the real environment, the VR virtual environment can achieve the learning effect of real environment, and the VR virtual environment can achieve more interaction, with good interaction. Therefore, the immersive learning system based on VR virtual detection technology can realize the cognition of 3D model structure and has a certain learning effect.

2. Method of Constructing Immersive Learning System for VR

Virtual reality technology combines multimedia and network technology, so multimedia design principle design virtual reality also has a great reference value; we should not only pay attention to the external form of teaching media but also pay attention to the value of education. Only according to the correct design principles the multimedia teaching software can fundamentally promote the students' meaningful learning [6, 7].

Virtual test is conducted through 3D human-computer interaction, realistic image generation, 3D sound positioning technology, and simulation information acquisition. The development path of virtual testing technology based on VR is shown in Figure 1.

3. Research Methods

3.1. Experimental Arrangement. A total of 20 qualified subjects were selected and divided into two groups. The ratio of males to females in each group tended to be the same, with 5 males and 5 females in each group. The experimental group 1 was in the real operating environment, and the experimental group 2 was in the VR virtual disassembly and assembly environment. The experimental task was to complete the disassembly and assembly tasks of the reducer assembly model with the help of the data and tools given by the team and to complete the knowledge investigation and test after the experiment according to the knowledge acquired in the disassembly and assembly learning process [8, 9]. In addition to different operating environments, the other conditions between the two experimental groups are consistent, as

shown in Table 1; that is, there is an equal corresponding relationship between experimental operating objects, experimental equipment, and experimental text data. For example, the solid model of the gearbox corresponds to the virtual model in the three-dimensional environment, actual model disassembly video animation corresponds to 3D model disassembly animation display in VR environment, and actual 2D text data corresponds to interface UI display in VR environment.

The specific description of the behavioral data to be recorded during the experiment and the mapping meaning of the results of the behavioral data are as follows:

Error times E1: the error times in the disassembly process whether the parts are placed correctly or not and the error times in the assembly process whether the parts are matched successfully or not. The error times are too high, indicating that the recognition of the parts at the disassembly position is insufficient [10, 11].

Knowledge questionnaire score: knowledge questionnaire mainly involves the structure cognition and working principle of the model and is used to judge whether learners understand the structure of the model in the process of model disassembly and assembly. The lower the score of the question test, the less helpful the learning system is to learners, and the lower the evaluation in the effectiveness index.

Subjective satisfaction score: obtains users' subjective evaluation of the design of the two operational learning environments.

3.2. Statistical Analysis. This experiment is a set of comparative experiments of learning styles, consisting of two groups, namely, physical disassembly environment (group 1) and VR virtual disassembly environment (group 2). Independent sample *t*-test is adopted to analyze all data, which is completed in SPSS software. If the *P* value of significance probability (i.e., Sig. in the table) is greater than 0.05 in Levene's test of the equation's variance, it indicates homogeneity of variance, and the final *P* value of independent sample *t*-test is subject to "assuming equal variance." On the contrary, we should deal with the *P* value when the strain variance is different. When the *P* value of *t*-test (i.e., Sig. (double tail) in the table) is less than the significance level of 0.05, it is considered that there is a significant difference between the two groups of data; otherwise, it is considered that there is no significant difference between the two groups of data.

4. Experimental Results

4.1. Error Times in Task Process. In the process of experimental tasks, task errors are mainly defined as the following three situations: one error and one record. Specifically, in the disassembly process, the parts should be placed in the specified parts tray, and the placement error is recorded as a task error. In the assembly process, the wrong parts are grabbed for assembly, which is recorded as a task error. The assembly position and direction of the parts are wrong, which is recorded as a task error. As shown in Table 2, in the process of task completion, the number of errors in the VR virtual situation was significantly lower than that in the real

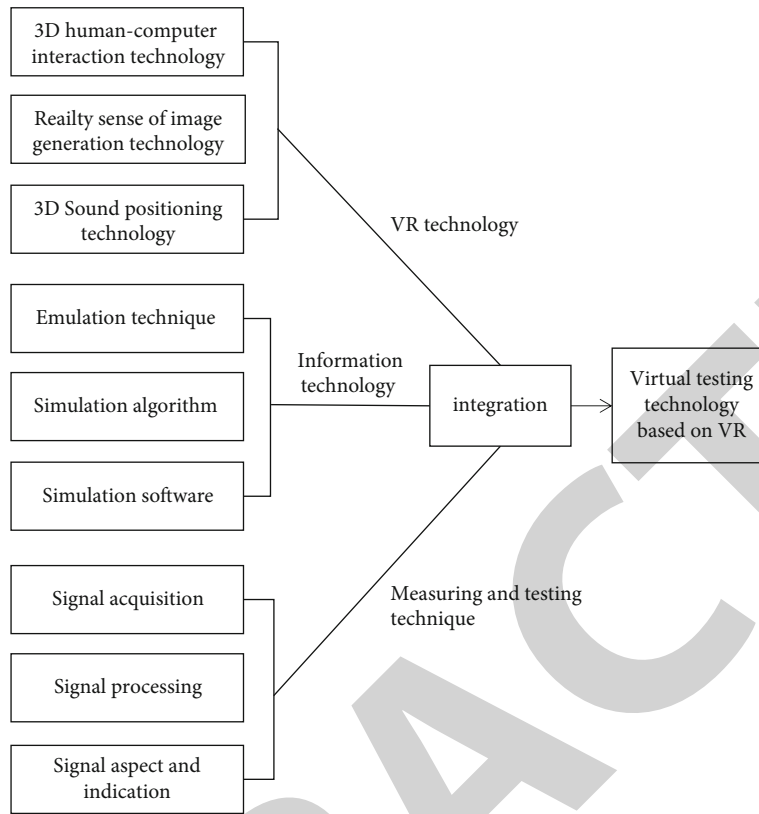


FIGURE 1: Development path of virtual testing technology based on VR. Virtual test is conducted through 3D human-computer interaction, realistic image generation, 3D sound positioning technology, and simulation information acquisition.

TABLE 1: Corresponding relation of each factor in the two groups of experiments.

	Physical disassembly group	VR disassembling group
Experimental environment	Real work drawing model laboratory operating environment	VR virtual disassembly and assembly experiment ring
The experiment task	Model disassembly and test	Model disassembly and test
Laboratory equipment	Wrenches and other commonly used tools, desks, part placement plates, etc.	VR headsets, leap motion, etc.
The subjects	Physical model	3D virtual model
Experimental data	Two-dimensional pictures, teaching materials Video animation of model disassembly	Virtual UI interaction, interface display 3D model disassembly animation demonstration

TABLE 2: Number of errors in the task process.

Experimenter code	1	2	3	4	5	6	7	8	9	10	The average
1_real environment	5	3	5	5	8	6	2	3	4	7	4.8
2_vr environment	2	1	1	1	2	3	3	2	4	3	2.2

environment. In the process of physical assembly, especially in the assembly process of shafting part group 1 and shafting part group 2, it is easy to make mistakes, and the most common mistake is the wrong assembly position of parts. In a VR virtual operation environment, the main reason for user operation error is that there are more than one bearing and adjustment ring in a shafting part group, but the matching

of the designed parts of the system is one to one; that is, the bearing located on the left side of the shaft must be assembled on the left side before the system can identify the assembly as successful. Due to the visual feedback of color highlighting after the successful matching of the system design, most users did not see visual feedback during the assembly process and would try repeatedly. The feedback information from the experimenters can provide guidance for the subsequent design and optimization of the learning system.

4.2. *Score of Knowledge Questionnaire.* As shown in Table 3, the average score of knowledge questionnaire in the VR virtual environment ($M = 84$) was slightly lower than that in the real operating environment ($M = 85.5$). The two sets of questionnaire score data are independent sample t -test, as

TABLE 3: Knowledge questionnaire scores.

Experimenter code	1	2	3	4	5	6	7	8	9	10	The average
1_ real environment	80	75	95	85	90	85	85	80	95	85	85.5
2 _vr environment	85	90	75	80	80	90	75	85	85	95	84

TABLE 4: Independent sample t -test of questionnaire scores.

	Levene's test of equation variance		t -test of mean value equation		
	F	Sig.	T value	Df (degrees of freedom)	Sig. (double tail)
Assumed equivariance	0.083	0.777	0.515	18	0.163

shown in Table 4; the analysis results show that two kinds of learning environment knowledge questionnaire score data in Levene's test in significant probability P value are 0.777, which is greater than the significance level of 0.05, homogeneous variance, so in the independent sample t -test, the final P values will be subject to "assume equal variance." The P value of significance probability of the t -test is 0.613, which is greater than 0.05. There is no significant difference in the overall scores of the two groups of experimenter, indicating that the VR virtual environment can achieve the learning effect of real environment. Knowledge questionnaire topic fills up the following topic: multiple choice, find the wrong topic, question of these four questions, fills up the topic focuses on the user of cognition, the basic structure of reducer model essay question inspects the knowledge for the user to the reducer between various parts of the assembly position and role of understanding, true or false user's understanding of the relation of the part assembly, and examine the user's learning degree of the assembly drawing of the reducer by finding the wrong questions. As for the drawing method of part assembly drawing, in VR headset, due to the influence of the resolution of the headset equipment, the presentation of VR virtual visual effect is not as clear as the two-dimensional paper data in the real world, leading to a large difference in the score of error finding in assembly drawing between the two groups. As VR virtual environment presents diversified and multisensory information, the learning effect of users on the working principle of gearbox model is better than that of the real environment. Users can quickly understand and enhance the cognition of this knowledge point in the three-dimensional dynamic environment. Therefore, the average score of students in group 2 in the question part is higher than that of students in group 1.

4.3. User Subjective Satisfaction. After sorting out and analyzing the scoring data of the user subjective satisfaction scale of the two groups of experiments, the mean value of the score is shown in Figure 2. The independent sample t -test is conducted on the subjective satisfaction score data of users, and the specific data description is shown in Table 5.

It can be seen from Table 5 that there are significant differences between the two operating environments in the evaluation indicators of user satisfaction such as Q1, Q3, Q6, Q8, Q9, Q10, and Q12. Among them, the user satisfaction score of the VR virtual learning environment is significantly higher

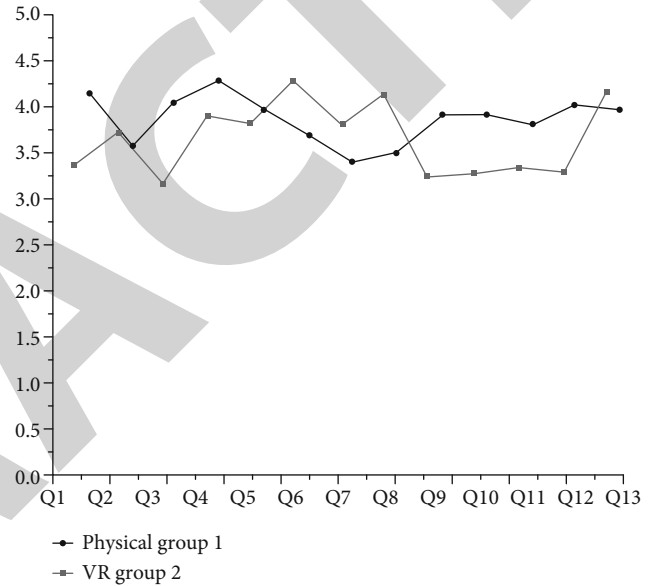


FIGURE 2: Average score graph. The scoring data of the user subjective satisfaction scale of the two groups of experimenters were sorted out and analyzed, and the mean map of the score was obtained.

than that of the real operating environment in Q1 immersion, Q3 fun, Q9 information guidance (reducing mistakes by providing feedback), Q10 help from visual feedback, and Q12 diversification of resource information presentation. In the two evaluations of Q6 realism and Q8 operating comfort, the user satisfaction of the VR virtual learning environment is significantly lower than that of the real operating environment.

Through interviews with experimental users, the specific reasons were obtained, which can be summarized as follows:

Q1 immersion: virtual environment can provide a closed learning environment for the operator to avoid external interference from other factors. The real environment is easily disturbed by other factors. Therefore, the immersive experience of the experimenters in the VR virtual learning environment is more obvious.

Q3 interesting: scenes in the virtual environment are of a relatively simple cartoon element style. Comfortable background music alleviates learning pressure. Interesting ways

TABLE 5: User satisfaction score in the VR environment.

Qid		Group 1	Group 2	Levene's test of equation variance		The <i>t</i> -test for the mean value equation	
		The average M1	The average M2	<i>F</i> value	Sig.	<i>t</i>	Sig. (double tail)
Q1	Immersive	3.700	4.500	0.336	0.569	-2.954	0.008
Q2	3D cognitive	4.000	3.900	2.903	0.106	0.361	0.722
Q3	Interesting	3.500	4.400	1.301	0.269	-3.250	0.004
Q4	Interactive	4.200	4.600	0.000	1.000	-1.549	0.139
Q5	Integrity	4.200	4.300	2.396	0.139	-2.777	0.785
Q6	Sense of reality	4.600	4.000	0.231	0.637	2.250	0.037
Q7	Ease of use	4.100	3.700	1.011	0.328	1.052	0.307
Q8	Comfort	4.400	3.800	0.000	1.000	2.324	0.032
Q9	Information to guide	3.500	4.200	5.063	0.037	-3.280	0.004
Q10	Visual feedback	3.500	4.200	0.590	0.452	-2.333	0.031
Q11	Auditory feedback	3.600	4.100	0.945	0.344	-1.301	0.210
Q12	Diversification of information	3.500	4.300	1.714	0.207	-3.539	0.002
Q13	Overall satisfaction	4.400	4.300	0.543	0.471	0.372	0.714

of interaction, especially gesture interaction, enhance learners' interest in learning and spirit of exploration. The real disassembly and assembly environment has a low evaluation of fun. Like the traditional learning method, there is not too much interactive operation, and the learners have no freshness.

Q6 sense of reality: users have a low score on the sense of reality of the VR virtual learning environment, in which there are only feedback and perception of visual and auditory channels. In the process of physical disassembly and assembly, there is not only the feedback of the two channels but also the multichannel information such as touch, which can truly grasp and move the model, which is very real.

Q8 operational comfort: user feedback that the VR environment is not suitable for long-term learning. Due to screen delay in HTC helmets, some users may experience discomfort such as visual motion sickness during learning, resulting in a low evaluation of the comfort level of the virtual learning system.

Q9 information guidance, by providing feedback to reduce mistakes: in the VR virtual environment, clear visual feedback is provided during the assembly process of the model, and the matching color of the parts becomes highlighted, effectively reducing mistakes.

Q10 visual feedback help: users believe that visual feedback information is more abundant in the virtual environment, which not only displays the structure of parts but also realizes the interaction that cannot be realized in the real environment, such as the prompts of virtual UI.

Q12 diversification of resource information presentation: the resource information in the virtual context is relatively rich, which can effectively help users to have a deeper understanding of the model structure. In addition to the physical model, the resource information of the real operating environment is mostly two-dimensional drawing data and video data. There is a lot of information, but the display way is single.

In addition, in terms of Q7 ease of use, although there was no significant difference in the score data between the

two groups, there was a significant difference in the mean value. The reason is that in the learning process of VR virtual situation, since users need to use gesture recognition devices for interactive operation, they need to learn the gestures and relevant operation instructions of the system in advance. In the physical disassembly environment, the user does not need additional operation training and can quickly grasp the basic operation methods of the operating environment. The definition of gesture in the VR environment needs to be familiar with in advance, and the experimenter who is familiar with gesture quickly has a higher evaluation on the usability of virtual environment.

Q2 3D cognition, Q4 interactivity, Q5 integrity, Q11 auditory feedback, and Q13 overall satisfaction: there is no significant difference between the two groups in these evaluations, indicating that the virtual learning environment can achieve the same learning effect as the real model learning under these several indicators. That is, under the virtual learning system, users can intuitively learn the three-dimensional structure of the body and observe the details of the model from multiple angles.

5. Conclusions

In general, the immersive learning system based on VR virtual detection technology can realize the cognition of the three-dimensional model structure and has a certain learning effect. Compared with traditional disassembly learning of physical model, VR disassembly learning is not as good as physical model learning in terms of realistic sense and assembly drawing learning, but VR virtual learning system has obvious advantages in terms of immersion, fun, and visual feedback, which can better stimulate learners' interest in learning. With the development of modern information technology, the display of large-scale data information has demand for virtual reality technology, and the development of virtual reality equipment provides a broad space and industrial background. The immersive learning system based

Retraction

Retracted: Research of Schema Evolution and Implementation Scheme Optimization in AI-Enabled Embedded Systems

Wireless Communications and Mobile Computing

Received 28 November 2023; Accepted 28 November 2023; Published 29 November 2023

Copyright © 2023 Wireless Communications and Mobile Computing. This is an open access article distributed under the Creative Commons Attribution License, which permits unrestricted use, distribution, and reproduction in any medium, provided the original work is properly cited.

This article has been retracted by Hindawi, as publisher, following an investigation undertaken by the publisher [1]. This investigation has uncovered evidence of systematic manipulation of the publication and peer-review process. We cannot, therefore, vouch for the reliability or integrity of this article.

Please note that this notice is intended solely to alert readers that the peer-review process of this article has been compromised.

Wiley and Hindawi regret that the usual quality checks did not identify these issues before publication and have since put additional measures in place to safeguard research integrity.

We wish to credit our Research Integrity and Research Publishing teams and anonymous and named external researchers and research integrity experts for contributing to this investigation.

The corresponding author, as the representative of all authors, has been given the opportunity to register their agreement or disagreement to this retraction. We have kept a record of any response received.

References

- [1] X. Zhang, Y. Zhang, F. Zhang, and X. Yang, "Research of Schema Evolution and Implementation Scheme Optimization in AI-Enabled Embedded Systems," *Wireless Communications and Mobile Computing*, vol. 2021, Article ID 3591427, 10 pages, 2021.

Research Article

Research of Schema Evolution and Implementation Scheme Optimization in AI-Enabled Embedded Systems

Xiaojuan Zhang ¹, Yongheng Zhang ¹, Feng Zhang ¹, and Xiuyun Yang ²

¹School of Information Engineering, Yulin University, Yulin 719000, China

²Business School of Xiamen Institute of Technology, Xiamen 361021, China

Correspondence should be addressed to Xiuyun Yang; yangxiuyun@xit.edu.cn

Received 11 May 2021; Revised 23 June 2021; Accepted 4 August 2021; Published 16 August 2021

Academic Editor: Balakrishnan Nagaraj

Copyright © 2021 Xiaojuan Zhang et al. This is an open access article distributed under the Creative Commons Attribution License, which permits unrestricted use, distribution, and reproduction in any medium, provided the original work is properly cited.

The demand of embedded artificial intelligence system for powerful computing power and diversified application scenarios will inevitably bring some new problems. This paper builds the system dynamics model of embedded system based on artificial intelligence (AI). By analyzing the causal relationship between the elements of the system dynamics model, the state equation is established, and the parameters are estimated and tested. At the same time, the influence of the model simulation experiment on the relevant factors is evaluated. The simulation results show that the proposed model is effective and efficient.

1. Introduction

With the rapid development of big data and deep neural network technology, artificial intelligence has made great breakthroughs in voice analysis, computer vision, and natural language processing and has been applied to smart city, smart home, and industrial manufacturing, which is gradually changing the operation mode of society and people's way of life. The demand of embedded artificial intelligence system for powerful computing power and diversified application scenarios will inevitably bring some new problems. From the perspective of the current urban development trend, urban development and expansion have sped up, and internal space resources have been maximized basically [1, 2]. Worse still, personalized transportation develops quickly, making the traffic conditions more and more complicated and traffic congestion more and more serious. In this context, the concept of intelligent transportation system (ITS) comes into being. In this age, artificial intelligence presents an application-driven trend of stepped-up breakthrough, and it is now deeply affecting the transportation management mode throughout the world [3]. As mainly reflected in its level of intelligence, the perception intelligence is becoming increasingly mature, and the cognitive intelligence continues to make breakthrough. The combination of big data and deep learning is the main-

stream intelligent computing paradigm, and it has played a big role in the field of transportation. As a whole, the development of urban traffic control has basically gone through timing control, inductive control, adaptive control, and intelligent control [4]. As detection technology, communication technology, automatic control technology, and AI-related technology develop rapidly, urban traffic signal control system is also becoming more and more intelligent. With the new techniques such as AI, big data, and cloud computing being promoted and applied, ITS will become an effective mean to relieve and even resolve traffic congestion [5]. ITS can also be considered applying advanced science and technology into traffic-related fields and strengthening the correlation among vehicles, roads, and users so as to constitute a comprehensive traffic management system. With the help of big data and AI, we can manage and control the existing transportation networks in an effective, intelligent, and coordinated manner, and by integrating advanced AI with practical issues in city traffic, we can better solve the control and optimization problems in city transport [6, 7].

The special contributions of this paper include the following:

- (i) This paper has introduced the principles and theories involved in ITS optimization scheme and made

in-depth analysis and research of the development of traffic governance model from every viewpoint

- (ii) This paper has summarized and concluded the generalized pattern of urban traffic governance and its evolution rule with a view to ITS and explored the congestion management mode and its evolution direction under ITS
- (iii) This paper has used system dynamics model and made analysis from such aspects as traffic supply, traffic demand, and information technology. Besides, it has also analyzed the user behaviors of traffic participants in the microlevel with big data, made in-depth analysis of travel intensity, trip purpose, spatial and temporal distribution of travel, trip distance, and evolution of traffic structure, and identified the key influence factors in traffic, laying a foundation for the concrete analysis of traffic governance pattern
- (iv) This paper has proposed an optimization scheme from planning and construction, innovation, and information technology. It has found the role AI technology plays in promoting the balance between traffic supply and traffic demand

The remainder of this paper is organized as follows. Section 2 discusses related works, and demand characteristics of ITS and its evolution are outlined in Section 3. ITS influence factors based on system dynamics model are presented in Section 4.1, Section 4.2 shows the experimental simulation results and analysis, and Section 5 concludes the paper with a summary and proposed directions for future research.

2. Related Work

Nowadays, urban modernization has encountered severe challenges from aggravated energy consumption, environmental pollution, traffic congestion, and public safety caused by continuously increased urban population, expandedly developed automobile industry, and unceasingly increased car ownership [8]. AI is to achieve in the computer such intelligent behaviors that surpass human perception, cognition, decision-making, and action; in short, AI means that a machine can do the things to be done by human intelligence. A smart city contains ITS, which is merely a part of smart city system, but ITS plays an indispensable part in the economic development of the city [9]. On the other hand, the construction level of the smart city which is closely related to the development level of ITS has in return boosted the development of ITS [10]. The rapid urbanization has been inevitably restricted by such problems as shortage of land and energy resources, and traffic problem is one of the most important problems which need to be solved by urban management. Urban traffic congestion has already become a major bottleneck that restricts the urban development and affects the quality of everyday life in today's society [11]. In the realistic plight that the number of automobiles has exceeded the carrying capacity of urban road networks, the common traffic jam generated in urbanization cannot be

eradicated; instead, to relieve or alleviate the current traffic congestion, importance can be attached to effectively handling the traffic jam caused by emergencies [12]. ITS is a hotspot of the cross-disciplinary research involving computer, automatic control, and traffic engineering, and it has effectively combined advanced AI technology, automatic control technology, computing technology, information and communication technology, and electronic sensor technology together and then applied it into the entire ground traffic management system so as to build a real-time, accurate, and highly efficient comprehensive transportation management system which can be brought into play in a large scope and in an all-round manner [13, 14].

In ITS, man-machine fusion has become an important direction, and AI is now developing towards more fusion and interaction with conventional transportation; as a result, a new form of ITS rises [15]. In the 1950s and 1960s, AI technology had made preliminary development. Its expert system, artificial neural network, fuzzy logic, genetic algorithm, and other advanced technology have been applied in traffic engineering successively, greatly promoting ITS development [16]. Ever since the 1980s, the road traffic control technology of every country was developing from conventional control to information and intelligent control with the great help of information technology [17]. Then, ITS emerged. In the 1990s, Europe and America had come up with the concept of ITS. US Department of Transportation and ITS America had put forward the "10-year Development Plan for Intelligent Transportation Systems in the United States," and in this Plan, it is pointed out that the ITS in the US shall be a system to be planned and constructed as a whole, not by every region independently [18]. At present, US ITS includes 6 modules: traffic management, e-payment operation, public transport management and operation, emergency treatment, vehicle control and management, and safety management system [19]. Early this century, Japan has set up many monitors and radars on roads so that it can monitor road conditions and collect information at any time; meanwhile, it has also actively promoted ETC (electronic toll collection) on highways, which improved the utilization of toll roads. By virtue of these techniques, the Japanese government wants to build a world-leading ITS [20]. Europe has studied ITS a long time ago, especially in vehicle safety and environmental protection. Germany mainly conducts intelligent management over its spacious road networks, strengthens the construction of traffic information collection and release facilities, and widely applies GPS (global position system) and intelligent transportation guidance technology [21]. Australia has studied and promoted the Sydney Coordinated Adaptive Traffic System (SCATS), in which plenty of sensors and video surveillance devices are put on highway pavement and traffic thoroughfares, with an aim to collect the traffic flow information and road operation status, use the data processing technology systematically, and get adapted to traffic changes [22]. With the popularization and application of big data, 5g communication technology, Internet of Things, cloud computing, artificial intelligence, and other new technologies in various countries, intelligent traffic management system will

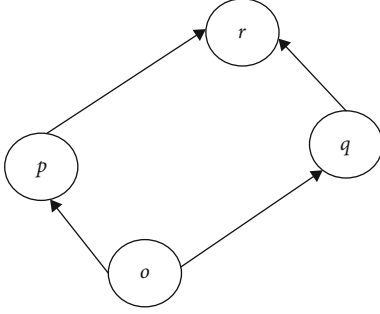


FIGURE 1: Four-section network.

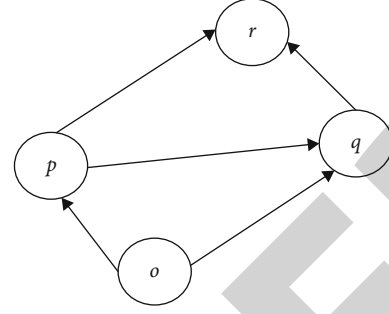


FIGURE 2: Five-section network.

become an effective mean to alleviate or even solve traffic congestion, which can be called “new fuel to promote urban mobility.”

3. Demand Characteristics of ITS and Its Evolution

3.1. Supply and Distribution of ITS. The core of urban road supply is to enhance the traffic capacity of traffic networks, which is usually done by expanding the existing roads or building new roads. Before taking this method, a thorough understanding of traffic demands within the city must be obtained in order to satisfy the travel demands of urban residents and maximize urban traffic networks. In the relationship between the density of urban road networks and the traffic flows, when the density exceeds the critical value, the steady state is the complete impedance of zero flow. Without a thorough grasp of traffic demands in advance, traffic congestion may aggravate only by expanding the existing roads or building new roads to strengthen the capacity of traffic networks [23].

In traffic network $G(N, L)$, it is defined that N is the set of network nodes, and L is the set of road sections. Assume that there are n_w elements in set W of O/D pairs. Mark the set of all paths connecting O/D as P and the set of paths connecting O/D to w as P_w . Define c_a as the travel time on section a , C_p as the travel time on path p , f_a as the traffic flow on section a , x_p as the traffic flow on path p , and d_w as the traffic demand from O/D to w .

Assume that the impedance of road section a is related not only to the flow of this section but also to that of other sections. To facilitate the calculation, other sections only include the sections that are adjacent to a and on the same path as a and they are marked as

$$c_a = c_a(f_a, f_1, f_2, \dots, f_\Lambda), \quad \forall a \in L, \quad (1)$$

where $\{1, 2, \dots, \Lambda\}$ is the set of sections which are adjacent to a and on the same path as a . The relationship between the path and the flow of the section is as follows:

$$f_a = \sum_{p \in P} x_p \delta_{ap}, \quad \forall a \in L. \quad (2)$$

If section a is on path p , $\delta_{ap} = 1$; if not, $\delta_{ap} = 0$. The path impedance calculated by Equation (1) and Equation (2) is as follows:

$$C_p = \sum_{a \in K} c_a(x_1, x_2, \dots, x_\Gamma) \delta_{ap}, \quad \forall p \in P. \quad (3)$$

Conservation of traffic flow:

$$d_w = \sum_{p \in P_w} x_p, \quad \forall w \in W. \quad (4)$$

Nonnegative constraints:

$$x_a \geq 0, \quad \forall a \in L. \quad (5)$$

Figure 1 is the four-section network. For a four-section network which includes one starting point o and one ending point r , Q is the constant of traffic demand.

The time of the section is related to the flows of all adjacent sections. At this point, the time of section can be presented as follows:

$$\begin{aligned} t_{op} &= \beta_1 (\gamma f_{op} + f_{pr}), \quad t_{qr} = \beta_1 (\gamma f_{qr} + f_{oq}), \\ t_{oq} &= \alpha_1 + \beta_2 (\gamma f_{oq} + f_{qr}), \quad t_{pr} = \alpha_1 + \beta_2 (\gamma f_{pr} + f_{op}), \end{aligned} \quad (6)$$

in which, t_{ij} represents the travel time between section ij , α is the time of free flow, β is the delay parameter, f is the traffic flow, and γ is the measurement factor to distinguish the impact of flows at different sections. So, the travel time of two paths from the starting point o to the ending point r can be shown as follows:

$$t_1 = t_{op} + t_{pr}, \quad t_2 = t_{oq} + t_{qr}. \quad (7)$$

The path flow meets:

$$\begin{aligned} f_{op} &= f_{pr} = f_1, \quad f_{oq} = f_{qr} = f_2, \\ Q &= f_1 + f_2. \end{aligned} \quad (8)$$

As the network has symmetry, the travel time t_1 of paths in the networks and the total impedance of T^4 the network under UE state are as follows:

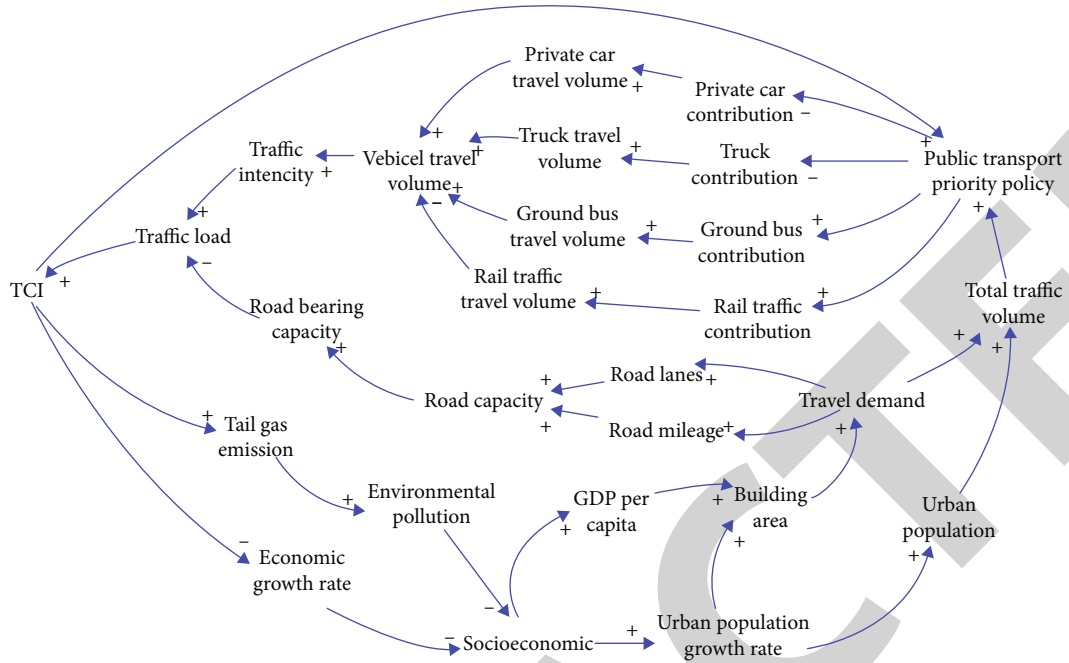


FIGURE 3: Cause-and-effect circuit diagram of megacity ITS.

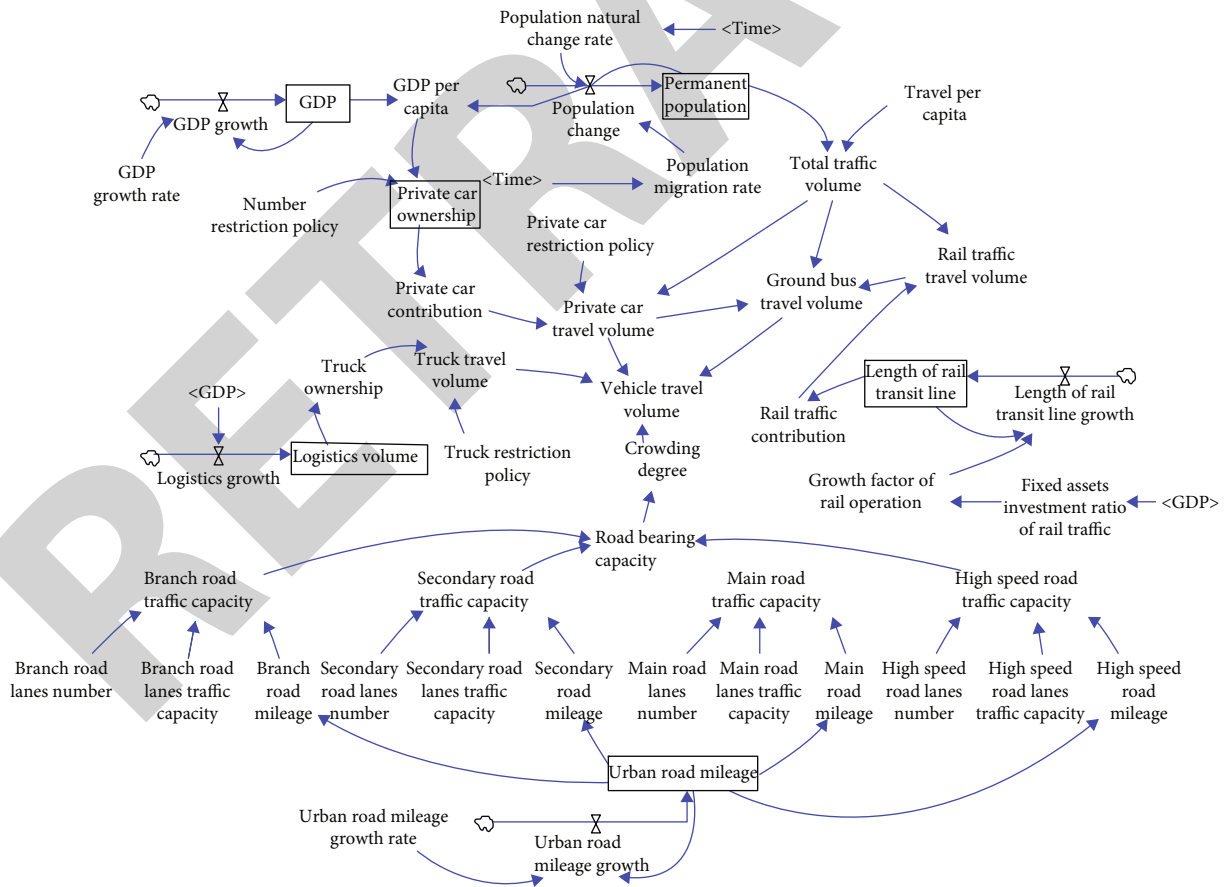


FIGURE 4: Stock flow chart.

TABLE 1: Description of model-related parameters.

Parameter or initial value	Value	Unit
Urban road mileage	5000.00	km
Urban road mileage growth rate	0.50	dmnl
High-speed road lanes traffic capacity	3000.00	Pcu/h
High-speed road lanes number	6.00	Lane(s)
Main road lanes traffic capacity	2800.00	Pcu/h
Main road lanes number	5.00	Lane(s)
Secondary road lanes traffic capacity	2600.00	Pcu/h
Secondary road lanes number	4.00	Lane(s)
Branch road lanes traffic capacity	2400.00	Pcu/h
Branch road lanes number	3.00	Lane(s)
Travel per capita	5.00	Times/day
Length of rail transit line	300.00	km
GDP growth rate	0.067	dmnl
Private car ownership	6210 thousand	Vehicle
Logistics volume	12,190 million	Ton

$$t_1 = t_2 = \frac{(\gamma + 1)(\beta_1 + \beta_2)Q}{2} + \alpha_1, \quad (9)$$

$$T^4 = \frac{(\gamma + 1)(\beta_1 + \beta_2)Q^2}{2} + \alpha_1 Q.$$

Figure 2 is the five-section network. When a four-section network becomes a five-section network, the function of section impedance has become

$$t_{op} = \beta_1 (\gamma f_{op} + f_{pr} + f_{pq}),$$

$$t_{qr} = \beta_1 (\gamma f_{qr} + f_{oq} + f_{pq}),$$

$$t_{oq} = \alpha_1 + \beta_2 (\gamma f_{oq} + f_{pr}),$$

$$t_1 = t_2 = t_3 = \frac{(\gamma(\gamma + 3)\beta_2^2 + 3\gamma(\gamma + 1)\beta_1\beta_2)Q + ((\gamma + 1)\beta_1 + (1 - \gamma)\beta_2)(\alpha_1 - \alpha_2)}{(\gamma + 1)\beta_1 + (3\gamma + 1)\beta_2} + \alpha_1. \quad (13)$$

When path 1 and path 2 have no traffic flow, $f_1 = f_2 = 0$, $f_3 = Q$ and $Q \leq ((\alpha_1 - \alpha_2)/((\gamma + 1)(\beta_1 + \beta_2)))$. When the third path also has no traffic flow, namely, $f_3 = 0$, $Q \geq ((2(\alpha_1 - \alpha_2))/((\gamma + 1)\beta_1 - (\gamma - 1)\beta_2))$, and both f_1 and f_2 are $Q/2$. So, in order to make these three paths have traffic flows, the traffic demand Q need to be within the scope of $((\alpha_1 - \alpha_2)/((\gamma + 1)(\beta_1 + \beta_2)))$, $((2(\alpha_1 - \alpha_2))/((\gamma + 1)\beta_1 - (\gamma - 1)\beta_2))$.

TABLE 2: Analysis results of stock flow chart.

Parameter	Simulation value	True value	Error
Permanent	2000.00	2153.60	0.0713
GDP	33577.05	35371.30	0.0507
Urban road mileage	7553.92	8000.00	0.0558
Logistics volume	4747.15	5000.00	0.0506

$$t_{pr} = \alpha_1 + \beta_2 (\gamma f_{pr} + f_{op}),$$

$$t_{pq} = \alpha_2 + \beta_2 (\gamma f_{pq} + f_{op} + f_{pr}). \quad (10)$$

The impedance of the new section and the relationship of the current traffic flows are as follows:

$$t_3 = t_{op} + t_{pq} + t_{qr},$$

$$f_{op} = f_1 + f_3, f_{pr} = f_1, f_{oq} = f_2,$$

$$f_{qr} = f_2 + f_3, f_{pq} = f_3, Q = f_1 + f_2 + f_3. \quad (11)$$

Make $t_1 = t_2 = t_3$ and show the flows of the paths in the five-section network under UE state:

$$f_1 = f_2 = \frac{(\gamma + 1)(\beta_1 + \beta_2)Q - (\alpha_1 - \alpha_2)}{(\gamma + 1)\beta_1 + (3\gamma + 1)\beta_2},$$

$$f_3 = Q - 2f_1 = \frac{(-(\gamma + 1)\beta_1 + (\gamma - 1)\beta_2)Q + (\alpha_1 - \alpha_2)}{(\gamma + 1)\beta_1 + (3\gamma + 1)\beta_2}. \quad (12)$$

The path time is represented as follows:

Represent the total impedance of the five-section network with T^5 and $T^5 = f_1 t_1 + f_2 t_2 + f_3 t_3$.

$$T^5 = (2\gamma\beta_1 + 2\beta_1 + 2\beta_2 + \gamma\beta_2)Q^2 + \alpha_2 Q,$$

$$\text{if } Q \leq \frac{\alpha_1 - \alpha_2}{(\gamma + 1)(\beta_1 + \beta_2)},$$

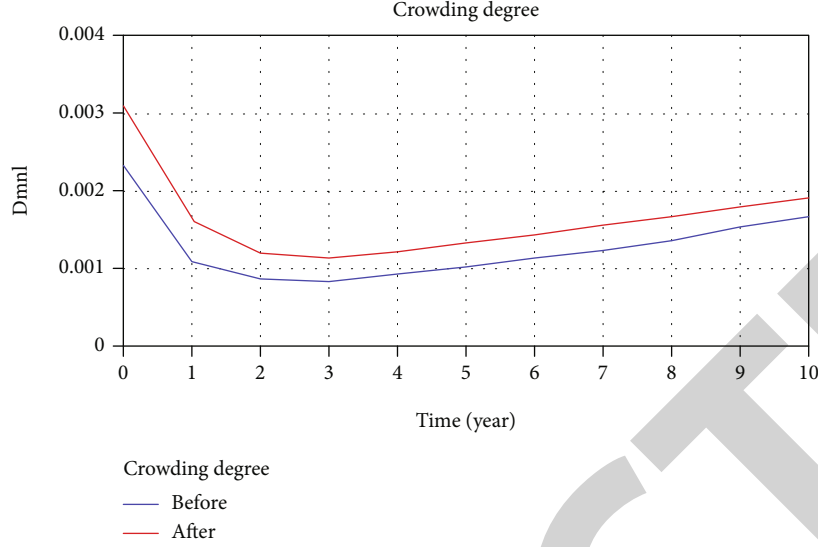


FIGURE 5: Crowding degree in different logistics volumes.

$$T^5 = Q \left[\frac{(\gamma(\gamma+3)\beta_2^2 + 3\gamma(\gamma+1)\beta_1\beta_2)Q + ((\gamma+1)\beta_1 + (1-\gamma)\beta_2)(\alpha_1 - \alpha_2)}{(\gamma+1)\beta_1 + (3\gamma+1)\beta_2} + \alpha_1 \right],$$

$$\text{if } \frac{\alpha_1 - \alpha_2}{(\gamma+1)(\beta_1 + \beta_2)} < Q < \frac{2(\alpha_1 - \alpha_2)}{(\gamma+1)\beta_1 - (\gamma-1)\beta_2},$$

$$T^5 = \frac{(\gamma+1)(\beta_1 + \beta_2)Q^2}{2} + \alpha_1 Q,$$

$$\text{if } Q \geq \frac{2(\alpha_1 - \alpha_2)}{(\gamma+1)\beta_1 - (\gamma-1)\beta_2}. \quad (14)$$

Make $T^5 > T^4$, and

$$Q \in \left(\frac{2(\alpha_1 - \alpha_2)}{3(\gamma+1)\beta_1 + (\gamma+3)\beta_2}, \frac{2(\alpha_1 - \alpha_2)}{(\gamma+1)\beta_1 - (\gamma-1)\beta_2} \right). \quad (15)$$

In other words, when the traffic demand Q is within the above range, to increase traffic supply will aggravate traffic jam [24, 25].

3.2. Evolution of Demand Characteristics. The supply of urban roads mentioned above belongs to government decision, and urban traffic demand is personal decision. Users play the role of pursuing the best personal interest in urban transportation (UE distribution). From a standpoint of game theory, many users will affect the capacity of traffic networks while pursuing the best personal interest, so the government needs to participate in the allocation of traffic resources and make decisions to optimize road resources in the macrolevel.

In UE distribution, the aim of every traveler is to minimize their travel time. $C_p(x^*)$ represents the path impedance under UE state, the minimum path impedance is λ_w , and x^* is the traffic flow of the path. Then,

$$\begin{aligned} C_p(x^*) &= \lambda_w, & \text{if } x_p^* > 0, \\ C_p(x^*) &= \lambda_w, & \text{if } x_p^* = 0. \end{aligned} \quad (16)$$

SO distribution is aimed at minimizing the total impedance of the system. $\widehat{C}_p(\cdot)$ is the path impedance under SO state; μ_w is the path impedance of the minimal border, and SO distribution can be shown as

$$\begin{aligned} \widehat{C}_p(x^*) &= \mu_w, & \text{if } x_p^* > 0, \\ \widehat{C}_p(x^*) &= \mu_w, & \text{if } x_p^* = 0. \end{aligned} \quad (17)$$

If traffic informationization is still in its infancy, traffic participants cannot share real-time information due to the fundamental attributes of transportation and neither can traffic users know about the travel demands of others; so, there exists a dynamic game of incomplete information between traffic actors, and they can only choose their travel modals and paths based on experience [26]. With the construction of smart city, ITS has developed unceasingly: traffic users can know the relevant travel information before they travel, and the dynamic game of incomplete information has been converted into the dynamic game of complete information, which will greatly reduce the travel cost and improve the traffic efficiency. Under this circumstance, the governance of traffic congestion has been developed from Traffic Demand Modal (TDM) to ITS.

4. Key Influence Factors of ITS and Analysis of Simulation Experiment

4.1. ITS Influence Factors Based on System Dynamics Model. Given the complexity and nonlinearity of urban transportation, this paper has studied the urban traffic congestion and its influence factors with system dynamics and with three parts: internal traffic factors, external traffic factors, and factors of traffic subject taking into consideration; it has built the system dynamic model for ITS. In this study, it will integrate many important elements including urban development, economic development, urban road supply, urban road

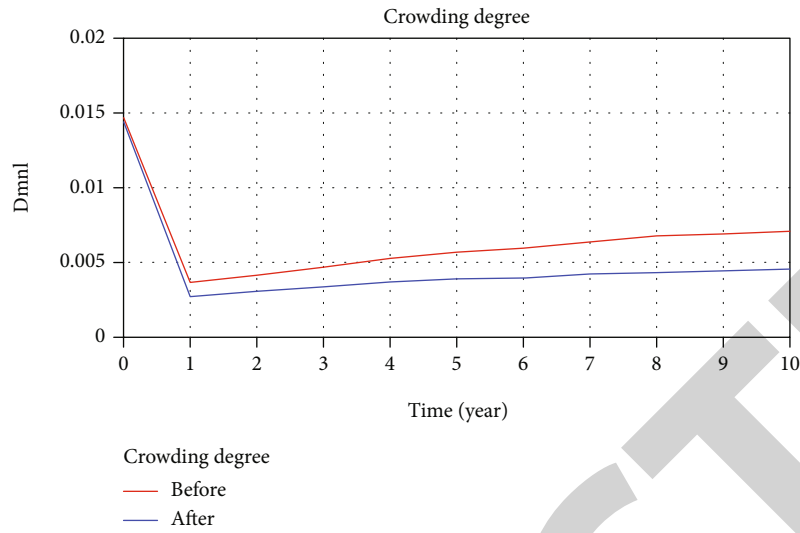


FIGURE 6: Crowding degree in different restriction policy.

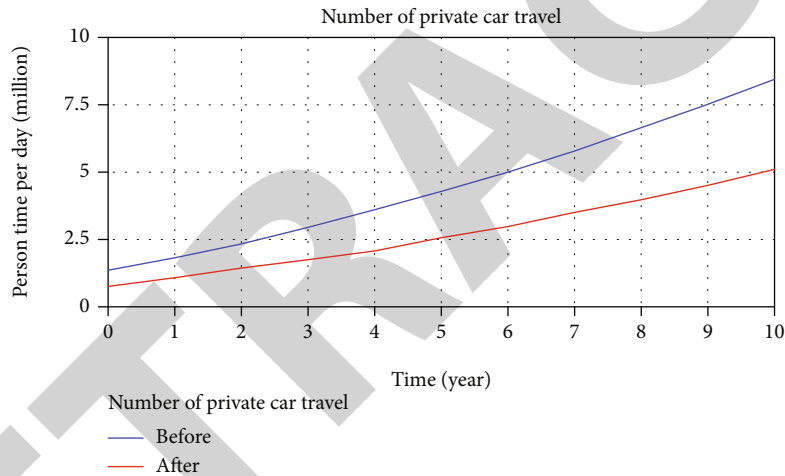


FIGURE 7: Private car trips under different traffic restriction policies.

demand, urban traffic operation elements, and environment elements; analyze the relationship between these elements; and study the impact different elements play on the whole system and the mutual impact between the elements by constructing the state equation and variable equation among different elements. Figure 3 is the cause-and-effect circuit diagram of megacity ITS. In Figure 3, the plus means the positive causal link, and the minus means the negative causal link. Figure 4 is the stock flow chart. Table 1 is the description of model-related parameters. Table 2 shows the analysis results of stock flow chart.

4.2. *Simulation Experimental Results and Analysis.* Integrating materials and data, the model in this paper has determined the relevant factors that affect urban traffic capacity. The first is the urban traffic state, including ground travel volume, transit travel volume, truck travel volume, and private car travel volume, and such factors as number restriction policy, traffic restriction policy, road bearing capacity, and

scale will have certain impact on traffic intensity. Next is traffic demand, including the traffic mode split rate of ground bus, private car, and rail traffic. These factors will directly affect the vehicle travel volume. Traffic supply, including the bearing capacity and traffic capacity of different types of roads, directly affects the maximum bearing capacity of different levels of roads and plays an important role on urban traffic capacity. Figure 5 shows the crowding degree in different logistics volumes.

As shown in Figure 5, with the rapid development of life and the continuous living needs of people, trunk travel volume has taken up a bigger and bigger ratio among the urban traffic participants. Through model simulation, it can be seen that as the total cargo volume increases continuously, the urban crowding degree will also increase; so, to carry out the corresponding truck restriction measures will effectively improve urban traffic conditions.

In order to reduce the increasing number of private cars and buses, the number of vehicles will be reduced in

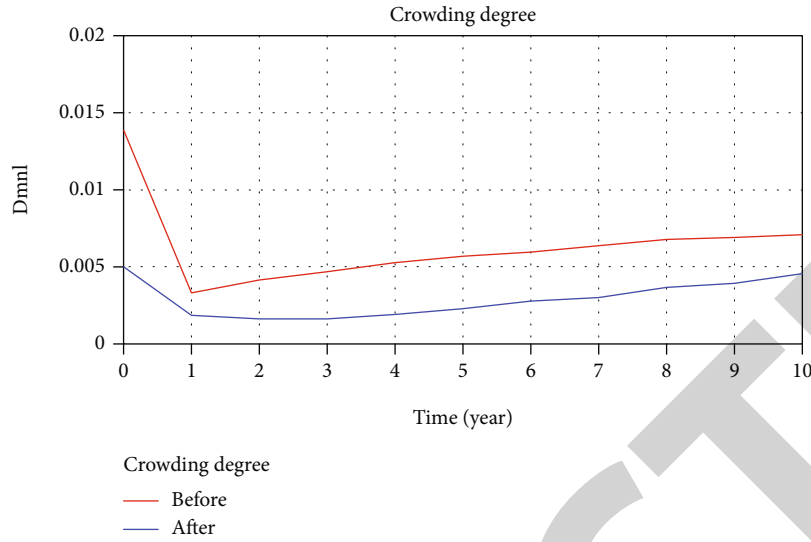


FIGURE 8: Congestion degree of rail transit lines with different lengths.

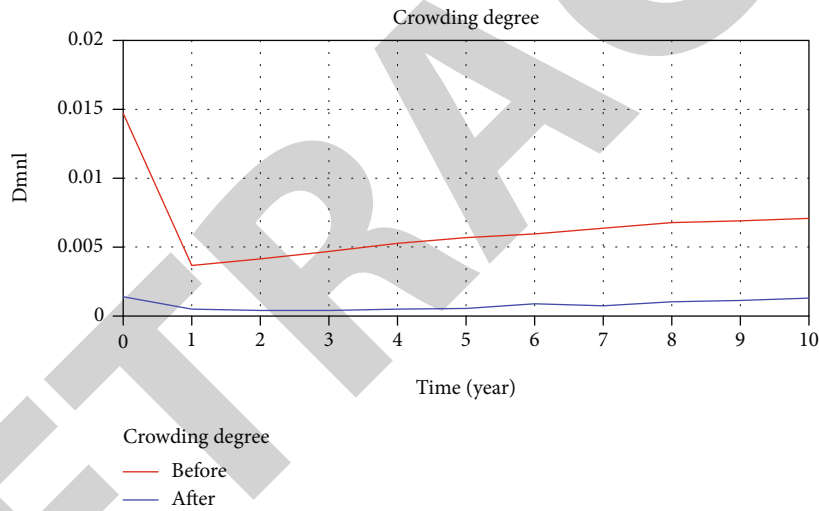


FIGURE 9: Congestion degree under different road capacities.

proportion after the implementation of the traffic restriction policy, so as to alleviate the total amount of urban traffic and reduce the degree of urban traffic congestion to a certain extent. It is clearly evident from Figure 6 that the proposed model simulation in the short term after the vehicle restriction policy is carried out, the number of vehicles decreases slightly, and in the long term, the vehicle volume increases compared with the decrease degree before restriction, and the crowding degree will gradually decrease over the increase of time. Therefore, the implementation of the number limit policy can significantly alleviate the urban traffic situation, and the effect will improve with the passage of time. Figure 7 shows the private car trips under different traffic restriction policies.

As shown in Figure 7, with regard to the traffic congestion caused by private car travel which takes up the largest part in urban traffic, the impact of restriction policy on pri-

mate car travel can be seen with the model. Through model simulation, it is obvious that after the restriction measures are taken, the private car travel drops greatly and the fall gradually increases over the time when the policy is implemented. Figure 8 shows the congestion degree of rail transit lines with different lengths.

As shown in Figure 8, the development of urban mass transit can effectively improve urban traffic capacity. From the model simulation, it can be seen that rail transit in Wulan city plays an important role in easing traffic congestion. With the increase of rail transit mileage, the traffic structure changes greatly. The sharing rate is improved, and the coverage is expanded. More passengers choose rail transit, which significantly improves the congestion. Figure 9 shows the congestion degree under different road capacities.

The road volume, mileage, and traffic capacity will directly affect the road traffic capacity. The simulation results

show that with the improvement of road carrying capacity, traffic congestion can be alleviated quickly in a short time and maintain this degree in a long time. Therefore, improving road capacity is the most fundamental and important way to improve urban traffic.

Through the above experimental results, it can be observed that the blind increase of traffic supply cannot solve traffic congestion fundamentally. In ITS construction, informationization technology can be utilized to collect real-time road traffic volume, road traffic load, travel demand generators, and other traffic data, to forecast the potential congestion points and guide the vehicle flow and give alarm, to achieve the traffic congestion governance pattern of emergency response, and to help the government to implement more rational and effective traffic control policies. The government needs to optimize public transport services. As the speed of urban expansion is far faster than the development of urban public transport, the development of public transport is mostly focused on the development of rail transit [27]. Rail transit construction takes a long time, and the line is fixed, which cannot meet the diversified travel needs of urban residents in the context of multicenter. Besides, conventional buses are not very appealing to residents due to the many stops, high crowding degree, and fixed lines. Therefore, to promote the development of public transportation shall be based on smart city.

With urban development, many new roads are built, and many traffic forks are set which is one of the biggest traffic congestion generators. To solve this problem, real-time traffic conditions of several adjacent forks shall be shown in each fork under the construction of smart cities so as to guide residents to avoid the roads with high traffic load, alleviate congestion pressure, and improve the utilization of other roads. On the other hand, adaptive control traffic light can be used to control the traffic flow in the fork. The relevant research of the impact of the traffic light played on road flow is very mature, and automatic control system can monitor road flows, calculate various vehicle-related data, and give autoalarm.

5. Conclusion

As science and technology develop consistently, such information technology as mobile Internet, the Internet of Things, big data analysis, and cloud computing are also becoming increasingly mature, and the information management solution which is applied in human society and life is improving constantly. In the future, these high-tech information technologies will be used to solve road traffic problems, which is also the future direction of smart city and its development. ITS has inherited the strengths of green and sustainable transport, and it has also made some innovations. Comparatively speaking, to greatly develop ITS can rapidly and effectively alleviate urban transportation problems with the minimum economic input. This paper, through the study of the internal and external factors of urban traffic, has summarized the key influence factors, made study from the urban development, urban economic level, external and internal urban resources, and traffic supply-and-demand level, constructed the model with system dynamics, and analyzed the

relationship between urban traffic factors, so as to provide the theoretical bases and implementation path to ITS development and provide a relatively complete ITS implementation and optimization scheme.

Data Availability

The raw/processed data required to reproduce these findings cannot be shared at this time as the data also form part of an ongoing study.

Conflicts of Interest

The authors declare that there are no conflicts of interest regarding the publication of this paper.

Acknowledgments

This work was supported by the National Science Foundation of China (Grant no. 72061030), Natural Science and Technology Project Plan in Yulin of China (Grant nos. 2019-78-3, CXY-2020-10, 2019-78-2, 2019-78-1, 2019-76-2, and 2019-106-6), Shaanxi Higher Education Teaching Reform Research Project (19ZY016 and 19BY111), and Shaanxi Education Scientific Planning Project in 2017 (SGH17H282).

References

- [1] X. Cai, K. Shi, S. Zhong, and X. Pang, "Dissipative sampled-data control for high-speed train systems with quantized measurements," *IEEE Transactions on Intelligent Transportation Systems*, vol. 22, pp. 1–12, 2021.
- [2] X. Cai, J. Wang, S. Zhong, K. Shi, and Y. Tang, "Fuzzy quantized sampled-data control for extended dissipative analysis of T-S fuzzy system and its application to WPGs," *Journal of the Franklin Institute*, vol. 358, no. 2, pp. 1350–1375, 2021.
- [3] Y. Yang, C. Hou, Y. Lang, T. Sakamoto, Y. He, and W. Xiang, "Omnidirectional motion classification with monostatic radar system using micro-doppler signatures," *IEEE Transactions on Geoscience and Remote Sensing*, vol. 58, no. 5, pp. 3574–3587, 2020.
- [4] H. Askari, A. Khajepour, M. B. Khamesee, and Z. Wang, "Embedded self-powered sensing systems for smart vehicles and intelligent transportation," *Nano Energy*, vol. 66, no. 12, article 104103, 2019.
- [5] D. Sirohi, N. Kumar, and P. S. Rana, "Convolutional neural networks for 5G-enabled intelligent transportation system: a systematic review," *Computer Communications*, vol. 153, no. 31, pp. 459–498, 2020.
- [6] L. Hua, H. Zhu, K. Shi, S. Zhong, Y. Tang, and Y. Liu, "Novel finite-time reliable control design for memristor-based inertial neural networks with mixed time-varying delays," *IEEE Transactions on Circuits and Systems I: Regular Papers*, vol. 68, no. 4, pp. 1599–1609, 2021.
- [7] F. Yin, X. Xue, C. Zhang et al., "Multifidelity genetic transfer: an efficient framework for production optimization," *SPE Journal*, vol. 26, pp. 1–22, 2021.
- [8] M. H. Hassan, A. Tizghadam, and A. Leon-Garcia, "Spatio-temporal anomaly detection in intelligent transportation systems," *Procedia Computer Science*, vol. 151, pp. 852–857, 2019.

Retraction

Retracted: Applications of Wireless Communication in a New Dual Branch CTS Charge Pump Based on Employing Clock Matched Technology

Wireless Communications and Mobile Computing

Received 28 November 2023; Accepted 28 November 2023; Published 29 November 2023

Copyright © 2023 Wireless Communications and Mobile Computing. This is an open access article distributed under the Creative Commons Attribution License, which permits unrestricted use, distribution, and reproduction in any medium, provided the original work is properly cited.

This article has been retracted by Hindawi, as publisher, following an investigation undertaken by the publisher [1]. This investigation has uncovered evidence of systematic manipulation of the publication and peer-review process. We cannot, therefore, vouch for the reliability or integrity of this article.

Please note that this notice is intended solely to alert readers that the peer-review process of this article has been compromised.

Wiley and Hindawi regret that the usual quality checks did not identify these issues before publication and have since put additional measures in place to safeguard research integrity.

We wish to credit our Research Integrity and Research Publishing teams and anonymous and named external researchers and research integrity experts for contributing to this investigation.

The corresponding author, as the representative of all authors, has been given the opportunity to register their agreement or disagreement to this retraction. We have kept a record of any response received.

References

- [1] J. Li, "Applications of Wireless Communication in a New Dual Branch CTS Charge Pump Based on Employing Clock Matched Technology," *Wireless Communications and Mobile Computing*, vol. 2021, Article ID 4014795, 9 pages, 2021.

Research Article

Applications of Wireless Communication in a New Dual Branch CTS Charge Pump Based on Employing Clock Matched Technology

Jiayang Li 

Nexperia (China) Ltd, China Design Center, Analog and Logic Business Group, Shanghai 200000, China

Correspondence should be addressed to Jiayang Li; dr.shenl@qq.com

Received 9 July 2021; Revised 22 July 2021; Accepted 30 July 2021; Published 16 August 2021

Academic Editor: Balakrishnan Nagaraj

Copyright © 2021 Jiayang Li. This is an open access article distributed under the Creative Commons Attribution License, which permits unrestricted use, distribution, and reproduction in any medium, provided the original work is properly cited.

With the increase in communication requirements, new communication technologies and implementation methods have developed rapidly. The rise of emerging markets such as the Internet of Things, smart homes, smart cities, and wearables has promoted the development of wireless communication integrated circuits in the direction of monolithic, low energy consumption, and high energy efficiency. This paper proposes a new dual branch charge pump based on CTS charge pump with enhanced current drive capability and undesired charge transfer completely eliminated. Clock matched technology is proposed to completely eliminate undesired charge transfer caused by delay turn on and off of the auxiliary transistors in the traditional CTS charge pump. The current drive capability is enhanced by employing NMOS transistors with $2V_{dd}$ gate drive voltage, while traditional dual branch CTS charge pumps are based on PMOS with $1V_{dd}$ gate drive voltage. The output voltage ripple is also reduced resulting from a dual branch structure. Simulation results of output voltage gain and power efficiency for the proposed charge pump and other traditional charge pumps are provided. Comparisons are made to show the improvement of the proposed charge pump compared with other traditional charge pumps.

1. Introduction

With Soc (system on chip) having been widely employed in electronic equipment in the recent decade, the blocks built in Soc are also significantly increased contributing to various power supply demands. A charge pump, a circuit consisting of switches and capacitors, becomes a preference in the application of nonvolatile memory [1], defect monitoring [2], energy harvesting [3], and so on resulting from its relatively high efficiency and integration simplicity compared with other step-up power converters such as the boost converter.

The most basic charge pump circuit was proposed by Dickson [4]. However, the traditional Dickson charge pump suffers from severe voltage drop caused by diode-connected transistors in each stage. The voltage drop caused by diode-connected transistors can be significantly reduced by employing a charge transfer switch [5]. The first charge pump without voltage drop loss was proposed in [6] based on [5]. However, undesired charge transfer occurs in [5, 6]

caused by the delay turn on and turn off of the auxiliary transistor with a nonideal clock signal, which reduces the power efficiency and output voltage gain. Some researchers designed dual branch charge pumps [7] based on [6] to reduce undesired charge transfer in traditional charge transfer switch charge pumps. However, undesired charge transfer still exists in [7], and conduction loss in [7] is increased caused by lower gate drive voltage contributing to lower power efficiency and output voltage gain.

This paper proposes a new dual branch charge pump based on [5, 7] with no undesired charge transfer and increased gate drive voltage, contributing to higher power efficiency and voltage gain. The conduction loss is significantly decreased by employing NMOS with $2V_{dd}$ gate drive voltage compared with PMOS and $1V_{dd}$ gate drive voltage in [7]. Undesired charge transfer is eliminated by employing a nonoverlapping clock [8] and accurate time delay circuit [9]. Section 2 discusses the undesired charge transfer in traditional charge pumps including [6, 7]. Section 3 introduces the

proposed charge pump. An optimized gate drive strategy for auxiliary transistors to completely eliminate undesired charge transfer is proposed in Section 4. The simulation result of the performance for the above charge pumps based on 0.18 μm technology is listed in Section 5. Section 6 is the conclusion of this paper.

2. Conventional Charge Pumps and Drawbacks

The Dickson charge pump proposed in [4] consists of diode-connected transistors and flying capacitors driving by clock signals. Figure 1(a) shows the schematic of N stage Dickson charge, while Figure 1(b) shows the clock signal for this N stage Dickson charge pump. The voltage drop loss in each stage approximately equals to the threshold voltage of the diode-connected transistor. The clock signal pumps the bottom plane of the flying capacitor and helps increase the voltage of the top plane to charge the next stage. The output voltage expression is given in [10]:

$$V_{\text{out}} = (N + 1)(V_{\text{DD}} - V_T) - \frac{NI_L}{C \cdot f}, \quad (1)$$

where V_{out} is the output voltage, N is the number of pumping stages, V_T is the threshold voltage of the diode connect transistor, f is the clock frequency, C is the capacitor, and I_L is the output current. According to the expression, there is a voltage drop in each pumping stage which significantly reduces the output voltage gain.

The schematic of the PMOS CTS charge pump proposed in [6] is shown in Figure 2(a). With the help of auxiliary of PN pair, there is no voltage drop in each pumping stage. However, charge transfer from high voltage node to low voltage node reduces the voltage gain and power efficiency. The following is the analysis of how undesired charge transfer occurs in the CTS charge pump. Let us take stage three as an example. Assume ϕ_1 is low and ϕ_2 is high, the voltage of node 1 is 1Vdd, and the voltage of node 2 and node 3 is 3Vdd. By this way, MN3 is on and MP3 is off, and M3 is on. Charge transfers from node 2 to node 3 occur in this period of time. When ϕ_2 transfer from 1Vdd to zero, the voltage of node 2 transfers from 3Vdd to 2Vdd. MP3 will turn on since the voltage of node 2 reaches $3V_{\text{dd}} - V_{\text{thp}}$ while MN3 will not turn off until the voltage of node 1 reached $2V_{\text{dd}} - V_{\text{thn}}$. Undesired charge transfer from node 3 to node 1 occurs in this period of time. Meanwhile, if ϕ_2 is low and ϕ_1 is high, when ϕ_1 transfer from 1Vdd to zero, MN3 starts to turn on since voltage of node 1 reached $2V_{\text{dd}} - V_{\text{thn}}$. This also contributes to undesired charge transfer from node 3 to node 1. What is more, the simultaneous turn on of MP3 and MN3 also causes M3 turning on, resulting in reverse current from node 3 to node 2.

The charge pump proposed in [7] is aimed at reducing the undesired charge transfer. Figure 3(a) shows the CP2 charge pump proposed in [7]. We use stage 3 to analyze the charge transfer again. When ϕ_2 is high and ϕ_1 is low, the voltage of node B4 and node B3 is about 4Vdd; then, MPA3 turns off. The voltage of node A2 is 3Vdd while the

node of B2 is 2Vdd; then, MNA3 turns on. In the clock transfer period, MPA3 turns on since $V_{B4} - V_{B3} > |V_{\text{thp}}|$, while MNA3 will not turn off until $V_{A2} - V_{B2} < |V_{\text{thn}}|$. The only condition that CP2 charge pump eliminates undesired charge transfer is that $V_{\text{thn}} + V_{\text{thp}} = V_{\text{dd}}$. Otherwise, undesired charge transfer happens in both node A3 to node A2 and node B4 to node B2. Another problem of the CP2 charge pump is that when MA3 turns on, the gate voltage is provided by node B2. By this way, the gate drive voltage is only 1Vdd, resulting in higher conduction loss and reducing voltage gain and current drive capability.

3. Proposed Charge Pump Circuit

The following dual branch charge pump is proposed based on traditional CTS charge pump [5] and CP2 charge pump [7]. The charge pump is composed of two branches with a complementary clock signal. The work principle is as follows.

3.1. First Stage. The first stage is the same as the CP2 charge pump proposed in [7], which is composed of a single NMOS transistor for each branch. When ϕ_1 is high and ϕ_2 is low, the voltage of node A1 is 1Vdd and the voltage of node B is zero. By this way, MA1 turns off and MB1 turns on, charging node B1 to 1Vdd. When the clock flips, the voltage of node B1 pumps to 2Vdd and MA1 turns on charging node A1 to 1Vdd. By this way, MA1 and MB1 can turn on and off effectively by the voltage from the complementary branch and do not need start up transistor.

3.2. Middle Stage. Since the work principle is the same for middle stages, we choose stage three to explain the mechanism. The clock signal of auxiliary NMOS transistor ϕ_1' is considered to be the same as ϕ_1 in this section. The NMOS transistor Ak3 is used to start up the circuit. When ϕ_2 is high and ϕ_1 is low, the voltage of node A4 is 5Vdd and node B4 is 4Vdd. MAP3 turns on, MAN3 turns off, and MA3 turns on. When the clock flips, the voltage of node A4 is 4Vdd and the voltage of node B4 is 5Vdd. By this way, MAP3 turns off and MAN3 turns on, resulting in the turning off of MA3. When MA3 turns on, the gate drive voltage is 2Vdd, which is much larger than that in the CP2 charge pump in [7], contributing to much smaller conduction loss.

3.3. Output Stage. The output stage for each branch is composed of a diode-connected NMOS and a PMOS. The diode-connected NMOS is aimed at providing a control signal to the previous stage, while the PMOS controlled by the complementary branch is aimed at controlling the output branch. It is shown in Figure 4.

When the voltage of Bn is low and the voltage of An is high, MAout turns on and the output voltage is provided by branch A. When the clock flips, MBout turns on and the output voltage is provided by branch B. This mechanism eliminates the voltage drop in [5] and reduces the output voltage ripple effective. This mechanism also provides better current drive capability.

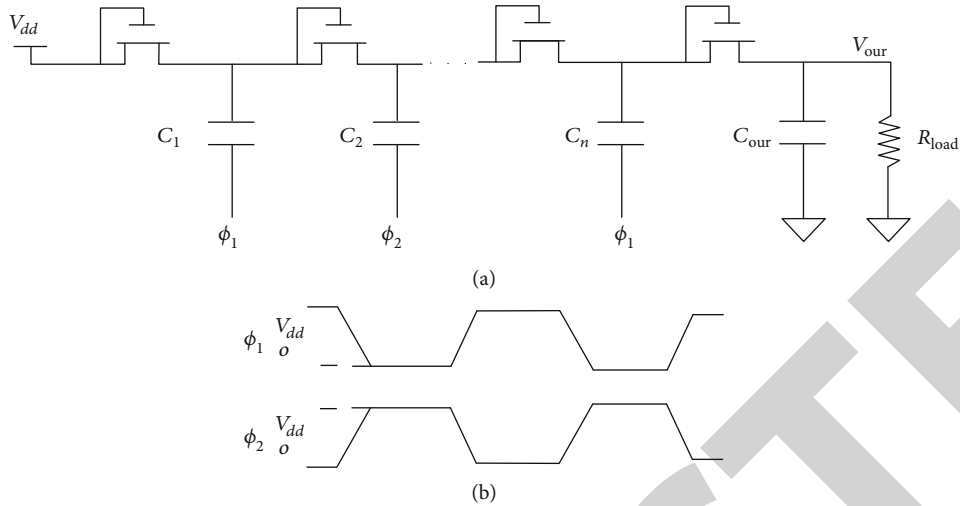


FIGURE 1: (a) N stage Dickson charge pump; (b) clock signal for Dickson charge pump.

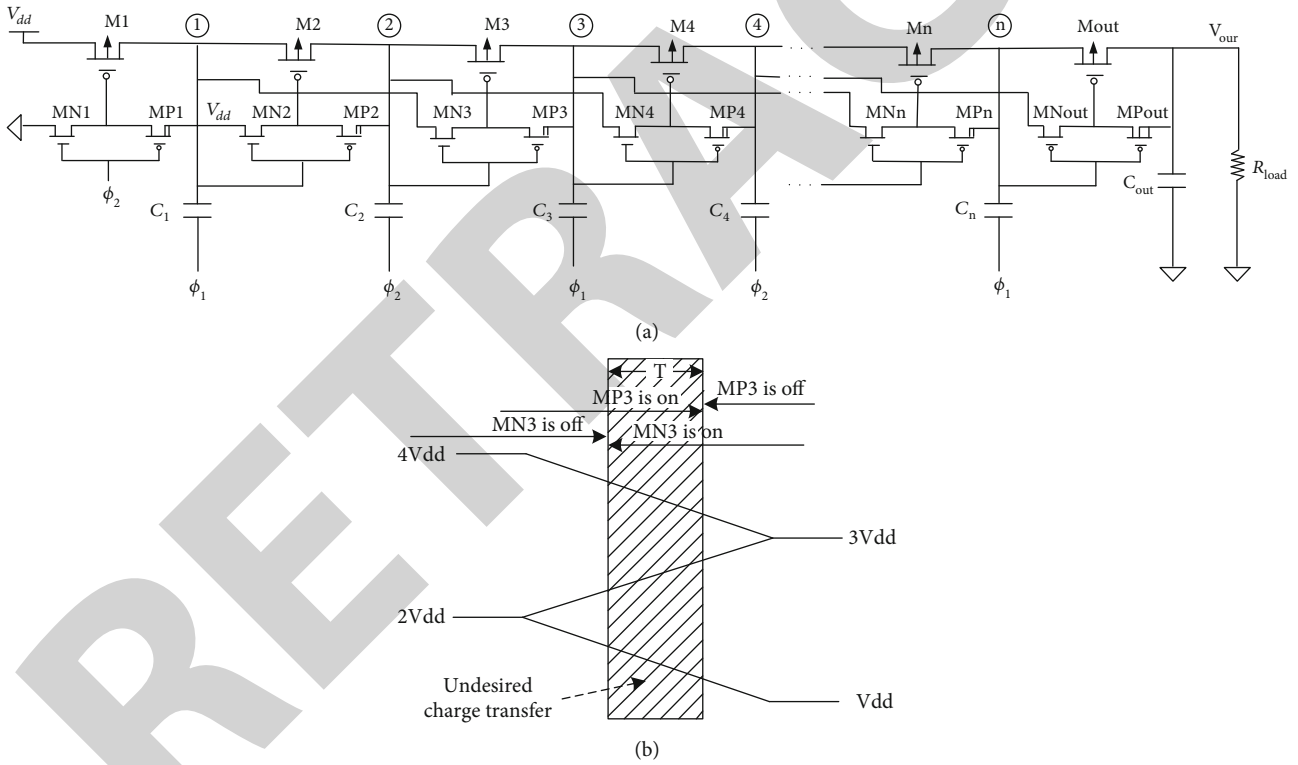


FIGURE 2: (a) Schematic of traditional CTS charge pump; (b) undesired charge transfer in traditional CTS charge pump.

4. Undesired Charge Transfer Eliminating Method

Before proposing the method of eliminating undesired charge transfer, we should first analyze the mechanism of undesired charge transfer in the proposed charge pump. Since the work principles are the same in the middle stage, stage 3 is used to explain. Firstly, we analyze the condition

that ϕ_1' equals to ϕ_1 . Assume at the beginning, ϕ_2 is high and ϕ_1 is low. The voltage of node A4 is $5V_{dd}$ and node B4 is $4V_{dd}$. $MAP3$ turns on, $MAN3$ turns off, and $MA3$ turns on. When ϕ_2 transfer to low and ϕ_1 transfer to high, $MN2$ will not turn on until ϕ_1 reaches V_{thn} , while $MP2$ will turn off since $V_{A4} - V_{B4} < V_{thp}$. If we use the original clock ϕ_1 and ϕ_2 to control the auxiliary NMOS in the PN switch pair, undesired charge transfer will happen as shown in

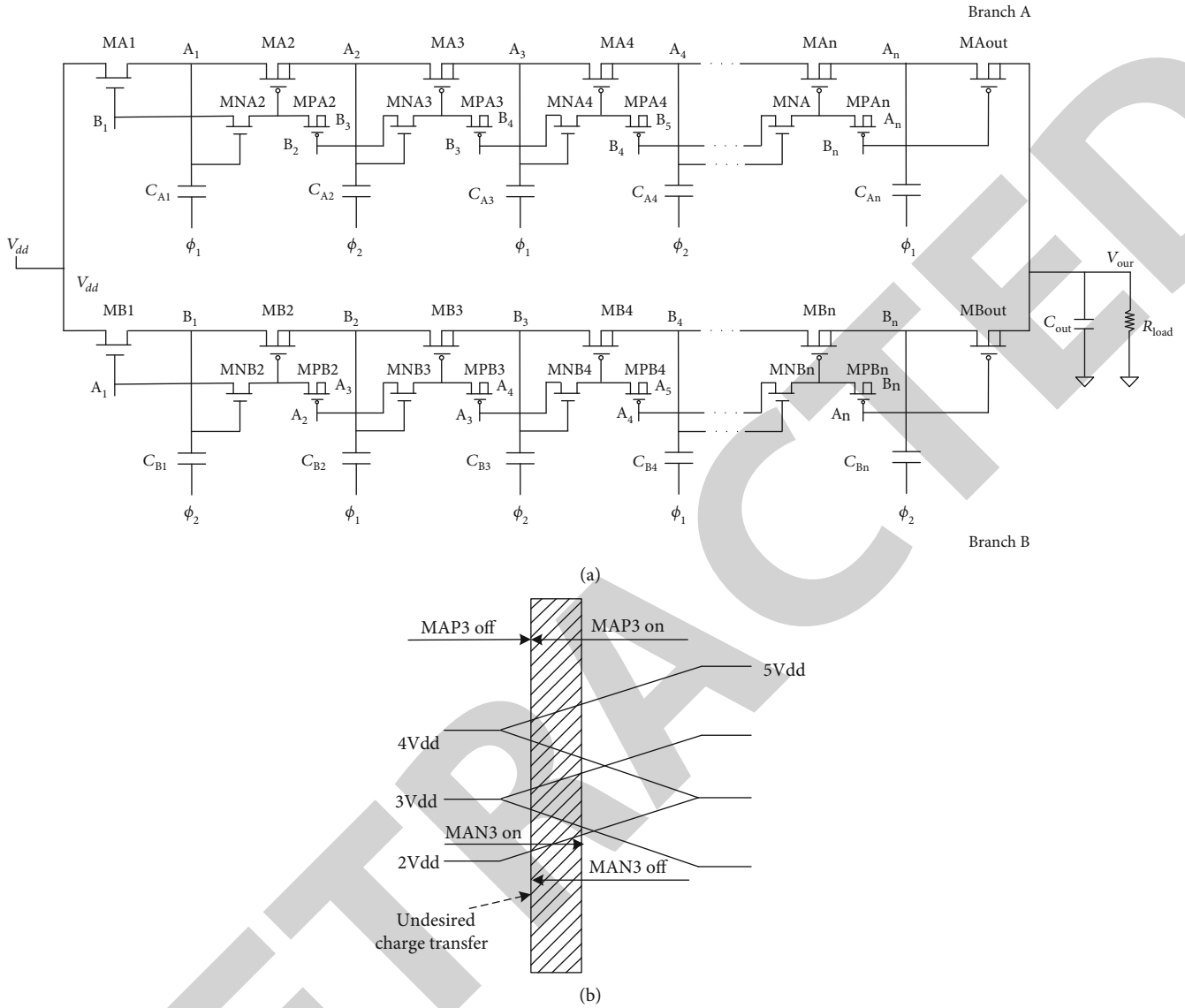


FIGURE 3: (a) Schematic of CP2 proposed in [7]; (b) undesired charge transfer in CP2 charge pump proposed in [7].

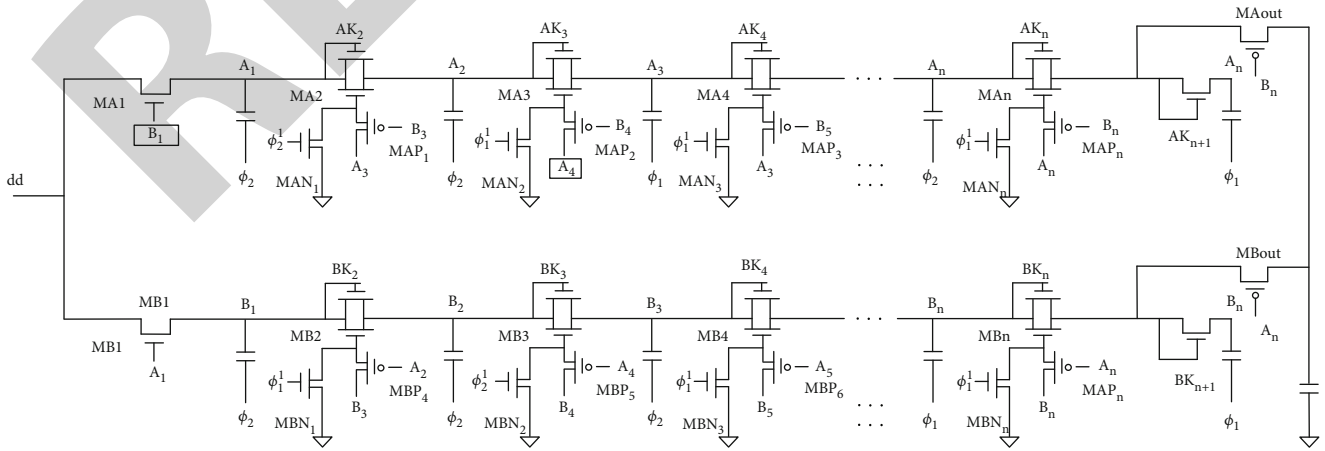


FIGURE 4: Schematic of proposed charge pump.

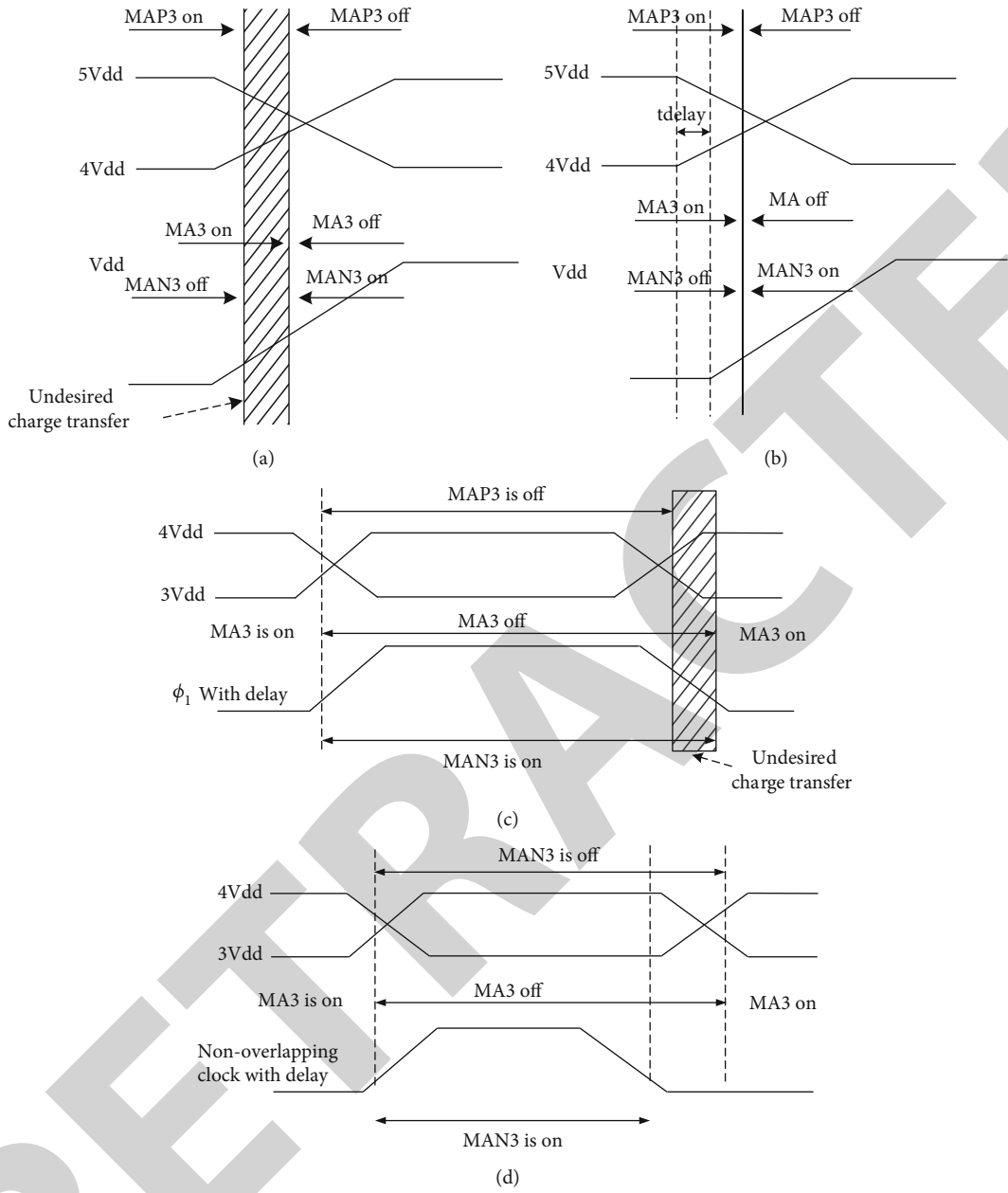


FIGURE 5: (a) Undesired charge transfer in original clock; (b) eliminating undesired charge transfer using delay block; (c) more severe undesired charge transfer in original clock with delay; (d) completely eliminating undesired charge transfer by using delay element and nonoverlapping clock.

Figure 5(a) unless $V_{thn} + 1/2V_{thp} = 1/2V_{dd}$. But the undesired charge transfer is significantly reduced compared with charge pumps proposed in [5, 6]. However, if we give a delay to the clock signal of the auxiliary NMOS transistor MAN3 to match the turn on and turn off time of MAN3 and MPN3, undesired charge transfer can be eliminated in this clock transfer period. The time delay element proposed in [9] can provide a time delay of 0.82 ps per resolution with very low power consumption. Figure 5(b) shows the elimination of undesired charge transfer by giving a delay to clock ϕ_1 . However, another problem occurs if we simply give a delay to ϕ_1 to elimi-

nate the undesired charge transfer in this clock transfer period; undesired charge transfer will become more severe in the complementary clock phase shown in Figure 5(c). The method to figure out this problem is to use nonoverlapping clock [8] shown in Figure 5(d). By employing a nonoverlapping clock and delay block, MAP3 will turn off simultaneously when MAN3 turns on. In the complementary clock transfer period, MAN3 will turn off before MAP3 turns on. A new clock signal ϕ'_1 is formed by this way. Undesired charge transfer is completely eliminated by employing the new clock signal ϕ'_1 , and we call it clock matched technology.

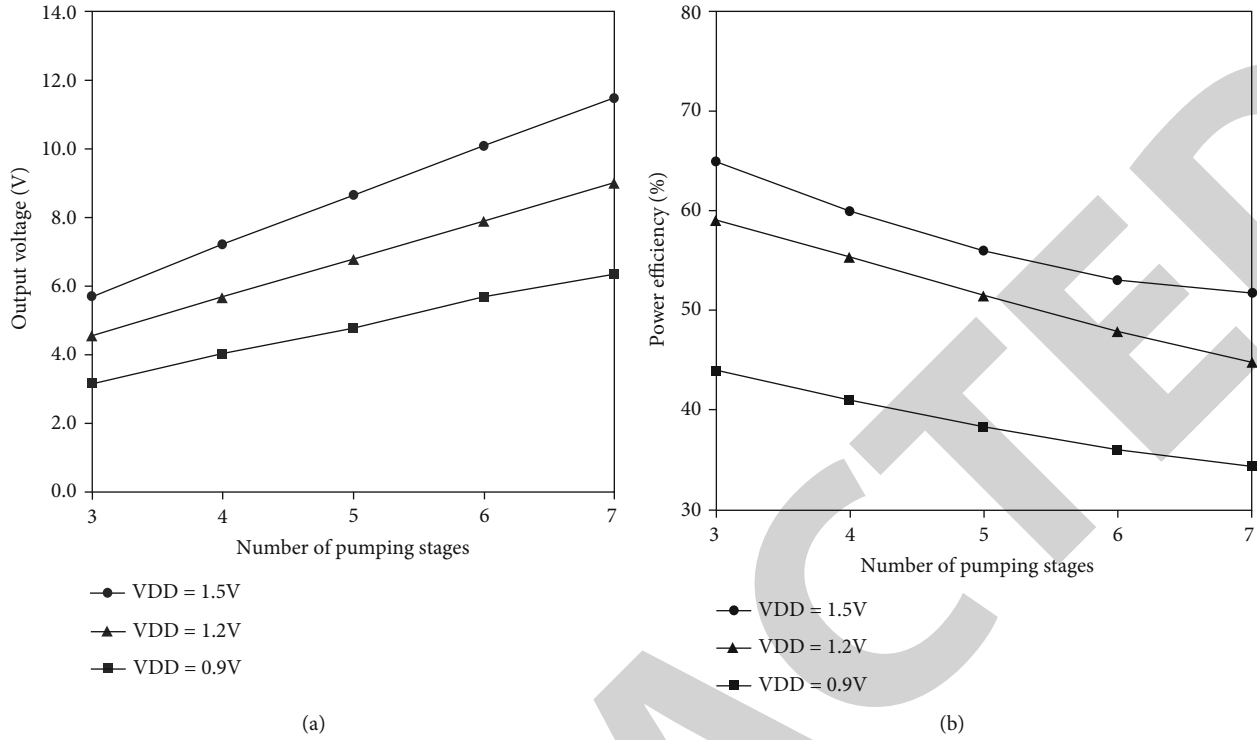


FIGURE 6: (a) Voltage gain with different power stages with 100 μA load current for the proposed charge pump; (b) power efficiency with different power stages with 100 μA load current for the proposed charge pump.

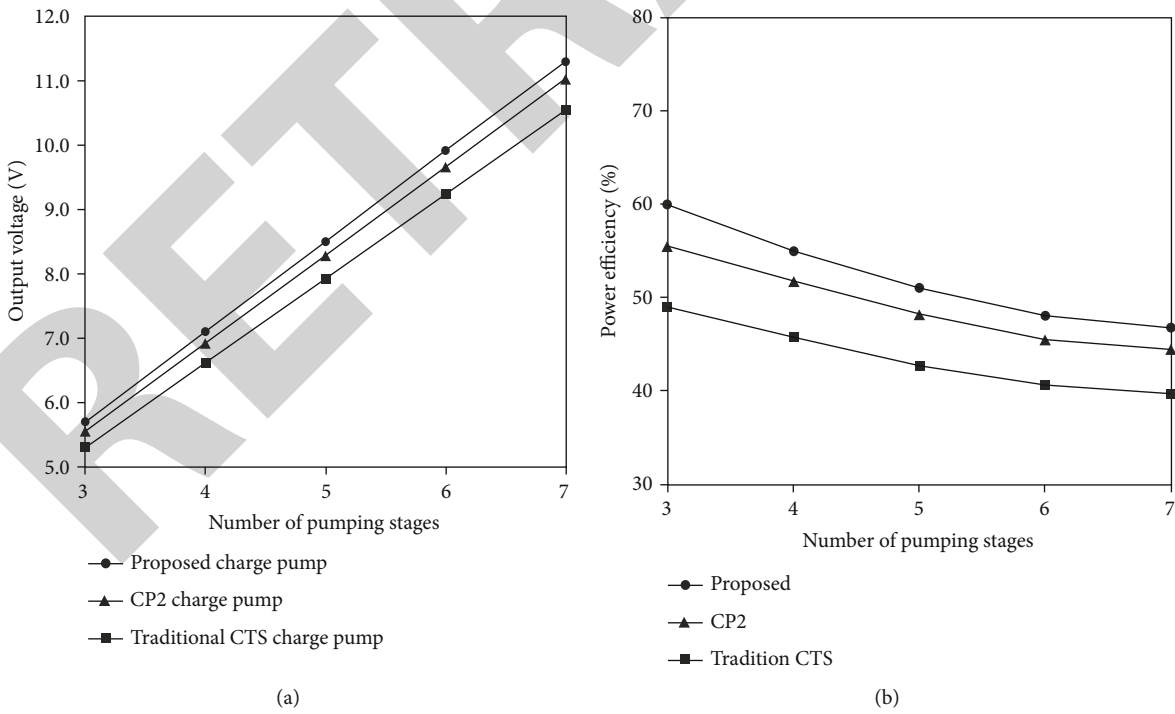


FIGURE 7: (a) Comparison of different charge pump voltage gains with 1.5 V power supply at 200 μA load current; (b) comparison of different charge pump power efficiencies with 1.5 V power supply at 200 μA load current.

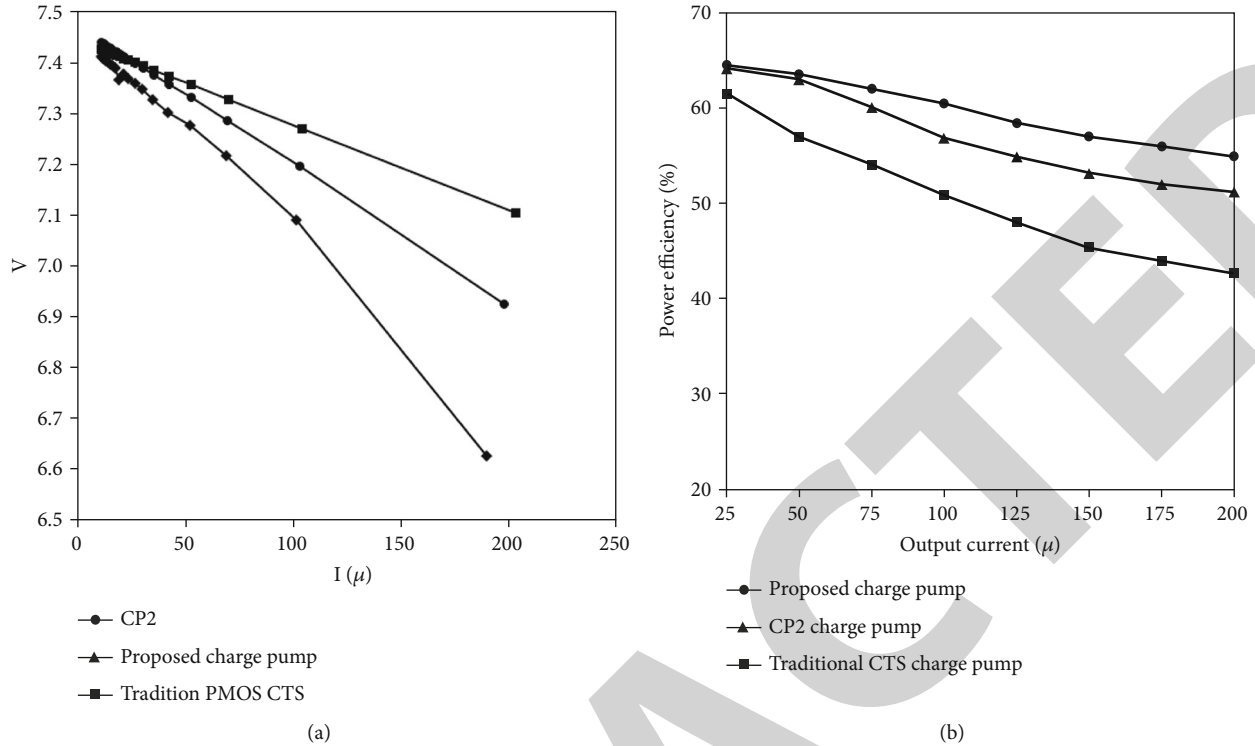


FIGURE 8: (a) The voltage gain for different charge pumps with different load current; (b) the power efficiency for different charge pumps with different load current.

5. Simulation Results

Simulation results are provided in this section to make a comparison between the proposed charge pump and traditional charge pumps. All simulation results are performed in $0.18\ \mu\text{m}$ CMOS technology with the Cadence Spectre Circuit Simulator. All charge pumps are simulated in the same branch conditions with 1 MHz clock and 1.5 nF flying capacitors.

All transistors are designed with the same dimension except for auxiliary transistors with much smaller size. A triple well structure is used to eliminate the body effect in all the charge pumps.

Figures 6(a) and 6(b) show the voltage gain and power efficiency for the proposed charge pump at a fixed load current of $100\ \mu\text{A}$ with supply voltage varying from 0.9 V to 1.5 V. According to the figure, the output voltage shows linear growth as the stage increases, while the power efficiency decreases with stage increasing. The proposed charge pump with higher supply voltage also has a better performance in power efficiency simulation.

Figures 7(a) and 7(b) show the comparison of the voltage gain and power efficiency of the proposed charge pump, CP2 charge pump in [7], and traditional CTS charge pump in [6] with different power stages with 1.5 V supply voltage at a fixed load current of $200\ \mu\text{A}$.

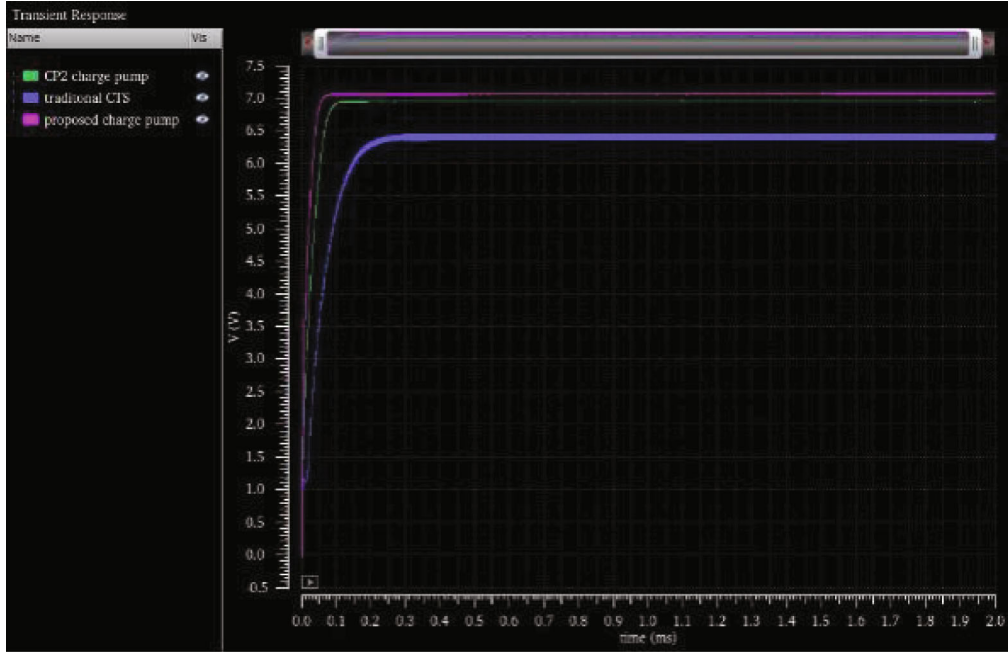
As shown in Figures 7(a) and 7(b), the proposed charge pump achieves the highest voltage gain and power efficiency among the three charge pumps. Figures 8(a) and 8(b) show

the comparison of voltage gain and power efficiency for 4 stage charge pumps with different load current and fixed 1.5 V supply voltage.

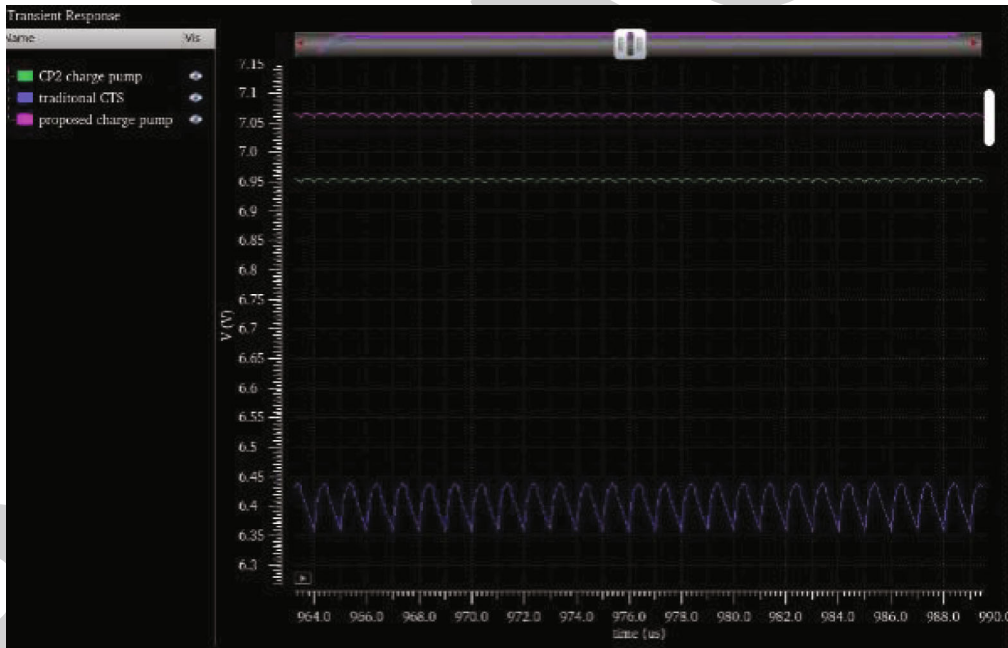
As shown in Figures 8(a) and 8(b), the proposed charge pump has the highest output voltage gain and power efficiency when the load current varies from $25\ \mu\text{A}$ to $200\ \mu\text{A}$ resulting from the elimination of undesired charge transfer and lower conduction loss. The employment of NMOS also helps the proposed charge pump to increase current drive ability. By this way, the advantage on voltage gain of the proposed charge becomes significant as the load current increases. The power efficiency for the proposed charge pump at low load current condition has not got obvious superiority resulting from extra auxiliary NMOS transistors used to start up the circuit, while it performs much better in high load current condition contributed by the lower conduction loss and the elimination of undesired charge transfer.

Figure 9(a) shows the output voltage waveform for the proposed charge pump, [6], and CP2 in [8] with 1.5 V supply voltage and $200\ \mu\text{A}$ load current. As shown in the figure, the proposed charge pump has the fastest startup time among the three charge pumps. Figure 9(b) shows the output voltage ripple in the same simulation condition. Details of output voltage gain performance for the three charge pumps are shown in Table 1.

According to the details shown in Table 1, the proposed charge pump achieves the highest voltage gain with the lowest voltage ripple and fastest startup time.



(a)



(b)

FIGURE 9: (a) Comparison of output voltage waveform for different charge pumps with 1.5 V power supply and 200 μA load current; (b) comparison of output voltage ripple for different charge pumps with 1.5 V supply voltage and 200 μA load current.

TABLE 1: Comparison of output voltage gain performance of the proposed charge pump, [6], and [7] with 1.5 V supply voltage and 200 μA load current.

	Proposed charge pump	CP2 charge pump	Traditional CTS charge pump
Output voltage (V)	7.066	6.956	6.437
Voltage gain (V/V)	4.71	4.63	4.29
Response time (μs)	88.5	119.5	306.4
Output voltage ripple (mV)	6.4	6.8	79
Output voltage percentage (V/V%)	0.0905	0.0978	1.2273

Research Article

Research on the Reform and Innovation of Preschool Education Informatization under the Background of Wireless Communication and Virtual Reality

Juan Li 

School of Arts, Shandong Management University, Jinan, Shandong 250357, China

Correspondence should be addressed to Juan Li; lijuan_smu@163.com

Received 1 July 2021; Revised 28 July 2021; Accepted 6 August 2021; Published 15 August 2021

Academic Editor: Raffaele Mascella

Copyright © 2021 Juan Li. This is an open access article distributed under the Creative Commons Attribution License, which permits unrestricted use, distribution, and reproduction in any medium, provided the original work is properly cited.

Nowadays, when various information technologies are constantly being updated, preschool children will inevitably need to use new technologies for knowledge learning. At present, preschool education informatization has begun to deploy new technologies in various colleges and universities, but there are still deficiencies. This article analyzes the significance of the combination of wireless communication and VR technology applied to preschool education for children and explores the status quo of children's participation in the use of information technology in kindergarten classrooms. Based on the problems existing in the status quo, try to use wireless communication and VR technology to improve preschool education in our country. Informatization of education proposes innovative strategies and analyzes the advantages and challenges of applying wireless communication and VR technology to the informatization of preschool education.

1. Introduction

Preschool education informatization mainly represents the preparation of various teaching aids through the use of new computer knowledge and technology in order to promote the learning effect of children and at the same time makes it easier for teachers to cultivate children's information technology sensitivity and enable them to obtain comprehensive integration ability [1].

In the context of the continuous emergence of various new information technology technologies, preschool children at home and abroad have been exposed to various electronic devices. Most children use electronic devices to perform some basic operations, such as playing games, learning small knowledge, and watching videos, but there are also many information technology devices that are not accessible to preschool children, including devices such as tape recorders and computers. When preschool children receive knowledge in domestic kindergartens, in most cases, the teacher operates the computer to play PPT to explain the knowledge to the children, and the children themselves cannot touch the computer. In developed countries abroad,

many kindergarten schools have arranged smart interactive tablets and other devices for children. Even in Florida, the tablet computer is an indispensable tool for almost every student in learning, and kindergarten teachers also like to try new technologies to teach knowledge to young children. It can be seen that the informatization of preschool education in China still needs improvement [2].

Since the beginning of this century, wireless communication and VR technology have developed rapidly. Wireless communication technology has developed the latest communication technologies and protocols other than Bluetooth and WIFI. VR technology equipment has been able to implement mobile phones, personal computers, all-in-one models, independent devices, etc. The existence and use of various forms, VR, and wireless communication technology itself are interrelated. The two technologies, as technologies generated by the progress of the new era, can help young children simplify complex knowledge and see through simulation screens that they have never seen it before or have already seen it [3]. The teaching method combining VR and wireless communication technology can bring many possibilities to preschool education, thus forming good learning habits at

the beginning of the preschool semester, cultivating great interest in learning, becoming an active learner as soon as possible, and knowing how to use it [4]. From a long-term perspective, wireless communication and virtual reality technology, as key applications for future development, require enlightenment from preschool education. The use of information technology by young children from an early age will lead to the formation of awareness of using new technology in the adult stage earlier, which also proves the significance of wireless communication and VR technology education in the early childhood stage [5].

2. Problems in the Development of Preschool Education Informatization

Although policies have repeatedly emphasized the importance of education informatization, the actual implementation is still not enough. Teachers also use videos or PPT graphics to explain the detailed analysis of difficult questions. They have not applied the latest technology in education; although, preschool education Informatization is constantly advancing, but there are still some key issues that need to be resolved [6].

2.1. No Customized Education for Preschool Children. Preschool education needs to focus on children's learning status and physical and mental health in the education process. Many children have not yet acquired an excellent learning habit at the preschool stage. However, many parents and kindergartens want to allow children to master more at the beginning stage. When children cannot accept more knowledge, they sacrifice their rest time to supplement knowledge, and it has become more and more intense. There are even many institutions that carry out elementary education in the pre-school stage [7].

In fact, the kindergarten or family in the current preschool education carrier needs a unified analysis platform for individual students' learning needs. It also needs to combine new technologies to analyze the learning situation of children and customize the learning content. There should be no blind education competitions. Otherwise, the complete informationization of preschool education will not improve the learning effect of children.

2.2. Preschool Education Information Resources Are Scarce. At present, there are still many remote areas in China that do not have information-based teaching equipment, and even computers are luxury teaching supplies. Even if they have computer equipment, they will not be used in schools. The probability of applying them to preschool education and teaching is even closer to zero. Statistics from related institutions found that the statistical comparison of informatization equipment among preschool teachers in remote villages and developed cities is shown in Table 1, and the specific visual display is shown in Figure 1.

Through the analysis of institutional statistics, it is found that the surveyed kindergarten classes are equipped with corresponding information equipment, and the types of information equipment are also relatively rich. The average ratio

of various corresponding characteristic devices has reached 0.6. Among them, the deployment rate of smart boards in preschool education places in remote areas is lower than only 0.05. The urban preschool education places are fully equipped, and all the equipment related to informatization teaching is available. It can be seen that preschool education in remote areas still lacks informatization equipment, and they need to solve the problem of lack of equipment through new information technology equipment [8].

2.3. Lack of Practical Ability Training for Preschool Education Information. Preschool education children are in the early stages of brain development and need to use hands to promote brain development. The current information-based teaching allows children to sit and listen without the opportunity to actually operate. This form of education is useful for cultivating children's hands-on ability not enough. After distributing the questionnaire survey, the author found that children in China have almost no opportunity to operate the equipment in person. Most of them are observing kindergarten teachers to operate the equipment. When the proportion reaches 0.916 and the proportion is 0.068, children can use technology products by themselves. The specific situation is shown in Table 2 and Figure 2. At present, the kindergartens where various preschool education institutions are located have different amounts of teaching materials (computers, cameras) and different teaching methods, so that children's participation in preschool education is different, and the final acceptance of children's knowledge is also different. It can be seen that the cultivation of children's hands-on ability is also related to the teaching path of kindergarten teachers and the equipment resources contained in it. In the end, the information teaching in kindergartens should be able to increase children's hands-on ability [9].

3. The Informatization Innovation Strategy of Preschool Education under the Background of Wireless Communication and Virtual Reality Technology

The current young children are growing up at a stage of rapid leap in information technology. The preschool education for young children cannot be the same as the traditional education in the past. It is the future education development trend to consider the introduction of new technologies in the preschool education. The introduction of digital technologies such as information technology will also have a positive impact on the development of children throughout their lives. Related scientific investigations have found that the latest information technology equipment in preschool education will bring beneficial factors to children's brain development and at the same time promote the cultivation of children's hands-on ability, logical thinking, and creative thinking. This section provides some strategies to solve the current problems in preschool education informatization and at the same time provide suggestions for the rational use of wireless communication and VR technology in preschool education informatization.

TABLE 1: Comparison of preschool education informatization equipment in remote villages and cities.

Device name	Unit ratio	Computer	Broadcasting	Smart board	Touch screen	Projector voice	Recorder	Television
Remote area	Amount	4	126	6	105	111	112	129
	Percentage	3%	95%	5%	79%	85%	86%	97%
City	Amount	12	20	20	20	20	20	20
	Percentage	100%	100%	100%	100%	100%	100%	100%

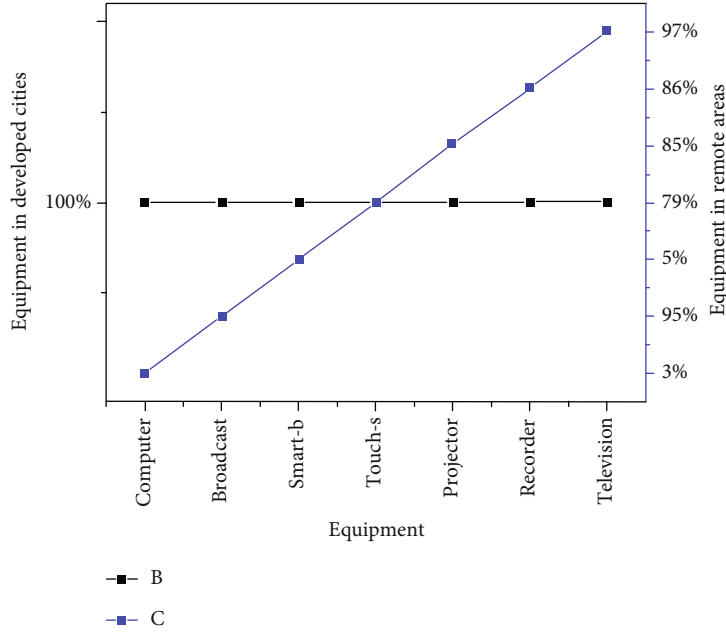


FIGURE 1: Comparison and visualization of preschool education informatization equipment in remote villages and developed cities.

TABLE 2: The use of technical equipment in preschool classrooms.

Organization	Unit ratio	Children operate by themselves	Children operate occasionally	Children only see teachers
Kindergarten	Times	0	9	121
Kindergarten	Percentage	0	6.83%	91.66%

3.1. Build a Child Learning Analysis Platform Based on VR and Wireless Communication Technology. Aiming at the problem that preschool children fail to achieve customized education, wireless communication and VR technology can be introduced, and then the big data technology in the application of wireless communication technology can be added to the problem-solving system, through wireless communication, VR, and big data technology. Data and other technologies are combined to build a children's learning data analysis platform. The platform can use big data to crawl informatized teaching materials from the Internet and provide teachers with more teaching suggestions through the best materials crawled to achieve the improvement of teachers' ability. In addition, after children use VR and wireless communication technology products, they can understand the development level of children in various aspects more accu-

rately according to the platform background data statistics. Through the learning data analysis of children operating VR devices, they can summarize the problems that children have in learning; so as to later, it can be customized to supplement the knowledge of the child.

3.2. Introduce VR and Wireless Communication Equipment. In fact, just a VR all-in-one machine can make up for all the shortcomings of scarcity of preschool education. You can see different realistic pictures during the class and learn different knowledge. You do not need to see actual objects or use other expensive equipment to simulate. This effectively solves the resource problem. Currently, companies such as Baidu have launched VR all-in-one machine, and its products have been used in a variety of scenarios and industries, such as VR industrial parks, training, party building, laboratories, and K12 classrooms. Through these cases, it can be found that the equipment has been applied to the preschool education industry. The price of the device is also more suitable for school introduction. A VR all-in-one machine can solve all resource problems. With the continuous development of technology, one all-in-one device can also be customized and developed to connect multiple VR head-mounted simulated eyes. It solves the problem of insufficient coverage.

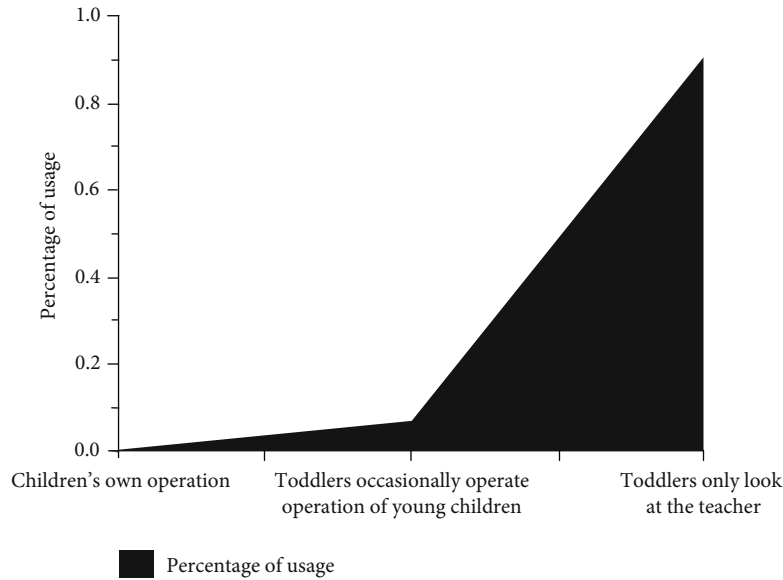


FIGURE 2: Proportion of operation technology equipment for preschool children.

3.3. Enhance Children's Hands-On Ability through VR Technology. VR and wireless communication technology can drive children to perform hands-on operations through immersion. Through the simulation of hands-on screens, children can climb mountains, swim, and pile wood in various sports and hands-on operations created by VR. In order for students to fully experience the real scene, it is necessary to integrate preschool education courses with VR technology, so that children can fully participate in activities and improve children's hands-on ability.

In addition, research has shown the shorter the time for young children to operate and use information technology. After children have been interacting with each other for a period of time using VR devices or electronic screens, encourage them to do another nontechnical activity. Therefore, teachers need to be able to control the various resources and learning modes provided by teachers. And it is necessary for teachers to limit the time, type, and form of children's technical use, as far as possible to prevent the occurrence of learning tasks that cannot be completed or even out of control and at the same time ensure healthy learning time for children.

4. Analysis of the Advantages and Challenges of the Integration of Wireless Communication +VR Technology and Preschool Education

At present, more than a thousand schools have been equipped with VR classrooms and laboratories. In the future, there will be more schools using wireless communication and VR technology. Compared with traditional information-based teaching, it has advantages and also brings many challenges.

4.1. Advantage

4.1.1. Improve Children's Comprehension Ability. Some scholars have found that if only pictures or texts of relevant

courses are provided, the effect of preschool education children's acceptance of knowledge can only reach 10%, and under the combination of video and PPT, the acceptance rate of children reaches 30%. When using VR and wireless in the teaching mode under the combination of communication technology, the acceptance rate of children is 70%, and we can infer from the data that it can improve children's comprehension [10].

4.1.2. Relieve the Confinement of Space and Time. For some historical scenes or demonstration teaching of extinct animals, conventional video playback effects are not realistic enough, and the impression of children in preschool education is not deep enough. Using VR and wireless communication technology cannot only simulate extinct animals such as dinosaurs but also detect dead animals. Go back to the historical scene. And many dangerous scenes can also be directly simulated, such as deep-sea exploration, experience the vastness of the sea next to sharks and whales, so as to realize the restoration of real scenes that cannot be achieved by traditional teaching methods, so that children can learn without specific restrictions on space and time, and also allow preschool education Children in middle school have a deeper understanding of the corresponding species and cultivate interest in subjects [11].

4.1.3. Reduce the Cost of Preschool Education. Through VR and wireless communication technology combined with preschool children's experimental teaching, VR methods can be used to replace traditional real object experiments. For example, chemical reaction experiments often waste materials after completing one time, while under VR and wireless communication technology, children can play repeatedly VR images continue to experiment to solve irreversible situations and reduce costs, which solves the irreversible situation that the material cost.

4.1.4. Improve Children's Interest and Motivation. Preschool children's brains are still in the early stages of development, and their ability to reason and understand things is not enough, but after a period of teaching by parents and relatives, they have the ability to independently carry out learning activities and then use wireless communication. The immersive experience of VR technology can further enhance the hands-on ability of children in preschool education and effectively enhance children's learning interest through visual and auditory stimulation [12].

4.2. Challenge. For preschool informatization education.. VR and wireless communication technology can bring a lot of beneficial factors, and it could also have an adverse effect on the growth of young children. Through analysis, the author found that children may have the following educational challenges under the application of wireless communication and VR technology [13]. At present, VR and wireless communication technology is mainly used in preschool education with the following challenges.

First, there are many ways to apply VR and wireless communication technology. If there is no fixed teaching standard guidance, teachers will not be able to teach effectively.

Second, the environment is more likely to cause certain adverse effects on young children. Excessive exposure to VR and wireless communication technologies may develop some negative effects, causing young children to mix reality with virtual.

Again, if young children are accustomed to the vivid experience and convenient knowledge brought by VR and wireless communication technology, they will no longer seriously think about the meaning behind the scenes they see. For example, after seeing dinosaurs, they feel accustomed to them and do not think about the development history of dinosaurs. This may affect children's own creative thinking and eventually lead to children's loss of creativity. This is a scenario that preschool education does not want to see.

Finally, children's single participation in VR and wireless communication technology may have a certain adverse effect on the child's body. Specifically, it may be manifested in obesity due to obesity, due to indulging in playing VR games and sedentary sitting, and vision loss due to long-term focus on the screen.

5. Conclusion

It is not only kindergarten teachers, family education, social education, and self-education that all affect the development of children. It is the general trend for children to participate in the use of information technology and kindergarten information technology education, and the informatization of the preschool education industry is also imperative, the application of wireless communication and virtual reality technology to the informationization of preschool education will realize a complete change in the way of preschool education and finally cultivate children who are qualified in moral, intellectual, physical, and artistic.

The application of wireless communication and VR technology has a significant positive impact on children's under-

standing of the world, raising interest in class, cultivating knowledge, and knowledge of various subjects. Applying wireless communication and VR technology to children's informatization teaching can enable children to have a deeper understanding of things and the laws of development of things and also enable them to understand the world in many aspects, angles, and directions. This article mainly regards the use of wireless communication and virtual reality technology in preschool education informatization as the theme, based on specific conceptual definitions, preschool education informatization status quo, and problem exploration, and the specific use of wireless communication and virtual reality technology in the preschool education informatization environment carries out comprehensive analysis and research to prepare a good theoretical analysis and practical research foundation for the use of wireless communication and VR technology in preschool education.

Data Availability

Data sharing not applicable to this article as no datasets were generated or analyzed during the current study.

Conflicts of Interest

The author declared no potential conflicts of interest with respect to the research, authorship, or publication of this article.

Acknowledgments

This paper is the periodic research results of "Research on the practice of Mixed Teaching Mode Based on Micro Video" (Project No. 21JX068), a teaching research project of Shandong Province in 2021. This paper is the periodic research results of "Exploration and Practice Research on the Improvement of College Students' Core Literacy Based on PAD Teaching Mode" (Project No. 21JG144), an education and teaching reform research project of Shandong Province in 2021. This paper is the periodic research results of "Research on the practice of vocational enlightenment education for 3-6-year-old children" (Project No. 21SC010), a educational science research project of Shandong Province in 2021.

References

- [1] X. Mei, "Research on higher education informatization construction promoting education and teaching reform and innovation," *Shaanxi Education (Higher Education)*, vol. 6, pp. 65-66, 2021.
- [2] J. C. Ge and C. Qi, "Cultivation of informationized teaching ability for normal students of preschool education major," *Journal of Anshan Normal University*, vol. 23, no. 2, pp. 61-65, 2021.
- [3] Z. Juanran and L. Juan, "Exploration of the reform and construction of practical teaching informatization of preschool education specialty," *Science and Technology Vision*, vol. 11, pp. 14-15, 2021.

- [4] Y. Wei, Z. Yufeng, and H. Wenyuan, "Feasibility study on the integrated development of "VR + preschool education"," *Journal of Weifang University*, vol. 20, no. 4, pp. 116–120, 2020.
- [5] D. Youjun, "Analysis of vocal music teaching reform in higher vocational colleges in the information age—an example of preschool education major of Lanzhou vocational and technical college," *Voice of the Yellow River*, vol. 18, pp. 37–38, 2015.
- [6] H. Lan, "Research on the informationization of dance teaching in preschool education major," *Journal of Ningbo Institute of Education*, vol. 21, no. 1, pp. 21–22, 2019.
- [7] L. Yang, T. Chunyu, and C. Wang, "Promoting higher vocational preschool education curriculum reform practice exploration with information technology—taking "social education for preschool children" as an example," *Future and Development*, vol. 43, no. 11, pp. 14–17, 2019.
- [8] A. Dun, "The teaching status and strategy analysis of preschool education professional courses," *Journal of Heilongjiang Teachers Development College*, vol. 39, no. 1, pp. 54–56, 2020.
- [9] P. Shuai, "The application of information technology in preschool education professional print teaching," *Art Education Research*, vol. 8, pp. 95–97, 2021.
- [10] C. Yan, "A brief discussion on the teaching and research of new era kindergarten facing educational informationization," *Western Journal*, vol. 6, pp. 116–118, 2021.
- [11] J. Zongzhen, "Preschool education information technology innovation and application research—comment on "basics and application of preschool education information technology"," *Science and Technology Management Research*, vol. 40, no. 24, p. 263, 2020.
- [12] Y. Ma, "Current status and prospects of preschool education informatization research," *China Educational Technology and Equipment*, vol. 15, pp. 66–69+79, 2020.
- [13] L. Xueping, "Educational informatization enhances the information literacy of kindergarten teachers," *Digital Communication World*, vol. 10, pp. 238–239, 2020.

Retraction

Retracted: Reform and Challenges of Ideological and Political Education for College Students Based on Wireless Communication and Virtual Reality Technology

Wireless Communications and Mobile Computing

Received 26 September 2023; Accepted 26 September 2023; Published 27 September 2023

Copyright © 2023 Wireless Communications and Mobile Computing. This is an open access article distributed under the Creative Commons Attribution License, which permits unrestricted use, distribution, and reproduction in any medium, provided the original work is properly cited.

This article has been retracted by Hindawi following an investigation undertaken by the publisher [1]. This investigation has uncovered evidence of one or more of the following indicators of systematic manipulation of the publication process:

- (1) Discrepancies in scope
- (2) Discrepancies in the description of the research reported
- (3) Discrepancies between the availability of data and the research described
- (4) Inappropriate citations
- (5) Incoherent, meaningless and/or irrelevant content included in the article
- (6) Peer-review manipulation

The presence of these indicators undermines our confidence in the integrity of the article's content and we cannot, therefore, vouch for its reliability. Please note that this notice is intended solely to alert readers that the content of this article is unreliable. We have not investigated whether authors were aware of or involved in the systematic manipulation of the publication process.

Wiley and Hindawi regrets that the usual quality checks did not identify these issues before publication and have since put additional measures in place to safeguard research integrity.

We wish to credit our own Research Integrity and Research Publishing teams and anonymous and named external researchers and research integrity experts for contributing to this investigation.

The corresponding author, as the representative of all authors, has been given the opportunity to register their agreement or disagreement to this retraction. We have kept a record of any response received.

References

- [1] X. Hang, "Reform and Challenges of Ideological and Political Education for College Students Based on Wireless Communication and Virtual Reality Technology," *Wireless Communications and Mobile Computing*, vol. 2021, Article ID 6151249, 7 pages, 2021.

Research Article

Reform and Challenges of Ideological and Political Education for College Students Based on Wireless Communication and Virtual Reality Technology

Xing Hang 

Business School, Chengdu University, Chengdu, Sichuan 610106, China

Correspondence should be addressed to Xing Hang; hangxing_edu@outlook.com

Received 5 July 2021; Revised 28 July 2021; Accepted 3 August 2021; Published 15 August 2021

Academic Editor: Balakrishnan Nagaraj

Copyright © 2021 Xing Hang. This is an open access article distributed under the Creative Commons Attribution License, which permits unrestricted use, distribution, and reproduction in any medium, provided the original work is properly cited.

With the continuous changes in ideological and political education methods in universities, the previous ideological and political teaching mode of blackboard plus PPT dictation is gradually facing the risk of being eliminated. Wireless communication and VR technology are the key points of the reform. The sense of situation, immersion, and participation that they bring is exactly what traditional ideological and political teaching lacks. This article will take college students' ideological and political teaching as the key object, analyze the possible application of VR technology and wireless communication technology in the process of college students' ideological and political teaching, use VR technology and wireless communication technology to simplify the process of college students' ideological and political teaching and the current wireless communication and the advantages and difficulties of VR technology in the application of college students' ideological and political teaching, explore how to scientifically and efficiently use wireless communication and VR technology to solve the difficulties encountered in the traditional teaching mode in the process of ideological and political teaching of college students, and provide direction for college students' ideological and political education reform.

1. Introduction

The current new round of education reform has put forward new requirements for the development of ideological and political education for college students. Ideological and political disciplines have ushered in the challenge of change under the framework of the key requirements of the new curriculum reform. In the traditional teaching process, there are many difficulties for students to realize the core quality education of ideological and political education. However, educational informatization has achieved corresponding results under the continuous promotion of departments at all levels. The development of this kind of informatization technology also places higher requirements on ideological and political teachers in colleges and universities, especially wireless communication and VR technology. In the case of social applications in various industries, the application of wireless communication and virtual reality technology in college ideological and political education has become an important trend [1].

In foreign countries, the first school to introduce virtual reality technology into the teaching experiment process was the Massachusetts Institute of Technology in the United States. Professors of the university established a virtual laboratory. As early as the 1980s, students of the university could pass this virtual laboratory. The laboratory conducts experimental design, circuit model modification, etc. and can also use remote test equipment to verify the success of its own experimental design. All of these only need to use their own computers, without the use of experimental equipment. In 2010, it was realized that only through mobile phones can complete the experiment [2]. In addition, virtual reality technology is also widely used in Italy, Singapore, Spain, and other countries. It can be seen that the development of virtual reality technology abroad is very rapid [3].

The domestic development of virtual reality technology is relatively slow compared to foreign development, but many domestic colleges and universities have virtual laboratories dedicated to their own students and teachers. Students and

teachers can conduct a large number of effective virtual experiments. Peking University has independently developed a virtual experimental system that can be used for large-scale calculations, and almost two experimental systems have been implemented, namely, cache and pipeline [4]. Similarly, my country's Tsinghua University, based on the State Key Laboratory of Power Systems, has established an automobile engine detection system using virtual instruments, which can be used to detect the overall performance of automobile engines [5]. In addition to Peking University and Tsinghua University, Beijing University of Aeronautics and Astronautics also has virtual laboratories. Based on virtual reality technology, many laboratories on virtual realization technology have been designed and constructed [6]. However, the University of Science and Technology of China is the first national-level virtual teaching simulation experiment center approved by the Ministry of Education for ideological and political education and possessing a set of virtual experiment teaching software. It can be seen that the development speed of virtual reality technology in domestic colleges and universities is very fast [7]. However, domestic research shows that the actual application of virtual reality technology in some ordinary colleges and universities is almost zero, and basically, there is no equipment to support virtual simulation experiments; so, virtual simulation experiments are still very large in the teaching of various subjects in China. Therefore, wireless communication and virtual reality technology still need to be further popularized and applied in the teaching of various disciplines [8].

As a continuously developing technology, the attempts of virtual reality technology in the field of education have never stopped. In order to fully understand the development status of domestic virtual reality technology, the author searched the CNKI database for related topics and analyzed its development status based on the line graph of the number of journal articles published. Among them, wireless communication and VR technology are the keywords. It can be seen from the broken line chart 1 that the number of papers has been on the rise from 1911 to 2020, and from 2015 to 2021, the upward trend is very obvious. It can be seen that the development of wireless communication and VR technology is the current hot spot as shown in Figure 1.

I used "wireless communication and VR technology + education," "wireless communication and VR technology + ideological and political teaching," and "wireless communication and VR technology + ideological and political experiment teaching" as keywords to search for the number of papers and make a line chart. Through the comprehensive analysis of the above four line graphs, it is found. Although wireless communication and VR technology are currently hotspots of development, the number of papers that combine wireless communication with VR technology and ideological education accounts for only 10% and the number of papers that combine wireless communication with VR technology and ideological and political teaching. There are only 55 articles in total, 35 of which are related to wireless communication and VR technology and ideological and political experimental teaching. From the above data, it can be seen that the application research of wireless communication

and VR technology in the ideological and political teaching of college students is still in the initial stage. The specific situation is shown in Figure 2.

Examples of applying wireless communication and VR technology to classroom teaching are mainly the way of creating VR classrooms. Through the combination of VR glasses and smart phones, an immersive virtual environment is created for students, combined with the explanation of university teachers and the creation of VR virtual environment, so that students can learn knowledge through observation in the classroom intuitively and vividly. In the future, wireless communication and virtual reality technology will be more closely integrated with university ideological and political education [9].

2. Actual Investigation and Analysis

This article mainly adopts literature research method, questionnaire survey method, and analogy analysis method. First, through reading the relevant literature, understand the current research situation at home and abroad and then determine your own research questions based on the actual survey situation. Design a questionnaire based on the needs of the research question and distribute the questionnaire to collect data. Combining the feedback results of the questionnaire survey, comparing traditional university ideological and political teaching, and analyzing the theoretical advantages and challenges of wireless communication and VR technology in university ideological and political teaching, it also provides a theoretical reference for the application of wireless communication and VR technology in university ideological and political teaching.

After analysis and thinking, the research questions of this thesis mainly include the following three questions. First, it studies the characteristics of wireless communication and VR technology and analyzes the changes in the research enthusiasm of the combination of wireless communication, VR technology, and university ideological and political teaching in recent years. Second, combine the results of the questionnaire survey to analyze the main problems in the process of ideological and political teaching in universities and the methods to solve these problems by using wireless communication and VR technology. Third, through examples, analyze the advantages and disadvantages of wireless communication and VR technology in university ideological and political teaching. Fourth, combine reality to find possible solutions to the shortcomings of wireless communication and VR technology in university ideological and political teaching.

2.1. Brief Introduction of Questionnaire Making. The author of this thesis has read a large number of references and discovered according to his own teaching experience that many scholars and teachers have investigated the current situation of university ideological and political teaching in most regions, as well as some major difficulties faced by college students in the process of learning university ideological and political. There are two main points:

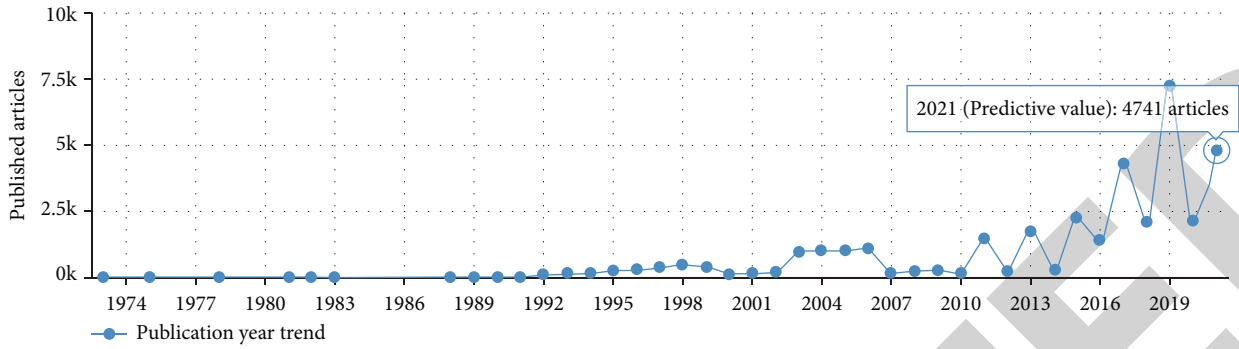


FIGURE 1: The trend of wireless communication and VR technology literature.

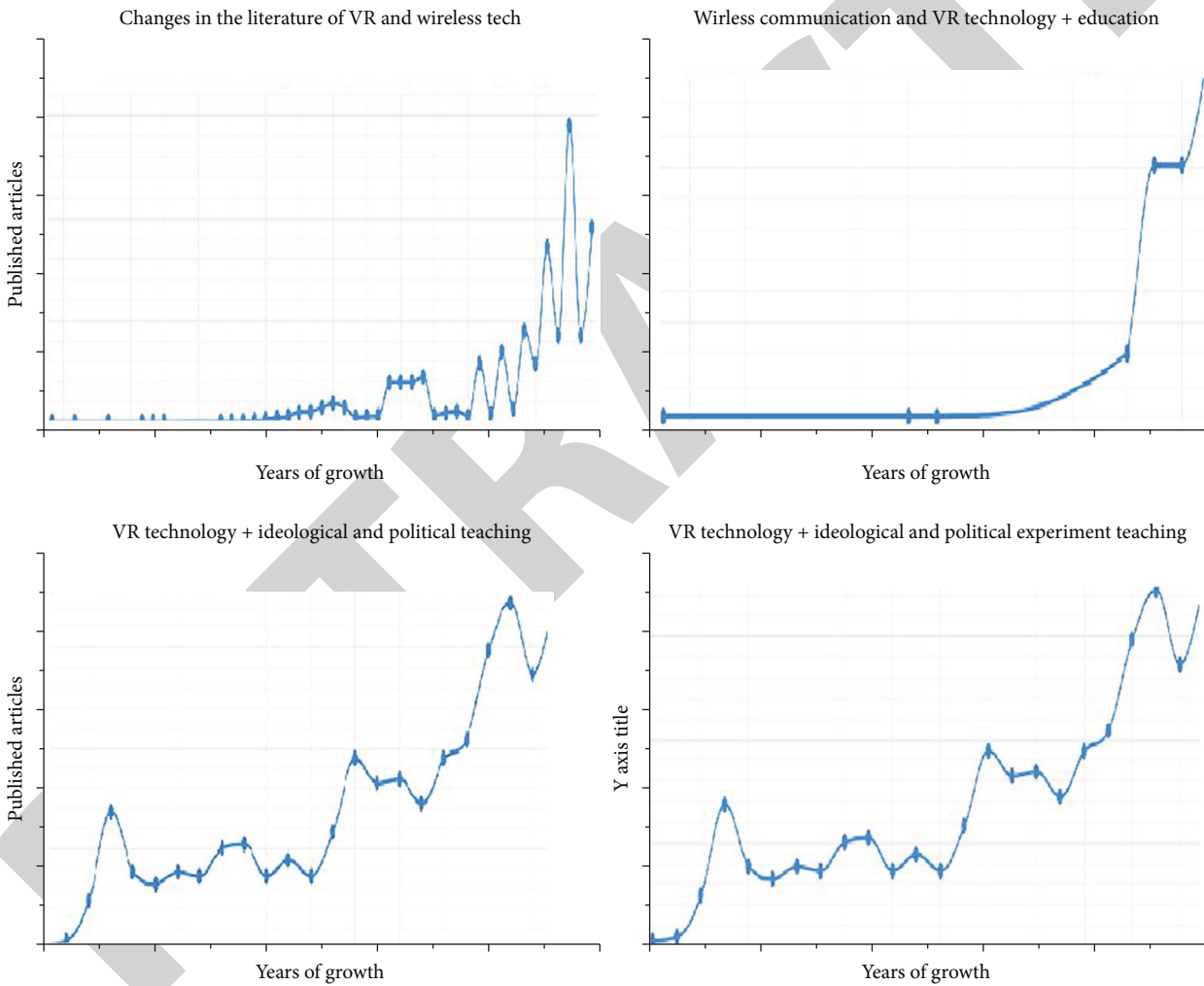


FIGURE 2: Literature change trends under different search terms for ideological and political and VR-wireless technologies.

(1) Ideological and political knowledge is relatively abstract. The understanding of ideological and political concepts and the establishment of ideological and political models require strong spatial imagination and understanding capabilities. Traditional language description and two-dimensional image display can hardly enable students to fully understand some

abstract ideological and political knowledge and complex ideological and political scene

(2) Many schools do not pay enough attention to the application of new technology in ideological and political teaching, mainly because of the lack of school laboratory equipment, less available funds,

school tasks are tight, teachers only pay attention to students' observation of the teaching results, and do not pay attention to the teaching process and other reasons. This affects the application of new technology in ideological and political teaching

This questionnaire survey was made based on the above questions. The content of this questionnaire survey can be divided into three parts as shown in Table 1.

2.2. Analysis of Survey Results. The subject of this questionnaire survey is for college students across the country. 211 valid questionnaires were recovered, and the results of the questionnaires are now analyzed.

First, analyze the basic information of the respondents. Among them, 110 are male students, and 101 are female students. 133 students from key universities accounted for 63.03% of the total, and 78 students from ordinary universities accounted for 36.97% of the total. 54 students from first-tier city universities accounted for 25.59% of the total, 64 from second-tier city schools accounted for 30.33% of the total, 61 from other city universities accounted for 28.91% of the total, and 32 from provincial capital universities accounted for 15.17% of the total. On the whole, the people participating in the questionnaire survey come from different regions, the sample coverage is wide, and the credibility is high.

3. Analysis of the Status Quo of College Students' Ideological and Political Study

The results of the questionnaire survey of these two questions in Table 2 show that 74.14% of students think ideological and political are very interesting, but only 20.38% of students can learn efficiently in ideological and political classrooms, and 43.60% of students have low or complete learning efficiency. I do not understand: the above data reflects that the current university ideological and political learning status is relatively poor. More than 60% of college students cannot effectively study ideological and political courses.

4. Problems Existing in College Ideological and Political Teaching

Ideological and political science is a science that combines logical thinking and debate. It is necessary for college students to conduct in-depth immersive thinking while studying, to feel the philosophical meaning behind the sentence. After analyzing the status quo of college students' ideological and political learning, it is found that the deficiencies in the teaching of college ideological and political courses mainly include the following aspects.

- (1) The participation of students in university ideological and political courses is not high. Due to the large number of students in large classes, it is impossible for the teacher to pay attention to every student. The participation of students in university ideological and political classes is not high. Due to the large

number of teachers in large classes, it is impossible for the teacher to pay attention to every student. Even if the students are very active, they will not get feedback and their enthusiasm will gradually decrease

- (2) Ideological and political courses involve more abstract philosophical concepts, for example, Marx's theory. In the past, ideological and political teaching in colleges used to be dictated by teachers to complete the teaching. The level of understanding of ideological and political courses by college teachers will directly affect the learning effect of students. Some philosophical concepts cannot be fully dictated by students in a single class. Understand its connotation, and only through other activities that are more immersive can students thoroughly understand
- (3) The current expectation of ideological and political teaching in colleges and universities of the Ministry of Education requires students to interact and bring in learning. In fact, colleges and universities only arrange PPT teaching at most, and the interaction and the sense of bringing in pictures and videos involved cannot really satisfy college students. Learning needs and college ideological and political topics need a more immersive device to stimulate students' interest in learning

5. Based on the Revolutionary Advantages of Wireless Communication and VR Technology in University Ideological and Political Teaching

Wireless communication technology and VR technology are essentially connected together, because the transmission of VR images and the collection of user actions involve wireless communication technology. The development of VR technology can be briefly divided into the following three types:

- (1) Completely immersed. Connect to the corresponding device through the VR eye, allowing the user to be fully immersed
- (2) Desktop VR system. Similar to watching the video directly, the user watches a more realistic VR scene through the computer screen, and the sense of immersion is weaker than that of the first one
- (3) Enhanced VR system. Convenient to carry, the user's senses are more intense, thus immersing in the virtual world

After analysis, the author found that the VR technology that is more suitable for teaching practice in the future is fully immersed wireless communication and VR technology, because this kind of VR technology can realize the function of a teacher tutoring dozens of students in college ideological and political classes, it can also observe and collect students' learning conditions, adjust teaching strategies in time, and correctly guide students' learning process. In general,

TABLE 1: Ideological, political, and wireless communication-VR technology questionnaire survey.

Survey question	Question number corresponding to survey
Basic information of the respondent	1-3
Status quo of university ideological and political teaching	4-23
Students' understanding of wireless communication and VR technology	24-26

TABLE 2: Current situation of college students' ideological and political learning.

Question	Options			
	Do not like it, feels hard	Do not like it, have no interest	Feel ideological and political is very interesting	It does not matter, it's just one subject
Do you like ideological politics?	8.06%	9.95%	74.41%	7.28%
High efficiency in learning ideological and political?	Very efficient 20.38%	Ordinary 36.02%	Low efficiency 25.12%	Do not understand 18.48%

immersive VR technology can achieve a win-win situation for teachers and students in ideological and political teaching in colleges and universities, teachers can more easily achieve better teaching results, and students can also grasp knowledge more firmly [10].

Because wireless communication and VR technology are still less used in college ideological and political classrooms, there is a lack of relevant references. I refer to online materials to summarize the possible advantages of wireless communication and VR technology in university ideological and political classroom teaching.

- (1) Wireless communication and VR technology can create more realistic teaching situations. When the fully immersive VR images are played, the students' sense of hearing and vision is thoroughly mobilized, and they devote themselves to the corresponding ideological and political teaching images. This kind of teaching is like the game images that students usually encounter and can even make students real experience the historical connotation of the picture, so as to better grasp the ideological and political knowledge [11]
- (2) Wireless communication and VR technology can optimize the ideological and political learning process of college students, mainly to improve personal presence and attention. In the VR teaching mode, every student is the master of the classroom and can easily participate in the interaction with the teacher. This teaching mode solves the problem of low efficiency of listening to the students in the back row in traditional teaching, so that every student has enough opportunities to participate, and it is easy to get a sense of satisfaction in learning and ultimately enhance the learning effect [12]
- (3) Wireless communication and VR technology can establish virtual models to help students understand ideological and political concepts and establish problem-solving ideas and methods. It can break through the limitations of the blackboard. The 3D

model established through wireless communication, and VR technology can enable students to have a concise and intuitive understanding of ideological and political models and can deepen students' understanding [13]

- (4) Convenient and fast. The use of wireless communication and VR technology for ideological and political experiment teaching breaks through the limitations of teaching venues, teaching equipment and teaching time in traditional teaching. Students do not even need to go to the teacher, and the teacher does not need to prepare related equipment in advance. They can conduct experiments in the classroom in time, which saves teaching time and makes ideological and political teaching more convenient
- (5) Economical. The use of wireless communication and VR teaching does not have to consider the wear and damage of some equipment such as chalk and blackboard in the teaching. There is no need to worry about the losses caused by operating errors. Students can continue to try and explore during the course. In some remote schools lacking teaching equipment, wireless communication and VR technology can also be used for experimental teaching, thereby reducing the cost of each school
- (6) The experimental resources are abundant, which can meet the teaching in different scenarios, using VR and wireless communication to teach can set the teaching conditions according to actual needs. For example, a certain course needs to play the VR images of Red Boat Spirit and Jinggangshan Reunion. These can all be adjusted by background needs. Breaking through the limitations of the real environment can enable students to observe the historical real situation in a more real situation
- (7) High safety. The use of VR for ideological and political teaching can enable students to conduct some more dangerous explorations in traditional teaching, avoid the possible harm to students in the

exploration, and also reduce the environmental pollution caused by harmful substances generated in the exploration. For example, students can experience dangerous scenes such as the Long March process that are simulated in the VR environment. VR ideological and political teaching does not have any pollution and danger, ensuring that every student can explore various ideological and political knowledge in a safe state

- (8) Ideological and political scenarios are intuitive and obvious and can directly analyze the results. The use of wireless communication technology and VR for ideological and political teaching can adjust the speed of the occurrence of the situation, slow down those ideological and political phenomena that reflect relatively quickly, and can also enlarge and observe the ideological and political phenomena that are not obvious. At the same time, you can use the computer to directly process the ideological and political knowledge data and reflect it in the form of tables and images, which is more beneficial for students to master the ideological and political knowledge

6. Conclusion

Although wireless communication and VR technology have great application prospects in university ideological and political teaching, there are still many challenges in applying wireless communication and VR technology to classrooms. The main problems at present are as follows.

- (1) High research and development costs. At present, the main form of wireless communication and VR technology used in teaching is the virtual laboratory developed under the desktop VR system. There is still a long way to go to the application of immersive VR teaching. Developing suitable software and maintaining the normal operation of the system requires a lot of consumption. But with the advancement of science and technology, this problem will definitely be solved reasonably
- (2) Teacher requirements are difficult to meet. After wireless communication and VR technology are applied to actual teaching, it is a big challenge for teachers. Teachers need to learn to develop teaching courseware suitable for VR systems and deal with the failures that may occur in the classroom. At present, these requirements are for the vast majority of It is difficult for teachers to achieve
- (3) The school hardware facilities are difficult to meet the requirements. To use wireless communication and VR technology for classroom teaching, the school should at least configure a distributed VR system for each class and at the same time ensure that the school achieves full coverage of the 4G network, or 5G network, equipped with a large number of wireless communication related equipment to collect

VR transfers. It is still difficult for most schools to complete the construction of the above supporting facilities, because it requires a lot of financial resources.

- (4) Lack of corresponding reference. VR teaching is a new thing, there is no corresponding theory to support, and there is no reference example. All teachers can only cross the river by feeling the stones; so, there may be many unexpected problems in the teaching practice
- (5) May cause social controversy. Wireless communication and VR technology is a new technology, while the education field is very traditional. In the process of integrating new technologies into traditional industries, many people may not be optimistic about it, and great controversy occurs

Data Availability

Data sharing not applicable to this article as no datasets were generated or analyzed during the current study.

Conflicts of Interest

The author declares that he has no conflicts of interest.

References

- [1] Y. Dong and B. Zhixiao, "Analysis of cultural security education in ideological and political theory courses in colleges and universities," *Journal of Mudanjiang Teachers College (Social Science Edition)*, vol. 3, pp. 107–109, 2021.
- [2] Y. Yuqin, *Research on the Design of the Living Scene of Ideological and Political Education*, Kashgar University, 2021.
- [3] C. Bao, "Analysis of the innovative education path of ideological and political education in secondary vocational education in the internet era," *Modern Vocational Education*, vol. 26, pp. 192–193, 2021.
- [4] J. Chunyan and S. Qi, "The current dilemma and development path of network ideological and political education in colleges and universities in the new era," *School Party Building and Ideological Education*, vol. 12, pp. 59–61, 2021.
- [5] Z. Miao, "A brief exploration of the integration of the spirit of scientists into the ideological and political education of college students," *School Party Building and Ideological Education*, vol. 12, pp. 88–90, 2021.
- [6] C. Yiwen, "The important role and reform direction of ideological and political education in the training of artificial intelligence talents in colleges and universities," *Science, Education and Culture Collection (Mid-term)*, vol. 6, pp. 106–110, 2021.
- [7] Z. Caixia, "Innovative practice of ideological and political education in secondary vocational schools," *Modern Vocational Education*, vol. 25, pp. 178–179, 2021.
- [8] X. Hu and H. Yu, "The historical mission of ideological and political education in the new era," *Journal of China Three Gorges University (Humanities and Social Sciences Edition)*, vol. 43, no. 4, pp. 34–36, 2021.
- [9] Z. Yan, "Strategies for ideological and political education of college students in the Internet age," *Journal of Liaoning*

Retraction

Retracted: Biobjective UAV/UGV Collaborative Rendezvous Planning in Persistent Intelligent Task-Based Wireless Communication

Wireless Communications and Mobile Computing

Received 28 November 2023; Accepted 28 November 2023; Published 29 November 2023

Copyright © 2023 Wireless Communications and Mobile Computing. This is an open access article distributed under the Creative Commons Attribution License, which permits unrestricted use, distribution, and reproduction in any medium, provided the original work is properly cited.

This article has been retracted by Hindawi, as publisher, following an investigation undertaken by the publisher [1]. This investigation has uncovered evidence of systematic manipulation of the publication and peer-review process. We cannot, therefore, vouch for the reliability or integrity of this article.

Please note that this notice is intended solely to alert readers that the peer-review process of this article has been compromised.

Wiley and Hindawi regret that the usual quality checks did not identify these issues before publication and have since put additional measures in place to safeguard research integrity.

We wish to credit our Research Integrity and Research Publishing teams and anonymous and named external researchers and research integrity experts for contributing to this investigation.

The corresponding author, as the representative of all authors, has been given the opportunity to register their agreement or disagreement to this retraction. We have kept a record of any response received.

References

- [1] Q. Wang, H. Chen, J. Tian, J. Wang, and Y. Su, "Biobjective UAV/UGV Collaborative Rendezvous Planning in Persistent Intelligent Task-Based Wireless Communication," *Wireless Communications and Mobile Computing*, vol. 2021, Article ID 9578783, 12 pages, 2021.

Research Article

Biobjective UAV/UGV Collaborative Rendezvous Planning in Persistent Intelligent Task-Based Wireless Communication

Qin Wang , Hua Chen , Junwei Tian , Jia Wang , and Yu Su 

School of Mechanical and Electronic Engineering, Xi'an Technological University, Xi'an, China

Correspondence should be addressed to Hua Chen; hc156131@163.com

Received 25 June 2021; Revised 26 July 2021; Accepted 3 August 2021; Published 15 August 2021

Academic Editor: Balakrishnan Nagaraj

Copyright © 2021 Qin Wang et al. This is an open access article distributed under the Creative Commons Attribution License, which permits unrestricted use, distribution, and reproduction in any medium, provided the original work is properly cited.

This paper addresses a multiobjective Unmanned Aerial Vehicle (UAV) and Unmanned Ground Vehicle (UGVs) collaboration scheduling problem in which UAVs must be recharged periodically during a persistent task, such as wireless communication and making aerial panoramic VR video by UAV. The proposal is to introduce a UGV/UAV cooperative system in which UAVs should be recharged by UGVs periodically, and also, the UGVs have to visit their task points expect for the recharge points. The objective of the problem is to schedule and plan paths with the tradeoff of path length and makespan for UAVs and UGVs. The mathematical model which can be considered a combinatorial multiobjective optimization problem is presented firstly, and the solution of the problem is composed of presubsolution and postsubsolution. The multiobjective adaptive large neighborhood is hybrid with the Pareto local search (MOALP) to resolve the problem. The experimental result shows that the proposed algorithm outperforms the compared algorithms on the rendezvous planning problem for UAVs and UGVs working collaboratively in intelligent tasks.

1. Introduction

Unmanned Aerial Vehicles (UAVs) have been successfully used for many applications in both civil and military scenarios, such as surveillance, precision agriculture, package delivery, and facility inspection. Multiple sensors can be equipped to obtain various information because UAVs are flexible; however, the endurance capability of UAV greatly limits its operation time. Recently, researches which try to enable UAVs working in persistent tasks have been drawn much attention.

It is a great challenge for the UAV/UGV collaboration system working in persistent tasks since UAVs have a short endurance. Previously, two kinds of methods are widely studied to improve the operation time of the UAV/UGV collaboration system in the literature; the first kind of method is to set recharging stations for UAVs in the environment to improve the endurance of UAVs; in this case, UAVs are required to visit recharging stations periodically and be replenished by battery swapping systems; for the second type of method, UGVs are used as mobile recharging stations, and UAVs need to be replenished by rendezvousing with a UGV periodically.

The problem of path planning for UAV/UGV collaboration systems has been widely investigated in existing literatures. Sunder and Rathinam [1] deployed multiple depots (charging stations) in the environment to refuel one UAV working in monitoring applications, the mixed integer linear programming (MILP) model is presented, and a local search heuristic was proposed for resolving the problem. [2] considered multi-UAVs and charging stations in the working scenario, and the problem is transformed into a generalized traveling salesman problem (GTSP) and then resolved by a GTSP solver.

Different from [1, 2], mobile robots were utilized in some literatures instead of using charging depots, and Maini and Sujit [3] proposed a model named FCURP-MRS which ensures that UAVs can be recharged by UGVs by generating UGV paths and UAV paths, respectively. [4–6] studied the path planning problem for mobile charging robots. In [4, 5], multiple working robots and one charging robot were considered in the problem, and the problem is resolved by using both dynamic programming and local search heuristics. In [6], the authors studied the single charging cycle problem and multirobot charging problem, and they

proposed the integer linear programming method and multi-robot Noon-Bean transformation to solve the problem, respectively.

Multiobjective path planning for the UAV/UGV collaboration system working in persistent tasks has been seldom studied in the previous related works while there exist a lot of researches on multiobjective path planning for robots, such as [7–12]. In [7, 10], NSGA-II which was introduced in [13] was used to obtain the Pareto front of the multiobjective path planning problem. Zhu et al. [8] proposed two multiobjective memetic algorithms (MOMAs) for the wheeled robot path planning problem, and the algorithm was evaluated in both simulation and real environment. In [9], the authors developed a new multiobjective optimization algorithm which is called the multiobjective firefly algorithm (MO-FA) to resolve a path planning problem which has three objectives. In [12], a local search heuristic was hybrid with SPEA2 to find the efficient solutions of the presented problem.

Researches on the combinatorial multiobjective problems (CMOPs) have a significant contribution to the study of multiobjective path planning, especially for scheduling problems. Heuristic algorithms have been widely studied for approximating the Pareto front of CMOPs because it is usually NP-hard to find the exact Pareto front of a CMOP. The Pareto local search (PLS) is one of the efficient algorithms for resolving CMOPs, and it is an extension of a single-objective local search [14]. Lust and Teghem [15] proposed 2PPLS, and it is a variant of PLS which consists of two phases of PLS in the algorithm. Based on PLS, various meta-heuristics have been proposed; in [16], the authors combined the idea of PLS and MOEA/D, and the proposed algorithm MOMAD contains three populations which represent subproblem solutions, PLS solutions, and external solutions, respectively. [17] proposed the Grid Weighted Sum Pareto Local Search (GWS-PLS), its main contribution is using the grid Pareto dominance instead of the Pareto dominance, and the grid Pareto dominance method enables the algorithm to adapt to both concave and convex problems; results show that GWS-PLS performs well in the multiobjective traveling salesman problem and multiobjective knapsack problem. Recently, [18–20] studied the multiobjective adaptive large neighborhood search (MOALNS), which is a heuristic algorithm based on the single objective of the adaptive large neighborhood search. In [21], the authors proposed MOALNS/D which is an improved version of MOALNS by combining the idea of decomposition with MOALNS.

In this paper, we mainly focus on multiobjective path planning for UAV/UGV collaboration systems working in persistent tasks; as mentioned above, the present related works often have the following shortcomings: firstly, path planning for charging robots was focused on while seldom works considered both replenishment robots and UAVs; secondly, the charging robots were only considered mobile charging stations while these robots can also complete other tasks; and thirdly, the single objective was considered in previous works while the decision-maker may need to tradeoff multiobjectives when planning paths for path planning for UAV/UGV collaboration systems.

In this paper, we firstly present a new scheduling problem and then propose an efficient algorithm for resolving the problem. The contributions of our work are shown as follows:

- (1) The problem is formulated as mixed integer linear programming, and planning paths for UAVs and UGVs simultaneously as well as UGVs have multi-task points to visit
- (2) The presented mathematical model is a biobjective optimization problem, which is firstly considered in this filed as far as we have known
- (3) A memetic algorithm which combines PLS and MOALNS is proposed for resolving the presented path planning problem
- (4) To resolve the problem efficiently, several heuristics and the local search procedure are developed for the algorithm

The remainder of the paper is organized as follows. In Section 2, we formally define the problem, and the corresponding mathematic model is presented. In Section 3, we present the framework of the proposed algorithm as well as the initialization method, solution representation, operators for the presubsolution, and proposed Hybrid Pareto Local Search (HPLS). In Section 4, we give details on MOALNS in HPLS, which contains five removal heuristics and three insertion heuristics. In Section 5, we implement the proposed algorithm for the presented problem and compare it with three other algorithms. In Section 6, we provide conclusions and avenues for future research.

2. Problem Statement

The problem we addressed in this paper is a combinatorial optimization problem, and we define and formulate it as follows.

Given a set of UAV and UGV working points, denote them as V_u and V_g , respectively; the number of UAVs and UGVs are M and N , respectively; UAVs have a fixed velocity of v_u while the maximum velocity of UGVs is v_{\max} , and UAVs have the maximum endurance of T_c , which means that all UAVs need to be replenished by UGVs periodically. A solution of the problem consists of paths of UAVs and UGVs, and two objectives, total length and makespan, should be optimized simultaneously to obtain an external set which contains a set of efficient solutions. The UAV and UGV paths should meet the following conditions: each UAV working point should be visited exactly once by any UAV, and according to the planned UAV path, all recharging points and the corresponding time will be generated, UGVs need to visit each UGV working point exactly, and also all recharging points should be visited by UAV before the UAV runs out of energy. Other notations used for the mathematical model are given as follows:

v_u^k : the k th UAV working point, where $k \in \{1, \dots, K\}$ and $V_u = \bigcup_{1 < k < K} v_u^k$ is the set of all UAV working points

v_g^h : the h th UGV working point, where $h \in \{1, \dots, H\}$ and $V_g = \bigcup_{1 < h < H} v_g^h$ is the set of all UGV working points

x_{ijm} : a binary variable which equals to 1 if the m th UAV travels from the i th UAV working point to the j th UAV working point and 0 if otherwise

$x_{i'j'n}$: a binary variable which equals to 1 if the n th UGV travels from the i' th UGV working point to the j' th working point and 0 if otherwise

c_{ij} : the Euclidean distance between the i th UAV working point and j th UAV working point

$c_{i'j'n}$: the Euclidean distance between the i' th UGV working point and j' th UGV working point

p_u^m : the m th UAV path, where $m \in \{1, \dots, M\}$ is the index of UAV

p_g^n : the n th UGV path, where $n \in \{1, \dots, N\}$ is the index of UGV

$t(v_c)$: the recharging time of v_c

τ_n^l : the l th recharging point in the n th UGV path, where $l \in \{1, \dots, L(n)\}$, $L(n)$ is the number of recharging points in p_g^n , and $V_c = \bigcup_{1 \leq n \leq N} \bigcup_{1 \leq l \leq L} \tau_n^l$ is the set of all recharging points

The formal definition of the problem is as follows: let $G_1 = (V_u, E_u, c)$ be an undirected graph, the problem is to find a path p_u , which contains M subpaths: p_u^m , and each sub-path has the same start position: v_u^1 ; meanwhile, for each vertex in $V_u \setminus v_u^1$, it should be visited exactly once by p_u . For the M subpaths, the set of recharging vertices V_c can be obtained by considering T_c , and let $G_2 = (V_g \cup V_c, c')$ be another undirected graph, finding a path p_g which contains N subpaths: p_g^n , and the start vertex of each subpath is v_g^1 ; in addition, each vertex in $V_g \cup V_c \setminus v_g^1$ should be visited by p_g exactly once, and the arrival time of each vertex in V_c should be less than its corresponding recharging time. A solution of the problem is composed of p_u and p_g . The optimization problem is biobjective; furthermore, the minimization of total length implies reducing the sum of the length of p_u and p_g , and the minimization of makespan implies reducing the time consumption of the UAV/UGV collaboration system.

The subsegment in one postsubsolution can be described as follows: for a postsubsolution p_g^m , its subsegments can have two cases: (1) the path formed between two adjacent recharging points and (2) the path between the last recharging point and the end of p_g^m . Figure 1 shows an example of the subsegment, in which s_{nz} denotes the z th subsegment in the n th UGV path; then, the length of subsegment s_{nz} is

$$l_n^z = \sum_{i=1}^{|s_{nz}|-1} c(s_{nz}^i, s_{nz}^{i+1}). \quad (1)$$

There have been two objectives in the proposed problem: path length and makespan. For the objective function of length cost L , it contains two components: L_u and L_g , which

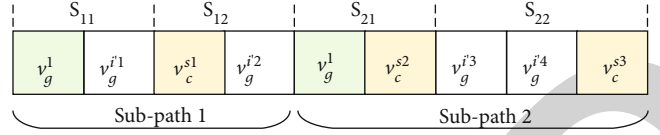


FIGURE 1: An example of the subsegments in the postsubsolution.

represent the length of UAV paths and the length of UGV paths, respectively, and the effect of the objective of makespan is to minimize the maximum working time of UAVs and UGVs. The two objectives can be, respectively, formulated as the following two equations.

$$\min \left(\sum_{m=1}^M L_u^m + \sum_{n=1}^N L_g^n \right), \quad (2)$$

$$\min \max \{ T_u^m, T_g^n \}, \quad (3)$$

where L_u^m and L_g^n represent the length of p_u^m and p_g^n , respectively, and T_u^m and T_g^n denote the makespan of p_u^m and p_g^n , respectively. L_u^m , L_g^n , T_u^m , and T_g^n can be calculated according to

$$L_u^m = \sum_{i=1}^K \sum_{j=1}^K c_{ij} x_{ijm}, \quad (4)$$

$$L_g^n = \sum_{i'=1}^H \sum_{j'=1}^H c_{i'j'n} x_{i'j'n}, \quad (5)$$

$$T_u^m = \frac{L_u^m}{v_u}, \quad (6)$$

$$T_g^n = t_n^{s(n)} + \sum_{e \in E_{p(n)}} c(e). \quad (7)$$

The objective functions are subjected to the following constraints:

$$\sum_{m=1}^M \sum_{i=1}^K x_{ijm} = 1, \quad \forall j \in \{2, \dots, K\}, \quad (8)$$

$$\sum_{m=1}^M \sum_{j=2}^K x_{ijm} = 1, \quad \forall j \in \{1, \dots, K\}, \quad (9)$$

$$\sum_{n=1}^N \sum_{i'=1}^{H+L} x_{i'j'n} = 1, \quad \forall j' \in \{2, \dots, H+L\}, \quad (10)$$

$$\sum_{n=1}^N \sum_{j'=2}^{H+L} x_{i'j'n} = 1, \quad \forall i' \in \{1, \dots, H+L\}, \quad (11)$$

$$t_n^s - t_n^{s-1} \leq T_c, \quad \forall n \in \{1, \dots, N\}, \forall s \in \{1, \dots, s(n)\}, \quad (12)$$

$$x_{ijm} = 1, \quad \forall i \in \{1, \dots, K\}, \forall j \in \{1, \dots, K\}, \forall m \in \{1, \dots, M\}, \quad (13)$$

$$x_{i'j'n} = 1, \quad \forall i \in \{1, \dots, K\}, \forall j \in \{1, \dots, K\}, \forall n \in \{1, \dots, N\}. \quad (14)$$

where equations (8) and (9) can guarantee that the edge that enters each node in V_u is selected and the edge that leaves each node in V_u is selected, respectively. Equations (10) and (11) make sure that every node in $V_g \cup V_c$ is selected to be visited exactly. Equation (12) implies that the solution should meet the constraint of recharging time windows; i.e., the time interval between two adjacent recharging points in the path shall not exceed the maximum interval T_c . Equation (13) formulates the domain of variable x_{ijm} , which expresses whether the m th UAV travels from v_u^i to v_u^j or not; similarly, equation (14) expresses whether the n th UGV travels from $v_g^{i'}$ to $v_g^{j'}$ or not.

3. Proposed Approach

In this section, the structure of the solution is presented firstly, and then, the framework of MOALP and operators for the presubsolution are given.

3.1. Solution Representation. The structure of the solution is shown in Figure 2, and it can be seen from the figure that the solution of the problem consists of two components: UAV path and UGV path, and v_u^1 and v_g^1 are the UAV start point and UGV start point, respectively; both UAV and UGV paths are composed of several subpaths, and every subpath is corresponding to a robot path; furthermore, the length of the UAV path is fixed at $M + K - 1$, and the UGV path length is not fixed since the recharging point set is determined by the UAV path.

3.2. Framework of MOALP. The proposed algorithm in this paper integrates the multiobjective adaptive large neighborhood search (MOALNS) into the PLS framework, and it is called multiobjective ALNS hybrid with PLS (MOALP); the detail of MOALP is shown in Algorithm 1.

Similar to MOMAD [16], MOALP maintains three populations during the optimization process, which are as follows:

- (1) P_p : the population will be undergone PLS
- (2) P_L : this population contains the solutions corresponding to subproblems
- (3) P_E : the external population contains all nondominated solutions found so far

3.3. Initialization. The initialization method for the postsolution is as follows: first of all, a temporary initial postsolution is set by random initialization; then, a reinforcement procedure for the postsolution which is shown in Figure 3 is applied in the temporary set to improve the number of feasible solutions in the initial set. The solution reinforcement

proposed in this paper is based on the following two facts: firstly, given a postsolution, recharging points are sequential for each UGV path, and secondly, in a UGV path, the distance of two adjacent recharging points is less than D_{\max} , where $D_{\max} = v_{\max}(t(\tau_n^{l+1}) - t(\tau_n^l))$.

The operators which are proposed for resolving the multiple travelling salesman problem are used to generate presubolutions, and in this paper, we use the PMX crossover operator and single-point mutation operator as the variation operators to generate presubolutions.

3.4. PLS Hybrids with MOALNS (HPLS). MOALNS is hybrids with PLS to resolve the presented combinatorial multiobjective optimization problem in this paper, and it is called Hybrid PLS (HPLS). The framework of HPLS is shown in Algorithm 2.

In HPLS, P_p refers to the population which will undergo HPLS; different from PLS, we here use the presented MOALNS as the local search heuristics. Once a postsolution p_g^i was input into MOALNS, a temporary set called P_T will be produced, where P_T is an efficient set for the input postsolution p_g^i ; the external set P_E will be updated by P_T during every iteration. MOALNS can be regarded as the problem-specific multiobjective local search for HPLS, while PLS often adapts a problem-specific single-objective local search heuristic.

4. MOALNS for the Postsolution

MOALNS is adopted as the solver for obtaining the postsolution, and its framework is shown in Algorithm 3. It is obvious that MOALNS is an extension of a single-objective ALNS [21].

Similar to ALNS, several different removal and insertion heuristics can be applied in the algorithm; in this work, we propose the following removal and insertion heuristics for MOALNS.

4.1. Removal Heuristics. The removal heuristics developed in this paper can be divided into two different types: removal heuristics for UGV working points and removal heuristics for recharging points. UGV working points and recharging points will be omitted to WP removal and CP removal, respectively, in the rest of the paper.

- (1) WP worst removal

Given a UGV working point $u_j \in p_g \setminus (V_c \cup v_g^1)$ which is served by the n th UGV in a postsolution p_g^n , we define the cost of the vertex u_j as r_j , and r_j can be calculated by the following equation:

$$r_j = c(u_{j-1}) + c(u_j, u_{j+1}) - c(u_{j-1}, u_{j+1}), \quad (15)$$

where $u_{j+1} \neq v_a^1$ and $r_j = c(u_{j-1}, u_j)$ when $u_{j+1} = v_a^1$; then, the WP which has the highest cost will be removed from the postsolution according to the following equation:

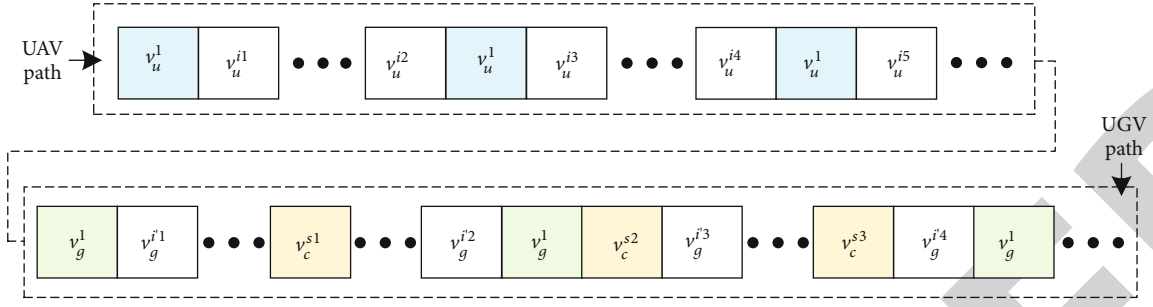


FIGURE 2: Structure of the solution.

Require: an instance; number of subproblems: N ; set of reference vectors $\lambda_1, \dots, \lambda_N$.
 Ensure: P_E
 1: Initialization ($N \downarrow, P_L \uparrow, P_P \uparrow, P_E \uparrow, \lambda \uparrow$)
 2: repeat
 3: HPLS ($P_P \downarrow, P_E \downarrow, P_L \downarrow$)
 4: for $k \in \{1, \dots, N\}$ **do**
 5: select_pop ($k \downarrow, P_L \downarrow, p^1 \uparrow, p^2 \uparrow$)
 6: PMX ($p^1 \downarrow, p^2 \downarrow, p_a \uparrow$)
 7: generate_pg ($p_a \downarrow, p_g \uparrow$)
 8: MOALNS/D ($p^a \downarrow, p^g \downarrow, P_T \uparrow, P_E \downarrow$)
 9: update ($P_T \downarrow, P_P \downarrow$)
 10: updateD ($P_T \downarrow, P_P \downarrow, \lambda \downarrow$)
 11: end for
 12: **until** stopping criteria was met

ALGORITHM 1: Framework of MOALP.

$$\arg \min_{1 \leq j \leq |p_g^n|} r_j. \quad (16)$$

(2) WP random removal

The WP random removal simply selects a UGV working point at random and removes it from the postsubsolution.

(3) WP segment removal

In this heuristic, a segment is randomly selected and removed from the current postsubsolution p_g ; this heuristic is inspired by the segment removal developed in [22], which was used for resolving the generalized traveling salesman problem.

(4) CP worst removal

Given a postsubsolution p_g , considering the j th recharging point in the postsubsolution p_g^n , where $n \in \{1, \dots, N\}$ and $j \in \{1, \dots, s(n)\}$, the removal cost of u_n^j is defined as the sum of r_n^j and d_n^j , where r_n^j and d_n^j represent the cost of length and time constraint penalty, respectively. For a recharging point τ_n^j in p_g^n , its cost of length is defined as $r_n^j = c(\tau_n^{j-1}, \tau_n^j)$

+ $c(\tau_n^j, \tau_n^{j+1}) - c(\tau_n^{j-1})$, where $j \neq L(n)$ and $r_n^j = c(\tau_n^{j-1}, \tau_n^j)$ when $j = L(n)$.

The cost of the time constraint of vertex τ_n^j is defined as $d_n^j = p(\tau_n^{j-1}, \tau_n^j) + p(\tau_n^j, \tau_n^{j+1}) - p(\tau_n^{j-1}, \tau_n^{j+1})$, where $j \neq L(n)$ and $d_n^j = p(\tau_n^{j-1}, \tau_n^j)$ when $j = L(n)$; $p(x, y)$ is a penalty function which is defined as the following equation.

$$p(x, y) = \begin{cases} 1, & \frac{c(x, y)}{v_{\max}} > t(x) - t(y), \\ 0, & \frac{c(x, y)}{v_{\max}} \leq t(x) - t(y). \end{cases} \quad (17)$$

The recharging point which would be removed can be found by calculating the following equation:

$$\arg \min_{1 \leq n \leq N} \min_{1 \leq j \leq L(n)} \beta d_n^j + r_n^j, \quad (18)$$

where $L_n^n < \beta < +\infty$ is a weight parameter. The positive effects of the calculation method of the cost for this heuristic are twofold: firstly, the existence of βd_n^j can make sure that the adjacent recharging points meet the recharging time window constraint, so the feasibility of the postsubsolution can be ensured during iterations. Furthermore, by considering r_n^j in the removal cost, not only can the total length of

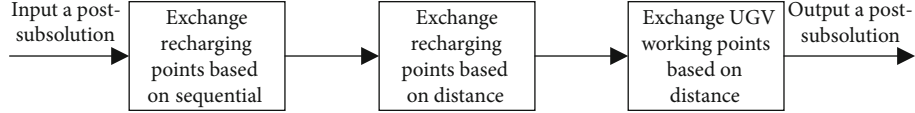


FIGURE 3: Solution reinforcement.

Require: P_p, P_E
Ensure: P_p, P_E
 1: $P = P_p$
 2: **while** $P \neq \emptyset$ **do**
 3: $P_a = \emptyset$
 4: **for** $s \in P$ **do**
 5: MO – ALNS($P_g^{\downarrow}, P_T^{\uparrow}$)
 6: update($P_E^{\uparrow}, P_T^{\uparrow}$)
 7: update($P_a^{\downarrow}, P_T^{\downarrow}$)
 8: **end for**
 9: **end while**

ALGORITHM 2: HPLS.

postsubsolution be decreased but also the makespan of it can be reduced since there will be more time redundancy for UGVs to visit UGV working points.

(5) CP random removal

Similar to the WP random removal, one recharging point in p_g will be selected and removed randomly in the CP random removal.

4.2. Insertion Heuristics. Two insertion heuristics for WP insertion and one insertion heuristic for CP insertion are proposed to insert WP or CP into the postsubsolution.

(1) WP cheapest insertion

Given a partial postsubsolution p_g^n , the vertex $u \in V_g \setminus p_g$ which has the minimum insertion cost and insertion position can be obtained by minimizing

$$I^{nzj}(u) = c(s_{nz}^j, u) + c(u, s_{nz}^{j+1}) - c(s_{nz}^j, s_{nz}^{j+1}), \quad (19)$$

where s_{nz} means the z th subsegment in the n th UGV path and $z \in \{1, \dots, L(n) + 1\}$.

(2) WP nearest insertion

Given a partial postsubsolution p_g^n , we first calculate the distance between every $u \in V_g \setminus p_g$ and each subsegment s_{nz} according to

$$\text{dist}(u, s_{nz}) = \min_{v \in s_{nz}} c(u, v). \quad (20)$$

And then, the nearest insertion can be formulated as

$$\arg \min_{u \in V_g \setminus p_g} \min_{1 \leq n \leq N} \min_{1 \leq h \leq H(n)} \text{dist}(u, s_{nz}). \quad (21)$$

When the insertion vertex u and insertion subsegment I_n^z were obtained by using equation (21), the vertex would be inserted into the selected subsegment s_{nz} by using the cheapest insertion.

(3) CP unified worst insertion

Given a partial postsubsolution p_g^n , the insertion cost in this heuristic is the weighted sum of penalty for the recharging time window constraint I_T^{nzj} , recharging point insertion cost I_H^{nzj} , and total length cost I_L^{nzj} , where n, z, j represent the index of UGV, subsegment, and point in the subsegment, respectively.

The insertion cost for the recharging time window constraint is defined as $I_T^{nzj}(u) = p(\tau_n^{z-1}, u) + p(u, \tau_n^z)$, where $z \neq L(n) + 1, \forall j \in 1, \dots, |s_{nz}|$, and $I_T^{nzj}(u) = p(\tau_n^{z-1}, u)$ when $z = L(n)$. The factor of the recharging point insertion cost is $I_H^{nzj}(u) = c(\tau_n^{z-1}, u) + c(u, \tau_n^{z+1}) - c(\tau_n^{z-1}, \tau_n^{z+1})$, where $z \neq L(n) + 1, \forall j \in 1, \dots, |s_{nz}|$, and $I_H^{nzj}(u) = c(\tau_n^{z-1}, u)$ when $z = L(n) + 1$. The total length cost is $I_L^{nzj}(u) = c(s_{nz}^j, u) + c(u, s_{nz}^{j+1}) - c(s_{nz}^j, s_{nz}^{j+1})$, where $j \neq |s_{nz}|$, and $I_L^{nzj}(u) = c(s_{nz}^j, u)$ when $j = |s_{nz}|$. The total insertion cost for a charging point in this heuristic can be calculated by

$$I_a^{nzj} = \beta I_T^{nzj}(u) + \lambda_1 I_H^{nzj}(u) + \lambda_2 I_L^{nzj}(u), \quad (22)$$

where λ_1 and λ_2 are the weight of CP insertion length cost and path length cost, respectively, and the smaller λ_1 is, the more minimization of makespan is considered, and the smaller λ_2 is, the more minimization of path length is considered. In addition, $L_g^n < \beta + \infty$, and $\beta I_T^{nzj}(u)$ represents the constraint of recharging time windows. The CP which is to be inserted and the corresponding insertion position can be obtained according to the following equation.

$$\arg \min_{u \in V_c \setminus p} \min_{1 \leq n \leq N} \min_{1 \leq h \leq L(n)} \min_{1 \leq j \leq |s_{nz}|} I_a^{nzj}. \quad (23)$$

4.3. Local Optimization. Except for removal and insertion heuristics given above, a local optimization method is also developed to improve the performance of the local solution during every iteration, and it can be regarded as a procedure for recharging points to be reallocated based on the current postsubsolution. Given a postsubsolution p_g , the basic idea of local optimization is solution reconstruction which firstly removes all recharging points from the postsubsolution p_g^n and then inserts them into p_g again by means of the local reallocation method.

Require: A solution: p .
Ensure: A temporary efficient set: P_T

- 1: $x = p_g$
- 2: initialize($T \uparrow, c \uparrow, \omega \uparrow$)
- 3: **repeat**
- 4: $x' = x$
- 5: Randomly select a removal heuristic R , and remove several vertices from x by using R .
- 6: Randomly select an insertion heuristic I , and repair x by using I .
- 7: local_optimization(x)
- 8: acceptance_criteria($x' \downarrow, x \downarrow, accept \uparrow$)
- 9: if $accept == 0$ **then**
- 10: $P_T = [P_T, x]$
- 11: **end if**
- 12: **until** stop criteria was met

ALGORITHM 3: MOALNS for the postsubsolution.

TABLE 1: Relation between m and S .

Parameter	Description
δ_1	T_{new} is a nondominated solution in the solution set
δ_2	T_{new} is not dominated in the solution set but is nondominated in the current neighborhood
δ_3	T_{new} is not a nondominated solution, but it dominates the current solution
δ_4	T_{new} is not dominated or dominates the current solution and is accepted by the algorithm
δ_5	T_{new} is dominated by the current solution and is accepted by the algorithm

TABLE 2: Scenario configuration.

Index	UAV scenario			UGV scenario				
	1	2	3	1	2	3	4	5
Num WPs	8	14	20	8	12	16	20	24

The insertion cost for recharging points of local optimization contains three components: recharging time window constraint cost I_W^{nzj} , path length cost I_L^{nzj} , and makespan cost I_M^{nzj} , where n, z, j represent the index of UGV, subsegment, and point in the subsegment, respectively. In detail, I_W^{nzj} is defined as equation (24); $I_L^{nzj} = c(\tau_n^{j-1}, \tau_n^j) + c(\tau_n^j, \tau_n^{j+1}) - c(\tau_n^{j-1})$, where $j \neq L(n)$ and $r_n^j = c(\tau_n^{j-1}, \tau_n^j)$ when $j = L(n)$; $I_M^{nzj} = (I_L^{nzj}(u))/v_{max}$ where $z = L(n) + 1$, $T_n + (I_L^{nzj}(u))/v_{max} > T_{max}$, and otherwise $I_M^{nzj} = 0$.

$$I_W^{nzj}(u) = \begin{cases} \infty, & \frac{I_n^z + I_L^{nzj}(u)}{v_{max}} > t(\tau_n^{z-1}) - t(\tau_n^z), \\ 0, & \frac{I_n^z + I_L^{nzj}(u)}{v_{max}} \leq t(\tau_n^{z-1}) - t(\tau_n^z). \end{cases} \quad (24)$$

The total insertion cost of local optimization is $I_o^{nzj} = I_W^{nzj}(u) + \epsilon I_L^{nzj}(u) + (1 - \epsilon) I_M^{nzj}(u)$, where $0 \leq \epsilon \leq 1$ is a coefficient which is used to tradeoff the path length and makespan by changing the value of ϵ . The total insertion cost is minimized to select the insertion point and position as defined in the following equation.

$$\arg \min_{u \in V_c \setminus p_g} \min_{1 \leq n \leq N} \min_{1 \leq h \leq L(n)} \min_{1 \leq j \leq |s_{nz}|} I_o^{nzj}. \quad (25)$$

4.4. Weight-Adaptive Approach, Acceptance Criteria, and Stopping Criteria. In MOALNS, the score of heuristics is updated during every iteration, and in this paper, we use the weight-adaptive approach in accordance with [23], and particularly, five different senses are considered when updating the score of insertion and removal heuristics, which is shown in Table 1, and $\delta_1 > \delta_2 > \delta_3 > \delta_4 > \delta_5$ is ensured. The standard simulated annealing is adopted as the search framework of the proposed MOALNS, and the acceptance criterion is as follows:

$$P_{accept} = \min \left\{ e^{\frac{f(s') - f(s)}{T}}, 1 \right\}, \quad (26)$$

where T is the temperature and its initial value is set to be T_{init} ; T is updated in every iteration of the algorithm as shown in equation (27), where c is the cooling rate.

$$T_{i+1} = T_i - cT_i. \quad (27)$$

The stopping criterion of MOALNS is as follows: the temperature will be reheating if no improvement is made to the current solution after the first R_1 iterations, and MOALNS ends if no improvement is made to the current solution after the first R_2 iterations. And no improvement is that the new solution cannot dominate the current solution.

5. Experimental Results

5.1. Performance Metrics

- (1) Set coverage (C-metric) [16]: let A and B be two efficient sets of an MOP; $C(A, B)$ is defined as the

TABLE 3: Parameter configuration of MOALP and the compared algorithms.

Parameter	ϵ	λ_1	λ_2	γ_1	γ_2	R_1	R_2	σ_1	σ_2	σ_3	σ_4	σ_5
Value	0.1	(0.3, 0.4)	0.3	0.5	0.05	$2N_c$	$5N_c$	10	7	5	3	2

TABLE 4: Coverage values (%) between MOALP and MOALNS, MOMAD, and PLS on the problem.

Instance	MOALNS		MOMAD		PLS	
	$C(A, B)$	$C(B, A)$	$C(A, B)$	$C(B, A)$	$C(A, B)$	$C(B, A)$
1-1-2-2	76.7	20.0	65.0	33.3	77.0	16.7
1-2-2-2	72.0	28.0	20.0	56.0	68.7	0.0
1-3-3-4	60.0	16.1	65.7	17.8	51.4	4.0
1-4-2-3	49.3	27.5	51.3	33.5	75.3	14.0
1-5-2-3	67.1	15.4	63.0	4.0	90.0	0.0
2-1-2-3	63.3	13.3	80.0	0.0	100.0	0.0
2-2-2-2	26.7	30.0	50.0	16.9	90.0	6.7
2-3-3-4	24.7	20.0	69.3	0.0	93.3	0.0
2-4-3-4	71.8	10.7	76.7	0.0	96.7	0.0
2-5-2-4	73.3	25.0	90.0	0.0	100.0	0.0
3-1-2-3	56.5	26.7	100.0	0.0	100.0	0.0
3-2-3-4	25.0	20.7	90.0	0.0	95.0	0.0
3-3-2-4	44.0	50.0	100.0	0.0	100.0	0.0
3-4-2-3	60.0	33.0	100.0	0.0	100.0	0.0
3-5-3-5	40.0	13.6	100.0	0.0	96.7	0.0

TABLE 5: Hypervolume values of MOALP, MOALNS, MOMAD, and PLS.

Instance	MOALP	MOALNS	MOMAD	PLS
1-1-2-2	1.526E+07	1.126E+07	1.876E+07	1.034E+07
1-2-2-2	2.323E+07	0.964E+07	1.720E+07	1.433E+07
1-3-3-4	3.312E+07	3.182E+07	3.284E+07	2.290E+07
1-4-2-3	2.769E+07	2.735E+07	1.869E+07	1.855E+07
1-5-2-3	2.417E+07	2.183E+07	1.863E+07	0.986E+07
2-1-2-3	0.840E+08	1.265E+08	0.408E+08	0.357E+08
2-2-2-2	1.617E+08	0.955E+08	0.937E+08	0.295E+08
2-3-3-4	2.810E+08	2.247E+08	0.907E+08	1.218E+08
2-4-3-4	1.952E+08	1.700E+08	0.796E+08	0.629E+08
2-5-2-4	2.112E+08	1.421E+08	0.351E+08	0.794E+08
3-1-2-3	4.848E+08	6.202E+08	0.563E+08	0.655E+08
3-2-3-4	8.900E+08	5.962E+08	1.090E+08	1.549E+08
3-3-2-4	4.435E+08	3.711E+08	0.762E+08	0.593E+08
3-4-2-3	7.478E+08	5.425E+08	0.895E+08	1.241E+08
3-5-3-5	4.353E+08	4.451E+08	1.209E+08	0.948E+08

TABLE 6: Running time (s) of MOALP, MOALNS, MOMAD, and PLS.

Instance	MOALP	MOALNS	MOMAD	PLS
1-1-2-2	16	16	7	28
1-2-2-2	19	17	7	31
1-3-3-4	30	21	11	45
1-4-2-3	30	23	10	53
1-5-2-3	36	29	14	62
2-1-2-3	47	44	36	137
2-2-2-2	47	38	17	103
2-3-3-4	77	59	47	173
2-4-3-4	72	67	45	182
2-5-2-4	98	92	67	292
3-1-2-3	100	86	217	475
3-2-3-4	130	100	110	508
3-3-2-4	157	121	211	818
3-4-2-3	146	110	172	555
3-5-3-5	211	168	558	954

percentage of the solutions in B that are dominated by at least one solution in A ; that is,

$$C(A, B) = \frac{|\{u \in B | \exists v \in A : v \text{ dominates } u\}|}{|B|}. \quad (28)$$

- (2) Hypervolume (HV) [16]: let $r = (r_1, r_2, \dots, r_m)^T$ be a reference point in the objective space which is dominated by all solutions in a PF approximation S . HV(S) indicates the volume of the region in the objective space which is dominated by S and dominates r .

$$HV(S) = \text{volume} \left(\bigcup_{x \in S} [f_1(x), r_1] \times \dots \times [f_m(x), r_m] \right). \quad (29)$$

5.2. *Test Instances.* Since the problem presented in this paper is a new problem in the literature and there are no established benchmark sets yet, we developed some instances for computational studies to test our proposed algorithm. Three different UAV working senses and five UGV working senses were generated, and the details of the tested instances are shown in Table 2.

15 instances were developed by combining UAV and UGV scenarios, and based on these instances, velocity of UAV (v_u), maximum velocity of UGVs (v_{\max}), number of UAVs (M), and number of UGVs (N) were set, and

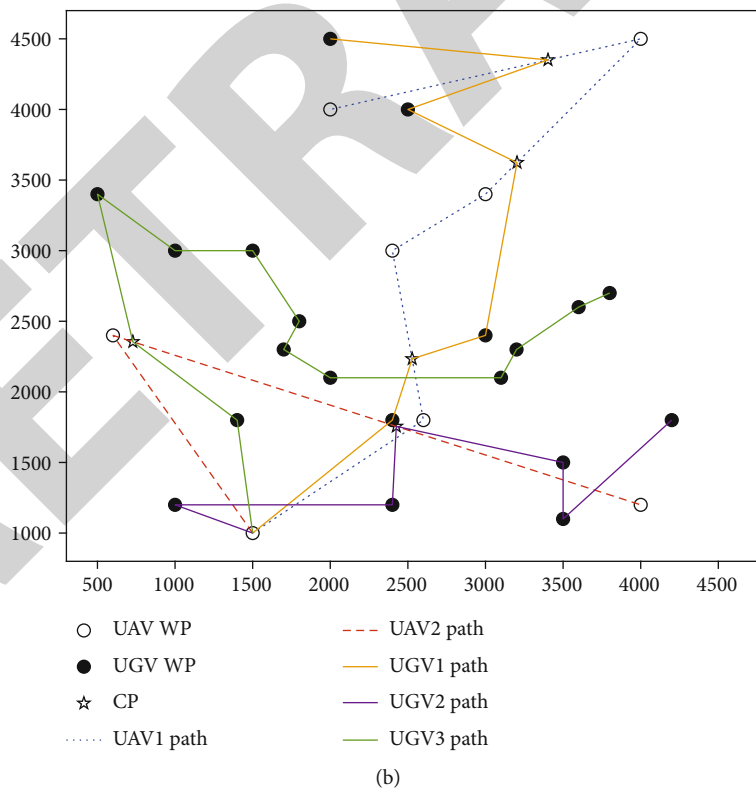
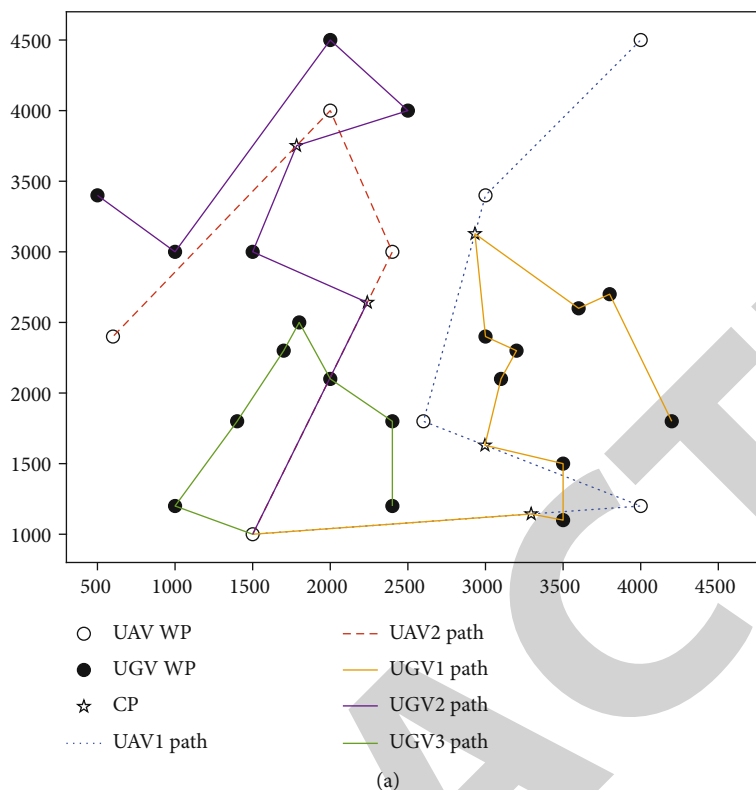


FIGURE 4: Continued.

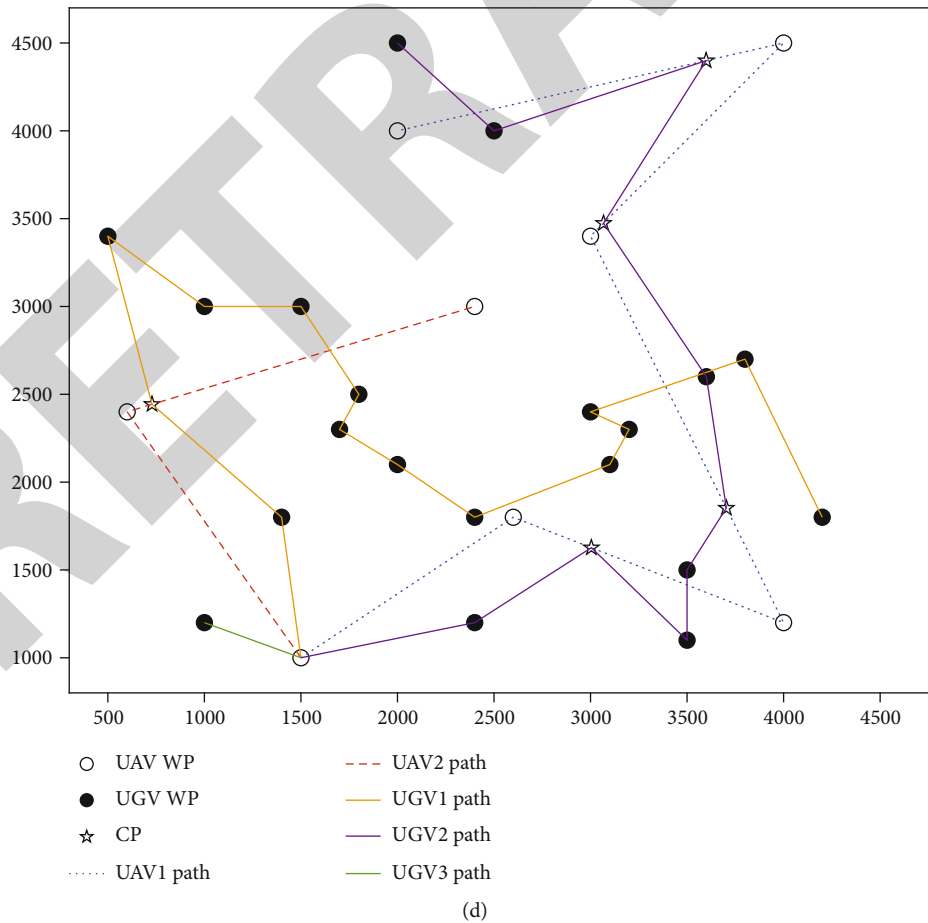
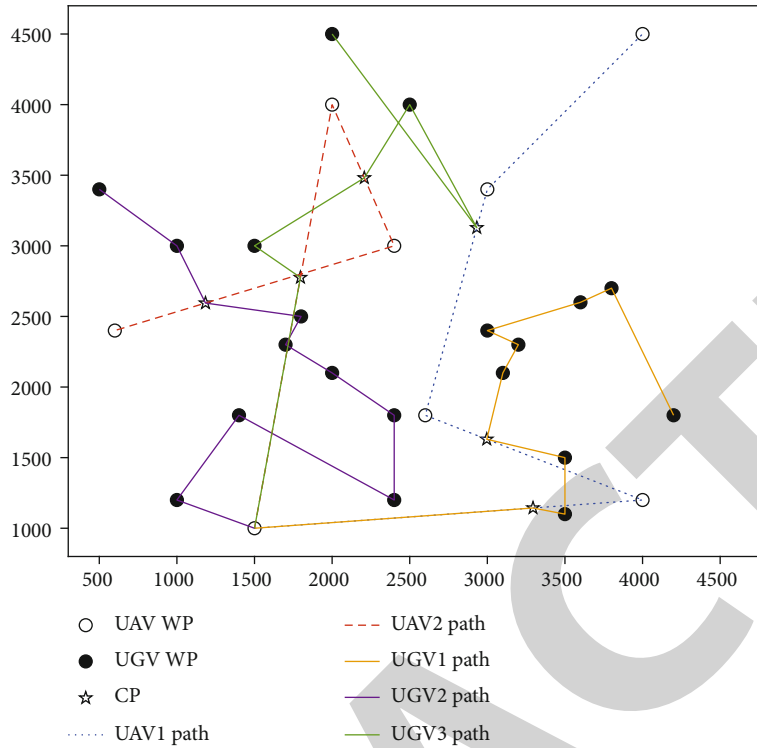


FIGURE 4: Nondominated solutions resolved by MOALP: (a) nondominated solution 1, (b) nondominated solution 2, (c) nondominated solution 3, and (d) nondominated solution 4.

particularly, $v_u = 2 \text{ m/s}$ and $v_{\max} = 2 \text{ m/s}$ were ensured. An example of instance is like 1-5-2-3, which means using UAV scenario 1 and UGV scenario 5; the number of UAVs and UGVs is 2 and 3, respectively.

5.3. Compared Algorithms. To show the performance of MOALP, we compare it with three other algorithms.

- (1) PLS [15]: this algorithm is designed for combinatorial MOP, and an external set and search set are maintained in the algorithm. In this paper, we use PMX to generate the neighborhood of the presubsolution, and then, local search heuristics proposed in this paper are integrated with PLS to find the efficient set of postsubolutions
- (2) MOMAD [16]: this algorithm is a memetic algorithm which is based on the framework of PLS, and it uses the idea of decomposition to improve the diversity of the attained PF. In the simulation experiments of this work, we implemented the framework of MOMAD and integrated local search heuristics with MOMAD to be adaptive to the problem presented in this paper
- (3) MOALNS [20]: multiobjective adaptive large neighborhood search (MOALNS) is an extension of ALNS in multiobjective optimization, its major components include solution destroy, solution repair, weight adaptive, solution acceptance. In this paper, we use a standard Simulated Annealing (SA) as the optimization framework, as well as the proposed removal and insertion heuristics, and also, PMX is implemented to generate the neighborhood of presubsolution.

5.3.1. Parameter Setting. For MOALP, PLS, MOMAD, and MOALNS, we set the size of PL to be 50, and the number of working points to be removed is $\text{rand}[0.2H, 0.3H]$, where H is the total number of working points. The number of recharging points to be removed is $\text{rand}[0.2H, 0.4H]$, where N_c is the total number of recharging points in the current solution. Table 3 shows the parameter setting of MOALP, where λ_1 has two values: 0.3 and 0.4, which means there exists two insertion heuristics for recharging points, while there have been two insertion heuristics for working points; four insertion heuristics are implemented in the algorithm since we combine a working point insertion with a recharging point insertion heuristic as one integral insertion heuristic; similarly, there have been 6 removal heuristics since three working removal and two recharging removal heuristics are implemented in the algorithm.

5.4. Results. Each algorithm runs independently for 5 times, and we use the average of indicators as the compared data resource. The C -metric values of all the comparisons on each instance are reported in Table 4. The hypervolume values of the efficient sets produced by these algorithms are plotted in Table 5. The average running time consumed by these algorithms is given in Table 6.

MOALP outperforms PLS on all test instances in the C -metric, and on 11 out of 15 test instances, $C(A, B)$ equals to 0.0% which means that solutions in the efficient set obtained by PLS cannot dominate that of MOALP at least once. MOALP has the better C -metric than MOMAD except for 1-2-2-2, and when compared with MOALNS, MOALP performs better than MOALNS on 13 out of 15 instances; furthermore, on 11 test instances, the C -metric of MOALP is more than 10% higher than that of MOALNS.

On 11 out of 15 test instances, the hypervolume values of MOALP are shown in Table 5; it can be seen that MOALP performs better than all compared algorithms, and except for instances 2-1-2-3, 3-1-3-2, and 3-5-3-5, MOALP outperforms MOALNS in the hypervolume indicator.

Regarding the running time, the average running time consumed by MOALP is lower than that of PLS, and compared with MOMAD, the running time of MOALP is shorter on large-scale instances, and PLS runs for the longest time in all test instances.

In Figure 4, four nondominated solutions resolved by our proposed algorithm MOALP are presented, and it can be seen that UAVs and UGVs can work collaboratively to enable them work in persistent tasks.

5.5. Result Visualization. Figure 4 shows four nondominated solutions of instance 1-4-2-3, obtained by using MOALP; we can see that there exist two UAV paths and three UGV paths in the solution; also, the start point of UGV is (1000, 1500); the objectives of the four solutions are $[2.548E + 04, 4489]$, $[2.696E + 04, 4433]$, $[2.798E + 04, 4264]$, and $[2.969E + 04, 3505]$, respectively.

6. Conclusions and Future Work

In this paper, we propose a multiobjective UAV/UGV collaboration path planning problem, which firstly considers multitasks for UGVs in persistent tasks. To resolve the presented problem, MOALP is proposed. The core of the algorithm is the hybridization of the Pareto local search and multiobjective large neighborhood search, and for the MOALNS in MOALP, we develop a mechanism for removal and insertion heuristics, which contains several removal and insertion heuristics for UGV working points and recharging points; besides, a local optimization method is also implemented after each iteration of MOALNS to improve the performance of the algorithm. The experiments have been conducted to verify MOALP. The comparisons of MOALP with three other algorithms (PLS, MOMAD, and MOALNS) show the efficiency of MOALP in 15 instances.

An important avenue of the proposed algorithm for future work is to extend MOALP to resolve more CMOPs, such as mTSP and mKP, and it also can be used to resolve more problems in applications of UAV/UGV collaborative systems.

Data Availability

Data sharing is not applicable to this article as no datasets were generated or analysed during the current study.

Retraction

Retracted: Research on Efficient Deep Learning Algorithm Based on ShuffleGhost in the Field of Virtual Reality

Wireless Communications and Mobile Computing

Received 28 November 2023; Accepted 28 November 2023; Published 29 November 2023

Copyright © 2023 Wireless Communications and Mobile Computing. This is an open access article distributed under the Creative Commons Attribution License, which permits unrestricted use, distribution, and reproduction in any medium, provided the original work is properly cited.

This article has been retracted by Hindawi, as publisher, following an investigation undertaken by the publisher [1]. This investigation has uncovered evidence of systematic manipulation of the publication and peer-review process. We cannot, therefore, vouch for the reliability or integrity of this article.

Please note that this notice is intended solely to alert readers that the peer-review process of this article has been compromised.

Wiley and Hindawi regret that the usual quality checks did not identify these issues before publication and have since put additional measures in place to safeguard research integrity.

We wish to credit our Research Integrity and Research Publishing teams and anonymous and named external researchers and research integrity experts for contributing to this investigation.

The corresponding author, as the representative of all authors, has been given the opportunity to register their agreement or disagreement to this retraction. We have kept a record of any response received.

References

- [1] B. Huang, H. Zhang, Z. Chen, L. Li, and L. Shi, "Research on Efficient Deep Learning Algorithm Based on ShuffleGhost in the Field of Virtual Reality," *Wireless Communications and Mobile Computing*, vol. 2021, Article ID 1382781, 11 pages, 2021.

Research Article

Research on Efficient Deep Learning Algorithm Based on ShuffleGhost in the Field of Virtual Reality

Bangtong Huang,^{1,2} Hongquan Zhang³, Zihong Chen,⁴ Lingling Li,⁵ and Lihua Shi¹

¹School of Management, Shanghai University of Engineering Science, China

²Key Lab of Information Network Security, The Third Institute of Ministry of Public Security, China

³Department of Computer Science and Engineering, The Chinese University of Hong Kong, China

⁴College of Engineering, Shantou University, China

⁵Department of Central Laboratory, Children's Hospital of Shanghai Jiao Tong University, China

Correspondence should be addressed to Hongquan Zhang; 03200001@sues.edu.cn

Received 24 May 2021; Revised 23 June 2021; Accepted 26 July 2021; Published 15 August 2021

Academic Editor: Balakrishnan Nagaraj

Copyright © 2021 Bangtong Huang et al. This is an open access article distributed under the Creative Commons Attribution License, which permits unrestricted use, distribution, and reproduction in any medium, provided the original work is properly cited.

Deep learning algorithms are facing the limitation in virtual reality application due to the cost of memory, computation, and real-time computation problem. Models with rigorous performance might suffer from enormous parameters and large-scale structure, and it would be hard to replant them onto embedded devices. In this paper, with the inspiration of GhostNet, we proposed an efficient structure ShuffleGhost to make use of the redundancy in feature maps to alleviate the cost of computations, as well as tackling some drawbacks of GhostNet. Since GhostNet suffers from high computation of convolution in Ghost module and shortcut, the restriction of downsampling would make it more difficult to apply Ghost module and Ghost bottleneck to other backbone. This paper proposes three new kinds of ShuffleGhost structure to tackle the drawbacks of GhostNet. The ShuffleGhost module and ShuffleGhost bottlenecks are utilized by the shuffle layer and group convolution from ShuffleNet, and they are designed to redistribute the feature maps concatenated from Ghost Feature Map and Primary Feature Map. Besides, they eliminate the gap of them and extract the features. Then, SENet layer is adopted to reduce the computation cost of group convolution, as well as evaluating the importance of the feature maps which concatenated from Ghost Feature Maps and Primary Feature Maps and giving proper weights for the feature maps. This paper conducted some experiments and proved that the ShuffleGhostV3 has smaller trainable parameters and FLOPs with the ensurance of accuracy. And with proper design, it could be more efficient in both GPU and CPU side.

1. Introduction

Deep learning has achieved great performance in computer vision and natural language processing tasks. The SOTA often makes use of a large-scale backbone, and ResNet-50 [1] has about 25.6M parameters and requires 4.1B FLOPs to process an image of size 224×224 . On the one hand, massive trainable parameters enhance the performance of these deep networks. On the other hand, the large-scale backbone faces a risk of costing much resources of memory and computation, which means it would be difficult to replant it to mobiles or cars with efficient and acceptable performance.

Over the years, a series of methods have been proposed to investigate compact deep neural networks such as network pruning [2], low-bit quantization [3], and knowledge distillation [4]. Ren and Lee [5] recently proposed using deep networks to learn high-level visual feature representations and synthetic images to train neural networks. Li et al. [6] used deep neural network and hash mapping to extract remote sensing image features with complex background. Since the feature dimensionality of the direct output of the classification network is high, the storage space is occupied with the efficiency reducing. Long et al. [7] constructed a complete convolutional network, which combines the semantic information of

the deep coarse layer with the appearance information of the shallow fine layer to generate an accurate and detailed segmentation set. At the same time, object recognition is one of the important contents of image recognition, and the number of object recognition will change according to different images, such as face recognition [8] and visual search engine [9].

Therefore, simplifying the output feature of the classification network is the key to improving the retrieval efficiency. However, performances of these methods are often upper bounded by pretrained deep neural networks that have been taken as their baselines. Besides them, efficient network design with fewer parameters and calculations have achieved considerable success such as MobileNet [10]. Thus, this paper focuses on how to reduce the trainable parameters and improve the efficiency of model training. We did a lot of experiments and tried to combine the advantages of several models like ShuffleNet [11], SENet, and GhostNet and found an architecture named ShuffleGhost, which has a better performance than the original GhostNet. Liu et al. [12, 13] proposed that edge computing method is used to solve the problems of supply chain network optimization, and good performance is obtained.

2. Related Models

2.1. GhostNet. Han et al. [14] found the abundant and even redundant information in the feature maps of well-trained deep neural networks. They came up with a method called Ghost module to generate the abundant information in a cost-efficient way. It reduces the trainable parameters and training time.

GhostNet contains two key parts: ghost convolution part and primary convolution part. And the feature maps produced from ghost convolution part donated as Ghost Feature Maps, as well as the feature maps produced from primary convolution part donated as Primary Feature Maps.

In GhostNet, researchers designed a module named Ghost module to do convolution, as shown in Figure 1. The key idea of GhostNet is to use one-half channels of feature maps to do convolution in primary convolution part, which shown as the green regions. The orange region in Figure 1, which is the ghost convolution part, adopted a ghost convolution to produce Ghost Features. The Ghost Features and the result of primary convolution are concatenated together as the output of the Ghost module. In the implementation of GhostNet, researcher used $C/2$ number of 3×3 kernels to do group convolution, with the number of the group is $C/2$, that is, the channel of each kernel is 1, and each kernel corresponds to one feature map. So the computation N_{CC} needed of this group convolution is much less than that of primary convolution N_{PC} :

$$\begin{aligned} N_{CC} &= (w - k_w + 1) \times (h - k_h + 1) \times k_w \times k_h \times \frac{C}{2}, \\ N_{PC} &= (w - k_w + 1) \times (h - k_h + 1) \times k_w \times k_h \times \frac{C}{2} \times \frac{C}{2}, \end{aligned} \quad (1)$$

where w , h , and C are the width, height, and channel of the feature map, respectively, and k_w and k_h are the width and height of kernels, respectively. In primary convolution module and ghost convolution module, the channels of input feature map and output feature map are all equal to $C/2$. It can be found that the ghost convolution module could produce $C/2$ Ghost Features with a low computation cost, which is $C/2$ lower than that of primary convolution module. Since the channels of feature maps from primary convolution and ghost convolution are all equal to $C/2$, after concatenating, the channel of Ghost module output is equal to the channel of input feature map.

The Ghost bottleneck is designed as an architecture like the block of ResNet, so that Ghost bottleneck could be used to build a deeper convolution network, as shown in Figure 2. Generally, each block in ResNet contains two or three convolutions and one shortcut, while in GhostNet, each Ghost bottleneck only contains two Ghost modules and one shortcut.

However, the GhostNet mainly has four drawbacks:

- (i) The Ghost Features are always placed at the end of the feature maps, which would introduce noise if the Ghost Features are used to predict new Ghost Features
- (ii) Convolution in Ghost module and shortcut have high computation cost
- (iii) When 1×1 kernel of convolution and one-padding are configured in the first convolution of Ghost module at the same time, the one-padding field is used to do 1×1 kernel of convolution and extract features which are meaningless and would introduce noise
- (iv) It is only downsampled by the large kernel. This drawback would make it hard to design GhostNet into other backbone

2.2. ShuffleNet. ShuffleNet has two key parts: shuffle layer and group convolution. These two components are used together to do convolution. As for group convolution, it could use sparse kernels to replace the original one, which allows it to have a partial dense field to extract features. And for shuffle layer, it is always placed after group convolution to shuffle the channels of feature maps together. ShuffleNet achieves great success in reducing the parameters and ensures the performance of the model in the meantime.

2.2.1. Shuffle Layer. As mentioned in the related paper of ShuffleNet, it was found that some state-of-the-art networks like Xception [15] use group convolution instead of doing 1×1 convolutions, namely, pointwise convolutions. If group convolution is applied, the channels would be divided into several parts, and group convolution would be conducted on them. However, the correlation among these feature maps from different channels would be block. In order to tackle this problem, ShuffleNet introduces shuffle layer to redistribute the feature maps, and it achieves a good performance.

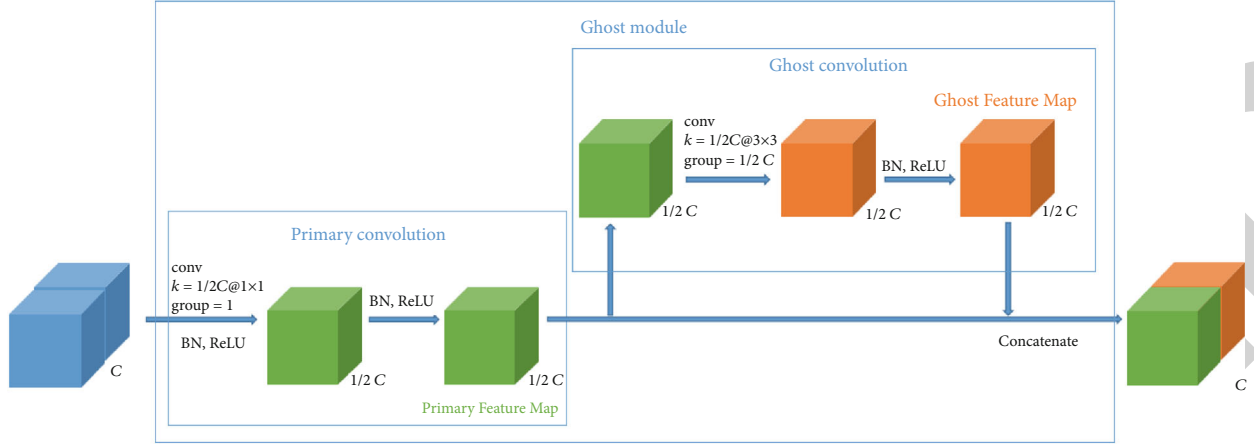


FIGURE 1: The structure of Ghost module in GhostNet.

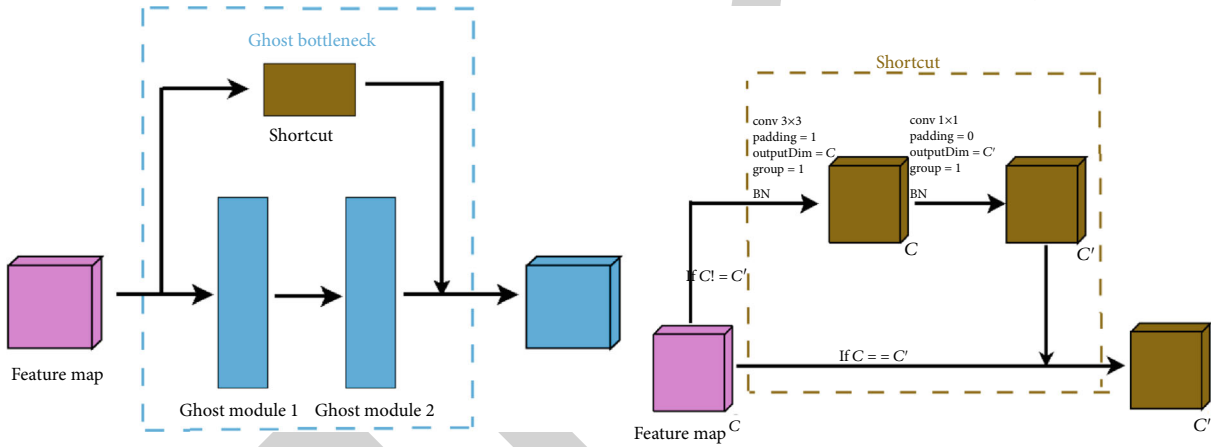


FIGURE 2: The structure of Ghost bottleneck and shortcut.

2.2.2. Group Convolution. Group convolution used sparse kernels to do convolution, and it can reduce the parameters and FLOPs of convolution. And Figure 3 shows the architecture of group convolution. As we know, if we do origin convolution (stride = 1, no padding) on figure maps with shape $1 \times C \times w \times h$ with k number of kernels with shape k_w, k_h, C , it would take computation N_{CON} :

$$N_{CON} = (w - k_w + 1) \times (h - k_h + 1) \times k_w \times k_h \times C \times k. \quad (2)$$

And it can be found that the computation of group convolution reduces significantly. If g groups and k' number of kernels are used, it would follow this ReLU.

$$C = g \times k'. \quad (3)$$

And the computation of group convolution N_{GC} is as follows:

$$N_{GC} = (w - k_w + 1) \times (h - k_h + 1) \times k_w \times k_h \times k' \times g. \quad (4)$$

It can be found that the computation of N_{CON} is k

times larger than that of N_{GC} . In fact, in group convolution, the zero field of kernels also joins the computation, and the advantage of group convolution might be less obvious.

2.2.3. SENet. Hu et al. [16] investigated the relationship between channels of network design and introduced a new architectural SE block unit, which allows the network to perform feature recalibration and learn to use the global information. Only a small amount of computation is needed to improve the performance.

For traditional CNN, the core computation is convolution operator, which learns new feature maps from input one by convolution kernel. A large part of existing works is improving the receptive field, that is, combining more features in space or extracting multiscale spatial information, while the SENet is more concentrating on the relationship between different channels and expecting that the model can automatically learn the importance of different channel features. To achieve this goal, SENet proposed the squeeze-and-excitation block [17–19].

In SE block, first stage is squeeze. The squeeze operation is performed on the feature map obtained by convolution to

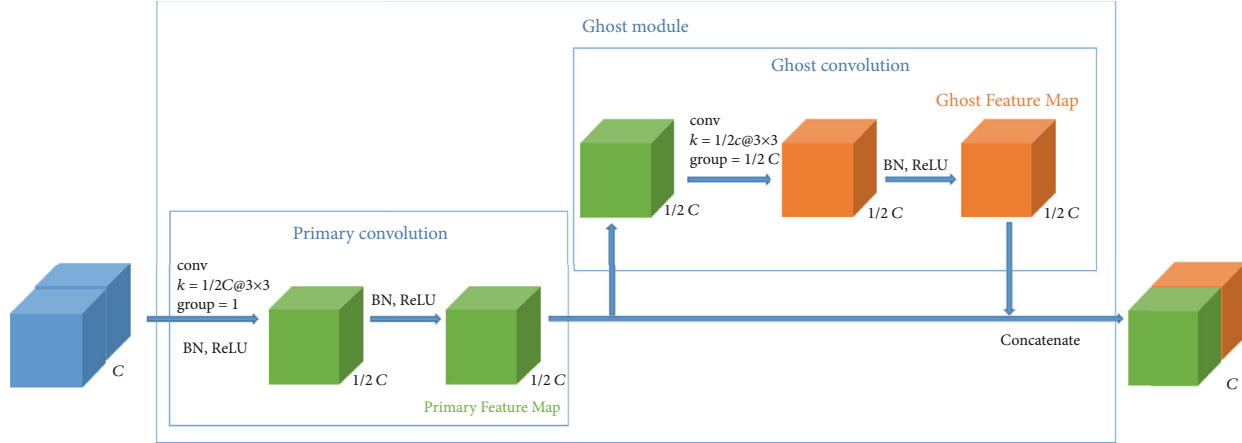


FIGURE 3: The structure of GhostNet-like module modified from Ghost module in GhostNet.

get the global information. Namely, it shrinks feature maps through spatial dimensions. Then, in the second stage, the excitation, it learns the relationship between channels and gets the weight of different channels. Finally, multiply the original feature map to get the final feature [20–22].

(1) Squeeze

Convolution is only operated in a local space, which means it is difficult for the output feature map to obtain enough information to extract the relationship between channels. This problem becomes more serious in the front layer of the network due to the relatively small receptive field. The essence of squeeze operation is to encode the whole spatial feature of a channel into a global feature, which is implemented by global average pooling. The following equation shows the computation of squeeze [23, 24].

$$Z_C = F_{sq}(u_C) = \frac{1}{h \times w} \sum_{i=1}^h \sum_{j=1}^w u_C(i, j), \quad (5)$$

where h and w are the height and width of feature maps, respectively, and u_C is the input of feature maps.

(2) Excitation

When we get the global feature, then we need another operation to learn the relationship between channels, which is the excitation. The excitation should meet the two criteria: firstly, it should be flexible. And it should be able to learn the nonlinear relationship between channels. Secondly, the learning relationship is not mutually exclusive because it allows multiple channel features instead of one hot form. Based on the criteria, there is the equation [25, 26].

$$S = F_{ex}(z, W) = \sigma(g(z, W)) = \sigma(W_2 \delta(W_1 z)), \quad (6)$$

where δ is the ReLU function, $W_1 \in R^{C^2/r}$ and $W_2 \in R^{C^2/r}$ are the trainable parameters, and z is the input feature maps.

In order to reduce the complexity of the model and improve the generalization ability, a bottleneck structure with two FC layers is adopted. The first FC layer is used to reduce the dimension. The final FC layer restores the original dimension.

3. Methods

In the paper, we proposed a model named ShuffleGhost and compared with a GhostNet-like network to discuss the performance. In this section, we would first introduce the GhostNet-like network we used as baseline to compare the performance with the ShuffleGhost. The GhostNet-like network maintained most features from GhostNet but a 1×1 convolution operation in Ghost module was replaced with 3×3 convolution, and we could have a fair discussion and comparison among them.

3.1. GhostNet-Like Network. The method ShuffleGhost we proposed would utilize shuffle operation and group convolution to mix the information from the Ghost Feature Maps and Primary Feature Maps. In order to evaluate the performance of ShuffleGhost fairly, we designed a Ghost-like module as illustrated in Figure 3. In the Ghost-like module, we used 3×3 convolution to replace the 1×1 convolution in primary convolution in Ghost module. This modification would not influence the principle of GhostNet, as we remained the primary convolution and ghost convolution. Apart from Ghost-like module, we still adopted Ghost bottleneck with GhostNet-like module. And we designed a GhostNet-like network as baseline, as illustrated in Figure 4.

3.2. ShuffleGhost. The GhostNet employs ghost convolution and primary convolution to design Ghost module, the computation of Ghost Feature Map would be cheap since the Ghost module adopted 3×3 group convolutions, and the number of groups equal to the channels, which means that the channel of all kernels is equal to one. In fact, they are a series of linear transforms, and in GhostNet, these linear transforms are assigned to 3×3 convolution on each intrinsic feature. In this paper, we tried other linear transforms. We

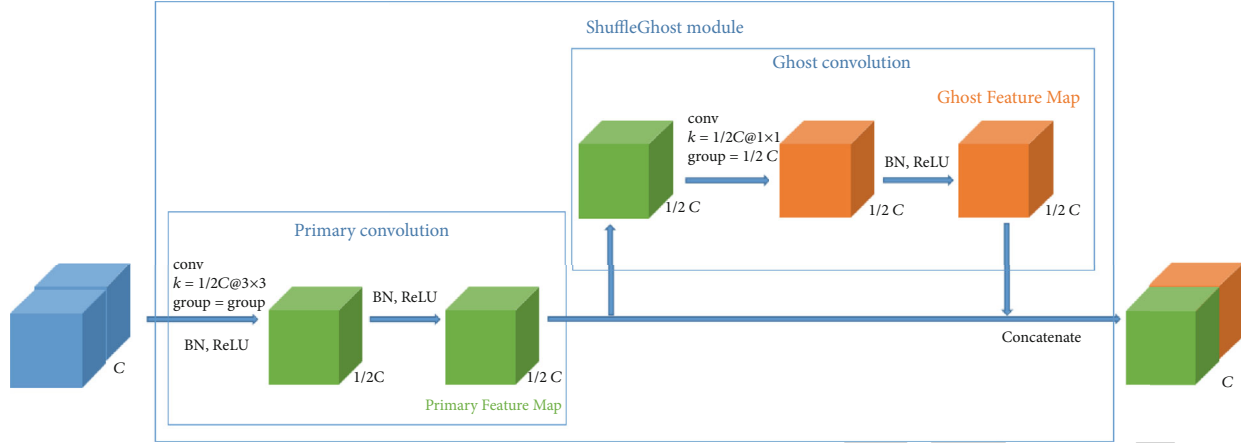


FIGURE 4: The structure of ShuffleGhost module.

found the Ghost Feature Maps from ghost convolution and the Primary Feature Maps from primary convolution are concatenated together, and the Ghost Feature Maps are always placed at a fixed position. In the next Ghost module, it introduces noise if the primary convolution is replaced with group convolution, especially if the group number is set to two. In this situation, all the Ghost Feature Maps would be used to produce half of the feature maps, and the real feature maps produce the other, and these two kinds of feature maps share the equal importance.

Apart from the ghost convolution to produce Ghost Feature, traditional convolution is adopted in Ghost module and shortcut in Ghost bottleneck, and this paper finds it possible to optimize them.

3.2.1. ShuffleGhost Module. This module is designed base on the GhostNet-like module. Since the computation of the first convolution in GhostNet-like module would take high cost of computations, ShuffleGhost replaced this first convolution with group convolution. But as mentioned above, group convolution in GhostNet-like module would reduce the robustness of the model due to the concatenate operation and cascade of Ghost module.

Comparing with GhostNet-like module and ignoring the trainable parameter reduction from the group convolution, ghost convolution mainly makes difference. In ghost convolution part, if ShuffleGhost follows the rule of GhostNet-like module with the kernel size set to 3×3 , then the trainable parameters and the computation cost of ShuffleGhost would be much higher. One possible way to solve it is replacing the 3×3 kernels in ghost convolution part with 1×1 kernels. Formally, the modification is to swap the places of two kinds of kernels, but in ShuffleGhost module, the expensive kernel, which is the 3×3 size one, produces the feature maps in primary convolution, and these feature maps are also utilized to produce Ghost Features. However, the feature maps produced by expensive kernel are only used in ghost convolution, as well as the Primary Feature Maps produced from ghost kernel, which are lack of precision and are utilized to conduct primary convolution and ghost convolution. So ShuffleGhost module has larger capacity and more precision

than Ghost module. Figure 4 shows the structure of ShuffleGhost module.

3.2.2. ShuffleGhost. In ShuffleGhost, we would introduce versions of bottlenecks, which use Ghost module or ShuffleGhost module to form themselves, so that this bottleneck could have some methods like residual block in ResNet. As mentioned before and illustrated in Figure 1, the Ghost module consists of two Ghost modules and one shortcut and adopts 3×3 convolution operation in shortcut part which would suffer from high computational cost. Meanwhile, group convolution in ShuffleGhost module would introduce noise because group would separate the information of Ghost Feature Maps from ghost convolution and Primary Feature Maps apart. To tackle this problem, one of direct ways is to mix the feature maps which concatenate from Ghost Feature Maps and Primary Feature Maps. Thus, each group of feature maps would contain the information from Ghost Feature Maps and Primary Feature Maps simultaneously.

(1) ShuffleGhostV1

In order to mix the channels of the primary feature maps and ghost feature maps, the shuffle layer is placed at the top of the ShuffleGhost BottleneckV1. Besides, 16 group convolutions with 3×3 kernels are configured after the shuffle layer to make combination and extract features from both Ghost Feature Maps and Primary Feature Maps. The ShuffleGhost BottleneckV1 contains two Ghost-like modules, which have the same architecture with the baseline, Ghost-like network. And in the first Ghost-like module, the padding could be set to zero or one, which depends on whether this bottleneck is going to do downsampling or not. The padding of the second Ghost-like module should be one, so that the feature map would not lose too much information and ensure the resolution of the feature map.

Since the bottleneck is modified, the shortcut should also be modified to ensure the dimension of the data from the second Ghost-like module that has the same shape as that from shortcut. In shortcut, the padding configure in the first convolution should be the same as the configure of the first

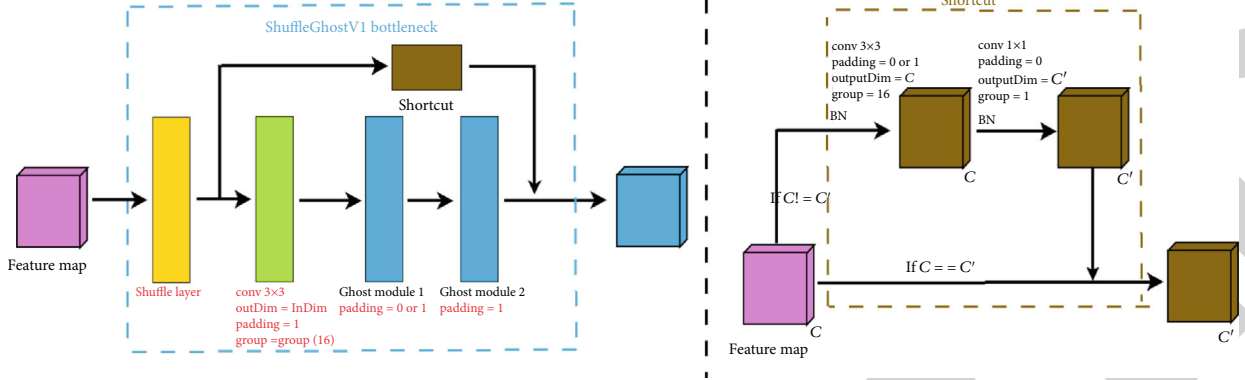


FIGURE 5: The structure of ShuffleGhostV1 bottleneck.

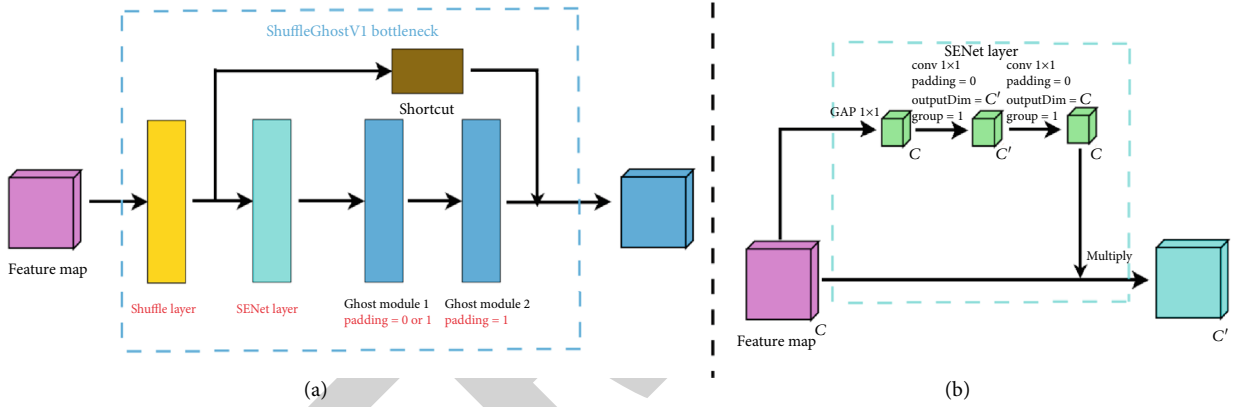


FIGURE 6: The structure of ShuffleGhostV3 bottleneck.

Ghost-like module in ShuffleGhost BottleneckV1, but this module also used group convolution in shortcut to lighten the computation.

ShuffleGhostV1 used ShuffleGhost BottleneckV1 and Ghost-like module and has the same layer configuration with Ghost-like network which is illustrated in Figure 5. It is found that ShuffleGhostV1 does not introduce more parameters than Ghost-like network although it used group convolution and shuffling in ShuffleGhost BottleneckV1. We placed the 3×3 group convolution in shortcut layer instead of 3×3 convolution, and the parameters we saved in shortcut layers are used to form group convolution in ShuffleGhost BottleneckV1.

(2) ShuffleGhostV2

ShuffleGhostV2 still used ShuffleGhost BottleneckV1 architecture to form a network, but ShuffleGhost module is used instead of Ghost-like module. The output of ShuffleGhost module shares the same shape with Ghost-like module, and the shortcut and bottleneck do not need modification.

(3) ShuffleGhostV3

In the bottleneck of ShuffleGhostV2, we adopted ShuffleGhost module and the same bottleneck structure as Shuffle-

GhostV1. We found in bottleneck of ShuffleGhostV2, the kernel size in group convolution after the shuffle layer is 3×3 , and it would suffer computation cost although it could integrate the information from shuffle layer across the channels and improve performance. In order to reduce the computation of this group convolution, we utilize SENet layer from SENet to design ShuffleGhost BottleneckV2 and build ShuffleGhostV3.

SENet layer used two steps to extract feature maps: squeeze and excitation. The first step is to squeeze the origin feature maps to a small-scale feature maps, and the second step is finding the importance of among these scale feature maps. Finally, the feature maps from excitation multiply with in origin feature maps. In ShuffleGhost, SENet layer could have a better performance than group convolution. On the one hand, SENet costs smaller computation. On the other hand, SENet could evaluate the importance of the feature maps which concatenated from Ghost Feature Maps and Primary Feature Maps and combine them together. The SENet layer and the structure of ShuffleGhostV3 are illustrated in Figure 6.

SENet layer is adopted to take the place of group convolution, and Figure 6(b) shows the detailed structure of SENet layer.

TABLE 1: The comparison of Ghost-like network and three visions of ShuffleGhost.

Layers	Output size	Ghost-like network	ShuffleGhostV1	ShuffleGhostV2	ShuffleGhostV3
conv	28×28	3×3 conv, stride 1	3×3 conv, stride 1	3×3 conv, stride 1	3×3 conv, stride 1
BatchNorm, ReLU	28×28				
Bottleneck	26×26	Ghost bottleneck (Ghost-like module $\times 2$)	ShuffleGhost BottleneckV1 (Ghost-like module $\times 2$)	ShuffleGhost BottleneckV1 (ShuffleGhost module $\times 2$)	ShuffleGhost BottleneckV2 (ShuffleGhost module $\times 2$)
Bottleneck	24×24	Ghost bottleneck (Ghost-like module $\times 2$)	ShuffleGhost BottleneckV1 (Ghost-like module $\times 2$)	ShuffleGhost BottleneckV1 (ShuffleGhost module $\times 2$)	ShuffleGhost BottleneckV2 (ShuffleGhost module $\times 2$)
Bottleneck	22×22	Ghost bottleneck (Ghost-like module $\times 2$)	ShuffleGhost BottleneckV1 (Ghost-like module $\times 2$)	ShuffleGhost BottleneckV1 (ShuffleGhost module $\times 2$)	ShuffleGhost BottleneckV2 (ShuffleGhost module $\times 2$)
Bottleneck	20×20	Ghost bottleneck (Ghost-like module $\times 2$)	ShuffleGhost BottleneckV1 (Ghost-like module $\times 2$)	ShuffleGhost BottleneckV1 (ShuffleGhost module $\times 2$)	ShuffleGhost BottleneckV2 (ShuffleGhost module $\times 2$)
Bottleneck	18×18	Ghost bottleneck (Ghost-like module $\times 2$)	ShuffleGhost BottleneckV1 (Ghost-like module $\times 2$)	ShuffleGhost BottleneckV1 (ShuffleGhost module $\times 2$)	ShuffleGhost BottleneckV2 (ShuffleGhost module $\times 2$)
Bottleneck $\times 3$	16×16	Ghost bottleneck (Ghost-like module $\times 2$)	ShuffleGhost BottleneckV1 (Ghost-like module $\times 2$)	ShuffleGhost BottleneckV1 (ShuffleGhost module $\times 2$)	ShuffleGhost BottleneckV2 (ShuffleGhost module $\times 2$)
Bottleneck	14×14	Ghost bottleneck (Ghost-like module $\times 2$)	ShuffleGhost BottleneckV1 (Ghost-like module $\times 2$)	ShuffleGhost BottleneckV1 (ShuffleGhost module $\times 2$)	ShuffleGhost BottleneckV2 (ShuffleGhost module $\times 2$)
Bottleneck $\times 3$	12×12	Ghost bottleneck (Ghost-like module $\times 2$)	ShuffleGhost BottleneckV1 (Ghost-like module $\times 2$)	ShuffleGhost BottleneckV1 (ShuffleGhost module $\times 2$)	ShuffleGhost BottleneckV2 (ShuffleGhost module $\times 2$)
conv	12×12	1×1 conv, stride 1	1×1 conv, stride 1	1×1 conv, stride 1	1×1 conv, stride 1
BatchNorm, ReLU	12×12				
Pooling	4×4		Global average pooling	Global average pooling	Global average pooling
Dense			10D fully connected, softmax	10D fully connected, softmax	10D fully connected, softmax

TABLE 2: The structure of Ghost-like network for tiny ResNet experiment.

Layers	Output size	Ghost-like network	Parameters
Convolution	28×28	3×3 conv, stride 1	216
BatchNorm, ReLU	28×28		6
Ghost bottleneck	26×26	Ghost-like module $\times 2$	3604
Ghost bottleneck	24×24	Ghost-like module $\times 2$	13800
Ghost bottleneck	22×22	Ghost-like module $\times 2$	34680
Ghost bottleneck	20×20	Ghost-like module $\times 2$	61214
Ghost bottleneck	18×18	Ghost-like module $\times 2$	116432
Ghost bottleneck $\times 3$	16×16	Ghost-like module $\times 2$	218960, 174880, 174880
Ghost bottleneck	14×14	Ghost-like module $\times 2$	276592
Ghost bottleneck $\times 3$	12×12	Ghost-like module $\times 2$	718288, 695360, 695360
Convolution	12×12	1×1 conv, stride 1	4800
BatchNorm, ReLU	12×12		960
Pooling	4×4	Global average pooling	0
Dense		10D fully connected, softmax	76810
			3266852

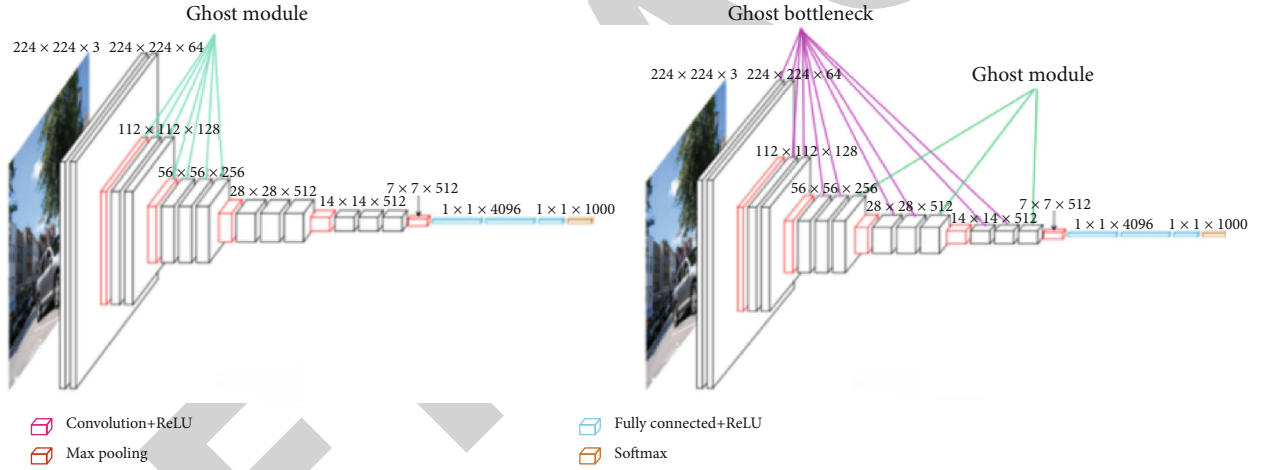


FIGURE 7: The structures of VGG16-like experiment.

In summary, the three visions of ShuffleGhost have the architectures and parameters as illustrated in Table 1. They have the same layer configuration with Ghost-like network.

4. Experiment

In tiny ResNet experiment, we used the bottleneck in ShuffleGhost or GhostNet-like network to replace the residual block and trained without pretrained models. This experiment focuses on comparing and discussing the appearance of bottleneck. The second experiment is VGG16-like [27] experiment. We used the bottleneck and the module in ShuffleGhost or GhostNet-like network to replace the convolution operations in VGG16. The strategy is that if two convolutions are cascaded, then we used one bottleneck to replace them; otherwise, we used one module to replace the convolution operation. We conducted the experiments on

TABLE 3: The comparison of trainable parameters and size of parameters of GhostNet-like network and three versions of ShuffleGhost.

Structure	Trainable parameters	Param size
GhostNet-like	3,271,594	12.48
ShuffleGhostV1	3,102,970 (-5.1%)	11.84
ShuffleGhostV2	3,087,802 (-5.6%)	11.78
ShuffleGhostV3	3,028,266 (-7.4%)	11.55

CIFAR-10 datasets and compared the performance on trainable parameters' effectiveness.

4.1. Tiny ResNet Experiment. The experiment focuses on finding the difference between the GhostNet-like network and ShuffleGhost.

TABLE 4: The trainable parameters, FLOPs, training time (CPU), and training time (GPU) from different structures.

Structure	Trainable parameters	FLOPs	Training time (CPU)	Training time (GPU)
Original VGG	14.728 M	314.032 M	1181 s	102.58 s
+ GhostNet-like module	7.388 M (-49%)	158.401 M	960 s	91.37 s
+ ShuffleGhost module	7.370 M (-50%)	157.295 M	931 s	90.84 s
+ Ghost bottleneck	8.337 M (-43%)	193.593 M	1111 s	110.32 s
+ ShuffleGhost BottleneckV1	7.795 M (-46%)	168.494 M	1112 s	114.82 s
+ ShuffleGhost BottleneckV2	7.670 M (-48%)	166.157 M	1097 s	122.05 s

Firstly, we build a tiny ResNet, whose structure illustrated as Table 2, with the original GhostNet as baseline to judge the performance of ShuffleGhost. Then, we implement ShuffleGhost in 3 versions to train on CIFAR-10 and compare the results with original GhostNet. We trained these models with 10^{-3} learning rate, 16 batch size, and 50 maximum epochs and employed Adam as the optimizer.

4.2. VGG16-Like Experiment. In a brief, for Ghost module, we use it to replace every convolution layer in VGG16. For Ghost bottleneck, since bottleneck is made up of 2 consistent convolution layers, we replace every 2 convolution layers by bottleneck and replace the left single one conv layer by Ghost module. The structure is like that of Figure 6. We use the same strategy for ShuffleGhost, and the structures of VGG16 experiment are shown in Figure 7.

Based on what we implemented, we have 6 structures in total. We will train them on the CIFAR-10 datasets and set epoch to be 50 and learning rate to be 0.01. Despite the fact that we focus on the portable devices' efficiency, which can be regarded as CPU, we would also try the GPU training too and prove we make some progress in both sides.

4.3. Result. Tables 3 and 4 described the models from 2 parts, the trainable parameters and accuracy. As shown in the 2 tables, firstly, for the model size, we can see the baseline GhostNet has around the size of 3.27 M trainable parameters while ShuffleGhost has smaller model size in both 3 versions. These 3 models decrease the model size more than 5% (-5.1%, -5.6%, and -7.4% separately), and the most outstanding model is the ShuffleGhost version 3; the size drops from 3.27 M to 3.02 M, and the FLOP drops from 989.25 M to 895.79 M; the FLOP drops around 9.4%; this could lead to a better performance of embedded devices in both efficiency and portability. Then, for the accuracy part, which is essential, we cannot sacrifice the accuracy to have a small model. The ShuffleGhostV2 has around 86.6% accuracy, which is 1% higher than the baseline GhostNet-like network. So, from this experiment, we can see that in the peer comparison, ShuffleGhost could perform better in both model size part and accuracy part.

After comparing the GhostNet-like network and ShuffleGhost, we will go deeper to see the performance of the different modules and bottlenecks. As mentioned before, we set the original VGG16 as the baseline model and redesigned VGG16-like models for experiment. In Table 4, it shows the parameters after replacing the convolution layers in VGG16

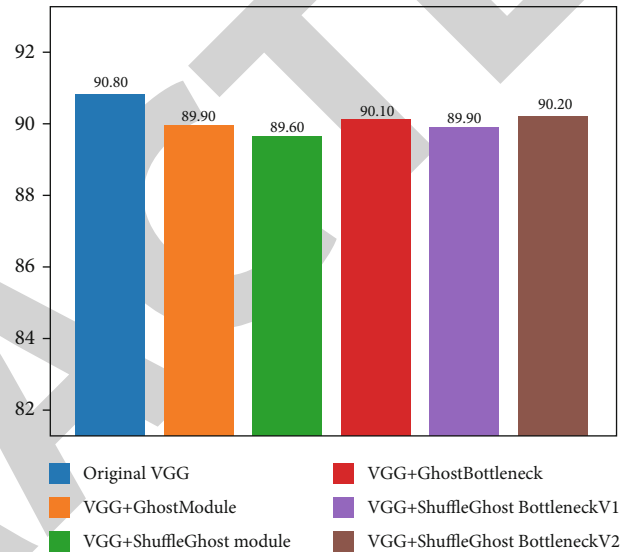


FIGURE 8: The overview accuracy from six different structures. And the models were trained with 50 epochs and batchsize 128.

network; it is known that GhostNet-like network and all the ShuffleGhost decrease the model size in a significant level (at least 40%). As for both ShuffleGhost module and ShuffleGhost bottleneck, they perform better than the original ones. Combining the accuracy in Figure 8 and the training time in Table 4, the advantages and disadvantages of applying modules and bottlenecks can be known from the data. Namely, for the model size part, ShuffleGhost module can bring us smaller model size than ShuffleGhost bottleneck, but the cost is worse accuracy. As for the accuracy consideration, ShuffleGhost bottleneck can guarantee a better accuracy, while the trade-off will be size. For the efficiency part, all the Ghost and ShuffleGhost run faster than the original one on CPU. But on GPU, only module can perform better; bottlenecks will be slower than the original one. In accuracy trend from Figure9, all the models get to the best result in almost the same epochs.

In VGG16-like experiment, Ghost module and ShuffleGhost module form an abstract comparison, that is, both modules used their module to take the place of the convolution in original VGG. And Ghost bottleneck forms the other abstract comparison, and each of them uses its bottleneck to replace two convolution layers in VGG.

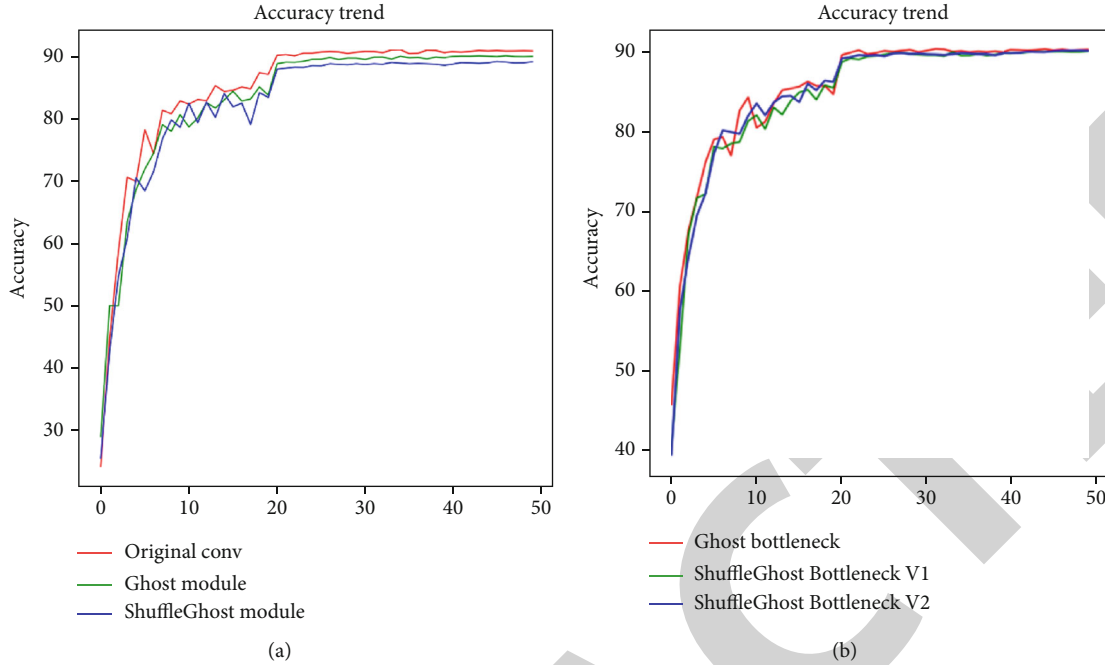


FIGURE 9: The accuracy of the VGG16-like experiment. (a) The accuracy of different modules. (b) The accuracy of different bottlenecks.

TABLE 5: The comparison of FLOPs and accuracy of GhostNet-like network and three versions of ShuffleGhost.

Structure	FLOP	Accuracy
GhostNet-like	989.259 M	85.20%
ShuffleGhostV1	933.156 M (-5.6%)	85.33%
ShuffleGhostV2	927.815 M (-6.2%)	86.61%
ShuffleGhostV3	895.796 M (-9.4%)	86.28%

5. Conclusion

In the tiny ResNet experiment, Tables 3 and 5 compare the original GhostNet and ShuffleGhost, and we can see that ShuffleGhost not only decreases the trainable parameters and FLOP, but also has a slightly better accuracy. In the VGG16-like experiment, Table 4 compares different modules and bottlenecks, and we can see that for the module, ShuffleGhost module has smaller trainable parameters and higher training speed both on CPU and GPU. But the speed to get the convergence of accuracy is a little slower. And for the bottleneck, both ShuffleGhost bottlenecks V2 and V3 have smaller trainable parameters than original Ghost. For the CPU training speed, they are similar, but for the GPU training speed, ShuffleGhost will be slower. As for the accuracy part in both experiments, as can be seen in Figure 8, the blue color one is the original VGG, which has the best performance, and all the other models have around 89.9% accuracy, 1% lower than the best. One thing needs to be noticed is that in ShuffleGhost BottleneckV3, the brown one with 90.2% accuracy has approximately the best accuracy result. Another thing we can notice in Figure 9 is that all the different modules and bottlenecks take nearly the same epoch to get to the best accuracy.

As discussed above, from the tiny ResNet experiment, we know that ShuffleGhost has smaller trainable parameters and a little higher accuracy compared to the original GhostNet-like network. From VGG16-like experiment, we can clearly see that the ShuffleGhost holds approximately the same accuracy result compared to the original one. But it has smaller trainable parameters and FLOPs and can be faster than the original one. All in all, we learn from GhostNet and design new ShuffleGhosts, which making use of the redundancy in feature maps properly and combined with shuffle to solve the too consistent problem in feature map produced by original GhostNet. Besides, we also implement different versions to tackle the problems we found in the original Ghost, which are already being introduced before.

Data Availability

The data used to support the findings of this study are available from the author upon request.

Conflicts of Interest

The authors declare that there are no conflicts of interest regarding the publication of this paper.

Acknowledgments

The finding is sponsored by the Key Lab of Information Network Security of Ministry of Public Security (Grant no. C20609) and Municipal Key Curriculum Construction Project of University in Shanghai (Grant no. S202003002).

Retraction

Retracted: Urban Fruit Quality Traceability Model Based on Smart Contract for Internet of Things

Wireless Communications and Mobile Computing

Received 28 November 2023; Accepted 28 November 2023; Published 29 November 2023

Copyright © 2023 Wireless Communications and Mobile Computing. This is an open access article distributed under the Creative Commons Attribution License, which permits unrestricted use, distribution, and reproduction in any medium, provided the original work is properly cited.

This article has been retracted by Hindawi, as publisher, following an investigation undertaken by the publisher [1]. This investigation has uncovered evidence of systematic manipulation of the publication and peer-review process. We cannot, therefore, vouch for the reliability or integrity of this article.

Please note that this notice is intended solely to alert readers that the peer-review process of this article has been compromised.

Wiley and Hindawi regret that the usual quality checks did not identify these issues before publication and have since put additional measures in place to safeguard research integrity.

We wish to credit our Research Integrity and Research Publishing teams and anonymous and named external researchers and research integrity experts for contributing to this investigation.



The corresponding author, as the representative of all authors, has been given the opportunity to register their agreement or disagreement to this retraction. We have kept a record of any response received.

References

- [1] C. Xu, K. Chen, M. Zuo, H. Liu, and Y. Wu, "Urban Fruit Quality Traceability Model Based on Smart Contract for Internet of Things," *Wireless Communications and Mobile Computing*, vol. 2021, Article ID 9369074, 10 pages, 2021.

Research Article

Urban Fruit Quality Traceability Model Based on Smart Contract for Internet of Things

Cheng Xu ^{1,2}, Kai Chen,¹ Min Zuo,² Hongzhe Liu ^{1,3} and Yanan Wu^{1,3}

¹Beijing Key Laboratory of Information Service Engineering, College of Robotics, Beijing Union University, China

²National Engineering Laboratory for Agri-Product Quality Traceability, Beijing Technology and Business University, China

³Beijing Key Laboratory of Traffic Data Analysis and Mining, Beijing Jiaotong University, China

Correspondence should be addressed to Hongzhe Liu; liuhongzhe@buu.edu.cn

Received 16 June 2021; Revised 9 July 2021; Accepted 22 July 2021; Published 15 August 2021

Academic Editor: Balakrishnan Nagaraj

Copyright © 2021 Cheng Xu et al. This is an open access article distributed under the Creative Commons Attribution License, which permits unrestricted use, distribution, and reproduction in any medium, provided the original work is properly cited.

In Internet of things, compared with the traditional traceability system, the existing system has difficulties in operation, data are easily lost, data are uncoordinated, standards are not unified, and so on. In this paper, based on the characteristics of blockchain, the traceability model of urban fruits is established to reduce the risk of counterfeit and shoddy urban fruits. The collected data is integrated into the chain for diversified display, providing different permissions and platforms for multiple roles. Blockchain and supporting intelligent hardware are used to realize the real record and tracking of the whole process of fruit. Improve the transparency and efficiency of supply chain, and reduce the supply chain cost. The experimental results show that the proposed algorithm model can be applied to the fruit service field and effectively improve the service level of smart city.

1. Introduction

The quality and safety of urban fruit in the Internet of things (IoT) have always been a hot topic of research. Agricultural product quality and safety traceability construction are an important trend and direction of agricultural product quality and safety supervision, as well as an important measure to promote agricultural quality in China [1]. The application of traceability in food has established and improved a set of food safety traceability system, from the production, processing, and sales to the consumer terminal, through the sharing of information through dedicated hardware equipment, to serve the final consumers [2]. Under the coverage of the whole process of the traceability system, once a problem occurs, the traceability system can quickly respond, obtain the information of the whole process of the production and circulation of the problem product, conduct troubleshooting and positioning [3], determine the root cause of the problem, and then solve the problem accordingly.

Previous incidents such as “tainted milk powder” and “gutter oil” have generally raised people’s awareness of quality and safety. “Seeing is believing” and “seeing is seeing” are the most assured [4]. Technological advances have made it possible to “see” food from where it is grown to where it is sold. Traceability is a production control system that can track products in a positive, reverse, and nondirectional manner. It is applicable to any product. At present, traceability technology can be divided into RFID traceability technology [5], two-dimensional code traceability technology [6], barcode traceability technology [7], and blockchain traceability technology [8]. Figure 1 shows the flowchart of the basic pattern of blockchain traceability.

Based on the traceability of blockchain and combined with big data [9], the traceability and security of commodities are greatly improved through in-depth combination of logistics management, production and manufacturing, anticounterfeiting of commodity traceability, and other fields. It provides solutions to problems such as data fraud tracing, “island of

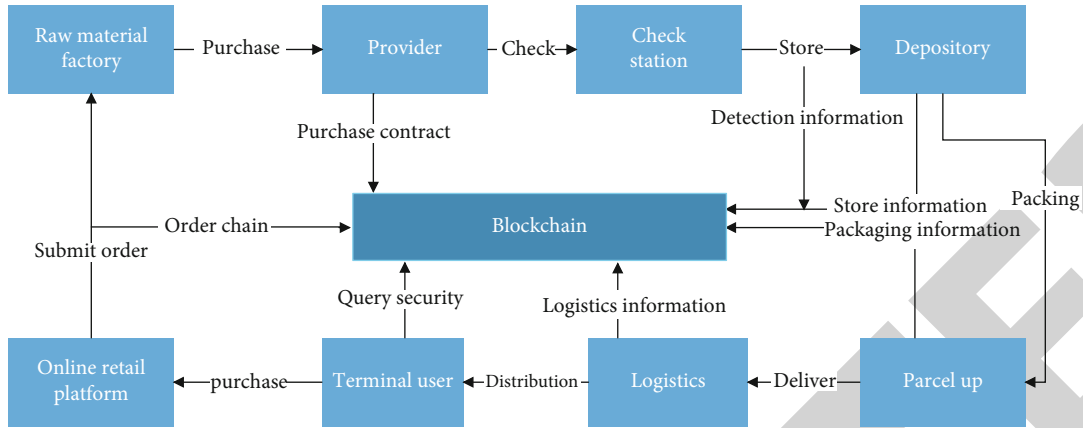


FIGURE 1: Flowchart of the basic pattern of blockchain traceability.

information” in the tracing chain, and difficulties in multiparty cooperation, making it possible to supervise the whole supply chain [10]. Therefore, it is also regarded as one of the most promising fields for the application of blockchain.

This paper makes three main contributions. (1) Propose the traceability model architecture research and design based on blockchain for IoT. (2) Use a distributed ledger and blockchain to design an asymmetric encryption authorization model. (3) Design the consensus mechanism and intelligent contract model of blockchain.

The rest of the paper is organized as follows. In Section 2, it briefly introduces the research key and design framework. In Section 3, it describes in detail the proposed model design route, decentralized technology route, and consensus mechanism technology route based on blockchain. In Section 4, the traditional traceability model and the blockchain-based traceability model are compared in terms of architecture and performance. Finally, it has the conclusion of the paper in Section 6.

2. Related Works

2.1. The Traceability Model Architecture Based on Blockchain for IoT. The data layer of the urban fruit quality traceability model based on blockchain contains the underlying data block, which is derived from the planting of urban fruit producers, the transportation of urban fruit transport enterprises, the distribution of urban fruit by distribution enterprises, and the sales of urban fruit by retail enterprises. In addition, it also includes the encryption of these data, timestamp, and other basic data and basic algorithms. This ensures that every complete transaction record of the city fruit can be verified and audited [11].

The data verification mechanism of the network layer is to verify the identities of government departments, enterprises, and urban fruit chain organizations; distributed networking makes data distributed in different node databases. The data transmission mechanism makes the data transparent and public.

The consensus layer contains the various consensus algorithms of the network nodes such as the POS algorithm—the government’s commerce and finance departments form an alliance [12]. Relevant government agencies and urban fruit

enterprises need to pass the review and verification of the alliance before they can enter the blockchain, thus ensuring the legitimacy and standardization of blockchain members.

At the contract level, national policies, legal provisions, and industry standards, such as the Agricultural Product Safety Law, the Quarantine Management Method of Entry Fruits, and the Provisional Methods for the Safety Supervision of Local Agricultural Products, are embedded into the blockchain in the form of smart contracts [13], which makes part of the supervision realize automation and greatly improves the supervision efficiency of government departments.

The application layer provides urban fruit information inquiry, quality tracking, and other services to consumers, urban fruit producers, transporters, distributors, retailers, and government departments who purchase urban fruits.

2.2. Distributed Ledger Based on Blockchain and Asymmetric Encryption Authorization in IoT. A distributed ledger means that transaction accounting is done by urban fruit suppliers, urban fruit transporters, urban fruit distributors, urban fruit retailers, and other local nodes [14]. And each node is a complete account. Different from the traditional distributed storage, each node of the blockchain stores the complete account data of urban fruits according to the blockchain structure, while the traditional distributed storage is to divide the relevant data of these urban fruits into several parts for storage according to certain rules. The security traceability system of urban fruits based on blockchain can ensure that no local node can record the ledger data of traded urban fruits separately, so as to avoid the centralization of the system and the control and tampering of system data by a single bookkeeper. In addition, a transaction chain is long and there are many accounting nodes [15]. Theoretically, unless all nodes are destroyed, the data of urban fruits will not be lost. The safety and reliability of urban fruit data can be guaranteed.

The city fruit quality traceability system based on blockchain highly encrypted the account identity information, and relevant information can only be accessed if the data owner of the city fruit is authorized, which ensures data security and personal privacy [16].

2.3. The Consensus Mechanism and Smart Contract. The consensus mechanism is an important component of blockchain technology. It completes the verification and confirmation of the transaction in a very short time through the voting of special nodes; for a transaction, if several nodes with unrelated interests can reach a consensus, we can think that the whole network can also reach a consensus. The purpose of the consensus mechanism in this paper is to reach a consensus among all the accounting nodes of urban fruits to determine the validity of records, to play the role of identification and tamperproofing [17]. There are two consensus mechanisms of urban fruit quality traceability systems based on blockchain. One is to compare the number of nodes of urban fruit, and the result agreed by more nodes is the final consensus result. It can also compare the computing power of urban fruit nodes or other characteristic quantities that can be compared by computers. The other is that all urban fruit nodes have the right to give priority to the consensus result. Only when the consensus result is agreed by other nodes can it become the final consensus result, thus avoiding the circulation of fake and inferior urban fruit in the market [18].

Smart contract is like the traditional paper contract. It is described by computer language and executed by computer. It is a computer protocol designed to spread, verify, or execute the contract in an informative way. It can trigger and execute the contract without the trust of a third party. Some legal provisions and government rules and regulations are set in advance in the system, such as the Agricultural Product Safety Law, the Quarantine Management Method of Entry Fruits, and the Interim Method of the Safety Supervision of Local Agricultural Products [19]. In case of any illegal event, the system can automatically identify and execute the relevant handling work, to improve the handling efficiency.

3. Urban Fruit Product Traceability System Design

The key problems of urban fruit quality traceability model based on blockchain mainly include the design of fruit traceability system architecture, the storage design of the urban fruit product traceability system, and the contract design of the urban fruit product traceability system.

3.1. Design of Fruit Traceability Architecture. Based on the blockchain system hierarchy, the operation rules of the fruit product quality and safety traceability system are superimposed. The system adopts service-oriented architecture (SOA) design and divides the system into an application layer, contract layer, consensus layer, network layer, and data layer. SOA is a method to design, develop, deploy, and manage discrete logical unit (service) models in the computing environment. It connects the different functional units of an application program through well-defined interfaces and contracts between these services. Interfaces are defined in a neutral way, and it is independent of the hardware platform, operating system, and programming language to realize the services and can interact in a unified and common way. Therefore, it is easier to maintain and has higher availability and better scalability. How to divide the urban fruit traceabil-

ity system according to different functions should be based on the production database, logistics database, storage database, sales database, and after-sales service database data layer service support, which is the key problem to be solved. Tracing to the source of production, logistics, storage, sales, and consumption can be realized. The traceability system platform for urban fruits can meet the traceability needs of regulatory authorities, platform managers, affiliated enterprises, and consumers.

3.2. Storage Design of the Urban Fruit Product Traceability System. Since the current chain structure of blockchain only supports query through trading address or block address and the traceability data needs to interact with multiple subsystems, how to design the way of combining blockchain with the database according to the data storage scheme is the key problem to be solved. Through blockchain transactions, the address is transferred to the database and the product ID is mapped to realize the backstage logical storage operation.

3.3. Contract Design of the Urban Fruit Product Traceability System. The smart contract mechanism of blockchain can convert textual contracts into computer transaction protocol codes and entrusts them with self-executing properties, thus minimizing the need for trusted intermediaries between trading parties and reducing the occurrence of malice and exceptions. How to design the protocol text such as urban fruit control and transaction payment embedded in the traceability system and how to automatically trigger the specified terms under the consensus and carry out rewards and punishments once the quality and transaction risks occur are the key problems to be solved. To achieve the purpose of saving the coordination cost and the unbalance of interests, it should distribute and punish the participants.

4. Fruit Quality Traceability Model Based on Blockchain

Through the design of the architecture, database storage, and intelligent contract of the city fruit product traceability system, we completed the framework construction of the model system and then introduced the specific implementation of the technical route.

4.1. Technical Route of Tracking Model Architecture Design. The system architecture of the food traceability system is divided into the front end and the back end. The design of the traceability model architecture is shown in Figure 2. The front end is a user interface. All participants in the supply chain, such as farms or farmers, consumers, food enterprises, supermarkets, and regulatory departments, can log in and access the food traceability system by scanning bar codes, QR codes, or RFID. The front end is based on Oracle's open-source framework JET. JET uses REST to invoke a smart contract deployed in the back end on a blockchain cloud service (BCS).

The back end consists of smart contracts and blockchain infrastructure services. The back end uses Oracle's BCS, a

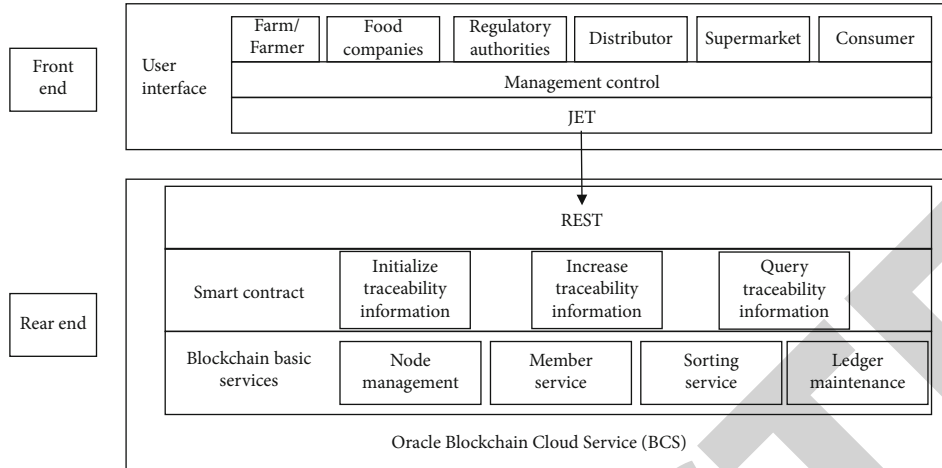


FIGURE 2: Design of traceability model architecture based on blockchain.

comprehensive distributed ledger cloud platform that can be used to preconfigure a blockchain network, join other organizations, and deploy and run smart contracts to update and query the ledger.

Blockchain basic services mainly include node management, member services, sorting services, and ledger maintenance functions.

Node management: it maintains account status and manages chain code. In a Hyperledger Fabric network, peer means that each fabric peer instance in the network is responsible for receiving transaction requests and maintaining a consistent ledger. These instances may run in bare-metal machines, virtual machines, or even containers. The nodes communicate with each other through gRPC messages. Functional peers are divided into endorser, committer, ledger, chain code, and event, and several nodes form a P2P gossip network.

Member service: the member service is the member management service, which provides identity management, privacy, confidentiality, and auditability services for the entire blockchain network. Member management services through Public Key Infrastructure (PKI) or ZKP (Zero-knowledge Proof) and a decentralized consensus mechanism platform can restrict the ability of access nodes and clients, making nonlicensed blockchain become licensed blockchain.

Sort service: it is a communication service run by a set of sort nodes that provides atomic broadcast services that use pluggable trust engines (CFT or BFT) to sort transactions. The sort service collects a set of transactions into a preblock and distributes them to the commit node. The GOSSIP synchronization block is used between nodes. Common sorting algorithms include SOLO, Kafka, and SBFT.

Ledger maintenance: it continuously forms blocks of newly linked data into the ledger in chronological order and updates other copies of the ledger in the blockchain network.

4.2. Decentralization Technology Route. The main characteristics of using blockchain to achieve traceability are as follows: the essence of the business level is decentralization,

while the essence of the technical level is dedatabase. To better understand this core feature, a comparison is made between the traditional traceability [20] approach using database technology and the blockchain-based traceability approach.

The database traceability scheme generally adopts a three-tier architecture, which is the database, the business logic layer, and the client. The application technology of the client and business logic layer is constantly evolving, but the underlying database has not changed much. With the increase in concurrent access and the need to improve the user experience, the response time is more and more demanding, and the caching layer is added, as shown in Figure 3. In the traditional database-based traceability scheme, the business logic layer and various applications on the client side all rely heavily on the underlying database. The database becomes the central and constraint bottleneck of this type of solution, and once it is tampered with or destroyed, the impact is global and catastrophic.

The difference between blockchain traceability and traditional database technology traceability is that the data is stored in a distributed ledger and read and write operation of the ledger is carried out through smart contract. The distributed ledger is a key value blockchain plus state library. A blockchain is a series of connected blocks, corresponding to files, written in an appended, immutable way, to record historical transactions that can take place at any node in the world's network; the status library can be constantly updated, corresponding to the current state of the books. The fabric of Oracle and IBM blockchain cloud services default to level DB, which can be replaced with other key value databases such as CouchDB. Blocks and transactions can be generated at any network node in the world, and cryptography methods such as PKI, asymmetric key encryption algorithm, and digital certificate can be used to guarantee the nonrepudiation and privacy protection of transactions. This new traceability scheme is a decentralized distributed network platform. The blockchain-based technology traceability scheme is shown in Figure 3(b).

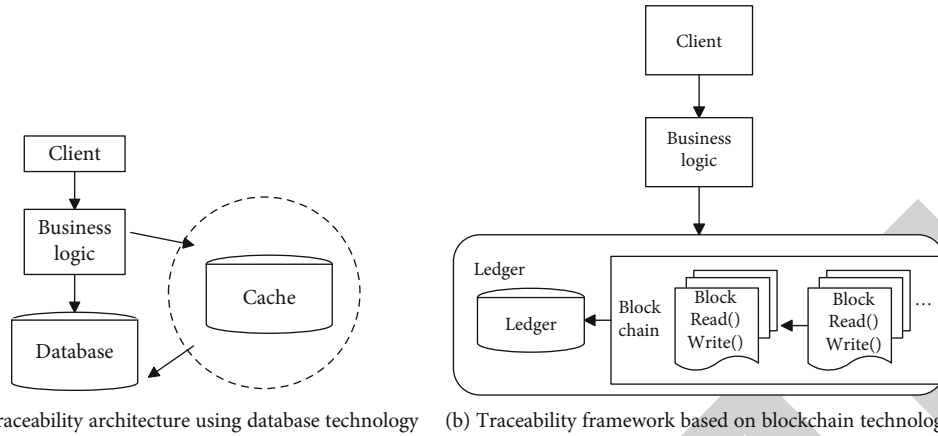


FIGURE 3: Comparison of the traceability architecture based on blockchain and traditional database technology.

Participants in the food supply chain such as farms, ranches, farmers, food enterprises, inspection and supervision departments, and supermarkets input their responsible information into the blockchain with their private keys to generate account books. The blockchain network uses the consensus mechanism to ensure the consistency of distributed account books. With distributed ledgers, if a participant in the food supply chain is tampered with or has falsified information (transactions), it is easy to identify who tampered with or falsified the information (transactions) because copies of the ledger are not changed at other nodes scattered across the network.

4.3. The Technical Route of the Consensus Mechanism. In blockchain, the consensus algorithm is adopted to ensure the consistency of the ledger. From bitcoin in 2009 to Ethereum in 2014, the POW (Proof-Of-Work) consensus algorithm is adopted in the public chain, while the modular/pluggable consensus algorithm is adopted in the alliance chain such as the Super Ledger Fabric from 2017. Therefore, a clearly defined and implemented consensus algorithm is probably the most important feature for the security, extensibility, and maturity of each blockchain protocol. Choosing the right consensus algorithm is crucial to support mutual trust in a distributed business network.

The Byzantine fault tolerance (BFT) algorithm is a general term for solving the Byzantine general problem. Its characteristic is that even if some nodes have shortcomings or malicious behavior, the Byzantine fault tolerance system can continue to operate. In essence, Byzantine fault tolerance is that the minority is subordinate to the majority. The practical Byzantine fault tolerance mechanism will specify that one node in the system is the primary node (leading node) and the other nodes are the secondary node (alternate node). When the primary node fails, all the legitimate nodes in the system are qualified to upgrade from the secondary node to the primary node and follow the principle of minority subordinate to majority to ensure that the honest nodes can reach a consensus. To produce agricultural and sideline products from farms to pastures to dinner tables, the collapse of fault-tolerant and Byzantine fault-tolerant consensus algorithms may be even more necessary. Since the SOLO consen-

sus model uses one node to verify all transactions, it is more suitable for the development network with relatively limited security requirements.

Currently, Hyperledger Fabric supports consensus-based voting in licensed networks. The combination of voting and licensing makes the network runtime far more efficient than many publicly owned Byzantine fault-tolerant networks. In our design of the food safety traceability system, because the cattle ranches in the food supply chain, farmers, food processing enterprises, inspection supervision department, distributors, and retailers are based on the identity of the participants, there is no unknown role throughout the supply chain, meaning that our food safety traceability system does not need to trouble the consensus algorithm, using super book Fabric providing out-of-the-box Apache Kafka and fault tolerance; it also supports collapse, namely, when there is a part of the network that is still functioning. Other consensus algorithms such as BFT-Smart and SBFT (simplified Byzantine fault tolerance) can also be considered to tolerate malicious actions in the consensus.

What is the operating mechanism of the traceability application designed and developed according to the system architecture in Figure 2? The following is a step-by-step description of the transaction flow diagram in Figure 4.

Here, E0, E1, and E2 are endorsement nodes; P3 and P4 are submission nodes; O is the sort node, and some sort nodes act as sort service; A, B, C, and D are smart contracts (chain codes in the Super Ledger Fabric). The transaction process is as follows:

- (1) The application initiates the transaction request

The client program submits a transaction request to smart contract (chain code) A. The smart contract must be endorsed by nodes {E0, E1, E2}.

The endorsement strategy is that E0, E1, and E2 must be signed; P3 and P4 do not need signature.

- (2) Endorsement node to execute the transaction proposal

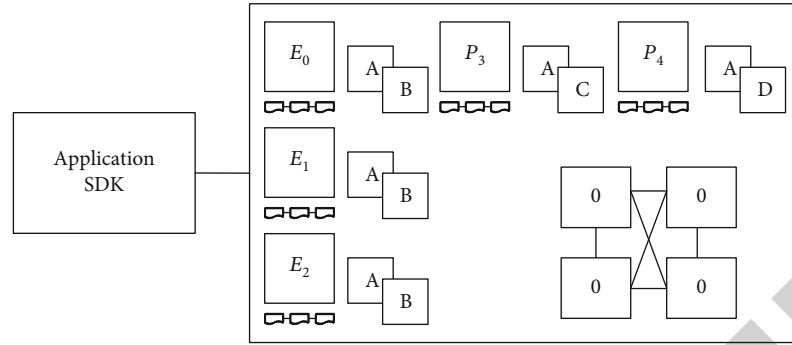


FIGURE 4: Schematic diagram of the transaction process.

E_0 , E_1 , and E_2 execute transaction proposals separately, and these executions do not update the books. Each execution produces a set of data, called RW sets, which are read and written.

(3) The application receives the response

The RW sets are signed by each endorsement node $\{E_0, E_1, E_2\}$ and returned to the application.

(4) Sort transactions

The application submits the response data to the sort node as a transaction that needs to be sorted. Sorting is done concurrently, and the execution of other applications can be processed simultaneously.

(5) Distribute transactions

Sort nodes distribute transactions to all commit nodes $\{E_0, E_1, E_2, P_3, P_4\}$. The sort service collects a set of transactions into a preblock and distributes them to the commit nodes $\{E_0, E_1, E_2, P_3, P_4\}$. Gossip is used between nodes to synchronize each commit node in the block.

(6) Verify the transaction

Each commit node $\{E_0, E_1, E_2, P_3, P_4\}$ verifies the endorsement policy to check that the RW sets are still valid against the current state to prevent double flowers. The transaction is written into the ledger, and the status information of the valid transaction is updated in the status DB.

(7) Notify the transaction result

The submission nodes $\{E_0, E_1, E_2, P_3, P_4\}$ notify the transaction results to the application. The application can register messages that need to be notified of the success of the transaction and the addition of a block, and then, the peer to which the application is connected notifies other events accordingly.

5. Experimental Results and Analysis

The traditional urban fruit traceability system has a central database, which can manage the data centrally. In the pro-

cess of each producer's participation, the data is likely to be tampered and destroyed. After users submit access to the system platform, they request central database access. In the process of access, there is the risk of human operation modification, and the traceability data may be inaccurate. Manufacturers, processors, and sellers of urban fruit quality traceability models based on blockchain need to enter and query data, and the government or organization can view the data entry. Users access the blockchain through the private key, obtain the transaction copy of the account, and then trade with other participants. The transaction records are encrypted and stored in the account book copy together with the timestamp. Then, the transaction records are propagated to the surrounding nodes through a consensus algorithm to complete data synchronization. Distributed data storage reduces the possibility of network attacks and human tampering. A comparison of the two architectures is shown in Figure 5.

The traditional urban fruit traceability system is to establish a centralized database, while the urban fruit quality traceability model based on blockchain is to establish a node database account and establish a copy to distribute to each participant. Through the analysis of Table 1, compared with the urban fruit quality traceability model based on blockchain, the traditional urban fruit traceability system requires higher costs and longer initial certification time. It is difficult for the government to supervise the internal system data of the enterprise, and the data interaction process may lead to inaccurate data due to human participation.

Table 2 and Figure 6, respectively, compare the traceability efficiency and system performance of RFID traceability technology, two-dimensional code traceability, commodity bar traceability, and blockchain traceability.

RFID has been piloted in several industries, but there is no unified standard. The cost of a complete SET of RFID equipment is relatively high, and different traceability systems are not compatible, so only the electronic tags of this system can be identified. Overall, the Xinjiang agricultural product quality traceability system is still in the state of "fragmentation," the traceability system incompatible problem is very serious, this is not only convenient for consumers to query trace information, and data security is low and is not conducive to government departments to use a real-time tracing system for food safety regulation, causing a serious waste of resources.

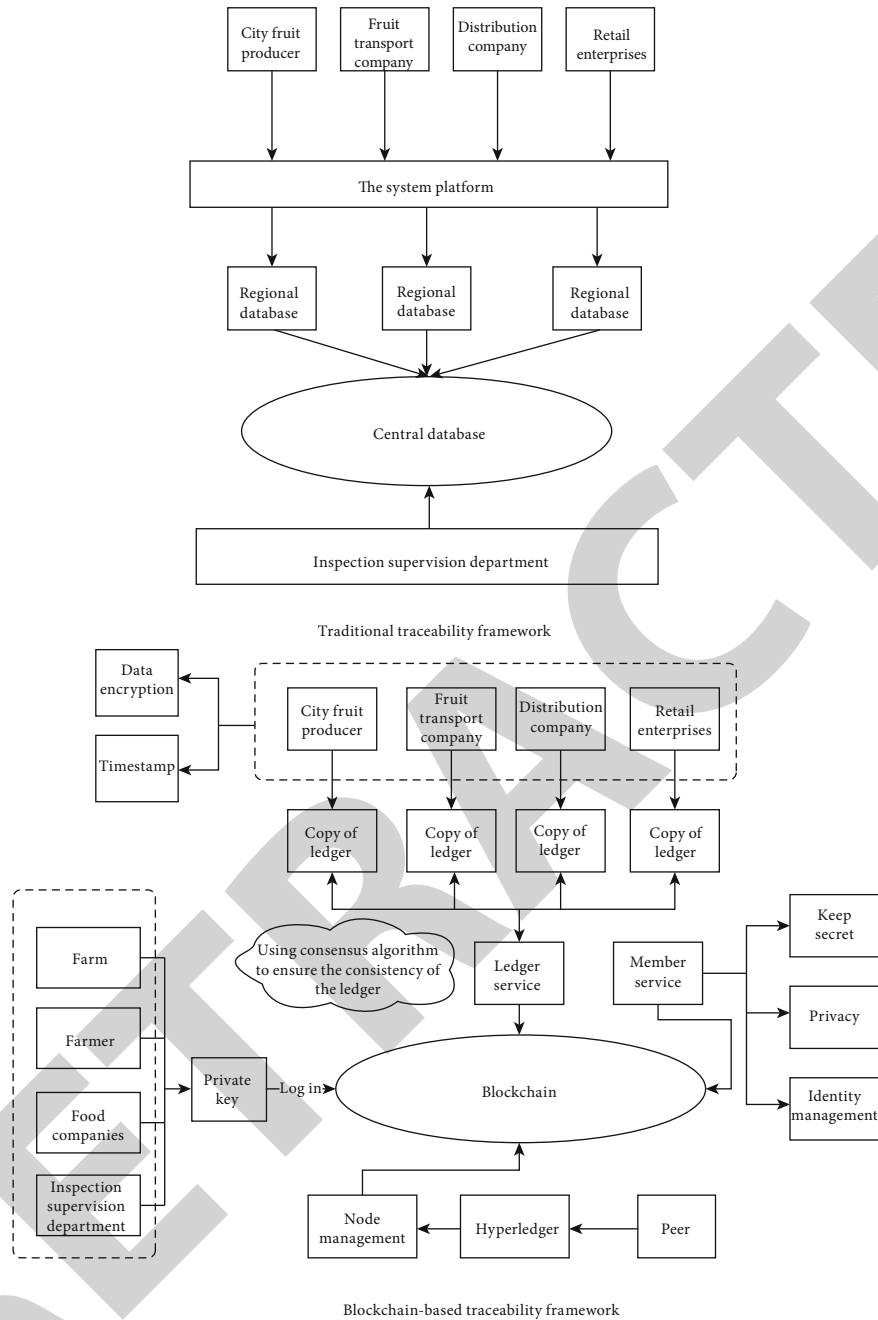


FIGURE 5: Comparison of traditional and blockchain database architecture.

Because the cost of two-dimensional code is much cheaper than that of RFID, it is widely used in life. With high information density and large information capacity, two-dimensional code can be independently applied without relying on a database and communication network. Moreover, it can encode digital information such as picture, voice, signature, and fingerprint to complete the description of items, thus providing consumers with more comprehensive food traceability information. However, two-dimensional code recognition technology has disadvantages such as reproducibility, easy to stain, and low data integrity and security.

Barcodes are now the main source of traceability used in shopping malls. Since barcode is unique, it is easy to trace and manage each workshop, different production lines, and each production process in the whole production process. At the same time, managers can carry out statistics, analysis, and feedback on all the information, to realize the traceability management of the whole production process. The bar code error proofing system collects raw data, which ensures the timeliness and accuracy of production information and makes the production process knowable and controllable. By mastering all information of the production process, the

TABLE 1: Comparison of the traditional system architecture with the blockchain system architecture.

System name	Traditional centralized system [20]	City fruit quality traceability model
Certification time	1.5~2.0 months	Expected within 1 month
Certification cost	13,000~18,000 yuan	Estimated within 10,000 yuan
Data integrity	Only a small amount of data owned by participants	Cover all data on the chain
Data tampering	Data can be tampered with at any time	The data is automatically synchronized and updated and cannot be tampered with
Government regulation	It is difficult for government regulators to monitor the data of enterprise systems	The government supervision department acts as a blockchain node and monitors traceable data at all times

TABLE 2: Performance comparison of the four traceability technologies.

	RFID traceability technology [5]	Two-dimensional code traceability technology [6]	Commodity barcode traceability technology [7]	Ours
Performance	√	√	√	√
Traceability	√	√	√	√
Data integrity	√	√	√	√
Data security	×	×	×	√
Supervisory capability	√	×	×	√
Traceability efficiency	√	√	√	√

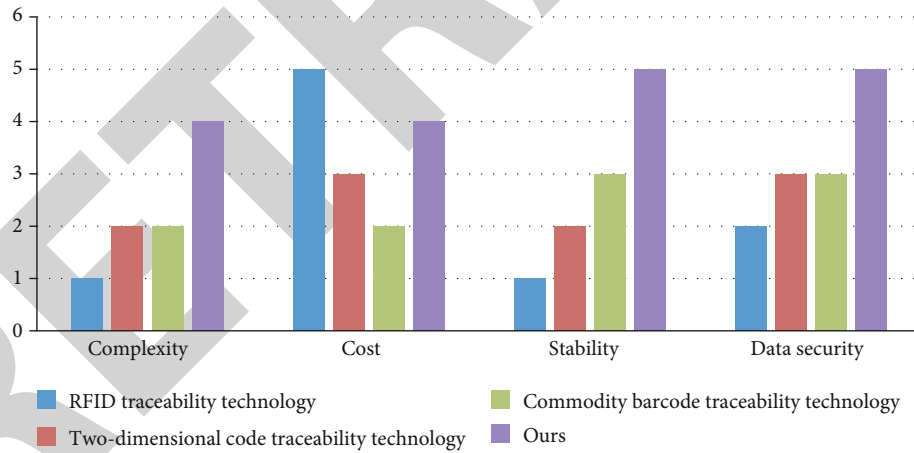


FIGURE 6: Performance comparison of the four traceability systems.

production technology can be adjusted in a planned way without worrying about the authenticity of the information. However, in the process of production and sales, there are still instances of obtaining improper benefits by forging bar codes, and the data security is low.

These technologies mitigate the harm caused by fake and inferior products to some extent, but in fact, they cannot fundamentally solve the problem of counterfeiting by copying and transferring anticounterfeit labels and cannot avoid centralized human operation. Recent scandals have further undermined its

credibility. Compared with the traditional technology, the blockchain with the characteristics of decentralization and nontampering can fundamentally trace the anticounterfeiting source of commodities and effectively strengthen people's trust in the market.

Figure 7 compares the traceability degree of the traditional fruit traceability system and the traceability model based on blockchain. A batch of fruit is marked and put on the market to ensure randomness of fruit circulation and eliminate human intervention as much as possible. Subsequently, the

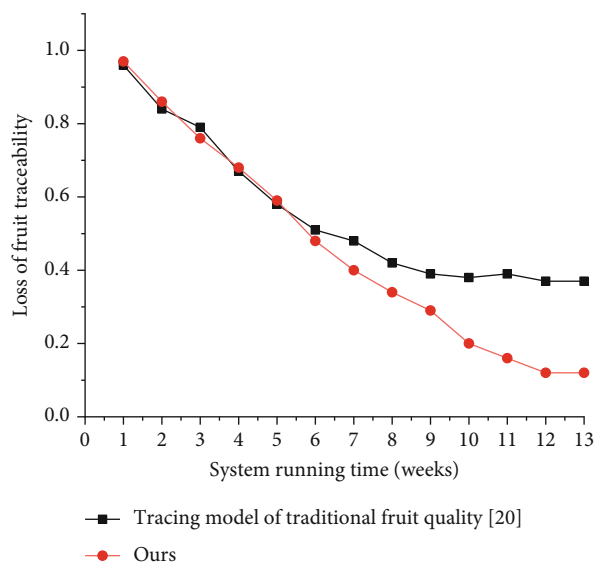


FIGURE 7: Comparison of traceability loss degree between traditional and blockchain models.

two models were used to track the whole region. Due to the short time and low fruit fluidity at the beginning, the loss degree of both models remained high. As time goes by, the loss rate of the traditional traceability model containing natural losses will eventually stabilize at about 40%, while the loss rate of the traceability model based on the blockchain will eventually stabilize at about 13%. The loss rate of the traceability model based on the blockchain will be lower, and the traceability performance will be better.

6. Conclusion

In the Internet of things, according to the characteristics of the blockchain, the traceability model of urban fruits is created, and the architecture design based on the traceability model of blockchain is proposed. Based on studying the architecture design of the traceability model of blockchain, the traceability model of urban fruit quality based on blockchain was established. The traceability model is connected to each participant through the blockchain network. Each participant will establish a node, and each node will be a peer. At the same time, each participant will be displayed as the client and server and has the right to view and modify the node data. The asymmetric encryption algorithm adopted by blockchain ensures the security of users' personal information. Farmers, farms and pastures, food enterprises, and regulatory agencies access the node through the decoding of the private key of the blockchain. The decentralized point-to-point network of blockchain solves the trust problem in the transaction process through distributed node management and automatic management of nodes by using a super ledger structure network. A blockchain network provides Internet of things account services. Each node has a copy of the ledger that is exactly consistent with the ledger data. The data information of participants' transactions is encrypted by an encryption algorithm, and the corresponding timestamp is

generated for each transaction to ensure that the changed data can be tracked and prevent forgery. The data information of each node is owned, managed, and supervised by all participants. Each transaction is a transaction, and the transaction is automatically executed by the smart contract code without the intervention of a legal person. The blockchain network also keeps the identity privacy of its members' secret to ensure the information security of its participants. Different from the traditional clustering method, the distributed technology of blockchain is used to reconstruct, and the point-to-point dispersion of blockchain is used to make the transaction of participants more fair, just, and open and reduce the risk of urban fruit counterfeiting or low quality.

Data Availability

The datasets used and/or analyzed during the current study are available from the corresponding author on reasonable request.

Conflicts of Interest

The authors declare that they have no conflicts of interest.

Acknowledgments

This work was supported by the National Engineering Laboratory for Agri-product Quality Traceability Project (No. AQT-2020-YB2), the Beijing Municipal Commission of Education Project (Nos. KM202111417001 and KM201911417001), the National Natural Science Foundation of China (Grant Nos. 61871039, 61906017, and 61802019), the Collaborative Innovation Center for Visual Intelligence (Grant No. CYXC2011), and the Academic Research Projects of Beijing Union University (Nos. ZK40202101, ZK120202104, ZB10202003, ZK80202001, and XP202015).

References

- [1] Y. Yong and F. Wang, "Current status and prospects of blockchain technology development," *Acta Automatica Sinica*, vol. 42, no. 4, pp. 481–494, 2016.
- [2] N. Zhang, Y. Wang, C. Kang, J. Cheng, and D. He, "Research framework and typical applications blockchain technology in the energy Internet: a preliminary study of research framework and typical applications," *Proceedings of the Chinese Society of Electrical Engineering*, vol. 36, no. 15, pp. 4011–4022, 2016.
- [3] W. Hongwei, W. Hua, and Q. Zhiwei, "A method of agricultural product traceability combining qualitative analysis and online identification," *Modern Agricultural Science and Technology*, vol. 19, pp. 223–227+231, 2020.
- [4] C. Yuejing, Z. Ailian, N. Xie et al., "Agricultural product quality and safety traceability system based on blockchain and Internet of things," *Journal of Agricultural Big Data*, vol. 2, no. 3, pp. 61–67, 2020.
- [5] L. Zongmei, "Research on "blockchain + radio frequency identification technology" empowering food traceability platform," *Food and Machinery*, vol. 36, no. 9, pp. 102–107, 2020.
- [6] H. Wang, L. Weiwei, H. Wu, B. Yanhong, and L. Junguang, "Design and implementation of a safety traceability system

Retraction

Retracted: Network Traffic Prediction via Deep Graph-Sequence Spatiotemporal Modeling Based on Mobile Virtual Reality Technology

Wireless Communications and Mobile Computing

Received 28 November 2023; Accepted 28 November 2023; Published 29 November 2023

Copyright © 2023 Wireless Communications and Mobile Computing. This is an open access article distributed under the Creative Commons Attribution License, which permits unrestricted use, distribution, and reproduction in any medium, provided the original work is properly cited.

This article has been retracted by Hindawi, as publisher, following an investigation undertaken by the publisher [1]. This investigation has uncovered evidence of systematic manipulation of the publication and peer-review process. We cannot, therefore, vouch for the reliability or integrity of this article.

Please note that this notice is intended solely to alert readers that the peer-review process of this article has been compromised.

Wiley and Hindawi regret that the usual quality checks did not identify these issues before publication and have since put additional measures in place to safeguard research integrity.

We wish to credit our Research Integrity and Research Publishing teams and anonymous and named external researchers and research integrity experts for contributing to this investigation.

The corresponding author, as the representative of all authors, has been given the opportunity to register their agreement or disagreement to this retraction. We have kept a record of any response received.

References

- [1] K. Zhang, X. Zhao, X. Li, X. You, and Y. Zhu, "Network Traffic Prediction via Deep Graph-Sequence Spatiotemporal Modeling Based on Mobile Virtual Reality Technology," *Wireless Communications and Mobile Computing*, vol. 2021, Article ID 2353875, 12 pages, 2021.

Research Article

Network Traffic Prediction via Deep Graph-Sequence Spatiotemporal Modeling Based on Mobile Virtual Reality Technology

Kai Zhang,^{1,2} Xiaohu Zhao ,¹ Xiao Li,^{1,2} Xingyi You,^{1,2} and Yonghong Zhu³

¹National and Local Joint Engineering Laboratory of Internet Application Technology on Mine, China University of Mining and Technology, Xuzhou, Jiangsu 221008, China

²School of Information and Control Engineering, China University of Mining and Technology, Xuzhou, Jiangsu 221008, China

³School of Information Engineering, Xuzhou University of Technology, Xuzhou, Jiangsu 221008, China

Correspondence should be addressed to Xiaohu Zhao; xhzhao76@gmail.com

Received 8 June 2021; Revised 25 June 2021; Accepted 12 July 2021; Published 1 August 2021

Academic Editor: Balakrishnan Nagaraj

Copyright © 2021 Kai Zhang et al. This is an open access article distributed under the Creative Commons Attribution License, which permits unrestricted use, distribution, and reproduction in any medium, provided the original work is properly cited.

Accurate and real-time network traffic flow forecast holds an important role for network management. Especially at present, virtual reality (VR), artificial intelligence (AI), vehicle-to-everything (V2X), and other technologies are closely combined through the mobile network, which greatly increases the human-computer interaction activities. At the same time, it requires high-throughput, low delay, and high reliable service guarantee. In order to achieve ondemand real-time high-quality network service, we must accurately grasp the dynamic changes of network traffic. However, due to the increase of client mobility and application behavior diversity, the complexity and dynamics of network traffic in the temporal domain and the spatial domain increase sharply. To accurately capture the spatiotemporal features, we propose the spatial-temporal graph convolution gated recurrent unit (GC-GRU) model, which integrates the graph convolutional network (GCN) and the gated recurrent unit (GRU) together. In this model, the GCN structure could handle the spatial features of traffic flow with network topology, and the GRU is used to further process spatiotemporal features. Experiments show that the GC-GRU model has better prediction performance than other baseline models and can obtain spatial-temporal correlation in traffic flows better.

1. Introduction

Accurate network traffic prediction is the basis of network performance optimization and network integrated management [1]. The prediction results can be used for traffic engineering, anomaly detection, and energy consumption management [2, 3]. Especially in the last decade, the complexity and the diversity of the network and the communication scenario increase dramatically, which promote researchers proposed many technologies such as ultra-dense deployment of cellular cells, device-to-device (D2D) network technology mobile virtual reality (MVR), and mobile edge computing to improve network capacity and service quality [4–6]. The successful application of these technologies is tightly related to the accurate cognition of network traffic features

and future trends. In the context of these scenarios, network resource optimization is accomplished by two key elements, traffic model and optimization algorithm. If we can more accurately and timely understand the dynamic trend of future traffic, high reliability and low delay communication could be achieved by dynamic content caching or service processing in vicinity [7–9].

However, the traditional network traffic prediction model gradually presents many deficiencies in processing of increasingly complex network traffic. In the context of the linear network traffic forecasting model such as autoregressive integrated moving average (ARIMA) model [10], support vector regression model (SVR) [11], and Bayesian model [12, 13], mainly through the linear correlation of traffic in temporal to achieve traffic modeling and prediction, with

the emergence of new network technology and new scenarios, new factors that could greatly affect network traffic features should be considered:

- (1) The trend of network traffic is constrained by network topology, every end-to-end traffic flow travels the network through a path composed of links, and a link converges flows from different paths. The performance change of any node on the transmission link will spread to the adjacent nodes. The booming 5G, the Internet of Things (IoT), MVR, and V2X bring more and more mobility to the network, which also bring great uncertainty in the spatial distribution of network traffic
- (2) The statistical value of network traffic flow shows the characteristics of proximity, periodicity, and trend in time. The closer the time interval, the higher the correlation between the two statistical values. In the scenarios such as MVR, IoT, or V2X, the terminal behaviors and traffic demands are more dynamic, that make the temporal patterns of the traffic too complicated to be captured [14–16].

To better handle the problem of spatial feature processing caused by terminal mobility and spatial dependence of applications, many studies use neural networks to network traffic modeling and prediction based on the big data of the network traffic [17]. The convolutional neural network (CNN) and RNN are the most representative in the proposals [17–19]. However, the method based on CNN also has some shortcomings. Different from Euclidean data such as image and grid, the communication network usually uses graph representation which is not suitable for CNN [17]. Unlike the Euclidean data, the structure of graph is irregular. It is difficult for CNN to hold a stable kernel size to realize parameter sharing. This kind of model cannot describe the spatial correlation of network in essence; consequently, the prediction accuracy of the trained model and the applicability of different topologies are limited. To solve these problems, we propose GC-GRU, a novel network model which could accurately forecast network traffic matrix by comprehensively understand the complex relation on traffic flow, node topology, and time. Our main contribution has three aspects:

- (1) This model firstly uses GCN to process network topology relationship, node input traffic, and network topology that are combined as input of the model to achieve spatial features capturing. Then, hidden states are input to a recursive network based on GRU to find the temporal dynamics. Through the parameter sharing method of spatial and temporal features, traffic prediction has a better universal correlation model for the future network. Our model is able to generalize over arbitrary topologies, routing schemes, and variable traffic intensity
- (2) We evaluated our model on real topology and traffic matrices of real traffic dataset. The result shows that our model can handle the time-varying information

of graph structure well and has higher accuracy than all baseline methods, which proves the superiority of the model in network traffic prediction. In addition, through experimental comparison, we find that our GC-GRU model can maintain stable prediction performance under different forecast time granularity, and it shows that it has better robustness

2. Related

Network traffic prediction methods include analytic model method and data-driven method. The representative methods of the first kind include queuing theory model, cell transmission model, and random geometry model [20–23]. Through the model method, a clear relationship between network traffic and other network parameters could be established, so as to complete the network planning and scheduling. For example, Krishnan et al. [23] introduce an analysis framework of random geometry that describes the spatial-temporal interference of adjacent locations and calculates the joint coverage probability of them; in this contest, the Poisson process is used to model the mobile behavior of the UE under the station. Kamath et al. [24] proposed a framework to handle the QoS of heterogeneous services in the network, in which a multiclass queuing model is used to analyze the heterogeneous services performance demands and combined with SDN technology to complete service classification and network slicing. Such models are either based on some idealized assumptions or based on realistic simplification. However, in reality, it is difficult to model UE arrival process as Poisson process, and the diversity of applications also makes the link service feature dynamic. These theoretical models are difficult to model these mobility, time-varying, and spatial dependence elements comprehensively; consequently, it is hard to accurately predict the current complex network traffic in reality [10, 18]. In addition, the model-driven approach relies on specific idealized scenarios; as a result, it lacks the ability of generalization and migration [25–27].

The data-driven methods are based on the statistical characteristics of network traffic history data, by using its self-similarity, long-term relevance, and periodicity to forecast the trend in time domain [1, 28]. This kind of methods does not specifically analyze the specific dynamics and behaviors of network elements and has high flexibility. These methods are mainly including parametric prediction and nonparametric prediction [10, 29]. The parameter model is based on the regression function, through the analysis in mathematical statistics of the history data to determine the quantitative relationship of interdependence between two or more parameters, so as to forecast next step traffic volume according to the regression function.

More representative methods include autoregressive integral moving average model (ARIMA) and its improved variants [10, 30, 31]. For example, Paxson and Sally [32] used the autoregressive integral moving average model (ARIMA) to predict Ethernet traffic in 1994. Subsequently, in order to improve the prediction accuracy of the model, many researchers proposed different kinds of improvements based

on it, such as seasonal-ARIMA (SARIMA), Kohonen-ARIMA, and subset ARIMA [10, 33]. Maciej and Anna [33] found that the latter SARIMA has better prediction accuracy than the ARIMA model through experimental. Furthermore, Chen et al. [34] used SARIMA to predict the short-term flow of the IEEE 802.11 network for the first time and achieved well prediction results on single traffic flow. Their advantages are that the mathematical foundations are relatively mature, and the system performance evaluation is easy to express mathematically. However, these methods are not robust. They assume that statistics and parameters' relationship of the traffic model hold steady which are not conform to the reality of network traffic nowadays. In addition, the nonparametric model has its advantages in this respect. The representative methods such as Bayesian network model [12, 13], support vector regression model (SVR) [35, 36], K-Nearest Neighbor model [37], and neural network model [38] use just historical traffic information to automatically learn statistics.

Recently, the deep learning model has been effectively devoted to promote complex pattern recognition and analysis in big data systems [28, 39–41]. Meanwhile, with the improvement of network big data collection ability, network traffic prediction methods based on the deep learning have attracted much attention because of its ability on capturing the nonlinear features of network traffic [1, 41]. For example, Azzouni and Pujolle [18] use recurrent neural networks (RNNs) to predict the traffic matrix (TM) and uses the prediction results to dynamically and actively allocate optical network resources to save network available capacity and alleviate the impact of peak traffic. To achieve traffic forecasting in data center, Laisen et al. [13] combined deep structure and deep trust networks to achieve traffic demand prediction through temporal dynamic features capturing. Tang et al. [42] proposed a prediction method of communication key indicators based on deep learning and combined software-defined network (SDN) to achieve intelligent dynamic channel allocation, which improves the channel utilization of wireless Internet of Things and avoids potential congestion. These methods mainly take the temporal correlation of network traffic sequence as prediction basis and the advantages recurrent neural network (RNN) structure to learn the characteristics in time to achieve adaptive traffic flow or traffic matrix prediction.

As mentioned before, the factors that affect network traffic are not only time but also in spatial. Without spatial relations such as network topology, dynamic content dependence, and client mobility, accurate forecasting and estimating could not be achieve. In order to explore the potential of spatial features on network traffic prediction, many studies had been proposed. For example, Zhao et al. [43] proposed a model that combined the multiscale wavelet analysis with the deep learning approach with; firstly, discrete wavelet decomposition was used to decompose the original TM sequence into multilevel time-frequency TM subsequences of different time scales; then, a CNN was used to find the spatial distribution pattern between network streams and finally, the LSTM in charge of exploring temporal dynamics in the TM sequences. In order to estimate the

future location and resource usage of UEs, Siracusano and La Corte [44] proposed a deep regression (DR) model based on a tightly connected convolutional neural network (CNN) to simulate its complex spatiotemporal dynamics to capture the multiscale of mobile data. LA-ResNet [41] is a model which combined the residual network and RNN to capture spatiotemporal correlations of wireless traffic, and the experimental results showed that it had higher accuracy than RNN models.

Although the CNN method has made great progress in network traffic prediction, its data operation process makes it more suitable for processing Euclidean data rather than graph topology. The complex topological structures of communication network limited its application in this field. Based on this background, we propose a novel network GC-GRU, which unifies the network nodes, links, and traffic input in space, and analyzes the inherent spatiotemporal correlation characteristics combined with the dynamics in time, so as to complete the accurate network traffic prediction.

3. Method

3.1. Problem Definition. The task of network traffic prediction is to estimate the future network traffic status as accurately as possible according to the network historical traffic data. The traffic information includes traffic volume, time delay, and packets loss. In this paper, we take traffic volume as main example in experiment.

Definition 1. In our model, unweighted graph $G = (V, E)$ was used to denote the network topology, where $V = \{v_1, v_2, \dots, v_N\}$ denotes N nodes (they could be switches or routers) in the network, and E represents the set of communication links between nodes. The adjacency matrix A describes the detail relationship among network nodes, where $A \in R^{N \times N}$. Its element $a_{ij} = 1$ if node v_i is connected to v_j , $a_{ij} = 0$ otherwise.

Definition 2. We use $X^{N \times P}$ to represent the traffic feature matrix in the network, where N represents nodes counts as mentioned above, and P denotes the length of historical sampling sequence of traffic. $X_t \in R^{N \times i}$ means the traffic on node connection at time i .

In this way, our spatiotemporal network traffic prediction problem model is represented as equation (1):

$$[x_{t+1}, \dots, x_{t+T}] = f([x_{t-n}, \dots, x_{t-1}, x_t]; G), \quad (1)$$

where f denotes the mapping function from G and historical X , to the next T step traffic information.

3.2. Model

3.2.1. Framework Overview. In this part, we will introduce our solution model GC-GRU, in which the temporal and spatial features are considered comprehensively. As shown in Figure 1, GC-GRU includes input layer, spatial feature processing, temporal feature processing, and a fully connected layer. Firstly, it takes n time series data between

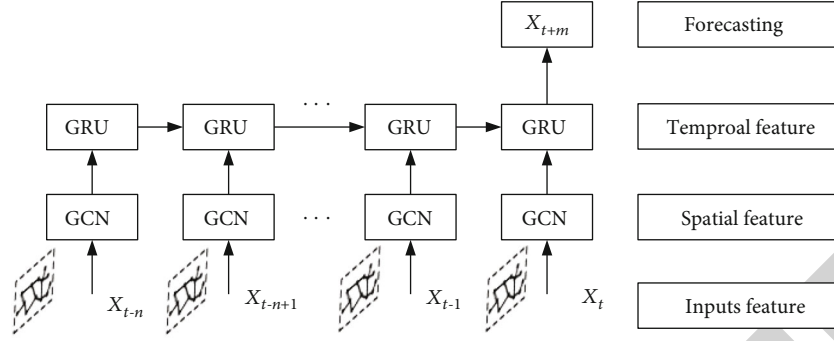


FIGURE 1: Framework overview of the GC-GRU model.

nodes in the network as the input and use graph convolution combined with the spatial topological relationship of communication network to obtain the spatial features of traffic; secondly, we use the processed time series with spatial features as the input of gated recursive unitary model and obtain the features in time domain through the information transmission between cells; finally, we use all connected network as the input. The prediction results are obtained through the layer.

As in Figure 1 shows, our model contains two main part: network topology GCN for spatial feature extraction and GRU for hidden spatial-temporal features capturing. Firstly, the GCN is used to learn the spatial features of the network topology, it takes the traffic feature matrix and network topology data both as input, in detail, X_i denotes the traffic on all node connections at time i , and the topology data is represented by adjacency matrix A introduced in Definition 1. Then, the output of the GCN model is fed into the second part which is constructed by gated recurrent units, to find out the traffic dynamics, so as to learn the temporal features. At last, a fully connected layer network is used to convert features mapping to original space; then, we get the predicted results.

3.2.2. Spatial Relation Feature Extraction Model. Accurately capturing the spatial dependence between nodes in the network is a key problem in this paper. As mentioned before, the CNN is suitable for Euclidean space data rather than non-Euclidean data like network topology [45]. In the graph representation of the network, each vertex has different numbers of adjacent vertices, and it is difficult to hold a convolution kernel with a same size. In recent years, the graph convolutional network (GCN) has been widely concerned, which can realize convolution operation on non-Euclidean structure, effectively learn the spatial characteristic information of nodes, and has been applied in action recognition, traffic network flow prediction, and so on [46–48].

From the perspective of graph signal processing (GSP), it applies discrete signal processing (DSP) to the field of graph signal. Through the transfer of basic concepts of signal processing such as Fourier transform and filtering, it studies the basic tasks of signal processing such as compression, transformation, and reconstruction of graph signal [49, 50]. In detail, given a graph $G = (V, E)$, graph signal is a kind of mapping from node field to real number field

[50], which is expressed as vector in the form of $X = [x_1, x_2, \dots, x_n]^T$, and x_i represents signal strength on vertex v_i strength. The Fourier transform of X is represented as $\mathcal{F}(X) = U^T X$, where $U = [u_0, u_1, \dots, u_{n-1}] \in R^{n \times n}$ represented the eigenvector. Its inverse Fourier transform is $\mathcal{F}^{-1}(\hat{X}) = U\hat{X}$, where \hat{X} represents the frequency domain signal obtained from the graph Fourier transform [46]. The graph convolution operation of two groups of graph signals can be transformed into the corresponding graph filtering operation. From this point of view, the graph convolution is equivalent to the graph filtering. We take X as signal on vertexes and $g \in R^N$ as the filter, and the graph convolution could be expressed as equation (2):

$$x *_G g = \mathcal{F}^{-1}(\mathcal{F}(x) \odot \mathcal{F}(g)) = U(U^T x \odot U^T g), \quad (2)$$

where \odot represents the Hadamard product [46]. If we denote a filter as $g_\theta = \text{diag}(U^T g)$, equation (2) could be simplified as

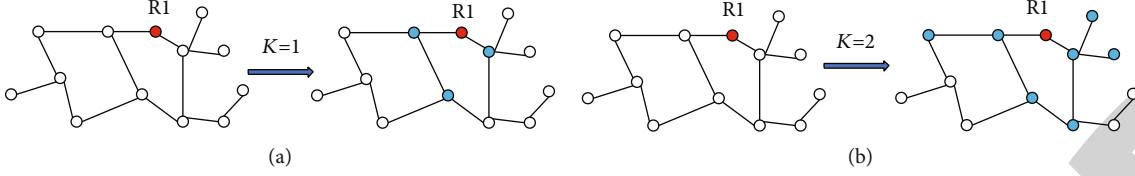
$$*_G g_\theta = U g_\theta U^T X. \quad (3)$$

This method was first proposed by [51], but it has many limitations in practical application. Firstly, the computation depends on the eigen decomposition of Laplacian matrix, which has high complexity. Secondly, when u is used for signal transformation, because u is dense, the complexity is very high, and the method is not localized. Therefore, the method has not attracted widespread attention.

In order to reduce the computational complexity, Chebyshev Spectral CNN (ChebNet) [45] used Chebyshev polynomials of the diagonal matrix of eigenvalues to approximate the filter g_θ . g_θ is a diagonal matrix composed of the parameter θ , and its polynomial expression is represented as equation (4):

$$g_\theta(\tilde{L}) = \theta_0 I + \theta_1 \tilde{L} + \theta_2 \tilde{L}^2 + \dots + \theta_k \tilde{L}^k, \quad (4)$$

where $\tilde{L} = I_n - D^{-1/2} A D^{-1/2}$, D denotes the degree matrix of A ($D_{ii} = \sum_j A_{i,j}$), and I_n denotes identity matrix. As the normalized Laplacian matrix has the property of real symmetric-positive semidefinite [51], \tilde{L} can be decomposed into $\tilde{L} = U \Lambda U^T$, where Λ is the diagonal matrix of eigenvalues [50]

FIGURE 2: Graph convolutional networks. (a) $k = 1$. (b) $k = 2$.

($\Lambda_{ii} = \lambda_i$). Then, g_θ could be expressed as a function of eigenvalue Λ :

$$g_\theta = g_\theta(\Lambda) = \sum_{k=0}^{K-1} \theta_k \Lambda^k, \quad (5)$$

and then convolution of g_θ and graph signals could be expressed as

$$X *_G g_\theta = U g_\theta(\Lambda) U^T x = \sum_{k=0}^{k-1} \theta_k L^k x. \quad (6)$$

In this way, the number of calculation parameters is reduced from n to k , and there is no need to explicitly calculate the feature matrix U in the calculation process; so, the computational complexity is greatly reduced. In addition, k -localized has local connectivity, because it is a k -order polynomial in Laplacian. As Figure 2 shows, each point represents a network node (router or switch), and the line represents link between nodes; for node R1, the GCN could get the spatial information directly linked to R1 and their links to other surrounding nodes and encode the network topology and the traffic attributes in nodes, so as to obtain the spatial correlation.

On the basis above, the first order approximation of chebNet is introduced into the graph convolution network to simplify the calculation process [45]. Moreover, in order to reduce parameters, Kipf [52] further assumes that $\theta = \theta_0 = -\theta_1$, the definition of graph convolution given as formula (7):

$$*_G g_\theta = \theta \left(I_n + D^{-\frac{1}{2}} A D^{-\frac{1}{2}} \right) x. \quad (7)$$

Then, a high availability graph convolution network without too much matrix multiplication operation is established. It can be expressed as

$$H^{(l+1)} = \sigma \left(\tilde{D}^{-\frac{1}{2}} \tilde{A} \tilde{D}^{-\frac{1}{2}} H^{(l)} \theta^{(l)} \right), \quad (8)$$

where σ denotes the sigmoid function, $\tilde{A} = A + I_n$, $\tilde{D} (\tilde{D} = \sum_j \tilde{A}_{ij})$ represents degree matrix, $H^{(l)}$ is the output of layer l , and $\theta^{(l)}$ denotes the parameters corresponding.

As shown in Figure 3, our spatial feature analysis model uses a two-layer graph convolution [52] structure. The first layer is $H^{(1)} = \sigma(\tilde{A}X\theta_0)$, $\theta_0 \in \mathcal{R}^{n_1 \times p}$, where n_1 is the number of hidden layer cells, and p is the length of input traffic

matrices. $\theta_0 \in \mathcal{R}^{n_1 \times p}$ represents the feature matrix from the hidden layer to the output layer. The second layer is $H^{(2)} = \sigma(\tilde{A}H^{(1)}\theta_1)$, $\theta_1 \in \mathcal{R}^{N \times T}$, where N represents the node number, and T represents the length of the sequence to be predicted. The whole graph feature extraction process is expressed as follows:

$$f(X, A) = \sigma(\tilde{A}\sigma(\tilde{A}X\theta_0)\theta_1). \quad (9)$$

3.2.3. Temporal Dependence Modeling. This section introduces the method to obtain temporal correlation in network traffic prediction. At present, RNN is the most used model for time sequence data processing. In order to calculate the gradient, the time reverse propagation algorithm is used in the training RNN network. However, it has the defects of gradient disappearance and gradient explosion [53]. For network traffic prediction, it may lose the ability of weighted long-term dependence, which makes it having limitations in long-term prediction. Two famous architectures proposed to solve this problem are LSTM and GRU, and they are improved variants of RNN, which have been proved to solve the above problems [18, 28, 54]. Here, we take the GRU model to find the temporal correlation of network traffic data which is relatively simple, because of less parameters and faster training speed.

As Figure 4 shows, x_t represents the input at time t ; h_{t-1} represents the hidden state at time $t-1$. The candidate activation \tilde{h}_t contains the previous information h_{t-1} and input x_t ; h_t denotes output state at time t which is a linear combination of the activation on the h_{t-1} and the candidate activation \tilde{h}_t ; r_t is the reset gate, which is in charge of controlling whether the previous state should be forgotten or not (e.g., if $r_t \approx 0$, h_{t-1} will not be passed to h_t); z_t is the update gate, and it decides the extent to which the unit updates its activation (e.g., if $z_t \approx 1$, h_{t-1} almost directly copied h_t . Instead, if $z_t \approx 0$, \tilde{h}_t will be passed directly to h_t).

3.2.4. Spatiotemporal Correlation Process. To better predict the impression of complex spatial dependence and dynamic time dependence on the distribution of network traffic, we devote a network traffic spatiotemporal correlation model. In this model, the gate structure and hidden state of GRU are reserved, but we use the convolution feature of graph as input to find the hidden spatiotemporal features.

In the model, the traffic matrix dynamics on network are associated with the network topology information through the graph product to find the spatial correlation of network traffic. Then, the GRU unit is used to further handle the dynamics in temporal, so as to get spatiotemporal

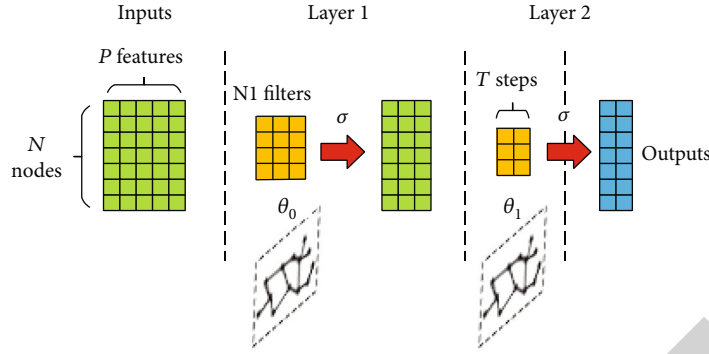


FIGURE 3: Spatial modeling in 2-layer graph convolutional networks (GCN).

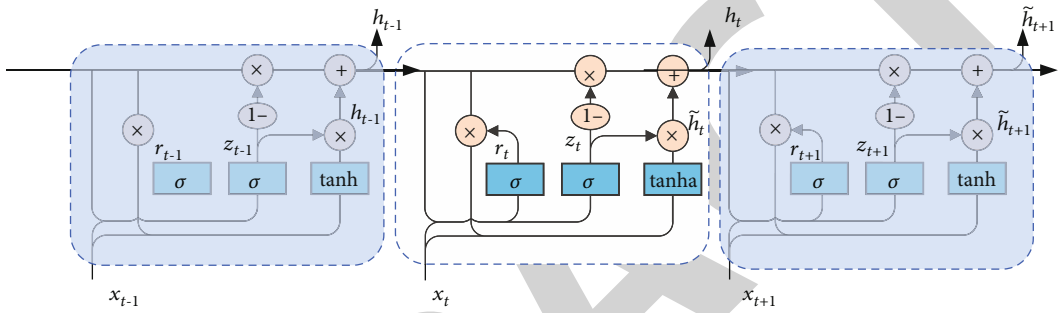


FIGURE 4: The structure of the GRU model.

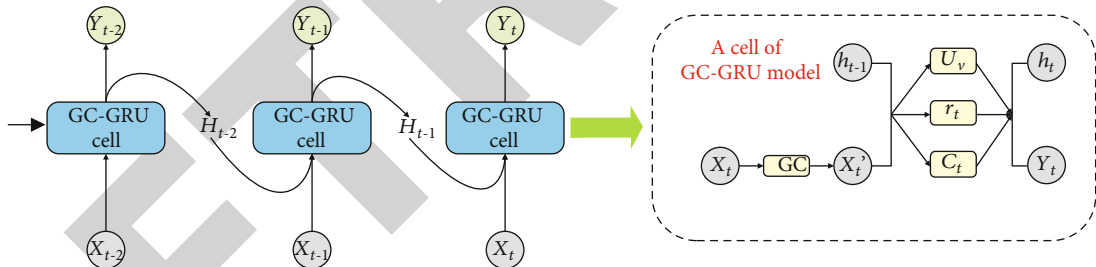


FIGURE 5: The process of spatial-temporal prediction.

correlation, and finally realizes the traffic prediction task. As Figure 5 shows, h_{t-1} denotes the output before time t , and h_t denotes the output at time t . X'_t is the spatial feature matrix after graph convolution, and GC represents the graph convolution process. z_t is the update gate, and r_t is the reset gate. The detail process is shown below:

$$\begin{aligned}
 r_t &= \sigma(W_r[X'_t, h_{t-1}] + b_r), \\
 z_t &= \sigma(W_z[X'_t, h_{t-1}] + b_z), \\
 \tilde{h}_t &= \tanh(W[X'_t, r_t \odot h_{t-1}] + b), \\
 h_t &= z_t \odot h_{t-1} + (1 - z_t) \odot \tilde{h}_t.
 \end{aligned} \tag{10}$$

W represents the weights, and b represents biases, which needs to be trained. \odot represents the point-wise multiplication. The loss function is defined as

$$\text{Loss} = \|X_t - \hat{X}_t\| + \lambda L_{\text{reg}}, \tag{11}$$

where X_t and \hat{X}_t represent the ground truth volume and the forecasted volume. λ is a hyperparameter, and λL_{reg} denotes the L2 regularization term to prevent overfitting.

4. Experiments

4.1. Data Description and Experimental Settings. We evaluate our prediction model by dataset from the Europe Research and Education Network (GÉANT) [55]. GÉANT

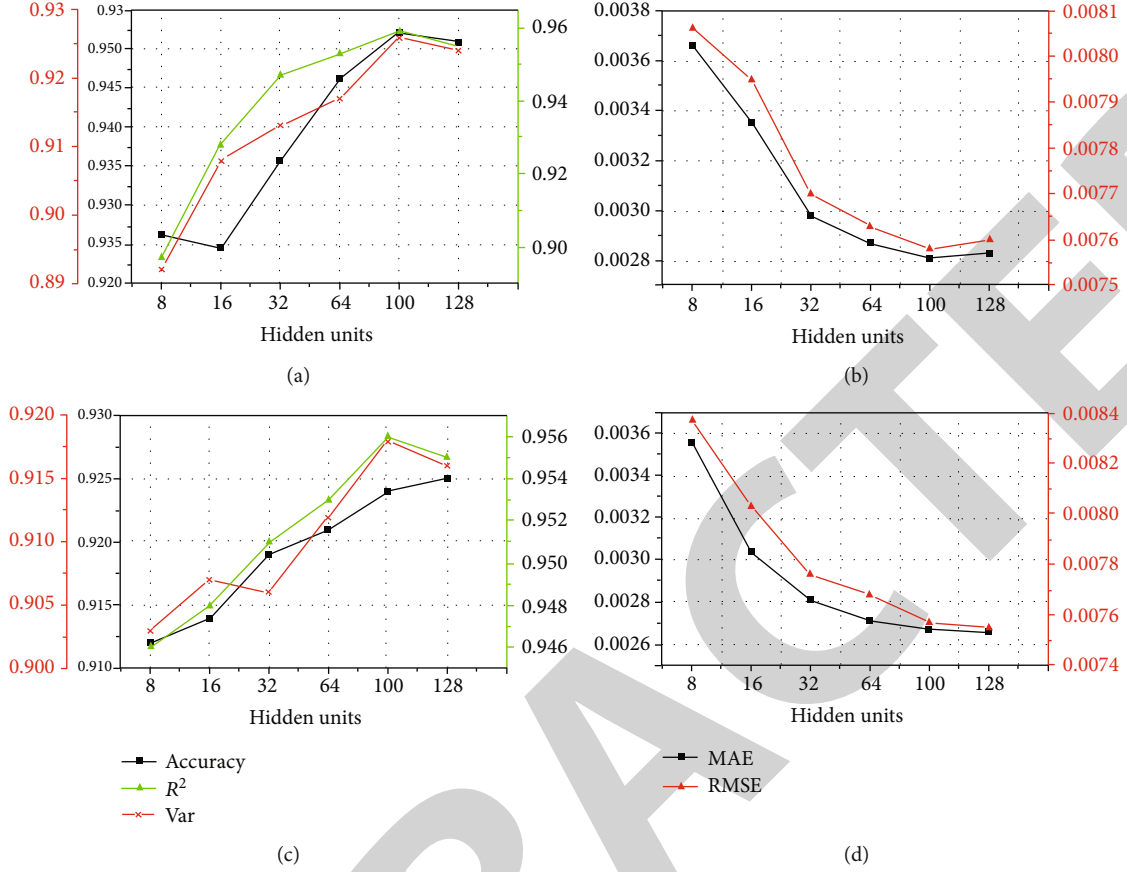


FIGURE 6: (a) Accuracy, R^2 , and var in training set under different hidden units. (b) MAE and RMSE in the training set under different hidden units. (c) Accuracy, var, and R^2 in test set under different hidden units. (d) MAE and RMSE in the test set under different hidden units.

TABLE 1: Instructions of baseline models used for comparison.

No.	Model name	Brief intrude
1	ARIMA [10]	A well-known series data prediction model which the parameter model is consistent with the observation data.
2	SVR [11]	A version of support vector machine (SVM) for regression, it is mainly used in nonlinear regression estimation.
3	GCN	As mentioned in section 3.2.2
4	LSTM [38]	Long-short term memory (LSTM). Here, we set up two LSTM layers and a fully connected layer.

network contains 23 router nodes and 74 undirected links (as of 2005); in addition, 11460 traffic matrices were recorded in every 15 minutes. In the experiment, we build a sliding window on each data sequence for continuous input and learning. 70% of the data is used at the training phase, and the rest 30% is used at test phase.

All experiments adopt Pytorch deep learning architecture. The workstation used for experiment is configured with 64 core Intel Xeon 2.40GHz CPU, tow 8G NVIDIA GTX-2080 graphics, and 192 G RAM. The workstation uses the windows server operating system.

4.2. Evaluation Metrics. In the experiment, 5 metrics are used to evaluate the performance of GC-GRU model:

(1) Root mean squared error (RMSE):

$$\text{RMSE} = \sqrt{\frac{1}{M} \frac{1}{N} \sum_{j=0}^M \sum_{i=0}^N (y_i^j - \hat{y}_i^j)^2}. \quad (12)$$

(2) Mean absolute error (MAE):

$$\text{MAE} = \frac{1}{N} \frac{1}{M} \sum_{j=0}^M \sum_{i=0}^N |y_i^j - \hat{y}_i^j|, \quad (13)$$

TABLE 2: The prediction results of the GC-GRU model and other baselines on GÉANT dataset.

Time	Metric	ARIMA	SVR	LSTM	GCN	GC-GRU
15 min	MAE	0.00742	0.00378	0.00317	0.00376	0.00279
	RMSE	0.0112	0.00898	0.00796	0.00833	0.00692
	Accuracy	0.4935	0.8337	0.8991	0.7635	0.9137
	R^2	*	0.8138	0.8536	0.7537	0.8811
30 min	MAE	0.00693	0.00366	0.00312	0.00384	0.00272
	RMSE	0.0098	0.00866	0.00762	0.0088	0.00708
	Accuracy	0.5375	0.8523	0.8903	0.7181	0.9113
	R^2	*	0.7835	0.8027	0.6957	0.8738
45 min	MAE	0.00726	0.00397	0.00299	0.00415	0.00259
	RMSE	0.01045	0.00857	0.00768	0.00855	0.00715
	Accuracy	0.5874	0.8497	0.8701	0.8499	0.8257
	R^2	*	0.7273	0.7745	0.6625	0.9023
60 min	MAE	0.00711	0.00341	0.00296	0.00409	0.00261
	RMSE	0.0976	0.00927	0.00748	0.00856	0.00712
	Accuracy	0.4973	0.8447	0.6894	0.5693	0.8932
	R^2	*	0.6438	0.6948	0.6204	0.8032

* means the value is very small to be ignored which indicates the model's prediction effect is poor.

where \hat{y}_i^j denotes the forecasted traffic value of traffic flow i at time j , and y_i^j denotes ground truth value, respectively. N is the index of traffic flows, and M represents the index of time slot

(3) Accuracy:

$$\text{Accuracy} = 1 - \frac{\|Y - \hat{Y}\|_F}{\|Y\|_F}. \quad (14)$$

Y and \hat{Y} represent the set of real values and predicted values, respectively

(4) Coefficient of determination (R^2):

$$R^2 = 1 - \frac{\sum_{j=1}^M \sum_{i=1}^N (y_i^j - \hat{y}_i^j)^2}{\sum_{j=1}^M \sum_{i=1}^N (y_i^j - \bar{Y})^2}. \quad (15)$$

\bar{Y} is the average of Y .

(5) Explained variance score (var):

$$\text{var} = 1 - \frac{\text{Var}\{Y - \hat{Y}\}}{\text{Var}\{Y\}}. \quad (16)$$

R^2 and var are the measures to represent fitting degree of the predicted value to observation value of the traffic.

4.3. Model Parameter Settings. In the experiment, the batch size is set to 32, and the training epoch is 200; the learning

rate is set to 0.001. We set 8, 16, 32, 64, 100, and 128 as the number of hidden units and record and analyze the experimental results under each configuration. As shown in Figure 6(a), experiments show that the best prediction accuracy and correlation are obtained when the size of hidden units is 100. Specifically, with the increase of the number of hidden cells, the prediction accuracy, R^2 , and var increase, but with the increase of hidden cells, the increase range of prediction accuracy and correlation declines, and when the number of hidden cells reaches 128, the prediction accuracy and R^2 drop. At the same time, Figure 6(b) shows the MAE and RMSE values under different units' numbers in the training stage. It can be seen that contrary to the accuracy and R^2 , MAE and RMSE decrease with the increase of the number of hidden units, which indicates that the error between the predicted value and the observed value can be reduced by appropriately increasing the number of hidden units. Similarly, when the number of hidden units is 100, the error is the smallest. Figures 6(c) and 6(d) show the experimental results on the test set, which are basically consistent with the training phase. At the same time, when the number of hidden units is set to 100, several indicators perform best. In conclusion, the appropriate number of hidden units can improve the performance of the model, but not the higher the better, and too many hidden units may cause over fitting problem and led to higher computing overhead which would decrease prediction performance.

4.4. Results. We compared our GC-GRU model with other reprehensive baselines model, as Table 1 shows.

Based on the GÉANT dataset, we make traffic prediction at 15, 30, 45, and 60 minutes. As shown in Table 2, it is clearly observed that our GC-GRU model obtained the best

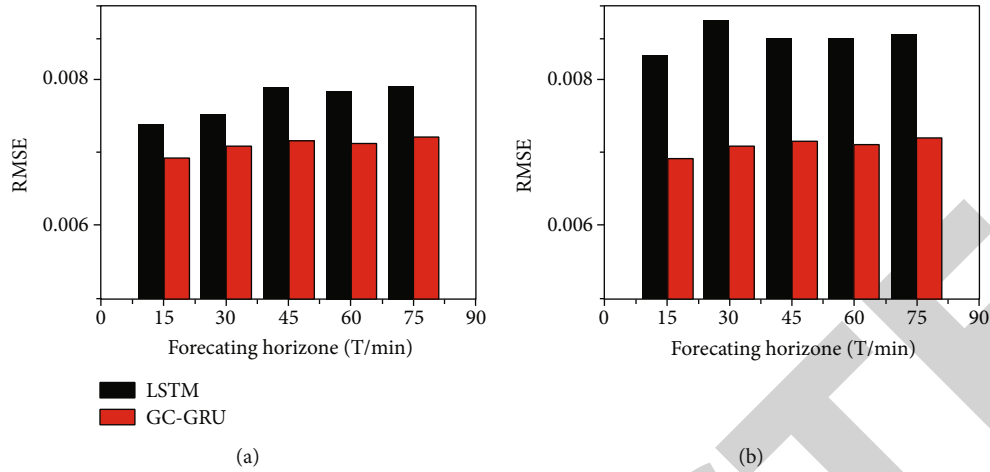


FIGURE 7: Spatiotemporal prediction capability of the GC-GRU model. (a) Comparison of the RMSE of GC-GRU model with the LSTM model. (b) Comparison of the RMSE of the GC-GRU model with the GCN model.

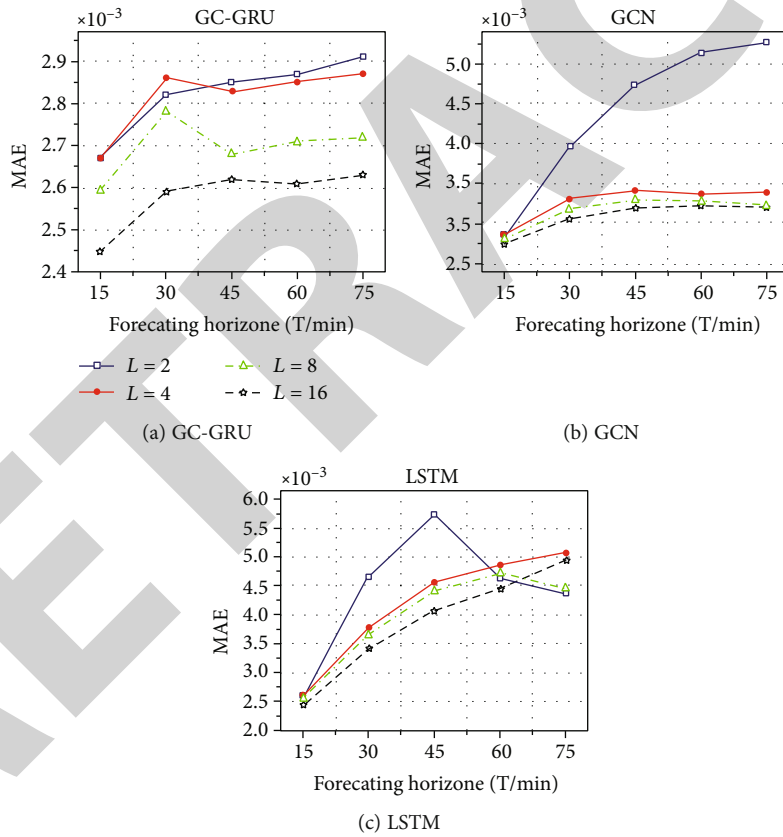


FIGURE 8: MAE comparison between different sliding window lengths L for different prediction horizons.

performance under all evaluation metrics and different prediction time granularity. In general, the prediction performance of deep learning methods (LSTM, GC-GRU) is significantly better than other model baselines (ARIMA, SVR) under each prediction horizon. For example, compared with the ARIMA model, the prediction accuracy of the GC-GRU model and LSTM model is about 46% and 45% higher,

and RMSE error is reduced by 38% and 29%, respectively. Also, compared with the SVR model, these metrics of the GC-GRU model and LSTM model are 22% and 11% lower, respectively, and the prediction accuracy is improved by 15% and 9%. Although the performance of the SVR model is better than ARIMA, it is also significantly lower than the LSTM and GC-GRU method. This may be caused by the lack

of the ability of these methods to process complex nonstationary time series data. In essence, LSTM and GRU could capture the temporal features of traffic matrix sequences than the time series model, because their cell states increase with time. Similarly, we can also clearly notice that the prediction effect of the GCN model is not good, which shows that it is not enough to only consider the spatial features of network traffic by ignoring the time-domain characteristics of network traffic.

4.4.1. Spatiotemporal Prediction Ability. In order to verify whether the GC-GRU model on the ability of handle spatiotemporal features from the dataset, we further analyzed the experimental results of the GC-GRU model, LSTM model, and GCN model. In detail, Figure 7(a) shows the RMSE of GC-GRU compared with the LSTM model which only considers the time domain features, the RMSE error of the GC-GRU model for 15-minute and 60-minute network traffic prediction is reduced by about 13% and 5%, respectively, and the prediction error is basically controlled at a low level, which indicates that the GC-GRU model can capture the time correlation well. In Figure 7(b), the multistep forecast result of GC-GRU is obviously better than the GCN model, and the RMSE of GC-GRU model is 16.9% lower than that of GCN model. For the 60-minute traffic volume forecast, the RMSE of GC-GRU model is reduced by 16.8%, which indicates that the GC-GRU model can capture the spatial correlation. It can be seen that GC-GRU has better prediction accuracy than the method based on spatial and temporal factors. Because GCN only considers the spatial feature of the network, the dramatic change of time domain may cause prediction error. LSTM can make a better one-step prediction because of its structure memory, but in the process of training, there is the possibility of modeling noise into the model, which leads to overfitting. In the GC-GRU model, we construct a local filter in the Fourier domain when dealing with the neighborhood node relationship and constantly move the filter to capture the spatial features, so that the local parameters can be shared. This process plays a role in noise suppression, which may reduce the possibility of overfitting issue.

4.4.2. Prediction Ability for Different Prediction Horizons. Figure 8 shows the difference of input sliding window lengths (L) for traffic prediction. Generally speaking, a longer input window length can improve the accuracy of long-term prediction because it contains more time-domain features. For the LSTM model, because of the memory of the hidden state, when the hidden state is updated for a long time, they will remember more information; so, the prediction accuracy is more affected by the history window. In contrast, the GCN model does not have explicit temporal modeling; consequently, it gets little responded to window size change. The MAE of our model for different prediction horizons under different history sliding windows holds small and stable, which means that the method has strong adaptability to both prediction horizon and input history horizon. In conclusion, we know that the GC-GRU model has strong adaptability in both long-term and short-term forecasting.

5. Conclusion

In view of the new characteristics of network traffic brought by the dynamic change of spatiotemporal correlation in the new application scenarios of mobile network, this paper proposes a novel network traffic prediction method based on traffic spatiotemporal features. It combines GCN and GRU, in which GCN is in charge of obtaining spatial correlation of the traffics on each node, and GRU is used to handle the spatiotemporal features hidden in spatial dynamic series, so as to achieve spatiotemporal network traffic prediction. Experimental results on real network traffic datasets show that the GC-GRU model has better prediction performance than other baseline models under different prediction horizons. It is not only more suitable for nonlinear network traffic prediction than ARIMA and SVR but also more suitable for nonlinear network traffic prediction than spatiotemporal model. The research results show that the model can capture the spatiotemporal correlation characteristics of network traffic, provide accurate network traffic distribution prediction for mobile network interactive applications, and provide more fine-grained and more accurate scheduling decision-making basis for wireless access management, content optimization cache, and computing resource scheduling tasks in these application scenarios [56].

In addition, we will further study the traffic characteristics of mobile networks. In reality, it is not only the traffic size but also the link delay, jitter, and other factors that reflect the network characteristics. In the future, we will explore the network demand forecasting method under multiparameter constraints.

Data Availability

All data, models, and code generated or used during the study appear in the submitted article.

Conflicts of Interest

The authors declared no potential conflicts of interest with respect to the research, authorship, and/or publication of this article.

Acknowledgments

This study was supported by (1) the Fundamental Research Funds for the Central Universities: 2020ZDPY0223 and supported by the Xuzhou Science and Technology Plan Funded Project-Research on Key Technologies for Three-dimensional Monitoring of Lake Water Environment based on 5G Internet of Things: KC19208.

References

- [1] A. D'Alconzo, I. Drago, A. Morichetta, M. Mellia, and P. Casas, "A survey on big data for network traffic monitoring and analysis," *IEEE Transactions on Network and Service Management*, vol. 16, no. 3, pp. 800–813, 2019.

- [2] P. Tsai, C. W. Tsai, C. W. Hsu, and C. S. Yang, "Network monitoring in software-defined networking: a review," *IEEE Systems Journal*, vol. 12, no. 4, pp. 3958–3969, 2018.
- [3] J. Feng, X. Chen, R. Gao, M. Zeng, and Y. Li, "DeepTP: an end-to-end neural network for mobile cellular traffic prediction," *IEEE Network*, vol. 32, no. 6, pp. 108–115, 2018.
- [4] B. K. J. al-Shammari, N. al-Aboody, and H. S. al-Raweshidy, "IoT traffic management and integration in the QoS supported network," *IEEE Internet of Things Journal*, vol. 5, no. 1, pp. 352–370, 2018.
- [5] A. Brogi and S. Forti, "QoS-aware deployment of IoT applications through the fog," *IEEE Internet of Things Journal*, vol. 4, no. 5, pp. 1185–1192, 2017.
- [6] A. Čolaković and M. Hadžialić, "Internet of Things (IoT): a review of enabling technologies, challenges, and open research issues," *Computer Networks*, vol. 144, pp. 17–39, 2018.
- [7] B. Hu, L. Fang, X. Cheng, and L. Yang, "In-vehicle caching (IV-cache) via dynamic distributed storage relay (D²SR) in vehicular networks," *IEEE Transactions on Vehicular Technology*, vol. 68, no. 1, pp. 843–855, 2019.
- [8] J. Bhatia, R. Dave, H. Bhayani, S. Tanwar, and A. Nayyar, "SDN-based real-time urban traffic analysis in VANET environment," *Computer Communications*, vol. 149, pp. 162–175, 2020.
- [9] C. Shu, Z. Zhao, G. Min, J. Hu, and J. Zhang, "Deploying network functions for multiaccess Edge-IoT with deep reinforcement learning," *IEEE Internet of Things Journal*, vol. 7, no. 10, pp. 9507–9516, 2020.
- [10] R. Madan and P. S. Mangipudi, "Predicting computer network traffic: a time series forecasting approach using DWT, ARIMA and RNN," in *2018 Eleventh International Conference on Contemporary Computing (IC3)*, pp. 1–5, Noida, India, August 2018.
- [11] Y. Liang and L. Qiu, "Network traffic prediction based on SVR improved by chaos theory and ant colony optimization," *International Journal of Future Generation Communication and Networking*, vol. 8, no. 1, pp. 69–78, 2015.
- [12] E. Castillo, J. M. Menéndez, and S. Sánchez-Cambronero, "Traffic estimation and optimal counting location without path enumeration using Bayesian networks," *Computer-Aided Civil and Infrastructure Engineering*, vol. 23, no. 3, pp. 189–207, 2008.
- [13] L. Nie, D. Jiang, and Z. Lv, "Modeling network traffic for traffic matrix Estimation and anomaly detection based on Bayesian network in cloud computing networks," *Annals of Telecommunications*, vol. 72, no. 5-6, pp. 297–305, 2017.
- [14] H. Elazhary, "Internet of Things (IoT), mobile cloud, cloudlet, mobile IoT, IoT cloud, fog, mobile edge, and edge emerging computing paradigms: disambiguation and research directions," *Journal of Network and Computer Applications*, vol. 128, pp. 105–140, 2019.
- [15] P. Duan, Y. Jia, L. Liang, J. Rodriguez, K. M. S. Huq, and G. Li, "Space-reserved cooperative caching in 5G heterogeneous networks for industrial IoT," *Journal of Network and Computer Applications*, vol. 14, no. 6, pp. 2715–2724, 2018.
- [16] M. Wollschlaeger, T. Sauter, and J. Jasperneite, "The future of industrial communication: automation networks in the era of the Internet of Things and industry 4.0," *IEEE Industrial Electronics Magazine*, vol. 11, no. 1, pp. 17–27, 2017.
- [17] X. Cheng, L. Fang, L. Yang, and S. Cui, "Mobile big data: the fuel for data-driven wireless," *IEEE Internet of Things Journal*, vol. 4, no. 5, pp. 1489–1516, 2017.
- [18] A. Azzouni and G. Pujolle, "NeuTM: a neural network-based framework for traffic matrix prediction in SDN," in *NOMS 2018 - 2018 IEEE/IFIP Network Operations and Management Symposium*, Taipei, Taiwan, April 2018.
- [19] X. Cheng, L. Fang, X. Hong, and L. Yang, "Exploiting mobile big data: sources, features, and applications," *IEEE Network*, vol. 31, no. 1, pp. 72–79, 2017.
- [20] M. Kim, "Network traffic prediction based on INGARCH model," *Wireless Networks*, vol. 26, no. 8, pp. 6189–6202, 2020.
- [21] J. Prados-Garzon, P. Ameigeiras, J. J. Ramos-Munoz, J. Navarro-Ortiz, P. Andres-Maldonado, and J. M. Lopez-Soler, "Performance modeling of Softwarized network services based on queuing theory with experimental validation," *IEEE Transactions on Mobile Computing*, vol. 20, no. 4, pp. 1558–1573, 2021.
- [22] E. Palkopoulou, C. Merkle, D. A. Schupke, C. G. Gruber, and A. Kirstädter, "Traffic models for future backbone networks – a service-oriented approach," *European Transactions on Telecommunications*, vol. 22, no. 4, pp. 137–150, 2011.
- [23] S. Krishnan and H. S. Dhillon, "Spatio-temporal interference correlation and joint coverage in cellular networks," *IEEE Transactions on Wireless Communications*, vol. 16, no. 9, pp. 5659–5672, 2017.
- [24] S. Kamath, S. Singh, and M. S. Kumar, "Multiclass queueing network modeling and traffic flow analysis for SDN-enabled mobile core networks with network slicing," *IEEE Access*, vol. 8, pp. 417–430, 2020.
- [25] A. Soule, A. Lakhina, N. Taft et al., "Traffic matrices: balancing measurements, inference and modeling," *ACM SIGMETRICS Performance Evaluation Review*, vol. 33, no. 1, pp. 362–373, 2005.
- [26] V. Paxson and S. Floyd, "Wide area traffic: the failure of Poisson modeling," *IEEE/ACM Transactions on Networking*, vol. 3, no. 3, pp. 226–244, 1995.
- [27] M. Malboubi, S. Peng, P. Sharma, and C. N. Chuah, "A learning-based measurement framework for traffic matrix inference in software defined networks," *Computers & Electrical Engineering*, vol. 66, pp. 369–387, 2018.
- [28] M. Abbasi, A. Shahraki, and A. Taherkordi, "Deep learning for network traffic monitoring and analysis (NTMA): a survey," *Computer Communications*, vol. 170, pp. 19–41, 2021.
- [29] D. Jiang, Z. Xu, and H. Xu, "A novel hybrid prediction algorithm to network traffic," *Annals of Telecommunications-Annales Des Télécommunications*, vol. 70, no. 9-10, pp. 427–439, 2015.
- [30] G. P. Zhang, "Time series forecasting using a hybrid ARIMA and neural network model," *Neurocomputing*, vol. 50, pp. 159–175, 2003.
- [31] Man-Chun Tan, S. C. Wong, Jian-Min Xu, Zhan-Rong Guan, and Peng Zhang, "An aggregation approach to short-term traffic flow prediction," *IEEE Transactions on Intelligent Transportation Systems*, vol. 10, no. 1, pp. 60–69, 2009.
- [32] W. E. Leland, M. S. Taqqu, W. Willinger, and D. V. Wilson, "On the self-similar nature of ethernet traffic (extended version)," *IEEE/ACM Transactions on Networking*, vol. 2, no. 1, pp. 1–15, 1994.
- [33] M. Szmit and A. Szmit, "Usage of pseudo-estimator LAD and SARIMA models for network traffic prediction: case studies,"

Retraction

Retracted: A Formal Verification Method of Compilation Based on C Safety Subset

Wireless Communications and Mobile Computing

Received 28 November 2023; Accepted 28 November 2023; Published 29 November 2023

Copyright © 2023 Wireless Communications and Mobile Computing. This is an open access article distributed under the Creative Commons Attribution License, which permits unrestricted use, distribution, and reproduction in any medium, provided the original work is properly cited.

This article has been retracted by Hindawi, as publisher, following an investigation undertaken by the publisher [1]. This investigation has uncovered evidence of systematic manipulation of the publication and peer-review process. We cannot, therefore, vouch for the reliability or integrity of this article.

Please note that this notice is intended solely to alert readers that the peer-review process of this article has been compromised.

Wiley and Hindawi regret that the usual quality checks did not identify these issues before publication and have since put additional measures in place to safeguard research integrity.

We wish to credit our Research Integrity and Research Publishing teams and anonymous and named external researchers and research integrity experts for contributing to this investigation.

The corresponding author, as the representative of all authors, has been given the opportunity to register their agreement or disagreement to this retraction. We have kept a record of any response received.

References

- [1] Y. Tan, D. Ma, and L. Qiao, "A Formal Verification Method of Compilation Based on C Safety Subset," *Wireless Communications and Mobile Computing*, vol. 2021, Article ID 8352267, 10 pages, 2021.

Research Article

A Formal Verification Method of Compilation Based on C Safety Subset

Yu Tan,^{1,2} Dianfu Ma,^{1,2} and Lei Qiao ³

¹State Key Laboratory of Software Development Environment, Beihang University, Beijing 100191, China

²School of Computer Science and Engineering, Beihang University, Beijing 100191, China

³Beijing Institute of Control Engineering, Beijing 100190, China

Correspondence should be addressed to Lei Qiao; 105133744@qq.com

Received 17 June 2021; Revised 3 July 2021; Accepted 12 July 2021; Published 1 August 2021

Academic Editor: Balakrishnan Nagaraj

Copyright © 2021 Yu Tan et al. This is an open access article distributed under the Creative Commons Attribution License, which permits unrestricted use, distribution, and reproduction in any medium, provided the original work is properly cited.

With the rapid increase in the number of wireless terminals and the openness of wireless networks, the security of wireless communication is facing serious challenges. The safety and security of computer communication have always been a research hotspot, especially the wireless communication that still has a more complex architecture which leads to more safety problems in the communication system development. In recent years, more and more wireless communication systems are applied in the safety-critical field which tends to need high safety guarantees. A compiler is an important tool for system development, and its safety and reliability have an important impact on the development of safety-critical software. As the strictest method, formal verification methods have been widely paid attention to in compiler verification, but the current formal verification methods have some problems, such as high proof complexity, weak verification ability, and low algorithm efficiency. In this paper, a compiler formal verification method based on safety C subsets is proposed. By abstracting the concept of C grammar units from safety C subsets, the formal verification of the compiler is transformed into the verification of limited C grammar units. In this paper, an axiom system of first-order logic and special axioms are introduced. On this axiom system, the semantic consistency verification of C grammar unit and target code pattern is completed by means of theorem proving, and the formal verification of the compiler is completed.

1. Introduction

With the rapid development of wireless communication technology, a wireless communication system has been widely used in various fields of national economy and national defense construction. An important part of all kinds of safety-critical systems and software have more and more complex internal structures and open application environments. These factors make people pay more attention to its safety and reliability. Therefore, it is very important to analyze, design, and verify the safety-critical software, especially the onboard software of large passenger aircraft.

At present, the certification standard mainly adopted in the aviation field is DO-178B [1], “Software Requirements in the Certification of Airborne Systems and Equipment”, issued by the American Aeronautical Radio Commission

(RTCA) in December 1992. DO-178B defines the design and development process for airborne software and describes the target traceability process. According to the impact on aircraft failure state, airborne software is classified into five software grades: A (catastrophic), B (serious), C (heavy), D (light), and E (no impact). The DO-178C was released by RTCA in 2012 [2]. DO-178C complements DO-178B in four aspects: software tool verification, model-based development and verification, object-oriented programming, and formal methods. With the rapid development of new software technologies, these additions and revisions are well adapted to the current process of safety-related software development.

Compiler, as an important tool in software development process, is the bridge between software design and hardware operation. How to ensure the correctness of compiler compilation process is an important problem in software

development. The traditional method to detect compilation errors is to conduct a lot of tests, but the tests can only prove that the software is wrong but cannot prove that the software is error-free. In recent years, formal verification methods have received continuous attention in compiler verification. The formal verification method is based on strict mathematical theory, and the software system and properties are regulated by logical methods. Through the formal system composed of axioms and inference rules, the software system is proved in the same way as the theorem proved in mathematics. At present, there are two mainstream methods for formal verification of compilers. One is model detection [3], whose main bottleneck is state explosion, so it is only suitable for analysis of systems with limited and small state space. The other is theorem proving technology [4]. At present, a better way of proving is to use the unified framework of programming and proving, such as PVS, Coq, and Isabelle. Its limitation lies in that it requires tool users to have a high theoretical foundation and technical background, which limits the learning and application of most programmers.

This paper proposes a compiler formal verification method based on secure C subset. By introducing MISRA-C [5], the automotive manufacturing embedded C coding standard, the C language used in safety-critical systems is restricted. The C language defined by this specification is considered to be readable, reliable, portable, and easy to maintain. Combined with the characteristics of MISRA-C and aerospace software, a series of programming criteria of C language software are redefined, and a C safety subset is formed. The C safety subset strictly requires the maturity and stability of the compiler. The compiler must truly reflect the structure and semantics of the source code for comparison and tracking before and after compilation. From the C safety subset, a finite C grammar unit can be obtained, and the source program can be identified by the push-down automata corresponding to the grammar unit. A correct source program must conform to the rules of the grammar unit. Therefore, the proof of the correctness of the compilation process of the source program can be transformed into the proof of the equivalence of the semantics of the grammar unit. This method greatly simplifies the problems of the traditional formal verification methods, such as the high complexity and long time of the proof.

2. Related Works

The study of theorem proving for programs began in the 1960s with the papers published by Hoare and Floyd [6]. In his paper, Hoare proposed a formal system called Hoare logic. In Hoare logic, there is a set of proof rules called Hoare rules. Hoare logic can be used for machine proof because Hoare rule can be used for formal proof of some correctness assertions.

Separation logic is an extension of Hoare logic, which eliminates the possibility of sharing by providing logical connectives to express separation and corresponding deduction rules, and can describe the properties and related operations of memory in a natural way in the process of calculation, thus simplifying the verification of pointer programs. Separate logic has been proven to be more verifiable, which is a big step forward in program verification and inference technology.

In recent years, the representative one is the work of the COMPCERT project team led by Leroy X [7, 8]. For the first time, they have completed the formal verification of the correctness of a complete and practical compilation process. The whole verification process is completely formalized and automatically generated by the machine. To support automatic formal verification, CompCert uses the Coq Assistant, an auxiliary theorem proving tool, to restructure the compilation process. The entire process consists of conversions between eight different intermediate languages, and then, the Coq Assistant is used to prove the correctness of the entire compilation process, i.e., semantic retention. At present, the CompCert compiler can only realize compilation verification for a subset of C language, and it cannot fully cover all C language elements. Moreover, the back-end optimization degree is relatively low, and the project is still under further study [9].

In 2011, Yang et al. [10] tested mainstream C compilers in their research work on CSmith, an automatic test case generation tool, and reported 325 previously unknown bugs to compiler developers, including famous Intel CC, GCC, and LLVM compilers. CompCert performed exceptionally well in all 11 C compilers it compared, not finding any wrong-code errors in its supported C subsets.

The most influential work in recent years is that CompCert puts forward a safe subset Clight in the compiler researched and developed. By adding ultralong types, variable-length parameters, and other features, and adding a safe subset in the front end of the compiler to analyze and trim unnecessary language features in the front end, the compiler complexity of the language is reduced. The range between the standard C (C90), Clight, and MISRA-C safety subsets is shown in Figure 1.

As shown in Figure 1, the C90 covers the latter two, being the first standard C specification to add a true standard library, new preprocessing commands and features, function prototypes that allow for function declarations, and new keywords for specifying parameter types. There is a large intersection between Clight and MISRA-C, but some of them are not covered by each other. This has the very important instructive significance to the future work. Part 1 represents the C language features included in the declaration definition, layout writing, branch control, pointer use, jump control, operational processing, and other parts that are not supported by MISRA-C. Part 2: the intersection of the C language subset supported by Clight and MISRA-C, including C language basic types, syntax, statements, and library functions. Part 3: restricted multiple label declaration, null switch language use, parameter pointer use, pointer nesting, and so on stipulated by MISRA-C are included in it. Part 4: this region is the point not covered by the two subsets, and it is the C language features such as extralong data type, triplet sequence, special type of structure, general representation of floating-point type, special definition of precursor volume, and special arithmetic library function, which are clearly defined in C90 standard.

After the investigation of related researches, it is found that the research content of safety C compilation mainly includes two aspects: the correctness of the design and

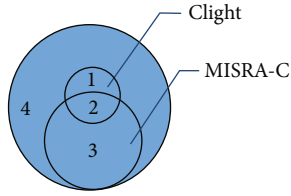


FIGURE 1: The scope of Clight, MISRA-C, and C90.

function of compilation, which ensures the correctness of the compiled object and the correctness of the compilation process itself, and thus guarantees the compilation security to a certain extent obviously; the security of the compiled object is the premise, and the security of the compiler itself is the ultimate goal. Both of them are purposes and motivations of each other, and together constitute the research contents of safety-critical compilation. The conclusions of the objects studied in this paper are shown in Table 1.

3. Formal Verification Method of Complication

3.1. Safety C Grammar Unit and Semantics. Abstract Syntax Tree Code (ASTC) is a tree representation of the abstract syntax structure of the source code, with each node on the tree representing a syntax structure in the source code. The source program and its corresponding abstract syntax tree are essentially equivalent, and the abstract syntax tree contains all the semantic information of the source program, so the verification of the source program can be transformed into the verification of the abstract syntax tree. From the definition of the tree, we can know that each tree is recursively defined by its subtree, so we can verify the whole grammar tree by verifying the subtree of the grammar separately.

Under the constraints of the C safety subset, the unsafe syntax specifications in C language, such as Pointers, are removed. Abstract and induction of the abstract syntax tree, we can get some common subsyntax tree structure, these subsyntax tree structures were extracted and restored to the form of C language, and we get the C grammar unit. Compilation verification of the source program is equivalent to verification of each C grammar unit, which can be achieved by verifying whether the semantics of each C grammar unit and the corresponding target code pattern are consistent before and after compilation.

In order to obtain the semantics of each C grammar unit, this paper introduces the concept of context, which can define the semantics of grammar unit according to context. Context represents the environment and context of each proof item in the sequence to be proved, including function local variables, global variables, and context. Table 2 shows some of the C grammar units and their corresponding semantics.

In the table, the sigma symbol σ represents the process of taking a value, and $\sigma(\langle \text{LOG-EXP} \rangle)$ represents the value of a logical expression that, according to the C safety subset specification, can only be 0 and 1. $\langle \text{STA-LIST} \rangle$ represents a statement block, which can include expression statement and conditional selection statement, and is generally handed over to the push-down automaton that identifies the state-

ment block for recursive processing. $\langle \text{ASS-EXP} \rangle$ represents an assignment statement that returns the value of the expression. $\langle \{.. \} ** n \rangle$ represents the statement inside the braces of the loop execution, which defines the semantics of the loop statement. SKIP means to jump directly to the next statement for execution. Under the 32-bit Power PC instruction set, define SKIP equals $\sigma(\text{PC} = \text{PC} + 4)$, where PC represents the program counter.

3.2. The Denotational Semantics of Target Language. The denotational semantics is the science of annotating the semantics of a definite formal language with corresponding mathematical objects (such as set and function) using the formal system method. The denotational semantics can also be explained as follows: there are two domains, one is the linguistic domain, in the grammatical domain defines a formal language system. The other is the mathematical domain (or formal system with known semantics). Within the scope of a 32-bit Power PC instruction set, this paper models assembly instruction and obtains corresponding the denotational semantics according to the operational semantics of each instruction given in the official Power PC document. Table 3 gives the denotational semantics of some Power PC assembly instructions.

In the table, the GPR (general-purpose register) represents the Power PC's general-purpose register, mainly used as a stack pointer, the first argument to a function, the return value, etc. CR (Conditional Register) is a condition register, which can reflect the results of some operations (such as CMP instruction) and assist in testing and execution of branch instructions. MEM is a memory space that stores the values of local, global, and other variables. @target represents the relative address, which is generally used in the jump instruction. $\text{PC} = \text{PC} + @\text{target}$ means to jump from the address currently pointed by PC to the address identified by the target. $\text{PC} = \text{PC} + 4$ means to directly execute the next instruction.

3.3. Target Code Patterns and Propositions. Target code pattern is a generalized representation of target code sequence obtained by compiling C grammar units in a certain context with GCC compiler and eliminating the influence of context on the target code sequence. Formal verification of compiler should be converted into semantic consistency verification of C grammar unit and target code pattern. Table 4 shows the target code patterns corresponding to some C grammar units under the 32-bit Power PC instruction set.

Formal proof of a program requires a specific system of axioms as the basis. The axiomatic system is to axiomatize a scientific theory and study it with axiomatic methods. Every scientific theory is a system composed of a series of concepts and propositions. Based on the referential semantics of Power PC assembly instruction in 2.2, the proposition mapping algorithm in 3.1 can be used to obtain the proposition of each target code pattern. The propositions of target code patterns about the condition statement ($\langle \text{if-statement} \rangle$) and loop statement ($\langle \text{while-statement} \rangle$) are given in Table 5.

3.4. Verification and Proof. The formal verification method proposed in this paper is based on the axiom system of

TABLE 1: Comparisons of related works.

Works and method		Advantages	Deficiency
Correctness of design	C safety subset	A safe subset is proposed, which can reduce the complexity of compilation by adding extralong types, variable-length parameters, and other features in the front end without changing the C semantics.	The coverage range is smaller than that of C90 standard, and MISRA-C standard is not covered, and the accuracy of detection and analysis is not complete.
Correctness of function	From C to ASM	It supports automatic formal proof and reconstructs the compilation process in Coq and completes the compilation from a structured functional language Clight to assembly code PowerPC. Finally, it proves the correctness of the whole compilation process by using Coq.	In the process, it has experienced compilation between eight different intermediate languages, and the language changes are complex. The project is still in progress.
Formal verification	Model checking	High degree of automation, error detection can be given after the counterexample.	State space explosion problem.
	Theorem proving	Using rigorous mathematical reasoning to prove clear attribute requirements and clear correctness standards, high credibility.	The degree of automation is low, the degree of formalization requirements is high, and the proof process is difficult.

TABLE 2: Safety C grammar unit and semantics.

Statement	Grammar unit	Grammar unit semantics
<if-statement>	<pre> if (<LOG-EXP>) { <STA-LIST_1> } else { <STA-LIST_2> } </pre>	$\sigma(\langle \text{LOG-EXP} \rangle) \rightarrow \sigma(\langle \text{STA-LIST}_1 \rangle)$ $\sim \sigma(\langle \text{LOG-EXP} \rangle) \rightarrow \sigma(\langle \text{STA-LIST}_2 \rangle)$
<while-statement>	<pre> while (<LOG-EXP>) { <STA-LIST> } </pre>	$\{\sigma(\langle \text{LOG-EXP} \rangle) \rightarrow \sigma(\langle \text{STA-LIST} \rangle)\} ** n$ $\sim \sigma(\langle \text{LOG-EXP} \rangle) \rightarrow \text{skip}$
<do-while-statement>	<pre> do { <STA-LIST> } while (<LOG-EXP>); </pre>	$\sigma(\langle \text{STA-LIST} \rangle)$ $\{\sigma(\langle \text{LOG-EXP} \rangle) \rightarrow \sigma(\langle \text{STA-LIST} \rangle)\} ** n$ $\sim \sigma(\langle \text{LOG-EXP} \rangle) \rightarrow \text{skip}$
<for-statement>	<pre> for(<ASS-EXP_1>; <LOG-EXP>; <ASS-EXP_2>) { <STA-LIST> } </pre>	$\sigma(\langle \text{ASS-EXP}_1 \rangle)$ $\{\sigma(\langle \text{LOG-EXP} \rangle) \rightarrow \sigma(\langle \text{STA-LIST} \rangle);$ $\sigma(\langle \text{ASS-EXP}_1 \rangle)\} ** n$ $\sim \sigma(\langle \text{LOG-EXP} \rangle) \rightarrow \text{skip}$

first-order logic. Starting from the axioms given in the axiom system in advance (such as the target code pattern proposition), a series of new propositions are deduced according to the inference rules and are added as the premise in the subsequent proof process. Since every item in the proof sequence is a premise, an axiom, or a theorem, and because the axiom system of first-order logic is reliable, every item in the proof sequence must be correct, so that the final inference proves the sequence must be correct.

The MP (Modus Ponens) rule, which is called detached argument or detached rule, is the most basic reasoning rule in the axiom system of first-order logic. The MP rule can be expressed as follows:

$$p \longrightarrow q, p \vdash q. \quad (1)$$

The implication is as follows: if p is true, then q is true, and then p is true, therefore q is true. The separation rule consists of three statements (or propositions, or statements): the first statement is a conditional statement, i.e., p implicates q ; the second statement is p , the premise of the conditional statement is true. The q follows from the first two statements that the conclusion of the conditional statement must also be true logically.

The CI (Conjunction Introduction) rule is called the Conjunction Introduction or combination rule. CI rule can be expressed as follows:

TABLE 3: The denotational semantics.

Instruction category	Instruction	Denotational semantics
li	li rD,SIMM	GPR[rD] = SIMM
lwz	lwz rD, D(rA)	GPR[rD] = MEM[D]
stw	stw rS,D(rA)	MEM[D] = GPR[rS]
b	b target	PC = PC + @target
beq	beq crfD,target	CR[crfD] == b100->PC = PC + 4 CR[crfD] == b010->PC = PC + 4 CR[crfD] == b001->PC = PC + @target
bne	bne crfD,target	CR[crfD] == b100->PC = PC + @target CR[crfD] == b010->PC = PC + @target CR[crfD] == b001->PC = PC + 4
cmp	cmp crfD,L,rA,rB	GPR[0] < 0->CR [7] = b100 GPR[0] > 0->CR [7] = b010 GPR[0] == 0->CR [7] = b001
cmpi	cmpi crfD,L,rA,SIMM	GPR[rA] < SIMM->CR[crfD] = b100 GPR[rA] > SIMM->CR[crfD] = b010 GPR[rA] == SIMM->CR[crfD] = b001
add	add rD,rA,rB	GPR[rD] = GPR[rA] + GPR[rB]
addic	addic	GPR[rD] = GPR[rA] + SIMM
subf	subf rD,rA,rB	GPR[rD] = -GPR[rA] + GPR[rB]
mullw	mullw rD,rA,rB	GPR[rD] = GPR[rA] * GPR[rB]
divw	divw rD,rA,rB	GPR[rD] = GPR[rA]/GPR[rB]

$$p, q \vdash p \wedge q. \quad (2)$$

Its meaning is as follows: if p, q is true, then $p \wedge q$ is true. The rule of conjunction is mainly used to convert multiple true propositions into a single one.

In the actual verification process, for the target code mode propositions such as expression grammar unit and conditional choice grammar unit, because they do not contain cyclic structure, it is convenient to complete the reasoning proof of propositions by using MP rule and axiom set and theorem set in the axiom system of first-order logic. However, for cyclic structure, such as <While-Statement> target code pattern proposition, after direct reasoning, the semantics of the target code pattern obtained is quite different from the semantics of the C grammar unit, so it is impossible to directly prove that the semantics of the two are consistent. Therefore, this paper introduces the limited mathematical induction method to prove the target code pattern proposition of cyclic structure.

The logical basis of limited mathematical induction is the axiom of natural numbers, also known as Peano's axiom. General mathematical induction logic expressions for the $P(0) \wedge (\forall n) (P(n) \longrightarrow P(s(n))) \longrightarrow (\forall n) P(n)$, limited mathematical induction is on the basis of general mathematical induction, limit n is poor, the program for loop structure, the loop is terminated, and termination conditions are given by the people. Table 6 and Algorithm 1 will give the proofs of the target code pattern propositions of <if-statement> and <while-statement>, respectively.

In Table 6, the final inference of the proof sequence is S12, and the semantics of the target code pattern obtained by the value (σ) operation on S12 are as follows:

$$\begin{aligned} \sigma(\langle \text{LOG-EXP} \rangle) &\rightarrow \sigma(\langle \text{STA-LIST}_1 \rangle) \\ \|\sim \sigma(\langle \text{LOG-EXP} \rangle) &\longrightarrow \sigma(\langle \text{STA-LIST}_2 \rangle). \end{aligned} \quad (3)$$

Combined with the semantics of <if-statement> in Algorithm 1, it can be seen that the semantics of the two are consistent, which is verified.

The inference of <while-statement> proof sequence is the same as that of <if-statement>, the proof sequence is directly derived here, and the proof sequence is proved by finite mathematical induction combining with the semantics of the grammar unit.

4. Formal Verification Algorithm

4.1. Proposition Mapping Algorithm. The function of the propositional mapping algorithm is to transform the object code pattern into the form of propositions, so as to facilitate subsequent reasoning proof. The algorithm needs to take the referential semantics corresponding to each instruction in the Power PC instruction set as the special axiom input, traverse the input object code pattern one by one, transform each object code into the corresponding form of referential semantics, and finally express the referential semantics of the object code pattern into the form of proposition set

TABLE 4: Grammar unit and patterns of target code.

Statement	C grammar unit	Target code pattern
<if-statement>	<pre> if (<LOG-EXP>) { <STA-LIST_1> } else { <STA-LIST_2> } </pre>	<pre> <LOG-EXP> cmpi 7,0,0,0 beq 7,.L1 <STA-LIST_1> b .L2 .L1: <STA-LIST_2> .L2: </pre>
<while-statement>	<pre> while (<LOG-EXP>) { <STA-LIST> } </pre>	<pre> .L1: <STA-LIST> .L2: <LOG-EXP> cmpi 7,0,0,0 bne 7,.L1 </pre>
<do-while-statement>	<pre> do { <STA-LIST> } while (<LOG-EXP>); </pre>	<pre> .L1: <STA-LIST> <LOG-EXP> cmpi 7,0,0,0 bne 7,.L1 </pre>
<for-statement>	<pre> for(<ASS-EXP_1>; <LOG-EXP>; <ASS-EXP_2>) { <STA-LIST> } </pre>	<pre> <ASS-EXP_1> b .L2 .L1: <STA-LIST> <ASS-EXP_2> .L2: <LOG-EXP> cmpi 7,0,0,0 bne 7,.L1 </pre>

TABLE 5: The propositions of target code patterns.

Statement	Target code pattern	Proposition
<if-statement>	<pre> <LOG-EXP> cmpi 7,0,0,0 beq 7,.L1 <STA-LIST_1> b .L2 .L1: <STA-LIST_2> .L2: </pre>	<p>P1: $GPR[0] = \langle LOG-EXP \rangle$</p> <p>P2: $(GPR[0] < 0 \rightarrow CR[7] = b100) \parallel (GPR[0] > 0 \rightarrow CR[7] = b010) \parallel (GPR[0] == 0 \rightarrow CR[7] = b001)$</p> <p>P3: $(CR[7] == b100 \rightarrow PC = PC + 4) \parallel (CR[7] == b010 \rightarrow PC = PC + 4) \parallel (CR[7] == b001 \rightarrow PC = PC + @.L1)$</p> <p>P4: $\langle STA-LIST_1 \rangle$</p> <p>P5: $PC = PC + @.L2$</p> <p>P6: $.L1:$</p> <p>P7: $\langle STA-LIST_2 \rangle$</p> <p>P8: $.L2:$</p>
<while-statement>	<pre> b .L2 .L1: <STA-LIST> .L2: <LOG-EXP> cmpi 7,0,0,0 bne 7,.L1 </pre>	<p>P1: $PC = PC + @.L2$</p> <p>P2: $.L1:$</p> <p>P3: $\langle STA-LIST \rangle$</p> <p>P4: $.L2:$</p> <p>P5: $GPR[0] = \langle LOG-EXP \rangle$</p> <p>P6: $(GPR[0] < 0 \rightarrow CR[7] = b100) \parallel (GPR[0] > 0 \rightarrow CR[7] = b010) \parallel (GPR[0] == 0 \rightarrow CR[7] = b001)$</p> <p>P7: $(CR[7] == b100 \rightarrow PC = PC + @.L1) \parallel (CR[7] == b010 \rightarrow PC = PC + @.L1) \parallel (CR[7] == b001 \rightarrow PC = PC + 4)$</p>

TABLE 6: The proof of <if-statement>.

Proof	Inference
S1 = GPR[0] = <LOG-EXP >	P1
S2 = (GPR[0] < 0->CR [7] = b100) (GPR[0] > 0->CR [7] = b010) (GPR[0] == 0->CR [7] = b001)	P2
S3 = (<LOG-EXP><0->CR [7] = b100) (<LOG-EXP>>0->CR [7] = b010) (<LOG-EXP> == 0->CR [7] = b001)	S1, S2, MP
S4 = (CR [7] == b100->PC = PC + 4) (CR [7] == b010->PC = PC + 4) (CR [7] == b001->PC = PC + @.L1)	P3
S5 = (<LOG-EXP><0->PC = PC + 4) (<LOG-EXP>>0->PC = PC + 4) (<LOG-EXP> == 0->PC = PC + @.L1)	S3, S4, MP
S6 = <STA-LIST_1 >	P4
S7 = PC = PC + @.L2	P5
S8 = .L1:	P6
S9 = <STA-LIST_2 >	P7
S10 = .L2:	P8
S11 = { (<LOG-EXP><0->PC = PC + 4) (<LOG-EXP>>0->PC = PC + 4) (<LOG-EXP> == 0->PC = PC + @.L1) ^ <STA-LIST_1 > ^ PC = PC + @.L2 ^ .L1: ^ <STA-LIST_2 > ^ .L2: }	S5, S6, S7, S8, S9, S10, CI
S12 = { (<LOG-EXP><0-><STA-LIST_1 >) (<LOG-EXP>>0-><STA-LIST_1 >) (<LOG-EXP> == 0-><STA-LIST_2 >) }	S11

<p>Proposition: $\{\sigma(\langle \text{LOG-EXP} \rangle) \rightarrow \sigma(\langle \text{STA-LIST} \rangle)\} **n \sim \sigma(\langle \text{LOG-EXP} \rangle) \rightarrow \text{skip}$</p> <p>Lemma: $PC = PC + @.L2 \wedge$</p> <p>.L1: \wedge $\langle \text{STA-LIST} \rangle \wedge$</p> <p>.L2: \wedge $(\langle \text{LOG-EXP} \rangle \langle 0 \rangle \rightarrow PC = PC + @.L1) (\langle \text{LOG-EXP} \rangle \rangle 0 \rightarrow PC = PC + @.L1) (\langle \text{LOG-EXP} \rangle == 0 \rightarrow PC = PC + 4)$</p> <p>Proof:</p> <p>(1) when $n = 1$, substitution propositions are: $\sigma(\langle \text{LOG-EXP} \rangle) \rightarrow \sigma(\langle \text{STA-LIST} \rangle) \sim \sigma(\langle \text{LOG-EXP} \rangle) \rightarrow \text{skip}$. To lemma, when n is 1, said only cycle time, use CI rules: $(\langle \text{LOG-EXP} \rangle \langle 0 \rangle \rightarrow \langle \text{STA-LIST} \rangle) (\langle \text{LOG-EXP} \rangle \rangle 0 \rightarrow \langle \text{STA-LIST} \rangle) (\langle \text{LOG-EXP} \rangle == 0 \rightarrow PC = PC + 4)$, Values, available lemma semantics: $(\langle \text{LOG-EXP} \rangle \langle 0 \rangle \rightarrow \langle \text{STA-LIST} \rangle) (\langle \text{LOG-EXP} \rangle \rangle 0 \rightarrow \langle \text{STA-LIST} \rangle) (\langle \text{LOG-EXP} \rangle == 0 \rightarrow PC = PC + 4)$, It can be obtained that the semantics of the two are consistent, so it is true when $k = 1$.</p> <p>(2) Assume $n = n$, get the proposition $\{\sigma(\langle \text{LOG-EXP} \rangle) \rightarrow \sigma(\langle \text{STA-LIST} \rangle)\} **N \sim \sigma(\langle \text{LOG-EXP} \rangle) \rightarrow \text{skip}$ was established. When $n = n + 1$, on the basis of $n = n$, a cycle is performed. If $\langle \text{LOG-EXP} \rangle == 0$, then $PC = PC + 4$, the whole loop is finished, and the semantics obtained after value operation are: $\sim \sigma(\langle \text{LOG-EXP} \rangle) \rightarrow \text{skip}$. If $\langle \text{LOG-EXP} \rangle != 0$, then PC jumps to the starting position of $\langle \text{STA-LIST} \rangle$, continues to execute the statement sequence, and the semantics obtained after value operation are: $\sigma(\langle \text{LOG-EXP} \rangle) \rightarrow \sigma(\langle \text{STA-LIST} \rangle)$, Apply the semantic and (2) the above assumptions, CI rules, have $\{\sigma(\langle \text{LOG-EXP} \rangle) \rightarrow \sigma(\langle \text{STA-LIST} \rangle)\} ** (N + 1) \sim \sigma(\langle \text{LOG-EXP} \rangle) \rightarrow \text{skip}$ was established. From (1), (2) and (3), it can be seen that the propositions to be verified are valid and have been verified.</p>
--

ALGORITHM 1: The proof of <while-statement>.


```

Input: TargetCodePatternSet
Output: PropositionSet
1: axiomSet = loadAxiom(denotationalSemanticsFileName)
2: for each line in TargetCodePatternSet do
3:   lines = line.split(regex)
4:   lines = filterOtherCharacter(lines)
5:   if lines.length == 0 then
6:     continue
7:   else if lines.length == 1 then
8:     add new Proposition(lines) to PropositionSet
9:   else
10:    paras = generateParas(lines)
11:    seman = generateSemantic (lines, paras, axiomSet)
12:    add new Proposition (lines, paras, seman) to PropositionSet
13:   end if
14: end for

```

ALGORITHM 2: Proposition mapping algorithm.

```

Input: PropositionSet
Output: SemantemeSet
1: for each p in PropositionSet do
2:   for each q in PropositionSet do
3:     if p == q then
4:       continue
5:     end if
6:     newProposition = applyInferenceRuleToTwoPropositions (p, q)
7:     if newProposition != null then
8:       add newProposition to PropositionSet
9:     end if
10:    if q's content is empty then
11:      remove q from PropositionSet
12:    end if
13:   end for
14: end for
15: for each p in PropositionSet do
16:   s = obtainSemantemeFromProposition (p)
17:   add s to SemantemeSet
18: end for

```

ALGORITHM 3: Automatic inference algorithm.

output. The pseudocode of the propositional mapping algorithm is shown in Algorithm 2.

4.2. Automatic Inference Algorithm. The automatic inference algorithm is the core of the formal verification method proposed in this paper. The algorithm takes the proposition set outputted by the proposition mapping algorithm in 3.1 and the axiom set of first-order logic as the premise, deduces a series of new propositions according to the inference rules, adds these new propositions to the premise for subsequent proof, and finally constructs the proof sequence and draws the conclusion. For the object code pattern propositions without cycles, we can directly value (σ) the sequence of the proof, so as to obtain the semantics of the object code pattern propositions. Compared with the semantics of C grammar

units, we can directly judge whether the semantics of the two are consistent. For the object code pattern proposition set containing cycles, the semantic consistency verification process cannot be completed by directly valuing the derived proof sequence, and the loop interactive proof algorithm in 3.3 can be introduced to complete the whole process. The pseudocode of the automatic reasoning algorithm for propositions is shown in Algorithm 3.

4.3. Loop Interaction Proof Algorithm. The theoretical basis of the loop interactive proof algorithm is limited mathematical induction. The algorithm first guide the user to enter n to 1 C unit of semantics, grammar, and then according to the loop condition is true or false, respectively, construct new proposition to join proposition 3.1 mapping algorithm output a

```

Input: PropositionSet
Output: Flag
1: Flag = true
2: for i from 1 to 2 do
3:   userSemantemeSet = ReadUserInputSemanteme ()
4:   copy PropositionSet to cpyPropositionSet
5:   add true loop condition Propositionto cpyPropositionSet
6:   trueSemantemeSet = AutomaticInferenceAlgorithm(cpyPropositionSet)
7:   copy PropositionSet to cpyPropositionSet
8:   add false loop condition Propositionto to cpyPropositionSet
9:   falseSemantemeSet = AutomaticInferenceAlgorithm(cpyPropositionSet)
10:  semantemeSet = trueSemantemeSet || falseSemantemeSet
11:  if i == 2 then
12:    semantemeSet=CI (semantemeSet, userSemantemeSet)
13:    update n from N to (N + 1) in userSemantemeSet
14:  end if
15:  if semantemeSet unequal to userSemantemeSet then
16:    Flag = false
17:    return Flag
18:  end if
19: end for

```

ALGORITHM 4: Loop interaction proof algorithm.

copy of the thesis set, call the automated reasoning algorithm to copy proposition 3.2 set reasoning, so as to get the target pattern proposition of semantics.

Contrast the semantics of object code pattern propositions with the semantics of user input. If the semantics of the two are inconsistent, it will give a direct reminder of the errors in the formal verification process and exit. If it is consistent, the user is reminded to input the semantics of the C grammar unit when n is N , and on this basis, the source semantic set is reasoned again. Through CI rules, the inferred semantic results are added to the semantics of the C grammar unit when n is N , and the semantics of the target code pattern when n is $N + 1$ are obtained. When the user input n is N , the semantics of the C grammar unit is replaced by $N + 1$, and the target code pattern semantics inferred by the program is compared with the semantics of the user input C grammar unit when n is $N + 1$, and the judgment result is returned. The pseudocode of the loop interaction proof algorithm is shown in Algorithm 4.

5. Discussion and Conclusion

In the safety C to the target code compilation process, different scenarios in the field of safety critical need to support more kinds of assembly instruction set, considering the method of this paper can be generalized to a variety of platforms, and the next step works consideration to expand to the academic and industry mainstream assembly instruction set, in order to better support security system application in key areas. This part of the work has been carried out in the laboratory where this paper is located. Up to now, it can support MIPS, x86, SPARC, etc. And RISC-V, the fifth generation of open source condensed instruction set, is also under research.

Also, optimization is a common method to improve the compilation efficiency, but the introduction of optimization will cause some details missing in the compilation process, making it difficult to verify the traceability of source code and object code. How to guarantee both compilation systems meet the demand of traceability in the field of security key, and the optimization technique in safety-critical software compilation; this paper is preliminary thought to compile step for progressive refinement, the architecture, development, and validation of refinement to enhance the analysis of particle size; it will be the issues worthy of challenges in the future research.

This paper proposes a safety subset of the C compiler form verification method towards wireless communication systems which are applied in the safety-critical field; this method is within the scope of C safety subset constraints C grammar unit which is introduced, the traditional directly to the source code of the overall transformation of formal verification in order to limit C verification of grammatical unit, by showing that C grammar unit and the target pattern of semantic equivalence completed form verification process. This method greatly reduces the complexity and time of formal verification and saves the development cost. At the same time, the verification tool developed based on the formal verification algorithm proposed in this paper can guide the user to complete the proof of the cyclic structure through very few interactions, and the whole proof process conforms to the principle of restricted mathematical induction.

The future work will focus on further refinement of C grammar unit and object code pattern, and further research on cyclic interaction proof algorithm will be needed, so that the algorithm can complete the reasoning process with less or even no artificial interaction.

Retraction

Retracted: A Method of Offline Reinforcement Learning Virtual Reality Satellite Attitude Control Based on Generative Adversarial Network

Wireless Communications and Mobile Computing

Received 28 November 2023; Accepted 28 November 2023; Published 29 November 2023

Copyright © 2023 Wireless Communications and Mobile Computing. This is an open access article distributed under the Creative Commons Attribution License, which permits unrestricted use, distribution, and reproduction in any medium, provided the original work is properly cited.

This article has been retracted by Hindawi, as publisher, following an investigation undertaken by the publisher [1]. This investigation has uncovered evidence of systematic manipulation of the publication and peer-review process. We cannot, therefore, vouch for the reliability or integrity of this article.

Please note that this notice is intended solely to alert readers that the peer-review process of this article has been compromised.

Wiley and Hindawi regret that the usual quality checks did not identify these issues before publication and have since put additional measures in place to safeguard research integrity.

We wish to credit our Research Integrity and Research Publishing teams and anonymous and named external researchers and research integrity experts for contributing to this investigation.

The corresponding author, as the representative of all authors, has been given the opportunity to register their agreement or disagreement to this retraction. We have kept a record of any response received.

References

- [1] J. Zhang and F. Wu, "A Method of Offline Reinforcement Learning Virtual Reality Satellite Attitude Control Based on Generative Adversarial Network," *Wireless Communications and Mobile Computing*, vol. 2021, Article ID 4238125, 9 pages, 2021.

Research Article

A Method of Offline Reinforcement Learning Virtual Reality Satellite Attitude Control Based on Generative Adversarial Network

Jian Zhang ¹ and Fengge Wu ²

¹University of Chinese Academy of Sciences, Institute of Software, Chinese Academy of Science, Beijing, China

²Institute of Software, Chinese Academy of Science, Beijing, China

Correspondence should be addressed to Jian Zhang; 16141191@qq.com

Received 24 June 2021; Revised 7 July 2021; Accepted 16 July 2021; Published 1 August 2021

Academic Editor: Balakrishnan Nagaraj

Copyright © 2021 Jian Zhang and Fengge Wu. This is an open access article distributed under the Creative Commons Attribution License, which permits unrestricted use, distribution, and reproduction in any medium, provided the original work is properly cited.

Virtual reality satellites give people an immersive experience of exploring space. The intelligent attitude control method using reinforcement learning to achieve multi-axis synchronous control is one of the important tasks of virtual reality satellites. In real-world systems, methods based on reinforcement learning face safety issues during exploration, unknown actuator delays, and noise in the raw sensor data. To improve the sample efficiency and avoid safety issues during exploration, this paper proposes a new offline reinforcement learning method to make full use of samples. This method learns a policy set with imitation learning and a policy selector using a generative adversarial network (GAN). The performance of the proposed method was verified in a real-world system (reaction-wheel-based inverted pendulum). The results showed that the agent trained with our method reached and maintained a stable goal state in 10,000 steps, whereas the behavior cloning method only remained stable for 500 steps.

1. Introduction

Virtual reality satellites enable people to explore space using any mobile, desktop, or virtual reality device. Traditional attitude control methods require single-axis alternate control. In order to track all kinds of observed celestial bodies in real time, efficient attitude control methods need to be studied. The attitude control method based on reinforcement learning gives a feasible path to achieve efficient three-axis synchronous control.

Reaction momentum wheels are widely used in modern satellites as executive mechanisms that can redistribute momentum between the satellite body and the momentum wheel. Studies on the attitude control algorithms for this kind of actuator have focused on how to control the attitude of the satellite body by adjusting the momentum. Methods based on classical control theory, such as proportional-integral-derivative (PID), linear-quadratic regulator (LQR), and iter-

ative linear-quadratic regulator (LQR), are widely used in this field, and these methods rely on an analytical model of the satellite's rigid body dynamics. The design stage requires sufficient system knowledge, manual parameter adjustment, and multiple experiments. The control algorithm in an experiment may fail due to unreasonable parameter selection (such as P , I , and D parameters). The reinforcement learning paradigm provides a powerful framework for problem solving and has proven to be a promising and nonintuitive problem-solving technology in many challenging environments, such as MuZero [1], Atari games [2], Go [3], and GYM [4]. However, the application of reinforcement learning in real-world systems has just started, mainly for the following reasons:

- (1) In a real-world environment, sample acquisition costs are high, and the incentive function cannot be accurately described since the function is typically a

multiobjective function and the objectives are related to each other

- (2) The system sensor contains noise
- (3) The actuator control frequency has a limiting value
- (4) Due to security issues, the system cannot be explored at will
- (5) It is impossible to effectively reset the system to the initial state at the end of each training session

Additional issues can arise in real-world systems. Applying reinforcement learning to satellite attitude control faces the challenges described above. In this study, we construct a physical system to introduce the characteristics of the real-world system.

Based on whether historical data is used to establish the environmental model transfer function explicitly, reinforcement learning methods can be divided into two broad categories: model-free and model-based methods. Model-free methods require continuous interactions with the environment during the learning process. To improve the performance of the policy during the training iterations, model-free methods often require a large number of samples to learn and are prone to problems of high collection times and costs caused by the low sampling efficiency. However, once a method converges, it can often obtain a policy with a better performance.

Depending on whether the policy for interacting with the environment is consistent with the policy that is required to improve performance and whether the collected samples can be reused, model-free methods can further be divided into two categories: on-policy and off-policy methods. On-policy methods use the same policy to interact with the environment. After the policy is updated, the data sampled by the current policy needs to be used to estimate the Q -value function or A -value function to ensure the correctness of the estimate. The samples collected in each iteration need to be discarded. Representatives of these methods include state-action-reward-state-action (SARSA) [5], policy gradient, trust region policy optimization (TRPO) [6], and proximal policy optimization (PPO) [7]. Off-policy methods allow the use of policies different from those that need to be updated to interact with the environment. Samples collected during each interaction can be collected and used in the next policy update. These methods are represented by Q -learning [8], deep deterministic policy gradient (DDPG) [9], twin delayed DDPG (TD3) [10], and soft actor-critic (SAC) [11].

Applying on-policy methods directly to a real system will amplify the many problems caused by the low utilization rate of the samples. Therefore, the application of this type of method is mainly in simulation environments. Elkins et al. [12, 13] trained a satellite attitude stabilization controller in a simulation environment. In comparison, off-policy methods alleviate the problem of sample utilization. In recent years, they have been applied in real-world systems. For example, Haarnoja et al. [14] used the improved SAC algorithm to directly train Minitaur quadruped robots, achieving gait control for a variety of sports.

Model-based reinforcement learning methods use historical data to explicitly learn environmental dynamics models and return functions, to learn policies, to evaluate actions, and to formulate plans using the learned models. This type of method is mainly concerned with two factors: the accuracy of the learning dynamics model and how to use the model effectively. In improving the accuracy of the environmental dynamics model predictions, challenges such as randomness and uncertainty must be addressed. For low-dimensional problems, Bayesian parameter-free models such as Gaussian processes have become an effective choice. Parameter-based neural networks have become a popular research topic in recent years, and a probabilistic ensemble (PE) dynamic model has been proposed and achieved state-of-the-art results.

In terms of how to effectively use the model, the first type of method does not consider the cumulative error. It only selects one action, such as random shot, model predictive control (MPC), or cross entropy method (CEM), and selects the current optimal action by simulating multiple paths in the learned environment. This type of method often requires powerful computing resources. The second type of method begins from the perspective of learning policies in the environment, makes the most efficient use of the dynamic models, represented by model-based policy planning (POPLIN) [15], stochastic lower bound optimization (SLBO) [16], and model-based policy optimization (MBPO) [17], and draws upon theories to determine how to correctly make choices in the interaction between the real environment and the model.

The above methods can be effectively applied to real-world systems, and they are mainly bridged in two ways. One is to build a simulation environment close to the real-world system and deploy the policies obtained after training in the simulation environment to the real system. The second is to learn the environmental model based on historical data and use mixed training in the environmental dynamics model and the real system to obtain the final deployment policy. In the scenario considered in this study, the following facts make it difficult to use existing methods directly: (1) it is impossible to accurately construct a scenario similar to the real world (such as an on-orbit environment in outer space), (2) it is impossible to interact with the real-world system during the training phase, and (3) real-time simulations are not supported.

Our method trains the policy set at different stages through the historical state-action trajectory data and takes the global data to train the discriminator. In the actual operation, the method relies on the discriminator to determine the action proposed by the policy set to select the optimal action and to reduce the upper bound of error that is proportional to the square of the number of steps with behavior cloning. The innovations of this paper are as follows. (1) This paper proposes a new imitation learning method to solve the continuous control problem. (2) Through training, a low-level control policy for a real system with a reverse momentum wheel as the actuator was obtained. (3) By only using the onboard original sensor information to achieve the end-to-end control of the multimotor pulse width modulation (PWM) signals, the control task of balancing on a corner was completed.

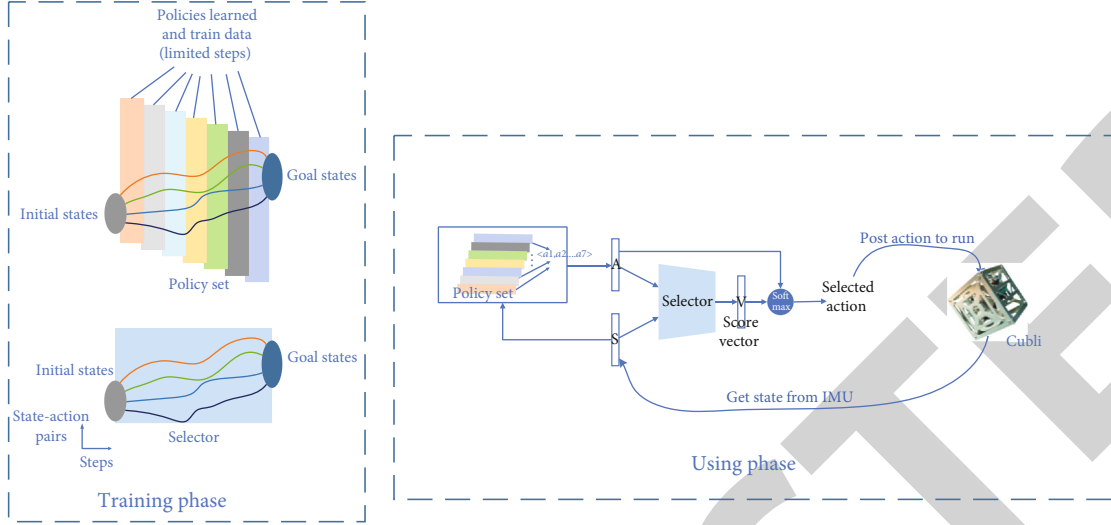


FIGURE 1: The overall idea of the method.

2. Methodology

Figure 1 shows the overall idea of the method in this paper. The method uses historical data to train the policy set and policy selector in the training stage. In the actual utilization stage, it applies the policy set to calculate the candidate action set based on the current state. Based on the current state and candidate action set, it then relies on the policy selector to calculate the final action submitted to the actual system for execution. As shown in the left part of Figure 1, each policy in the policy set uses part of the data for training, which is called local training, where the data used is marked in different colors. The selector uses global data. Training is called global training, and only one selector is marked with a unique color. Sections 2.1 and 2.2 describe the details of the policy set training and policy selector design, respectively.

2.1. Policy Set Training. Behavior cloning transforms the learning problem into a supervised learning problem of fitting expert demonstration behavior. That is, given expert state-action pair trajectory data, the deterministic policy function receives a state as an input and then outputs an action that should be close to the expert's action in the historical data. For a random policy function, it outputs the distribution of actions in the current state. Under this distribution, the expert's actions in the current state should have a high probability value. When using a neural network to characterize a policy function, π , the policy function is typically determined by the neural network architecture and parameters θ , so it can be written as π_θ . The policy network training task is to adjust θ and find θ^* to minimize the loss function. The task and the loss function are expressed as follows:

$$\theta^* = \operatorname{argmin}_\theta (L(\theta)),$$

$$L(\theta) = E_{(s,a) \sim D} \left[\frac{1}{2} (\pi_\theta(\bullet|s) - a)^2 \right], \quad (1)$$

where E denote the expectation and $\langle s, a \rangle \sim D$ denote the state, action pair sampled from the data D to estimate the expectation.

Ross et al. presented the following conclusion. The policy (s) is obtained by supervising training with a labeled training set. When the action a_t given in the state s and the optimal action a^* are evaluated with a 0-1 loss, $L(\pi) = E_{\tau \sim \pi} [\sum_0^{t=H} 1(a_t \neq a^*)]$ (τ is the trajectory collected by policy π) will be within the upper bound given as follows.

$$L(\pi) \leq C + H^2 \epsilon, \quad (2)$$

where ϵ is the generalization error in the distribution $s \sim d^\pi(s)$ and C is constant. This means that when the time length is H , the deviation of the error will grow as the square of H , which will cause to deviate significantly from the expert policy. Thus, the state distribution $d^\pi(s)$ obtained by executing the policy π is far away from the state distribution $d^E(s)$ obtained by using the expert policy.

To address this issue, the collected expert trajectories are segmented, and policies of different stages are trained for different state sets. This allows the policy selector to control the length of time used by each policy and to reduce the overall accumulated error, as shown in Figure 2. Rectangles of one color represent the training data used in one policy. The overlapping area is set in the segmented data of the interval. Given the training set $\tau_1, \tau_2, \dots, \tau_N$, the trajectory length is H , and the policy set is $\pi_1, \pi_2, \dots, \pi_K$, the width of the data used to train each policy is W , and the width of the overlapping area is S . The following relationship $W * K - S * (K - 1) = H$ must be satisfied. For the i -th policy in the policy set π_{θ_i} during training, minimize the following loss function:

$$L(\theta_i) = E_{\tau \sim \pi} \left[\sum_{W*(i-1)-S*(i-1)}^{t=W*i-S*(i-1)} \frac{1}{2} (\pi_{\theta_i}(\bullet|s_t) - a_t)^2 \right]. \quad (3)$$

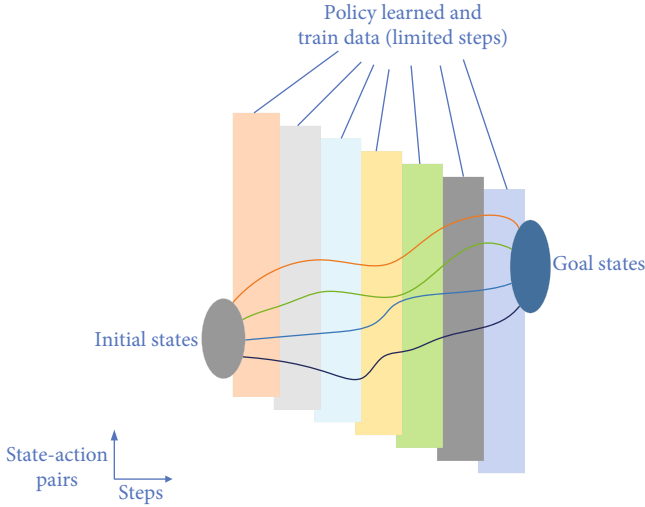


FIGURE 2: An example of policy set training.

2.2. Design of Policy Selector Based on Generative Adversarial Network. The generative adversarial network (GAN) was first proposed by Goodfellow [18]. It is a generative model that uses deep neural networks. The generative adversarial network consists of two components: a generative model and a discriminator model. The generative model is used to generate new samples, and the discriminator model distinguishes the generated samples from the real samples. In the training, the training goal of the generative model is to make the generated samples for the discriminator to recognize its real samples, and the training goal of the discriminator is to correctly distinguish between true and false samples. The two models improve performance in adversarial mode so that the generative model can converge to generate data that is similar to the distribution represented by the real sample data. Meanwhile, the discriminator model has a high accuracy rate that can distinguish between true and false samples.

As shown in Figure 3, a policy selector architecture is proposed based on a GAN. A discriminator is trained to distinguish whether a given state-action pair is an expert demonstration. The fake data used for training consists of two parts. The first is the state-action pair (s, a) formed by inputting random noise Z (sampled from a normal distribution) and state S (sampled from real historical data) to the generator $G(S, Z)$ to obtain the current action a . The second is the data obtained by the action of both the selector and the policy set (trained by the method described in Section 2.1). A state S (sampled from real historical data), it corresponds to the policy set $\pi_1, \pi_2, \dots, \pi_K$, which is used to form the output action vector $A = a_1, a_2, \dots, a_K$, where $a_i (i = 1, 2, \dots, K)$ corresponds to the action proposal given by the i -th policy, and the policy selector takes $(s, a_1), (s, a_2), \dots, (s, a_K)$ as inputs to obtain the scoring vector to judge whether each action pair is an expert behavior $V = D(s, a_1), D(s, a_2), \dots, D(s, a_K)$. The final action can be calculated as follows:

$$\text{action} = A \cdot \frac{V}{\sum_{i=1}^K e^{D(s, a_i)}}. \quad (4)$$

The resulting action pair $\langle s, a \rangle$ is used as a sample of the fake dataset. The real data comes from the demonstration of expert data.

The training objective of the discriminator is the maximization of equation (5), the training objective of the generator is the maximization of equation (6), and the parameter update process is marked by the dotted line in Figure 3.

$$L(D) = E_{(s,a) \sim \text{Fake Data}} [\log (1 - D(s, a))] + E_{(s,a) \sim \text{Real Data}} [\log (D(s, a))], \quad (5)$$

$$L(G) = E_{s \sim \text{history states set}} [D(s, G(s, z))]. \quad (6)$$

2.3. Summary of Algorithm. According to the description above, the algorithm is summarized as shown in Algorithm 1. After the training, the algorithm outputs the discriminator D_{w^*} and the policy set $\{\pi_1^*, \pi_2^*, \dots, \pi_K^*\}$. In actual use, at every moment t , the state s is obtained from the real system, and the action candidate set $A = \{a_1^*, a_2^*, \dots, a_K^*\}$ is obtained after the policy set is processed. The discriminator D_{w^*} is used as a selector to obtain the score vector, $V = \{D_{w^*}(s, a_1^*), D_{w^*}(s, a_2^*), \dots, D_{w^*}(s, a_K^*)\}$, and output action, $\text{action} = A \cdot e^V / (\sum_{i=1}^K e^{D_{w^*}(s, a_i^*)})$. These are submitted to the real system for execution, and closed-loop control is formed over and over again. The process is shown in Figure 1.

3. Experiments and Results

Cubli is a 15 cm \times 15 cm \times 15 cm cube. Momentum wheels are arranged on the three planes of the cube. It is a typical nonlinear, unstable, and multidegree-of-freedom control system. The rotation of the motor drives the flywheel to produce momentum changes. Momentum is transferred between the flywheel and the body to control the posture. Cubli is shown in Figure 4.

Inverted pendulum has been used to verify control theory for a long time [19, 20]. Chaturvedi et al. [21] pointed out that the three-dimensional inverted pendulum can be used as a simplified aircraft version to study control theory. As a reaction-wheel-based inverted pendulum, Cubli has the similar structure as a satellite and be used to verify the method proposed in the study.

Cubli is mainly composed of three brushless motors with encoders, three sets of brake devices, an MPU6050 digital motion processor, a main control chip STM32F103RCT6, and Raspberry Pi 4B. The STM32 and the Raspberry Pi were connected through a serial port. The onboard data was collected by STM32 through MPU6050 and submitted to the Raspberry Pi for processing through the serial port. The communication protocol sent by Cubli to the Raspberry Pi was floating-point data of the Euler angles (roll, yaw, and pitch), angular velocities (rotation rates around the x , y , and z axes), motor speeds (one for each of the three motors), and motor PWM values (one for each of the three motors). The first two data entries were read from the MPU6050 DMP register. As the calculation unit and control unit, the Raspberry Pi calculated the current actions (the PWM target values of the three motors) to be performed after obtaining the current

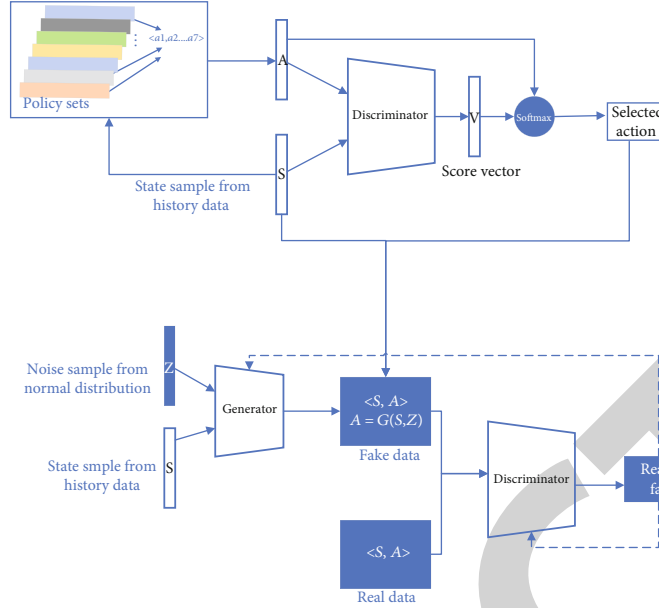


FIGURE 3: The architecture of policy selector based on GAN.

Input: expert state-action trajectories $\{\tau_1, \tau_2, \dots, \tau_N\}$, and the i th trajectory $\tau_i = (s_0^i, a_0^i, s_1^i, a_1^i, \dots, s_H^i, a_H^i)$'s length is H .
Initialize policy set $\{\pi_1, \pi_2, \dots, \pi_K\}$ which size is K , and the i th policy's parameter is θ_i .
Training set's width is W , and the overlap size between two adjacent training sets is S .
Initialize generator's parameter ϕ and discriminator parameter w

Output: trained discriminator D_{w^*} and policy set $\{\pi_1^*, \pi_2^*, \dots, \pi_K^*\}$

- 1: **for** $i = 1$ to K **do**
- 2: Initialize training set D_i
- 3: **for** $j = 1$ to N **do**
- 4: Collect state-action pairs from trajectory $\tau_j = (s_{W^*(i-1)-D^*(i-1)}^j, a_{W^*(i-1)-D^*(i-1)}^j, \dots, s_{W^*i-D^*(i-1)}^j, a_{W^*i-D^*(i-1)}^j)$, and save into training set D_i .
- 5: **end for**
- 6: Train policy π_i with gradient descent to minimize the loss $L(\theta_i) = -E_{(s,a) \sim D_i}[\log(\pi_{\theta_i}(a|s))]$
- 7: **end for**
- 8: **for** $k = 1$ to MAX **do**
- 9: **for** $i = 1$ to M **do**
- 10: Sample state-action pairs (s_i, a_i) from expert state-action data, and save into real data set R
- 11: Sample states s_i from expert data, input the state into policy set, and get action vector $A = \{a_1^i, a_2^i, \dots, a_K^i\}$
- 12: Calculate the score vector $V = \{D_{w_i}(s_i, a_1^i), D_{w_i}(s_i, a_2^i), \dots, D_{w_i}(s_i, a_K^i)\}$
- 13: Calculate the action with $a_{fake} = A \cdot e^V / \sum_{i=1}^K (e^{V_i})$
- 14: Save (s_i, a_{fake}) into fake data set F
- 15: Save the action $a_{generated}$ generated from generator $(s_i, a_{generated})$ into fake data set F
- 16: **end for**
- 17: Update the discriminator parameters with gradient ascent to maximize the function $E_{(s,a) \sim R}[\log(D_{w_i}(s, a))] + E_{(s,a) \sim F}[\log(1 - D_{w_i}(s, a))]$'s value
- 18: Update the generator parameters with gradient ascent to maximize the function $L(\phi) = E_{s \sim \tau}[\log(D_{w_i}(s, G_\phi(s, z)))]$
- 19: **end for**

ALGORITHM 1: GAN-based offline reinforcement learning method.

Cubli status information, which was sent to the Cubli main control chip and was executed by the motor after it was written into the register. The on-board data sampling interval time was 5 ms. The time to calculate the action through the Raspberry Pi was about 3 ms, and the time from acquiring

the status to executing the action was about 8 ms, that is, the control frequency was 125 Hz.

The environment constructed in this paper was mainly used to achieve point balance on a corner, as shown in Figure 5. After turning Cubli to the side balancing state, the

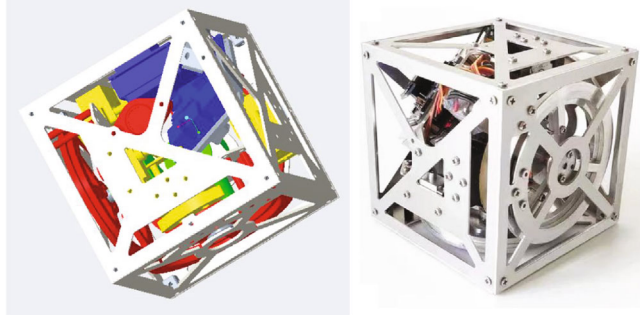


FIGURE 4: Cubli and its structure.

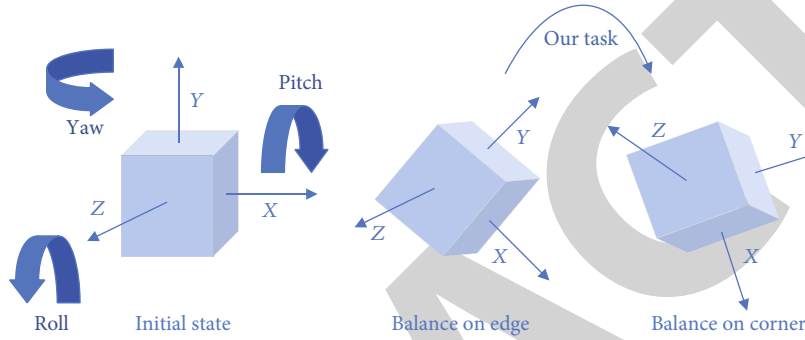


FIGURE 5: Schematic diagram of spot balance task.

momentum exchange between the body and the flywheel was implemented by controlling the rotation of the three flywheels to achieve the attitude movement. In the vicinity of the balance point, the angular momentum of the body was again reduced to close to 0 to implement the point balance control.

The current state of Cubli is represented as $s_t = [\phi, \theta, \varphi, \dot{x}, \dot{y}, \dot{z}, \text{Encoder_A}, \text{Encoder_B}, \text{Encoder_C}]^T$, where ϕ, θ , and φ represent roll, pitch, and yaw, respectively; \dot{x}, \dot{y} , and \dot{z} represent the angular velocities around the x, y , and z axes, respectively; and Encoder_A, Encoder_B, and Encoder_C represent the speed data of the devices on the three plane flywheels. The action is expressed as $at = [a1, a2, a3]$, where $a1, a2$, and $a3$ correspond to the PWM values of the three

motor voltage signals that control the rotation of the motor.

The Euler angles and triaxial angular velocities in each state were directly measured by the onboard MPU6050 six-axis inertial measurement unit. Encoder_A, Encoder_B, and Encoder_C were written into the main control chip by the encoder of the motor. The state was standardized, and the cosine and sine function values were used instead of the Euler angles. For the shaft angular velocity and motor speed, the measured data was obtained from the board and divided by the maximum value for normalization so that each state component was limited to the value range of $[-1, 1]$. Therefore, the actual state of use is expressed as follows:

$$s_t = \left[\begin{array}{cccccc} \cos(\phi), \sin(\phi), \cos(\theta), \sin(\theta), \cos(\varphi), \sin(\varphi) \\ \dot{x}, \dot{y}, \dot{z}, \text{Encoder_A}, \text{Encoder_B}, \text{Encoder_C} \end{array} \right]^T \cdot \left[\begin{array}{cccccc} \text{MAX_X}, \text{MAX_Y}, \text{MAX_Z}, \text{MAX_ENCODER}, \text{MAX_ENCODER}, \text{MAX_ENCODER} \end{array} \right] \quad (7)$$

A fully connected neural network was used to represent the policy model. The neural network had three hidden layers, each with 128 neurons, initialized with random values for each parameter. A three-layer, fully connected neural network was used to represent the generative model and discrimination model in the policy selector. The specific neural network architecture, initialization parameters, learn-

ing method, sample batch number, and learning rate are shown in Table 1.

At the beginning of the experiment, the expert policy was deployed on Cubli and used to collect data for simulating to get control data on orbit, and 200 expert state-action pair trajectory data were collected, with 2000 steps per trajectory. This dataset was used to train the policy through behavior

TABLE 1: Parameter settings of policy, policy set, and policy selector.

	Behavioral cloning	Policy set	Policy selector (discriminator)	Generator
Number of input layer units	12	12	15	12
Number of output layer units	3	3	1	3
Means of parameter initialization	Censored normal distribution randomly generated	Censored normal distribution randomly generated	Censored normal distribution randomly generated	Censored normal distribution randomly generated
Number of hidden layer units	128	128	256	256
Hidden layers	3	3	3	3
Optimization algorithm and learning rate	Adam/0.003	Adam/0.003	Adam/0.003	Adam/0.003
Number of batch samples	256	64	256	64

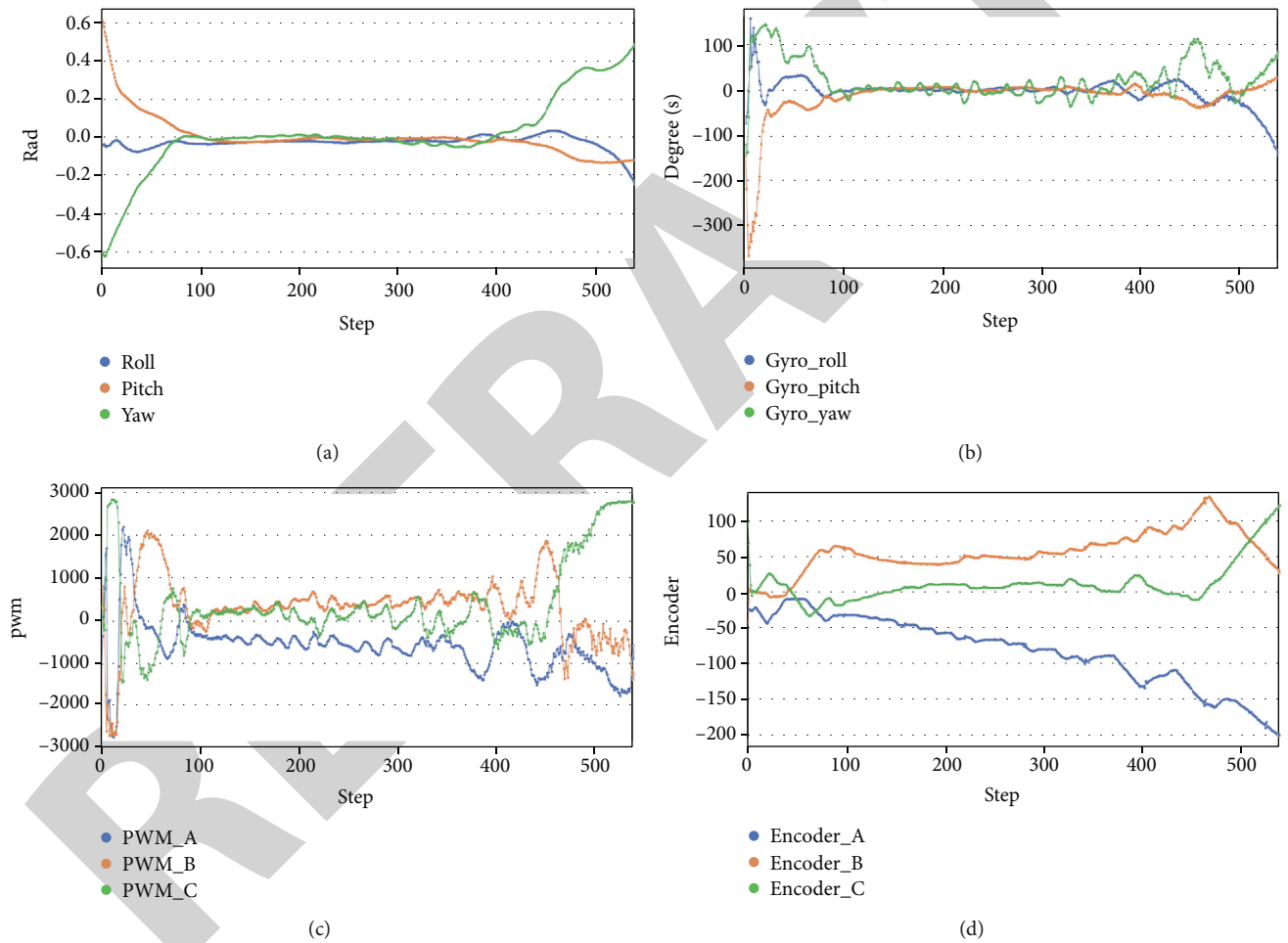


FIGURE 6: Experiment results: BC method was used. (a) Euler angles, (b) gyro value, (c) PWM value, and (d) encoder value.

cloning, and the same dataset was used to train the policy set and policy selector of the method proposed in this paper. The behavioral cloning method used 400,000 entries of the sample data of the entire training set for training a single policy, and the number of sample batches for each training process was 256. The training was performed in 1,562,500 times with the 400,000 samples. A policy set with a set number of seven was used, the 2000-step data of each trajectory was divided

into seven training sets, and the number of steps in each training set was 290 steps. The number of overlapping steps in the training set used by the interval policy was five.

After the training, π_{BC} and π_{OUR_METHOD} were deployed in the same real system to verify the effects of the two policies. Figure 6 shows that the policy trained using the behavioral cloning method could adjust Cubli to the equilibrium point at the beginning of the experiment so that the Cubli Euler

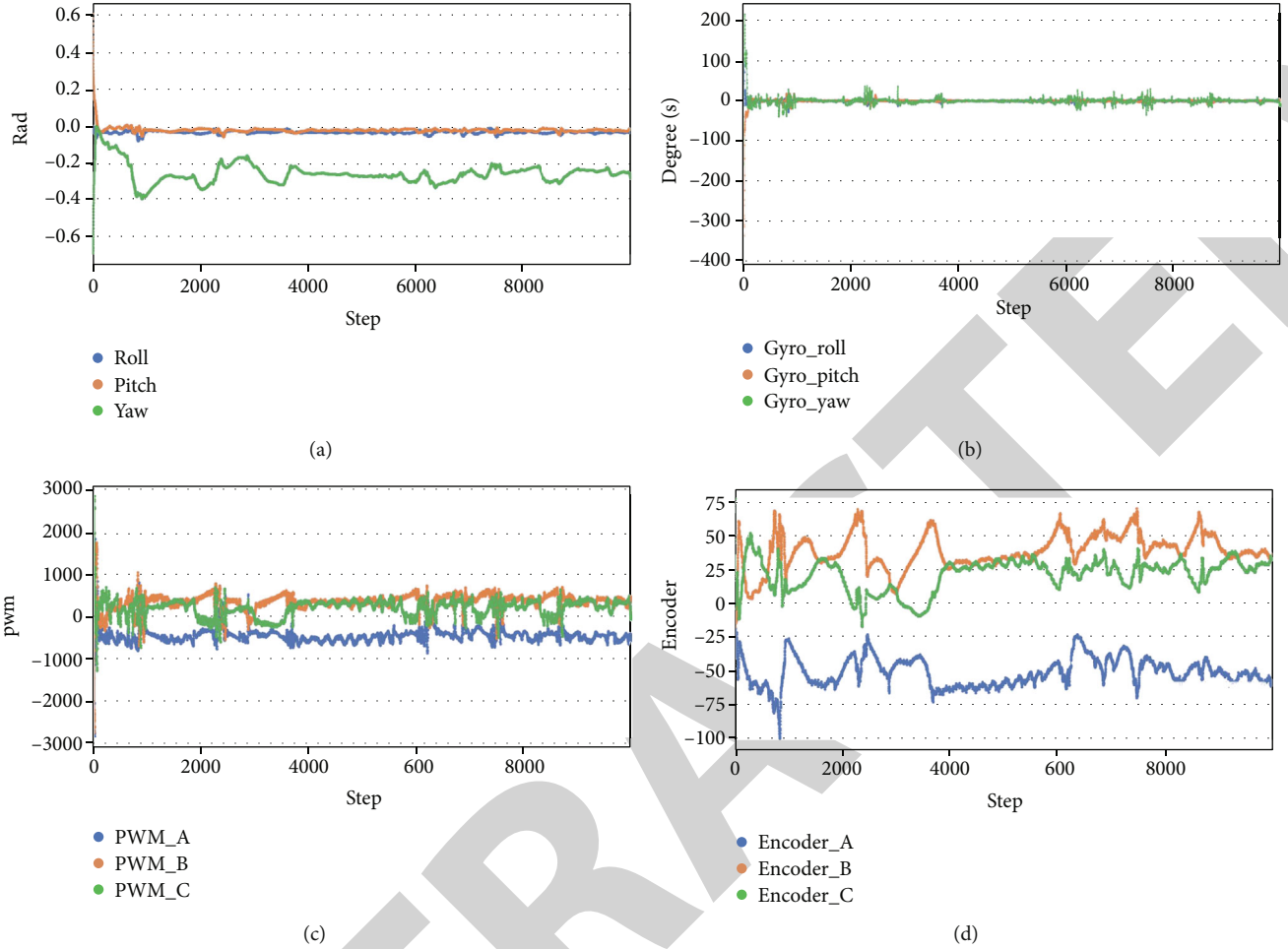


FIGURE 7: Experiment results: our method. (a) Euler angles, (b) gyro value, (c) PWM value, and (d) encoder value.

angle was close to 0. The three-axis angular velocities were nearly 0, which means a balance was maintained in the experiment of nearly 500 steps. However, after 500 steps, it gradually deviated from the balance point, which caused errors to accumulate and eventually resulted in the loss of balance.

The experimental results verify Ross's conclusion that the accumulation of errors is proportional to the square of the number of steps. The test results using the method in this paper are shown in Figure 7. To better display the data, the entire record is not presented; only the first 10,000 steps in the trajectory are shown. This is sufficient to demonstrate the performance of the proposed method. The data of 10,000 steps shows the system adjusted from the initial state to the equilibrium point (the Euler angle error and angular velocity were close to 0), and the system remained near the equilibrium point. The PWM and flywheel speed values showed that Cubli was always relatively stable during operation, and the adjustment was maintained within a small range, achieving better performance.

Analysis of the results showed that the reason the proposed method achieved a better performance was that by dividing the expert trajectories, each policy in the policy set was trained for a different initial state set. Moreover, in actual

use, the policy that is suitable for the current state is selected through the policy selector. Consequently, the probability of the same policy being used continuously is significantly reduced compared to the behavioral cloning method with only one policy, thereby reducing the cumulative error caused by using only one policy.

4. Conclusion

In this paper, a data-driven offline reinforcement learning method is proposed that can learn effective control policies in an attitude control system that uses momentum exchange as the actuator. The method learns a single policy from different stages by dividing the trajectories of experts, making it possible to select policies with fewer accumulated errors from the policy set based on the state. The method also adopts global data to train the policy selector. When deployed in the actual system, an effective policy is selected through the evaluation of the policy selector based on the current state. This yields a good performance for control over long time periods. Unlike previous works that verified algorithms in a simulation environment, the physical system constructed in this study was closer to a satellite attitude control system with momentum wheels as the actuators. The method also avoids

Research Article

A Wireless Network Communication Capacity Control Technology Based on Fuzzy Wavelet Neural Network

Bing Zheng and Dawei Yun 

Department of Information Engineering, Hainan Vocational University of Science and Technology, Haikou 571126, China

Correspondence should be addressed to Dawei Yun; yundw@hvust.edu.cn

Received 11 March 2021; Revised 24 April 2021; Accepted 10 May 2021; Published 26 July 2021

Academic Editor: Yong Deng

Copyright © 2021 Bing Zheng and Dawei Yun. This is an open access article distributed under the Creative Commons Attribution License, which permits unrestricted use, distribution, and reproduction in any medium, provided the original work is properly cited.

The communication capacity control of the computer wireless network is the basis for realizing the efficient communication of massive data. In order to study the communication capacity control technology of the computer wireless network, improve the control effect of a large amount of data communication, and calculate the capacity of the wireless network in real time, this paper uses the fuzzy wavelet neural network to predict the wireless network channel. After the interference-free channel is obtained, the load balancing strategy of the ant colony optimization algorithm is used to filter the channel, and the channel allocation sequence with the most balanced load distribution is obtained, and a priority selection list is generated. After discretizing the channels in the largest discretization selection list, the channel sequence is allocated to the pair of nodes with communication requests according to the greedy coloring algorithm, so as to realize the communication capacity control of the computer wireless network. The test results show that the technology can guarantee good communication performance in both static and dynamic networks and can effectively complete network communication of massive data, and the communication capacity control effect is good.

1. Introduction

Wireless network communication capacity refers to the maximum amount of information that can be transmitted in a unit time, which is the embodiment of the advantages and disadvantages of wireless network communication ability, and it is greatly related to communication lines, work efficiency, and information passing time. At present, the Internet has covered people's daily life. With the continuous integration of wireless communication technology and computer network technology, computer network technology has also developed rapidly. It has developed from simple data transmission in the past to multimedia data transmission such as voice, image, and video [1]. With the rapid development of computer technology, network technology, and communication technology, wireless network communication performs the functions of traditional network communication, such as file transmission, peripheral sharing, Web browsing, e-mail, and database access. Its main characteristics are high data transmission rate, relatively low price, and

fast network construction speed [2]. Because the wireless communication link has the characteristics of high burst error rate, signal attenuation and background noise, interference conflict, and so on and because of the distributed random access characteristics of DCF, it will be greatly affected by network congestion, resulting in communication bottlenecks and other problems [3]. Because the communication line is the main reason that affects the wireless network communication, the communication line is also called the channel, and the capacity of the channel determines the capacity of the network communication [4]. Channel capacity is a parameter of the channel, which can reflect the maximum amount of information that can be transmitted by the channel. At present, the single-channel protocol is the main protocol in the practical application of wireless network, which simplifies the implementation of the protocol, reduces the difficulty of mutual discovery between nodes, and makes the networking more rapid and convenient [5]. However, when the amount of data is very large, many nodes will apply for communication on this channel at the same time,

resulting in increased communication competition. Therefore, it is studied in this paper, and the communication capacity control technology of computer wireless network is proposed, which is used to solve the problem of communication capacity control and ensure the efficient transmission of data communication [6].

The key contributions of this work are as follows:

- (1) This paper uses fuzzy wavelet neural network to predict wireless network channels
- (2) This paper uses the load balancing strategy of the ant colony optimization algorithm to filter the channels, obtain the channel allocation sequence with the most balanced load distribution, and generate a priority selection list
- (3) The channel sequence is allocated to the pair of nodes with communication requests according to the greedy coloring algorithm to realize the communication capacity control of the computer wireless network

The rest of this paper is organized as follows: Section 2 discusses communication capacity control technology of computer wireless network, followed by the experimental test which is discussed in Section 3. Section 4 concludes the paper with summary and future research directions.

2. Communication Capacity Control Technology of Computer Wireless Network

In this paper, a multichannel MAC protocol is used, which can make many nodes in wireless sensor network and use multiple channels for parallel communication, so as to greatly improve the utilization of network bandwidth resources, reduce communication competition, and improve the network communication capacity [7].

The communication capacity control of computer wireless network is divided into three steps: channel prediction, screening, and allocation. In the communication process of computer wireless network, the prediction model of fuzzy wavelet neural network is used to get the channel without interference in the next stage [8]. Then, the load balancing strategy based on ant colony algorithm is applied to filter the channels, and the channel sequences without interference and with low load are recorded in the priority choice lists (PCL). Then, the maximum discretization algorithm is applied to select the channel from the PCL for channel discretization [9]. After the maximum discretization of the channel is completed, the channel sequence is assigned to the node pair with communication request to realize the communication capacity control of computer wireless network [10].

2.1. Channel Prediction Based on Fuzzy Wavelet Neural Network. Fuzzy wavelet neural network is composed of fuzzy neural network and wavelet network. The first half realizes a TSK fuzzy model, and the second half is wavelet network.

The outputs of the two network models are the outputs of the model [11]. The network structure is shown in Figure 1.

It can be seen from Figure 1 that the neural network has a three-layer structure including an input layer, a calculation layer, and an output layer. There is a close connection between each level. In the structure of fuzzy wavelet neural network, the number of nodes in fuzzy rules is the same as the number of input signals [12]. In the second layer, each node has its corresponding language rules [13]. The membership value of each input signal to the network belongs to a part of the fuzzy system set. The membership function is expressed by Gauss function as

$$\mu_j(x_i) = \exp \left[-\frac{(x_i - \xi_{ij})^2}{\tau_{ij}^2} \right], \quad i = 1, 2, \dots, k, j = 1, 2, \dots, m, \quad (1)$$

in which the input signal variables of the fuzzy wavelet neural network, the number of nodes of the second layer network, and the center and width of the membership function of the j th term of the i th input are represented by x_1, x_2, \dots, x_k ; m ; ξ_{ij} ; and τ_{ij} , respectively [14].

The output of the third layer of the fuzzy network can be expressed as follows:

$$\mu_\theta(x) = \prod_j \mu_j(x_i) \theta = 1, 2, \dots, n, \quad j = 1, 2, \dots, m, \quad (2)$$

in which the output of the fuzzy network is $\mu_\theta(x)$, which is also the input signal of the final network. Therefore, the common output of the wavelet network and fuzzy network can be expressed as

$$u = \frac{\sum_{\theta=1}^n \mu_\theta(x) y_\theta}{\sum_{\theta=1}^n \mu_\theta(x)}, \quad (3)$$

in which the output of the upper wavelet network and the final output of the network are $\mu_\theta(x)$; y_1, y_2, \dots, y_n ; and U , respectively [15].

When using the fuzzy wavelet neural network to predict a channel, the spectrum state β of binary sequence with length T in the channel is decomposed into vector $\beta_{t-\tau+1}^t = [\beta_t, \beta_{t-1}, \dots, \beta_{t-\tau+2}, \beta_{t-\tau+1}]$ with length τ as an input vector of the fuzzy wavelet network, the output is Y° , and its equation is

$$\beta_t = \begin{bmatrix} \beta_t & \cdots & \beta_t & \cdots & \beta_{T-1} \\ \beta_{t-1} & \vdots & \beta_{t-1} & \vdots & \beta_{T-2} \\ \vdots & \vdots & \vdots & \vdots & \vdots \\ \beta_2 & \vdots & \beta_{t-\tau+2} & \vdots & \beta_{T-\tau+1} \\ \beta_1 & \cdots & \beta_{t-\tau+1} & \cdots & \beta_{T-t} \end{bmatrix}, \quad (4)$$

$$Y^\circ = [\beta_{\tau+1}, \beta_{t+1}, \dots, \beta_T].$$

Each column of β_t is sent to the input layer neuron as the input sequence of the fuzzy wavelet neural network. Because

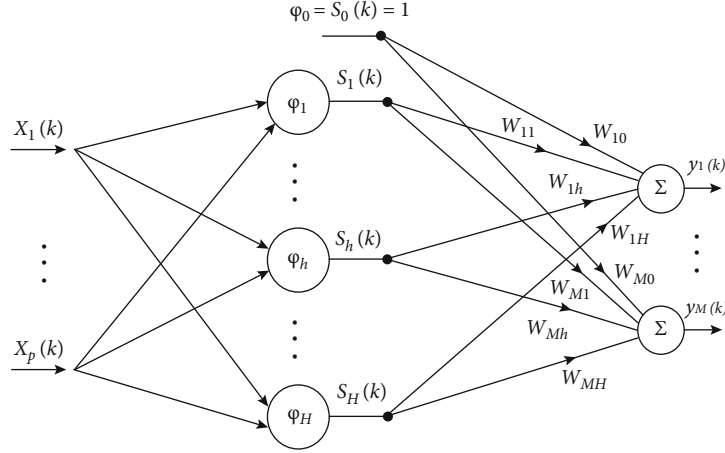


FIGURE 1: Structure of fuzzy wavelet neural network.

the determination of the fuzzy rules of the sample set affects the network structure and the initial parameters of the network, it can reduce the complexity and improve the generalization performance [16]. Therefore, we first extract the rules from the sample set and use the fuzzy C-means clustering algorithm to complete the rule extraction; that is, for N samples $\{(x_j, y_j)\}, j = 1, 2, \dots, N$, the number of clusters c is set; then, the problem is transformed into an optimization problem that meets the constraint conditions [17].

$$\min_{\mu_{ki}, y_j} J = \sum_{j=1}^N \sum_{k=1}^c (\mu_{kj})^m d_{kj}^2. \quad (5)$$

The constraint conditions are as follows:

$$\begin{cases} \sum_{k=1}^c \mu_{kj} = 1, & 1 \leq j \leq N, \\ \mu_{kj} \geq 0, & 1 \leq j \leq N, 1 \leq k \leq c, \end{cases} \quad (6)$$

in which the fuzzy index of clustering is expressed by m , and $m > 1$; the membership degree of sample x_j belonging to cluster k is expressed by μ_{kj} ; the Euclidean distance and diagonal matrix between the sample point and cluster center are $d_{kj}^2 = A_j(x) = (x_j - v_k)^T (F_k)^{-1} (x_j - v_k)$ and F_k , respectively [18].

Let the partition matrix and center matrix of clustering be $U = [\mu_{kj}], K = 1, 2, \dots, C, J = 1, 2, \dots, N$, and $V = [v_1, v_2, \dots, v_c]$, and the number of cycles and the ending error be $l = 1$ and $\varepsilon > 0$, respectively. The process of fuzzy clustering is as follows:

(1) Calculate the fuzzy clustering model:

$$v_k^{(l)} = \frac{\sum_{j=1}^N (\mu_{ki}^{(l-1)})^m Z_j}{\sum_{j=1}^N (\mu_{ki}^{(l-1)})^m}, \quad k = 1, 2, \dots, c, \quad (7)$$

in which Z_j is sample set

(2) Calculate the covariance matrix:

$$F_k = \frac{\sum_{j=1}^N (\mu_{ki}^{(l-1)})^m (Z_j - v_k^{(l)}) (Z_j - v_k^{(l)})^T}{\sum_{j=1}^N (\mu_{ki}^{(l-1)})^m} \quad (8)$$

(3) Calculate the distance to the cluster:

$$d_{kj}^2 = (Z_j - v_k^{(l)})^T D_k (Z_j - v_k^{(l)}), \quad 1 \leq l \leq n, 1 \leq k \leq c \quad (9)$$

(4) Update partition matrix:

$$v_{k,j}^{(l)} = \frac{1}{\sum_{i=1}^c (D_{k,j}^2(z_j, v_k) / D_{i,j}^2(z_j, v_i))^{1/(m-1)}} \quad (10)$$

(5) Using orthogonal least square method, according to the principle of maximum error change rate, M_s important clusters are found and saved [19]. $M = M_s$; $U^{(l)} = [u_i], i = 1, \dots, M_s$; and U is regularized

- (6) If $\|U^{(l)} - U^{(l-1)}\| < \varepsilon$ ends, otherwise $l = l + 1$, return (1) to continue running

For the generated fuzzy rule, if x_1 is A_1^j and x_n is A_n^j , then $\widehat{y}_j = \widehat{Y}_{\text{WNN}}$, where R_j is the j th fuzzy rule and \widehat{y}_j is the output corresponding to the j th fuzzy rule R_j . A_i^j Gaussian membership function μ_{ij} is

$$\mu_{ij}(\beta_i) = \exp\left(-\frac{(\beta_i - \xi_{ij})^2}{\tau_{ij}^2}\right). \quad (11)$$

In this case, the output rule μ_j can be expressed as

$$\mu_j = \prod_{i=1}^n \exp\left(-\left(\frac{(\beta_i - \xi_{j,i})}{\tau_{j,i}}\right)^2\right). \quad (12)$$

The output \widehat{Y}_{WNN} of the wavelet network is calculated as follows:

$$\widehat{Y}_{\text{WNN}_j} = \sum_{a=1}^M \sum_{b=0}^a \omega_{a,b,j} \cdot \varphi_{a,b} \left(\sum_{i=1}^n C_{a,b}^i \cdot X_i \right), \quad (13)$$

in which the scale factor and displacement factor are a and b , respectively.

The prediction output of the whole network is \widehat{Y} :

$$\widehat{Y} = \frac{\sum_{j=1}^M (\mu_j \cdot \widehat{Y}_{\text{WNN}_j})}{\sum_{j=1}^M \mu_j}. \quad (14)$$

$C_{a,b}^i$ and $\omega_{a,b}$ use the least square difference of gradient descent.

$$E = \frac{1}{2i} \sum_{i=1}^n (\widehat{Y} - y(i))^2, \quad (15)$$

in which E is the error and y is the expected output.

The gradient descent method is used to adjust the parameters ξ , τ , C , and weight ω in equations (10) and (14). The first two parameters depend on the fuzzy membership function, the last two parameters come from the wavelet network

model, and α is the learning rate [20].

$$\begin{aligned} \tau(q+1) &= \tau(q) - \alpha \cdot \frac{\partial E}{\partial \tau} \Big|_q = \tau(q) - \alpha \cdot \frac{1}{i} \cdot (\widehat{Y} - Y_i) \cdot \frac{\partial \widehat{Y}}{\partial \tau} \Big|_q, \\ \xi(q+1) &= \xi(q) - \alpha \cdot \frac{\partial E}{\partial \xi} \Big|_q = \xi(q) - \alpha \cdot \frac{1}{i} \cdot (\widehat{Y} - Y_i) \cdot \frac{\partial \widehat{Y}}{\partial \xi} \Big|_q, \\ \omega(q+1) &= \omega(q) - \alpha \cdot (\widehat{Y} - y(i)) \cdot \frac{1}{i} \cdot \frac{1}{a} \cdot z_j \cdot \frac{\partial \widehat{Y}_{\text{WNN}}}{\partial \omega} \Big|_q, \\ c(q+1) &= c(q) - \alpha \cdot (\widehat{Y} - y(i)) \cdot \frac{1}{i} \cdot \frac{1}{a} \cdot z_j \cdot \frac{\partial \widehat{Y}_{\text{WNN}}}{\partial c} \Big|_q. \end{aligned} \quad (16)$$

If node j is connected to rule node l , then

$$\frac{\partial \mu_l(\beta_j)}{\partial \xi_{ji}} = \mu_l(\beta_j) \frac{2(\beta_j - \xi_{ji})}{\tau_{ji}^2}, \quad \frac{\partial \mu_l(\beta_j)}{\partial \tau_{ji}} = \mu_l(\beta_j) \frac{2(\beta_j - \xi_{ji})^2}{\tau_{ji}^3}. \quad (17)$$

2.2. Load Balancing Based on Ant Colony Algorithm. Load balancing problem for wireless sensor network channel allocation is to make the data traffic balanced allocation to each channel. Load balancing is very important for the performance of communication capacity and average delay of wireless sensor networks [21]. The reason is that if the network load cannot be evenly distributed, the channel with large load will lead to the backlog of data services, while the channel with small load will produce the phenomenon that the channel is idle after the transmission of data services, thus affecting the communication capacity of wireless sensor networks [22]. In this paper, low overhead MAC protocol and ant colony optimization algorithm are used to integrate and exchange information between data links and networks, establish certain connections, work cooperatively, remove redundant operations, and allocate network resources more effectively [23].

In the algorithm, pheromone updating is divided into iterative optimal updating and local pheromone updating. The search path selection methods of searching solution space include two kinds: according to the prior law and according to the probability [24]. The purpose of this algorithm is as follows: at a certain time, when the data traffic set in the network comes, the ant colony algorithm is used to find a channel allocation sequence which makes the load most balanced distribution. Whether the channel load distribution is balanced or not can be expressed by the standard deviation of the channel load distribution [25].

$$B = \sqrt{\frac{1}{n} \sum_{j=1}^n (x_j - q)^2}, \quad q = \frac{1}{n} \sum_{j=1}^n x_j, \quad (18)$$

in which j is the total number of available channels, x_j is the load ratio of channel j , q is the average load ratio of channel,

and B is the standard deviation of the load ratio of channel. The smaller the value of B is, the smaller the fluctuation of channel load is and the more balanced the load distribution is. The algorithm first updates the channel load ratio for the channel with low load [26]. With the increase of the overall load, the update mechanism gradually releases the restriction of the load ratio update, allowing more channels with relatively high load to join the algorithm scheduling; when the system load drops, the scheduling of individual channels with relatively high load will be closed in the global update [27], so as to achieve the purpose of overall load balancing.

(1) Iterate and update equation

$$\begin{aligned} \tau(r, s) &= (1 - \rho) \times \tau(r, s) + \rho \Delta \tau(r, s), \\ \Delta \tau(r, s) &= \begin{cases} K \sigma \tau(r, s)^{-1}, & (r, s) \in \text{IOP}, \\ 0, & \text{otherwise,} \end{cases} \end{aligned} \quad (19)$$

in which $i(r, s)$ is the pheromone content of the channel rs , that is, the ratio of the load of the channel rs to the total load; $\Delta i(r, s)$ is the increment of the ratio of the load on the channel to the total load; ρ is the volatile factor of the iterative optimal update load ratio; and $(1 - \rho)$ is the residual factor of the new load ratio. By changing the values of ρ and K , the growth rate of channel load is adjusted [28]. $\sigma \tau(r, s)$ is the standard deviation of the optimal channel sequence load generated in each iteration, and the channel sequence with no interference and low load is recorded in the priority choice lists (PCL); IOP is the iterative optimal path [29, 30].

(2) Local update equation

$$\tau(r, s) = (1 - \vartheta) \tau(r, s) + \vartheta \tau(0), \quad (20)$$

in which ϑ is the volatility coefficient of the local update load ratio, $\tau(0)$ is the initial value of the load ratio, and the introduction of ϑ can reduce the load ratio on the selected channel, which is conducive to the discovery of new paths [31].

(3) Path transfer rule equation

$$S = \begin{cases} \arg \max \left\{ [\tau(r, u)]^\alpha \cdot [\varphi(r, u)]^\beta \right\}, & q \leq q_0, \\ P_{ij}^k, & q > q_0, \end{cases} \quad (21)$$

in which q_0 ($0 < q_0 < 1$) is a parameter of the algorithm, and q_0 is a random number between 0 and 1. α is the heuristic factor, which is the adjustment parameter of load ratio; β is the expected heuristic factor, which is the adjustment parameter of visibility. $\varphi(r, u)$ is heuristic information. When $q > q_0$, the channel is searched according to the probability; when $q \leq q_0$, the channel is selected according to the prior law [32].

(4) Calculation equation of transition probability

$$P_{ij}^k(t) = \begin{cases} \frac{\tau_{ij}^\alpha(t) * \varphi_{ij}^\beta(t)}{\sum_{\text{scalloved}_k} \tau_{is}^\alpha(t) * \varphi_{ij}^\beta(t)}, & j = \text{allpved}_k, \\ 0, & \text{otherwise,} \end{cases} \quad (22)$$

in which $P_{ij}^k(t)$ is the probability that the k th ant selects channel ij at time t , and allpved_k represents the set of nodes connected with the edge of node i , that is, the set of nodes that can be selected by the k th ant at node i . If the node is in the set, its probability is calculated according to the concentration of load ratio; otherwise, the probability is 0. The transfer probability equation indicates that the k th ant of an iteration is calculated according to the proportion of the channel load to the total load. If the load of the channel accounts for the greater proportion of the total load, the probability of transfer is also greater [33].

The algorithm description of multichannel load balancing scheduling algorithm based on ant colony algorithm is as follows:

Step 1. Parameters are set to initialize the load ratio of the channel.

Step 2. The ants in the ant colony choose a channel according to the selection probability.

Step 3. If the load ratio of each channel after scheduling is less than the set threshold.

Step 4. The data service is allocated to the channel.

Step 5. The channel load ratio is updated according to the channel searched by ants in ant colony.

Step 6. If there is a channel after scheduling, the load ratio is greater than the set threshold.

Step 7. Return to Step 2, and reselect a channel.

The maximum discretization is used to process the channel in the PCL list. The equation is as follows:

$$G(i) = [i + OH, i + 1H, i + kH], \quad i = 1, 2, 3, 4, k = 3, \quad (23)$$

in which k is the maximum value satisfying the inequality $i + kH \leq 16$. Each group includes at least n channels, and the equation is as follows:

$$n = \text{floor} \left(\frac{C}{H} \right). \quad (24)$$

In order to ensure the maximum discretization and the maximum separation of each group of channels, the channel expression equation of group j is as follows:

$$\text{Group}(j) = [G(j); G(j + n); G(j + tn)]. \quad (25)$$

Channel maximum discretization is completed. When

TABLE 1: Details of wireless network node parameters.

Parameter	The values	Meaning
Chan	Channe/wirelessChanne	The channel type is a wireless channel
Prop	Propagation/FreeSpace	The transport model is free space
Mac	Mac/Mmac	Protocol used
ifqlen	50	Size of the interface queue
X	500	Topological range length
Y	500	Width of topology range
Stop	100	Set model time
nn	200	Number of wireless nodes
N	10	The total number of channels

there is a node pair to transmit data, the channel is selected from the channel list after the maximum discretization according to the greedy coloring algorithm to assign the channel to the node pair, so as to control the communication capacity of the computer wireless network.

3. Experimental Test

In order to test the communication capacity control effect of the wireless network, NS2 simulation platform is used to complete the simulation experiment. During the experiment, the details of wireless network node parameters are shown in Table 1.

The performance of the multichannel MAC protocol has a great impact on the result of communication capacity control. Throughput average packet delay and average handshake time are used to measure the performance of the multichannel MAC protocol. One of the main goals of multichannel MAC protocol design is to increase the throughput of the network. The parameter can directly reflect the performance of the protocol. Packet delay refers to the time from the sending node to the receiving node, which is composed of queue delay, sending delay, and backoff delay. The average packet delay is an important index to measure the quality of a MAC protocol. The calculation equations are as follows:

$$\begin{aligned}
 & \text{Cumulative throughput} \\
 &= \frac{\text{Group size} \times \text{number of packets sent successfully}}{\text{Simulation time}}, \\
 & \text{Average packet delay} \\
 &= \frac{\sum \text{Packet delay of successfully received packets}}{\text{Number of packets received successfully}}.
 \end{aligned} \tag{26}$$

The transmission performance of the proposed technology in static network and dynamic network is tested, and the performance of the multichannel MAC protocol and typical single transceiver multichannel protocol (MMAC protocol) is compared under different packet arrival rates. Comparison results of the two protocols in static network and dynamic network are shown in Table 2. Packet average delay results in static and dynamic networks are shown in Table 3.

TABLE 2: Comparison results of the two protocols in static network and dynamic network (bit).

Network type	Arrival rate (Kbps)	This paper presents a multichannel MAC protocol	Single transceiver multichannel MMAC protocol
Static network	0	0	0
	20	0.30	0.30
	40	0.38	0.38
	60	0.79	0.61
	80	0.82	1.22
	100	0.98	1.62
	120	1.04	1.71
	140	1.18	1.78
	160	1.21	1.82
	180	1.2	1.78
Dynamic network	200	1.21	1.84
	0	0	0
	20	0.28	0.30
	40	0.31	0.41
	60	0.42	0.68
	80	0.79	1.12
	100	0.88	1.29
	120	1.22	1.71
	140	1.22	1.54
	160	1.21	1.61
180	1.2	1.77	
200	1.21	1.78	

According to the test results in Table 2, in the static network and dynamic network, when the packet arrival rate is lower than 40 Kbps, the throughput difference between the multichannel MAC protocol and the typical single transceiver multichannel protocol (MMAC protocol) is small; this phenomenon is because the network load is small, the multichannel can meet the transmission needs of the network, and there will be no more serious data conflict; when the packet arrival rate is lower than 40 Kbps, the throughput difference between the multichannel MAC protocol and the typical single transceiver multichannel protocol (MMAC protocol) is small; when the packet rate is higher than 60 Kbps, the

TABLE 3: Packet average delay results in static and dynamic networks (sec).

Network type	Arrival rate (Kbps)	This paper presents a multichannel MAC protocol	Single transceiver multichannel MMAC protocol
Static network	0	0.01	0.01
	20	0.02	0.02
	40	0.03	0.03
	60	0.03	0.03
	80	0.03	0.03
	100	0.04	0.08
	120	0.05	0.12
	140	0.05	0.18
	160	0.07	0.27
	180	0.12	0.28
200	0.18	0.33	
Dynamic network	0	0	0
	20	0.04	0.05
	40	0.06	0.09
	60	0.08	0.13
	80	0.10	0.17
	100	0.12	0.27
	120	0.27	0.34
	140	0.31	0.39
	160	0.32	0.41
	180	0.36	0.55
200	0.43	0.61	

throughput of the multichannel MAC protocol is significantly higher than that of the typical single transceiver multichannel protocol (MMAC protocol), and with the gradual increase of the packet arrival rate, the difference between the throughput of the two protocols becomes larger and larger. This is because the multichannel MAC protocol is based on the maximum discrete channel allocation, which can effectively avoid the mutual interference between adjacent channels and alternate channels and greatly improve the utilization of wireless network channel resources, so it can effectively increase the throughput of wireless network communication. Packet average delay results in static and dynamic networks are shown in Table 3.

According to the test results in Table 3, in a static network, when the packet arrival rate is lower than 80 Kbps, the average delay of the multichannel MAC protocol and the typical single transceiver multichannel protocol (MMAC protocol) is equal; with the increase of the packet arrival rate, the load of the wireless network also increases; at this time, the average delay of the multichannel MAC protocol begins to be lower than the typical single transceiver multichannel protocol (MMAC protocol), and the average delay of the network is reduced greatly. In the dynamic network, the average delay of the two protocols increases slowly when the packet arrival rate is 20 Kbps, but the average delay of the multichannel MAC protocol is lower than that of the typical single

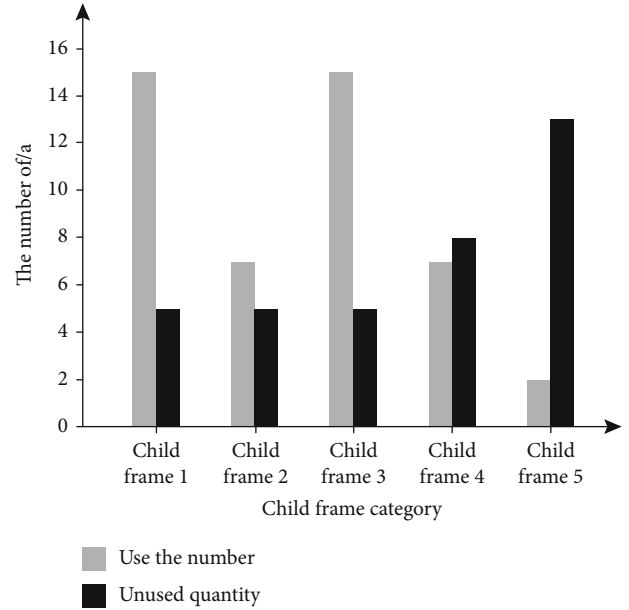


FIGURE 2: Wireless network communication capacity before control.

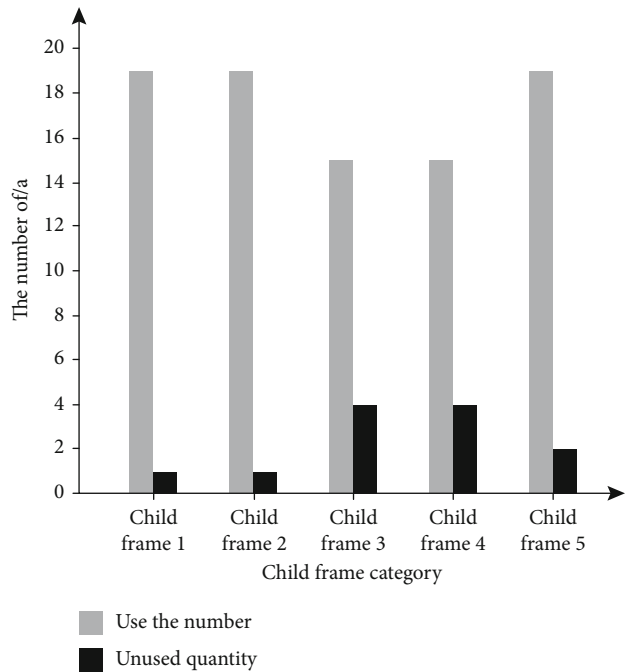


FIGURE 3: Wireless network communication capacity after control.

transceiver multichannel protocol (MMAC protocol). It shows that the transmission performance of the proposed technology is better.

In order to test the communication capacity control effect of the proposed method, the wireless network communication capacity before and after the control is counted. Wireless network communication capacity before control is shown in Figure 2. Wireless network communication capacity after control is shown in Figure 3.

According to the test results of Figures 3 and 4, before the control, there is a large amount of spare capacity in the

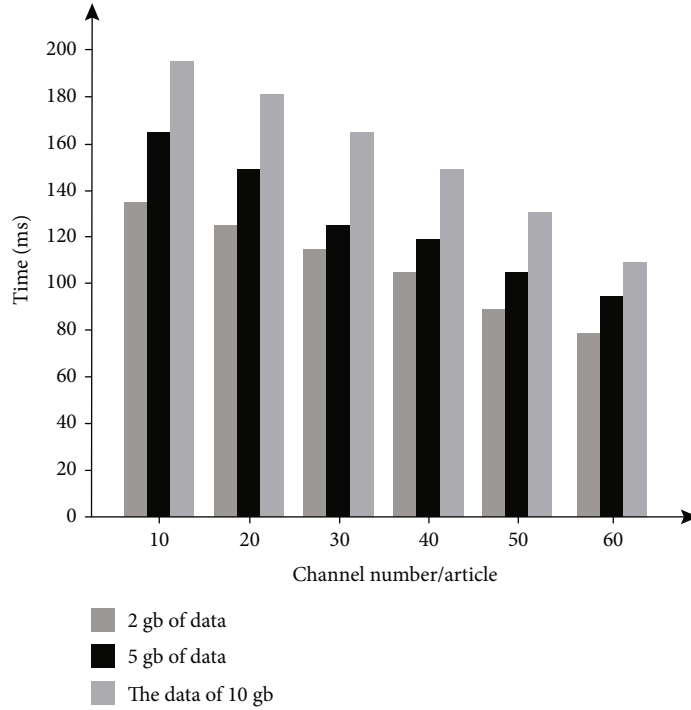


FIGURE 4: Data transmission time before control.

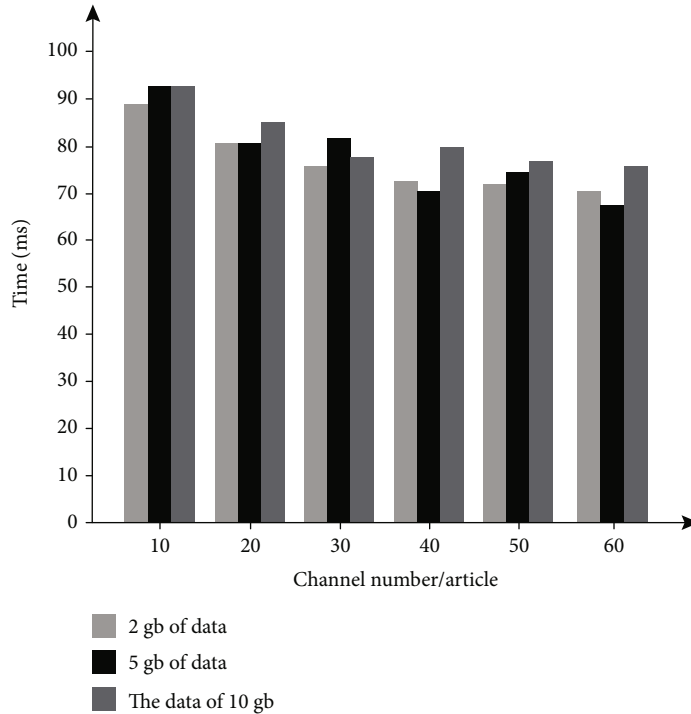


FIGURE 5: Data transmission time after control.

network, which does not make full use of the channel to complete the effective allocation of capacity; after using the technology in this paper, the use and allocation of spare capacity can be completed by using the channel reasonably. It shows that this technology has good control effect on the communi-

cation capacity of computer wireless network and can make full use of the channel to achieve capacity allocation.

In the case of different numbers of channels, the time required for data transmission of different sizes before and after control is tested. Data transmission time before control

is shown in Figure 4. Data transmission time after control is shown in Figure 5.

According to the test results of Figures 4 and 5, when the data volume is 2 GB, 5GB, and 10GB, the larger the data volume is before the communication capacity control, the more time-consuming the transmission is, because the larger the data volume is, many nodes will send communication applications to the channel at the same time, resulting in communication competition, and there will be interference between nodes, resulting in the increase of transmission time-consuming; after the communication capacity control, it can realize multi-channel parallel communication, and improve the utilization of network broadband and transmission efficiency.

4. Conclusion

The communication capacity control of computer wireless network is the main means to meet the current communication needs of computer wireless network, so this paper studies the communication capacity control technology of wireless network based on fuzzy wavelet neural network and ant colony algorithm. In order to ensure good network connectivity as the premise, according to the channel load to carry out channel allocation, the reasonable use of the channel can be realized, to reduce the cost of nodes, so as to ensure the effective control of communication transmission capacity. The test results show that the technology is effective for the communication capacity control of computer wireless network, and the network communication performance is good. In the future research, how to calculate the capacity of wireless network communication in real time has become a main research direction. This link should be added to the research of this article.

Data Availability

The datasets used and/or analyzed during the current study are available from the corresponding author on reasonable request.

Conflicts of Interest

The authors declare that they have no conflict of interest.

Acknowledgments

This study was funded by Beichuang teaching assistant Fund-University industry research innovation fund of Science and Technology Development Center, Ministry of Education (Grant No. 2018A05031).

References

- [1] S. Shan, X. Duan, Y. Zhang, and T. T. Zhang, "Research on collaborative governance of smart government based on Blockchain technology: an evolutionary approach," *Discrete Dynamics in Nature and Society*, vol. 21, no. 4, pp. 1–23, 2021.
- [2] X. Hao, J. Liu, N. Yao, and L. Xie, "Research of network capacity and transmission energy consumption in WSNs based on game theory," *Dianzi Yu Xinxi Xuebao/Journal of Electronics and Information Technology*, vol. 40, no. 7, pp. 1715–1722, 2018.
- [3] J. Cui and F. Zhang, "Design and development of GPS navigation and positioning system based on AutoCAD platform," *Computer-Aided Design and Applications*, vol. 18, no. S3, pp. 46–57, 2020.
- [4] S. Sayed and A. Massoud, "General classification and comprehensive performance assessment of multi-objective DC voltage control in multi-terminal HVDC networks," *IEEE Access*, vol. 9, pp. 34454–34474, 2021.
- [5] O. Kennedy, E. Chukwu, O. Shobayo, E. Noma-Osaghae, I. Okokpujie, and M. Odusami, "Comparative analysis of the performance of various active queue management techniques to varying wireless network conditions," *International Journal of Electrical and Computer Engineering*, vol. 9, no. 1, pp. 359–368, 2019.
- [6] L. Jin, Z. Zhang, N. Wang, Z. Liu, and Y. Fu, "Intensity distribution of partially coherent array finite airy beams propagating in atmospheric turbulence," *International Journal of Optics*, vol. 2021, Article ID 6649144, 11 pages, 2021.
- [7] H. Li, H. Ishidaira, K. SOUMA, and J. Magome, "Assessment of the flood control capacity and cost efficiency of sponge city construction in Mianyang City, China," *Journal of Japan Society of Civil Engineers Ser G (Environmental Research)*, vol. 76, no. 5, pp. 46–57, 2020.
- [8] F. R. Z. Hasibuan and I. Indayani, "The effect of application of SAK-ETAP, internal control system, and capacity of cooperatives on the development of business in cooperatives in Banda Aceh City," *Journal of Accounting Research Organization and Economic*, vol. 2, no. 3, pp. 262–270, 2020.
- [9] E. B. Aleksandrova, A. A. Shtyrkina, and A. V. Yarmak, "Isogeny-based cryptographic access control," *Automatic Control and Computer Sciences*, vol. 54, no. 8, pp. 803–812, 2020.
- [10] M. Yoshida, T. Kan, K. Kasai, T. Hirooka, K. Iwatsuki, and M. Nakazawa, "10 channel WDM 80 Gbit/s/ch, 256 QAM bi-directional coherent transmission for a high capacity next-generation mobile fronthaul," *Journal of Lightwave Technology*, vol. 39, no. 5, pp. 1289–1295, 2021.
- [11] F. P. L. Sanico, "Organizational capacity assessment as input to policy direction in the University of Eastern Philippines, Cataraman Northern Samar," *International Journal of Research-GRANTHAALAYAH*, vol. 7, no. 3, pp. 120–129, 2020.
- [12] C. Xia, Y. Zhang, and Y. Liu, "Path planning and energy flow control of wireless power transfer for sensor nodes in wireless sensor networks," *Turkish Journal of Electrical Engineering and Computer Sciences*, vol. 26, no. 5, pp. 2618–2632, 2018.
- [13] Z. P. Liu, "Research on risk control of relay protection under Hainan Power Grid with large capacity generators," *Yunnan Electric Power Technology*, vol. 47, no. 12, pp. 63–66, 2019.
- [14] M. Sivaram and V. Porkodi, "FCCP-NS: a fair congestion control protocol with N-sinks in wireless sensor networks," *International Journal of Advanced Trends in Computer Science and Engineering*, vol. 8, no. 12, pp. 43–51, 2019.
- [15] G. F. Liu, X. S. Han, Y. Tian, and H. K. Li, "Research on prevention and control technology of oxide scale of boiler in 350 MW supercritical unit," *Reneng Dongli Gongcheng/Journal of Engineering for Thermal Energy and Power*, vol. 33, no. 8, pp. 144–148, 2018.
- [16] C. M. Meng and H. J. Liang, "Research on existing problems in maintenance and management of mobile communication

- network,” *Digital technology and application*, vol. 37, no. 1, pp. 36–38, 2020.
- [17] T. A. Podshibyakina, “Political discourse in online communities as a communication technology of network control,” *Opcion*, vol. 35, no. 23, pp. 1301–1314, 2020.
- [18] B. G. Ibrahimov, M. Q. Hasanov, R. T. Humatov, and R. F. Ibrahimov, “Research on the performance of intelligent communication networks,” *IFAC-PapersOnLine*, vol. 51, no. 30, pp. 768–770, 2020.
- [19] Y. Qiu, H. Zhang, K. Long, and M. Guizani, “Subchannel assignment and power allocation for time-varying fog radio access network with NOMA,” *IEEE Transactions on Wireless Communications*, vol. 3, no. 8, pp. 1–1, 2021.
- [20] R. Zhou, B. Li, M. Yang, and Z. J. Yan, “Simulation research on multi-user media access control technology for the next generation WLAN,” *Computer Simulation*, vol. 36, no. 8, pp. 288–292, 2019.
- [21] Z. Niu, B. Zhang, J. Wang et al., “The research on 220GHz multicarrier high-speed communication system,” *China Communications*, vol. 17, no. 3, pp. 131–139, 2020.
- [22] B. Zhang, Z. Niu, J. Wang et al., “Four-hundred gigahertz broadband multi-branch waveguide coupler,” *IET Microwaves, Antennas & Propagation*, vol. 14, no. 11, pp. 1175–1179, 2020.
- [23] B. Zhang, D. Ji, D. Fang, S. Liang, Y. Fan, and X. Chen, “A novel 220-GHz GaN diode on-chip tripler with high driven power,” *IEEE Electron Device Letters*, vol. 40, no. 5, pp. 780–783, 2019.
- [24] A. Li, D. Spano, J. Krivochiza et al., “A tutorial on interference exploitation via symbol-level precoding: overview, state-of-the-art and future directions,” *IEEE Communications Surveys and Tutorials*, vol. 22, no. 2, pp. 796–839, 2020.
- [25] J. Zhang and G. Qu, “Physical unclonable function-based key sharing via machine learning for IoT security,” *IEEE Transactions on Industrial Electronics*, vol. 67, no. 8, pp. 7025–7033, 2019.
- [26] J. Zhang and C. Shen, “Set-based obfuscation for strong PUFs against machine learning attacks,” *IEEE Transactions on Circuits and Systems. I: Regular Papers*, vol. 68, no. 1, pp. 288–300, 2021.
- [27] J. Shi, Y. Lu, and J. Zhang, “Approximation attacks on strong PUFs,” *IEEE Transactions on Computer-Aided Design of Integrated Circuits and Systems*, vol. 39, no. 10, pp. 2138–2151, 2020.
- [28] P. Wang and Y. Liu, “SEMA: secure and efficient message authentication protocol for VANETs,” *IEEE Systems Journal*, vol. 15, no. 1, pp. 846–855, 2021.
- [29] B. Li, Y. Liu, A. Zhang, W. Wang, and S. Wan, “A survey on blocking technology of entity resolution,” *Journal of Computer Science and Technology*, vol. 4, no. 35, pp. 769–793, 2020.
- [30] Q. Jiang, F. Shao, W. Gao, Z. Chen, G. Jiang, and Y. Ho, “Unified no-reference quality assessment of singly and multiply distorted stereoscopic images,” *IEEE Transactions on Image Processing*, vol. 28, no. 4, pp. 1866–1881, 2019.
- [31] Y. Sun, C. Xu, G. Li et al., “Intelligent human computer interaction based on non redundant EMG signal,” *Alexandria Engineering Journal*, vol. 59, no. 3, pp. 1149–1157, 2020.
- [32] D. Jiang, G. Li, Y. Sun, J. Hu, J. Yun, and Y. Liu, “Manipulator grabbing position detection with information fusion of color image and depth image using deep learning,” *Journal of Ambient Intelligence and Humanized Computing*, vol. 4, 2021.
- [33] F. Xiao, G. Li, D. Jiang et al., “An effective and unified method to derive the inverse kinematics formulas of general six-DOF manipulator with simple geometry,” *Mechanism and Machine Theory*, vol. 159, article 104265, 2021.

Retraction

Retracted: Research on Book Recommendation Algorithm Based on Collaborative Filtering and Interest Degree

Wireless Communications and Mobile Computing

Received 28 November 2023; Accepted 28 November 2023; Published 29 November 2023

Copyright © 2023 Wireless Communications and Mobile Computing. This is an open access article distributed under the Creative Commons Attribution License, which permits unrestricted use, distribution, and reproduction in any medium, provided the original work is properly cited.

This article has been retracted by Hindawi, as publisher, following an investigation undertaken by the publisher [1]. This investigation has uncovered evidence of systematic manipulation of the publication and peer-review process. We cannot, therefore, vouch for the reliability or integrity of this article.

Please note that this notice is intended solely to alert readers that the peer-review process of this article has been compromised.

Wiley and Hindawi regret that the usual quality checks did not identify these issues before publication and have since put additional measures in place to safeguard research integrity.

We wish to credit our Research Integrity and Research Publishing teams and anonymous and named external researchers and research integrity experts for contributing to this investigation.

The corresponding author, as the representative of all authors, has been given the opportunity to register their agreement or disagreement to this retraction. We have kept a record of any response received.

References

- [1] Z. H. Wang and D. Z. Hou, "Research on Book Recommendation Algorithm Based on Collaborative Filtering and Interest Degree," *Wireless Communications and Mobile Computing*, vol. 2021, Article ID 7036357, 7 pages, 2021.

Research Article

Research on Book Recommendation Algorithm Based on Collaborative Filtering and Interest Degree

Zhi Hui Wang¹ and De Zhi Hou²

¹Wuxi Vocational College of Science and Technology, Wuxi 214101, China

²R&D Department, Beijing Huapin Borui Network Technology Co., Ltd., Beijing 100020, China

Correspondence should be addressed to Zhi Hui Wang; wzh@wxsc.edu.cn

Received 26 May 2021; Revised 17 June 2021; Accepted 29 June 2021; Published 12 July 2021

Academic Editor: Balakrishnan Nagaraj

Copyright © 2021 Zhi Hui Wang and De Zhi Hou. This is an open access article distributed under the Creative Commons Attribution License, which permits unrestricted use, distribution, and reproduction in any medium, provided the original work is properly cited.

With the increase of library collections, it is difficult for readers to quickly find the books they want when choosing books. Book recommendation system is becoming more and more important. Based on the previous research, this paper proposes a book recommendation algorithm based on collaborative filtering and interest. Take the interest of the book itself as an important measurement index, including the number of searches, borrowing time, borrowing times, borrowing interval, and renewal times. Through the analysis of MAE and RMSE experiments, the results show that the method proposed in this paper converges faster than the traditional method.

1. Introduction

With the continuous deepening of the informatization process, all walks of life are carrying out informatization reforms. In this context, the process of digitalization of library management information is gradually improving [1]. Digital libraries are deeply loved by readers for their convenient and quick document retrieval methods, personalized recommendations, and other characteristic services [2]. It is difficult for readers to find books of interest in a short period of time in the face of various bibliographies. Therefore, the user experience of the traditional library borrowing method is poor. At present, many scholars have proposed book recommendation methods, including content-based recommendation algorithms, which recommend products similar to the products he liked in the past according to the products that the user liked in the past [3]. A recommendation algorithm based on association rules [4], the same user borrows different books can be considered as having an association relationship [5]. Searching for the collection of books with the highest degree of association from the borrowing information

can be used as an important reference for book recommendation [6]. A combination recommendation model based on tagging and association rule mining and user-based collaborative filtering has nothing to do with items [7]. Find the most similar neighboring users of the current user, and recommend the books borrowed by neighboring users to the current user [8]. A collaborative filtering recommendation algorithm is based on the popularity of the item scoring system combined with average preference weights [9]. A book recommendation algorithm is based on social networks and so on [10].

This paper proposes a book recommendation algorithm based on collaborative filtering and interest degree. Collaborative filtering uses cosine similarity to calculate; interest degree includes search times, borrowing time, borrowing times, borrowing interval, and renewing times according to book attributes. Finally, the average deviation and the root mean square error are used to measure.

The rest of this paper is organized as follows: Section 2 analyzes the factors that affect book recommendation from the two aspects of interest and similarity. The book recommendation algorithm based on collaborative filtering and

interest degree is discussed in Section 3. Section 4 shows the experimental analysis, and Section 5 concludes the paper with summary and future research directions.

2. Analysis of the Factors Affecting Book Recommendation

Recommending books to users can be analyzed in terms of interest and similarity, as shown in Figure 1.

In interest degree, interest is the characteristic of the book itself, and it is recommended from the perspective of attractiveness to the target user [11]. It includes the interest of the book itself and the interest of the user. Book interest refers to the attributes of the book itself, including search times, borrowing time, borrowing interval, borrowing times, and renewing times [12]. User interest refers to books that users like, books that have already been borrowed, and so on.

In similarity, the similarity is to recommend the target user from the perspective of relevance to the user. There are two situations for being associated with users [13]. Either they have common attributes, including major, grade, and gender, or they have a common borrowing group with the books borrowed by the user, and the books borrowed by these people can also be recommended to the user [14].

After comprehensively analyzing the interest and similarity, the relevant model is used to make predictions, and a recommendation list is generated [15]. Finally, comprehensive evaluation is carried out through evaluation indicators, and the prediction results are analyzed.

3. Book Recommendation Algorithm Based on Collaborative Filtering and Interest

3.1. Book Interest Model. Attributes related to books include search times, borrowing time, borrowing times, borrowing interval, and renewing times.

The proportion of search times of a certain book is the proportion of search times to the search times of all books. For normalization, the proportion is divided into five levels; the formula is as follows:

$$A = \frac{M}{N} = \left\{ \begin{array}{l} 5 \quad 0 - 20\% \\ 4 \quad 21 - 40\% \\ 3 \quad 41 - 60\% \\ 2 \quad 61 - 80\% \\ 1 \quad 81 - 100\% \end{array} \right\}. \quad (1)$$

In which, A is the grade score of the search proportion, M is the number of searches, and N is the total number of searches for all books. The higher the ranking means the higher the score.

The length of the borrowing time can basically reflect the popularity of a book [16]. Of course, the borrowing time may be too long because you forget to return the book, or you cannot return the book because of the holiday. This special case

is not considered here for the time being, and the formula is as follows:

$$B = \frac{\sum_1^K \left(\frac{t'(i) - t(i)}{t} \right)}{K} = \left\{ \begin{array}{l} 5 \quad 0 - 20\% \\ 4 \quad 21 - 40\% \\ 3 \quad 41 - 60\% \\ 2 \quad 61 - 80\% \\ 1 \quad 81 - 100\% \end{array} \right\}. \quad (2)$$

In which, B is the grade score of the borrowing time, K is the number of borrowers of the book, t is the longest borrowing time of the book, $t'(i)$ is the book return time, and $t(i)$ is the book borrowing time. The higher the ranking means the higher the score.

The number of borrowings can accurately reflect the popularity of the book [17]. The more borrowing times, the higher the popularity. The formula is as follows:

$$C = \frac{Q}{Q'} = \left\{ \begin{array}{l} 5 \quad 0 - 20\% \\ 4 \quad 21 - 40\% \\ 3 \quad 41 - 60\% \\ 2 \quad 61 - 80\% \\ 1 \quad 81 - 100\% \end{array} \right\}. \quad (3)$$

In which, C is the rating value of the number of borrowings, Q is the number of borrowings of the book, and Q' is the total number of borrowings of all books. Divide the number of borrowings into five levels, and rank according to the number of borrowings. The ranking is within 20%, the highest level. The ranking is 81%-100%, the level is the lowest, and the score is the lowest.

The borrowing interval refers to the time interval for a book to be borrowed after being returned [18]. If the time is shorter, the demand for the book is greater, or the popularity of the book is greater. On the contrary, if it is returned and is no longer borrowed, it means that the popularity of the book is very low. The formula is as follows:

$$D = \frac{\sum_1^K \left(\frac{t(i+1) - t'(i)}{t} \right)}{K} = \left\{ \begin{array}{l} 5 \quad 0 - 20\% \\ 4 \quad 21 - 40\% \\ 3 \quad 41 - 60\% \\ 2 \quad 61 - 80\% \\ 1 \quad 81 - 100\% \end{array} \right\}. \quad (4)$$

In which, D is the grade score of the borrowing interval, K is the number of borrowers of the book, t is the longest borrowing time of the book, $t'(i)$ is the return time, and $t(i+1)$ is the next person's borrowing time. \sum is the sum. The higher the ranking means the higher the score.

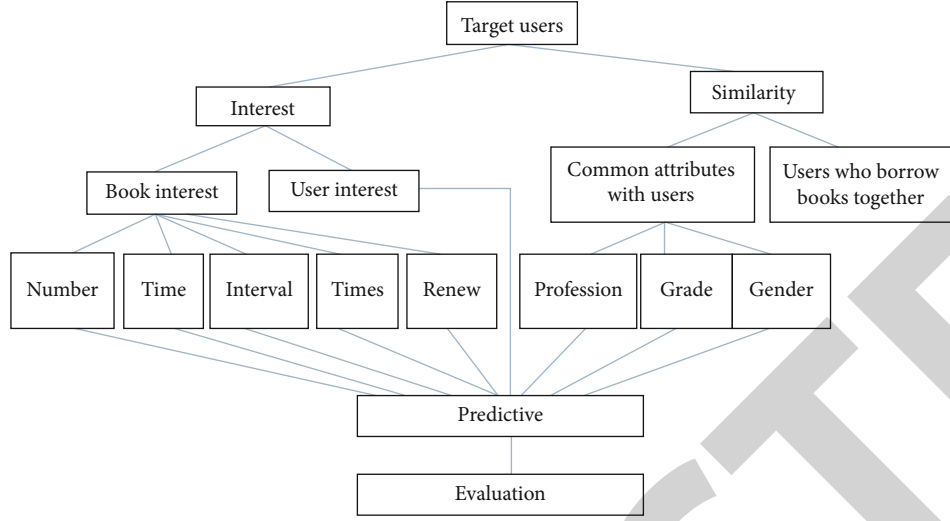


FIGURE 1: Recommended elements for target users.

The number of renewals of a book can also reflect the popularity of the book to a certain extent. The formula is as follows:

$$E = \frac{P}{P'} = \left\{ \begin{array}{l} 5 \quad 0 - 20\% \\ 4 \quad 21 - 40\% \\ 3 \quad 41 - 60\% \\ 2 \quad 61 - 80\% \\ 1 \quad 81 - 100\% \end{array} \right\}. \quad (5)$$

In which, E is the grade score of the proportion of the number of renewals, P is the number of renewals of the book, and P' is the total number of renewals of all books. The higher the ranking means the higher the score.

Finally, the average of the five indicators is used as a comprehensive indicator of book interest; the formula is as follows:

$$X = \frac{A + B + C + D + E}{5}. \quad (6)$$

3.2. Collaborative Filtering Recommendation Model. The basic idea of the collaborative filtering algorithm is to find similar users of the current user and predict the current user's score based on the similar user's score information to make recommendations. A recommendation system based on collaborative filtering does not analyze information from data but establishes an effective evaluation feedback mechanism to allow users to form a good feedback [19]. In other words, the recommendation users get may not be mined from the data at all but contributed by other users. There are three main steps: collecting scoring data, finding neighbors, and generating a recommendation list.

The scoring data is shown in Table 1.

The user-based collaborative filtering algorithm is to find neighbor users with high similarity for the current user and

TABLE 1: The scoring data.

	Profession	Grade	Gender	Same borrower
User 1	D_{11}	D_{12}	D_{13}	D_{14}
User 2	D_{21}	D_{22}	D_{23}	D_{24}
\vdots	\vdots	\vdots	\vdots	\vdots
User m	D_{m1}	D_{m2}	D_{m3}	D_{m4}

then recommend items that the neighbor users have rated, and the current user has not rated to the current user. The steps include calculating the similarity between the current user and other users, sorting according to the similarity from the highest to the bottom and the user with the highest ranking as the current user's neighbor, filtering the current user's rating items from the neighboring user's rating list, predicting the current user's rating of unrated item scoring, selecting the one with the highest score, and recommending it to the current user.

Cosine similarity can describe the linear correlation between two sets of data, and its value range is between -1 and 1. The cosine similarity is calculated based on the set of items jointly evaluated by two users [20]. When using this method to calculate, it is necessary to remove the average value of all commodities evaluated by the user. Generally, the following calculation formula is used to calculate the similarity.

$$\text{Sim}(u, v) = \frac{\sum_{i \in I_{uv}} (R_{ui} \times R_{vi})}{\sqrt{\sum_{i \in I_u} R_{ui}^2} \times \sqrt{\sum_{i \in I_v} R_{vi}^2}}. \quad (7)$$

In which, I_u is the set evaluated by user u , I_v is the set evaluated by user v , R_{ui} is the rating of user u on item i , and R_{vi} is the rating of user v on item i .

In this paper, the interest degree and collaborative filtering are averaged for a comprehensive analysis.

TABLE 2: 2020 classified borrowing statistics.

Class name	Class number	Jan.	Feb.	...	Jun.	Jul.	Aug.	Sept.	Oct.	Nov.	Dec.
Marxist	A	2	0	...	0	4	0	3	14	5	5
Philosophy	B	30	0	...	9	7	0	18	92	126	55
Social science	C	26	0	...	6	3	0	6	24	49	44
Politics	D	0	0	...	1	13	0	5	9	32	34
Military	E	0	0	...	0	0	0	0	4	5	4
Economic	F	18	0	...	17	10	0	34	51	145	102
Culture	G	17	0	...	13	0	0	31	42	27	43
Language	H	65	0	...	35	9	0	88	370	480	330
Literature	I	127	0	...	131	43	0	115	788	1528	765
Art	J	24	0	...	22	0	0	23	98	102	59
History	K	23	0	...	11	14	0	23	78	110	61
Natural	N	0	0	...	12	0	0	2	1	8	1
Mathematical	O	9	0	...	4	0	0	7	41	47	73
Astronomical	P	0	0	...	1	0	0	0	2	6	1
Biological	Q	1	0	...	2	0	0	0	2	8	1
Medicine	R	2	0	...	10	0	0	13	8	18	15
Agriculture	S	1	0	...	0	0	0	1	0	2	1
Industry	T	98	0	...	36	27	3	92	147	296	233
Traffic	U	0	0	...	1	0	0	0	3	1	3
Aviation	V	0	0	...	0	0	0	0	0	0	0
Surroundings	X	1	0	...	0	0	0	0	0	0	2
Comprehensive	Z	9	0	...	18	1	0	16	20	21	17

TABLE 3: Part of MAE data.

Number	MAE	Number	MAE	Number	MAE
1	0.89	160	0.6	320	0.58
10	0.88	170	0.6	330	0.57
20	0.83	180	0.61	340	0.57
30	0.74	190	0.6	350	0.56
40	0.64	200	0.59	360	0.56
50	0.64	210	0.59	370	0.56
60	0.64	220	0.59	380	0.56
70	0.64	230	0.59	390	0.55
80	0.62	240	0.59	400	0.55
90	0.62	250	0.57	410	0.56
100	0.62	260	0.57	420	0.54
110	0.62	270	0.58	430	0.54
120	0.62	280	0.57	440	0.54
130	0.61	290	0.57	450	0.54
140	0.61	300	0.57	460	0.54
150	0.61	310	0.57	470	0.54

3.3. *Evaluation Model.* Mean deviation and root mean square error are usually two standards to measure the accuracy of the recommended system.

Divide the attributes into five levels and rank them according to the data. The ranking is within 20%, the highest level; the ranking is 81%-100%, the lowest level, and the score is the lowest.

The formula for mean deviation is as follows:

$$MAE = \frac{\sum_{i=1}^n |p_i - q_i|}{n}. \quad (8)$$

In which, p_i is the predicted user rating, and q_i is the user's actual rating. The smaller the deviation of the average value, the closer the predicted score of the recommendation algorithm is to the actual score.

The formula for the root mean square error is as follows:

$$RMSE = \sqrt{\frac{\sum_{(u,i) \in T} (r_{ui} - r'_{ui})^2}{|T|}}. \quad (9)$$

In which, T represents the test data, $|T|$ represents the size of the test data set, u represents the user, i represents the book, r_{ui} represents the user's actual score for the book, and r'_{ui} represents the user's predicted score for the book.

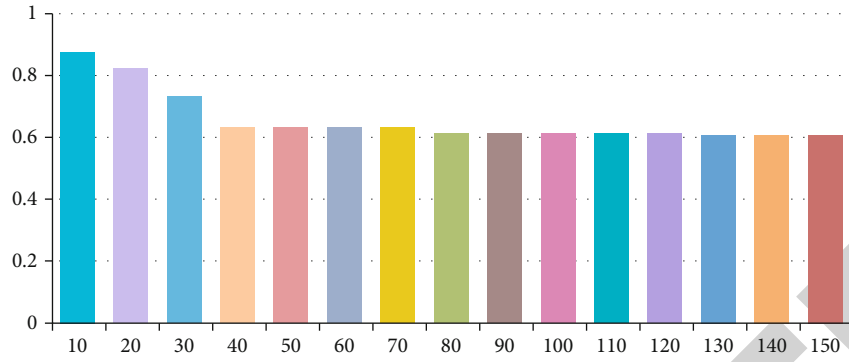


FIGURE 2: MAE comparison chart.

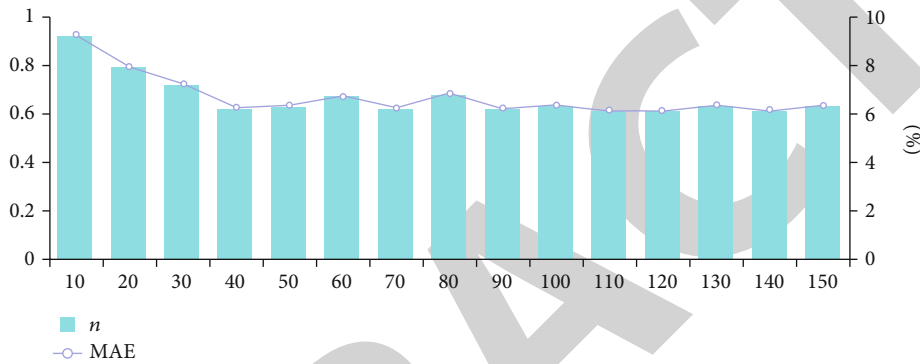


FIGURE 3: MAE comparison chart of science and engineering.

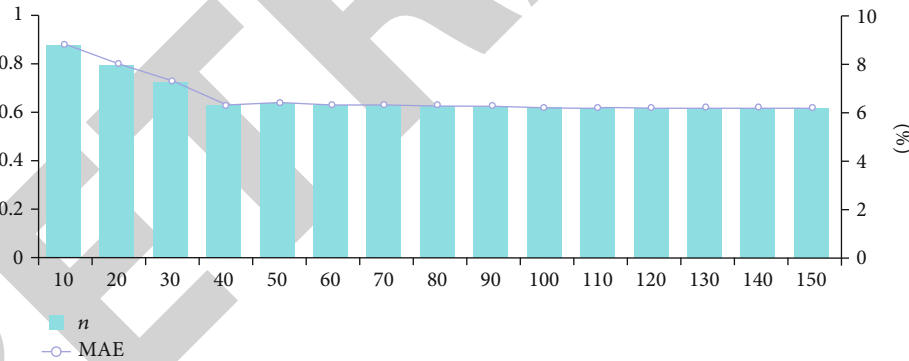


FIGURE 4: MAE comparison chart of literature and history.

4. Experimental Results and Analysis

The experimental data selected the borrowing data and user data of Wuxi Vocational College of Science and Technology from 2014 to 2020, and the data was copied and expanded to three times the original data volume. The borrowing data for 2020 is shown in Table 2. In the experiment, the data set is divided into training set and test set in an 8:2 manner.

The MAE is calculated according to formula (8), and the partial comprehensive data obtained is shown in Table 3, and the MAE of the first 150 neighbors is shown in Figure 2.

It can be seen from Figure 2 that in the comparison of the first 150 neighbor users, it gradually decreased at the begin-

ning, and the maximum value was 0.89. When it reaches about 40 neighbor users, it basically tends to be stable, and the stable value is around 0.6. The data is divided into literature and history and science and engineering for analysis. Figure 3 is the MAE value of science and engineering, and Figure 4 is the MAE value of literature and history. It can be seen that the literature and history category basically tends to be stable when it reaches about 40 neighboring users, similar to Figure 2. The science and engineering category also tends to be stable among 40 neighbor users, but there are some fluctuations. This shows that the data of literature and history accounts for a higher proportion of the whole data, and the frequency of borrowing is also higher.

TABLE 4: Part of RMSE data.

Number	Literature and history	Science and engineering	Number	Literature and history	Science and engineering
10	0.97	1.02	160	0.61	0.64
20	0.96	1	170	0.61	0.63
30	0.84	0.9	180	0.62	0.63
40	0.67	0.83	190	0.6	0.63
50	0.64	0.77	200	0.6	0.61
60	0.63	0.65	210	0.59	0.61
70	0.63	0.65	220	0.59	0.62
80	0.64	0.69	230	0.6	0.6
90	0.62	0.66	240	0.58	0.6
100	0.63	0.65	250	0.58	0.59
110	0.62	0.64	260	0.58	0.59
120	0.62	0.67	270	0.58	0.6
130	0.63	0.63	280	0.57	0.59
140	0.62	0.65	290	0.57	0.59
150	0.62	0.64	300	0.57	0.59

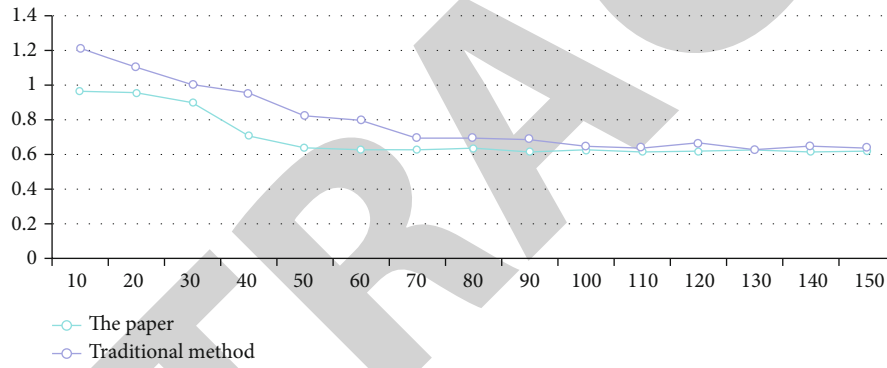


FIGURE 5: RMSE comparison chart of literature and science.

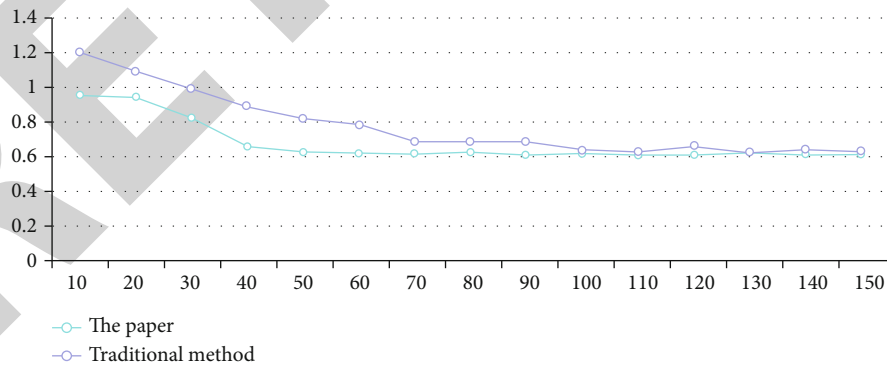


FIGURE 6: Comparison chart with traditional method RMSE.

The RMSE is calculated according to formula (9), and the partial comprehensive data obtained is shown in Table 4, and the RMSE of the first 150 neighbors is shown in Figure 5.

It can be seen from Figure 5 that the literature and history category also tends to be stable with 40 neighbor users. The science and engineering category tends to be stable with 60 users. This is the same as the previous article, indicating that

the data of literature and history account for a higher proportion of the entire data, and the frequency of borrowing is also higher.

This article analyzes from two perspectives of collaborative filtering and interest and compares it with the traditional single cosine similarity collaborative filtering, as shown in Figure 6. It can be seen that the method proposed in this

Retraction

Retracted: A Novel Model-Based Reinforcement Learning Attitude Control Method for Virtual Reality Satellite

Wireless Communications and Mobile Computing

Received 28 November 2023; Accepted 28 November 2023; Published 29 November 2023

Copyright © 2023 Wireless Communications and Mobile Computing. This is an open access article distributed under the Creative Commons Attribution License, which permits unrestricted use, distribution, and reproduction in any medium, provided the original work is properly cited.

This article has been retracted by Hindawi, as publisher, following an investigation undertaken by the publisher [1]. This investigation has uncovered evidence of systematic manipulation of the publication and peer-review process. We cannot, therefore, vouch for the reliability or integrity of this article.

Please note that this notice is intended solely to alert readers that the peer-review process of this article has been compromised.

Wiley and Hindawi regret that the usual quality checks did not identify these issues before publication and have since put additional measures in place to safeguard research integrity.

We wish to credit our Research Integrity and Research Publishing teams and anonymous and named external researchers and research integrity experts for contributing to this investigation.

The corresponding author, as the representative of all authors, has been given the opportunity to register their agreement or disagreement to this retraction. We have kept a record of any response received.

References

- [1] J. Zhang and F. Wu, "A Novel Model-Based Reinforcement Learning Attitude Control Method for Virtual Reality Satellite," *Wireless Communications and Mobile Computing*, vol. 2021, Article ID 7331894, 11 pages, 2021.

Research Article

A Novel Model-Based Reinforcement Learning Attitude Control Method for Virtual Reality Satellite

Jian Zhang ¹ and Fengge Wu ²

¹Institute of Software, Chinese Academy of Science, University of Chinese Academy of Sciences, Beijing, China

²Institute of Software, Chinese Academy of Science, Beijing, China

Correspondence should be addressed to Jian Zhang; 16141191@qq.com

Received 20 May 2021; Revised 1 June 2021; Accepted 16 June 2021; Published 1 July 2021

Academic Editor: Balakrishnan Nagaraj

Copyright © 2021 Jian Zhang and Fengge Wu. This is an open access article distributed under the Creative Commons Attribution License, which permits unrestricted use, distribution, and reproduction in any medium, provided the original work is properly cited.

Observing the universe with virtual reality satellite is an amazing experience. An intelligent method of attitude control is the core object of research to achieve this goal. Attitude control is essentially one of the goal-state reaching tasks under constraints. Using reinforcement learning methods in real-world systems faces many challenges, such as insufficient samples, exploration safety issues, unknown actuator delays, and noise in the raw sensor data. In this work, a mixed model with different input sizes was proposed to represent the environmental dynamics model. The predication accuracy of the environmental dynamics model and the performance of the policy trained in this paper were gradually improved. Our method reduces the impact of noisy data on the model's accuracy and improves the sampling efficiency. The experiments showed that the agent trained with our method completed a goal-state reaching task in a real-world system under wireless circumstances whose actuators were reaction wheels, whereas the soft actor-critic method failed in the same training process. The method's effectiveness is ensured theoretically under given conditions.

1. Introduction

SpaceVR's Overview 1 virtual reality satellites enable us to experience space firsthand using any mobile, desktop, or virtual reality device. Observing the universe with virtual reality is an exciting application of satellites. As one of the core subsystems in satellite, the attitude control system needs to be developed to meet the requirement for space virtual reality applications. An intelligent method of attitude control plays a role part in the subsystem. Reinforcement learning gives a remarkable achievement to prove potentiality to realize intelligent control.

In recent years, a significant progress has been made in the research of reinforcement learning (RL) [1]. Researchers have proposed many RL methods, such as the deep deterministic policy gradient (DDPG), trust region policy optimization (TRPO), proximal policy optimization (PPO), soft actor-critic (SAC), and twin-delayed deep deterministic policy gradient (TD3) methods [2–6]. These methods have been applied for playing Atari games [7] completing control tasks

in OpenAI Gym [8] and defeating human players in Go [9]. However, compared with simulation environments, successful cases in real-world systems are relatively rare. Application of RL methods directly in real-world systems faces a series of problems, such as sample limitations, exploration of the state space leading to system damage, unspecified reward functions, unknown delays in the system actuators, and unstable measurements from sensors [10].

In a real-world system, goal-state reaching is a task in which the control actuators adjust the system to reach a specified goal state. For example, attitude control of a satellite, including attitude maneuvering and attitude stabilization, can be defined as a task to reach a goal attitude state. The control tasks, such as balancing a car or an inverted pendulum, are also goal-state reaching problems in which the balancing point is specified as the goal state.

Approaches to tackle the challenges of real-world systems without expert knowledge can be roughly divided into two categories: “simulation to real” and “real experience data to model to real.” “Simulation to real” methods build a

simulation environment based on the real-world system and use RL methods for training. After training, the policies obtained from the simulation environment are applied in the real-world system. A number of previous studies have examined this type of method to learn robotic skills in real-world systems, including locomotion [11], robotic control [12], and vision-based autonomous flight [13].

“Real experience data to model to real” methods learn the model of the environment dynamics based on experience data from real-world systems and interact with a learned dynamics model using RL methods, and then, they apply the learned policy in a real-world system. Nagabandi et al. [14] built an environment dynamics model with neural networks, used a model predictive controller to simulate the transition trajectory in the learned environment model, and selected the best actions for the real-world system, thus realizing four-legged robot motion along a specified path. Lambert et al. [15] built an environment model with real-world system data, simulated the transition trajectory in the environment model running on multiple computing nodes, obtained the best action, and realized the attitude stability of a four-wing aircraft with low-level control, where the input was sensor data and the output was a pulse-width modulation signal.

The “simulation to real” methods depend on knowledge of the real-world system, the accuracy of the simulator, and the effectiveness of shifting the experience distribution between the simulator and the real-world system. The existing “real experience data to model to real” methods face two major challenges. First, sufficient experience data must be collected initially to model the environment dynamics. Second, the state space visited by the untrained policy without expert knowledge is insufficient for modelling the environment dynamics. In this paper, we present a method that overcomes the shortcomings of both classes of methods. Our method iterates in the loop of “collecting data using the latest policy-learning environment dynamics model-learning policy.” By using the latest policy to collect data from the real environment, it can gradually improve the model’s accuracy regarding the dynamics and policy’s performance without building a simulator. Although SAC was used for learning the latest policy, the difference from the original SAC method is that when exploring the unknown state space, we use the verified policy in the learned dynamics model, thus making the exploration more effective and safer.

Compared with the “simulation to real” methods, our method does not require knowledge of the real-world system. Existing “real experience data to model to real” method collects training samples at one time. The policy used to collect data should cover all the state space to support modelling the environment dynamics precise. But it is impossible. The difference between our method and existing “real experience data to model to real” is that the data used to train the model in our method is collected gradually, which reduces the dependence on the initial random data and thus reduces the probability of falling into a state space that will lead to disasters of the system. At the same time, it can cover a wider state space, which makes the dynamics model more precise.

The proposed method was tested using Cubli, a reaction-wheel-based inverted pendulum system. Cubli [16] is a cube whose height, width, and depth are 15 cm. It is equipped with three reaction wheels in three different planes. It is a typical nonlinear, unstable, and multidegree of freedom control system. The three reaction wheels are driven by motor rotation to generate torque to achieve attitude adjustment. Research on Cubli’s control is mainly based on classical methods of control, such as proportional–integral–derivative (PID), linear–quadratic regulator (LQR), and nonlinear control theory [16–19]. These controllers operate based on analytical models for Cubli’s dynamics, manual parameter tuning, and long design times. In our paper, we address the challenge of generating controllers without system knowledge in an end-to-end learning method.

The main work of this paper includes the following: (1) A learning system for Cubli is constructed in Section 2.1. The policy learned with our method achieves motor control from raw sensor data on board to drive the Cubli reaction wheels. The required torque produced by changing the spinning speeds of the reaction wheels leads the system to reach the goal state. (2) To solve the problems of an unknown delay of the actuator and inaccurate state information from the sensor data, a mixed environment dynamics model whose input window size varies is proposed (Section 2.3). (3) A method that can be used to learn the environment dynamics and policy based on the SAC method is presented. The convergence of the method was ensured theoretically (Section 2.5), and the effectiveness of the method was verified by experiments (Section 3).

2. Methodology

2.1. Learning System Construction. The state is generally composed of Euler angle and angular velocity around axis in a real-world system. Especially, in a goal-reaching system, the state is given by a measurement unit on board. The policy to learn outputs the control signal to the execution unit which is regarded as an action in a given state.

This section mainly describes how the learning system was built. As shown in Figure 1, the learning system was composed of four parts. (1) A real-world system called Cubli was used to collect state-action pair trajectory data. (2) The execution node executed the latest policy and interacted with Cubli via Bluetooth. (3) Real trajectory data was used to train an environmental dynamics model represented by a neural network. (4) In the environment modelled by the trained neural network, SAC method was used to train agents to obtain the latest policy. The latest policy was verified at the execution node.

At any time step t , Cubli obtained the state from an onboard sensor and submitted the state s_t to the execution node. The execution node used the latest policy neural network for inference and obtained the current action a_t . After Cubli executed the action, the execution node collected the next state data s_{t+1} , judged whether the current trajectory had ended through the feedback state data, and saved the trajectory into the trajectory buffer. The trajectory buffer was used to train the dynamics model $P(s_{t+1} | s_t, a_t)$.

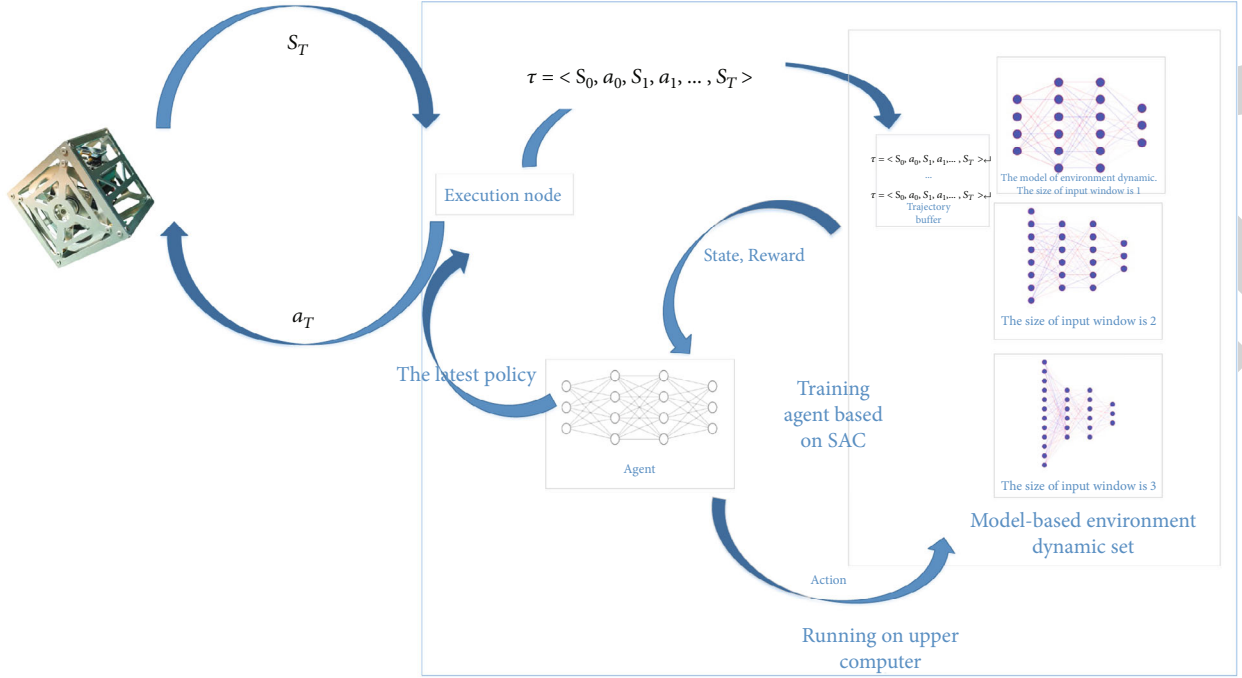


FIGURE 1: The overall structure of the learning system.

The training process is described in detail in Section 2.4. The training of the agent was carried out through the interaction with the environment represented by the trained model. At time step t , s_t and a_t are submitted to generate s_{t+1} by the model of the environment dynamics, and the reward signal is given based on s_{t+1} . In this study, the agent was trained by the SAC method, and the gradient of the value network and the policy network parameters estimated with batch samples were used to update the parameters. The execution node, the training of the agent, and the model of the environment dynamics were run on the upper machine. The entire learning process could operate automatically and independently, except that manual intervention was required in cases of Cubli power exhaustion or abnormalities. Although the new trajectory stored in the buffer was paused, the training of the agent did not stop. The tasks of training can be distributed between multiple machines. At the same time, the learning system can be connected with multiple systems to provide more trajectories and allow the dynamics model, the agent's value network, and policy network's parameters to converge faster.

2.2. Definition of Goal-State Reaching under Reinforcement Learning Paradigm. Reinforcement learning is a machine learning paradigm that maximizes expected cumulative return. The problem to be solved is defined as a Markov process. A Markov process is defined by the five-tuple $\langle S, A, r, P, \gamma \rangle$, where S is the state space, A is the action space, and r is the reward function. In the problem of goal-state reaching, the reward function is often related to the current state s_t and the goal state s_{goal} . It can be written as $r(s_t, s_{\text{goal}})$. P is the state transition probability function. $P: S \times A \rightarrow S$ is a function that maps the state-action pair space to the state space, which we also call it in this paper the environmental dynamics model as $P(s_{t+1} | s_t, a_t)$. γ is the discount factor

used to calculate the discount cumulative return. The policy function is represented by $\pi: S \rightarrow A$, which is a function that maps the state space to the action space. The agent uses the policy function to obtain the current action according to the current state $a_t = \pi(s_t)$ and interacts with the environment to get the next state s_{t+1} . This process continuously loops to form a state-action trajectory $\tau = \langle s_1, a_1, \dots, s_T \rangle$. When using a neural network to represent the policy function, π is determined by the neural network architecture and the parameter θ , so it can be written as π_θ , and the policy network training is to adjust the parameter θ . The process can be formalized as

$$\operatorname{argmax}_{\theta} E_{\tau \sim \pi_{\theta}} \left[\sum_t \gamma^t \cdot r(s_t, s_{\text{goal}}) \right] \text{ where } r(s_t, s_{\text{goal}}) = -\|s_t - s_{\text{goal}}\|. \quad (1)$$

The SAC is an RL method based on maximum entropy, which emphasizes the policy's randomness when exploring an unknown state space. While maximizing the cumulative discount return, SAC prevents the parameters of the policy network from converging to the local optimum. The following equations describe the loss functions that need to be optimized:

$$J_Q(\phi_i) = E_{(s,a,r,s') \sim D} \left[Q_{\phi_i}(s, a) - \left(r + \gamma \left(\min_{j=1,2} Q_{\text{target},j}(s', a') - \alpha \log \pi_{\theta}(a' | s') \right) \right) \right], \quad (2)$$

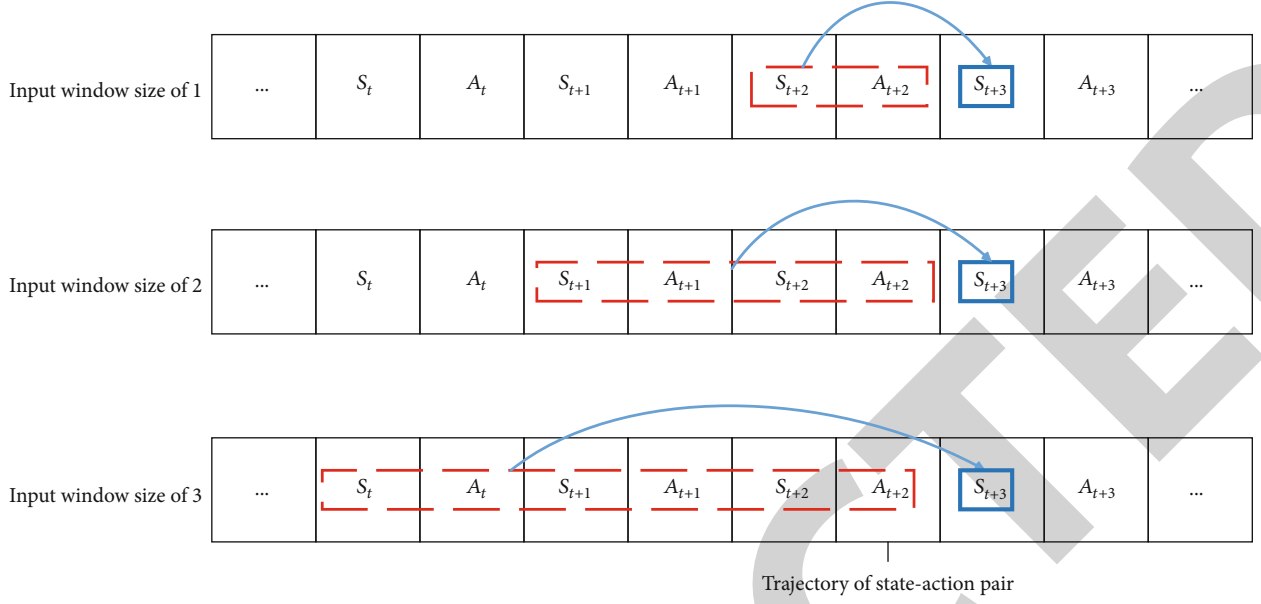


FIGURE 2: Schematic diagram of models with different input window sizes.

$$J_{\pi}(\theta) = E_{s \sim D, a \sim \pi} \left[\alpha \log \pi_{\theta}(a | s) - \min_{i=1,2} Q_{\phi_i}(s, a) \right], \quad (3)$$

$$J(\alpha) = E_{s \sim D, a \sim \pi} [-\alpha \log \pi_{\theta}(a | s) - \alpha H], \quad (4)$$

where $H = -\text{Dimensions of action space}$.

SAC concurrently learns a policy π_{θ} and two Q-functions Q_{ϕ_1}, Q_{ϕ_2} . Q-function $Q^{\pi}(s, a)$ describes the cumulative reward following policy π after executing action a from current state s . Equation (2) is the loss function of the Q-function, which is also known as the mean squared bellman error (MSBE), Equation (3) is the loss function of the policy function that can be optimized for improving the policy's Q value, and Equation (4) is the loss function of the temperature parameter α , which defines the explore-exploit tradeoff, with a higher α corresponding to more exploration, and a lower α corresponding to more exploitation. The SAC takes the minimum value of two sets of independent Q-function parameters to solve the problem of overestimating the Q-function, and it uses the target Q value network parameter to solve the training instability problem caused by using the same set of Q value network parameters to bootstrap. These techniques were first proposed by van Hasselt et al. [20]. The optimization of the temperature parameter α is used to control the trade-off between the exploration and the utilization and to ensure the stability of the policy in the later stage of training.

2.3. Learning the Environmental Dynamics Model. Because of the noise in the onboard sensor data, only using the state-action pair at one timestep as the input of the model will affect the accuracy of the environmental dynamics model. We propose a model that predicts the next state by combining state-action pairs of different sizes as the input. As shown in Figure 2, for a state-action pair trajectory, the state at a cer-

tain moment is assumed to be S_{t+3} , which is marked by blue boxes with solid lines. The environmental dynamics model needs to predict the state at this moment with the historical state-action pairs. The red boxes with dashed lines in the figure represent the input, and we define the number of state-action pairs as the size of the input window. The sizes of the input windows in the first, second, and third parts in Figure 2 are 1, 2, and 3, respectively. A single model is represented by a fully connected neural network. Each model uses data with different sizes of the input windows as inputs to predict the state change value Δs_{t-1} for the next state, and the output of the K models are averaged as the actual predicted state change value. The parameters of the i th model are defined as φ_i , and a single-environment dynamic model is expressed as

$$P_{\varphi_i}(s_t | s_{t-i}, a_{t-i}, \dots, s_{t-1}, a_{t-1}) + s_{t-1}. \quad (5)$$

When the size of the input window is K , a state-action pair trajectory of length N can construct $N - K + 1$ "prediction-truth" pairs represented by $\langle S_t', S_t \rangle$ where $S_t' = (1/K) \sum_{i=1}^K P_{\varphi_i}(\cdot | s_{t-i}, a_{t-i}, \dots, s_{t-1}, a_{t-1}) + S_{t-1}$. The training of the model is minimizing the mean square error between the prediction and the truth. The process is formalized as

$$\operatorname{argmin}_{\varphi_i} E_{\langle s_{t-i}, a_{t-i}, \dots, s_{t-1}, a_{t-1}, s_t \rangle \sim D} \left\| \frac{1}{K} \sum_{i=1}^K P_{\varphi_i}(\cdot | s_{t-i}, a_{t-i}, \dots, s_{t-1}, a_{t-1}) + s_{t-1} - s_t \right\|^2 \quad (6)$$

2.4. Training Environment Construction. In this section, we describe the construction of the learning environment. The state consisted of Euler angles (roll, yaw, and pitch) and the

three-axis angular velocities. The state was directly measured by the MPU-6050 inertial measurement unit. Action outputs the pulse-width modulation to control the rotation of the motor.

A state $s_t = [\phi, \theta, \varphi, \dot{x}, \dot{y}, \dot{z}]^T$ is a six-dimensional vector, where ϕ, θ , and φ represent roll, yaw, and pitch, and \dot{x}, \dot{y} , and \dot{z} represent the angular velocity of the rotations around the x -, y -, and z -axes, respectively. An action $a_t = [a_1, a_2, a_3]^T$ is a three-dimensional vector, where a_1, a_2 , and a_3 represent the values of the pulse-width modulation (PWM) to control the rotational speeds of the motors.

To standardize the state value, we replaced the Euler angles with their cosine and sine values. For the axis angular velocity, the measured data was obtained from the IMU and divided by the maximum value of each measurement, and each state component was limited to the value range of $[-1, 1]$. Therefore, the actual state is expressed as follows:

$$s_t = \left[\begin{array}{c} \cos(\phi), \sin(\phi), \cos(\theta), \sin(\theta), \cos(\varphi), \\ \sin(\varphi), \frac{\dot{x}}{\text{MAX}_X}, \frac{\dot{y}}{\text{MAX}_Y}, \frac{\dot{z}}{\text{MAX}_Z} \end{array} \right]^T. \quad (7)$$

The control task of balancing Cubli on an edge is defined as follows. When the Cubli flips, the error from the balance point is ϵ , and only the IMU measurement data and PWM signal of the control motor are used to maintain balance on the edge. Based on the position of the momentum wheel, three edges that can achieve the balance task are determined. Euler angles (roll, yaw, and pitch) can be used to describe the distance from the balance point. As described above, the reward function of the balance task is given as follows:

$$r(s_t, s_{\text{goal}}) = \begin{cases} -\left((\phi)^2 + 0.1 * \left(\frac{\dot{x}}{\text{MAX}_X} \right)^2 \right)^{1/2} & \text{balance around X axis,} \\ -\left((\theta)^2 + 0.1 * \left(\frac{\dot{y}}{\text{MAX}_Y} \right)^2 \right)^{1/2} & \text{balance around Y axis,} \\ -\left((\varphi)^2 + 0.1 * \left(\frac{\dot{z}}{\text{MAX}_Z} \right)^2 \right)^{1/2} & \text{balance around Z axis.} \end{cases} \quad (8)$$

2.5. Theoretical Analysis. Theory 1: when the reward function satisfies $r(s, s_{\text{goal}}) = -\|s - s_{\text{goal}}\|$, the value function V^{π^{k+1}, P^*} of the policy π^{k+1} acts on the real environment model P^* will be greater than or equal to the value function V^{π^k, P^*} while the policy π^{k+1} is obtained from $\pi^{k+1}, P^{k+1} = \text{argmax}_{\pi, P} (V^{\pi, P} - D_{TV, \pi^k}(P, P^*))$ (Condition 1) in the $k + 1$ th iteration, where

$$V^{\pi^{k+1}, P^*} \geq V^{\pi^k, P^*}. \quad (9)$$

P^* is the dynamics model in real environment, P^k is the dynamics model learned in the k th iteration, and $D_{TV, \pi^k}(P, P^*)$ is the absolute value of the maximum state difference between the experience trajectory collected in the real environment P^* and the learned environment dynamics model P following the policy π^k . From the definition, $D_{TV, \pi^k}(P^*, P^*)$ is zero. $V^{\pi^{k+1}, P^{k+1}}$ is the value function of π^{k+1} acting on the dynamics model P^{k+1} learned in the $k + 1$ iteration, and V^{π^k, P^*} is the value function of π^k acting on the real environment P^* . $\rho_t^{\pi^k, P^*}$ is the probability density function of the state distribution at time t when the policy π is used to interact with the dynamics model P . \hat{s}_t is the state at step t when acting on the learned dynamics, and s^* is the goal state.

Proof.

$$\begin{aligned} & V^{\pi^{k+1}, P^*} - V^{\pi^k, P^{k+1}} \\ &= E_{s_t \sim \rho_t^{\pi^{k+1}, P^*}, \hat{s}_t \sim \rho_t^{\pi^k, P^{k+1}}} \left[-\sum_{t=0}^{\infty} \gamma^t (\|s_t - s^*\| - \|\hat{s}_t - s^*\|) \right] \\ &\geq E_{s_t \sim \rho_t^{\pi^{k+1}, P^*}, \hat{s}_t \sim \rho_t^{\pi^k, P^{k+1}}} \left[-\sum_{t=0}^{\infty} \gamma^t (\|s_t - \hat{s}_t\|) \right] \\ &\geq -E_{s_t \sim \rho_t^{\pi^{k+1}, P^*}, \hat{s}_t \sim \rho_t^{\pi^k, P^{k+1}}} \left[\sum_{t=0}^{\infty} \gamma^t \max_t (\|s_t - \hat{s}_t\|) \right] \\ &= -D_{TV, \pi^k}(P^*, P^{k+1}) \\ &\geq -D_{TV, \pi^k}(P^*, P^{k+1}) \text{ (inequality 1)}. \end{aligned} \quad (10)$$

From inequality 1,

$$\begin{aligned} V^{\pi^{k+1}, P^*} &\geq V^{\pi^{k+1}, P^{k+1}} - D_{TV, \pi^k}(P^*, P^{k+1}) \\ &\geq V^{\pi^k, P^*} - D_{TV, \pi^k}(P^*, P^*) \text{ (According to condition 1)} \\ &\geq V^{\pi^k, P^*} \text{ (because } D_{TV, \pi^k}(P^*, P^*) = 0). \end{aligned} \quad (11)$$

□

```

Input: initialize three input length environment dynamic model parameters  $\varphi_1, \varphi_2, \varphi_3$ .
Initialize policy parameters  $\theta$ , Q-function parameters:  $\varnothing_1, \varnothing_2$ 
Empty replay buffer  $D$ , empty trajectory buffer  $T$ .
Set target Q-function parameters:  $\varnothing_{\text{target},1} \leftarrow \varnothing_1, \varnothing_{\text{target},2} \leftarrow \varnothing_2$ 
1: repeat
2: Collect state-action trajectory  $\tau = (s_0, a_0, s_1, a_1, \dots, s_T)$ , store trajectory into replay buffer  $T$ .
3: Randomly sample a batch  $B_1$  of trajectory from replay buffer  $T$ , construct  $|B_1|^* (N - 2)$  (prediction, truth) pair training samples.
4: Update dynamic model by gradient decent using

$$\nabla_{\varphi_i} (1/|B_1|^* (N - 2)) \sum_{s_{t-3}, a_{t-3}, \dots, s_{t-1}, a_{t-1} \in B_1} \|1/3 \sum_{i=1}^3 P_{\varphi_i}(\bullet | s_{t-i}, a_{t-i}, \dots, s_{t-i}, a_{t-i}) + s_{t-1} - s_t\|^2$$

5: until convergence
6: repeat
7: for  $i$  in range(three dynamic models) do
8: Based on current state  $s_{t-1}$  and sample action  $a_{t-1} \sim \pi_{\theta}(\bullet | s)$ 
9: calculate next state  $s'$  with executing action in dynamic models  $P_{\varphi_i}$  with previous state-action pair
10: end for
11: Record latest action  $a$ , observe latest two state  $s, s'$ , reward  $r$ , and done signal  $d$ 
12: Store  $(s, a, s', d)$  into replay buffer  $D$ 
13: if done signal  $d$  is True then
14: Reset environment state.
15: end if
16: for  $j$  in range(update times) do
17: Randomly sample a batch  $B_2$  transitions from replay buffer  $D$ 
18: Update Q-functions by gradient decent using

$$\nabla_{\varnothing_i} (1/|B_2|) \sum_{(s,a,r,s') \in D} (Q_{\varnothing_i}(s, a) - (r + \lambda (\min_{j=1,2} Q_{\text{target},j}(s', a') - \alpha \log \pi_{\theta}(a' | s'))))$$

19: Update policy network by gradient decent using

$$\nabla_{\theta} (1/|B_2|) \sum_{s \in B} (\alpha \log \pi_{\theta}(a | s) - \min_{j=1,2} Q_{\varnothing_j}(s, a))$$

20: Update target Q-function networks with

$$Q_{\text{target},j} \leftarrow \rho \varnothing_{\text{target},j} + (1 - \rho) \varnothing_j, \text{ for } j = 1, 2$$

21: end for
22: if it is time to test in real system then
23: Run latest policy in real system, collect state-action trajectory, collect state-action trajectory  $\tau = (s_0, a_0, s_1, a_1, \dots, s_T)$ , store trajectory into replay buffer  $T$ .
24: Observe the result running in real system
25: if task is completed then
26: completed  $\leftarrow$  true
27: else
28: Update dynamic model as step 4.
29: end if
30: end if
31: until completed

```

ALGORITHM 1: Learning algorithm with hybrid window's length dynamic model.

Therefore, according to the steps described in Theory 1, the policy sequence $\pi^0, \pi^1, \dots, \pi^k$ with a monotonically increasing value function will be generated such that $V^{\pi^k, P^*} \geq \dots \geq V^{\pi^1, P^*} \geq V^{\pi^0, P^*}$.

The procedure is presented in Algorithm 1. The environment dynamics model represented by mixed models with different sizes of the input window is trained to convergence using trajectory data from the real environment. The agent is trained by the SAC. The update rule of the parameters in the policy function's network is given by Equation (3), and the value function is given by Equation (2). During the application of the algorithm, Condition 1, which considers all the policy and environment dynamics models, is not satisfied. In our algorithm, we assume that the model represented by the neural network architecture includes the real environment

dynamics model and that the error between the learned model trained with more real data and the real environment model is decreasing.

3. Results and Discussion

A Cubli is shown as Figure 3. The yellow area marks the brake components, the blue area marks the control unit and the onboard measurement unit, and the green area marks 3 sets of motors. It is mainly composed of three brushless motors with encoders, three sets of brake devices, an MPU6050 digital motion processor, and a main control chip STM32F103RCT6. The communication with the host computer depends on the Bluetooth module. The communication protocol between Cubli and the upper computer

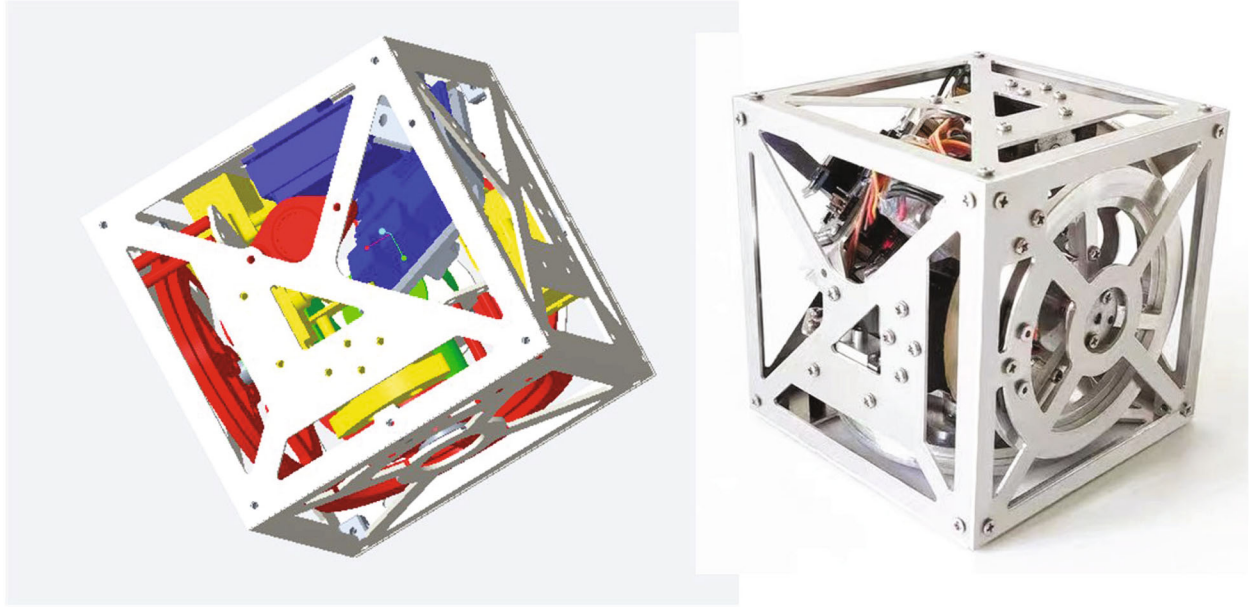


FIGURE 3: Cubli and its structure.

consisted of seven floating-point numerical data (roll; pitch; yaw; angular velocities of rotation around the x -, y -, and z -axes; current motor speed code value; and current motor PWM value). The data were read from the DMP register in the MPU6050. The upper computer sent the target PWM value of the motor to the STM32F103RCT6 on Cubli, and the instruction was executed by the motor after it was written into the register. The frequency of setting the PWM value was 62.5 Hz, and the frequency of obtaining the onboard data was also 62.5 Hz, i.e., the period of the PWM value and obtaining onboard data were both 16 ms. The control loop is shown as Figure 4.

A single model of the environmental dynamics was represented by a fully connected neural network. The neural network had two hidden layers, each with 256 neurons, and it used random values to initialize each parameter. In the experiment, we used input windows with different sizes to test the actual effect. The neural network architecture, initialization parameters, learning method, batch size, and learning rate were fixed, and it was ensured that the experimental training conditions were as constant as possible. Table 1 shows the specific conditions. At the beginning of the experiment, a random policy was used to collect 200 state-action pair trajectories at the execution node by interacting with the real environment, corresponding to about 40,000 state-action-state transition sample data. These data were used to train the three models. As shown in Figure 5, the collection of these training data began from the initialization state.

As shown in Figure 6, using these 40,000 samples to train the environment dynamics model, we randomly initialized the parameters of each model and trained each model multiple times to evaluate the loss. After 50 times training with batch size of 256, all three models converged.

Theoretically, the larger the input window length, the more mixed models, and the higher the prediction accuracy of the final environmental dynamics model. However, as

the size of the input window and the number of mixed models increase, the number of final model parameters will increase, and the training and inference time will be extended.

There was a trade-off between the size of the input window and the training time, and we found through experiments that the accuracy of the model and the requirements of the task could be satisfied when the size of input window was 3.

Algorithm 1 was used to train the agent, where the SAC was used as the controller training method to interact with the model of the environment dynamics. The agent's policy and value functions were represented by a fully connected neural network, and it had two hidden layers, each with 256 neurons. To compare the model of the environment dynamics and verify the effectiveness of the method proposed in this paper, for each model, the same method was used to train the agent with the same setting for 100,000 steps, and the trained controller was used for verification in the real-world system. Each controller interacted with the environment for 100 epochs, and the results are shown in Figure 7. The controller trained using the model when the size of the input window was 1 was unable to complete the task in the real environment. The controller trained with the environment dynamics model with a window length of 2 could complete the task in some initial states of the real environment, but it still encountered initial states for which it could not complete the task. According to the method proposed in this paper, the controller trained using the model of the environment dynamics with an input window length of 3 could complete the task in the random initial state and quickly stabilize at the target point.

In addition, the method described in this paper was compared with the SAC. After 140,000 training steps, the controllers trained with our method and the SAC were used in a real environment. The PWM value output by the two controllers

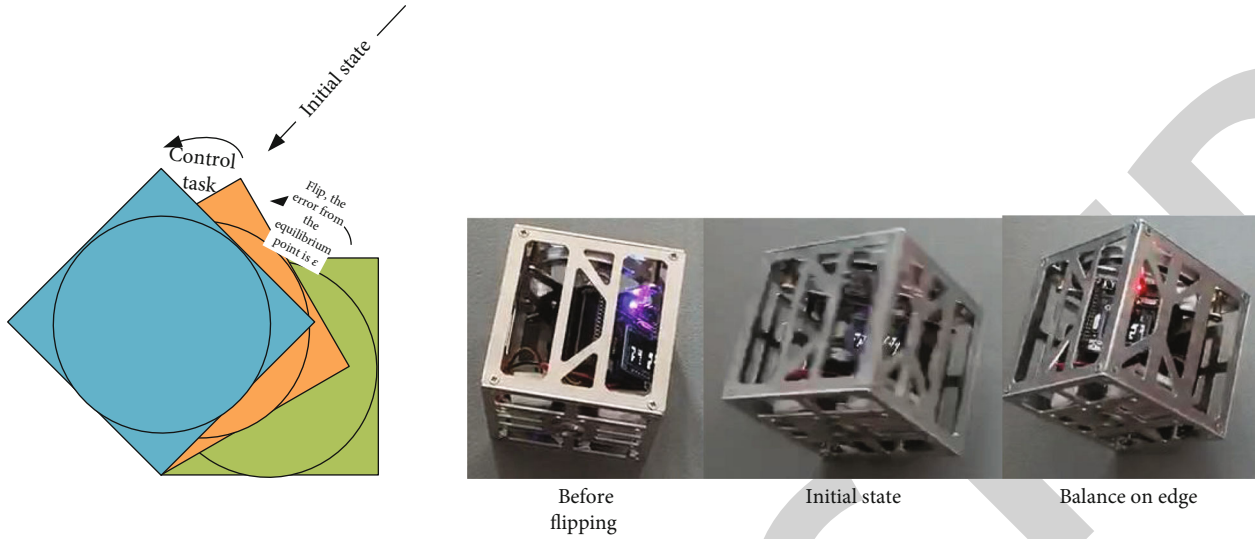


FIGURE 5: Balance task on edge.

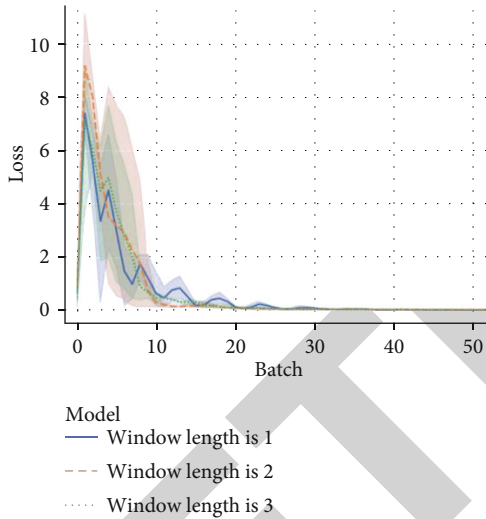


FIGURE 6: Training of different models (the shaded regions represent min-max loss at the current step).

is shown in Figure 8. The controller trained by our method completed the task and kept the PWM value around 600 in 15 steps, but the controller trained by the SAC failed, and the motor remained in a saturated state with a PWM value of 7200.

4. Conclusion

As a promising method, reinforcement learning could be used to realize intelligent attitude control for virtual reality satellites in which the method of attitude control needs to have sufficient adaptability for meeting the various creative virtual reality satellite applications. To cope with the challenges of a high sample data acquisition cost and noise of the raw sensor data when using RL methods in real-world systems, a new method to learn the model of the environment dynamics and train the controller was developed in this

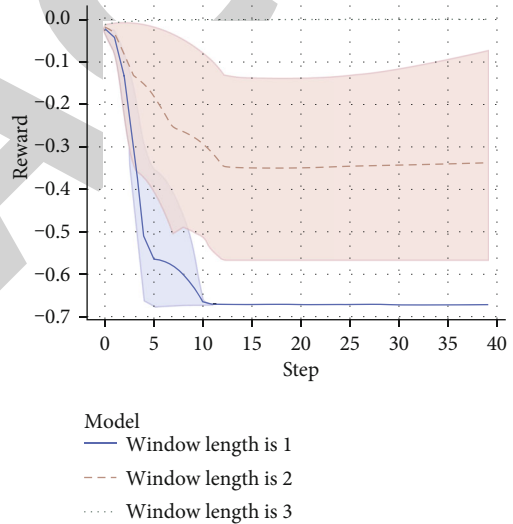
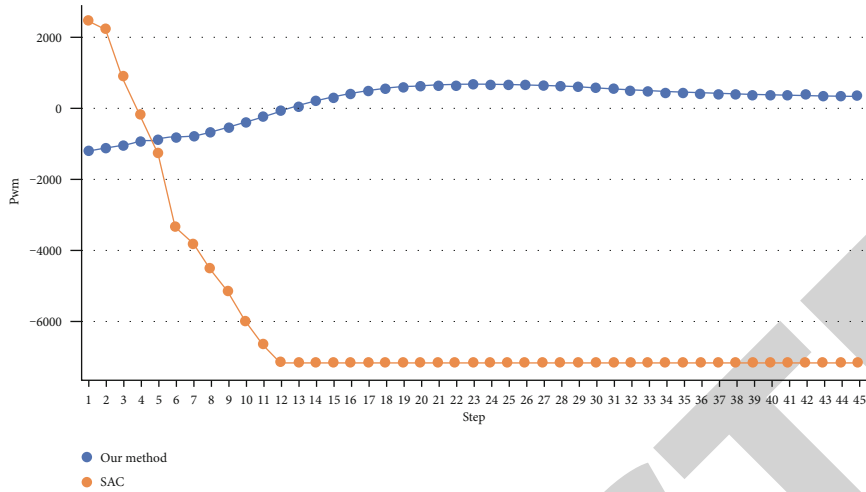
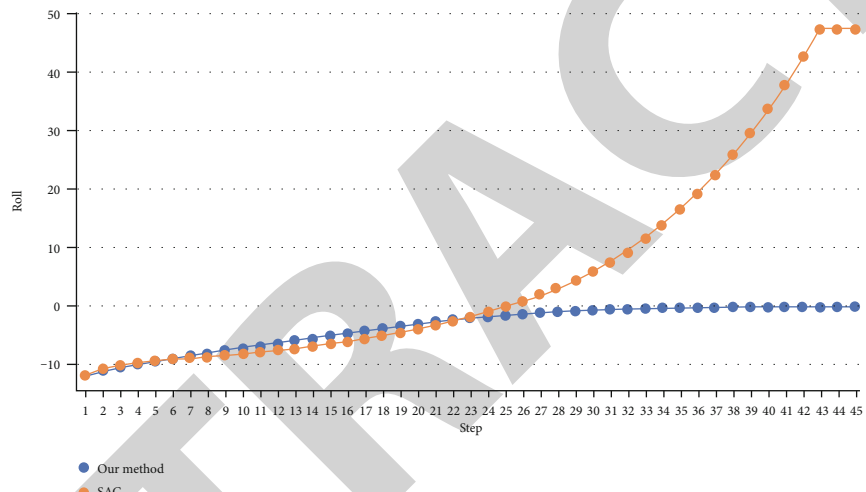


FIGURE 7: The verification effect of the controller in the real environment (training: 100,000 steps in the model of the environment dynamics with different sizes of input window. The shaded regions represent the min-max reward at the current step).

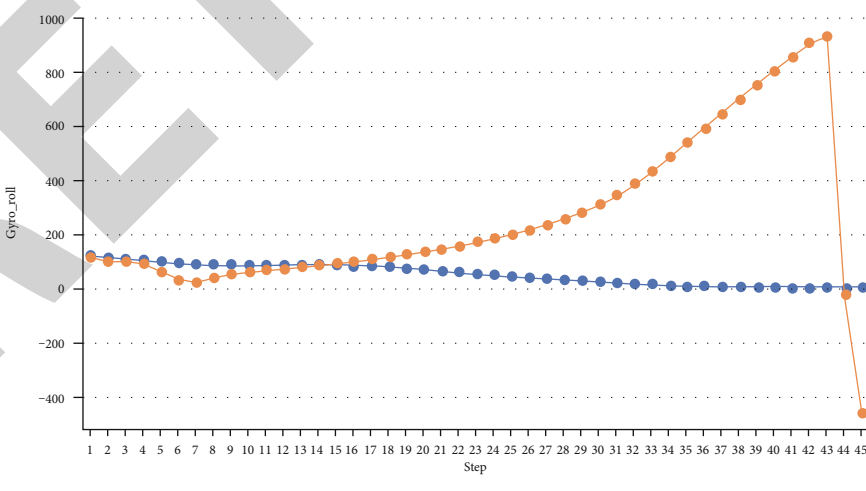
study. Compared with the two main current methods, our method does not require knowledge of the system and has high coverage of the state space. Our method was verified to learn to reach the goal-state in a real-world system, Cubli, without prior knowledge. In our work, we found that the mixed model describing the environment model with different sizes of the input was effective for reducing the impact of noisy data on the model's prediction accuracy. In our experiments, the models representing the environment dynamics with different architectures were trained to converge with the same samples, and the controllers were trained in environments with different models. Based on the results, the effectiveness of the model was verified. We found that our method of training based on the environmental dynamics and the policy gradually achieved better performance than



(a)



(b)



(c)

FIGURE 8: (a) Pulse-width modulation (PWM) value output by trained controllers; (b) roll value when running trained controllers; and (c) gyro value for roll when running trained controllers (note: SAC: soft actor-critic).

Retraction

Retracted: An Intelligent Code Search Approach Using Hybrid Encoders

Wireless Communications and Mobile Computing

Received 28 November 2023; Accepted 28 November 2023; Published 29 November 2023

Copyright © 2023 Wireless Communications and Mobile Computing. This is an open access article distributed under the Creative Commons Attribution License, which permits unrestricted use, distribution, and reproduction in any medium, provided the original work is properly cited.

This article has been retracted by Hindawi, as publisher, following an investigation undertaken by the publisher [1]. This investigation has uncovered evidence of systematic manipulation of the publication and peer-review process. We cannot, therefore, vouch for the reliability or integrity of this article.

Please note that this notice is intended solely to alert readers that the peer-review process of this article has been compromised.

Wiley and Hindawi regret that the usual quality checks did not identify these issues before publication and have since put additional measures in place to safeguard research integrity.

We wish to credit our Research Integrity and Research Publishing teams and anonymous and named external researchers and research integrity experts for contributing to this investigation.

The corresponding author, as the representative of all authors, has been given the opportunity to register their agreement or disagreement to this retraction. We have kept a record of any response received.

References

- [1] Y. Meng, "An Intelligent Code Search Approach Using Hybrid Encoders," *Wireless Communications and Mobile Computing*, vol. 2021, Article ID 9990988, 16 pages, 2021.

Research Article

An Intelligent Code Search Approach Using Hybrid Encoders

Yao Meng 

State Key Laboratory of Mathematical Engineering and Advanced Computing, Zhengzhou 450001, China

Correspondence should be addressed to Yao Meng; mengyao@ncwu.edu.cn

Received 23 March 2021; Revised 2 June 2021; Accepted 18 June 2021; Published 1 July 2021

Academic Editor: Balakrishnan Nagaraj

Copyright © 2021 Yao Meng. This is an open access article distributed under the Creative Commons Attribution License, which permits unrestricted use, distribution, and reproduction in any medium, provided the original work is properly cited.

The intelligent code search with natural language queries has become an important researching area in software engineering. In this paper, we propose a novel deep learning framework At-CodeSM for source code search. The powerful code encoder in At-CodeSM, which is implemented with an abstract syntax tree parsing algorithm (Tree-LSTM) and token-level encoders, maintains both the lexical and structural features of source code in the process of code vectorizing. Both the representative and discriminative models are implemented with deep neural networks. Our experiments on the CodeSearchNet dataset show that At-CodeSM yields better performance in the task of intelligent code searching than previous approaches.

1. Introduction

In the modern world, the application of computer software has already penetrated every aspect of our lives. The necessities of life, such as medical care, resources, transportation, and public security, depend on the running of high-quality software. For code quality and efficiency, programmers repeatedly involve successful code snippets developed by other authors. It has been a key task in the field of software engineering to locate target code snippets, which are returned by natural language queries, in code repositories such as GitHub and SourceForge.

The traditional code search algorithms are mostly implemented with information retrieval methods, which are widely used in the field of natural language processing. These approaches usually treat the source code as a plain text or a sequence of tokens, and then return the related code snippets by computing the similarity of queries and code documents. The token-based code search toolkits have been already used in industry, e.g., Sourcerer and Krugle. They treat both the query words and code snippets in codebase as plain text and return the target codes by key word-matching or template-matching technology. In the academic area, McMillan et al. propose a searching model Portfolio [1], which returns a chain of functions through keyword matching and the PageRank algorithm. Lv et al. developed a famous code-searching engine CodeHow [2], which com-

bines text similarity and API matching through an extended Boolean model.

Source code search algorithms based on text retrieval strategy often fail in practice. Different from plain text, code snippets usually contain both the structural and semantic information. The source code snippets made by programmers and queries written in natural languages are essentially heterogeneous. They may not share common lexical tokens, synonyms, or language structures. Sometimes programmers are extremely unsatisfied with searching results from traditional information retrieval algorithms. To improve code search according to natural language queries, researchers tend to use various code representations. They construct different code encoders with machine learning methods, which map source code and query words to the same vector space. The most related code vectors are returned as searching results according to the distance [3] between adjacent vectors.

In recent years, with the rapid development of deep learning technology, researchers in the field of software engineering begin to analyze the structural and semantic features of source code with deep learning approaches. Based on the common neural networks such as the convolutional neural network, the recursive neural network, and the recurrent neural network, scholars exploit various deep encoders to represent source code in different vector spaces [4–6]. Compared to traditional approaches, deep neural networks can extract the structural and semantic information hidden in

the source code snippets during code embedding, which might improve the representation ability of code vectors.

In this paper, we propose a novel source code search model using deep learning algorithms. The model maps both the code snippets in the codebase and natural language queries to the same high-dimensional vector space and then return the most related code snippets by computing the cosine similarity between code vectors and query vectors. Different from previous research, At-CodeSM vectorizes the source code with three independent encoders, e.g., the method name encoder, the lexical encoder, and the structural encoder. The lexical encoder extracts the tokens from the source code and encodes them with an attention-based LSTM network. The core tokens are strengthened with heavy attention scores. The structural encoder firstly transforms the source code into an AST, and then encodes the whole tree using a tree-LSTM network in a recursive way. The combination of three encoders in At-CodeSM retains both the lexical and syntactics of code in the process of representation, which improves the searching performance.

In practice, At-CodeSM firstly updates the parameters of the source code encoder and query encoder by offline learning on the training set. It then conducts an offline embedding on all the code snippets in the search base. Finally, At-CodeSM uses an online matching algorithm to compare the cosine similarity between the query vector and code vectors from the search base. The code snippets with higher similarity scores are returned as the searching results.

The main contributions of this work are as follows:

- (i) We propose a novel source code representation model based on the deep neural network. The model implements the encoding of method name, method body, and method grammar tree, respectively, with three independent encoders. Compared with other models, the representation process in At-CodeSM effectively retains both the lexical and semantic characteristics of the code snippets
- (ii) To our knowledge, we are the first to introduce a self-attention mechanism, which was developed in NLP, into the area of intelligent code search. With the self-attention mechanism, key words in the source code are strengthened, which finally improve the searching performance
- (iii) The big achievements are made when we apply our representation model in the intelligent code search area. We improve the model parameters with supervised learning on a large-scale dataset CodeSearchNet, which is made by Microsoft. The experiments show that our model is superior to the state-of-art approaches

The remainder of this paper is organized as follows: Section 2 describes related work in the code search area. Section 3 presents background materials of various LSTM structures and the self-attention mechanism. Section 4 elaborates on the details of At-CodeSM. Section 5 gives the experiment and evaluation. In Section 6, we discuss the crucial

factors which may affect the searching performance. Finally, we conclude the paper in Section 7.

2. Related Work

2.1. Traditional Approaches. Using common NLP methods, most traditional code search approaches treat source code as plain text or a set of tokens, ignoring its structure and semantics. Such models often extract code features manually or with NLP methods, and then return related code snippets via a text similarity algorithm [7, 8]. Mostly applied in the early stage, these models completed simple search tasks with keyword matching. Due to the low complexity and cross-platform features, these approaches have been widely used in industry. For instance, Lucene is a successful code search platform implemented with traditional approaches.

In 1993, Chang and Eastman [9] proposed a famous code search tool SMART, which was based on keyword searching. SMART identified the code snippets as token sequences and then returned the target code according to a common keyword-matching algorithm. The early SMART model implemented an exact matching algorithm on keywords. Inspired by SMART, software companies such as Google and GitHub improved matching strategies in their code search tools with fuzzy search algorithms.

People began to study different matching algorithms for code search performance. LV et al. [2] proposed CodeHow, which transformed the queries into corresponding APIs. The target code was returned by API matching in codebase. Reiss et al. [10] presented a semantic search engine, which improved the searching performance by filtering unrelated code snippets. The structural semantic indexing model proposed by Bajracharya et al. [11] could establish the connection between natural language queries and source code keywords.

Marcus et al. [12] attempted to introduce Latent Semantic Analysis (LSA) into the field of code search. Their model made a good achievement by semantic code analysis. Inspired by a previous study, Jiang et al. [13] proposed ROSF, which combined IR and supervised learning technology during code embedding. It performed well in the task of code search when applying multiple structural extraction approaches.

2.2. Deep Learning Approaches. With the development of deep learning theory, people tend to solve problems in every field with deep learning approaches [14–18]. In recent years, researchers in the field of software engineering have introduced deep neural networks [19–22] such as multilayer perceptron network, recurrent neural network and convolutional neural network to solve the problems. The researchers carefully update their models with supervised or unsupervised learning on large-scale datasets. The neural network model through supervised or unsupervised training. Compared with previous coding encoding algorithms, deep neural encoders can automatically extract the structural and semantic features hidden in the source code.

Iyer et al. [23] presented LSTM networks with attention to produce summaries that describe C# code snippets and

SQL queries. Their model codeNN is built on a classical encoder-decoder framework, which takes the source code as plain text and models the conditional distribution of the summary. Allamanis et al. [24] applied a neural convolutional attentional model to vectorize the source code snippets. These learning-based approaches mainly learn the latent features from source code with neural networks.

Gu et al. [25] proposed a code search model called codeNN with complicated neural networks. Inspired by joint embedding in the image processing field, codeNN treats the code snippet as a combination of function names, API calls, and a sequence of tokens. The code encoder is implemented with bi-LSTM and MLP networks. They build their own dataset by collecting Java source code snippets from GitHub. The first sentence of the code comment is identified as the data label. The typical questions posted on StackOverflow are accumulated as the queries in the test set, and corresponding code snippets for each query are also collected with other code search engines. The matching scores between snippets and queries are judged by experts. The construction of datasets and evaluation methods have been used by scholars for contrast experiments. codeNN makes full use of the structural characteristics of source code in the process of code encoding. It outperforms the classical code search engines Lucene and CodeHow. Although inaccurate results might be returned, or partial-related items are ahead of exact matching ones in the result list, it is still the most effective code search method right now. Cambroneiro et al. [19] reconfirmed this ranking in their latest review in 2019, but they declared the complex network structure also resulted in low embedding efficiency.

The searching models with unsupervised learning has attracted the attention of researchers for lack of labeled data, although their performance might not match one with supervised learning models. Sachdev et al. [3] trained their search model on large-scale corpus with unsupervised learning. The model encodes all the snippets in a codebase with common document embedding and TD-IDF techniques, and then returns related code vectors according to a specific vector similarity algorithm.

The famous pretrained model BERT [26], which was proposed in 2018, has played an important role in word-embedding techniques in the area of NLP. Researchers Kanade et al. [27] were the first to introduce BERT into the field of code retrieval. The contrast experiments show that their model with BERT embedding outperforms searching models based on LSTM networks with word2vec embedding. They declare that their pretrained model also outperforms the Transformer [28], which is trained from scratch.

Recent scholars manage to improve the models' searching ability by intensifying the expressiveness of queries [29–31]. Programmers often apply code search with few words for simplicity so that queries lack semantic information, which fails to meet the requirements of developers. In 2019, Liu et al. [32] proposed a NQE model which is capable of enlarging query words. The query enhancer in the model inputs a small number of query keywords and outputs an extended query statement with new words. The searching models are trained on a specific corpus with supervised

learning. Experiments show that the searching performance is obviously improved by the query enhancer in NQE.

3. Preliminaries

In this section, we briefly give some well-accepted definitions in the area of source code search and deep learning.

3.1. Abstract Syntax Tree. Abstract syntax tree is a kind of syntax tree representing the abstract syntactic structure of the source code. It has been widely used by programming compilers and software engineering tools due to the powerful representation ability. Different from concrete syntax trees (CTS), abstract syntax trees do not contain all the details of source code such as the punctuation and delimiters. They only include the syntax structure of the source code at an abstract level. AST contains both the lexical and syntax information of the source code, which is often employed in the industry as an intermediate tool to extract the hidden information

Figure 1 is the structure of an AST. Nodes of the AST correspond to the constructs or symbols of the source code. We conclude from the graph that the AST fully retains the structural information of the source code.

3.2. Attention. The attention mechanism is the internal process for machines to imitate the human observation of things in the world. When processing images, our vision quickly obtains the target area by a global scan, i.e., the focus of attention. Then, the brain pays more attention to the focus area for details, while suppressing irrelevant information.

Bahdanau et al. [33] firstly applied the attention mechanism in the field of machine translation, i.e., sequence to sequence learning. He successfully solved the problem of long-term dependency in machine translation, i.e., the translation models based on fixed vector representations often lost history information of long sentences in the decoding process. After that, people began to study deep encoders with attention layers, which achieved amazing effects in all areas of NLP.

Mathematically, the attention is essentially a mapping function composed of Query, Key, and Value. The calculation of attention values is divided into three steps:

Step 1. Query is combined with each Key to calculate the attention weight. The similarity function $f(Q, K)$ can be defined in multiple ways. The simplest calculation is shown as follows:

$$f(Q, K) = K^T Q. \quad (1)$$

Step 2. The softmax function is used to normalize the attention weight obtained in Step 1, as shown in equation (2). Sometimes, we have to scale the attention scores later as the original ones are too large to calculate:

$$a_i = \text{softmax}(f(Q, K)). \quad (2)$$

Step 3. The final attention is the weighted sum of normalized weights a_i and corresponding values, which is shown as follows:

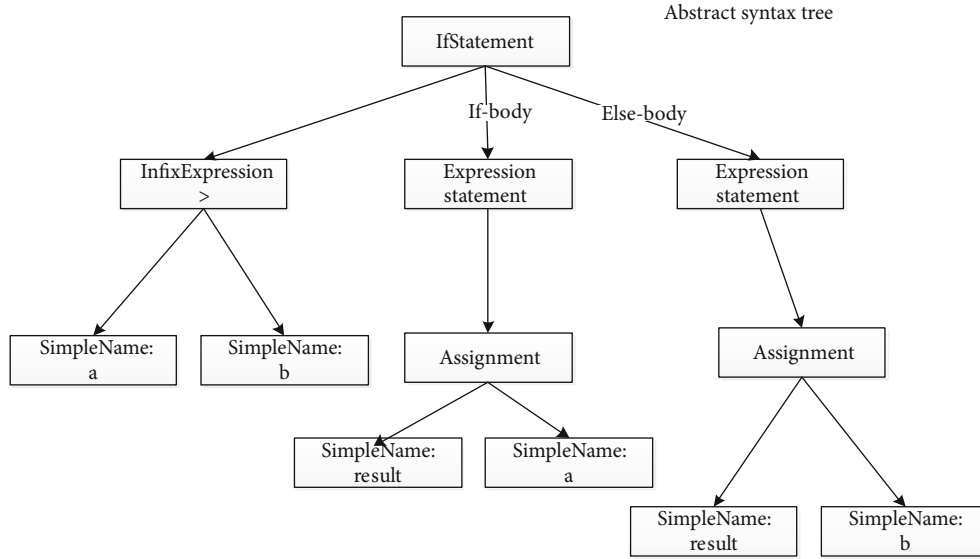


FIGURE 1: Abstract syntax tree.

$$\text{Attention}(Q, K, V) = \sum a_i V. \quad (3)$$

The attention mechanism is widely used in RNN-based encoder-decoder models. The input of the decoder's current state is determined by the weighted average of all hidden layers' output values in the encoder. The attention algorithm is transformed to the self-attention algorithm when $Q = K = V$ in the encoder [28]. Our lexical encoder in At-CodeSM is implemented with a specific self-attention LSTM layer.

3.3. LSTM Networks. Recurrent neural networks (RNN) can process input sequences of arbitrary length via the recurrent structure with shared weights. Unfortunately, a common problem with the traditional RNN is that components of the gradient vector can grow or decay exponentially over long sequences during training. Therefore, the LSTM architecture [34], which was invented by Hochreiter and Schmidhuber in 1997, addresses this problem of learning long-term dependency by introducing a memory cell that is able to preserve states over long periods of time. The core part of the LSTM is a cell memory C_t , including an input gate i_t , an output gate o_t , and a forget gate f_t . Figure 2 describes the basic structure of LSTM. Different from the original RNN, the LSTM solves the problem of long-term dependency effectively with the special structure memory cell, discarding the trivial information in the history to avoid the gradient vanishing.

The cell memory of LSTM is composed of three gate controllers. The forget gate f_t controls the extent to which the previous memory cell is forgotten, which is essential a sigmoid function. The entry of f_t is a weighted combination of the previous output value and the current input value. The input gate i_t controls how much each unit is updated, and the output gate o_t controls the exposure of the internal memory state. The LSTM transition equations are the following:

$$\begin{aligned}
 f^t &= \sigma(W_f \bullet [h_{t-1}, x_t] + b_f), \\
 i_t &= \sigma(W_i \bullet [h_{t-1}, x_t] + b_i), \\
 C_t &= f_t \times C_{t-1} + i_t \times \tan h(W_c \bullet [h_{t-1}, x_t] + b_c), \\
 o_t &= \sigma(W_o \bullet [h_{t-1}, x_t] + b_o), \\
 h_t &= o_t \bullet \tan h(C_t),
 \end{aligned} \quad (4)$$

where W_i, W_f, W_o are the weighted matrices, and b_i, b_f, b_o are the biases of LSTM to be learned during training, parameterizing the transformations of the input, forget, and output gates, respectively. σ and $\tan h$ are the activation functions, and \bullet denotes the element-wise multiplication. x_t is the input of the LSTM cell unit, and h_t is the output of the hidden layer at the current time step.

In order to deal with structural data, Tai et al. [35] invented tree-based LSTM networks (Tree-LSTM) from the standard LSTM networks. Figure 3 shows the difference between standard LSTM and tree-LSTM networks. Figure 3(a) is the common LSTM network designed for sequential data, while Figure 3(b) is the tree-LSTM network used for structural data. Unlike traditional LSTM networks, tree-LSTM contains an output and n inputs at time step t , for which it is convenient to handle data stored in trees. Normally, it is used for binary trees when $n = 2$. The updating equations of tree-LSTM are detailed in Section 4.2.3.

4. Our Proposed Approach

4.1. General Framework. In this section, we detail the workflow of At-CodeSM, which is summarized in Figure 4. It contains a source code encoder E_c and a query encoder E_q . E_c maps the source code into representation vectors with a neural network, while E_q maps the queries written in natural languages into vectors with another neural network. Both encoders are trained with supervised learning on large corpora.

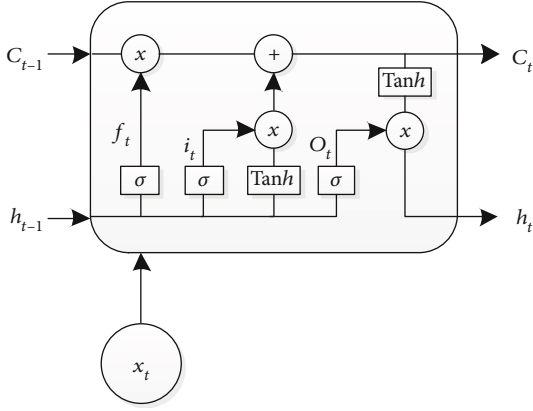


FIGURE 2: Structure of standard LSTM.

The code search usually contains an offline data preprocessing and an online search. In the process of offline data preprocessing, At-CodeSM updates E_c and E_q on the training corpus, and then apply an offline embedding on the search corpus with E_c . All the snippets in the search base are transformed to code vectors. In the process of online search, E_q firstly encodes the users' query, and then matches the query vector with each code vector on the search corpus. The top k snippets are returned as search lists according to the cosine similarity between vectors. All the encoders of At-CodeSM are detailed in the following subsections.

4.2. Source Code Encoder. As the core component of our model, E_c applies lexical embedding and structural embedding, respectively, during encoding process, so that the output vector maintains both the structural and semantic characteristics of the source code.

Figure 5 shows the structure of the source code encoder. It is a combined model, which includes a method name encoder, a lexical encoder, and a structural encoder. The method name encoder inputs the full name of the function and output a representation vector V_{name} . The lexical encoder inputs the body of the function and outputs a representation vector V_{token} . The structural encoder outputs a representation vector V_{ast} by embedding the corresponding AST with a specific traversal algorithm. Finally, V_{name} , V_{token} , and V_{ast} are fused into a unified vector v_c through a fully connected layer in At-CodeSM.

We present all the encoders in the following sections.

4.2.1. Lexical Embedding. The body of source code methods contains many core words which describes the functionality. During lexical embedding, At-CodeSM extracts core tokens from the method body, and then embeds them with common word-embedding technology in NLP by treating the source code snippets as plain texts. Finally, the output vector is generated with an attentional LSTM network. We use an independent attention layer at the back of lexical encoder, as the contribution of each token varies in implementing the functionality.

The process of lexical embedding is divided into three steps:

- (1) **Data preprocessing:** in order to collect tokens from a Java method, we tokenize the method body and split each token according to a camel case, e.g., *changeToPDF* and *parseXML*. All the duplicated tokens, stop words, and Java keywords are removed as they frequently occur in source code and are not discriminative
- (2) **Token embedding:** let $T = \{\text{token1}, \text{token2}, \text{token3}, \dots\}$ denote the sequence of tokens from source code after step (1). The lexical encoder includes a transformation f , which makes $f(\text{token1}, \text{token2}, \text{token3}, \dots) = v_{\text{token1}}, v_{\text{token2}}, v_{\text{token3}}, \dots$. By contrast, we implement the transformation f with Word2vec [36].
- (3) **Source code vector generation:** the sequence of token vectors $v_{\text{token1}}, v_{\text{token2}}, v_{\text{token3}}, \dots$ are loaded into a standard bi-LSTM. Equation (5) shows the calculation of LSTM, where \vec{h}_t and h_t denote the forward and backward hidden status at step t , and h_t is the concatenation of \vec{h}_t and h_t

$$\begin{aligned} \vec{h}_t &= \overrightarrow{\text{LSTM}}(v_{\text{token}t}) t \in [1, n], \\ h_t &= \overleftarrow{\text{LSTM}}(v_{\text{token}t}) t \in [n, 1], \\ h_t &= [\vec{h}_t, h_t] t \in [1, n]. \end{aligned} \quad (5)$$

However, the effect of each token is different in high-level programming languages, e.g., the token XML is more important than other tokens in a method dealing with the data storage in XML files. In this paper, we attempt to introduce the self-attention algorithm in the process of lexical embedding. To our knowledge, it is the first time to use attention mechanism in the field of code search. Since our model only includes the encoder, we decide to use the self-attention algorithm. The attention scores can be calculated in many ways as there are various definitions of similarity function. In our paper, equation (6) and equation (7) are used to calculate the attention scores, which are defined in [37]:

$$\alpha_i = \frac{\exp(h_i^T K)}{\sum_i \exp(h_i^T K)}, \quad i \in [1, n], \quad (6)$$

$$v_{\text{token}} = \sum_i \alpha_i h_i, \quad (7)$$

where h_i denotes the hidden states of the bidirectional LSTM, K denotes a context vector which is initialized randomly. Hu et al. [38] indicates that the inner product of h_i and K denotes the contribution of h_i to the source code vector. The value of K is updated continuously with other parameters via supervised learning. α_i denotes the i th attention score, corresponding with the hidden state h_i . v_{token} is the representation vector of the given code fragment, which is generated by the weighted sum of all the hidden states. Figure 6 shows the encoding process with the self-attention layer.

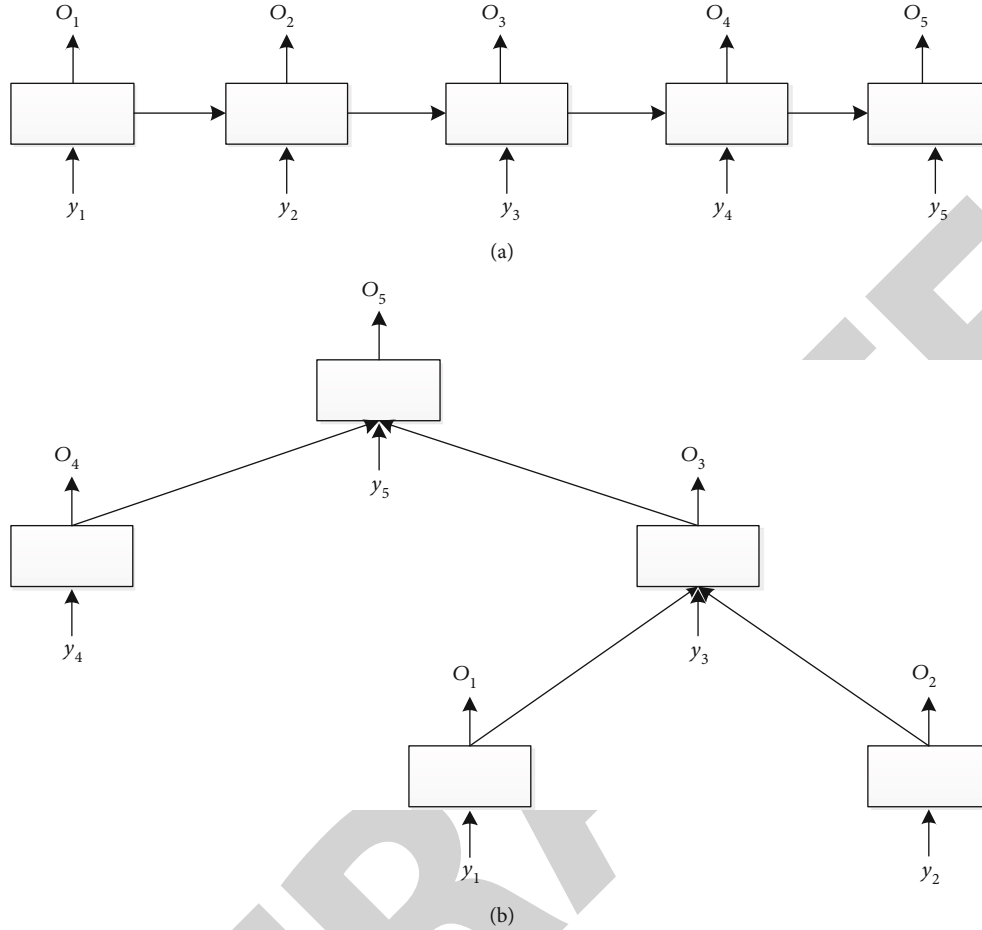


FIGURE 3: Comparison between standard LSTM and tree-LSTM.

4.2.2. Method Name Embedding. The method name is a description of the method functionality, which is composed of a small amount of keywords. Early code search algorithms apply a simple keyword matching between queries and method names. At-CodeSM uses an independent encoder for the embedding of method names, which is simpler than lexical embedding. Let $T = \{\text{name1}, \text{name2}, \text{name3}, \dots\}$ denote the sequence of small names extracted from the method name; after that, the encoder applies a transformation f , which makes $f(\text{name1}, \text{name2}, \text{name3}, \dots) = v_{\text{name1}}, v_{\text{name2}}, v_{\text{name3}}, \dots$ with Word2vec technology. Finally, At-CodeSM outputs the representation vector for the method name with a bi-LSTM network, which is shown as follows:

$$v_{\text{name}} = h_{mt} = \left[\overrightarrow{h_{mt}}, h_{mt} \right], \quad (8)$$

where $\overrightarrow{h_{mt}}$ and h_{mt} are the forward and backward hidden states of the bi-LSTM, v_{name} is the final semantic vector of the method name, generated from the concatenation of $\overrightarrow{h_{mt}}$ and h_{mt} . We tried to implement self-attention in the embedding layer, which had no performance improvement by experiments. Experimental results with various self-attention layers are discussed later.

4.2.3. Structural Embedding. We employ javalang to generate an abstract syntax tree (AST) from the source code snippet. The structural encoder then transforms the AST into a high-dimensional vector V_{ast} according to a specific AST traversal algorithm. Recent researchers have proposed several AST embedding algorithms, e.g., RvNN embedding algorithm [6], structure-based algorithm (SBT) [38], tree-LSTM embedding algorithm [35], and tree-CNN embedding algorithms [39]. We implement the structural encoder in At-CodeSM with a special tree-LSTM embedding algorithm, which is used by Hu et al. in their code clone detector CDLH.

Tai et al. proposed the tree-based LSTM networks, which is used for the embedding of ASTs in CDLH. Different from standard LSTM networks, neural cells in tree-LSTM contain several forget gates, each of which corresponds with an input. The transition equations for tree-LSTM are the following:

$$i = \sigma \left(W_i x + \sum_{l=1}^L U_{ilr_l} + b_i \right),$$

$$f_l = \sigma (W_f x + U_{flr_l} + b_f), \quad l = 1, 2, \dots, L,$$

$$o = \sigma \left(W_o x + \sum_{l=1}^L U_{olr_l} + b_o \right),$$

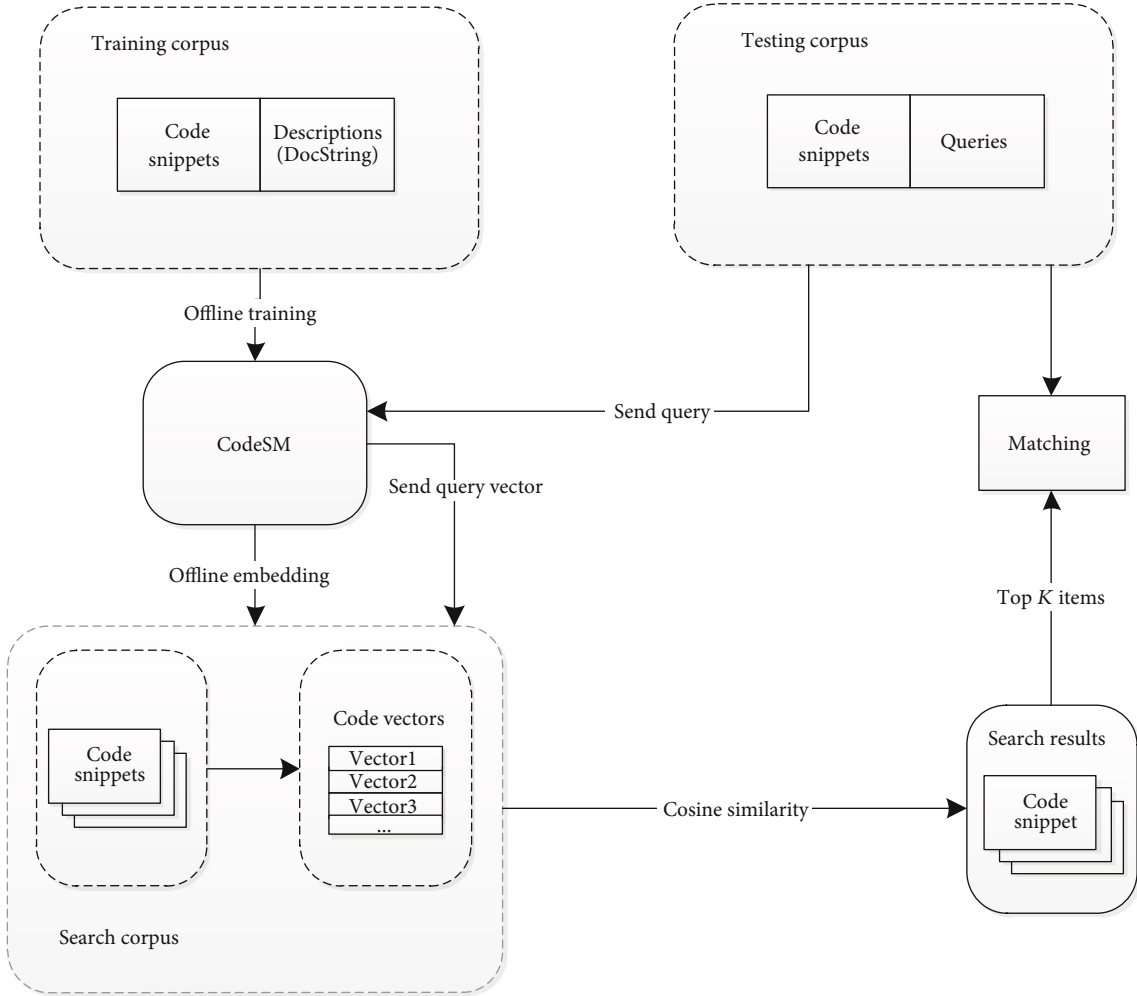


FIGURE 4: The workflow of At-CodeSM.

$$\begin{aligned}
 u &= \tan h \left(W_u x + \sum_{i=1}^L U_{ulr_i} + b_u \right), \\
 c &= i \odot u + \sum_{i=1}^L f_l \odot c_i, \\
 r &= o \odot \tan h(c),
 \end{aligned} \tag{9}$$

where x is the embedding of the corresponding token, L denotes the number of children, f_l are L forget gates for the children of the AST node, l is the index number for its children, r is a control variable for the output, W_i , W_f , W_o , W_u , U_{il} , U_{fl} , U_{ol} , and U_{ul} are weight matrices, and b_i , b_f , b_o , b_u are bias vectors. \odot denotes the element-wise multiplication, and σ is the sigmoid function.

The original ASTs generated from source code might have multiple branches. The classical tree-LSTM networks can be used for the embedding of ASTs with multiple branches. The number of children L varies for different AST nodes, which might cause problems in the parameter-sharing of weight matrices. We transform the original ASTs into binary trees, whose nodes contain 0 or 2 children.

The transform algorithm for binary trees is divided into two steps:

- (1) We split nodes with more than 2 children and generate a new right child together with the old left child as its children, and then put all children except the left-most as the children of this new node. Repeat the operation in an up-down way until only nodes with 0, 1, and 2 children are left
- (2) The nodes with 1 child are merged with its child

After transformation, the AST is transformed into a full binary tree, nodes of which contain 0 or 2 children. Figure 7 describes the transformation of a subtree. The binary tree on the right part of the figure is transformed from the left one, and node 6 and node 7 are generated after two splits.

For implementation, we input the embeddings of the two children into the Tree-LSTM networks, and the hidden state for each internal node is computed recursively in a bottom-up way. The final output from the AST root V_{ast} is the representation for the code snippet.

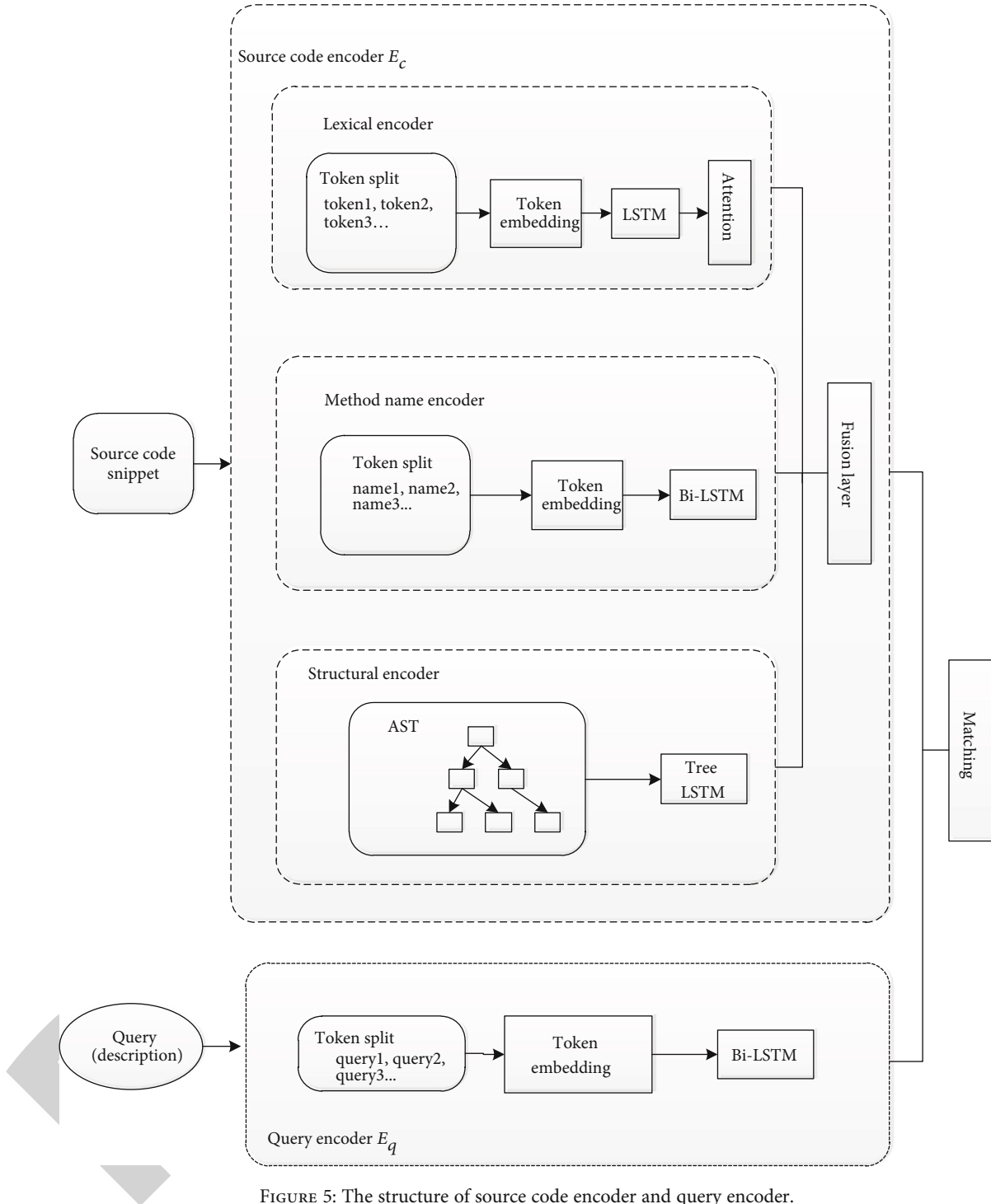


FIGURE 5: The structure of source code encoder and query encoder.

4.3. *Query Embedding.* In practice, programmers input queries in the repositories for code search. In the training process, the query encoder is updated with target descriptions. Both queries and descriptions are a sequence of natural language words. The lower part of Figure 5 describes the structure of the query encoder equation. The process of query embedding is similar to the embedding of method names in source code. The query encoder transforms a sequence of tokens to a sequence of vectors $v_{\text{query}1}$, $v_{\text{query}2}$, and $v_{\text{query}3}$ with

word-embedding technology. Finally, the embedding network embeds this sequence of vectors into a query vector using bi-LSTM, which is shown as follows:

$$v_{\text{query}} = h_{qt} = \left[\overrightarrow{h_{qt}}, \overleftarrow{h_{qt}} \right], \quad (10)$$

where $\overrightarrow{h_{qt}}$ and $\overleftarrow{h_{qt}}$ are the forward and backward hidden

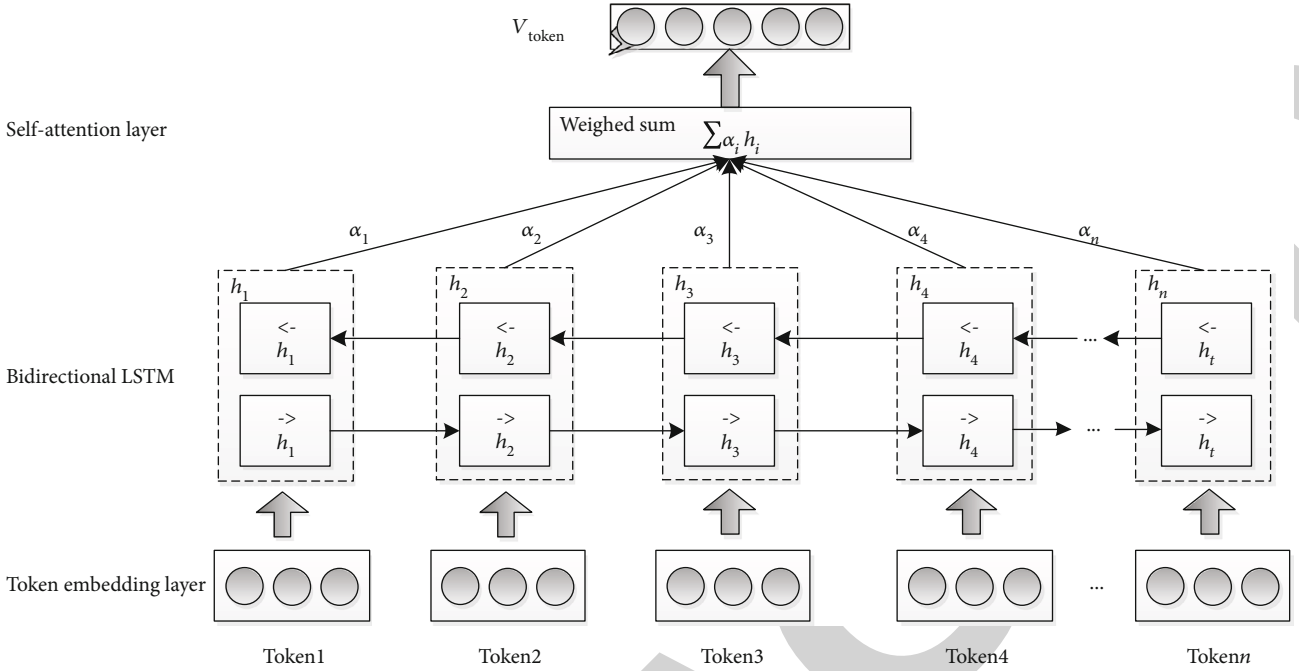


FIGURE 6: Lexical embedding with self-attention.

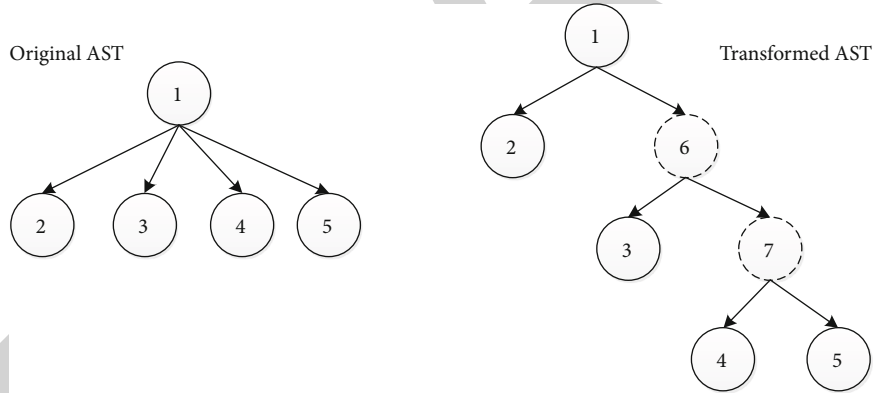


FIGURE 7: The transformation for binary trees.

states produced by the final layer of LSTM in the query encoder, and v_{query} is the output vector of the query sentence. We tried to add a self-attention layer in the query encoder, which had no performance improvement by experiments.

4.4. Loss Function. In this section, we present the loss function used in At-CodeSM. With carefully trained encoders, and At-CodeSM maps both the source code and queries to different vectors in a unified vector space. The goal of training is as follows: if a code snippet and a description have similar semantics, their embedded vectors should be close to each other. In other words, given an arbitrary code snippet C and an arbitrary description D , we want it to predict a distance with high similarity if D is an exact description of C , and a little similarity otherwise.

We build each training instance as a triple $\langle C, D+, D- \rangle$ for supervised training. For each code snippet C , there is a positive description $D+$ (correct description) and a negative

description $D-$ (false description) randomly chosen from the collection of other $D+$. In the training process, the search model predicts the cosine similarities of both $\langle C, D+ \rangle$ and $\langle C, D- \rangle$ pairs and minimizes the ranking loss [40], which is defined as follows:

$$L(\theta) = \sum_{\langle C, D+, D- \rangle \in P} \max(0, \epsilon - \cos(c, d_+) + \cos(c, d_-)), \quad (11)$$

where θ indicates the model parameters, P indicates the training corpus, ϵ is a constant margin. c , d_+ , and d_- are the embedded vectors of C , $D+$, and $D-$, respectively. The lost function $L(\theta)$ encourages the similarity between a code snippet and its correct description to increase, and the similarity between a code snippet and its false description to decrease.

4.5. Evaluation Metrics. The objective of code search models is to locate suitable code snippets in code repositories. They often return many results based on similarity algorithms due to the big capacity of codebase. In most cases, developers only focus on the snippets ahead in the result list. In our experiment, we select MRR and NDCG as evaluation metrics which are often used in the field of information retrieval [2, 25, 41, 42], to compare the performances of At-CodeSM and other baselines.

5. Experiments

All the experiments are conducted on a server, having a CPU of 16 cores with GPU acceleration. The framework is built on python 3.6 and CUDA 9.0. All the tokens are embedded using word2vec with the Skip-gram algorithm, and we set the embedding size to be 128.

The standard LSTM and tree-LSTM networks are used to build the encoders, respectively, where the hidden dimensions are set to be 128. We use SGD to train the model and set Batch_size to 64. We employ the optimizer Adam with a learning rate of 0.005 to train the model.

5.1. Dataset Preparation. There are very few public datasets for source code search as it is very difficult to collect exact descriptions for code snippets in the code repositories with massive code data. Especially, the similarity scores between code snippets and queries should be judged by experts, which might cause human bias. Researchers usually construct three datasets for contrast experiments in code search area.

- (1) Training corpus: it refers to a dataset of paired code and the natural language description. A common example for the natural language description could be the code snippet's corresponding docstring. A training corpus is used to update the searching models with supervised labeling. Unsupervised learning models use only code snippets from the training corpus
- (2) Search corpus: it refers to a dataset of unique code entries after data preprocessing. Entries are unique to avoid repetition in search results. Code search engines take effort to apply an offline embedding on each code snippet in the search corpus with their code encoders before an online search. Data in the search corpus are not necessarily like the ones in training corpus. Sometimes, code snippets in the search corpus might not be paired with descriptions
- (3) Testing corpus (benchmark queries): it refers to a set of evaluation queries and corresponding code snippets used to gauge the performance of trained models. It is defined as $\{ \langle \text{query}_i, C_i \rangle \mid i \in N, |C_i| \geq 1 \}$. Depending on the size of C_i , testing sets generally fall into two categories in code search:
 - (a) Each test case includes a query and a corresponding code snippet, i.e., $\forall \text{query}_i, |C_i| = 1$. These test cases can be automatically collected and evaluated. However, due to the complexity of the code structure, it is possible for search engines in prac-

tice to return heterogeneous code snippets with the same functionality, e.g., type 4 clone pairs. These correct cases are probably identified as "false." The evaluation for code snippets with similar functionality, which are returned by search engines, will lose effectiveness

- (b) Each test case includes a query and several corresponding code snippets, i.e., $\exists \text{query}_i, |C_i| > 1$. Test cases of this kind successfully solve the problem of code snippets with similar functionality but different shapes. Based on these test cases, we can evaluate the search engine's performance with traditional methods in the IR field. However, it is difficult to find all the target snippets related to the same query and judge the relatedness between them. Recent scholars manage to collect similar code snippets according to the same query by various search models, and the relatedness scores are often obtained manually. Hence, the testing corpus does not have a large capacity. We believe that the problem of collecting test cases will be solved with the development of deep learning methods in the field of source code clone detection

5.2. Dataset Description. Previous researchers [3, 43] build their own datasets by collecting source code from code repositories, due to the lack of public datasets for code search and summarization. In order to solve the problem, Microsoft Cambridge Research Center and GitHub company released a large-scale dataset CodeSearchNet [44] for machine learning in 2020. The dataset contains more than 6 million code snippets extracted from GitHub, an open-source code repository with massive code data, among which more than 2 million snippets are commented methods. The code extraction is applied according to "popularity" as indicated by the number of stars and forks in GitHub. The dataset authors generate the label for each code snippet by extracting the first sentence from its comment. Table 1 shows the data in CodeSearchNet, which are grouped by programming language. These labeled data on the second column of Table 1 can be used for code search and code summarization tasks. We conduct contrast experiments on the Java subset.

The dataset for java in CodeSearchNet is split in 80-10-10 train/valid/test proportions after data preprocessing. We use the labeled java dataset as the search corpus, the original training set as our training corpus. Figure 8 shows the partition of Java dataset in our experiments.

At-CodeSM and other baseline models are evaluated with two different testing sets, which are described in Section 5.1:

- (1) Test A: we apply an automatic testing on the Java testing set from CodeSearchNet. Table 1 shows that the Java testing set contains 26909 method-description pairs. The experimental results are unbiased due to the exclusive partition of training and testing sets [45]. We calculate the MRR values of all the searching models in Test A

TABLE 1: Data statistics in CodeSearchNet.

Language	Labeled data (functions with descriptions)	All
Go	347789	726768
Java	542991	1569889
Javascript	157988	1857835
PHP	717313	977821
Python	503502	1156085
Ruby	57393	164048

- (2) Test B: expert scoring are employed in the evaluation of ranking models in order to cope with heterogeneous code snippets with similar functionality. Experts score each item in the result list by the relatedness between the snippet and query. Traditional IR-based methods such as NDCG are then applied for evaluation depending on the matching scores. Test B is rarely used by researchers due to the luxury manual work. Hence, the authors of CodeSearchNet construct a new dataset called CodeSearchNet Challenge for code evaluation. It is defined as $\{D_i, \langle C_{in}, R_{in} \rangle \mid i = 1, 2, \dots, 99; n = 1, 2, \dots, 100\}$, where D_i denotes the description or query, C_{in} is a corresponding code snippet according to D_i , R_{in} is a matching score between C_{in} and D_i given by experts

CodeSearchNet Challenge contains 99 natural languages queries paired with likely results for each of six programming languages. All the queries are obtained from the famous search engine Bing with high click-through rates, each of which contains around 10 corresponding code snippets, returned by baseline code search models. Every query-result pair is labeled by a human expert, indicating the relevance of the result for the query. Table 2 shows some examples in CodeSearchNet Challenge. Table 3 shows the criterion of relevance followed by experts.

5.3. *Contrast Experiments.* We compare At-CodeSM with three baseline models in the field of source code search by different experiments on CodeSearchNet dataset:

- (1) NBoW model (Neural Bag of Words) [45]: as a classical code search model, NBoW has already been implemented in CodeSearchNet. It applies code embedding with common NLP methods by treating source code as the plain text. The tokens extracted from the code snippet are embedded with a transformation matrix, which is updated by training. The representation vector for the code snippet is generated by a max-pooling function over all the token vectors. NBoW implements the query embedding with the same embedding algorithm. Finally, NBoW returns the most related code snippets in the vector space as search results with a similarity algorithm between vectors
- (2) NCS model (Neural Code Search) [3]: built in Facebook, NCS generates the representation vector of

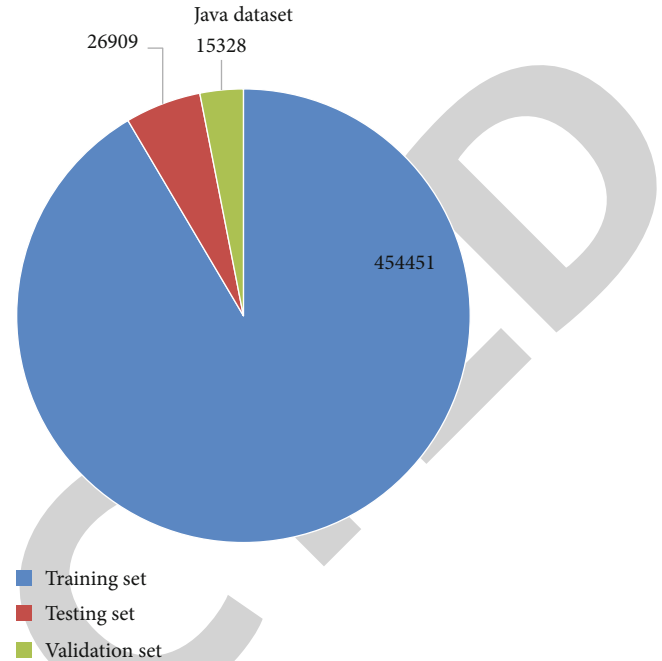


FIGURE 8: Java dataset.

the code with a combination of token-level embedding with fastText [45], which is similar to Word2vec, and conventional IR techniques, such as TF-IDF. The encoders of NCS are not implemented with conventional deep neural networks nor supervised training

- (3) CODenn model [25]: all the encoders in CODenn are implemented with complicated neural networks, compared to former baselines. CODenn includes three encoders for method names, APIs, and method body, respectively. The encoders for method names and APIs are implemented with a standard LSTM, while the lexical encoder uses a simple MLP for the embedding of method body. Finally, CODenn outputs a unified vector by merging three subvectors through a MLP layer. For query embedding, a bi-LSTM network is employed to process the sequence of token vectors extracted from the query sentence. CODenn returns the result list according to the cosine similarity algorithm. Unlike NCS, authors of CODenn update their model with supervised learning. The labeled data are collected from code repositories by themselves. The authors provide the framework of CODenn in GitHub, which we use for our contrast experiments on CodeSearchNet

Figure 9 shows the experimental results of At-CodeSM and baseline models on the test corpus of CodeSearchNet. The figures above the bars are the MRR values of search models, which are the rank of the first hit results. We see that the search performance of CODenn and At-CodeSM, which is evaluated by MRR, is much higher than the former models.

TABLE 2: Examples in CodeSearchNet challenge.

Query	The path of the returned code	Score
Connect to sql	https://github.com/druid/.../DruidPool.java#L31-L51	0
Connect to sql	https://github.com/Teddy-Zhu/.../jdbc/JDBCPOOL.java#L97-L105	1
Convert html to pdf	https://github.com/Coveros/.../Reporter.java#L741-L752	2
Convert json to csv	https://github.com/GCRC/nunaliit/.../ExportRecordsCSV.java#L118-L150	0
Convert string to number	https://github.com/b3log/.../JSONObject.java#L2074-L2126	3

TABLE 3: Criterion of relevance.

Description	Score	Criteria
Totally irrelevant	0	I would never want to see this for this query.
Weak match	1	That is not exactly what I was looking for, but there are some useful elements I would use (e.g., APIs and code structure) and can form the basis of a new query or exploration towards solving my query.
Strong match	2	This is more or less what I was looking for. I would use the code in here as a backbone for my purpose, but I will not necessarily copy-paste it or use this library.
Exact match	3	It is exactly what I was looking for. I would copy-paste the code and make minor adaptations or will use this functionality of the library in my code.

Figure 10 shows the experimental results of At-CodeSM and baseline models on CodeSearchNet Challenge. We see that At-biLSTM and CODEnn once again take the lead in the search performance evaluated by NDCG.

6. Discussion

In this chapter, we take a detailed discussion about the performance of At-CodeSM and other code search models based on ablation tests. We try to find the key components which affect searching accuracy by further experiments.

6.1. Comparing with Baseline Models. Compared to other baseline models, we conclude from the contrast experiments that At-CodeSM model outperforms the other models in both MRR values, which are generated from automated testing, and NDCG values which are generated with manual evaluation. NCS model encodes the source code with common NLP methods. The unsupervised learning has a negative influence on the searching performance, although unlabeled data are easily collected. Figures 9 and 10 show the poor performance of NCS, of which the searching accuracy and ranking in the result list are lower than codeNN and At-CodeSM. The performance of NBoW is not ideal, because its code encoder ignores both the sequential information of tokens and structural information in source code.

CodeNN is a successful code search model trained with supervised learning. It introduces deep learning technology into the field of code search. It makes great achievement in source code search by using a combination of method names, tokens, and APIs during code embedding. Inspired by codeNN, we propose the At-CodeSM model. The performance of our model is slightly better than codeNN. We guess it is the introduction of self-attention and tree-LSTM networks that improve the searching performance. The core words are strengthened with a self-attention mechanism,

which highlight the behavior and logic hidden in function bodies. The AST encoder in our model, which is implemented with tree-LSTM networks, further extracts the structural features hidden in source code, compared to API revocations in codeNN. Both models outperform NCS and NBoW, which only extract lexical features.

6.2. AST Traversal Algorithms. A traversal algorithm for ASTs is introduced in At-CodeSM. The corresponding AST maintains the structural feature hidden in the source code snippet. We use a tree-based LSTM network in the embedding of AST. In the field of software engineering, many AST-based traversal algorithms are proposed, with which corresponding ASTs are transformed to representation vectors.

In order to investigate the effects of the embedding algorithms for ASTs, we conduct contrast experiments on the same dataset, and the results are shown in Table 4. Models in the table are the same except that the structural encoders are implemented with three different traversal algorithms for AST embedding. Model 1 embeds the source code with a combination of the lexical encoder and method name encoder, which ignores the structural embedding completely. Model 2 implements the AST embedding with SBT, which convert the ASTs into special formatted sequences of nodes. A bi-LSTM network is used to generate the representation vector according to the sequence of nodes. The authors of SBT claim the transformation keeps the structural information. Model 3 is an At-CodeSM model, whose structural encoder is implemented with a Tree-based LSTM. We compare both the MRR and NDCG values in Table 4.

Through the above experimental results, it can be observed that model 1 shows the poorest performance, as it fails to extract the structural information hidden in the AST. The search performance of model 2 is slightly inferior to that of model 3. We guess the one-dimensional sequence

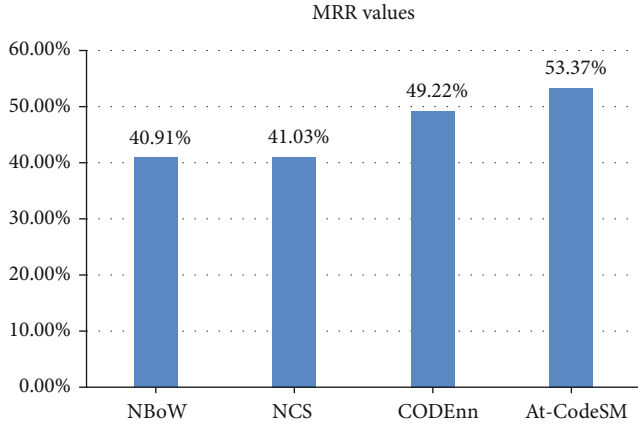


FIGURE 9: The MRRs for various models on CodeSearchNet.

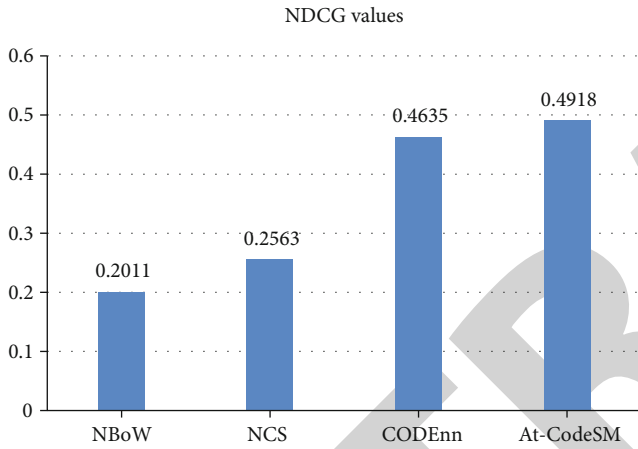


FIGURE 10: The NDCGs for various models on CodeSearchNet.

TABLE 4: Search performance depending on various AST traversal algorithms.

Descriptions	MRR	NDCG
Without AST (model 1)	46.45%	0.4149
SBT (model 2)	51.03%	0.4683
Tree-LSTM (model 3)	53.37%	0.4918

generated from SBT might lose the structural information of some tree nodes.

6.3. Self-Attention Algorithms. The use of a self-attention layer, which stresses the effect of key words in source clone embedding, is a great innovation in our paper. In this section, we investigate the effect of self-attention layers on the search performance by contrast experiments. Figure 11 shows the experimental data we collect from five code search models, each of which is built on the basic At-CodeSM model. The detailed structure of At-CodeSM is presented in Section 4.2, including three encoders for method names, code tokens,

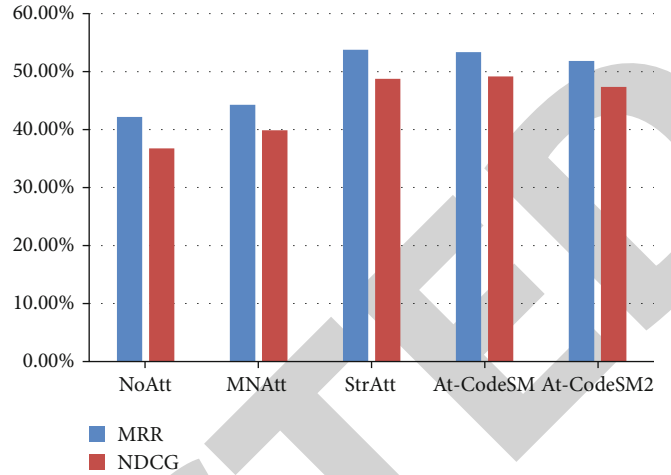


FIGURE 11: Search models with various self-attention layers.

and the code structure, respectively. The structures of these models are the same except the self-attention layers:

- (1) NoAtt model: it does not include the self-attention layer at all. The vectors generated from three independent encoders are merged via a fusion layer
- (2) MNAtt model: the self-attention layer is placed at the back of the name encoder, which assigns weights to the tokens extracted from method names
- (3) StrAtt model: the self-attention mechanism is used during structural embedding. Each node vector is assigned with an attentional weight
- (4) At-CodeSM model: it is proposed in Section 4. The self-attention layer is used during lexical encoding
- (5) At-CodeSM2 model: it is a variant of the original At-CodeSM model, where the attention scores are computed according to equation (12). Many formulas are proposed to calculate the attention scores in the NLP field. Equation (12) is a simple implementation for the self-attention algorithm without other model parameters. We want to investigate the effects of various attention algorithms by contrast experiments

Figure 11 shows that the self-attention layer greatly improves the search performance of the model. The contributions of different words are various in high-level programming languages. The core words implementing the logical functionality are more important than the normal ones. The encoder with self-attention layers can strengthen the effectiveness of core words and weaken the impact of common words such as variable declaration. Both the MRR and NDCG values of NoAtt substantially fall behind the other models. The performance improvement in MNAtt is not obvious. We guess that all the words extracted from the method name are important, the contributions of which are similar. The performance of StrAtt is close to that of At-CodeSM. However, it takes more time to train StrAtt due to the complicated structure encoder with attention.

We find that the search performance of At-CodeSM and At-CodeSM2 are slightly different. The performance of At-CodeSM is higher when involving an independent parameter K in equation (7). We suspect that the search performance of the second model is slightly affected due to the lack of some adjustments to the input when calculating the attention scores.

$$\alpha_i = \frac{\exp(h_i^T h_i)}{\sum_i \exp(h_i^T h_i)}. \quad (12)$$

7. Conclusion

In this paper, we have presented a novel source code-searching model At-biLSTM based on deep learning with a self-attention mechanism. It contains a query encoder and three independent source code encoders, which successfully capture both the lexical and syntactic information of the code during embedding. The searching results are returned by computing the cosine similarity between the query vector and code vectors in a unified high-dimensional vector space. Contrast experiments show that our model significantly outperforms most of the existing code search models.

We will focus on three aspects in the future. First, the At-CodeSM should be used in large-scale codebase. At present, both the algorithms for clone search and data collected in the labs cannot be applied in the real world. We will study and improve the searching performance of our model in industry. Second, we will focus on the code-embedding technology. In recent years, many pretrained models for embedding have made great achievements in NLP applications. We plan to rebuild our code encoders with BERT, which is the most popular pretrained model in the world. Third, we will make a study of query expansion technology. We plan to add a special component for the expansion of keywords in queries, which might improve the searching performance.

The threats to the validity stem from the datasets used in our experiments. The models are trained on a new dataset called CodeSearchNet which was created by Microsoft in 2020, as the labeled data for code search are difficult to accumulate. The labeled data in CodeSearchNet are collected in the same way as in other datasets. The first sentence of the method comment is identified as the query description, which is far away from the real query in practice. The matching scores for 99 queries are all given manually. The introduction of human evaluation might have a negative influence on searching results when we evaluate the models' NDCG values.

Data Availability

The data used to support the findings of this study are included in the article.

Conflicts of Interest

The authors declare that they have no conflicts of interest.

Acknowledgments

This work was supported by the National Key Research and Development Program of China under Grant No. 2019QY1300.

References

- [1] C. McMillan, M. Grechanik, D. Poshyvanyk, Q. Xie, and C. Fu, "Portfolio: finding relevant functions and their usage," in *2011 33rd International Conference on Software Engineering (ICSE)*, pp. 111–120, New York, NY, USA, 2011.
- [2] F. Lv, H. Zhang, J. Lou, S. Wang, D. Zhang, and J. Zhao, "CodeHow: effective code search based on API understanding and extended boolean model (E)," in *2015 30th IEEE/ACM International Conference on Automated Software Engineering (ASE)*, pp. 260–270, Lincoln, NE, USA, 2015.
- [3] S. Sachdev, H. Li, S. Luan, S. Kim, K. Sen, and S. Chandra, "Retrieval on source code: a neural code search," in *Proceedings of the 2nd ACM SIGPLAN International Workshop on Machine Learning and Programming Languages*, pp. 31–41, New York, NY, USA, 2018.
- [4] H. Yu, W. Lam, L. Chen, G. Li, T. Xie, and Q. Wang, "Neural detection of semantic code clones via tree-based convolution," in *2019 IEEE/ACM 27th International Conference on Program Comprehension (ICPC)*, pp. 70–80, Montreal, QC, Canada, 2019.
- [5] H. Wei and M. Li, "Supervised deep features for software functional clone detection by exploiting lexical and syntactical information in source code," in *Proceedings of the Twenty-Sixth International Joint Conference on Artificial Intelligence, IJCAI*, pp. 3034–3040, New York, NY, USA, 2017.
- [6] M. White, M. Tufano, C. Vendome, and D. Poshyvanyk, "Deep learning code fragments for code clone detection," in *2016 31st IEEE/ACM International Conference on Automated Software Engineering (ASE)*, pp. 87–98, New York, NY, USA, 2016.
- [7] E. Hill, L. Pollock, and K. Vijay-Shanker, "Improving source code search with natural language phrasal representations of method signatures," in *2011 26th IEEE/ACM International Conference on Automated Software Engineering*, pp. 524–527, Lawrence, KS, USA, 2011.
- [8] Y. Ye and G. Fischer, "Supporting reuse by delivering task-relevant and personalized information," in *Proceedings of the 24th International Conference on Software Engineering*, pp. 513–523, Orlando, FL, USA, 2002.
- [9] Y. F. Chang and C. M. Eastman, "An information retrieval system for reusable software," *Information Processing & Management*, vol. 29, no. 5, pp. 601–614, 1993.
- [10] S. P. Reiss, "Semantics-based code search," in *Proceedings of the 31st International Conference on Software Engineering*, pp. 243–253, New York, NY, USA, 2009.
- [11] S. K. Bajracharya, J. Ossher, and C. V. Lopes, "Leveraging usage similarity for effective retrieval of examples in code repositories," in *Proceedings of the Eighteenth ACM SIGSOFT International Symposium on Foundations of Software Engineering*, pp. 157–166, Santa Fe, NM, USA, 2010.
- [12] A. Marcus, A. Sergeev, V. Rajlich, and J. I. Maletic, "An information retrieval approach to concept location in source code," in *11th Working Conference on Reverse Engineering*, pp. 214–223, Delft, Netherlands, 2004.

- [13] H. Jiang, Z. Sun, Z. Ren et al., "ROSF: leveraging information retrieval and supervised learning for recommending code snippets," *IEEE Transactions on Services Computing*, vol. 12, no. 1, pp. 34–46, 2019.
- [14] Y. Meng and L. Liu, "A deep learning approach for a source code detection model using self-attention," *Complexity*, vol. 2020, Article ID 5027198, 15 pages, 2020.
- [15] A. Li, D. Spano, J. Krivochiza et al., "A tutorial on interference exploitation via symbol-level precoding: overview, state-of-the-art and future directions," *IEEE Communications surveys and tutorials*, vol. 22, no. 2, pp. 796–839, 2020.
- [16] Q. Yue and L. Zhang, "Two-sided matching for hesitant fuzzy numbers in smart intelligent technique transfer," *Mechanical Systems and Signal Processing*, vol. 139, article 106643, 2020.
- [17] J. Zhang and G. Qu, "Physical unclonable function-based key sharing via machine learning for IoT security," *IEEE Transactions on Industrial Electronics*, vol. 67, no. 8, pp. 7025–7033, 2020.
- [18] M. Zhang, J. Montewka, T. Manderbacka, P. Kujala, and S. Hirdaris, "A big data analytics method for the evaluation of ship-ship collision risk reflecting hydrometeorological conditions," *Reliability Engineering & System Safety*, vol. 213, article 107674, 2021.
- [19] J. Cambroner, H. Li, S. Kim, K. Sen, and S. Chandra, "When deep learning met code search," in *Proceedings of the 2019 27th ACM Joint Meeting on European Software Engineering Conference and Symposium on the Foundations of Software Engineering*, pp. 964–974, New York, NY, USA, 2019.
- [20] J. Zhang and C. Shen, "Set-based obfuscation for strong PUFs against machine learning attacks," *IEEE Transactions on Circuits and Systems. I: Regular Papers*, vol. 68, no. 1, pp. 288–300, 2021.
- [21] J. Shi, Y. Lu, and J. Zhang, "Approximation attacks on strong PUFs," *IEEE Transactions on Computer-Aided Design of Integrated Circuits and Systems*, vol. 39, no. 10, pp. 2138–2151, 2020.
- [22] Z. Niu, B. Zhang, J. Wang et al., "The research on 220 GHz multicarrier high-speed communication system," *China communications*, vol. 17, no. 3, pp. 131–139, 2020.
- [23] S. Iyer, I. Konstas, A. Cheung, and L. Zettlemoyer, "Summarizing source code using a neural attention model," in *Proceedings of the 54th Annual Meeting of the Association for Computational Linguistics (Volume 1: Long Papers)*, pp. 2073–2083, Berlin, Germany, 2016.
- [24] M. Allamanis, H. Peng, and C. Sutton, "A convolutional attention network for extreme summarization of source code," in *Proceedings of the 33rd International Conference on Machine Learning*, pp. 2091–2100, New York, NY, USA, 2016.
- [25] X. Gu, H. Zhang, and S. Kim, "Deep code search," in *2018 IEEE/ACM 40th International Conference on Software Engineering (ICSE)*, pp. 933–944, Gothenburg, Sweden, 2018.
- [26] J. Devlin, M. W. Chang, K. Lee, and K. Toutanova, "BERT: pre-training of deep bidirectional transformers for language understanding," 2018, <https://arxiv.org/abs/1810.04805/>.
- [27] A. Kanade, P. Maniatis, G. Balakrishnan, and K. Shi, "Pre-trained contextual embedding of source code," 2019, <https://arxiv.org/abs/2001.00059/>.
- [28] A. Vaswani, N. Shazeer, N. Parmar et al., "Attention is all you need," in *Proceedings of the 31st International Conference on Neural Information Processing Systems*, pp. 6000–6010, Red Hook, NY, USA, 2017.
- [29] B. Zhang, Z. Niu, J. Wang et al., "Four-hundred gigahertz broadband multi-branch waveguide coupler," *IET Microwaves, Antennas & Propagation*, vol. 14, no. 11, pp. 1175–1179, 2020.
- [30] K. Xiang, C. Xu, and J. Wang, "Understanding the relationship between tourists' consumption behavior and their consumption substitution willingness under unusual environment," *Psychology Research and Behavior Management*, vol. 14, pp. 483–500, 2021.
- [31] B. Zhang, D. Ji, D. Fang, S. Liang, Y. Fan, and X. Chen, "A novel 220-GHz GaN diode on-chip tripler with high driven power," *IEEE Electron Device Letters*, vol. 40, no. 5, pp. 780–783, 2019.
- [32] J. Liu, S. Kim, V. Murali, S. Chaudhuri, and S. Chandra, "Neural query expansion for code search," in *Proceedings of the 3rd ACM SIGPLAN International Workshop on Machine Learning and Programming Languages*, pp. 29–37, New York, NY, USA, 2019.
- [33] D. Bahdanau, K. Cho, and Y. Bengio, "Neural machine translation by jointly learning to align and translate," 2016, <https://arxiv.org/abs/1409.0473/>.
- [34] S. Hochreiter and J. Schmidhuber, "Long short-term memory," *Neural Computation*, vol. 9, no. 8, pp. 1735–1780, 1997.
- [35] K. S. Tai, R. Socher, and C. D. Manning, "Improved semantic representations from tree-structured long short-term memory networks," in *Proceedings of the 53rd Annual Meeting of the Association for Computational Linguistics and the 7th International Joint Conference on Natural Language Processing*, pp. 1556–1566, Beijing, China, 2015.
- [36] T. Mikolov, K. Chen, G. Corrado, and J. Dean, "Efficient estimation of word representations in vector space," in *Proceedings of Workshop at ICLR*, New York, NY, USA, 2013.
- [37] Z. Yang, D. Yang, C. Dyer, X. He, A. Smola, and E. Hovy, "Hierarchical attention networks for document classification," in *Proceedings of the 2016 Conference of the North American Chapter of the Association for Computational Linguistics: Human Language Technologies*, pp. 1480–1489, San Diego, California, 2016.
- [38] X. Hu, G. Li, X. Xia, D. Lo, and Z. Jin, "Deep code comment generation," in *Proceedings of the 26th Conference on Program Comprehension*, pp. 200–210, New York, NY, USA, 2018.
- [39] L. Mou, G. Li, L. Zhang, T. Wang, and Z. Jin, "Convolutional neural networks over tree structures for programming language processing, 2015," <https://arxiv.org/abs/1409.5718/>.
- [40] A. Frome, G. Corrado, J. Shlens et al., "DeViSE: a deep visual-semantic embedding model," in *Proceedings of the 26th International Conference on Neural Information Processing Systems - Volume 2*, pp. 2121–2129, Red Hook, NY, USA, 2013.
- [41] K. Jarvelin and J. Kekalainen, "Cumulated gain-based evaluation of IR techniques," *ACM Trans Inf Syst*, vol. 20, no. 4, pp. 422–446, 2002.
- [42] Y. Wang, L. Wang, Y. Li, D. He, T.-Y. Liu, and W. Chen, "A theoretical analysis of NDCG type ranking measures," *Journal of Machine Learning Research*, vol. 30, 2013.
- [43] Y. Wan, Z. Zhao, M. Yang et al., "Improving automatic source code summarization via deep reinforcement learning," in *Proceedings of the 33rd ACM/IEEE International Conference on Automated Software Engineering - ASE 2018*, pp. 397–407, Montpellier, France, 2018.

Research Article

Application of Virtual Display Technology of LCD Backlight Spectrum Optimization Algorithm Based on Linear Programming

Yuan Cui , Zhuyang Chen, Cheng Huang, and Qian Gao

School of Electric Information Engineering, Jiangsu University of Technology, Changzhou 213001, China

Correspondence should be addressed to Yuan Cui; cuiyuan@jsut.edu.cn

Received 23 March 2021; Revised 18 April 2021; Accepted 15 May 2021; Published 26 May 2021

Academic Editor: Yong Deng

Copyright © 2021 Yuan Cui et al. This is an open access article distributed under the Creative Commons Attribution License, which permits unrestricted use, distribution, and reproduction in any medium, provided the original work is properly cited.

In order to make the color of image display more realistic, optimize the use of energy, and improve the light efficiency of the module through reasonable spectral distribution, this paper proposes a backlight spectral optimization algorithm based on linear programming. With the goal of maximizing the backlight luminous efficiency, the theoretical maximum of the luminous efficiency of the backlight spectrum can be achieved by constructing a linear programming model. The research process is to obtain the optimal distribution of transmittance spectrum by linear programming method on the premise of ensuring the color gamut standard of display system. The results show that the light efficiency can be increased to 335.5 lm/W, while the original light efficiency of the system is less than 150 lm/W. With the goal of maximizing the light efficiency, light sources with narrow bandwidths such as lasers and quantum dot materials can be used to simulate and reconstruct these characteristic wavelengths. There will be easier to approach the ideal optimization spectrum and achieve the theoretical maximum luminous efficiency of 610.8 lm/W.

1. Introduction

In recent years, many display devices have been introduced. In particular, the digital flat panel display technology represented by the LCD has been rapid developed [1, 2]. For further improving the effect of the display device and enhancing the performance of the display, the color gamut, as an important indicator of the display quality, will become the focus in the research area of display. At the same time, the polarizer and color filter in the LCD panel structure have a huge impact on the luminous efficiency, which lead to the low light effect. At present, RGB color light source can remove the color filter to improve the luminous efficiency, but there are still some limitations. As the light source of the display, the spectral components contained in the backlight spectrum will directly affect the final color rendering effect. The backlight spectrum is the key to color gamut expansion as well. In this paper, a linear programming-based algorithm is proposed for optimization of the backlight spectrum. Through constructing a linear programming model, the spectrum distribution of the primary colors of

any display and the calculation of the limit value of the light efficiency can be optimized.

The rest of this paper is arranged as follows: Section 2 studies the structure of liquid crystal display and the phenomenon of metamerism; Section 3 illustrates the optimization model of the backlight spectrum; Section 4 reports the analysis of the backlight optimization model. Finally, Section 5 concludes the proposed algorithm and presents several aspects of future work.

2. Structure of Liquid Crystal Device and Phenomenon of Metamerism

Since the liquid crystal layer cannot emit the light, the traditional LCD uses a multilayer module for reconstruction of the image by modulating the backlight through diffusers, polarizers, liquid crystal layers, and filters. According to the distribution of the backlight light source, common modules can be divided into two types: edge type and direct type [3, 4]. The schematic diagram of these two structures is shown in Figure 1.

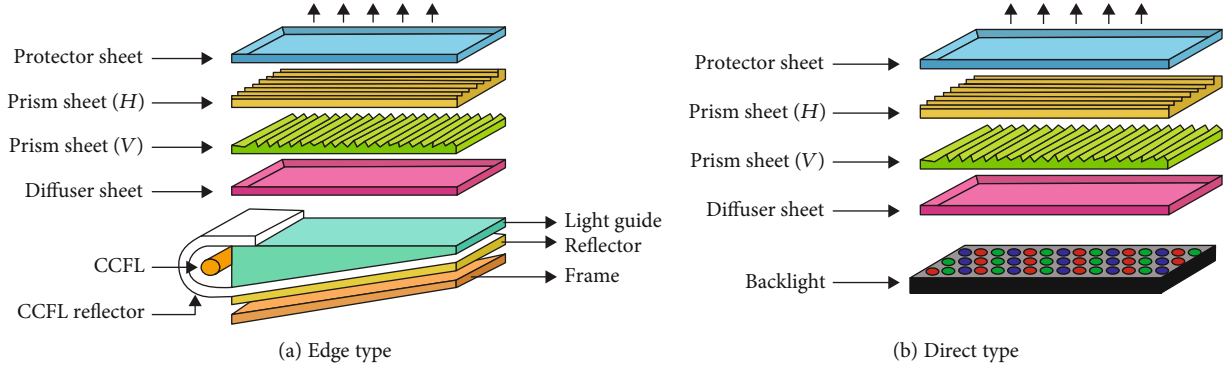


FIGURE 1: Schematic of the LCD module structure.

As for the edge type, the backlight source is placed on the side of the liquid crystal panel. The light guide plate is used for color mixing and can directly couple the light to the liquid crystal panel as the input light energy. However, in the direct type, the light emitted from the backlight is reflected by the reflector. After that, the light is dispersed upward through the diffuser. Eventually, the light can be transmitted from the front side. Taking the direct backlight structure as an example, the basic structure of the module and the transmittance level of each layer are shown in Figure 2. Compared with the direct type, the side type has a lower overall utilization rate of the light energy due to the energy loss of the light guide plate [5, 6].

Because of the multilayer structure of the module, there are only 5% of the light from the direct type module that can be emitted by the screen for forming the final image. This means that the utilization rate of light energy in the LCD system is rather low. To ensure the quality of the reconstructed image, most of the light is absorbed or uniformed by various materials during the layer-by-layer modulation. This phenomenon not only exacerbates the heating problem of the display but also increases the power consumption of the device. Generally, the luminous efficiency (lm/W) is used as an index to measure the electro-optical conversion efficiency of the light source. The luminous efficiency can be calculated as follows:

$$\eta = \frac{k \int_{380}^{780} \Phi(\lambda) V(\lambda) d\lambda}{\int_{380}^{780} \Phi(\lambda) d\lambda}. \quad (1)$$

In which, the coefficient k represents the maximum optical efficiency, i.e., 683 lm/W, which is also the luminous efficiency value when human watches the yellow-green light (555 nm). $\Phi(\lambda)$ is the radiance spectral energy distribution of the light source. $V(\lambda)$ is the light efficiency function of human eyes' optical spectrum. In the LCD system, whether it is a traditional CCFL backlight or a new LED backlight, the luminous efficiency of the device does not exceed 150 lm/W, and the luminous efficiency of the whole system does not exceed 10 lm/W.

The light emitted from the backlight of the flat panel display system is filtered by the module. Under the CIE-1931

XYZ color space, the color is calibrated by its color coordinates (x, y) . Equation (2) for calibration is given as follows:

$$\begin{cases} X = \int_{380}^{780} \Phi(\lambda) \bar{x}(\lambda) d\lambda, \\ Y = \int_{380}^{780} \Phi(\lambda) \bar{y}(\lambda) d\lambda, \\ Z = \int_{380}^{780} \Phi(\lambda) \bar{z}(\lambda) d\lambda, \\ x = \frac{X}{X + Y + Z}, \\ y = \frac{Y}{X + Y + Z}. \end{cases} \quad (2)$$

In which, X , Y , and Z represent the tristimulus values of the red, green, and blue channels, respectively. $\Phi(\lambda)$ is the spectral distribution of the color. $\bar{x}(\lambda)$, $\bar{y}(\lambda)$, and $\bar{z}(\lambda)$ are the standard observations of X , Y , and Z .

Deduced from the integral calculation of the color coordinates, there are infinite possibilities for the color light spectrum distribution that meets the color coordinates. Theoretically, if the color coordinates (x, y) are the same and have the same brightness, the human eyes cannot distinguish them and will judge these colors as the same color. This phenomenon is also elaborated by Glassman's law [7–9]. In fact, whether in daily life or the industrial production, most of the colors are metameres [10, 11]. This phenomenon is much more common, especially in the industries such as printing, dyes, and painting. Since the actual color perception of the human eye is directly related to the tristimulus value instead of the spectral composition, the optimization of many light sources and spectral analysis can be achieved by using the metamerism. For instance, the metamerism can be used for improving the color accuracy of the multiprimary color display systems [12]. Wyszecki et al. proposed the concept of metamerism black to decompose the spectral reflectance of objects [13]. Cohen et al. proposed an R matrix mathematical model for spectral reconstruction calculations [14, 15]. Similarly, metamerism also provides the possibility to optimize the backlight of liquid crystal displays.

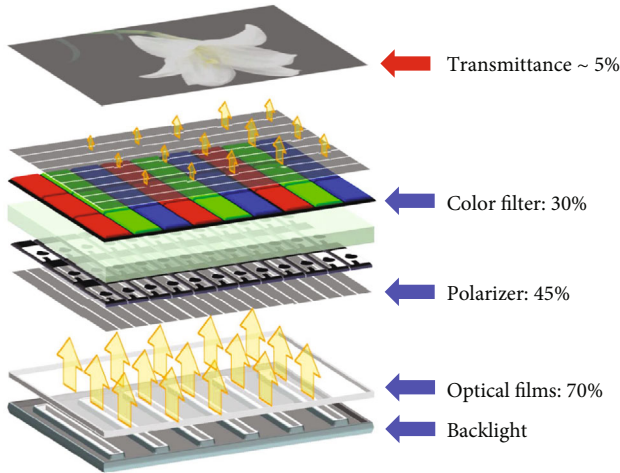


FIGURE 2: Structure of the LCD backlight module and the transmittance of each layer.

The energy consumption of displays is used as another important indicator. In the optimization, the light efficiency of the display is used as a reference indicator to measure the quality of the backlight spectrum, and the high luminous efficiency light source is of great significance for the display. Normally, the power consumption of the general liquid crystal display (LCD) backlight accounts for most of the entire power consumption. Backlight modulation can also be used to improve the luminous efficiency of LCD module, such as flicker backlight technology and scanning backlight technology. Flicker backlight is to make the backlight glow only for a certain period in a frame instead of continuously illuminated. This method can reduce energy consumption but may lead to a decrease in the overall image brightness, which makes the brightness output of the backlight more demanding. Based on the flickering of the backlight, scanning backlight adds the process of controlling the phase of the backlight; that is, lighting up and closing the backlight at the phase when the LCD pixel are completely on and completely off. The advantage of backlight scanning is that the light energy utilization of the backlight is high and can obviously improve the phenomenon of LCD image motion blur, but in order to achieve a constant background light brightness, it is necessary to improve the brightness of the scanned background light. Therefore, the reduction of the power consumption caused by the backlight source is crucial. The utilization of LCDs with higher light efficiency in portable devices can improve the endurance of the device under the same battery capacity which can enhance the practicability and competitiveness of the product.

Besides, the spectral optimization of the display backlight source is also applicable to the field of lighting. In recent years, with the development of cities, the fossil energy has become increasingly tense. The prices of the conventional energy, such as oil and coal, have continued to rise. In particular, international oil prices have reached to the peak leading to an increasingly severe energy supply situation. The sustainable development and utilization of energy has attracted more and more attention. Lighting is one of the main areas

where humans consume energy. Therefore, it is of great significance to achieve energy saving in the lighting field [16]. For alleviating the ever-increasing energy crisis, the “green lighting concept” has been proposed internationally in the early 1990s. The Energy Independence and Security Act of 2007 (EISA2007) signed by the United States specifically requires the inclusion of the “Next Generation Lighting Initiative” (NGLI) [17]. Currently, European and American markets generally adopt the Energy Star (ES) indicator jointly promoted by the US Department of Energy and the US Environmental Protection Agency [18], China, also began to implement the promotion of “green lighting projects” in 1996 [19, 20]. An important step to realize this plan is to develop and promote efficient and energy-saving lighting fixtures. Saving the electricity for lighting, reducing the lighting pollution, and establishing a high-quality, efficient, economical, comfortable, safe, and reliable lighting system are beneficial to the whole system. The high-efficiency lighting source means that the source consumes less energy under the same light output. It is of great significance to save energy and reduce power costs.

Compared with the lighting, the color gamut range should be taken into consideration in the display system while improving the light efficiency. Otherwise, the image quality of the display will be affected due to the decrease in color saturation, which will be harmful to the final quality of the display. By using the metamerism, the simulation and optimization of the spectral distribution of the light source can be achieved with the optimal light efficiency.

3. Optimization Model of the Backlight Spectrum

The reconstruction of color images of LCD can be achieved by mixing multiple primary colors. Under the premise of ensuring the color gamut area, the light efficiency of the display should be maximized. The optimized spectrum of each primary color is the basis for the optimized spectrum of the entire backlight. Based on the passive light-emitting principle of LCD, the light of the display received by the viewer is the backlight by passing through the liquid crystal layer and the filter. The absorption of other optical film layers such as polarizers can be treated as a fixed value. In order to achieve a real simulation effect, the spectral distribution of the backlight, $\Phi_{BL}(\lambda)$, the transmittance line distribution of the filter, $T_{CF}(\lambda)$, and the transmittance distribution of the liquid crystal, $T_{LC}(\lambda)$, should be set as unknown parameters. Since these three parameters are unknown, solving the function directly can be very difficult [21]. In order to simplify the process, the optimization of the process can be divided into three steps. Step one is the spectrum optimization of the primary color light. Step two is the spectral synthesis of the display optimization backlight; the final step is the spectral distribution of the color filter transmittance. During the process, the optimized result in each step can be the basis of the next calculation. In the first step of optimization, the transmittance spectrum of the color filter and the liquid crystal can be set as an ideal state, i.e., 100%. Following these three steps, the optimized spectral distribution of the backlight

and the corresponding distribution of the filter and the transmittance spectral of the liquid crystal can be obtained.

3.1. Spectral Optimization of Primary Colors. The spectrum optimization of the primary colors is the basis of the display backlight optimization. As for displays that comply with a specific color gamut standard, the color coordinates of each primary color have been determined. Each color coordinate of the primary color is different and vary with each other. Optimizing a certain primary color is equal to optimize the color light spectrum distribution of any known color coordinate. The calculation of color coordinates and light effects can refer to equation (1) and equation (2). $\bar{w}(\lambda)$ is the white spectrum curve value. $\Phi(\lambda)$ is the spectral distribution of the color. $\bar{x}(\lambda)$, $\bar{y}(\lambda)$, and $\bar{z}(\lambda)$ are the standard observations of X and Y . According to the principle of metamerism, there are countless chromatic light spectrum distribution, $\Phi(\lambda)$, that satisfy the given color coordinate theoretically. With the goal of maximizing the light efficiency, finding one or more optimized distributions among countless kinds of spectral distributions and improving light efficiency while satisfying the color perception are the task of optimization of primary colors. Using the chromaticity formula, the problem can be transformed into the following mathematical model. Assuming that the function $\Phi(\lambda)$ satisfies the following equations, we should find $\Phi(\lambda)$ when η reaches to the maximum.

$$\begin{cases} \bar{w}(\lambda) = \bar{x}(\lambda) + \bar{y}(\lambda) + \bar{z}(\lambda), \\ \int_{380}^{780} \Phi(\lambda)[x\bar{w}(\lambda) - \bar{x}(\lambda)]d\lambda = 0, \\ \int_{380}^{780} \Phi(\lambda)[y\bar{w}(\lambda) - \bar{y}(\lambda)]d\lambda = 0, \end{cases} \quad (3)$$

$$\eta = \frac{k \int_{380}^{780} \Phi(\lambda)\bar{y}(\lambda)d\lambda}{\int_{380}^{780} \Phi(\lambda)d\lambda}. \quad (4)$$

The solution of equation (3) is in the form of a function distribution, which is a functional problem. The tristimulus values, $x(\lambda)$, $y(\lambda)$, and $z(\lambda)$, are subjective experimental statistical results. There is no recognized analytical formula corresponding to it. In order to simplify the solution process and reduce the difficulty of the solution, the idea of function discretization is used to reconstruct all the function distributions into discrete functions. The integral operation is converted to accumulation operation [22, 23]. Eventually, the problem can be transmitted into a discrete function for a nonlinear programming model. Assuming that the discrete function $\Phi(\lambda)$ satisfies the following equations, we should find $\Phi(\lambda)$ when η reaches to the maximum.

$$\begin{cases} \bar{w}(\lambda) = \bar{x}(\lambda) + \bar{y}(\lambda) + \bar{z}(\lambda), \\ \sum_{\lambda=380\text{nm}}^{780\text{nm}} \Phi(\lambda)[x\bar{w}(\lambda) - \bar{x}(\lambda)] = 0, \\ \sum_{\lambda=380\text{nm}}^{780\text{nm}} \Phi(\lambda)[y\bar{w}(\lambda) - \bar{y}(\lambda)] = 0, \end{cases} \quad (5)$$

$$\eta = \frac{k \sum_{\lambda=380\text{nm}}^{780\text{nm}} \Phi(\lambda)\bar{y}(\lambda)}{\sum_{\lambda=380\text{nm}}^{780\text{nm}} \Phi(\lambda)}. \quad (6)$$

The discrete functions involved in which all have the same sampling rate. Taking into consideration of the calculation accuracy and time, the sampling interval is set as 1 nm in this paper. In addition, due to the physical meaning of the function, the value of each wavelength in $\Phi(\lambda)$ is the intensity of the energy distribution. Therefore, the value of $\Phi(\lambda)$ is non-negative, i.e., $\Phi(\lambda) \geq 0$, ($380 \text{ nm} \leq \lambda \leq 780 \text{ nm}$). Eventually, the nonlinear programming problem takes equation (6) as the objective function, which contains 401 unknown parameters, 2 equality constraints, and 401 inequality constraints.

The nonlinear programming problem is solved by substituting the corresponding constraints and objective functions. After normalization, the solution is the optimal relative spectral power distribution of any color light. In the solving process, it is necessary to substitute the spectral distribution data for satisfying the color coordinates as the initial value. If the initial value is unknown, the approximate color coordinates can be substituted into the calculation. However, the value calculated by the first optimization may not be the best result. The first optimization result can be used as an initial value and then substituted into the mathematical tool for the next round of calculation. The result after two iterations will converge to the final optimal result. The final result maximizes the light efficiency under the premise that the color coordinate is unchanged. Figure 3 shows the optimized results of a certain white light (color coordinates (0.271, 0.234)). Before the optimization, the theoretical luminous efficiency of the original spectral distribution of the illuminator is 237.6 lm/W. After the optimization, the theoretical luminous efficiency is increased to 321.8 lm/W.

Through the optimization, the spectral distribution of the color light represented by any point other than the edge in the tongue diagram of the color gamut in the CIE-1931 XYZ color space can be optimized [24, 25]. Figure 4 shows the optimized contour distribution of the tongue diagram with the maximum light effect. The optimizable range covers the entire tongue-shaped chart color gamut, which provides a basis for the spectrum optimization of the primary colors and the backlight of the display.

3.2. Synthesis of Backlight Spectrum. As for traditional displays, the standard of the color gamut provides four sets of color coordinates for the four primary colors, i.e., red, green, blue, and white field. For example, in the NTSC standard (National Television Standards Committee, American Standard Television Broadcast Transmission and Reception Protocol), the color coordinates of red, green, blue, and white are specified as $(x_r, y_r) = (0.67, 0.33)$, $(x_g, y_g) = (0.21, 0.71)$, $(x_b, y_b) = (0.14, 0.08)$, and $(x_w, y_w) = (0.31, 0.316)$. Briefly, the standard color coordinates of each primary color should be calculated. Then, the aforementioned steps can be used to construct an equivalent nonlinear programming problem. After that, the constructed nonlinear programming problem can be solved. Eventually, the optimal spectral distribution of the light efficiency of each primary color can be obtained. Taking the NTSC standard as an example, the optimized

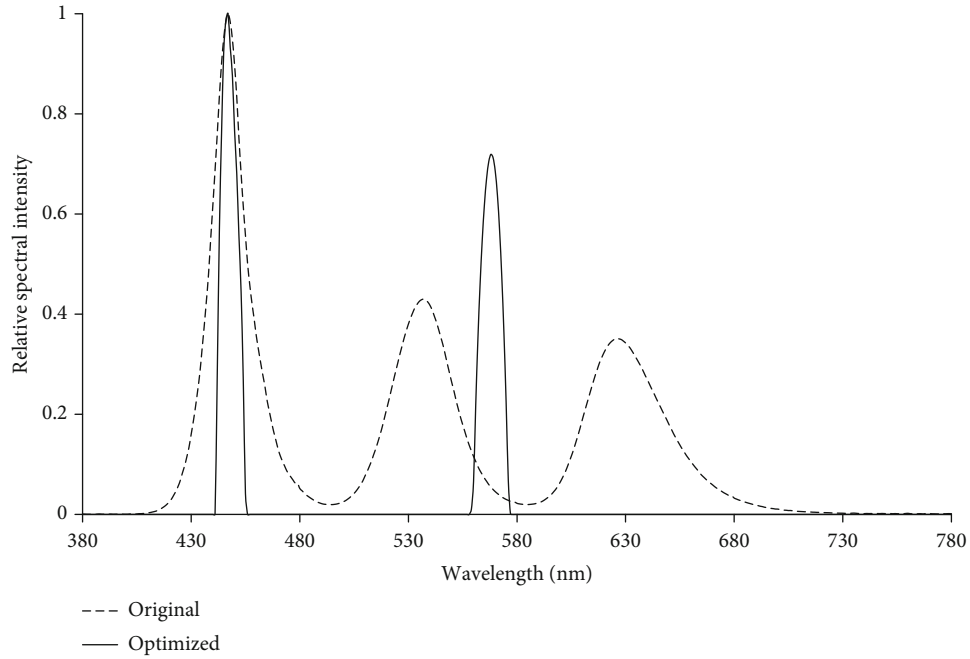


FIGURE 3: The optimized spectral distribution of the white light with color coordinate of (0.271, 0.234).

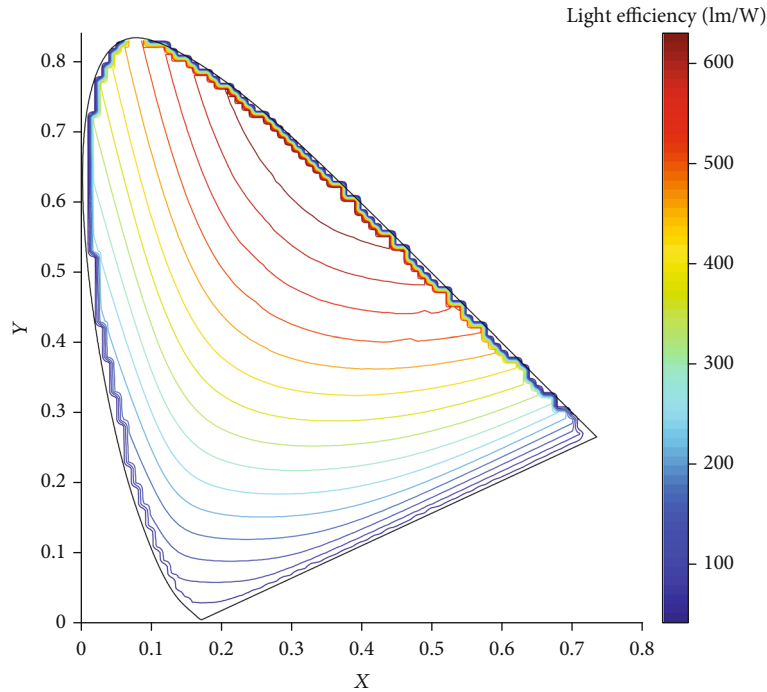


FIGURE 4: The contour map of the maximum light efficiency.

spectral distributions of the three primary colors, i.e., $\Phi_r(\lambda)$, $\Phi_g(\lambda)$, and $\Phi_b(\lambda)$, are shown in Figure 5. The theoretical light effects of the three primary colors after the optimization are 330.8 lm/W, 612.9 lm/W, and 101.9 lm/W, respectively.

Since the color coordinates of the white field are also specified in the color gamut standard, the relative intensity of each primary color spectrum needs to be calculated after

obtaining the optimized spectrum of each primary color. To tackle this issue, the synthesized white should be exactly equal to the color coordinates of the white field when the primary colors reach the maximum. Meanwhile, the light intensity of each primary color should be used to maximize the total brightness in the white field. The gain coefficients of the three primary colors of red, green, and blue channels

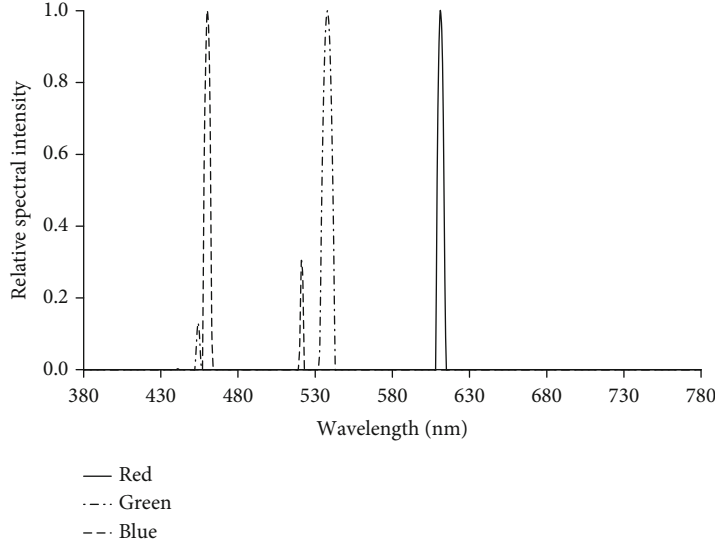


FIGURE 5: The optimized spectral distribution of the red, green, and blue channel under the standard of NTSC.

can be set as n_r , n_g , and n_b . In order to ensure the white field color coordinates, the intensity coefficient should satisfy the following equations:

$$\begin{cases} [y_g y_b Y_r (x_r - x_w)] n_r + [y_r y_b Y_g (x_g - x_w)] n_g + [y_r y_g Y_b (x_b - x_w)] n_b = 0, \\ [y_g y_b Y_r (y_r - y_w)] n_r + [y_r y_b Y_g (y_g - y_w)] n_g + [y_r y_g Y_b (y_b - y_w)] n_b = 0. \end{cases} \quad (7)$$

In which, Y_r , Y_g , and Y_b represent the luminous flux of the three primary colors in the optimal spectral distribution of light efficiency, respectively. The expression of these three parameters is given as follows:

$$\begin{cases} Y_r = \sum_{\lambda=380\text{nm}}^{780\text{nm}} \Phi_r(\lambda) \bar{y}(\lambda) \Delta\lambda, \\ Y_g = \sum_{\lambda=380\text{nm}}^{780\text{nm}} \Phi_g(\lambda) \bar{y}(\lambda) \Delta\lambda, \\ Y_b = \sum_{\lambda=380\text{nm}}^{780\text{nm}} \Phi_b(\lambda) \bar{y}(\lambda) \Delta\lambda. \end{cases} \quad (8)$$

In which, $\Delta\lambda = 1 \text{ nm}$. The total luminous flux, Y_w , of the white field of the display is expressed as the sum of the luminous fluxes of the three primary colors:

$$Y_w = n_r Y_r + n_g Y_g + n_b Y_b. \quad (9)$$

On the premise that the color temperature of the white field does not deviate and in order to maximize the brightness of the white field, equation (7) can be set as the constraint condition, and equation (9) can be set as the objective function. In order to maximum the solution of equation (9), a linear programming problem can be proposed for solving the gain strength of each primary color. It should be

noted that each gain coefficient is nonnegative, i.e., $n_r \geq 0$, $n_g \geq 0$, and $n_b \geq 0$. Besides, the final constructed linear programming problem contains three unknown parameters, two equality constraints, and three inequality constraints. By using some calculation tools, n_r , n_g , and n_b can be solved. Taking the NTSC standard as an example, the brightness of the white field formed by the combination should be the largest when the white field color coordinates are (0.31, 0.316), $n_r = 0.8875$, $n_g = 0.5742$, and $n_b = 1.0000$.

After obtaining the spectral intensity gain coefficients of each primary color, the optimized spectra of all primary colors are combined into the display backlight spectrum according to the coefficient ratio. Due to the passive light emitting principle of liquid crystal displays, the backlight of the display should pass through filters for selecting the specific wavelength. Therefore, the final backlight spectrum value at a certain wavelength is the maximum value of the optimized spectrum of all primary colors at that point. The final optimized backlight spectrum $BL(\lambda)$ is given as follows:

$$BL(\lambda) = \max_{380\text{nm} \leq \lambda \leq 780\text{nm}} (n_r \Phi_r(\lambda), n_g \Phi_g(\lambda), n_b \Phi_b(\lambda)). \quad (10)$$

In which, the optimized backlight spectrum distribution synthesized by the NTSC standard is shown in Figure 6. The theoretical light efficiency of the optimized backlight spectrum is 335.5 lm/W.

3.3. Spectral Optimization of the Transmittance of the Filter. Due to the passive light emitting principle of the LCD, the backlight of the display should be selected by passing through filters. A large amount of backlight energy is absorbed by the filter layer causing a low lighting efficiency. Based on the aforementioned principle, the optimization of the transmittance distribution of the filter can also be achieved by constructing a linear programming problem [26, 27]. Assuming that the spectral distribution of the display backlight is $BL(\lambda)$, the transmittance distribution functions of the red, green,

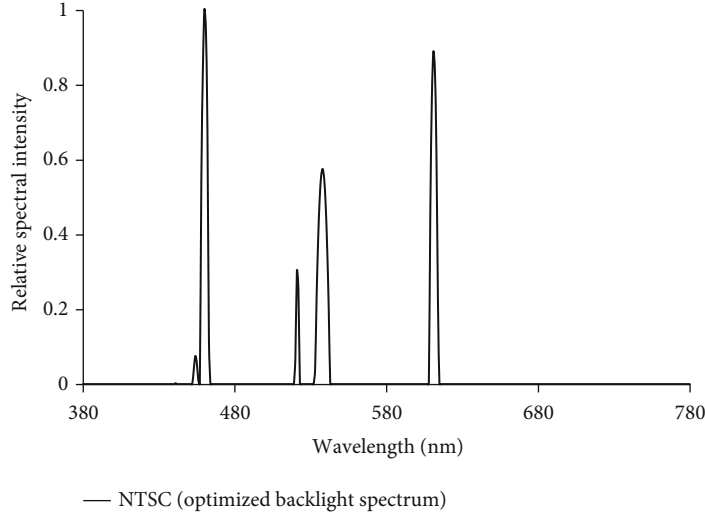


FIGURE 6: The optimized spectral distribution of the backlight under the standard of NTSC.

and blue filters are $CF_r(\lambda)$, $CF_g(\lambda)$, and $CF_b(\lambda)$, respectively. According to the provision of the color gamut standard, the final color coordinate calculation of the primary color light received by the human eyes meets equation (11) as follows:

$$\bar{w}(\lambda) = \bar{x}(\lambda) + \bar{y}(\lambda) + \bar{z}(\lambda), CF_w(\lambda) = CF_r(\lambda) + CF_g(\lambda) + CF_b(\lambda),$$

$$\left\{ \begin{array}{l} x_r = \frac{\sum_{\lambda=380nm}^{780nm} BL(\lambda)CF_r(\lambda)\bar{x}(\lambda)}{\sum_{\lambda=380nm}^{780nm} BL(\lambda)CF_r(\lambda)\bar{w}(\lambda)}, y_r = \frac{\sum_{\lambda=380nm}^{780nm} BL(\lambda)CF_r(\lambda)\bar{y}(\lambda)}{\sum_{\lambda=380nm}^{780nm} BL(\lambda)CF_r(\lambda)\bar{w}(\lambda)}, \\ x_g = \frac{\sum_{\lambda=380nm}^{780nm} BL(\lambda)CF_g(\lambda)\bar{x}(\lambda)}{\sum_{\lambda=380nm}^{780nm} BL(\lambda)CF_g(\lambda)\bar{w}(\lambda)}, y_g = \frac{\sum_{\lambda=380nm}^{780nm} BL(\lambda)CF_g(\lambda)\bar{y}(\lambda)}{\sum_{\lambda=380nm}^{780nm} BL(\lambda)CF_g(\lambda)\bar{w}(\lambda)}, \\ x_b = \frac{\sum_{\lambda=380nm}^{780nm} BL(\lambda)CF_b(\lambda)\bar{x}(\lambda)}{\sum_{\lambda=380nm}^{780nm} BL(\lambda)CF_b(\lambda)\bar{w}(\lambda)}, y_b = \frac{\sum_{\lambda=380nm}^{780nm} BL(\lambda)CF_b(\lambda)\bar{y}(\lambda)}{\sum_{\lambda=380nm}^{780nm} BL(\lambda)CF_b(\lambda)\bar{w}(\lambda)}, \\ x_w = \frac{\sum_{\lambda=380nm}^{780nm} BL(\lambda)CF_w(\lambda)\bar{x}(\lambda)}{\sum_{\lambda=380nm}^{780nm} BL(\lambda)CF_w(\lambda)\bar{w}(\lambda)}, y_w = \frac{\sum_{\lambda=380nm}^{780nm} BL(\lambda)CF_w(\lambda)\bar{y}(\lambda)}{\sum_{\lambda=380nm}^{780nm} BL(\lambda)CF_w(\lambda)\bar{w}(\lambda)}. \end{array} \right. \quad (11)$$

Since the backlight is determined, the difference in the transmittance spectrum of the filter will directly determine the luminous efficiency of the display. Therefore, the optimization of the luminous efficiency is equal to the maximization

of the luminous flux. The luminous flux of the brightness of the white field, i.e., Y , can be calculated as follows:

$$Y = \sum_{\lambda=380nm}^{780nm} BL(\lambda)CF_w(\lambda)\bar{y}(\lambda). \quad (12)$$

Since there are three independent spectral distributions, each solution contains 401 unknown parameters, if the sampling interval is set as 1 nm. In order to simplify the problem, the three functions can be combined into one function, and this function can be solved by some mathematical tools. The synthesis process is to connect the transmittance distribution functions of the red, green, and blue filters in sequence to form a discrete function, i.e., $CF_{all}(m)$, containing 1203 elements. The synthesis equation (13) is given as follows:

$$CF_{all}(m) = [CF_r(380), \dots, CF_r(780), CF_g(380), \dots, CF_g(780), CF_b(380), \dots, CF_b(780)]. \quad (13)$$

Taking equation (13) as the function to be solved, equation (11) and equation (12) can be transmitted into:

$$A = \begin{bmatrix} BL(380)(\bar{x}(380) - x_r\bar{w}(380)) & \dots & BL(780)(\bar{x}(780) - x_r\bar{w}(780)) & 0 & \dots & 0 & 0 & \dots & 0 \\ BL(380)(\bar{y}(380) - y_r\bar{w}(380)) & \dots & BL(780)(\bar{y}(780) - y_r\bar{w}(780)) & 0 & \dots & 0 & 0 & \dots & 0 \\ 0 & \dots & 0 & BL(380)(\bar{x}(380) - x_g\bar{w}(380)) & \dots & BL(780)(\bar{x}(780) - x_g\bar{w}(780)) & 0 & \dots & 0 \\ 0 & \dots & 0 & BL(380)(\bar{y}(380) - y_g\bar{w}(380)) & \dots & BL(780)(\bar{y}(780) - y_g\bar{w}(780)) & 0 & \dots & 0 \\ 0 & \dots & 0 & 0 & \dots & 0 & BL(380)(\bar{x}(380) - x_b\bar{w}(380)) & \dots & BL(780)(\bar{x}(780) - x_b\bar{w}(780)) \\ 0 & \dots & 0 & 0 & \dots & 0 & BL(380)(\bar{y}(380) - y_b\bar{w}(380)) & \dots & BL(780)(\bar{y}(780) - y_b\bar{w}(780)) \\ BL(380)(\bar{x}(380) - x_w\bar{w}(380)) & \dots & BL(780)(\bar{x}(780) - x_w\bar{w}(780)) & BL(380)(\bar{x}(380) - x_w\bar{w}(380)) & \dots & BL(780)(\bar{x}(780) - x_w\bar{w}(780)) & BL(380)(\bar{x}(380) - x_w\bar{w}(380)) & \dots & BL(780)(\bar{x}(780) - x_w\bar{w}(780)) \\ BL(380)(\bar{y}(380) - y_w\bar{w}(380)) & \dots & BL(780)(\bar{y}(780) - y_w\bar{w}(780)) & BL(380)(\bar{y}(380) - y_w\bar{w}(380)) & \dots & BL(780)(\bar{y}(780) - y_w\bar{w}(780)) & BL(380)(\bar{y}(380) - y_w\bar{w}(380)) & \dots & BL(780)(\bar{y}(780) - y_w\bar{w}(780)) \end{bmatrix}, A \cdot \begin{bmatrix} CF_{all}(1) \\ \dots \\ CF_{all}(1203) \end{bmatrix} = \begin{bmatrix} 0 \\ \dots \\ 0 \end{bmatrix},$$

$$Y = k[BL(380)\bar{y}(380), \dots, BL(780)\bar{y}(780), BL(380)\bar{y}(380), \dots, BL(780)\bar{y}(780), BL(380)\bar{y}(380), \dots, BL(780)\bar{y}(780)] \cdot CF_{all}(m). \quad (14)$$

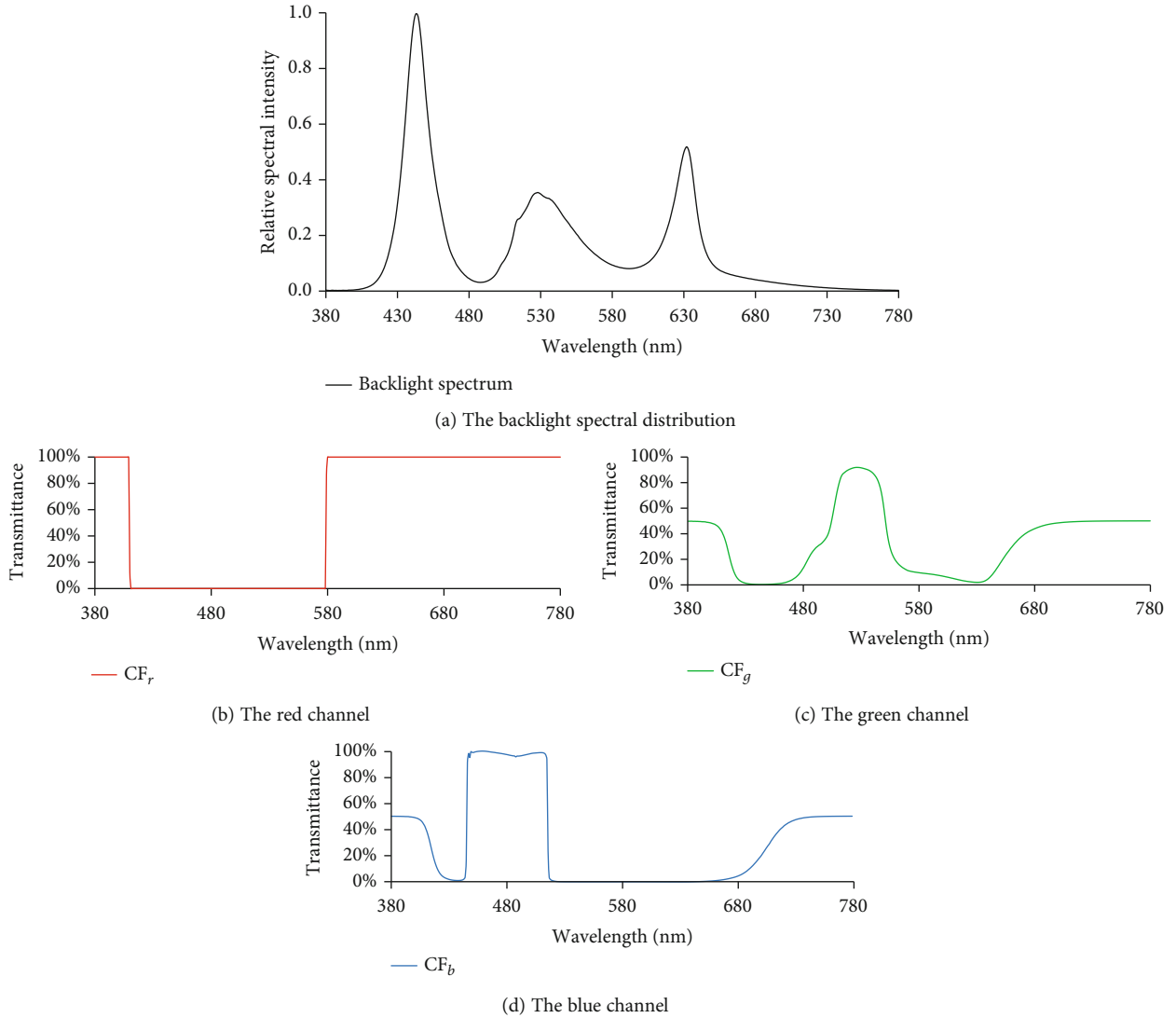


FIGURE 7: The optimization results of transmission spectrum line of the three primary color filter.

In addition, the value of the function $CF_{all}(m)$ is the transmittance of the material, which should fall in the interval $(0, 1)$, i.e., $1 \geq CF_{all}(m) \geq 0$ ($1 \leq m \leq 1023$). Finally, the linear programming problem contains 1203 unknown parameters, 8 equality constraints, and 2406 inequality constraints. The optimized distribution of $CF_{all}(m)$ can be solved. The first to 401th values, the 402th to 802th values, and the 803th to 1203th values of the solution correspond to the red filter, green filter, and blue filter, respectively. By combining these three sets of transmittance spectral distribution and the known backlight, the color coordinates of the three primary colors of the red, green, blue, and white field are all the same, and the light efficiency reaches the maximum.

Through the proposed method, the transmittance optimization spectral distribution of any known backlight of the three primary color filters can be solved. Taking the spectral distribution shown in Figure 7(a) as an example, using NTSC color gamut standard, the abscissa is taken as the

wavelength length, and the ordinate is taken as the relative spectral intensity to calculate the relative intensity of RGB tri-color at the corresponding wavelength. Finally, the transmission spectrum line of the three primary color filters is optimized, and the results are shown in Figures 7(b)–7(d). The final light efficiency is 197.1 lm/W.

If the backlight spectrum is the result shown in Figure 6, the corresponding optimized transmittance distribution of the filter can also be obtained. The result is shown in Figures 8(a)–8(c).

Since the energy of the optimized backlight spectrum shown in Figure 6 is concentrated in some narrow bandwidths, the energy of the backlight can be retained to the maximum if the transmittance of the color filter at the corresponding wavelength is in a high-pass state. The light efficiency of the overall module can reach to the theoretical limit value of 335.5 lm/W. Compared with the common backlight, the loss of the light energy caused by the filter is smaller and easier to achieve.

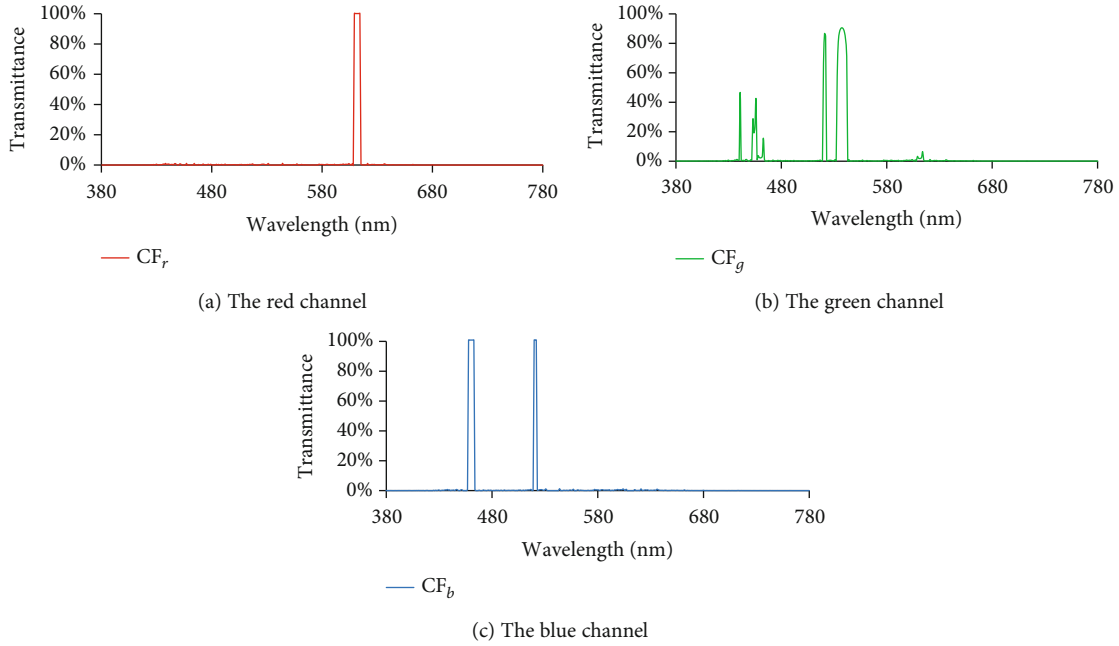


FIGURE 8: The result of filter transmittance lines for optimizing backlight spectrum.

4. Analysis of the Backlight Optimization Model

According to the metamerism in colorimetry, the optimization of any color light spectrum and the LCD backlight spectrum can be achieved by constructing linear programming equations. However, from the simulation results, the spectrum with the theoretical maximum light effect has the characteristic of pulsed distribution. Since the liquid crystal displays is commonly used in the traditional LCD backlight source, the spectrum is difficult to approach the theoretical limit in practical applications. Then, the characteristics of the optimal spectral distribution of monochromatic light will be discussed. Combined with the new quantum dot backlight technology, the optimization of the spectrum in the application of improving the display backlight will also be discussed.

4.1. Characteristic of Optimization of Primary Colors. According to the aforementioned algorithm, any color light with known color coordinates can be optimized. Via the simulation of many colored lights, the distribution characteristics of the optimized spectrum of monochromatic light can be found. For a fixed color coordinate, the spectral distribution with the greatest light effect is often concentrated in two segments or a very narrow range, showing a pulse-like distribution. The power of the remaining wavelengths is zero. These wavelengths of zero value mean that they are ineffective or less effective to a given color coordinate. Therefore, the optimized backlight spectrum should avoid letting the power distribute at these wavelengths for reducing the waste of the light energy. The feature of the pulsed distribution simplifies the process of the optimized spectrum. Therefore, the wavelength and the relative intensity of the pulse can be used to determine an optimized spectrum distribution. In Figures 9(a)–9(c), the pulse wavelength and

the relative intensity of the optimized spectrum of three primary colors under the NTSC standard in Figure 5 is annotated, respectively.

It can be seen from Figure 9 that the optimized spectrum for color coordinates (0.67, 0.33) (NTSC standard red) contains a main peak at 611 nm. The optimized spectrum for color coordinates (0.21, 0.71) (NTSC standard green) contains a main peak at 538 nm and a secondary peak at 454 nm, where the intensity is 13.0% of the main peak. The color coordinate (0.14, 0.08) (NTSC standard blue) optimized spectrum contains a main peak at 460 nm and a secondary peak at 521 nm where the intensity is 30.2% of the main peak. These wavelengths of the main peaks are close to the optimization results obtained by Senfar Wen, according to the color difference statistical algorithm [28, 29].

The wavelength positions and relative intensities of the main and secondary peaks of the optimized spectra vary with the color gamut. According to the algorithm discussed above, for any given gamut standard, the characteristic peak position of each primary color can be obtained. In the actual application, the backlight spectrum should be adjusted to the corresponding main and secondary peak positions, and the relative intensity should be maintained to continuously approach the theoretically optimized spectrum. Eventually, the light efficiency of the backlight can be improved when the color gamut is unchanged.

4.2. Optimization of the Quantum Dots. As for the optimized spectrum characteristics of the pulsed distribution, the traditional broad spectrum light source is difficult to achieve. In addition to lasers, new quantum dot materials offer great possibilities for approaching the ideal spectrum. As for fitting the ideal backlight, quantum dot materials should be used to meet the wavelength of the primary and secondary peaks in

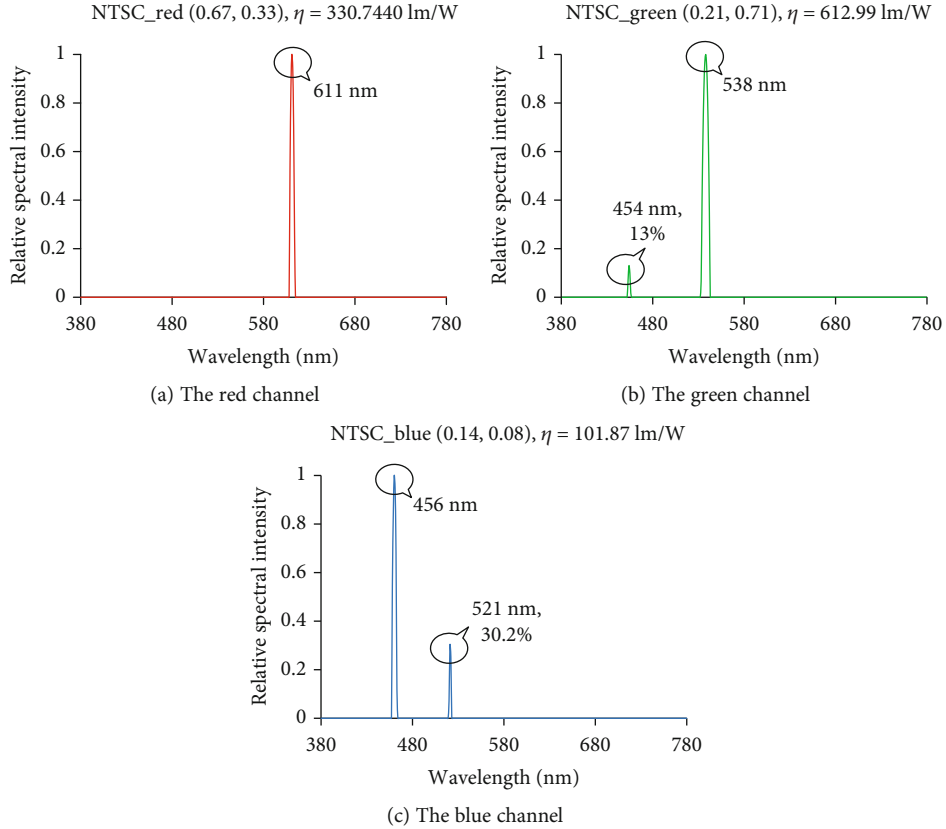


FIGURE 9: The wavelength and relative intensity of the optimized spectral distribution of the NTSC standard.

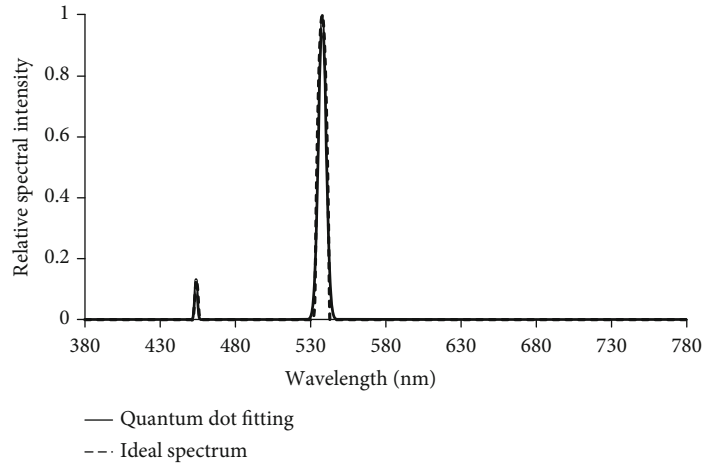


FIGURE 10: The simulation spectrum of the quantum dot backlight.

the optimized spectrum. The relative intensity of each primary color can be controlled by changing the concentration of the quantum dot materials. However, even for quantum dot materials, the spectrum is not strictly in the pulse distribution. In the mathematical model, Gaussian distribution can be used to simulate the spectrum [30, 31]. Equation (15) is given as follows:

$$\Phi_{\text{QD}}(\lambda) = e^{-\ln 2((\lambda-\lambda_p)/d)^2}. \quad (15)$$

In which, λ_p represents the center wavelength of the quantum dot spectrum, and d represents the half-wave width. In order to study the approximation degree of fitting and optimizing backlight by using quantum dot materials, under the NTSC green standard, the simulation results is shown in Figure 10.

The results show that the position and relative intensity of the main and secondary peaks are consistent with the ideal spectrum. The half-wave width of the main peak is 3 nm, and the secondary peak is 1 nm. The actual color coordinates of

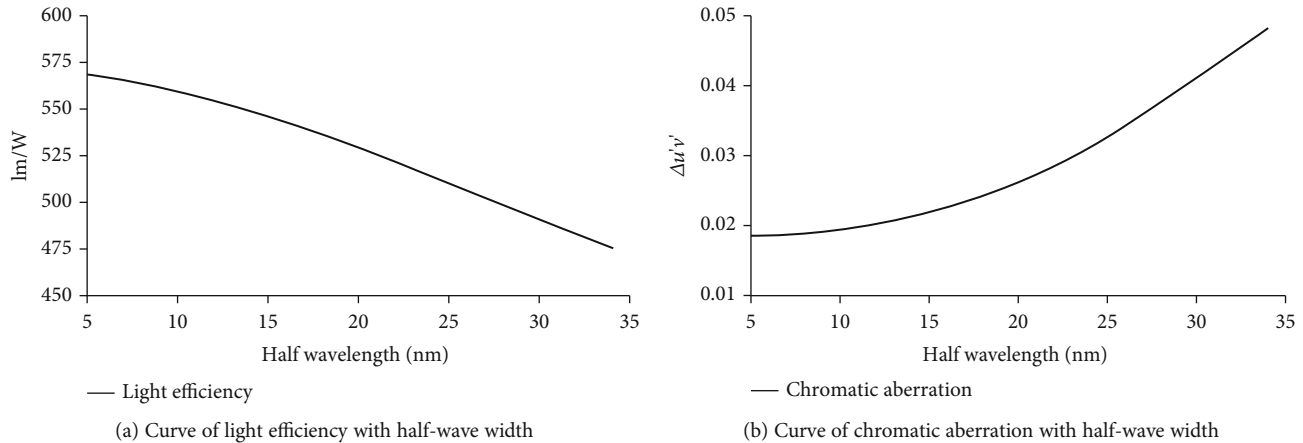


FIGURE 11: The curves of luminous efficiency and chromatic aberration with half-wave width, respectively.

the simulated waveform are (0.21, 0.71), and the luminous efficiency is 610.8 lm/W. The simulated waveform almost coincides with the ideal waveform. The luminous efficiency is improved on the premise that the green color coordinate remains unchanged, showing the importance of the position of the main peak of the spectrum. However, the half-wave width of the actual quantum dot material is wider than the simulation one. The excessively wide spectral distribution will not only generate unnecessary energy consumption but also affect the reproduction of the target color. Figures 11(a) and 11(b) show the variation curves of the luminous efficiency and the chromatic aberration with half-wave width, respectively. The chromatic aberration is characterized by the distance between two color coordinate points, i.e., $\Delta u'v'$, under the CIE-1976 $u'v'$ color space.

It can be seen from Figure 11 that as the half-wave width of the quantum dot material increases, the chromatic aberration of the fitted waveform continues to increase, and the light efficiency continues to decrease. In order to correct the error caused by the half-wave width, it is necessary to further adjust and optimize the primary and secondary positions of the waveform on the basis of the original waveform.

5. Conclusion and Future Work

In summary, based on the aforementioned results, using the metamerism of the human visual system, this paper proposes a linear programming-based algorithm for optimization of the backlight spectrum within the range of any given display system color gamut. On the premise of keeping the color gamut of the display system, the maximum theoretical luminous efficiency of the backlight is calculated by the proposed algorithm. The simulation results provide a design reference and characteristic standard for the future low-power display. At the same time, this paper shows that the utilization of narrow-bandwidth light sources such as lasers and quantum dot materials can make it easier to approach the maximum value of theoretical light efficiency. Besides, as the bandwidth of the nonideal backlight source increases, the positions of the primary and secondary peaks of the original optimized waveform may shift. Therefore, the next research can be

focused on optimization of the algorithm by using the specific material. In addition, it needs to be further considered that the Gaussian function spectral distribution characteristics should be combined in the spectral distribution optimization design. At the same time, by reasonably changing some parameters and constraints in the metamerism equation, targeted simulation optimization is realized, and the error is continuously reduced.

Data Availability

The data in this paper are valid and available from the corresponding author.

Conflicts of Interest

This paper does not contain any conflict of interest.

Acknowledgments

The study is supported by the National Natural Science Foundation of China (61601208) and the Industry-university-research cooperation project of Jiangsu Province (Grant No. BY2018139).

References

- [1] H. Ishino, M. Miike, T. Nakamura, T. Okamura, and I. Iwaki, "Novel wide-color-gamut LED backlight for 4K LCD embedded with mixing cup structure for isotropic light source," *Sid Symposium Digest of Technical Papers*, vol. 45, no. 1, pp. 241–244, 2014.
- [2] M. Xu, C. Li, Z. Chen, Z. Wang, and Z. Guan, "Assessing visual quality of omnidirectional videos," *IEEE Transactions on Circuits and Systems for Video Technology*, vol. 29, no. 12, pp. 3516–3530, 2019.
- [3] M. Anandan, "Progress of LED backlights for LCDs," *Journal of the Society for Information Display*, vol. 16, no. 2, pp. 287–310, 2008.
- [4] B. Zhang, "Analysis of LCD backlight module and its components," *Display Device Technology*, vol. 1, no. 3, pp. 22–27, 2009.

- [5] D. Ye, *Research on LCD Display Characteristics Based on the LED Backlight*, Southeast University, 2011.
- [6] Y. Sun, C. Xu, G. Li et al., "Intelligent human computer interaction based on non redundant EMG signal," *Alexandria Engineering Journal*, vol. 59, no. 3, pp. 1149–1157, 2020.
- [7] P. Vandersteegen, G. Schwartz, P. Bienstman, and R. Baets, "Luminous power efficiency optimization of a white organic light-emitting diode by tuning its spectrum and its extraction efficiency," *Applied Optics*, vol. 47, no. 11, pp. 1947–1955, 2008.
- [8] J. J. Wang, N. F. Liao, W. M. Wu, B. Cao, Y. S. Li, and H. B. Cheng, "Spectral reflectance reconstruction with nonlinear composite model of the metameric black," *Spectroscopy and Spectral Analysis*, vol. 37, no. 3, pp. 704–709, 2017.
- [9] R. Yang, M. Xu, T. Liu, Z. Wang, and Z. Guan, "Enhancing quality for HEVC compressed videos," *IEEE Transactions on Circuits and Systems for Video Technology*, vol. 29, no. 7, pp. 2039–2054, 2019.
- [10] S. Q. Tang, *Colorimetry*, Beijing Institute of Technology Press, 1990.
- [11] D. Jiang, G. Li, Y. Sun, J. Hu, J. Yun, and Y. Liu, "Manipulator grabbing position detection with information fusion of color image and depth image using deep learning," *Journal of Ambient Intelligence and Humanized Computing*, 2021.
- [12] F. Koenig, K. Ohsawa, M. Yamaguchi, N. Ohya, and B. Hill, "Multiprimary Display: Discounting Observer Metamerism," in *9th Congress of the International Colour Association*, International Society for Optics and Photonics, 2002.
- [13] G. Wyszecki, "Valenzmetrische Untersuchung des Zusammenhanges zwischen normaler und anomaler Trichromasie," *Psychophysical investigation of relationship between normal and abnormal trichromatic vision, Farbe*, vol. 2, pp. 39–52, 1953.
- [14] J. B. Cohen and W. E. Kappauf, "Metameric color stimuli, fundamental metamers, and Wyszecki's metameric blacks," *American Journal of Psychology*, vol. 95, no. 4, pp. 537–564, 1982.
- [15] J. B. Cohen and W. E. Kappauf, "Color mixture and fundamental metamers: theory, algebra, geometry, application," *American Journal of Psychology*, vol. 98, no. 2, pp. 171–259, 1985.
- [16] K. Y. Qian and Y. Luo, "Optical efficiency analysis of LED road lighting luminaires," *China Illuminating Engineering Journal*, vol. 20, no. 1, pp. 21–25, 2009.
- [17] H. P. Mo, "United States' national strategy of supporting the development of solid-state lighting and the policy suggestion for China," *China Illuminating Engineering Journal*, vol. 23, no. 4, pp. 7–17, 2012.
- [18] H. Wang, "Design of backlight for liquid crystal display energy star 6.0," *Chinese Journal of Liquid Crystals and Displays*, vol. 28, no. 4, pp. 577–581, 2013.
- [19] M. Q. Jiang, Z. Y. Xue, and W. Wu, "Research on the energy saving technology of green-lighting," *Building Technology Development*, vol. 30, no. 11, pp. 100–101, 2003.
- [20] H. J. Huang, G. Chen, and Y. B. Lv, "On green lighting planning and design of the city," *Journal of Civil, Architectural and Environmental Engineering*, vol. 27, no. 5, pp. 10–12, 2005.
- [21] L. Ding, L. Huang, S. Li et al., "Definition and application of variable resistance coefficient for wheeled mobile robots on deformable terrain," *IEEE Transactions on Robotics*, vol. 36, no. 3, pp. 894–909, 2020.
- [22] J. M. Zoido, F. Carreño, and E. Bernabeu, "Improved linear programming method to generate metameric spectral distributions," *Applied Optics*, vol. 34, no. 11, pp. 1938–1943, 1995.
- [23] F. Xiao, G. Li, D. Jiang et al., "An effective and unified method to derive the inverse kinematics formulas of general six-DOF manipulator with simple geometry," *Mechanism and Machine Theory*, vol. 159, no. 2, pp. 104–265, 2021.
- [24] D. L. Macadam, "Maximum attainable luminous efficiency of various chromaticities," *Journal of the Optical Society of America*, vol. 40, no. 2, pp. 120–120, 1950.
- [25] B. Li, Y. Liu, A. Zhang, W. Wang, and S. Wan, "A survey on blocking technology of entity resolution," *Journal of Computer Science and Technology*, vol. 4, no. 35, pp. 769–793, 2020.
- [26] C. Gong, Y. Hu, J. Gao, Y. Wang, and L. Yan, "An improved delay-suppressed sliding-mode observer for sensorless vector-controlled PMSM," *IEEE Transactions on Industrial Electronics*, vol. 67, no. 7, pp. 5913–5923, 2019.
- [27] K. Xiang, C. Xu, and J. Wang, "Understanding the relationship between tourists' consumption behavior and their consumption substitution willingness under unusual environment, psychology research and behavior," *Management*, vol. 14, pp. 483–500, 2021.
- [28] S. Wen, "Primary Design of Wide-Color-Gamut Displays for Matching the Color Gamut of Objects," in *Sid Symposium Digest of Technical Papers*, Blackwell Publishing Ltd, Oxford, UK, 2007.
- [29] J. Shi, Y. Lu, and J. Zhang, "Approximation attacks on strong PUFs," *IEEE Transactions on Computer-Aided Design of Integrated Circuits and Systems*, vol. 39, no. 10, pp. 2138–2151, 2020.
- [30] L. U. O. Zhi-hui, H. E. Jun-fang, W. A. N. G. Min-qiang, S. J. Zhang, and P. E. N. G. Yan-xiang, "Spectral property of ZnSe/SiO₂ semiconductor quantum dots glass," *Acta Photonica Sinica*, vol. 36, no. 3, pp. 471–475, 2007.
- [31] Z. Liu, L. Lang, B. Hu, L. Shi, B. Huang, and Y. Zhao, "Emission reduction decision of agricultural supply chain considering carbon tax and investment cooperation," *Journal of Cleaner Production*, vol. 294, no. 4, article 126305, 2021.